

Sunday Afternoon, October 17, 2010

Biomaterials Plenary Session
Room: Taos - Session BP-SuA

Detecting, Characterizing and Controlling Biofouling
Moderator: S.L. McArthur, Swinburne University of Technology, Australia

3:00pm **BP-SuA1 The Effect of a Polymer Brush Coating on Protein Adsorption, Bacterial Adhesion, and Biofilm Formation, W. Norde, Wageningen University, University Medical Center Groningen and University of Groningen, the Netherlands**

INVITED

Adsorption of proteins from biofluids is considered to be the first event in the biofouling process. Subsequently, micro-organisms and/or biological cells (e.g. blood platelets, erythrocytes) adhere to the surface and a biofilm may be developed. In this paper, generic principles of the interaction between a polymer brush and indwelling particles (globular proteins; micro-organisms) are explained and illustrated with some experimental results. Furthermore, the influence of a polymer brush on the development and characterization of a biofilm is discussed.

3:40pm **BP-SuA3 Biomaterials-Associated Infections – In Vitro and In Vivo Studies, H. Busscher, University Medical Center and University of Groningen, the Netherlands**

INVITED

Modern health care is greatly dependent on the use of biomaterials implants and devices for the restoration of function, after trauma, (oncological) intervention surgery or simply wear due to old age. Biomaterials implants surfaces in the human body are prone to infection, as can develop through three distinctly different routes. Peri-operative infection is the best documented route and usually causes early infection of an implant. Also immediate post-operative infection can be a cause of early failure. Late post-operative infections spreading from infections elsewhere in the body have also been described to be a cause for implant infection and failure. Since a biomaterial-associated infection (BAI) is difficult to treat with antibiotics due to the protection offered by the biofilm mode of growth and intra-cellular shelter, the fate of an infected implant often is removal, at great discomfort to the patient and costs to the healthcare system. Frequently even, the condition of a patient does not allow replacement surgery or removal of a device. BAI can be lethal when spreading through the body. Whereas the infection rate of primary implants may be considered low (4-6% on average depending on the implant type), infection rates in revision surgery are much higher around 15%.

Prevention strategies under investigation are numerous, but no generally effective way to prevent BAI has been found. Moreover, prevention of BAI of a primary implant may require different approaches than the prevention of BAI of secondary implants after treatment of BAI.

Numerous prevention strategies based on biomaterials surface modification that discourage microbial adhesion and biofilm formation have been forwarded in the literature, but none of them have clinically provided a breakthrough. The lack of a clinical breakthrough is partially due to the low incidences of BAI (though still being unacceptably high), requiring large numbers of patients to be enrolled in a study. Therefore, novel evaluation technologies are required that indicate whether new preventive strategies work under in vivo conditions.

Bioluminescence and Fluorescent Imaging are new evaluation technologies (BLI and FLI) that offer the opportunity to observe the *in vivo* course of BAI in small animals without the need to sacrifice animals at different time points after the onset of infection. BLI is highly dependent on the bacterial cell metabolism which makes BLI a strong reporter of viable bacterial presence. Fluorescent sources are generally more stable than bioluminescent ones and specifically targeted, which renders the combination of BLI and FLI a promising tool for imaging BAI.

In the concept of the race for the surface, successful implant coatings should favour tissue integration over microbial colonization. This suggests that new prevention strategies abandoning the concept of mono-functional fully non-adhesive, tissue-supporting, or immune-friendly coatings may have to be developed on the basis of multi-functional coatings better mimicking natural tissue. The efficacy of macrophages in removing adhering bacteria from a surface for instance, is much higher on cross-linked PEG coatings than on glass because bacteria do not switch on their natural defences on such highly hydrated coatings exerting only weak interaction forces, while macrophages are less immobilized for the same reasons. Polymer brush coatings, designed with an occasional RGD-group for instance, keep their non-adhesive functionality, while at the same time supporting tissue integration.

The coming decade is without becoming the decade of effective antimicrobial coatings for biomedical implants and devices. Societal pressure is huge and with the current developments of new evaluations technologies and better insights in the different functionalities with which effective coatings should be equipped, clinical breakthrough should be within reach.

4:20pm **BP-SuA5 Engineered Surface Designs for Directed Attachment on Topographies, A.B. Brennan, C.M. Magin, University of Florida, L.K. Ista, University of New Mexico, G.P. Lopez, Duke University, M.E. Callow, J.A. Finlay, J.A. Callow, University of Birmingham, UK**

INVITED

Biofouling is a technically complex issue that directly impacts our economic stability and environmental health. Recent identification of the long term negative effects of chemical antifouling compounds led to a world ban of TBT in 2008. We are investigating the impact of physical/chemical characteristics of surfaces on the attachment process. Our focus on topography led to the development of the Sharklet AFT™ pattern, which is a bio-inspired structure embossed into polymeric surfaces. The Sharklet AFT™ pattern was the first example of a physical attribute capable of strongly inhibiting the attachment of the zoospore of *Ulva* green algae and the cells of *Cobetia marina* bacteria. A model is presented for bacteria and algal zoospores, correlating attachment density with surface roughness. Our model demonstrates, for the first time, that organisms respond in a uniform manner that can be described in terms of surface energy and a Reynolds number associated with the organism.

Monday Morning, October 18, 2010

Actinides and Rare Earths Topical Conference

Room: Isleta - Session AC+SS-MoM

Surface Science of Actinides

Moderator: J.G. Tobin, Lawrence Livermore National Laboratory

9:00am **AC+SS-MoM3 High Resolution Auger Electron Spectroscopy of Plutonium Metal and Oxide Surfaces**, *D.P. Moore, A.L. Broach, D.L. Pugmire*, Los Alamos National Laboratory, *H.G. Garcia Flores*, University of Nebraska-Lincoln, *P. Roussel*, Atomic Weapons Establishment

There has been considerable new study of the oxidation of plutonium in recent years. Much of this study has focused on the properties of the thin film oxide layers that form on the plutonium metal surface under exposure to oxygen. For these studies, x-ray photoelectron spectroscopy (XPS) has typically been the technique of choice as it is ideally suited for the study of oxidation states by analyzing XP peak shape and position changes. This allows for the identification of relative changes in the Pu 4f manifold in going from Pu metal, to the Pu sesquioxide (Pu₂O₃), to the Pu dioxide (PuO₂). But there are advantages of other surface science techniques, specifically Auger electron spectroscopy (AES), over XPS for certain types of studies. Prime among them is that AES has a much higher spatial resolution than XPS allowing for analysis of specific areas and features on a surface down to a few tens of nanometers. And although AES typically suffers from less sensitivity and specificity to chemical state differences in its peak shape and position, modern Auger systems with field emission sources and hemispherical electron analyzers have alleviated much of this shortcoming.

For plutonium, Auger peaks for the metal and dioxide have been used for investigation whereas the Auger peaks for the sesquioxide have not received the same study. Peak positions from derivative spectra have been used for distinguishing between metal and oxide with quantification of the oxides from peak-to-peak heights and estimates of relative sensitivity factors. In order to more fully utilize AES for the study of the oxidation of plutonium surfaces, the relative changes in the Auger peaks in going from Pu metal to all its oxides must be quantified. We have used high resolution AES to identify the Auger peak structure of Pu metal, PuO₂, and Pu₂O₃. We have studied the OPP and OVV Auger transitions in the 80 – 110 eV range as well as the NOV transitions at approximately 315 eV via oxygen dosing on Pu metal surfaces. Oxygen doses from less than a Langmuir up to over 500 Langmuirs have been investigated. Relative changes in both the integrated and derivative Auger peak structures for Pu metal, PuO₂, and Pu₂O₃ have been identified and will be presented. Using this new information we will be able to take advantage of the higher spatial resolution of AES to further study plutonium oxide properties such as layer structure, oxidation kinetics, and auto reduction on polycrystalline plutonium samples.

9:20am **AC+SS-MoM4 The Behavior of Gallium During the Initial Stages of Plutonium/Gallium Alloy Oxidation**, *D.L. Pugmire*, Los Alamos National Laboratory, *H.G. Garcia Flores*, University of Nebraska-Lincoln, *D.P. Moore, A.L. Broach*, Los Alamos National Laboratory, *P. Roussel*, Atomic Weapons Establishment

An area of significant importance to the oxidation of any alloy is the role that the constituent metals play. It has been previously shown that the oxidation rate for the δ -phase stabilized, plutonium/gallium alloy can be significantly affected by the gallium content as well as composition of the oxidizing atmosphere (O₂, O₂/H₂O, H₂O). Reasons for the observed rate changes upon alloying with gallium are not understood. A previous study of a variety of δ -plutonium alloys shows that the significant structure difference between unalloyed α -plutonium and alloyed δ -plutonium cannot be the sole cause of different oxidation rates. This implies that the alloying metal must play some role in the slower oxidation rates observed for gallium-stabilized δ -plutonium. In order to elucidate the oxidation mechanism of this commonly employed alloy, it is important to understand the role gallium plays during oxidation. The relatively low concentrations of alloying metals used, typically several atomic percent, can make the activities of gallium during oxidation of δ -plutonium difficult to follow. This complication is compounded by the fact that the initial stages of oxidation are inherently a surface phenomenon, thereby significantly limiting the relative amount of affected material. Significant questions remain as to what is a realistic description for the Pu/Ga-oxide, thin-film system during the initial stages of oxidation.

An ultra-high vacuum (UHV) system equipped with surface sensitive techniques, such as x-ray photoelectron spectroscopy (XPS) and Auger

electron spectroscopy (AES), provides a controlled environment ideally suited to study the behavior of gallium during the initial stages of Pu/Ga oxidation. In addition to information about the oxidation states of the plutonium species in the near surface region provided by XPS, both XPS and AES are very useful for studying the relative atomic concentration of elements present at the sample surface (such as oxygen and gallium). While these surface sensitive techniques suffer from relatively high limits of detection, we have been able to qualitatively, and in some cases quantitatively, study the behavior of gallium during the oxidation of the δ -plutonium alloy. The gallium content relative to plutonium is observed to decrease within the oxide film during oxidation, with the displaced gallium apparently moving to the oxide/metal interface to form a thin gallium rich region. The results of these studies and their implications on the mechanism of gallium-stabilized, δ -plutonium oxidation will be discussed.

9:40am **AC+SS-MoM5 Angle-Resolved Photoemission and the 5f Electronic Structure of Pu Materials**, *J. Joyce, T. Durakiewicz, K.S. Graham, E.D. Bauer, J.N. Mitchell, D.P. Moore, J.A. Kennison, T.M. McCleskey, A.K. Burrell, E. Bauer, Q. Jia*, Los Alamos National Laboratory

INVITED

The electronic structure of Pu compounds ranging from Mott insulators to strongly correlated metals is investigated using angle-resolved photoemission (ARPES). The electronic properties of the Pu compounds PuCoGa₅, PuSb₂, and PuO₂ are compared with angle-integrated and temperature-dependent photoemission results for Pu metal. The balance in strongly correlated materials between the central and periodic potentials is directly probed through ARPES. For the strongly correlated metals, details of the sharp quasiparticle peak at the Fermi energy are presented, including crystal momentum dispersion, giving insight into the self-energy and ground state properties of these Pu materials. In PuSb₂, the ARPES data at a photon energy of 21.2 eV, indicates a quasiparticle peak that disperses through the Fermi energy. At 40.8 eV photon energy, PuSb₂ shows f-electron intensity periodic with the lattice. Photoemission results for the Fermi level spectral intensity as well as the more localized 5f states well-removed from the Fermi energy are used to quantify adaptive character for these materials. Both PuSb₂ and PuCoGa₅ ARPES data show a dispersive peak which crosses the Fermi energy at a photon energy of 21.2 eV where the conduction states have a larger cross section than the 5f states. The results for 40.8 eV photon energy, with enhanced 5f strength, indicate a peak dispersing through the Fermi energy for PuCoGa₅ but the PuSb₂ data indicate an intensity modulated peak near the Fermi energy. The first ARPES results for the Mott insulator PuO₂ show substantial dispersion consistent with hybrid functional calculations which predict significant covalency for PuO₂ compared with the earlier ionic actinide dioxides such as UO₂. The ARPES, photon energy dependence, and the temperature dependent data for Pu materials will be discussed in terms of 5f adaptive character and the implications for Pu ground state properties.

Work supported by the U.S. Department of Energy, Basic Energy Sciences, the Los Alamos National Laboratory LDRD program, and Campaign II.

10:40am **AC+SS-MoM8 Novel Band Renormalization Mechanism in f-electron Systems**, *T. Durakiewicz, J. Joyce*, Los Alamos National Laboratory, *P.S. Riseborough*, Temple University, *P.M. Oppeneer*, Uppsala University, Sweden, *J.-C. Griveau*, ITU, Germany, *E.D. Bauer*, Los Alamos National Laboratory, *E. Guziewicz*, Polish Academy of Sciences, Poland

Several mechanisms may lead to band renormalization in strongly correlated systems. Inter-band scattering was recently shown to produce significant renormalization effects in high temperature superconductors. Here we show, for the first time, that inter-band processes may lead to strong band renormalization in the vicinity of Fermi level in a 5f-electron system, USb₂. The Fermi surface of this compound consists of several uniaxial cylindrical sheets. We show that the bare band LDA calculation over-counts the number of sheets, because it lacks the renormalization part. But our high resolution angle resolved photoemission (ARPES) experiments demonstrate that one of the calculated cylinders shrinks below the Fermi level, forming a closed cigar-shaped Fermi surface rather than an open cylindrical one. In normal emission experiments, we measure the dispersion of the bands of interest in the Gamma-Z direction. The measured results disagree with the LDA result, but the bare LDA bands can be renormalized by using a low order self-energy expansion in three-band inter-band scattering model, and very good fit is obtained. We conclude that inter-band scattering in USb₂ influences the fermiology of this system in terms of changing the shape and number of Fermi sheets.

11:00am **AC+SS-MoM9 The Initial Oxidation of Polycrystalline Thorium**, *M. Bagge-Hansen, R.A. Outlaw, D.M. Manos*, College of William & Mary

The initial oxidation of clean, polycrystalline α -Th from background CO/CO₂ and saturation of the Th surface by O₂ has been examined in ultrahigh vacuum ($p < 2 \times 10^{-11}$ Torr, H₂) by angle resolved Auger electron spectroscopy (ARAES) and time of flight secondary ion mass spectrometry (ToF-SIMS). Following dissociative adsorption of background CO/CO₂, the accompanying oxygen surface population increased at a rate roughly one third that of the carbon, suggesting significant oxygen incorporation into the bulk. The admission of O₂ following heating and sputter cleaning of the Th, showed similar behavior in that some oxygen atoms continued to diffuse into the bulk until formation of stoichiometric ThO₂ was observed at ~ 37 L. The thickness of the oxide complex was determined by both ARAES and ToF-SIMS and found to be ~ 5 nm. The thermal stability of the ThO₂ over the temperature range of 25 – 1000°C was also studied. Rapid decomposition of the oxide by CO desorption and subsequent oxygen dissolution into the bulk was observed to occur within a temperature range of ~ 550 -750°C.

11:20am **AC+SS-MoM10 The Non-Equilibrium Nature of Uranium Oxide Surfaces**, *R.K. Schulze, D.P. Johnson, M.A. Hill*, Los Alamos National Laboratory

We examine the surface reactions of bulk single crystal uranium oxide (UO₂) and thin films of uranium oxide on metal using Kelvin probe (surface work function and chemical potential) measurements and x-ray and ultraviolet photoelectron spectroscopy. The processes of surface and sub-surface reactions with small gas phase molecules are examined through in-situ work function measurements (dynamic) while the surface chemistry and configuration are probed with photoemission and LEED measurements (equilibrium). The hyperstoichiometric uranium oxide (UO_{2+x}) is shown to be composed of, in the surface region, labile interstitial oxygen that can be moved relatively easily in and out of the fluorite structure lattice through control of the headspace oxygen activity. The transport of oxygen in this near surface region of the oxide is examined through changes in the surface work function with exposure to various partial pressures of oxygen. The amount of excess oxygen in the oxide lattice of the surface is shown to affect the reactivity of this surface with small gas phase molecules directly. A measurement and description of the band structure of the uranium oxide surface for different levels of oxygen content (UO₃, UO_{2+x}, UO₂, UO_{2-x}) is presented.

11:40am **AC+SS-MoM11 Characterization of the Surface Changes During the Activation of Erbium/Erbium Oxide for Hydrogen Storage**, *M.T. Brumbach, K.R. Zavadil, C.S. Snow, J.A. Ohlhausen*, Sandia National Laboratories

Erbium is known to effectively load with hydrogen when held at high temperature in a hydrogen atmosphere. To make the storage of hydrogen kinetically feasible, a thermal activation step is required. Activation is a routine practice, but very little is known about the physical, chemical, and/or electronic processes that occur during Activation. This work presents *in situ* characterization of erbium Activation using variable energy photoelectron spectroscopy at various stages of the Activation process. Modification of the passive surface oxide plays a significant role in Activation. The chemical and electronic changes observed from core-level and valence band spectra will be discussed along with corroborating ion scattering spectroscopy measurements.

§Sandia National Laboratories is a multi-program laboratory operated by Sandia Corporation, a wholly owned subsidiary of Lockheed Martin Company, for the U.S. Department of Energy's National Nuclear Security Administration under contract DE-AC04-94AL85000.

Energy Frontiers Topical Conference

Room: Mesilla - Session EN+PS-MoM

Plasmas for Photovoltaics & Energy Applications

Moderator: B. Lane, TEL Technology Center America

8:20am **EN+PS-MoM1 Combinatorial Plasma CVD of Si Thin Films with a Multihollow Discharge Plasma CVD Reactor**, *M. Shiratani, K. Koga, T. Matsunaga, Y. Kawashima, W. Nakamura, G. Uchida, N. Itagaki*, Kyushu University, Japan

A-Si and micro-crystalline thin films for solar cells are widely deposited by plasma CVD in industry. To realize combinatorial plasma CVD of such Si thin films, we have developed a multi-hollow discharge plasma CVD method, by which fluxes of H and SiH₃ as well as their flux ratio on the

substrate placed perpendicular to the electrodes depend on the distance from the discharges [1-4]. Thus, we can simultaneously deposit Si thin films with various structures and properties. For 60 MHz discharges of H₂+SiH₄ (0.3%), no films were deposited just near the discharge regions due to Si etching by H, micro-crystalline films were deposited in a rather narrow area around the no film regions, and a-Si:H films were obtained in the rest wide area far from the discharges. The spatial distribution of film structures indicate that the density ratio of H to SiH₃ decreases sharply with increasing the distance from the discharges and the surface reaction probability of H is much higher than that of SiH₃, being consistent with the reported surface reaction probabilities [5, 6]. For 2-6 Torr, the micro-crystalline film structure such as crystalline volume fraction and grain size varies sharply not only along the direction perpendicular to the electrodes but also along the direction parallel to the electrodes. These results suggest that the micro-crystalline film structure is highly sensitive to spatial and temporal uniformity of fluxes of H and SiH₃ as well as their flux ratio.

[1] K. Koga, et al., *Jpn. J. Appl. Phys.* **44**, L1430 (2005).

[2] W. M. Nakamura, et al., *IEEE Trans. Plasma Sci.* **36**, 888 (2008).

[3] W. M. Nakamura, et al., *J. Phys.: Conf. Series* **100**, 082018 (2008).

[4] H. Sato, et al., *J. Plasma Fusion Res. SERIES*, **8**, 1435 (2009).

[5] A. Matsuda, et al., *Surface Sci.* **227**, 50 (1990).

[6] J. Perrin, et al., *J. Vac. Sci. Technol. A*, **16**, 278 (1998).

8:40am **EN+PS-MoM2 Infrared Solar Cells Using Plasma-Processed Carbon Nanotubes**, *T. Kaneko, S. Kodama, Y. Li, R. Hatakeyama*, Tohoku University, Japan

Since the conventional silicon solar-cell conversion is limited to a certain window of solar cell photon energies over 1 eV, a full use of the solar spectrum is one of the crucial issues in order to greatly increase the solar cell efficiency. In this sense, carbon nanotubes (CNTs) are attracting much interest for photovoltaic energy conversion because of their broad absorption bands including the infrared range (0.2 ~ 1.3 eV) as well as other advantages such as large surface areas, high mobility of charge carrier, high mechanical strength, chemical stability, and so on. In this connection, we have developed a plasma-ion irradiation method, which enables pristine single-walled carbon nanotubes (SWNTs) to selectively encapsulate various kinds of atoms and molecules, such as metals and fullerenes, serving as electrons donors or acceptors inside their cavities. Then these enhanced p-type, n-type, and pn-junction housed semiconductor-SWNTs are applied toward the realization of high-efficient photovoltaic devices, which is composed of thin films of p- and n-types semiconductor SWNTs or an individual SWNT with p-n junction inside. Here, as a first step, electrical properties of p-n junctions fabricated using a combination of the thin films of pristine (empty) SWNT or C₆₀-encapsulated SWNT (C₆₀@SWNT), and n-doped Si (n-Si) are investigated.

The electrical properties of these SWNT film/n-Si devices show an obvious rectifying characteristic, and a short-circuit current I_{sc} and an open-circuit voltage V_{oc} through a downward shift of I - V curves are observed under illumination of light with wavelength of 1550 nm which corresponds to the photon energy of 0.8 eV. Moreover, it is found that the device fabricated with the C₆₀@SWNT film has a larger V_{oc} caused possibly by a large diffusion voltage in the interface of p-n junction compared with the device fabricated with the pristine SWNT film, due to the enhanced p-type behavior of SWNTs after C₆₀ encapsulation. To investigate undesirable photovoltaic effects of n-Si, we fabricate a schottky barrier solar cell consisting of silver (Ag) and n-Si in the absence of SWNTs. It is confirmed that the Ag/n-Si schottky barrier solar cell generates photo currents in the visible range (1.5 ~ 3 eV), while there is almost no difference between with and without light in the infrared range (0.8 eV) because the light with photon energy less than 1 eV cannot be absorbed by Si.

Based on these results, high performance solar cells which work in the infrared region are for the first time demonstrated to be formed using SWNTs, especially p-type enhanced C₆₀@SWNT.

9:00am **EN+PS-MoM3 A Novel Method of Controlling Plasma Uniformity in a Large Area VHF Plasma Source for Solar Applications**, *T. Tanaka, J. Kudela, E. Hammond, C. Boitnott, Z. Chen, J.A. Kenney, S. Rauf*, Applied Materials Inc. **INVITED**

Processing a large area substrate in a capacitively coupled plasma (CCP) reactor is becoming increasingly more difficult as the driving frequency required by the process is becoming higher and the size of the substrates is becoming larger. At the VHF (very high frequency) range the wave length of the driving signal is approaching the size of the substrate, and the resulting standing wave causes a severely non-uniform process. In this presentation, we will present a novel approach using magnetic boundary conditions in conjunction with phase modulation between multiple power feed points to improve process uniformity for a CCP reactor operating in the VHF range. The substrate size we consider is Gen 8.5 (2.2 m × 2.6 m

substrate) and the VHF power applied to generate the plasma is 40 and 60 MHz. At 60 MHz, with the vacuum wavelength of 5 m, the size of the substrate is approximately $\frac{1}{2}$ of the vacuum wavelength. An electromagnetic simulation with a pseudo plasma showed that, when 60 MHz is applied in a conventional manner, i.e. it is fed from the center of the back of one of the electrodes, it generates a dome shape electromagnetic field profile, which falls off sharply to almost zero at the voltage node before rising again towards the edges. A similar field pattern was also generated even when the VHF was fed from two feed points located at the opposing edges. The plasma distribution pattern measured with a 4×8 grid of optical emission spectroscopic (OES) probes revealed that the plasma was localized in the center when VHF the signal applied to the feed points were in phase. To modify the wave propagation pattern to change the shape of the standing wave in the central area, we placed ferrite material along two of the edges (edges that are away from the feed points) of the powered electrode. In this case, the peak in the central area was significantly stretched towards the ferrite-lined edges. We also found that the stretched "bar" of plasma could be moved over the substrate area by dynamically modifying the relative phase between the feed points in a manner similar to the technique employed by Yamakoshi *et al.* [1], and effectively distribute the processing plasma to much larger area.

[1] H. Yamakoshi *et al.* Appl. Phys. Lett. 88, 081502 (2006)

9:40am **EN+PS-MoM5 Novel Plasma Processing Routes of Si Nanocrystals for Photovoltaic Applications**, *I. Doğan, N.J. Kramer, M.A. Verheijen*, Eindhoven University of Technology, Netherlands, *T.H. van der Loop*, University of Amsterdam, Netherlands, *A.H.M. Smets*, Eindhoven University of Technology, Netherlands, *T. Gregorkiewicz*, University of Amsterdam, Netherlands, *M.C.M. van de Sanden*, Eindhoven University of Technology, Netherlands

10:00am **EN+PS-MoM6 Characterisation of Thin Film CdTe Multilayer Photovoltaic Devices Deposited by Closed Field Magnetron Sputtering**, *J.K. Bowers, S. Moh, A. Abbas, P.N. Rowley, H.M. Upadhyaya, J.M. Walls*, Loughborough University, UK

A new magnetron sputtering strategy is introduced that utilises high plasma densities ($\sim 5 \text{ mA cm}^{-2}$) to avoid or reduce high temperature processing. The technique uses magnetrons of opposing magnetic polarity to create a "closed field" in which the plasma density is enhanced without the need for high applied voltages. A batch system has been used which employs a rotating vertical drum as the substrate carrier and a symmetrical array of four linear magnetrons. The magnetrons are fitted with target materials for each of the thin films required in the photovoltaic (PV) stack viz. CdTe absorber layer, CdS buffer layer, metal contact and the back transparent conducting oxide (TCO) contact using the superstrate configuration. The "closed field" sputtering technology allows scale up not only for larger batch system designs but it is also configurable for "in-line" or "roll to roll" formats for large scale production. The morphology of each of the layers is characterised together with the overall device performance.

10:40am **EN+PS-MoM8 Material Properties of Hydrogenated Nanocrystalline Silicon Thin Films by RF-PECVD using He-SiH₄ Mixture**, *I.K. Kim, J.H. Lim, K.N. Kim, G.Y. Yeom*, Sungkyunkwan University, Republic of Korea

11:00am **EN+PS-MoM9 Surface Composition and Gas-Phase Passivation of Plasma-Synthesized Si Nanoparticles**, *B.N. Jarivala**, Colorado School of Mines, *N.J. Kramer*, Eindhoven University of Technology, Netherlands, *B.G. Lee, P. Stradins*, National Renewable Energy Laboratory, *M.C.M. van de Sanden*, Eindhoven University of Technology, Netherlands, *C.V. Ciobanu, S. Agarwal*, Colorado School of Mines

Tunable band gap of c-Si nanoparticles (NPs) (<5 nm) along with the possibility of multiple exciton generation has led to an increased interest in this form of Si as a material for 3rd generation photovoltaic (PV) devices. In addition to a high degree of control over the particle size, surface passivation of the NPs is key to their utilization in PV applications. In this presentation, we will primarily focus on understanding the growth of Si NPs in a dusty plasma, determining the surface composition of the NPs, and demonstrating novel techniques for passivation and encapsulation through the gas-phase. The particles are grown in a SiH₄/Ar plasma generated in a tubular flow rf discharge. The plasma source is attached to an in-house-built vacuum chamber equipped with *in situ* attenuated total reflection Fourier-transform infrared (ATR-FTIR) spectroscopy and a quadrupole mass spectrometer. Using this technique, we have synthesized Si NPs in the size range of 3-7 nm, which transition from amorphous to crystalline over the rf

power range of 5 to 40 W. The *in situ* IR data show that the surface hydride composition of the NPs is related to their crystallinity, which in turn depends on particle heating during synthesis. The as-synthesized NPs surfaces are terminated with Si mono-, di- and tri-hydrides. The higher hydride concentration decreases with increasing particle crystallinity, similar to previous observations on the amorphous Si surfaces, where higher Si hydrides are known to decompose with increasing deposition temperatures. These results also are consistent with the particle heating models proposed for dusty plasmas. In the first surface passivation approach, the as-synthesized H-terminated Si NPs, which oxidize even under high-vacuum conditions, are passivated *in situ* through hydrosilylation using 1-alkenes of different chain lengths. We have used density functional theory calculations to investigate the detailed reaction mechanism for various alkene chain lengths, and to understand the effects of alkene coverage on the oxidation of the surface. The surface reaction kinetics for hydrosilylation is observed *in situ* by monitoring the C-H and Si-H stretching vibrations. The ligand coverage is determined to be roughly 50% of the surface sites, which is sufficient to prevent oxidation for several hours. The quality of surface passivation is further determined through the photoluminescence quantum yield measurements, which show a higher yield for surface passivated NPs. In the second approach, the NPs are passivated with metal oxides using atomic layer deposition that involves the two different oxidation steps with O₃ and H₂O to achieve deposition at <200 °C.

11:20am **EN+PS-MoM10 Effects of Hole-Array-Electrode on the Characteristics of Radio Frequency Capacitively Coupled Plasma Sources for uc-Si Thin Film PECVD**, *H.-J. Lee, S.-S. Wi*, Pusan National University, Republic of Korea, *D. Kim, D. Hwang, W.S. Chang*, LG Electronics, Republic of Korea

In order to improve the productivity of thin film growth in rf capacitively coupled plasma based chemical vapor deposition system, modifications of electrode surface geometry has frequently been used. Array of holes in the shower head electrode is probably the most popular one. In this paper, using self-consistent fluid approximation with collisional sheath model, we have analyzed the effects of the hole array on the plasma characteristics in terms of plasma density, electron temperature, ion current density, sheath voltage and electron heating efficiency. It is shown that electron heating efficiency of the hole array electrode increases more than 10 % compared with that of flat electrodes. DC bias voltage at the substrate side increases with hole depth and pitch due to increase in surface area ratio between powered and substrate electrode. Peak electron density near throat region of the hole structure becomes more than 2 time higher than that of flat parallel electrode at the same voltage driving condition. It was experimentally verified that these variations of plasma properties is beneficial for high rate of Si thin film deposition

11:40am **EN+PS-MoM11 Arc Energy in Large Scale Magnetron Sputtering**, *D. Carter, H. Walde*, Advanced Energy Industries, Inc.

A detailed analysis of sputtering arcs on a large scale (3400 cm²) magnetron source reveals some common trends related to energy absorbed in these events and the progression of current and voltage through their duration. Examination of these trends provides insight into the rapid release of arc energy and some of the practical limitations of the techniques used to minimize their impact on deposition processes. Two very different but equally important materials were studied, metallic aluminum and ceramic, aluminum-doped, zinc oxide. While the characteristics and behaviors of arcs from these two materials are generally similar, subtle distinctions in the evolution of current and voltage explain a significant difference in measured arc energies. These observations present factors for consideration regarding arc suppression and also raise the question of what is the minimum achievable arc energy. In an attempt to answer this fundamental question a stored energy model for a large scale magnetron system is proposed. Using practical assumptions for sheath capacitance and source inductance, minimum arc energy is calculated to serve as the ultimate goal for a next generation arc detection and suppression system.

* Coburn & Winters Student Award Finalist

Graphene Focus Topic

Room: Brazos - Session GR+SS+TF+EM-MoM

Epitaxial Graphene on SiC

Moderator: P.E. Sheehan, Naval Research Laboratory

8:20am **GR+SS+TF+EM-MoM1 Controlling Carriers in Graphene.** *G.G. Jernigan, P.E. Thompson, C.S. Hellberg, J.L. Tedesco, V.D. Wheeler, L.O. Nyakiti, P.M. Campbell, D.K. Gaskill*, Naval Research Laboratory

No technique for graphene synthesis yields controllably doped material. Measurements of carrier density and carrier type produce results that are dependent on extrinsic factors. For example, exfoliated graphene and metal-catalyzed graphene on SiO₂ often obtain carriers through unwanted charges in the oxide[1] or by gas adsorption[2] making graphene p-type. Similarly, epitaxial graphene on SiC should be n-type due to work function differences with the underlying SiC substrate[3]. Our recent measurements of graphene grown on Si-face SiC show that device processing steps can cause it to switch between carrier types. Additionally, we have found graphene grown on C-face SiC to be highly doped by Si impurities, which can produce either electrons or holes.

We have begun a series of investigations to impart properties after growth on epitaxial graphene formed on Si- and C-face SiC[4-5]. Substitutional incorporation of impurity atoms can lead to doping in a graphene sheet, if their concentration does not drastically affect the pi-network. This can be achieved by selective oxidation to remove C atoms from the graphene lattice and by molecular beam deposition (MBE) of dopants with controllable ultra-low fluxes to fill the C vacancies. It is important to note that Group III and V dopants can maintain the 2D geometry of the graphene sheet without producing an unsaturated bond (as they do when incorporated into the bulk of Si.) Thus, the extra p-orbital electrons from the Group V elements can be added to the graphene pi-network, or Group III elements can provide extra holes, without adversely affecting carrier mobility. Using MBE, we have substitutionally doped graphene with B and P. Ultraviolet photoelectron spectroscopy (UPS) is used to observe shifts in the Fermi level resulting from doping, and we have seen up to a 110 meV shift with 1% B in the lattice of graphene. Discussion of scanning tunneling microscopy (STM) observations of dopant placement and electrical properties will be presented. Density functional theory has been used to compute the density of states for the doped system in support of the STM and electrical measurements.

[1] S. S. Datta, D. R. Strachan, E. J. Mele, and A.T.C. Johnson, *Nano Lett.* 9 (2009) 7.

[2] Y. Dan, Y. Lu, N.J. Kybert, Z. Luo and A.T.C. Johnson, *Nano Lett.*, 9 (2009) 1472.

[3] T. Filleter, K. V. Emtsev, Th. Seyller, and R. Bennewitz, *Appl. Phys. Lett.* 93 (2008) 133117.

[4] G.G. Jernigan, et al., *Nano Lett.* 9, 2605 (2009).

[5] J.L. Tedesco, B.L. VanMil, R.L. Myers-Ward, J.M. McCrate, S.A. Kitt, P.M. Campbell, G.G. Jernigan, J.C. Culbertson, C.R. Eddy, Jr., and D.K. Gaskill, *Appl. Phys. Lett.*, 95, 122102 (2009).

8:40am **GR+SS+TF+EM-MoM2 The Role of Carbon Surface Diffusion on the Growth of Epitaxial Graphene on SiC.** *T. Ohta, N.C. Bartelt, S. Nie, K. Thürmer, G.L. Kellogg*, Sandia National Laboratories

Growth of high quality graphene films on SiC is regarded as one of the more viable pathways toward graphene-based electronics. Graphene films are readily formed on SiC by preferential sublimation of Si at elevated temperature. Little is known, however, about the atomistic processes of interrelated Si sublimation and graphene growth. We have observed the formation of graphene on SiC by Si sublimation using low energy electron microscopy, scanning tunneling microscopy, and atomic force microscopy. This work reveals unanticipated growth mechanisms, which depend strongly on the initial surface morphology. Carbon diffusion governs the spatial relationship between Si sublimation and graphene growth. Isolated bilayer SiC steps generate narrow ribbons of graphene by a distinctive cooperative process, whereas triple bilayer SiC steps allow large graphene sheets to grow by step flow. We demonstrate how graphene quality can be improved by controlling the initial surface morphology to avoid the instabilities inherent in diffusion-limited growth. This work is supported by the LDRD program at Sandia Labs and the US DOE Office of Basic Energy Sciences, Division of Materials Science and Engineering (DE-AC04-94AL85000), and was performed in part at CINT (DE-AC04-94AL85000). Sandia is a multiprogram laboratory operated by Sandia Corporation, a Lockheed Martin Co., for the U.S. DOE NNSA (DE-AC04-94AL85000).

9:00am **GR+SS+TF+EM-MoM3 Epitaxial Graphene on SiC(0001).** *T. Seyller*, Universität Erlangen, Germany **INVITED**

The properties of graphene, its fabrication, and its application are very active fields of research. The large carrier mobility and prospects for room-temperature ballistic transport raise hopes for application of graphene in electronic devices. Applications, however, demand growth methods suitable for producing graphene layers on a wafer scale. While this goal is impossible to reach with mechanical exfoliation, epitaxial graphene (EG) grown on the basal plane surfaces of silicon carbide (SiC) offers a much better prospective. In this talk I shall review studies of the structural, electronic, and transport properties of EG grown on SiC by solid-state decomposition at elevated temperatures. The first part describes a study of the electronic structure and structural properties of EG which can conveniently be determined using surface science techniques. In the second part I demonstrate how the growth of EG is improved by going from the traditional growth environment, namely ultrahigh vacuum, to an Argon atmosphere. The latter method leads to vastly improved EG films with properties similar to those of exfoliated graphene. Finally I shall discuss how the interface between SiC and graphene can be controlled by intercalation of foreign atoms.

9:40am **GR+SS+TF+EM-MoM5 Structural Defects in Epitaxial Graphene Layers Synthesized on 4H-SiC(000-1) Substrate - Transmission Electron Microscopy (TEM) Studies.** *J. Borysiuk*, University of Warsaw, Poland, *S.K. Krukowski*, Polish Academy of Sciences, Poland

Main structural defects in graphene layers, synthesized on the carbon-terminated face, i.e. SiC(000 $\bar{1}$) face of 4H-SiC substrate, are discussed. The discussed structures include in-plane edge dislocations, grain boundaries, puckers, etc. These defects are investigated using High Resolution Transmission Electron Microscopy (HRTEM), revealing their atomic arrangement. The mechanism of creation of such defects, in relation to the misalignment to the underlying crystallographic structure of the SiC substrate is elucidated. The relation between the SiC surface structure, including the presence of the single atomic steps, the sequences of atomic steps, and also the macrosteps, and the emergence of edge dislocations or boundaries between the regions having different crystallographic orientation in the graphene layers, is shown. In addition, the structures containing different stacking sequences of carbon atoms in the graphene layers are presented. The presented C-layers stacking includes AA, AB, ABC sequences, and also the stacking close to turbostratic stacking.

10:00am **GR+SS+TF+EM-MoM6 Controlling the Growth Rate of Graphene on Silicon Carbide.** *D.B. Torrance, D.L. Miller, M. Phillips, H. Tinkey, E. Green, P.N. First*, Georgia Institute of Technology

Controlled thermal decomposition of silicon carbide is so far the most effective method for growing high-quality graphene epitaxially and at the wafer scale. In this work we simultaneously study the graphenization of SiC(0001) and SiC(000-1) as a function of temperature and buffer-gas pressure in a custom-built ultrahigh vacuum (UHV) induction furnace. The buffer gas is modeled as a homogeneous diffusion medium using kinetic theory. In-situ characterization by both Auger electron spectroscopy and low-energy electron diffraction (LEED) was used to determine the pressure- and temperature-dependent growth rate of graphene layers. Sample quality was further assessed ex-situ using a variety of techniques such as Raman spectroscopy and scanning tunneling microscopy.

10:40am **GR+SS+TF+EM-MoM8 Evidence of Screw Dislocations in Epitaxial Graphene Islands.** *J.K. Hite, J.C. Culbertson*, Naval Research Laboratory, *J.L. Tedesco*, National Institute of Standards and Technology, *M.E. Twigg, A.L. Friedman, P.M. Campbell, R.L. Myers-Ward, C.R. Eddy, Jr., D.K. Gaskill*, Naval Research Laboratory

Epitaxial graphene (EG) has lately garnered enormous interest, due to its high free-carrier mobility and compatibility with semiconductor processing. In fact, the first EG RF field effect transistor has been demonstrated.¹ However, the growth mechanism of this material is not well understood. Current RF device work has been on the Si polar face of (0001) semi-insulating SiC substrates as EG on this face mainly consists of 1 monolayer of graphene. In contrast, the C-face consists of a dozen or more graphene layers and has a rougher morphology. Yet, there is significant interest in obtaining few layer, smooth EG on the C-face of SiC due to its better electrical properties as compared to the Si-face. Recently, it was shown that C-face EG grown in Ar ambient slows the growth rate, and under certain conditions results in islanding of the graphene on the C-face.² These islands open the possibility of investigating the initial stages of graphene growth.

Electron channeling contrast imaging (ECCI) has previously been used to investigate threading dislocations in semiconductors such as GaN and SiC.^{3,4} In this work, ECCI is used for the first time to investigate graphene island morphology as a function of island size and growth conditions. Using

this characterization tool, single threading screw dislocations (TSDs) have been found in the center of small EG islands (>20 μm diameter). ECCI images confirm that these small graphene islands are forming in hexagonal recesses below the surface of the SiC substrate. For larger islands, the evidence of TSDs disappears suggesting that as the islands grow or coalesce to larger diameters either the TSD becomes buried or no longer contributes to growth. Once the islands become this large, the graphene begins to grow above the SiC surface, unlike the smaller islands. After removal of the EG by various methods, TSDs are still observed in the centers of the pits formed by the small island graphene growth. After some removal efforts, many pits retained small triangles of graphene around the TSD. These results are consistent with Raman and AFM maps of the islands that demonstrate that the centers of the islands are much deeper and the graphene thicker than the surrounding graphene. The evidence of TSDs in the centers of these C-face EG islands strongly suggests that these dislocations serve as nucleation sites for EG growth, where the TSD may provide an escape pathway for sublimated silicon atoms during the growth process.

¹J.S. Moon *et al.*, IEEE Electron Dev Lett **31**, 260, 2010

²J.L. Tedesco *et al.*, Appl Phys Lett, in press

³Y.N. Picard *et al.*, Scripta Materiala **61**, 773, 2009

⁴Y.N. Picard *et al.*, Appl Phys Lett **90**, 23401, 2007

11:00am **GR+SS+TF+EM-MoM9 Direct Measurement of the Energy Gaps Involved in the Lifting of the Valley and Spin Degeneracies in Epitaxial Graphene**, *Y.J. Song, A.F. Otte*, CNST/NIST; Maryland NanoCenter UMD, *D.B. Torrance, Y. Hu, P.N. First, W.A. de Heer*, Georgia Institute of Technology, *J.A. Stroscio*, CNST/NIST

Landau levels on epitaxially grown graphene were recently mapped both spatially and energetically using scanning tunneling spectroscopy in magnetic fields at 4 K [1]. In this talk we present new measurements, made at ≈ 10 mK, of all four electron states resulting from the lifting of the fourfold spin- and valley-degeneracy of the $N = 1$ Landau level in applied magnetic fields. We show that the energy splitting from the broken valley degeneracy is ten times larger than electron spin splitting in our samples. When the Fermi level lies inside the four-fold Landau manifold, significant electron correlation effects result in an enhanced valley splitting at even filling factors, and an enhanced electron spin splitting at odd filling factors. Most surprisingly, we observe new many body states with top-layer Landau level filling factors $7/2$, $9/2$, and $11/2$.

[1] David L. Miller, Kevin D. Kubista, Gregory M. Rutter, Ming Ruan, Walt A. de Heer, Phillip N. First, and Joseph A. Stroscio, Science **324**, 924-927 (2009).

11:20am **GR+SS+TF+EM-MoM10 Morphology of Epitaxial Graphene on SiC: Nano-Objects, Nano-Cracks, and Ribbons**, *S. Chiang*, Univ. of California at Davis, *N. Camara*, IMB-CNM-CSIC, Spain, *S. Vizzini, D. Martinotti*, CEA-Saclay, France, *H. Oughaddou*, Univ. de Cergy-Pontoise & CEA Saclay, France, *H. Enriquez*, Univ. de Paris-Sud/Orsay & CEA-Saclay, France, *Ph. Godignon*, IMB-CNM-CSIC, Spain, *J. Camassel*, GES, UMR-CNRS, France, *P. Soukiasian*, Univ. de Paris-Sud/Orsay & CEA-Saclay, France

We use scanning tunneling microscopy/spectroscopy (STM/STS) and low energy electron microscopy (LEEM) to investigate epitaxial graphene grown under vacuum on a 4H-SiC(000-1)-C-face substrate and self-organized parallel graphene ribbons grown in a furnace on a 6H-SiC(000-1) C-face sample covered by a graphite cap. On the vacuum grown graphene, we observed two types of nanostructures including nano-objects and nano-cracks. The results reveal that these nano-objects are located at the graphene/SiC interface leading to electronic interface states. Their height profiles suggest that these objects are made of packed carbon nanotubes confined vertically and forming mesas at the SiC surface. We also find nano-cracks covered by the graphene layer that, surprisingly, is not broken going deep into the crack, with no resulting electronic interface state. Therefore, unlike the above nano-objects, these cracks should not affect the carrier mobility. LEEM has been used to observe the formation of graphene ribbons grown on SiC in a furnace. The morphology and distribution of the ribbons has been examined, and their typical size is about 1 μm wide and 10 μm long.

Work supported by Agence National pour la Recherche (ANR) under GraphSiC program

Frontiers in Inkjet Technology Topical Conference Room: Tesuque - Session IJ+BI+MN-MoM

Frontiers in Inkjet Technology

Moderator: T. Boland, University of Texas at El Paso

8:20am **IJ+BI+MN-MoM1 Drop Impact on Liquid, Solid and Porous Surfaces**, *A.L. Yarin*, University of Illinois at Chicago **INVITED**

The talk covers drop impacts on thin liquid layers, dry impermeable surfaces, and porous surfaces with nano-scale texture. Splashing and corona formation and propagation on liquid layers are discussed first. Then, some additional kindred, albeit non-splashing, phenomena like drop spreading and deposition, receding (recoil), jetting, fingering and rebound on liquid and dry impermeable solid surfaces are covered. A number of practical applications of drop impacts are mentioned and relevant experimental, theoretical and computational aspects are considered.

After that, a novel method of enhancement of drop and spray cooling for microelectronic, optical and radiological elements and server rooms, which require extremely high heat fluxes, is discussed. The key idea of the method is to cover the heat transfer surfaces with electrospun nonwoven polymer nanofiber mats. The experiments reveal that drop impacts on nanotextured surfaces of nanofiber mats produce spreading similar to that on the impermeable dry surfaces. However, at the end of the spreading stage the contact line is pinned and drop receding is prevented. All the mats appear to be dynamically permeable for water drops. The enhanced efficiency of drop cooling in the presence of nanofiber mats observed experimentally results from a complete elimination of drop receding and bouncing characteristic of the current spray cooling technology. Therefore, the drops evaporate completely, and the large cooling potential associated with the latent heat of water evaporation is more fully exploited. This is paradoxical: the best cooling can be provided by a "furry overcoat"! The results on drop impact on porous surfaces are also relevant for drop impacts on paper and nonwovens in the context of ink-jet-printed microelectronics.

9:00am **IJ+BI+MN-MoM3 Upper and Lower Bounds for the Stability of Inkjet Printed Lines**, *B. Derby, J. Stringer*, University of Manchester, UK

Many applications for inkjet printing require the ability to print continuous linear features. Inkjet printing achieves this through the overlap and coalescence of a series of liquid drops on a planar substrate, which then transform to a solid through phase change or solvent loss. In order to produce regular parallel sided printed lines, the intermediate fluid thread must retain morphological stability prior to solidification. Drying fluid drops often show considerable hysteresis between the advancing and receding contact angles. This behaviour is shown to impose upper and lower bounds for the width of a line formed by the overlap of printed drops. The lower bound for line width is determined by the minimum separation distance for spreading drops to spread, overlap and coalesce. However, for liquids with zero receding contact angles (as is the case for many evaporating solvents) there is a further limit for parallel sided lines [1]. The upper bound for line width is determined by a dynamic fluid instability that occurs through competing fluid flows between the spreading and coalescence processes [2]. This dynamic instability is a function of both drop spacing and the rate of droplet deposition. By considering both the upper and lower bound limits we can construct a map in a parameter space defined by drop size, drop spacing, drop/substrate contact angle and linear printing velocity that shows the conditions under which stable linear features can be printed.

9:20am **IJ+BI+MN-MoM4 Particle Deposition and Assembly of Inkjet-Printed Colloidal Drops in Line and Pattern Printing**, *A. Joshi, V. Chhasatia, Y. Sun*, Drexel University

Precise control of process parameters during inkjet printing is essential to enable uniform, accurate and repeatable deposition of functional materials. In this work, we present a combined in-situ observation and computational study to examine particle deposition and assembly during evaporation of inkjet-printed colloidal drops. Unlike previous computational models that use tracer particles and known velocity fields inside the drop, our computational model uses a multi-phase lattice Boltzmann method (LBM) that directly simulates the flow of the liquid drop, surrounding vapor phase and the motion of the liquid-vapor interface. The motion of suspended particles within the liquid phase is directly coupled to the fluid flow and also influences the velocity field in the liquid. Evaporation is accomplished

by reducing the vapor pressure above the drop and different evaporation modes including evaporation with contact line pinning and self-similar evaporation with a constant contact angle are examined. A novel visualization technique is developed wherein aqueous suspensions of fluorescent particles are jetted onto transparent surfaces and the evaporation dynamics are observed in real-time using a fluorescence microscope. The effects of drop spacing, jetting frequency, substrate wettability, particle size and volume fraction, and environmental conditions (temperature and humidity) on the final deposition morphology are presented for line and pattern printing of functional materials on substrates.

9:40am **IJ+BI+MN-MoM5 Inkjet Printing of Flexible Hybrid Solar Cells based on P3HT and ZnO**, *G. Carryon, J.B. Baxter, Y. Sun*, Drexel University

Inkjet printing of organic solar cells offers an inexpensive alternative to conventional solar cell fabrication methods. Despite the attractiveness of organic solar cells, they have demonstrated some degradation problems and have yet to achieve the efficiencies necessary to make them economically viable. In contrast to their organic counterparts, inorganic semiconductors have demonstrated advantages in their high dielectric constant which facilitates carrier generation processes, high carrier mobility, and thermal morphological stability. In recent years, improvements in device performance have been seen in the development of organic-inorganic hybrid materials (e.g., ZnO nanoparticle-polymer composites or CdSe quantum dot-polymer composites) as the photoactive layer. To date, most studies on hybrid solar cell fabrication have focused on using lab-scale spin-coating methods to deposit ZnO nanoparticle-polymer materials. In this paper, we present our results in using an industrial piezoelectric-driven printing device for inkjet printing of ZnO nanoparticles/nanorods-polymer [e.g., poly(3-hexylthiophene (P3HT))] ink materials for large-scale processing of hybrid solar cells. The deposition morphology and properties of printed photoactive layer are examined as a function of the solvent properties (e.g., wettability and vapor pressure), particle size, volume fraction, and polydispersity, as well as the aspect ratio of nanorod. The effects of jetting parameters (e.g., wave form and jetting frequency) and printing patterns on film thickness and uniformity are also discussed in detail. Finally, the feasibility of printing P3HT onto aligned ZnO nanorod arrays for novel heterogenous nanostructures for reduced exciton diffusion lengths is explored.

10:00am **IJ+BI+MN-MoM6 Anomalies in Applications of Inkjet Printing in Microfluidic Device Fabrication**, *W.E. Dieterle, C.P. McNary*, California University of Pennsylvania

Utilization of inkjet-generated masks for UV photosensitive materials as a cost-effective method for the generation of microfluidic devices requires resolution of certain anomalies related to combinations of various color components. These anomalies are demonstrated for UV exposures with a high-pressure mercury vapor source and possible solutions are discussed, including implications for inkjet manufacture designs targeted to similar applications.

10:40am **IJ+BI+MN-MoM8 Fabrication of Miniature Drug Screening Platform Utilizing Low Cost Bioprinting Technology**, *J. Rodriguez, T. Xu*, University of Texas at el Paso

In the pharmaceutical industry, new chemicals and substances are being tested to find appropriate compounds for treating a specific disease. The demand for screening large compound collections against and increasing number of therapeutic targets has stimulated technology development in the areas of assay automation and miniaturization. Current methods for evaluating the reactions of cells use a relatively large volume in the range from microliters to milliliters; since reliability has to be met, it exists the need to have several assays to confirm the biochemical reactions, which ultimately cause the usage of large amounts of volume for each substance. Unfortunately, some of these new compounds are rather hard to obtain, which causes an expensive researched and limited material availability; therefore, increasing the time development for future cures. We have developed a new and low-cost deposition method to fabricate miniature drug screening platform that can realistically and inexpensively evaluate biochemical reactions up to 4 substances per trial in a picoliter-scale volume.

This study focuses on the development of the controls for a deposition method (inkjet printing technology) which will simultaneously place therapeutic drugs and cells onto target sites to fabricate cell/drug chips for drug screening application. Using a modified HP 5360 CD printer, droplets of GFP expressing *Escherichia coli* have been deposited in an agar coated coverslip chip as small reliable volume of 180 picoliters per each colony dot, along with this bacteria it has been patterned different antibiotics in such a way that we evaluated the growth of the bacteria under antibiotics

presence. The viability and function of the printed cells were evaluated by the live/dead and plasmid gene transfection experiments resulting in 98% viability and maintaining DNA function. Moreover, it has been recorded as high throughput process printing 250,000 droplets/second. Due to the reduction of volume, this method will increase the effectiveness of the resources utilized for emerging drug screening processes. The results show promising usage of resources for future drug screening through new biochemicals.

11:00am **IJ+BI+MN-MoM9 Inkjet Printing of Oxygen Releasing Materials for Improved Cell Survival and Growth**, *A. Arteaga, T. Xu*, University of Texas at el Paso

Introduction: A major barrier in tissue engineering is the impossibility of providing adequate oxygen to all cells within the engineered tissue before a full vascularization is achieved. To overcome this limitation, a variety of oxygen-producing particles have been developed for improving tissue survival. However, most of these particles are used in random mixtures with scaffolding materials, which usually leads to an uneven distribution of oxygen in bioengineered tissues. An ideal oxygen supply requires a precise spatial-temporal control of the oxygen-producing particles in scaffolds. Unfortunately, current oxygen delivering scaffold techniques are unable to perform as described and to precisely incorporate oxygen particles into the scaffolds. Cell inkjet printing is a novel tissue fabrication approach, in which a special inkjet printer can be programmed to deposit cells and/or biomaterials of various types and sizes in a very precise pattern. In this study we have applied the inkjet printing technology to allocate oxygen releasing materials to their designed positions for optimal cell viability and growth.

Methods: The controlled oxygen-releasing platform is fabricated by printing different patterns ("Black", "White", "Grey", and "Dots" to represent different densities of the oxygen particles on the substrates) of encapsulated calcium peroxide (CPO) particles that were analyzed against C2C12 mouse myoblast cell line for cell viability. CPO has been found to release its oxygen over an extended timeframe. The effects of controlled oxygen-releasing particles on cell viability were analyzed using the cell morphology study, live/dead assay, and the MTS assay.

Results: These analyses showed the concentration of the oxygen-releasing particles in "Black" was toxic to the cells based on the decreasing trend in cell viability. The "White" did not have oxygen-releasing particles, which correlates to the decrease in cell viability over time due to oxygen deprivation. Both "Grey" and "Dots" showed a similar trend in absorbency, in which the absorbency was low at 24 hours, there was an increase in absorbency at 48 hours, and then an abrupt decrease at 72 hours. Both these results suggest that the amount of oxygen released was beneficial to the cells within the first 48 hours, yet may not have been sufficient to sustain cell viability after that time span. The cells treated in the printed "Dots" showed to have the most compatible treatment for an overall increase in cell viability.

Conclusion: The amount of oxygen released can be controlled to optimize the cell by bioprinting different densities of the oxygen releasing materials onto a substrate.

11:20am **IJ+BI+MN-MoM10 Understanding Volume Ejection of Complex Fluids through Pressure Measurements**, *G.E. Mårtensson, W. Holm*, Micronic Mydata AB, Sweden

In conventional ink jetting applications, a pressure difference is used to ensure the continuous and prompt filling of the jetting chamber between jetting actuations. The delivery of precise fluid volumes utilizing inkjet-like drop-on-demand jetting technology is primarily controlled by the piezo voltage that actuates the jetting chamber (Gerhauser et al. 1983, SID 83 Digest). The jetting of large volumes, in excess of 1 nL, of complex viscous fluids is complicated by the difficulty of filling the ejection chamber quickly after the previous droplet ejection.

A novel jetting mechanism for highly viscous complex fluids, that utilizes a viscous micropump to control the amount of fluid that is ejected by a piezo actuated mechanism, has been developed and implemented by the authors. In this paper, we report results of volume, exit velocity, and pressure measurements. The piezo voltage, V_p , and the angular speed, N , of the viscous pump has been varied. A chosen V_p translates directly to displaced volume and N to flow rate.

The ejected volume has been measured by weighing a large number of droplets and via 3D profilometry methods. It has been shown in the experimental jetting setup that the volume of a jetted deposit is only affected to a minor degree, of the order of 5% of the target volume, by the chosen piezo voltage, V_p . Thus the ejected volume is almost independent of the displaced volume within the experimental range and determined by the flow rate, which in turn is controlled by N .

The exit velocity of the jet has been measured using high speed double exposure imaging. It has been shown that the speed of the ejected droplet has a nearly linear response to V_p (at least for all but the smallest N). For a given V_p , the exit velocity increase with increasing N . Thus, it seems that a larger displaced volume results in a higher exit velocity, but the ejected amount is unaffected.

In order to probe these seemingly counterintuitive results, the pressure in the ejection chamber, as well as in the viscous micropump, was measured over a large number of ejection cycles. The volume of the resulting depositions were correlated with the chamber and pump pressures. Additional measurements were performed to correlate the speed of the resulting shot with the chamber and pump pressures. Simple models are proposed to correlate the above mentioned quantities.

11:40am **IJ+BI+MN-MoM11 Determination of Effective Jet Radius from Measurements of the Perturbation Growth Rate in Thermally Stimulated Continuous Microjets**, *J.M. Grace, G. Farruggia, E.P. Furlani, Z.J. Gao, K.C. Ng*, Eastman Kodak Company

Drop formation in continuous inkjet devices is based upon the Rayleigh-Plateau instability – a phenomenon in which surface tension drives the break-up of a column of fluid into droplets. In thermally stimulated continuous inkjet devices, heat pulses applied to the jet at the nozzle couple to the instability to stimulate drop formation. The level of stimulation depends upon the size of the effective perturbation and its growth rate along the jet. While the growth rate depends upon characteristics of the jet itself (fluid properties and jet diameter), the effective perturbation depends upon coupling between the source of stimulation and the jet, as well as the fluid properties. The coupling efficiency can be inferred from measurements of the perturbation growth rate and the jet diameter. For liquid microjets with diameters of 10 micrometers or less, direct determination of the jet diameter by optical microscopy is extremely challenging. Although the lateral dimensions of the microjets may be difficult to measure precisely, the break-up length can be determined with relatively good precision. Measurements of break-up length as a function of input power provide a means to determine the perturbation growth rate. From the experimentally determined growth rate as a function of stimulation frequency, the diameter of the microjet can be determined by fitting to a model for jet break-up. The experimentally determined growth rate and jet diameter provide a basis for comparing the effective coupling for different designs of jetting modules. Measurements of jet break-up and methods for determining the effective jet diameter will be presented and discussed.

Marine Biofouling Topical Conference Room: Navajo - Session MB+BI-MoM

Understanding Marine Biofouling

Moderator: S. Zauscher, Duke University

8:40am **MB+BI-MoM2 Colloidal Theories of Bacterial Attachment as Applied to Marine Bacteria: A Necessary Revision?**, *L.K. Ista*, University of New Mexico, *G.P. Lopez*, Duke University

The majority of our knowledge of bacterial attachment and subsequent biofilm formation has been gleaned from studies on human pathogens and commensal bacteria with specialized attachment mechanisms and attachment substrata. In contrast many marine microorganisms have a variety of substratum choices, with the added challenge of new types of introduced substrata (boats, piers, pilings) as possible biofilm supports. Maintaining the genetic information needed to produce specific attachment mechanisms for each possible substratum would be maladaptive; it is very likely that marine bacteria exploit their colloid-like size and rely on colloidal interactions to drive attachment. Thus, colloidal models of bacterial attachment are of particular interest to understanding marine microbial attachment. Current models of bacterial attachment are useful for describing some bacterial attachment, but cannot predict attachment behavior in most cases. In this work we examine 3 basic assumptions of the preeminent model used for bacterial attachment, the Lewis Acid Base (LAB) model proposed by van Oss. We used gold-alkanethiolate self-assembled monolayers (SAMs) and three marine bacteria to test these assumptions. The first assumption is that apolar interactions include both London dispersion (induced dipole/induced dipole) interactions and those

based on fixed dipoles. Using apolar contact angle liquids of either purely London dispersion or London dispersion and dipole/induced dipole interactions we calculated the apolar component of the surface tensions of SAMs and bacteria and observed differences in the estimation of the apolar surface tension and, thus, the total surface tension on polar surfaces. The second assumption is that the Lewis acid and base components of H_2O surface tension are equal, which frequently leads to overestimation of Lewis basicity. We calculated surface tensions of bacteria and SAM surfaces with both LAB values and those based on solvatometric hydrogen bonding calculations and observed that the latter gave more reasonable estimation of the free energy of attachment. The third assumption is that interactions can be correlated with average surface energy for the cell. Both our observations and those in the literature have led us to believe this is untrue. We present scanning electron microscopy data that demonstrate that different parts of bacterial cells are in contact with the surface of different SAMs and that SAMs on nanoparticles can identify specific regions of heterogeneity on bacterial cell surfaces. Based on our results we propose modifications to the LAB model that may make it more able to model and predict marine bacterial attachment.

9:00am **MB+BI-MoM3 Reversible Adhesion in Barnacle Cyprids: the Weak Link in Surface Colonisation?**, *N. Aldred*, Newcastle Univ., UK, *I.Y. Phang*, MESA+ Institute for Nanotech. and Dutch Polymer Inst., Netherlands, *T. Ekblad*, *O. Andersson*, *B. Liedberg*, Linköping Univ., Sweden, *G.J. Vancso*, MESA+ Institute for Nanotech. and Dutch Polymer Inst., Netherlands, *A.S. Clare*, Newcastle Univ., UK **INVITED**

Reversible or temporary adhesion allows barnacle cyprids to explore surfaces before they commit to permanent settlement. As such this scarcely studied system is an obvious point of attack for fouling control. The remarkable paired antennules of the cyprid bear attachment discs; hairy adhesive structures that enable the cyprid to walk over surfaces in a stilt-like fashion while resisting detachment by hydrodynamic forces. A proteinaceous secretion at the surface of the disc has been postulated to function as a 'temporary adhesive'. Here evidence is presented that suggests the antennular secretion is related to the adult settlement pheromone – the settlement-inducing protein complex – and that it functions as a reversible adhesive, but in a hybrid wet/dry adhesive system somewhat akin to insect reversible adhesion. While a complete characterisation of the antennular secretion remains an aim, the application of surface analytical techniques (atomic force microscopy and imaging surface plasmon resonance) and direct measures of cyprid behaviour, go some way to providing a mechanistic understanding of why cyprids settle at low rates on certain surfaces, which can be applied to future developments in antifouling technology.

9:40am **MB+BI-MoM5 Chemical Insights on How Shellfish Stick**, *J.D. White*, *C.R. Matos-Perez*, *J.R. Burkett*, *T.W. McCarthy*, *J.W. Wilker*, Purdue University **INVITED**

Since the very first mariners traversed ocean waters, hulls have become encrusted with fouling organisms such as barnacles, oysters, tube worms, and algae. Antifouling coatings can prevent the resulting loss of vessel performance, but at a cost. Current coatings release toxins into the water, thereby killing the foulers as well as other species. Rather than destroying marine life, stopping bioadhesion processes may provide a benign means of antifouling. Consequently we have been seeking detailed knowledge of how shellfish attach themselves to surfaces. The resulting insights can be used to develop mechanism-based antifouling coatings for inhibiting the production of bioadhesives. Our characterization efforts have focused on the intractable glues and cements of mussels, barnacles, and oysters. A fruitful approach has been to work simultaneously with synthetic peptide models, extracted adhesive proteins, and material produced by the animals. Perspectives from each class of experiments can be complimentary and used to build pictures of how the animals generate their adhesives. Themes in marine bioadhesion are beginning to emerge as well as evidence for unique aspects within each system. Cross-linking of proteins plays a prominent role in curing the glues. Inorganic reactions and related oxidative chemistry also contribute to formation of the materials. Here we will present a summary of our latest findings on how shellfish stick.

10:40am **MB+BI-MoM8 Investigation of Early Marine Biofouling Events on Model Organic and Polymeric Surfaces**, *G.P. Lopez*, Duke University **INVITED**

Marine biofouling -the accumulation of unwanted biomass on solid structures- is of major concern to maritime pursuits. Biofouling can not only decrease performance of deployed marine equipment, such as ships or oil rigs, but can also result in the transport of invasive species between ports of call. The problem of biofouling is at first a problem of microbial interaction with the water-solid interface; bacteria and diatoms themselves can form detrimental biofilms and can further enable the settlement of macrofoulers. This talk will present studies that seek to shed light on underlying chemical

factors that lead to the initial attachment of metabolically homogenous populations of model marine bacterial populations to well-defined organic and polymeric surfaces. It will also present studies of the use of stimuli-responsive surfaces to allow release of attached marine biofilms.

11:20am **MB+BI-MoM10 The Promise of Fouling Deterrence as a Natural Marine Antifouling Strategy**, *A.S. Mount*, Clemson University
INVITED

Marine biofouling is the unwanted accumulation of bacteria, algae, plants and marine animals on submerged structures including ships. Unfortunately, man's attempts to develop effective antifouling coatings have had deleterious effects on marine life and a less toxic deterrent to cuprous oxide based paints are needed. Larval marine invertebrates have highly developed sensory organs which investigate surfaces prior to settlement, attachment and metamorphosis. We investigated this tactile chemical sense as a potential natural antifouling strategy by covalently linking the neuroendocrine hormone noradrenaline (NA) to poly(hydroxyethylmethacrylate) and to poly(methacrylic acid) polymer surfaces. NA was selected since it is well established that the soluble form it inhibits larval settlement in mollusks, barnacles, bryozoans and annelid tube worms, all of which are major macrofoulers. The NA conjugate polymer surfaces induced oyster cellular apoptosis when compared to negative controls and also deter the settlement of barnacle and oyster larvae. Fouling deterrence is promising strategy in that only treated surfaces would deter biofouling thus eliminating the need to release of any toxic substances into the oceans.

Nanometer-scale Science and Technology

Room: La Cienega - Session NS-MoM

Oxide Based Nanoelectronics

Moderator: C. Nakakura, Sandia National Laboratories

8:40am **NS-MoM2 Oxidation Kinetics of Electron Beam Evaporated Nano Copper Thin Films by Kelvin Probe Measurements**, *A. Subrahmanyam*, IIT Madras, India

Copper is a very good interconnect in microelectronics because it has a high thermal and electrical conductivities and low electromigration resistance. However, the formation of an oxide layer on Cu (even at room temperature) induces trap states at the Cu/Cu oxide interface that can ultimately cause a decrease in its thermal and electrical conductivities, as well as a significant degradation in its interconnection capabilities. These effects become more and more critical when the copper is in nano form for use in ULSI. The partial oxides of copper can also be a very good candidate for plasmonic structures.

Copper exhibits two valences. The size effects and partial oxidation of copper bring significant changes in the electrical resistivity. Thus the surface oxidation kinetics of nano copper are important. In the present communication, pure copper thin films have been prepared by electron beam evaporation technique on cleaned glass substrates at 500 K. The thickness is varied in the range : 20 nm to 300 nm. The electrical resistivity of these films ranges from $5.201 \times 10^{-6} \Omega \text{ cm}$ to $9.206 \times 10^{-6} \Omega \text{ cm}$. The carrier concentration and electron mobility have been evaluated by Hall measurements. In order to follow the surface oxidation kinetics of copper thin films with varying grain sizes exposed to the ambient at 300K, the contact potential (cpd) / work function measurements by Kelvin probe technique have been performed. The increase in the contact potential difference (cpd) indicates the oxidation kinetics of these films.

9:00am **NS-MoM3 Hot-wire Chemical Vapor Deposition of Tungsten Oxide Nanoparticles for Use in Energy Applications**, *C.-P. Li, C.A. Wolden*, Colorado School of Mines, *R. Tenent, A.C. Dillon*, National Renewable Energy Laboratory

Crystalline tungsten oxide nanoparticles were synthesized by hot-wire chemical vapor deposition (HWCVD). These materials are being examined for use in numerous energy related applications including electrochromic windows and fuel cells. It is possible to tune the particle morphology by changing key synthesis parameters including filament temperature, substrate temperature, and oxygen partial pressure. The resulting nanostructures are characterized by a number of techniques including transmission electron microscopy, X-ray diffraction, and Raman spectroscopy. The dependence of nanoparticle size and morphology will be described both as a function of HWCVD synthesis conditions as well as post-deposition annealing treatments. The resulting nanoparticles are suspended in solution and used to form thin films on transparent conducting oxide coated glass substrates using an ultrasonic spray deposition process. Ultrasonic spray coating is a cost effective, scalable deposition process that

offers an excellent route to achieve large-scale implementation of electrochromic films. Important ultrasonic spray variables include substrate temperature, precursor concentration, carrier solvent and other parameters related to solution atomization. The electrochromic properties of these films were characterized by performing cyclic voltammetry in registry with *in situ* measurements of optical transmission. Particular attention is paid to optimizing performance metrics such as coloration efficiency and cycling stability. Using the measurements described above, we will evaluate the important process-structure-performance relationships in these systems.

9:20am **NS-MoM4 Monitoring Charge Storage Processes in Nanoscale Oxides using Electrochemical Scanning Probe Microscopy**, *K.R. Zavadil, J. Huang, P. Lu*, Sandia National Laboratories

Advances in electrochemical energy storage science require the development of new or the refinement of existing *in situ* probes that can be used to establish structure – activity relationships for technologically relevant materials. The drive to develop reversible, high capacity electrodes from nanoscale building blocks creates an additional requirement for high spatial resolution probes to yield information of local structural, compositional, and electronic property changes as a function of the storage state of a material. In this paper, we describe a method for deconstructing a lithium ion battery positive electrode into its basic constituents of ion insertion host particles and a carbon current collector. This model system is then probed in an electrochemical environment using a combination of atomic force microscopy and tunneling spectroscopy to correlate local activity with morphological and electronic configurational changes. Cubic spinel $\text{Li}_{1-x}\text{Mn}_{2-x}\text{O}_4$ nanoparticles are grown on graphite surfaces using vacuum deposition methods. The structure and composition of these particles are determined using transmission electron microscopy and Auger microprobe analysis. The response of these particles to initial de-lithiation, along with subsequent electrochemical cycling, is tracked using scanning probe microscopy techniques in polar aprotic electrolytes (lithium hexafluorophosphate in ethylene carbonate:diethylcarbonate). The relationship between nanoparticle size and reversible ion insertion activity will be a specific focus of this paper.

This work is funded within the Nanostructures for Electrical Energy Storage, an Energy Frontier Research Center funded by the U.S. Department of Energy, Office of Science, Office of Basic Energy Sciences under Award Number DESC0001160. Sandia is a multiprogram laboratory operated by Sandia Corporation, a Lockheed Martin Company, for US DOE's NNSA under contract DE-AC04-94AL85000.

9:40am **NS-MoM5 Tuning Superconductivity at the $\text{LaAlO}_3/\text{SrTiO}_3$ Interface**, *A.D. Caviglia, S. Gariglio, N. Reyren, C. Cancellieri, A. Fête*, University of Geneva, Switzerland, *M. Gabay*, University of Paris-Sud, France, *J.-M. Triscone*, University of Geneva, Switzerland
INVITED

Electronic states with unusual properties can be promoted at interfaces between complex oxides [1]. A striking example is the interface between the band insulators LaAlO_3 and SrTiO_3 , which displays conductivity with high mobility and 2D superconductivity [2,3]. We will discuss recent experiments that revealed the sensitivity of the normal and superconducting state to external electric fields. Using the electrostatic field effect, the phase diagram of the system has been mapped out, revealing a quantum phase transition between a superconducting state and an insulating state [4]. We will also lay out an example of an electronic property arising from the interfacial breaking of inversion symmetry, namely a large spin-orbit interaction, whose magnitude can be modulated by the application of an external electric field [5].

[1] E. Dagotto, *Science* **318**, 1076 (2007)

[2] A. Ohtomo, H. Y. Hwang *Nature* **427**, 423 (2004)

[3] N. Reyren, S. Thiel, A. D. Caviglia, L. F. Kourkoutis, G. Hammerl, C. Richter, C. W. Schneider, T. Kopp, A.-S. Ruetschi, D. Jaccard, M. Gabay, D. A. Muller, J.-M. Triscone, J. Mannhart *Science* **317**, 1196 (2007).

[4] A. D. Caviglia, S. Gariglio, N. Reyren, D. Jaccard, T. Schneider, M. Gabay, S. Thiel, G. Hammerl, J. Mannhart, J.-M. Triscone *Nature* **456**, 624 (2008).

[5] A. D. Caviglia, M. Gabay, S. Gariglio, N. Reyren, C. Cancellieri, J.-M. Triscone *Phys. Rev. Lett.* **104**, 126803 (2010).

10:40am **NS-MoM8 Fabrication and Characterization of Ferroelectric BiFeO₃ Nanocapacitors for Next Generation FeRAMS**, *L.E. Ocola, S. Hong, R. Nath Premnath, W. Li*, Argonne National Laboratory, *S. Jackson*, Illinois Mathematics and Science Academy, *R. Katiyar*, University of Puerto Rico, *O.H. Auciello*, Argonne National Laboratory

11:00am **NS-MoM9 Polarization-Dependent Electron Transport in Thin Films of Uni- and Multiaxial Ferroelectrics**, *P. Maksymovych*, Oak Ridge National Laboratory, *J. Seidel*, University of California, Berkeley, *S. Jesse*, Oak Ridge National Laboratory, *P. Yu, Y.-H. Chu*, University of California, Berkeley, *A.P. Baddorf*, Oak Ridge National Laboratory, *R. Ramesh*, University of California, Berkeley, *S.V. Kalinin*, Oak Ridge National Laboratory

The intrinsic coupling of soft-phonon order parameters and electron transport in ferroic materials can usher a wide range of novel physical phenomena with potential for new applications in information technology, energy harvesting and quantum computing. In this talk we will present local conductivity and piezoresponsive measurements on the surfaces of uniaxial (Pb(Zr_{0.2}Ti_{0.8})O₃) and multiaxial (BiFeO₃) perovskite ferroelectrics, with film thicknesses ranging from 30 nm to 100 nm. Conductive atomic force microscopy revealed that most of these films possesses highly non-linear, and often hysteretic current-voltage characteristics, and in many cases the hystereses could be correlated to local polarization switching induced by the electric field of the AFM tip. In lead zirconate titanate, the large spontaneous polarization produced up to 500-fold enhancement of local conductivity, and the film remained sufficiently conducting in the bias-region significantly smaller than the switching voltage. As a result, this effect can be used for a non-destructive and resistive read-out of the polarization state on length-scales down to 10 nm, implementing a prototypical memory function. Extending the I-V measurements to low-temperatures revealed a strong exponential dependence of the conductivity. We developed a novel analysis scheme, which enabled identifying trap-assisted Fowler-Nordheim tunneling and Poole-Frenkel hopping as two dominant mechanisms behind non-linear I-V curves. Curiously, we have been able to separate the contributions due to interface- and bulk-limited conduction, as well as to visualize spatially-resolved variations due to each transport regime.

We will further discuss the peculiarities of local electron transport through BiFeO₃, and in particular the mechanism behind local conductivity of 10⁹ ferroelastic domain walls. Based on a statistical analysis of I-V curves and simultaneous measurements of local transport and piezoresponse, we suggest that the domain wall is not a static conducting object under a biased tip, but instead that a transient, local and microscopically reversible topological distortion of polarization structure at the wall contributes to enhanced electron transport. In particular, it produces a seminal example of ferroic memristive functionality.

The measurements were conducted at the Center for Nanophase Materials Sciences sponsored at Oak Ridge National Laboratory by the Division of Scientific User Facilities, U.S. DOE.

[1] P. Maksymovych, S. Jesse, P. Yu, R. Ramesh, A. P. Baddorf, S. V. Kalinin,

Science 324 (2009) 1421.

[2] P. Maksymovych, J. Seidel et al, submitted (2010)

11:20am **NS-MoM10 Observation of Unintentionally Incorporated Nitrogen Complexes in Vapor-Liquid-Solid Grown ZnO and GaN Nanowires**, *A. Souidi, Y. Gu*, Washington State University

Semiconductor nanowires have been intensively explored as building blocks for the next-generation electronic and opto-electronic devices. Further advances towards real-world applications require a reliable and precise control of material properties, which, to a large extent, are determined by impurities. Controlled incorporation of functional impurities enables an impurity-engineering approach, whereby novel material properties can be engineered based on the interactions between impurities and the one-dimensional material host. On the other hand, unintentional impurity incorporation can be significant in determining nanowire electronic properties. Therefore, efforts towards identifying impurity species, especially those incorporated unintentionally, as well as understanding their microscopic structures and effects on material properties, are critical to advancing nanowire-based device technologies.

To this end, Raman scattering spectroscopy provides an effective approach to probing impurity incorporation in various materials. When complemented by mass spectrometry studies, this technique can enable unambiguous identifications of impurity species by their vibrational frequencies (i.e. impurity vibrational modes). As impurity vibrational characteristics are sensitive to the surrounding environment, the lattice locations of these impurity atoms can also be determined. Furthermore, the

nanoscale spatial resolution of Raman scattering spectroscopy can provide insightful information on the possible routes of impurity incorporation, shedding light on the relationship between nanowire synthesis conditions and material properties.

In this work, using Raman scattering spectroscopy complemented by mass-selected time-of-flight particle emission techniques, we show the presence of unintentionally incorporated nitrogen complexes (most likely interstitial nitrogen molecules) in ZnO and GaN nanowires grown via the vapor-liquid-solid (VLS) process. Spatially resolved Raman scattering spectra obtained at various locations on single nanowires suggest a possible route of nitrogen incorporations via metal nanocatalysts during the growth. As nitrogen impurities have profound effects on electronic properties of ZnO and GaN, these results have significant implications for current efforts on realizing high-performance opto-electronic device applications based on these nanomaterials. In addition, with the VLS process as one of the most common growth modes for synthesizing semiconductor nanowires, these experimental findings might be relevant for many nanowire systems, signifying the necessity of more studies on unintentional impurity incorporation in these nanomaterials.

Plasma Science and Technology Room: Aztec - Session PS-MoM

Advanced BEOL / Interconnect Etching I

Moderator: K. Kumar, TEL Technology Center America

8:20am **PS-MoM1 Plasma Processes Challenges for Porous SiOCH Patterning in Advanced Interconnects**, *N. Posseme*, CEA-LETI-MINATEC, France, *T. Chevolleau*, CNRS-LTM, France, *T. David*, CEA-LETI-MINATEC, France, *M. Darnon*, CNRS-LTM, France, *F. Bailly*, *R. Bouyssou*, *J. Ducote*, *C. Verove*, STMicroelectronics, France, *O. Joubert*, CNRS-LTM, France

INVITED

The choice of copper/Low-k interconnects architecture is one of the keys for integrated circuits performances, process manufacturability and scalability. Today, the implementation of porous low-k material becomes mandatory in order to minimize the signal propagation delay in the interconnections. In this context, the traditional plasma processes issues (the plasma-induced damages, dimension and profile control, selectivity) and new emerging challenges (sidewalls surface roughness, dielectric wiggling) become the critical points to control the reliability and defectivity.

Based on plasma-surface interaction understanding, the main issues and also the potential solutions will be illustrated through different process architecture using metallic or organic hard masks strategies.

9:00am **PS-MoM3 TiN Selectivity Improvement by DC Voltage Effect in a DC+ Dual Frequency Capacitive Coupled Plasma Etcher**, *M. Nishino*, *M. Honda*, *Y. Ooya*, *R. Shimizu*, Tokyo Electron AT Limited, Japan

Metal Hard Mask (TiN) damascene scheme has been chosen by many logic semiconductor manufacturers for 2x or beyond BEOL processes. Due to issues related to Aspect Ratio, wiggling, and integration with low mechanical stress resistant porous low-k dielectric materials, TiN hard mask has become thinner and less resistant to etch. As the technology node decreases to sub 20nm, Self-Aligned Via (SAV) process will be introduced for MHM dual damascene scheme to maintain Via CD within the confined specifications of the MHM. With this scheme, TiN MHM is exposed to RIE etch twice: once during partial via formation and another in trench etch. Due to such tight process margins, many semiconductor manufacturing companies are focusing on high selective chemistry for TiN during both Via and Trench dielectric etch process. The DC+ Dual frequency etcher is a capacitive coupled plasma etcher with a superimposed DC voltage. This configuration has been proven to be more effective for maintaining TiN hard mask during dielectric etching. A negative DC bias is applied to the upper Si electrode. The Si electrode surface reacts with CF_x radicals from fluorocarbon based plasma and the fluorine component of bulk plasma was reduced. This phenomenon is the interaction between fluorocarbon based plasma and Si electrode which was induced by DC voltage. This paper presents an investigation of TiN hard mask high selective process from this interaction. We measured Ne and Vdc areas of MHM trench process both with and without DC voltage conditions and investigated the direction of Ne/Vdc windows as MHM trench process at first. We evaluated this interaction effect from Ne and Vdc trend with DC voltage and observed that DC voltage did not only acquire higher TiN selectivity to dielectric (maintain TiN thickness) but also reduce TiN HM facet etching rate (control

CD shift) in dielectric etching. This is one of the advantages for the DC+ Dual frequency capacitive coupled plasma etcher .

9:20am **PS-MoM4 RIE Process Challenges in sub 30nm node Trench First Metal Hard Mask Scheme**, *K. Zin, Y. Feurprier, Y. Chiba, H. Kida*, Tokyo Electron Limited, *M. Ishikawa*, Toshiba America Electronic Components, *Y. Mignot*, STMicroelectronics, *Y. Yin*, IBM Systems and Technology Group

As scaling of microelectronic devices approaches sub 30nm nodes, many material and module process challenges in BEOL plasma patterning have been reported. One of the methods that has gained traction over recent years for enabling sub 20nm feature patterning is the Trench First metal Hard Mask (TFmHM) scheme. While this scheme solves or mitigates many challenges that are inherent with Via First Trench Last (VFTL) Scheme, it introduced other dielectric RIE process and hardware challenges. One of the root causes of the former is the fact that all patterns and materials are exposed to plasma at the same time. As such, the simultaneous control of via, trench and chamfer profiles (i.e. Critical Dimensions, depth, taper profile, etc), the need to control selectivity between multiple patterning layer (TiN, TEOS, ULK, Barrier cap, etc), and ULK damage control has become more pertinent in the dielectric etch. As the direct result of such tight process guidelines, the hardware challenges arise and new dimensions in process controls are needed. The prolonged exposure of the TiN to the plasma created the need for more robust production worthy hardware. The required selectivity of the materials necessitate temperature controllable chucks. The more complex patterning techniques require ULK preservation and other uniformity controls. In this paper, the RIE efforts on process controls of the profiles, material selectivity, associated hardware challenges and possible future roadmaps under TFmHM scheme will be discussed.

This work was performed by the Research team at TEL Technology Center America in joint development with IBM Research Alliance Teams in Albany, NY.

9:40am **PS-MoM5 BEOL Double Patterning: Challenges for Etch**, *Y. Yin, J.C. Arnold, M. Colburn, S. Burns, S. Holmes, C. Koay*, IBM Systems and Technology Group, *R. Kim*, Global Foundries, *G. Landie*, STMicroelectronics, *D. Horak*, IBM Systems and Technology Group, *Y. Mignot*, STMicroelectronics, *H. Tomizawa*, Toshiba Corporation

As feature critical dimension (CD) shrinks towards and beyond the 22nm node, limitations of traditional patterning processes become critical. Conventional 193nm immersion lithography is not able to resolve trenches below 40nm half pitch with a single exposure. Patterning vias at appropriate CD and spacing is equally challenging. Extreme ultraviolet (EUV) lithography offers appropriate k1 reduction to solve these problems, but the equipment and metrology infrastructure is not in place to support 15nm node development on a large scale. Thus, much of the industry's attention is being paid to double patterning techniques based on existing 193nm imaging capability. In this paper, we will discuss various double patterning schemes and the associated technical challenges for plasma etching - both for generating patterns with sub-40nm half pitch and for utilizing the resultant masking stacks for BEOL etching. In particular, we will review the issues associated with applying "double-exposure double-etch" sequences, "double-exposure single-etch" approaches, and sidewall image transfer to formation of dual-damascene structures in advanced ultra low-k dielectrics.

This work was performed by the Research Alliance Teams at various IBM Research and Development Facilities.

10:40am **PS-MoM8** , *J. Lee, D.B. Graves*, University of California, Berkeley

The degradation of porous ultra-low-k material, like SiCOH, under plasma processing continues to be a problem in the next generation of integrated-circuit fabrication. Due to exposure with many species during plasma treatment, such as photons, ions, radicals, etc., it is difficult to identify the mechanisms responsible for plasma-induced damage. Some studies have attempted to decouple plasma-generated species in order to study the effect of individual components and possible synergistic effects [1,2]. Using a vacuum beam apparatus with a calibrated VUV lamp and Ar ion gun, we show that 147 nm VUV photons and the presence of molecular O₂ cause a loss of methylated species in SiCOH, creating a silica-like structure on the upper layer of the exposed material. The extent of the VUV/O₂ induced damage as well as the effect of Ar ion bombardment is dependent on the interconnectivity, and thus diffusivity, of the material. In highly interconnected material, Ar⁺ bombardment may seal pores, restricting O₂ diffusion into the film and reducing damage compared to VUV/O₂ alone. The effects of vacuum beam exposures are shown to be comparable to plasma exposures under 'plasma cure' (no energetic ion bombardment) and some rf-biased conditions. Using Fourier-transform infrared (FTIR) spectroscopy and mercury probe measurements, we show that VUV/O₂ exposure causes loss of carbon, resulting in a hydrophilic, damaged layer

that is susceptible to H₂O absorption, which leads to an increased dielectric constant. These results suggest that both VUV photons and high-energy ions can play important roles in the generation of plasma-induced damage.

[1] Jinnai B, Nozawa T, Samukawa S 2008 *J.Vac. Sci. Technol. B* **26** 1926.

[2] Uchida S *et al.* 2008 *J. Appl. Phys.* **103** 073303

11:00am **PS-MoM9 Oxygen Containing Photoresist Ashing Chemistries with Less Damage to Low-k Films**, *R. Gupta, N. Stafford, C. Dussarrat, V. Omarjee*, Air Liquide

Oxygen-based plasma has been traditionally used for ashing patterned photoresist on low dielectric SiCOH (low-k) thin films. During the ashing process, energetic plasma species remove carbon (or CH₃ group) from the exposed regions of the low-k film causing an increase in the dielectric constant of the film. The modified low-k film is also susceptible to water absorption which leads to higher dielectric constant and a degraded performance of the patterned device structure (such as collapsing and loss of critical dimensions) [1,2]. Moreover, higher porosity films will be required in future to achieve even lower dielectric constant and these films will be even more susceptible to plasma damage. Therefore, there was a need for new ashing chemistries to reduce the level of damage to the porous low-k film. A systematic study was performed with mixtures of O₂ and selected molecules such as the standard CO₂, CH₄ or newly thought ashing chemistries. The ashing performance of the selected gas mixtures was compared with pure O₂ for a similar thickness of resist removal. In order to highlight the chemistry effects of gas mixtures, the ashing was performed in similar conditions (i.e. RF power, temperature and pressure) as used for pure O₂ using a CCP RIE chamber.

A parametric study completed with pure O₂ indicates that an increase in RF power and pressure generally leads to an increase in low-k damage. However, flow rate change with constant pressure did not show significant modification in damage characteristics. Damage to low-k film is improved by using gas mixture of the new chemistries and O₂. The Hg-probe dielectric measurements reveal a least increase in dielectric constant with this mixture. Dilute Hydrofluoric (HF) acid tests also reveal the higher etch resistance of low-k films ashed with this mixture. Auger/XPS depth profile metrology is used to obtain elemental profiles of the damaged low-k films. In addition, residual gas analyzer data is being reviewed to understand better the etch gas chemistry to correlate to the damaging behavior of selected chemistries.

References:

Lee et al., Thin Solid Films, 517, (2009)

Zhou et al. AVS 2009.
http://www.avsusergroups.org/pag_pdfs/2009_6zhou.pdf .

11:20am **PS-MoM10 Ultra-low k Integration Challenges and Plasma Etch Solutions For 22nm Node**, *Y. Zhou, Z. Cui, J. Pender, S. Nemani, M. Naik*, Applied Materials Inc.

Higher porosity and new film chemistry are required to drive down k value of porous ultra low k (ULK) dielectrics integrated in advanced BEOL stacks. The challenge of integrating ULK dielectrics is compounded by shrinking dimensions. Taking a tri-layer resist via-first-trench-last integration scheme as an example, as the technology nodes progress, lower k value dielectrics are more prone to ashing damage. The resulting damaged layer accounts for a larger percentage of remaining film, resulting in higher integrated k value. Therefore, ashing improvement achieved for earlier nodes is not sufficient for the 22nm node. A particular ULK integration challenge is via to line spacing. The tight pitches at 22nm leave little tolerance for enlargement of the via size and shape. Previously acceptable levels of profile bowing can now directly lead to shorting. In this work, the challenges of ashing damage and via profile bowing are examined with a via first trench last integration scheme. It is identified that ashing is responsible for the majority of via profile bowing, and the key to reducing via bowing and ashing damage is to improve the ashing selectivity of organic mask to dielectrics. Different approaches are taken to improve ashing selectivity, including the traditional ashing chemistry/plasma optimization and a new pre-ash dielectric passivation scheme. These optimizations have significantly improved both physical and electrical performance.

11:40am **PS-MoM11 Highly Selective Etching of SiOCH over SiC Films by Dual Frequency CCP with DC Bias Superimposed to Upper Electrode**, *T. Yamaguchi, K. Takeda*, Nagoya University, Japan, *C. Koshimizu*, Tokyo Electron AT Limited, Japan, *H. Kondo, K. Ishikawa, M. Sekine, M. Hori*, Nagoya University, Japan

The dual frequency capacitively coupled plasma (CCP) with negative DC bias superimposed to the upper electrode has been proposed to realize high performance etching technologies. Denpoh *et al.* have discussed a mechanism under the DC bias superimposition that secondary electrons generated at the upper electrode transport through a bulk Ar plasma to the counter electrode. Kawamura *et al.* have also discussed about effects of the secondary electrons and a characteristic of the superimposed DC/RF sheath. Since the fluorocarbon (CF) etching plasma with the DC bias has not ever analyzed, we have measured various parameters and discuss the effect of the DC bias on the selective etching of SiOCH over SiC.

We used a CCP reactor for 300 mm wafer. VHF (60 MHz) power and DC bias were simultaneously applied to the upper electrode. RF (13.56 MHz) power was applied to the lower electrode where the samples were placed for etching experiments. A mixture gas of Ar, N₂ and C₄F₈ introduced with flow rates of 800, 100, and 10 sccm, respectively. Pressure was kept at 5.3 Pa.

Bulk plasma parameters such as electron density and CF_x densities were measured when the DC bias changed. The electron density was 1.3×10^{11} cm⁻³ without the DC bias. In contrast, with the bias of -1200V, that gained up to 2.1×10^{11} cm⁻³. This increase can be interpreted that positive ions accelerated by the DC bias bombarded the upper electrode with higher energy and then generated and supply more secondary electrons to the bulk plasma.

Notably, CF₂ radical density was decreased from 2.5 to 1.5×10^{13} cm⁻³ with the DC bias. It is well known that the bulk density depends on the surface loss probability, α , of the CF₂ radical. The α gained by dangling bonds creation by the ion bombardments. As the result, we believed that more fluorine-rich compounds in bulk plasma were lost by the adsorption and reaction on the reactive surfaces. In fact, with the DC bias of -1200V, SiOCH/SiC selectivity was improved significantly to 68 from 5.5 without the DC biasing. This improvement was mainly brought by the etch rate decreasing SiC from 18.5 to 1.3 nm/min while the etch rate of the SiOCH film was maintained almost constant.

Surface analysis results showed that CF polymerized layer was not grew thicker on the SiOCH by such chemical reactions as C + O → CO, C + N + H → HCN. However, in the SiC case, a polymerized layer was relatively thicker because removal reactions were suppressed by lack of F-rich compound. Consequently, the highly selective etching for SiOCH/SiC films was achieved by differentiating the polymerized layer formation.

Advanced Surface Engineering

Room: Cimmaron - Session SE+PS-MoM

Atmospheric Pressure Plasmas

Moderator: H. Barankova, Uppsala University, Sweden

8:20am **SE+PS-MoM1 Plasmajet Atmospheric Pressure Plasma: Effects of H₂ Addition in N₂ Main Plasma Gas on the Optical and Electrical Plasma Characteristics and on Si-based Film Composition**, *D. Debrabandere, X. Vanden Eynde*, CRM (Centre for Research in Metallurgy), Belgium, *F. Reniers*, Université Libre de Bruxelles, Belgium
Si-based coatings were deposited with a cold plasma jet (Plasmabrush® PB1 from Reinhausen Plasma) at atmospheric pressure with nitrogen as main plasma gas and hexamethyldisilazane (HMDSN) as precursor. Effects of hydrogen addition on the plasma characteristics and the coating composition have been evidenced with optical emission spectroscopy (OES), power measurements and XPS in-depth analyses of deposited coatings. The evolution of the nitrogen line (at 315.9 nm) intensity with the applied voltage (ranging from 3.0 kV to 4.5 kV) has a sigmoid shape for the pure nitrogen plasma but it is quite linear with hydrogen addition (up to 3%). Based on OES spectra, the presence of the NH specie in the nitrogen-hydrogen plasmas has been evidenced (around 336.0 nm) but not in the pure nitrogen plasma. The power measured showed the same evolution with the applied voltage as the nitrogen line optical emission intensity: sigmoid shape for the pure nitrogen plasma and straight line for the nitrogen-hydrogen mixture. Although the plasma power is in similar range for both gases (except for applied voltages from 3.2 to 3.6 kV), the nitrogen concentrations in the films as evidenced by XPS were lower with the nitrogen-hydrogen plasma than with the pure nitrogen plasma indicating a chemical effect of the presence of hydrogen in the plasma.

Acknowledgements

Monday Morning, October 18, 2010

The authors would like to thank the Walloon Region (Belgian authorities) for financial support in the framework of a FIRST DOCA program.

8:40am **SE+PS-MoM2 Plasma Polymerization at Atmospheric Pressure: an Environmental Friendly Approach to Synthesize (ultra)hydrophobic, Biocompatible, Hybrid, Barrier or Ion - Exchange Coatings**, *D. Merche, J. Hubert, F. Dabeux, B. Nisol, A. Batan, N. Vandecasteele, F. Reniers*, Université Libre de Bruxelles, Belgium

Plasma treatments are widely used in various applications, such as surface modification (etching, grafting, cross-linking...), cleaning, pollutant removal, and thin films deposition. They are advantageous since they have a low energy cost, they do not release toxic organic solvents into the environment, they are easy to control (the main parameters to control the plasma are the current, voltage, frequency and the gas pressure and composition) and they can be run at room temperature. The plasma polymerization technologies at atmospheric pressure were developed more recently. They allow avoiding expensive vacuum set up, and can be easily implemented in a continuous production line. Two major configurations were used for the deposits: direct (in a DBD system) and remote mode (atmospheric torch). The synthesis conditions (in one step, starting from a liquid precursor, and using an atmospheric pressure plasma) of various types of coatings will be presented and discussed: PEG[1] and PTFE-like coatings [2] (for biocompatible coatings), multifunctional hybrid coatings for barrier properties [3]; sulfonated polystyrene membranes for fuel cell applications [4,5]. The chemical structures of the various coatings were studied by XPS, FTIR and SIMS spectrometry. Correlations between the chemical structure and composition of the coatings and the plasma parameters were established.

[1] B. Nisol, C. Poleunis, P. Bertrand, F. Reniers, "Poly(ethylene glycol) Films Deposited by Atmospheric Pressure Plasma Liquid Deposition and Atmospheric Pressure Plasma-Enhanced Chemical Vapour Deposition: Process, Chemical Composition Analysis and Biocompatibility", Plasma processes and polymers, (2010) under press

[2] N. Vandecasteele, O. Bury, F. Reniers "Process to deposit a fluorinated layer on a support", WO/2009/030763

[3] A. Batan, F. Brusciotti, I. De Graeve, J. Vereecken, M. Wenkin, M. Piens, J.J. Pireaux, F. Reniers and H. Terryn, "Comparison between wet deposition and plasma deposition of silane coatings on aluminium", Progress in Organic Coatings, (2010) under press

[4] D. Merche, C. Poleunis, P. Bertrand, M. Sferrazza, F. Reniers, "Synthesis of PS thin films by means of an atmospheric pressure plasma torch and a dielectric barrier discharge", IEEE trans. on plasma science, 37 (2009), 951-960.

[5] Delphine Merche, Julie Hubert, Claude Poleunis, Patrick Bertrand, Philippe De Keyser, François Reniers "Synthesis of sulfonated PS films using a Dielectric Barrier Discharge high pressure plasma" plasma processes and polymers, submitted

9:00am **SE+PS-MoM3 Surface Treatment of Energy Conversion Device Components by Cold Atmospheric Plasma**, *L. Bardos, H. Barankova*, Uppsala University, Sweden

Advantage of virtually unlimited substrate sizes makes the cold atmospheric plasma very attractive for treatments of surfaces e.g., for improving the lifetime and performances of renewable energy conversion systems. Samples of fiberglass-reinforced vinyl ester with a vinyl ester based gelcoat from windmill turbine blades and steel sheets used for ocean buoys in the linear wave energy converters have been treated by the Fused Hollow Cathode (FHC) and Hybrid Hollow Electrode Activated Discharge (H-HEAD) atmospheric plasma, generated in Ar, Ne and a mixture of air with water. The resulting surface energy has been examined by contact angle measurements. Turbine blade surface becomes hydrophilic after the treatment, sticking of the water droplets is reduced and the surface dries fast after rain, snow or icing. An increased surface tension after plasma treatment of steel relaxes within about 60 min. However, the SEM observations of paint-steel interfaces after an immediate application of the protective paint on treated surfaces have confirmed a considerable improvement of the paint adhesion that can provide better corrosion resistance and lifetime of buoys. Results of tests under different plasma parameters are presented and discussed.

9:20am **SE+PS-MoM4 Smooth and Self-Similar SiO₂-like Layers on Polymers Synthesized using Dielectric Barrier Discharge Assisted CVD at Atmospheric Pressure**, *P. Antony Premkumar, S.A. Starostin*, Eindhoven University of Technology, Netherlands, *H. de Vries*, FUJIFILM Manufacturing Europe BV, Netherlands, *M. Creatore, M.C.M. van de Sanden*, Eindhoven University of Technology, Netherlands

High quality inorganic oxide thin films applied over polymers are of significant technological interest in the field of optics, vapour barrier

coatings, microelectronics, flat panel displays and protective coatings. The layers prepared by PECVD at atmospheric pressure (AP-PECVD) is considered as a promising technology due to its economical and technological advantages. Despite these benefits, the major challenge of this coating technology is the usually reported poor film quality which arises mainly due to the intrinsic instabilities of the plasma as well as from the complex reactions of the deposition process.

In this investigation, we demonstrate the remarkable SiO_x film properties synthesized using AP-PECVD in a roll-to-roll configuration [1]. The depositions were performed, in He free gas mixtures, using uniform glow-like dielectric barrier discharge as the electrical sources to assist CVD at atmospheric pressure. As a generic characteristic of the developed technology, it is observed that, irrespective of precursors (TEOS or HMDSO) and process gases (Ar, N₂ or air) employed, the films are smooth, both in short and long range length scales, and of near stoichiometric silica with very low carbon content (<2%). Detailed AFM morphology description and surface statistical analysis on SiO₂ dynamics showed that no dynamical film roughening in growth front and lateral directions are observed and the synthesized layers (~350 nm) follow the topology of the substrate, mimicking its surface texture characteristics. The value of the roughness exponent (α), close to 1, determined from the height-height correlation function analysis, indicates a self-similar scaling of the SiO₂-like film morphology with the polymer substrate. The films are uniform with no defects or particle being incorporated during the deposition process and exhibit excellent barrier performances towards O₂ and H₂O permeation.

[1] P. Antony Premkumar, S.A. Starostin, M. Creatore, H. de Vries, R.M.J. Paffen, P.M. Koenraad, M.C.M. van de Sanden, *Plasma. Proc. Polym.* (2010) In Press

9:40am **SE+PS-MoM5 Atmospheric-pressure Plasma Activation of Silicon and Glass Surfaces for Low-Temperature Direct Bonding.** C.-P. Klages, M. Eichler, Fraunhofer Institute for Surface Engineering and Thin Films (IST), Germany, B. Michel, Technische Universität Braunschweig / Institut für Oberflächentechnik (IOT), Germany **INVITED**

Low-temperature direct bonding of silicon wafers has been industrially established for several years now. To achieve a lowered annealing temperature required for sufficient bond strength from about 1000 °C to a few 100 °C only, low-pressure plasma treatment came into use more than 20 years ago. As shown at Fraunhofer IST more recently, also plasma activation at 1 bar is capable of reducing required annealing temperatures to around 100 °C while still achieving bond energies 2 to 3 times higher compared to RCA-cleaned reference wafer pairs.

Many questions concerning the key effects, responsible for lowering the required annealing temperature, are still under investigation, especially for the attractive atmospheric-pressure method. At IOT and IST, the effects of dielectric barrier discharge (DBD) treatments performed under a wide range of conditions at 1 bar pressure on the properties of native or thermal SiO₂ layer on silicon wafers and on the achieved bond strength have been investigated in the recent years. The presentation will give an overview of the results from these investigations which were obtained using several surface analytical methods.

Recently, main interest has shifted from silicon to other materials and to alternative atmospheric-pressure plasma processes. With special gases used for the plasma activation, an increased bonding strength is also achievable for borosilicate glass bonding. However, while the mechanism of bonding enhancement in case of native oxide layers on Si can clearly be attributed to a surprisingly rapid growth of a porous oxide film, a convincing explanation for the effects achieved with glasses is still missing.

A common attribute of surface activation by DBD and low-pressure plasmas is a direct access of the plasma to the surface. By contrast, corona discharge makes use of the inhomogeneity of the electric field near a needle tip. Plasma zone and wafer are spatially separated and the electric field stress at the wafer surface is greatly reduced. Promising results of corona discharge treatment as an activation method for low-temperature wafer bonding have been obtained, indicating that relatively stable charged species play an important role. On the other hand, excimer UV radiation was virtually ineffective.

New insights into the kinetics of silanol condensation were also made possible by continuous measurements of the bonding strength *in situ* during annealing. Results of these studies show that the bond strength increase can be attributed to the expansion of bonded micro regions instead of statistical formation of siloxane bridges between the wafers.

10:40am **SE+PS-MoM8 Atmospheric Pressure Microcavity Plasma Arrays for Spatial Surface Modification.** R.D. Short, S. Al-Bataineh, E. Szili, C. Priest, Ph. Gruner, University of South Australia, E. Anglin, Flinders University, Australia, H.J. Griesser, University of South Australia, N. Voelcker, Flinders University, Australia, D. Steele, University of South Australia

Microplasmas, a rapidly growing technology, are normally operated at or near atmospheric pressure with dimensions ranging from microns to millimetres. [1] We are developing this technology for surface modification without using a physical mask or additional processing steps to increase the versatility and cost-effectiveness of the technology. Micropatterning of various chemistries and biomolecules is seen as vital to the successful development of new and emerging technologies, such as microfluidics and high throughput cell screening tools. [1, 2] In this presentation, the fabrication process of microcavity plasma array devices will be introduced, followed by a demonstration of the utility of these devices for generating specially well-controlled micron-scale surface treatment and polymer deposition. Two issues regarding the utility of these devices for localised surface modification were investigated: 1) Can these devices be used to modify a surface with micron-scale features without having the substrate pressed against the array? 2) Can this be achieved with control over diffusion of the plasma reactive components? We explored this through XPS imaging and small spot analysis, which gave insights into the surface chemistry of the micron-scale modified areas. Finally, we demonstrate the utility of microcavity plasma array surface engineering in the development of biological cell arrays.

1. Iza, F., et al., *Microplasmas: Sources, particle kinetics, and biomedical applications*. Plasma Processes and Polymers,

2008, 5(4): p. 322-344.

2. Klages, C.-P., et al., *Microplasma-Based Treatment of Inner Surfaces in Microfluidic Devices*. Contributions to Plasma

Physics, 2007, 47(1-2): p. 49-56.

11:00am **SE+PS-MoM9 Electrical Characterization of Dielectric Barrier Discharges of Various Electrode Geometries.** V. Rodriguez-Santiago, J.K. Hirvonen, B.E. Stein, U.S. Army Research Laboratory, D.R. Boris, S.G. Walton, U.S. Naval Research Laboratory, D.D. Pappas, U.S. Army Research Laboratory

The increased use of atmospheric-pressure plasmas for the surface modification of materials has drawn particular interest in understanding the basic phenomena underlying dielectric barrier discharges (DBDs). One of the main advantages of using DBDs is the generation of cold, non-equilibrium plasma at atmospheric pressure conditions without the need of vacuum equipment. A typical DBD setup consists of one or both electrodes covered with a dielectric material with a sufficiently high applied voltage to ignite the plasma. The plasma can be either filamentary or spatially uniform depending on parameters such as dielectric and electrode material, interelectrode gap, carrier and reactive gas mixture, and the type of applied voltage among others. Another important aspect is the geometry of the electrode assembly, which will determine the electric field configuration and thus influence the discharge characteristics.

In this study, we investigate the electrical characteristics of He and He-O₂ dielectric barrier discharges using a pulsed, sinusoidal signal in the kHz frequency range with a (1-10) kV peak-to-peak amplitude. Full characterization of the plasma will be carried out using rod, sheet and planar electrode assemblies, while materials of various dielectric constants such as mica, quartz and polyethylene will be employed. Voltage, current and power distributions will be analyzed aiming to identify the optimal electrode geometries and dielectric materials needed to produce uniform and large scale plasmas for materials processing.

11:20am **SE+PS-MoM10 ICP Atmospheric Plasma Torch with Saddle-like Antennas for Yttrium Oxide Nanocoating.** Y. Glukhoy, H. Schiesser, American Advanced Ion Beam Inc.

ICP atmospheric plasma torch is the most powerful electrode-less heat generating system with relatively small dimensions and a reasonable consumption of power and gases. It serves as an universal tool for nanocoating of surfaces where the gaseous, liquid as well as powder precursors can be used. A total melting, evaporation and plasma chemical reaction of precursor can be achieved with torches that provide a sufficient residential time a high temperature plasma fluid. But a conventional torches are supplied by a coil inductor pinching this fluid due to an axial magnetic field. In result, a high temperature area is reduced and a sufficient part of precursor is converted in dust. In order to broaden and lengthen this area for a sufficient increasing of a residential time the inductor has been replaced with two saddle-like ICP antennas with the different frequencies, i.e. 27.12

and 13.56 MHz. Each antenna comprises two or more spiral coils in a mirror position and in series or parallel connection. These coils are distributed with an angular uniformity and envelop a quartz tube of a plasma reactor. Such a non-axisymmetric design allows generation of a transversal RF field directed normally to axis of this reactor. But a plasma fluid is fixed on the axis due to buoyancy in the centrifugal force field created by a swirling injection of a discharge and sheath gases. However, the temperature gradient and a pressure drop caused by a cold carrier gas injected with a high velocity axially into a plasma bulk generate turbulence disrupting and distorting the plasma fluid. In result, a heat transfer from plasma to the wall is increased, becomes non-uniform and creates a hot spot melting the quartz wall. Mechanisms of the non-axisymmetric coupling, torch generation, contribution of different factors in distortion of the plasma fluid and method elimination of the hot spot have been investigated. In addition, we will discuss recent effort to extend applications such a torch in different areas including fabrication of yttrium oxide anti-corrosive nanocoating of focusing rings used in plasma etching processes in semiconductor industry.

1. Y.Glukhoy, I. Ivanov RF Atmospheric Plasma Systems for Nanopowder Production and Deposition of Nanocrystallines. AVS 53rd International Symposium, San Francisco, California, November, 2006 CA, USA.

2. Y.Glukhoy. Saddle-like ICP Antenna for RF Atmospheric Plasma Processes. AVS 56th International Symposium, San Jose, California, November, 2009 CA, USA.

Surface Science

Room: Picuris - Session SS1-MoM

Reactivity and Selectivity on Catalytic Surfaces

Moderator: C.T. Campbell, University of Washington

8:20am **SS1-MoM1 Structure and Reactivity of Alkyl Ethers Adsorbed on Hydroxylated CeO₂(111) Model Catalysts.** *F.C. Calaza*, Oak Ridge National Laboratory, *T.-L. Chen*, Brookhaven National Laboratory, *D.R. Mullins*, *S.H. Overbury*, Oak Ridge National Laboratory

The study of adsorption and reactivity of oxygenated molecules on model oxide catalysts is of great interest to gain a better understanding of the mechanism of industrial reactions. Cerium oxide is commonly used in three-way auto exhaust and WGS catalysts. Our experimental design is intended to find the conditions where UHV experiments could mimic the real catalytic processes and from these results explain the reaction pathway from the atomistic level.

From the surface science point of view, previous studies of alcohols, ketones and aldehydes adsorbed on the surface of cerium oxide model catalysts have shown a variety of pathways for decomposition and reactivity. In the present work we have examined these pathways for two ethers, diethyl ether (DEE) and dimethyl ether (DME). Both ethers adsorb on fully oxidized CeO₂(111) and highly reduced CeOx(111) under UHV conditions but only at low temperature (~150 K) and they do not decompose. If the catalyst surface is pre-covered by hydroxyls, by adsorbing water at room temperature on the reduced CeOx(111) surface, then the adsorption geometry of the ether on this hydroxylated surface changes, indicating interaction with OH groups. Regarding their reactivity towards decomposition, the two ethers behave differently when exposed to hydroxylated CeOx(111) at 300-400 K. In the case of DEE, this molecule promptly reacts by breaking the C-O bond presenting a very interesting chemistry. By means of Reflection Absorption Infrared Spectroscopy (RAIRS) and soft X-Ray Photoelectron Spectroscopy (sXPS), we could detect ethoxide and possibly carboxylate species as adsorbed intermediates for the reaction. However, when the hydroxylated CeOx(111) is exposed to DME at same conditions, the ether shows no reactivity, indicating the importance of H on a carbon atom β to oxygen. Possible explanations for the role of hydroxyls in helping break the C-O bond of ether molecules will be given.

Research sponsored by the Division of Chemical Sciences, Geosciences, and Biosciences, Office of Basic Energy Sciences, US Department of Energy, under contract DE-AC05-00OR22725 with Oak Ridge National Laboratory, managed and operated by UT-Battelle, LLC. Use of the National Synchrotron Light Source, Brookhaven National Laboratory, was supported by the US Department of Energy, Office of Science, Office of Basic Energy Sciences, under Contract No. DE-AC02-98CH10886.

8:40am **SS1-MoM2 Adsorption and Activation of n-alkanes on a PdO(101) Thin Film.** *J.F. Weaver*, *C. Hakanoglu*, *J.A. Hinojosa, Jr.*, *A. Antony*, *J.M. Hawkins*, *A. Asthagiri*, University of Florida

The formation of palladium oxide (PdO) is thought to be responsible for the exceptional activity of supported Pd catalysts toward the complete oxidation of alkanes under oxygen-rich conditions. In this talk, I will discuss our recent investigations of the adsorption and activation of n-alkanes on a PdO(101) thin film that is prepared by oxidizing Pd(111) in ultrahigh vacuum (UHV) using an oxygen atom beam. We find that alkanes adsorb relatively strongly on the PdO(101) surface by forming σ -complexes along the rows of coordinatively unsaturated Pd atoms. The formation of σ -complexes causes the alkane binding energies on PdO(101) to exceed those of alkanes physisorbed on Pd(111). We also find that the alkane σ -complexes on PdO(101) act as precursors for initial C-H bond cleavage; propane and n-butane undergo facile C-H bond cleavage below about 215 K in UHV. Finally, I will discuss density functional theory calculations which show that dative bonding between the alkane and σ -Pd atoms weakens the coordinated C-H bonds, thereby lowering energy barriers for C-H bond scission by as much as 100 kJ/mol. These findings provide insights for understanding the role of molecularly chemisorbed precursors in the initial activation of alkanes on PdO(101) and possibly other transition-metal oxide surfaces.

9:00am **SS1-MoM3 Stereo and Enantioselectivity in Surface Reactions.** *F. Zaera*, University of California, Riverside **INVITED**

Achieving high selectivity is arguably the main upcoming challenge in heterogeneous catalysis for the 21st century. In complex reaction with competing parallel pathways, small changes in the relative values of the different activation energies are sufficient to switch the selectivity of those processes from one product to another. We in our laboratory have been carrying out mechanistic studies on the conversion of hydrocarbons on model metal surfaces to try to identify the key factors that control such selectivity. In this talk we will present a couple of examples of increasing subtlety from that work. In the first, we will discuss a reaction involving a C=C double bond isomerization, in particular cis-trans isomerization reactions. The second example will be focused on issues of bestowing enantioselectivity on solid surfaces by using cinchona alkaloid modifiers. In both cases, it will be shown how the mechanistic information obtained from surface-science studies can be extended to design more selective real catalysts.

9:40am **SS1-MoM5 Enantioselective Explosions on Chiral Surfaces.** *A.J. Gellman*, *Y. Huang*, *F. Xu*, *V.V. Pushkarev*, Carnegie Mellon University

The high Miller index surfaces of single crystal metals have chiral structures and interact enantiospecifically with chiral adsorbates. The enantiospecificity of surface reaction kinetics is dictated by the enantiospecificity of surface reaction energetics but can also be influenced by reaction order. Recently, it has been shown that tartaric acid decomposes with explosive reaction kinetics on Cu(110) surfaces. Tartaric acid is chiral and on naturally chiral Cu surfaces such as Cu(643), Cu(653), Cu(17,5,1), and Cu(531) the non-linear nature of the reaction kinetics leads to extremely high enantiospecificity. The explosive reaction kinetics originate with the need for empty surface sites for the decomposition process. At high coverages of tartaric acid the limited availability of empty sites constrains the decomposition process. Once nucleated, however, the reaction proceeds autocatalytically and occurs over a very narrow temperature range during heating. The decomposition kinetics of R,R- and S,S-tartaric acid depend on the handedness of the Cu substrate and the decomposition features observed during temperature programmed reaction spectroscopy are completely resolved. Peak enantiospecificities in the decomposition reaction rates can reach a factor of fifty.

10:00am **SS1-MoM6 C-H Bond Activation of Light Alkanes on Pt(111): Dissociative Sticking Coefficients, Evans-Polanyi Relation, and Gas-Surface Energy Transfer.** *G. Cushing*, *J. Navin*, *S. Donald*, *I. Harrison*, University of Virginia

Effusive molecular beam experiments were used to measure alkane dissociative sticking coefficients, $S(T_g, T_s)$, for which the impinging gas temperature, T_g , and surface temperature, T_s , could be independently varied. The 500-1000 K temperature range primarily examined should be relevant to heterogeneously catalyzed industrial processes such as the steam reforming of alkanes. Methane, ethane, and propane all showed increasing dissociative sticking as either T_g or T_s was increased – indicative of activated dissociation reactions. Effusive beam experiments with gas impinging along the surface normal and $T_g = T_s = T$ determined $S_n(T)$, a close approximation and formal upper bound to the thermal dissociative sticking coefficient, $S(T)$, appropriate to reaction with a thermal ambient gas. Activation energies determined from $S_n(T)$ for methane, ethane, and propane are $E_a = 58 \text{ kJ mol}^{-1}$, 43 kJ mol^{-1} , and 34 kJ mol^{-1} , respectively. An

Evans-Polanyi plot of E_a for alkane dissociative chemisorption versus the alkane thermal desorption energy, E_d , is linear with a slope of -0.94. Assuming that the alkane E_d serves as a good approximation to the Van der Waals stabilization of the chemisorbed alkyl radical product of dissociative chemisorption, the slope of the Evans-Polanyi plot indicates a late transition state for alkane dissociative chemisorption on Pt(111). A microcanonical unimolecular rate theory model of dissociative chemisorption was used to model the effusive molecular beam experiments. Explicit accounting of the gas-surface energy transfer for the non-equilibrium experiments became increasingly important as the alkane size was increased. A simple exponential down model of the molecule/phonon collision step size distribution with a mean energy down parameter of $\alpha = 350 \text{ cm}^{-1}$ for ethane, and $\alpha = 1400 \text{ cm}^{-1}$ for propane, sufficed to provide a good description of the $S_n(T_g, T_s)$ data.

10:40am **SS1-MoM8 Heat of Formation of Adsorbed Methoxy on Pt(111) by Adsorption Microcalorimetry**, *E. Karp, M. Crowe, C.T. Campbell*, University of Washington

The heat of adsorption of methanol on clean and oxygen pre-covered Pt(111) surfaces was measured in the temperature range of 100 to 160 K using Single Crystal Adsorption Calorimetry (SCAC). Our ultrahigh vacuum calorimeter, which also includes capabilities for AES, LEED and ISS, routinely achieves pulse-to-pulse standard deviations in heat measurements of 0.5 kJ/mol using methanol pulses containing only 0.02 ML. Averaging 8 runs reduces this to below 0.2 kJ/mol. These measurements provide the heat of formation of methoxy, an important intermediate in several catalytic reactions, including methanol reforming for highly pure H₂. Above 125K, methanol is known to react with pre adsorbed oxygen adatoms to form methoxy and co-adsorbed OH (Akhter et al., Surf. Sci., 167, 1986, 101):

$\text{CH}_3\text{OH}(\text{g}) + \text{Oads} \rightarrow \text{CH}_3\text{Oads} + \text{OHads}$, at $125\text{K} < T < 160 \text{ K}$.

Recently our group experimentally determined the heat of formation of OHads on Pt(111) to be -226.8 kJ/mol, using this value we have determined the heat of formation of adsorbed methoxy and compared this value to theoretical DFT work. Heats of adsorption of methanol were also measured on clean Pt(111) at 100K, as well as on the amorphous methanol multilayer, and compared to prior TPD measurements.

11:00am **SS1-MoM9 Interaction of Ethylene and Nitrogen Atoms on the Pt (111) Surface**, *J. Yin, R. Meyer, M. Trenary*, University of Illinois at Chicago

The selective catalytic reduction (SCR) of NO_x by hydrocarbons on noble metals is critically important to the implementation of leaner burning more fuel efficient processes. Understanding the reaction mechanisms and pathways is essential for designing an effective catalytic system. As one small part of this effort, we focus on the interaction of nitrogen atoms and simple alkenes such as ethylene on the Pt(111) surface under UHV conditions in an effort to understand the potential intermediates in NO_x reduction. The adsorption of ethylene on a nitrogen pre-covered Pt(111) surface has been investigated using reflection absorption infrared spectroscopy (RAIRS) and thermal desorption spectroscopy (TDS) as well as density functional theory calculations. Three interesting observations have been made. First, we observed the presence of π -bonded ethylene below 220 K, indicating a switch in the preferred binding site for ethylene on N-Pt (111) as compared to the clean surface. Second, above 500 K, CN coupling occurs as indicated by the desorption of HCN and the identification of CNH₂ with RAIRS. Third, the formation of ammonia is observed through NH₃ desorption as well as by observation of the δ_s (NH₃) mode of NH₃ at $\sim 1170 \text{ cm}^{-1}$ with RAIRS. The appearance of ammonia is believed to be the result of a reaction between N atoms (or NH) with coadsorbed ethylidyne.

11:20am **SS1-MoM10**, *D.J. Stacchiola, S.D. Senanayake, J. Hrbek, J.A. Rodriguez*, Brookhaven National Laboratory

The water-gas shift (WGS) is an important reaction for the production of molecular H₂ from CO and H₂O. An inverse CeO_x/Au(1 1 1) catalyst exhibits a very good WGS activity, better than that of copper surfaces or Cu nanoparticles dispersed on a ZnO substrate which model current WGS industrial catalysts. In this work we report on intermediates likely to arise during the CO + H₂O reaction over CeO_x/Au(1 1 1) using soft X-ray photoemission (sXPS) and near-edge X-ray absorption fine structure (NEXAFS). Several potential intermediates including formates (HCOO), carbonates (CO₃) and carboxylates (HOCO) are considered. Adsorption of HCOOH and CO₂ is used to create both HCOO and CO₃ on the CeO_x/Au(1 1 1) surface, respectively. HCOO appears to have greater stability with desorption temperatures up to 600 K while CO₃ only survives on the surface up to 300 K. On the CeO_x/Au(1 1 1) catalysts, the presence of Ce³⁺ leads to the dissociation of H₂O to give OH groups. We demonstrate experimentally

that the OH species are stable on the surface up to 600 K and interact with CO to yield weakly bound intermediates. When there is an abundance of Ce⁴⁺, the OH concentration is diminished and the likely intermediates are carbonates. As the surface defects are increased and the Ce³⁺/Ce⁴⁺ ratio grows, the OH concentration also grows and both carbonate and formate species are observed on the surface after dosing CO to H₂O/CeO_x/Au(1 1 1). The addition of ceria nanoparticles to Au(1 1 1) is essential to generate an active WGS catalyst and to increase the production and stability of key reaction intermediates (OH, HCOO and CO₃).

11:40am **SS1-MoM11 Reactivity of CO towards Nanocrystals and Continuous Films of α -Fe₂O₃ on Au(111) at Ambient Pressure: Implications for the Water-Gas Shift Reaction**, *X. Deng, J. Lee, C. Wang, C. Matranga*, National Energy Technology Laboratory (NETL), F. Aksoy, Z. Liu, Lawrence Berkeley National Laboratory

Surface Science

Room: Santa Ana - Session SS2+EM-MoM

Semiconductor Surfaces and Interfaces

Moderator: J. Millunchick, University of Michigan, Ann Arbor

8:20am **SS2+EM-MoM1 Spontaneous Microfaceting and Pyramidal Growth during Si(100) Etching**, *M.F. Faggin, A. Gupta, M.A. Hines*, Cornell University

The spontaneous, etching-induced transformation of an initially flat Si(100) surface to a completely nanofaceted morphology consisting of overlapping pyramidal hillocks has been observed using a combination of morphological and spectroscopic probes and modeled using a fully-atomistic kinetic Monte Carlo (KMC) simulator of Si(100) etching. A novel silicon etchant has been developed that catalyzes the complete chemical transformation of a Si(100) surface into H-terminated Si{111} and Si{110} nanofacets. This finding was confirmed by infrared absorption spectroscopy, atomic force microscopy (AFM), and scanning electron microscopy (SEM). The formation of pyramidal hillocks is highly reproducible and occurs on a time scale of several hours, enabling detailed studies of initial hillock formation and subsequent growth. The formation of microfaceted pyramidal hillocks during etching of Si(100) has previously been attributed to local masking on the surface by deposited impurities, etch products or gas bubbles. These mechanisms assume that an adsorbed impurity or gas bubble decorates the apex of every pyramid. Our atomistic simulations uncovered a second mechanism, one that is *intrinsic* to the etchant and that generates dynamically self-propagating pyramidal structures. Attempts to distinguish between these two mechanisms through rational modifications of the etchant chemistry will be described. For example, the kinetics of pyramidal growth were followed spectroscopically, enabling quantitative assessment of the effects of chemical additives. These observations are more than an intellectual curiosity, as the silicon solar cell industry is actively searching for inexpensive, environmentally-friendly means of pyramidally texturing Si(100) surfaces to reduce reflection losses. Conversely, in microfabricated devices, suppression of pyramid formation is critical to high-yield manufacturing processes. An understanding of the hillock formation process may lead to the rational design of better etchants.

8:40am **SS2+EM-MoM2 Selective Ablation of Xe on Silicon Surfaces: MD Simulation and Experimental Laser Patterning**, *O. Stein, M. Asscher*, The Hebrew University in Jerusalem, Israel

Laser induced ablation of multilayer Xe on Si has been studied employing molecular dynamics (MD) simulations. 5nsec long laser pulse at $\lambda = 337\text{nm}$ was applied to a Xe slab at thicknesses of 16 32 and 40ML (7744, 15488, 19360 atoms, respectively) adsorbed on top of a 8 layers 5408 atoms Si slab. Evaporative and explosive ablation thresholds were identified at absorbed laser power of 12 and 16MW/cm² which corresponds to surface temperature rise of 500 and 658K, respectively. Selective ablation was studied, where only a fraction of the lateral dimension of the computation cell was actually ablated. Extremely strong lateral dissipation among the Xe layers, has led the ablation threshold to shift to higher laser power as the fraction of heated area shrinks. Heated fraction (HF) less than 10% results in practically no ablation at laser power below substrate damage threshold. The MD studies were assessed and verified by experimental laser ablation measurements. A 10nsec Nd:YAG laser pulse operating at $\lambda = 532\text{nm}$ was employed. It was found that for 80 and 160ML Xe layer thickness, full ablation was reached at laser power of 6.9 and 8.4MW/cm² which corresponds to surface temperature rise of 180 and 220K respectively. Line-edge profile resulting from fractional laser induce desorption- coverage grating formation followed by metallic lift-off experiments were compared

to the MD simulations of selective ablation, revealing a remarkable similarity.

Key words: Molecular Dynamics Simulations, Laser Ablation, adsorbed Xe on Si, Coverage Grating.

9:00am **SS2+EM-MoM3 Tuning Properties of Thin Films by Aminofunctionalization**, *A.V. Teplakov*, University of Delaware

Surfaces and interfaces play an important role in development of modern microelectronics, optoelectronics, biosensing and other fields. This work will describe the approaches to tune the properties of interfaces, surfaces, and subsurface layers of participating materials by aminofunctionalization. The amino-groups of a general formula NH_2 have been used in our group to control surface reactions on semiconductor surfaces, to promote deposition schemes on surfaces of thin solid diffusion barrier films, and to provide a reliable surface sites for biofunctionalization of self-assembled monolayers. In all of these cases, the reactivity of the amino-group can be designed to fit the required application. We will use selected temperature regimes, alkyl, aryl, and other substituents to alter the reactivity of amino-terminated surfaces and to reversibly tune the properties of surface and subsurface layers in thin solid films. Infrared spectroscopy was used to determine the chemical nature of the surface termination, X-ray photoelectron spectroscopy was applied to discover the stability of the surfaces and interfaces produced and to assist in assessing the chemical state of nitrogen-containing functional groups, microscopic techniques, including atomic force microscopy and transmission electron microscopy were employed to uncover the topographic properties and structure of the films based on titanium carbonitride that serve as a diffusion barrier and of the self-assembled amino-terminated layers utilized as platforms for biosensing devices. The preparation, structure, reactivity, and stability of these aminofunctionalized surfaces and interfaces will be discussed.

9:20am **SS2+EM-MoM4 Helium Atom Diffraction Measurements of the Surface Structure and Vibrational Dynamics of CH_3 -Si(111) and CD_3 -Si(111) Surfaces**, *J.S. Becker, R.D. Brown*, University of Chicago, *E. Johansson, N.S. Lewis*, California Institute of Technology, *S.J. Sibener*, University of Chicago

The surface structure and vibrational dynamics of CH_3 -Si(111) and CD_3 -Si(111) surfaces were measured using helium atom diffraction. The elastic diffraction patterns exhibited a lattice constant of 3.82 Å, in accordance with the spacing of the silicon underlayer. The high quality of the observed diffraction patterns indicates a high degree of long-range ordering for this novel interface. The vibrational dynamics were investigated by measurement of the Debye-Waller decay of the elastic diffraction peaks as the surface temperature was increased. The angular dependence of the specular ($\theta_i = \theta_r$) decay revealed perpendicular mean-square displacements and He-surface well depths of $1.0 \cdot 10^{-5} \text{ \AA}^2 \text{ K}^{-1}$ and 7.5 meV for the CH_3 -Si(111) surface and $1.2 \cdot 10^{-5} \text{ \AA}^2 \text{ K}^{-1}$ and 6.0 meV for the CD_3 -Si(111) surface. Effective surface Debye temperatures of 983 K for CH_3 and 824 K for CD_3 were calculated. These unusually large Debye temperatures suggest that collisional energy accommodation at the surface occurs primarily through Si-C local mode. The parallel mean-square displacements were $4.3 \cdot 10^{-4} \text{ \AA}^2 \text{ K}^{-1}$ and $4.5 \cdot 10^{-4} \text{ \AA}^2 \text{ K}^{-1}$ for CH_3 - and CD_3 -Si(111) surfaces, respectively. The increase in thermal motion is consistent with interaction between the helium atoms and Si- CH_3 bending modes. These experiments yield new information on the dynamical properties of these robust and technologically interesting semiconductor interfaces.

9:40am **SS2+EM-MoM5 Comprehensive Descriptions of Surface Atomic Structure**, *J.C. Thomas, J. Mirecki Millunchick*, The University of Michigan, Ann Arbor, *N.A. Modine*, Sandia National Laboratories, *A. Van der Ven*, The University of Michigan, Ann Arbor

INVITED

Comprehensive descriptions of surface atomic structure have been developed over the years for a wide range of metals and covalent crystals, but this understanding has typically been obtained only after extensive trial and error. Unfortunately, experimental and theoretical characterization of surfaces is complicated significantly in systems that can exhibit metastable surface reconstructions or in alloy systems, where atomic size mismatch and lattice mismatch strains play an important role and can give rise to phase coexistence. Clearly, a systematic and rigorous approach to determining surface structure is needed in order to explore surface phenomena in alloy systems or away from equilibrium. We have developed an approach that uses prior knowledge about the surface atomic structure of a pure system, along with first principles energy calculations and statistical mechanical methods, to systematically and efficiently explore new ground-state and near-stable surface reconstructions, finite temperature behavior, and alloying effects. We describe the automated generation of III-V (001) surface reconstruction candidates in the group V-rich regime and discuss how our approach is used to study the complex surface structure of the $\text{In}_{1-x}\text{Ga}_x\text{As}$ (001) alloy, which exhibits nanoscale coexistence domains and

where an unexplained ($\sqrt{3} \times \sqrt{3}$) reconstruction is observed over a wide range of conditions.

10:40am **SS2+EM-MoM8 The Structure of Metal-Rich (001) Surfaces of InAs and InSb**, *J.J. Kolodziej*, Jagiellonian University, Poland

Based on electron diffraction experimental observations the reconstructions of the indium-rich indium antimonide and indium arsenide (001) surfaces are assigned as $c(8 \times 2)$ or closely related $c(8 \times 2)/(4 \times 2)$. At room temperature scanning tunneling and atomic force microscopy studies also evidence highly symmetric $c(8 \times 2)$ or (4×2) reconstructions. However, microscopic studies done at cryogenic temperatures indicate lowering of the surface structures symmetry from $c2mm/p2mm$ to $p2$, structural domains, disorder and fluctuations. In the present paper we will show that the surfaces are well described by a so called zeta-family models with certain atomic rows occupied slightly above 50%. Atomic vacancies are confined to these rows and rapidly fluctuate at room temperature. Averaging effects cause that experiments done at elevated temperatures using slow methods evidence symmetric structures. In contrast, at low temperatures, the vacancies stabilize to form regular double-period structures along the rows, but this spontaneously leads to the complete surface structure having only $p2$ symmetry group, structural domains and partial disorder on the surface. We have also identified a variety of local structures appearing at the domain walls. This complex surface structure is inherent to the thermodynamic equilibrium of the system as indicated by failed attempts to increase surface indium content by adsorption of In atoms from a gas phase. Density functional theory calculations confirm that the new surface structure is a minimum energy configuration at fixed stoichiometry. Simulated scanning tunneling microscopy images confirm proposed model of the structure.

11:00am **SS2+EM-MoM9 Monolayer Passivation of Ge(100) Surface via Nitridation and Oxidation**, *J.S. Lee, S. Bishop, T. Kaufman-Osborn, A.C. Kummel*, University of California at San Diego

The monolayer passivation of Ge(100) surface via formation of Ge-N and Ge-O surface species was studied using scanning tunneling microscopy (STM) and density functional theory (DFT) to develop a process of minimizing interface defect density between Ge and a high-k dielectric layer in a highly scaled device. Direct nitridation was performed on a Ge(100) surface using an electron cyclotron resonance (ECR) plasma source with pure N_2 gas. It was hypothesized that plasma nitridation at elevated temperature (500°C) would form an ordered nitride structure that would combine the low defect density of GeO_2 with the higher thermal stability of GeON via formation of a Ge-N ordered structure. Experimental and theoretical modeling showed that bandgap states are produced from the ordered nitride structure resulting in Fermi level pinning of the surface; however, it is predicted that H-passivation on the nitride structure would unpin the Fermi level by reducing the dangling bonds and the bond strain. The best method to passivate a Ge(100) surface is to form a layer of GeO_2 which is free of suboxides. However, this process is difficult to scale using thermal oxidation by O_2 , so alternative oxidants, H_2O and GeO_2 , were studied. At room temperature, the H_2O -dosed Ge surface showed Ge-OH sites with very few Ge adatoms, while the e-beam deposition of GeO_2 formed semi-ordered Ge-O structures and Ge ad-species. It is likely the H_2O dosing produces an ideal passivation layer since it displaces few surface Ge atoms. Nevertheless, annealing above 300°C converts the surface oxides into suboxide rows on both H_2O and GeO_2 dosed Ge surfaces due to the reactivity of GeO_2 with Ge. Scanning tunneling spectroscopy (STS) shows that the Fermi level of the *n*-type Ge surfaces covered by suboxides is near the valence band edge, consistent with formation of Ge suboxide rows likely causing Fermi level pinning. The atomic layer deposition (ALD) of GeON and SiO_2 are being studied to form a monolayer or bilayer of passivation with a minimum defect density and the improved thermal stability.

11:20am **SS2+EM-MoM10 Formation of Titanium Sub-Oxide from TiO_2 ALD Films on Si and Ge Substrates after Vacuum Anneal**, *R.M. Methaapanon, P. Ardalan, S.F. Bent*, Stanford University

The formation of an oxide interlayer between a Si or Ge substrate and a metal oxide dielectric film has a direct influence on the physical and electrical properties of the field effect transistors made from these components. An oxide interlayer may form either during the deposition process or during a subsequent high temperature step. It is usually desirable to control or eliminate the formation of this oxide interlayer; one approach used is to create an oxide-free surface by chemically etching away the native oxide layer and adding a surface modifier such as hydrogen or halogens to inhibit further oxide formation.

In this work, we study the interlayer oxide formation on hydrogen-terminated silicon and halide-terminated germanium following TiO_2 atomic layer deposition (ALD). The surface analysis of TiO_2 films on silicon substrates is conducted immediately after the ALD process without

exposure to ambient conditions by an integrated X-ray photoelectron spectroscopy (XPS)/ALD system. The results on hydrogen-terminated silicon show that no silicon oxide forms between the two materials during ALD at 100 °C. However, a silicon oxide interlayer is detected after annealing in ultrahigh vacuum. A concomitant depletion of oxygen in the TiO₂ films occurs, leading to generation of a Ti sub-oxide. The effect is shown to be correlated with both the annealing temperature and the thickness of the TiO₂ film. Control experiments carried out on TiO₂ film deposited by ALD on SiO₂-coated silicon show significantly less depletion of oxygen in the TiO₂ films. Our results indicate that TiO₂ is the source of O for Si oxidation, and that migration of oxygen to this interface is a driving force for oxygen depletion in the TiO₂ film. The TiO₂ films on Br- and Cl-terminated germanium substrates are deposited by ALD at temperatures in the range of 100-300 °C and analyzed using *ex-situ* synchrotron radiation photoemission spectroscopy (SR-PES). Formation of titanium germanate (TiGeO_x) was observed after annealing to 400 °C. Upon annealing to 700 °C, titanium sub-oxide formation is also observed for this system. However, this reduction was more pronounced in thinner TiO₂ films. The stability of these oxide structures upon annealing, and the prospect for eliminating the oxide interlayer in the TiO₂/Si and TiO₂/Ge systems will be discussed.

11:40am **SS2+EM-MoM11 Interfacial Effects of Near-surface Dopant Diffusion and Electrical Activation in Silicon**, *P. Gorai, Y. Kondratenko, E.G. Seebauer*, University of Illinois at Urbana-Champaign

Defect behavior in silicon can be controlled by manipulating the chemical state of nearby surfaces and solid-solid interfaces, with important implications for transistor fabrication by ion implantation and annealing. Silicon interstitials formed during the ion implantation step are responsible for unwanted transient enhanced diffusion (TED) of dopants, and affect the degree of dopant activation as well. Earlier work in our laboratory has shown that certain chemical treatments of surfaces and interfaces changes its ability to act as sinks for interstitials. The fundamental kinetic quantity describing “sink” behavior can be described by an annihilation probability (S). Yet surfaces and interfaces also support electrically charged defects, which create local strong electric fields that influence the local motion of interstitials that are charged. The degree of charge buildup can be quantified by an electric potential (V_i). The combined effects of S and V_i not only influence the annihilation of interstitials, but lead under some conditions to the pile up of electrically active dopant near the surface or interface. However, up to now, the precise nature of the interplay, including the most relevant time scales during annealing, has never been quantified. Through continuum modeling on the nanometer length scale, the present work provides such quantification. Differential equations describing the diffusion and reaction of silicon and boron interstitials are solved to yield the time evolution of boron profiles that are compared in important cases to experiment.

Thin Film

Room: Ruidoso - Session TF+EM-MoM

Nanostructuring Thin Films

Moderator: A. Melechko, North Carolina State University

8:20am **TF+EM-MoM1 Nanostructured Magnetic Thin Film Heterostructures: Fabrication, Exchange Interactions and Tailored Anisotropies**, *K.M. Krishnan*, University of Washington **INVITED**

Ultrathin metallic heterostructures show richness in magnetic behavior driven, in part, by exchange, interface, proximity, size and dimensionality effects. One of the most widely studied and technologically important, but still not well-understood, magnetic behavior is the phenomenon of exchange bias (EB) observed in ferromagnetic (FM)/antiferromagnetic (AFM) structures. In this talk, I will first discuss epitaxial growth of such MnPd/Fe bilayers with tailored AFM spin-lattices (compensated and uncompensated) at the interface exhibiting in-plane EB and (Co_xAlPt_y)_n/IrMn multilayers with perpendicular EB. Assymmetric magnetization reversals in *exchange*-biased Fe/MnPd bilayers were confirmed by photoemission electron microscopy (PEEM) with x-ray magnetic circular dichroism (XMCD) for magnetic contrast. Further, the element-specific magnetic structure of the Mn₅₂Pd₄₈/Fe bilayer was investigated with atomic-layer depth sensitivity at the antiferromagnet/ferromagnet interface by soft-XMCD and magnetic reflectivity (XMR). A complex magnetic interfacial configuration, consisting of a 2-monolayer-thick induced ferromagnetic region, and pinned uncompensated Mn moments that reach far deeper (~13 Å), both in the antiferromagnet, were found. These epitaxial EB samples also show in-plane reorientation transitions, determined by the competition between the interface exchange coupling and the intrinsic uniaxial energies, and is

driven by the temperature, as well as the thickness of MnPd and Fe layers. Complementing these results, work on multilayers show that perpendicular EB arise from a complex interplay between unidirectional anisotropy at the terminating FM/AFM interface, the perpendicular anisotropy of the FM/nonmagnet (NM) multilayer stack and the overall magnetostatic energy of the structure. Finally, we have developed and implemented nanoimprint lithography (NIL) to fabricate wire and particle arrays of exchange biased elements at the 300nm length scale. A mask transfer NIL process has also been developed to grow epitaxial structures. The role of size and dimensionality as well as competing anisotropies, introduced by particle shape, on EB heterostructured elements has been studied. Details will be presented.

9:00am **TF+EM-MoM3 Self and Directed Assembly of Thin Metallic Films by Pulsed Laser Induced Dewetting**, *Y. Wu*, University of Tennessee, *J.D. Fowlkes*, Oak Ridge National Laboratory, *P.D. Rack*, University of Tennessee

The synthesis and assembly of functional metallic nanomaterials is critical for realizing many important applications of nanoscience and nanotechnology. In this study, we investigated thin film dewetting of metal films via pulsed nanosecond laser melting. We studied film instabilities induced by capillary forces and the subsequent mass transport which can lead to thin film break-up and subsequent nanoparticle formation. We have also explored the dewetting and nanopattern formation of nano-lithographically patterned thin films of various shapes to understand how various initial and boundary conditions can guide the assembly. In this presentation we will discuss the various spinodal and Rayleigh-Plateau instability mechanisms and the inertial, visco-inertial and viscous flow regimes involved in the thin metal film assembly. Finally we will discuss how nano-lithographically defined features can be used to direct the assembly of multi-functional nanoparticle ensembles.

9:20am **TF+EM-MoM4 Plasma-assisted Metallorganic Chemical Vapor Deposition of ZnO Nanostructures: Impact of Process Parameters on Dimensionality and Morphology**, *M. Bonvalot, G.M. Rosaz*, Ltm-Cnrs, Cea-Leti, France

ZnO is a II-VI semiconductor with a large band gap (3.4 eV) and excitonic binding energy (60 meV), which make it particularly attractive for a great diversity of potential emerging applications in the field of nanotechnologies (UV light emitters, laser diodes...). Several synthesis routes of ZnO nanostructure arrays have been reported in the literature, essentially on sapphire substrates. However, very few studies have been reported on growth of ZnO nanostructures on Si(111) substrates due to the difficulty of matching materials with different spatial symmetry group.

In this study, ZnO nanostructures have been prepared on Si(111) by plasma assisted pulsed injection MOCVD (metallorganic chemical vapor deposition). This technique of elaboration offers the advantage of large area growth and is compatible with existing semiconductor processing technologies. The key role of the plasma during material preparation is to allow lower substrate temperature (as low as 350°C), thus providing lower activation energies. It also allows in situ thermal treatment of substrates and prepared nanostructures. Moreover, the active chemical species of the plasma can help force in situ doping of the semiconducting nanostructure, which opens up a large spectrum of metastable phase formation possibilities.

We have investigated the effect of several process parameters (precursor flow rate, O₂/Ar partial pressure, plasma incident power) on the morphology of the produced nanostructures. Three growth regimes have been identified: 2 dimensional very fine grain thin films, ordered hexagonal shaped plates and oriented columnar grains with a very large density corresponding to nanowire growth. These results will be presented in the light of literature data [1, 2]. The transition between these three different growth regimes is induced by a careful adjustment of the substrate temperature and Ar/O₂ plasma flowrate. The role of these process parameters will be highlighted based on gas phase OES and SEM analyses, and the growth mechanism of densely packed 1D ZnO nanostructures will be presented.

[1] S. Agouram, J.A. Bastos-Segura and V. Munoz-Sanjos, <http://www.sciencedirect.com/science/journal/07496036> **42**, 140 (2007).

[2] J. B. Baxter and E. S. Aydil, *J. Electrochem. Soc.* **156** (1) H52-H58 (2009).

9:40am **TF+EM-MoM5 Self-assembled and Engineered Nanostructures in $\text{Hf}_{1-x}\text{Al}_x\text{N}/\text{MgO}(001)$ Single-Crystal Alloys: Effects on Physical Properties**, B. Howe, E. Sammamn, J.-G. Wen, M. Sardela, T. Spila, J. Greene, University of Illinois at Urbana-Champaign, L. Hultman, Linköping University, Sweden, I. Petrov, University of Illinois at Urbana-Champaign

Transition metal nitrides (TMN) are well known to have a remarkable range of unique physical properties. One method used to further enhance the physical properties of many transition metal nitrides is to alloy them with a second, thermodynamically immiscible nitride. The most famous example is $\text{Ti}_{1-x}\text{Al}_x\text{N}$; many have reported drastically enhanced physical properties including super hardness, increased oxidation resistance, age-hardening behavior, and the formation nanoscale compositional modulations during film growth and post annealing experiments. However, very little has been reported on the ability to control this nanostructure, nor has the effect of these nanostructures on the physical properties of the films. We have chosen $\text{Hf}_{1-x}\text{Al}_x\text{N}$ as a model system to study the nanostructures of interest. We begin by reporting on the effects of nanostructure on the optoelectronic, thermal transport and elastic constant properties of $\text{Hf}_{1-x}\text{Al}_x\text{N}$ single crystal layers grown on $\text{MgO}(001)$ using ellipsometry, temperature dependent hall effect, and picosecond probe acoustic transport measurements, respectively. We continue by summarizing a systematic study into the effects of growth parameters (ion energy, E_i , ion-to-metal flux ratio, $J_{\text{ion}}/J_{\text{me}}$, and substrate temperature, T_s) on single crystal reactively sputtered $\text{Hf}_{0.7}\text{Al}_{0.3}\text{N}/\text{MgO}(001)$ layers in order to controllably manipulate the nanostructure and study its effects on the physical properties. Films are deposited from a Hf/Al 70/30 (at. %) target in 5% N_2/Ar mixtures while $J_{\text{ion}}/J_{\text{me}}$ is varied from 0.7 to 12.6, T_s from 400 to 700 °C, and E_i from 10 to 80 eV. $J_{\text{ion}}/J_{\text{me}}$ has a strong effect on the formation of 3D nanoscale (2-3nm) compositional modulations as indicated by HR-XRD and HR-TEM. Nanoindentation experiments reveal an increase in film hardness from 31.7 ± 0.6 GPa to 38.9 ± 0.6 GPa. E_i has a strong effect on the AlN incorporation probability, which can be adjusted between ~0 and 100% by varying the ion energy (E_i) incident at the growing film over a narrow range, 10-40 eV. Epitaxial film compositions vary from $x = 0.30$ with $E_i = 10$ eV, to 0.27 with $E_i = 20$ eV, 0.17 with $E_i = 30$ eV, and ≤ 0.002 with $E_i \geq 40$ eV. This extraordinary range in real-time manipulation of film chemistry during deposition is due to the efficient resputtering of Al atoms (27 amu) by Ar^+ ions (40 amu) backscattered from Hf atoms (178.5 amu). We demonstrate that this effect can be used to grow superlattices with abrupt interfaces at high deposition rates from a single target by switching E_i . We grew superlattices with bilayer thicknesses from 1-6nm and films exhibited an increase in hardness from 32.5 ± 0.9 GPa to 37.8 ± 1.2 GPa.

10:00am **TF+EM-MoM6 Lowering the Epitaxial Growth Temperature of Ge Quantum Dots on $\text{Si}(100)-(2 \times 1)$ by Electronic Excitation**, A.O. Er, H. Elsayed-Ali, Old Dominion University

Low temperature epitaxy is important for device fabrication because it can lead to suppressing the introduction of defects such as dislocations and stacking faults. The effect of laser-induced electronic excitations on the self-assembly of Ge quantum dots (QDs) on $\text{Si}(100)-(2 \times 1)$ grown by pulsed laser deposition is studied. The experiment was conducted in ultrahigh vacuum. A Q-switched Nd:YAG laser (wavelength $\lambda = 1064$ nm, 10 Hz repetition rate) was split into two beams; one used to ablate a Ge target while the other to electronically excite the substrate. In-situ reflection high-energy electron diffraction (RHEED), scanning tunneling microscopy (STM), and ex-situ atomic force microscopy (AFM) were used to study the morphology of the grown QDs. The dependence of the QD morphology on substrate temperature and ablation and excitation laser energy density was studied. Electronic excitation is shown to affect the surface morphology. For Ge coverage of 22 monolayer, it was observed that excitation laser reduces the epitaxial growth temperature to 250 °C. Applying excitation laser to the substrate during the growth changes the QD morphology and island density and improves the size uniformity of QDs at 390 °C. Applying the excitation laser during growth decreases the surface roughness at room temperature. RHEED recovery curves show that applying excitation laser increases the surface diffusion. A purely electronic mechanism of enhanced surface diffusion of the Ge adatoms due to a phonon-kick mechanism following two-hole localization could explain the results. Ongoing experiments using a femtosecond laser for excitation and in-situ STM for detection of the early stages of island nucleation will be presented.

10:40am **TF+EM-MoM8 Novel Nanoparticle and Thin film Growth Via Matrix Assisted Pulsed Laser Evaporation of Metal Based Acetates**, M.A. Steiner, J.M. Fitz-Gerald, University of Virginia

Until recently, the majority of research surrounding Matrix Assisted Pulsed Laser Evaporation (MAPLE) has been concentrated on preserving the structure and properties of polymeric and biomaterials. Deviating from this course, novel research will be presented illustrating the feasibility of applying matrix-assisted processing to grow inorganic materials from

precursor solutions in the form of complex nanoparticles and thin films. By replacing the preferentially absorbing matrix material with a transmitting solvent, laser energy is instead absorbed by a precursor solute which decomposes and is subsequently ejected onto the substrate in the form of nanoparticles. [1] [2] Acetates are a widely favored metallorganic precursor for thin film processing on various substrates because they decompose under ultraviolet irradiation. Results will be presented in the form of thin films and nanoparticle systems of Au-Ag-Pd, ZnO, and YBaCuO material systems.

[1] Allmond, C., Sellinger, A., Gogick, K., & Fitz-Gerald, J. (2007). Photochemical synthesis and deposition of noble metal nanoparticles. *Applied Physics A: Materials Science & Processing*, 86(4), 477-480

[2] Sellinger, A., Aburada, T., & Fitz-Gerald, J. (2008). Synthesis of multimetallic nanoparticles using a solution-based pulsed laser deposition approach. In *Proceedings of SPIE* (Vol. 7005, p. 700516)

11:00am **TF+EM-MoM9 Nanocomposite Vanadium Oxide Thin Films**, B.D. Gauntt, M.W. Horn, O.M. Cabarcos, E.C. Dickey, Penn State University

Thin film vanadium oxide is used as the active layer in un-cooled, infrared imaging devices based on microbolometer structures. In this type of imaging device, infrared radiation is detected via a temperature driven resistivity change in the active layer. Underlying readout circuitry and the need for increased detection sensitivity require low electrical resistivity material with high thermal coefficient of resistivity (TCR). Vanadium oxide thin films deposited via reactive pulsed direct current (DC) sputtering have properties in the range of interest with room temperature resistivity varying from 0.01 to 6×10^4 Ohm cm and TCR's varying from -0.1 to -4.2 %/°C. Films with resistivity in the range of interest (0.1 to 1.0 Ohm cm) contain the rocksalt structured FCC VO_x phase ($0.8 < x < 1.3$) accompanied by significant structural disorder, while those with greater resistivity are amorphous. The relationship between TCR and room temperature resistivity is exponential, and throughout the present series of films is fixed, i.e. a film with a given resistivity has a set TCR. Energy filtered electron diffraction patterns collected in the transmission electron microscope (TEM) reveal a diffuse scattering feature at low scattering angle for both amorphous and nanocrystalline films, suggesting that films containing nanocrystals also contain an amorphous phase. Raman spectroscopy results from amorphous films show a broad feature around ~ 890 cm^{-1} , while spectra from nanocrystalline films exhibit the "amorphous" feature and a second broad feature at ~ 300 cm^{-1} . The feature at ~ 300 cm^{-1} was the only feature present in the most crystalline of the films, suggesting it represents the disordered FCC VO_x phase. Film stoichiometry, as measured with Rutherford backscattering spectroscopy, puts the overall chemistry of the nanocrystalline films outside the FCC VO_x phase field, with many of the samples having a V:O ratio greater than 1.3. A pre-peak feature in the V-K edge was observed with X-ray absorption spectroscopy (XAS), and the intensity of the pre-peak, which is known to result from local octahedral disorder, increased with increasing oxygen content and correlates with diffraction observations of increasing disorder. The combined TEM, RBS, Raman, and XAS analyses suggest vanadium oxide films with properties in the range of interest for microbolometer-based devices consist of a two-phase material containing FCC VO_x nanocrystals embedded in an oxygen-rich amorphous matrix. Films lacking sufficient disorder have resistivity in the range of interest but insufficient TCR magnitude, suggesting the need for both the nano-crystalline phase and the amorphous matrix.

11:20am **TF+EM-MoM10 Titanium-doped Carbon-based Nanocomposite Coatings, Mechanical and Tribological Properties, Biocompatibility and Cell-Attachment Properties: Implications in Orthopedic Implants**, P. Epaminonda, University of Cyprus, Y. Christou, A. Odysseos, EPOS-IASIS R&D, Cyprus, C. Reholz, C. Tsotsos, University of Cyprus

Stress shielding due to uneven load distributions at the bone-prosthesis interface affect joint prostheses and can lead to wear and loosening. Commonly used cobalt-chromium-molybdenum alloys can degrade during wear at an average rate of 0.02–0.06 mm/year. Other alloys such as titanium-aluminum-vanadium although biocompatible and highly corrosion resistant, exhibit relatively low mechanical properties and poor wear resistance. Nanocomposite nanocrystalline (nc-) Ti(N,C)/ amorphous diamond-like-carbon (a-C:H) coatings exhibit high hardness (H), low friction coefficients, high wear resistance and resilience to substrate deformation thus making them promising candidates for prosthetic implant applications. In this work we investigate the influence of the microstructure of nc-Ti(N,C)/a-C:H coatings on the mechanical, tribological and biological properties with the aim of using such materials not only as wear resistant films in biomedical implants, but also as a bioactive surface that can promote bone ingrowth at areas of medical implants, such as the femoral

stem or the acetabular cell in hip replacement joints, that are in direct contact with bone. Approximately 2 μm thick, nc-Ti(N,C)/ a-C:H coatings were deposited on Si wafer and implant alloy coupons using low temperature ($\sim 200^\circ\text{C}$) DC reactive magnetron sputtering. The carbon content was varied from 41 to 57 at % and the obtained a-C:H phase ranged from 31 – 47 at. % in order to form the desired nanocomposite structure of 2-4 nm wide Ti(N,C) with 1 to 2 monolayer coverage of a-C:H. An increase in the amorphous phase results in a decrease in mechanical and a decline in tribological performance, however the change in structure and surface morphology at increased carbon content favours the bioactivity of the films. Coating chemical composition and microstructure was investigated by means of x-ray photoelectron spectroscopy (XPS), x-ray diffraction (XRD) and transmission electron microscopy (TEM). The mechanical and tribological properties of the films were determined using nanoindentation and nanotribo-scope methods. In order to assess the biocompatibility of nc-Ti(N,C)/a-C:H coatings and investigate their osteoblast - attachment properties and thus determine their efficacy as implant coatings, the osteoblastogenic osteosarcoma immortalised cell lines Saos-2 and Hos were seeded and allowed to grow on the coating surface. Cell attachment properties were assessed in terms of viability of seeded cells. Viable attached cells were quantified by a mitochondrial enzymatic activity-based colorimetric assay against cultures seeded on conventional tissue-culture treated plastic surface.

11:40am **TF+EM-MoM11 Magnetic Responsive Polymer Nanocomposites Thin Films: Synthesis, Characterization and Implementation in RF/Microwave Applications**, *C. Morales, J. Dewdney, S. Skidmore, S. Pal, K. Stojak, H. Srikanth, T. Weller, J. Wang*, University of South Florida

Newly-developed magnetic responsive polymer nanocomposites were elaborated using low complexity equipments and low-cost lab materials and apparatus. Sub-10nm CoFe₂O₄ and Fe₃O₄ nanoparticles with tightly controlled size distribution were synthesized using a chemical coprecipitation procedure, which involves Iron and Cobalt salts and oleic acid and oleylamine as surfactants. This polymer nanocomposite is dissolved in hexane together with calculated amount of surfactant-coated nanoparticles to obtain the polymer nanocomposites with uniform nanoparticle dispersion at desired concentration. Excellent dispersion of magnetic nanoparticles in the polymer matrix is very important for a low-loss material at microwave and RF frequencies, as it minimizes magnetic hysteresis losses by reducing magnetic coupling amongst particles. The amount and composition of all the constituent solvents is critically-controlled for the purpose of maintaining the desired viscosity to control the exact thickness of the thin film after solvent evaporation and the curing process.

The electrical microwave properties of Fe₃O₄-based polymer nanocomposites (e.g., permeability, permittivity and loss tangent) were tuned under externally-applied DC magnetic fields. In addition, two novel microstrip-based test structures were used to extract the complete set of microwave properties and their dependence on externally-applied magnetic field. The transmission of microwave signals through these structures is susceptible to variation in the dielectric/magnetic properties of the polymer nanocomposites, which facilitates the demonstration of the tunability and extraction of properties at different magnetic field strengths.

The required magnetic field is achievable by small commercial permanent magnets, which justifies the use of this new class of materials for implementation of practical microwave and RF devices and circuits. Magnetic polymer nanocomposites are very easy to process, which enables them to be employed in both PCB board and chip levels using conventional manufacturing processes. They exhibit unique and very attractive properties for many microwave applications that require tunability and flexible materials.

Thin Film

Room: Pecos - Session TF+EN-MoM

ALD: Energy Applications

Moderator: S.M. George, University of Colorado at Boulder

8:20am **TF+EN-MoM1 ALD Applications in Heterogeneous Catalysis**, *P.C. Stair*, Northwestern University & Argonne National Lab, *J. Lu*, Northwestern University, *H. Feng, J.E. Libera, J.W. Elam, M.J. Pellin*, Argonne National Laboratory, *H.-S. Kim*, Northwestern University

INVITED

Atomic Layer Deposition (ALD) has enormous potential for the synthesis of advanced heterogeneous catalysts with controlled composition and

structure at the atomic scale. The ability of ALD to produce conformal oxide coatings on porous, high-surface area materials offers the possibility to provide completely new types of catalyst supports. At the same time ALD can achieve highly uniform catalytically active metal and oxide phases with (sub-) nanometer dimensions.

Vanadium oxide species supported on high surface area oxides are among the most important catalytic materials for the selective, oxidative conversion of hydrocarbons to useful chemicals. In our laboratory ALD has been used to synthesize both the catalytic vanadium oxide and the supporting oxide on both high surface powders and anodic aluminum oxide (AAO) nanoliths. These materials have been characterized by SEM, XRF, ICP, UV-Vis absorption spectroscopy, Raman spectroscopy and evaluated for the oxidative dehydrogenation (ODH) of cyclohexane.

More recently we have studied what we call "ABC-type" ALD in which metal nanoparticles and support materials are grown sequentially in each ALD cycle. This method makes possible metal deposition at lower temperatures than conventional AB-type ALD and exceptionally small particles, ca. 0.5 nm. Using additional ALD support layers at the conclusion of the growth, the metal particles are stabilized against sintering at high temperatures and reaction conditions.

9:00am **TF+EN-MoM3 Process and Materials Optimization for Ru/RuO₂ ALD using a Novel Cyclohexadienyl Precursor**, *K. Gregorczyk, L. Henn-Lecordier*, University of Maryland, *J. Gatineau, C. Dussarrat*, Air Liquide, *G.W. Rubloff*, University of Maryland

Ruthenium is of particular interest to the semiconductor industry and others due to its low bulk resistivity ($7\mu\Omega\text{ cm}$) and high work function (4.7eV). In addition, its complementary oxide, RuO₂, can exhibit high specific capacitance (up to 750 F/g) and conductivity ($80\text{-}100\mu\Omega\text{ cm}$), making it attractive for energy storage applications. We report results for Ru and RuO₂ ALD using a novel Ru cyclohexadienyl precursor and oxygen. This precursor is attractive because it is liquid at room temperature, stable in air and non-reactive with water, while its vapor pressure is similar to that of common ALD Ru precursors RuCp₂ and Ru(EtCp)₂, i.e., 0.1 Torr at 60°C and 1 Torr at 100°C. ALD Ru deposition was achieved in a wafer scale (100mm), cross-flow ALD reactor. Self-limiting ALD surface chemistry is observed between 250-300°C with a growth rate of $\sim 0.5\text{Å}/\text{cycle}$ and across-wafer uniformity $>98\%$. Four point probe measurements show a low sheet resistance of $16\mu\Omega\text{ cm}$. Ru nucleation is improved compared to RuCp₂ and Ru(EtCp)₂ based processes, with no nucleation delay on SiO₂ or TiO₂, a slight delay on Si, and a significant delay on Al₂O₃. Growth rates are constant with the number of deposition cycles. Conformality studies were conducted using high aspect ratio anodic aluminum oxide (AAO) thin films, using a thin TiO₂ nucleation layer before Ru ALD. This Ru ALD process converts to a RuO₂ ALD process at higher oxygen partial pressure, with an oxide conductivity of $\sim 80\mu\Omega\text{ cm}$. Post-process thin film characterization using XRD, XPS and AFM will be also presented.

This work was supported by the US Department of Energy, Office of Basic Energy Sciences as part of an Energy Frontier Research Center.

9:20am **TF+EN-MoM4 Atomic Layer Deposition Enabled Metal-Insulator-Metal Tunnel Diode for Infrared Energy Rectifying System**, *I.-T. Wu*, University of South Florida, *N. Kislov*, NanoCVD Inc., *J. Wang*, University of South Florida

Amongst present-day renewable energy sources, solar cells have been widely considered as the most viable solution. However, the energy conversion efficiency for the solar cells is limited to 30% or below due to the device physics. Rectifying antenna (rectenna) is an ideal supplement that is able to efficiently capture the abundant infrared (IR) energy from the solar radiation in part due to IR antenna's inherent high efficiency. The rectenna system consists of two key elements: antenna and rectifying diode. The IR antenna captures the solar radiation within the wavelength of interest to be delivered to the ultrafast diode that rectifies the received signal into usable DC power.

Rectennas operating at microwave frequencies with efficiency up to 85% has been routinely demonstrated. However, the key remaining challenge for the infrared counterparts can be ascribed to the insufficient cutoff frequency of the semiconductor-based diodes owing to their excessive depletion-induced capacitance. In order to obtain the desired response times less than 10-12seconds, metal-insulator-metal (MIM) tunnel diodes with junction area in the range of $100\text{nm}\times 100\text{nm}$ were implemented herein to enable the coveted terahertz frequencies due to the greatly reduced junction capacitance and ultrafast quantum tunneling.

In this work, MIM tunnel diodes with sub-micron sized junction have been mass produced using CMOS-compatible processes without the need for E-beam lithography or sophisticated chemical etching. Standard

photolithography and atomic layer deposition (ALD) were used to allow formation of a micrometer-wide finger in the second metal layer separated from the electrode in the first metal layer by an ALD-deposited sidewall dielectric spacer, thus forming a nm-thick vertical tunnel junction. The nano-scale junction is defined by the width of the finger and the thickness of the electrode, while the junction thickness is controlled by the ALD process.

On par to nano-scale devices, MIM tunnel diodes with micron-scale self-aligned cross-fingers have been successfully developed. Through this process, we have investigated a wide variety of metal and insulator materials such as Au, Cu, Pt, Ni, Al, Al₂O₃, HfO₂ to advance the performance of the MIM diode with particular focus on its efficiency. Some preliminary DC and RF characterization have been carried out to study the device characteristics such as responsivity, nonlinearity and asymmetry of I-V, and frequency responses. Ongoing research for modeling of MIM tunneling diode based on measured S-parameter data and further reduction of the device junction area will be detailed in the final manuscripts.

9:40am **TF+EN-MoM5 New Semiconductor-Insulator-Semiconductor Solar Cell Concept based on Wet Chemically Etched Silicon Nanowires: Processing and Electro-Optical Properties**, *B. Hoffmann, V.A. Sivakov, G. Broenstrup, F. Talkenberg*, Institute of Photonic Technology, Germany, *S.H. Christiansen*, Max Planck Institute for the Science of Light, Germany

Silicon nanowire (SiNW) ensembles with vertical geometry have been realized using wet chemical etching of bulk silicon wafers (n-Si(100)) with an etching hard mask of silver nanoparticles that are deposited by wet chemical electroless deposition on silicon surfaces.

The new concept of the solar cell is based on the semiconductor-insulator-semiconductor (SIS) layer sequence produced by Atomic Layer Deposition (ALD). A thin tunnelling oxide (SiO₂, Al₂O₃) with a thickness of 5-20 Å and a 300 nm transparent conductive oxide (Al doped ZnO or In doped SnO₂) around 1D silicon nanostructures have been realized using Plasma Assisted ALD approach (Oxford Plasma, OpAL).

The first prototype reached an open-circuit voltage of 80mV and a short-circuit current density of 23mA/cm².

The influence of the thickness and chemical nature of the tunnelling oxide will be discussed. Back side contacts of Ti/Al or Ti/Ag were realized using sputtering. From literature it is known that the planar SIS solar cell can reach an energy conversion efficiency of approx 15%. Absorption of visible and infra-red light is significantly enhanced in nanowires compared to planar layers of identical thickness. Thus, wet chemically etched silicon nanowires have the potential for even higher energy conversion efficiencies compared to the planar SIS solar cells. The morphology, crystallographic and surface structure, optical and solar cell properties will be presented and discussed in details.

10:00am **TF+EN-MoM6 Ultrathin Al₂O₃ for c-Si Solar Cells: Differences in Passivation by Thermal and Plasma ALD-Synthesized Films**, *G. Dingemans, N.M. Terlinden, M.L.C. Adams, H.B. Profijt, M.M. Mandoc, M.C.M. van de Sanden, E.W.M.M. Kessels*, Eindhoven University of Technology, Netherlands

Ultrathin films of Al₂O₃ synthesized by ALD at low substrate temperatures (200 °C) have recently demonstrated their potential as surface passivation material in c-Si photovoltaics enabling solar cell efficiencies up to 23.4%. So far, the best results were obtained by plasma ALD Al₂O₃ but recently it was shown that similar excellent results can be obtained by thermal ALD [1]. For both methods, Al₂O₃ yield excellent lifetimes after annealing (at 400 °C) on both *p*- and *n*-type Si wafers with the best results corresponding to ultralow surface recombination velocities < 1 cm/s (for 3.5 Ohm cm *n*-type *c*-Si). However, also several striking differences have been observed in terms of the underlying passivation mechanism as will be addressed in this contribution. From capacitance-voltage (C-V) measurements, corona charging experiments and optical second harmonic generation (SHG) it was found that Al₂O₃ deposited with thermal ALD contains a lower negative fixed charge density (~10¹² cm⁻²) than plasma ALD (> 5·10¹² cm⁻²). This indicates that field-effect passivation (i.e., shielding of one type of charge carriers from the surface) is less important for thermal ALD. On the other hand, it was observed that chemical passivation (i.e., reduction of interface defect states) is very important for both thermal and plasma ALD Al₂O₃. Relatively low interface defect densities *D_i* of <10¹¹ eV⁻¹ cm⁻² were found for both methods after anneal. However, for as-deposited Al₂O₃, the interface defect density (and correspondingly the surface recombination velocity) is significantly poorer for plasma ALD Al₂O₃ than for thermal ALD Al₂O₃. From vacuum ultraviolet (VUV) emission measurements, it has been found that the high *D_i* can be attributed to plasma radiation damage by photons with an photon energy of ~9.5 eV. Furthermore, it will be shown that the difference in importance of field-effect passivation explains several

differences observed in the passivation performance for thermal and plasma ALD Al₂O₃ (e.g., the minimum thickness required for excellent passivation).

[1] G. Dingemans, M. C. M. van de Sanden, W. M. M. Kessels, *Electrochem. Solid-State Lett.*, 13, H76 (2010).

10:40am **TF+EN-MoM8 Cathodoluminescent and Photoluminescent Properties of Pulsed Laser Deposited Thin Phosphor Films**, *O.M. Nwaeeborwa*, P.D. Nsimama, J.J. Dolo*, University of the Free State, South Africa, *M.S. Dhlamini*, University of the Free State and CSIR, South Africa, *E. Coetsee, J.J. Terblans, H.C. Swart*, University of the Free State, South Africa **INVITED**

Phosphors have many uses today, such as information display, medical imaging, and theft prevention. The phosphors are often used as powders, even though thin films offer higher resolution and better chemical stability. We have investigated the cathodoluminescent (CL) and photoluminescent (PL) properties of thin films of several phosphors (e.g. SrAl₂O₄:Eu²⁺, Dy³⁺; SiO₂:PbS; Gd₂O₂S:Tb³⁺; SiO₂:Ce³⁺, Tb³⁺ and Y₂SiO₅:Ce³⁺) that were ablation deposited onto Si (100) substrates using either conventional pulsed laser deposition (PLD) or pulsed reactive crossed beam laser ablation (PRCLA). Several deposition parameters were varied, including vacuum versus partial pressure of gas (O₂ or Ar), type of laser pulse, and substrate temperature using either a 307 nm XeCl or 248 nm KrF excimer laser. The CL spectrum and intensity were measured in vacuum from films irradiated with 2 keV electrons for a prolonged period of time, while PL data were collected in air under excitation by either a 325 nm HeCd laser or a monochromatized xenon lamp. Both the CL and PL intensities were strongly dependent on the deposition conditions and post-deposition annealing. Data from scanning electron microscopy (SEM) and atomic force microscopy (AFM) show that the major influence of the deposition conditions on the CL/PL intensity was through changes in the morphology and topography of the films, which affects light scattering and out-coupling. Finally, the CL intensity from the films decreased significantly during prolonged electron beam irradiation. The degraded CL intensity resulted from the formation of non-luminescent oxide layers on the film surfaces. The chemical composition and electronic states of the 'dead' layers were analyzed using x-ray photoelectron spectroscopy (XPS). The influence of the various deposition conditions on the luminescent intensities will be discussed. The mechanism leading to lower CL intensities will be concluded to be electron stimulated surface chemical reactions.

Vacuum Technology

Room: Laguna - Session VT+MN-MoM

MEMS Sensors, Vacuum Gauges, Measurements and Pumps

Moderator: J. Fedchak, National Institute of Standards and Technology

8:20am **VT+MN-MoM1 Practical Issues and Applications for Vacuum and Hermetic Microsystems Packaging**, *L. Fang, D. Chu, K. Ewsuk*, Sandia National Laboratories **INVITED**

Microsystems packaging involves physically placing and electrically interconnecting a microelectronic device in a package that protects it from and interfaces it with the outside world. When the device requires a hermetic or controlled microenvironment, it is typically sealed within a cavity in the package. Sealing involves placing and attaching a lid, typically by welding, brazing, or soldering. Materials selection (e.g., the epoxy die attach), and process control (e.g., the epoxy curing temperature and time) are critical for reproducible and reliable microsystems packaging. This paper will review some hermetic and controlled microenvironment packaging at Sandia Labs, and will discuss materials, processes, and equipment used to package environmentally sensitive microelectronics (e.g., MEMS and sensors).

9:00am **VT+MN-MoM3 New NIST Comparison Method Calibration Service for Vacuum Gauges Based on MEMS Pressure Sensors**, *J.H. Hendricks, D.A. Olson*, NIST

A new calibration service based on a secondary pressure transfer standard spanning the pressure range from 0.65 Pa to 130 kPa (5 mTorr to 975 Torr) has been developed at NIST. Until now, vacuum gauges in this range could only be calibrated using the NIST Ultrasonic Interferometer Manometers (UIMs). However, many customers desire direct traceability to NIST but

* Paul Holloway Award Winner

cannot justify the cost of the NIST UIM calibrations. The new service follows a similar model of other calibration services where a lower cost, and less accurate service is offered to customers who do not require the lowest uncertainty possible but still desire direct NIST tracibility. The comparison method utilizes a high accuracy transfer standard package that consists of a 133 Pa (1 Torr) Capacitance Diaphragm Gauge (CDG), a 13.3 kPa (10 Torr) CDG and a 130 kPa (975 torr) MEMS type Resonance Silicon Gauge (RSG) all encased in a temperature controlled enclosure that is periodically calibrated against the NIST 160 kPa UIM and 140 Pa oil UIM primary pressure standards. Due to the superior calibration stability of the MEMS based RSG, the transfer standard package, and ultimately the comparison method vacuum gauge service, provides expanded uncertainties as low as 0.05 % from 1.33 kPa to 130 kPa (10 Torr to 975 Torr) and 0.3 % from 1.33 Pa to 1.33 kPa (0.01 Torr to 10 Torr).

9:20am **VT+MN-MoM4 Pirani for Industrial Processes**, *B. Andreaus, R. Enderes, M. Wuest*, INFICON Ltd, Liechtenstein

In modern Pirani heat transfer gauges a filament is usually kept at a constant temperature and the necessary heating power is measured as a function of pressure.

Pirani gauges operated in coating and etching applications suffer from degradation due to process contamination or corrosion. Eventually, the Pirani may fail because the filament is etched away, its resistance and/or its emissivity have changed. Standard procedure for those processes is to use a corrosion resistant filament material adapted to the process in question, e.g. Nickel. Yet the choice of suitable filament material is limited as it needs to be manufactured as very thin coils, be electrically conducting, have a high and well-defined temperature coefficient for the resistance and be chemically inert. For some of the latest manufacturing processes in semiconductor industry none of the available filament materials is sufficiently resistant against corrosion.

We will present here a different approach in that we present first data on a coated Pirani sensor. The coating allows for a much broader field of application as electrical and mechanical requirements of the filament are separated from its chemical properties. Chemical stability is solely due to the coating, all other requirements, unaffected by the coating, can be met using a standard filament material.

9:40am **VT+MN-MoM5 Nitrogen Incorporated Ultrananocrystalline Diamond as a Robust Cold Cathode Material for Miniature Mass Spectrometry Application in Space Exploration**, *X. Wang*, University of Puerto Rico; Argonne National Laboratory, *S. Getty*, NASA Goddard Space Flight Center, *A.V. Sumant, O.H. Auciello*, Argonne National Laboratory, *D. Glavin, P. Mahaffy*, NASA Goddard Space Flight Center

Ultrananocrystalline diamond (UNCD) thin films have been investigated for over a decade for application to electron field emission devices since they offer very low threshold voltage (1-3 V/ μm) and reasonably stable field emission with time. Due to the small grain size (2-5 nm) and unique atomically abrupt grain boundary structure containing mixed sp^2/sp^3 carbon bonding, it has been postulated that field emission occurs mainly at the grain boundary due to the high field enhancement effect at the grain boundary and stable field emission has been observed independent of surface geometry or film thickness. In addition to low power consumption and potential for miniaturization, robust field emission materials are compelling for applications as long life electron sources for mass spectrometers for space exploration where electron sources are exposed to harsh environments. A miniaturized mass spectrometer under development for *in situ* chemical analysis on the moon and other planetary surfaces requires a robust, long-lived electron source, to generate ions from gaseous sample using electron impact ionization. To this end, we have explored the field emission properties and lifetime testing of nitrogen-incorporated ultrananocrystalline diamond (N-UNCD). The N-UNCD films were synthesized in a microwave plasma chemical vapor deposition system by introducing nitrogen in the Ar/CH_4 gas chemistry. Characterization of the N-UNCD films were carried out by using visible and UV Raman spectroscopy confirming characteristic signature of a good quality N-UNCD film. We will present results revealing that UNCD films with nitrogen incorporation during growth yield stable/high field-induced electron emission in high vacuum for up to 1000 hours.

This work was done with support from the NASA Astrobiology Science and Technology Instrument Development Program, under Grant Number 07-ASTID07-0020, and the NASA Goddard Space Flight Center Internal Research and Development Program. Use of the Center for Nanoscale Materials was supported by the U. S. Department of Energy, Office of Science, Office of Basic Energy Sciences, under Contract No. DE-AC02-06CH11357.

10:40am **VT+MN-MoM8 The Pumping Synergies of Integrated NEG and SIP Pumps for UHV Applications**, *A. Bonucci, A. Conte, L. Caruso, L. Viale, P. Manini*, SAES Getters S.p.A., Italy

A variety of vacuum systems, such as particle accelerators, synchrotrons, surface science chambers or laboratory equipments, do require the achievement of very high or even extremely high vacuum conditions (UHV-XHV). To this purpose, Ion pumps and Non Evaporable Getter (NEG) technologies are widely applied, since they complement each other effectively. Ion pumps remove ungetterable species like noble gases and methane, while the NEG provides a constant and large pumping speed for all the other gases, in a very compact volume.

So far ion and NEG pumps have been mostly used as separate units mounted in separate part of the vacuum system. In this paper, we investigate how overall pumping performances are influenced by the mounting geometry of the two pumps. In particular we will show that a remarkable synergic effect arises when the two pumps are integrated into one unit having optimized design, known as NEG^+ .

This configuration allows to minimize the detrimental effect given by outgassed species released by the SIP [^{1,2}] This increases the real pumping speed of the SIP, generally masked in the UHV range by gas desorption from SIP internal surfaces. This effect is particularly noticeable for ungetterable gases like Argon and Methane.

The resulting pumping speed of the NEG^+ is therefore larger than the sum of the pumping speed of the two separated pumps.

Reducing the degassing effect also increases the overall pumping efficiency at the lower pressure.

In fact, the presence of oxides and nitride compounds onto the cathode surface are known to slow down the diffusion of hydrogen and helium into the cathode [³], which is mainly an ion implantation driven process.

In the present paper we discuss some of these effects as well as the synergies arising from the NEG^+ integrated design. A specific focus will be given to argon [⁴] and methane, which are important gases to consider in a variety of application including electron microscopy and electron/ion optics.

[1] K.M. Welch, D.J. Pate and J. Todd, "Pumping of helium and hydrogen by sputter-ion pumps. II. Hydrogen pumping", *J. Vac. Sci. Technol. A* 12(3), May/June 1994

[2] A. Calcatelli et al. "Study of outgassing of sputter-ion pump materials treated with three different cleaning procedures", *Vacuum* vol. 47 n. 6-8, 1996

[3] M. Audi and M. De Simon, "The influence of heavier gases in pumping helium and hydrogen in a an ion pump", *J. Vac. Sci. Technol. A* 6 (3), May/June 1988

[4] D. Andrew, D.R. Sethna and G.F. Weston, "Inert-Gas pumping in a magnetron pump", *proc. 4th AVS*, (1968)

11:00am **VT+MN-MoM9 NEG+: A Novel Route to Compact, High Performance Pumping in UHV-XHV Vacuum Systems**, *P. Manini, A. Bonucci, A. Conte, L. Viale, L. Caruso*, SAES Getters S.p.A., Italy

The need to miniaturize and reduce the footprint of vacuum systems is growing in a variety of industrial and R&D applications, encompassing scanning and transmission microscopes, vacuum chambers for surface science, material preparation or portable analyzers.

This is posing serious challenges to the UHV pumping groups in term of design, space constraints and weight. Even in large vacuum systems, like synchrotrons and particle accelerators, fitting the vacuum pumps is becoming increasingly difficult, due to the presence of magnets, power stations, a variety of diagnostic tools and instrumentation, as well as service and experimental devices. Non Evaporable Getter (NEG) pumps are very compact and light, vibration-free devices, able to deliver extremely high pumping speed per unit volume with minimal power requirement. One of the main drawbacks of NEG pumps is their inability to pump noble gases and methane. In the present paper the design of a novel combination pump, called NEG^+ , is introduced. In the NEG^+ , the getter cartridge acts as the main pumping element, leaving to an ancillary and small sputter ion pump the task of removing noble gases and methane, which are not pumped by the NEG. Pumping of all the gases as well as the ability to provide a pressure reading, so helpful in a variety of applications, is therefore possible in one single and compact unit. The design of the NEG^+ is optimized to ensure a high integration between the getter element and the ion pump. This provides large pumping speed in a very compact volume as well as interesting synergies in the pumping of gases at the UHV level. The design and general properties of this new pump, including pumping tests and example of applications will be reported.

11:20am **VT+MN-MoM10 Direct Simulation Monte Carlo Modeling of Miniature Vacuum Pumps**, *B.J. Davis, R.W. Hill, P.H. Sorensen, R.J. Kline-Schoder*, Creare Incorporated

NASA and other organizations have pressing needs for miniaturized high vacuum systems. Recent advances in sensor technology at NASA and commercial laboratories have led to the development of highly miniaturized time-of-flight, quadrupole, and ion trap mass spectrometers. However, high vacuum systems of adequate performance continue to be too large, heavy, and power hungry for man-portable mass spectrometers or spectrometers deployed on UAVs, balloons, or interplanetary probes. Terrestrial, man-portable applications impacted by this problem include military and homeland defense systems for detecting hazardous materials as well as portable leak detectors for commercial use.

For over 10 years, Creare has been developing the technologies required to design and build miniature high vacuum pumps. We have designed and built pumps that are as small as a D-cell battery, reach an ultimate pressure of $10e-7$ torr, have a flow rate in excess of 5 L/s, and spin at 200,000 RPM. As mass spectrometers are reduced in size, the vacuum system requirements can be relaxed. As a consequence, Creare is developing an extremely low-cost and rugged high vacuum system whose performance is optimized for miniature mass spectrometers. The vacuum system is based on an innovative molecular drag pump designed to match the requirements of portable analytical instruments.

To support our miniature vacuum pump design efforts, Creare has developed statistical models of molecular drag pumps (MDP) in the free molecular flow regime. In this method, individual molecular trajectories through a simplified three-dimensional representation of the pump are calculated. The initial positions and velocities of the particles as they enter the pump are randomly generated, with statistics consistent with the gas states at the inlet and outlet of the pump. The free-molecular statistical simulation can be used to determine the probability that a molecule entering the pump at the inlet (outlet) exits through the outlet (inlet). In the free-molecular regime, these probabilities are sufficient to determine the pump's capabilities for compression, flow rate, etc.

We will describe the modeling methods, the verification of the models using previously published data, and the results of special experiments performed to verify that the models can be used to support new miniature pump designs.

11:40am **VT+MN-MoM11 Improvements in the Performance of Turbomolecular Pumps Beyond the Molecular Range**, *A. Chew, B. Brewster, I. Olsen, S. Ormrod*, Edwards Ltd, UK

A new range of turbomolecular pumps, nEXT, has been developed. This incorporates a new damping mechanism and pumping stage options. A new Siegbahn drag stage in combination with a regenerative mechanism are described in their combination with pure turbomolecular stages. Consequent increased backing pressures, high compression ratios and the facilitation of a boost port being used to back other turbos will be described.

Monday Afternoon, October 18, 2010

Actinides and Rare Earths Topical Conference

Room: Isleta - Session AC+TF-MoA

Actinide and Rare Earths Thin Films

Moderator: S.W. Yu, Lawrence Livermore National Laboratory

2:00pm **AC+TF-MoA1 EUV and in situ Spectroscopic Ellipsometric Analysis of the Oxidation of Uranium Thin Films, H. Dumais, D.D. Allred, R.S. Turley, Brigham Young University**

2:20pm **AC+TF-MoA2 Atomic Layer Deposition of Rare Earth Ion Co-doped Oxides for Optical Applications, J. Hoang, C. Pham, J.P. Chang, University of California, Los Angeles**

Rare earths (REs) exhibit unique shielded f-electrons giving rise to sharp spectral transitions. These transitions are dictated by the RE identity and can be manipulated by engineering the interactions of multiple RE ions. In this work, radical enhanced atomic layer deposition (RE-ALD) is used to design complex metal oxides with multiple dopants, whose concentration variation and spatial distribution control enable the synthesis of a wide range of multifunctional materials with tunable properties including magnetic, spectral, and electronic. Specifically, the control of sensitizer proximity and concentration is used to enhance amplification at 1.54 μm ($\text{Er } ^4\text{I}_{13/2} \rightarrow ^4\text{I}_{15/2}$) for compact planar optical amplifier applications and promote Er upconversion at 535 nm ($^2\text{H}_{11/2}, ^4\text{S}_{3/2} \rightarrow ^4\text{I}_{15/2}$) and at 670 nm ($^4\text{F}_{9/2} \rightarrow ^4\text{I}_{15/2}$). The spatial distributions between Er^{3+} and RE (RE = Yb^{3+} , Eu^{3+} , Ce^{3+}) are investigated with 1.54 μm emission promotion via direct energy transfer for Yb sensitizers and via cross relaxation for Eu and Ce sensitizers. Polycrystalline thin films are synthesized by sequential radical-enhanced ALD of Y_2O_3 , Er_2O_3 , Yb_2O_3 , and Eu_2O_3 at 350°C using 2,2,6,6-tetramethyl-3,5-heptanedionato analog of the corresponding metal (e.g. RE(TMHD)_x) and reactive oxygen atoms from a plasma. The composition, microstructure, cation distribution, local chemical bonding and optical properties of the synthesized thin films are determined by x-ray and Rutherford backscattering spectroscopies, electron microscopy and photoluminescence measurements. The effect of concentration is examined using a 8:1:x Y:Er:RE cycle sequence with x = 0, 1, 3, 5, 7, while the spatial distribution is investigated using a y:5:y:5 Y:Er:RE ratio with y = 0, 2, 4, 6, 8, 10. High resolution transmission electron microscopy on thin films deposited on nanotubes verify the construction of nanolaminates. Extended x-ray absorption fine structure Yb L2 edge scans show that the Yb local environment possesses more 2nd nearest neighbor Yb ions as the Yb cycles increases. Photoluminescence (PL) spectra using both 488 nm and 980 nm laser excitations show sharp Er intra 4f peaks with peak intensity centered at 1535 nm at low pump powers (~50 mW for 980 nm excitation). ~8x luminescence enhancement is achieved using a 8:1:3 Y:Er:Yb cycle ratio, while a slight decrease in PL intensity is apparent as the Er and Yb distance increases. Individual PL studies of Eu and Ce codoped Er:Y₂O₃ samples were found to require higher excitation powers, while tri-doped samples (Yb:Eu and Yb:Ce codoped Er:Y₂O₃) are currently under investigation to study further attainable PL enhancement and upconversion efficiency.

2:40pm **AC+TF-MoA3 Electronic Structure and Surface Reactivity of Actinide Systems, Th. Gouder, A. Seibert, European Commission, JRC, Institute for Transuranium Elements, Germany** **INVITED**

Actinide research is motivated by the peculiar properties of the 5f states which are on the verge from itinerancy to localization. These states confer to the actinides rich, yet often unpredictable chemical and physical properties. In this context surface science, focusing on the few topmost atomic layers, plays a particularly important role. In this region decreased bonding leads to 5f-band narrowing and enhances localization effects. On the other hand, the interaction of actinide surface atoms with the environment dominates the reactivity of spent nuclear fuel. Detailed knowledge of these surface reactions is required for the prediction of the long term storage behavior of spent fuel.

In the talk we will discuss the evolution of the electronic structure of actinide elements confined to thin films. We will describe film preparation by sputter deposition from elemental targets (Th, U, Np, Pu and Am) on strongly and weakly interacting substrates (Mg, Al, Si). Information on the electronic structure is obtained by photoemission spectroscopy. 5f localization occurs both with increasing Z and with decreasing layer thickness. In Pu, which is the last actinide where in the bulk the 5f states are itinerant, the 5f states become localized at one monolayer. For thicker films, photoemission shows precursor effects manifesting as final state multiplets.

For Np, the 5f states are always itinerant, even at the submonolayer level, but also here, deviation from the pure band behaviour is observed.

We will then compare actinide surface compounds, focusing on the oxides. The difference between surface and bulk oxides, and the specific contribution of the 5f states will be discussed. In late actinides oxides (down to Pu) the 5f states are well localized and only rare-earth like (An₂O₃) sesquioxides and (AnO₂) dioxides are observed. There is no higher oxide. With decreasing Z, the increasingly bonding 5f states destabilize the An₂O₃ favoring AnO₂, and simultaneously enable higher oxidation states beyond AnO₂. Here again, the presence of the surface with its lowered coordination and increased tendency for 5f localization leads to oxidation states different from the bulk.

Finally, we will give a brief overlook on actinide surface reactions with the environment, where 5f states are involved (catalysis and photochemistry). We will present the surprising surface reduction of PuO₂ thin films by water, which we attribute to a photochemically driven surface reaction involving 5f states. Such processes may fundamentally influence the long term storage properties of spent fuel.

3:40pm **AC+TF-MoA6 Observation of Strong Resonant Behavior in the Inverse Photoelectron Spectroscopy of Ce Oxide, J.G. Tobin, S.W. Yu, B.W. Chung, Lawrence Livermore National Laboratory, G.D. Waddill, Missouri University of Science and Technology, L. Duda, J. Nordgren, Uppsala University, Sweden**

X-ray Emission Spectroscopy (XES) and Resonant Inverse Photoelectron Spectroscopy (RIPES) have been used to investigate the photon emission associated with the Ce3d_{5/2} and Ce3d_{3/2} thresholds. Strong resonant behavior has been observed in the RIPES of Ce Oxide near the 5/2 and 3/2 edges. Inverse Photoelectron Spectroscopy (IPES) and its high energy variant, Bremstrahlung Isochromat Spectroscopy (BIS), are powerful techniques that permit a direct interrogation of the low-lying unoccupied electronic structure of a variety of materials. Despite being handicapped by counting rates that are approximately four orders of magnitude less than the corresponding electron spectroscopies (Photoelectron Spectroscopy, PES, and X-ray Photoelectron Spectroscopy, XPS) both IPES [1,2,3,4,5] and BIS [6,7,8] have a long history of important contributions. Over time, an additional variant of this technique has appeared, where the kinetic energy (KE) of the incoming electron and photon energy (hν) of the emitted electron are roughly the same magnitude as the binding energy of a core level of the material in question. Under these circumstances and in analogy to Resonant Photoelectron Spectroscopy, a cross section resonance can occur, giving rise to Resonant Inverse Photoelectron Spectroscopy or RIPES. [9-13] Here, we report the observation of RIPES in an f electron system, specifically the at the 3d_{5/2} and 3d_{3/2} thresholds of Ce Oxide.

References

1. G. Denninger, V. Dose, and H. P. Bonzel, Phys. Rev. Lett. 48, 279 (1982); V. Dose, Appl. Phys. 14, 117 (1977).
2. P. D. Johnson and N. V. Smith, Phys. Rev. Lett. 49, 290 (1982).
3. F. J. Himpsel and Th. Fauster, Phys. Rev. Lett. 49, 1583 (1982).
4. B.J. Knapp and J.G. Tobin, Phys. Rev. B 37, 8656 (1988).
5. J.G. Tobin, "Photoemission and Inverse Photoemission," in "Determination of Optical Properties," Vol. VIII in Physical Methods of Chemistry, 2nd edition, Ed. B.W. Rossiter and R.C. Bretzold, John Wiley and Sons, New York, 1993 and references therein.
6. E. Wuilloud, et al, Phys. Rev. Lett. 53, 202 (1984); E. Wuilloud, et al, Phys. Rev. B 28, 7354 (1983);
7. J.W. Allen, J. Magn. Mater. 47/48, 168 (1985). check
8. P. Kuiper, et al, Phys. Rev. B 44, 4570 (1991).
9. R. J. Liefeld, A.F. Burr and M.B. Chamberlain, Phys. Rev. A 9, 316 (1974); M.B. Chamberlain, A.F. Burr, and R.J. Liefeld, Phys. Rev. A 9, 663(1974).
10. F. Reihle, Phys. Status Solidi 98, 245 (1980).
11. Y.Hu, et al, Phys. Rev B 38, 12709 (1988).
12. P. Weibel, et al, Phys. Rev. Lett. 72, 1252 (1994); M. Grioni, et al, Phys. Rev. B 55, 2056 (1997).
13. B.E. Mason, R.J. Liefeld, J. Vac. Sci. Tech. A 8, 4057 (1990).

4:00pm **AC+TF-MoA7 Growth and Reactivity of CeO₂(100) Thin Films**, *D.R. Mullins, T.-L. Chen, F.C. Calaza, S.H. Overbury, M.D. Biegalski, H.M. Christen*, Oak Ridge National Laboratory

Cerium oxide is a principal component in many heterogeneous catalytic processes. One of its key characteristics is the ability to provide or remove oxygen in chemical reactions. The different crystallographic faces of ceria present significantly different surface structures and compositions that may alter the catalytic reactivity. The structure and composition determine the availability of adsorption sites, the spacing between adsorption sites and the ability to remove O from the surface.

To investigate the role of surface orientation on reactivity, CeO₂ films were grown with two different orientations. CeO₂(100) films were grown *ex situ* by pulsed laser deposition on Nd-doped SrTiO₃(100). The structure was characterized by RHEED, XRD and reflectometry. CeO₂(111) films were grown *in situ* by thermal deposition of Ce metal onto Ru(0001) in an oxygen atmosphere. The structure of these films has been studied by LEED and STM. Attempts to grow CeO₂(100) *in situ* by physical vapor deposition on Pt(100) and Pd(100) failed due to preferential growth of CeO₂(111) on these supports.

The chemical reactivity was characterized by the adsorption and decomposition of methanol and 2-propanol. Reaction products were monitored by TPD and surface intermediates were determined by soft x-ray photoelectron spectroscopy and infrared spectroscopy. Both of these alcohols readily chemisorbed on either surface in UHV. The decomposition of methanol was less selective on CeO₂(100) than on CeO₂(111) with CO and H₂ resulting even from a fully oxidized surface. Water was also produced as on CeO₂(111), and the CeO₂(100) surface could be reduced by exposure to methanol at 700 K. Unlike on reduced CeO_x(111), methanol adsorption on reduced CeO_x(100) produced only a small increase in reactivity and inhibited formaldehyde formation. 2-propanol produced primarily propene and water with a small amount of acetone.

Research sponsored by the Division of Chemical Sciences, Geosciences, and Biosciences, Office of Basic Energy Sciences, US Department of Energy, under contract DE-AC05-00OR22725 with Oak Ridge National Laboratory, managed and operated by UT-Battelle, LLC. Use of the National Synchrotron Light Source, Brookhaven National Laboratory, was supported by the US Department of Energy, Office of Science, Office of Basic Energy Sciences, under Contract No. DE-AC02-98CH10886. Research at Oak Ridge National Laboratory's Center for Nanophase Materials Sciences was sponsored by the Scientific User Facilities Division, Office of Basic Energy Sciences, U.S. Department of Energy.

4:20pm **AC+TF-MoA8 Photoemission Study of Au-Schottky Barrier Formation on YbGaN Thin Films using Synchrotron Radiation**, *S.R. McHale, J.W. McClory, J.C. Petrosky*, Air Force Institute of Technology, *Y.B. Losovyj*, Louisiana State University

Au-YbGaN Schottky barrier formation was observed using Au evaporation on multiple concentrations of Yb_xGa_{1-x}N thin films deposited on (111) Si substrates. Low Energy Electron Diffraction was performed to verify the integrity of the Au deposition. Energy dependent, synchrotron generated photoemission spectroscopy ranging from 15 to 26 eV under UHV conditions clearly determined a valence band shift of up to 0.62 eV.

The experiments were conducted at the Louisiana State University (LSU) Center for Advanced Microstructures and Devices (CAMD), using synchrotron radiation dispersed by the 3m toroidal grating monochromator (TGM) beamline, where resolution of the experimental apparatus is approximately 70 meV. Thin films were fabricated using RF plasma-assisted molecular beam epitaxy (PAMBE) at the University of Nebraska (Lincoln) Center for Materials and Nanoscience (NCMN). Yb temperatures during deposition were 500 °C, 700 °C, and 860 °C, resulting in slightly coarse, uniform, and very coarse grained films, respectively. The XRD patterns show a high degree of order in the films.

A least squares fit was used to calculate the valence band maximum (VBM) for each spectrum. Comparing the calculated VBM values for the bare YbGaN sample spectra with those following Au deposition shows that Au clearly affects the YbGaN electronic structure by shifting the valence band toward the Fermi energy by a maximum value of 0.62 eV at a monolayer of Au coverage. This valence band shift yields a calculated Schottky Barrier, ϕ_{SB} , of 0.83 eV, determined by the relationship $E_{\text{g}} - (E_{\text{F}} - E_{\text{VBM}})$, where the energy gap, E_{g} , was approximated at 3.5 eV.

SB calculation via direct spectroscopic data will be supplemented by SB calculation via I-V measurements of the sample surface, using a Keithley 4200 Semiconductor Characterization System and a Signatone Probe Station.

Our research efforts are motivated by radiation detection materials and devices. Radiation detector diodes typically operate in the reverse bias mode, where Schottky contacts are desirable to optimize the signal-to-noise

ratio. Therefore, we intend to extend these results to facilitate additional measurements using other Lanthanide-doped III-nitride compounds in a future research endeavor involving potential radiation detection materials. We anticipate that this effort will improve researchers' determination of suitable combinations of materials, and will produce novel, efficient, and more accurate neutron detection devices than currently available.

Electronic Materials and Processing

Room: Dona Ana - Session EM+MI-MoA

Semiconducting and Highly Correlated Oxides

Moderator: L.J. Brillson, The Ohio State University

2:00pm **EM+MI-MoA1 Oxide Superconducting Semiconductors**, *H.Y. Hwang*, University of Tokyo, Japan **INVITED**

3:00pm **EM+MI-MoA4 X-ray Photoemission Spectroscopy of Sr₂FeMoO₆ Film Stoichiometry and Valence State**, *M.M. Rutkowski, A.J. Hauser, F.Y. Yang, R. Ricciardo, T. Meyer, P.M. Woodward, A. Holcombe, P.A. Morris, L.J. Brillson*, The Ohio State University

We have used a combination of monochromatized X-ray photoemission spectroscopy and Rutherford backscattering spectrometry to determine bulk compound stoichiometry and charge state of Sr₂FeMoO₆ epitaxial films. Complex oxides are an attractive class of materials for the creation of novel electronic devices due to their diverse properties. Sr₂FeMoO₆ (SFMO) is one such material due to the discovery of low field colossal magnetoresistance at room temperature and its half metallic character making it suitable in applications from magnetic read heads and nonvolatile magnetic random access memory to spin injectors in spintronic devices. But in order to create functional devices from such materials, it is necessary to have complete control over the crystal stoichiometry and ordering. Complicating this is that many of these materials, SFMO included, are not point compounds and small changes in stoichiometry can lead to the formation of other material phases which would strongly influence the materials properties.

Using standard samples with known stoichiometries of Fe₂O₃ and SrMoO₃, we were able to obtain sensitivity factors relative to oxygen for Sr, Fe, and Mo. In conjunction with RBS measurements, these sensitivities allowed us to determine sensitivity factors specific to SFMO for measuring stoichiometry. These studies also identify an optimum ion sputtering process for removing surface contaminants and an SrMoO₄ overlayer while avoiding preferential sputtering of film constituents or alteration of their characteristic valence states. For Sr₂FeMoO₆, low energy (500 eV), glancing incidence Ar⁺ sputtering for short (tens of seconds) periods is successful in achieving stoichiometric compositions and characteristic charge states of the film constituents. Furthermore, the adventitious surface carbon content dropped from 10% to less than 2% in the first 15s of sputtering. With longer sputtering times we observed the oxygen content to fall below its stoichiometric value (60%) and continue to fall with further sputtering indicating the preferential removal of oxygen from the film. We also observed the emergence of a metallic component to the iron and molybdenum valence states after 120s of sputtering indicating damage to the crystal lattice. Thus XPS reveals both a different surface overlayer stoichiometry as well as a 'window' of sputter time that provides bulk stoichiometry. The evolution of composition and valence state with sputtering provides a guide to measure stoichiometry and charge state of SFMO and complex oxide thin films in general.

4:00pm **EM+MI-MoA7 Electronic Structure of Ferrimagnetic Co_{1-x}Fe_{2+x}O₄ Determined by Soft X-ray and Ultraviolet Spectroscopies**, *J.A. Moyer, C.A.F. Vaz, Yale University, D.A. Arena*, Brookhaven National Laboratory, *V.E. Henrich*, Yale University

Developing new materials with large spin polarizations, high Curie temperatures and resistivities similar to those of semiconductors would greatly benefit the field of spintronics. Cobalt ferrite (CoFe₂O₄), like its parent compound magnetite (Fe₃O₄), is a promising material for spintronic applications due to its high Curie temperature ($T_c=793$ K) and large predicted spin polarization; however, CoFe₂O₄ is an insulator. Cobalt ferrite becomes an *n*-type conductor when doped with excess iron - Co_{1-x}Fe_{2+x}O₄; the origin of the conduction is electron hopping between Fe²⁺ cations in octahedral sites. The strong localization of electrons on the Fe²⁺ cations in this highly correlated oxide keeps the conductivity in the semiconducting range. In this work, heteroepitaxial Co_{1-x}Fe_{2+x}O₄ thin films have been grown on MgO (100) and MgAl₂O₄ (100) and (110) with *x* ranging from 0 to 0.5. The electronic band structure near the Fermi energy is measured with ultraviolet photoelectron spectroscopy (UPS), and the results are correlated with resistivities determined from transport measurements. This range of

doping allows for the resistivity to be tailored over two orders of magnitude. The cation valence states and occupation sites are determined with x-ray photoelectron spectroscopy (XPS) and x-ray absorption spectroscopy (XAS). Bulk magnetic moments are obtained with SQUID magnetometry, while bulk and site specific orbital and spin magnetic moments are obtained using x-ray magnetic circular dichroism (XMCD). The XMCD measurements provide a view of the spin polarization of the Fe^{2+} octahedral cations responsible for conduction. The wide variety of measurements enables us to determine the electronic structure of $\text{Co}_{1-x}\text{Fe}_{2+x}\text{O}_4$, an important development for the goal of determining the viability of $\text{Co}_{1-x}\text{Fe}_{2+x}\text{O}_4$ as a spin-polarized source or detector in spintronic devices.

This research is primarily supported by NSF Grant MRSEC DMR-0520495.

4:20pm EM+MI-MoA8 Effects on the Electronic Band Structure of EuO Films upon Gd Doping, *J.A. Colón, J. An, K.D. Belashchenko*, University of Nebraska - Lincoln, *Y.B. Losovyj*, Louisiana State University, *P. Liu, X.J. Wang, J. Tang*, University of Wyoming, *P.A. Dowben*, University of Nebraska - Lincoln

High quality films of EuO and Gd doped EuO were successfully grown on Si (100) via pulse laser deposition (PLD). The addition of 4% Gd introduces considerable effects on the texture growth direction, although the crystal structure remains intact. This Gd doping also has a strong influence on the electronic structure of these films, in particular the apparent band offsets, making the material appear considerably more n-type in combined photoemission and inverse photoemission studies. There are also concomitant changes to the conductivity properties. To further elucidate the influence of Gd doping on the electronic band structure of the EuO films, heterojunction devices were constructed resulting in diodes with very distinct properties a negative differential current that depends on magnetic field.

4:40pm EM+MI-MoA9 Catalytic Performance for Soot Combustion of Lanthanum-Based Cobalt-Iron Perovskite Materials, *L.M. Petkovic, S.N. Rashkeev*, Idaho National Laboratory, *V. Ugikar*, University of Idaho Perovskite-type oxide materials with a general formula $\text{La}_{0.8}\text{A}_{0.2}\text{Fe}(1-y)\text{Co}(y)\text{O}(3-\delta)$, where A is Sr or Ba and $y=0.4$ or 0.5 , were prepared and tested in the combustion of carbon black, which can be regarded as a conservative soot model. Maximum combustion rates under temperature programmed combustion conditions were found at temperatures about 150°C lower than blank combustion experiments. A combination of density-functional-theory (DFT) calculations and characterization analyses such as surface area, infrared spectroscopy, X-ray diffraction, and temperature programmed oxidation and reduction were applied to elucidate the main processes that contribute to the activity of these catalysts for soot combustion. The results suggest the importance of the kinetics of oxygen adsorption and reaction at the surface and oxygen migration in the bulk.

Energy Frontiers Topical Conference Room: Mesilla - Session EN-MoA

Excitonic and Third Generation Solar Cells Moderator: J.B. Baxter, Drexel University

2:00pm EN-MoA1 Beyond the Adiabatic Limit: Charge Separation in Organic Photovoltaic Materials, *R.D. Pensack, J.B. Asbury*, Penn State University **INVITED**

The dynamics of charge separation in photovoltaic polymer blends following photoinduced electron transfer from the conjugated polymer, CN-MEH-PPV, to the electron accepting functionalized fullerene, PCBM, are observed with ultrafast vibrational spectroscopy. The investigators take advantage of a solvatochromic shift of the vibrational frequency of the carbonyl (C=O) stretch of PCBM to directly measure the rate of escape of electrons from their Coulombically bound charge transfer (CT) excitons at donor/acceptor interfaces on ultrafast time scales. The data reveal that the rate of dissociation of CT excitons is temperature independent from 200 to 350 K indicating that excess energy in hot CT excitons plays an important role in mediating charge separation. These observations suggest that conceptual and theoretical descriptions properly taking into account the strong coupling of electronic and nuclear degrees of freedom in organic semiconductors are essential to understand the mechanism of charge separation in organic photovoltaic materials. From a practical stand-point, efforts to develop new low band-gap polymers for organic solar cells should target electron donor and acceptor pairs capable of advantageously redistributing excess energy in hot CT excitons to enable efficient charge separation with minimal donor-acceptor energy level offsets.

2:40pm EN-MoA3 Third Generation Photovoltaics: Multiple Exciton Generation in Colloidal Quantum Dots, Quantum Dot Arrays, and Quantum Dot Solar Cells, *A.J. Nozik*, National Renewable Energy Lab and Univ. of Colorado, Boulder, *M.C. Beard, J.M. Luther*, National Renewable Energy Lab, *A.G. Midgett, O.E. Semonin*, Univ. of Colorado, Boulder, *J.C. Johnson*, National Renewable Energy Lab **INVITED**

One potential, long-term approach to more efficient future generation solar cells is to utilize the unique properties of quantum dot (QD) nanostructures to control the relaxation pathways of excited QD states to produce enhanced conversion efficiency through efficient multiple exciton generation (MEG) in QDs.

We have observed efficient multiple exciton generation (MEG) in PbSe, PbS, PbTe, and Si QDs at threshold photon energies of 2-3 times the HOMO-LUMO transition. We have studied MEG in close-packed QD arrays where the QDs are electronically coupled in the films and thus exhibit good carrier mobility. We have developed simple, all-inorganic QD solar cells that produce large short-circuit photocurrents via both nanocrystalline Schottky junctions and nanocrystalline p-n junctions without the need for QD sintering, superlattice order or separate phases for electron and hole transport. The latter shows an NREL-Certified conversion efficiency of 3%. We have demonstrated that the MEG efficiency in conductive Pb chalcogenide QD films after certain chemical treatments can be comparable to isolated QDs in colloids, but the QY varies greatly depending upon the specific chemical treatment and subsequent QD surface chemistry.

Selected aspects of this work will be summarized and recent advances will be discussed. Various possible configurations for novel QD solar cells that could produce very high conversion efficiencies will be presented, along with progress in developing such new types of solar cells. Recent controversy about MEG and its application to photovoltaic cells will also be addressed.

3:40pm EN-MoA6 Solar Cells Based on Semiconductor Quantum Dots and Nanowires, *K.S. Leschkies*, University of Minnesota **INVITED**

Solar cells based on colloidal semiconductor nanocrystals, or quantum dots (QDs) may have the potential to achieve high power conversion efficiencies at low cost. Quantum confinement of electrons and holes in these nanometer-size crystals endows them with properties that may be advantageous for efficient solar-to-electric energy conversion. For example, varying the QD size changes the electronic energy levels and optical absorption in QDs. This allows the optimization of their optical absorption for maximum overlap with the solar spectrum. In addition, QDs can be prepared in large quantities as stable colloidal solutions under mild conditions and deposited as thin films using inexpensive, high-throughput coating processes to form solar cells.

After a brief review of the literature on QD solar cells, I will focus on a new type of QD solar cell based on heterojunctions between PbSe QDs and thin ZnO films designed to improve on the current state-of-the-art. These QD solar cells were fabricated by depositing thin films of ZnO and PbSe QDs onto a glass substrate coated with conductive indium-tin-oxide (ITO), which forms the bottom contact of the device. Absorption of light produces electron-hole pairs in the QDs that dissociate, either at a QD-electrode interface or within the QD film and generate photocurrent. Specifically, electrons lower their energy by transferring into the ZnO film, which forms a type-II heterojunction with the PbSe QDs. These electrons move across the ZnO film and are collected at the ITO contact while the positive charges are transported to and collected at a top gold electrode.

Under simulated sunlight, the QD solar cells exhibit short-circuit currents as high as 15 mA/cm^2 and open-circuit voltages up to 0.45 V . The solar cell open-circuit voltage depends on the QD size and increases linearly with the QD effective band gap energy. Charge collection in these devices can be increased further by using nanostructured interfaces between PbSe QDs and ZnO. Specifically, the ZnO film can be replaced with a vertical array of ZnO nanowires, and infiltrating this array with colloidal PbSe QDs. These nanowire-quantum-dot solar cells exhibited power conversion efficiencies of 2%, nearly three times higher than that achieved with thin-film ZnO devices constructed with the same amount of QDs. Supporting experiments using field-effect transistors made from these QDs also show that the QDs' electrical properties are strongly influenced by the presence of nitrogen and oxygen atmospheric gases. Such results have important implications with respect to the assembly, characterization, and exposure of QD-based solar cells to an ambient environment.

4:20pm EN-MoA8 PbSe and PbS Nanocrystal Solar Cells, *J.J. Choi, J. Luria, B.-R. Hyun, A.C. Bartnik, L. Sun, Y.-F. Lim, J.A. Marohn, F.W. Wise, T. Hanrath*, Cornell University **INVITED**

Rational progress towards nanocrystal based solar cells demands an improved understanding of electronic and optical interactions of proximate nanocrystals in functional assemblies. We combined transient

photoluminescence spectroscopy and electric force microscopy to probe photogenerated exciton dissociation in PbS nanocrystal assemblies. We show that excitons dissociate via charge tunneling between neighboring nanocrystals. Implications in the context of nanocrystal photovoltaic devices will be discussed. We also present the design, fabrication and characterization of excitonic solar cells based on PbSe and PbS nanocrystal active layers. The best performing device shows a 1-sun power conversion efficiency of 4%.

5:00pm EN-MoA10 Solid-State Quantum Dot Sensitized Solar Cells: Atomic Layer Deposition versus Successive Ionic Layer Adsorption and Reaction, P. Ardalan, T.P. Brennan, J.R. Bakke, S.F. Bent, Stanford University

Narrow band gap nanostructures such as cadmium sulfide quantum dots (QDs) are known to show size quantization effects. In quantum dot sensitized solar cells (QDSSCs), these QDs can be engineered to transfer an electron to a wide band gap semiconductor such as titanium dioxide (TiO₂). However, performance in such devices is reduced by charge recombination at the TiO₂ surface and hence use of organic linkers such as self-assembled monolayers (SAMs) on these devices could provide a means of eliminating recombination sites and lead to increased efficiency. In this study, we investigated the effects of different aliphatic and aromatic SAMs with phosphonic acid headgroups and varied tailgroups on the bonding and performance of cadmium sulfide (CdS) solid-state QDSSCs. TiO₂ was deposited on piranha-cleaned Si or microscope glass via atomic layer deposition (ALD) and the resulting surfaces were characterized by ultraviolet photoelectron spectroscopy (UPS), X-ray photoelectron spectroscopy (XPS), Auger electron spectroscopy (AES), scanning electron microscopy (SEM), and atomic force microscopy (AFM). Next, different SAMs were attached from solution to either ALD-deposited (planar) or doctor-bladed (nanoporous) TiO₂ substrates, and the effects of chain length, aromaticity, and tailgroup on the quality of the SAMs were investigated. CdS QDs were then grown on the SAM-passivated TiO₂ surfaces by either successive ionic layer adsorption and reaction (SILAR) from solution or by atomic layer deposition (ALD) from the gas phase, and the bonding and performance of the resulting materials were evaluated by UV-visible and other spectroscopic techniques. Our results show that CdS QDs with particle sizes in the range of 2 to 6 nm are grown by SILAR on TiO₂ both with and without SAMs, but more CdS can be deposited on samples with SAMs with the exception of the long-chain methyl-terminated monolayer. Furthermore, it is determined that the SAM chain length affects the SILAR CdS deposition at the TiO₂ surfaces more significantly than does the identity of the tailgroup. ALD also is effective for depositing CdS QDs, but less CdS is deposited by ALD than by SILAR at TiO₂ surfaces for the same number of cycles. QDSSC devices have been made using both SILAR and ALD, and we will present results on the dependence of solid-state QDSSC performance and efficiency on the deposition technique employed to grow the CdS QDs, as well as on the properties of the SAM. Overall, we observed higher efficiencies in devices with SAMs and we propose that this result can be attributed to the presence of a charge recombination barrier.

5:20pm EN-MoA11 Synthesis and Application of Branched Titania Nanotubes in Dye-Sensitized Solar Cells, G. Butail, P. Gopal, M. Raddiar, R. Teki, N. Ravishankar, G. Ramanath, Rensselaer Polytechnic Institute

Titania is a promising photocatalyst used in a variety of photovoltaic, optoelectronic and biofiltering applications. There is great interest in synthesizing high surface area titania nanostructures by inexpensive means for low-cost power generation, among which titania nanotubes offer higher efficiencies because of unidirectional charge transport and low scattering losses. Here we demonstrate, for the first time, the formation of branched titania nanotubes using potentiostatic anodization of titanium thin films. The realization of branched titania nanotubes provides a means to tune the electronic properties of titania and to functionalize them with multi-sized quantum dots and other metallic/semiconducting nanostructures.

Experimental analysis show anodization diameter to be a linear function of applied voltage. We exploit the relationship between the anodization voltage and nanotube diameter to obtain and control the extent of branching and tune branch diameters between 30 to 110 nm. Branching achieved through single step voltage induced anodization offers the added advantage of control of point of branching depending on rate of anodization at each voltage. We also evaluate the morphology and the optical properties of branched titania nanotubes and compare their light-harvesting efficiency with unbranched nanotubes in dye-sensitized solar cells. We specifically compare branched titania nanotubes formed by ramping down the voltage from 60 to 33 V and compare the them with titania nanotubes formed at 60 V and 33 V. Preliminary results show a 33% increase in active surface area of branched titania nanotubes as compared to unbranched nanotubes formed at 60 V which is further confirmed through BET analysis.

Application of straight (unbranched) titania nanotubes for fabrication of dye-sensitized solar cells using a ruthenium based dye (N719) results in an efficiency of 0.58±0.2% with short circuit current density of 6.3±1.0 mA/cm² and fill factor of 22.4±0.2. Use of branched titania nanotubes of same thickness under same conditions reports an efficiency of 1.04±0.1% with increase in short circuit current density to 9.1±0.8 mA/cm² and a fill factor of 23.7±0.1%. A two-fold enhancement of photovoltaic efficiency of branched samples as compared to straight nanotubes correlates well to the difference in surface area and optical properties of the two structures.

Graphene Focus Topic

Room: Brazos - Session GR+NS-MoA

Graphene: Chemical Reactions

Moderator: T. Seyller, Universität Erlangen, Germany

2:00pm GR+NS-MoA1 Chemical Interactions during Thermal Reduction of Multilayered Graphene Oxide, M. Acik, University of Texas at Dallas, C. Mattevi, Imperial College London, C. Gong, G. Lee, K.J. Cho, University of Texas at Dallas, M. Chhowalla, Imperial College London, Y.J. Chabal, University of Texas at Dallas

Graphene/graphite oxide (GO), with its non-stoichiometric chemical structure and highly hygroscopic functionalized graphene backbone, has been of interest for chemical energy storage applications such as supercapacitors and ultracapacitors as well as its reduced form for bioelectronic applications such as sensor networks and for printed electronics. For all these applications, it is important to characterize and control the chemical nature of GO at various stages of thermal reduction. In particular, the formation and evolution of defect structures within GO can greatly impact the resulting properties. Similarly, the properties of species intercalated between individual planes can alter the reduction chemistry. The interplay between intercalated species and defect sites can lead to interesting new chemistry.

To understand these chemical interactions, we have studied the deoxygenation process of both single- and multi-layer(s) of GO and focused on comparing the removal of oxygen upon heating both from the basal plane and the edges, by bringing to bear a number of methods. In particular, we have carried out a series of experiments using *in-situ* IR absorption spectroscopy (FTIR), x-ray diffraction technique (XRD), *ex-situ* raman scattering, thermogravimetric analysis (TGA), transmission electron microscopy (TEM), and x-ray photoelectron spectroscopy (XPS), together with density functional (DFT) calculations and molecular dynamic (MD) simulations of various oxygen structures and resulting electronic states. The IR absorption spectra reveal the formation of ketones, ethers and sp²-hybridized C=C as well as a loss of hydroxyls, carboxyls and epoxides upon gradual annealing. They also confirm that defect formation is a direct result of CO₂ and CO formation, and highlight the role of intercalated species, such as water. At higher temperatures (~850°C), oxygen is found to remain at the edges of defective sites in a very stable configuration, involving the alignment of edge ether. Overall, the structure of GO upon annealing exhibits interesting, and in some cases unexpected features, which could have a crucial role and applicability to various systems such as vibration-powered energy scavenging, night vision tracking systems and optoelectronics.

*The authors acknowledge funding from the SWAN/NRI program and Texas Instruments.

2:20pm GR+NS-MoA2 Non-bonding State formed Around Defects on HOPG, J. Nakamura, T. Kondo, J. Oh, D. Guo, Y. Honma, T. Machida, University of Tsukuba, Japan

Understanding the interface interaction between metal nano-clusters and carbon supports composed of graphite materials is one of the most important needs in the development of carbon related-catalysts. We have studied the carbon support effects on the electrocatalysts for fuel cells as well as the interface interaction using model catalysts of Pt-deposited highly oriented pyrolytic graphite (HOPG) by IETS-STs-STM, TPD, and molecular/atomic beam technique. Here, we report the formation of non-bonding state in the vicinity of defects on the HOPG surface. We have measured STS spectra at many different points in the vicinity of the point defect. STS spectra were very different depending on the point of the measurement. In the directions perpendicular to short zigzag edges at the point defect, STS peaks appear near the Fermi level, suggesting the edge state or non-bonding state. The non-bonding state propagates 3-4 nanometers away from the defect with three-fold symmetry. No such a STS peak was observed near the point defect in the other directions. We thus constructed a STS map showing the distribution of the non-bonding state. We also observed spatial "oscillations" in the *dI/dV* peak position and the

intensity. The oscillations have been explained as electron-electron interaction or electron-hole interaction. We currently consider that the non-bonding state is responsible for the chemical reactivity such as adsorption of atom, molecules, and clusters.

References

1. E. Yoo, J. Nakamura, et al., Nano Letters 9 (2009) 2255.
2. T. Kondo, J. Nakamura, et al., Phys. Rev. B 80 (2009) 233408.
3. J. Oh, T. Kondo, J. Nakamura, et al., J. Phys. Chem. Lett. 1 (2010) 463.
4. T. Kondo, J. Nakamura, et al., J. Phys. Chem. C 112 (2008) 15607.

2:40pm GR+NS-MoA3 Opto-electronic Properties of Solution Processable Chemically Derived Graphene Oxide, M. Chhowalla, Rutgers University **INVITED**

A solution based method that allows uniform and controllable deposition of reduced graphene oxide thin films with thicknesses ranging from a single monolayer up to several layers over large areas will be described. Transport of carriers in reduced GO is limited by the structural disorder. However, conductivity of 10^3 S/m and mobilities of ~ 10 cm²/V-s are sufficiently large for applications where inexpensive and moderate performance electronics are required. The oxidation treatment during synthesis of GO creates sp^3 C-O sites where oxygen atoms are bonded in the form of various functional groups. GO is therefore a two dimensional network of sp^2 and sp^3 bonded atoms, in contrast to an ideal graphene sheet which consists of 100% sp^2 carbon atoms. This unique atomic and electronic structure of GO, consisting of variable sp^2/sp^3 fraction, opens up possibilities for new functionalities. The most notable difference between GO and mechanically exfoliated graphene is the opto-electronic properties arising from the presence of finite band gap. In particular, the photoluminescence can be tuned from blue to green emission. The atomic and electronic structure along with tunable photoluminescence of graphene oxide at various degrees of reduction will be described.

3:40pm GR+NS-MoA6 Structural Evolution during the Reduction of Chemically Derived Graphene Oxide, V.B. Shenoy, Brown University / Rhode Island Hospital

The excellent electrical, optical and mechanical properties of graphene have driven the search to find methods for its

large-scale production, but established procedures (such as mechanical exfoliation or chemical vapour deposition) are not

ideal for the manufacture of processable graphene sheets. An alternative method is the reduction of graphene oxide, a

material that shares the same atomically thin structural framework as graphene, but bears oxygen-containing functional

groups. Here we use molecular dynamics simulations to study the atomistic structure of progressively reduced graphene

oxide. The chemical changes of oxygen-containing functional groups on the annealing of graphene oxide are elucidated and

the simulations reveal the formation of highly stable carbonyl and ether groups that hinder its complete reduction to

graphene. The calculations are supported by infrared and X-ray photoelectron spectroscopy measurements. Finally, more

effective reduction treatments to improve the reduction of graphene oxide are proposed [1].

[1] Akbar Bagri, Cecilia Mattevi, Muge Acik, Yves J. Chabal, Manish Chhowalla and

Vivek B. Shenoy, Nature Chemistry (in press, 2010).

4:00pm GR+NS-MoA7 Perfluorographane: Synthesis and Properties, J.S. Burgess, National Research Council, J.A. Robinson, Naval Research Laboratory, M. Zalaludinov, SFA, inc, K. Perkins, P.M. Campbell, E. Snow, B.H. Houston, J.W. Baldwin, Naval Research Laboratory

Graphene was grown by CVD on a copper substrate. The as-grown samples and samples transferred to silicon on insulator (SOI) and SiO₂ substrates were then exposed to XeF₂ gas resulting in fluorination of the graphene sheets. The samples were characterized using XPS and Raman spectroscopies. XPS showed maximum fluorine content in the graphene of 20 % for the graphene on copper and 50 % on SOI. The marked difference is owed to the etching of the silicon layer on the SOI substrate, allowing exposure of the underside of the graphene sheet to the XeF₂ gas and fluorination of both sides of the graphene sheet. The fluorine was removed from the film using both thermal and chemical (hydrazine reduction) methods. Chemical, mechanical, and electrical properties of these materials will also be discussed.

4:20pm GR+NS-MoA8 Stability and Activity of Pt Nanoclusters Supported on Graphene Monolayers on Ru(0001), O. Alves, C. Lorenz, H.E. Hoster, R.J. Behm, Ulm University, Germany

Being an atomically thin half-metal and exhibiting moiré-type nm-scale superstructure, graphene monolayers supported on metal single crystals [1-3] can serve as a template for the growth of ordered arrays of nanosized metallic (electro-)catalyst particles. These particles, which are fabricated by simple metal vapour deposition in ultrahigh vacuum [4-6] and comprise monodispersed Pt clusters seeded on the graphene monolayer on Ru(0001), were found to nucleate preferentially at a unique region in the Moiré unit cell and displayed heights of 1-5 atomic layers and lateral diameters within the range 1-4 nm. The size selectivity of the Pt nanoclusters, jointly with their self-assembled array, assign them as interest and promising system for (electro-)catalytic model studies.

We will report on the activity and stability either of a single graphene monolayer or of the Pt clusters. The graphene layers and the cluster arrays are prepared in ultrahigh vacuum, whilst the potential-dependent reaction studies are measured in a wall-jet type flow cell sited in an electrochemical pre-chamber attached to the main UHV system. Cluster arrays with different total Pt coverages and cluster size distributions were tested as electrodes for elementary reactions as hydrogen evolution/oxidation, CO oxidation, or O₂ reduction. According to STM analyses before and after the electrochemical tests, we discuss in how far the stabilities of clusters of various sizes can be rationalized in terms of reaction conditions and applied potentials. The general electrochemical behaviour of the Pt cluster arrays will be discussed in comparison to bulk Pt. As a main (electro-)catalytic result, we find a surprisingly high activity for hydrogen evolution.

[1] C. Oshima et al., J. Phys. Condens. Matter 9,1 (1997).

[2] S. Marchini et al., Phys. Rev. B 76, 075429 (2007).

[3] Coraux et al., Nano Lett. 8, 565 (2008).

[4] N'Diaye et al., New J. Phys. 11, 103045 (2009).

[5] Yi Pan et al., Appl. Phys. Lett. 95, 093106 (2009).

[6] K. Donner and P. Jakob, J. Chem. Phys. 131 164701 (2009).

4:40pm GR+NS-MoA9 Writing Graphene Electronics Into Chemically Modified Graphene, P.E. Sheehan, Z. Wei, Naval Research Laboratory, D. Wang, Georgia Institute of Technology, W.-K. Lee, M.K. Yakes, Naval Research Laboratory, W.P. King, University of Illinois at Urbana-Champaign, E. Riedo, Georgia Institute of Technology, A.R. Laracuente, J.A. Robinson, S.G. Walton, Naval Research Laboratory

Graphene is the most likely carbon-based successor material for CMOS electronics. Recently, interest in chemically modified graphene (CMG) has risen for producing large-scale flexible conductors and for its potential to open an electronic gap in graphene structures. We have developed a means to tune the topographical and electrical properties of several CMGs with nanoscopic resolution by local thermal processing with an AFM tip. Heating converts the CMG back towards graphene with nanoscale resolution. Nanostructures of one CMG, graphene oxide, show an increase in conductivity up to four orders of magnitude as compared to pristine material. Variably conductive graphene nanoribbons have been produced in a single step that is clean, rapid and reliable. Critically, the "carbon skeleton" is continuous across the CMG/graphene boundary. Recent work suggests that ribbons formed this way may be superior to ribbons that were cut.

5:00pm GR+NS-MoA10 Oxygen Etching of Graphene on Ir and Ru, E. Starodub, N.C. Bartelt, K.F. McCarty, Sandia National Laboratories

We have used low-energy electron microscopy to investigate how graphene is removed from Ru(0001) and Ir(111) by reaction with oxygen. We find two mechanisms on Ru(0001). At short times, oxygen reacts with carbon monomers on the surrounding Ru surface, decreasing their concentration below the equilibrium value. This undersaturation causes a flux of carbon from graphene to the monomer gas. In this initial mechanism, graphene is etched at a rate that is given precisely by the same nonlinear dependence on carbon monomer concentration that governs growth. Thus, during both growth and etching, carbon attaches and detaches to graphene as clusters of several carbon atoms. At later times, etching accelerates. We present evidence that this process involves intercalated oxygen, which destabilizes graphene. On Ir, this mechanism creates observable holes. It also occurs most quickly near wrinkles in the graphene islands, depends on the orientation of the graphene with respect to the Ir substrate, and, in contrast to the first mechanism, can increase the density of carbon monomers. We also observe that both layers of bilayer graphene islands on Ir etch together, not sequentially. Work at Sandia was supported by the Office of Basic Energy Sciences, Division of Materials Sciences, U. S. Department of Energy under Contract No. DE-AC04-94AL85000.

Marine Biofouling Topical Conference
Room: Navajo - Session MB+BI+AS-MoA

Preventing & Characterizing Marine Biofouling

Moderator: G.P. Lopez, Duke University

2:00pm **MB+BI+AS-MoA1 Zwitterionic Polymers for Non-Fouling Coatings, G. Tew**, University of Massachusetts Amherst **INVITED**

Biofouling remains a challenging problem for various fields ranging from biomedical applications and marine coatings technology, to water purification, transport, and storage systems. To date, the most widely employed protein repellent materials are poly(ethylene glycol) (PEG) or oligo(ethylene glycol) (OEG) based. Even though PEG shows excellent nonfouling character, it has low stability in the presence of oxygen and transition metal ions found in most biochemical solutions, which pushed the field to search for more robust non-fouling materials. Having hygroscopic nature similar to PEG as well as a biomimetic character, arising from their structural similarity to the head groups of lipids comprising cell membranes, zwitterions such as 2-methacryloyloxyethyl phosphorylcholine (MPC) and more recently carboxy/sulfobetaines have also been investigated as protein resistant materials. These materials concentrate only on hydrophilic modification of the substrates. However, the real biological environment is populated by different species, which have different attachment mechanisms; some prefer to adhere more on hydrophilic surfaces whereas others prefer more hydrophobic substrates. The solution to this problem has been investigated by engineering surfaces that reconstruct depending on the environment they are being exposed to, which has been found to be relatively easy to obtain with amphiphilic materials. However, these approaches are either still not sufficient to inhibit bioadhesion by themselves or they suffer from complex or labor intensive coatings preparation conditions. In this work, we are introducing a new polymeric system which carries dual functionality at the repeat unit level, a zwitterionic functionality coupled with an alkyl moiety that can be varied to adjust the amphiphilicity of the overall system. The alkyl group is varied to include PEG based, hydrocarbon, and fluorinated chains. Using these ring-opening metathesis polymerization (ROMP) based zwitterionic polymers as the foundation for non-fouling coatings, we are trying to understand what role the overall hydrophilicity/amphiphilicity of the materials play in fouling prevention.

2:40pm **MB+BI+AS-MoA3 Resistance of Saccharide-Terminated Alkylthiol Self-Assembled Monolayers to Protein Adsorption and Marine Biofouling, T. Ederth, T. Fyrner, T. Ekblad, M. Hederos, H.-H. Lee, A. Mangone, P. Konradsson, C.-X. Du**, Linköping University, Sweden, **M.E. Pettitt, M.E. Callow, J.A. Callow**, University of Birmingham, UK, **S.L. Conlan, A.S. Clare**, University of Newcastle, UK, **F. D'Souza, G.T. Donnelly, A. Bruin, P.R. Willemsen**, TNO Science and Industry, The Netherlands, **B.G. Liedberg**, Linköping University, Sweden

The protein resistance of galactoside-terminated alkanethiol self-assembled monolayers (SAMs) can be tuned by partial methylation of the terminating saccharides, and has a non-trivial dependence on the degree of methylation [1], and for other mono- and oligosaccharide-terminated SAMs, protein resistance may vary considerably with small changes in sugar structure. We have used such mono- and oligosaccharide-terminated SAMs in a series of assays using marine fouling organisms as biological model systems, representing common micro- and macrofoulers. We investigate to what extent protein resistance properties are related to effective prevention of fouling by the marine model organisms, and discuss the results in terms of physicochemical properties of the SAMs.

[1] Hederos, M.; Konradsson, P.; Liedberg, B., *Langmuir* **2005**, 21(7), 2971-2980. DOI: 10.1021/la047203b

3:00pm **MB+BI+AS-MoA4 Influence of the Characteristics of a Mineral Coating on its Ability to Resist to the Biofouling, T.H. Tran**, Ecole Nationale Supérieure des Mines de Saint Etienne, France

Mortars are building material with a high primary bioreceptivity and thus, they are easily colonized by different microorganisms... But green algae and cyanobacteria are the main which affect the aesthetics of the facade. Besides the aesthetical problem, an economical problem exists because of the expensive restoration of facade.

This work aimed to study the influence of the intrinsic parameters of a Portland cementitious mortar (roughness, porosity and surface alkalinity) on the algae development in laboratory and also in situ experiments. The degree of fouling was evaluated by means of colorimetric measurements and image analysis.

The roughness played an important role in algae establishment: the higher the roughness, the easier the algae adhesion. The carbonation, reducing surface alkalinity, shortened remarkably the latency time of the fouling onset.

From experimental results, a model was built to predict the fouling of mortar. This model was based on processes such as "germination" - growth. Each rate law was determined separately by image analysis.

3:40pm **MB+BI+AS-MoA6 Influence of Physicochemical Surface Properties on the Settlement of Biofouling Microorganisms, A. Rosenhahn**, Karlsruhe Institute of Technology, Germany **INVITED**

When manmade surfaces are immersed into the ocean, biofouling rapidly occurs. To support the outphase of toxic coating formulations from the market we derive design rules for environmental benign alternatives. Therefore we study the interaction of biofouling organisms such as zoospores of the green seaweed *Ulva linza* with well defined surfaces and disentangle the influence of wetting, hydration, morphology, and charge. The obtained results are discussed in the context of time depending formation of conditioning layers. Especially because of its motility, the settlement step of *Ulva* is highly selective and crucial in their life cycle. A detailed investigation of the relevant phases of approach, exploration and eventually settlement is desired but challenging due to the quick, three dimensional swimming motions of spores. Digital in-line holography is suited for this application as time lapse holograms recorded with a single detector provide the 3D position of microorganisms with high accuracy and at a high frame rate. From such 4D tracking data, the sensitive response of spores and their interaction with surfaces has been studied. Statistical analysis of the motion pattern occurrence, velocity distributions and turning motions on surfaces with different chemical termination can be correlated with the accumulated biomass. By this we obtain quantitative access to the interaction between single spores and surfaces.

4:20pm **MB+BI+AS-MoA8 Interfacial Spectroscopy: In situ Approaches to Understand Sticky Contacts, K.J. Wahl, D.E. Barlow, R.K. Everett, C.M. Spillmann**, Naval Research Laboratory, **G.H. Dickinson, B. Orihuela, D. Rittschof**, Duke University Marine Laboratory **INVITED**

Proteinaceous secretions are widely recognized to be significant contributors to marine biofouling. The resulting interfacial films can be physisorbed or chemisorbed, and have varying degrees of permanency – they may be highly polymerized and cross-linked, or simply sticky enough to allow surface exploration. Conventional approaches to examining interfacial films derived from bioadhesive junctions is forensic in nature – foulant removal (separating the surfaces) followed by *ex situ* examination of the adhesive composition and surface morphology. While “what” the adhesive is may be gleaned from *ex situ* approaches, “how” the adhesive is applied and cures cannot. These time dependent changes can’t be examined “after the fact” and instead require real-time measures of interfacial interactions.

At NRL, we have made significant progress in developing *in situ* methods to demonstrate the chemical, mechanical and rheological processes in interfaces. We are now applying and extending these approaches to examine underwater adhesion in marine organisms, specifically the little striped barnacle, *Balanus amphitrite*. We are developing *in situ* and *in vivo* spectroscopic approaches to determine how protein structure and chemistry influence marine foulant adhesion. We are particularly interested in determining the structure and chemistry of the cement, the biochemical processes influencing polymerization, cross-linking, and water displacement, as well as the physicochemical nature of the adhesion. Our *in situ* approaches include performing temporally- and spatially-resolved microscopy and spectroscopy through adhesive interfaces transparent at UV, visible, IR, and x-ray wavelengths. I will describe how we have used these tools to develop new understanding of the properties and development of the adhesive interface of barnacles.

5:00pm **MB+BI+AS-MoA10 Solid State Circular Dichroism of Insoluble Bioadhesive Films: Determining Protein Secondary Structure by Concentration Independent Analysis, D.E. Barlow, J.L. Kulp, K.J. Wahl**, U.S. Naval Research Laboratory

Far-UV circular dichroism (CD) is a valuable method for estimating protein structure components. Analysis of protein CD spectra typically requires deconvolution to resolve overlapping bands and standard methods require that the concentration and pathlength of the sample are accurately known. While this is usually not an issue for the solution state, it is sometimes desirable or a necessity to analyze samples as solid films, complicating deconvolution. Barnacle cement is one example of a proteinaceous bioadhesive that is insoluble by standard biochemical methods and of

inconsistent thickness in the native state. To analyze such samples by CD, we have applied g-factor analysis,¹ where the CD spectra are normalized by absorption spectra. This has been demonstrated as a valid, concentration independent deconvolution method, but so far has not been widely used. We will present proven secondary structure estimation results of barnacle cement films as determined by g-factor analysis and show how these results compare with those obtained by infrared spectroscopy. Potential issues and further applicability of solid state CD for bioadhesion studies will be discussed.

¹ McPhie, P. *Anal. Biochem.* **2001**, *293*, 109.

5:20pm **MB+BI+AS-MoA11 Dissipative Microbalance (QCM-D) Studies of Interfacial Processes at the Nanoscale, M.A. Poggi**, Biolin Scientific

Currently there are many technologies that can study the bulk properties of nanoparticles in solution (such as light scattering) as well as experimental methods that allow one to visualize particles (microscopy or fluorescence). However, there are few technologies that can provide real-time in-situ information regarding how nanoparticles interact with other molecules or materials. Recently we have been using the quartz crystal microbalance with dissipation monitoring technology (QCM-D) to quantify the interaction of particles with surfaces and other materials (biological and organic). We will first present recently published results that address the effect of stagnant and dynamic motion of chemically modified nanoparticles on their adsorption onto silica surfaces. We were able to follow the real-time assembly (in liquid) of these chemically-modified particles. By simultaneously quantifying the changes in surface mass and viscoelasticity during the adsorption process, we were subsequently able to model the adsorption characteristics of these nanoparticles. We will also discuss recent advances that have been made in regards to using QCM-D to follow the assembly of biological nanoparticles (such as cells, viruses and lipids) and polyelectrolytes and touch upon recent electrochemical work that we have been using to study electroactive processes at interfaces.

Nanometer-scale Science and Technology
Room: La Cienega - Session NS-MoA

Nanomaterials in the Environment

Moderator: U.D. Schwarz, Yale University

3:40pm **NS-MoA6 Nanotechnology in the Environment: Safety by Design, V. Colvin**, Rice University **INVITED**

Nanotechnology-enabled systems offer much promise for solving difficult environmental problems ranging from water purification to waste remediation. These solutions must not only be cost-effective and sustainable, but they must also be safe for people and the environment. Our emerging understanding of the interface between nanomaterials and biological systems gives us the critical ability to approach the latter issue early in the development of nanotechnology. This talk will discuss in some detail how the chemical and physical properties of engineered nanomaterials impact their biological effects in model systems. Three case studies, ranging from fullerenes to metal oxides, illustrate the vast diversity of nanomaterial features and biological response. The composition of a nanomaterial is the primary factor in describing acute biological effects, and among the different examples nanoparticle charge and surface coating can be of equal importance. Interestingly, the size of the inorganic material itself – such an important feature for applications development – in these three examples is secondary in defining the materials' acute biological effect. In all cases, the biological and environmental compartments experienced by nanomaterials lead to substantial modification of their hydrodynamic size and charge. The bio-modified material that results is the central element to understand and characterize in order to detect the underlying correlations between the inorganic nanomaterial phase, composition and size with biological outcomes. These correlations form the basis for guidelines that permit researchers creating new nanoparticles to focus their energy on materials that are 'safe by design'.

4:20pm **NS-MoA8 Surface Functionalization of TiO₂ Nanoparticles: Photo-stability and Reactive Oxygen Species (ROS) Generation, K. Louis, O. Bar-Ilan, W. Heideman, M. Konrath, J. Pedersen, R. Peterson, S. Yang, R.J. Hamers**, University of Wisconsin-Madison

Nanoparticles made from TiO₂ and other metal oxides are of increasing interest for applications including sunscreens, cosmetics, paints, biomedical imaging, and photovoltaic devices. While TiO₂ is generally considered to be non-toxic, TiO₂ and other metal oxides can generate highly toxic reactive oxygen species when exposed to water and sunlight. The ROS species can, in turn, modify the stability of the TiO₂ nanoparticles by altering the organic

ligands that typically are present on the exterior of the nanoparticles. We are investigating the formation of ROS species by TiO₂ nanoparticles and the relationship between organic ligands, ROS generation, and nanoparticle stability. These factors all affect the bioavailability of TiO₂ nanoparticles and consequently are important factors in understanding the safety and health impacts of nanomaterials. As model systems, we have investigated TiO₂ nanoparticles functionalized with several ligands including citrate, 3,4-dihydroxybenzaldehyde, and rutin, a model of humic substances. Using fluorescent probes we are measuring the amount of ROS species produced from nanoparticles of different sizes and relating this to the chemical alteration/degradation of the ligands using XPS and FTIR, and examining the impact on stability of nanoparticles in aqueous media. Concurrent measurements are being made of the toxicity of the nanoparticles using zebrafish in the presence and absence of ultraviolet light in order to understand how surface chemistry of nanoparticles ultimately impacts bioavailability and environmental impact of engineered nanomaterials.

4:40pm **NS-MoA9 Environmental Effects on Nanoparticle Properties and Chemical Reactivity, D.R. Baer, J.E. Amonette, A. Dohnalkova, M.H. Engelhard**, Pacific Northwest National Laboratory, *R.L. Penn*, University of Minnesota, *P. Nachimuthu, J. Liu*, Pacific Northwest National Laboratory, *J.T. Nurmi, P.G. Tratnyek*, Oregon Health and Sciences University, *C.M. Wang*, Pacific Northwest National Laboratory

Nanoparticles of many types are increasingly used in a variety of applications. Parts of our work have focused on the reactions of Fe metal-core oxide-shell nanoparticles with water and solution contaminants that may be found in ground water. An important factor in understanding the ability of such particles to reduce environmental contaminants and the ultimate fate of such particles is knowledge of how the particles and their properties change with time in a variety of environments. Our work has demonstrated that these particles can change rapidly over periods of hours to days in water. Our research has focused attention on three aspects of these time dependent phenomena: 1) developing the ability to extract particles from solution, thereby stopping the reaction process and preserving, to the extent possible, the chemical and structural information; 2) how changes in the solution (adding buffers and organics) alter particle reactivity and aging in solution; and 3) using *in situ* methods to track particle changes and chemical properties. A variety of *ex situ* methods have been used to characterize the particles, including XPS, TEM, BET and XRD. Electrochemistry measurements have been used as an *in situ* real-time method. The method of sample extraction involves handling samples in a nitrogen atmosphere, a solvent rinse, and vacuum pumping to remove excess solvent. Even when particles appear dry, aggregates of particles may retain significant solvent. In addition to examining the influence of a variety of common buffers, we have examined the impact of natural organic material on the oxidation and chemical behavior of nanoparticles. Although natural organic matter (NOM) slows aging of the particles, the NOM coating helps the particles migrate relatively quickly through soil. Electrochemical measurements of various types including the open-circuit potential demonstrate the time dependence of particle changes and highlight the effects of varying environments on particle properties. Surface-potential measurements also highlight the impact of differing solutions on particle behavior.

5:00pm **NS-MoA10 Functionalized Ceria Nanoparticles – Influence of Coating Thickness and Density on Their Reactivity, A. Karakoti**, University of Central Florida, *S. Kuchibhatla, G. Orr, H. Wang, D.R. Baer*, Pacific Northwest National Laboratory, *S. Seal*, University of Central Florida, *S. Thevuthasan*, Pacific Northwest National Laboratory

Topical interest in the biomedical applications of cerium oxide nanoparticles (CNPs) has emerged from its radical scavenging, antioxidant like, behavior. The ability of CNPs to carry these single electron redox processes (radical scavenging) stems from the ability of cerium to switch between the Ce³⁺ and Ce⁴⁺ oxidation states. It is essential to test and increase the biocompatibility and solubility of CNPs to be able to use these in biomedical applications as it involves a direct interface of nanoparticles with the intracellular environment. The biocompatibility as well as solubility of CNPs can be increased by modifying the surface with biocompatible polymers as ligands. Such a composite system should be able to demonstrate the unaltered characteristics of the parent CNPs and biocompatibility as well as high solubility of the polymeric system. Thorough characterization of CNP-polymer system such as thickness of polymeric coating, surface coverage and number density of the polymer per nanoparticle is necessary to relate its properties with biocompatibility.

CNPs were synthesized using two different wet chemical methods and coated with different concentration of polymer (polyacrylic acid) using conventional precipitation and redispersion technique. The molecular weight of the polymer was varied between 2,000 and 250,000 g/mol and composite system was characterized for particle size, stability/solubility of dispersion, surface charge, surface density of the polymer and thickness of

the polymeric coating. Dynamic light scattering measurements were used to characterize the size as well as surface charge of the coated nanoparticles. A combination of surface area and thermogravimetric analysis was used to ascertain the number density of the polymers per unit surface area of the nanoparticles. The extent of polymeric functionalization will be determined by estimating the number of carboxyl groups on the surface of nanoparticles by chemical probing. Non linear optical (NLO) measurements are becoming increasingly popular to quantify the surface of nanoparticles. NLO analyses such as Sum Frequency Generation Vibrational Spectroscopy (SFG-VS) will be used to quantitatively estimate the polymeric ligands on the surface of CNPs. The presentation will be concluded by some of the preliminary results from the biocompatibility tests carried out on the well analyzed composite/functional CNPs.

Plasma Science and Technology

Room: Aztec - Session PSI-MoA

Advanced FEOL / Gate Etching I

Moderator: A. Metz, TEL Technology Center America

2:00pm **PSI-MoA1 Reduction of Plasma Induced Silicon-Recess During Gate Over-Etch Using Synchronous Pulsed Plasmas.** *M. Darnon, C. Petit-Etienne, F. Boullard, E. Pargon, L. Vallier, G. Cunge, P. Bodart, M. Haass, CNRS-LTM, France, S. Banna, T. Lill, Applied Materials Inc.*

With the downscaling of CMOS devices in semiconductor industry, very thin layers (<1.5nm) are now introduced in transistor gate stacks. Integrating such thin layers presents tremendous challenges, particularly for the etch processes which have to be stopped selectively without inducing damage to the thin materials below. For instance, bulk silicon may be oxidized during the gate over-etch step through the thin gate oxide, which leads to silicon recess during the subsequent wet cleanings. In this contribution, we will precise the mechanisms of silicon oxidation through the thin gate oxide, and we will propose solutions to minimize this phenomenon by pulsing the plasma.

The experiments are performed on a state of the art 300mm AdvantEdge™ etch reactor equipped with the Pulsync™ system which provides full plasma pulsing capabilities at frequencies between 100 Hz and 20 kHz, with duty cycles between 10 and 90 %. In-situ spectroscopic ellipsometry is used to determine etch rates on thick silicon oxide and polysilicon layers, and to investigate plasma induced oxidation through a 2.5nm thin silicon oxide coated on bulk silicon. An angle resolved XPS system connected to the reactor allows quasi in-situ surface characterizations.

We show that an infinite selectivity of polysilicon over SiO₂ is obtained using an HBr/O₂/Ar gate over etch process on thick layers. However, when a thin layer of silicon oxide is exposed to the same process, the thin oxide layer thickness increases with the plasma exposure time. This thickness increase is related to plasma induced oxidation through the thin gate oxide. XPS analysis show that a Si-Br_x interface layer builds up between SiO₂ and Si, and that some bromine is incorporated in the oxide. This suggests that bromine implantation through the SiO₂ layer may generate a path in the oxide layer facilitating the oxygen and water diffusion (from the plasma or from the atmosphere) down to the SiO₂/Si interface

We show that plasma induced oxidation can be minimized by using synchronous pulsed plasmas. This way, we move from a highly dissociated plasma to a highly recombined plasma. As a consequence, radicals are larger and less prone to diffuse, and ions are molecular rather than atomic, which decreases the net energy of their components. Hence, bromine incorporation is highly limited and no Si-Br_x interface layer is created, which minimizes silicon oxidation through the thin gate oxide.

These experiments clarify the mechanisms of plasma induced oxidation through the thin gate oxide, and show the promises of synchronous pulsed plasmas to reduce silicon recess.

2:20pm **PSI-MoA2 Control of Si Damage in Dry Etch Beyond 22nm Technology Node.** *J. Guha, C. Lee, V. Vahedi, Lam Research Corporation*

The continuous shrinking of CMOS device node have put stringent requirement on reducing plasma induced damage and under layer film loss during dry etch. It is always almost the case that when a film is etched in a plasma the under layer film sustains some extent of damage and in some cases this film is etched leading to recess. Up until now this was within the noise to some extent, but beyond 22nm technology node this will be critical in defining device performance. Si roughness and recess during FEOL etch (like gate and spacer) results in degradation of device performance; like shift in threshold voltage, high leakage current leading to increased power consumption. These are some of the roadblocks in achieving high device

performance at high packing density. Therefore, it is desirable to attain infinite selectivity between the film that is intended to be etched and its underlying film such that the under-layer film is damage free. In many cases strategies to control Si damage leads to tradeoffs like tapered profile which is not acceptable. This talk will discuss some of the issues in controlling Si damage in FEOL applications and some interesting results.

2:40pm **PSI-MoA3 Structural and Electrical Characterization of HBr/O₂ Plasma Damage to Si Substrate.** *M. Fukasawa, Sony Corporation, Japan, Y. Nakakubo, A. Matsuda, Y. Takao, K. Eriguchi, K. Ono, Kyoto University, Japan, M. Minami, F. Uesawa, Sony Corporation, T. Tatsumi, Sony Corporation, Japan*

Suppression of Si substrate damage caused by energetic ion bombardment is one of the most critical issues in advanced devices. Si substrate damage during gate electrode etching causes the "Si recess" structure, which is reported to degrade device performance. In previous work, we developed a bilayer model (surface oxide/dislocated Si) of the damaged layer and studied monitoring methods. In this paper, we have investigated the damage generation by plasma exposure and the removal of damage by wet treatment. We have also studied the impact of the damage on electrical performance. A dual frequency (60/13.56 MHz) CCP reactor was used in this study. A SiO₂ layer (1.7 nm) was formed on the Si substrate and exposed to HBr/O₂, H₂, and O₂ plasma. The pressure and V_{pp} were kept constant at 60 mTorr and 420 V. Diluted HF (100:1) was used to perform a wet treatment. The Si substrate damage was analyzed by spectroscopic ellipsometry (SE), HRBS, and TEM. In the SE analysis, data was fitted using a four-layer model (ambient/SiO₂/dislocated Si/substrate). Dislocated Si was modeled as a mixing of SiO₂ and polysilicon. C-V characteristics were measured with a mercury probe system. HBr/O₂ plasma generates a thicker surface oxide layer than O₂ plasma. The root cause of the thick oxide layer is enhanced diffusion of oxygen in the dislocated Si layer generated by deep penetration of H⁺ from the plasma. The thickness of the oxide layer (T_{ox}) increased monotonically with increased exposure time (t) and reached about 10 nm at 600 s. The T_{ox} was found to depend on t^{1/2}, which is a so-called parabolic relationship (diffusion-controlled oxidation) in the Deal-Grove model. The T_{ox} and the thickness of the underlying dislocated Si layer (T_d) were compared by SE, HRBS, and TEM. The results were quite consistent across all analyses. The T_{ox} and T_d after dHF treatment were also analyzed. The surface SiO₂ was completely removed and the upper part of the dislocated Si was also eliminated (generation of Si recess). As the remaining dislocated Si was mainly caused by H⁺ ion penetration, the C-V characteristics for H₂ plasma-exposed samples were analyzed. A negative bias voltage shift was observed, which implies the generation of positive charge trapping in the interface between the surface oxide and the dislocated Si layer. To minimize the Si damage during gate etching, it is necessary to control the H⁺ penetration depth within the thickness of the thin gate oxide by controlling the IEDF precisely. Thus, quantitative control of the IEDF, precise monitoring of surface structure, and understanding the effects on device performances are indispensable for creating advanced devices.

3:40pm **PSI-MoA6 FEOL Etch Challenges for Beyond 2x Technology Node: What does it mean for Energy Consumption?** *C. Lee, M. Davis, V. Vahedi, Lam Research Corporation*

INVITED

Energy reduction has become an emerging trend for semiconductor equipment manufacturing; as the technology evolves, demands for higher throughput on the etching of high aspect ratio structures (as driven by DRAM and NAND devices) have placed more demands on the amount of RF power required. A direct consequence of this is more energy is required, both to drive the RF generators and to provide the cooling necessary in order to remove heat generated. This talk will provide an overview on direct energy resource usage, such as power, water, thermal load, process gas usage, and what role does each of these play in the beyond 2x technology node.

4:20pm **PSI-MoA8 Advanced Gate Patterning of Novel Multi-Gated Devices for 15nm Node and Beyond.** *S.U. Engelmann, Y. Zhang, M.A. Guillorn, S. Bangsaruntip, N.C. Fuller, W.S. Graham, E.M. Sikorski, IBM T.J. Watson Research Center*

To continue scaling CMOS devices at the traditional pace following Moore's law, Short Channel Effects (SCE) are the major issues limiting the use of planar device geometries for future technology nodes. Alternative device integration schemes are currently being tested to test the impact on SCE and extend technology nodes even further. The device candidates that are currently being tested include planar devices, FinFETs, Trigates and Nanowires (gate all around device). The gate formation on these advanced, multi-gated devices imposes completely new challenges on the plasma etch conditions, which translates to the demand to control the plasma process in a second (and a third) dimension. E-beam lithography has been proven to be a very valuable tool to explore plasma processing at device sizes

unattainable by state-of-the-art optical lithography. We have demonstrated the fabrication of gates above a Fin of varying dimensions of gate and fin for SRAM cells down to 0.025 μm^2 . Significant challenges for this integration lie in the gate as well as the spacer formation, while maintaining the Si fin that has no hardmask to prevent plasma damage. While maintaining a vertical gate profile, no Silicon loss was observed on the Si Fin. A more significant challenge is the spacer formation, where Nitride needs to be removed from the fin sidewall, while maintaining it on the gate sidewall to prevent device shorts. An even higher degree of process control is needed in the fabrication of nanowire or gate all around devices. Maintaining a vertical gate profile while not damaging or destroying nanowires of diameters less than 5nm is critical. A gate recess process was employed to release the nanowire structures. A highly selective spacer etch process was developed to yield nanowires down to 3nm in diameter.

4:40pm **PS1-MoA9 Plasma Etching Challenges for Patterning Advanced Gate Stacks for 22nm Node and Beyond**, *Y. Zhang, S.U. Engelmann, Q. Yang, R.M. Martin, E.A. Joseph, M.A. Guillorn, E.M. Sikorski, W.S. Graham, B.N. To, N.C. Fuller*, IBM T.J. Watson Research Center

There are increasingly more challenges facing by patterning advanced gate stacks due to continuously scaling of CMOS device dimensions to 22 nm node and beyond. The major causes are from the following: (1) new materials being introduced for advanced gate stacks to enable continuously scaling of T_{inv} ; (2) continuously shrinking of pitch and higher density; (3) complex gate patterning integration schemes, such as double or multiply exposures and double or multiply etching with multiply layer mask schemes due to the delay of EUVL; (4) 3D active area and gate structures, such as finFET, tri-gate, Si nanowire (SiNW) FET, etc.; and (5) move to the deep-nanometer regime, such as ETSOI with < 5nm Si channel. The 3D structures with the combination of novel materials and sub-50nm pitches for gate stacks impose unique challenges and demands on plasma etch process technology and news integration schemes and plasma etch tooling innovations. To meet all the requirements of target pitches, device feature profile, line edge roughness (LER) or line width roughness (LWR), and device performance/functionality, Different and unconventional approaches have to be introduced in plasma etching processing to fabricate 3D fins/active area, gates and spacers, particularly with the use of metal/high-k dielectric gate stack materials. Recent results illustrating some of these etching challenges including the progresses developed aiming on improving 3D profiles and achieving increased control of LER/LWR for fin, gate and spacer structures will be presented.

5:00pm **PS1-MoA10 High Selectivity SiN Etching with Low Damage by RLSA Microwave Plasma**, *M. Inoue, M. Sasaki, Y. Ohsawa*, Tokyo Electron, LTD., Japan

New materials such as High-K/Metal Gate and three-dimensional structures such as Tri-Gate have been introduced at the 22nm node and beyond. In addition, high selectivity and reduced Plasma Induced Damage (ex. Charge up damage and Si crystal damage, etc.) are required of the etching process. Especially, Fin Spacer of Tri-Gate is required high selectivity to thin oxide. RLSA (Radial Line Slot Antenna) microwave plasma has several features that overcome these new challenges. The characteristics of RLSA plasmas include high density, low electron temperatures and low plasma potential. In addition, Radical/ion ratio is higher than conventional plasma source. These characteristics enable highly selective etching with decreased Plasma Induced Damage on the wafer surface. A high SiN/SiO selectivity process has been achieved due to the features of RLSA plasma and low bias (low Vpp) conditions.

We have recently developed a high selective SiN/Si etching process under low bias conditions. It is thought that the mechanism for this etch includes minimum oxidation (native oxide level) of the Si surface to SiO₂, creating a highly selective etch similar to the SiN/SiO₂ process that was previously developed.

5:20pm **PS1-MoA11 Impact of Plasma and Annealing Treatments on 193nm Photoresist Line Width Roughness and Profile**, *L. Azarnouche*, STMicroelectronics, France, *E. Pargon, K. Menguelti, M. Fouchier*, Ltm - Umr 5129 Cnrs, France, *R. Tiron*, CEA-LETI-MINATEC, France, *P. Gouraud, C. Verove*, STMicroelectronics, France, *O. Joubert*, Ltm - Umr 5129 Cnrs, France

As the Critical Dimension (CD) of gate transistors scales down to the nanometer range, line width roughness (LWR) becomes a serious issue, which directly impacts the electrical performance of CMOS devices. It has previously been shown that the photoresist (PR) sidewall roughness present after lithography (6nm, 3 σ) is transferred during the subsequent plasma etching processes into the gate, resulting in a final LWR far above the ITRS requirements for the 32nm technological node (1.7nm, 3 σ). The key to decrease the final gate LWR is to minimize the photoresist LWR before the

plasma etching steps involved in the gate patterning process. The best and simplest way is to expose the photoresist patterns to plasma treatments prior to gate patterning. Indeed, it was observed that Vacuum Ultra Violet (VUV) light emitted by plasmas plays a key role in the photoresist LWR decrease. In the present study, we have used CD-SEM and CD-AFM techniques to investigate the impact of plasma treatment on the photoresist LWR and profiles. Several plasmas (HBr, Ar, He, H₂) emitting strongly in the VUV region (100-200nm) have been investigated. LiF windows placed between the plasma and the photoresist patterns have been used to evaluate the role of the plasma VUV light only on the LWR evolution. The role of the substrate temperature has also been studied. Many characterization techniques have been used to characterize the physico-chemical modifications of photoresist films exposed to the same plasma treatments (Multiple Internal Reflection infrared spectroscopy (MIR), Raman, gas chromatography (GC)).

The results obtained indicate that all plasma treatments lead to a LWR decrease. We have observed that for all plasma investigated, VUV light only seems to induce a slight reflow of the resist which is probably correlated with the LWR decrease. On the other hand, in HBr and Ar plasmas, resist patterns remain square indicating that no reflow occurs. Heating resist patterns up to 200°C without plasma exposure also leads to a LWR decrease, resist reflow being only observed above 200°C. All treatments generate the cleavage of the side groups (lactone group for plasma treatment and protecting group for annealing treatment) and the decrease of the glass transition temperature which is potentially correlated to the LWR decrease. GC analysis also reveals that under Ar and HBr plasma exposure, cleaved side groups can be trapped in the resist polymer matrix because of the presence of a denser surface layer. This dense layer could prevent the resist reflow leading in final to the square profiles observed in HBr plasmas.

Plasma Science and Technology Room: Galisteo - Session PS2-MoA

Atmospheric Plasma Processing and Micro Plasmas Moderator: A. Rousseau, Ecole Polytechnique, France

2:20pm **PS2-MoA2 High Current Diffuse Dielectric Barrier Discharge in Atmospheric Pressure Air for Thin Silica-Like Film Deposition**, *S.A. Starostin*, Eindhoven University of Technology, Netherlands, *P. Antony Premkumar*, Materials Innovation Institute (m2i), Netherlands, *M. Creatore*, Eindhoven University of Technology, Netherlands, *H. de Vries*, FUJIFILM Manufacturing Europe BV, Netherlands, *M.C.M. van de Sanden*, Eindhoven University of Technology, Netherlands

The dielectric barrier discharge (DBD) is recognized as a promising tool of thin films deposition on various substrates at atmospheric pressure. Emerging applications including encapsulation of flexible solar cells and flexible displays require large scale low costs production of transparent uniform dense layers with low level of surface defects. Unfortunately the common operational mode of the atmospheric pressure DBD is filamentary, resulting in strong spatial non-uniformity of plasma chemistry and affecting the quality of the deposited films. Sustaining of the filament-free non-thermal plasma over the large area substrate at atmospheric pressure remains a challenging task especially considering the discharge in ambient air [1].

In present contribution the diffuse dielectric barrier discharge in atmospheric pressure air was applied for the thin film deposition on polymeric web in industrially relevant roll-to-roll configuration. The silica-like film deposition was performed using the admixture of hexamethyldisiloxane precursor to air flow. Discharge diagnostics was realized by means of fast ICCD imaging; time resolved optical emission spectroscopy and electrical characteristics analysis. ICCD discharge imaging confirms plasma uniformity in a microsecond time scale, while at nanosecond time scale shows fast propagating lateral ionization waves. Morphology and composition analyses, performed by means of AFM, ATR-FTIR and XPS methods, indicate that the process results in ultra-smooth films (roughness comparable to initial substrate roughness) and shows the possibility to synthesize carbon-free layers.

[1] S.A. Starostin, P. Antony Premkumar, H. de Vries, R.M.J. Paffen, M. Creatore, and M.C.M. van de Sanden *Appl. Phys. Lett.* **96**, 061502 (2010)

2:40pm **PS2-MoA3 Microscale, Atmospheric-Pressure Plasmas for Nanomaterials Synthesis**, *R.M. Sankaran*, Case Western Reserve University **INVITED**
Large-scale, low-pressure plasmas play an essential role in the manufacturing of integrated circuits that are now ubiquitous in consumer

electronics. In recent years, new challenges have arisen for these top-down approaches to materials processing. Future electronic devices will incorporate nanoscale materials such as nanoparticles, carbon nanotubes, and silicon nanowires that cannot be fabricated by current plasma technology because of limitations associated with photolithography. In addition, emerging applications in sensors, energy, and medicine require materials that must be prepared from the “bottom-up”. The aim of our research is to develop a new class of plasmas, termed “microplasmas”, for nanomaterials synthesis.

Microscale plasmas or microplasmas are a special class of electrical discharges formed in geometries where at least one dimension is less than 1 mm. As a result of their unique scaling, microplasmas operate stably at atmospheric pressure and contain large concentrations of energetic electrons (1-10 eV). These properties are attractive for a range of nanomaterials applications. Vapor-phase metal-organic precursors can be dissociated at ambient conditions (i.e. room temperature and atmospheric pressure) to homogeneously nucleate metal¹ and alloyed² nanoparticles. The formation of metal nanoparticles in the gas phase allows direct introduction of these materials as catalysts for carbon nanotube and silicon nanowire growth³. Recently, we have also coupled microplasmas with liquids or polymeric films to nucleate nanoparticles from metal ions⁴. In this talk, I will discuss these topics in detail, highlighting the advantages of microplasma-based systems for the synthesis of well-defined nanomaterials.

1. W-H. Chiang and R. M. Sankaran, “Microplasma synthesis of metal nanoparticles for gas-phase studies of catalyzed carbon nanotube growth,” *Appl. Phys. Lett.*, Vol. 91, 121503 (2007).
2. W-H. Chiang and R. M. Sankaran, “Synergistic effects in bimetallic nanoparticles for low temperature carbon nanotube growth,” *Adv. Mater.*, Vol. 20, 4857 (2008).
3. W-H. Chiang and R. M. Sankaran, “Linking catalyst composition to chirality distributions of as-grown single-walled carbon nanotubes by tuning Ni Fe nanoparticles,” *Nat. Mater.*, Vol. 8, 882 (2009).
4. C. Richmonds and R. M. Sankaran, “Plasma-liquid electrochemistry: Rapid synthesis of colloidal metal nanoparticles by microplasma reduction of aqueous cations,” *Appl. Phys. Lett.*, Vol. 93, 131501 (2008).

3:40pm PS2-MoA6 Micro-discharge Plasma using Silicon Platform, M.K. Kulsreshath, T. Dufour, P. Lefauchaux, O. Aubry, S. Dozias, P. Ranson, CNRS/Université D’Orleans, France, J.-B. Lee, M.J. Goeckner, L.J. Overzet, University of Texas, Dallas, R. Dussart, CNRS/Université D’Orleans, France

Micro-discharges can be produced in a variety of different configurations and using a variety of different technologies. The properties of these micro-discharges have been examined with increasing interest during the past decade. There has also been intense interest in new fabrication techniques for the production of micro-discharges. In this paper we present the fabrication technology used to make micro-discharge “reactors” on a silicon (Si) substrate along with selected plasma properties. For the fabrication of these reactors we have used 4” Si wafers and standard cleanroom facilities. The fabrication technology used is compatible with standard CMOS device fabrication and the micro-discharge reactors fabricated can be used to produce either DC or AC discharges. The micro-discharges operate well at high-pressure. They were given planar cathodes and ring-shaped anodes separated by a SiO₂ dielectric with a thickness of approximately 5-6 μm rather than the much more common ~100 μm. The micro-discharge reactors can consist of either a single hole or multiple holes and we have built devices with holes from 25 to 150 microns in diameter. The micro-discharge measurements were obtained for inert gas, DC plasmas between 100 and 1000 Torr. Although we used only a single ballast resistor, many hole micro-discharges were obtained because the cathode surface area of each micro-discharge was limited. This also acts to limit the discharge power. In addition, we will report on current leakage and parasitic sparks during high pressure operation. Finally, we discuss the spread of the micro-discharge over the anode and cathode surfaces as well as the life time of the micro-discharge reactors.

4:00pm PS2-MoA7 Electron Current Extraction from rf Micro-Dielectric Barrier Discharges, J.-C. Wang, University of Michigan, Ann Arbor, N. Leoni, O. Gila, Hewlett Packard Research Labs, M.J. Kushner, University of Michigan, Ann Arbor

Micro dielectric barrier discharges (mDBD’s) consist of micro-plasma devices (10-100 μm diameter) in which the electrodes are fully or partially covered by dielectrics, and operate at atmospheric pressure driven with radio frequency (rf) wave forms. After the plasma is generated charging of the dielectric terminates the discharge. At atmospheric pressure, particularly in attaching gases, the plasma formation and decay times can be as short as a few to tens of ns whereas the rf period may be tens to hundreds of ns. So the micro-plasma may need to be re-ignited with each discharge pulse. In certain applications, it may be desirable to extract electron current out of the

mDBD plasma, which necessitates a third electrode. As a result, the physical structure of mDBD and the electron emitting properties are important to its operation. In this presentation, we will discuss the properties of mDBD’s sustained in atmospheric pressure N₂ and air using results from a two-dimensional plasma simulation. The micro-DBD’s are sandwich structures with an opening of ten-of-microns excited with rf voltage waveforms of up to 25 MHz up to 0.5 mm away. The model, nonPDPSIM, solves Poisson’s equation and transport equations for charge species and electron energy conservation equation for electron temperature. Rate coefficients and transport coefficients are obtained from local solutions of Boltzmann’s equation for the electron energy distribution. Radiation transport is addressed using a Green’s function approach. We find that following avalanche by electron impact ionization in the mDBD cavity, the plasma can be expelled from the mDBD’s cavity towards the collection electrode during the part of the rf cycle when the collection electrode appears anodic. This extraction can be enhanced by biasing the extraction electrode. At lower frequencies, the plasma needs to be reformed every cycle. Long lived neutral species facilitate the generating of plasma by production of UV photons that continuously seed secondary electrons at surfaces until the potential is favorable to re-ignite plasma. The amount of extracted charge per pulse is not a strong function of rf frequency for values up to 25 MHz, but is sensitive to the dielectric constant of the barrier. For applied voltages of up to 2-3 kV, electric field emission appears not to play an important role.

4:20pm PS2-MoA8 Ignition and Extinction of a Micro Hollow Cathode Discharge Operating in DC Regime, R. Dussart, M.K. Kulsreshath, T. Dufour, CNRS/Université D’Orleans, France, L.J. Overzet, University of Texas at Dallas, P. Lefauchaux, T. Tillocher, O. Aubry, S. Dozias, P. Ranson, CNRS/Université D’Orleans, France, M.J. Goeckner, University of Texas at Dallas, J.-B. Lee, University of Texas, Dallas

Microdischarges have gained the interest of the plasma community for the 15 past years. Among them, Micro Hollow cathode Discharges (MHCDs) have the very interesting property to operate at atmospheric pressure in a stable non thermal regime. We have studied the ignition and extinction of such microdischarges. Our samples are made in alumina, covered by a 5 μm thick Nickel layer on both sides and drilled by a laser process. We made experiments in helium and argon at a pressure between 100 and 1000 Torr. To initiate the plasma, we increase the discharge voltage linearly and slowly (20 sec) until the voltage breakdown was reached. During the microplasma ignition, a high current pulse as high as several tens of microamps appeared before a stable and constant lower value was obtained. We will compare these current pulses to those obtained in the so-called self pulsing regime. We will also show electrical and optical measurements carried out to characterize the phenomenon. Finally, we will show the discharge current and voltage temporal evolution at the very last moments of the microplasma, just before its extinction. The physical mechanism of the ignition and extinction will be discussed to explain the measured waveforms.

4:40pm PS2-MoA9 Characterization and Applications of Three Different Configured Atmospheric Pressure Plasma Sources, Z. Ouyang, V. Surla, S. Jung, M.J. Neumann, D.N. Ruzic, University of Illinois at Urbana-Champaign

The Center for Plasma-Material Interactions (CPMI) at the University of Illinois at Urbana-Champaign has developed large-scale microwave-induced atmospheric plasma sources for use in various manufacturing applications. The microwave source employed has a working frequency at 2.45 GHz, and a maximum input power of 6 kW. Plasma sources of three different configurations have been developed in order to tailor the plasma configuration to various specific applications. A cold plasma torch has the ability to generate an atmospheric plasma with a temperature range from room temperature (20°C) to more than 1,000 °C. A thermal plasma torch has been developed such that the temperature range extends to 2,000 °C. A linear line source suitable for production line integration has the ability to sustain a 20-centimeter long atmospheric plasma. Various gas compositions (He, Ar, N₂ and O₂) are used to reveal the functionalizations of different radicals and particles. OES system has been used to analyze critical characteristics such as electron density ($n_e \sim 10^{14} \text{cm}^{-3}$) and temperature ($T_e \sim 1\text{eV}$), plasma temperature ($T_g \sim 300\text{-}2,000\text{K}$) under different operating conditions and results of material processing correlated to those measurements so that a selectable and repeatable material process can be obtained. Hydrophilicity tests on polymer substrates reveal that the “cold” atmospheric plasma has the ability to modify the surface energy within seconds of exposure at a relatively low flux of incident particles, without deforming bulk material substrates; while the “thermal” atmospheric plasma is used to assist in Nd:YAG laser ablation ($f=100\text{Hz}$, $P_{av} = 2.0\text{W}$ at 266 nm, 12.5W at 532nm, and 32.5W at 1064nm) of metal or ceramic materials, to provide a means to deposit high quality contamination free films on

substrate with better lamination at a relatively higher deposition rate (~5,000 nm/min) in comparison to traditional PVD methods.

5:00pm PS2-MoA10 Study of Atmospheric Pressure Plasma Jets: The Influences of Ambient Air and the Application on ZnO Thin Film Deposition. *Y.J. Yang, Y.W. Hsu, Y. Lin, C.C. Hsu*, National Taiwan University, Taiwan, Republic of China

This presentation includes the diagnostic studies of an atmospheric pressure plasma jet (APPJ) and the use of this plasma jet to perform ZnO thin film deposition. The APPJ under investigation is sustained by a pulsed power supply with a repetitive power frequency up to 25 kHz using N₂ or O₂ as the plasma gas. The assessment of how the ambient air influences the plasma characteristics and how it can effectively be minimized are the focus of the diagnostic work. To minimize the ambient air influence, the exit of the jet is shielded with a glass tube with the inside diameter ranging from 3 to 5 cm. The exit of the tube is covered by a metal plate and leaving a gap of 0.5 to 3 mm. When the N₂ plasma is used, the visible jet length is much longer with such an arrangement. The effective area within which the jet is treated increases by more than a factor of two, as confirmed by the contact angle measurement made on the treated glass surface. In O₂ plasmas, the intensity of atomic oxygen emission (777.4 nm) increases by more than one order of magnitude with the presence of the glass tube. When photoresist is etched using this oxygen plasma jet, the jet with the presence of the glass tube shows a increase in the etching rate by more than 50 % than the case without the presence of glass tube.

The use of this APPJ to perform ZnO thin film deposition is studied as the second part of this presentation. ZnO thin films are deposited on a silicon wafer by spraying nebulized zinc-containing salt solutions, namely ZnCl₂ and Zn(NO₃)₂, into the downstream of the plasma jet. Preliminary studies show that by using N₂ plasmas, a better quality film can be obtained comparing with using O₂ plasmas. The film quality is found to be sensitive to the plasma conditions. With properly adjusted process parameters, dense and smooth films can be deposited with a rate higher than 75 nm/min. Improvement of the electrical conductivity and the study of the photoluminescence properties of the film are currently underway.

5:20pm PS2-MoA11 Atmospheric-Pressure Microplasma-Jet Modified Polystyrene Surfaces as Substrates for Epithelial Cell Growth. *J.-S. Oh, J.W. Bradley, K.G. Doherty, C.M. Sheridan, R.L. Williams, A. Bowfield, P. Unsworth, P. Weightman*, The University of Liverpool, UK

Non-thermal atmospheric pressure plasma jets (APPJs) have recently been the subject of much interest as an alternative to low-pressure plasma treatment since they are relatively simple to construct, and have the advantages that expensive vacuum equipment and high grade gases are not needed. APPJs have potentially numerous applications such areas such as deposition, surface modification and particularly, in biomedicine, sterilization and wound treatment. Here we focus on developing micro-plasma jet technology based on capillary dielectric barrier (DBD) discharges for the localized surface modification of polystyrene (PS) as a substrate for biomaterial processing. The micro-capillaries have an internal diameter of 280 μm and an outer diameter of 330 μm. The surface modification is spatially investigated by dynamic water contact angle (WCA) measurement with about ~0.2 μL water droplets. The results show that the WCA of untreated PS is 90° reducing to angles between 30° and 20° for exposure times between a few seconds and several minutes. The treated areas have typically radial extensions of several millimeters varying with discharge voltage, excitation frequency, gas flow rate and capillary-substrate distance. The modified surface properties will be discussed in more detail with focus on X-ray photoelectron spectroscopy measurements of the surface chemistry and the relationship to epithelial cell culture growth and proliferation.

Advanced Surface Engineering

Room: Cimmaron - Session SE+PS-MoA

Pulsed Plasmas in Surface Engineering

Moderator: J. Patscheider, EMPA, Switzerland

2:00pm SE+PS-MoA1 2010 AVS Peter Mark Award Lecture - High Power Impulse Magnetron Sputtering (HIPIMS) - Fundamentals and Applications. *A.P. Ehiasarian**, Sheffield Hallam University, UK

INVITED

High power impulse magnetron sputtering (HIPIMS) is one of the youngest magnetron sputtering technologies. It provides new parameter space and

new level of control of deposition parameters which are unattainable by conventional sputtering or cathodic arc evaporation technologies.

HIPIMS utilises a short (impulse) gas discharge with duration of ~100 μs and duty cycles of <1% allowing it to access high peak power densities of 3000 Wcm⁻² at voltages of several hundred volts and current density of 1-4 Acm⁻². Within each HIPIMS pulse the discharge is ignited through a hot electron ionisation wave and then develops into a cold metal plasma. The properties of the target material such as sputter yield, secondary electron emission coefficient, atomic mass and ionisation potential determine the power dissipated in the discharge, the density of plasma and the transport from the target to the substrate. The lifetime of both gas and metal ions spans over several milliseconds after the pulse often extending to the next pulse, thus creating a constant bombardment of ions at the substrate.

The degree of metal ionisation is controlled by the peak power density dissipated at the target and reaches 50% for Ti and 70% for Ta. The high metal ionization fraction of the HIPIMS technology has been utilised in applications for metalizing high-aspect vias with depth-to-width ratio of 30:1 achieving 10% bottom coverage for Ti, Ta and Cu films. The technology has been upscaled to a production cycle for through-silicon via (TSV) interconnects on 200 mm wafers.

HIPIMS pretreatment can implant metals and rare earths in substrates whilst maintaining the crystalline character, promoting local epitaxial growth over large lateral areas and excellent adhesion. This enables the introduction of oxidation- and corrosion- barriers at the coating-substrate interface.

Reactive sputtering in Ar and N₂ atmosphere in HIPIMS are characterised with a strong dissociation of the nitrogen molecule. In conditions of high power density, the N¹⁺ : N₂⁺ ratio and Ti¹⁺:Ti⁰ ratio can exceed 1 thus promoting a fully dense intercolumnar boundaries in TiN films and increase their hardness. A preferred growth orientation of (200) is observed even without substrate biasing.

Nanoscale multilayer (superlattice) structured coatings based on CrAlN/CrN have been grown with very low waviness and strongly improved density. These coatings provide excellent oxidation resistance and reduced fatigue deficit of aerospace turbine blades.

Nanocomposite coatings based on CrAlSiN were also deposited by HIPIMS for applications in high-temperature oxidation protection. Closer packing and reduced misorientation of nanocrystals as well as increased size of nanoclusters in which they are grouped are crucial mechanisms crucial in enhancing the film hardness.

The technology is finding new applications in the deposition of Cu(InGa)Se₂ in industrial photovoltaic cell coaters where a 3% improvement in efficiency over conventional sputtering has been achieved.

2:40pm SE+PS-MoA3 Influence of Plasma Conditions on the Properties of Hafnium and Titanium Films Deposited using HIPIMS. *A.N. Reed*, Air Force Research Laboratory, *M.A. Lange*, Air Force Research Laboratory/Universal Technology Corp., *J.G. Jones, C. Muratore, J.J. Gengler, A.A. Voevodin*, Air Force Research Laboratory

The orientation of a film can have a significant effect on its physical properties, for example the thermal conductivity of hexagonal materials. There has been a significant amount of work in the area of controlling the microstructure of films using deposition parameters. High power impulse magnetron sputtering, HIPIMS, is a PVD technique that produces a sputtered flux with a higher ion content than conventional DC magnetron sputtering. The ionization fraction of material upon the substrate permits some control of the film characteristics. In this study films were grown at pressures ranging from 5-30 mTorr, and pulse duration from 20-200μs. The resulting films exhibited pressure dependent deposition rates as well as changing crystalline structure based on pulse duration. Energy resolved mass spectrometry and optical emission spectroscopy allowed correlation of ion energy distributions to deposition rates. Material characterization techniques, such as XRD, XPS, and SEM, have been used to correlate film structure to processing conditions for hafnium, titanium, and their nitrides. Time-domain thermal reflectance was used to measure the films' thermal conductivities. Differences in these values were related to the film microstructure.

3:40pm SE+PS-MoA6 High Power Impulse Magnetron Sputtering for the Growth of Functional Amorphous and Nanocrystalline Films. *K. Sarakinos, A. Aijaz, M. Samuelsson, U. Issaksson, U. Helmersson*, Linköping University, Sweden

INVITED

Growth of films by condensation from the vapor phase frequently proceeds far from thermodynamic equilibrium giving rise to metastable configurations with unique attributes which are largely determined by the energy of the film forming species. One way of transferring energy to the growing film is via bombardment by ionized species which are present in plasma assisted physical vapor deposition (PVD) techniques. High power impulse magnetron sputtering (HiPIMS) is a novel plasma assisted PVD

* Peter Mark Memorial Award Winner

technique in which large fluxes of energetic ions are made available at the growing film. This is achieved by applying the power to the target in short unipolar pulses of low duty cycle (<10%) and frequency (<10 kHz). This mode of operation results in the generation of ultra dense plasmas (electron densities 10^{18} - 10^{19} m⁻³) and a subsequent high degree of ionization for both gas atoms and sputtered material. HiPIMS has been extensively used for the deposition of polycrystalline elemental and compounds films facilitating control over their microstructure, phase composition, optical, mechanical and electrical properties. In the present talk the use of HiPIMS for the deposition of amorphous and nanocrystalline carbon and metal nitride based films is demonstrated. Discharges are generated using a variety of experimental parameters with respect to the pulse width, pulsing frequency, composition and pressure of the gas atmosphere. Time-averaged and time-resolved plasma diagnostics reveal that the variation of the above mentioned process parameters allows for control over the flux, the energy and the nature of the bombarding ionized species. Growth of films at those conditions enables to tune their bonding properties, their microstructure and their crystallinity and through this tailor important functional attributes such as their mechanical performance and high temperature stability.

4:20pm SE+PS-MoA8 New Development in Modulated Pulse Power Sputtering of Aluminum Oxide, Aluminum Nitride and Carbon Films, R. Chistyakov, Zond Inc, B. Abraham, Zpulsor LLC

Modulated pulse power (MPP) sputtering is a versatile high power pulse magnetron sputtering technique in which there can be multiple voltage steps within a pulse. In this study, multiple voltage steps have high amplitude voltage oscillations. It was found that at certain level of voltage oscillations amplitude and frequency it is possible to sustain near arc free discharge in reactive gas environment. A special plasma generator with adjustable voltage oscillations amplitude and frequency was developed. The maximum output voltage is 1400 V. Aluminum oxide and aluminum nitride films have been reactively deposited with new approach in near arc free mode. The deposition rate, film structure, orientation, and mechanical properties were analyzed and measured, and the results of the film property measurements will be presented. Carbon films were sputtered with high average and peak power. It was found that with particular voltage pulse shapes there is no cones formation on the target surface during the deposition

Surface Science

Room: Picuris - Session SS1-MoA

Nanocluster Reactivity

Moderator: G.B. Fisher, University of Michigan

2:00pm SS1-MoA1 Size and Shape of the Au/TiO₂(110) Nanoparticles That Catalyze the Oxidation of CO, J. Jupille, Inst. des Nanosciences de Paris, France, M.-C. Saint-Lager, A. Bailly, Inst. Néel, France, G. Cabailh, Inst. des Nanosciences de Paris, France, S. Garaudée, Inst. Néel, France, R. Lazzari, Inst. des Nanosciences de Paris, France, P. Dolle, Inst. Néel, France, O. Robach, CEA, France, I. Laoufi, Inst. Néel, France, H. Cruguel, Inst. des Nanosciences de Paris, France

The catalytic activity of supported gold nanoparticles [1] has generated great excitement over the two last decades. In contrast with the inertness of the bulk gold, the catalytic activity of gold nanoparticles increases dramatically as their size decreases. Most studies have focused on the catalytic oxidation of CO in particular because gold catalyzes that reaction at temperature as low as 200 K with an even better activity than platinum [2]. The origin of the property is still debated. Following the earlier suggestion that reactive sites are at the edge of the Au/oxide interface [2], it was alternatively proposed from density functional approaches, in the frame of a pure gold pathway, that the activity of gold nanoparticles mostly comes from low coordinated atoms [3]. In a very different manner, the activity of gold nanoparticles was attributed to a quantum size effect with a maximum in activity for two-atom-thick clusters [4].

To date, a direct characterization of the morphology of gold nanoclusters during catalytic reactions is lacking. The present works reports on observations by Grazing Incidence Small Angle X-Ray Scattering (GISAXS) of Au/TiO₂(110) supported particles during the catalytic oxidation of CO, by using a dedicated set up. The analysis chamber, operated from ultra-high vacuum to normal pressure, is acting as a reactor [5]. The reactivity is determined by mass spectrometry. In the present case (20 mbar O₂ + 0.1 mbar CO on Au/TiO₂(110) at 200 K), it rapidly increases for particles < 5 nm. GISAXS demonstrates that reacting gold particles are always three-dimensional with an aspect ratio H/D ≈ 0.6 (H and D are the height and diameter of the particles, respectively) which, for the smallest particles under study (D = 2 nm) still corresponds to 4 atomic layers of

gold. The reaction mechanism is discussed via the relationship between the reactivity and the particle geometry.

- [1] M. Haruta et al., Chem. Lett. 2 (1987) 405.
- [2] G. R. Bamwenda et al., Catal. Lett. 44 (1997) 8.
- [3] I. N. Remediakis et al., Angew. Chem. Int. Ed. 44 (2005) 1824.
- [4] M. Valden et al., Science 281 (1998) 1647.
- [5] M.-C. Saint-Lager et al., Rev. Sci. Instrum. 78 (2007) 083902.

2:20pm SS1-MoA2 Formation and Thermal Stability of Platinum Oxides on Size-Selected Platinum Nanoparticles: Support Effects, L.K. Ono, J.R. Croy, H. Heinrich, B. Roldan Cuenya, University of Central Florida

Metal-loaded diblock-copolymer micelles have been used to synthesize size-selected self-assembled Pt nanoparticles (NPs). Ex-situ atomic force microscopy (AFM) and transmission electron microscopy (TEM) as well as in-situ X-ray photoelectron spectroscopy (XPS) measurements were performed to investigate the formation and thermal stability of PtO_x species on Pt NPs supported on SiO₂, ZrO₂, and TiO₂ thin films. For a given particle size distribution, the role played by the NP support on the stability of Pt oxides was studied. Our findings are: (i) the formation of PtO_x species upon atomic oxygen exposure and a two-step thermal decomposition process (PtO₂ → PtO → Pt) from 300 K to 600 K upon annealing in vacuum; (ii) the enhanced stability of PtO_x species on ZrO₂ as compared to SiO₂ and TiO₂ upon annealing in O₂, and in vacuum, possibly due to its stabilization at the NP/support interface; (iii) the onset of strong NP/support interactions above 600 K and the formation of Pt-Ti and/or Pt-Ti-O alloys for the Pt-NP/TiO₂ system associated with the creation of O-vacancies on TiO₂ upon annealing in vacuum, leading to the encapsulation of Pt by TiO_x above 700 K.

The size-dependent stability of PtO_x species in Pt NPs supported on SiO₂ as compared to bulk Pt(111) will be demonstrated based on temperature programmed desorption measurements.

2:40pm SS1-MoA3 Catalytic Reactivity of Mass Selected Nanoparticles, I. Chorkendorff, Technical University of Denmark

INVITED

It has recently been shown that for both the technologically important steam reforming process [1] and the methanation reaction [2] the rates are strongly dependent on the particles' size. This is ascribed to the nature of the nanoparticles and in particular the presence of step and kink sites on the nanoparticles. The abundance of such sites is expected to be very dependent on the size and the synthesis procedure. In this work we have investigated the nature of mass selected Ruthenium nanoparticles and specifically their reactivity with respect to gasses relevant for the above mentioned processes. Ruthenium is known to be a very good catalyst for both processes, and in some situations it may be superior to the commonly used Nickel catalyst despite its much higher price. Nanoparticles of sizes relevant for the above mentioned processes (2-10 nm) are manufactured by a sputter magnetron and subsequently mass selected by a quadrupole mass spectrometer. The nanoparticles are soft landed on various substrates (HOPG or SiO₂) and the influence and the advantages of the substrates will be discussed. The nanoparticles have been characterized in situ by SEM, AES, ISS,TPD and STM while ex-situ TEM has been used. The surface area and the stability of the nanoparticles were initially determined by temperature programmed desorption, and their ability to dissociate CO was evaluated using isotopically labeled gasses. The nature of the CO bonding and dissociation will be correlated with similar investigations on purpose stepped single crystals of Ruthenium (Ru(0 1 54)) demonstrating how the activity can be evaluated as a function of size. The reactivity of such mass selected nanoparticles has also been measured in a newly developed micro reactor on a chip with a volume of only 235 nl. This small volume combined with the fact that all the reactants and products can be led directly into a quadrupole mass spectrometer for analysis allows for a close correlation of size and overall reactivity at high pressure and temperature conditions.

References:

- [1] G. Jones, J. G. Jakobsen, S. S. Shim, J. Kleis, M. P. Andersson, J. Rossmeisl, F. Abild-Pedersen, T. Bligaard, S. Helveg, B. Hinnemann, J. R. Rostrup-Nielsen, I. Chorkendorff, J. Sehested, and J. K. Nørskov, "First Principles Calculations and Experimental Insight into Methane Steam Reforming over Transition Metal Catalysts", J. Catal. 259 (2008) 147-160.
- [2] M. P. Andersson, F. Abild-Pedersen, I. Remediakis, J. Engbaek, O. Lytken, S. Horch, J. H. Nielsen, J. Sehested, J. R. Rostrup-Nielsen, J. K. Nørskov, and I. Chorkendorff, "H₂ Induced CO dissociation on nickel surfaces", J. Catal. 255 (2008) 6-19.

3:40pm **SSI-MoA6 Optical Nanocalorimetric Measurements of Catalytic Light-Off Temperature and Catalytic Activity of Pd Nanoparticles-Size Dependent Effects**, C. Langhammer, M.K. Larsson, B.H. Kasemo, I.L. Zorić, Chalmers University of Technology, Sweden

Nanocalorimetric studies of reaction rates for the $H_2 + O_2 \rightarrow H_2O$ reaction on supported Pd nanoparticles were performed, under realistic (T, p) conditions, by measuring *local* temperature of catalytic nanoparticles using the indirect nanoplasmonic sensing method^{1, 2}. This method utilizes a sensing platform consisting of a 2D array of nanoplasmonic Au sensor nanodisks, coated with a few nm thick SiO₂ spacer layer onto which Pd nanoparticles, with an average size of 2.2, 3.9, 6.5 and 18 nm, were prepared. The chemical power generated by the above exothermic reaction causes a temperature rise of the nanocatalyst and the sensing Au nanodisks, which in turn leads to a spectral shift of the localized surface plasmon resonance (LSPR) of the latter. During the experiments the surrounding temperature was scanned from RT to 300°C for each reactant concentration. By subtracting the calibrated temperature dependence of the Au LSPR from the observed spectral shifts during the reaction we obtain local temperature changes on the Pd nanocatalysts, which is directly proportional to the reaction rate, as a function of surrounding temperature for different reactant concentration $a=H_2/[H_2+O_2]$ in the feed gas and for Pd nanocatalysts of different sizes. A clear transition in the measured reaction rate, from the kinetically limited, low temperature regime, via a light-off, into the mass transport limited regime was observed. In the low temperature kinetically limited regime an Arrhenius analysis yields apparent activation energies, for a given catalyst size, that vary as a function of reactant concentrations in agreement with the data in the literature. A shift of the light-off temperature towards higher values, observed at higher a values, is accounted for by an increased catalyst self poisoning by hydrogen. By following a nonmonotonic change of the light-off temperature, at a given a value, for four different sizes of the Pd nanocatalyst, we were able to extract information about the size dependence of the catalytic activity for our systems. This was achieved by subtracting away the size dependence of the surface area as obtained from the TEM pictures of the nanocatalysts. The catalytic activity of the smallest nanoparticles (2.2 nm) shows an almost three fold increase compared to the activity of 18nm nanoparticles.

1. Larsson, E.M., Langhammer, C., Zorić, I. & Kasemo, B. Nanoplasmonic Probes of Catalytic Reactions. *Science* **326**, 1091-1094 (2009).

2. Langhammer, C., Zhdanov, V.P., Zorić, I. & Kasemo, B. Size-Dependent Kinetics of Hydriding and Dehydriding of Pd Nanoparticles. *Physical Review Letters* **104**, 135502 (2010).

4:00pm **SSI-MoA7 Photochemistry on Metal Nanoparticles: Comparison of Nanosecond and Femtosecond Laser Induced NO Photodesorption from NO Dimer Layers on Supported Ag Nanoparticles**, K.H. Kim, D. Mulugeta, Fritz-Haber-Inst. der Max-Planck-Gesellschaft, Germany, K. Watanabe, Tokyo Univ. of Science, Japan, D. Menzel, Fritz-Haber-Inst. der Max-Planck-Gesellschaft and TU München, Germany, H.-J. Freund, Fritz-Haber-Inst. der Max-Planck-Gesellschaft, Germany

Metal nanoparticles (MNP) have special electronic and optical properties due to their dimensions being smaller than many length parameters of electrons and photons with solids; this leads to drastic changes of surface photochemistry [1]. For oxide-supported Ag nanoparticles (AgNPs), we have reported before on strong influences of the initial excitation (2.3 – 4.7 eV, in particular of Mie plasmons at 3.5 eV), and of the mean particle size (2 to 12 nm), on the photodesorption cross sections (PCSS) of NO from NO dimer layers [2,3], using nanosecond laser pulses. However, the mechanism of desorption remains the same as on Ag(111) [2-4], as indicated by detailed measurements of final state energy distributions (translational, rotational, and vibrational) of the desorbing molecules [5], except for the smallest particles at the highest excitation energy [2] where much higher final state energies are found. These results are compatible with desorption via a transient ion, negative (TNI) in most cases [4], and positive (TPI) in the latter case [2]. In the entire range of nanosecond laser excitation, strictly linear behavior is found.

We have now done similar measurements using femtosecond laser excitation (3.1 eV photons only), increasing the excitation density by more than 10⁴ for the same photon fluences. No change is seen on Ag(111), while for AgNPs femtosecond plasmon excitation drastically increases the PCSS as well as changes the dynamics, as indicated by different final state energies of the desorbed NO. We interpret this behavior as due to the confinement of excitation in the NPs which then leads to multiple pump-up of hot electrons during the laser pulse.

After a general survey of the basics of photochemistry on nanoparticles as compared to surfaces of bulk crystals, and of the indicated previous results, the recent measurements will be described and discussed, aiming at conclusions about their relevance for the understanding of excitations and photochemistry on nanoparticles.

[1] K. Watanabe, D. Menzel, N. Nilius, and H.-J. Freund, *Chem. Rev.* **106**, 4301 (2006)

[2] D. Mulugeta, K. H. Kim, K. Watanabe, D. Menzel, and H.-J. Freund, *Phys. Rev. Lett.* **101**, 14613 (2008)..

[3] K. H. Kim, K. Watanabe, D. Menzel, and H.-J. Freund, *J. Am. Chem. Soc.*, **131**, 1660 (2009).

[4] F.M. Zimmermann and W. Ho, *Surf. Sci. Rep.* **22**, 127 (1995), and references therein.

[5] D. Mulugeta, Ph.D. Thesis, TU Berlin 2010; and D. Mulugeta, K. Watanabe, D. Menzel, and H.-J. Freund, to be published.

4:20pm **SSI-MoA8 H/D Exchange on Pd Nanoparticles: Effects of cis-2-butene Co-adsorption, and Implications for Isomerization and Hydrogenation of Alkenes over Pd**, A. Savara, W. Ludwig, Fritz-Haber-Institut der Max-Planck-Gesellschaft, Germany, R.J. Madix, Harvard University, S. Schauermann, H.-J. Freund, Fritz-Haber-Institut der Max-Planck-Gesellschaft, Germany

4:40pm **SSI-MoA9 Cu/CuOx Nanoclusters on ZnO(1010): Electronic, Catalytic, Morphological Structure**, Z. Zhang, M. Patterson, M. Ren, Y. Losovyi, J. Flake, R.L. Kurtz, P.T. Sprunger, Louisiana State University ARUPS, STM, and EELS has been used to study the electronic, atomic and chemical structure of Cu and CuO nanoclusters on non-polar ZnO(1010) surface. Within the backdrop of developing high performance CO₂ reduction catalyst (methanol production), our studies show that higher yield rate are found for Cu(I) surface species. ARPUS results from nanocluster CuOx/ZnO reveals that the oxidation process is highly dependent on the cluster size (smaller size). Moreover, CO adsorption (BE and vibrational) are distinctly different between Cu and CuOx nanoclusters supported on ZnO. Reaction studies confirm that methanol production is 4 times higher on partially oxidized Cu nanoclusters. Photoemission shows a small amount of Cu(II) even upon repeated oxidation/annealing processes, indicating a preferential stability of Cu(I) in the supported nanoclusters, due to interfacial effects with the substrate. This talk will include results from EELS/TPD and STM/AFM studies to better elucidate the chemical adsorption and intermediates as a function of CuOx size and structure.

5:00pm **SSI-MoA10 Femtosecond-laser Photoemission of Deposited MoxSy Clusters on Al2O3/NiAl(110)**, J. Zhou, State University of New York at Stony Brook, N. Camillone III, Brookhaven National Laboratory, M.G. White, State University of New York at Stony Brook

The electronic structures of supported size-selected Mo_xS_y clusters on an ultrathin aluminum oxide film on NiAl(110) are studied by two-photon photoemission spectroscopy. The Mo_xS_y clusters are produced by magnetron sputtering in gas phase and selected by a quadrupole mass filter. The mass-selected clusters are deposited on the ultrathin aluminum oxide film which has wide band gap to minimize the electronic interaction between clusters and NiAl(110) substrate. The formation of the aluminum oxide film on NiAl(110) results in a 0.3 eV decrease in work function and disappearance of the surface state of NiAl(110). With 0.1 ML Mo₄S₆ deposited on the surface, the photoemission spectrum is similar with that of bare alumina oxide film because of the absence of interaction between isolated clusters on the film. When the cluster coverage increases to 0.2 ML, some features origin from the cluster are observed and reveal that the clusters are semiconductor with a band gap of about 0.6 eV. A variety of other molybdenum sulfide clusters, Mo_xS_y (x/y: 2/6, 3/7, 5/7, 6/8, 7/10), are also investigated and they exhibit different electronic properties with specific molybdenum to sulfide ratio.

5:20pm **SSI-MoA11 Formation of Homogeneous Rh Clusters on Al₂O₃ from [Rh^{II}(OAc)₂]₂ Precursor Elucidated by STM and XAFS Analyses**, Z.W. Chen, Osaka University, Japan, W.-J. Chun, International Christian University, Japan, K. Fukui, Osaka University, Japan

Choice of a catalyst precursor sometimes affects the activity and selectivity of the catalyst due to local structures of precursors apart from the thermodynamically favored one. We have studied on precursor dependent structure of Rh/Al₂O₃ catalysts by using STM and X-ray absorption fine structure (XAFS). Our STM results showed that homogeneous Rh clusters can be randomly dispersed on the Al₂O₃ thin film (5 Å) on NiAl(110) by thermal decomposition of [Rh^{II}(OAc)₂]₂ precursors in vacuum. By statistical analyses of density, height, and diameter of the particles as a function of heat treatment temperature, we concluded that the particle typically included two Rh atoms, hence reflected the precursor composition. In situ STM measurements during heating process also showed that the precursors decomposed around 420 K. The Rh clusters were stable against aggregation up to 800 K. These features were quite different from the typical Rh/Al₂O₃ catalyst prepared from RhCl₃ precursor, where particle size was larger and aggregation easily occurred at such high temperature.

In order to determine the local structure of the clusters and elucidate the precursor dependency on the final structures, we performed XAFS measurements for Rh K-edge at NW-10A station in KEK-IMSS-PF. The Rh/Al₂O₃ catalysts were prepared from three Rh precursors, [Rh^{II}(OAc)₂]₂, Rh^{III}(OAc)₃, RhCl₃ on γ -Al₂O₃. The precursor Rh^{III}(OAc)₃ was selected because of its similar local structure to RhCl₃. The as-deposited samples were heated to 500 K, 650 K, 800 K, respectively in vacuum and XAFS were measured after each heat treatment.

In the case of RhCl₃, only one peak assignable to Rh-Rh bond appeared after heat treatment above 500 K and its coordination number was increased at higher temperature. It indicated that metallic Rh particles formed just after decomposition of RhCl₃, and they aggregated at high temperature. In contrast, in the case of Rh acetate precursors, both of [Rh^{II}(OAc)₂]₂ and Rh^{III}(OAc)₃, the peak assignable to Rh-O bond was predominant. A weak peak of Rh-Rh bond was also observed in the case of [Rh^{II}(OAc)₂]₂. Curve-fitting results suggested that the particle roughly included two Rh atoms each, which was qualitatively consistent with the STM results. In the case of Rh^{III}(OAc)₃ precursors, Rh species were dispersed as single atoms after decomposition and they agglomerated at above 650 K. We supposed that Rh-O bond was formed in the process of the acetate-containing precursors decomposition stabilized the small Rh particles on the Al₂O₃ surface.

Surface Science

Room: Santa Ana - Session SS2-MoA

Stress and Bonding Energetics in Nucleation and Growth

Moderator: G.L. Kellogg, Sandia National Laboratories

2:00pm **SS2-MoA1 Epitaxy of Disilane on Si(100)-H using Scanning Tunneling Microscope-induced Hydrogen Depassivation Patterns**, *J.B. Ballard, J.R. Von Ehr, J.N. Randall, J. Alexander, R. Saini*, Zyvex Labs, *M. Huang, H.-S. Choi, K.J. Cho, J.-F. Veyan, Y.J. Chabal*, University of Texas at Dallas, *J.W. Lyding*, University of Illinois at Urbana-Champaign
INVITED

2:40pm **SS2-MoA3 Stress Balance in Nanopatterned N/Cu(001) Surfaces**, *T.S. Rahman, S. Hong*, University of Central Florida, *E.Z. Ciflikli, B.J. Hinch*, Rutgers University

Helium atom scattering (HAS) and density functional theory (DFT) within pseudopotential methods have been used to investigate stress balance in nano-patterned N/Cu(001) surfaces. HAS shows that the stress-relief-driven lateral expansion of the averaged lattice parameter within finite-sized N containing patches reduces, with increasing N coverage (and decreasing stripe widths), from 3.5% to 1.8% and then, beyond a critical exposure, the patches' lateral expansion increases again slightly to 2.4%. This implies that, in this higher coverage range, the compressive stress is partially relieved with another mechanism; namely Cu vacancy trenches are nucleated. The trenches serve to enable further surface stress reduction and expansion in the N lattice parameters. In full agreement with above and previous experimental observations, DFT calculations show that an optimized N-induced $c(2 \times 2)$ structure has a net surface stress level ~ 4 N/m and such stress is effectively relieved when stripes of clean Cu(001) form along the $\langle 100 \rangle$ direction or when trench-like steps of Cu atoms form along the $\langle 110 \rangle$ direction. On the other hand, the calculations demonstrate that (contrary to the suggestions of Driver *et al.*[1]) rumpling displacements within the outermost Cu layer do not act to relieve the compressive surface stress levels while clock-like displacements could relieve stress levels, although such displacements are energetically unstable.

[1] S. M. Driver, J-T Hoefl, M. Polcik, M. Kittel, R. Terborg, R. L. Toomes, J-H. Kang, and D. P. Woodruff, *J. Phys. Cond. Mat.* 13, L601 (2001).

Work supported in part by NSF Grant CHE-0741423

3:00pm **SS2-MoA4 The Effect of Lattice Strain on Adatom Diffusion Barriers on Terraces and Step Edges**, *T.S. Rahman, H. Yildirim*, University of Central Florida

While it is well known that lattice strain has an effect on adatom diffusion barriers, its material specificity has not yet been explored. In a comparative study based on density functional theory, we find that self diffusion barriers for Pd(100) terraces and step edges are not affected by tensile strain (up to 5%) as much as their counterparts on Ag(100) and Cu(100). This difference is particularly significant for the step edge barriers (Ehrlich-Schwoebel) which for the cases of the Ag and Cu surfaces may be reduced to zero (or become negative) under strain but remain positive for the Pd surface. In other words, growth modes on Pd surfaces are less susceptible to changes in strain, as compared to Ag and Cu surfaces. We trace these differences to

local geometric response and characteristics in the electronic structure. In particular we argue that strain is less effective in changing diffusion barriers on transition metal surfaces than on the coinage metal surfaces.

3:40pm **SS2-MoA6 Long-range Self-ordered Ge Nanostressors on Silicon Nanomembranes**, *M. Huang, F. Chen*, University of Wisconsin-Madison, *Y. Zhang*, University of Utah, *D.M. Paskiewicz, F.S. Flack, D.E. Savage*, University of Wisconsin-Madison, *F. Liu*, University of Utah, *M.G. Lagally*, University of Wisconsin-Madison

Silicon nanomembranes (SiNMs) are defect-free, single-crystal Si sheets with thickness ranging from 2 to 500 nm. This thinness makes them flexible, transferable, bondable and, most importantly, mechanically ultracompliant. This compliance makes nanomembranes fundamentally different from bulk materials [1,2]. Growth of three-dimensional Ge islands (Ge "huts", or quantum dots) on freestanding Si membranes exploits this unique mechanical behavior to induce self-organization of the dots, resulting in a periodic strain in Si nanomembranes or nanoribbons [1,2].

To understand better the effects of strain and substrate compliance on lattice-mismatched heteroepitaxy, we grow Ge islands on stretched (i.e., tensile strained), freestanding, (001)-oriented SiNMs. We drape a SiNM over a substrate patterned with high ridges. The bending of the SiNM over the edges of the ridges creates regions of local strain that enhance and direct Ge island nucleation. The ridge height and separation are varied to manipulate the draped-membrane strain. Ge 3D islands are grown on the draped SiNM via chemical vapor deposition or molecular beam epitaxy. We demonstrate two-dimensional self-ordering of a single layer of Ge dots, with uniform dot size and spacing. The islands, however, differ from the classic [105]-faceted structures. We find that, while our new Ge dots still have square or rectangular bases, they have steeper facets than those of conventional Ge "huts". We perform finite-element analysis to map the local strain in the draped membrane and to investigate the influence of membrane thickness and substrate ridge height on the dot ordering.

This work is supported by DOE, NSF, and AFOSR.

References:

- [1] M. Huang et al., *ACS Nano* 3, 721 (2009)
- [2] H-J. Kim-Lee et al., *Phys. Rev. Lett.*, 102, 226103 (2009)

4:00pm **SS2-MoA7 Atomic Layer Epitaxy of Ge on Si(100)-(2x1)**, *J.-F. Veyan, M.P. Nadesalingam, M. Huang, H. Dong*, University of Texas at Dallas, *J.N. Randall, Zyvex Labs, W.P. Kirk, J. Cho, R.M. Wallace, Y.J. Chabal*, University of Texas at Dallas

4:20pm **SS2-MoA8 The Influence of Metal – Substrate Bonding Energetics on Metal Atom Adsorption, Cluster Nucleation and Film Growth**, *C.T. Campbell*, University of Washington
INVITED

Oxide-supported late transition metal nanoparticles form the basis for many important industrial catalysts. The activity, selectivity and sintering rates of these catalysts can depend strongly on the particle size, the oxide support, and the extent of reduction of the oxide. The microkinetics of sintering are essentially the same as for nucleation and growth. All of these kinetic properties are closely related to the variation of metal atom energy (chemical potential) with nanoparticle size. We will review our calorimetric measurements of the energies of metal atoms in nanoparticles supported on different oxide surfaces, and relate those to nucleation/growth kinetics. We will discuss these results in the light of DFT calculations by our collaborators, H. Jonsson, G. Henkelman and L. Xu. The stability of Ag nanoparticles increases with particle size on both MgO(100) and reduced CeO₂(111), until the number of atoms per particle exceeds ~ 5000 . At any given size, Ag nanoparticles have much higher stability on reduced CeO₂(111) than on MgO(100). This difference is due to the much larger adhesion energy of Ag nanoparticles to reduced CeO₂(111) compared to MgO(100). Increasing the extent of reduction of the CeO₂ surface increases Ag particle stability. The energetics and growth of Li and Ca on MgO(100) are dominated by defect sites, and differences in migration barriers there. The migration rates of Pd clusters on MgO(100) vary in unusual ways with size below 5 atoms, and this impacts nucleation.

The above results for oxide surfaces will be contrasted with similar studies of metal film growth on polymer surfaces, where diffusion of metal atoms below the surface and highly exothermic reactions with subsurface heteroatoms can dominate the early stages of growth.

Work supported by NSD and DOE-OBES.

5:00pm **SS2-MoA10 Growth of Ag on Ge(110) and Ge(111) Studied by LEEM**, C. Muller*, S. Chiang, University of California, Davis

We studied Ag island growth on reconstructed Ge(110) and Ge(111) surfaces with low energy electron microscopy (LEEM). At 480 C, one-dimensional (1D) island growth was observed on Ge(110). Island nucleation proceeds from defects in the Ge substrate, with island thickness corresponding to the size of the substrate defect where the island nucleation occurred. As Ag is deposited, islands lengthen but do not thicken. At 9 ML, Ag coverage islands were up to 10 μm long, and thicknesses varied from 100 nm to 250 nm. One-dimensional islands were also produced by Ag deposition at room temperature followed by sample heating. Round Ag islands resolvable in LEEM were observed and coalesced into many long 1D islands as temperature was increased. Islands formed by deposition at room temperature followed by heating to a particular temperature were shorter and thicker than islands grown by deposition on a substrate held at that same temperature. Ag growth on Ge(111) is Stranski-Krastanov. Multilayer Ag island formation begins after the Ag ($\sqrt{3}\times\sqrt{3}$)R30° phase completes at one monolayer. Ag islands exhibit hexagonal faceting. For both the Ge(111) and Ge(110) surfaces, Ag islands induce changes in the Ge substrate that leave a "footprint" observable in LEEM after all Ag has been desorbed from the surface.

*Funding from NSF CHE-0719504; NSF PHY-0649297 (REU)

5:20pm **SS2-MoA11 Growth of Au Islands and Thin Films on NiAl(110): STM Experiments and DFT - Based Analysis**, C. Yuen, T. Duguet, Iowa State University & Ames Laboratory U.S. D.O.E., Y. Han, Institute of Physical Research and Technology, J. Evans, Iowa State University, P.A. Thiel, Iowa State University & Ames Laboratory U.S. D.O.E.

Both Au(110) and Ag(110) have a $0.29\times 0.41\text{ nm}^2$ rectangular surface unit cell matching almost perfectly that for NiAl(110). This provides the opportunity to grow epitaxial thin films free of lateral mismatch strain. One might expect in both cases layer-by-layer growth of two-dimensional fcc(110) islands given the low surface energy of Au and Ag. However, observed behavior is distinctly different for the two metals. Our STM experiments of Au deposition on NiAl(110) between 200-350 K reveal initial formation of islands with a height of 0.23-0.25 nm. Island densities and size distributions are determined. At 300 K, islands are irregular and regions with 3x1 periodicity are sometimes evident. For the coverage of about 60%, there is significant population by islands of second "layer" or level with heights of $\sim 0.24\text{ nm}$. Extensive DFT analysis were performed to determine low-energy structures of supported Au films for various coverages. Isolated Au atoms on NiAl(110) prefer sites between two Ni separated by 0.29 nm. However, rather than a simple (110) overlayer with Au at these sites, lower energy structures exist also populating 3-fold sites (e.g., NiAl₂) and displaying combinations of square and hexagonal motifs of adatoms. We believe that observed islands have such structures and present a model for their formation. Behavior is contrasted with Ag/NiAl(110) where bilayer Ag(110) islands form due to quantum size effects (QSE) [1]. However, Ag/NiAl(110) is known to exhibit a bilayer-by-bilayer growth mode due to QSE [1], and the bulk Au(110) surface exhibits 2x1 and 3x1 reconstructions.

[1] Y. Han et al. PRL 100, 116105 (2008); PRB 81, 115462 (2010).

Thin Film

Room: Pecos - Session TF-MoA

Organic ALD

Moderator: G.N. Parsons, North Carolina State University

2:00pm **TF-MoA1 Inorganic/Organic Interface Structure on ALD Modified Polymer Fibers**, J.S. Jur, J.C. Spagnola, W.J. Sweet, B. Gong, Q. Peng, G.N. Parsons, North Carolina State University

2:20pm **TF-MoA2 Molecular Layer Deposition of Hybrid Siloxane/Alumina Polymer Films**, A.I. Abdulagatov, B. Yoon, V.R. Anderson, Z.M. Gibbs, A.S. Cavanagh, S.M. George, University of Colorado at Boulder

Polydimethylsiloxane (PDMS) is an important polymer with excellent flexibility and low elastic modulus. The properties of PDMS are also tunable based on varying the cross-linking between the polymer chains. PDMS MLD was initially attempted using the sequential dosing of bis(dimethylamino)dimethylsilane or dimethylmethoxychlorosilane

(DMMCS) and water at different temperatures. Unfortunately, the surface reactions appeared to terminate and no mass gain was measured after about 20 MLD cycles. After precursor dosing was stopped, the deposited film was observed to decrease in mass. This loss of mass is believed to be related to desorption of cyclic siloxanes from the PDMS MLD film. Cyclic siloxane desorption is entropically favored at longer PDMS chain lengths and higher temperatures and is facilitated by the high flexibility of the PDMS chains. To prevent desorption of the cyclic siloxanes, hybrid siloxane/alumina films were grown by mixing aluminum into the siloxane film using trimethylaluminum (TMA). The new hybrid MLD films contain [-Si(CH₃)₂-O-] units that are separated by [-Al-O-] linkages. The hybrid siloxane/alumina polymer films were grown using the precursor sequence: DMDCS; H₂O, TMA; and H₂O. Quartz crystal microbalance studies revealed linear growth with growth rates of $\sim 22\text{ ng/cm}^2$ at 200°C. FTIR vibrational studies revealed -Si(CH₃)₂OCH₃, -Si(CH₃)₂OH, -AlCH₃, and -AlOH surface species after the DMDCS; H₂O, TMA; and H₂O exposures, respectively. FTIR studies also observed self-limiting adsorption during the individual precursor exposures. X-ray reflectivity (XRR) measurements revealed a hybrid siloxane/alumina growth rate of $\sim 1.0\text{ \AA/cycle}$ at 200°C and a film density of $\sim 2.3\text{ g/cm}^3$. Elemental analysis of films using X-ray photoelectron spectroscopy (XPS) indicated that the films were chlorine-free. Hybrid siloxane/alumina polymer films could be grown at temperatures as low as 120°C, and these films showed some chlorine impurities.

2:40pm **TF-MoA3 Quantum Chemical Simulations of ALD and MLD; Insights from Simulations**, C. Musgrave, University of Colorado at Boulder

INVITED

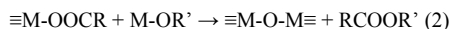
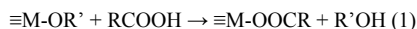
Ab Initio simulations have become widely used tools in the materials, surface science and chemistry communities for predicting molecular and materials properties and for studying atomistic processes. In this talk we will give an overview of how these methods can be used to understand ALD and MLD from an atomistic viewpoint and what you can learn from simulations. We will also discuss the limits of quantum chemistry and provide guidelines for those interested in using simulations to study ALD. Examples from our past and current work as well as that of others will be used to illustrate the application of these methods to surface reactions relevant to ALD and MLD. Examples include; the effect of using precursors with different ligands, including alkoxides, alkylamides and halogens, to deposit HfO₂ and Al₂O₃; the effect substrate type and functionalization on the initial ALD nucleation reactions; the ability to grow oxynitrides; and the use of simulations as a computational spectroscopy tool to complement experiment in the determination of ALD intermediates and products.

3:40pm **TF-MoA6 Nonaqueous Sol-Gel Chemistry in Atomic Layer Deposition**, N. Pinna, University of Aveiro, Portugal and Seoul National University, Korea

INVITED

Nonaqueous sol-gel routes are elegant approaches for the synthesis of high quality metal oxide nanomaterials such as pure inorganic nanocrystals [1], ordered hybrid organic-inorganic materials [2] or thin films by atomic layer deposition (ALD) [3]. In this communication, after a short introduction to nonaqueous sol-gel chemistry we will focus on the ALD using nonaqueous sol-gel. In particular, the similarities and differences of the chemical processes taking place in solution and in ALD will be discussed through two examples of recent approaches of metal oxide film deposition

Our approach makes use of metal alkoxides and carboxylic acids as metal and oxygen source, respectively [4]. In the first step, it is expected that the reaction of surface alkoxide species with carboxylic acids leads to surface carboxylate species (eq. 1). In the second step an aprotic condensation reaction between surface carboxylate species and metal alkoxides leads to metal-oxide bonds formation (eq. 2).



This process enables the growth of metal oxides at temperatures as low as 50 °C on various supports.

A comparison of this nonaqueous sol-gel route to ALD approaches using ozone as oxygen source will be made. Although, from a first look it seems that the chemistry responsible for metal oxide formation is very different, this is certainly not the case. As a matter of fact it was recently reported that during the ALD of metal oxides, the exposure to ozone leads to formate, carbonate and hydroxyl groups on the surface [5-7]. According to Goldstein et al., a large amount of formate surface species were formed by the reaction of trimethylaluminum (TMA) and O₃ [5]. Therefore, the formation of surface carboxylic species upon reaction with ozone leads to similar surface states as in the case of reaction with carboxylic acids [4]. These findings will be used to discuss the chemical reactions responsible for the deposition of PbTiO_x using lead bis(3-N,N-dimethylamino-2-methyl-2-propoxide), titanium(IV) isopropoxide and a combination of water and ozone as oxygen sources as recently reported by Hyun Ju Lee et al. [8]

* Morton S. Traum Award Finalist

References:

- [1] Pinna, N. & Niederberger, M. *Angew. Chem. Int. Ed.*, **2008**, *47*, 5292
- [2] Pinna, N. *J. Mater. Chem.*, **2007**, *17*, 2769
- [3] Clavel, G. et al. *J. Mater. Chem.*, **2009**, *19*, 454
- [4] Rauwel, E. et al. *Angew. Chem., Int. Ed.*, **2008**, *47*, 3592
- [5] Goldstein, D. N. et al. *J. Phys. Chem. C*, **2008**, *112*, 19530
- [6] Rai, V. R.; Agarwal, *J. Phys. Chem. C*, **2008**, *112*, 9552
- [7] Kwon, J. et al. *Chem. Mater.*, **2008**, *20*, 3248
- [8] Lee, H. J. et al. *ECS Transactions*, **2009**, *19*, 829

4:20pm TF-MoA8 Combined Atomic Layer Deposition and Molecular Layer Deposition for Encapsulation of Electrospun Nylon Nanofibers, C. Oldham, B. Gong, J.C. Spagnola, North Carolina State University, K. Senecal, T. Godfrey, Natick Soldier RD&E Center, J.S. Jur, G.N. Parsons, North Carolina State University

Electrospun nanofibers are of interest for air filtration, thermal insulation, biochemical sensing, and a range of other applications. Nanofibers can be readily electrospun from polyamide-6 (PA-6) nylon, but nylon is highly susceptible to water uptake and rapid degradation when exposed to chemical reactants, including those used in ALD. The high surface area of nanofibers makes these issues more acute and difficult to manage. We have recently investigated the deposition of Al₂O₃ and ZnO on nylon nanofibers and found distinctly different results for these two material processes. Aluminum oxide ALD from trimethylaluminum and water resulted in significant fiber degradation, whereas fibers remained intact upon ALD using diethyl zinc and water. The ZnO coating was not sufficient, however, to impede attack and degradation during subsequent exposure to Al₂O₃ ALD using TMA. We have recently explored a new MLD process in our lab using TMA and glycidol, where the resulting film is a hybrid organic-metal oxide polymer. This MLD coating onto a ZnO-coated nylon nanofiber results in only minimal reaction with the polymer under the ZnO. After 75 MLD cycles, exposing the nylon nanofibers to 25 cycles of trimethylaluminum/water results in no visible degradation, indicating successful encapsulation by the ZnO/MLD bilayer. We will present the chemistry associated with the reaction between the TMA and PA-6. Additionally, the surface chemistry of the PA-6 nanofibers after encapsulation, and the air stability of the hybrid organic-metal oxide coatings will be discussed.

4:40pm TF-MoA9 Structure and Properties of Ultra-High Molecular Weight PHEMA Synthesized Using Solvent-Free Initiated Chemical Vapor Deposition (iCVD), R.K. Bose, K.K.S. Lau, Drexel University

Initiated chemical vapor deposition (iCVD) is a low temperature variant of hot-wire chemical vapor deposition (HWCVD) which has been used to produce a wide variety of free radical polymers like fluoropolymers, acrylic polymers and silicone polymers without the use of solvents. An initiator is activated in the gas phase by a resistively heated filament array. The radicals thus generated undergo surface polymerization on a cooled substrate by attaching to multiple monomer units. In this work, we produced thin films of poly(2-hydroxyethyl methacrylate) (PHEMA), an important hydrogel, for potential biomaterials applications such as skin substitutes. Fourier transform infrared (FTIR) and nuclear magnetic resonance (NMR) spectroscopies showed that the chemistry of PHEMA obtained by iCVD synthesis matched closely to PHEMA obtained from solution synthesis. Deposition kinetics were tuned to achieve high deposition rates (~1.5 μm/min), which yielded mechanically robust ultra-high molecular weight polymer films. As a result, the films displayed a high degree of physical chain entanglement giving rise to high tensile modulus and storage modulus. This eliminates the need for chemical crosslinking, thus preserving maximum hydrophilicity for cell growth. The films showed good water transport and swellability. *In vitro* cytotoxicity studies of adult human dermal fibroblasts on PHEMA showed these films were non-cytotoxic and displayed viable cell adhesion. Non-specific protein adsorption was shown to be reduced compared to controls.

5:00pm TF-MoA10 Molecular Layer Deposition of Alucones Using Trimethylaluminum and Glycerol or Glycidol, R.A. Hall, B. Yoon, Y. Lee, S.M. George, University of Colorado at Boulder

Molecular layer deposition (MLD) can be used to grow hybrid organic-inorganic films using organic MLD and inorganic ALD precursors. The alucones are the most studied of these hybrid organic-inorganic films. Alucone MLD depends on the sequential, self-limiting reactions between trimethylaluminum (TMA) and various organic alcohols. In this work, alucone MLD was performed using glycerol, a sugar alcohol with three hydroxyl groups or glycidol, an alcohol molecule that contains an epoxide group. Both of these alcohols should promote cross-linking in the alucone film for enhanced film stability and film toughness.

Studies of alucone MLD using TMA and glycerol (GL) or glycidol (GLY) were performed using *in situ* quartz crystal microbalance (QCM), Fourier transform infrared (FTIR) and quadrupole mass spectrometry (QMS) techniques. The FTIR studies showed that the TMA and GL or GLY reactions were both self-limiting. For the TMA + GL reaction, the FTIR spectra observed the growth/loss of AlCH₃ and C-OH vibrations versus TMA/GL exposures. The mass gain measured by the QCM was 43 ng/cm²/cycle at 150°C. QMS confirmed the presence of TMA and GL parents and observed the CH₄ reaction products. *Ex situ* XRR measurements yielded a growth rate of 2.40 Å/cycle after 50 cycles at 150°C.

Alucone films grown using TMA and GL or GLY were more stable than alucone films grown using TMA and ethylene glycol. The instability of alucone films has been attributed to unreacted AlCH₃ species. To explore this issue, alucone films were grown using TMA, GL and H₂O exposures in an ABC sequence. QCM measurements showed that the mass gain increased to 56 ng/cm²/cycle for this ABC sequence at 150°C. In addition, the QMS observed CH₄ intensities during H₂O exposures that were ~1/4 the intensity observed during GL exposures. These results indicate that H₂O exposures can remove unreacted AlCH₃ species and increase the mass gain per cycle.

Vacuum Technology

Room: Laguna - Session VT+MS-MoA

Gas Analysis in Vacuum and Process Applications

Moderator: S. Thornberg, Sandia National Laboratories

2:00pm VT+MS-MoA1 Miniature Mass Spectrometers and Ambient Analysis by Mass Spectrometry, R.G. Cooks, R.J. Noll, Z. Ouyang, Purdue University

INVITED

Two inter-related areas of rapid growth in mass spectrometry are i) Ambient ionization and ii) miniature mass spectrometers. This talk covers both topics. It attempts to provide the conceptual basis for these developments as well as summarizing the state of the technology and citing typical applications.

The authors believe that mass spectrometers are in the early stages of a radical transformation that will make them much more versatile and much more widely applied *in situ* than in the laboratory in future. At the same time they will increasingly be operated by non-technical staff including nurses, production line workers, industrial hygiene and food safety inspectors, surgeons and others who are not skilled in scientific instrumentation. The essential features needed for these developments are already in place, namely the rapid growth of regulatory and other demands for chemical analysis and the laborious nature of current standard laboratory methodology in many areas of chemical analysis.

Miniature and micro mass spectrometers are of great current interest. For many reasons, quadrupole ion traps are the most appropriately miniaturized mass analyzers and both microscale (10's of microns) and miniscale (100's of microns) instruments have been used. Arrays of such analyzers have further advantages in terms of reduction in power requirements. Most attention has gone to the mass analyzer but full systems (sampling, ion source, data capture and reduction) have been built and will be discussed, including a series of Mini mass spectrometers built in our labs. These handheld mass spectrometers have good performance (unit mass resolution to m/z 500) and allow gases, solutions and surfaces to be analyzed using a variety of ionization methods including internal electron impact and external electrospray ionization and desorption electrospray ionization (DESI). These systems are pressure-tolerant, they provide tandem mass spectrometry capabilities and satisfies critical size and weight criteria while providing essentially instantaneous chemical analysis.

Ambient ionization - in which samples are examined without preparation in their native state is readily applied with miniature mass spectrometers. These methods, of which DESI is the prototypical example, do not require sample preparation and operate in the ambient environment. High throughput analysis of complex mixtures - with tandem mass spectrometry being used to resolve the overlapping chemical signatures - is possible. Examples range from benzene vapor in urban air to agrochemical residues in produce to phospholipid distributions in diseased tissue.

2:40pm VT+MS-MoA3 Accurate Determination of Molar Quantity for Gas in a Vacuum Chamber with Extreme Temperature Variations, H.C. Peebles, M.S. Benner, Sandia National Laboratories, T.K. Mehrhoff, Independent Contractor to Sandia National Laboratories

Mass spectrometry is routinely used to quantify gases in analytical measurements and process diagnostics. In many of these applications, gases enter the ion source of the mass spectrometer through a molecular leak.

Sections of the gas manifold on the high pressure side of the leak may contain extreme temperature gradients such as a gas source operating at a very high temperature or a cryogenic trap at low temperature with the remaining manifold components near room temperature. Calibration of the mass spectrometer response to the molar quantity of gas present in the manifold must take into account the thermal gradient over pressures that can span the range from viscous flow to the molecular flow regime where thermal transpiration dominates. This paper will present a method for calibrating the molar quantity of gas present in a manifold with a large but constant temperature gradient using a pressure gauge and molar calibration source (MCS) attached to a room temperature section of the manifold. The MCS is a calibrated gas volume and integrated pressure gauge maintained at constant temperature. Molar quantities of gas released from the MCS into the manifold are related to the response of the pressure gauge using empirical n/P functions. These functions accurately relate the manifold pressure to the molar quantity of gas in the manifold as long as the temperature distribution across the manifold remains stable. An example will be presented showing the application and stability of n/P functions used in thermal desorption measurements of hydrogen isotope concentrations in thin metal films. The construction and critical performance characteristics of the MCS will also be described.

Sandia National Laboratories is a multi-program laboratory operated by Sandia Corporation, a wholly owned subsidiary of Lockheed Martin company, for the U.S. Department of Energy's National Nuclear Security Administration under contract DE-AC04-94AL85000.

3:00pm VT+MS-MoA4 Hydrocarbon Measurements at ppb Level at 10Pa Absolute Pressure, R. Versluis, M.F. Dekker, TNO Science and Industry, Netherlands

In Extreme UltraViolet lithography (EUVL), 13.5 nm light is used for imaging the reticle pattern onto the wafer. Since EUV light is absorbed by all materials (including gases) a reflective optical system is used in EUV wafer steppers. Wafer resist outgassing during exposure is one of the most important contributors to mirror contamination. Just one or a few monolayers of Carbon on the multi-layer reflective optics of the system leads to an unacceptable reflectivity loss. Considering the fact that a large fraction of the EUV induced wafer resist outgassing constitutes of hydrocarbons, suppression and mitigation of these molecules is absolutely necessary.

Different methods exist to suppress hydrocarbons and other contamination from wafer, or 'dirty' components. In order to qualify such methods, very sensitive hydrocarbon measurements need to be done at relatively high pressures.

We built a test rig capable to detect hydrocarbons at ppb level. The hydrocarbon levels that need to be measured are at the order of $1E-9$ Pa, while the absolute pressure is at the order of 10 Pa. The test rig therefore needs to be extremely clean during the measurements. The test rig includes six large Turbo Molecular Pumps to keep the test rig at an absolute pressure of 10 Pa, while the component under test is continuously being flushed. The electro-polished setup (about 4 meters long and one meter high) can be completely baked at 150°C to reach the extreme clean conditions needed to measure the low concentrations of hydrocarbons. Measurements are done with a very sensitive residual gas analyser (RGA) which can be baked to 200°C. The RGA has been optimized in such a way that the sensitivity for heavy gases is increased with respect to the sensitivity for lighter gases (patent appointed). Test gases (hydrocarbons, Ar, N₂) can be injected at different locations in the test rig. This way a contamination source in the wafer stage as well as wafer resist outgassing can be simulated.

With the test rig we can also do a thermal qualification of the component under test, to determine heat loads to the test component and heat load distributions.

The presentation will focus on design and engineering aspects of the test rig, the qualification of the test rig and the qualification of the component under test.

3:40pm VT+MS-MoA6 Ratiometric and Absolute Partial Pressure Measurements with Low Mass Range Mass Spectrometers, G. Brucker, J. Rathbone, K. Van Antwerp, M.N. Schott, Brooks Automation, Inc.

Low mass range mass spectrometers are routinely used to obtain partial pressure information in high vacuum and ultrahigh vacuum systems. Absolute and ratiometric partial pressure measurements are both applied to monitor and control vacuum processes and experiments. Mass spectrometers provide indirect partial pressure measurements, and require advanced data interpretation and analysis procedures in order to generate accurate partial pressure measurements from their raw spectral output. This presentation describes some of the modern methodologies used by commercial equipment manufacturers to derive accurate absolute and ratiometric partial pressure information using both quadrupole mass spectrometers and a new generation of electrostatic ion trap mass

spectrometers. The advantages of combining accurate total pressure readings with native ratiometric partial pressure information from electrostatic ion traps is also described and compared to standard partial pressure measurement methodologies. Fast process control, in the millisecond timescale, based on partial and total pressure measurements is also described.

4:00pm VT+MS-MoA7 Accurately Modeling the Natural Frequencies of Ions Ejected from an Anharmonic Resonant Ion Trap, M.N. Schott, Brooks Automation, Inc.

A mathematical model is demonstrated that accurately predicts the natural frequencies of ions ejected from an Anharmonic Resonant Ion Trap (ion trap). The model is based upon a force balance equation of motion, which is comprised of a forcing function, a mass, a damper and a spring. The forcing function is a low amplitude RF signal, swept from high frequencies to low frequencies over a given period, which locks-up, bunches and then ejects ions with a common mass-charge ratio using the principal of autoresonance. The ionized gas particles provide the mass portion of the equation, where specific autoresonant mass selection is dependent upon the selected ion's mass-charge ratio. The equation damping, or ion trap losses, are primarily dependent upon ion trap pressure. The spring in this model is provided by the trap's static anharmonic voltage gradient, which is a function of ion trap geometry and the associated relative-voltage-potentials distributed across the ion trap's geometric structures. The ejected ions natural frequencies are then proportional to the square root of the anharmonic voltage gradient, the pressure dependent damping and the autoresonant selected mass-charge ratio. Experimental results are presented that vary the independent anharmonic voltage gradient, pressure, and ionized gases versus dependent ejected ion natural frequencies on the ion trap compared with the model's predicted natural frequencies.

4:20pm VT+MS-MoA8 Solving the Low Mass Range Mass Spectrometer Limitations (Zero Blast) using Electrostatic Ion Traps, P.C. Arnold, G. Brucker, J. Rathbone, Brooks Automation, Inc.

The phenomena of typically unavailable resolution of low mass spectroscopic peaks (zero blast) will be presented along with a solution that allows clear resolution of those low mass peaks, for example, masses 1 to 4. A new mass spectrometer design composed of an electrostatic ion trap using anharmonic resonant trapping potentials will be shown to resolve this issue. The primary causes of poor low mass resolution will be presented. The background of the physical electronics of the problem will be discussed. The new mass spectrometer design will be described with respect to its effect on zero blast. A test program to demonstrate the solution and show results at scans of low mass will be presented.

4:40pm VT+MS-MoA9 Ion Residence Times for Electron-Impact Ion Sources of Mass Spectrometers, R.E. Ellefson, REVac Consulting, M.F. Vollero, INFICON, Inc.

Electron impact ionization is a common method of ion production for mass spectrometers. The mass spectrum produced is affected by the electron energy and ion residence time in the ionization region. The residence time is the time between the initial direct ionization event and the extraction and focus of the ion(s) from the ionization region into the mass analyzer. During the residence time, additional ionization, fragmentation and ion-molecule reactions can occur. In closed ion sources or other high-pressure ion sources, ion-molecule reactions can be significant; the ions extracted and analyzed can exhibit a bias in inferred gas composition due to the addition or depletion of the species-related ions of interest by the ion-molecule reactions. The presence of a potential well created by the ionizing electron beam and the ion extraction potentials dictate the residence time for ions in the ion source. Models for the depth of the potential well as a function of electron emission current and ion extraction potentials are given and estimated ion residence times are calculated. Evidence for change in residence time with emission current is provided by monitoring mass 80-Ar₂⁺ abundance relative to mass 40-Ar⁺ at a fixed ion source pressure for different emission currents. Other ion-molecule reactions (e.g. N₂⁺⁺ + N₂ gives N₃⁺ + N) and charge-exchange reactions (e.g. He⁺ + Ar yields He + Ar⁺) are presented together with pressure dependence and magnitude of the reactions. Recommendations are given for ion source operation to minimize biases in compositional analysis of gas mixtures.

5:00pm VT+MS-MoA10 Performance Characteristics of a New Wide Range, Fast Settling Electrometer Design for a Residual Gas Analysis Mass Spectrometer, S. Billington, MKS Spectra Products UK, J. Blessing, MKS Instruments, R. Fletcher, P. Shaw, MKS Spectra Products UK

The use of faraday or electron multiplier detectors in mass spectrometry has always presented the electronics engineer with the challenge of having to choose some compromises in a design for the electrometer. The maximum measurable signal usually determines the value for the feedback resistor that

is required. However, with a conventional electrometer where a high impedance input Operational Amplifier is used in an inverting configuration with a feedback resistor, the noise is dominated by the feed-back resistor value. A typical quadrupole mass spectrometer design is capable of generating partial pressure ion currents from a scan of masses which encompasses the full range of the detector output. In order to utilise this full range, more than one feedback resistor is used with switching between gain ranges or a logarithmic amplifier is used. Intrinsicly, the logarithmic amplifier requires significantly longer settling times for lower signal levels which tends to make it impractical for a mass spectrometer where two signals at the extremes of the dynamic range of measurement can be only a few milliseconds apart. Traditionally a gain switching electrometer has been the choice of RGA designers but this has resulted in the compromise of having to either choose which gain range to use for a particular scan of masses or wait for several tens of milliseconds each time the range is switched during the scan.

This work will describe a new electrometer design which allows the use of two gain ranges in a scan of masses with settling times of less than 20ms per measurement point. Data will be presented to show the effectiveness of the design for speed of measurement and the wide dynamic range available. RGA data will also be shown of common applications that traditionally would have required a compromised speed of acquisition or reduced dynamic range. Data will also be shown on the improved accuracy offered for fast transient peak measurements with the faster data acquisition rates of the new RGA design.

Tuesday Morning, October 19, 2010

Actinides and Rare Earths Topical Conference

Room: Isleta - Session AC+MI-TuM

Actinide and Rare Earth Magnetic Interfaces & Nanostructures

Moderator: T. Durakiewicz, Los Alamos National Laboratory

8:20am **AC+MI-TuM2 An Alternative Model for Electron Correlation in Pu**, *S.W. Yu, J.G. Tobin, P. Soderlind*, Lawrence Livermore National Laboratory

Using a density functional theory based approach that treats the 5f electrons relativistically, a Pu electronic structure with zero net magnetic moment is obtained, where the 5f orbital and 5f spin moments cancel each other. By combining the spin and orbital specific densities of states with state, spin and polarization specific transition moments, it is possible to reconstruct the experimentally observed photoemission spectra from Pu. Extrapolating to a spin-resolving Fano configuration, it is shown how this would resolve the extant controversy over Pu electronic structure. See *J. Phys.: Condens. Matter* 20 (2008) 422202 for more detail. Lawrence Livermore National Laboratory is operated by Lawrence Livermore National Security, LLC, for the U.S. Department of Energy, National Nuclear Security Administration under Contract DE-AC52-07NA27344. This work was

supported by the DOE Office of Science, Office of Basic Energy Science, Division of Materials Science and Engineering.

8:40am **AC+MI-TuM3 Correlation Effects in Gadolinium Compounds: Comparison of Theory and Experiment**, *P.A. Dowben*, University of Nebraska - Lincoln **INVITED**

The apparent Gd 4f binding energy in photoemission spectroscopy is strongly affected by both correlation energy contributions, and final state effects in photoemission. The latter are clearly strongly influenced by metallicity and screening [1]. To understand these various contributions to the observed electronic structure of gadolinium compounds, we compare a series of studies on gadolinium compounds and clusters with pure and alloyed gadolinium films [2]. These materials range from the metallofullerenes, in which a metal atom or cluster is encapsulated inside a fullerene, such as in the "buckyball" C₆₀, to more conventional rare earth compounds like GdN, Gd₂O₃, Gd doped HfO₂ and Gd-Ni alloys. The Gd³⁺ ion exhibits bonding and hybridization that is quite different for these various compounds. While the total spin multiplicity of Gd is maximum because of its half-filled 4f state, and the atomic orbitals are strongly hybridized with the C₆₀ molecules in the example of Gd@C₆₀ [3] or oxygen in the case of Gd doped HfO₂ [4], while the highest possible symmetry site for gadolinium is generally not favored. These results are to some extent a confirmation of theoretical expectations but there are complications. There is experimental evidence for intra-atomic hybridization with both the unoccupied and occupied Gd 4f states, as well as band dispersion even for the occupied Gd 4f states in some systems [2] and spin dependent screening [5].

[1] J.E. Ortega, F.J. Himpsel, Dongqi Li and P.A. Dowben, *Solid State Commun.* **91** (1994) 807-811

[2] T. Komesu, H. K. Jeong, David Wooten, Ya. B. Losovyj, J. N. Crain, M. Bissen, F. J. Himpsel, J. Petrosky, Jinke Tang, Wendong Wang, I.N. Yakovkin, and P. A. Dowben, *Physica Status Solidi B* **246** (2009) 975-980

[3] R. F. Sabirianov, W. N. Mei, Jing Lu, Y. Gao, X. C. Zeng, R.D. Bolskar, P. Jeppson, Ning Wu, A.N. Caruso, and P. A. Dowben, *J. Phys. Cond. Matter* **19** (2007) 082201

[4] Ya. B. Losovyj, I. Ketsman, A. Sokolov, K. D. Belashchenko, P.A. Dowben, J. Tang, Z. Wang, *Appl. Phys. Lett.* **91** (2007) 132908

[5] Hae-Kyung Jeong, R. Skomski, D. Wisbey, P.A. Dowben, *Physics Letters A* **341** (2005) 508-515

This work has been undertaken with Y. Losovyj, T. Komesu, Hae-Kyung Jenong, I. Ketsman, N. Wu, A. Sokolov, J. Colon Santana, W. Choe, K. D. Belashchenko, R. F. Sabirianov, W. N. Mei, Jinke Tang, A.N. Caruso, D. Wooten, R. Skomski, F. Himpsel, E. Vescovo

9:20am **AC+MI-TuM5 Electronic Phase Diagram of Rare Earth Mono-Pnictides and Mono-Chalcogenides**, *L. Petit, R. Tyer*, Daresbury Laboratory, UK, *A. Svane*, Aarhus University, Denmark, *Z. Szotek, W.M. Temmerman*, Daresbury Laboratory, UK **INVITED**

The self-interaction corrected local spin density (SIC-LSD) approximation is used to predict the ground state valency configuration of the manifold of rare earth mono-pnictides and mono-chalcogenides. This is a first-principles methodology that adequately describes the dual character of f-electrons, itinerant vs. localized, and the goal is to combine it with high throughput computing, in order to achieve predictive capability in the search for and design of new materials with specific physical properties. For the rare earth mono-pnictides and mono-chalcogenides we predict an electronic phase diagram composed of metallic, semi-conducting and heavy fermion like regions, and exhibiting valency transitions brought about by a complex interplay between ligand chemistry and lanthanide contraction. Our findings, including the ground state lattice parameters, and the "intermediate valent" character of compounds such as SmO and TmSe, are in excellent agreement with the available experimental data.

10:40am **AC+MI-TuM9 Nanotechnology in the Actinides: Uranium Thin Films and Multilayers**, *R.S. Springell*, University College London, UK **INVITED**

From the modern scientific landscape of nanotechnology research, the manipulation of elements and compounds on a near-atomic scale has contributed to innovations, some of which affect our everyday life. The growth of thin films and multilayers has allowed systematic studies of reduced dimensionality and the electronic interplay between dissimilar materials. Important applications have emerged, notably the GMR effect. However, such studies of systems containing actinide elements are, to our knowledge, absent, but offer exciting possibilities because of potential hybridization involving the 5f electronic states.

The samples are prepared by a dedicated sputtering facility at Oxford University, UK2.

Our investigation into uranium multilayers, which involves both bulk as well as element specific techniques, compares the structural properties² and electronic interactions^{3,4,5} of uranium interleaved with layers of ferromagnetic Fe, Co, Ni, and Gd. Only in the case of U/Fe is a large magnetic moment induced on the U atoms, close to the interface⁵.

The study of epitaxial uranium films is initially concerned with the nature of the structural constraints incurred by the substrate and buffer⁶ and the potential for stabilizing structures otherwise absent in the bulk. a-U (which is the normal ambient orthorhombic phase) grows well on a Nb buffer on sapphire. In the bulk it exhibits a charge-density wave (CDW) at 43 K, so in epitaxial films an interesting question is the minimum thickness for the CDW to appear; we have already observed the CDW down to 10 nm. Using epitaxial *hcp*-Gd as a buffer, we have produced *hcp*-U for the first time⁷. The observed *c/a* = 1.90 is larger than for any other hexagonal element. We report also our first efforts to prepare epitaxial UO₂ films.

11:20am **AC+MI-TuM11 Growth and Characterization of Dy/Y Superlattices**, *J. Yu, H. Sato, P.R. LeClair, G.J. Mankey*, University of Alabama, *J.L. Robertson, R.S. Fishman*, Oak Ridge National Laboratory

Inelastic neutron scattering is the world's most powerful tool to study the magnetic excitations of solids. We aim to study spin wave dispersion relations in multilayer structures and how they are affected by the indirect RKKY exchange interaction through nonmagnetic spacers. Dy was chosen as the magnetic film since it has a huge magnetic moment of 10.2 Bohr magnetons and the neutron scattering cross section is directly proportional to the atomic moment. For elastic scattering, a film with thickness of order 100 nm is sufficient, but inelastic neutron scattering has a considerably lower cross-section requiring much more material for measurement. To enable such a study, many samples with tightly-controlled thickness and crystallinity must be fabricated. The neutron experiments can then be performed by stacking 8-10 samples, each with 50-100 superlattice repeats. The number of repeats for each sample is limited by the accumulation of defect structures over the growth front. Using a home-built sputtering system, we have achieved the ability to make suitable samples. The system has computer-controlled magnetron sputtering guns and a sample transfer system which enables continuous sample rotation of a 2" diameter wafer at 900°C during sputtering in an ultra-pure environment. Maintaining a good vacuum is essential since both Y and Dy are highly reactive and form stable

oxides with only a minute amount of oxygen in the sputtering environment. In addition, the dispersion relations of the spin wave modes are highly sensitive to thickness variations, so it is essential to create samples with uniform and repeatable layer thicknesses. We report the growth and characterization of epitaxial Dy/Y multilayer samples and our optimization of the growth temperature to produce samples with well-defined superlattice Bragg peaks in high-angle x-ray diffraction.

Funded by US-DOE through DE-FG02-08ER46499 and research at Oak Ridge National Laboratory's High Flux Isotope Reactor was sponsored by the Scientific User Facilities Division, Office of Basic Energy Sciences, U.S. Department of Energy.

11:40am **AC+MI-TuM12 Study of f Electron Correlations in Uranium- and Cerium-Oxides by BIS and XES**, *S.W. Yu, B.W. Chung*, Lawrence Livermore National Lab, *D.G. Waddill*, Missouri University of Science and Technology, *J.G. Tobin*, Lawrence Livermore National Lab

When a high energy electron beam impinges on a material, some electrons of the incident electron beam are decelerated into the unoccupied states of the material with a spontaneous emission of electromagnetic radiation (bremsstrahlung). This bremsstrahlung process can be considered as the inverse of the photoemission process if the initial and final states are exchanged and the occupied state is replaced by the unoccupied one. BIS (Bremsstrahlung Isochromat Spectroscopy) is a very powerful tool to study the bulk unoccupied electronic structures of materials, minimizing the impact of surface effects.

Recently, we have developed a BIS capability, using an XES-350 system from VG SCIENTA, at the Lawrence Livermore National Laboratory, to investigate the electronic structure of actinides, in which 5f electrons play important roles to determine their physical and chemical properties. Similar to the resonant photoemission, the measured BIS signal can be resonantly enhanced when the electron energy reaches the threshold of the binding energy of a core electron, as a result of the interference between the BIS signal and the x-ray emission signal emitted by a radiative decay of the core hole. In case of cerium-oxide, the BIS signal is enhanced significantly at the 3d → 4f resonance. However, in the case of uranium-oxide, the BIS signal is enhanced only slightly at the 4d → 5f resonance.

The x-ray emission can be described as a spontaneous emission of photons in a transition that are allowed by the dipole selection rules between two electronic states. The implication of the dipole selection rules is that, for example, in the case of K-emission, where 1s holes are created, only states with p-character are allowed to decay and the partial p-type density of state is measured in a x-ray emission spectrum. Therefore, the x-ray emission spectra from a variety of core levels allow us to study the symmetries of the occupied electronic states.

We will present the resonant BIS spectra and x-ray emission spectra (U 4f, 4d, O1s, Ce 3d) of the uranium- and cerium-oxides. Based on these data, we will discuss the detailed electronic structures of f electrons in uranium- and cerium-oxides.

Lawrence Livermore National Laboratory is operated by Lawrence Livermore National Security, LLC, for the U.S. Department of Energy, National Nuclear Security Administration under contract DE-AC52-07NA27344. This work was supported by the DOE Office of Science, Office of Basic Energy Science, Division of Materials Science and Engineering.

Applied Surface Science

Room: Cochiti - Session AS-TuM

Electron Spectroscopies

Moderator: S.R. Bryan, Physical Electronics

8:00am **AS-TuM1 Recent Developments in Quantitative XPS and AES**, *C.J. Powell*, National Institute of Standards and Technology **INVITED**

An overview will be given of some recent developments to improve quantitative XPS and AES [1]. First, guidance is now available for choosing integration limits in the measurement of XPS peak intensities [2]. A recent comparison of reported peak intensities in simulated XPS spectra with known intensities showed large deviations if the integration limits were chosen inappropriately. Second, Tanuma et al. have reported a new set of inelastic mean free paths (IMFPs) for 41 elemental solids that were calculated from experimental optical data for electron energies from 50 eV to 30 keV [3]. These IMFPs agree well with recent calculations and measurements. Third, examples will be given of the use of simple predictive formulae that are available for the effective attenuation length, mean escape depth, and information depth in AES and XPS [4]. Fourth, the effects of

elastic scattering and analyzer-acceptance angle on the analysis of angle-resolved XPS data have recently been analyzed [5]. Calculations were made of photoelectron intensities at selected emission angles for films of SiO_{1.6}N_{0.4} and HfO_{1.9}N_{0.1} of various thicknesses on Si with the NIST SESSA Database [6]. Ratios of intensities for each line from the film for the least realistic model condition (elastic scattering "off", small analyzer-acceptance angle) to those from the most realistic model condition (elastic scattering "on", finite analyzer-acceptance angle) changed relatively slowly with emission angle but the corresponding intensity ratios for the Si(substrate) 2p line changed appreciably with emission angle; such changes can lead to erroneous results in the analysis of angle-resolved XPS data [5]. Fifth, examples will be given of a new NIST database to provide backscattering correction factors for AES using an advanced model that accounts for attenuation of the primary beam in the surface region of the sample and the instrumental configuration [7]. Finally, mention will be made of a set of reference energies for 59 Auger transitions in 42 elemental solids that should be useful for the determination of chemical shifts in AES and XPS [8].

[1] C. J. Powell and A. Jablonski, *J. Electron Spectrosc. Relat. Phenom.* 178-179, 331 (2010).

[2] C. J. Powell and J. M. Conny, *Surf. Interface Anal.* 41, 804 (2009).

[3] S. Tanuma, C. J. Powell, and D. R. Penn, *Surf. Interface Anal.* (to be published).

[4] A. Jablonski and C. J. Powell, *J. Vac. Sci. Technol. A* 27, 253 (2009).

[5] C. J. Powell, W. S. M. Werner, and W. Smekal (to be published).

[6] <http://www.nist.gov/srd/nist100.htm>.

[7] A. Jablonski and C. J. Powell (to be published).

[8] C. J. Powell, *J. Electron Spectrosc. Relat. Phenom.* (to be published).

8:40am **AS-TuM3 Effect of Monochromator X-ray Bragg Reflection on Photoelectric Cross Section**, *A. Herrera-Gomez*, CINVESTAV, Mexico

The photoelectric differential cross section plays a fundamental role for assessing the relative concentration of the various elements present within the XPS probing depth. Accounting for the different issues affecting the cross section is paramount not only for quantitative chemical studies (including angle-resolved XPS) but also for a proper comparison between the results obtained in different XPS tools, or in the same tool but with different X-ray sources. In XPS experiments employing monochromatized light, the X-ray Bragg reflection undergone by the beam at the monochromator crystal causes a partial polarization of the X-rays. The photoelectric cross section is affected since it depends on the angle between the electric field vector and the direction of the escaping electrons. **An expression for the photoelectric differential cross section is presented that accounts for the effect of the monochromator and of the geometrical configuration of the XPS tool.** The correction is as large as 9% for s-orbitals and reduces to up to 5% for orbitals with the asymmetry factor $\beta \sim 1$. The differences are directly related to the β factor within the dipole approximation, which is the first order treatment of photoemission; i.e., they are not due to higher order quadruple terms.

9:00am **AS-TuM4 Photovoltage, Photoconductivity and Charging Probed by Dynamical XPS Measurements**, *S. Suzer*, Bilkent University, Turkey

We have developed a technique for recording the shifts in the positions of the XPS peaks in response to different forms of electrical stimuli for probing dynamics of charging/discharging processes of thin dielectric films, which we have named as Dynamic XPS. Modulation of the electrical signals in the forms of square, sinusoidal and triangular waves at different frequencies enables us to extract some dielectric properties of surface structures, such as effective resistance, and capacitance values in a chemically resolved fashion. We have also introduced photo-illumination as an additional form of the stimuli and have been using this technique for investigating the combined optical + electrical responses of semiconductive (Si and GaAs) as well as photoactive (CdS and TiO₂) materials towards better understanding of the different photo-processes, like photoconductivity and/or photovoltage development, etc. We use our dynamic measurements to help in distinguishing various fundamental processes, by using the frequency dependence as an additional tool. This makes XPS a more powerful technique for characterizing today's demanded nano or optoelectronic devices. The methodology will be introduced, and several examples will be presented.

9:20am **AS-TuM5 Order-Disorder Transition for Corrugated Au Layers**, *K. Fukutani*, University of Nebraska-Lincoln, *N. Lozova*, Louisiana State University, *S.M. Zuber*, University of Wroclaw, Poland, *N. Wu*, *P.A. Dowben*, University of Nebraska - Lincoln, *P. Galiy*, Ivan Franko National University of Lviv, Ukraine, *Y.B. Losovyj*, Louisiana State University

Atomic-scale structure of the growth of a gold film on Mo (112) was investigated by means of low energy electron diffraction (LEED) and scanning tunneling microscopy (STM) up to several monolayers (ML) of gold coverage. Both LEED and STM results establish that Au grows on Mo(112) in a layer-by-layer mode, for at least the first two monolayers. A number of ordered structures are formed and both the first and second layers adopt the Mo(112) 1x1 surface structure upon completion. For some gold layers on Mo(112), notably the 1.66 monolayer 3x1 and 1.75 monolayer 4x1 gold overlayers, we find evidence of a phase transition associated with increasing disorder in gold layers with structural corrugation and anisotropic band structure. The signature of this phase transition, at temperatures in the range of 400–500 K, is a sharp decrease in the overlayer effective Debye temperature. Angle-resolved photoemission spectroscopy (ARPES) suggests coverage dependent changes in the electron-phonon coupling for gold adlayer.

9:40am **AS-TuM6 Surface Characterization of Gold Nanoparticles and Their Interaction with Protein G B1 Domain**, *S. Techane*, *L. Baugh*, *L.J. Gamble*, *P.S. Stayton*, University of Washington, *D.R. Baer*, Pacific Northwest National Laboratory, *D.G. Castner*, University of Washington

The purpose of this research is to study the interactions of biomolecules with nanoparticles using model systems. Model proteins and nanoparticle surfaces are used to simplify the complex biological/nanoparticle surface environment and develop a fundamental understanding of the interactions at this interface. Protein G B1 domain was used as a model protein. Wild type Protein G B1 (WT) has a uniform distribution of negatively charged residues on its surface. Using site-directed mutagenesis to neutralize six charged residues at one end of the protein, a mutant ($\Delta 6$) was created possessing a global charge dipole along its long axis. This variation in surface charge affected the biomolecular interaction with nanoparticle surfaces. Gold nanoparticles (AuNPs) with self-assembled monolayers of carboxylic alkanethiols (COOH-SAM) were used as the well-defined model surface.

We previously reported that AuNPs 14nm in diameter and functionalized with C16 COOH-SAM were more monodisperse in size and shape relative to those with larger diameter, and more stable in solution relative to those functionalized with shorter-chain COOH-SAMs. To accurately interpret XPS data and account for the curvature effect, and to quantitatively analyze overlayer thickness (T) and roughness (R), we used SESSA combined with geometric correction methods. The C16 COOH-SAM on flat Au was modeled with SESSA at photoelectron take-off angles from 5 to 85°. Corresponding ARXPS experiments were also performed. T and R were optimized to find the best agreement between the simulated and experimental results. It was necessary to add a hydrocarbon contamination layer (CL) at the surface of the COOH-SAMs in the simulations. For the C16 COOH-SAM on flat Au, the best conditions were $T=1.1\text{\AA}/\text{CH}_2$, $R=1.05$ and $CL=1.5\text{\AA}$. After applying a geometric correction, $T=0.9\text{\AA}/\text{CH}_2$ and $R=1.05$ was obtained for the SAM on AuNPs with similar CL. Studies to minimize CL are underway.

WT and $\Delta 6$ B1-protein G were adsorbed onto 14nm-AuNP-C16 COOH-SAM at various protein concentrations. Following adsorption and centrifugation, the final supernatant containing unbound protein and AuNPs with bound protein were analyzed by colorimetric assay and XPS, respectively. Both methods showed that $\Delta 6$ adsorbed more than WT. As $\Delta 6$ concentration increased, the N signal (unique to the protein) increased and the Au signal (unique to the surface) decreased, following similar trends as observed in the adsorption isotherm curve. Based on our preliminary study, a %N of 13.6 ± 0.3 corresponded to a monolayer of $\sim 0.95\mu\text{g}/\text{cm}^2$. Further studies to accurately determine thermodynamic adsorption parameters and the AuNP concentration are underway.

11:00am **AS-TuM10 Charging Compensation Method in XPS with Positive Voltage and Low Energy Electron Beam**, *M. Shima*, *K. Tsutsumi*, *T. Tazawa*, JEOL Ltd., Japan

X-ray photoelectron spectroscopy (XPS) is widely used for qualitative, quantitative and chemical state analysis on various material surfaces, because XPS can obtain more stable spectra even in charged insulator surfaces than Auger electron spectroscopy. However in many cases, XPS spectra would be even distorted and shifted to high binding energy side by the positive surface charging caused by photoelectron emission. And we identify the chemical state of materials from peak position and peak shape. As a result, such a charging effect reduces the usefulness of XPS. The most widely used method for suppression of surface positive charging is to

irradiate low energy electron to the sample surface. But operator should select electron flood gun conditions carefully such as accelerating voltage and the amount of the electron flux, because once the electron flux and accelerating voltage is set too high, peak shape will be distorted again and peak position turn to the lower binding energy side.

At this time, we propose a new charge compensation method that electrons irradiated from flood gun will be maintained efficiently on an insulator surface by applying positive voltage underside of insulator sample. The mechanism of this method is to accumulate excess electrons on the top of an insulator like a capacitor. Electrons maintained on insulator sample surface remove the differential positive charging, even when X-ray irradiation makes another differential charging. In addition, our experiment results shows that surface potential of insulator sample is determined simply by accelerating voltage of flood gun and it is independent of applied positive voltage for sample under the conditions that adequate electrons are supplied from flood gun. It is found that this charge compensation method has ideal mechanism; we can control not only peak shape in ideal shape but also its peak position.

In the presentation we will show some XPS experimental results with this method and discuss them.

11:20am **AS-TuM11 Applications of Hard X-ray Photoelectron Spectroscopy for Characterization of a Hybrid Ti-Si Sol-Gel**, *J.L. Fenton*, *G. Mitchell*, *Y. Srivastava*, *Y.Q. Rao*, *B. Weaver*, *R. Auger*, The Dow Chemical Company

Hard x-ray photoelectron spectroscopy (HAXPS), in particular variable kinetic energy photoelectron spectroscopy (VKE-XPS), is becoming increasingly useful to determine chemical and elemental information from the "bulk" of materials compared to traditional XPS. In addition, VKE-XPS allows for non-destructive depth profiling of materials that pose a greater challenge for Angle-Resolved XPS (ARXPS) such as materials with rough surfaces. This talk will present the application of VKE-XPS to hybrid Ti-Si based sol-gels to understand potential chemical or elemental changes as a function of excitation kinetic energy.

11:40am **AS-TuM12 Inline Production Monitoring of Carbon Doped Polysilicon Using X-Ray Photoelectron Spectroscopy**, *B. Dickson*, ReVera Incorporated, *H. Lee*, *W. Namkoong*, Samsung Electronics Co., *M. Kwan*, *H. Pois*, *T.C. Larson*, ReVera Incorporated

X-ray photoelectron spectroscopy [XPS] is a well respected compositional and thickness metrology technique. Historically, XPS has been used as an off-line characterization method limited to laboratories. The introduction of fully automated, small spot XPS systems in the fab now enables in-line metrology with results in minutes instead of days. This paper details the production control monitoring of carbon composition in carbon doped polysilicon films which are used in flash devices. Measuring carbon doped polysilicon for inline production has two main challenges: sensitivity and stability. Sensitivity to different carbon dosage processes as well as the process variation of day to day production has been demonstrated. In addition to compositional sensitivity, high resolution XPS can measure the different chemical bonding states of C. Because the carbon doped polysilicon surface is very unstable, with surface carbon accumulating on the wafers' surface over time in the form of amorphous carbon and an atomic molecular contamination [AMC] layer, the main carbon dopant bonding state signal is separated from non-doped carbon bonding state signals. For stability, the ReVera Veraflex has developed an application to separate the naturally increasing AMC carbon from the stable doped carbon atomic composition, enabling a robust statistical process control [SPC] method.

Biomaterial Interfaces

Room: Taos - Session BI-TuM

Cells on Surfaces

Moderator: M.R. Alexander, University of Nottingham, UK

8:00am **BI-TuM1 Co-Culturing of Osteocytes and Neurons on a Unique Micropatterned Surface: Bone Pain in Cancer**, *M.E. Boggs*, *W. Thompson*, University of Delaware, *M.C. Farach-Carson*, Rice University, *R.L. Duncan*, *T.P. Beebe*, University of Delaware

Bone pain is a debilitating problem for patients with bone cancer. Bone pain is the result of communication between the neural and skeletal systems of the body, and yet the mechanisms of communication or signal transduction between cells and tissues comprising these bodily systems is poorly understood. We have developed and are now using a unique micropatterned

substrate as a platform consisting of two different proteins to investigate the mechanisms of cell-cell communication between co-cultured osteocyte-like cells and neurons. We have found that an optimal matrix for neurons is laminin type-1, while an optimal matrix for osteocytes is the perlecan domain-IV peptide. The use of micropatterned lanes 40-micron-wide by 1-cm long consisting of alternating laminin type-1 and perlecan domain-IV peptide creates a unique environment in which several osteocyte-neuron meeting events can be observed and probed under controlled conditions. This presentation will build upon our prior work with neuronal cell culture substrates, starting from how they are made, characterized, and then used in experiments to study cell-cell interactions for different cell types.

8:20am BI-TuM2 Patterned Growth of Human Neural Stem Cells on Surfaces Prepared by Microcontact Printing. *A. Ruiz*, University Milan, Italy, *L.M. Buzanska, M. Zychowicz*, Polish Academy of Sciences, Poland, *P. Colpo, F. Rossi*, Joint Research Centre, Italy

This work relates to a method of patterning human neural stem cells as a suitable platform for performing different studies of cell proliferation, migration, and differentiation. The patterning of cells has been achieved by using microcontact printing (MCP) to create micropatterns of Poly-L-Lysine (PLL) and Fibronectin (FN), on substrates coated with cell repellent poly ethylene glycol (PEG) deposited by plasma. This substrate is particularly interesting since it is anti adhesive in liquid, but protein adhesive in the dry state. More details of the preparation method are described in [1]. Briefly, microstructured polydimethylsiloxane stamps have been fabricated by casting silicon masters produced by photolithography. The PDMS stamps have been inked with a FN or PLL solution, then dried with a nitrogen stream and put in conformal contact with the PEG substrate. By this method we are able to create fouling (PLL, FN) / antifouling (PEG) contrast on the surfaces where the cells are incubated and by modification of the spot size and distance, the influence of the cell environment on stem cells maintenance and fate studied.

Human Umbilical Cord Blood - Neural Stem Cells [2] were grown on the platforms with PLL or fibronectin pattern. After incubation for 4 days on PLL patterns consisting of 105µm squares spaced 300 µm, the cells are predominantly localized within the square. Such behavior is conditioned by agents added to the incubating medium. After being exposed to dBcAMP, the cells extend neuronal projections outside the squares, but cell bodies are patterned within the active domain. Immunocytochemistry was applied to trace neuronal lineage specific markers and their redistribution on the pattern domain upon influence of differentiating agents. It is found that the maintenance and fate of stem cells can be controlled by a combination of the protein type layer deposited by MCP and culture medium composition: presence of serum, neuromorphogenes and growth factors. Proper arrangement of soluble factors and bioactive surface domains allowed to work out conditions for developmental stage-specific immobilization of neural stem cells to the surface.

1. A. Ruiz, L. Buzanska, D. Gilliland, T. Sobanski, L. Ceriotti, S. Coecke, P. Colpo, F. Rossi. *Micro-stamped surfaces for the patterned growth of neural stem cells*. *Biomaterials* 29 (2008) 4766-4774.

2. Buzanska, L., Jurga, M., Stachowiak, E.K., Stachowiak, M.K., Domanska-Janik, K. *Stem cells Dev.*, 15, 391-406, 2006.

9:00am BI-TuM4 Biomolecule Microarrays in Neural Stem Cell Assay Development. *D. Mehn, J. Nowak*, Joint Research Centre, Italy, *L.M. Buzanska*, Polish Academy of Sciences, Poland, *A. Ruiz, H. Rauscher, G.R. Marchesini, P. Colpo, F. Rossi*, Joint Research Centre, Italy

Human umbilical cord blood originated neural stem cells (HUCB-NSC) are promising candidates for developing human cell based *in vitro* neurotoxicity assays. The origin of the cells makes possible to avoid species specificity extrapolation problems and avoid ethical issues compared to the embryonic stem cell research. Besides the easy cell line like culturing procedure of these cells they were shown to be able to differentiate to neuronal, astrocytic and oligodendroglial phenotypes. This feature makes them also excellent subjects for developmental neurotoxicity studies.

The extracellular matrix compounds (ECM) used for anchoring the cells on culture dish or device surfaces may induce various ECM-dependent stem cell developmental responses mediated by integrin receptors. Investigation of stem cell - extracellular matrix interactions on biomolecule microarrays provides fundamental knowledge on neural differentiation as well as key inputs for stem cell based assay development.

The most powerful tools for microarray fabrication are microspotting and microcontact printing, offering flexibility regarding composition, concentration, spotted volumes or printed pattern geometry. Both methods are proven to be gentle enough to handle biomolecules for cell interaction studies.

In this work, the piezoelectric spotting and microcontact printing technologies were tested for rapid fabrication of biomolecule arrays on cell repellent surfaces.

Cell anchoring molecules, like extracellular matrix proteins (fibronectin and vitronectin) and poly-L-lysine (a polycationic polypeptide) were printed on anti-adhesive poly(ethylene) oxide-like films deposited by plasma-enhanced chemical vapor deposition. The microspotted and printed patterns were characterized by ellipsometry and microscopic techniques. The morphology of seeded stem cells and expression of certain differentiation marker proteins (GFAP, beta-tubulin III) were visualized by immunostaining and fluorescent microscopy, including also characterization after treatment with various concentrations of a known neurotoxic compound (MeHgCl). Toxicity results obtained on adhesive molecule spots were compared with results of a conventional neutral red uptake assay performed in coated 96 well plates.

Effect of the nature of biomolecules on cell behavior (including cell adhesion, morphology and survival) were investigated and are discussed focusing on generation long term cell-pattern stability, as well as stem cell differentiation into particular cell types.

9:20am BI-TuM5 Imaging Conformational States of Fibronectin on Patterned Poly(dimethylsiloxane) Surfaces. *J. Dechene, A. Leclair, P.R. Norton*, University of Western Ontario, Canada

The ability to both understand and direct cellular adhesion is vital in a variety of fields including bioanalysis, medical diagnostics and implant materials design. When a cell approaches a material, its ability to adhere and proliferate will depend greatly on the surface properties of the underlying material. One such material, poly(dimethylsiloxane) (PDMS), has many ideal bulk characteristics but its surface is hydrophobic and does not inherently promote cell growth. To remedy this, many surface treatments of PDMS, particularly plasma treatments, have been used to increase the adhesion strength and bioactivity of PDMS towards cells.

We have recently reported a novel method of patterning the bioactivity of PDMS [1]. We have further exploited the patterning by spatially-selective modification with various biologically active functionalities that permit cell patterning. A different, photolithographic technique has also been developed that exploits the hydrophobic recovery of PDM S, and while we were successful at patterning hydrophobic and hydrophilic areas using this method, cell growth was unfortunately not limited to only the hydrophilic regions on the photolithographically produced patterns.

To understand why the photolithographic method was unsuccessful, we looked both at the ability of a cell to proliferate on the different surfaces, as well as the adsorption of serum proteins, the presence and conformation of which directly affect the adherence of a cell to the surface. To better understand the cell selectivity or lack thereof, fibronectin was adsorbed on the patterned surfaces. A monoclonal antibody HFN7.1 was used to identify exposed integrin binding sites. The antibody was immunofluorescently labeled using a secondary FITC conjugated antibody. The difference in relative availability of binding sites was visualized using confocal microscopy and compared to the relative adsorption of fibronectin, and cell proliferation on the patterned surfaces. The availability of binding sites was shown to correlate with cell attachment on the stencil-masked patterned surfaces. However an increased availability of binding sites was seen on the hydrophobic recovered regions of the photolithographic patterned surfaces. We plan to directly measure the adhesion forces of chosen cells on the areas of "good" and "bad" conformation.

[1] N. Patrio, C. McCague, P. R. Norton, N. O. Petersen, *Langmuir* 2007; 23, 2, 715 - 719

9:40am BI-TuM6 Measuring Contractile Cell Forces on Rigid Substrates. *B. Müller*, University of Basel, Switzerland, *J. Köser*, University of Applied Sciences, Switzerland

Mechanical properties of substrates have been shown to be crucial factors for cell behavior, which includes the differentiation of stem cells or the malignant transformation into cancerogeneous cells (Engler et al. (2006) *Cell* 126, 677 and Cross et al. (2007) *Nature Nanotechnol* 2, 780). There have been published several techniques to measure contractile forces of cells, exerted onto the underlying substrate, since 1980. These approaches, however, only rely on compliant substrates and not on rigid ones as well known from load-bearing implants and culture dishes.

We present an approach to quantify the contractile forces of an ensemble of cells growing on rigid substrates based on nanomechanical cantilever sensors. In particular, we measured the relaxation of micro-cantilevers as the result of trypsin-release of about 100 fibroblasts. The optically measured change in cantilever bending, detected by means of the Cantisens Research system (Concentris GmbH, Basel), together with the number of fibroblasts counted was converted to the contractile cell force using the STONEY formula.

For the measurement of the contractile cell forces the selected cells were cultured on silicon cantilever arrays. The arrays consist of 8 micro-cantilevers each 500 μm long, 100 μm wide and 1 μm thin that enables us to detect stresses as small as 0.01 mN/m. Following adhesion and contractile force generation over night, the cantilever arrays were introduced into the Cantisens Research system to monitor the cantilever relaxations upon trypsin-mediated release of the cells from the substrate.

When rat2 fibroblasts are seeded on the silicon cantilevers they adhere and develop the morphology indistinguishable from that on standard culture dishes. Upon trypsin-induced release of the cells from the silicon substrate bending, the free end of the cantilever changes its position according to the following function $D = 0.5D_0 (1 - \tanh(t/\tau))$, where D_0 corresponds to the deflection amplitude and τ the time constant of the cell release. While τ is apparatus and process specific, D_0 directly relates to the contractile forces of an ensemble of cells. The contractile force of an individual rat2 fibroblast on silicon corresponds to $(17 \pm 7) \mu\text{N}$. This value is reasonable, but high compared to the contractile forces of fibroblasts exerted on compliant substrates, a behavior expected from the studies on differently stiff compliant substrates. The contractile cell forces are strongly dependent on the state of the cell that explains the rather large error bar.

The method will support the fundamental understanding of cell-materials interactions with implications for cell-based biosensing and implant design.

10:40am **BI-TuM9 Biological Cell Detachment from Poly(*N*-Isopropyl Acrylamide) and its Applications**, *H.E. Canavan*, University of New Mexico **INVITED**

Over the past two decades, poly(*N*-isopropyl acrylamide) (pNIPAM) has become widely used for bioengineering applications. In particular, pNIPAM substrates have been used for the non-destructive release of biological cells and proteins. In this work, we review the applications for which pNIPAM substrates have been used to release biological cells, including for the study of the extracellular matrix (ECM), for cell sheet engineering and tissue transplantation, the formation of tumor-like spheroids, the study of bioadhesion and bioadsorption, and the manipulation or deformation of individual cells. The work reviewed includes that of our own group, as well as from those performing research in the field world-wide.

11:20am **BI-TuM11 Rare Earth Nanoparticles - Biocompatibility Studies: Interaction with Human Neutrophil Granulocytes**, *N. Abrikosova, C. Skoglund, M. Ahren, L. Selegård*, Linköping University, Sweden, *T. Bengtsson*, Örebro University, Sweden, *K. Uvdal*, Linköping University, Sweden

Rare-earth metal nanoparticles are among the most promising candidates to be used as probes for visualization and targeted drug delivery. Compared to the ion-based gadolinium containing complexes used clinically as contrast agents today, gadolinium oxide (Gd_2O_3) nanoparticles show a considerably improved relaxivity and thus enable an increased resolution and an increased contrast enhancement. However, surface modification of these nanoparticles is essential in order to improve the biocompatibility and diminish any potential toxic effects. In the present study we have evaluated the impact of Gd_2O_3 nanoparticles (as synthesized, dialyzed, and functionalized with polyethyleneglycol, PEG) on the production of reactive oxygen species (ROS) from human neutrophils.

Gd_2O_3 nanoparticles were synthesized (via the polyol route), functionalized with PEG and characterized as previously described in Ahren *et al.*¹. Neutrophil granulocytes were isolated from heparinized whole blood using density gradient centrifugation. Generation of ROS by neutrophils upon addition of IgG-opsonized yeast, in presence and/or absence of as synthesized, dialyzed and functionalized Gd_2O_3 nanoparticles was studied with luminol-dependent chemiluminescence. In addition, the morphology of neutrophils after interaction with Gd_2O_3 nanoparticles was evaluated by fluorescence microscopy.

The ROS production from neutrophils challenged with IgG-opsonized yeast after exposure to as synthesized Gd_2O_3 nanoparticles was significantly decreased compared to control without nanoparticles. This indicates that the as synthesized nanoparticles are not well suited to be directly used in a living system without further modification. However, after dialysis and functionalization with PEG, no inhibitory effects were observed, possibly indicating that the high concentration of diethylene glycol (DEG) present in the as synthesized nanoparticle preparation is responsible for the inhibitory effects. Indeed, we in the present study also show that even a low concentration of DEG (0.3%) inhibits neutrophil ROS production. Our results indicate that dialyzed and PEG-functionalized Gd_2O_3 particles may be suitable in an in vivo situation as they do not impair the neutrophils capacity to produce ROS in response to a pray.

¹ Ahren M, Selegård L, Klasson A, Söderlund F, Abrikosova N, Skoglund C, Bengtsson T, Engström M, Käll P.O, and Uvdal K, *Synthesis and characterization of PEGylated Gd₂O₃ nanoparticles for MRI contrast enhancement*. Langmuir 2010, 26 (8) 5753-5762

11:40am **BI-TuM12 Synchrotron Radiation X-Ray Fluorescence Mapping of Cobalt Ferrite Nanoparticles in BALB 3T3 Fibroblast Cells**, *G. Ceccone, P. Marmorato, J. Ponti, F. Rossi*, EC-JRC-IHCP, Italy, *B. Kaulich, A. Gianoncelli, M. Kiskinova*, Elettra Sincrotrone Trieste, Italy, *M. Salomé*, ESRF Grenoble France, *R. Ortega, G. Deves, A. Carmona*, University of Bordeaux, France, *L. Pascolo*, Elettra Sincrotrone Trieste, Italy

Recent efforts in development of multifunctional nanoscale materials, and in particular nanoparticles (NPs) for use as drugs delivery, targeted therapeutic and imaging agent have made significant progress [1, 2]. Magnetic NPs and in particular cobalt ferrites (CoFe_2O_4), offer some attractive possibilities in biomedicine as drug delivery carriers, hyperthermia treatments in cancer therapy and magnetic resonance imaging (MRI) contrast enhancement [3, 4]. However, along with developing their vast implementation there is a growing concern about the health hazards related to the possible toxic effects of the NPs. The lacking information about the NPs impact on environment and on human health as well as data on risk assessment requires reliable methodology for control and prediction. Among the promising detection methods is the synchrotron radiation x-ray fluorescence (SRXRF) that has already demonstrated its potential in biomedical research exploring e.g. neurodegenerative disorders [5, 6]. Extending the application of SRXRF using soft X-rays [7] has also provided access to light elements natural constituents of the living matter. In this work we report SRXRF investigation of the distribution and chemistry of CoFe_2O_4 nanoparticles on balb3T3 mouse fibroblast cells exposed to NPs concentrations ranging between 40 and 1000 μM for 24h. The SRXRF maps and micro-spot spectra indicate that, for concentrations below 500 μM , the NPs are localized in the perinuclear region, whilst at higher concentration they penetrate also in the nuclei, where the Fe/Co ratio indicates that the cells are not able to counteract the toxic effect of NPs chemical components (i.e. cobalt). A co-localization of P, Ca and Fe at high concentration has also been observed indicating intracellular sequestration mechanisms as a response or in an attempt to reduce the nanoparticles toxic effects. Preliminary PIXE (Proton Induced Ion Emission) measurements support the XRF results indicating that at 250 μM the Fe and Co are localized around the nucleus whilst Ca, P, S, K, Zn and Na are uniformly distributed in the cell.

References

- [1] T. Paunesku et al., Nanoletters, 7(3), (2007), 596.
- [2] L.A. Nagahara, M. Ferrari, T. Grootzinski, MRS bulletin, 34(6), (2009), 406.
- [3] D.H. Kim et al, J. Mag. Mat. 320(2008), 2390
- [4] J.A. Ritter, et al., J. Mag. Mat., 288, (2005), 403
- [5] A. Ide-Ektesabi, Application of Synchrotron Radiation: Microbeams in cell Microbiology and Medicine, Springer, (2007)
- [6] R. Ortega et al., Nucl. Inst. Met. B210 (2003), 325
- [7] R. Alberti et al., X-ray Spectrometry 38 (2009), 205-209

Electronic Materials and Processing Room: Dona Ana - Session EM-TuM

Contacts and Transport

Moderator: L. Porter, Carnegie Mellon University

8:00am **EM-TuM1 Resistivity Increase due to Electron Surface Scattering in Nanoscale Metal Films**, *J.S. Chawla, D. Gall*, Rensselaer Polytechnic Institute

The resistivity increase due to electron surface scattering can be reduced by facilitating specular scattering, as demonstrated by *in-situ* transport measurements on single crystal Cu, Ag, and TiN layers. However, metal barrier layers and surface exposure to oxygen/air perturb the periodic surface potential, causing diffuse electron scattering which increases the resistivity. These findings are important for the development of future generation narrow low-resistivity Cu interconnects and TiN metal gates. Epitaxial Cu(001), Ag(001), and TiN(001) layers exhibit a minimum continuous thickness of 20, 50, and 1.8 nm, respectively, when grown on MgO(001) substrates by ultra-high vacuum magnetron sputter deposition at 80, 140, and 750 °C, respectively, while Cu grown on a 2-nm-thick TiN(001) buffer layer at room temperature shows a minimum continuous thickness of 4 nm. X-ray diffraction θ - 2θ scans, ω -rocking curves, and pole figures show the layers are single crystals with a cube-on-cube epitaxy. The surface and interface roughness, and layer thickness were determined by Rutherford backscattering spectrometry, x-ray reflectometry, and *in-situ* scanning tunneling microscopy. *In-situ* electron transport measurements at room temperature show a resistivity increase with decreasing thickness *d*,

from (i) 1.7 to 6.4 $\mu\Omega\text{-cm}$ for Cu layers with $d = 1400$ to 4 nm, (ii) 13 to 150 $\mu\Omega\text{-cm}$ for TiN layers with $d = 760$ to 1.8 nm, and (iii) 1.6 to 2.1 $\mu\Omega\text{-cm}$ for Ag layers with $d = 1250$ to 50 nm. The data for Cu and Ag layers is consistent with the Fuchs-Sondheimer model and indicates specular scattering at metal-vacuum boundary with an average specularly parameter $p = 0.6$ and 0.4, respectively. In contrast, layers measured *ex-situ* show completely diffuse surface scattering ($p = 0$) due to sub-monolayer oxidation.

In-situ deposition of 0.3 to 7 nm thick Ta barrier layers on Cu(001) films leads to a resistance increase that indicates transition to $p = 0$, independent of the Ta thickness. *In-situ* exposure of Cu(001) layers to O_2 between 10^{-3} and 10^5 Pa-s results in a sequential increase, decrease and increase of electrical resistance which is attributed to partial specular surface scattering for smooth clean Cu(001) and for surfaces with a complete adsorbed monolayer, but diffuse scattering at partial coverage and after chemical oxidation. A model relates the surface coverage to p and provides values for the oxygen adatom and advacancy scattering cross-sections of 0.8 and 0.06 nm^2 , which are qualitatively validated by non-equilibrium *ab initio* transport simulations. The rates for resistance change are proportional to the O_2 pressure, indicating a high-sensitivity gas sensing mechanism.

8:20am EM-TuM2 Extracting Inelastic and Elastic Hot Electron Attenuation Lengths from nm-Thick Metal Films using BEEM, J.J. Garramone, J.R. Abel, I.L. Sinitzky, V.P. LaBella, University at Albany

Measuring the scattering of electrons in nm-thick structures of metals such as Cu and Ag is both technologically and fundamentally significant. For example, sidewall and grain boundary scattering in nanoscale Cu-metal interconnects dramatically increases the resistance, which is detrimental to device performance. A highly accurate method for studying hot electron transport on the nanometer length scale is ballistic electron emission microscopy (BEEM). BEEM is a three terminal scanning tunneling microscopy (STM) based technique, where electrons tunnel from a STM tip into the grounded metal base of a Schottky diode [1]. The BEEM current is a measurement of the electrons that traverse the metal film and are collected in the semiconductor. Results from BEEM measurements of the hot electron attenuation length of the metal films will be presented. A Fermi liquid based model is utilized to extract the inelastic and elastic contributions to the scattering. The metal films are deposited on H-terminated Si(001) under ultra-high vacuum (UHV). The BEEM measurements are taken at 77K under UHV. Recently we fabricated a contact to the metal layer on the silicon utilizing standard lithography prior to deposition of the metal in UHV [2]. This allowed these BEEM measurements to be performed *in situ*. The process utilized to fabricate this contact will be presented along with the *in situ* BEEM results.

References:

- [1] L. D. Bell and W. J. Kaiser, Phys. Rev. Lett. 61 2368 (1988)
- [2] J. J. Garramone, et al., J. Vac. Sci. Technol. A (in press) (2010)

8:40am EM-TuM3 Influence of Spontaneous Polarization and Intrinsic Gap States in Schottky Contacts to ZnO, M.W. Allen, University of Canterbury, New Zealand, S.M. Durbin, University at Buffalo

INVITED

Zinc oxide is an interesting test case for evaluating theoretical Schottky contact formation models as it is significantly more ionic than most semiconductors. This results in weaker Fermi level pinning, which in turn allows the barrier height of Schottky contacts to vary with metal properties. Equally important is the fact that contacts can be prepared on laterally homogeneous, bulk-grown, single crystals with minimal surface processing as there is no requirement, as with most semiconductors, to remove native surface oxide layers with potentially damaging etching treatments. As a result, we have been able to fabricate very low ideality factor, laterally homogeneous Schottky contacts to 'intrinsic' ZnO surfaces for a wide variety of metals using a novel eclipse pulsed laser deposition technique. Using these contacts, we have evaluated the two leading contemporary Schottky contact formation models – Tung's 'chemical bond polarization model' and Mönch's 'metal induced gap states and electronegativity model'. The lack of broad agreement with either of these models suggests the involvement of additional mechanisms, perhaps involving the large spontaneous polarization of ZnO and ionic surface charge screening effects, with important consequences for other oxide semiconductors.

9:20am EM-TuM5 Dynamics of the Charge Transfer through the Individual Molecules in Alkanethiolate Self-Assembled Monolayers, P. Kao, Pennsylvania State University, S. Neppel, P. Feulner, Technische Universität München, Germany, D.L. Allara, Pennsylvania State University, M. Zharnikov, Universität Heidelberg, Germany

Emergence of molecular and organic electronics as frontier fields of modern science and technology require reliable experimental data regarding the

charge transport (CT) in individual molecules and their functional units. Whereas static conductance of molecules arranged in self-assembled monolayer (SAM) fashion on a suitable substrate has been extensively studied, little is known about the CT dynamics in these systems. By the example of alkanethiolate films on Au(111), we show that the latter phenomena can be successfully addressed by resonant Auger spectroscopy, using the core hole clock method. The charge transfer pathway was unambiguously defined by resonant excitation of the nitrile tailgroup attached to the alkyl backbone. The length of this backbone was varied to monitor the respective dependence of the CT time. It was found that, similar to the static conductance, this dependence can be coarsely described by an exponential function with an attenuation factor of 0.93 per a methylene unit. As a result, the CT time is quite long even for a relatively short alkyl chain; in particular, it is ca. 100 fs for the chain consisting of only four methylene units. In contrast, the CT time associated with the thiolate headgroup anchor was found to be quite short, viz. 2.3 fs (upper limit), which suggests an efficient interfacial electronic coupling between the aliphatic backbone of the molecules and substrate over the thiolate-gold linkage.

9:40am EM-TuM6 Electronic Properties and Assembly of Zinc Metalloporphyrin Islands on Au(111) Surfaces, A.E. Schuckman, K.M. Webb, L.M. Perez, Texas A&M University, M. Jurow, Hunter College of the City University of New York, L.H. Yu, National Institute of Standards and Technology, C.M. Drain, Hunter College of the City University of New York, J.G. Kushmerick, National Institute of Standards and Technology, J.D. Batteas, Texas A&M University

Porphyrins are stable, highly conjugated compounds and the choice of metal ion and substituents bound to the macrocycle as well as other effects such as chemical surrounding and cluster size modulate the electronic and photonic properties of the molecule. Porphyrins and their derivatives are relatively non-toxic, and due to their very rich photo- and electro-chemistry as well as their small HOMO-LUMO gaps, this makes them outstanding candidates for use in molecularly-enhanced electronic applications.

For this study, the transport properties of self-assembled zinc coordinated tri-pyridyl porphyrin thiol islands inserted into a dodecanethiol matrix on Au(111) were investigated using scanning tunneling microscopy (STM) and cross-wire inelastic tunneling spectroscopy (IETS). The zinc porphyrin thiol islands observed by STM exhibited reversible bias-induced switching at high surface coverage due to the formation of Coulomb islands of ca. 10 nm diameter driven by porphyrin aggregation. Low temperature measurements (~ 4 K) from crossed-wire junctions verified the appearance of a Coulomb staircase and blockade which was not observed for single molecules of this compound or for the analogous free base. Scanning probe lithography via nanografting has been implemented to fabricate nanoscale patterns of the zinc porphyrin thiols on Au surfaces and ultimately ~ 10 nm islands which is the optimal size for the observed switching effect.

10:40am EM-TuM9 Deposition of Nickel Nanostructures by Electroless Deposition on Micron-Scale Patterned SAMs, Z. Shi, A.V. Walker, University of Texas at Dallas

We have investigated the reaction pathways involved in the electroless deposition of nickel on -COOH, -OH, and -CH₃ terminated functionalized alkanethiolate self-assembled monolayers (SAMs) adsorbed on gold, using time-of-flight secondary ion mass spectrometry (TOF SIMS), scanning electron microscopy (SEM) and x-ray photoelectron spectroscopy (XPS). This work has important applications in molecular/organic electronics as well as other technologies.

We observe that the nickel electroless deposition rate increases as the plating bath pH increases. For -COOH, terminated SAMs, this is effect is very pronounced, with the largest deposition rates observed at above pH = 9. This is most likely due to the -COOH terminated groups deprotonating to form forming carboxylate ions, COO⁻. These carboxylate ions can easily complex with Ni²⁺ ions in solution, forming Ni-carboxylate complexes which serve as the nucleation sites for Ni deposition. Furthermore on -COOH terminated SAMs the nickel overlayer forms almost immediately, while on -CH₃ and -OH terminated SAMs the nickel overlayer forms after 15-20 minutes deposition. The nucleation of the Ni overlayer is slightly faster on the hydrophobic -CH₃ terminated SAM than on the hydrophilic -OH terminated SAM.

By exploiting the different nickel deposition rates on -COOH, -OH, and -CH₃ terminated SAMs we demonstrate that a variety of nanostructures can be produced, including nanowires and rings, using micron-scale patterned SAM surfaces.

11:00am EM-TuM10 Rapid DNA Sequencing via Transverse Electronic Transport, M. Zwolak, Los Alamos National Laboratory, M. Di Ventra, University of California at San Diego

A rapid and low-cost DNA sequencing method would revolutionize medicine: a person could have their full genome sequenced so that

treatments could be tailored to their specific conditions; doctors could know in advance a patient's likelihood to develop a given ailment; cures to major diseases could be developed faster. These goals of "personalized medicine" is hampered today by the high cost and slow speed of DNA sequencing methods. I discuss a sequencing protocol we suggest that uses the measurement of transverse electronic currents during the translocation of single-stranded DNA through nanopores. I present support for our conclusions using molecular dynamics simulations coupled to quantum mechanical calculations of electrical current in experimentally realizable systems. Several recent experiments also support our theoretical predictions. In addition to their possible impact in medicine and biology, the above methods offer ideal test beds to study open scientific issues in the relatively unexplored area at the interface between solids, liquids, and biomolecules at the nanometer length scale [1].

[1] M. Zwolak, M. Di Ventra, "Physical Approaches to DNA Sequencing and Detection", *Rev. Mod. Phys.* 80, 141 (2008).

11:20am EM-TuM11 Using Scanned-Probe Microscopy to Study Surface-Induced Fluctuations as a Tool for Microscopically Probing Organic Materials, N. Hoepker, Cornell University

The development of organic electronics calls for new tools to study organic thin films. By measuring the frequency noise experienced by a cantilever near a surface, we are able to microscopically probe organic materials. In previous work, we have used custom-fabricated ultrasensitive cantilevers to measure frequency noise ("jitter") due to dielectric fluctuations as a function of cantilever height and voltage over polymer of various compositions and thicknesses [1]. In parallel, we have developed a zero-free parameter linear-response theory of thermally induced dielectric fluctuations [2] that successfully describes our observations. Having understood dielectric fluctuations, we are now investigating fluctuations induced by carrier motion in organic materials in order to extract the local charge mobility.

11:40am EM-TuM12 High Precision Local Electrical Probing: Potential and Limitations for the Analysis of Nanocontacts and Nanointerconnects, A. Bettac, J. Koebler, M. Maier, A. Feltz, Omicron NanoTechnology GmbH, Germany, D. Jie, N. Chandrasekhar, Institute of Materials Research & Engineering, Singapore, C. Joachim, CEMES-CNRS, France

The variety of approaches for individual nanoscale devices is tremendous. In contrast however, comprehensive concepts towards electrically integrated and therefore functional devices are rare. The individual (metallic) contact interface represents one of the main challenges and high precision local electrical probing has the potential to increase efficiency in evaluating different approaches. To meet the involved requirements, we have established and being advancing an approach integrating SPM technology with high resolution electron microscopy: (1) Rapid and simultaneous SEM navigation of four local STM probes; (2) Localization of nanostructures by high resolution SEM; (3) Individual probe fine positioning by atomic scale STM imaging; (4) STM based probe approach for "soft-landing" of sharp and fragile probes and controlled electrical contact for transport measurements; (5) approaches towards sharp and clean STM tips; (6) suitable low noise signal re-routing for transport measurements; and (7) chemical or magnetic analysis by complementary analysis techniques.

We will report on recent technical enhancements and illustrate achievements and limitations along specific applications. As a model system, we have chosen Au islands on MoS₂ [1]. These islands represent contact pads, each electrically connected by an individual STM probe. As good band gap (approx. 1.3eV transverse gap) semiconductor, MoS₂ has the potential to sufficiently decouple nanostructures electrically at low voltage. Those Au triangular islands have a lateral size of typically 10-30nm and form an "atomically" clean and defined metal-semiconductor interface. We will present measurements on (1) probe navigation and electrical contacting with contact distances in the 10nm regime. (2) reproducible Schottky like IV properties for the individual STM tip/Au island/substrate contact; (3) surface conductance measurements with variable inter-island distance down to 17nm; and (4) we also show that the individual STM probe can be employed under SEM to manipulate those Au islands [2] with high precision in order to generate arbitrary multi probe planar contact configurations.

Furthermore, we will present a newly developed probing system. The complete stage including probes is cooled down to LHe temperatures, while each probe is capable of atomic resolution STM. A major challenge is the integration of an high performance UHV Gemini SEM into the thermally shielded probe stage compartment, while maintaining the sample temperature below 10K during SEM operation.

[1] MSM Saifullah et al., *Nanotechnology*, 13, 659 (2002)

[2] J.S. Yang et al., *J. Vac. Sci. Tech. B*, 25, 1694 (2007)

**Energy Frontiers Topical Conference
Room: Mesilla - Session EN-TuM**

Flexible Solar Cells

Moderator: C.A. Wolden, Colorado School of Mines

8:40am EN-TuM3 Control of the Structural, Electrical and Mechanical Bending Properties of Highly Transparent Conductive Ga-doped ZnO Films Deposited on Polyester Substrates, K. Nagamoto, Y. Matubayashi, T. Kondo, LINTEC Corporation, Japan, Y. Sato, H. Makino, N. Yamamoto, T. Yamamoto, Kochi University of Technology, Japan

In this work, we report the structural, electrical and mechanical bending properties of highly transparent conductive Ga-doped ZnO (GZO) films deposited on flexible substrates for use in electrodes for flexible devices. GZO films were deposited on polyester substrates covered with under-coat layers by ion plating deposition with direct-current arc discharge at a temperature of less than 100 degree Celsius (The glass transition temperature (T_g) of polyester substrates are approximately 120 degree Celsius). Polycrystalline GZO films with high (0002) orientation perpendicular to the substrate have obtained. The resistivity of GZO films of a 100 nm thickness on polyester substrates was 5.0×10^{-4} ohm-cm and the average transmittance of more than 80 % in the visible wavelength region.

The mechanical bending properties of GZO films were investigated by bend test: sheet resistance of GZO films as a function of bending diameter before and after bending was determined by Hall-effect measurement. When the substrate is bent by an external force, the outer side surface experiences tensile stress and inner side surface experiences compressive stress. The analysis of data obtained by the bend test shows that sheet resistance for GZO films at 12 mm bending diameter were 150 ohm/sq. (before bending test : 50 ohm/sq.) for compressive stress direction whereas sheet resistance was 1770 ohm/sq. for tensile stress direction. In addition, the bend test was carried out for GZO films deposited at different process temperature. GZO films deposited at lower substrates temperature exhibit improved bending performance. GZO films deposited on polymer substrates have residual stress including intrinsic stress and thermal stress caused by the difference in thermal expansion coefficient between GZO films and the substrates. The bending property of GZO films can be improved by controlling the residual stress affected by process temperature.

We developed multiple depositions to reduce polymer substrates temperature and obtained the relationship between bending properties of GZO films and process temperature.

The financial support from the Japan Science and Technology Agency is gratefully acknowledged.

9:00am EN-TuM4 Low-Temperature Deposition of Transparent Conducting Oxides on Plastic Substrates, E. Ritz, University of Illinois at Urbana-Champaign, T. Dockstader, Kurt J. Lesker Company, L. Meng, M.J. Neumann, D.N. Ruzic, University of Illinois at Urbana-Champaign

The future of electronic devices such as touchscreen phones and large flat panel displays is bright, with their usage only becoming more prevalent in our daily lives. Such devices are dependent on transparent conducting oxides (TCOs) and their continued growth necessitates a manufacturing process that is able to deposit an inexpensive coating with high transparency and high conductivity. Operating using a dual unbalanced DC magnetron system with a secondary RF antenna running at 13.56MHz, a process has been developed that can deposit TCO films such as Indium Tin Oxide (ITO) and Aluminum-doped Zinc Oxide (AZO) without significantly heating the substrate while maintaining high transmission and electrical properties. The system utilizes two 75mm-diameter circular magnetrons with a 2-loop immersed inductive RF antenna between them in order to provide increased ionization. By adjusting RF power from 0W to 300W, ionization fraction can be increased from 20% to over 80% for unbalanced configuration as measured by a gridded energy analyzer. In addition, plasma density is increased with RF enhancement from 10^{10} cm⁻³ to 10^{11} cm⁻³. This RF enhancement allows for substrate temperatures to remain below 100°C while still achieving film resistivity on the order of 10^{-3} - 10^{-4} Ohm-cm (measured by four-point probe method) and transparency of greater than 90% in the visible wavelengths (measured by spectrophotometry.) Low-temperature deposition expands the possibilities for substrate choice to include plastics, such as polyethylene terephthalate (PET), resulting in flexible TCO films. Adjusting process gas oxygen content (from 0-5%) and RF power allows for a means to tune the film properties to the desired transparency and conductivity. Experiments performed using ITO and 2%-doped AZO with glass and PET substrates. Plasma monitoring accomplished through use of Langmuir probe and optical emission spectroscopy. Additional film quality analysis by means of x-ray diffraction (XRD) and x-ray photoelectron spectroscopy (XPS).

9:20am **EN-TuM5 Flexible Solar Cells Based On Monocrystalline Silicon and GaAs**, *J.A. Rogers*, University of Illinois at Urbana-Champaign **INVITED**

Solar modules that involve large collections of small, ultrathin photovoltaic cells on thin plastic or rubber substrates offer mechanical properties (e.g. stretchability) and other features (e.g. curvilinear shapes; lightweight designs) that cannot be achieved with conventional approaches. This talk describes the use of inorganic micro/nanomaterials in systems that provide the performance of state-of-the-art, wafer-based technologies but with the mechanical properties of a rubber band. We explain the materials science and mechanics of these approaches in the context of monocrystalline silicon and gallium arsenide solar cells, and key mechanics aspects of their use in flexible and stretchable modules.

10:40am **EN-TuM9 Thin Film Photovoltaics from Nanocrystal Inks**, *M. Law*, University of California, Irvine **INVITED**

Colloidal semiconductor nanocrystals (NCs) are metastable objects prone to thermal and oxidative degradation driven by their large surface-to-volume ratios. The fabrication of practical electronic devices based on NC solids hinges on developing methods to prevent oxidation, diffusion, sintering and other undesirable physical and chemical changes to which these materials are susceptible. In this talk, I first describe systematic measurements of the room-temperature electron and hole field-effect mobilities of alkanedithiol-treated PbSe NC films as a function of NC size and the length of the alkane chain. These results establish a baseline for mobility trends in PbSe NC solids and have implications for fabricating high-mobility NC-based optoelectronic devices. Optical, electrical and photoelectron spectroscopy measurements are combined to monitor the room-temperature oxidation of films of PbSe NCs that are treated in solutions of short-chain thiols or carboxylic acids to produce electronically-coupled NC solids. I show that surface oxidation can be prevented by infilling NC films with thin (10-20 nm) Al₂O₃ layers deposited by low-temperature atomic layer deposition (ALD). ALD treatment of complete PbSe NC field-effect transistors yields high-performance devices that operate indefinitely in air. ALD infilling is a promising route to the preparation of stable, all-inorganic NC solids with tunable electrical properties, and may prove an important breakthrough in the fabrication of robust, high-efficiency quantum dot solar cells.

11:20am **EN-TuM11 Architectures for Enhanced Exciton Harvesting in Organic Photovoltaic Cells**, *R.J. Holmes*, University of Minnesota **INVITED**

Organic semiconductors are attractive for application in photovoltaic cells due to their compatibility with lightweight, flexible substrates, and high-throughput processing techniques. Optical absorption in these materials leads to the creation of tightly-bound, mobile excitons. In order to generate photocurrent in an organic photovoltaic cell (OPV), excitons must diffuse to a dissociating, electron donor-acceptor (D-A) interface. Most organic semiconductors are characterized by exciton diffusion lengths that are considerably smaller than the optical absorption length. This trade-off between diffusion and absorption often necessitates the use of thin active layers to maximize exciton harvesting. Among the approaches that have been demonstrated to mitigate the short exciton diffusion length, the use of a D-A bulk heterojunction has been widely studied. In these structures, the D-A materials are blended to realize a large interface area for exciton dissociation. The film morphology is typically optimized by thermal annealing, which results in the formation of pathways for charge carrier collection. This talk will explore two alternate OPV architectures designed to overcome the exciton diffusion bottleneck. The first involves the use of composite donor layers that contain both a fluorescent host and a phosphorescent guest sensitizer. The inclusion of the phosphor sensitizer in the donor layer enables the population of the long-lived triplet exciton state of the fluorescent host. Diffusion via the host triplet leads to a near-doubling in the exciton diffusion length and an increase in device efficiency. The second architecture relies on the use of OPVs containing a continuously graded D-A film composition as a means to simultaneously optimize the exciton diffusion and charge collection efficiencies. In these graded heterojunction OPVs, the power conversion efficiency is observed to exceed that of comparable devices containing either planar or uniformly mixed heterojunctions. In both of these approaches, improved performance is realized by utilizing architectures that enable an increased level of control over the exciton diffusion and charge collection efficiencies.

Exhibitors & Manufacturers Technology Spotlight
Room: Southwest Exhibit Hall - Session EW-TuM

Exhibitors & Manufacturers Technology Spotlight
Moderator: D.J. Surman, Kratos Analytical Inc., R. Langley, Consultant

10:20am **EW-TuM8 Multifrequency Techniques for AFM/SPM**, *A. Gannepalli, R. Proksch*, Asylum Research, *S. Jesse*, ORNL

In multifrequency AFM, as the name suggests, the AFM cantilever is excited at more than one frequency, typically two, but could be more. The motivation is to increase the amount of information on the tip-sample forces that can be measured. When the excitation frequencies coincide with the resonant modes of the cantilever, it is called modal imaging. In harmonic imaging the excitation frequencies are the harmonics of a resonant mode. A different technique called Dual AC Resonance Tracking (DART) uses two excitation frequencies to track the contact resonance of the cantilever in contact resonance applications. A methodology to extract the conservative and dissipative nature of the tip-sample interactions in DART mode will be presented. A new technique called Band Excitation, where the cantilever is excited in a band of frequencies, allows mapping conservative interactions, nonlinearities, and energy dissipation at the nanoscale. The presentation will focus on the technology, instrumentation, and application examples.

Graphene Focus Topic
Room: Brazos - Session GR+TF-TuM

Characterization, Properties, and Applications
Moderator: M. Chhowalla, Rutgers University

8:00am **GR+TF-TuM1 Near-field Scanning Microwave Microscopy of Few-Layer Graphene**, *N.G. Kalugin*, New Mexico Tech

Near-field microwave microscopy can be used as an alternative to atomic-force microscopy or Raman microscopy in determination of graphene thickness. We evaluated the values of AC impedance for few layer graphene. The impedance of mono and few-layer graphene at 4GHz was found predominantly active. Near-field microwave microscopy allows simultaneous imaging of location, geometry, thickness, and distribution of electrical properties of graphene without device fabrication. Our results may be useful for design of future graphene-based microwave devices.

Sandia is a multiprogram laboratory operated by Sandia Corporation, a Lockheed Martin Company, for the

United States Department of Energy's National Nuclear Security Administration under contract DE-AC04 94AL85000.

8:20am **GR+TF-TuM2 Molecular Simulation of the Indentation of Free-Standing Graphene Films in the Presence of Defects**, *J.D. Schall, R.V. Petrach*, Oakland University

Recent experimental advances in the synthesis of graphene have enabled the construction of free-standing graphene-based "nanobridges" (for example: Shivaraman, Nanoletters, 9, 2009, 3100). This has allowed for the first time to probe the mechanical properties of this unique material directly through experiment. In the past, mechanical properties had been estimated theoretically via various molecular simulation techniques. With these new experimental advances, many new questions arise. To list a few: How do defects affect mechanical properties? How do molecular adsorbates modify these materials? Again, molecular simulation is expected to play a significant part in the future of graphene research. In this talk, results of simulated indentation of free-standing graphene films mimicking recent force-probe experiments will be presented. Simulations are conducted using Brenner's second generation reactive empirical bond order potential. This method allows for accurate determination of mechanical properties and chemical modification of the films. Using indentation and a simple force balance approach, the Young's modulus of a pristine free-standing graphene nano-bridge was estimated to be in excess of 1 Terapascal. Results from films with Stone-Wales defects, vacancies, and chemical adsorbates also will be presented.

8:40am **GR+TF-TuM3 Mechanical Characterization of Freestanding Graphenoid Nanomembranes from Self-Assembled Monolayers**, *X. Zhang, C.T. Nottbohm, A. Turchanin, A. Beyer, A. Götzhäuser*, Bielefeld University, Germany

We report on the fabrication and mechanical characterization of novel graphenoid nanomembranes with a thickness of approximately 1 nm. The

nanomembranes are prepared from electron cross-linked aromatic self-assembled monolayers (SAMs). The membranes are then transferred to window-substrates (Si) for mechanical characterization. Bulge testing of such freestanding nanomembranes within an atomic force microscope is utilized to investigate their mechanical properties.

A series of biphenyl-based molecules were used to prepare the nanomembranes, such as carbonitrile-biphenyl-trimethoxysilyl (CBPS), biphenyl-thiol (BPT) and nitro-biphenyl-thiol (NBPT). Biphenyl-based nanomembranes have elastic moduli ranging from 6 to 12 GPa. They display outstanding performance in the ultimate tensile strength with values of 400 to 500 MPa, which is several times higher than the values of other carbon based membranes. Furthermore, annealing of the cross-linked nanomembranes in ultra high vacuum systematically increase of the Young's moduli from 10 GPa to ~45 GPa for an annealing temperature of ~1000 K. Strain relaxation lowers the residual strain from 0.9 % to ~0.35 % for temperatures of 800 K and above. This is caused by a structural transformation in which the nanomembrane is converted into nanocrystalline graphene.

9:00am GR+TF-TuM4 Chemical Vapour Deposition (CVD) Growth of Graphene on Copper. *C. Mattevi, H.K. Kim, G. Eda, M. Chhowalla,* Imperial College London, UK

Uniform large-scale fabrication of graphene thin films with controllable thickness represents a key challenge for integration of graphene into practical electronic devices. Recently, graphene of high quality has been synthesized by chemical vapor deposition (CVD) on transition metal catalysts [1,2]. The graphene growth by CVD on polycrystalline copper [2] is particularly interesting because it allows single graphene layer over 95% of the surface and the residual 5% is covered by 2-3 layered graphene film. Hence, this is the first [2] reported reproducible method to synthesize uniform graphene thickness over large area. Then the as grown graphene can be transferred by different processes, onto a variety of substrates. An appealing challenge is to selectively obtain different graphene thicknesses over large area, to satisfy different applications. Here we report a detailed study of the multilayer graphene domains that appear in limited regions of the copper surface. The lateral size as well as the graphene thickness and stacking order, has been carefully investigated as a function of copper pre-treatment and growth parameters. In particular the role of the feed stock gas pressure and ratio between the etching gas (H₂) and the precursor (CH₄) has been demonstrated to affect the lateral size and the thickness. Optoelectronic properties of the transferred graphene films onto SiO₂ are also presented.

References

1. K. S. Kim, Y. Zhao, H. Jang, S. Y. Lee, J. M. Kim, K. S. Kim, J. H. Ahn, P. Kim, J. Y. Choi and B. H. Hong, *Nature* **457**, 706 (2009).
2. X. Li, W. Cai, J. An, S. Kim, J. Nah, D. Yang, R. Piner, A. Velamakanni, I. Jung, E. Tutuc, S. K. Banerjee, L. Colombo, and R. S. Ruoff, *Science* **324**, 1312 (2009).

9:20am GR+TF-TuM5 Structural and Electronic Properties of Graphene Synthesized by Chemical Vapor Deposition. *Y. Chen,* Purdue University **INVITED**

We have studied the structural and electronic properties of large scale (up to several inches) graphitic and graphene thin films synthesized by chemical vapor deposition (CVD) on polycrystalline Ni_{1,2} and Cu₃ foils then transferred onto insulating substrates (SiO₂ on doped Si). For films grown on Ni_{1,2}, structural characterizations by atomic force microscopy (AFM), scanning tunneling microscopy (STM), *cross-sectional* transmission electron microscopy (XTEM) and spectroscopic Raman mapping confirm that such large scale graphitic thin films contain both thick graphite regions and thin regions of few layer graphene. The films also contain many wrinkles, with sharply-bent tip and dislocations revealed by XTEM, yielding insights on the growth and buckling processes of the film. Measurements on mm-scale back-gated transistor devices fabricated from the transferred film show ambipolar field effect with resistance modulation ~50% and carrier mobilities reaching ~2000 cm²/Vs. We also demonstrate quantum transport of carriers with phase coherence length over 0.2 μm from the observation of 2D weak localization in low temperature magnetotransport measurements. Our results show that despite the non-uniformity and surface roughness, such large-scale, flexible thin films can have electronic properties promising for device applications. For films grown on Cu₃, we show they consist dominantly of monolayer graphene as indicated by Raman mapping. STM imaging shows monolayer graphene lattice. Low temperature transport measurements are performed on micro devices fabricated from such CVD graphene, displaying ambipolar field effect (with on/off ratio ~5 and carrier mobilities up to ~3000 cm²/Vs) and “half-integer” quantum Hall effect, a hall-mark of intrinsic electronic properties of monolayer graphene. We also observe weak localization and extract information about phase coherence and scattering of carriers by disorder in

the graphene. We have measured the thermal conductivity of suspended CVD graphene to be ~3000 W/m-K, comparable with that of exfoliated graphene, by combining electronic transport and Raman thermometry. Finally, I will present some results on graphene layers grown by CVD directly on insulating substrates. Work in collaboration with Q. Yu, H. Cao, L. Jauregui, R. Colby, E. Stach, N. Guisinger and H. Li.

1. Q. Yu *et al.*, *Appl. Phys. Lett.* **93**, 113103 (2008)
2. H. Cao *et al.*, *J. Appl. Phys.* **107**, 044310 (2010)
3. H. Cao *et al.*, *Appl. Phys. Lett.* **96**, 122106 (2010)
4. R. Colby *et al.*, *Diamond Relat. Mater.* **19**, 143 (2010)
5. L. A. Jauregui *et al.*, *ECS Trans.* **28** (5), 73 (2010)

10:40am GR+TF-TuM9 Scanning Tunneling Spectroscopy of a Gated Single-Layer Graphene Device in the Quantum Hall Regime. *S. Jung, G.M. Rutter, N.N. Klimov, D.B. Newell, N.B. Zhitenev, J.A. Stroscio,* NIST

We have performed scanning tunneling spectroscopy (STS) measurements to investigate Dirac particle interactions and localization by local impurities in a gated single-layer exfoliated graphene device in the quantum Hall regime at a temperature of 4.3 K. At the Dirac point, electron-hole puddles created by the disorder potential in SiO₂ substrate are observed at zero magnetic field. In an applied magnetic field, the carriers are condensed into well-resolved Landau levels (LLs), whose general evolution as a function of both charge density and magnetic field is well described by the context of “massless” Dirac particles. Tunneling spectroscopy measurements as a function of magnetic field and applied gate potential are shown to give insight into the localization of carriers and their relation to the disorder potential. At low magnetic fields, tunneling spectra display long-range scattering features related to the graphene disorder potential variation. The disorder potential also determines the spatial distribution of LLs in higher magnetic fields. We observe that isolated compressible LL regions surrounded by incompressible strips behave like graphene quantum dots (QDs). Single-electron charging of the QDs is seen as four-fold Coulomb oscillations in individual *dI/dV* curves. These results show that the plane of the graphene 2DEG breaks into a checkerboard pattern of electron- or hole-rich QDs localized at either maxima or minima of the disorder potential.

11:00am GR+TF-TuM10 Scanning Tunneling Spectroscopy of Gated Bilayer Graphene Device in the Quantum Hall Regime. *N.N. Klimov, CNST/EEEL/NIST and Maryland NanoCenter UMD, G.M. Rutter, CNST/NIST, S. Jung, CNST/NIST and Maryland NanoCenter UMD, D.B. Newell, EEEL/NIST, N.B. Zhitenev, J.A. Stroscio,* CNST/NIST

It has been shown recently, both theoretically [1] and experimentally [2-3], that a bandgap can be opened and even tuned continuously in bilayer graphene (BLG) in the presence of a strong electrical field, which induces asymmetry of the electrostatic potential of the two graphene layers. This makes BLG an attractive material for future digital electronic applications, infrared nanophotonics, pseudospintronics, and terahertz technology. On the other hand a complete understanding of the physics of BLG and the effect of disorder on a microscopic scale is missing. In this work, we present local tunneling measurements of bilayer graphene exfoliated on SiO₂/Si using scanning tunneling spectroscopy at a temperature of 4.3 K. The graphene bilayer is probed with both the application of a perpendicular magnetic field and with an external gate voltage applied to the Si substrate. We study the effect of disorder potential induced by SiO₂/Si on the electronic properties of bilayer graphene. We find that disorder potential causes a bandgap opening in BLG, while a backgate voltage has a secondary effect on the density of states. We also find that the magnetic quantization of the carriers, evidenced by the formation of Landau levels (LL), does not obey the simple scaling of LL energy versus magnetic field for an ideal graphene bilayer.[4] The LL spectra are seen to vary greatly depending on the local potential variation and associated charge density. We have investigated these variations with detailed spectroscopic maps of the LL spectra as a function of energy, gate voltage, and local potential variation. We find the assignment of the spectral features to be much more complex than expected, and may require the introduction of an intrinsic electrical bias in the bilayer system. In this talk, we will discuss the possible theoretical models that may account for our observations.

- [1] E. McCann, V. I. Fal'ko, *Phys. Rev. Lett.* **96**, 086805 (2006).
- [2] J. B. Oostinga, *et al.*, *Nature Mater.* **7**, 1510157 (2008).
- [3] E. V. Castro *Phys. Rev. Lett.* **99**, 216802 (2007).
- [4] E. A. Henriksen *et al.*, *Phys. Rev. Lett.* **100**, 087403 (2008).

11:20am **GR+TF-TuM11 Monolayer Graphene on 150mm Substrate**, *H.J. Chung, J. Heo, H. Yang, S.-H. Lee, S. Seo*, Samsung Advanced Institute of Technology, Korea

Monolayer graphene over a 150 mm substrate was fabricated using Cu-Ni multilayer growth substrates with Inductively Coupled Plasma-Enhanced Chemical Vapor Deposition (ICPCVD) over 700°C. It was confirmed with Raman spectroscopic mapping after metal etching and transfer process. Over 2000 FETs were fabricated on a 150 mm wafer and on-off ratio and Dirac shift were measured for each device and compared to ones from the graphene grown on Ni substrate. In addition, the result from SPM investigation will be presented.

11:40am **GR+TF-TuM12 Probing the Electronic Structure, Surface Chemistry, and Alignment of Graphene using Soft X-ray Absorption Spectroscopy**, *C. Jaye*, NIST, *V. Lee*, SUNY at Buffalo, *P. Lysaght*, SEMATECH, *S. Banerjee*, SUNY at Buffalo, *D.A. Fischer*, NIST

Graphene, a single layer of graphite packed in a honeycomb lattice, has been the subject of intense scientific research since its discovery in 2004 owing to its remarkable properties such as the half-integer quantum Hall effect, ballistic conduction, and the extremely high mobilities of its charge carriers. Graphene has numerous potential applications in the electronics industry including within ultra-high frequency transistors, electrical interconnects and as a replacement for indium-tin-oxide. Nevertheless, the fabrication of large-area graphene remains a challenge. We present systematic studies of the electronic structure, defect density, and alignment of relatively large-area graphene thin films prepared by a) solution/sonochemical methods and b) chemical vapor deposition (CVD). The solution-chemistry-based approaches have the advantage of ease of scalability, making it an attractive approach for industry. We have been able to achieve the fabrication and transfer of large-area graphene films on both conductive and non-conductive substrates. The fabricated films have been characterized by Raman spectroscopy, near-edge X-ray absorption spectroscopy, and four-point-probe conductivity measurements. This battery of measurements allows evaluation of the role of different reducing agents in reducing graphene oxide to graphene. We have also performed systematic measurements of single- and few-layered graphene grown by CVD onto Cu and Ni substrates. X-ray absorption spectroscopy in particular provides strong evidence for substrate hybridization and rippling of graphene. The ripping of graphene induced during transfer to insulating substrates represents a formidable challenge that will need to be solved since corrugations and electronic asperities in graphene induce local scattering potentials. Finally, we will present some X-ray absorption spectroscopy imaging data showing local electronic asperities in graphene.

In Situ Microscopy and Spectroscopy Topical Conference

Room: Acoma - Session IS+SS-TuM

In Situ Spectroscopy – Interfacial Chemistry/Catalysis

Moderator: D.R. Baer, Pacific Northwest National Laboratory

8:00am **IS+SS-TuM1 Oxidation and Reduction of Pd(100) and Supported Pd Nanoparticle Model Catalysts**, *R. Westerstrom, S. Blomberg, N. Martin, J. Gustafson, E. Lundgren, J.N. Andersen, M.E. Messing, K. Deppert*, Lund University, Sweden, *H. Bluhm*, Lawrence Berkeley National Laboratory, *O. Balmes, R. van Rijn*, ESRF Grenoble, France

Using *in situ* high pressure X-ray photoelectron spectroscopy, we study the oxidation and reduction by O₂ and CO in the mbar pressure regime of Pd(100) and Pd nanoparticles of 15 or 35 nm diameter supported on a SiO_x substrate. We find the oxidation behavior of these model catalysts to be qualitatively similar, with an ultra-thin surface oxide forming prior to the onset of bulk PdO formation. However, the Pd nano particles are observed to bulk oxidize at sample temperatures 40 degrees lower than Pd(100). For the PdO surface, we identify a core level shift of the Pd 3d and O 1s levels of -0.3 and -1.3 eV, respectively, relative to the corresponding levels in bulk PdO. In a CO atmosphere, the Pd 3d shift changes by +0.55 eV due to CO adsorption, and CO adsorbed on the oxide can be identified in the C1s. Also the reduction by CO is similar between the single crystal and the nanoparticle samples, but after the complete removal of the oxide, the nanoparticles incorporate carbon to form a Pd carbide. This is not observed for the single crystal sample.

8:20am **IS+SS-TuM2 In-situ XPS Studies of CO₂ Captured by Aqueous Monoethanolamine (MEA) Solutions**, *T. Lewis, A. Chaudhuri*, University of California, Irvine, *M. Faubel*, Max-Planck Institut für Dynamik und Selbstorganisation, Germany, *B. Winter*, Helmholtz-Zentrum Berlin für Materialien und Energie, Germany, *J.C. Hemminger*, University of California, Irvine

XPS on a micro liquid jet has been used to study solutions of monoethanolamine (MEA), which is commonly used in gas stream scrubbing for carbon dioxide capture. It is likely that interactions between CO₂ and the aqueous MEA solution at the gas/liquid interface are important to this process, yet there is little information available concerning the spatial distribution of species at the interface of such solutions. In the present work, aqueous solutions of MEA with a range of pH values as well as solutions of MEA reacted with CO₂ have been measured using tunable synchrotron radiation from the BESSY facility in Berlin, where the photoelectron kinetic energy can be varied to obtain depth dependent composition information. N1s photoemission spectra allow for the identification of protonated versus unprotonated MEA by the different binding energies of the two species, and likewise, C1s spectra allow for the determination of CO₂-reacted versus unreacted MEA. Depth profiling reveals that deprotonated MEA is more surface active than both protonated MEA and the CO₂-reacted species. The mechanism of the reaction of CO₂ with aqueous solutions of monoethanolamine will be discussed in light of our results.

8:40am **IS+SS-TuM3 Photoelectron Spectroscopy Under Humid Conditions**, *H. Bluhm*, Lawrence Berkeley National Laboratory **INVITED**

The interaction of water with surfaces plays a major role in many processes in the environment, atmosphere and technology. Weathering of rocks, adhesion between surfaces, and ionic conductance along surfaces are among many phenomena that are governed by the adsorption of molecularly thin water layers under ambient humidities. The properties of these thin water films, in particular their thickness, structure and hydrogen-bonding to the substrate as well as within the water film are up to now not very well understood. Ambient pressure photoelectron spectroscopy (APXPS) is a promising technique for the investigation of the properties of thin water films. We will discuss the basics of APXPS as well as the particular challenges that are posed by investigations in water vapor at Torr pressures, as well as show examples of the application of APXPS to the study of water films on metals and oxides.

9:20am **IS+SS-TuM5 Chemistry of Aminoacids at the Water – Metal Interfaces under UHV and AP Conditions**, *A. Shavorskiy*, Lawrence Berkeley National Laboratory, *T. Eralp*, The University of Reading, UK, *F. Aksoy, Z. Liu, H. Bluhm*, Lawrence Berkeley National Laboratory, *A. Cornish, D. Watson*, The University of Reading, UK, *K. Schulte, J.N. Andersen*, Lund University, Sweden, *G. Held*, The University of Reading, UK

Many important catalytic reactions take place at the interface between a solid catalyst and a solution, in particular aqueous solutions play a crucial role in all biological systems. The presence of the solvent at the solution-catalyst interface can dramatically change the chemical surface properties and, therefore, the entire catalytic process. Although surface science has been very successful in studying gas-surface reactions, most UHV-based surface science techniques cannot be applied to the co-adsorption of solvent and reactant molecules of important reaction systems because the solvent desorption temperature in UHV is too low to allow co-adsorption at realistic reaction temperatures. In order to keep significant amounts of water adsorbed near room temperature pressures of up to 1 mbar are needed for most metals. Recently, ambient pressure X-ray photoelectron spectroscopy (APXPS), has become available for studying these systems at close-to-real conditions [Bluh09].

For the experiments reported here we chose to study the influence of water on the adsorption of glycine and alanine on Pt[111] and Pt[110] in UHV and on Cu[110] at near-ambient pressure. The comparison between results obtained in UHV and at AP allows us to reveal importance of the reaction conditions (in particular reaction pressure and temperature) on the chemical composition and stability of the molecular adlayers on metals. It also bridges the pressure gap in studies of such kind of bio-related systems. Our results show an absence of any noticeable changes in the chemical composition of the aminoacids on Pt[111] and Pt[110] when co-adsorbed with water in UHV. On the other hand we observed clear decrease of the amino acid desorption temperature and a change of the desorption pathway (compared to UHV [Barl05]) on Cu[110] when the H₂O pressure is increased above 10⁻⁵ mbar. Two possible mechanisms of lowering the stability of the amino acids in the presence of water are discussed: (a) oxidation of the amino acid by OH or O or (b) hydrogenation of the anionic amino acid followed by desorption of the less stable intact form [Jone06].

[Bluh09] H. Bluhm, J. El. Spec. Rel. Phen., doi:10.1016/j.elspec.2009.08.006, 2009.

[Jones06] G. Jones et al Surf. Sci. 600 (2006) 1924.

[Barl05] S. M. Barlow et al Surf. Sci 590 (2005) 243.

[Ande07] K. Andersson et al. J. Phys. Chem. C 111 (2007) 14493.

9:40am **IS+SS-TuM6 In-situ Ambient Pressure XPS Observations of Reversible Charge Storage in Ni Electrodes**, *A.H. McDaniel, F. El Gabaly*, Sandia National Laboratories, *M. Grass, Z. Liu*, Lawrence Berkeley National Laboratory, *K.F. McCarty*, Sandia National Laboratories, *H. Bluhm*, Lawrence Berkeley National Laboratory

Electrochemical technologies will be increasingly used to supply energy to the world without contributing to climate change. These technologies can store and convert energy with unsurpassed efficiencies through, for example, the charging and discharging of batteries or the inter-conversion of electrical and chemical energy via fuel cell and electrolyzer. Perhaps the most important phenomena to understand in electrochemical energy storage/conversion is how electric charge is transferred across interfaces and subsequently stored in material phases and/or double layers. Currently, detailed knowledge is lacking of critical pathways such as which chemical reactions are responsible for charge transfer, what species are involved, and where charge transfer reactions occur in heterogeneous devices. These limitations arise in no small degree from the physical complexities of these devices, which consist of a variety of electrified materials undergoing chemical reactions. Lacking this knowledge, development proceeds largely using engineering approaches.

To help answer these questions we have spectroscopically characterized electrochemical charge-transfer and storage as it occurs. This is accomplished by primarily using a new diagnostic based on synchrotron X-ray spectroscopies that we have been developing at the Advanced Light Source (ALS, LBNL, Berkeley, CA). Photoelectrons are used as a contactless probe for the direct measurement of the electric inner potential everywhere in a Ni-YSZ based electrochemical cell operating at near ambient pressure. This information, in addition to space-resolved chemical characterization of the surface species showing phase changes relevant to Ni-metal-hydride batteries, will be discussed. The experimental configuration consists of a thin-film Ni electrode that is electrochemically modified by injection of O₂- ions. During an applied bias, charge is stored in the electrode by the conversion of the Ni to NiOOH. This leads to dramatic changes in the XPS spectra as well as the existence of a constant discharge potential plateau resulting from the equilibrium of NiOOH with two other phases, Ni and H₂O. Thus, our approach has the ability to identify the phases that store charge, which are only stable under electrical bias. This rich data will provide new understanding on how electrochemically driven phases form.

10:40am **IS+SS-TuM9 Hard X-ray Photoelectron Spectroscopy: an Effective Probe for Electronic Structure in Materials Science**, *W. Drube*, Deutsches Elektronen-Synchrotron DESY, Germany **INVITED**

The use of hard X-ray excitation in the range from about 2 to 15 keV for photoelectron spectroscopy (HAXPES) is a rapidly emerging technique at synchrotron sources worldwide since it significantly widens the range of applications, in particular in the study of complex materials and buried nano-structures or interfaces. Due to the increased electron inelastic mean free paths, it becomes possible to probe chemical composition and electronic structure in the bulk of materials with considerable sensitivity, down to typically 10-20 nm at 10 keV kinetic energy. This not only is essential in the study of complex correlated materials which often exhibit a modified surface electronic structure but also is very relevant for technologically interesting multi-layered materials with buried interfaces. As an additional benefit, "as-grown" materials can be measured without need for prior surface treatment.

A drawback is the rapidly decreasing photoelectric cross section in the hard X-ray range, especially for shallow core levels and valence states, and - until recently - the limited availability of suitable high-voltage electron spectrometers. The latter are available meanwhile and the high X-ray flux at undulator beamlines has been shown to effectively compensate the cross section decrease. In addition, the X-ray tunability over a large energy range not only allows to significantly vary the electron probing depths and the photoelectric cross sections, but also enables the study of resonance phenomena at deep inner-shell thresholds. Further, the excitation of X-ray standing wave fields within single crystals or multi-layered structures can be effectively used to correlate geometric and electronic structure information.

In the past five years, HAXPES activities at synchrotron laboratories worldwide have increased dramatically and the trend continues as new instruments are currently being built and planned. A brief overview is given on the current activities worldwide, both on instrumental developments and results obtained. At DESY, HAXPES experiments routinely use a dedicated spectrometer at an X-ray wiggler with moderate energy resolution (~0.5 eV), well suited for many core level studies. Very recently, high-resolution

studies also became possible at DESY with the availability of PETRA III, a new storage ring source providing the highest X-ray brilliance.

11:20am **IS+SS-TuM11 Novel Applications in Surface Science – In situ Sample Analysis in Extreme Environments**, *A. Thissen*, SPECS Surface Nano Analysis GmbH, Germany

Modern devices are often only functional in environments far away from ultrahigh vacuum, still being the standard operation conditions for all Surface Science techniques. In parallel the importance of surfaces for the correct device operation is continuously increasing due to miniaturization down to the nanoscale. To contribute to advanced materials analysis in future means using Photoelectron spectroscopy, Scanning Probe Microscopies and related techniques in the generic or near generic device environments. This means high, elevated or near ambient pressures of defined working gas mixtures, liquid media, potentials or magnetic fields applied. Also extremely low or high temperatures might be necessary. In past all standard Surface Science Techniques did not work under these *extreme* environments. This work summarizes and presents existing solutions nowadays and future development routes to new instruments and materials analysis methods being functional under these working conditions. Opportunities and limits will be discussed. from the perspective of a supplier of scientific instruments. Finally applications, examples and results from existing *In situ* methods like high pressure treatments cells, complete High Pressure or Near Ambient Pressure Photoelectron Spectroscopy Systems (NAP-PES or HP-SPM), liquid and electrochemical cells, Liquid sample "manipulators", and concepts and status of equipment working in highest or lowest temperatures, high magnetic fields and static or dynamic potentials will be demonstrated.

Nanometer-scale Science and Technology
Room: La Cienega - Session NS-TuM

Nanomanufacturing and Nanomachines

Moderator: M. Hersam, Northwestern University

8:00am **NS-TuM1 Nanomanufacturing Processes using Mechanosynthesis Applications**, *S.L. Sullivan*, NanoSource Inc.

Quality, production capacity and production cost have been identified as the current barriers to the implementation of carbon nanotubes and nanofibers within the industrial markets and military applications where such materials offer superior performance benefits. Significant use of nanotubes and nanofibers will require substantial increases in production volume coupled with decreases in production cost of < \$ 15/Kg. Based on low cost, high-volume, high yield, and the ability to highly control diameter, length and chirality, a Mechanosynthesis process was selected as the most viable approach for a scalable, top down mass manufacturing process of nanoscale structures such as nanoparticles, nanotubes and nanofibers that are continuous.

Index Terms- Mechanosynthesis, nanomanufacturing, nanoimprinting, nanofibers, material science.

8:20am **NS-TuM2 Enabling Surface Patterning on Polyhedral and Curved Nanoparticles**, *J.-H. Cho*, Los Alamos National Laboratory, *T. James, D. Gracias*, Johns Hopkins University

It is well known that surface patterning on three dimensional (3D) nanostructures can alter their physical and chemical properties. However, present day nanoparticles such as nanowires and nanopolyhedra have limited to no surface patterning. Lithographic processes enable precise patterning and are very well developed. There are several nanolithographic techniques such as electron beam (e-beam), imprint, and dip pen lithography that can enable patterning, but in an inherently two dimensional manner.

In this talk, we describe strategies to curve and rotate precisely patterned thin film templates to form 3D nanostructures such as cubes, pyramids, tubes, scrolls and talons. The highlight of the approach is that the process leverages already existing nanolithographic techniques and enables structures to be formed with any desired surface patterns in all three dimensions; a line width resolution of 10 nm was achieved.

We utilized multiple layers of electron beam lithography to pattern 2D templates. Patterns with homogeneous (pores in nickel panels) or dissimilar materials (e.g. gold lines on nickel or alumina) were defined. Curvature of hingeless templates and rotation of hinged panels was achieved by triggering grain coalescence in tin (Sn). Polyhedral particles ranging in size from 100-900 nm and surface patterning of 15 nm could be achieved. In

addition, curved nanostructures with both homogeneous (rings, tubes) and variable (spirals, talons) radii of curvature could be formed.

Our demonstration of patterning of self-assembly of precisely patterned polyhedral and curved nanoparticles has material versatility and we believe that this strategy can be utilized to integrate optical, electronic and biological elements on the surfaces of nanoparticles with unprecedented precision and in all three dimensions for a range of applications.

8:40am NS-TuM3 Atomic Precision Fabrication Using Patterned Si Atomic Layer Epitaxy: Processing Capabilities, Throughput Limitations, and Applications, J.N. Randall, J.B. Ballard, J.R. Von Ehr, J. Alexander, R. Saini, Zyvex Labs, J.W. Lyding, Univ. of Illinois at Urbana-Champaign, R.M. Wallace, Y.J. Chabal, Univ. of Texas at Dallas, R.M. Silver, J. Gorman, National Inst. of Standards and Tech., N. Sarkar, Univ. of Waterloo, Canada, T. Toth-Fejel, General Dynamics **INVITED**

Atomically precise Si fabrication technology is being pursued via atomic-precision, H-depassivation lithography with a scanning tunneling microscope (STM) and silicon atomic layer epitaxy (ALE). The details of this process and progress towards its realization are published elsewhere. In this presentation we will cover the expected process capabilities, throughput limitations, applications that will be feasible in spite of these limitations, extensions of the processing capabilities, and paths to scaleup of the throughput. Initially the fabrication process will involve simply patterned homo-epitaxy of Si on Si surfaces, but will allow arbitrary three dimensional structures with some design rules imposed by the Si lattice. The limitations imposed by the physics of the H depassivation lithography and the need for repeated patterning is the principal process bottleneck and leads to estimations of a cost per unit volume of atomically precise fabricated material that seems extremely high. However, the ability to create structures with atomic precision will enable very valuable applications and products that can be cost effectively manufactured in the relatively near term. This process, which can be conceived of as spatially controlled deprotection, appears to be general enough to adapt to the large number of materials that may be deposited with ALE or atomic layer deposition (ALD). Further, there are clear paths to scaling up the process via MEMS-based STM scanner arrays that would significantly widen the range of products and applications resulting from this Atomically Precise Manufacturing technology.

This material is based upon work supported by the Defense Advanced Research Project Agency (DARPA) and Space and Naval Warfare Center, San Diego (SPAWARSYSCEN-SD) under contract N66001-08-C-2040. It is also supported by a grant from the Emerging Technology Fund of the State of Texas to the Atomically Precise Manufacturing Consortium.

9:20am NS-TuM5 Axial Ge/Si Nanowire Heterostructures: Synthesis and Asymmetric Band-gap Engineered Tunnel FETs, S.A. Dayeh, Los Alamos National Laboratory, J. Huang, A. Gin, Sandia National Laboratories, S.T. Picraux, Los Alamos National Laboratory

While new materials and device concepts are being developed to extend CMOS device scaling beyond the 22 nm node, the potential of combining Si/Ge heterostructured materials with the dimensionality of semiconductor nanowires (NWs) remains to be explored. The vapor-liquid-solid (VLS) mechanism allows modulation of doping and alloy composition in the axial NW direction which is the transport direction for NW FETs. This provides an additional degree of freedom for energy band-edge engineering in the transport direction which is difficult to access in planar devices. Such unique aspect of semiconductor nanowires when added to Ge compatibility for integration with Si technology, makes Ge/Si axial NW heterostructures advantageous over other existing material and device possibilities, in particular for tunnel FETs.

This work reports on two significant advances in the area of heterostructure nanowires and tunnel FETs: (i) the realization of 100 % compositionally modulated Si/Ge axial heterostructure nanowires with lengths suitable for device fabrication and (ii) the design and implementation of Schottky barrier tunnel FETs on these nanowires for high-on currents and suppressed ambipolar behavior. A growth procedure was devised to eliminate Au diffusion on the NW sidewalls and minimize random kinking in the heterostructured NWs as deduced from detailed electron microscopy analysis. Our prototype devices resulted in a current drive in excess of 100 $\mu\text{A}/\mu\text{m}$ ($I/\pi D$) and $10^5 I_{\text{on}}/I_{\text{off}}$ ratios over a wide range of source-drain biases, thus exceeding earlier performance results in the literature of tunnel FET devices made of semiconductor nanowires and carbon nanotubes by ~ 2-3 orders of magnitude. These results demonstrate the potential of such asymmetric heterostructures (both in the semiconductor channel and metal-semiconductor barrier heights) for low-power and high performance electronics.

9:40am NS-TuM6 Direct Writing of Polymers using a Heated Probe for Patterning Nanoparticles and Graphene, W.-K. Lee, J.A. Robinson, A.R. Laracuente, Naval Research Laboratory, Z. Dai, W.P. King, University of Illinois at Urbana-Champaign, P.E. Sheehan, Naval Research Laboratory
In thermal Dip Pen Nanolithography (tDPN), a heatable AFM cantilever regulates the deposition of an ink through controlled melting, much like a nanoscale soldering iron. Control over writing is exceptional—deposition may be turned on or off and the deposition rate easily changed without breaking surface contact. tDPN has been successful at depositing polymers ranging from semiconductors to insulators at speeds up to 200 $\mu\text{m}/\text{s}$. Recently, we developed the technique depositing polymer-nanoparticle composites. Nanoparticles and nanoparticles-polymer composites may offer many new capabilities that could greatly advance nanoelectronics, data storage, biosensors, and optical imaging applications. With tDPN, we could deposit with nanoscale precision a wide range of polymers (PMMA, P(VDF-TrFE), polyethylene) that contain nanoparticles or small molecules. An oxygen plasma can remove the polymer to reveal evenly dispersed nanoparticles or, for some combinations, precisely-placed 10 nm wide rows of nanoparticles.

Another substrate, a single layer of graphene on a SiO_2 , was also used to deposit polymers by tDPN. We used the deposited polymer on graphene as an etch mask to pattern graphene nanoribbons (GNRs). Background graphene was then either etched by oxygen plasma to expose SiO_2 or modified by graphene fluoride to form an insulating substrate. The electrical measurements of nanopatterned graphene structures will also be presented.

10:40am NS-TuM9 Understanding and Controlling Rotation at the Single-Molecule Level: Turning Rotors into Motors, H.L. Tierney*, A.D. Jewell, A.E. Baber, E.V. Iski, E.C.H. Sykes, Tufts University

While molecular machines driven by chemical, light or thermal energies can be found throughout nature, little progress has been made toward creating synthetic counterparts. The gap between nature and nanotechnology remains due to the limited fundamental understanding of the transfer of energy to mechanical motion at the nanoscale. Understanding and actuating the rotation of individual molecules on surfaces is a crucial step towards the development of nanoscale devices such as fluid pumps, sensors, delay lines, and microwave signaling applications. Towards this end we have used a group of small molecules in order to understand the fundamental aspects of molecular rotation. Thioethers constitute a simple, robust system with which molecular rotation can be actuated thermally, mechanically and electrically, and can be studied using scanning tunneling microscopy (STM) as a function of molecular chemistry and proximity of neighboring molecules. Interestingly, the thermal onset to rotation was found to be nearly identical for studied thioether molecules with alkyl tails of two carbons or more. It is proposed that this plateau in thermal onset was due to an interplay between degrees of freedom in the alkyl tail vs. the S-metal bond length. While small amounts of thermal energy are capable of inducing rotation, thermodynamics dictates that thermal energy alone cannot be used to perform useful work in the absence of a temperature gradient. Therefore, for molecules to meet their full potential as components in molecular machines, methods for coupling them to external sources of energy that selectively excite the desired motions must be devised. To this end, we have studied using an electrical current to rotate individual dibutyl sulfide molecules on command. For these studies the source of energy is supplied via high energy electrons from the STM tip. By monitoring the rate of rotation as a function of tunneling electron energy (action spectroscopy) we have demonstrated that the rotors can be driven electrically via a mechanism that involves excitation of a C-H stretch. Finally, using theoretical methods the minimum energy adsorption site was determined and the mechanism of rotation was elucidated for the simplest thioether, dimethyl sulfide. These theoretical results indicate that the rotation of a small, simple molecule is actually rather complex; as the CH_3 groups of dimethyl sulfide rotate around the Au-S bond, the central S atom precesses around a surface Au atom.

11:00am NS-TuM10 Atomic Layer Deposition on Self-Assembled Block Copolymer Films, Q. Peng, Y.-C. Tseng, S.B. Darling, J.W. Elam, Argonne National Laboratory

We establish a new method for preparing ordered nanoscale patterns of various materials with tunable domain sizes by applying atomic layer deposition onto block copolymer thin films. The mechanism is based on the selective interaction of the ALD precursors with moieties in one of the polymer blocks. Well aligned, patterned Al_2O_3 and TiO_2 stripes with controllable dimensions were fabricated by applying ALD onto PS-*b*-PMMA block copolymer templates. Moreover, due to the self-limited cyclic deposition nature of ALD, a seed layer generated from Al_2O_3 ALD provides a secondary selective chemistry, which in turn enables a far broader suite of

* Morton S. Traum Award Finalist

materials to be patterned into the PMMA domains. For example, ZnO and W nucleate easily on the PMMA-Al-OH domains formed from one cycle of Al₂O₃ ALD. By carefully designing block copolymers and selecting ALD parameters, patterned designer materials with controlled size, center-to-center space, and composition could be synthesized onto a broad range of substrates.

11:20am **NS-TuM11 In Control of Molecular Motion From Molecular Motors to Nano-Machines, B.L. Feringa**, The University of Groningen, the Netherlands **INVITED**

Inspired by Nature we design nano-scale systems in which the control of dynamic properties of molecules is coupled to specific functions. Molecular machines ultimately require control over structure, organization and function of multi-component molecular assemblies at different hierarchical levels. Major challenges are the integration of kinetic driven processes in multifunctional molecular systems and control over translational and rotary motion.

Molecular switches and motors offer ample opportunity to control functions in a dynamic way. Following the development of the first light-driven unidirectional molecular motor, the focus is now on the control of dynamic functions in more complex systems as well as autonomous motion. Synthetic approaches to various molecular switches and motors and the construction of integrated systems featuring trigger and motor elements are discussed.

Specific challenges that we address are the acceleration of molecular rotary motors and the construction of a nanoscale "windmill park" powered by light. Recent advances in the design of new generation motors that allow the increase of the speed of rotation over a million fold are presented. Furthermore the design of molecular motors in which the rotary direction can be reversed, a molecular crankshaft and brake and molecular transmission phenomena are discussed. Besides rotary motion induced by light, we present unique molecular motors that run on a chemical fuel and discuss our attempts to achieve autonomous motion.

Plasma Science and Technology

Room: Aztec - Session PS1-TuM

Advanced FEOL Etching II

Moderator: A. Agarwal, Applied Materials Inc.

8:20am **PS1-TuM2 Sidewall Polymer Management of sub 20nm Shallow Isolation Trench (STI) Etch via Pulsed Plasma, X. Hua, X. Ji, J. He, J.H. Choi, A. Khan**, Applied Materials Inc.

The thickness of sidewall polymer accumulated on feature is typically a few nanometers during plasma etching. How to manage this thin polymer layer becomes critical to successful pattern transfer by plasma etch, because it equals >10% of the actual feature size as semiconductor devices are aggressively scaled down below 20nm. The impact of this thin layer on conductance of species in the features is not negligible any more when feature size is shrunk below 20nm, especially in high aspect ratio applications. To make minimum depth loadings, i.e. into cell/micro loadings, and ideal feature profiles are extremely challenging and strongly dependent on how we manage this sidewall polymer. In this work, we will discuss how we can utilize pulsed plasmas to manage this polymer layer. Since the residence times of typical plasma etch conditions are in order of ms~s and the period of pulsed plasma is ~ms, species has extra time to move into or out of the feature when it is the off cycle, as compared conventional plasma sources of continuous wave mode. This unique property of pulsed plasma leads to 1) thinner polymer coverage (less redeposition, radicals moving out of the feature) or 2) thicker polymer accumulation (more deposition, radicals moving into the feature from the gas phase), depending on plasma conditions. Better introcell/ micro loadings, more rounded/less pinch off trench bottom are demonstrated by using low duty cycle (<60%) pulsed plasmas than continuous wave plasmas. The influence of duty cycles/frequency of the pulsed plasmas on feature profile, depth loading was investigated in details. In synchronized pulsed plasmas, continuous tapered trench profile is demonstrated with no pinchoff bottom. With optimized duty cycle ratio between source and bias powers, microloading is achieved below 5% of etch depth (>300nm). Pulsed plasma has shown enormous advantage over conventional continuous wave plasma source to control the pattern transfer of future semiconductor fabrications.

8:40am **PS1-TuM3 Feature Scale Model of Shallow Trench Isolation (STI) Etch in HBr Plasma and Comparison with Experiments, S. Sriraman, T. Panagopoulos, A. Paterson, H. Singh, V. Vahedi**, Lam Research Corporation

Continued scaling in the semiconductor industry provides new challenges for critical etch applications in front-end logic and memory devices. As device sizes shrink, control of Shallow Trench Isolation (STI) features to create active area islands become more important. Typical logic STI performance metrics for a 300mm wafer include trench angle, trench depth and iso-dense depth loading and their corresponding within-wafer uniformity. In addition to these metrics, memory STI application includes a challenging requirement for intra-cell depth loading that arises due to within-feature variation of the space critical dimensions (CD) in the dense feature array. These stringent profile control requirements are typically met by operating halogen-based Transformer Coupled Plasma (TCP™) in the mid-pressure operating regime.

This paper will discuss the semi-empirical feature scale model of STI etch in HBr plasma to address iso-dense and intra-cell trench depth loading for an etch stack representative of memory STI features. Plasma diagnostics and reactor-level models are implemented to characterize the HBr plasma produced in the TCP configuration process chamber. Kinetic parameters in the model are constrained by matching simulated feature profiles with those experimentally obtained at various process conditions that are a subset of the process space of interest. The feature scale model is quantitatively calibrated to the experimental profiles and validated for prediction within the process space. The validated profile simulator is used to identify reactor-level process knobs that minimize iso-dense and intra-cell depth loading. The advantages of calibrated process-specific profile simulation in enabling efficient exploration of parameter space during process development and future challenges facing STI trench depth etch will be discussed.

9:00am **PS1-TuM4 Synchronous Plasma Pulsing For Etch Applications, M. Haass*, M. Darnon, E. Pargon, C. Petit-Etienne, L. Vallier, P. Bodart, G. Cunge, CNRS-LTM, France, S. Banna, T. Lill, Applied Materials Inc., O. Joubert, CNRS-LTM, France**

Plasma processes have been used for many years in the manufacturing of semiconductors. They have been so far the only technological solution to address the critical dimension control at the nanometer range imposed by the continuous downscaling of the CMOS devices dimensions.

However, the current etch processes are reaching their limits of controlling the etch selectivity and the critical dimensions at the atomic scale. In this study we investigate the potential of pulsed plasmas to further improve dry etching processes.

The experiments are carried out in a commercially available 300 mm AdvantEdge™ tool from Applied Materials Inc. The inductively coupled plasma is sustained by two RF generators operating at 13.56 MHz, one to generate the plasma and the other mainly to polarize the wafer. These generators have been modified using the Pulsync™ system to allow pulsing at frequencies between 10 Hz and 20 kHz and duty cycles between 10 and 90 %. Even though a delay can be applied between the generators only the synchronous case is studied here. Several modifications of the plasma chamber were carried out in order to use advanced plasma diagnostics like in situ ellipsometry, UV absorption spectroscopy and mass spectroscopy. Furthermore an angle resolved XPS system is connected to the plasma chamber under vacuum allowing quasi in-situ analysis of the wafer surface after etching.

This article focuses on HBr/O₂ plasmas dedicated to STI (Shallow Trench Isolation) etch processes. We demonstrate the ability of synchronously pulsed etch plasmas at different frequencies and duty cycles to modify the etched profiles strongly compared to the standard continuous case. Especially experiments carried out at a frequency of 1 kHz and a duty cycle of 20 % show a very distinct alteration. In this case, ellipsometry measurements indicate a sharp increase in time compensated etch rate (etch rate relative to the actual plasma ON time of the etch process). Additionally, the etched profiles show a strongly enhanced quality, in particular a high selectivity, uniformity and a minimization of the aspect ratio dependent etching phenomena. We demonstrate that these improvements are linked to the balance between plasma dissociation and recombination during the ON and OFF time of the pulsed plasma which can directly influence the composition of neutral and ion flux. This balance is controlled by the duty cycle rather than the pulsing frequency.

* Coburn & Winters Student Award Finalist

9:20am **PS1-TuM5 Characterization of Pulsed Plasma Etch Reactors with an Integrated Global Plasma-Feature Scale Model**, *A. Balakrishna, A. Agarwal, P. Stout, S. Rauf, K. Collins*, Applied Materials Inc.

Uniformity requirements (both etch rate and critical dimensions) for plasma etching of very small features (< 32 nm) are more stringent than ever. One particular challenge is minimizing feature distortion due to plasma induced damage. If the feature aspect ratio is high, via-like features in dielectric materials may physically twist/turn due to the stochastic nature of fluxes entering the feature as the size of the opening shrinks [1]. Limited quantity of polymer on the sidewalls exaggerates this feature distortion. Pulsed plasma operation is a promising approach to improve uniformity while reducing feature distortion [2]. Although pulsing of both capacitively and inductively coupled plasma (CCP/ICP) sources has been investigated before, novel pulsing schemes such as synchronously pulsed ICPs allow for expanded operating regime for damage-free etching of nanoscale features.

In this paper, pulsed and continuous plasma operation of an ICP reactor in electronegative gas mixtures will be discussed using results from a computational investigation. Earlier investigations [3] have linked a 2-dimensional plasma equipment model (HPEM) to a Monte Carlo feature profile model to assess the consequences of pulsed plasma operation on etching. Long computational times restricted the range of conditions that could be investigated, e.g. more complex chemistries or lower pulse frequencies. We have addressed this constraint by using a global plasma model (*Zephyr*) combined with analytical expressions for behavior in the sheath. The global plasma model is based on the methods described by Meeks et al [4]. This model calculates all the species (neutrals, ions and electrons) concentrations and their temperatures using time-dependent conservation equations, including both gas and surface reactions. The impact of different surface materials on plasma chemistry is also captured. The global plasma model is validated using more detailed 2-dimensional plasma modeling and experimental diagnostic results for simple chemistries (Ar, O₂). The validated model is then applied to pulsed plasmas of highly electronegative chemistries used for silicon etching (Cl₂ and HBr based). Results will be discussed for impact of pulse characteristics such as duty cycle, pulsing frequency, and phase lag between source and bias pulses on etching in an ICP chamber.

¹ M. Wang and M.J. Kushner, *J. Appl. Phys.* 107, 023308 (2010).

² S. Banna, et al., *Trans. Plasma Sci.* 37, 1730 (2009).

³ A. Agarwal et al, *J. Appl. Phys.* 106, 103305 (2009).

⁴ E. Meeks, H.K. Moffat, J.F. Grcar and R.J. Kee, SAND96-8218 (1996)

9:40am **PS1-TuM6 Atomic Layer Etching of Graphene using O₂ Radical and Ar Neutral Beam**, *W.S. Lim, Y.Y. Kim, G.Y. Yeom*, Sungkyunkwan University, Republic of Korea

10:40am **PS1-TuM9 Etching of Magnetic Stack for Development of Thermally-assisted Magnetic Access Random Memory**, *J. Pereira, X. Mellhaoui, LTM - UMR 5129 CNRS, France, J. Shin, Crocus Technology, France, E. Pargon, LTM - UMR 5129 CNRS, France, J. Reid, Crocus Technology, France, O. Joubert, LTM - UMR 5129 CNRS, France*

Magnetoresistive Random Access Memories (MRAM) is of great interest since they combine the best characteristics of FLASH, SRAM and DRAM memories: non-volatility, low voltage operation, unlimited read and write endurance, fast read and write operation. One of the key parameters for MRAM technology development is the etching of the Magnetic Tunneling Junction (MTJ). Today, one of the main methods used for MRAM patterning is based on a pure sputtering dual Ion Beam Etching (IBE). However, IBE technique shows some technological limitations that increases the difficulty of MRAM device manufacturing. Indeed, it has low throughput and cannot be used to pattern very dense structures because of shadowing effects. The process can lead to magnetic materials redeposition on the pattern sidewalls that can short-circuit the dielectric tunnel junction. In this paper, we propose to develop plasma etching technologies to pattern complex stacks of MRAM devices as an alternative to IBE process, improving the manufacturability of MRAM devices.

The aim of this work is to investigate a full RIE process for the patterning of Thermally Assisted MRAM (TA-MRAM) dots in ICP reactors (Decoupled Plasma Source from AMAT).

We propose to investigate innovative plasma chemistries (without O₂, Cl₂ to avoid corrosion) to etch the magnetic materials composing the MTJ junction. CO/NH₃ plasmas assisted by temperature could be very promising plasma chemistries to form volatile metal-carbonyl etch by products and avoid redeposition on the pattern sidewalls.

Optical Emission spectroscopy and reflectometry is used to monitor the plasma process. The etching profile, critical dimensions (CD) and possible redeposition on sidewalls are analysed using Scanning Electron Microscopy (SEM), and Focused Ion Beam devices (FIB-SEM, FIB-TEM). The nature

of non-volatile by-products re-deposition is studied using X-Ray Photoelectron Spectroscopy.

11:00am **PS1-TuM10 III-V Etch Challenges for Beyond 20nm Node**, *U. Shah, B. Turkot, M. Radosavljevic, M. Shaw, S. Clendenning, B. Chukung*, Intel Corp.

Plasma Science and Technology

Room: Galisteo - Session PS2-TuM

Plasma Diagnostics, Sensors and Control

Moderator: U. Czarnetzki, Ruhr-University Bochum, Germany

8:00am **PS2-TuM1 Wafer-level Plasma Parameters Measurements in a Multi-Frequency Capacitively Coupled Plasma Discharge**, *L. Dorf, S. Rauf, J.A. Kenney, K. Bera, N. Misra, K. Collins*, Applied Materials Inc.

8:20am **PS2-TuM2 In-situ Measurement of High-Frequency Current and Voltage in Etching Chambers**, *S. Kobayashi, H. Hanawa, K. Ramaswamy, S. Rauf*, Applied Materials Inc.

A set of electrical probes have been developed to measure high-frequency current and voltage, close to electrode surfaces in inductive and capacitive etching chambers. Attenuating radio-frequency (RF) voltage probes are often used for voltage measurements in plasma chambers. However, at high frequencies over 50 MHz, the reading of RF voltage by these probes strongly depends on how the grounding wire is connected to a posited earth point. On the other hand, a voltage probe of the capacitive divider-type provides the voltage reading defined by the direction of dominant electric field, resulting in physically meaningful data even over 100 MHz. The latter approach is therefore taken. Since this voltage probe is designed with a high input impedance, the 50 ohm cable of an arbitrary length can be connected so as to place its sensing part in a small space of a chamber. Our current probe design is based on the pick-up coil approach. However, this current probe is designed to remove contamination of electric field from current reading. After precise calibration, both the probes can be mounted at any surface of the plasma etching chamber.

The probes are firstly used to monitor the etching uniformity in a capacitive plasma discharger operated at 162 MHz. The experimental concept is based on the electrical control methodology proposed by Sobolewski et al. (1999). Due to the 162 MHz standing wave built up in the transmission part of the chamber, the interpretation of current and voltage measurements is not so straightforward. However, the voltage probe, mounted close to the wafer position shows better correlation with etching uniformity compared with another commercialized voltage probe mounted at the exit of the RF match box.

In the second experiment, these electrical probes are used to monitor the phase difference between two floating electrode in a capacitive discharging etching chamber. This experiment is aimed at testing the approach suggested by Bera et al. (2008). While experiments on uniformity-control via RF-phase was reported in the literature of Sung et al. (2009), one problem with these experiments is that the phase shift was monitored in the pre-match position. Unless special care is taken to characterize the match state, the phase change controlled by the phase-shifter would not have provided precise information on phase between the two electrodes. In our experimental set-up, this issue will be overcome by monitoring voltages close to the electrode surfaces.

These preliminary experiments indicate that these high-frequency voltage/current probes have a broad range of in-situ applications in the future design of etching chambers.

8:40am **PS2-TuM3 The Determination of Energy Fluxes in Plasma Surface Interaction**, *H. Kersten*, University of Kiel, Germany **INVITED**

Since the thermal conditions at substrate surfaces affect essentially the interaction of elementary processes during plasma treatment of solid surfaces (deposition, etching, modification), the experimental determination of the energy influx from plasma to substrate is of great importance.

The total energy influx can be measured by special calorimetric sensors (thermal probes). One method is based on the determination of the temporal slope of the substrate surface temperature in the course of the plasma process. The heating curve as well as the cooling curve (after switching-off) are fitted by suitable functions and the time derivatives at same environmental temperature are calculated. By knowing the calibrated heat capacity of the sensor the difference of the time derivatives yields the integral energy influx to the surface. Simultaneously, the electrical current

to the substrate can be obtained and by variation of the sensors bias voltage the energetic contribution of charge carriers can be determined. By using thermal probes of different materials it is even possible to verify the effect of surface recombination, secondary electron emission and sputtering in respect to the energy balance of a substrate in plasma processing. By comparison of the experiments with model assumptions on the involved plasma-surface mechanisms the different energetic contributions to the total energy influx can be separated.

The method will be demonstrated for various process plasmas, e.g. magnetron sputtering (HiPIMS), asymmetric rf-discharge, ion beam source, and ECR afterglow.

9:20am PS2-TuM5 Noninvasive Electrical Monitoring of Ion Current, Ion Energy, Electron Temperature, and Electron Yield, M.A. Sobolewski, National Institute of Standards and Technology

Traditional plasma diagnostic techniques that require inserting a probe into a plasma are not compatible with commercial plasma reactors and the manufacturing environment. In contrast, the radio-frequency (rf) current and voltage across a discharge can easily be measured outside the reactor, without perturbing the plasma or process. Furthermore, the waveforms of rf current and voltage contain information about process-relevant plasma properties. For example, one technique [1,2] has been developed which uses a numerical model of the plasma and its sheaths to analyze the waveforms and determine from them the total ion current and ion energy distributions. This method, however, assumes that the electron temperature is constant, and it neglects any emission of electrons from the electrode or substrate surfaces. To investigate errors arising from these assumptions, variations in electron temperature were measured by a Langmuir probe during fluorocarbon plasma etching of silicon dioxide films, and values for the yield of ion-induced and photon-induced electron emission were estimated. These results allow the resulting uncertainties in ion current and ion energy to be quantified. They also provide tests of how well the existing technique can be extended to also provide monitoring of electron temperature and emitted electron yield, in addition to ion current and ion energy.

[1] M. A. Sobolewski, J. Vac. Sci. Technol. A 24, 1892 (2006).

[2] M. A. Sobolewski, J. Appl. Phys. 95, 4593 (2004).

9:40am PS2-TuM6 Controllable Electron Beam for Optical Emission Studies in Real-Time Process Plasmas, G. Padron-Wells*, P.L.S. Thamban, University of Texas at Dallas, J. Hosch, Verity Instruments, M.J. Goeckner, University of Texas at Dallas

Process control in etch plasma systems are often achieved by optical emission spectroscopy (OES) signals. One such application is etch endpoint detection. In systems where plasma emissions are low, OES signals for process control cannot be employed. To address this problem, a versatile electron extraction method has been developed and used in conjunction with an OES diagnostic system to reliably measure changes in gas composition and emission cross sections for CF₄ plasma etch environments. An inductively coupled plasma source is employed to source electrons in an excitation region where optical emission measurements are conducted. Unique to this design is the control it offers to measure electron impact optical excitation of gas phase species. Cross section response for Argon emission lines with respect to electron beam energy correlates well with published data. Cross section behaviors for the strongest emission lines characterizing the CF_x molecular system are presented. Also, ability to detect 0.1% changes in feedstock gas chemical composition makes this design a highly sensitive end point detection system for analysis of semiconductor process chemistries. Work supported in part by NSF (Grant CBET- 0922962) and Verity Instruments.

10:40am PS2-TuM9 A New Diagnostic Tool of Electron Energy Distribution Function in Capacitive Modes in High Frequency Plasmas, H. Shindo, Y. Nakazaki, Tokai University, Japan

A new diagnostic tool to measure Electron Energy Distribution Function (EEDF) by an emissive probe has been proposed[1] and applied to radio-frequency (RF) plasmas. In particular, the measurements are made in the capacitive mode which is occurred at the various frequencies of 2 to 60 MHz. It is generally difficult for a conventional probe method to measure EEDF in RF plasmas, because of the plasma potential fluctuation, particularly in the capacitive mode. On the contrary, one of the advantages of the present method is that the measurements are free from the high frequency potential fluctuation.

The method is based on measurement of the functional relationship between the floating potential change ΔV_F and the heating voltage V_H of emissive probe. If the Maxwellian plasma is concerned, the following equation can be obtained as a practical and useful formula.[1]

It is important to know that the value of ΔV_F contains information of electron energy distribution with several electron volt interval along the floating potential V_F , because ΔV_F is determined only by the current of plasma electrons with an energy interval.

In the experiments, the values of ΔV_F were measured in the Ar plasmas which were produced by a single-loop antenna[2] in the frequencies of 2 to 60 MHz and the gas pressures of 5 to 100 mTorr. The values of ΔV_F behave quite differently, depending on the frequency and the gas pressure, hence the plasma mode. It is found that the capacitive mode is appeared at the pressures below 20 mTorr at 2 MHz, 10 mTorr at 13 MHz, and at 60 MHz, the behavior of floating potential change ΔV_F is fairly complicated, hence non-Maxwellian plasma. In all capacitive modes, from the data set of ΔV_F and V_F , the electron energy probability function (EEDF) is calculated, and the EEDF thus obtained reveals a bi-Maxwellian with the two electron temperatures depending on the frequencies. For an example, the data set of ΔV_F and V_F at the pressures of 3 to 7 mTorr at 13 MHz revealed the high energy tail with the temperature of 3.0 to 5.0, while at 10 mTorr the EEDF showed a straight line, hence a Maxwellian. At 2 MHz, on the other hand, the capacitive mode was appeared even in higher RF power, but the two temperature mode was not so typical. It should be emphasized that the present diagnostic method becomes powerful in observation of the plasma mode transition in a variety of frequencies.

References:

[1] K.Kusaba and H.Shindo, Review of Scientific Instruments, **78**, 123503-1(2007).

[2] Y.Jinbo and H.Shindo, Applied Physics Express, **2**, 016001-1(2009).

11:00am PS2-TuM10 Frequency Probe Measurements in Processing Plasmas, D.R. Boris, NRL/NRC Postdoctoral Research Associate, S.G. Walton, Naval Research Laboratory, M. Baraket, NRL/NRC Postdoctoral Research Associate, E.H. Lock, R.F. Fernsler, Naval Research Laboratory

Plasma density measurements are an essential tool in understanding and controlling processing plasmas across a wide range of applications. Charge collection probes (Langmuir probes) are of limited utility in depositing plasmas, high pressure applications or in processes that require the use of reactive gases, as these environments result in unreliable data acquisition. Plasma frequency probes are an attractive alternative to Langmuir probes in such applications since they do not suffer significant performance degradation in these environments. Frequency probes are capable of measuring plasma density over a range of 10^8 to 10^{12} cm⁻³ and, it is possible to extract the plasma potential and electron temperature. This presentation details the use of plasma frequency probes, in a variety of different geometries, to measure plasma parameters in unique systems, such as plasma produced by electron beams, operating at higher pressures, or in reactive gases (O₂ and SF₆). Where possible these measurements are compared with Langmuir probe measurements for identical experimental parameters.

11:20am PS2-TuM11 Probe Geometry Induced Electron Energy Distribution Function (EEDF) Distortion, A.E. El Saghir*, E.M. Martin, S.S. Shannon, North Carolina State University

One of the most valuable plasma characteristics that can be obtained from a Langmuir probe is the Electron Energy Distribution Function (EEDF). This is carried out by subtracting the ion contribution of the probe current, the shape of the electron current for probe potentials lower than the plasma potential is used to reconstruct the EEDF. The integral relationship for electron current in the transition region of a single probe voltage-current characteristic has been previously derived for planar probe configurations¹. The Druyvesteyn relation for obtaining EEDF's from Langmuir probes is derived based on a model that assumes that only an electron's energy component perpendicular to the electric field generated by the biased probe determines whether an electron is collected or deflected by the probe when operating with an electron retarding potential. Cylindrical and spherical probe geometries have an additional electron retarding mechanism not accounted for in the Druyvesteyn relation. This additional mechanism comes in the form of a centrifugal retarding potential whose strength is determined by the initial angular momentum when the electrons are far away from the probe. In this work, formulations for cylindrical and spherical geometries are presented. These integral relationships are used to demonstrate the impact of ignoring probe geometry in EEDF extraction and highlights distortion of EEDF's when these geometric considerations are not taken into account. Finally, by combining the integral formulation for cylindrical and spherical probes with the analytical findings of Hoskinson for a finite cylindrical probe², we present a study of the effect of finite length cylindrical probe geometries on EEDF solutions.

¹Druyvesteyn M.J, Z. Phys., vol. 64,1930, pp. 781-798.

²R. Hoskinson, and N. Hershkowitz, Plasma Sources Sci. Technol. vol. **15**, 2006,pp. 85-90.

* Coburn & Winters Student Award Finalist

This work is supported by the UNC General Assembly and a generous gift from Applied Materials

11:40am **PS2-TuM12 How Fast do Ions Fall Out of a Two Ion Species Plasma? Experimental Test of a New Theory**, *N. Hershkovitz, C.-S. Yip*, University of Wisconsin-Madison, *G. Severn*, University of San Diego

Recent experiments have shown that ions in weakly collisional plasmas containing two ion species of comparable densities nearly reach a common velocity at the sheath edge. A new theory suggests that collisional friction between the two ion species enhanced by two stream instability reduces the drift velocity of each ion species relative to each other near the sheath edge and finds that the difference in velocities at the sheath edge depends on the relative concentrations of the species. It is small when the concentrations are comparable and is large, with each species reaching its own Bohm velocity, when the relative concentration differences are large. To test these findings, ion drift velocities were measured near the near sheath edge in Argon-Xenon plasmas as a function of the concentration ratio using the laser-induced fluorescence technique. We show that the predictions are in good agreement with a revised version of the model. This is the first experimental test of the collisional friction model.

Advanced Surface Engineering

Room: Cimmaron - Session SE-TuM

Hard and Nanostructured Coatings

Moderator: I. Petrov, University of Illinois at Urbana-Champaign

8:00am **SE-TuM1 PVD-Oxide Coatings for Tribological Applications**, *H. Rudigier, J. Ramm*, OC Oerlikon Balzers AG, Liechtenstein **INVITED**

In the past, oxide coatings for tribological applications were almost exclusively deposited using chemical vapour deposition technology. The synthesis of corundum type Al-Cr-O coatings at temperatures of the order of 500°C using physical vapour deposition - cathodic arc evaporation in the case of Al-Cr-O - has triggered research activities to explore the potential of oxide materials for wear protection and other tribological applications. An overview of the various attempts to deposit oxides will be given, as well as a discussion of their properties and applications.

8:40am **SE-TuM3 Nanostructure, Bonding, and High Temperature Oxidation of SiZrON Thin Films**, *M.S. Byrne, R.J. Lad*, University of Maine

SiZrON thin films have potential applications as hard high temperature coatings since they combine the oxidation resistance and hardness of oxides with the toughness of nitrides. In this study, a range of $\text{Si}_x\text{Zr}_y\text{O}_z\text{N}_{1-x-y-z}$ thin films with a nominal thickness of 200 nm were deposited onto r-cut sapphire and fused silica substrates at 200°C using reactive RF magnetron co-sputtering of Zr and Si targets in $\text{N}_2/\text{O}_2/\text{Ar}$ gas mixtures. The films were characterized using high resolution scanning electron microscopy (SEM), X-ray diffraction (XRD) and X-ray photoelectron spectroscopy (XPS) in the as-deposited state as well as after annealing treatments up to 1000°C both in air and in vacuum. Grazing incidence XRD indicates that the as-deposited are amorphous for oxygen-rich and Si-rich film stoichiometries, but nanocrystalline ZrN or ZrO_2 phases form within an amorphous matrix for N-rich and Zr-rich films. XPS shows a decrease in the Si, Zr, O, and N Auger parameters as the chemical bonding becomes more ionic with increasing O+Si content. For the different films, the N1s XPS lineshape indicates different states involving Si-N-O, Zr-N-O, and/or O-N bonding. When annealed to 1000°C in vacuum, negligible changes in stoichiometry or nanostructure are observed. However, when the films are heated to 1000°C in air, N depletion and Si enrichment at the film surface is observed, accompanied by the formation of tetragonal phase ZrO_2 nanocrystallites and changes in nanomorphology as observed by SEM. Argon ion depth profiling with XPS was used to investigate the kinetics of the high temperature oxidation process.

9:00am **SE-TuM4 Spinodal Decomposition of $\text{Ti}_{0.33}\text{Al}_{0.67}\text{N}$ Thin Films Studied by Atom Probe Tomography**, *L.J.S. Johnson*, Linköping University, Sweden, *M. Thuvander, K. Stiller*, Chalmers University of Technology, Sweden, *M. Odén, L. Hultman*, Linköping University, Sweden
The metastable solid solution of fcc-TiAlN is of interest both from an industrial perspective, since it is extensively used as a coating for cutting tools, and from a scientific perspective; as questions pertaining to the details of phase transformations in the system, not least spinodal decomposition,

remain [1]. Here, the isostructural decomposition of $\text{Ti}_{0.33}\text{Al}_{0.67}\text{N}$ thin films deposited by cathodic arc evaporation has been studied by atom probe tomography with close to atomic resolution. As-deposited films were found to deviate slightly from a random solid solution, and so be in the earliest stage of decomposition. After annealing at 900 °C for 2 h the films exhibited a spinodally decomposed nanostructure, in an intermediate stage. Results indicate that N segregates to the Al-rich domains in the annealed sample, causing the TiN-domains to be understoichiometric. Furthermore, a possible Kirkendall effect was detected in the annealed sample, with a modulation of the local stoichiometry by 1-2 at. % along the decomposition gradient. The implication of the findings for the age hardening of TiAlN alloy films will also be discussed.

[1] L. J. S. Johnson, Nanostructuring and Age Hardening in TiSiCN, ZrAlN, and TiAlN Thin Films, Licentiate Thesis no. 1442, Linköping University, 2010, <http://urn.kb.se/resolve?urn=urn:nbn:se:liu:diva-56221>

9:20am **SE-TuM5 Structure, Mechanical Properties and Thermal Stability of Zr-Al-N Thin Films**, *P.H. Mayrhofer, L. Chen, D. Holec, D. Luef, R. Rachbauer*, University of Leoben, Austria, *Y. Du*, Central South University

$\text{Zr}_{1-x}\text{Al}_x\text{N}$ thin films were synthesized by magnetron sputtering with AlN mole fractions x ranging from 0 to 0.9. We reveal, via X-ray diffraction (XRD) and transmission electron microscopy (TEM) that the films crystallize in the cubic NaCl (c) structure with $x \leq 0.32$ and the wurtzite ZnS (w) structure with $x \geq 0.75$. For AlN mole fractions between 0.32 and 0.75 the films crystallize with multiple phases and contain a fully percolated disordered phase. This is in agreement with ab initio calculations suggesting that within a broad x range of 0.38–0.75 the cubic, wurtzite and hexagonal (BN structure) are equally preferred with respect to their energy of formation. Lower AlN mole fractions prefer the cubic structure whereas higher AlN fractions favor the wurtzite structure. The maximum hardness of $H \sim 36$ GPa with an indentation modulus of $E \sim 303$ GPa is observed for the single-phase cubic $\text{Zr}_{0.68}\text{Al}_{0.32}\text{N}$ coating. For higher Al contents the hardness rapidly decreases to ~ 22 GPa with $x \sim 0.45$ and then slightly decreases further to ~ 21 GPa for even higher Al contents. This is in perfect agreement with the structural investigations. During thermal annealing to 1500 °C in inert atmosphere the supersaturated phases of the films decompose towards their stable constituents c-ZrN and w-AlN. This is connected with a change in their mechanical properties where two major differences can be observed. The hardness of as deposited single-phase cubic $\text{Zr}_{1-x}\text{Al}_x\text{N}$ slightly increases with annealing to $T_a \sim 1000$ °C due to the formation of cubic Zr- and Al-rich domains. Contrary to this observation the hardness of as deposited multi-phase $\text{Zr}_{1-x}\text{Al}_x\text{N}$ coatings with x values between 0.38 and 0.5 increases by ~ 10 GPa during annealing to ~ 900 °C. Here, the observed hardness increase is mainly based on the structural rearrangement during annealing which results in the formation of crystalline areas with compact interface boundaries. As soon as w-AlN is formed, at around 1100 °C, the hardness decreases for as deposited single-phase cubic and multi-phase $\text{Zr}_{1-x}\text{Al}_x\text{N}$ coatings.

9:40am **SE-TuM6 Growth and Microstructure Analysis of Hafnia-Based Nanostructured Coatings**, *M. Noor-A-Alam, C.K. Roy, C.M. Bradely, A.R. Choudhuri, C.V. Ramana*, University of Texas at El Paso

The aim of this work is to develop nano-structured Hafnia-based coating which can withstand with high temperature environment. Ytria stabilized hafnia (YSH) coatings have been fabricated on Nickel-based super alloy Inconel-738 and stainless steel using PVD method. The coatings have been produced at various temperatures. The thickness of the coating was about 500 nm as demonstrated in the cross-sectional imaging by Scanning Electron Microscopy (SEM). The structural characterization performed by X-ray diffraction (XRD) indicates the cubic crystal structure of YSH coating. Columnar structure has been noticed in all the coatings. The microhardness investigated by using a diamond tip microhardness testing machine indicates 3 Gpa hardness coatings. The temperature stability of these coatings has been examined. The result will be discussed in detail.

10:40am **SE-TuM9 Low Temperature Synthesis of $\alpha\text{-Al}_2\text{O}_3$ Films**, *K. Jiang, F. Nahif*, RWTH Aachen University, Germany, *K. Sarakinos*, Linköping University, Sweden, *S. Konstantinidis*, University of Mons, Belgium, *D. Music, J.M. Schneider*, RWTH Aachen University, Germany
In this study, we deposit Al_2O_3 films using plasma assisted chemical vapor deposition (PACVD) in an $\text{Ar-H}_2\text{-O}_2\text{-AlCl}_3$ atmosphere and by filtered cathodic arc.

During PACVD a novel generator is employed delivering four times larger power densities than those obtained in conventional PACVD approaches. This mode of operation enables the increase of the efficiency of the AlCl_3 dissociation in the gas phase, as well as a more intense energetic bombardment of the growing film. We demonstrate that these deposition conditions allow for the growth of dense films $\alpha\text{-Al}_2\text{O}_3$ with negligible Cl

incorporation and elastic properties similar to those of the bulk α - Al_2O_3 at a temperature of 560 ± 10 °C.

α - Al_2O_3 films are deposited employing a monoenergetic Al^+ beam generated by a filtered cathodic arc. A critical Al^+ ion energy of 40 eV for the formation of the α - Al_2O_3 phase at a substrate temperature of 720 °C is determined. This energy is used as input for classical molecular dynamics and Monte-Carlo based simulations of the growth process, as well as *ab initio* calculations. The combination of theory and experiment indicates that in addition to the well known surface diffusion the previously not considered diffusion in sub-surface regions is an important atomistic mechanism in the phase formation of Al_2O_3 .

11:00am **SE-TuM10 Al-Si-N-O Hard Coatings Prepared by Reactive Magnetron Sputter Deposition from Composite Targets**, *J. Patscheider, M. Parlinska-Wojtan, A. Pélisson, Empa, Switzerland, P. Polcik, Plansee Composite Materials GmbH, Germany, P. Pecher, Glas Troesch AG, Switzerland*

The applicability of hard nitride coatings on a large industrial scale often depends on the sensitivity of their properties on oxygen contaminations. Following the experience of reactive magnetron sputter deposition of optically transparent Al-Si-N thin films by co-sputtering from two elemental targets in a confocal arrangement, the possibility to prepare similar films from powder metallurgical Al-Si targets of different Al/Si ratios in mixed $\text{Ar-N}_2\text{-O}_2$ is investigated. This arrangement is especially interesting when such coatings have to be prepared on an industrial scale. In this work, the effect of oxygen on the coating properties is examined, as reactive elements like Al often cause oxygen to be incorporated as a contamination. It is shown that hardness values up to 28 GPa are reached at oxygen concentrations of several atomic percent. The deliberate addition of O_2 to the reactive gas mixture of Ar/N_2 leads to the incorporation of oxygen up to 20 atomic %. Despite these very high concentrations hardness values of 25 GPa are reached. Similar to silicon, oxygen additions cause grain refinement and a gradual disappearance of the columnar structure with increasing oxygen content. It is shown that the hardness is primarily influenced by the plasma density and to a lower extent by other factors like silicon content and preferred orientation.

11:20am **SE-TuM11 A New Approach to the Synthesis of Adherent Hard Coatings with High Toughness**, *A.N. Ranade, Northwestern University, L.R. Krishna, International Advanced Research Centre (ARCI), India, Y.W. Chung, Northwestern University*

Traditional ceramic coatings provide abrasive wear protection due to high hardness. However, these coatings have low fracture toughness, making them susceptible to surface or internal flaws and failure under high impact loads. In addition, when ceramics are deposited onto metal substrates, lower thermal expansion coefficients compared to those of metals can cause thermal stress that may result in delamination. This paper explores a new approach to the synthesis of adherent hard coatings with high toughness. The approach begins with a metal matrix identical to that of the substrate, followed by the incorporation of nanoscale hard particles to increase hardness by Orowan strengthening. Theoretical estimates indicate that incorporation of 10 vol. % of such nanoscale particles can raise the hardness by as much as 20 GPa. The coating matrix is identical to that of the substrate, resulting in maximum adhesion and minimum thermal stress. Furthermore, by choosing nanoscale particles whose structure is semi-coherent with the metal matrix, local stress at the particle-matrix interface may activate the motion of screw dislocations, thus preserving the high fracture toughness of the matrix. This paper will present initial results of this exploration, using Ti as the matrix and semi-coherent TiB_2 nanoparticles as the strengthening agent. Characterization tools include x-ray diffraction (structure), AFM (surface roughness), SEM/TEM (size and distribution of nanoparticles), nanoindentation (elastic modulus, hardness, and fracture toughness), and scratch testing (adhesion), as a function of nanoparticle concentration. These studies should provide a general strategy for designing adherent hard coatings with high toughness.

11:40am **SE-TuM12 Oxidation and Diffusion Study on AlCrVN Hard Coatings using Oxygen Isotopes ^{16}O and ^{18}O** , *R. Franz, University of Leoben, Austria, J. Schnoeller, H. Hutter, Vienna University of Technology, Austria, C. Mitterer, University of Leoben, Austria*

In the commonly applied procedure to study the oxidation behavior of hard nitride and carbide coatings, the sample is heated to a certain temperature and exposed to an oxygen-containing atmosphere during a defined period of time. Subsequently, the oxidized specimen is analyzed as to the thickness and morphology of the oxide layer or the composition and chemical nature of the oxides. In order to gain more information about the mechanisms active during oxidation the procedure can be split into two stages where different isotopes, ^{16}O and ^{18}O , are introduced in each step. An analysis by means of secondary ion mass spectrometry depth-profiling with its inherent

isotope selectivity allows for an investigation of the general oxidation behavior as well as the oxygen diffusion during the oxidation process. In the present case, two AlCrVN coatings of equal composition but different crystal structure were studied. The single-phase coating with its face-centered cubic (fcc) structure presents a higher oxidation resistance as compared to the dual-phase coating containing a wurtzite and a fcc phase. After the annealing treatment, the surface of the latter is entirely covered by VO_2 and V_2O_5 as evidenced by Raman spectroscopy. The single-phase coating, on the other hand, reveals unoxidized coating material and AlVO_4 crystals. However, even though exhibiting a significantly different oxidation resistance, the oxygen diffusion is similar. In both cases peak values of ^{18}O , which was introduced in the second stage, were found near the oxide-nitride interface indicating that O atoms diffused through the already formed oxides. Additional experiments using a gas mixture comprising natural water vapor H_2^{16}O and $^{18}\text{O}_2$ revealed that mainly the molecular oxygen serves as source for the formation of oxides as with increasing water vapor partial pressure the oxide layer thickness was significantly reduced.

Surface Science

Room: Picuris - Session SS1-TuM

Catalysis on Metal and Alloy Surfaces

Moderator: A.J. Gellman, Carnegie Mellon University

8:00am **SS1-TuM1 Sulfur-Induced Reconstruction of the Ag(100) Surface**, *S.M. Russell, M. Shen, Iowa State University, C.J. Jenks, D.-J. Liu, Ames Laboratory, US-DOE, P.A. Thiel, Iowa State University & Ames Laboratory, US-DOE*

Sulfur adsorption on Ag(100) is the object of this investigation because sulfur affects reshaping and decay of Ag nanostructures on this, and other, surfaces. We have studied sulfur on Ag(100) using STM. Consistent with prior LEED work [1-2], we find two structures that coexist at room temperature: a $\sqrt{2} \times \sqrt{2}$ chemisorbed phase, and a $(\sqrt{17} \times \sqrt{17})R14^\circ$ reconstruction, the latter being the phase with higher sulfur coverage. As sulfur coverage increases, sulfur atoms replace Ag in the surface plane to form the $\sqrt{17}$, resulting in ejection of Ag and development of $\sqrt{17}$ islands on the terraces. DFT supports a model in which 5 Ag atoms are ejected per unit cell. In STM, the dominant local motif of the $\sqrt{17}$ reconstruction consists of rectangular groups of (primarily) four sulfur atoms, very similar to sulfur on Cu(100) in the $\sqrt{17}$ phase [3]. At room temperature, the $\sqrt{17}$ islands are dynamic, and can develop extensions of disordered material that link and island, transiently, to another $\sqrt{17}$ island or domain.

References

- [1] G. Rovida and F. Pratesi, *Surf. Sci.* **104**(2-3), 609 (1981).
- [2] M. P. Sotito and J. C. Boulliard, *Surf. Sci.* **162**(1-3), 285 (1985).
- [3] M. L. Colaiani and I. Chorkendorff, *Phys. Rev. B* **50**(12), 8798 (1994).

8:20am **SS1-TuM2 In-situ Spectroscopic Investigation of Adsorption and Reaction of Pyridine Molecules on Modified Pt Surfaces**, *R. Denecke, C. Wöckel, K. Fischer, S. Wickert, Universität Leipzig, Germany, R. Streber, Universität Erlangen, Germany*

Using high-resolution and time-dependent x-ray photoelectron spectroscopy (XPS) adsorption and reaction processes can be followed in-situ. From the data, adsorbed species as well as reaction intermediates and products can be determined and quantitatively analyzed. Time-dependent data allow for the determination of kinetic parameters.

We are applying this method to pyridine molecules adsorbed on flat and stepped Pt surfaces. Using a regularly stepped Pt(355) surface with (111) oriented terraces which are five atomic rows wide and (111) oriented monatomic steps, C 1s and N 1s core level data are recorded during adsorption at various temperatures. As additional parameter, the free Pt terrace width is varied by deposition of Ag atoms on the surface. At 300 K, they form rows along the step edges, thus effectively reducing the terrace width. Following the core level data while increasing the temperature with a fixed heating rate, temperature-programmed XPS data allow to follow the thermal reaction of the adsorbed species. The experiments have been performed at the synchrotron radiation facility BESSY II in Berlin.

Literature reports a temperature- and coverage-dependent reorientation of the pyridine molecules on Pt(111) [1]. While at 300 K an upright molecule is proposed, the situation changes for low temperatures from flat-lying at low to upright at higher coverages. In line with these reports, we observe distinct changes in the core level binding energies and intensities. While at 200 K only one strong N 1s feature is observed for all coverages, there is a change from two features to one for 300 K. Here, the remaining feature is

observed at a higher binding energy. Temperature-dependent data show the change from the low to the high energy feature. This is accompanied by respective changes in the C 1s data, thus suggesting again temperature- and coverage-dependent changes.

The presence of steps and especially their decoration by Ag changes the situation quite drastically. This manifests itself in changed binding energies and reaction schemes. From a comprehensive analysis a scheme for adsorption and thermal reaction of pyridine on Platinum surfaces is derived.

[1] S. Haq, D.A. King, *J. Phys. Chem.* 100 (1996) 16957.

8:40am **SSI-TuM3 Mechanisms of Catalytic Processes on Au: Imaging, Spectroscopy and Reactivity.** *C. Friend, Xu, Liu, Baker, Haubrich, R.J. Madix*, Harvard University **INVITED**

The need for energy-efficient catalytic processes and the long fascination with Au as a material has spurred intense activity in the investigation of gold-based catalysis. There is on-going discussion of the origin of the activity of gold for oxidation reactions, including changes in the oxidation state and electronic properties of Au nanoparticles. We have demonstrated that atomic oxygen bound to Au is highly active for a range of oxidative transformations on metallic Au. Well-prepared gold crystal surfaces are inactive for O₂ dissociation, so that ozone was used as an oxidant in order to probe the bonding and reactivity of O on Au. Oxidation of Au(111) leads to the release of Au nanoparticles on which O is adsorbed. A combination of scanning tunneling microscopy (STM), high resolution electron energy loss spectroscopy experiments complemented by density functional theory calculations show that the local bonding and degree of longer range order of the O-Au islands depends on the temperature of oxidation and the overall O coverage. Reactivity studies show that low coverages of O bound in sites of local three-fold coordination are most active for selective reactions. Investigations of the molecular-scale mechanism for oxidative coupling reactions promoted by atomic oxygen on Au will be presented. Oxidative coupling of oxygenates—alcohols and aldehydes—will be the focus of the talk. The coupling reactions yield organic esters, which are important products industrially because of their widespread use as precursors for fragrances, flavorings, and fabrics. We construct a general mechanism for this class of reactions that provides insight into the optimum conditions of selectivity for even complex mixtures of alcohols. These fundamental studies will also be related to parallel studies using nanoporous Au as a catalyst at atmospheric pressure to illustrate the value of fundamental studies of catalytic processes. In this case, the reactions of Au under ultrahigh vacuum conditions provide an understanding of reactions at higher pressure because of the low intrinsic reactivity of Au itself, the weak bonding of water to Au, and the low steady state concentration of reactants on the surface even at high pressure because of the low rate of O₂ dissociation on Au. This is an unprecedented success in bridging the pressure gap between fundamental studies and working catalytic conditions.

9:20am **SSI-TuM5 An Atomic-scale View of Metal Alloy Surface Chemistry.** *E.C.H. Sykes*, Tufts University

Palladium and its alloys play a central role in a wide variety of industrially important applications such as hydrogen reactions, separations, storage devices, and fuel cell components. The exact mechanisms by which many of these processes operate have yet to be discovered. Low-temperature scanning tunneling microscopy (STM) has been used to investigate the atomic-scale structure of Pd/Au and Pd/Cu bimetallics created by depositing Pd on both Au(111) and Cu(111) at a variety of surface temperatures. We demonstrate that *individual isolated* Pd atoms in an inert Cu matrix are active for the dissociation of hydrogen and subsequent spillover onto Cu sites. The same mechanism does not operate for Pd in Au(111) surfaces, however, because the spillover is thermodynamically unfavorable. These results demonstrate the powerful influence an inert substrate has on the catalytic activity of individual Pd atoms supported in its surface. In addition, differential conductance spectroscopy has enabled the electronic structure of these active sites to be measured and quantitatively compared to that of the host metal.

9:40am **SSI-TuM6 Prediction of Surface Ensembles in Au-based Bimetallic Alloys using Combined DFT and Monte Carlo Simulations.** *J.A. Stephens, H.C. Ham, G.S. Hwang*, University of Texas at Austin

Bimetallic materials have shown great promise for the development of superior catalysts. The recent surge of new interest in catalysis by gold has led researchers to investigate the effects of adding gold to other metals. While mechanisms underlying the alloying effect are still not understood in detail, recent evidence suggests that the enhanced reactivity of bimetallic catalysts can be attributed to a combination of metal-metal interactions (ligand effect) and unique mixed-metal surface sites (ensemble effect). The ability to accurately predict the arrangements of constituent atoms in a surface alloy is indispensable to unraveling the roles played by the ensemble and ligand effects in the performance of bimetallic model

catalysts. We have developed a scheme to predict the equilibrium arrangement of atoms in surface alloys at finite temperatures. It is based on the Ising model and is capable of reproducing DFT-predicted total energies to within no more than a few meV per surface atom. We have used it successfully to predict monomer and dimer concentrations in Au-Pd and Au-Pt fcc (111) surface alloys. The scheme will be presented in detail, as well as what we have learned about the effects of temperature and composition on ensemble formation in both fcc (111) and (100) surface alloys, including the size and shape distributions of larger ensembles. We will also discuss how the atomic arrangements affect the reactivity of gold-based alloy surfaces, particularly towards oxidation of hydrogen and carbon monoxide.

10:40am **SSI-TuM9 Structure and Segregation at Clean and Oxidized Pd₃Fe(111) Alloy Surfaces.** *X. Yang, B. Koel*, Lehigh University

Pd/Fe alloy catalysts have attracted attention in PEM fuel cell research because they have been found to be comparable to Pt electrocatalysts in oxygen reduction reaction (ORR) kinetics at the cathode. Higher electrocatalytic activity is also found when these bimetallic nanoparticles act as a support of Pt or Pd monolayers. The mechanism of enhancing ORR kinetics with this alloy is not well understood. We report here on the structure and segregation at a clean and oxidized Pd₃Fe(111) alloy using LEED, LEIS, XPS, and STM. Pd starts to segregate at the surface at 600 K and reaches a coverage of 0.9 monolayers at 1100 K. STM reveals a complex structure with 0.17 monolayers of Pd adatoms on top of the outmost alloy layer, which is different from other well-studied binary alloy systems. The experimental observation of this unusual Pd structure is supported by DFT calculations. Adsorption of oxygen reverses the segregation trend and causes Fe atoms to accumulate on the surface. Fe at the surface is oxidized by oxygen and initially protects Pd oxidation. Oxygen adsorption at different temperatures caused the formation of nanoclusters at lower temperatures (300-500 K) and several well-organized surface structures at higher temperatures. Such studies of structure, segregation and oxidation of these model Pd/Fe alloy catalysts may help explain the origin of enhanced ORR kinetics using these alloys.

11:00am **SSI-TuM10 Role of Ensembles in Determining the Catalytic Activity of Au-Pd and Au-Pt Surface Alloys towards CO Oxidation and Oxygen Reduction Reaction: A First Principles Study.** *H.C. Ham, J.A. Stephens, G.S. Hwang*, University of Texas at Austin

Gold-based bimetallic alloys have been found to significantly increase catalytic efficiency, compared to their monometallic counterparts in various reactions including low temperature oxidation of CO, direct synthesis of H₂O₂ from H₂ and O₂, and production of vinyl acetate monomers. Recent experimental and theoretical studies have suggested that the reactivity of bimetallic catalysts can be governed by creation of unique mixed-metal surface sites (ensemble effect) and/or electronic structure change by metal-metal interactions (ligand effect), while mechanisms underlying the alloying effect still remain unclear. In this talk, we will present the recent results of our first principles calculations on the mechanisms of CO oxidation and oxygen reduction reaction (ORR) on AuPd and AuPt alloy surfaces. Using periodic density functional theory calculations, we find that the rate of CO oxidation can be a strong function of Pd/Pt ensembles, while the ensemble effect is likely to be more important in the AuPd case. In addition, we find that ORR tends to be promoted on PdAu alloys, compared to the pure Pd case. This work provides valuable hints on the importance of the interplay of the ensemble and ligand effects in determining the catalytic activity of Au-based bimetallic catalysts particularly toward CO oxidation and ORR.

11:20am **SSI-TuM11 Adsorption Studies on Unsupported PdZn Alloy Powders.** *B. Halevi*, University of New Mexico, *B. Kiefer*, New Mexico State University, *K. Artyushka, P. Atanassov, A. Datye*, University of New Mexico

Estimating the true catalytically active surface area for complex 3-D surfaces such as powders is both important for evaluating the true catalytic performance of the material and difficult. Since most industrially relevant catalysts are metallic particles supported on Carbon or Oxides evaluating their chemically relevant surface area is even more difficult. In an effort to better quantify the active surface area of supported catalysts we synthesized an unsupported phase pure and compositionally homogeneous PdZn powder and evaluated by DFT and experiments the thermo- and electro-chemical adsorption of H₂, O₂, and CO on the powder. These benchmark values can be used to evaluate the available surface area of supported catalysts as well.

11:40am **SSI-TuM12 Reactivity of Epitaxial Vanadium Oxide Layers.** *M. Li, E.I. Altman*, Yale University

Monolayers of vanadia supported on other oxides can be uniquely active and selective for a number of reactions including the selective catalytic reduction of NO and the partial oxidation of methanol to formaldehyde. A

number of explanations have been offered in the literature to explain the unique properties of vanadia monolayers and the influence of the support, but these have been hampered by the inability to control both the chemical interaction of the vanadia with the substrate and the structure of the vanadia layer. We have addressed this issue by using oxygen plasma-assisted molecular beam epitaxy (OPA-MBE) to grow ordered vanadia monolayers and multilayers on rutile (110), anatase (001) and (101), $\text{WO}_3(100)$ and $\text{LaCoO}_3(100)$. By control of the atomic oxygen flux, monolayers and multilayers with the same surface structure can be obtained. For the monolayers, oxygen adsorption oxidizes all of the vanadium to 5+ while for the multilayers the bulk stoichiometry is VO_2 but oxygen adsorption oxidizes the surface to V_2O_5 . Comparing the reactivity of monolayers and multilayers of vanadia on rutile (110) and anatase (001) reveals the importance of direct chemical interactions with the support versus the importance of maintaining non-bulk V_2O_5 structures. For both the rutile and anatase support, we find that as long as the films are epitaxial that the direct chemical interaction with the support is not required to observe oxidative dehydrogenation of 1-propanol to propionaldehyde in thermal desorption; vanadia on both supports desorbed 1-propionaldehyde in a peak at ~ 400 K independent of the thickness of the vanadia layer. Differences between anatase and rutile as well as monolayers and multilayers were observed however. In particular, the fraction of adsorbed alcohol that reacted on the vanadia monolayer was much higher than any other vanadia surface, a finding attributed to the propensity of the rutile (110) surface to form defects that are highly active for alcohol deprotonation, the first step in the reaction. Thus the titania supports can influence the reactivity by both stabilizing reactive, non-bulk structures, and by facilitating the first step in reactions of alcohols. The reactivity data will be compared with results for vanadia on $\text{LaCoO}_3(100)$ which has the same surface unit cell as anatase (001), and thus in the monolayer regime the influence of chemical interactions on the reactivity of the vanadia are characterized with the structure held constant.

Surface Science

Room: Santa Ana - Session SS2-TuM

Aromatic Molecular Films

Moderator: C. Wöll, Karlsruhe Institute of Technology, Germany

8:00am SS2-TuM1 Relating Aromatic Molecule Structure to Film Structure/Property Relationships, J.E. Anthony, University of Kentucky
INVITED

The ease with which small-molecule organic semiconductors can be functionalized allows a single chromophore framework to be tuned for use in a myriad of electronic applications. Careful selection of substituents allows tuning of both solubility and crystal packing, allowing optimum structures for both film morphology and charge transport to be dialed in by careful structure-property studies. Additional substituents on the chromophore can be added to improve stability, shift phase transitions, or change the dominant carrier type for the material. Using 4, 5 and 6 fused-ring acenes and heteroacenes as the chromophore, our straightforward functionalization approach has created organic materials for use in high-performance organic transistors and organic solar cells. The crystal-packing arrangements for these two types of devices are dramatically different. This talk will examine how materials with two-dimensional π -stacking arrangements yield high-performance transistors, and how subtle tuning of the substituents can further improve performance and alter solubility. In the optimum case, hole mobility as high as $5 \text{ cm}^2/\text{Vs}$ was observed from a dip-cast film. Structure-property relationships in organic transistors are also explored in high-quality single crystals, showing how changes in crystalline order changes the intrinsic carrier properties of a homologous series of materials. In the case of bulk heterojunction organic solar cells, substitution of the acene chromophore with small electron-withdrawing groups yielded effective acceptors in blends with polythiophene donors. In this case, materials with strong π -stacking interactions yielded the poorest-performing solar cells. In contrast, materials with weak, 1-dimensional π -stacking interactions yielded the best performance, with power conversion efficiencies greater than 1.5% in these fullerene-free blends.

8:40am SS2-TuM3 Optimal Electron Doping of a C_{60} Monolayer on Cu(111) via Interface Reconstruction, W.W. Pai, National Taiwan Univ., H.T. Jeng, Academia Sinica, Taiwan, C.-M. Cheng, National Synchrotron Radiation Research Center, Taiwan, C.-H. Lin, National Taiwan Univ., X.D. Xiao, A.D. Zhao, X.Q. Zhang, Hong Kong Univ. of Sci. and Tech., G. Xu, X.Q. Shi, M.A. Van Hove, City Univ. of Hong Kong, C.-S. Hsue, National Tsing Hua Univ., Taiwan, K.-D. Tsuei, National Synchrotron Radiation Research Center, Taiwan

We demonstrate the charge state of C_{60} on a Cu(111) surface can be made optimal, i.e., forming C_{60}^{3-} as required for superconductivity in bulk alkali-doped C_{60} , purely through interface reconstruction rather than with foreign dopants [1]. We link the origin of the C_{60}^{3-} charge state to a reconstructed interface with ordered (4×4) 7-atom vacancy holes in the surface. In contrast, C_{60} adsorbed on unreconstructed Cu(111) receives a much smaller amount of electrons. Specifically, we used multiple techniques of scanning tunneling microscopy and spectroscopy (STM/STS), angle-resolved and angle-integrated photoemission spectroscopy (AR-AI-PES), ab initio calculations, and low-energy electron diffraction I-V analysis (LEED I-V) to convincingly establish the C_{60}^{3-} charge state and the reconstructed interface model. With STM, in-situ monitoring of C_{60} growth at ~ 400 K revealed that each C_{60} removes 7 atoms. STS showed the LUMO band sits nearly at the Fermi energy when the interface is reconstructed, or ~ 0.8 eV above the Fermi energy at unreconstructed interface. AI-PES indicated the initial charge state of C_{60} over reconstructed interface is already close to C_{60}^{3-} because very few extra K atoms are needed to reach maximal LUMO spectra intensity. AR-PES showed two hole-like bands crossing Γ bar that account for most of the charge transfer, and a shallow electron-like band near Γ bar. An extensive LEED I-V analysis using a total fitting range of ~ 3500 eV and 33 independent beams resolved the preferred structure model as the unfaulted fcc 7-atom monolayer vacancy model. We obtained a very good Pendry factor of ~ 0.27 . Finally, although the C_{60} has an optimal doping level for bulk superconductivity, we did not observe surface superconductivity down to ~ 5 K. Our result adds a new dimension in understanding functional molecular thin films; it illustrates a definitive interface structure-doping effect that affects the electronic properties of molecule-electrode contact.

[1] Woei Wu Pai et al., *Phys. Rev. Lett.* **104**, 036103 (2010)

9:00am SS2-TuM4 Pattern Formation of Arenes and their Derivates on Cu(111), D.Z. Sun, D.H. Kim, Z.H. Cheng, Y.M. Zhu, W.H. Lu, M. Luo, University of California at Riverside, S. Hong, T.S. Rahman, University of Central Florida, L. Bartels, University of California at Riverside

Intermolecular force plays an important role in self-assembly and surface pattern formation. Unsubstituted arenes, such as anthracene, attach to a metallic substrate predominantly through van der Waals interaction leading to substrate binding that is less sensitive to the precise adsorption configuration and allows a range of ordered surface patterns. In contrast, substitution of the arenes can lead to strong intermolecular forces within the film and amplified substituent-substrate interactions that strictly define the adsorption configuration and film pattern. In this contribution we present the pattern formation of anthracene on Cu(111) and show how addition of thiol and carbonyl groups can vary the resultant surface pattern. For each case we investigate the chemical and physical interaction underlying the pattern formation using a combination of variable temperature scanning tunneling microscopy (STM) imaging and density functional theory (DFT) simulation.

9:20am SS2-TuM5 Step Edge Barriers and Island Nucleation in Organic Thin Film Growth, C.K. Teichert, A. Hlawacek, S.B. Lorbek, P.C. Puschnig, D. Nabok, C.E. Ambrosch-Draxl, University of Leoben, Austria, P.F. Frank, T.G. Potocar, A.H. Winkler, Graz University of Technology, Austria

Crystalline films of conjugated organic semiconductors offer attractive potential for optoelectronic and electronic applications on flexible substrates. Due to the complexity and anisotropy of the molecular building blocks, novel growth mechanisms can occur as is demonstrated for the growth of the rod-like oligophenylene molecule paraxiphenyl (6P) on mica surfaces. On clean mica(001), the self-organization of crystallites into one-dimensional chains is observed on a wetting layer where the 6P molecules lie flat with their long molecular axis parallel to the surface [1].

Here, we demonstrate by atomic force microscopy that on an ion bombarded mica surface, the formation of terraced mounds composed by almost upright standing molecules is observed. In inorganic growth systems such a mound morphology is frequently due to a kinetic effect, the so-called Ehrlich-Schwoebel barrier for step-edge crossing [2]. Quantitative analysis of the mound morphology together with transition state theory calculations revealed the existence of molecule bending during step edge crossing and level dependent step edge barriers [3]. A lower barrier due to a larger molecular tilt angle (with respect to the surface normal) in the first layer

results in the completion of one monolayer before mound formation starts. This is convincingly demonstrated by transverse shear microscopy measurements.

By temperature and rate dependent growth experiments we also determined the size of the critical nucleus to be significantly larger than one. These findings are again complemented by force-field calculations revealing the size of an energetically stable island of upright standing molecules.

Our analysis shows that procedures developed and verified for inorganic systems [2] can be successfully applied to organic thin film growth. However, we have also demonstrated that the complexity and anisotropy of the molecular building blocks lead to additional effects [3] that are not observed in atomic inorganic growth systems.

[1] C. Teichert G. Hlawacek, A. Andreev, H. Sitter, P. Frank, A. Winkler, N.S. Sariciftci, Appl. Phys. A **82** (2006) 665.

[2] T. Michely and J. Krug; Islands, Mounds and Atoms (Springer, Berlin 2004).

[3] G. Hlawacek, P. Puschnig, P. Frank, A. Winkler, C. Ambrosch-Draxl, C. Teichert, Science **321** (2008) 108.

This work has been funded by Austrian Science Fund (FWF) within NFN "Organic Thin Films" Projects S9707 + S9714 as well as P19197.

9:40am **SS2-TuM6 Filamentous C₆₀ Structures at C₆₀:ZnPc Interfaces**, L. Tskipuri, W. Jin, Q. Liu, J. Weeks, University of Maryland, D.B. Dougherty, North Carolina State University, S.W. Robey, NIST, J.E. Reutt-Robey, University of Maryland

Since the introduction of the bulk heterostructure concept, efficiencies of organic photovoltaic devices have improved markedly. This has spurred intense interest in controlling chemical morphologies to achieve more efficient charge separation. Unfortunately, there is surprisingly little guidance on how to achieve vertical nanophase separation in small-molecule materials. Basic studies of interface formation and nanophase separation in molecular materials are needed to understand how local chemical forces direct chemical morphology.

We present STM investigations of interface-formation and nanophase separation in binary films of zinc phthalocyanine (ZnPc) and C₆₀ on Ag(111) and Au(111) supports. Physical vapor deposition provides exquisite control of the growth kinetics, allowing access to both metastable and thermodynamic phases. We demonstrate the controlled formation of ZnPc:C₆₀-1D and 2-D interfaces with distinctive molecular orientations and packing densities. Of particular interest is the formation of filamentous C₆₀ structures at the ZnPc surface. C₆₀ chains of single-molecular width wander the ZnPc substrate without registration to the underlying ZnPc template, islanding into a disordered chain phase. (Similar structures are also observed on Pn and 6-T surfaces.) These structures are reminiscent of dipole fluids (albeit of single molecular widths!) We present detailed measurements and analysis of C₆₀ wandering chain formation on ZnPc/Ag (111) and ZnPc/Au (111) substrates. We then explore the physical origin of these structures through simulations with a model potential that incorporates short-range C₆₀ - C₆₀ attraction and a long-range dipolar repulsion. From simulations of realized structures, we estimate the effective dipole needed for chain formation. We account for unexpected magnitude through the combined influences of the charge-transfer (interface) moment and the induced moment in these highly polarizable materials.

**This work has been supported by the UMD MRSEC (DMR 0520471) and NSF Surface and Analytical Chemistry (CHE0750203)

10:40am **SS2-TuM9 Manipulating Island Density and Shape in Organic Thin Film Growth: the Nucleation of Perfluoropentacene on Self-Assembled Monolayers**, T.V. Desai, A.R. Woll, J.R. Engstrom, Cornell University

We have examined the nucleation and growth of perfluoropentacene (PFP) on SiO₂ and on a variety of surfaces possessing different terminating self-assembled-monolayers (SAMs) using *in situ* synchrotron x-ray scattering and *ex situ* atomic force microscopy (AFM). The SAMs ranged from very low surface energy hydrophobic surfaces (perfluorooctyltrichlorosilane, FOTS), to higher surface energy hydrophilic surfaces (3-methacryloxypropyltrichlorosilane, MAOPTS). From real time x-ray scattering we find that the growth of PFP, while crystalline, becomes very 3D after completion of the first 1-2 monolayers, independent of the substrate surface termination. Concerning growth in the submonolayer regime, we find that nucleation is homogeneous, and that the absolute density of islands depends strongly on the surface termination, while the relative change of the island density with increasing growth rate is essentially independent of the underlying SAM. From the latter we find that a critical island size of ~ 3 molecules can describe all the data. On the other hand, the dependence of the island density on termination implicates a significant change in the diffusivity of PFP with the identity of the SAM, with values differing by over 2 orders of magnitude. The shape of the

islands also depends on the surface termination, but somewhat unexpectedly—the islands are most compact and faceted on surfaces where the diffusivity of isolated PFP molecules is the smallest. The shapes of the islands on these surfaces can be interpreted by arguments based on equilibrium, where polygonal islands expose low energy facets. These results demonstrate the sensitivity of the initial stages of nucleation to the nature and identity of the underlying substrate.

11:00am **SS2-TuM10 Surface Structure Directed Chemistry: A Scanning Tunneling Microscopy Study of Chemically Reactive Self-Assembled Monolayers**, D.H. Dahanayaka, The University of Oklahoma, R.D. Abrahams, University of Maryland, A. Singh, L.P. Jackson, L.A. Bumm, R.L. Halterman, The University of Oklahoma

Self-assembled monolayers (SAMs) are flexible substrates for surface chemistry. A wide variety of SAM-surface functionalities can be prepared using alkanethiols with different terminal functional groups. Typically this requires a different alkanethiol for each. Another strategy uses a single alkanethiol to create a reactive surface which can be chemically modified post self-assembly. We are exploring azido-functional monolayers, which are reactive under mild conditions. The best known reaction is the copper catalyzed catalytic 1,3-dipolar cycloaddition with terminal alkynes. This approach has already been demonstrated for general surface chemical modification. We demonstrate molecularly-resolved STM imaging of these SAMs before and after the reaction. The surface structure affects the local reactivity and can be used to direct the reaction at the nanometer scale.

This work has been supported by NSF CAREER grant No. CHE- 0239803, NSF MRSEC No. DMR-0080054, and NSF No. DMR-0805233.

11:20am **SS2-TuM11 Molecular Organization and Odd-Even Effects in in Perfluoroterphenyl-Based Monomolecular Films**, F. Chesneau, Universität Heidelberg, Germany, B. Schüpbach, Universität Frankfurt, Germany, K. Szelągowska-Kunstman, Jagiellonian University, Poland, N. Ballav, Universität Heidelberg, Germany, P. Cyganik, Jagiellonian University, Poland, A. Terfort, Universität Frankfurt, Germany, M. Zharnikov, Universität Heidelberg, Germany

Self-assembled monolayers (SAMs) formed by perfluoroterphenyl-substituted alkanethiols (PFTP-ATs) with variable length of the aliphatic linker (either 2 or 3 methylene units) were prepared on (111) Au and Ag and characterized by a combination of several complementary spectroscopic and microscopic techniques. A specific feature of these systems is the helical conformation of the PFTP moieties, which, along with the high electronegativity of fluorine, distinguishes them from the analogous non-fluorinated systems and makes them attractive for different applications. The SAMs were found to be well-defined, highly ordered, and densely packed, which suggests a perfect correlation between the orientations and, in particular, twists of the PFTP helices in the adjacent molecules. Significantly, the SAM exhibited pronounced odd-even effects, i.e. a dependence of the molecular orientation and packing density on the length of the aliphatic linker in the target molecules, with parity of *n* being the decisive parameter and the direction of the effects on Au opposite to that on Ag. The presence of the odd-even effects in the FTPn system brings new aspects into the discussion about the origin and mechanism of these phenomena. Specifically, the helical conformation of the FTP moieties in the dense phase excludes a variation of the intramolecular torsion and molecular twist as the mechanism behind the odd-even effects.

11:40am **SS2-TuM12 From Selective Adsorption to Substrate Reconstruction: A Scanning Tunneling Microscopy Study of 4'-nitro-1,1'-biphenyl-4-thiol Self-Assembled Monolayers on Au(111)**, H. Muzik, L. Kankate, A. Turchanin, A. Götzhäuser, University of Bielefeld, Germany

Self-assembled monolayers (SAMs) of 4'-nitro-1,1'-biphenyl-4-thiol (NBPT) on gold surfaces are extensively used for applications in chemical nanolithography and fabrication of chemically functionalized ultrathin (down to 1 nm) nanomembranes. However, the structure of NBPT SAMs has not yet been investigated in detail. Here we present the first scanning tunneling microscopy (STM) study of NBPT SAMs on the Au(111) surface. NBPT SAMs were prepared both in solvent and by vapor deposition in vacuum. We show by complementary STM and X-ray photoelectron spectroscopy (XPS) measurements that NBPT SAMs exhibits a complex polymorphic phase behavior which strongly correlates with the surface density of NBPT molecules. We have found that at low NBPT coverage, the molecules selectively adsorb outside the bridging regions of the herringbone reconstructed Au(111) surface, whereas at high coverage intermolecular interactions lead to a reorganization of the Au(111) substrate. These findings can be very relevant for the tuning of nanomaterials and devices fabricated by chemical nanolithography from NBPT SAMs and give new insights in the molecular self-assembly of aromatic thiols on gold surfaces.

[1] A. Turchanin, A. Tinazli, M. El-Desawy, H. Großmann, M. Schnietz, H. H. Solak, R. Tampé, and A. Götzhäuser, Molecular self-assembly, chemical

lithography, and biochemical tweezers: A path for the fabrication of functional nanometer-scale protein arrays: *Adv. Mater.* 20, 471-477 (2008).

[2] L. Kankate, A. Turchanin, and A. Götzhäuser: On the Release of Hydrogen from the S-H groups in the Formation of Self-Assembled Monolayers of Thiols. *Langmuir* 25, 10435-10438 (2009).

[3] M. Schnietz, A. Turchanin, C. T. Nottbohm, A. Beyer, H. H. Solak, P. Hinze, T. Weimann, A. Götzhäuser, Chemically functionalized carbon nanosieves with 1 nm thickness. *Small* 5, 2651-2655 (2009).

Thin Film

Room: Pecos - Session TF1-TuM

ALD: Dielectrics for Semiconductors

Moderator: H. Kim, Yonsei University, Korea

8:00am **TF1-TuM1 Feasibility of Wrinkle Free Graphene Process.** **B.H. Lee, C.H. Cho, S.K. Lim, S.Y. Lee, H.J. Hwang, Y.-G. Lee, U.J. Jung, C.G. Kang,** Gwangju Institute of Science and Technology, Korea **INVITED** Graphene is an attractive material for advanced device applications due to its excellent electrical conductivity. Up to now, the best quality graphene in terms of electrical properties are obtained only from the graphene mechanically exfoliated from a natural graphite. Other processes such as a thermal graphitization of SiC and a precipitated graphene from metal films super saturated with carbon atoms did generate a good quality graphene in terms of Raman analysis. However, the morphology of graphene shows a high density of physical defects such as micro size wrinkles, island growth etc. For practical application of nanoscale device fabrication, global size wrinkles should be eliminated like a flat silicon substrate. Major sources of global defects in graphene are 1) a mismatch of thermal expansion coefficient between the graphene and the growth templates (metal, SiC etc), 2) a preferential out-diffusion or adoption of carbon along the grain boundary of metal. In this talk, a novel process that can detour these problems and generate a wrinkle free graphene will be discussed.

8:40am **TF1-TuM3 The Effects of Interfacial Organic Layers on the Growth of Thin Al₂O₃, HfO₂ and TaN_x Films by Atomic Layer Deposition.** **K.J. Hughes, S. Issacson, J.R. Engstrom,** Cornell University

One of the most poorly understood aspects of atomic layer deposition involves the initial stages of growth. As growth via ALD is almost always conducted on a substrate of different composition than the film being grown on top of it, there are often issues related to what are the best ways to initiate growth. Over the past few years we have been examining the use of interfacial organic layers (IOLs) as way to tailor the nucleation and growth of ALD thin films. Here, unlike essentially all work we have reported previously, we have conducted ALD using a conventional hot wall, viscous flow-type reactor, operating at pressures of ~ 1-100 mTorr. We focus here on the growth of two oxides: the benchmark Al₂O₃ and high-k HfO₂, and one nitride, TaN_x. As to the IOLs we consider one vapor phase deposited self-assembled monolayer, perfluorooctyltrichlorosilane (FOTS), which is expected to provide no active sites for ALD growth. We also consider a solution phase deposited polymer, poly(ethylene imine) (PEI), which possesses a high density of -NH₂ groups expected to act as active sites for growth. Concerning the latter IOL, from synchrotron x-ray reflectivity we confirm that PEI forms a thin (~ 7 Å) smooth film on the substrates we have examined. For ALD growth of Al₂O₃ on both bare SiO₂, and SiO₂ treated with PEI we observe linear growth, and no detectable incubation period. Growth on FOTS/SiO₂ on the other hand clearly exhibits an incubation period of ~ 15 cycles. Thus, for Al₂O₃, growth on unmodified SiO₂ and SiO₂ modified with PEI are indistinguishable. In contrast, growth of both HfO₂ and TaN_x is definitely perturbed by the presence of the PEI interfacial organic layer: compared to growth on unmodified SiO₂, growth on PEI/SiO₂ exhibits an incubation period of ~ 10 cycles for HfO₂, and > 40 cycles for TaN_x. A common question is what is the fate of the IOL? Concerning the growth of Al₂O₃, from *ex situ* angle-resolved x-ray photoelectron spectroscopy (ARXPS) we find that the elemental species associated with the IOL (F for FOTS, and N for PEI) are located at the IOL/Al₂O₃ interface, indicating the IOL has not migrated to the top surface during growth.

9:00am **TF1-TuM4 Property of Interfacial Layer Induced V_{FB} Shift in Al-related Gate Oxide Deposited by Remote Plasma Atomic Layer Deposition.** **H.T. Jeon, H. Kim, S. Woo, J. Lee, H. Lee,** Hanyang University, Republic of Korea

With the continuous dimensional scaling down of Si based devices has called for using high-k dielectrics to replace SiO₂ or nitrided SiO₂ as the gate oxide in CMOS devices. However, the untrollability of flatband voltage (V_{FB}) is still a crucial issue for CMOS devices with high-k gate

dielectrics. This undesirably flatband voltage shift is highly related to the interfacial defects, such as interface defect density, fixed charge density and oxygen vacancy. Therefore, it is significant to understanding the physical and chemical properties of the interface regions.

To grow thin films with excellent properties, plasma-enhanced atomic layer deposition (ALD) has been widely used as a thin film deposition method. PEALD commonly produces better quality of films at lower growth temperatures than dose thermal ALD because the required activation energy is provided by a plasma source. Some processes require the presence of radicals to enhance chemical reactions without having to use ion bombardment, as it can cause plasma-induced damage. Remote plasma ALD (RPALD), wherein the plasma is created in a remote chamber using RF power, was developed to meet these processing demands. The radicals generated in the plasma enter into the process chamber for deposition.

In order to understand the interfacial influence on the V_{FB} shift in high-k based MOS structure, it is need to investigate the dependence of the V_{FB} shift on the properties of interfacial layer. In this paper, to modify the Si surface, N₂ plasma was treated on Si surface at RF powers of 100 W, 200 W and 300 W. The Al₂O₃ was deposited by remote plasma ALD at 250°C. The Pt/Al₂O₃/Si MOS structure was fabricated to investigate the impact of interfacial layer between Al₂O₃ and Si substrate on change in V_{FB}. In addition, plasma was monitored by optical emission spectroscopy (OES). The physical and chemical properties of high-k dielectric films and interfacial layer were examined by XPS and AES.

We found that the nitrogen content at Si substrate increased during N₂ plasma pre-treatment at high RF power which results in a negative shift of V_{FB}. Therefore, the properties of the interfacial layer which are critical in determining the V_{FB} are affected by N₂ plasma pre-treatment.

9:20am **TF1-TuM5 Atomic Layer Deposited Pb(Zr,Ti)O_x Films Composed as Ferroelectric and Multiferroic Materials.** **F. Zhang, T.E. Quickel, Y.-C. Perng, S. Tolbert, J.P. Chang,** University of California, Los Angeles

Atomic layer deposition (ALD) of complex oxides is a viable method to tailor the composition and microstructure of the resulting thin films, thereby generating multi-functionality that is needed in various device applications. Another desirable feature of ALD is its ability to uniformly and conformally coat complex surface structures of high aspect ratios, making it possible to interface distinct materials to form composite materials that may show exciting properties, such as multiferroic behavior.

In this work, lead zirconium titanate (PZT) films were synthesized by depositing PbO, ZrO₂ and TiO₂ ALD layers with a sequence of (Pb-O)-(Ti-O)-(Pb-O)-(Zr-O). The deposition rate for PZT was approximately 0.7nm/cycle-sequence. The as-deposited materials were amorphous but crystallized into perovskite structure upon annealing to 950°C. The polarization properties found in the P-V measurements including remanent polarization (Pr), saturation polarization (Ps), and coercive field (Ec) are promising and are strongly affected by the ALD sequence which dictates the composition and structuring of the resulting thin film.

One example of the advantages of ALD produced PZT can be seen in our work on composite multiferroic materials, which can be created by coupling together nanoscale ferroelectric and ferromagnetic materials. In this work, mesoporous cobalt ferrite (CFO) thin films formed by block-copolymer templating methods with pores 14 nm in diameter were used as the ferromagnetic framework. Ultra-thin ALD PZT films were used to create a uniform and conformal coating over and on all CFO pore spaces and generate a nano-structured PZT-CFO hybrid material, as confirmed by scanning electron microscope (SEM), transmission electron microscope (TEM), and ultraviolet photoelectron spectroscopy (UPS) measurements. Superconducting quantum interference device (SQUID) magnetometry is underway to assess the multiferroic properties of this PZT/CFO composite, including both in-plane and out-of-plane saturation magnetization measurements after electrical poling and polarization voltage (P-V) measurements.

9:40am **TF1-TuM6 Y₂O₃ Atomic Layer Deposition from a Novel Process and its Integration in a Gate First Approach for 0.8 nm Equivalent Oxide Thickness.** **C. Dubourdieu,** CNRS and IBM Research, **M.M. Frank, E. Cartier, J. Bruley, S.M. Rossnagel,** IBM T.J. Watson Research Center, **A. Kellock,** IBM Almaden Research Center, **V. Narayanan,** IBM T.J. Watson Research Center

A large part of the high-k dielectric stacks investigated for the replacement of the SiO₂ or Si₃N₄ gate oxide in metal-oxide-semiconductor (MOS) field-effect transistors consists of a Hf-based oxide or silicate deposited on top of an ultrathin interfacial SiO₂ layer. We report here the formation of yttrium lanthanum silicate in direct contact with silicon for the fabrication of MOS capacitors with a resulting highly competitive equivalent oxide thickness (EOT) of 0.8nm. Such a low EOT is remarkable as it is obtained with a non Hf-based dielectric and following a high-temperature gate first

route. This result is achieved by integrating Y_2O_3 films grown on buffer layers by a novel atomic layer deposition process that combines an original yttrium precursor and an innovative liquid injection source.

The growth of Y_2O_3 thin films by ALD from $Y(EtCp)_3$ and water precursors will be presented. The yttrium precursor was introduced using a novel delivery scheme consisting of a pulsed injection system from Kemstream®. The control of the growth as a function of various process parameters (precursor supply time, water purging time, temperature) was investigated. Film stoichiometry was determined by Rutherford backscattering spectrometry. The reactivity of $Y(EtCp)_3$ with water and the frontiers between ALD and CVD regimes will be discussed.

We describe MOS capacitors prepared from ALD- Y_2O_3 thin films deposited onto Si(p-type)/ SiO_2 (0.8 nm)/ La_2O_3 (1 nm) structures. The Y_2O_3 thickness ranges from 1.5 to 3.5 nm. The metal gate electrode consists of 10 nm TiN and implanted polysilicon on top. The complete stack undergoes a high-temperature RTA at 1000°C for 5 s under N_2 for dopant activation in the poly-Si, which simulates gate first process of CMOS transistor fabrication. Finally, a forming gas anneal is performed at 475°C. The stack microstructure and composition were studied by transmission electron microscopy, electron loss spectroscopy and energy dispersive x-ray spectrometry. Interdiffusion reactions occur between SiO_2 , La_2O_3 and Y_2O_3 layers upon the RTA and result in an yttrium lanthanum silicate film in direct contact with Si. The elemental distribution within the silicate layer will be discussed. C-V and I-V were performed on $10 \times 10 \mu m^2$ size capacitors in a frequency range of 1 kHz up to 300 kHz. EOTs as low as 0.8 nm were obtained for stacks with initially 3 nm Y_2O_3 deposited films. The leakage current density for such stacks is of $2.1 \times 10^{-3} A/cm^2$ at -1V. The formation of silicate enables an appropriate V_{FB} , which is tunable for nFET and pFET. Results obtained for stacks prepared from different buffer layers such as Al_2O_3 and HfO_2 will also be discussed.

10:40am **TF1-TuM9 Direct Liquid Injection Chemical Vapor Deposition of Nickel Ferrite and Barium Titanate Thin Films**, *N. Li, A. Wang, A. Gupta, T.M. Klein*, University of Alabama

Multiferroic heterostructures, such as the ferromagnetic-ferroelectric bilayered structures, have attracted a lot of attention due to their potential application in multifunctional devices. The simultaneous tunability of magnetic and electric fields in such structures is very useful for microwave and millimeter wave planar devices such as tunable phase shifters, resonators and delay lines. Growth of high quality and thick (10 μm -100 μm) ferromagnetic and ferroelectric thin films is an essential step to obtain satisfactory final devices. In this work, the growth of single crystal nickel ferrite (NFO, ferromagnetic) and barium titanate (BTO, ferroelectric) thin films with high growth rate by direct liquid injection chemical vapor deposition is investigated. The liquid precursor source for injection was prepared by dissolving corresponding metalorganic precursors into a solvent. In our case, Ni(acac)₂•PMDTA adduct (acac=acetylacetonate, PMDTA= N,N,N',N',N"-pentamethyldiethylenetriamine) and Fe(acac)₃ were dissolved in toluene as NFO precursor solution; Ba(hfa)₂•tetraglyme adduct (hfa=hexafluoroacetylacetonate) and Ti(tmhd)₂(ipo)₂ (tmhd= 2,2,6,6-tetramethyl-3,5-heptanedionate, ipo=isopropoxide) were dissolved in toluene as the BTO precursor solution. The as-prepared metal organic precursor solution was fed into a commercial vaporizer system through a liquid mass flow controller (10g/h range). Epitaxial growth of NFO and BTO thin films on MgO(100) were observed using X-ray diffraction. X-ray photoelectron spectroscopy showed the existence of trace amount of fluorine on the BTO surface. Scanning electron microscopy and atomic force microscopy showed the grain sizes to be around 100nm and the surface roughness around 20nm. The growth rates of both the NFO and BTO thin films are in the range of 0.5~1 $\mu m/h$ under our experimental conditions.

11:00am **TF1-TuM10**, *L.C. Haspert, P. Banerjee, L. Henn-Lecordier, G.W. Rubloff*, University of Maryland

Thin film TiO_2 is a relatively high permittivity material with applications in electronic and energy devices. However, TiO_2 crystallizes easily, forming grain boundaries and creating current percolation pathways which increase leakage current and power consumption. Al-doped TiO_2 (ATO) increases the thermal stability of TiO_2 , reducing leakage currents by suppressing phase transformation and limiting grain growth. To achieve the benefits of Al doping which retaining those of TiO_2 , structure-property relationships must be optimized as a function of processing parameters.

Raman spectroscopy (RS), a highly sensitive technique for observing the evolution of nano-crystalline phases - their time evolution, volume fraction, defect states and stresses, is employed here to characterize ATO films grown by atomic layer deposition (ALD) and their correlation with electrical performance. 25nm TiO_2 thin films were deposited at 150°C in a Beneq TF500 cross-flow ALD reactor by sequentially pulsing TDMAT and water precursors. Aluminum doping was controlled from 0 to 15 at% by

introducing a single TMA / water pulse sequence at pre-determined intervals of multiple TDMAT/water pulse sequences during oxide growth, producing reproducible compositions estimated from their TiO_2 to Al_2O_3 pulse ratios. Following ALD the films were rapid thermal annealed (RTA) in an oxygen-rich environment ranging from 600°C to 1000°C from 5 to 300 sec.

The degree of crystallization was determined primarily through lineshape analysis of the Raman-active 144 cm^{-1} frequency mode. RS (and XRD) detected only the TiO_2 anatase phase, even at annealing temperatures where rutile formation was expected. RS data clearly shows the crystallization of TiO_2 with thermal anneal and that the crystallization onset shifts to higher temperatures with Al-doping while producing smaller grains. Pure TiO_2 films show a dielectric constant of 28.5 with high leakage currents (up to $10^{-3} A/cm^2$). Annealed ATO films have a slightly lower dielectric constant (24) but leakage currents are dramatically reduced to $\sim 1.0 \times 10^{-7} A/cm^2$. The clear correlation between the microstructure measured by RS and the electrical performance of ALD TiO_2 and ATO thin films shows that RS can be a rapid, valuable monitor of thin film material nanostructure for correlation and optimization with electrical properties.

This work was supported by Laboratory for Physical Science, UMD

11:20am **TF1-TuM11 In-situ XPS and Half-Cycle Studies of Atomic Layer Deposited Al_2O_3 on Group-III Nitride Substrate for MOS-HEMT Applications**, *P. Sivasubramani, T.J. Park, B.E. Coss, S. McDonnell, R.M. Wallace, J. Kim*, University of Texas at Dallas, *Y. Cao, D. Jena, H. Xing*, University of Notre Dame

Group-III nitride (III-N) technology has been widely used in optoelectronics, RF transistors and power switching due to a suitable bandgap, excellent transport properties, high breakdown field, low power losses, as well as the possibility of forming a heterojunction structure on low cost, large area substrate templates such as Si, sapphire, etc. [1] X-N alloy on Ga-N (where X = Ga, In, or Al) are expected to achieve high-speed switching performance due to a high carrier mobility of 2-D electron gas formed at the heterojunction interface. The introduction of a high-quality, ultrathin, atomic layer deposited (ALD) dielectric in between the metal and semiconductor has been shown to effectively decrease the diode leakage current without compromising the MOS-HEMT transfer characteristics. [2, 3] The evaluation of interfacial and bulk bonding configurations as a function of ALD dielectric growth parameters could provide valuable information for III-N device application. Therefore, in this work, we have investigated the growth, interfacial, and bulk properties of ALD Al_2O_3 dielectric on top of Ga-N on top of a low-cost sapphire template. Immediately after surface preparation, the samples were loaded in an ultra high vacuum (UHV) custom tool which has an integrated x-ray photoelectron spectroscopy (XPS), ALD, and a UHV transfer tube for in-situ analysis of ALD half-cycle reactions with the III-N substrate. The surfaces were pre-cleaned using atomic H cleaning and/or solvent-wet chemical cleaning. XPS of III-N substrates indicates that a small, higher oxidation state component, possibly a hydroxide or an oxynitride (e.g. Ga-O-N) exists on the as-grown surface. The hydroxide and residual carbon components on the clean substrate and during the half-cycle reactions are simultaneously monitored. Significant charging of the semiconductor during XPS is circumvented by using a doped substrate along with suitable charge references. ALD half-cycle studies of the TMA (tri-methyl aluminum)/water and TMA/ O_3 reactions on the III-N surface will be presented. References: [1] Phys. Status Solidi C 6, No. 6, 1361 (2009) [2] Appl. Phys. Lett. 86, 063501 (2005) [3] IEDM09-15

11:40am **TF1-TuM12 Defect Mechanisms for Chlorosilane Based Self-Assembled Monolayers**, *S. Miller, A.J. Muscat*, University of Arizona

Self-aligning manufacturing processes could allow smaller device structures to be made as well as significantly reduce the number of manufacturing steps required. By utilizing selective chemistry it is possible to control where growth occurs for many different materials. Self assembled monolayers (SAMs), such as octadecyltrichlorosilane (OTS), have been used to inhibit the atomic layer deposition (ALD) of materials spanning from high-k dielectrics to metals such as Ir or Pt. By tailoring the selective chemistry, it is possible to chemically activate and deactivate the surface for multiple materials. SAMs such as 3-mercaptopropyltriethoxysilane have been used to attach a variety of nanoparticles where desired, and when combined with other SAMs such as OTS can prevent adsorption or deposition where undesired. Simple patterning techniques such as photolithography, AFM lithography, or electron lithography can be combined with selective chemistries to allow high resolution spatial control over the growth and deposition of materials. One limitation of this technology is the long time scales required to fully deactivate deposition using SAMs, which are on the order of 48 hours. Molecular defects such as water in the SAM, unblocked hydroxyl groups, exposed Si-O bonds, misaligned boundaries between forming SAM islands, or polymerized SAM molecules in the SAM layers also leads to an eventual failure point for

deposition deactivation. We found that they can be largely eliminated by forming the SAM on a uniformly hydroxylated surface, using a chloroform rinse step, and removing any polymerized or physisorbed SAM molecules from the surface during SAM formation. Using TiCl_4 as a probe for defect sites, the level of each defect type has been determined. The number of defects sites on the surface on a typical OTS SAM is on the order of 10^{12} molecules/cm². 1/3rd of the defects are associated with the physisorbed SAM molecules. Of the other 2/3^{ds} of SAM defects nearly half are unblocked hydroxyl groups while the other half are likely open Si-O bonds at grain boundaries. Water has been shown not to be a contributing cause for nucleation of deactivation failure. TiO_2 deposition from a TiCl_4 and H_2O ALD process at 170°C has been deactivated for at least 100 cycles after treating for only 4 hours in 10mM OTS in toluene solution, as long as the sample is removed every hour and rinsed. The extraction step removes unwanted SAM molecules and exposes open surface areas allowing for new SAM molecules to quickly fill the gaps. These improvements in both the quality and the time scale of SAM formation could be feasible to begin incorporating these technologies into manufacturing.

Thin Film

Room: Ruidoso - Session TF2-TuM

Nonvolatile Memory

Moderator: C. Vallee, Université Joseph Fourier, France

8:00am TF2-TuM1 MRAM: A Practical Application of Spintronics, D.W. Abraham, IBM INVITED

Magnetic random access memory (MRAM) is a new class of solid state memory which is based on the spin of the electron (as opposed to its charge). This technology is a relative newcomer to the constellation of non-volatile memories, and offers a unique combination of non-volatility, density and speed. I will review the scientific discoveries that enabled the first MRAM chips, and then will discuss several distinct generations of the technology which have evolved in the last decade, including both field-switched and spin-torque-switched devices. Finally I will describe promising new structures which are currently under development which exploit the separation of spin and charge to allow more reliable and lower power operation.

8:40am TF2-TuM3 Bipolar Resistive Switching Characteristics of HfO_x with Anode-Interface HfAlO_x Layer, H.-C. Sohn, J.G. Kim, H.D. Na, K.-M. Lee, S.-H. Lee, Yonsei University, Republic of Korea

In this work, we investigated the effect of anode-interface HfAlO_x layer on the resistance switching characteristics of ALD HfO_x films. HfAlO_x on TiN bottom electrode with the thickness and the cycle ratio of HfO_2 and Al_2O_3 was deposited and then HfO_2 thin film was grown by atomic layer deposition (ALD) process. The resistance switching behavior of the Pt/ HfO_2 / HfAlO_x /TiN MIM stack was characterized in conjunction with physical property such as chemical bonding of HfO_x and HfAlO_x . HfAlO_x layer with increasing the ratio of Al_2O_3 improved the endurance, the variance of V_{SET} and V_{RESET} , and the variance of R_{LRS} and R_{HRS} . Also, the resistances of LRS during first RESET processing were decreased with increasing the ratio of Al_2O_3 in HfAlO_x films. X-ray photoemission spectroscopy showed that the cycle ratio of Al_2O_3 in HfAlO_x layer caused an increase of metallic Hf (Hf^0) concentration. It was considered that an increase of metallic Hf (Hf^0) concentration is closely related to the migration of oxygen ions or vacancies at interface between transition metal oxide and TiN electrode, resulting in the enhanced endurance, the current level of LRS and HRS, and the narrowed distribution of $V_{\text{SET}} \& \text{RESET}$ and $R_{\text{LRS}} \& \text{HRS}$.

9:00am TF2-TuM4 Plasma Treatments of HfO_2 Resistive RAM, C. Vallée, P. Gonon, Ujf - Ltm, France, C. Mannequin, T. Chevolleau, Ltm - Umr 5129 Cnrs, France, H. Grampeix, N. Rochat, C. Licitra, V. Jousseau, CEA-LETI-MINATEC, France

9:20am TF2-TuM5 Growth of GeTe Films by MOCVD and PE-MOCVD for Phase Change Memory, E. Gourvest, STMicroelectronics, France, C. Vallée, Ujf - LTM, France, P. Michallon, CEA-LETI-MINATEC, France, J. Vitiello, Altatech Semiconductor, France, R. Blanc, CNRS-LTM, France, D. Jourde, CEA-LETI-MINATEC, France, S. Lhostis, STMicroelectronics, France, S. Maitrejean, CEA-LETI-MINATEC, France Phase-Change Memory (PCM) is one of the promising candidates for next-generation nonvolatile memory thanks to their low cost, low programming voltage and their excellent scalability to the nanoscale cell size [1]. This technology is based on fast and reversible phase change effect in the chalcogenide materials but suffers of the inherent lack of amorphous state

stability which affects archival life of the memory cell. This problem is critical for embedded applications where a high retention time at high working temperature is required. In this case, binary compound GeTe material has been shown to be a good candidate since a phase transition temperature higher than the usual $\text{Ge}_2\text{Sb}_2\text{Te}_5$ material has been found and 10 years-fail time at 105°C has been estimated [2]. Moreover the reduction of the current pulse needed to change material from crystal phase to amorphous phase implies the confinement of phase change materials at dimensions below 100 nm [3]. In this case the growth of GeTe materials by chemical vapour deposition (CVD) or Plasma Enhanced CVD is required in order to fill confined structures.

For this purpose, this work investigates the deposition of GeTe materials by a pulsed liquid injection Metal Organic CVD system allowing storing the precursor at ambient temperature. The deposition is made in a 200 mm MOCVD tool that can be assisted by a Low Frequency as well as Radio Frequency plasma. The liquid precursors are injected into a heated evaporator where flash evaporation occurs. A sequential injection leads to a precise control of the deposited material stoichiometry. Furthermore deposition in amorphous or crystalline state is performed by setting the substrate temperature. This chamber is connected to a cluster tool which allows quasi in situ analysis of the deposited films crystalline state by Spectroscopic Ellipsometry (SE) and of the growth mechanisms by angle-resolved X-ray Photoelectron Spectroscopy (ARXPS). Impact of process parameters on the films properties are then evaluated in the MOCVD and PECVD mode. In the case of plasma assistance the impact of the Low to Radio Frequency ratio on the thin film deposition is also studied. Direct informations on Ge/Te ratio and carbon contamination are given by the plasma analysis thanks to optical emission spectrometry. In addition to the chemical and physical properties investigations, the phase change performances and the electrical properties of the deposited materials are evaluated.

[1] S. J. Hudgens, *J. Non-Crys. Solids*, **354**, 2748 (2008)

[2] L. Perniola *et al.*, *IEEE Electron Device Lett.*, **31**, 5 (2010), pp. 488-490.

[3] S. L. Cho *et al.*, *Symp. VLSI Tech. Dig.* (2005), p. 96

9:40am TF2-TuM6 Effects of Halogenated Plasma Chemistries on Degradation of Magnetic Material Properties, R.M. Martin, D.W. Abraham, E.A. Joseph, Y. Zhang, IBM T.J. Watson Research Center

Patterning of magnetic materials with plasma processes is an integral step in the fabrication of magnetic devices such as magnetic tunnel junctions (MTJs) for magnetoresistive random access memory (MRAM). Obtaining optimal device performance requires preservation of the magnetic material properties throughout the fabrication process, and thus places limitations on the process window (e.g. temperature, gas chemistry) for patterning devices. Due to this, the use of halogenated plasma chemistries, which are commonly used in reactive ion etching (RIE) processing, must be carefully employed when patterning MTJ devices, as they can significantly degrade magnetic properties during the etch. One method used to minimize magnetic degradation is the incorporation of metallic capping layers which potentially isolate the halogen etch chemistry from the critical magnetic layers. However, the optimal thickness and/or properties of these layers have yet to be fully explored. For example, when a Cl_2 based plasma is exposed to a 300 Å Ru capping layer, the magnetic moment/area of the underlying magnetic free layer is reduced 11% from 1.64 to 1.46×10^{-4} emu/cm². Therefore in this work, the effects of the plasma etch chemistry on magnetic materials is explored using various halogenated chemistries and capping layer materials to understand the mechanisms by which patterning of magnetic devices can be achieved without degradation of magnetic properties.

10:40am TF2-TuM9 Phase Change Materials for Random Access Memories: Deposition, Characterization and Performance, C. Wiemer, CNR-IMM, Italy INVITED

11:20am TF2-TuM11 Bipolar Switching Behaviors in TiN/ HfO_2 /Pt Systems for Nonvolatile Resistive Memory Applications, D.-H. Ko, D.S. Lee, Y.H. Sung, Yonsei University, Republic of Korea

Resistive random access memory devices based on transition metal-oxides (TMO) have been considered as the most promising candidates for the next generation nonvolatile memories because of its simple structures and compositions, low voltage operation and process compatibility with CMOS.

In this presentation, stable bipolar resistive switching behaviors of TiN/ HfO_2 /Pt structures will be discussed for the first time. The HfO_2 films were grown by reactive sputter at room temperature using O_2 and Ar gas, and the subsequent heat treatment was performed in an ambient of O_2 at 300°C. TiN and Pt layers were used as the top and bottom electrode materials, respectively. For the characterization of stable bipolar resistive switching, current-voltage measurements were used in compliance with 1

mA. Excellent memory characteristics including low set/ reset voltages and long retention time were demonstrated without additional electroforming process. The bipolar resistive switching behavior can be explained by the formation of conductive path consisting of oxygen vacancies. We analyzed a composition and chemical bonding of HfO_2 by x-ray photoelectron spectroscopy. In addition, microstructures of the films were analyzed by transmission electron microscopy.

Vacuum Technology

Room: Laguna - Session VT+MS-TuM

Outgassing, Contamination Control, and Process Modeling

Moderator: M. Wuest, INFICON, Liechtenstein

8:00am **VT+MS-TuM1 Reduction of Hydrogen Content in Stainless Steel Vacuum Components**, *L.L. Wang, R.Y. Weinberg, K.A. Lao*, Los Alamos National Laboratory

Hydrogen is dissolved in stainless steel during the initial phases of production and fabrication. At room temperature, the dissolved hydrogen slowly diffuses out of the stainless steel. For stainless steel vessels assembled from commercially available vacuum components, we consistently measured constant rates of gas pressure increase in these sealed stainless steel vessels after they had been evacuated to 1×10^{-7} torr. The pressure in a 97 cc stainless steel vessel can reach up to 0.8 torr in six months at room temperature. The gas accumulated in these vessels, previously vacuum baked at 150°C for 48 hours to remove adsorbed gas, was analyzed to be essentially hydrogen. To determine how effective high-temperature vacuum bake out is in reducing the hydrogen content in the stainless steel components, we undertook a study that involved vacuum bakeout of the components at 400°C for 10 days and analysis of the hydrogen contents of the components with and without the vacuum bakeout. The hydrogen concentrations were measured by a LECO analyzer. The results will be presented and compared with that predicted by the Fick's law of diffusion.

8:20am **VT+MS-TuM2 Hydrogen Outgassing in a Small Vacuum Chamber**, *R.F. Berg*, National Institute of Standards and Technology

In a closed vacuum chamber, the problem of hydrogen outgassing from stainless steel increases with both the temperature and the chamber's surface-to-volume ratio. This talk will describe the outgassing in a chamber that is used to measure the vapor pressures of organic compounds in the range from 1 Pa to 100 kPa. The chamber, which is a small manifold built from stainless steel fittings and two capacitance diaphragm gauges, has a combination of challenges not usually present in a larger apparatus at room temperature. (1) Its volume of only 29 cm^3 created a relatively large surface-to-volume ratio. (2) Operating at temperatures as high as 200 °C greatly increased the outgassing rate. (3) The pressure gauges limited the maximum allowed bakeout temperature.

Closing the valve to the vacuum pump caused the pressure to increase nonlinearly with time. The initial rate slowed during several hours and usually became linear with time within one day. Intermittent pumping during one month at 200 °C showed that the linear rate decreased with an exponential time constant of approximately 11 days, which was consistent with the diffusion of hydrogen from the stainless steel fittings. Understanding this behavior is important because a pressure increase of 1 Pa/day (3×10^{-10} Pa m^3/s) can cause a significant error in the vapor pressure measurement. A model that accounts for the diffusion of hydrogen in the chamber wall and its nonlinear accumulation in the chamber volume will be compared to the pressure measurements.

8:40am **VT+MS-TuM3 Point-of-Use Abatement Devices and Exhaust Management Strategies**, *M. Sherer*, Sherer Consulting Services, Inc. **INVITED**

Semiconductor processes emit various contaminants which require exhaust management and in some cases point-of-use (POU) abatement. It is important to understand process exhaust management strategies, and to select the best, lowest cost-of-ownership POU abatement devices. This presentation will discuss these topics and provide relevant technical information.

9:20am **VT+MS-TuM5 Novel Instrument Capable of Efficient Gas Exchange to Remove Gas-phase Contamination in Complex Volumes Without Purging or High Vacuum**, *J. Brown, J. Hochrein, S. Thornberg*, Sandia National Laboratories

Countless systems used in research and in industry contain complex assemblies that are sealed in some type of enclosure, meant to isolate them from the harsh operating environment of the open atmosphere and to maintain a pristine internal atmosphere. Unfortunately, the internal atmosphere of any sealed component or system is, in the long-term, only as clean as the materials sealed within its enclosure. Over time, moisture or other volatile contaminants initially trapped in the materials can begin to evolve and accumulate with potentially detrimental effects on the functionality of the component. This problem can be extremely difficult to address, depending on the physical and mechanical constraints of the particular system. Recently, an instrument was developed at Sandia National Laboratories that can "clean" the internal atmosphere of a critical optical component that cannot be subjected to conventional conditioning methods (such as N_2/Ar purge, high-vacuum pumpdown, etc.). By using multiple pressurization and evacuation cycles tightly controlled within a narrow ± 2 psig window, the instrument fully and efficiently exchanges the liters of moisture- and contamination-laden internal gas of the component with clean, dry N_2 . This process is repeated as moisture from the internal materials diffuses back into the gas phase until, over time, the source of the moisture is depleted. This instrument has been successful in reducing the equilibrium gas-phase moisture levels in the optical component from the thousands of PPMv (parts per million by volume) to single-digit PPMv. This instrument, called the "Automated Pressure Cycler," will be discussed in detail.

10:40am **VT+MS-TuM9 Modeling, Design, Fabrication, and Characterization of a Pulsed Vacuum System**, *Z.C. Leseman, J. Butner*, University of New Mexico

Systems utilizing low to medium vacuum levels are becoming increasing popular due to packaging of micro and nanoelectronic devices, exploration of surface phenomena, and gas-phase etching of materials. In this work, pulsed vacuum systems are modeled, designed, fabricated, and characterized. Modeling efforts focus on methods for calibration of volumes, pump-down / pressure-up times, and vacuum system configuration considerations. As a result of this systems of linear equations are developed and solved, as well as systems of coupled differential equations which are solved analytically and numerically (when necessary). As a result of this modeling effort a new method has emerged for vacuum processing at discrete pressures and discrete times. Experimental validation is presented in regards to specific applications: MEMS environmentally dependent stiction failure, vapor phase lubrication of MEMS, and XeF_2 vapor phase etching of Si.

11:00am **VT+MS-TuM10 Effects of Inlet Pipe Diameters on Pumping Performance of Turbomolecular Pump**, *F.-C. Hsieh, D.R. Liu, F.-Z. Chen*, National Applied Research Laboratories, Taiwan

The effects of inlet pipe diameters on pumping performance of turbomolecular pump (TP) are evaluated by commercial software VacTran. The result indicates that at inlet pipe diameter (D_i) of 0.25 m the delivered pumping speed (DPS) of TP decreases from peak value (PV) of 680 L /s to about 430 L /s. However, DPS approaches to PV as D_i increases to the largest one (1.0 m). Besides, the conductance of TP increases when D_i increases. The conductance is proportional to the pipe radius at molecular flow. The pumping speeds (PS) versus the inlet pressure of TP and foreline (scroll pump) are evaluated. The PS for TP is higher than those obtained with foreline. Also, the DPS of TP is tested on an evaluation system constructed according to ISO-5302 standard. Good agreement between analysis and experimental data are shown. Finally, the throughput versus the inlet pressure of TP reveals linear trend in log-log scale within pressure ranged from 3.1×10^{-5} to 9.3×10^{-1} torr.

11:20am **VT+MS-TuM11 Optimal Configuration of a Radiometer Array for Low Pressure Applications**, *B. Cornella, A. Ketsdever*, University of Colorado at Colorado Springs, *N. Gimelshein, S. Gimelshein*, University of Southern California

A thin vane with a temperature gradient immersed in a rarefied gas will experience a force which tends to move the vane from the hot to the cold side. The radiometric force, as it is called, is the force that drives the Crookes radiometer. Applications of radiometric forces have been limited to date to high-density microdevices, most notably the atomic force microscope. However, applications can also involve larger devices in the low pressure regime (same equivalent Knudsen number). For an example, radiometric forces can act as a propulsion system to compensate disturbing forces on a vehicle traveling high in the atmosphere. Recent studies have shed new light on the relative influence of bulk radiometer area versus edge on force production, indicating that these effects are on the same order of

magnitude in the Knudsen regime where the force is maximized ($Kn=0.05$). An experimental study has been conducted to investigate the impact of vane separation distance for a multiple-vane radiometer. This study is a first step in maximizing the force per unit volume (or mass) by optimizing the area versus edge geometries. Furthermore, this study provides experimental validation for today's numerical models involving rarefied radiometric flows. To emulate a near space environment, a 39" diameter vacuum chamber was used to set a range of pressures for the experiment from 0.1 to 10 Pa (corresponding to Knudsen numbers of 1.3 to 0.01). The experiment measures the total force of a one by three array radiometer configuration and compares it to a single vane with the same active area. Each individual radiometer vane consisted of a 40 mm square Peltier thermoelectric cooler where the temperature difference across the two surfaces was actively maintained at approximately 25 K. The relative separation between the vanes was varied from 0% (single vane setup) to 100% of the size of the individual vane element and the maximum forces between these varying configurations compared. Preliminary experimental results suggest that the total force produced by the overall radiometer increases with gap distance. Numerical results suggest that the optimum separation distance for maximum force production is around 75% of the vane height.

Tuesday Lunch, October 19, 2010

Exhibitors & Manufacturers Technology Spotlight

Room: Southwest Exhibit Hall - Session EW-TuL

Exhibitors & Manufacturers Technology Spotlight

Moderator: D.J. Surman, Kratos Analytical Inc., R.

Langley, Consultant

12:20pm **EW-TuL2 A Multi-technique Approach to the Characterization of Patterned Polymers Using ESCALAB 250Xi.** *P. Mack, R.G. White, A. Wright*, ThermoFisher Scientific, UK

Surface treatment of polymers produces materials that exhibit a wide range of surface compositions, properties and structures. The chemical and structural properties of these novel materials can be exploited for the fabrication of devices for bio-medical and electronics applications. The combination of a variety of complementary surface-sensitive electron spectroscopies maximizes the information available to the analyst for full quantitative surface characterization of standard and patterned polymer surfaces

This presentation will show how the new Thermo Scientific ESCALAB 250Xi, a multi-technique surface analysis system, can be used to investigate the chemistry and structure of various standard and patterned polymer samples. Chemical changes produced by surface treatments were examined by high energy resolution XPS and angle resolved XPS. Complementary REELS measurements were used to examine the level of carbon unsaturation at the uppermost surface of each of the polymer samples. Ultraviolet Photoelectron Spectroscopy (UPS), REELS and XPS valence band analysis were used together to comprehensively evaluate the valence electronic structure of the polymers.

Chemical and elemental changes as a function of X, Y coordinate were evaluated on both the microscopic and macroscopic scale, employing techniques such as high spatial resolution parallel imaging. The continuous position imaging detector on the ESCALAB 250Xi allows fully quantitative images to be acquired, with full XPS region spectra at each imaging pixel. The ability of ESCALAB 250Xi's advanced Principal Components Analysis algorithms to streamline the processing of such imaging data will be demonstrated.

12:40pm **EW-TuL3 A New Cluster Ion Beam for Depth Profiling Challenging Organic Materials.** *J.S. Hammond*, Physical Electronics

C₆₀ and coronene cluster ion sources have been recently introduced for XPS and TOF-SIMS sputter depth profiling of many polymer materials. These sources have also been very successful for the removal of common organic contamination before XPS and TOF-SIMS surface analysis. This experience with C₆₀ and coronene cluster ion sources has revealed several polymer systems for which these cluster sources can not produce "non-destructive" chemical depth profiling with XPS and TOF-SIMS. Typically these polymers are either cross-linked, highly susceptible to radiation induced cross-linking, or are polymerized with bonds that are not amenable to sputter depth profiling. A new gas cluster ion beam (GCIB) source that produces massive argon cluster ions will be shown to successfully produce XPS and TOF-SIMS depth profiles on challenging materials such as polyimide thin films. The GCIB source can also be used to remove ion beam and plasma induced damaged layers on polymer materials.

This new ion source will greatly expand the breadth of materials for which XPS can produce chemical state depth profiles on multi-layer thin films. In addition, the use of a dual beam depth profiling approach with GCIB and LMIG sources on TOF-SIMS instruments will expand the applications for 3D characterization of polymer and biomaterial samples. Examples will be presented demonstrating the benefits of the GCIB for both XPS and TOF-SIMS analyses.

1:00pm **EW-TuL4 Recent Developments in X-ray Photoelectron Spectroscopy Data Acquisition and Processing.** *D.J. Surman, C. Moffitt, Kratos Analytical Inc., C.J. Blomfield, A.J. Roberts, S.J. Hutton, G. Mishra, Kratos Analytical Ltd., UK*

Tuesday Afternoon, October 19, 2010

Actinides and Rare Earths Topical Conference

Room: Isleta - Session AC-TuA

Science and Technology of Actinides and Rare Earths

Moderator: R.K. Schulze, Los Alamos National Laboratory

2:00pm **AC-TuA1 Enhanced Photoluminescence from Europium-Doped Gadolinium-Based Nanocrystal Scintillators**, *T.-K. Tseng, J. Choi, M.R. Davidson, P.H. Holloway*, University of Florida

Scintillator crystals have traditionally been grown with complex single crystal methods such as Czochralski and Bridgman techniques, which frequently result in high costs and small crystal size. Therefore, development of processes for larger area, polycrystalline ceramic scintillators with high luminescence is of great interest due to their potential for mass production, versatility in shape and size, and low cost. In this study, spherical $\text{Gd}_2\text{O}_3:\text{Eu}^{3+}$ and almond-like $\text{GdVO}_4:\text{Eu}^{3+}$ nanocrystals were synthesized using a water-based solution precipitation method at low reaction temperatures ($<90^\circ\text{C}$) in short times (3 min~1 h). Core/Shell nanostructures with mono-dispersed 220 nm SiO_2 cores and an ~13 nm Gd_2O_3 shell, i.e. $\text{SiO}_2/\text{Gd}_2\text{O}_3:\text{Eu}^{3+}$, were prepared. With an additional undoped Gd_2O_3 shell to form a $\text{SiO}_2/\text{Gd}_2\text{O}_3:\text{Eu}^{3+}/\text{Gd}_2\text{O}_3$ nanostructure, the quantum yield was 28% higher than that of $\text{SiO}_2/\text{Gd}_2\text{O}_3:\text{Eu}^{3+}$. This enhanced photoluminescence (PL) is attributed to a Gd_2O_3 surface shell serving (i) as a sensitizer with energy transfer to the Eu^{3+} in the $\text{Gd}_2\text{O}_3:\text{Eu}^{3+}$ shell, plus (ii) passivation of non-radiative surface quenching sites. Enhanced PL was also demonstrated from polyol-synthesized $\text{Gd}_2\text{O}_3:\text{Eu}^{3+}/\text{Y}_2\text{O}_3$ nanocrystals. Increased PL can also be achieved by incorporating Bi^{3+} sensitizer ions into colloidal $\text{GdVO}_4:\text{Eu}^{3+}$ nanocrystals which were self-assembled into almond-like clusters composed of ~60 nm nanorods. With 2% Bi^{3+} co-doped in $\text{GdVO}_4:\text{Eu}^{3+}$ nanocrystals, PL was enhanced by 45%, 90% and 570% when excited by 280, 323 and 347 nm photons, respectively. This enhancement is attributed to increased absorption from Bi-O bonds, plus extension of the excitation band edge to longer wavelength. For Bi^{3+} ion concentrations $>10\%$, PL from co-doped nanocrystals decreased due to non-radiative decay from Bi^{3+} -induced trapping centers, as well as increased Bi^{3+} - Bi^{3+} energy transfer instead of Bi^{3+} - Eu^{3+} transfer.

2:20pm **AC-TuA2 Memory Effects of UF_6 Adsorption and Reaction at Metallic Surfaces**, *M.T. Puffett, D.P. Moore, J.D. Farr, R.K. Schulze, K.D. Ianakiev*, Los Alamos National Laboratory

In this study we explore memory effects that arise from the reactivity of UF_6 with surface hydroxyls (and other entities with a reactive H bond) that may be present at metallic surfaces. These chemical interactions are noted to leave behind low but measurable quantities of uranium oxy fluorides (UO_2F_2 , UOF_4 and related extended solids). Uranium re-depositions are noted to occur following sequential exposures to varying isotopic content in the UF_6 gas stream. We explore the role that additional fluorinating agents (HF , ClF_3) play in promoting uranium surface re-fluorination and memory effects in these deposits. The primary surface and radiochemical characterization techniques utilized in this study and include x-ray photoelectron spectroscopy, Auger electron spectroscopy depth profiling, static SIMS and alpha emission spectroscopy. The importance of these memory effects in enabling higher accuracy isotopic determinations and in forensic knowledge

2:40pm **AC-TuA3 Nanocomposites for Thermoelectrics : Erbium Mono-Antimonide Nano Crystals Embedded in Group III -AsSb Host Materials**, *T. Onishi*, University of California, Santa Cruz and NASA Ames Research Center, *T. Favaloro*, University of California, Santa Cruz, *A. Shakouri*, University of California, Santa Cruz and NASA Ames Research Center, *E. Coleman, G.S. Tompa*, Structured Materials Industries Inc., *S. Kraemer, H. Lu, A. Gossard*, University of California, Santa Barbara, *N.P. Kobayashi*, University of California, Santa Cruz and NASA Ames Research Center

3:00pm **AC-TuA4 TRU Waste Disposal in Waste Isolation Pilot Plant, WIPP**, *M. Borkowski, H. Khaing, J.-F. Lucchini, D.T. Reed, M.K. Richmann, J.S. Swanson, D. Ams*, Los Alamos National Laboratory

The mobility and potential release of actinides into the accessible environment continues to be the key performance assessment concern of nuclear repositories. Actinide, in particular plutonium speciation under the wide range of conditions that can exist in the subsurface is complex and depends strongly on the coupled effects of redox conditions, inorganic/organic complexation, and the extent/nature of aggregation. Understanding the key factors that define the potential for actinide

migration is, in this context, an essential and critical part of making and sustaining a licensing case for a nuclear repository. Herein we report on recent progress in a concurrent modeling and experimental study to determine the speciation of plutonium, uranium and americium in high ionic strength Na-Cl-Mg brines. This is being done as part of the ongoing recertification effort in the Waste Isolation Pilot Plant (WIPP).

A key feature of salt-based repositories is the relatively rapid self-sealing nature of the salt. This feature leads to geologic isolation of the waste form, and when reduced metals are present (e.g., iron containers), the system is driven anoxic by corrosion leading to strongly reducing environments. The consequence of this is that the combination of anaerobic microbial activity, reactions of reduced metals, and, when present, reactions of organics leads to the reduction of higher valent Pu(V) and Pu(VI) species to the lower valent Pu(III) and Pu(IV) species. The reduction of Pu(V/VI) species has been studied extensively. Less is known about microbial effects with halophiles although there is no question that bioreduction of higher valent plutonium occurs readily by soil bacteria under anoxic conditions. These lower valent oxidation states have lower solubilities and correspondingly lead to lower solubility and mobility of the plutonium.

The oxidation-state specific solubility of actinides were established in brine as function of pC_{H^+} , brine composition and the presence and absence of organic chelating agents and carbonate. An oxidation-state invariant analog approach using Nd^{3+} and Th^{4+} was used for An^{3+} and An^{4+} respectively. These results show that carbonate and hydrolysis predominate at pC_{H^+} above 8. Organic complexation is more important for An^{3+} . Carbonates are the key factor for U(VI) solubility. Modeling efforts are focused on the use of Pitzer parameters to correct for high-ionic strength effects and show that there is still some uncertainty about the predominant carbonate and hydrolytic species, particularly when longer-term timeframes are considered.

4:00pm **AC-TuA7 Elastic Moduli of Pure Alpha, Beta, Gamma Plutonium—Three Different Metals**, *A. Migliori*, Los Alamos National Laboratory

From 10 K to 580K plutonium changes phase from monoclinic alpha to body centered monoclinic beta to orthorhombic gamma structures. Each crystal structure is rare or unique for an elemental metal. Measurements presented here provide the first high-accuracy values for a single high-purity specimen of the elastic moduli of unalloyed polycrystal plutonium as a function of temperature throughout the entire range of existence of the alpha, beta, and gamma phases. The bulk and shear moduli, essential thermodynamic material properties, reflect important and huge changes with temperature, such that these phases present as three different metals. Unlike phase transformations in many other elements where the bonding, nearest-neighbor distances, and physical properties are closely related among phases, in the three lowest-temperature phases of plutonium, the relationships are missing, and support the extreme sensitivity of plutonium properties to phase, temperature, and almost-certainly, electronic structure. We describe here the characteristics and implications of these newly-observed properties.

4:20pm **AC-TuA8 Self Diffusion Coefficients of Trivalent Element Ions in Moderately Dilute Aqueous Solutions: Comparative Study between Lanthanum and f-elements**, *H. Latrous*, Faculté des sciences de Tunis, Tunisia, *R. Besbes*, IPEST, Tunisie, Tunisia, *N. Ouerfelli*, Faculté des Sciences de Tunis, Tunisia, *A. manef*, IPEST, Tunisie, Tunisia

Our work continues our studies on the trivalent ions 4f and 5f elements. In this paper, we have summarized data relatives to measurements of self-diffusion coefficients, conductance, mobility and activity coefficients for trivalent f-elements ions. Self-diffusion coefficients, D_i of the trivalent f-elements aquo ions series have been determined in aqueous electrolyte support at 25°C using the open-end capillary method (O.E.C.M.), from concentration 0 to 1.5M. We verify its variation with concentration and ionic strength of medium.

Variation of D_i/D_i° versus \sqrt{C} (C : molar concentration) for La^{3+} in acid medium $\text{pH}=2.5$, verify Nernst-Hartley expression. Activity coefficients $\gamma \neq 1$ for LaCl_3 at $\text{pH} = 2.5$ deduct from diffusion measurements are compared with recent data measured by *f.e.m* and are discussed in term of association phenomena (ion-pairing).

4:40pm **AC-TuA9 Synthesis and Characterization of Scintillating $\text{Gd}_2\text{SiO}_5:\text{Ce}$ Nanoparticles using Hot-Solution Growth**, *J. Choi, T.-K. Tseng, M.R. Davidson, P.H. Holloway*, University of Florida

Scintillation detectors are commonly used for measuring radiation from nuclear materials. To date the scintillating material has been a single crystal, commonly doped with a rare earth ion that controls the wavelength and

intensity of radioluminescence. Scintillating nanoparticles have the potential to replace the expensive, energy-intensive, limited volume single crystal detectors. In this study, scintillating $Gd_2SiO_5:Ce^{3+}$ (GSO) nanoparticles with 5–10 nm diameters were prepared by a two-pot hot-solution growth (HSG at 200–300 °C) method. The Ce dopant concentration was varied between 0.2%–5% and concentration quenching was examined by photoluminescence (PL). Low (0.5% Ce) doped GSO nanoparticles exhibited good PL from both as-synthesized and calcined (1100 °C for 2 h in air) nanoparticles. Concentration quenching for nanoparticles occurred at higher Ce concentrations than for bulk samples; this will be discussed. The PL emission was from the 5d to two 4f levels (2T_2 to ${}^2F_{7/2}$ and ${}^2F_{5/2}$ transitions) of Ce^{3+} at 420–450 nm. Photoluminescent excitation (PLE) spectra showed that the emission resulted from the direct excitation of the 4f–5d transition of Ce^{3+} excited between 270–375 nm. X-ray diffraction (XRD) and transmission electron microscopy (TEM) data showed that the GSO nanoparticles were amorphous as grown, but well crystallized after calcining. Quantum yield and radioluminescence data will be presented and discussed.

Applied Surface Science

Room: Cochiti - Session AS-TuA

Advances in Surface and Interface Imaging

Moderator: A.V. Walker, University of Texas at Dallas

2:20pm **AS-TuA2 Advanced Chemical State Analysis Method with Standard Spectra Measured with a Higher Energy Resolution of 0.1 % in Auger Electron Spectroscopy**, *K. Tsutsumi, M. Shima, A. Tanaka, T. Tazawa*, JEOL Ltd., Japan

Auger electron spectroscopy (AES) and X-ray photoelectron spectroscopy (XPS) are very famous for elemental and chemical state analysis at a solid surface. In generally, XPS has been utilized for these analysis in an area of more than a few 100 nm² on a solid surface. In contrast, AES has been used rarely for chemical state analysis, but for elemental analysis at a minute area of less than 100 nm². The reason for it is approximately caused by the following three problems.

It is difficult to detect any peak shifts between chemical state differences because almost peaks in an AES spectrum are broader than XPS.

It is difficult to measure stably a standard AES spectrum for an insulator sample because a focused electron beam irradiation causes stronger surface charging.

A focused electron beam often makes some elements change to another chemical state.

Among these problems, No.2 and No.3 can be solved in many cases by some special pre-sampling and measurement techniques. However No.1 has been recognized as the biggest problem for the chemical state analysis in AES because some commercial Auger instruments could not obtain sharper peaks in a spectrum with a poor energy resolution of 0.5-0.6 % or the others could not have a sufficient sensitivity with an energy resolution of higher 0.1 %. So, the chemical state analysis in AES has been carried out only for some specific elements showing a bigger chemical shift of more than a few eV.

Now we had measured more than 400 standard spectra by the latest analyzer for pure materials or compounds with the energy resolution of higher than 0.1 %, which included sharper peaks and fine structures with little electron beam damage. Those spectra show that Auger spectra for compounds have different peak shapes and different peak positions. So, it is possible to distinguish them by the peak shape difference, even if some standard spectra of different chemical states have quite similar peak positions each other.

In this report, we can propose an advanced chemical state analysis by higher energy resolution AES, which is a spectrum separation method from a practical spectrum including several chemical states by comparison of peak shape difference. As an example application, this method was applied for the depth profile result of a natural oxide layer on a pure tin oxide plate with an energy resolution of 0.1 %. The result showed that it was clearly consisted of three layers ($SnO_2/SnO/Sn$ subst.) by the waveform separation of Sn MNN to each chemical condition of Sn^{4+} , Sn^{2+} , and Sn^0 . Moreover, it was found that the quantitative analysis of chemical state of Sn was also possible by comparison of the absolute intensity of standard spectrum.

2:40pm **AS-TuA3 3D Atom Probe Analysis of Embedded Nanoclusters in Oxide Matrix**, *S. Kuchibhatla, V. Shutthanandan, B. Arey*, Pacific Northwest National Laboratory, *R. Ulfzig, T. Prosa*, Cameca Instruments Inc., *C.M. Wang, S. Thevuthasan*, Pacific Northwest National Laboratory, *P. Clifton*, Cameca Instruments Inc.

The influence of embedded nanoclusters on the optical, magnetic and electrical properties of bulk and surface oxides has been an active area of investigation. The establishment of new atom probe tomography (APT) and related high-resolution chemical imaging facilities at EMSL, the Environmental Molecular Sciences Laboratory, provides a world-class user facility for performing nanoscale microscopy. In this study we report on Au-rich nanoclusters that have been embedded into MgO and TiO₂ substrates. The effect of high temperature annealing on the properties of the matrix and the secondary phase (Au) are studied in detail. Electron microscopy analysis has shown that the embedded metal particles are often associated with various defects, which further contribute to property modification.

We report the first Local Electrode Atom Probe (LEAP[®]) analysis of bulk MgO and TiO₂ implanted with 2 MeV Au ions using the accelerator facility at EMSL. Both as-implanted and annealed samples were critically analyzed using a combination of APT and the results are compared with high-angular annular dark-field scanning transmission electron microscopy (HAADF STEM) imaging. High-resolution transmission electron microscopy (HRTEM) clearly resolves the Au-rich nanoclusters and allows observation of the pronounced vacancy clustering associated with these features [1]. These Au-rich nanoclusters were also observed in the atom probe data with the average cluster size (~ 5 nm diameter) in good agreement with those seen using HRTEM. The APT technique, however, due to the high three-dimensional (3D) spatial resolution, is also able to detect the presence of finer-scale Au clusters. It can also directly measure residual Au composition within the MgO matrix and any MgO-Au mixing within the clusters. Besides variations in compositional microstructure, evolution of mass spectrum quality as a function of Au content is also observed. Efforts are ongoing in EMSL to confirm this observation and eliminate the possibility of any contribution from experimental artifacts.

During the course of this presentation we will highlight the advantages of using 3D APT in combination with electron microscopy. Specifically, correlative microscopy provides a means to evaluate the capability of APT to detect the presence of the vacancy clusters.

[1] Wang et al., Applied Physics Letters **87**, 153104, 2005

3:00pm **AS-TuA4 Novel Nanoscopic Light Source for Tip-Enhanced Raman Spectroscopy**, *Y.-T. Li*, University of Cambridge, UK, *D. Roy*, National Physical Laboratory, UK, *M.E. Welland*, University of Cambridge, UK

The invention of the Atomic Force Microscope (AFM) in 1986 has pushed the frontier of nanoscience, particularly in the semiconductor industry and biosciences. These instruments allowed atomic scale imaging of surfaces at ambient conditions. Researchers around the world are working to add new functionalities to the AFM probe to acquire both chemical and topographical information at the nanoscale.

In this work the authors present a novel nano-probe designed for Tip-Enhanced Raman Spectroscopy (TERS), which provides chemical and structural information with nanometer scale spatial resolution. This probe can act as a sensor for chemical analysis either by Raman or fluorescence Spectroscopy.

In TERS, a sharp metal (gold or silver) tip (<50 nm) is produced by electrochemically etching and a laser beam is focused onto the tip-end. There is an enhancement in the electric field at the end of the tip which gives a near-field enhancement of the Raman signal. Results obtained shows chemical and topological information with ~30nm spatial resolution of single Carbon Nanotubes. However, the two major challenges in TERS are (a) coupling the light at the tip-end to achieve a high enhancement factor, (b) reducing the background (far-field) signal. There are significant inconsistencies in the reported values of the enhancement factor in literature. In this work we present a new approach for calculating the Raman enhancement factor. This was performed by near-field and far-field measurements on a bi-layer film made of two different materials having distinct Raman signatures. This method eliminates the errors in calculating the enhancement factor arising from measurements on single layer/nanostructures.

To address the issue of background signal, a novel approach is demonstrated by coupling light through a grating etched onto the tip-shaft fabricated by Focused Ion Beam (FIB). The grating is purposely used to couple the laser beam with the surface plasmon to generate a new localised light source at the tip end. This new nanoscopic light source is equivalent to the size of the tip apex thereby overcoming the diffraction limit. With this new light source, background free TERS and fluorescence measurements can be performed at ambient conditions. This tip can also be used in various

other applications including fluorescence correlation spectroscopy with concentrated samples.

4:00pm AS-TuA7 Imaging of Coal Speciation Using TOF-SIMS and Scanning Transmission X-Ray Microscopy (STXM), B.P. Yatzor, University at Buffalo, *H.D. Liang*, China University of Mining and Technology, China, *J.A. Gardella Jr.*, University at Buffalo

A significant problem in the combustion of coal is the release of toxic elements into the atmosphere in gaseous and solid (particulate) forms. In China, villagers use coal, exposed at the surface by erosion, to heat their homes and cook their meals. It is believed that coal combustion is a potential source of endemic diseases [1, 2].

Coal samples were collected from the province of Guizhou in China. In this study, an ION-TOF V equipped with a bismuth primary ion source was used to analyze coal directly without any chemical treatment. Mechanical polishing was performed to create a flat surface for analysis. Analyses revealed that there are distinctions between the organic and inorganic phases of coal. Fluorine was determined to come from an inorganic phase rather than an organic phase. Two different forms of elemental sulfur were determined through ion imaging. The first one was determined to be organic in nature, while, the second derives from pyrite (FeS₂).

The high spatial resolution of TOF-SIMS can be used to distinguish between different domains in coal, revealing the relationship between specific components suspected of involvement in toxicity of particulate emissions and the coal components.

STXM images, from powder samples suspended on Si₃N₄ windows, show complementary chemical images of carboxylic, aromatic and carbonate species from the C_{1s} edge. Studies were performed using the third generation Canadian Light Source synchrotron facility located in Saskatoon, Saskatchewan. The soft microscopy beamline (10ID-1) was used for analyses.

Spectral shifts in STXM NEXAFS spectra allow carbonate species to be distinguished from carboxylic species. With the help of reference materials, aromatic species could be distinguished from aliphatic species. However, using TOF-SIMS for distinguishing such species would prove to be very difficult, which is why STXM is a good complementary technique for coal studies.

[1] Finkelman *et al.* (2004) *Int. J Coal Geol.* **59**, 19–24.

[2] Finkelman *et al.* (2002) *Int. J Coal Geol.* **50**, 425–443.

4:20pm AS-TuA8 From Depth Profiling to FIB Sectioning for 3D TOF-SIMS Imaging of Organics, G.L. Fisher, S.R. Bryan, Physical Electronics, *P. Lu*, General Motors Company, *N. Smith*, Oregon Physics, *C. Szakal*, NIST

TOF-SIMS characterization of materials in the range of several microns from the sample surface has become somewhat routine. Nevertheless, there are practical limitations to the use of ion beam sputtering for probing both organic and inorganic specimens beyond the surface region. Certain matrix components do not sputter well and are susceptible to ion beam-induced molecular damage. This accumulated beam damage gives rise to incorrect molecular distributions. Some matrix components may sputter at a different rate than others which results in a misrepresentation of the elemental and molecular distributions. Finally, the time requirements to achieve uniform (i.e. representative) depth profile analysis under ideal instrumental conditions can become prohibitive. Even under optimized experimental conditions, the efficacy of sputter depth profiling for 3D TOF-SIMS imaging is limited to < 5 μm in the case of a favorable matrix and to < 300 nm in the case of an unfavorable matrix. An alternative approach for 3D TOF-SIMS imaging the interior of a specimen is to utilize FIB milling and sectioning. With FIB milling, the interior of a specimen is revealed to depths of ~ 50 μm within a reasonable analytical timeframe. Additionally, 3D chemical imaging of ~ 10 μm deep volumes may be achieved in the same time it would take to perform a low voltage sputter depth profile. The advantage of the FIB-TOF approach is that the artifacts caused by sputter depth profiling, i.e. differential sputtering and accumulated ion beam damage to matrix molecules, are avoided. The union of successive FIB sectioning and TOF-SIMS analysis cycles to achieve 3D chemical imaging will be discussed and illustrated using inorganic and organic examples.

4:40pm AS-TuA9 Mapping of a Polymer Surface Reaction: Determination of the Spatially Resolved, Hydrolytic Degradation Kinetics of a Micropatterned Bioresorbable Membrane, M.D. Marchany, I.T. Ozbolat, B. Koc, J.A. Gardella, Jr., SUNY at Buffalo

Poly(L-lactic acid) (PLLA) is a synthetic, bioresorbable polyester that is extensively used and studied for many [FDA-approved] commercial applications – such as therapeutic drug delivery and tissue engineering scaffolds.¹ It is generally accepted that the degradation process of bioresorbable polyesters: a) is diffusion-based,² b) occurs in a region of

finite thickness, forming an erosion front that moves towards the center of a polymer structure,² and c) its rate increases with higher polymer surface area.³ Time-of-Flight Secondary Ion Mass Spectrometry (ToF-SIMS) has been previously used to determine initial (before the onset of weight loss) degradation kinetics at bioresorbable polymer surfaces.⁴ This analytical method, combined with the high lateral resolution capabilities of imaging with a bismuth ion source, and image processing algorithms, allowed us to determine the spatially-resolved initial degradation kinetics of micropatterned PLLA membranes at several pH levels. The results show that the degradation reaction occurs at different rates, and that these rates depend on the area of the feature. The findings of this study imply that polymer degradation can be controlled not only in a temporal manner, but also in a microspatial manner, by altering micropattern geometry and size distribution across the polymer membrane.

1. Lee, J, Gardella, Jr., *J. Analytical and Bioanalytical Chemistry.* **2002.** 373. 526.

2. Mathiowitz, E, Jacob, J, Pekarek, K, Chickering III, D. *Macromolecules.* **1993.** 26. 6756.

3. Buchanan, FJ, 2008. *Degradation Rate of Bioresorbable Materials: Prediction and Evaluation.* Cambridge, UK. Woodhead Publishing Limited.

4. Lee, J, Gardella Jr., *J. Analytical Chemistry.* **2003.** 75. 2950.

5:00pm AS-TuA10 Approaches towards Analyzing XPS Multispectral Image Series (Multi-Sample Analysis) and Combining Multiple Spectroscopic, Microscopic and Macroscopic Analytical, K. Artushkova, University of New Mexico

Applications of multivariate analysis (MVA) methods to surface analysis imaging datasets have increased quite significantly in recent years. Multivariate analysis of 3D imaging TOF-SIMS and XPS data is now quite widely applied (even routinely used by some research groups). Data preprocessing, scaling and selection of appropriate multivariate analysis method have been discussed in the literature quite extensively in a couple of recent years.

What has been addressed in a lesser extent is an important problem of combining quantitative analysis of imaging datasets from the same analytical method from various samples (multi-sample 3D imaging) or combining various analytical data (spectroscopic, imaging, or scalar) obtained for the same sample (multi-modal analysis).

Approaches to quantitatively combine imaging datasets from multiple samples will be discussed on example of multispectral XPS imaging data sets acquired from various paper samples.

Multi-modal analysis will be discussed on example of combining spectroscopic (XPS, XANES), microscopic (SEM) and macroscopic (BET surface area and pore size distribution) data from set of non-Pt group metal electrocatalysts for oxygen reduction reaction treated at different temperatures.

5:20pm AS-TuA11 Atomic Scale Structural and Chemical Analysis of Internal Interfaces in Inorganic Materials, B.P. Gorman, H.L. Guthrey, Colorado School of Mines, *A.G. Norman, Y. Yan, M. Al-Jassim*, National Renewable Energy Laboratory, *R.P. O'Hayre*, Colorado School of Mines

INVITED

Fundamentally, photovoltaic and fuel cell devices rely upon interfaces for electrical power generation. However, the undesirable formation of poor quality interfaces can also serve to decrease power efficiency. In the case of photovoltaics, interfaces control the generation and extraction of photogenerated charge carriers; however, the formation of dislocations and dopant clustering can result in recombination centers, thus reducing the ability to extract charge carriers. In fuel cells, the three phase boundary between the electrode, gas, and electrolyte controls the cell power output; however, surface contamination at this interface can reduce the electrochemical reaction rate, and thus the power output of the cell. Understanding both of these interfaces at the atomic structural and chemical level allows for a greater understanding of the formation of interface degradation. In order to fully understand the atomic scale chemistry and structure of interfaces in photovoltaics and fuel cells, we have applied a combination of in-situ FIB / SEM electrical probing using EBIC and ex-situ impedance spectroscopy with high resolution analytical STEM imaging and laser pulsed atom probe tomography. These techniques have been applied to III-V based photovoltaics to gain an understanding of dopant profiling across quantum structures and tunnel junctions, and to probe the initial stages of phase separation in multicomponent epilayers. Similarly, EBIC has been used to identify dislocations and grain boundaries in polycrystalline Si photovoltaics, and to determine the atomic level chemistry and structure at these interfaces that leads to an interface acting as a recombination center. Finally, a combination of STEM and atom probe tomography have illustrated 10⁻¹⁷ / cm³ changes in local Pt, C, and O

chemistry and structure around Pt catalysts for use in polymer electrolyte fuel cells. In order to enable atom probe analysis on materials with widely varying field evaporation characteristics, new FIB specimen preparation techniques were required. Details on the complex experimental methods and instrumentation developed in order to enable all of these investigations are illustrated.

Biomaterial Interfaces

Room: Taos - Session BII-TuA

Bacteria on Surfaces

Moderator: L.J. Gamble, University of Washington

2:00pm **BII-TuA1 High Throughput Methodologies for the Discovery of Materials Resistant to Biofilm Formation**, A.L. Hook, J. Yang, C.-Y. Chang, University of Nottingham, UK, D.G. Anderson, R. Langer, Massachusetts Institute of Technology, S. Atkinson, P. Williams, M.C. Davies, M.R. Alexander, University of Nottingham, UK

Biofilm formation leads to a 1000 times increase in antibiotic tolerance compared with planktonic bacteria and is associated with 80% of hospital acquired infections, resulting in \$3.0 billion in excess health-care costs each year in the U.S alone. Thus, new materials for biomedical devices that prevent biofilm formation would offer enormous benefits to the health industry and patient welfare. Polymer microarrays are emerging as a key enabling technology for the discovery of new biomaterials.¹ This platform enables a large combinatorial space to be rapidly screened by a biological assay to identify new materials that fulfil a given performance criterion.² Furthermore, utilising a high throughput surface characterisation approach the surface chemical and physical properties of each material can be understood and related to the biological performance in order to understand the material-biological interaction.³ A method for forming polymer microarrays has been developed using contact printing to deposit nanolitre volumes of premixed acrylate monomer and initiator to defined locations on a poly(HEMA) coated glass slide with UV photo-initiation.⁴ We have developed a high throughput bacterial attachment assay based on GFP transfected pathogens that is compatible with the polymer microarray format. In our high throughput strategy we initially produced an array containing hundreds of unique materials that was designed to maximise the combinatorial space explored. From this array 'hit' monomer compositions were identified that were used to design a second generation array that explored systematic variations in material compositions in order to focus onto the optimal material composition. This has been utilised to identify new materials that resist the formation of bacteria and show promise for implementation to various biomedical devices such as urinary tract catheters that are susceptible to bacterial colonisation.

¹ A. L. Hook, D. Anderson, R. Langer, P. Williams, M. C. Davies, and M. R. Alexander, *Biomaterials* **2010**, *31*(2), 187.

² Y. Mei, S. Gerecht, M. Taylor, A. J. Urquhart, S. R. Bogatyrev, S. W. Cho, M. C. Davies, M. R. Alexander, R. S. Langer, D. G. Anderson, *Adv. Mater.* **2009**, *21*(27), 2781.

³ A. J. Urquhart, D. G. Anderson, M. Taylor, M. R. Alexander, R. Langer, M. C. Davies, *Adv. Mater.* **2007**, *19*(18), 2486.

⁴ D. G. Anderson, S. Levenberg, R. Langer, *Nat. Biotechnol.* **2004**, *22*(7), 863.

2:20pm **BII-TuA2 Surface Self-Assembled PEG Gel Particles to Control Bacteria-Biomaterial Interactions**, Y. Wu, Q. Wang, M. Libera, Stevens Institute of Technology

The fact that desirable tissue cells and undesirable bacteria compete for the surface colonization of an implanted biomaterial is now well recognized. When bacteria win this competition, the resulting infection can lead to device failure with substantial consequences to both the patient and the health-care system. We are developing poly(ethylene glycol) [PEG]-based gel particles with which to modify surfaces and differentially control surface interactions with both tissue cells and bacteria. We are particularly interested in modulating the surface cell adhesiveness at micro/nano length scales with the goal of reducing staphylococcal adhesion while still enabling the adhesion, spreading, and proliferation of desirable tissue cells. In short to preserve healing while reducing the probability of infection. We have synthesized anionically charged PEG-acrylic acid (AA) copolymer hydrogel particles by inverse emulsion polymerization and used a bottom-up electrostatic self-assembly approach to modify otherwise cell-adhesive surfaces with cell-repulsive gel particles. Zeta potential measurements confirm that the gel particles are negatively charged because of the acid groups. SEM imaging and dynamic light scattering show that the particle diameters range from ~10's to ~100's of nm. We have electrostatically

deposited them on both polylysine-modified silicon wafers and titanium metal coupons. By varying the concentration of gel particles in solution and the deposition time, we can control the area density of particles deposited on the substrate surface to levels of ~ 0.1 – 2 particles/sq micron. Immunofluorescence imaging shows that, relative to unmodified Si and PLL primed Si, PEG-modified Si has substantially lower colonization by *S. epidermidis* after inoculation and 4 hrs of culture. Confocal imaging of PEG-modified surfaces after 4 days of osteoblast culture show good osteoblast spreading and proliferation. SEM images indicate that the osteoblasts grow over the cell-repulsive particles while adhering to the remaining adhesive surface. Such surfaces may be useful in reducing the susceptibility of biomedical devices to biomaterials-associated infection.

2:40pm **BII-TuA3 Some Strategies and Results for Antibacterial Coatings**, H.J. Griesser, K. Vasilev, H. Ys, C.P. Ndi, S.S. Griesser, S. Al-Bataineh, S. Semple, University of South Australia **INVITED**

Bacterial attachment and subsequent biofilm formation might be reduced by application of a thin coating that deters bacterial colonisation. For biomedical devices a coating should also allow good attachment of human tissue to facilitate wound healing, or for catheters and contact lenses be lubricious and not bio-adhesive. Requirements differ for antibacterial coatings for different implants and devices; accordingly we have used different approaches for the fabrication of several antibacterial coatings. For long-lasting effect, we prefer the approach of covalently immobilising antibacterial molecules; we have also investigated the alternative approach of release of silver ions. This presentation will review advantages and disadvantages of various approaches, and discuss open questions.

Our strategies are based on plasma polymer thin film coatings, because this approach can be transferred to coat many polymeric, metallic and ceramic materials. Plasma polymers with chemically reactive surface groups enable covalent immobilisation of antibacterial compounds onto their surface. Alternatively, we load plasma polymer coatings with silver nanoparticles, from which Ag⁺ ions can outdiffuse. Organic antibacterial compounds investigated were furanones, novobiocin, and serrulatanes, the latter are novel substituted diterpenes extracted from Australian plants used in traditional medicine. The chemical composition of coatings was assessed by XPS and ToF-SIMS to ensure that the intended coatings were achieved. Samples were tested for bacterial attachment and for biofilm formation, as well as for mouse 3T3 fibroblast cell attachment.

Surface-immobilised furanones, Novobiocin, and serrulatanes reduced bacterial attachment by up to 99.8%. While large biofilm communities formed on control surfaces within 48 hrs, these coatings prevented biofilm formation. Plasma polymer coatings loaded with Ag nanoparticles also were effective; Ag⁺ delivery can be adjusted via the properties and thickness of the plasma polymer film and the silver loading. Testing of coatings with m3T3 fibroblast cell cultures showed, however, that in many cases there were adverse effects. Silver in particular affected 3T3 cells. With organic antibiotics, the surface density appears important and an optimum must be found between deleterious cell effects and antibacterial effectiveness.

Important questions remain: do surface-immobilised antibiotics act as in solution, as quorum sensing inhibitors (furanones) or gyrase inhibitors (Novobiocin)? Do in vitro and in vivo tests correlate? How to mitigate adverse effects on mammalian cells? Why is there contradictory literature especially on Ag?

Biomaterial Interfaces

Room: Taos A - Session BI2+AS-TuA

Combining Techniques for Bointerface Characterization

Moderator: L.J. Gamble, University of Washington

4:00pm **BI2+AS-TuA7 Spatial and Depth Characterisation of Immobilised Biomolecules on Surfaces**, G. Mishra, A.J. Roberts, Kratos Analytical Ltd., UK, D.J. Surman, Kratos Analytical Ltd., S.L. McArthur, Swinburne University of Technology, Australia

4:20pm **BI2+AS-TuA8 Measuring the Orientation of Electrostatically Immobilised Proteins by Time-of-Flight Secondary Ion Mass Spectrometry and Sum Frequency Generation: From a Model Protein G B1 System to Cytochrome**, J.E. Baio, T.M. Weidner, L. Baugh, P.S. Stayton, L.J. Gamble, D.G. Castner, University of Washington

The ability to orient proteins on surfaces to control exposure of their biologically active sites will benefit a wide range of applications including protein microarrays and biomaterials that present ligands to bind cell receptors. As methods to orient proteins are developed, techniques are required to provide an accurate picture of their orientation. Since no single

technique provides a high-resolution image of surface-bound proteins, combinations of surface analytical techniques are required. In this study, we have developed a model system based on the electrostatic immobilization of a small rigid protein (Protein G B1 domain, 6kDa) to further develop the capabilities of time-of-flight secondary ion mass spectrometry (ToF-SIMS) and sum frequency generation (SFG) spectroscopy as tools to probe the orientation of surface immobilized proteins. A Protein G mutant (D4) exhibiting net positive and negative charges at either end (for pH 6-8) was produced by neutralizing four negatively charged residues closest to the end of the protein (Asp to Asn or Glu to Gln mutations). These mutants were then immobilized onto NH_3^+ and COO^- terminated self assembled monolayers (SAMs) to induce opposite end-on orientations. ToF-SIMS data from the D4 variant on both NH_3^+ and COO^- SAMs showed intensity differences from secondary ions originating from asymmetric amino acids (Asn:70, 87, and 98m/z; Met:62m/z; Tyr:107 and 136m/z at the N-terminus. Leu:86m/z at the C-terminus). For a more quantitative examination of orientation, we developed a ratio comparing the sum of the intensities of ions stemming from residues at either end of the protein. The 50% increase in this ratio, observed between the NH_3^+ and COO^- SAMs, indicated opposite orientations of the D4 variant on the two different surfaces. In addition, SFG spectral peaks characteristic of ordered α -helix (1645cm^{-1}) and β -sheet (1624 and 1675cm^{-1}) elements were observed, with a phase that indicated a predominantly upright orientation for the α -helix, consistent with an end-on protein orientation. We then moved from this model system and extended this analysis to examine the change in orientation of horse heart Cytochrome c on both NH_3^+ and COO^- SAMs. The positively charged region at one end of Cytochrome c binds to the COO^- substrate while the NH_3^+ surface elicits the opposite binding orientation. Again, within the SFG spectra, ordering of the protein α -helices were confirmed by the feature at 1645cm^{-1} and the change in orientation, induced by the two different substrates, is confirmed by intensity differences within ToF-SIMS spectra between ions stemming from asymmetric amino acids (Glu:84 and 102m/z; Asp:72 and 88m/z).

4:40pm **BI2+AS-TuA9 NanoBio Imaging for Cardiovascular Researches**, *D.W. Moon, T.G. Lee, J.Y. Lee, W. Jegal, S.W. Kim*, KRIS, Republic of Korea

INVITED

NanoScience has been developed to meet the demands on atomic scale characterization and manipulation of materials and devices from semiconductor industries based on the scaling down law. KRIS has been trying to extend the application scope of nanoscience and technology from microelectronics to biomedical areas. Biochemical imaging of cells and tissues is a basic infra-technology in various bio-medical applications. Instead of conventional labeling methodology for bio-molecular imaging with fluorescent dyes, label-free biochemical imaging methodologies for single cells and tissues such as coherent anti-stokes Raman scattering (CARS), secondary ion mass spectrometry (SIMS), and surface plasmon resonance imaging ellipsometer (SPRIE) has been developed and integrated for new biomedical applications, especially for cardiovascular researches.

Preliminary results of nanobio imaging for cardiovascular researches will be reported on the following issues 1) Three-dimensional visualization of atherosclerotic tissue and prompt on-site analysis of chemical profiles by multiplex CARS with intracellular lipids at the single-cell level as well as crystallized cholesterol in necrotic cores. ⁽¹⁾ 2) Histological Imaging based on SIMS analysis of myocardial infarction tissues. ⁽²⁾ 3) cell adhesion dynamics of human carotid smooth muscle cells and human umbilical endothelial cells on fibronectin thin films with SPRIE.

Finally, the present status and future challenges of nano-bio technology based on laser, mass spectrometry, and nanoprobe for biochemical imaging of single cells and tissues at KRIS will be discussed for practical applications in bio, medical, and pharmaceutical researches.

(1) "Multiplex coherent anti-Stokes Raman spectroscopy images intact atheromatous lesions and concomitantly identifies distinct chemical profiles of atherosclerotic lipids", Se-Hwa Kim, Eun-Soo Lee, JaeYong Lee, EunSeong Lee, Bok-Soo Lee, JeongEuy Park, and DaeWon Moon, Circulation Research, in press (2010)

(2) "ToF-SIMS Analysis of Myocardial Infarcted Tissue", J.-W. Park, M.-J. Cha, H. K. Shon, S.-H. Kim, T. G. Lee, D. W. Moon, and K.-C. Hwang, Surface and Interface Analysis, in press (2010)

5:20pm **BI2+AS-TuA11 Determining Antibody Orientation using ToF-SIMS and Fluorescence Imaging of Affinity-generated Patterns**, *M. Dubey*, Los Alamos National Laboratory, *F. Liu, H. Takahashi, D.W. Grainger*, University of Utah, *D.G. Castner*, University of Washington

This study assesses the capability of high-resolution surface analytical tools to distinguish immobilized antibody orientations on patterned surfaces designed for antibody affinity capture. High-fidelity, side-by-side co-patterning of protein A (antibody Fc domain affinity reagent) and fluorescein (antibody Fab domain hapten) was achieved photo-

lithographically on commercial amine-reactive hydrogel polymer surfaces. This was verified from fluorescence imaging using fluorescently labeled protein A and intrinsic fluorescence from fluorescein. Subsequently, dye-labeled murine anti-fluorescein antibody (4-4-20), and antibody Fab and Fc fragments were immobilized from solution onto respective protein A- and fluorescein- co-patterned or control surfaces using antibody-ligand affinity interactions. Fluorescence assays support specific immobilization to fluorescein hapten- and protein A-patterned regions through antigen-antibody recognition and natural protein A-Fc domain interactions, respectively. Affinity-based antibody immobilization on the two different co-patterned surfaces generated side-by-side full antibody "heads-up" and "tails-up" oriented surface patterns. Time-of-flight secondary ion mass spectrometry (ToF-SIMS) analysis, sensitive to chemical information from the top 2-3 nm of the surface, provided ion-specific images of these antibody patterned regions, imaging and distinguishing characteristic ions from amino acids enriched in Fab domains for antibodies oriented in "heads-up" regions, and ions from amino acids enriched in Fc domains for antibodies oriented in "tails-up" regions. Principal component analysis (PCA) improved the distinct ToF-SIMS amino acid compositional and ion-specific surface mapping sensitivity for each "heads-up" versus "tails-up" patterned region. Characteristic Fab and Fc fragment immobilized patterns served as controls. This provides first demonstration of pattern-specific, antibody orientation-dependent surface maps based on antibody domain- and structure- specific compositional differences by ToF-SIMS analysis. Since antibody immobilization and orientation are critical to many technologies, orientation characterization using ToF-SIMS could be very useful and convenient for immobilization quality control and understanding methods for improving the performance of antibody-based surface capture assays.

5:40pm **BI2+AS-TuA12 Molecular Depth Profiling and 3D Imaging of Biological Samples by ToF-SIMS: From Model Amino Acid Films to Real Biological Cells**, *J.P. Brison, N. Wehbe*, University of Namur, Belgium, *D.G. Castner*, University of Washington, *L. Houssiau*, University of Namur, Belgium

Time-of-Flight Secondary Ion Mass Spectrometry is now routinely used to obtain molecular information about the surface of complex biological samples and biomaterials. The recent advent of cluster ion beams such as Bi_3^+ and C_{60}^+ provides enhanced sensitivity for high mass fragments, which in turn allows 2D imaging of specific biomolecules with improved sensitivity and sub-micrometer lateral resolution. Molecular depth profiling of biological samples with low chemical damage and high depth resolution (*i.e.*, < 10 nm) has also been shown to be possible by etching with cluster projectiles such as C_{60} and with low energy cesium ions. Since ToF-SIMS also allows the detection of all elements without the need of specific markers, the technique shows great potential for molecular 3D imaging of single cells and could become an inevitable complementary tool to MALDI and fluorescence microscopy for biomedical research in the near future.

However, only few examples of full 3D images of biological cells have been reported in the literature at this time. This limitation probably comes from the facts that preparing the cells for chemical analysis under UHV environment is tedious, and that our understanding of energetic primary ions/biological matter interactions is limited. Fundamental studies of these aspects are indeed difficult during 3D imaging because the cells are complex, heterogeneous, non-flat samples with relatively unknown molecular composition.

In this work, fundamental biological matter/projectile interactions were studied by depth profiling model amino acid films under different ToF-SIMS conditions. The influence of the experimental parameters on the quality of the depth profiles was investigated by measuring the sputter rates, the depth resolutions and the intensities of the molecular ion signals with respect to the chemistry of the target (*e.g.*, arginine vs phenylalanine), the nature of the primary ion species (*e.g.*, C_{60}^+ vs Cs^+) and the bombardment conditions (*e.g.*, fluence and energy). Then the complexity of the model samples was increased by mixing several amino acids and by creating multilayer films. This approach was another step toward the analysis of real biological samples. Again, ToF-SIMS fundamentals were investigated by measuring, *e.g.*, the interface widths between the different organic layers and the signal decay due to the increasing etching fluence. Finally, optimal 3D images of single HeLa cells were acquired and were discussed based on the data obtained for the model amino acid films. The effect of the sample preparation on the quality of the images was also investigated.

Electronic Materials and Processing
Room: Dona Ana - Session EM-TuA

Defects in Semiconductors and Oxides

Moderator: J. Drucker, Arizona State University

2:00pm **EM-TuA1 Influence of N-induced Point Defects on the Electronic Properties of Dilute Nitride GaAsN Alloys**, *Y. Jin, R.M. Jock, H. Cheng, C. Kurdak, R.S. Goldman*, University of Michigan **INVITED**
(In)GaAsN alloys with a few percent nitrogen have potential applications in long wavelength optoelectronic devices, such as infrared laser diodes, heterojunction bipolar transistors, and high efficiency solar cells. However, due to the large size and electronegativity differences between As and N, the formation of several point defect complexes has been predicted, likely leads to the limited optical emission efficiency and minority carrier transport properties in (In)GaAsN alloys. In this work, we investigate the influence of two types of N-related point defect complexes, Si-N complexes and N interstitials, on the electronic and optical properties of InGaAsN alloys.

The presence of Si-N defect complexes is first suggested by a decrease in carrier concentration, n , with increasing N-composition observed in GaAsN:Si films but not in modulation-doped heterostructures. In addition, for GaAsN:Te (GaAsN:Si), n increases substantially (minimally) with annealing-T, suggesting a competition between annealing-induced Si-N complex formation and a reduced concentration of N-related traps. Since Si-N complex formation is enhanced for GaAsN:Si growth with the (2 x 4) reconstruction, which has limited group V sites for As-N exchange, the (Si-N)_{As} interstitial pair is identified as the dominant Si-N complex.

For the investigation of N interstitial defects, we compared the structural and electronic properties of GaAsN films before and after annealing. Nuclear reaction analysis (NRA) reveals an annealing-induced decrease in the interstitial N concentration, f_{int} , while the total N composition remains constant. Corresponding signatures for the reduced f_{int} are apparent in Raman spectra. For as-grown GaAsN films, low T transport measurements reveal two distinct T-dependent regimes of n : a T-independent regime > 150K, and a thermally-activated regime <150K. Meanwhile, persistent photoconductivity effect (PPC) was observed up to 160K, with the photo-capture barrier determined to be 350 - 400 meV. These two phenomena are reminiscent of the behavior of n-type AlGaAs due to the presence of DX-center levels, suggesting the presence of similar N-induced defect levels in GaAsN. After annealing, the thermal activation of n and the PPC effect are both suppressed, accompanied by the decrease in f_{int} revealed by NRA, suggesting the association of these two phenomena with N interstitials.

This work is supported by NSF-FRG, grant # DMR-0606406, monitored by L. Hess

2:40pm **EM-TuA3 Identification of the Dominant Recombination Centers in Dilute Nitrides**, *I.A. Buyanova, M. Chen*, Linköping University, Sweden **INVITED**

Dilute nitride alloys have in past years sparked a considerable interest because of their unusual physical properties and their potential device applications in visible light emitting diodes (LEDs), long wavelength telecommunications lasers on a GaAs substrate and highly efficient hybrid solar cells. Up to now, however, a major obstacle for full exploration of these devices is degradation of the radiative efficiency and carrier mobility of dilute nitrides when N content increases, mainly due to severe non-radiative (NR) recombination and carrier scattering. Many theoretical and experimental efforts were devoted to identifying the NRR centers, however, their origin is still being debated.

In this talk we will review our recent experimental results that have positively identified Ga interstitial defects as the dominant NR defects in Ga(In)NP and Ga(In)NAs epilayers and quantum wells by optical and spin resonance spectroscopy. Their formation is shown to strongly depend on growth methods (MBE or MOCVD) and conditions (growth temperature, bombardment by N ions, N flow, etc) as well as post-growth rapid thermal annealing and hydrogenation. In Ga(In)NAs, the carrier recombination process via these defects is shown to be strongly spin-dependent, which opens a door for spin manipulation of the process [1]. We demonstrate that strong spin-blockade of NR carrier recombination via these Ga interstitial defects can be achieved once the defect electrons are spin polarized. This results in a significant enhancement of light emission efficiency by up to 8 times, accompanied by a sizable increase in the non-equilibrium carrier lifetime. The defects formation is concluded to become thermodynamically favorable under the presence of N, possibly because of local strain compensation and seems to be unavoidable at least with the current technology. Therefore, demonstrated spin blockade of the associated carrier

recombination appears to offer an attractive approach to strongly suppress NR shunt path.

Besides the Ga interstitial defects, we will show that severe nitrogen ion bombardment under non-equilibrium growth conditions during solid-source MBE could also trigger formation of an interfacial defect at a GaNP/GaP interface. The defect is identified to involve a P_{Ga} antisite or a P_i interstitial with a neighboring partner aligned along a <111> direction. The defect could be important in restricting carrier mobility in the related transistor structures and in reducing radiative efficiency of the GaNP-based LEDs.

[1] X.J. Wang, I.A. Buyanova, F. Zhao, D. Lagarde, A. Balocchi, X. Marie, C.W. Tu, J.C. Harmand and W.M. Chen, Nature Materials, 8, 198 (2009).

4:00pm **EM-TuA7 Band Bending and Surface Defects in Ga₂O₃**, *T.C. Lovejoy, R. Chen, S.X. Zheng*, University of Washington, *E.G. Villora, K. Shimamura, H. Yoshikawa, Y. Yamashita*, NIMS, Japan, *S. Ueda, K. Kobayashi*, SPring-8, Japan, *S. Dunham, F.S. Ohuchi, M.A. Olmstead*, University of Washington

Wide-band-gap oxides like Ga₂O₃, In₂O₃, SnO₂, and ZnO, are of key importance as transparent conductors and gas sensing materials. The conductivity in these materials is almost-always observed to be n-type, although the mechanism is under debate. An inverse correlation between oxygen partial pressure, p(O₂), during growth and measured conductivity has been reported, leading to a commonly held model that oxygen vacancy defects in the crystals are responsible for the conductivity. This model is supported by some density functional theory (DFT) calculations, in SnO₂ for example, but excluded by others. beta-Ga₂O₃ has the largest band gap of the oxides listed above, ~4.8 eV, making it unique among them for near-UV applications. We report on a combined experimental and theoretical study of beta-Ga₂O₃ single crystals. Using density functional theory we compute the formation energies of various intrinsic defects as function of the Fermi level position relative to the valence band maximum (E_F-E_{VBM}). We show by a combination of hard x-ray photoemission (HAXPS) and Hall measurements that the near-surface value of E_F-E_{VBM} is very different from that in the bulk due to band bending. By comparing the experimental results with the calculations we conclude that oxygen vacancies have too high an activation energy in the bulk to contribute substantially to the conductivity, but band bending enables them to play a role near the surface.

4:40pm **EM-TuA9 Control of Oxygen Diffusion in Titanium Dioxide for Nanoelectronic Applications**, *A. Hollister, P. Gorai, E.G. Seebauer*, University of Illinois at Urbana-Champaign

The technologically useful properties of semiconductor oxides such as titania often depend on the concentration and motion of defects. Native point defects such as interstitial atoms and vacancies strongly affect the operation of nanoelectronic gas sensors, light emitting diodes and memory resistors. Past work in our laboratory with silicon has shown that semiconductor surfaces serve as efficient pathways for generation and annihilation of point defects in the underlying bulk. Such pathways should play an especially important role in nanoelectronics fabrication, where devices have high surface-to-volume ratios. The present work extends the findings for silicon to the oxide semiconductor TiO₂, wherein we have identified a new pathway for interstitial-mediated diffusion of oxygen in titanium oxide. Oxygen diffusion rates were measured by exposing natural-abundance single-crystal rutile TiO₂ to isotopically labeled oxygen gas. The resulting profiles were measured by secondary ion mass spectrometry and subsequently modeled with continuum equations for the reaction and diffusion of the key point defects that control oxygen diffusion. The exponential diffusion profile shapes, together with the increase of the diffusion coefficients with oxygen pressure, strongly suggest the diffusion is mediated by oxygen interstitials. The measured diffusion coefficients were nearly two orders of magnitude higher than those expected from the literature, but could be decreased substantially by the adsorption of submonolayer quantities of sulfur to saturate surface dangling bonds. These latter observations suggest that the pristine TiO₂ surface is especially efficient at creating oxygen interstitials that then sink into the bulk and mediate diffusion there.

5:00pm **EM-TuA10 Effect of Vacuum Ultraviolet and Ultraviolet Irradiation on Capacitance-Voltage Characteristics of Low-k-porous Organosilicate Dielectrics**, *H. Sinha, J. Lauer, M. Nichols, A. Sehgal*, University of Wisconsin-Madison, *N.M. Russell, M. Tomoyasu*, Tokyo Electron Limited, *G.A. Antonelli*, Novellus Systems, Inc., *Y. Nishi*, Stanford University, *J.L. Shohet*, University of Wisconsin-Madison

5:20pm **EM-TuA11 Effect of Strain Relaxation on Electron Mobility in InAs/GaAs Nanowire Heterowires**, *K.L. Kavanagh*, Simon Fraser University, Canada, *J. Salfi, I. Saveliev*, University of Toronto, Canada, *D. Susac*, Simon Fraser University, Canada, *M. Blumin, H. Ruda*, University of Toronto, Canada

The structure and electrical properties of InAs-GaAs core-shell nanowires grown by molecular beam epitaxy on GaAs (001) substrates has been investigated by scanning transmission electron microscopy (STEM) and field-effect measurements of nanowire conductance. Zincblende and wurtzite phase wires are found growing preferentially along

(001) directions. The InAs core radii varied from 10 to 60 nm, with GaAs shell thicknesses from 3 to 20 nm, depending on the growth time.

The ZB wires show a rectangular cross-section with $\langle 110 \rangle$ side facets while the WZ are hexagonal in cross-section. Strain relaxation via dislocations in individual wire is observed from the analysis of electron diffraction and Moire fringe patterns. Close to complete relaxation (95%) occurs preferentially in the longer radial $\langle 110 \rangle$ direction while a large residual strain of 30% to 50% is found along the wire length. Less strain relaxation in the perpendicular radial $\langle 110 \rangle$ direction is occurring consistent with a large radius of curvature in the wire morphologies.

The room temperature field effect mobility of unencapsulated InAs nanowires increases from approximately 1000 to several thousand as diameter increases from 30 to 80 nm, consistent with scattering from charged surface states or surface roughness. In comparison, InAs-GaAs core-shell nanowires have lower field effect mobility which does not increase with increasing diameter. A different, diameter-independent scattering mechanism related to strain relaxation limits the electronic mean-free-path in InAs-GaAs core-shell nanowires.

Energy Frontiers Topical Conference

Room: Mesilla - Session EN+EM-TuA

Electronic Materials for Energy Conversion & Storage

Moderator: G.W. Rubloff, University of Maryland

2:00pm **EN+EM-TuA1 High-capacity and High-rate Metal Oxide Anodes for Li-ion Batteries**, *A.C. Dillon, C. Ban*, National Renewable Energy Laboratory, *L.A. Riley, A.S. Cavanagh, S.M. George*, University of Colorado, *Y.S. Jung, Z. Wu, Y. Yan*, National Renewable Energy Laboratory, *S.-H. Lee*, University of Colorado **INVITED**

Significant advances in both energy density and rate capability for Li-ion batteries will be necessary for implementation in next generation electric vehicles. By employing metal oxide nanostructures, it is possible to achieve Li-ion anodes that have significantly higher capacity than the state-of-the-art graphite technology. For example we have demonstrated that thin film MoO_3 nanoparticle electrodes ($\sim 2 \mu\text{m}$ thick) have a stable reversible capacity of $\sim 630 \text{ mAh/g}$ when tested at $C/2$.¹ By fabricating more conventional electrodes ($\sim 35 \mu\text{m}$) with a conductive additive and binder, an improved reversible capacity of $\sim 1000 \text{ mAh/g}$ is achieved.² The increased capacity for the MoO_3 coin cell electrode compared to the thin film electrode may be attributed to improved electronic/ionic mobility with the conductive additive and more complete access to the nanostructures. We have also demonstrated that by applying a thin atomic layer deposition coating of Al_2O_3 , improved rate capability for the high volume expansion MoO_3 is achieved for thick more conventional electrodes³.

More recently we have focused our work on iron oxide nanostructures, as iron is an inexpensive, abundant and a non-toxic material. Furthermore, we have synthesized binder-free, high-rate capability electrodes. The electrodes contain Fe_3O_4 nanorods as the active lithium storage material and carbon single-wall nanotubes (SWNTs) as the conductive additive. The highest reversible capacity is obtained using 5 wt.% SWNTs, reaching 1000 mAh/g ($\sim 2000 \text{ mAh/cm}^3$) at C rate when coupled with a lithium metal electrode, and this high capacity is sustained over 100 cycles. Furthermore, the electrodes exhibit high-rate capability and stable capacities of 800 mAh/g at 5C and $\sim 600 \text{ mAh/g}$ at 10C. Scanning electron microscopy indicates that this high-rate capability is achieved because Fe_3O_4 nanorods are uniformly suspended in a conductive matrix of SWNTs. Raman spectroscopy is employed to understand how the SWNTs function as a highly flexible conductive additive. We expect that this method can be used to achieve

other binder-free anodes as well as cathodes with similar high-rate capability⁴.

(1) Lee, S.-H.; Kim, Y.-H.; Deshpande, R.; Parilla, P. A.; Whitney, E.; Gillaspie, D. T.; Jones, K. M.; Mahan, A. H.; Zhang, S. B.; Dillon, A. C. *Adv. Mat.* 2008, 20, 3627-3632.

(2) Riley, L. A.; Lee, S.-H.; Gedvilias, L.; Dillon, A. C. *Journal of Power Sources* 2010, 195, 588-592.

(3) Riley, L. A.; Cavanagh, A. S.; George, S. M.; Jung, Y.-S.; Yan, Y.; Lee, S.-H.; Dillon, A. C. *ChemPhysChem* 2010, *in press*.

(4) Ban, C.; Wu, Z.; Gillaspie, D. T.; Chen, L.; Yan, Y.; Blackburn, J. L.; Dillon, A. C. *Advanced Materials* 2010, *in press*.

2:40pm **EN+EM-TuA3 Engineering $\text{Li}_x\text{Al}_y\text{Si}_z\text{O}$ Thin Films as a Solid Electrolyte for 3D Microbatteries**, *Y.-C. Perng, J. Cho, D. Membreno, B. Dunn, J.P. Chang*, UCLA

The development of secondary lithium-ion batteries has been directed primarily at portable electronics applications. However, these batteries also have the potential to function as a power source for micro-systems through engineering of electrodes into 3D architectures based on high aspect ratio pillars. In order to utilize this potential, an ultra-thin and highly conformal solid electrolyte layer is required to coat the 3D electrode array. The solid electrolyte lithium aluminosilicate (LiAlSiO_4), is a promising candidate for this application due to high ionic conductivity along its c-axis resulting from channels formed by the alternating tetrahedra of aluminum-oxygen (Al-O) and silicon-oxygen (Si-O). The length of c-axis of lithium aluminosilicate can be adjusted by changing the crystallization temperature for desired conductivity characteristics.

Atomic layer deposition (ALD) was employed in this work to synthesize thin film lithium aluminosilicate. The self-limiting characteristic of ALD allows for precise control of thickness and composition of complex oxides and results in a highly conformal and pinhole-free coating suitable in 3D micro-battery applications. The metal precursors used in this work are tetraethyl orthosilicate (TEOS), trimethylaluminum (TMA) and lithium t-butoxide (LTB). We also investigated the use of tri-t-butoxy-hydroaluminate (LTBA) but found that the metal composition was difficult to control and high carbon contents. Using the three precursors mentioned above with water vapor as the oxidant, we deposited SiO_2 , Al_2O_3 and Li_2O , at deposition rates in the range of $0.8\text{-}2 \text{ \AA}/\text{cycle}$. The overall deposition rate of stoichiometric LiAlSiO_4 was $\sim 5 \text{ \AA}/\text{cycle}$ using a chamber base pressure of 10^{-2} Torr and substrate temperature of 300°C . The concentration of each metal element in $\text{Li}_x\text{Al}_y\text{Si}_z\text{O}$ thin films is found to correlate closely to ALD cycles and the associated incubation times. The crystalline structures as well as the local environment of the Li-conducting channels are also affected by the ALD cycles and sequences, as indicated by ultraviolet photoelectron spectroscopy (UPS), transmission electron microscopy (TEM) imaging and nuclear magnetic resonance (NMR) analyses. The Li-ion conductivities of ALD $\text{Li}_x\text{Al}_y\text{Si}_z\text{O}$ thin films were determined by impedance measurements using a four-point probe setup with contacts made to the film surface. The films have high ion conductivity and low electronic conductivity, the values of which are strongly influenced by the lithium content and distribution in the synthesized thin films.

3:00pm **EN+EM-TuA4 Laser-Deposition and Characterization of Amorphous Thermoelectric Films**, *G.B. Wilks*, Air Force Research Laboratory, *P.T. Murray*, University of Dayton, *S.B. Fairchild, N.W. Gothard, J.E. Spowart*, Air Force Research Laboratory

From the Efficient Cluster Packing model describing the topology of metallic glasses, it is understood that certain compositions are favored for glass-formability based on the ratio of atomic sizes between constituents. In this regard, the half-Heusler composition $\text{Zr}_{0.5}\text{Hf}_{0.5}\text{NiSn}$ is nearly ideal. Although the crystallized form of this material has been widely studied because of its high thermoelectric power factor, it has been suggested that partial vitrification may enhance the thermoelectric figure of merit by preserving the favorable aspects of electronic structure while significantly disrupting thermal transport. Capitalizing on the high quench rates possible during pulsed laser deposition, a spectrum of thin films including amorphous and partially-amorphous duplex microstructures has been grown under various conditions. Transport characteristics relevant to the thermoelectric effect are rationalized in light of accompanying microstructure characterization.

4:00pm **EN+EM-TuA7 Probing Charge Transport in Exploratory Nanocrystal-Based Devices**, *P. Nagpal, V.I. Klimov*, Los Alamos National Laboratory **INVITED**

Colloidally synthesized semiconductor nanocrystals offer the exciting opportunity to exploit unique physical properties, such as size tunable band gap, in low-cost, solution-processed thin film devices. However, charge transport in as-deposited thin films of colloidal nanocrystals is hindered by

organic ligands. At the Center for Advanced Solar Photophysics (CASP), a DOE Energy Frontier Research Center, we are investigating the mechanism of charge transport in nanocrystal films by employing them in a range of simple device architectures, with the goal of optimizing them for photovoltaic application. As an example, I will present recent work in nanocrystal-based optical field effect transistors specifically designed to study electron transport and the dynamics of the photogenerated carriers in these semiconductor thin films. These devices offer invaluable information regarding field dependant mobility, optical gating and changes in the Fermi-level at the nanocrystal film interface. I will then discuss other exploratory device efforts at CASP, and how the information generated will be used collectively for the development of solar cells and other energy-related applications.

4:40pm EN+EM-TuA9 Investigation of GaTIP for Use in Multijunction Photovoltaics, C. Downs, T. Vandervelde, Tufts University

To achieve the highest possible conversion efficiencies in multijunction photovoltaics, the individual layers of the device must both be lattice-matched and have optimal band-gap spacing. Lattice-matched or strain-compensated epitaxy is required for the growth of junctions thick enough to elicit high quantum efficiency. Ideally, for spectral matching, one would have an infinite number of junctions that are current-matched; however, fabrication of a large number of junctions is neither easy nor desirable because of problems that arise from series resistance. In the end, it becomes a balancing act where the optimal number of junctions for a high efficiency concentrator cell is 3-6 junctions, with the conversion efficiency directly linked to how well spacing of the band gaps of the cell are optimized for absorption of the solar spectrum. Unfortunately, many of the optimal lower band-gaps for these multijunction cells do not occur in the dominant materials system (i.e. Ge and mixtures of In, Ga, Al, As, and P). As such, of late there has been a strong push to characterize new materials in hopes of providing more design options for photovoltaic cells. GaTIP is one such material, theorized to be useful as one of the lower junctions of 3+-junction cells while still being lattice-matched to GaAs and Ge. In this research, the change in lattice constant and band gap of GaTIP with varying compositions are investigated first by computational simulation and then with physical devices. New efficiency records should be achievable by incorporating these new optimal junction materials into the design for multijunction cells. This development will help solar concentrator cells achieve grid parity, thereby becoming a viable renewable energy choice.

5:00pm EN+EM-TuA10 Photo Induced Ferroelectric Properties of $Pb_{0.95}La_{0.05}Zr_{0.54}Ti_{0.46}$ Thin Films, H.V. Nampoori, S. Kotru, University of Alabama

Thin films of lanthanum doped lead zirconate titanate (PLZT) have gained attention due to the large photostrictive response, and their possible use for contact less actuators and sensors. Variation in composition and doping are known to influence the photostrictive responses as well as ferroelectric behavior of these materials. PLZT is also a potential material for photovoltaic devices due to its high electro-optic coefficient and optical transparency.

In this work, thin films of $Pb_{0.95}La_{0.05}(Zr_{0.54}Ti_{0.46})O_3$ (PLZT) were prepared using Metal-Organic Decomposition technique (MOD). The films are deposited by spin coating. Sputter deposited Pt electrodes serve as top contacts for the films. Thickness of the grown films varied from 70-350 nm and the growth temperature was chosen in the range of 550-700°C. Details of the film growth process including effects of temperature, thickness and annealing, and electrical and optical characterization will be presented. In addition parameters which affect the electrical properties like ferroelectric hysteresis and leakage behavior mechanisms will be discussed. The photo induced effects on the ferroelectric and the leakage properties, giving insight to the photovoltaic properties of ferroelectric thin films would be presented

**Energy Frontiers Topical Conference
Room: Pecos - Session EN+TF-TuA**

Thin Films for Photovoltaics

Moderator: L.W. Rieth, University of Utah

2:00pm EN+TF-TuA1 Ar/H₂ Plasma Treatment of a-Si:H Thin Films: On the Role of Atomic Hydrogen in μ c-Si:H Thin-Film Deposition, A.C. Bronneberg, A.M. Creatore, M.C.M. van de Sanden, Eindhoven University of Technology, the Netherlands

The transition from amorphous (a-Si:H) to microcrystalline (μ c-Si:H) silicon film growth has been ascribed to the interaction of atomic hydrogen with the (sub)surface of the growing film [1]. To gain more insight into the

formation of microcrystalline silicon and to the role of atomic hydrogen, several studies have been dedicated to hydrogen treatment of a-Si:H films [2,3,4,5]. However, the observed film crystallization is often wrongly ascribed to the impinging hydrogen atoms. What tended to be overlooked, is that the counter electrode is covered with an a-Si:H film during the deposition step. Interaction of the H₂ plasma with the coated electrode will result in formation of molecules and radicals originating from silane [4]. Hence, the resulting plasma conditions are similar to those used for μ c-Si:H, which explains the observed crystal formation.

Here, we show that this is not only true for direct plasmas, but that also in remote plasmas the reactor wall has big influences on the growth process. By using *in situ* spectroscopic ellipsometry and *ex situ* Raman spectroscopy, we show that H₂ plasma treatment of a-Si:H only results in the formation of crystals when there is a source of silicon-based molecules and radicals. Together with a plasma study, comprising mass spectrometry and ion probe measurements, we address the origin and kinetics of the crystal formation and discuss the implications for μ c-Si:H growth.

1. A. Matsuda, Journal of Non-Crystalline Solids **338**, 1-12 (2004).
2. A. F. I. Morral, J. Bertomeu, and P. R. I. Cabarrocas, Materials Science and Engineering B-Solid State Materials for Advanced Technology **69**, 559-563 (2000).
3. A. F. I. Morral and P. R. I. Cabarrocas, Journal of Non-Crystalline Solids **299**, 196-200 (2002).
4. K. Saitoh, M. Kondo, M. Fukawa, T. Nishimiya, A. Matsuda, W. Futako, and I. Shimizu, Applied Physics Letters **71**, 3403-3405 (1997).
5. G. Dingemans, M. N. van den Donker, A. Gordijn, W. M. M. Kessels, and M. C. M. van de Sanden, Applied Physics Letters **91**, (2007).

2:20pm EN+TF-TuA2 Spectroscopic Analysis of the Role of Hydrogen in Amorphous Silicon, P. Schäfer, F. Nobis, O.D. Gordan, H. Kupfer, F. Richter, D.R.T. Zahn, Chemnitz University of Technology, Germany

Amorphous hydrogenated silicon (a-Si:H) is widely used in photovoltaic applications. The high absorption renders a-Si:H technically relevant especially for thin film solar cells. Despite lower efficiency, an amorphous silicon solar panel possesses the advantage of higher absorption rate and easier processing at lower production cost.

Here the focus lies on highly (p and n) doped amorphous silicon films. The samples are prepared using d.c.-pulsed magnetron sputtering of crystalline silicon targets. A controlled hydrogen flow is added to the sputtering plasma. Hydrogen in amorphous silicon is known to saturate dangling bonds and improves the short range atomic order [1]. To probe the influence of hydrogen in the sputtering process various spectroscopic techniques were applied for sample characterisation.

Raman spectroscopy is a technique sensitive to the morphological aspects of the film. The relaxation of quasi-momentum conservation in amorphous films results in drastically different spectra of amorphous and crystalline silicon. A broad band at $\sim 485\text{ cm}^{-1}$ appears instead of the sharp crystalline phonon feature at 520 cm^{-1} . Its shape and asymmetry unveils further information on the short range order like the average dispersion angle from tetrahedral conformation. With the help of Fourier transformed transmission infrared spectroscopy the concentration of hydrogen in the sample is studied. Vibrational hydrogen-silicon stretching modes in the region around 2000 cm^{-1} are therefore assessed by a modified [2] Brodsky-Cardona-Cuomo approach [3]. Access to the optical constants n and k and therefore the complex dielectric function ϵ of the sputtered material is granted by variable angle spectroscopic ellipsometry. Thereby important parameters like the Tauc-Lorentz band gap which is mainly determined by interband gap defects are revealed. The combination of these spectroscopic techniques provides a detailed picture of morphological, electrical, and optical parameters of the system. An in depth discussion of the degree of structural improvement, the decrease of interband gap defects, the saturation of hydrogen content, and evolution of optical properties in correlation with the hydrogen flow will be presented.

-
- [1] R. A. Street, "Hydrogenated Amorphous Silicon", chapter 2.3, Cambridge University Press.
 - [2] A. A. Langford, M. L. Fleet, B. P. Nelson, W. A. Lanford, N. Maley: Phys. Rev. B **45** (1992) 13367.
 - [3] M. H. Brodsky, M. Cardona, J. J. Cuomo: Phys. Rev. B **16** (1977) 3556.

2:40pm EN+TF-TuA3 Improved Efficiency and Air Stability of Hybrid Thin Film Solar Cells with a ZnO Nanoparticle Layer, P.H. Holloway, L. Qian, J. Yang, R. Zhou, A. Tang, Y. Zheng, J. Xue, University of Florida

Hybrid solar cells with active and transport layers based on conjugated polymers and/or inorganic semiconductor nanoparticles are an alternative to

all-organic or all-inorganic solar cells. In hybrid cells, inorganic nanoparticles complement the absorption of the organic phase and provide better charge transport properties due to higher carrier mobility, while still maintaining the ability to solution-process. These properties will be illustrated first in hybrid solar cells with a mixed active layer based on poly(3-hexyl thiophene) (P3HT) and colloidal CdSe nanospheres, and with a ZnO nanoparticle buffer layer. The CdSe and ZnO nanoparticles were synthesized using a micelle and a sol-gel method, respectively. Both the active and buffer layers were spin-coated from solution onto a poly(3,4-ethylene dioxythiophene) doped with polystyrenesulfonic acid (PEDOT:PSS) layer on an ITO/glass substrate, and finished by deposition of the Al cathode. Compared to control devices without the ZnO layer, devices with the layer showed only slight changes in open-circuit voltage and fill factor, but showed 40-70% higher short-circuit current density, depending on the size of the CdSe nanospheres. ZnO-containing devices showed a maximum power conversion efficiency of 2.5-2.8%, compared to approximately 1.6-1.9% for the best P3HT/CdSe nanosphere devices without the ZnO layer. Using a ZnO layer and a low-gap poly[2,6-(4,4-bis-(2-ethylhexyl)-4H-cyclopenta[2,1-b;3,4-b']-dithiophene)-alt-4,7-(2,1,3-benzothiadiazole)] (PCPDTBT) to better harvest near-infrared photons, we have achieved a maximum power conversion efficiency of 3.3-3.5%. In addition to the efficiency enhancement, the ZnO layer also drastically improved the air stability of both types of hybrid solar cells. While devices without the ZnO layer degraded completely after one to three days of air exposure, devices with the ZnO layer exhibited only a modest 35% efficiency decrease after >70 days of storage in laboratory air. The mechanisms leading to higher efficiencies and reduced degradation will be discussed.

4:00pm **EN+TF-TuA7 Energy Band Alignments and Influence of Doping on Ga-doped ZnO, CuO and Si**, *S.Y. Chiam, S.J. Wang, J.S. Pan, L.M. Wong*, Institute of Materials Research & Engineering, Singapore, *W.K. Chim*, National University of Singapore

It is important to investigate new materials for thin film solar cells for 2nd generation devices. Materials extraction cost and annual electricity production considerations highlighted several potential new materials including cuprous oxide (Cu₂O). In this work, we report on the growth of Cu₂O and highlighted the importance of the oxygen partial pressure during growth. Namely, the partial pressure of oxygen determines the transition of Cu₂O to CuO with increasing partial pressure. This is accomplished at a fixed total pressure as this may influence Cu₂O formation. We then discuss about the interface energy alignments, first between Cu₂O/ZnO and then ZnO/Si. The former is of importance as inorganic thin film p-n junction that is suitable for 2nd generation solar cell devices. For the latter case, we fabricated device structure on differently doped Si, to investigate influence on doping on the transport characteristics of the hetero-pn junction. It is found that forward bias characteristics for a heterojunction, is not critically dependant on the band offsets, but rather the build-in-field at the heterojunction. If the physics is considered from the point of view of quasi-fermi level separation during light illumination, this build-in-field will also determine the V_{oc}. In this sense, band offset measurements can only give an indication of the maximum limit of the V_{oc} for differently doped semiconductors (non-degenerate) heterojunction solar cells. In addition, we show that under illumination, the current conduction for the ZnO/Si at zero-bias is a "forward bias" current, unlike all homojunction devices. This can be understood with a detail examination of the energy band diagrams. This work shows the importance of using measured band offsets to aid in understanding the relative Fermi-level alignment instead of using bulk electron affinity values. The work also demonstrates a whole array of playground possible for thin film heterojunction of different materials to engineer an ideal junction for solar cell devices.

4:20pm **EN+TF-TuA8 Growing Low-Dislocation-Density Ge on Si through Nanometer Sized Voids in Chemical Oxide and Subsequent Integration of III-V Films for Multijunction Solar Cells**, *D. Leonhardt, J.J. Sheng*, University of New Mexico, *J.G. Cederberg, M.S. Carroll*, Sandia National Laboratories, *M.J. Romero*, National Renewable Energy Laboratory, *S.M. Han*, University of New Mexico

In an effort to reduce the manufacturing cost of multijunction solar cells, which currently utilize Ge substrates, we have scaled up a process to produce low-defect-density Ge films on 2-inch-diameter Si substrates. This process begins with the nucleation of over 1x10¹¹/cm² Ge islands on Si through 3-to-7 nanometer diameter voids in chemical SiO₂. It is shown that upon Ge island coalescence, the Ge film primarily contains stacking faults as opposed to threading dislocations. We have found that annealing the Ge islands at an early stage of island growth removes the stacking faults, but results in the formation of 5x10⁷/cm² threading dislocations upon further growth. Herein, we report on a detailed investigation using transmission electron microscopy (TEM) to clarify the mechanism of the stacking fault formation in the Ge. We will also discuss the effect of annealing both on the

Ge island morphology and in eliminating the stacking faults. Additionally, the origin of the threading dislocations obtained after annealing is revealed through the TEM study. Lastly, we report characterization results of GaAs-based double heterostructures integrated on the annealed Ge films, whose photoluminescence intensity over the entire 2-inch wafer is comparable to the same structures grown on commercially available GaAs and Ge substrates.

4:40pm **EN+TF-TuA9 Optimizing Heterojunctions of ZnTe/ZnSe Solar Cells: Effect of Surface Treatment and Growth Conditions**, *F. Fang, B. McCandless, R. Opila*, University of Delaware

II-VI direct band gap semiconductors are attractive for thin film solar cell (TFSC) applications owing to their potential flexibility in tunable optoelectronic properties and possible application in tandem cells for being band gap materials (E_g > 2 eV). For the n-ZnSe/p-ZnTe heterojunction solar cell, the defect states and electronic band alignment at the ZnSe/ZnTe interface are crucial for device performance. We have employed Al-Kα X-ray photoelectron spectroscopy as well as synchrotron source ultra-violet photoelectron spectroscopy to study the surface chemical composition and electronic structures at heterojunction interface. Scanning electron microscopy (SEM) was used to study observe the film microstructure morphology of the interface.

We used two different deposition techniques: Close Space Sublimation (CCS), a low-cost deposition method already demonstrated for high efficiency and commercial CdTe TFSC, and conventional thermal evaporation. Our preliminary results indicated that surface oxides on CCS-grown ZnSe film formed once open to air, and a significant valence band offset induced by this oxide is observed which acts like additional energy barrier for carrier transport, resulting in low open circuit voltage. Also, during sequential CSS deposition of the two stacking films, the covering ZnTe thin film layer growth damage the microstructure of the underlying ZnSe film, i.e., enlarged pores are observed in ZnSe films in the locations where partially covering ZnTe film was deposited. A degraded device performance is expected and low short circuit currents and fill factors of the cells are detected. By analogy to CdS/CdTe TFSC, we are aiming for close-packed column polycrystalline of ZnSe/ZnTe film growth. Therefore, we are exploring etching processes, annealing temperatures and ambient settings to optimize the growth conditions. Evaporation is under investigation, since we have the option of dual-sources in the self-designed chamber, sequential growth of ZnSe and ZnTe films without vacuum break is feasible. Film morphology as well as energy band alignment at the heterojunctions using evaporation growth is being studied.

5:00pm **EN+TF-TuA10 Investigation of NbSe₂ as Potential High Work Function Back Contact for CdTe Solar Cells**, *M.A. Wolak, S. Gutmann, M.M. Beerbom, C.S. Ferekides, R. Schlaf*, University of South Florida

The layered semi-metal NbSe₂ combines a chemically inert van der Waals surface with a high work function of about 5.8 eV. This motivated an investigation of NbSe₂ as Ohmic hole injection contact for CdTe solar cells. Current back contacts made from Cu suffer from interdiffusion issues leading to cell degradation. In the discussed experiments, the interface between NbSe₂ and CdTe was investigated using x-ray and ultraviolet photoemission spectroscopy (XPS, UPS). In these experiments CdTe and NbSe₂ thin films were grown in-situ in a vacuum chamber attached to the photoemission system. This enabled the investigation of the CdTe/NbSe₂ interface without interference by ambient contamination. After growth of a CdTe thin film, the NbSe₂ film was prepared in several steps. Photoemission spectroscopic characterization between each of the deposition steps allowed the observation of the formation of the band line-up at the interface. The results of the experiments indicate that an intermixed layer forms at the interface. This layer causes the formation of an interface dipole, preventing the formation of an Ohmic contact. A Schottky-type band line-up formed instead.

5:20pm **EN+TF-TuA11 In-Rich InGa_{1-x}N Films for Efficient Photovoltaic Devices Grown by ENABLE**, *T.L. Williamson, M.A. Hoffbauer*, Los Alamos National Laboratory, *K.M. Yu, L.A. Reichertz, W. Walukiewicz*, Lawrence Berkeley National Laboratory

The wide band gap tunability of In_xGa_{1-x}N thin films (0.7 eV to 3.4 eV, 1 > x > 0) makes them ideal for efficient photovoltaic (PV) devices. However, growing high-quality In-rich In_xGa_{1-x}N films with strong photoluminescence in the green-to-red portions of the visible spectrum has faced considerable challenges due to indium phase segregation and other materials issues. These challenges have precluded the growth of both In-rich InGa_{1-x}N and compositionally graded InGa_{1-x}N materials, and make it difficult to grow higher bandgap Ga-rich materials on top of lower bandgap In-rich materials. Overcoming these difficulties using conventional epitaxial techniques is challenging due to the low decomposition temperatures of In-

rich materials (e.g. InN~550°C) and the relatively high growth temperatures for Ga-rich materials (e.g. GaN >800°C).

Energetic neutral atom beam lithography & epitaxy (ENABLE) is a low-temperature thin film growth technology recently developed at LANL that utilizes a collimated beam of energetic neutral N atoms (kinetic energies 0.5 to 5.0 eV) to react with evaporated Ga and In metals to grow InGaN. ENABLE is similar to MBE, but provides a much larger N atom flux and correspondingly high film growth rate. The high kinetic energy of the reactive N atoms substantially reduces the need for high substrate temperatures, making isothermal growth over the entire InGaN alloy composition range possible at rates of >3 microns/hr with no toxic precursors or waste products.

Data on film photoluminescence, crystallinity, electrical properties, doping, and electro-luminescence of $\text{In}_x\text{Ga}_{1-x}\text{N}$, graded $\text{In}_x\text{Ga}_{1-x}\text{N}$, and GaN films grown using ENABLE over the full composition range will be presented. ENABLE-grown $\text{In}_x\text{Ga}_{1-x}\text{N}$ films show strong photo- and electro-luminescence spanning the entire visible region of the spectrum, with reasonable carrier mobilities background carrier concentrations typically in the low 10^{17} range. Evidence for p-type doping of In-rich InGaN films and characterization of p/n junctions will be discussed along with the prospects for using ENABLE to fabricate efficient PV devices.

5:40pm EN+TF-TuA12 Copper Oxide Thin Films: Preparation and Modulation of Semiconducting Properties by Electrochemical Methods, F. Caballero-Briones, CICATA-IPN/Universitat de Barcelona, Spain, A. Palacios-Adrós, Instituto de Bioingeniería de Catalunya, Spain, F. Sanz, Instituto de Bioingeniería de Catalunya/CIBER-BBN, Spain

Copper oxide is a p-type semiconductor with a direct band gap of 2 eV, suitable for photovoltaic applications. In this work we present an electrochemical method to prepare p-type semiconducting Cu_2O films around 100 nm thick with noticeable photocurrent response. The film properties were modulated by varying different conditions such as the time at a dissolution potential and the film doping with alkaline ions. The modification of the time of exposure to the dissolution potential allows the tailoring of the crystallinity, the band gap energy and the disorder parameter E_0 and also provided elements to outline the growth mechanism of the Cu_2O films that involve surface reaction, diffusion of oxygen species that react in the solid state accordingly to the point defect model, and heterogeneous deposition of Cu_2O from the Cu^+ ions dissolved in a chemical bath-like fashion. On the other side, the study of the behavior of different alkaline metal ions (A: Li, Na, K, Cs) present in the electrolyte used to prepare the Cu_2O films lead to important results. It was observed that important amounts of the alkaline ion (around 1%) can be incorporated to the film and that are indeed electrically active impurities that modify the band gap energy probably by introducing states within the band gap in the case of Cs or by getting incorporated to the crystalline lattice for Na or Li. Changes in the optical absorption, thickness, density of carriers and in defects are related with the size of the employed ion. To complete the study, an electronic diagram of the $\text{Cu}/\text{Cu}_2\text{O}/\text{Electrolyte}$ interface was prepared by using a combination of techniques including Electrochemical Impedance and Electrochemical Tunneling Spectroscopy/Microscopy.

Exhibitors & Manufacturers Technology Spotlight

Room: Southwest Exhibit Hall - Session EW-TuA

Exhibitors & Manufacturers Technology Spotlight

Moderator: D.J. Surman, Kratos Analytical Inc., R. Langley, Consultant

3:40pm EW-TuA6 RJ Lee Group's Advanced FESEM, STEM, and XPS Analytical Consulting Services for Exploring the Nano-World, K.L. Bunker, J.L. Sturgeon, T.L. Lersch, B.R. Strohmeier, J.D. Piasecki, RJ Lee Group, Inc.

RJ Lee Group, Inc. (RJLG, www.rjlg.com) is an organization of experts who provide the highest quality microscopy, analytical, and consulting services to our clients and partners. Leading organizations come to RJLG for more than data and information. They come for an innovative approach and technical solutions developed through our commitment to quality, reliability, and customer satisfaction. RJLG's multi-technique approach to materials characterization offers comprehensive solutions to complex problems. RJLG is presently the exclusive commercial analytical laboratory in the United States to offer analytical services with a number of advanced instruments that provide unique complementary information for the study of nanomaterials. These instruments include: 1) Hitachi S-5500 ultrahigh resolution electron microscope, which is capable of performing field emission scanning electron microscopy (FESEM) and low energy (30 kV)

scanning transmission electron microscopy (STEM); 2) Hitachi HD-2300 high energy (200 kV) STEM, which can also generate FESEM images; and 3) Thermo Scientific K-Alpha X-ray photoelectron spectrometer (XPS). The S-5500, HD-2300, and K-Alpha are three of the most powerful materials and surface characterization instruments available to scientists today. The electron optical designs of the Hitachi S-5500 and HD-2300 microscopes place the sample at the optimum imaging and analytical working distance, allowing concurrent acquisition of high-resolution FESEM and/or STEM images, as well as energy dispersive X-ray spectroscopy (EDS). Both microscopes are equipped with the latest silicon drift detector (SDD) technology for EDS, which allows for high resolution elemental analysis and mapping of nanostructures. A variety of signals can be collected simultaneously including secondary electron (SE) and backscattered electron (BSE) FESEM images and bright field (BF) and dark field (DF) STEM images. A semiconductor-based Protochips Aduro™ sample heating system allows for *in situ* microscopic analysis at elevated temperatures up to 1,200 °C. Therefore, the S-5500 and HD-2300 can provide unique information on samples that single standard microscopy techniques, such as SEM and TEM, are not able to accomplish when used alone. XPS is a highly surface-sensitive and quantitative technique for materials characterization. The Thermo Fisher Scientific Model K-Alpha XPS is a compact, fully integrated, state-of-the-art surface analysis instrument. Nanometer scale sampling depth and its ability to provide chemical state information makes XPS an ideal analytical technique for investigating the elemental and chemical surface composition of nanoparticles and other complex advanced materials. This presentation will give a brief overview of the advanced capabilities of each instrument along with examples of combined applications of these instruments for the characterization of nanomaterials.

Graphene Focus Topic

Room: Brazos - Session GR+TF-TuA

Graphene and 2D Nanostructures

Moderator: Y. Chen, Purdue University

2:00pm GR+TF-TuA1 Graphene and Its Progeny: from Fundamental Material Properties to Device Applications, A.W. Ghosh, University of Virginia

INVITED

The incredible material properties of graphene have spurred intense interest among chemists, physicists and engineers towards potentially exciting electronic applications. Much like nanotubes, graphene electrons have high mobilities due to the sharp curvature of their bands at the Gamma point that reduces their effective masses, as well as long scattering lengths due to symmetry selection rules among their pseudospin separated bands. However, a potential problem with graphene is its metallicity, which makes its ON-OFF ratio unacceptable for digital logic. Effort is under way to mitigate this by opening bandgaps through various chemical and electrostatic means. I will argue that any such band-gap opening leads to an inevitable reduction in mobility *even if we manage to do so without affecting its scattering length*. The trade-off arises from a fundamental asymptotic constraint on all graphitic materials (epitaxial graphene, strained graphene, nanoribbons, nanotubes, and bilayer graphene) that pins the high energy electrons away from the Gamma point to an ultimately linear dispersion. However, opening a bandgap by width confinement, e.g. in a nanoribbons, can provide distinct electrostatic if not material advantages. The presence of diffuse boundary conditions at the edges, along with strain and edge roughness, systematically erases any signs of chirality and metallicity in GNRs, making their widths the single arbiter of metallicity. This allows us to envisage wide-narrow-wide (WNW) nanoribbons monolithically patterned out of a single template into both switches and interconnects. The 2-D electrostatics of the source-drain contact edge capacitances improves the gate control, allowing the current to show a highly desirable saturation characteristic. Furthermore, the presence of C-C bonds at the channel-contact interface makes metal induced gap states relatively ineffective in pinning the bands, promoting Ohmic behavior. I will quantify the advantages and disadvantages of WNW devices, and compare with alternate GNR switches, such as utilizing electron focusing in p-n junctions.

2:40pm GR+TF-TuA3 Electronic Structure of Graphene/BN Heterojunctions formed by Graphene CVD: Doped Graphene, C. Bjelkevig, Z. Mi, University of North Texas, J. Xiao, P.A. Dowben, Nebraska Center for Nanostructures and Materials, S. Gaddam, S. Pokharel, J.A. Kelber, University of North Texas

Graphene has been grown by chemical vapor deposition of C_2H_4 on a monolayer of h-BN(0001) formed by atomic layer deposition (BCl_3 , NH_3)

on Ru(0001). AES, STM and LEED confirm a graphene-like overlayer, with near-zero DOS near the Fermi level, in registry with a BN R30($\sqrt{3}\times\sqrt{3}$) substrate. Raman spectra reveal graphene "G" and "2D" features with relative intensities indicative of single layer graphene. A large (350 cm^{-1}) redshift in the 2D feature relative to HOPG indicates significant BN-to-graphene charge transfer. The charge transfer is confirmed by photoemission/angle-resolved inverse photoemission spectroscopies (PES/ARIPES), that demonstrate filling of the lowest unoccupied graphene state (π^*) near the Brillouin zone center. These results are in direct contrast to PES/ARIPES results for graphene/ Cu, and reported results for graphene/SiC(0001), that show empty graphene π^* states. The data show that the BN layer acts as an n-type dopant for graphene. For the graphene/BN heterojunctions, the ARIPES-determined dispersion of the unoccupied graphene $\sigma^*(\Gamma_1^+)$ state yields an effective mass of $0.05 m_e$, in excellent agreement with reported transport measurements on graphene sheets, and indicating that BN doping does not fundamentally alter the graphene electronic structure. The direct growth of graphene on dielectric substrates, and the controlled exploitation of graphene/substrate heterojunction properties, are critical issues for practical device fabrication. The implications of direct CVD of undoped graphene and graphene/BN heterojunctions on high dielectric constant substrates for device applications will be discussed in light of recent results in our laboratories for graphene thermal and free radical-assisted CVD on OH-terminated MgO(111).

Acknowledgements: Work at UNT was supported by the Global Research Consortium of the Semiconductor Research Corporation through Task ID 1770.001, and through ONR under award no. N00014-08-1-1107 through a subcontract with Texas State University at San Marcos. Work at UNL was supported by the Defense Threat Reduction Agency (Grant No. HDTRA1-07-1-0008), and the NSF "QSPINS" MRSEC (DRM-0820521) at UNL. The authors also thank Luigi Colombo and Adam Pirkle for acquisition of the Raman spectra.

3:00pm **GR+TF-TuA4 Electrical Transport in Graphenoid and Graphene Nanomembranes from Pyrolyzed Self-Assembled Monolayers**, *A. Turchanin*, Univ. of Bielefeld, Germany, *D.H. Weber*, National Metrology Inst., Germany, *M. Bünenfeld*, Univ. of Bielefeld, Germany, *J. Mayer*, Ernst Ruska-Centre for Microscopy, Germany, *C. Kisielowski*, National Center for Electron Microscopy, *T. Weimann*, National Metrology Inst., Germany, *A. Götzhäuser*, Univ. of Bielefeld, Germany

Ultrathin carbon nanomembranes have recently attracted enormous interest. We report a molecular route to the fabrication of a monolayer or few layers of free-standing graphenoid and graphene nanomembranes based on molecular self-assembly, electron processing and pyrolysis. Aromatic biphenyl self-assembled monolayers (SAMs) are cross-linked by electron irradiation. The cross-linking results in mechanically stable graphenoid sheets with the thickness of a single molecule ($\sim 1\text{ nm}$) and arbitrary sized. The graphenoid sheets can be lifted from their surface and transferred to another solid substrate or holey structures, where they become free-standing nanomembranes. Upon annealing (pyrolysis) up to 1300 K the molecular sheets transform into nanocrystalline graphene phase. This transformation is accompanied by a drop of the sheet resistivity from $\sim 10^8$ to $\sim 10\text{ k}\Omega/\text{sq}$ and a 2D insulator to metal transition. We characterize the insulator to metal transition by electrical transport measurements as well as by complementary spectroscopic and microscopic techniques. A plethora of applications of the suggested molecular route to free-standing ultrathin carbon materials is feasible that take advantage from the fact that the large scale fabrication, control over the thickness and nanostructuring are easily controlled.

[1] A. Turchanin, A. Beyer, C. T. Nottbohm, X. H. Zhang, R. Stosch, A. Sologubenko, J. Mayer, P. Hinze, T. Weimann, and A. Götzhäuser: One Nanometer Thin Carbon Nanosheets with Tunable Conductivity and Stiffness, *Adv. Mater.* 21, 1233-1237 (2009)

[2] A. Turchanin, D. Käfer, M. El-Desawy, C. Wöll, G. Witte, and A. Götzhäuser: Molecular Mechanisms of Electron-Induced Cross-Linking in Aromatic SAMs, *Langmuir* 25, 7342-7352 (2009).

[3] C. T. Nottbohm, A. Turchanin, A. Beyer, A. Götzhäuser: Direct e-beam writing of 1 nm thin carbon nanoribbons, *J. Vac. Sci. Technol. B* 27, 3059-3062 (2009).

4:00pm **GR+TF-TuA7 From 2D to 1D - Supramolecular Architectures on Rippled Graphen**, *M. Roos*, *H.E. Hoster*, *R.J. Behm*, Ulm University, Germany

Bis(terpyridine)derivatives (BTP) form highly ordered hydrogen-bonded 2D networks on solid surfaces.¹⁻⁴ The preferred hydrogen bond configurations and thus the resulting structures are steered via the positions of the nitrogen atoms within the BTP molecules. Elaborate synthesis procedures allow varying these positions without altering the footprint shape of the molecules.¹ On smooth surfaces like graphite or metal single crystals, the molecule-substrate interactions play a secondary role for the

structures, mainly by determining the orientations of the molecules and thus of the ordered networks.²⁻⁴ In this contribution, we will demonstrate that more pronounced template effects arise for substrates where the molecule-substrate interaction laterally varies at nm-scales. As an example, we will show the ordering behaviour of two different types of BTP molecules on Graphene monolayers grown on Ru(0001). The moiré-type pattern of these surfaces has a periodicity of 3 nm, i.e., in the order of the BTP dimensions and the network meshes they usually form. Submolecularly resolved STM images show that the BTP molecules are confined to the valleys of the graphene ripple structure. We will compare the resulting supramolecular 1D and 2D assemblies to the ordered 2D networks formed by the same molecules on smooth substrates, and we will discuss in how far the template effect can be quantitatively explained by a lateral modulation of the van der Waals interactions due to the height corrugation of the Graphene sheet.⁵

1C. Meier et al., *J Phys Chem B* 109 (2005) 21015.

2 M. Roos et al., *Phys. Chem. Chem. Phys.* 9 (2007) 5672.

3 H. E. Hoster et al., *Langmuir* 23 (2007) 11570.

4 T. Waldmann et al., *ChemPhysChem* 11 (2010) 1513.5 W. Moritz et al., *Phys. Rev. Lett.* 104 (2010) 136102.

4:20pm **GR+TF-TuA8 Understanding the Functionalization of Graphene by Electron-Beam Generated Plasmas**, *M. Baraket*, *S.G. Walton*, *E.H. Lock*, *J.A. Robinson*, *F.K. Perkins*, Naval Research Laboratory
Graphene is a single monolayer thick carbon sheet with remarkably high electron mobility. Its unique structural and electronic properties make it an interesting material for nanoscale electronic and sensing devices. The addition of functionalities increases its reactivity toward certain materials and thus broadens its applications. One significant impediment to realizing the potential of graphene is the development of an industrially viable approach to producing precisely engineered functionalities over large areas. In this respect, plasmas are an ideal candidate but problems associated with the large fluxes of high-energy ions are a significant concern. Electron beam generated plasmas, characterized by low incident ion energies ($< 5\text{ eV}$), have been used to functionalize graphene without any damage [1]. We discuss the use of this system to controllably introducing oxygen, hydrogen, fluorine, nitrogen or ammine containing groups at different concentrations. The reversibility of the functionalization via low-temperature annealing will also be discussed. This work was supported by the Office of Naval Research. M.B. appreciates the support of the National Research Council.

[1] M. Baraket, S.G. Walton, E.H. Lock, J. T. Robinson, and F.K. Perkins. The functionalization of graphene using electron beam generated plasmas. *Applied Physics Letters* 96, 231501 (2010)

4:40pm **GR+TF-TuA9 Chemically Tailoring Graphene via Organic Self-Assembled Monolayers**, *M.C. Hersam*, Northwestern University

INVITED

Chemically functionalized semiconductor surfaces have been widely explored due to their potential for enabling molecular electronic and sensing devices that are compatible with conventional microelectronic technology [1]. Thus far, the vast majority of work in this field has focused on established semiconductors including silicon, germanium, and gallium arsenide. Meanwhile, the condensed matter physics community has diverted substantial experimental and theoretical effort to graphene, an emerging electronic material with superlative carrier mobility and exotic charge transport phenomena such as the quantum Hall effect.

In an attempt to unify these two fields, we have been exploring strategies for forming and interrogating organic self-assembled monolayers on graphene surfaces. In particular, we have recently demonstrated that self-assembled monolayers of perylene-3,4,9,10-tetracarboxylic-dianhydride (PTCDA) can be formed on graphene surfaces via gas-phase deposition in ultra-high vacuum (UHV) environments at room temperature [2]. Molecular-scale resolution scanning tunneling microscopy (STM) images reveal long-range order in the PTCDA monolayers, while scanning tunneling spectroscopy (STS) measurements yield distinct electronic features associated with the PTCDA that are not observed on pristine graphene.

In addition to UHV STM characterization, this talk will summarize our most recent efforts to nanopattern self-assembled monolayers on graphene at the sub-10 nm scale. Nanopatterning chemically functionalized graphene presents opportunities for tailoring the electronic and chemical properties of graphene nanoribbons in addition to providing a molecular-scale resolution template for subsequent materials growth on graphene surfaces.

[1] M. A. Walsh and M. C. Hersam, "Atomic-scale templates patterned by ultrahigh vacuum scanning tunneling microscopy on silicon," *Annual Review of Physical Chemistry*, **60**, 193 (2009).

[2] Q. H. Wang and M. C. Hersam, "Room-temperature molecular-resolution characterization of self-assembled organic monolayers on epitaxial graphene," *Nature Chemistry*, **1**, 206 (2009).

5:20pm **GR+TF-TuA11 Stability of Continuous Graphene Sheet and Graphene Flake on the Si(111) Surface**, *B.B. Kappes, T.E. Davies*, Colorado School of Mines, *S. Jun*, University of Wyoming, *A.C.T. van Duin*, Penn State University, *C.V. Ciobanu*, Colorado School of Mines

While rapid use of carbon nanostructures in the silicon-based nanoelectronics industry will involve the direct integration of graphene with silicon chips, so far graphene has not been grown on pristine silicon surfaces because usual synthesis routes would likely lead to the formation of stable silicon carbide instead of the precipitation of carbon at the surface. Here we show that if graphene can be deposited on pristine Si(111) surfaces, then it forms moiré superstructures and binds strongly to the substrate over a wide range of in-plane orientations. The binding energies depend on the orientation of graphene as well as the strain applied to achieve commensurability with the substrate; the strongest binding estimated from density functional theory calculations is approximately 1.5 eV/carbon atom. Using molecular dynamics simulations based on bond-order and reactive force field interatomic potentials, we present evidence that graphene remains stable and bonded to the substrate for temperatures up to 80% of the substrate melting temperature. Bonding information, study of the local density of states, and simulated scanning tunneling microscopy show graphene on Si(111) is semiconducting, with a sizable number of carbon hybridized sp^3 and a bandgap affected by the orientation of graphene with respect to the substrate.

5:40pm **GR+TF-TuA12 Effect of Point-like Defects on the Atomic Structure and Electronic Properties of Graphene Supported on Amorphous SiO₂**, *K.E. Kweon, G.S. Hwang*, University of Texas at Austin
Graphene supported on the common gate dielectric, SiO₂, has been considered as a highly promising candidate for future electronics. Therefore, it is important to understand the interfacial interaction between graphene and SiO₂. Most of the existing theoretical studies have modeled the underlying SiO₂ surface using defective or H-terminated crystalline structures. However, the gate oxide is amorphous and possibly has a number of point-like defects, yet no detailed study has been undertaken on the defect effect. In this talk, based on first principles calculations we present how the SiO₂-graphene binding and consequent graphene electronic structure are influenced by the presence of point-like defects in not only SiO₂ surface but also graphene sheet. We considered six different surface defects on SiO₂: silyl radicals [(≡Si-O)₃Si•], oxy radicals [(≡Si-O)₂Si-O•], silylene center [(≡Si-O)₂Si:], silanone [(≡Si-O)₂Si=O], peroxide radicals [(≡Si-O)₃Si-O-O•], and dioxasilirane [(≡Si-O)₂Si-O-O₂], along with defective graphene that contains vacancies. This talk will mainly touch on the pathways and energetics of the defect-mediated graphene binding to SiO₂, and how the covalent graphene-SiO₂ binding affects the electronic properties of graphene.

In Situ Microscopy and Spectroscopy Topical Conference

Room: Acoma - Session IS+SS-TuA

In Situ Microscopy/Spectroscopy – Interfacial Chemistry/Catalysis

Moderator: S. Kodambaka, University of California Los Angeles

2:00pm **IS+SS-TuA1 In-situ LEEM Study of Ceria Growth on Cu(111)**, *J.T. Sadowski, S.D. Senanayake, F. Yang, Y.M. Choi*, Brookhaven National Laboratory, *J.I. Flege, J. Falta, B. Menkens*, University of Bremen, Germany, *J.A. Rodriguez, J. Hrbek*, Brookhaven National Laboratory

The use of CeO₂-based materials in catalysis has attracted considerable attention in recent years. Ceria has shown great potential as a novel reducible oxide support with unique oxygen storage capacity (OSC) [1]. Ceria can accommodate a large number of oxygen vacancies and the oxidation states of the Ce cation can be switched readily between Ce³⁺ and Ce⁴⁺ depending on the ambient conditions. Hence ceria can actively participate in redox chemical reactions.

The formation of well-ordered, flat CeO₂ films is required in order to minimize substrate effects in surface chemistry of ceria. An earlier successful approach to this problem involved growth of ceria films on Ru(0001) [2]. More recently, CeO₂(111) was grown on a Cu(111) substrate [3]. High activity of ceria-based model catalysts was demonstrated on the inverse catalyst [4, 5] with ceria nanoparticles supported on noble metal substrates. Overall, there is still little known about the mechanism for the growth of ceria film on metal surfaces, its structure and stoichiometry.

In the present work the growth of thin ceria films on Cu(111) has been investigated *in-situ* by means of low-energy electron microscopy (LEEM). Ce was deposited from an e-beam evaporator onto Cu(111) under O₂ atmosphere (5x10⁻⁷ Torr). Real-time observation of the film growth revealed that at relatively high substrate temperature (above 800K) flat, highly crystalline, epitaxial CeOx(111) film has been formed. In this presentation we will discuss in detail the mechanism of the nucleation and growth, and the atomistic structure of the CeOx film on Cu(111) under varying growth conditions and Cu(111) oxidation state.

[1] A. Trovarelli, *Catalysis by Ceria and Related Metals*, Imperial College Press, London, 2002.

[2] D. R. Mullins, P. V. Radulovic, S. H. Overbury, *Surf. Sci.* **429**, 186 (1999).

[3] V. Matolin, J. Libra, I. Matolinova, V. Nehasil, L. Sedlacek, F. Sutara, *Appl. Surf. Sci.* **254**, 153 (2007).

[4] J. A. Rodriguez, S. Ma, P. Liu, J. Hrbek, J. Evans, and M. Pérez, *Science*, **318**, 1757 (2007).

[5] J. A. Rodriguez, J. Hrbek, *Surf. Sci.*, **604**, 241 (2010).

The authors are thankful to the US Department of Energy (Chemical Sciences Division, contract no. DE-AC02-98CH10886) for financial support. Research carried out in part at the Center for Functional Nanomaterials, Brookhaven National Laboratory, which is supported by the U.S. Department of Energy, Office of Basic Energy Sciences, under contract no. DE-AC02-98CH10886.

2:20pm **IS+SS-TuA2 Quantitative Speciation of Zn(II) During the Solution Synthesis of ZnO Nanowires Using In-Situ XANES Spectroscopy**, *K.M. McPeak*, Drexel University, *M. Becker, B.A. Bunker*, University of Notre Dame, *J.B. Baxter*, Drexel University

Low temperature, aqueous solution synthesis is widely used to deposit ZnO nanowire arrays for applications such as dye sensitized solar cells. Zinc nitrate and hexamethylenetetramine (HMTA) are the most common precursors for the solution synthesis of ZnO nanowires; but after ten years of using this chemistry, the underlying mechanisms of the reaction remain unclear. We report on the in-situ x-ray absorption spectroscopy of ZnO nanowire growth from HMTA and zinc nitrate precursors. Time-resolved, in-situ x-ray absorption near-edge structure (XANES) spectra, at the Zn K-edge, give detailed information about the local structure of both Zn(II) in solution and the solid phases formed throughout the reaction. A principal component analysis (PCA) algorithm was employed to determine the number and type of probable species present during the growth of ZnO nanowires under real reaction conditions, with temperatures up to 90 °C and concentrations ranging from 4 – 25 mM. Only two species were present for ZnO nanowire growth at all concentrations and temperatures studied: [Zn(6H₂O)]²⁺ and ZnO_(s). The proportions of these Zn species as a function of reaction time were determined quantitatively by least-squares fitting (LSF) the experimental time-dependent XANES spectra with linear combinations of the principal component spectra. PCA and target testing conclusively refute previous theories that ZnO nanowire growth from HMTA and zinc nitrate precursors occurs due to the thermal decomposition of an intermediate zinc-amine or zinc-HMTA complex. Additionally, XANES analysis shows that no zinc hydroxide intermediates exist above the detection limit of 0.05 mM. Beyond the focused investigation of ZnO, this study also establishes in-situ XANES spectroscopy, in combination with PCA and LSF, as an excellent quantitative tool to understand the solution synthesis of semiconductor nanostructures and thin films.

2:40pm **IS+SS-TuA3 X-ray Spectromicroscopy of Organic and Inorganic Nanostructures**, *S.G. Urquhart*, University of Saskatchewan, Canada

INVITED

Understanding the composition and structure of complex surfaces is essential for many scientific questions, from understanding processes in surface corrosion to the development of organic electronic devices. X-ray

Spectromicroscopy provides surface sensitive chemical speciation with high lateral spatial resolution, by combining the chemical sensitivity of X-ray absorption and photoemission spectroscopy with the high spatial resolution of X-ray microscopy. This presentation will discuss x-ray spectromicroscopy studies to study phase segregation in mixed Langmuir Blodgett thin films as well as efforts to develop a new zone-plate based surface sensitive spectromicroscopy.

1.) We have used surface sensitive X-ray Photoelectron Emission Microscopy (X-PEEM) to study the mechanisms of phase separation and growth in mixed Langmuir Blodgett thin films.[1,2] Here, the chemical sensitivity of x-ray absorption spectroscopy provides spatially resolved composition information to complement the morphology information provided by AFM.

2.) We are developing of a new form of new surface sensitive x-ray microscopy, based on electron-yield detection in a scanning zone plate microscope. Preliminary results from the development of this new method will be presented.

References:

- 1.) Christensen et al., J. Electron Spectrosc. and Rel. Phenom. (2008) **162**, 107-114.
- 2.) S.E. Qaqish, Langmuir (2009) **25**, 7401-7409.

Research supported by NSERC (Canada) and performed at the Canadian Light Source (CLS) and the Advanced Light Source (ALS). The CLS is supported by NSERC, NRC, CIHR, U. Saskatchewan, and the ALS is supported by the Director, Office of Science, Office of Basic Energy Sciences, of the U.S. Department of Energy under Contract No. DE-AC02-05CH11231.

4:00pm IS+SS-TuA7 The Use of *in-situ* Spectro-Electrochemical Tools on the Way to R&D of Rechargeable Li and Mg Batteries, D.A. Aurbach, Bar-Ilan University, Israel

INVITED

The performance of high energy density rechargeable Li and Li ion batteries depends on passivation phenomena. On thermodynamic basis, both the negative electrodes: Li metal or lithiated carbonaceous materials and the positive electrodes: lithiated transition metal oxides are reactive with the electrolyte solutions that are relevant to these systems (polar-aprotic solvents and Li salts).

Thereby, it is highly important to understand the complicated surface chemistry that characterizes all kinds of rechargeable Li batteries. Based on understanding the correlation between surface phenomena, performance and safety features, it is possible to optimize electrolyte solutions in which irreversible phenomena and electrodes capacity fading will be minimized. Consequently, it was highly important to develop specific spectroscopic and microscopic tools that can be used in conjunction with electrochemical techniques and can be specifically suitable for such highly reactive systems. In this talk we demonstrate the development and use of *in-situ* FTIR spectroscopy for mapping the complicated surface reaction of Li metal electrodes in most relevant electrolyte solutions. Especially important was an approach based on internal reflection modes. The use of *in-situ* Raman spectroscopy for understanding lithiation processes of graphite in ionic liquids will be demonstrated. Application of spectroscopy enables to follow detrimental processes such as co-intercalation of the solvents' cations together with Li insertion, what interferes badly with the passivation phenomena, on which the reversibility and stability of Li-graphite anodes depend. The same techniques were applied to non-aqueous electrochemistry of magnesium, in the framework of R&D of rechargeable Mg batteries. The use of EQCM was helpful in characterizing passivation free Mg electrodes, in ethereal solutions with contain magnesium organo-chloro-aluminate complex electrolytes. Highly useful for the study of surface phenomena related to Li batteries were *in-situ* AFM measurements, with which it was possible to follow delicate phenomena related to surface films formation, exfoliation of Li-graphite electrodes and break down and repair of passivation phenomena on both Li metal and Li graphite electrodes. The study of Mg anodes was nicely promoted by the use of *in-situ* STM measurements. This technique was very suitable for characterization of Mg anodes in passivation free electrolyte solutions. New directions for development of *in-situ* techniques suitable for highly reactive electrochemical systems, will be discussed.

4:40pm IS+SS-TuA9 Electrochemistry Platforms for In Situ Transmission Electron Microscopy of Li-ion Batteries, A. Subramanian, J.P. Sullivan, J. Huang, M.J. Shaw, N. Hudak, Sandia National Laboratories, Y. Zhan, J. Lou, Rice University

Nanoscale materials offer a number of potential advantages for Li-ion batteries: examples include low-cost LiFePO₄ nanoparticle cathodes that exhibit good rate performance despite having low electrical conductivity and high-capacity conversion anodes that have high cycle life despite large volume changes per cycle, e.g. Si nanowires. However, one of the challenges with the use of nanoscale materials is their electrochemical characterization, particularly assessing structural changes in nanoscale particles, or reaction product layer interfaces, such as the solid-electrolyte-interphase (SEI). This requires tools with atomic to nanoscale spatial resolution. To meet this need, we have developed a micro-electromechanical systems (MEMS)-based platform for performing electrochemical measurements using volatile electrolytes inside a transmission electron microscope (TEM). This platform uses flip-chip assembly with special alignment features and multiple buried electrode configurations. The nanoscale materials of interest are assembled into the viewing area using dielectrophoresis (DEP). This permits the incorporation of a diverse array of nanoscale particles, including the co-assembly of anode materials in proximity to cathode materials. As an initial realization of the MEMS-based platform, we have developed an unsealed platform that permits *in situ* TEM electrochemistry using ionic liquid electrolytes or *ex situ* electrochemistry and TEM imaging using conventional battery electrolytes. We have demonstrated these approaches using β -MnO₂ nanowire cathodes that were individually assembled using DEP. These wires were lithiated over a range of potentials, in ethylene carbonate-based electrolytes with lithium metal as a counter electrode, in order to produce a range of lithium content. Using TEM and solid-state electrical characterization, we observed that lithiation introduces increasing lattice disorder particularly at the nanowire surfaces; yet, the wires remain β -phase. The electrical measurements revealed a monotonic decrease in electrical conductivity with increasing lithium content, consistent with electronic localization at defects or an increased band gap. From these results, we conclude that *in situ* TEM characterization tools will enable important mechanistic understanding of Li-ion battery materials. This work was supported by LDRD and EFRC projects and was performed, in part, at CINT, a U.S. DOE, Office of Basic Energy Sciences user facility. Sandia is a multiprogram laboratory operated by Sandia Corp., a wholly owned subsidiary of Lockheed Martin Company, for the U.S. DOE's NNSA under contract DE-AC04-94AL85000.

5:00pm IS+SS-TuA10 In-Situ Heating, Imaging, and Analysis of Nanoparticles Using SEM, STEM, and XPS, J.L. Sturgeon, RJ Lee Group, Inc., Z. Liu, University of Pittsburgh, K.L. Bunker, T.L. Lersch, J. Mastovich, B.R. Strohmeier, RJ Lee Group, Inc., J.C. Yang, University of Pittsburgh

Use of an *in-situ*, semiconductor-based heating stage in high-resolution scanning electron microscope (SEM) and scanning transmission electron microscope (STEM) instruments permits rapid, but controlled, temperature changes and the ability to collect images and videos in real time with minimal drift. A Protochips Aduro™ system utilized on a Hitachi S-5500 SEM/STEM allows analysis at elevated temperatures coupled with low voltage SEM/STEM imaging. Catalyst nanoparticles consisting of an iron core surrounded by a carbon shell have been studied using this technology. Elevated temperatures result in a variety of changes to the core-shell structure as well as migration and agglomeration of the iron nanoparticles. X-ray photoelectron spectroscopy (XPS) was also used to study the surface chemistry of these materials before and after heating. These experiments give critical insights into the kinetics of reaction of the iron nanoparticles. Additional analysis at higher accelerating voltages is possible using a dedicated STEM instrument. Other applications using elevated heating of nanoparticles will be discussed.

5:20pm IS+SS-TuA11 Understanding the Role of Fe Catalyst in Carbon Nanotube Growth Using Atomic-Scale (S)TEM, A. Mkhoyan, M.J. Behr, E.S. Aydil, University of Minnesota

The combination of unique mechanical, thermal, optical, and electronic properties of carbon nanotubes (CNTs) make them a desirable material for use in a wide range of applications. Many of these unique properties are highly sensitive to how carbon atoms are arranged within the graphene nanotube wall. Plasma-enhanced chemical vapor deposition (PECVD) from methane-hydrogen gas mixtures using Fe catalytic nanoparticles enables large-scale growth of CNT films, however, much is still unknown about what happens to the catalyst particle during growth and how it dictates the final nanotube structure. To investigate the fundamental processes of CNT growth by PECVD (S)TEM based characterization techniques were used including convergent-beam electron diffraction (CBED), high-resolution

(S)TEM imaging, energy dispersive x-ray spectroscopy and electron energy-loss spectroscopy (EELS).

It is found that hydrogen plays a critical role in determining the final CNT structure through controlling catalyst crystal phase and morphology. A variety of tube structures grow, via a base-growth mode, from single crystalline BCC iron and cementite catalyst particles. At low hydrogen concentrations in the plasma, well-graphitized nanotubes grow from elongated Fe₃C crystals, while at high hydrogen concentrations, poorly-graphitized nanofibers grow from BCC iron crystals. Although catalyst particles are single crystals, they exhibit combinations of small-angle rotations, twists, and bends along their axial length between adjacent locations. Distortions are most severe away from the base up into the nanotube where the number of walls is large. This suggests that the stresses generated by the surrounding nanotube distort the catalyst particle during growth. The much larger thermal expansion coefficient of Fe₃C compared to that of the nanotube may also play a role in shaping the crystal into the observed tear-drop morphology. No preferential catalyst orientation relative to the nanotube axis was observed, suggesting that what is required for nanotube growth is not an epitaxial relationship with the catalyst, but rather, only formation of an initial graphitic carbon seed. Z-contrast STEM images combined with atomic-scale EELS measurements also revealed an iron-oxide shell at the very base of each BCC and Fe₃C catalyst crystal.

Magnetic Interfaces and Nanostructures

Room: Zuni - Session MI+EM-TuA

Spintronics

Moderator: S.-W. Hla, Ohio University

2:00pm **MI+EM-TuA1 All-Electric Spintronics with Quantum Point Contacts: From Spin Physics to Spin Electronics, P. Debray, University of Cincinnati** **INVITED**

The controlled creation, manipulation, and detection of spin-polarized currents by purely electrical means remains a central challenge and objective of spintronics. One approach to meet this challenge has been to rely on coupling of the electron orbital motion to its spin. Attempts have been made to use the Rashba spin-orbit coupling as a tool to achieve this objective. Despite intense effort there has so far been no report of any success. In this talk, I will present experimental evidence that a quantum point contact made from a semiconductor with intrinsic spin-orbit coupling can generate completely spin-polarized current when its lateral confinement is made highly asymmetric by tuning the bias voltages of the side gates that create it. Such quantum point contacts can be used as all-electric spin polarizer or detector. I will discuss how they can replace the ferromagnetic electrodes of conventional spin valves to yield all-electric spin valves with very high On/Off values. By avoiding the use of ferromagnetic contacts or external magnetic fields, the use of such quantum point contacts will make feasible the development of a variety of semiconductor spintronic devices.

2:40pm **MI+EM-TuA3 Incorporation of Mn Atoms into N-polar Wurtzite GaN(000-1) Surface Studied using Scanning Tunneling Microscopy, A.V. Chinchore, K. Wang, M. Shih, A.R. Smith, Ohio University Nanoscale and Quantum Phenomena Institute**

There has been much interest in dilute magnetic semiconductors. Mn-doped gallium nitride was proposed as a possible dilute magnetic semiconductor with Curie temperature above room temperature [1]. Consequently, many studies have been carried out to investigate the growth and properties of Mn-doped GaN. Despite much work however, not much is known about the location of Mn atoms in the GaN surface. We present in this new study evidence for the precise position of Mn atoms in the nitrogen polar wurtzite GaN (000-1) surface.

The N-polar GaN (000-1) surface is prepared by molecular beam epitaxy using a Ga effusion cell and a rf N-plasma source on sapphire substrates. The growth is monitored in-situ using reflection high energy electron diffraction. The as-grown GaN surface shows a smooth 3×3 reconstruction. The sample is transferred in-situ to the analysis chamber where it is imaged using room-temperature scanning tunneling microscopy (STM). The as-grown sample surface shows large terraces of 3×3 reconstruction. Transferring the sample back to the growth chamber, Mn is then deposited onto the 3×3 surface at a rate of about 0.01 monolayers (ML's) per second for a total of about 0.3 ML, at a sample temperature of 250 °C. After this, the surface remains in a 3×3 structure.

STM images of the surface after Mn deposition show a modified 3×3 reconstruction including almost uni-axial trench-like structures over large areas which are not seen on the clean GaN surface. The closely-spaced trenches run along [11-20], and they are separated by an even number of

gallium adlayer rows. The position of these features also coincides precisely with Ga adlayer row positions. A model for this structure involving Mn atoms within the GaN(000-1) adlayer has been developed. Additional work exploring the coverage dependence of this structure is also underway. This work has been supported by DOE (Grant No.DE-FG02-06ER46317) and NSF (Grant No.0304314). Equipment support from ONR is also acknowledged.

[1] T. Dietl, H. Ohno, F. Matsukura, J. Cibert, and D. Ferrand, *Science* 287, 1019 (2000).

3:00pm **MI+EM-TuA4 Formation of Ferromagnetic MnGa Monolayers on GaN(0001) Studied by STM, K. Wang, A.V. Chinchore, M. Shi, A.R. Smith, Ohio University Nanoscale and Quantum Phenomena Institute**

4:40pm **MI+EM-TuA9 Chemical Switching of Coupled Molecular Spins: On and Off, C. Waeckerlin, D. Chylarecka, A. Kleibert, K. Mueller, Paul Scherrer Institute, Switzerland, C. Iacovita, University of Basel, Switzerland, F. Nolting, T.A. Jung, N. Ballav, Paul Scherrer Institute, Switzerland**

Herein we present a unique approach to reversibly control between the *on* and *off* state of the spin of an organometallic molecule coupled to a ferromagnetic substrate by a chemical switch. Such an ultimate degree of control was achieved via modification of the coordination strength of the central metal ion of the organometallic molecule by an external ligand. Thus the regulation of oxygen affinity in hemoglobin by iron-porphyrin moiety as shown in nature has been used as a designed concept to perform the switching event of single molecular spin. Use of external stimuli to control single molecular spins at magnetic-interfaces is of potential interest for spintronics and quantum information.

5:00pm **MI+EM-TuA10 The Spin-Resolved Electronic Structure of the Strongly Correlated M^{II}[TCNE]^{•-} Magnets, S.J. Janjua, University of Missouri-Kansas City, K.I. Pokhodnya, North Dakota State University, J. Trunk, Brookhaven National Laboratory, C.S. Olson, North Dakota State University, J.C. Sutherland, E. Vescovo, Brookhaven National Laboratory, A.N. Caruso, University of Missouri-Kansas City**

M^{II}[TCNE]^{•-} organic-based magnets are an important class of solids for both application and magnetic exchange and correlation study. The detailed spin polarized occupied electronic structure of M^{II}[TCNE]^{•-} magnets has eluded description from conventional ligand field theory, the results of elementally- or spin-sensitive photon and electron spectroscopies as well as spin resolved density functional calculations. This talk will present heuristic models for M=V, Fe and Ni in the context of the local physical structure and recent less conventional electronic structure studies (UV/Vis MCD), but with a new twist to the onsite and nearest neighbor Coulomb repulsion based correlation.

Nanometer-scale Science and Technology

Room: La Cienega - Session NS-TuA

Carbon-Based Nanomaterials

Moderator: N.A. Burnham, Worcester Polytechnic Institute

2:00pm **NS-TuA1 Covalent Synthesis and Optical Characterization of Double-Walled Carbon Nanotube - Nanocrystal Heterostructures, X. Peng, State University of New York at Stony Brook, M.Y. Sfeir, J.A. Misewich, Brookhaven National Laboratory, S.S. Wong, State University of New York at Stony Brook**

Double-walled carbon nanotubes (DWNs) have been a key focus material of research in recent years owing to their unique electronic structure and properties. However, the incorporation of DWNs with quantum dots (QDs) into nanocomposites via a covalent chemical approach as well as the optical properties of the composites have rarely been explored. In particular, the investigation based on CNT-QD systems, one of well-studied nanomaterial heterostructures, provides insights into a fundamental understanding of efficient charge separation within heterostructures via charge transfer relative to other relaxation pathways such as exciton recombination. In this specific work, DWNT-CdSe heterostructures were obtained by covalently conjugating 2-aminoethanethiol (AET)-modified CdSe QDs with terminal amino groups onto the surfaces of oxidized DWNs via the formation of amide bonds. For AET-CdSe, a characteristic emission in NIR was observed due to the trap states induced by the presence of AET capping ligands. Besides, the magnitude of the trap emission was found to be associated with the concentration of AET added into systems. Interestingly, the observed trap emission is effectively quenched upon

conjugation with the DWNT as a result of the charge transfer from trap states of CdSe to DWNTs. More strikingly, the time-resolved photoluminescence studies showed the exciton decay of DWNT-CdSe composites was recovered from multi-exponential to nearly mono-exponential behavior, thereby suggesting that a unique exciton dynamic occurred in the DWNT-CdSe heterostructure. More careful kinetic studies are in progress.

2:20pm NS-TuA2 Carbon Nanotube Nonvolatile Memory, K. Matsumoto, Osaka University, Japan

Since single-walled carbon nanotubes (SWNTs) have small diameter of ~1 nm, high-electric field concentration is easily generated around SWNTs. Therefore, the carbon nanotube field-effect transistors (CNTFETs) using SWNTs as a channel are expected for low power consumption nonvolatile memory. The conventional CNTFETs, however, whose channels are exposed to the atmosphere, exhibit large hysteresis due to charge trapping by impurities, such as water molecules, around SWNT channels. In the present paper, we have fabricated nonvolatile memory based on top-gated CNTFETs with double gate insulator layers after removal of the impurities around SWNT channels.

A double layer thin SiNX /SiO₂ films were deposited on SWNT channels using catalytic chemical vapor deposition. After the double layers deposition, a top gate electrode was fabricated. The interface between SiNX and SiO₂ films in the device is expected as a charge storage node of nonvolatile memory. The transfer characteristics of the CNTFET as a function of back- and top-gated voltages at 300 K in vacuum were measured. The negligible hysteresis is observed for sweeping the back-gated voltage, indicating that impurities around the SWNT channel are completely removed. In contrast, hysteresis increases with increasing sweep range for top-gated voltage. The counterclockwise hysteresis loops are due to the charging and discharging processes of holes in the top-gated CNTFETs. These results mean that the charge was trapped at the interface of SiNX /SiO₂ films by the applied top gate bias. Due to the small diameter of the CNT, the electric field concentration occurs, and only 2V application of the top gate bias produces the hysteresis. This gate bias is 10 times smaller value than that of the conventional planer type memory. The single-charge effects are observed using the CNT-based memory devices. When top-gated voltage was swept forth and backward for the ranging of ± 0.7 V, the abrupt peaks on the currents are observed for both directions. The abrupt drop or increase in drain currents corresponds to single-hole charging and discharging phenomena in CNT-based memory devices, respectively. The same measurements were carried out twenty times, and four discrete Id-Vg curves are clearly observed, which are attributed from the effect of single-holes traps.

We have fabricated the CNTFETs nonvolatile memory, which operate 10 times smaller bias owing to the electric field concentration effects. Single charge detection was also demonstrated in the CNT memory device.

2:40pm NS-TuA3 Single Walled Nanotube (SWNT) Fiber Field Emission Cathodes, S.B. Fairchild, B. Maruyama, J.J. Boeckl, D.A. Shiffler, N.P. Lockwood, Air Force Research Laboratory, M. Pasquali, Rice University

High power THz sources and amplifiers hold the potential to revolutionize the remote sensing and communication industries. Traveling wave tubes (TWT) are the most promising technology for compact high power amplifiers at THz frequencies. High frequency applications necessitate the need for small diameter beam tunnels and thus small diameter high current electron beams. Small diameter beams are typically achieved by emitting electrons from a thermionic cathode surface much larger than the THz TWT beam tunnel and focusing the beam using either electrostatic or magnetic field electron beam optics. To avoid using focusing optics, a micron sized high aspect ratio field emission (FE) cathode can be immersed in the confining magnetic field and used to generate an electron beam with a smaller diameter than the THz TWT beam tunnel. The key technical challenge with using a micron sized FE cathode is achieving the high current densities, long life time, and uniform current densities within the electron beam. The Air Force Research Laboratory (AFRL) began research on small diameter (<100 micron) single fiber DC cathodes for this application. Two types of fibers were tested, 1) those made from carbon with graphitized outer shells, and 2) fibers made solely from single walled carbon nanotubes (SWNT) that are densely packed and highly aligned along the axial direction of the fiber. Carbon fiber cathodes suffered serious degradation due to joule heating after only 25 hours of operation while only producing up to 200 microamps of current. A single SWNT fiber cathode has emitted approximately 3 milliamps of current for hundreds of hours while suffering minimal damage, as well as an 8x reduction in turn-on voltage over carbon fiber cathodes. Efforts are currently underway to optimize these SWNT fiber FE cathodes by tip shaping and applying low work function coatings.

3:00pm NS-TuA4 Spectroscopic Identification of Bond Strain and P Interactions in a Series of Saturated Carbon-Cage Molecules: Adamantane, Twistane, Octahedrane, and Cubane, T.M. Willey, J.R.I. Lee, Lawrence Livermore National Lab, D. Brehmer, SLAC National Accelerator Lab, L. Landt, Lawrence Livermore National Lab, P.R. Schreiner, A.A. Fokin, B.A. Tkachenko, N.A. Fokina, Justus-Liebig Univ. Giessen, Germany, T. van Buuren, Lawrence Livermore National Lab

Novel nanocarbons such as fullerenes, nanotubes, graphene, and nanodiamond reside at the cutting edge of nanoscience and technology. Along with chemical functionalization, geometrical constraints (such as extreme curvature in nanotubes or graphene, or defects within or at the surfaces of nanodiamond crystallites) can modify the electronic states of the nanocarbon material. Understanding the effects of bond strain on electronic structure is critical to developing nanoelectronic applications based on these materials. This paper presents a fundamental study of how bond strain affects electronic structure in a benchmark series of novel saturated carbon cage compounds. Adamantane, C₁₀H₁₆, the smallest diamondoid, and arguably the smallest nanodiamond crystallite, has carbon atoms essentially commensurate with diamond lattice positions and possesses by far the least bond strain of the series. Twistane has the same stoichiometry (C₁₀H₁₆), but introduces some strain into the cage. Octahedrane (C₁₂H₁₂) and cubane (C₈H₈) contain increasing amounts of bond strain, culminating in cubane where carbon-carbon bonds lie either parallel, or orthogonal to one another. Using gas-phase near-edge x-ray absorption fine structure spectroscopy to probe the unoccupied electronic states, we observe two major progressions across this series. First, a broad C-C σ^* resonance in the absorption splits into two more narrow and intense resonances with increasing strain. Second, the first manifold of states previously associated with tertiary C-H σ^* in the diamondoid series appears to broaden and shift to lower energy. This feature is more than twice as intense in cubane as octahedrane, even though these two molecules have similar stoichiometries (C_xH_x). We attribute the additional intensity to π^* states, indicating a high degree of π interaction between parallel C-C bonds in the cubane.

4:00pm NS-TuA7 Self-Assembly of Photo-reduced Graphene-Titanium Films, C.A. Chavez, T.N. Lambert, C.M. Washburn, N.S. Bell, B.B. McKenzie, M.T. Brumbach, D.R. Wheeler, Sandia National Laboratories

In an aim to develop photo-responsive composites, the UV photo-reduction of aqueous titanium oxide nanoparticle-graphene oxide (TiO₂-GO) dispersions (Lambert et al. J Phys. Chem. 2010 113 (46), 19812-19823) was undertaken. Photo-reduction led to the formation of a black precipitate as well as a soluble portion, comprised of titanium oxide nanoparticle-reduced graphene oxide (TiO₂-RGO). When allowed to slowly evaporate, self assembled titanium oxide nanoparticle-graphene oxide (SA-TiO₂-RGO) films formed at the air-liquid interface of the solution. The thickness of SA-RGO-TiO₂ films range from ~30-100 nm when deposited on substrates, and appear to be comprised of a mosaic assembly of graphene nanosheets and TiO₂, as observed by scanning electron microscopy. Raman spectroscopy and X-ray photoelectron spectroscopy indicate that the graphene oxide is only partially reduced in the SA-TiO₂-RGO material. These films were also deposited onto inter-digitated electrodes and their photo-responsive behavior was examined. UV-exposure lead to a ~ 200 kOhm decrease in resistance across the device, resulting in a cathodically biased film. The cathodic bias of the films was utilized for the subsequent reduction of Ag(NO₃) into silver (Ag) nanoparticles, forming a ternary Ag-(SA-RGO-TiO₂) composite. Various aspects of the self assembled films, their photoconductive properties as well as potential applications will be presented.

This work supported by the Department of Energy, Office of Basic Energy Sciences and the United States Department of Energy under contract number DE-AC04-94AL85000. Sandia is a multi-program laboratory operated by Sandia Corporation, a Lockheed-Martin Company, for the United States Department of Energy.

4:20pm NS-TuA8 Temperature Dependence of Carbon Nanofiber Resistance, S. Maeda, T. Yamada, H. Yabutani, T. Saito, C. Yang, Santa Clara University

Carbon nanostructures such as nanotube (CNT) and nanofiber (CNF) are the most promising materials for applications in next-generation silicon integrated circuits. Knowledge of the temperature dependence of these materials is critically important as it relates directly to circuit performance. However, in practice, it is extremely difficult to measure and control the temperature of each test device and maintain thermal equilibrium because of its small thermal capacity. Therefore, one must determine the temperature of test devices by other means. Here we report results of such a study on vertical via and horizontal CNF test devices. CNF can potentially be a replacement for copper in on-chip via interconnects [1], as well as in through-silicon-vias (TSVs) in three-dimensional chips [2,3]. The horizontal CNF test device can be used as a prototype of interconnect lines between adjacent transistors in the same silicon layer. In the horizontal

structure, the temperature of the CNF is extracted from current stress measurements using our heat transport model [4]. For the via test device, the CNF temperature is estimated from that of the temperature-controlled measurement system [1]. In both cases, the conductivity of CNF is determined from the measured current-voltage characteristics. We find that in either case, the conductivity increases with increasing temperature as expected. However, the measured resistance of the test device in each case contains a very different contact resistance component, due to the much higher contact resistance in the horizontal structure [5]. From the conductivity versus temperature behavior, we extract the activation energy, which turns out to be about 30 meV in each case. This finding suggests that the change in conductivity in CNF, regardless of device configuration, is due to electron trapping and detrapping at defect sites within the carbon nanostructure.

[1] Q. Ngo, T. Yamada, M. Suzuki, Y. Ominami, A. M. Cassell, J. Li, M. Meyyappan, and C. Y. Yang, *IEEE Trans. Nanotech*, **6** (2007) 688.

[2] T. Wang, K. Jeppson, N. Olofsson, E. E. B. Campbell and J. Liu, *Nanotechnology*, **20** (2009) 485203.

[3] J. U. Knickerbocker, C. S. Patel, P. S. Andry, C. K. Tsang, L. P. Buchwalter, E. J. Sprogis, H. Gan, R. R. Horton, R. J. Polastre, S. L. Wright, and J. M. Cotte, *IEEE J. of Solid State Circuits*, **41** (2006) 1718.

[4] T. Yamada, T. Saito, D. Fabris, and C. Y. Yang, *IEEE Elect. Dev. Lett.*, **30** (2009) 469.

[5] W. Wu, S. Krishnan, T. Yamada, X. Sun, P. Wilhite, R. Wu, K. Li, and C. Y. Yang, *Appl. Phys. Lett.*, **94** (2009) 163113.

4:40pm NS-TuA9 New Concepts in Molecular and Energy Transport Within Carbon Nanotubes: Thermopower Waves and Stochastically Resonant Ion Channels, M. Strano, Massachusetts Institute of Technology
INVITED

Our laboratory has been interested in how carbon nanotubes can be utilized to illustrate new concepts in molecular and energy transfer. In the first example, we predict and demonstrate the concept of thermopower waves for energy generation. Coupling an exothermic chemical reaction with a thermally conductive CNT creates a self-propagating reactive wave driven along its length. We realize such waves in MWNT and show that they produce concomitant electrical pulses of high specific power >7 kW/kg. Such waves of high power density may find uses as unique energy sources. In the second system, we fabricate and study SWNT ion channels for the first time and show that the longest, highest aspect ratio, and smallest diameter synthetic nanopore examined to date, a 500 μm SWNT, demonstrates oscillations in electro-osmotic current at specific ranges of electric field, that are the signatures of coherence resonance, yielding self-generated rhythmic and frequency locked transport. The observed oscillations in the current occur due to a coupling between stochastic pore blocking and a diffusion limitation that develops at the pore mouth during proton transport.

5:20pm NS-TuA11 All-Diamond Particles Prepared by Layer-by-Layer Deposition for High Performance Liquid Chromatography, M.R. Linford, L.A. Wiest, D.S. Jensen, Brigham Young University, A. Dadson, M.A. Vail, U.S. Synthetic

All-diamond, core-shell particles for HPLC have been prepared by layer-by-layer deposition. The process begins with the amine functionalization of ca. 2 micron diamond particles by their immersion in an aqueous solution of a primary amine-containing polymer, polyallylamine (PAAm). The amine-functionalized microdiamond is then immersed in an aqueous suspension of nanodiamond, which leads to adsorption of the nanodiamond. Alternating immersions in the solutions of PAAm and the nanodiamond suspension are continued until the desired number of nanodiamond layers is formed around the core particle. Finally, the core-shell particles are functionalized with 1,2-epoxyoctadecane to create a C18 phase. Other surface modifications, including cross linking of the PAAm polymer have been demonstrated. Scanning electron microscopy and Brunauer Emmett Teller (BET) surface area and pore size measurements show formation of the expected particles. To date, we have made core-shell particles that can be used for an HPLC separation of a four-component mixture with more than 40,000 plates/m.

5:40pm NS-TuA12 Fabrication of High-Performance Carbon Nanotube Field-Effect Transistors with Dense and Aligned Nanotubes, Z. Xiao, Alabama A&M University

Multilayered dense single-walled carbon nanotubes (SWCNTs) were deposited and aligned for fabrication of carbon nanotube field-effect transistors (CNTFETs) using the alternating electric field-directed dielectrophoresis (DEP) method. Ultrapurified high-pressure carbon monoxide (HiPCO)-grown SWCNTs were ultrasonically dispersed in *n*-methyl pyrrolidone (NMP) for deposition and alignment. High-performance CNTFETs with high on/off drain-source current ratios and good saturation

of drain-source current were fabricated using semiconductors as the source/drain contact materials. The current-voltage (IV) electrical property of the fabricated CNTFETs was measured. The processes for alignment of multilayered dense SWCNTs and fabrication of CNTFETs and the electrical property of the fabricated CNTFETs will be reported in the conference.

Plasma Science and Technology
Room: Aztec - Session PS1-TuA

Advanced BEOL/Interconnect Etching II
Moderator: Y. Zhou, Applied Materials Inc.

2:00pm PS1-TuA1 Reaction Mechanism and Profile Evolution for Cleaning and Sealing Porous Low- k Dielectrics using He/H₂ and Ar/NH₃ Plasmas, J. Shoeb, Iowa State University, M.J. Kushner, University of Michigan, Ann Arbor

Porous dielectric materials offer lower capacitances that reduce RC time delays in integrated circuits. Typical *low-k* materials include SiO₂ – silicon dioxide with carbon groups, principally CH₃, lining the pores. Fluorocarbon plasmas are often used to etch *low-k* materials. These processes leave a fluorocarbon polymer on the *low-k* surface that must be removed. This is often done with oxygen containing plasmas. With porosities as high as 0.5, pores open to the surface and which are internally connected provide pathways for reactive species to enter into the porous network. Reactions during plasma cleaning of, for example, O atoms with the CH_x groups, can increase the *k* value of the material by removing C atoms. To maintain the *low-k* value, cleaning the CF_x polymer and sealing of the surface must be performed without significantly altering the SiOCH material properties, and not removing the CH_x groups. Plasma cleaning with He/H₂ mixtures is capable of removing these CF_x residues without harming the underlying *low-k* surface and can also strip off the hydrocarbon photoresist (PR) mask.

In this talk, we discuss results from modeling of the plasma cleaning and sealing of porous SiOCH in sequentially applied He/H₂ and Ar/NH₃ plasmas. The HPEM (Hybrid Plasma Equipment Module) was employed to obtain the ion energy and angle distributions of reactive fluxes from inductively coupled plasmas. These are used as input to the MCFPM (Monte Carlo Feature Profile Module) with which profiles of the *low-k* materials after the plasma exposures are predicted.

We found that hot hydrogen atoms can remove the CF_x polymer, generating mainly HF and fluorohydrocarbons such as CHF₂. These hot H-atoms can simultaneously remove H from the surface resident CH₃ groups thereby activating the SiOCH surface by creating C dangling bonds. He ions are also effective at breaking Si-O bonds creating dangling while also removing H-atoms from CH₃ group, both of which activate the SiOCH surface. Unlike O₂ plasma cleaning, the He/H₂ clean creates more reactive CH_x (*x* = 1,2) sites without significantly damaging the substrate. Following the He/H₂ plasma cleaning, NH₃ plasma treatment seals the pores by NH_x (*x*=1,2 and 3) species passivating previously produced dangling bonds, forming Si-N and C-N bonds.[1] Initial results indicate that combined He/H₂ and Ar/NH₃ plasma treatment of SiOCH with pores having radii of 0.8 nm can seal nearly 100% of the surface pores.

* Work supported by Semiconductor Research Corp.

[1] A. M. Urbanowicz, M. R. Baklanov, J. Heijlen, Y. Travaly, and A. Cockburn, *Electrochem. Solid-State Lett.* **10**, G76 (2007).

2:20pm PS1-TuA2 Mechanism of Modification in Si-O-Si Structure in Porous SiOCH Low- k Films by H₂/N₂ Plasmas, H. Yamamoto, K. Takeda, K. Ishikawa, H. Kondo, M. Sekine, M. Hori, Nagoya University, Japan, T. Imamura, H. Hayashi, I. Sakai, T. Ohiwa, Toshiba Corporation, Japan

Introduction of porous low-dielectric-constant (*low-k*) materials such as porous (p-) SiOCH film, to the interlayer dielectric is important for improving performances of ULSI devices. The trench sidewall in the p-SiOCH film is known to suffer serious damage during the plasma processes. The *in-situ* evaluation is crucial for the clarification of damage generation mechanism because the damaged films are easily modified during air exposure. In this work, we have investigated the impact of ions, radicals and light from H₂/N₂ plasma and subsequent air exposure on Si-O-Si bond structure in the film using *in-situ* Fourier transform infrared reflection absorption spectroscopy. A 75-nm-thick p-SiOCH film was coated on 150-nm-thick Tungsten film deposited on Si substrate. A Si plate or an MgF₂ window which transmits light (greater than 115 nm in wavelength) was set 1 mm above or just on the film during the plasma exposure. Samples were placed on the lower electrode in a VHF-CCP etcher with (a) no plate for evaluating the interaction of ions, radicals, and light, (b) Si plate for

evaluating the impact of radicals, (c) MgF₂ window for evaluating the effect of light and radicals, and (d) MgF₂ window with no space for evaluating the light effect. To investigate the Si-O-Si bond modification in the films, IR absorption signal in 985-1250 cm⁻¹ were decomposed to three bands with peaks at 1035, 1065, and 1149 cm⁻¹, which correspond to the linear, network and cage structures, respectively. The change in the three peak area ratios were investigated after H₂/N₂ plasma and air exposures. The peak area ratio of the linear structure decreased and the ratio of network and cage structure increased after the H₂/N₂ plasma exposure in all samples. The ratio of linear structure decreased and the ratio of cage structure increased after the air exposure in all samples. In the case of sample (a), that was exposed to ions, radicals, and radiation, the amount of change in Si-O-Si structure was relatively smaller than the amount of decrease in Si-CH₃ bond. It was confirmed that a portion of Si-O-Si linear structure in the SiOCH film changed to network and cage structure with decrease in Si-CH₃ bond during the H₂/N₂ plasma exposure. Si-NH₂ bonds and dangling bonds formed by the plasma exposure reacted with water in the atmosphere and the Si-O-Si structure was modified with Si-OH bonds formation. Ion bombardment made the top surface shrink and the densified layer inhibited moisture uptake into the film during air exposure. This work was supported by Grant-Aid for Scientific Research (21 · 10187).

2:40pm PS1-TuA3 Effect of UV-wavelength on Hardening Process of Porogen-containing and Porogen-free Ultra-low-k PECVD Glasses, A.M. Urbanowicz, K. Vanstreels, P. Verdonck, E. Van Besien, Ch. Trompoukis, D. Shamiryan, S. De Gendt, M.R. Baklanov, IMEC, Belgium

The ITRS scaling of ultra-large-scale integrated circuits requires mechanically robust materials with low *k*-value. Low-*k* materials recently used in the Cu/low-*k* integration scheme have *k*-values between 2.5 and 3.0. One of the limiting factors in further reduction of *k*-value is mechanical robustness, since major way to decrease *k*-value is increasing the material porosity. The PECVD low-*k* deposition of ultra low-*k* films uses a porogen-based approach. The matrix material is deposited by oxidation of alkylsilanes in a plasma-enhanced chemical vapor deposition (PECVD) process. The porogen molecules, usually cyclic hydrocarbons, are introduced into a SiOCH film by co-deposition with the matrix material. To create porosity, the porogen is removed from the films using UV-assisted-thermal curing. The porogen molecules are photo-dissociated by UV-light with the formation of volatile hydrocarbons and non-volatile carbon-rich residues (porogen residue) [1]. We have shown recently that SiOCH glasses with improved mechanical properties and ultra-low-*k* value could be obtained by controlled decomposition of the porogen molecules prior to the UV-hardening step [2]. The controlled removal of porogen can be performed by H₂-based afterglow plasma treatment of PECVD film [1,2].

In this work we study the effect of narrow band 172 nm and broadband >200 nm UV-sources in the new curing scheme of the PECVD dielectrics. The data are compared with the PECVD films fabricated in the conventional UV-curing scheme. The effect of both 172 nm and >200 nm UV-sources is comparable for porogen-containing conventional PECVD films. However, the porogen-free films cured with 172 nm UV-source shows approximately twice as higher Young's modulus (YM) of 6.64 GPa (*k*100kHz ~ 2.2, 44% open porosity) than those cured with >200 nm UV with YM of 3.38 GPa (*k*100kHz ~ 2.0, 48% open porosity). The mechanical properties, optical properties 150 nm - 800 nm, dielectric constants at 100 kHz and 4 GHz, porosities and pore size distributions, bonding structure are presented. The impact of porogen on optical characteristic and therefore on photochemical UV-hardening mechanism is discussed. The achieved mechanical properties are explained on a basis of the percolation of rigidity theory and random network concepts.

References

- [1] A. M. Urbanowicz, K. Vanstreels, D. Shamiryan, S. De Gendt and M. Baklanov, *Electrochem. Solid State Lett.*, 12, H292 (2009).
 [2] A. M. Urbanowicz, K. Vanstreels, P. Verdonck, D. Shamiryan, S. De Gendt and M. R. Baklanov, accepted at *J. Appl. Phys.* 107,xxx, (2010).

3:00pm PS1-TuA4 CF₃I for Low-k Etching: Overcoming Current Technology Limitations, V. Omarjee, American Air Liquide – Delaware Research and Technology Center, A.G. Gildea, E. Eisenbraun, The University at Albany-SUNY, N. Stafford, F. Doniat, C. Dussarrat, American Air Liquide – Delaware Research and Technology Center
 Every technology node brings new processing challenges. The etching of low-*k* and ultra-low-*k* (*k*=2.4 and below) materials that are currently used in leading edge interconnects is very demanding. With a porosity varying from ~15 to 30%, the films are easily damaged during the various processing steps and it is easy to have undesired film modifications (physical defects,

collapse, impurity penetration, roughening of the surfaces, moisture uptake...) that degrade interconnect reliability and performance.

In this talk we will present recent work done on optimization of dielectric etching using CF₃I, a promising replacement gas for CF₄ in interconnect etch applications. Using a Design of Experiment (DOE) approach through a Taguchi-like Method combined with the capabilities of a State-of-the-Art Unaxis 200mm wafer etch system, the influences of the key parameters on the etching mechanism and performance will be presented. The DOE approach is introduced here to minimize the number of experiments while maximizing the process understanding. For instance, one of the results of the experimental matrix suggests an etching rate contribution of CF₃I that is non-linear. In addition to characterization of etch rate, the samples are characterized using RBS, AES and SEM to fully understand the impact of the process parameters on overall film quality. Baseline data as well as structure patterning will be presented after the optimization process using CF₃I alone and also using CF₃I mixed with well established fluorocarbons.

4:00pm PS1-TuA7 Challenges in sub-100nm Dual Damascene Etch of Porous Oxycarbosilane Ultra Low-k Dielectrics for BEOL Integration, R.L. Bruce, S.U. Engelmann, S. Purushothaman, IBM T.J. Watson Research Center, T.J. Frot, IBM Almaden Research Center, M. Darnon, M. Lofaro, S. Cohen, IBM T.J. Watson Research Center, W. Volksen, T.P. Magbitang, L. Krupp, G. Dubois, IBM Almaden Research Center

There has been much interest recently in porous oxycarbosilane (POCS)-based materials as the interconnect layer dielectric (ILD) in back-end-of-line (BEOL) manufacturing due to their superior mechanical properties compared to conventional porous SiCOH at equivalent porosity and dielectric constant. [1-4] While it is well known that plasma etching and ashing processes can cause significant damage to porous ultra-low *k* dielectric materials in general, little has been reported about the effect of plasma damage to POCS as the ILD material. In this work, we discuss the effect of plasma etching and ashing processes on POCS during the fabrication of single and dual damascene structures for BEOL integration. We used TEM-EELS to quantify chemical composition changes at the top, bottom, and sidewalls of POCS trenches after each plasma etching and ashing step. After plasma processing, POCS structures undergo extensive plasma damage such as pitting, microtrenching, and the generation of trench bottom roughness. Opening of the cap layer exacerbates these etch damage features. Damage is reduced by increasing the neutral-to-ion ratio of the gas discharge in the ULK trench etch and eliminating O₂ from the ashing process. The use of vapor phase silylation between etch process steps is also shown to repair plasma-damaged POCS. However, we show that the most significant improvement to post-plasma damage occurred by reducing the pore size of the starting POCS material while maintaining comparable porosity, i.e. dielectric constant.

- [1] W. Volksen, *et al.*, *Chem. Rev.* 110, 56 (2010).
 [2] G. Dubois, *et al.*, *J. Of Sol-Gel Science and Technology* 48, 187 (2008).
 [3] G. Dubois, *et al.*, in *Dielectric Films for Advanced Microelectronics*, edited by M. Baklanov, *et al.*, (Wiley, New York, 2007), p. 33.
 [4] G. Dubois, *et al.*, *Adv. Materials* 19, 3989 (2007).

4:20pm PS1-TuA8 Mechanism of Highly Selective SiO₂ Etching over Photoresist Using New Alternative Gas, C₃HF₇, Y. Miyawaki, Y. Kondo, K. Takeda, K. Ishikawa, M. Sekine, H. Kondo, Nagoya University, Japan, A. Ito, M. Nakamura, Zeon Corporation, Japan, M. Hori, Nagoya University, Japan

With the continuous demand for increasing the storage capacity of semiconductor memory devices, a much precise etching process for high aspect ratio contact holes in SiO₂ film is indispensable. The aspect ratio of more than 20 will be required for 45-nm node in 2010. Furthermore, deterioration of the SiO₂ selectivity over a fragile, thin photoresist would cause the sidewall roughness and poor pattern-width definition. In this study, we utilized a newly designed environmentally-friendly (low global warming potential) gas, C₃HF₇, and compared the etch performances with conventional C₃F₈ gas. A very-high-frequency (VHF) capacitively coupled plasma (CCP) etcher was used with 1800 W VHF power and 2 MHz bias of 1200 W. C₃F₈ or C₃HF₇ gas was introduced with O₂ and Ar (C₃F₈ or C₃HF₇/O₂/Ar = 15 / 10-35 / 300 sccm). We evaluated the dependence of O₂ flow rate on the etching rates of SiO₂ and KrF photoresist and SiO₂ selectivity to the resist. The gas phase species, O radical (O*) and CF₃⁺, were measured using Vacuum Ultraviolet Laser absorption spectroscopy (VUVLAS) and a

quadruple mass spectroscopy (QMS). The C_5F_8 gas chemistry showed the maximum selectivity of 3.7 with the etching rate of 416 nm/min at 20 sccm O_2 flow rate. In contrast, C_3HF_7 chemistry realized much higher selectivity (more than 13.5) with the etching rate of 356 nm/min at 25 sccm O_2 flow rate. It was confirmed that almost four times higher selectivity than that of the conventional C_5F_8 gas was obtained by using the new C_3HF_7 gas. In the both gas chemistry, the density of CF_3^+ ion, that could be one of the dominant etch species for SiO_2 , showed the maximum value at the maximum etch rate conditions. The variation trends for O^* densities were similar to the resist etch rate in $C_3HF_7/O_2/Ar$ plasma. It was also speculated that the H atoms from C_3HF_7 reduced the density of F radical that would enhance the resist etch rate. The reason for the high selectivity would be examined by measuring the surface chemical compositions and the gas phase species, such as CF_x and F.

4:40pm **PS1-TuA9 Etch Characteristics of SiO_2 in the C,F_y Dual-Frequency Capacitive Coupled Plasma**, *M.H. Jeon, S.K. Kang, J.Y. Park, G.Y. Yeom*, Sungkyunkwan University, Republic of Korea

5:00pm **PS1-TuA10 Ultra-high Selectivity Silicon Nitride Liner Etch: Mitigating Substrate Damage in Logic-based Contact Level Interconnects**, *A. Metz, H. Cottle, Y. Chiba, P. Biolsi*, TEL Technology Center America, *M. Luo, E. Geiss*, Global Foundries, *S.H. Sung*, Samsung Electronics, *M. Aminpur, R. Wise*, IBM Microelectronics

Reactive Ion Etch [RIE] of Silicon Nitride films, utilized primarily as spacers, hard masks or etch stop layers [ESLs], is pervasive throughout logic and flash microelectronics fabrication processes. While the most critical RIE-related specifications vary widely depending on the specific application and photolayer, contact level liner/ESL removal is among the most challenging. This application ideally requires high etch selectivities to multiple material types [including NiSi, SiO_2 , Si, and Si_xGe_y] at the bottom of a high aspect ratio feature where etch stop marginality in a polymer rich regime can impact opens yield. Furthermore, relying on high radical density, low ion energy, primarily chemical etch processes utilized for Si_xN_y type spacer applications often lack profile control where sidewall bowing can result in metallization related yield fallout.

This work characterizes a new contact RIE process developed for 28nm and beyond technology nodes. Reported is the successful integration of an ultra high selectivity Si_xN_y liner removal process [$> 40:1$ in hole selectivity for $Si_xN_y : Si$]. Cross-sectional characterization of contact profile and in hole selectivity data will be provided. High Opens/Shorts yield [equal or better than baseline] as determined by voltage contrast metrology and inline E-Test will be shown. In addition, a 10x reduction in gate leakage will be shown based in-line E-Test attributable to reduced active area Si loss/recess.

5:20pm **PS1-TuA11 Achieving Lithographically Independent sub-35nm Vias for Phase Change Memory Applications**, *E.A. Joseph, R. Dasaka, M. Breitwisch, A.G. Schrott, C.H. Lam*, IBM T.J. Watson Research Center

Non-volatile phase change based memory has recently garnered significant interest due to its potential for scalability beyond that of conventional DRAM and Flash memory technologies.[1] However, multiple etch challenges exist in the fabrication of robust PCM devices and not all have been thoroughly discussed and/or researched. For instance, patterning of the novel phase change material without causing material modification and performance degradation is a well known issue and has been reviewed in the past.[2,3,4] On the other hand, the ability to fabricate robust and uniform sublithographic contacts (to the phase change material) is rarely discussed from an etch perspective. In this presentation, this latter issue is explored in detail and a lithographically independent etch process scheme with the capability of yielding sub-35nm vias is presented. Critical factors such as oxide and nitride etch selectivity, taper angle and etch stop phenomenon are all reviewed. Lastly, the application of this method for logic applications such as gate contacts and BEOL via patterning will also be discussed with a focus on the ultimate scaling limitations of this process.

[1] Y.C. Chen, C.T. Rettner, S. Raoux *et al.*, IEDM Tech. Dig., p. S30P3, 2006.

[2] P. Petruzza, Paper PS-MoA4, AVS 54th International Symposium, 2007

[3] E. A. Joseph, T. D. Happ, S.-H. Chen, S. Raoux, *et al.*, Symp. VLSI-Technology Systems and Applications, 2008. pg 142-143, 2008

[4] E. A. Joseph, S. Raoux, J. L. Jordan-Sweet, D. Miller, H-Yu Cheng, A. Schrott, C-F. Chen, R. Dasaka, B. Shelby, Y. Zhang, C. Lam, J. Washington, G. Lucovsky and M. Paesler, Paper PS1-ThM11, AVS 56th International Symposium, 2009

5:40pm **PS1-TuA12 The Evaluation of Sidewall Polymerization during Platinum Dry Etching Process using Inductively Coupled $Cl_2/O_2/Ar$ and CH_3OH Plasmas**, *J.Y. Moon, J.W. Park, M.S. Lee, B.G. Jyun, W.J. Choi, S.H. Cho, J.S. Roh, S.-K. Park*, HYNIX Semiconductor Inc., Republic of Korea

It has been reported that platinum is the most appropriate resistive switching RAM (ReRAM) electrode material due to its good oxidation-resistance, high electrical conductivity and low leakage current characteristics. However, platinum does not easily form the volatile products, and the unwanted sidewall polymer which is produced during plasma etch process gives a large shift in the pattern size of the etched pattern and also makes it difficult to remove. In this study, experimental studies of platinum etching process have been performed to understand the characteristics of sidewall polymerization using inductively coupled $Cl_2/O_2/Ar$ and CH_3OH plasmas etching process. The effects of etch parameters such as gas combination and substrate temperature on the characteristics of etch properties of platinum were also investigated to minimize sidewall polymer re-deposition in the point of re-deposited sidewall polymers. The thickness of re-deposited polymers related to platinum were measured and studied by high resolution transmission electron microscopy (HR-TEM). The chemical reactions on the etched surface also have been studied by X-ray photoelectron spectroscopy (XPS).

Plasma Science and Technology Room: Galisteo - Session PS2-TuA

Plasma Sources

Moderator: D.J. Economou, University of Houston

2:00pm **PS2-TuA1 Plasma Study in Modulated Pulse Power (MPP) Magnetron Sputtering with Different Magnetron Configurations**, *D.N. Ruzic, L. Meng, S. Jung, M.J. Neumann*, University of Illinois at Urbana-Champaign

As a derivative of high power pulsed magnetron sputtering (HPPMS), modulated pulse power (MPP) technology is used to apply arbitrary voltage waveforms to the cathode. It not only retains the distinctive features of HPPMS as the intense pulsed plasma density and potentially high ionization fraction of metal atoms, but also offers high degree of freedom for additional process control. In a 1000 cm^2 circular planar magnetron, discharges were initiated using a 10 kW average power MPP generator (capable of a pulse peak power up to 147 kW). To optimize the MPP discharge for the future applications, the effects of pulse waveforms and other discharge parameters on the plasma were studied first using a time-resolved triple Langmuir probe. A typical electron temperature (T_e) of 10 eV and an electron density (n_e) close to $10^{12} cm^{-3}$ during the pulses were determined. Higher pulse current, lower pulse repetition frequency, higher gas pressure and closer to the target were revealed to exhibit higher n_e , while T_e was also affected. The ion fluxes were then measured using an electrostatic gridded energy analyzer, showing typical ion energies of about 10 eV. Combined with a quartz crystal microbalance, the analyzer was further employed to measure the ionization fractions of sputtered metal atoms under various conditions. Finally, the effects of magnetron configurations were investigated using a specially-designed magnet pack in which both the positions and the strengths of the magnets were fully adjustable. Several configurations showed obvious superiorities to the normal balanced DC magnetron configuration, maintaining a higher pulse current and consequently a higher plasma density. A qualitative plasma model was proposed to explain the observed results and further understand the underlying mechanisms of the MPP discharge.

2:20pm **PS2-TuA2 Spatial Evolution of Plasma Generated VUV in a Microwave Surface-Wave Plasma**, *J.P. Zhao, L. Chen, M. Funk, R. Bravenec, R. Sundararajan*, Tokyo Electron America Inc., *K. Koyama, T. Nozawa*, Tokyo Electron Limited, Japan, *S. Samukawa*, Tohoku University, Japan

Vacuum ultraviolet (VUV) radiations generated in low temperature plasmas (e.g., CCP and ICP) has been reported to cause wafer damage, alteration of morphology of polymers and electrical properties of dielectrics. Electron-hole pairs generated in dielectric films by VUV radiations can be trapped in dielectrics and interfaces. This results in charge buildup and dielectric breakdown as well as the decrease of device reliability. Synergistic effects of VUV exposure and energetic ion bombardment have been addressed to increase photoresist roughening. In order to improve the device and plasma process reliability, monitoring and evaluation of plasma generated VUV radiations have become important and highly demanded in plasma processing. Herein, characterization and spatial evolution of VUV radiations generated in a microwave surface-wave plasma is reported.

Microwave surface-wave discharges operating within a wide power and pressure window can be used to produce large area plasmas of high density. Due to its inherent diffusion characteristics, apart from the discharge source, quiescent, uniform, and low-temperature Maxwellian plasma near wafer region can be obtained. In spite of these promising features, understanding the evolution of plasma generated VUV radiations can help the development of microwave surface-wave plasma based hardware and the design of process recipes. The plasma source used in this work consists of a radial line slot antenna (RLSA) which transmits 2.45 GHz microwaves into a large quartz resonator disk which then couples to the plasma. VUV radiations in RLSA plasma are monitored by measuring VUV induced electron-hole pair generation in dielectric films using VUV monitoring sensors developed by Samukawa et al.¹ Three kinds of VUV sensors consisting of SiO₂, Si₃N₄, and SiO₂/Si₃N₄ films are used, which monitor VUV radiations in the wavelength range of <140 nm, <250 nm, and >250 nm, respectively. Measurements in N₂, Ar, and O₂ plasma are carried out from 23 mm to 203 mm below top plate surface. A wide pressure-power spectrum has been investigated. Experimental results indicate that VUV radiations in RLSA plasma are dramatically reduced as a function of distance from the top plate. For better understanding on the evolution of VUV radiations in RLSA plasma, the electron energy distribution functions (EEDFs) are also measured using a Langmuir probe as a function of vertical location. Mechanisms on the evolution of VUV radiations are discussed based on the measured EEDFs and VUV absorption process.

¹ S. Samukawa et al., J. Vac. Sci. Technol. A 23(6), 1509 (2005)

2:40pm **PS2-TuA3 PM Helicons: A Better Mousetrap, F.F. Chen***,
UCLA **INVITED**

Helicon discharges are known to very efficient in generating high plasma densities at low pressures for such applications as etching. The reason for this efficiency is that helicon plasmas depend on resonant waves in a magnetic field which couple the rf energy into electrons in a complicated way involving nonlinear physics. To generate the magnetic field, commercial helicon reactors employ large, heavy electromagnets and a correspondingly large dc power supply to drive them. A new type of helicon discharge has been developed that uses the remote field of annular permanent magnets (PMs) and an array of small tubes that incorporate constructive interference of a reflected helicon wave [1-3]. With 3kW at 13.56 MHz, an 8-tube test device has produced argon plasmas of density $2-6 \times 10^{11} \text{ cm}^{-3}$ over $\sim 20 \times 50 \text{ cm}$ areas with $\pm 3-5\%$ uniformity [4]. The source needs only 15 cm of vertical space. A code HELIC is used for the design of the wave properties, and a new code EQM has recently been developed to predict the equilibrium profiles of plasma and neutral densities and of electron temperature. With 27.12 MHz it is possible to design a very compact plasma thruster for spacecraft.

*mail to:ffchen@ee.ucla.edu

1. F.F. Chen and H. Torreblanca, Plasma Phys. Control. Fusion **49**, A81 (2007).
2. F.F. Chen and H. Torreblanca, Phys. Plasmas **16**, 057102 (2009).
3. F.F. Chen and H. Torreblanca, Plasma Sources Sci. Technol. **16**, 593 (2007).
4. H. Torreblanca, Ph.D. thesis, UCLA (2008).

4:00pm **PS2-TuA7 Modeling of a Transformer-type Toroidal Plasma Source, S. Rauf, Z. Chen, K. Collins**, Applied Materials Inc.

4:20pm **PS2-TuA8 Self-Consistent Electrodynamics of Large-Area High-Frequency Capacitive Plasma Discharge, Z. Chen, S. Rauf, K. Collins**, Applied Materials Inc.

Large-area capacitively coupled plasmas (CCP) generated by high frequency (HF, 3-30 MHz) and very high frequency (VHF, 30-300 MHz) RF sources are used for thin film deposition in the production of thin film transistors for flat panel display and thin film photovoltaic solar panels. Economic considerations are driving a rapid increase in substrate size and adoption of VHF sources for improved film quality and higher deposition rate. As a consequence of these trends, electromagnetic wave effects are becoming the dominant factor in determining processing uniformity. Because the effective RF wavelength in plasma depends upon both RF frequency and plasma process conditions such as RF power and gas pressure, a self-consistent model including both RF power delivery system and plasma discharge is highly desired to capture a more complete physical picture of plasma behavior. In this paper, we present a three-dimensional model for self-consistently studying both electrodynamic and plasma dynamic behavior of large-area ($> 8 \text{ m}^2$) CCP. The model couples Maxwell's equations with transport equations for charged and neutral

species in the time domain. Maxwell's equations are discretized and solved using the finite-difference time-domain (FDTD) method. The plasma discharge is modeled by solving the continuity equations for charged and neutral species and the electron energy conservation equation. The complete RF plasma discharge chamber including RF power delivery sub-system, electrodes and plasma domain is modeled as an integrated system. The RF power source is naturally applied onto the transmission line of the RF feed system in the form of an electromagnetic wave. Based on the full-wave solution model, we are able to study the important limitations for processing uniformity imposed by electromagnetic wave effects in a rectangular reactor having electrode size of $3.05 \text{ m} \times 2.85 \text{ m}$. We examine the behavior of H₂ plasmas in such a reactor at a pressure of 2 Torr when we incrementally scale the frequencies from 13.56 to 200 MHz and the power from 20 kW to 80 kW. We show that various rectangular harmonics of electromagnetic fields can be excited as RF frequency or power is increased. These rectangular harmonics, mathematically described by the hyperbolic functions, can create not only the plasma profiles where plasma density is high at the center and low at the corners of the reactor, but also the profiles where plasma density is high at the corners and along the edges of the reactor and low in the inner area. Such highly nonuniform plasma distribution at VHF or high power level is challenging to compensate and has important implications for large-area plasma processing.

4:40pm **PS2-TuA9 Independent Control of Ion Energy and Flux in CCPs by the Electrical Asymmetry Effect, U. Czarnetzki**, Ruhr-University Bochum, Germany **INVITED**

Technical plasmas are often generated by radio-frequency (RF) fields in the MHz regime. In particular, capacitively coupled RF plasmas have found wide industrial application ranging from semiconductor etching to thin film deposition as e.g. in large area production of solar-cells. In all cases the processes on the substrate surface are critically dependent on the energy and flux of the impinging ions. Therefore, independent control of these parameters is the major aim of various alternative concepts developed in the past. Despite some general progress, in practice independent control has been realized only within certain constraints.

The recently invented electrical asymmetry effect provides a novel solution by adjusting as a control parameter the relative phase between two harmonic RF frequencies [1]. This meets not only the above requirements in an almost ideal way but allows in addition for the first time breaking the symmetry in geometrically geometric discharges, which are common in large area processing. There the phase can be set so that the ion energy is increased on one electrode and reduced on the other or vice versa. The physics of the resulting non-linear system can be reduced to a few basic principles that allow an analytic treatment. The results of the analytical model are compared with particle-in-cell (PIC) / Monte Carlo (MC) simulations and experiments [1-6]. Although the system is characterized by a high degree of complexity all three approaches show remarkable agreements. Ultimately this leads to a detailed understanding not only of the dynamics of the electrical asymmetry effect but also of the physics of capacitively coupled plasmas in general.

Finally, first applications in industry on thin-film solar-cell production demonstrate superior performance by immediately more than doubling the deposition rate of silicon without loss in quantum efficiency.

References:

- [1] Brian G. Heil, U. Czarnetzki, R. P. Brinkmann, T. Mussenbrock, Journal of Physics D: Applied Physics. **42**, 165202 (2008)
- [2] Z. Donkó, J. Schulze, B.G. Heil and U. Czarnetzki, Journal of Physics D: Applied Physics **42**, 025205 (2009)
- [3] Z. Donkó, J. Schulze, U. Czarnetzki, and D. Luggenhölscher, Applied Physics Letters **94**, 131501 (2009)
- [4] J. Schulze, E. Schüngel and U. Czarnetzki, Journal of Physics D: Applied Physics **42**, 092005 (2009)
- [5] J. Schulze, E. Schüngel, U. Czarnetzki and Z. Donkó, Journal of Applied Physics **106**, 063307 (2009)
- [6] J. Schulze, E. Schüngel, Z. Donkó, and U. Czarnetzki, Journal of Physics D: Applied Physics, in print (2010)

5:20pm **PS2-TuA11 Inhomogeneous Magnetic Field Interaction with VHF and HF Capacitively Coupled Plasmas, K. Bera, S. Rauf, K. Collins**, Applied Materials, Inc.

Both electromagnetic and electrostatic power deposition play important role in very high frequency (VHF) capacitively coupled plasma source to determine the plasma spatial profile. The electromagnetic effect enhances the plasma density near the chamber center, while electrostatic and inductive effects increase the density near the electrode edges. The electrostatic effect prevails for high frequency (HF) plasma sources. Secondary electron emission also plays an important role in determining the

HF plasma profile. It has been shown earlier that the plasma profile generated due to VHF and HF sources can be modified using static magnetic fields. In this study, we further investigate the interaction of inhomogeneous static magnetic fields with plasmas. Various magnetic coil configurations, such as solenoid, cusp, mirror and dual solenoids, are considered. Our plasma model includes the full set of Maxwell equations in their potential formulation. The equations governing the vector potential, A , are solved in the frequency domain after every cycle for multiple harmonics of the driving frequency. The electron transport coefficients become tensor quantities in the magnetized plasma. The coupled set of equations governing the scalar potential, Φ , and drift-diffusion equations for all charged species are solved implicitly in time. Static magnetic field from dc current sources has been simulated for different coil configurations, and imported to our plasma model. The plasma modeling result shows that radial magnetic field component limits electron loss to the electrodes and locally enhances the electron density. The axial magnetic field component primarily limits plasma diffusion in the radial direction thereby preserving the effect of improved electron confinement by the radial magnetic field component. For VHF plasmas, using solenoid coil, the magnetic field decreases the electron density in the chamber center and the peak in electron density gradually moves to the edge of the lower electrode. For HF plasmas, the peak density near the electrode edge increases with magnetic field. The effect of magnetic field on the plasma profile is enhanced using the cusp configuration. With dual solenoid, the radial and axial components of magnetic field are modified locally using different coil current ratios and directions. Depending on the nature and location of power deposition in the plasma chamber, the plasma profile is modified in different manner using various coil configurations, current directions, and current ratios.

5:40pm **PS2-TuA12 Properties of Corona Bar Discharges for Production of Preionizing UV Light**, *Z. Xiong, M.J. Kushner*, University of Michigan, Ann Arbor

In electric discharge-pumped excimer lasers as used for photolithography sources in microelectronics fabrication, corona discharges are often used to provide UV photons to preionize the gas mixture. The preionization source, often called a *corona bar*, typically consists of a cylindrical metal rod surrounded by a dielectric. A discharge initiated by a high voltage pulse propagates around the surface of the corona bar, producing a surface-hugging avalanche wave similar to a gas phase streamer. The high electron temperature in the avalanche front produces radiating excited states that in turn produce the desired UV photons. We present results from a numerical study of an idealized corona bar discharge sustained in a multi-atmosphere Ne/Ar/F₂/Xe gas mixture as used in ArF excimer lasers. The corona bar consists of a grounded metal cylinder surrounded by an annular dielectric layer of a few cm diameter. A point electrode (cathode) is located on the surface of the dielectric layer and is subject to a stepwise initial voltage change. The ensuing corona surface discharge was investigated using a 2-dimensional plasma hydrodynamics model with radiation photon transport. Continuity equations for charged and neutral species, and Poisson's equation are solved coincident with the electron energy equation with transport coefficients obtained from solutions of Boltzmann's equation. The ionization front, initiated from the point electrode, propagates along the cylinder surface (with speeds up to 3×10^8 cm/s that depend on the dielectric constant) charging the surface as it propagates. The ionization front usually stops before completing a full circle as the corona bar becomes progressively charged. The strength and propagation speed of the ionization wave are characterized by the electron density and temperature distributions along the cylinder circumference. The photon fluxes are collected on a surrounding circular surface. With radiation from short lived states such as Ne₂^{*}, the UV emission sweeps around the corona bar coincident with the ionization wave. The effects of dielectric constants, gas mixture and voltage on the corona discharge dynamics will be presented.

* Work supported by Cymer, Inc. and the Department of Energy Office of Fusion Energy Sciences.

Advanced Surface Engineering

Room: Cimmaron - Session SE-TuA

Surface Engineering for Thermal Management

Moderator: A.A. Voevodin, Air Force Research Laboratory

2:00pm **SE-TuA1 Nanometer-Scale and Interfacial Thermal Transport and Thermal Properties Characterization**, *W.P. King*, University of Illinois at Urbana-Champaign **INVITED**

This talk discusses recent work on measurements of nanometer-scale and interfacial heat transfer as well as measurements of nanometer-scale thermophysical properties of solid materials. The research combines atomic

force microscope (AFM)- based measurements, nanometer-scale thermal processing, and nanometer-scale infrared spectroscopy.

In the first research thrust, an AFM cantilever probe can be used to measure thermomechanical expansions with spatial resolution smaller than 10 nm and out-of-plane displacements as small as 3 pm. Such displacements correspond to about 10 mK temperature changes. We use this technique to measure temperature distributions in graphene and carbon nanotube devices. It is possible to make a quantitative measurement of temperature rise in carbon nanoelectronic devices that are one atom thick.

In the second research thrust, we use AFM cantilever probes with integrated heaters. When the AFM tip is in contact with a solid substrate, the tip-substrate contact is an ultrasmall hotspot with a diameter as small as 1 nm. This tip can be used to measure nanometer-scale temperature-dependent mechanical, chemical, and electronic properties of surfaces.

2:40pm **SE-TuA3 Determination of Thermal Accommodation Coefficients from Heat Transfer Measurements Between Parallel Plates**, *W.M. Trott, J.R. Torczynski, M.A. Gallis, D.J. Rader, J.N. Castañeda*, Sandia National Laboratories

Thermal accommodation coefficients have been derived for a variety of gas-surface combinations using an experimental apparatus developed to measure the pressure dependence of the conductive heat flux between parallel plates at unequal temperature separated by a gas-filled gap. The heat flux is inferred from temperature-difference measurements across the plates in a configuration where the plate temperatures are set with two carefully controlled thermal baths. Temperature-controlled shrouds provide for environmental isolation of the opposing test plates. Since the measured temperature differences in these experiments are very small (typically 0.3° C or less over the entire pressure range), high-precision thermistors are used to acquire the requisite temperature data. High-precision components have also been utilized on the other control and measurement subsystems in this apparatus, including system pressure, gas flow rate, plate alignment, and plate positions. The apparatus also includes the capability for *in situ* plasma cleaning of the installed test plates. Measured heat-flux results are used in a formula based on Direct Simulation Monte Carlo (DSMC) code calculations to determine the thermal accommodation coefficients. Thermal accommodation coefficients have been determined for three different gases (argon, nitrogen, helium) in contact with various surfaces. Materials include metals and alloys such as aluminum, gold, platinum, and 304 stainless steel. A number of materials important to fabrication of Micro Electro Mechanical Systems (MEMS) devices have also been examined. For most surfaces, coefficient values are near 0.95, 0.85, and 0.45 for argon, nitrogen, and helium, respectively. Only slight differences in accommodation as a function of surface roughness have been seen. Surface contamination appears to have a more significant effect: argon plasma treatment has been observed to reduce thermal accommodation by as much as 0.10 for helium. Mixtures of argon and helium have also been examined, and the results have been compared to DSMC simulations incorporating thermal-accommodation values from single-species experiments. Sandia National Laboratories is a multi-program laboratory operated by Sandia Corporation, a wholly owned subsidiary of Lockheed Martin Corporation, for the U.S. Department of Energy's National Nuclear Security Administration under contract DE-AC04-94AL85000.

3:00pm **SE-TuA4 The Nanoscale Surface Modification of the Wettability on Enhancements of Two Phase Change Heat Transfer Coefficient and Critical Heat**, *C.H. Li*, The University of Toledo, *G.P.B. Peterson*, Georgia Institute of Technology

Nanoscale surface modification has been an emerging technology for many engineering applications; particularly it could enable the two phase change heat transfer of an order of magnitude higher performance compared to the untreated smooth surface. Moreover, a micro scale surface structure modification will enhance the liquid replenishment by separating the vapor and liquid flow paths. By integrating those two surface modification methods, the critical heat flux and heat transfer coefficient of two phase change heat transfer have been significantly improve.

4:00pm **SE-TuA7 Surface Engineering for Thermoelectric Energy Conversion**, *D.S. Dudis, M. Check, J. Ferguson*, Air Force Research Laboratory **INVITED**

Thermoelectric energy conversion encompasses both the conversion of thermal energy to electricity (energy harvesting and power generation), as well as the conversion of electrical energy to thermal energy (refrigeration and heat pumping). Since 1993 a renaissance has taken place in quest for better thermoelectric materials offering improved thermoelectric energy conversion efficiencies. An obstacle to achieving improved thermoelectric properties is to increase the electrical conductivity to thermal conductivity ratio (σ / κ), while not negatively impacting thermopower (Seebeck coefficient). Surface engineering has proven particularly important in this

quest, as the transport of thermal energy across boundaries is intimately tied to surface effects. This talk will review recent progress in thermoelectric materials research and highlight some challenges tied to surface and materials engineering.

4:40pm **SE-TuA9 Thermal Conductance of Pt/VO₂/Pt Heterointerfaces**, *D.-W. Oh, D.G. Cahill*, University of Illinois at Urbana-Champaign

5:00pm **SE-TuA10 Synthesis and Thermoelectric Properties of RuO₂ Nanorods**, *D. Music, F.H.-U. Basse*, RWTH Aachen University, Germany, *J.J. Gengler, A.A. Voevodin*, Air Force Research Laboratory, *J.M. Schneider*, RWTH Aachen University, Germany

We have explored the effect of the O/Ru ratio on the morphology and the Seebeck coefficient of RuO₂ nanorods (space group *P4₂/mnm*) synthesized by reactive sputtering. At an O/Ru ratio of 1.69, a faceted surface is observed, while nanorod formation occurs at O/Ru ratios of 2.03 and 2.24. Using classical molecular dynamics with the potential parameters derived in this work, we show that volatile species enable nanorod formation. Based on *ab initio* calculations, two effects of the nanorod formation on the Seebeck coefficient are observed: (i) increase due to additional states in the vicinity of the Fermi level and (ii) decrease due to oxygen point defects (volatile species). These two competing effects give rise to a moderate increase of the Seebeck coefficient upon nanorod formation.

5:20pm **SE-TuA11 Thermal Conductivity Measurements of RuO_x Thin Films**, *J.J. Gengler, A.A. Voevodin*, Air Force Research Laboratory, *D. Music, F.H.-U. Basse, J.M. Schneider*, RWTH Aachen University, Germany

Thermal conductivity trends in RuO_x thin films of varying stoichiometry were characterized with a time-domain thermoreflectance (TDTR) technique. At an O/Ru ratio of $x = 1.69$, a faceted film surface is observed with a measured thermal conductivity value of $28.8 \pm 0.8 \text{ W m}^{-1} \text{ K}^{-1}$. With an O/Ru ratio of $x = 2.24$, nanorod formation occurs. These films were grown by a reactive magnetron sputtering technique with nonrotating substrates oriented 20° normal to the Ru target. Such material synthesis conditions resulted in a gradient sample structure at the onset of nanorod formation. As a result, the RuO_{2.24} samples exhibited gradually changing surface roughness (rms of 12 nm – 200 nm) and thermal conductivity values ($22 \text{ W m}^{-1} \text{ K}^{-1} - 5 \text{ W m}^{-1} \text{ K}^{-1}$), respectively. The thermal conductivity of the thin film samples studied here are all well below that of single crystal RuO₂ with tetragonal rutile structure ($50 \text{ W m}^{-1} \text{ K}^{-1}$ [1]). The samples also have an inverse relationship of thermal conductivity with Seebeck coefficient [2], which is desirable for improving the figure of merit for thermoelectric performance.

References

[1] Ferizovic D, Hussey LK, Huang Y-S, Munoz M. Determination of the room temperature thermal conductivity of RuO₂ by the photothermal deflection technique. *Appl Phys Lett* 2009;94:131913.

[2] Music D, Basse F H-U, Habdorf R, Schneider JM. Synthesis and thermoelectric properties of RuO₂ nanorods. *J Appl Phys*, submitted for review.

5:40pm **SE-TuA12 Heat Transport at Water Interfaces in the Proximity of Micro- and Nano-Structured Surfaces**, *S.A. Putnam, J.G. Jones*, Wright Patterson Air Force Base

Breakthroughs in many of today's advanced technologies depend on the ability to reliably dissipate enormous amounts of thermal energy (heat) from very small areas. The most demanding applications are managed with nucleate boiling-based cooling schemes (e.g. spray cooling, heat pipes, thermosyphons, flow boiling, and jet impingement), where the cooling effectiveness is dictated by both the cooling configuration and the coolant itself. Surface features can also play a crucial role in boiling/cooling processes because they can, for example, i) increase the total wettable surface area, 2) control the bubble nucleation dynamics at the surface (e.g. vapor bubble release rate and size), and iii) change the effective surface energy (i.e., the intrinsic driving mechanism for wetting the hot surface with a coolant). Here we present our studies on thermal transport at liquid interfaces, focusing on 1) our recent experimental data and corresponding numerical simulations of water microdroplets evaporating, wetting, and bouncing on micro- and nano-structured surfaces and 2) our time-domain thermoreflectance (TDTR) experiments for the interfacial thermal conductance (G) of evaporating water microdroplets on aluminum thin-films as a function of surface temperature.

Surface Science

Room: Picuris - Session SS-TuA

Chemical Dynamics at Surfaces

Moderator: I. Harrison, University of Virginia

2:00pm **SS-TuA1 Gently Lifting Gold's Herringbone Reconstruction by Tuning Adsorbate Chemistry**, *A.D. Jewell, E.C.H. Sykes*, Tufts University

Recently it was discovered that the structure of the molecule-metal interface in alkane thiol-based self-assembled monolayers (SAMs) is more complex than first believed. Thiols have been shown not only to lift the herringbone reconstruction of Au(111) but remove a significant fraction of the Au surface atoms. The etch pits formed by these vacancies are thought to be one of the weakest areas of the SAM films in terms of susceptibility to and degradation by oxidizing species.

In an effort to slightly weaken the molecule-metal interaction and prevent the formation of etch pits, we have chosen to study the interaction and assembly of trimethylphosphine (PMe₃) on Au(111) using a scanning tunneling microscope (STM). This is to our knowledge the first atomic-scale characterization of a phosphine species adsorbed on a metal surface.

At full monolayer coverage PMe₃, the molecules formed a hexagonally packed layer which exhibited a $(\sqrt{7} \times \sqrt{7})R19^\circ$ unit cell. The interaction between PMe₃ and Au caused Au atoms to be ejected from the herringbone reconstruction, but not the substrate surface itself (as in the thiol case) and led to the formation of small Au islands. This effect manifested in the herringbone spacing increasing from that of native gold (6.33 nm) to 11.2 ± 0.9 nm. As this system was exposed to various annealing treatments, a fraction of the molecules desorbed, the Au islands coalesced, and the herringbones disappeared entirely, indicating that the underlying Au surface adopted a 1×1 reconstruction. The data indicate that the PMe₃/Au island formation is a kinetically limited process.

Finally, we have developed a mathematical equation that gives the theoretical island coverage (q) as a function of the maximum island coverage (q_{max}), the native herringbone spacing (x_0) and the experimental herringbone spacing (x): $q = q_{\text{max}}(1 - x_0/x)$. This should be useful in future studies of many types of SAMs on Au(111), or any similarly reconstructed surface.

2:20pm **SS-TuA2 Tunneling and Guidance in the Diffusion of Polyatomic Molecules at a Metal Surface**, *Z.H. Cheng, E. Chu, D.Z. Sun, D.H. Kim, Y.M. Zhu, M. Luo, G. Pawin, K.L. Wong, K.-Y. Kwon, R. Carp, M. Marsella, L. Bartels*, University of California at Riverside

Pentacene derivatives that have two and four carbonyl groups attached to them diffuse on a Cu(111) surface in a uniaxial fashion, i.e. exclusively along a substrate atomic row, despite the threefold symmetry of the substrate. In this, they resemble the behavior of dithioanthracene and anthraquinone, previously dubbed "molecular walkers", which move across Cu(111) sequentially stepping the thiol/carbonyl linkers on each side of the molecule. This poses the question of how a fourfold substituted, i.e. quadrupedal, molecule can accomplish uniaxial motion: will it move its substrate linkers on opposite ends of the molecule at the same time resembling the gait of trotting, or will it instead move both linkers on one side at the same time, resembling the gait of pacing? Density functional theory (DFT) suggests the latter. Variable temperature scanning tunneling microscopy (STM) monitoring of the molecular motion reveals a striking difference between the diffusion prefactors of the quadrupedal and bipedal species, with the latter being very low. Wentzel Kramers Brillouin-based modeling of the motion of the substrate linkers in the calculated diffusion barriers suggest that the origin of this discrepancy lies in the relevance of the tunneling of the substrate linkers, allowing bipedal species, which only need to move one substrate linker at a time, to accomplish motion through tunneling of the linker, whereas quadrupedal species, whose diffusion requires concerted motion of two substrate linkers, cannot move in this way, resulting in significantly higher diffusion temperatures.

2:40pm **SS-TuA3 Scanning Tunneling/Atomic Force Microscopy of Individual Atoms/Molecules on Insulating Films**, *G. Meyer, L. Gross, F. Mohn, N. Moll*, IBM Zurich Research Laboratory, Switzerland, *P. Liljeroth*, Utrecht University, Netherlands, *J. Repp*, University Regensburg, Germany

INVITED

Ultrathin insulating films on metal substrates are unique systems to use the scanning tunneling / atomic force microscope to study the electronic and structural properties of single atoms and molecules, which are electronically

decoupled from the metallic substrate. Individual gold atoms on an ultrathin insulating sodium chloride film supported by a copper surface exhibit two different charge states, which are stabilized by the large ionic polarizability of the film [1]. The charge state and associated physical and chemical properties such as diffusion can be controlled by adding or removing a single electron to or from the adatom with a scanning tunneling microscope tip. The simple physical mechanism behind the charge bistability in this case suggests that this is a common phenomenon for adsorbates on polar insulating films. Employing a low temperature tuning fork AFM the different charge states can be observed directly in the force signal[2]. In the case of STM of molecules on ultrathin insulating films the electronic decoupling allows the direct imaging and manipulation of molecular orbitals [3]. As we have recently demonstrated detailed structural information can be attained by Atomic Force Microscopy which leads to the direct imaging of the molecular geometry. I.e. the complete chemical structure of single molecules can be accessed in scanning probe microscopy [4].

1. J. Repp, G. Meyer, F.E. Olsson, M. Persson, 'Controlling the Charge State of Individual Gold Adatoms', *Science* 305, 493 (2004)

2. L. Gross, F. Mohn, P. Liljeroth, J. Repp, F. J. Giessibl, G. Meyer, "Measuring the Charge State of an Adatom with Noncontact Atomic Force Microscopy" *Science*, 324, 1428-1431 (2009)

3. P. Liljeroth, J. Repp, G. Meyer, Current-Induced Hydrogen Tautomerization and Conductance Switching of Naphthalocyanine Molecules *Science*, 317, 1203-1206 (2007)

4. L. Gross, F. Mohn, N. Moll, P. Liljeroth, G. Meyer 'The Chemical Structure of a Molecule Resolved by Atomic Force Microscopy', *Science*, 325, 1110-1114 (2009)

4:00pm **SS-TuA7 STM Tip Induced Chemistry of Anthracene Derivatives on TiO₂(110)**, *D.V. Potapenko, R.M. Osgood*, Columbia University

Surface chemistry in photocatalysis is driven by the charge carriers that are created in the bulk of the catalyst and then are transferred to the adsorbed molecules. Both electrons and holes can be injected into molecules from the scanning tunneling microscope tip thus allowing mechanistic studies of photocatalytic processes on a single-molecule basis. We have studied adsorption and tip-induced surface chemistry of anthracene, as well as a number of anthracene derivatives on the TiO₂(110) surface. These molecules form ordered monolayers on the surface at room temperature with their structure dictated by the surface-charge distribution on TiO₂(110). Passing the electric current pulses from the STM tip into molecules causes dissociation and in some cases desorption of the molecules as indicated by the changes in the STM images. Halogenated organic molecules were especially susceptible to electron-induced dissociation with an energy threshold of ~ 2.5V. We report on the conditions of the tip-induced chemistry and propose a mechanism for the observed phenomena.

4:20pm **SS-TuA8 A New Mechanism of Atomic Manipulation: Bond-Selective Molecular Dissociation via Thermally Activated Electron Attachment**, *S. Sakulsermsuk, P.A. Sloan, R.E. Palmer*, University of Birmingham, UK

We report a new mechanism of (bond-selective) atomic manipulation in the scanning tunneling microscope (STM). We demonstrate a channel for one-electron induced C-Cl bond dissociation in chlorobenzene molecules chemisorbed on the Si(111)-7x7 surface, at room temperature and above, which is thermally activated. We find an Arrhenius thermal energy barrier to one-electron dissociation of 0.8 ± 0.2 eV, which we correlate explicitly with the barrier between chemisorbed and physisorbed precursor states of the molecule. Thermal excitation promotes the target molecule from a state where one-electron dissociation is suppressed to a transient state where efficient one-electron dissociation, analogous to the gas phase negative ion resonance process, occurs. We expect the mechanism will obtain in many surface systems, and not just in STM manipulation, but in photon and electron beam stimulated (selective) chemistry.

4:40pm **SS-TuA9 State-Resolved Molecular Beam Reflectivity Measurements of Methane Activation on Ni(111)**, *N. Chen, Y. Huang, V. Campbell, A. Utz*, Tufts University

State-resolved measurements of CH₄ reactivity on Ni(111) and Ni(100) have yielded detailed insights into how methane's vibrational energy promotes reactivity. To date, such measurements have relied on post-dose quantification of reaction products to measure reactivity as a function of methane's translational energy, internal vibrational and rotational state, and

surface temperature. Here, we describe a new detection scheme for measuring state-resolved reaction probabilities. This method uses a variation of the "King and Wells" molecular beam reflectivity method to improve reproducibility and significantly decrease the data acquisition time for state-resolved measurements. Rather than modulate the flux of molecules incident on the surface, we modulate laser excitation. In this way, the partial pressure change due to modulation reveals the difference in reactivity with and without laser excitation, which is the key quantity needed to obtain state resolved reaction probabilities. We demonstrate the method for methane incident on Ni(111) and show that it provides real-time coverage dependent reaction probabilities while decreasing data acquisition time and permitting a more expansive exploration of how energy and chemical identity influences reactivity at the gas-surface interface. We use this experimental method to extend our study of CH₄ activation to additional vibrational states, including the 2v₄ bend overtone, and different surfaces. Comparing the reactivity of these states provides insight into key features of energy flow during the reaction, and data to assess the generality of non-statistical behavior in gas-surface reactivity.

5:00pm **SS-TuA10 Dynamical Heterogeneity in Surface Reactions**, *A. Utz, D.R. Killelea, V. Campbell, N. Chen*, Tufts University

The rates and pathways of energy flow within the reagent-surface complex play central roles in determining whether or not a given molecule will react during its encounter with the surface. State-resolved experimental studies, in combination with dynamical calculations, are beginning to paint a detailed picture of these energy flow dynamics, particularly for the model system of methane's dissociative chemisorption on low-index Ni surfaces. Four key features of the reaction dynamics have emerged. First, the barrier to reaction can depend very sensitively on bond lengths and bond angles in the reaction complex; second, vibrational motions and their phase can modulate transition state access and the resulting energy threshold for reaction; third, such motion can be slow relative to the duration of the reagent-surface encounter; and fourth, the extent of vibrational energy flow and redistribution within the reaction complex can range from very limited to significant depending on the details for the reactive system.

We will present a conceptual framework for understanding and predicting general energy flow propensities for surface reactions. State-resolved experimental measurements, including prior examples of mode- and bond-selective surface chemistry and very recent results that explore the generality of these results for a broader range of chemical systems, will illustrate these principles. We will also include data that clearly show the ability of surface phonon excitation to modulate the energy threshold for reaction and that support recent theoretical predictions. The data point to a significant role for surface atom displacement in promoting methane activation under thermal conditions. Taken together, these studies show that the dynamical vibrational motion of reagent and substrate and the relative phase of these motions for a particular encounter can modulate the energy threshold for reaction and introduce significant energetic heterogeneity at the single molecule level.

5:20pm **SS-TuA11 Adsorbate Distribution and Dynamics inside Nanometer-Scale Metal Facets**, *J. Wyrick, Z.H. Cheng, M. Luo, D.Z. Sun, D.H. Kim, Y.M. Zhu, W.H. Lu*, University of California at Riverside, *K. Kim, T.L. Einstein*, University of Maryland, *L. Bartels*, University of California at Riverside

We use low temperature scanning tunneling microscopy to investigate the diffusion and arrangement of CO molecules adsorbed on Cu(111) facets of ~4 nm diameter formed by self-assembly of a honeycomb network of anthraquinone molecules. CO molecules and adlayers exhibit properties under such nanoscale confinement that markedly depart from those of extended adlayers: a) the confinement stabilizes dislocation lines (anti-phase domain boundaries) in the adlayer that affect roughly 1/4 of the adsorbed molecules; b) confinement prevents the formation of dense islands of adsorbed molecules, depending on coverage either causing dispersion of vacancies in the adlayer or preventing the growth of molecular islands; c) at a coverage of just a few molecules on the facet, we observe that a molecular shell structure is formed, resembling in its underlying mathematics the atomic model. Confined structures are an ideal test bed for measurement of the coverage dependence of molecular diffusion and in this study we find a reduction of the diffusion barrier at a slope of 57%/ML.

5:40pm **SS-TuA12 Ab Initio Calculations of the Preexponential Factor for the Diffusion of CO on Ag(001): The Importance of Inclusion of the Full Phonon Dispersion**, *M. Alcántara Ortigoza, T.S. Rahman*, University of Central Florida, *K.P. Bohnen, R. Heid*, Karlsruhe Institute of Technology, Germany

Knowledge of factors that determine the diffusivity of CO on catalytic surfaces is of utmost importance for understanding why some surfaces render higher reaction rates (e.g. CO oxidation) than others. A rigorous

calculation of the diffusion prefactor is not only the first approximation one should target to analyze diffusivity but also a prerequisite to adequately take into account dissipative anharmonic processes since calculation of both the prefactor and anharmonic processes rates require the full dispersion of all phonons in the system as input information. In this work, we obtain from first principles calculations the diffusion path of CO on Ag(001), the corresponding energy barrier, diffusion prefactors, and diffusion rate. The latter have been calculated via the total phonon density of states in the surface Brillouin zone from density functional perturbation theory calculations. Comparison of the results for the prefactors obtained using the full phonon dispersion curve with those confined only to the adsorbate modes on a frozen substrate point to significant differences and to the importance of having a knowledge of the full vibrational dynamics of the system, particularly at (low) temperatures which are relevant to experimental measurements.

Thin Film

Room: Ruidoso - Session TF-TuA

ALD/CVD: Surface Chemistry and Fundamentals

Moderator: S.M. Rossnagel, IBM Research

2:00pm **TF-TuA1 Studying Roll-to-Roll ALD Process Conditions Using a Moving Substrate Under a Gas Source Coating Head.** R. Fitzpatrick, Z.M. Gibbs, S.M. George, University of Colorado

Continuous roll-to-roll ALD processing is currently being developed for economical and efficient ALD on polymer and other flexible substrates. One of the key implementations of roll-to-roll ALD was introduced by Kodak (D. H. Levy et al., *Appl. Phys. Lett.* **92**, 192101(2008)). To understand the dependence of roll-to-roll ALD on process conditions, we have constructed a laboratory-scale apparatus featuring a fixed gas source coating head that sits in ambient above a moving substrate that is driven by a programmable stepper motor. The gas source coating head consists of a series of rectangular channels that spatially separate the ALD reactions. As the substrate moves under the gas source coating head, the channel sequence for each reactant is: precursor; exhaust; N₂ purge; and exhaust. The gas source head was built for 1.5 ALD cycles. Using Al₂O₃ ALD as a model system, the gas source head has the trimethylaluminum (TMA) channel sequence in the middle and the water channel sequence on each side of the TMA. This design allows for the deposition of two Al₂O₃ ALD cycles during one complete back-and-forth translation of the moving substrate. A low conductance gap between the precursor and exhaust channels allows for nearly "static" reactant exposures and prevents intermixing of the reactants. A higher conductance gap was machined into the gas source head between the exhaust and purge channels to create a "high flow" entrainment region that further isolates the precursor channels. The spacing between the gas source head and substrate is fixed and can be controlled with micron precision. This new apparatus can test how roll-to-roll ALD depends on the gap spacing, substrate speed, gas flow rates, and pressure difference between reactant and purge channels. An understanding of these process parameters will be necessary for the successful implementation of continuous, large scale roll-to-roll ALD.

2:20pm **TF-TuA2 Reactive Intermediates during Atomic Layer Deposition of Aluminum Oxide from Ozone and an Oxygen Plasma.** V.R. Rai, Colorado School of Mines, V. Vandalon, Eindhoven University of Technology, Netherlands, S. Agarwal, Colorado School of Mines

In this presentation, the authors will elucidate the surface reaction mechanisms during the atomic layer deposition (ALD) of aluminum oxide from trimethyl aluminum (TMA) in conjunction with O₃ and an O₂ plasma. The deposition mechanism was explored over a substrate temperature range of 70–200 °C using in situ attenuated total reflection Fourier transform infrared spectroscopy. Our IR data show that both –OH groups and carbonates are formed on the surface during the oxidation cycle. Gas-phase IR data indicate that oxidizer-assisted combustion of methyl ligands in chemisorbed TMA produces CO₂ and H₂O, which react simultaneously on the Al₂O₃ surface to produce carbonates. The origin of the –OH groups was attributed to the reaction of the uncombusted methyl ligands with gas-phase H₂O. While the type of surface sites are common to both oxidizing agents, in the case of O₂-plasma-assisted ALD, surface carbonates are simply reactive intermediates, which completely decompose upon prolonged plasma exposure. The ratio of carbonates to –OH groups is strongly dependent on the oxidizing agent, and its dose in case of plasma-assisted ALD. Surface reactions such as chemisorption of TMA, formation of –OH groups and Al₂O₃ were pseudo first order. On the other hand, the kinetic behavior of the carbonates suggests a series reaction of the type, A (CH₃) →

B (carbonates) → C (Al₂O₃). Although carbonate sites contribute to Al₂O₃ growth, their contribution was determined to be insignificant.

2:40pm **TF-TuA3 Synthesis of Micro/Mesoporous Alumina Fibers by Gas Phase Infiltration of Polyesters with Trimethyl Aluminum and Water.** B. Gong, Q. Peng, C. Devine, K. Lee, G.N. Parsons, North Carolina State University

Preparation of inorganic micro/mesoporous materials has attracted considerable attention because of their function in catalytic, separations, and other applications. Although many approaches are known to synthesize porous materials, methods to form mesoporous materials with pre-determined shape and morphology are not readily known. Sub-surface deposition, recently observed during atomic layer deposition (ALD) on polymer substrates, provides a potential method to transform polymers from fully organic solids into organic-inorganic hybrid and micro/mesoporous materials. Moreover, the transformation allows polymers with well defined micro and nano-structure, such as polymer fiber matrices, to maintain their shape and structure to form new replica materials. In this presented work, we apply this process to synthesis of Al-O/organic hybrid micro fibers by gas phase infiltration of tri-methyl aluminum and water alternatively into polyesters, such as polybutylene terephthalate (PBT). Through in-situ infrared analysis, we show that TMA acts as a strong Lewis acid and attacks the nucleophilic ester groups in polyesters to insert Al-O bonds into the polymer chains. The organic components are removed by post annealing to produce a micro/mesoporous alumina fiber. Surface area, pore volume, and pore size distribution of the porous alumina fibers were tested by nitrogen adsorption/desorption experiments, and surface areas exceeding 400 m²/g were obtained. SEM was used to track the morphology change along the process, and cross-section TEM images of annealed samples confirmed the formation of porous structures.

3:00pm **TF-TuA4 Growth Rate Control in ALD by Surface Functionalization: Alkyl Alcohols on Metal Oxides.** A. Yanguas-Gil, J.W. Elam, Argonne National Laboratory

In this work we explore the effect that alkyl alcohols (ROH) have on the saturation growth rate during the ALD of metal oxides. The traditional dosing sequence for metal oxide ALD is: M/O/M/O... where M is the metal precursor and O is the oxygen source. We find that by dosing organic molecules prior to dosing the metal precursor (e.g. ROH/M/O...) we can modify the surface chemistry and control the saturation growth rate. We will present results describing the effect of alkyl alcohols (R=Me, Et, iPr, and Bu) using H₂O as the oxygen source and the metal precursors Ti(iPr)₄ for TiO₂ ALD, TMA for Al₂O₃ ALD, and DEZ for ZnO ALD. Furthermore, we demonstrate this effect in the ALD of doped metal oxides.

Our results show that the ROH/M/H₂O sequence causes a substantial reduction in the growth per cycle for all of the ALD systems studied. For instance, the growth per cycle reduces from 0.31 to 0.06 Å/cycle in the case of TiO₂ ALD using MeOH/Ti(iPr)₄/H₂O, and from 1.2 to 0.4 Å/cycle in the case of Al₂O₃ ALD using MeOH/TMA/H₂O at 200°C.

Previous studies in the literature indicate that ROH reacts with basic sites on the metal oxide surface. Alcohol deprotonation followed by metal oxygen heterolytic bond formation leads to the formation of alkoxide functional groups bound to metal cations. To investigate this process, we performed *in situ* mass spectrometry and quartz crystal microbalance studies during the ROH/M/H₂O dosing sequence. We discovered that the ROH adsorbed on the surface desorbs intact as ROH during the subsequent water pulse, but no alcohol is released during the metal precursor pulse. Furthermore, the reduction of the growth rate per cycle is not affected by purge times, suggesting that the ROH molecules bond strongly to the metal oxide surface. Finally, no reduction in growth per cycle is observed using the dosing sequence: ROH/H₂O/TMA/H₂O. This finding suggests that the ROH and H₂O are able to displace one another, and signifies an almost complete elimination of the alkoxide groups during the water pulse. This observation agrees with the many reports of successful metal oxide ALD using metal alkoxide and water.

The ability to tune the saturation growth rate by modifying the surface chemistry can be of great utility for the ALD of doped materials where a homogenous distribution of dopants at a low concentration is desired.

4:00pm **TF-TuA7**, V.R. Anderson, A.S. Cavanagh, A.I. Abdulagatov, Z.M. Gibbs, S.M. George, University of Colorado

Most processes for TiO₂ atomic layer deposition (ALD) utilize water or other oxidants that can oxidize some substrates of interest. To avoid this oxidation, waterless or oxidant-free surface chemistry can be used that involves titanium halides and titanium alkoxides. This waterless surface chemistry approach for metal oxide ALD was originally proposed by the University of Helsinki group (M. Ritala et al., *Science* **288**, 319 (2000)). In this study, TiO₂ ALD was accomplished using titanium tetrachloride (TiCl₄) and titanium tetraisopropoxide (TTIP). In situ Fourier transform infrared

(FTIR) studies revealed that the mechanism for TiO₂ ALD using TiCl₄ and TTIP changed with temperature. At high temperatures between 250 and 300 °C, the isopropoxide species after TTIP exposures quickly underwent beta-hydride elimination to produce TiOH species on the surface. The observation of propene by quadrupole mass spectrometry confirmed the beta-hydride elimination reaction pathway. The TiCl₄ exposure then reacted with the TiOH species to deposit TiCl_x species on the surface. At low temperatures between 125 and 200 °C, the isopropoxide species remained after TTIP exposures to react with TiCl₄. However, this reaction was much less efficient than the reaction of TiCl₄ with TiOH species. Quartz crystal microbalance (QCM) studies were also used to monitor TiO₂ ALD at low and high temperatures. The QCM studies measured low TiO₂ growth rates of ~3 ng/cm² at a low temperature of 150°C. In contrast, much higher TiO₂ growth of ~15 ng/cm² were observed at a higher temperature of 250°C under similar reaction conditions. X-Ray reflectivity measurements determined that TiO₂ ALD using TiCl₄ and TTIP at 250°C produced a growth rate of 0.5-0.6 Å per cycle. X-Ray photoelectron studies also confirmed TiO₂ film growth with a chlorine contamination of less than 0.5 at%. This waterless TiO₂ ALD process using TiCl₄ and TTIP should be valuable for preventing substrate oxidation during TiO₂ ALD on oxygen-sensitive substrates such as cobalt.

4:20pm TF-TuA8 Growth Mechanism and Properties of Mg_xZn_(1-x)O Nanocomposites by Atomic Layer Deposition, Q. Peng, A.U. Mane, J.W. Elam, Argonne National Laboratory

Magnesium-zinc oxide (Mg_xZn_(1-x)O) ternary films are an interesting class of alloy materials in which the band gap can be tuned by adjusting the Mg doping concentration. Consequently, Mg_xZn_(1-x)O has been widely studied for application in the fields such as electronics, optics, photoelectronics, and solar cells. Mg_xZn_(1-x)O thin films have been fabricated through a variety of methods including chemical vapor deposition, physical vapor deposition, molecular beam deposition, and ALD. Although there have recently been a few reports describing ALD Mg_xZn_(1-x)O for application in photovoltaics, there has been no detailed study of the growth mechanism and properties of the ALD Mg_xZn_(1-x)O thin films.

In this work, the ALD Mg_xZn_(1-x)O was systematically explored with different doping concentration of Mg by using diethyl zinc (DEZ), bis-cyclopentadienyl-magnesium (Cp₂Mg) and H₂O as the precursors. The growth mechanism was investigated using quartz crystal microbalance and quadrupole mass spectrometry measurements. The growth rate of the Mg_xZn_(1-x)O alloy films was determined using spectroscopic ellipsometry. The crystal structures of the films before and after thermal treatment were analyzed using x-ray diffraction. In addition, the optical properties of the Mg_xZn_(1-x)O with different Mg concentrations were analyzed using UV-vis absorption spectroscopy and the electrical properties were evaluated using mercury probe current-voltage measurements. The thermal stability of the conductivity and structure of the Mg_xZn_(1-x)O films were studied as well. The system will be compared with Al doped ZnO system fabricated by ALD, to illustrate the conduction mechanism in doped ZnO synthesized by ALD process.

4:40pm TF-TuA9 Nucleation and Growth of Conformal and Ultrathin Pt Films on Al₂O₃ and W Substrates Using Plasma Enhanced ALD, L. Baker, A.S. Cavanaugh, D. Seghete, S.M. George, University of Colorado, A.J.M. Mackus, E.W.M.M. Kessels, Eindhoven University of Technology, Netherlands, Z.Y. Liu, F.T. Wagner, General Motors Research & Development

Pt ALD using thermal chemistry has nucleation difficulties and leads to the deposition of Pt nanoclusters. In contrast, Pt ALD using O₂ plasma nucleates much more readily and spectroscopic ellipsometry (SE) studies are consistent with continuous Pt films (H.C.M. Knoops et al., *Electrochem. Solid-State Lett.* 12, G34 (2009)). However, SE measurements alone were insufficient to characterize the early stages of the Pt ALD process. In this investigation, we have examined Pt ALD with MeCpPtMe₃ and O₂ plasma as the reactants using SE, X-ray reflectivity (XRR), X-ray photoelectron spectroscopy (XPS) and scanning electron microscopy (SEM) studies versus the number of ALD cycles. Analysis of the XRR and XPS results indicates that plasma Pt ALD on Al₂O₃ ALD substrates has a short nucleation delay. The nucleation delay is followed by a brief period of rapid Pt ALD film growth of 0.1 nm per cycle that is followed by a slower steady-state Pt ALD film growth of ~0.05 nm per cycle. During the Pt ALD nucleation and growth on the Al₂O₃ ALD substrate, SEM images show that the Pt film morphology evolves from isolated nanoclusters to worm-like nanostructures and finally to a conformal film at a Pt film thickness of approximately 7 nm. Nucleation and growth of Pt ALD on W ALD substrates led to very different results. In this case, a H₂ plasma was used instead of an O₂ plasma to prevent oxidation of the W ALD substrate. XRR and XPS studies revealed that Pt ALD with MeCpPtMe₃ and H₂ plasma as the reactants on W ALD substrates nucleated immediately and a continuous and conformal Pt ALD film was formed at a Pt ALD thickness of less than

5 nm. These results indicate that Pt ALD can be tuned to produce Pt nanoclusters or a continuous and conformal ultrathin Pt film using either thermal or plasma Pt ALD.

5:00pm TF-TuA10 Homogeneous Thermal Decomposition of Triethylaluminum: Effect of NH₃, J. Lee, T.J. Anderson, University of Florida

Thermal decomposition pathways of triethylaluminum ((C₂H₅)₃Al, TEAL) were investigated in a custom, up-flow, cold-wall CVD reactor. The extent of homogeneous decomposition of TEAL in N₂ as well as with added NH₃ was measured using *in situ* Raman spectroscopy measurement. The results of Density Functional Theory (DFT) calculations were used to assist in assignment of the observed Raman shifts to the decomposition products TEAL:NH₃, DEAlH, TEAL:NH₃, H₂N-AlH-NH-AlH₂, H₂Al-NH₂, MEAlH, MEAlH-AlH₂ and DEAl-AlH₂ as well as the estimating the rates of selected pathways. For the case of thermal decomposition of TEAL with N₂ carrier gas, the species H₂Al-NH₂ was observed. This is believed to result from the reaction of ammonia with the product of β-hydride elimination. This species is a possible reactant for AlN formation. Raman shifts of 600, 1989, 2025, 2580, 2835, 2849, 2900, 2918, 2939, and 3173 cm⁻¹ were recorded for TEAL in N₂, while shifts of 452, 1462, 1525, 1639, 2580, 2853, 2841, and 2849 cm⁻¹ were observed for a mixture of TEAL with ammonia in N₂. In addition, four vibrational bands (930, 965, 3230, and 3334 cm⁻¹) for ammonia were observed with high intensity. The temperature profile along the reactor centerline was measured and this was compared to the simulated results using a custom-FEM Galerkin method. DFT calculations using B3LYP/LanL2DZ level of theory were carried out to find the optimized geometry of each intermediate and transition structure and to calculate activation energy. This methodology, which uses the results from *in situ* Raman spectroscopy, DFT calculations, and FEM reactor modeling, is a powerful approach to understanding thermal decomposition mechanisms.

5:20pm TF-TuA11 Surface Reactions of TiCl₄ and Al(CH₃)₃ on GaAs(100), B. Granados, A.J. Muscat, University of Arizona

III-V materials have been considered as alternative channel materials for future high-speed low-power digital logic applications mainly because of their higher electron mobility compared to silicon. However, the integration of III-V materials into device structures faces multiple challenges due to the lack of a high quality native oxide and the high density of traps at metal-oxide interface, resulting in Fermi level pinning.

Most of the recent work on GaAs passivation has been done using atomic layer deposition (ALD) method. ALD offers precise control of film thickness, low processing temperatures, and excellent conformality. Additionally, a self-cleaning effect has been reported during Al₂O₃, HfO₂, and TiO₂ ALD on GaAs leading to the reduction or removal of GaAs oxides. Understanding the surface reactions involved in this self-cleaning effect is important in order to improve the GaAs-oxide interface, while depositing high-k dielectric films using ALD.

In this study, the ALD of trimethylaluminum (TMA, Al(CH₃)₃) and titanium tetrachloride (TiCl₄) on hydrofluoric acid (HF) treated GaAs (100) samples was conducted to investigate the similarities and differences in the surface chemistry of these precursors. After aqueous HF etching and air re-oxidation, the oxides were composed of As₂O₃ and Ga₂O. Annealing the sample desorbed volatile compounds such as As₂O₃ from the surface resulting in an As-rich (2.7:1, As:Ga ratio) surface. The precursors, TiCl₄ and TMA, reacted with As and Ga oxides and completely removing them from the surface. This is the first time that a TiCl₄ self-cleaning effect on GaAs is reported. TMA, as expected, produced a film of Al₂O₃ (2.3 monolayers thick) on top of the GaAs surface when the reaction was performed at 170°C.

In contrast to TMA, the oxygen and titanium levels remained below the XPS detection limits with TiCl₄ exposures in the temperature range from 170°C to 230°C, while a 0.03 monolayer-thick film was deposited at temperatures ranging from 89°C to 170°C. XPS results showed that in the higher temperature range, TiCl₄ reacted with the GaAs oxides on the surface producing only volatile compounds, leading to a clean, sharp GaAs surface. The proposed mechanism consists of two processes: TiO₂ formation on the surface and in-situ etching of these TiO₂ islands by chlorine atoms from breakdown of the precursor. This novel GaAs oxide cleaning method produced an oxygen-free surface, which has potential applications for GaAs integration in microelectronics and optoelectronics devices.

5:40pm TF-TuA12 Atomic Layer Deposition of Co-Al Films Studied by In-Situ Infrared Spectroscopy, J. Kwon, Y.J. Chabal, University of Texas at Dallas, J. Anthis, R. Kanjolia, SAFC Hitech

Cobalt-aluminum alloys are of great interest due to their unique properties such as corrosion resistance, high thermal stability, and unusual magnetic properties. In a search for appropriate precursors, we have investigated the growth of Co-Al thin films by atomic layer deposition (ALD) using

CCTBA (μ^2 - h^2 -('Buacetylene)dicobalthexacarbonyl) and DMAH (Dimethylaluminumhydride) on H-terminated Si(111) and on 2-nm TaN films. In-situ infrared absorbance spectra show that upon the first CCTBA pulse on H/Si(111), alkynes (CC triple bonds) bound to $\text{Co}_2(\text{CO})_6$ are converted to a benzene ring, as evidenced by the ring C=C stretching mode at 1475 and 1610 cm^{-1} . This transformation is not completely unexpected because cobalt carbonyl complexes ($\text{Co}_x(\text{CO})_y$) are used to catalyze cyclotrimerization reactions in organotransition-metal chemistry. IR spectra also show that the presence of hydrogen enhances the adsorption of carbonyl groups on the H/Si(111) surface. After the first CCTBA pulse which reacts almost completely with H-Si bonds (2083 cm^{-1}), the amount of adsorbed CO on the surface (1970 cm^{-1}) is found to decrease. The subsequent DMAH pulse is effective to remove the surface carbonyl groups, leaving Al-CH₃ and/or Al-H bonds on the surface. In contrast, the adsorption of carbonyl on a TaN surface where H is absent is negligible after the first CCTBA pulse.

In all cases, CH_x ligands are not removed during CCTBA or DMAH cycles, leading to accumulation of carbon species in the film. The growth of metallic Co-Al films is hindered due to Al-O bond formation during deposition. The source of oxygen is likely associated to a surface Fischer-Tropsch (FT) process. It appears that reaction of cobalt particles with hydrogen (originating from the DMAH precursor) generates water as a by-product through a FT-like process, thus forming Al-O bonds. This formation of Al-O bonds through a FT process is greatly suppressed (~50%) by annealing the sample to 300 °C in N₂ ambient before exposure to DMAH, which removes the carbonyl group from the surface and therefore the source of oxygen. Although the growth pattern is similar for both H/Si(111) and TaN substrates, a part of Ta atoms in the original TaN films are reduced to metallic Ta⁰ during growth, according to XPS Ta 4f core level spectrum after deposition of Co-Al(O_x) films.

Tuesday Afternoon Poster Sessions

Applied Surface Science

Room: Southwest Exhibit Hall - Session AS-TuP

Applied Surface Science Poster Session

AS-TuP1 Application of an Electrospray Technique to Secondary Ion Mass Spectrometry (SIMS), Y. Fujiwara, N. Saito, H. Nonaka, T. Nakanaga, S. Ichimura, National Institute of Advanced Industrial Science and Technology (AIST), Japan

An electrospray technique can generate a continuous stream of charged droplets at currents exceeding 1000 nA. We expect that it has a great potential in Secondary Ion Mass Spectrometry (SIMS). Consequently, we investigated beam generation characteristics using the electrospray technique operated at atmospheric pressure and under reduced pressure (i.e., vacuum).

When electro spraying is performed at atmospheric pressure or above, emitted charged droplets and ions are required to be sampled through an aperture into a vacuum chamber, and then accelerated toward a target. It was confirmed that a beam current was considerably reduced in the process passing through the aperture; for instance, passing efficiency through the 120-mm aperture was on the order of 10^{-3} . This loss mainly results from the spreading of electro sprayed ions at atmospheric pressure.

When electro spraying is done in a vacuum, freeze and evaporation of a solution will be a serious problem. In other words, in the case of frequently-used solutions such as water and ethanol, it is difficult to achieve stable electro spraying in a vacuum because of the freeze and evaporation around a capillary tip. To solve the problem, we have proposed a vacuum electro spray beam source using pure ionic liquids for SIMS application. Ionic liquids have very low vapor pressure as well as high ionic conductivity; its use will enable us to perform stable electro spraying in a vacuum. We investigated the electro spray characteristics of an ionic liquid in a high vacuum environment with pressures around 10^{-5} Pa using the stainless-steel capillary. The experimental results demonstrated that stable electro sprayed currents of the order of 1000 nA can be continuously generated in both positive and negative modes. Experimental results indicate that the electro spray technique seems to be applicable to SIMS.

AS-TuP2 Structure and Chemical Composition of Thiol-SAMs on Au Surfaces for Biological Applications, M. Bruns, S. Engin, V. Trouillet, D. Wedlich, Karlsruhe Institute of Technology, Germany, P. Br uner, T. Grehl, S. Kayser, ION-TOF GmbH, Germany, P. Mack, R.G. White, ThermoFisher Scientific, UK

Structured and oriented immobilization of bio-molecules has become subject of great interest in recent years due to the expected diversity of applications, e.g. bio sensors in diagnosis, lab-on-chip technology, and modern cell culture focused on cell adhesion, migration, and differentiation. Therefore, a lot of effort has been spent to develop strategies for covalent and non-covalent immobilization of proteins, respectively. A very promising approach is surface patterning by micro-contact printing (μ CP) to produce self-assembled-monolayers (SAMs) on gold surfaces based on mixtures of benzylguanine thiol (BGT) and matrix thiol. In this case BGT is the substrate for the SNAP-tag system, allowing for covalent attachment of any protein of interest fused to this tag, whereas the inert matrix thiol acts as spacer for BGT and moreover prevents from non-specific protein adsorption.

The present contribution focuses on the characterization of pure benzylguanine and matrix thiols as well as mixtures of both using a combination of complementary surface analytical methods. For this purpose all SAMs were prepared on gold films deposited onto glass substrates by r.f. magnetron sputtering directly prior to the thiol exposure. The chemical composition and the covalent binding of the thiols were proved by time-of-flight secondary ion mass spectrometry (ToFSIMS) and X-ray photoelectron spectroscopy (XPS) as well. The orientation of the SAMs together with thickness information were achieved by high-sensitive low-energy ion scattering (LEIS), and were justified by non-destructive depth profiles reconstructed from parallel angle-resolved XPS data applying a maximum entropy algorithm. Finally the μ CP micro-structures were verified by ToFSIMS.

S. Engin, V. Trouillet, C. M. Franz, A. Welle, M. Bruns, and D. Wedlich, *Benzylguanine Thiol Self-Assembled Monolayers for Immobilization of SNAP-tag Proteins on Microcontact Printed Surface Structures*, Langmuir, DOI: 10.1021/la904829y.

H. H. Brongersma, Th. Grehl, P. A. van Hal, N. C. W. Kuijpers, S. G. J. Mathijssen, E. R. Schofield, R. A.P. Smith, H. R.J. ter Veen, *High-*

sensitivity and high-resolution low-energy ion scattering, Vacuum 84 (2010) 1005-7.

AS-TuP3 Thickness and Composition of the HfO₂/Si Interface Layer As a Function of Aperture-Time of Oxidant-Agent for ALD-grown HfO₂ Nanofilms, P.G. Mani-Gonzalez, M.O. Vazquez-Lepe, A. Herrera-Gomez, CINVESTAV Queretaro, Mexico

Hafnium oxide nanofilms were grown with ALD (Atomic Layer Deposition) on H-terminated Si(001) wafers employing TDMA-Hf (tetrakis dimethyl amino hafnium) and water as precursors. The structure of the films was characterized with angle-resolved X-ray photoelectron spectroscopy (ARXPS). While the aperture-time for TDMA-Hf was kept constant at 0.08 s during the ALD deposition, the aperture-time (t_{H_2O}) for the oxidant-agent (H₂O) was varied from 0 to 0.1 s among the different samples. The water exposition-time has a direct effect on the thickness of the HfO₂ layer, which saturates at ~ 1.7 nm for 30-cycle ALD processes. The composition and thickness of the interface between Si and hafnia is approximately constant at Hf_{0.5}Si_{0.5}O₂ and 1 nm for $0.02 < t_{H_2O} < 0.06$ s. For larger aperture-times, the Hf contribution to the composition rises slowly; the thickness of the layer also rises slowly. The total film thickness, including the hafnium silicate and hafnium oxide layers, saturates at ~ 3 nm. Our results are in accordance with prior results, which estimate the film growth rate at ~ 1 Å per ALD cycle.

AS-TuP4 Defect States in Amorphous GaInZnO Thin Film Grown on SiO₂/Si Substrates, S. Heo, J.G. Chung, H.I. Lee, E.H. Lee, J.C. Lee, G.S. Park, Samsung Advanced Institute of Technology, Korea, J.S. Oh, H.Y. Cho, Dongguk University, Korea, D. Tahi, L.S. Son, S.K. Oh, H.J. Kang, Chungbuk National University, Korea, T. Nagatomi, Y. Takai, Osaka University, Japan

Transparent oxide conductor and semiconductor are useful for us to develop electronic components in various applications such as flat panel display and solar cells. In particular, amorphous Ga-In-Zn-O (a-GIZO) thin films are promising channel materials for thin film transistors (TFTs) because a-GIZO TFTs exhibit large field-effect mobility (>10 cm²/V s) irrespective of their fabrication on various substrates, such as silicon, glass, plastic, polyimide, polyethylene terephthalate (PET), cellulose paper and flexible substrates. In addition, they have superior uniformity, low processing temperature, possibility of large-area deposition and long term stability, and moreover they are cost effective.

In recent years, a large progress has been made in high performance TFTs based on a-GIZO as channel layers. Amorphous semiconductors have defect states originating from structural disorder and defect, which strongly affect carrier transport properties and devices performances. However, fundamental material properties of a-GIZO such as the band alignment and defect states, which are important for devices structure and circuit configuration have not been investigated in detail so far. Moreover, any investigation of band alignment and defect states of a-GIZO thin films is very important to understand the transport mechanism and to improve device performances.

In this study, we have investigated the band gap, valence band offset and defect states of GIZO thin films by using reflection electron energy loss spectroscopy (REELS), X-ray photoelectron spectroscopy (XPS), thermally stimulated exo-electron emission (TSEE) and photoinduced current transient spectroscopy (PICT). The band gap and valence band offset (VBO or ΔE_V) allow us to determine the conduction band offset (ΔE_C) by using the relation: $\Delta E_C = E_g(\text{SiO}_2) - \Delta E_V(\text{GIZO/SiO}_2/\text{Si}) - E_g(\text{a-GIZO})$. The band gap is 3.2eV, and the conduction band offset of GIZO is 3.62 eV. The shallow defect states obtained via PICT were at 0.24eV and 0.53eV below the conduction band minimum of a-GIZO thin film, and the deep defect state obtained by means of TSEE is 1.827eV below the conduction band minimum of GIZO thin film.

AS-TuP5 Band Alignment and Defect States in Amorphous Si-N Compounds on Si Substrates, H.I. Lee, Samsung Advanced Institute of Technology

Silicon nitride (SiN_x) has an important application in the photovoltaics. First, plasma SiN films have provided effective surface passivation of silicon solar cells. Secondly, SiN has an important application in electronic memory devices. The memory property of the amorphous silicon nitride (a-SiN_x) is due to its electronic structure dominated by many deep traps.

Electronic properties of a-Si₃N₄ are determined mainly by deep traps of electrons and holes as well as by hollow traps responsible for the spreading of charges captured by deep traps. In other words, they are responsible for the degradation of nonvolatile memory devices based on NMOS. Because of this, a correct knowledge about the nature of levels is extremely

important in selecting the technology for the preparation of layers intended for specific application.

In this study, in order to obtain band alignment as well as defect state of SiN_x thin films, we have investigated the band gap and valence band offset with the variation in the composition of N contents by using reflection electron energy loss spectroscopy (REELS) and X-ray photoelectron spectroscopy (XPS), respectively. The defect states were investigated by using thermally stimulated exo-electron emission (TSEE), which have been specially designed for in-situ measurement of a defect state in analysis chamber without any electrodes.

Our result shows that the valance band offsets were increased from 0.033 eV to 1.24 eV with increasing N contents. The band gap was changed from 3.2 eV to 4.7 eV for the above materials. The defect state energy of the a-SiN_x films were observed at 1.85 eV by using thermally stimulated exo-electron emission. This energy is related to hydrogen migration or a dangling bond ($\cdot\text{Si}\equiv$), called the K center, in the silicon nitride.[1] The values of deep trap energy below the conduction band are independent of N content.[2] The defect state energy are properly assigned.

AS-TuP6 X-ray Degradation of Oxygen Plasma Treated and Chemically Reduced Poly(propylene) Surfaces in Comparison to Conventional Polymers. *T. Gross*, BAM Federal Institute for Materials Research and Testing, *W.E.S. Unger, G. Kühn*, BAM Federal Institute for Materials Research and Testing, Germany

X-ray induced sample damage during mono XPS analysis of an oxygen plasma oxidized and subsequently wet-chemically reduced poly(propylene) film was investigated as a example for plasma modified or plasma deposited samples. By doing this the degradation index approach as introduced by Beamson and Briggs in the Scienta ESCA300 high resolution XPS data base of organic polymers has been adopted. As to be expected the sample degrades by loosing oxygen as revealed by observation of decreasing O/C and C-OR/Csum ratios. However, the X-ray degradation indices are definitely higher than those of conventional reference polymers. Moreover, the C-OR/Csum degradation index is significantly higher in comparison to this one obtained for the O/C ratio. In that context there is no difference between the plasma sample and a conventional poly(vinyl alcohol) polymer. It is concluded that for reliable quantitative surface chemical analysis the quality of spectra in terms of acquisition times must be optimized aimed to a minimization of X-ray degradation. Finally it is proposed to describe the photon flux of a X-ray gun in an XPS experiment, which defines the degradation rate at the end, by using the sample current simply measured with a carefully grounded sputter-cleaned reference silver sample.

AS-TuP7 Analysis of Friction and Wear Mechanisms on Hard Coatings Deposited by Reactive Magnetron Sputtering. *J.S. Restrepo*, Universidad Autonoma de México, *M.F. Cano, J.M. Gonzalez, A. Ruden, F. Sequeda*, Universidad del Valle, Colombia

AS-TuP8 Tribological and Mechanical Properties of Multilayer TiN/Cr_xN Coatings Deposited by Reactive Magnetron Sputtering. *F. Correa*, Universidad Autonoma de Occidente, Colombia, *M.F. Cano, J.M. Gonzalez, A. Ruden*, Universidad del Valle, Colombia, *J.S. Restrepo*, Universidad Autonoma de Mexico, *F. Sequeda*, Universidad del Valle, Colombia

AS-TuP9 Multi-scale Characterization Studies of Li-ion Batteries. *S. Nagpure, B. Bhushan, S. Babu, G. Rizzoni*, The Ohio State University

Advanced Li-ion batteries with high energy and power density are fast approaching compatibility with automotive demands. While the mechanism of the operation of these batteries is well understood the aging mechanisms are still under investigation. While aging at the macroscopic level is directly measurable by increase in the internal resistance, at material level that include cathode, anode, separator and electrolyte aging can be attributed to many degradation mechanisms. As, the degradation of the material is caused by several simultaneous physiochemical processes that occur within the batteries, material characterization in automotive application batteries is a challenging task. We have identified and tested a set of experimental techniques for multi-scale characterization of the cathode in the Li-ion batteries. The electrical properties are studied using the electrochemical impedance spectroscopy and scanning spreading resistance microscopy. The structural degradation is studied using the infrared thermal imaging (meters), scanning electron microscope (micro), X-ray diffraction (micro), atomic force microscope (micro to nano), transmission electron microscope (micro) and electron energy loss spectroscopy. Finally, a relatively new neutron depth profiling technique was successfully used in these studies to study the transport and concentration of lithium within the few microns of the cathode thickness. We present the results obtained from this set of experiments when applied to the samples extracted from an unaged and an aged LiFePO_4 based Li-ion battery.

AS-TuP10 Improved Tougaard Background Calculation using Predetermined Inelastic Electron Scattering Cross Section Functions K(T) using the Software UNIFIT 2011. *R. Hesse, R. Denecke*, Universität Leipzig, Germany

The shape of the background in x-ray photoemission spectra may be affected by secondary electrons and inelastic energy loss processes. A polynomial of low order has very often turned out to model the secondary electron background. The Tougaard background model [1] has been successfully used to characterise the inelastic loss processes. However, the correct usage of the Tougaard background needs a well defined K(T) function (T = energy loss). The introduction of a four parameter loss function $K(T) = BT/(C-C'T)^2+DT^2$ with the fitting parameters B, C, C' and D implemented in the fittable background function [2] allows the improved estimation of the K(T) function. The results will be compared with the recommended parameters by Tougaard. The calculation of inelastic electron scattering cross sections of clean surfaces from different materials using UNIFIT will be demonstrated.

[1] S. Tougaard, Surf. Interface Anal. 25 (1997) 137

[2] R. Hesse, T. Chassé, R. Szargan, Fresenius J. Anal. Chem., 365 (1999) 48

AS-TuP11 Comparative Study of Two Different Methods for Film Thickness Determination on Model and Real Systems using the Software UNIFIT 2010. *R. Hesse, P. Streubel, R. Denecke*, Universität Leipzig, Germany

The accuracy of thickness determination of laterally homogenous films by XPS in the range of few nm may be improved by combining two different methods. The results of the well established angle resolved photoelectron spectroscopy (ARXPS) for determining film thicknesses will be compared with the ones determined using the relative quantification of photoelectron lines at two different kinetic energies (i.e. energy-resolved) and the same emission angle (ERXPS). Only the substrate intensities were used. The advantages and disadvantages of both methods will be shown. The reliability and accuracy of the thickness determination by the two different methods is discussed for suitable model and real systems. The easy handling of the data analysis for estimating film thicknesses using UNIFIT will be demonstrated.

AS-TuP12 Non-destructive In-Depth Chemical Characterization of Air Exposed Plasma Polymers by Energy Resolved XPS. *P.-L. Girard-Lauriault, I. Retzko, S. Swaraj*, BAM Federal Institute for Materials Research and Testing, Germany, *N. Matsubayashi*, National Institute of Advanced Industrial Science and Technology (AIST), Japan, *T. Gross, W.E.S. Unger*, BAM Federal Institute for Materials Research and Testing, Germany

Plasma polymers can be deposited on a wide range of substrates in order to introduce a desired surface chemistry intended for a wide range of applications. For many of these, only the chemistry of the outermost surface layer is relevant and therefore, many works have favoured the use of surface-specific techniques such as X-ray photoelectron spectroscopy (XPS) or time of flight secondary ion mass spectrometry (ToF-SIMS), which have various sampling depth under the surface. Recently, a technique enabling XPS depth resolution by the modulation of the photoelectron attenuation length for non-destructive chemical depth profiling, known as energy-resolved XPS (ERXPS), has emerged. In the best case, the minimum attainable 95 % information depth value is about 22 % of its value under standard $\text{Al K}\alpha$ XPS conditions, thus permitting a better surface sensitivity than angle resolved XPS (ARXPS). ERXPS has also many other positive points that are thoroughly discussed.

In this study, plasma polymers containing oxygen and nitrogen based surface chemistries were prepared from allyl alcohol, allylamine and acrylic acid. Established selective chemical derivatisation procedures with trifluoroacetic anhydride (TFAA) and 4-trifluoromethyl benzaldehyde (TFBA), are used to determine alcohols and amines, respectively. All samples were analysed by energy resolved XPS (ERXPS). By analysing the high resolution spectra we demonstrate that slightly aged plasma polymers prepared from allyl alcohol and allylamine present a homogeneous in-depth chemistry in the range of XPS information depth (≈ 10 nm) while this was clearly not the case for their acrylic acid counterparts. Furthermore, it is shown that standard derivatisation reactions result in homogeneous changes of the chemistry in the above-mentioned information depth.

AS-TuP13 MVSA Analysis of 3D MCs⁺ ToF-SIMS Data. *V. Smentkowski*, GE Global Research Center, *M.R. Keenan*, Consultant

Depth profiling via ToF-SIMS is a well established technique that is used to determine the depth distribution of trace species in samples. 3D depth profiling techniques are now being heavily utilized in the ToF-SIMS community since it enables the measurement of both the depth distribution and the lateral distribution of the species. 3D ToF-SIMS analysis are

revealing that many samples are not uniform in the lateral dimension. Since a full mass spectrum is saved at every volume element, unexpected species are often found sub-surface, especially in real-world sample. Unfortunately, one often needs to perform two depth profile measurements in order to fully characterize a sample – a positive ion measurement to look for electropositive species with the highest sensitivity and a negative ion measurement in order to analyze electronegative species with the highest sensitivity. The two depth profile measurements are often performed using different erosion sources and experimental conditions which have been optimized for the species to be analyzed and often have significant differences in the erosion rate. Since the analysis are performed in two different regions of the sample, one can not correlate species observed in the two independent measurements. Additionally, there are instances where the amount of material is limited and one can not perform two measurements. MCs⁺ analysis have been reported in the ToF-SIMS literature. For MCs⁺ analysis one uses a Cs⁺ ion beam to erode the sample, and a Bi₃⁺ ion beam to perform the analysis in the positive ion polarity. Electropositive species are detected as M⁺ and/or M+Cs⁺ and the electronegative species are detected as M⁻ and/or M+Cs₂⁻ (where M is the element being analyzed). In this paper, we will demonstrate, for the first time, the ability to analyze complicated 3D MCs⁺ ToF-SIMS data sets using MVSA techniques. We will show the advantages of MVSA analysis over univariate analysis.

AS-TuP14 Metal Silicide Nanoscale Chemical Characterization with Scanning Auger Microscopy, D.F. Paul, J.S. Hammond, D.G. Watson, Physical Electronics

Scanning Auger Microscopy is a powerful compositional analysis technique for surfaces and nanostructures. It is well known that Auger instruments based on full CMA analyzers provide a stable imaging platform and analytical capability that can be successfully applied to a wide range of material systems. Recently a high energy resolution spectroscopy mode that provides enhanced chemical characterization was added to a CMA Auger instrument. This new functionality is integrated with the instrument while maintaining all the existing capabilities and benefits associated with the CMA based Auger instrument.

The usefulness of this new high energy resolution spectroscopy mode will be demonstrated with detailed chemical information from annealed metal silicide ultra thin films on silicon wafers. Low energy ion beam depth profiling facilitates a chemical state evaluation of the silicide/wafer interface induced by the annealing process. Auger mapping and high energy resolution Auger spectroscopy also characterizes the three dimensional nanostructures formed on the surface and at the interfaces of these metal silicide ultra thin films.

AS-TuP15 Influences Finish Quality in Machining Austempered Ductile Iron, W. Mattes, SENAI-SC, Brazil, A.C. Bottene, LOPF/NUMA, Brazil, R. da Silva, UNERJ, Brazil

The austempered cast iron (ADI - Austempered Ductile Iron), has been successfully applied in diesel trucks, class 8 trucks and agricultural tractors power train parts. This material has also been used in high performance gears, applied in various segments of the mechanical industry, especially in the automotive field because of their properties and technical advantages associated to the combination of strength and ductility of the material. The main technical limitation of the ADI is attributed to its machinability. This problem is related to the hardening that occurs by the transformation of austenite, characteristic of the microstructure of austempered ductile, which affects the steps of the production process and achieve common cropping the part before the heat treatment and finish machining right after them. This paper discusses a study on the behavior of the surface finish quality, technical and financial feasibility of the machining process. Comparing the use of grinding, CBN wheel, and the hard turning operation, cemented carbide coated TiAlCrN, of ADI by comparative analysis of lifetime of the tools in terms of speed of cutting, using as a criterion to end the life of the tool flank wear of 0.3 mm.

AS-TuP17 Tougaard Background Parameters - Simpler Than One Might Expect, P.J. Cumpson, Newcastle University, UK

Several methods of calculating - or subtracting - inelastic backgrounds from XPS spectra have been published over the years. Perhaps the most successful for practical XPS analysis has been the Tougaard background [1,2]. Tougaard proposed Universal Backgrounds that apply to most materials of analytical interest, yet are determined by only three or four parameters. In principle this allows the automatic removal of a large proportion of the inelastic background in many cases, but in practice there is often a problem in selecting appropriate Tougaard background parameters. These parameters do not have immediate physical interpretations, and it is often difficult to see which values are physically possible and which are not.

Therefore it seems difficult, for example, to include all four of these parameters in a fit to an experimental spectrum; the fit would be ill-conditioned and underdetermined. The problem is made worse by the necessarily narrow energy ranges of backgrounds available for background fitting in practical applications.

We show that there are significant relationships between the four parameters in the Tougaard model, and connect these with materials parameters. The result is a background that depends upon a single parameter that can be included in a least-squares fit to any practical multi-element spectrum.

[1]. S. Tougaard og I. Chorkendorff, Differential Inelastic-Electron Scattering Cross Sections from Experimental Reflection-Electron Energy-Loss Spectra: Application to Background Removal in Electron Spectroscopy. *Phys. Rev.* **B35**, 6570 (1987).

[2] S. Tougaard, Universality Classes of Inelastic Electron Scattering Cross Sections. *Surface Interface Analysis*, **Vol 25**, 137-155 (1997).

AS-TuP18 XPS Analysis of Surface Films Formed on Common Metals on Exposure to Ethanol-Blended Fuels, H.M. Meyer III, S.J. Pawel, Oak Ridge National Laboratory

Most automobile fuels contain some amount of ethanol, typically around 10% by volume, and fuels with higher ethanol levels are available. In Brazil mandated ethanol levels are 25% (E25 fuel) and in 2009 over 9 million vehicles were on the road using pure ethanol (E100) as fuel. Certainly, in the years ahead increasing levels of ethanol will be available in US fuels. As such, most automobile manufacturers are producing engines that can handle a variety of ethanol-blends. This poster examines several common metals used in fuel storage and fuel handling equipment, namely brass, galvanized steel, and nickel, and compares unexposed material to material that has been exposed to (1) reference gasoline and (2) E10 fuel and (3) E25 fuel. Samples were cleaned (acetone + ultrasonic), weighed, and placed in a stainless steel vessel. Fuel was added and the vessel was purged with Ar and sealed. After raising the temperature to 60 C, the samples were left for 28 days. Upon removal, the samples were rinsed with pure ethanol, dried, and weighed. X-ray photoelectron spectroscopy was used for determining surface composition. Sputter profiling was used to monitor changes in composition as a function of depth. For some samples, XPS mapping was employed to determine lateral distribution of chemical species. Results presented in this poster clearly show greater oxidation and the formation of metal sulfide species for the ethanol-blended fuels as compared to the reference gasoline. Increasing the ethanol content above E10 to E17 showed an increase in the extent of oxidation and formation of metal sulfides.

AS-TuP19 Sputtering of Lunar Regolith Simulant by Singly and Multicharged Constituents of the Solar Wind, F.W. Meyer, P.R. Harris, H.M. Meyer III, Oak Ridge National Laboratory, N. Barghouty, J.H. Adams, Jr., Marshall Space Flight Center NASA

We report preliminary results on sputtering of a lunar regolith simulant sample by H⁺, Ar⁺, Ar⁶⁺ and Ar⁹⁺ at solar wind-relevant energies. Such interactions are an important determinant of lunar exosphere composition, and may provide a possible pathway leading to the production of water on the moon. The presence of lunar water was recently confirmed by a number of orbiting lunar missions. The ions are generated using an electron cyclotron resonance (ECR) ion source at source potentials between 10-15kV. After being extracted, transported, and decelerated, the ions are normally incident on a pressed lunar regolith simulant sample that is situated within a floating UHV scattering chamber. The relative bias between the ECR source and the surface end station was adjusted to produce a constant impact energy of 0.375keV/amu for each of the 4 ion beams investigated. To simulate the effect of the dominant proton component, which constitutes >90% of the solar wind, the lunar regolith simulant sample was prepared by exposure to a proton beam up to total fluences of ~2x10¹⁸ H⁺/cm² prior to each of the Ar beam sputtering runs. Both transient and steady state conditions of sputtered species were monitored by a quadrupole mass spectrometer situated within the UHV scattering chamber. SEM and XPS analyses of the JSC-1A AGGL simulant were performed to monitor possible changes in surface morphology and composition during the pressing of the loose powder into the sample holder.

AS-TuP20 Chemical Depth Profiling: Relating Interfacial and Sub-surface Characterization to Electrical Performance, K.G. Lloyd, L. Zhang, J.P. Wyre, J.R. Marsh, M.A. Plummer, DuPont Corporate Center for Analytical Sciences

Thin multi-layered structures form the basis for photovoltaic/solar cells, OLED displays, and many other electronic devices. Electrical performance can be influenced by the thickness of these layers, the widths of interfaces between layers and/or development of interfacial chemistry, and the extent and location of dopants within layers. Depth profiling, i.e., obtaining chemical information as a function of depth, can provide this information,

especially for systems where cross-sectioning is not an option, species of interest are present below 1%, or sampling with better than 1 micron depth resolution is required.

ToF-SIMS (Time-of-Flight Secondary Ion Mass Spectrometry) and X-ray Photoelectron Spectroscopy (XPS, a.k.a. ESCA) are typically used in conjunction with a high-current ion sputter beam to analyze the outermost surfaces as they are freshly revealed. ToF-SIMS depth profiling offers high mass resolution, spatially-resolved chemical information, and the collection of the entire mass spectrum at each depth interval. The combination of ToF-SIMS depth profiling and multivariate methods of data analysis allows better definition and characterization of interfacial regions between layers.

Examples include characterization of the BSF (back surface field) layer on solar cell backsides, monitoring layered oxide growth on annealed stainless steels, and study of interdiffusion in organic electronic layered structures.

AS-TuP21 In-situ XPS Analysis of Co and Co²⁺ during Steam Reforming of Ethanol on Supported Cobalt Catalysts, A. Karim, Y. Su, M.H. Engelhard, D. King, Y. Wang, Pacific Northwest National Laboratory

In catalysis, the oxidation state of metal nanoparticles on the surface is often unknown, especially under oxidizing conditions. The redox properties of the catalyst are typically investigated by temperature programmed reduction and oxidation or x-ray absorption spectroscopy. However, these are not the surface sensitive techniques and provide limited surface details especially under H₂/H₂O environments. We report the use of in-situ x-ray photoelectron spectroscopy (XPS) to determine the oxidation state of Co following exposure to O₂, H₂, and H₂/H₂O. We found that the type of support and catalyst pretreatment (calcinations and/or reduction temperature) have a strong effect on the Co⁰/Co²⁺ ratio. Our results indicate that Zn helps stabilize Co against oxidation by O₂ or H₂O. The in-situ XPS measurements allowed us to study the effect of Co⁰/Co²⁺ ratio on the catalytic activity and understand the role of Co²⁺ in the ethanol reforming reaction pathways. The catalytic tests show that both Co⁰ and Co²⁺ were active in the C-C bond cleavage and water gas shift reactions. However, Co⁰ is shown to be much more active than Co²⁺. Also, the reaction pathways for CO₂ and CH₄ formation appear to be different on Co⁰ and Co²⁺. Catalysts with higher Co⁰/Co²⁺ surface ratio exhibited lower selectivity to CH₄. Our results show that ethanol decomposition and CO methanation are more favored on Co²⁺ relative to Co⁰. In addition, we show that on both Co⁰ and Co²⁺, CO₂ is a secondary product forming by the water gas shift reaction.

AS-TuP22 Surface Characterization of Al-Si-Fe-X (X = none, Sb, V) Rapidly Solidified Ribbons, V.N. Gaidarova, Bulgarian Academy of Sciences, Bulgaria, Y.T. Yordanov, Sofia Technical University, Bulgaria

Al-Si alloys are used in the automotive industry. Improvement of their properties is achieved by rapid solidification (RS) [1]. Highly developed surface of RS material is of importance in both interaction with the environment and processing of materials during ingots production. Surface formation and development under thermal treatment depends on the alloying and modifying elements.

Al-Si under-eutectic alloys with addition of Fe, Sb, V in different combinations are produced by RS using Planar Flow Casting technique. As-cast and thermally treated samples are studied using Auger Electron Spectroscopy (AES) combined with argon ion sputtering.

AES depth profiles of as-cast specimens demonstrate formation of nanoscale aluminum based oxide, enriched layer (EL) with solute elements and a region of constant Al/Si content following in depth. Annealing up to moderate temperatures (≤ 638K) causes changes in thickness of both oxide scale and EL. Availability of Fe (≤ 2wt.%) promotes diffusion of solute elements in oxide and EL while addition of Sb, even in a minor quantity 0.17 wt.%, to the last alloy content decreases Si-segregation. Changes are not detected in the oxide or EL of (Fe+V) doped RS ribbons. Annealing up to temperatures ≥ 673K leads to ceasing of oxidation and diminishing of silicon enrichment for all studied Fe-containing RS alloys. These remarkable changes of elements distribution can be connected with crystallization of Fe-containing phase at oxide/bulk interface and growth of silicon precipitations. Registered solute enrichment is in agreement with the segregation prediction [2], which is based on the phase diagrams of alloys. Comparison with micro hardness measurements on the surface of the ribbon samples shows proportional dependence on the uniform distribution of the fine silicon precipitations. With their growth the micro hardness declines, excluding for the RS alloy doped with Fe+V. In the last case dopants content does not allow iron segregation at the surface, which evidently leads to hardening by finely dispersed Fe-containing particles in the Al-matrix under.

Investigation is sponsored by the National Science Fund (Bulgaria), Grant DO 02-93/2009. We are thankful for the use of Frederick Seitz Mat. Res. Lab. Central Facilities, University of Illinois.

References:

- [1]. E. Lavernia, J. Ayers, T.S. Srivatsan, *Int. Materials Rev.* 37(1992)1.
- [2] J.J. Burton, E.S. Machlin, *Phys. Rev. Lett.*, 37(1976)1433.

AS-TuP23 Characterization of a Self-assembled Molecular Nanolayer at Buried Cu-silica Interface, S. Garg, R. Teki, A. Jain, K. Chinnathambi, B. Singh, Rensselaer Polytechnic Institute, V. Smentkowski, GE Global Research Center, M. Lane, Emory and Henry College, G. Ramanath, Rensselaer Polytechnic Institute

Integration of metal-dielectric interfaces using molecular nanolayers (MNLs) is attractive for prospective applications such as laminates in high frequency electronics and packaging, nanodevice wiring and composites. Recent works have shown that annealing-induced siloxane bridging can toughen organosilane-functionalized copper-silica interfaces. While strong bonding of the MNL with the under- and over-layers is essential for promoting adhesion, the nature of the MNL structure and bonding, especially at temperatures where the MNLs are known to degrade on bare surfaces, are unclear. But tracking atomic-level intermixing and interfacial phase formation in a sub-nm-layer is an exacting challenge due to difficulties in distinguishing Si atoms in the organosilane MNL from Si atoms in the silica substrate, and obtaining sufficient contrast by electron microscopy. Here, we study organogermane-tailored interfaces using a combination of electron spectroscopy and microscopy, and density functional theory calculations to obtain insights into the interface chemical changes. Our results reveal that annealing decomposes the organic monolayer into an inorganic Cu-O-Si network, leading to interface toughening.

We assembled Benzyl-trichlorogermane (BTCG) on silica to form a 0.7-nm-thick nanolayer. Four-point bending fracture tests on as-prepared Cu/BTCG/SiO₂ sandwiches revealed a low interface toughness of 2.1 J/m², comparable to pristine Cu/SiO₂ structures. However, interfacial toughness increased monotonically with annealing temperature, yielding values as high as 23.3 J/m² for T_{anneal} = 500 °C. Core-level spectra from silica fracture surfaces show a strong Ge signature for T_{anneal} ≤ 300 °C that becomes undetectable for T_{anneal} ≥ 400 °C, suggesting Ge transport and destruction of the organic MNL. This result is corroborated by time-of-flight secondary ion mass spectroscopy (SIMS) profiles showing the smearing of the interfacial Ge spike into the silica layer upon annealing. Incorporation of Ge in the silica weakens the Si-O-Si network, leading to intermixing of Si, O and Cu, forming nanoscale islands of rhombohedral CuSiO₃ observable by cross-sectional transmission electron microscopy and X-ray spectroscopy. For pristine Cu/SiO₂ structures there were no changes at the interface and the toughness value was ~ 3 J/m² for T_{anneal} ≤ 700 °C. Our findings suggest that molecular degradation of the organic MNL to form nanoscopic layer of inorganic metal-oxide-silicon bonds could be an attractive approach for toughening interfaces.

AS-TuP24 Experiences with the High Energy Resolution Optics (HERO) Update on a Physical Electronics 690 Auger System, W. Wallace, J.A. Ohlhausen, M.T. Brumbach, Sandia National Laboratories

We will present our experiences with the new High Energy Resolution Optics (HERO) upgrade on a Physical Electronics Auger 690 system. This upgrade allows the single pass cylindrical analyzer in the Auger system to achieve higher energy resolution than in the standard mode. With this upgrade, it should be possible to separate chemical states for certain elements. Also, it should be possible to separate closely spaced peaks from selected elements that have been difficult or impossible to separate without the upgrade. Specifically, we will investigate practical use of this upgrade in the analysis of materials systems where overlapping peaks have historically been an issue, such as Kovar, which consists of the elements Ni, Fe and Co. Strategies for the successful use of the technique as well as its current limitations will be shown.

[§]Sandia National Laboratories is a multi-program laboratory operated by Sandia Corporation, a wholly owned subsidiary of Lockheed Martin Company, for the U.S. Department of Energy's National Nuclear Security Administration under contract DE-AC04-94AL85000.

AS-TuP25 A Device for Traceable Force Probe Calibration, J.F. Portoles, P.J. Cumpson, Newcastle University, UK

AFM has become in the last two decades an instrument for the measurement of forces in the piconewton range, including forces at the single molecule level. Although many methods have been developed for the force calibration of AFM cantilevers [1], these use to be affected by high uncertainties and sometimes difficulty of use. Furthermore there is a growing need for a traceable force calibration standard that provides traceability to the units of the SI [2] and therefore allows comparison between instruments and with related force measurement techniques such as the Optical Tweezers and the Biomembrane Force Probe. We present the development of a device that provides fast and easy force calibration of

AFM cantilevers and other force probes, simultaneously facilitating the dissemination of force and providing traceability to the units of the SI.

[1] J.L. Hutter and J. Bechhoefer, *Rev. Sci. Instrum.* 64 (7) 1993, pp. 1868-1873

[2] P.J. Cumpson and J. Hedley, *Nanotechnology* 14 (12) 2003, pp. 1279-1288

AS-TuP26 Synthesis and Characterization of System Sr(Ru_{1-x}Fe_x)O₃ type Perovskite. L. Huerta, J.L. Mazariago, M. Quintana, Universidad Autónoma de México, E. Ramirez, Universidad Autónoma de la Ciudad de México, M. Flores, Universidad de Guadalajara, México, R. Escamilla, Universidad Nacional Autónoma de México

Polycrystalline samples of the SrRu_{1-x}Fe_xO₃ system with x = 0, 0.25, 0.5, 0.75 and 1.0, were synthesized by solid state reaction of stoichiometric quantities of oxides of RuO₂, Fe₂O₃ and SrCO₃. The samples were characterized by X-ray diffraction (XRD), x-ray photoelectron spectroscopy (XPS) and ac magnetization vs. temperature measurements. XRD results shown that the lattice parameter decreases with the iron content; as a consequence the unit cell volume decreases. The Sr 3d, Ru 3d Fe 3d and O 1s spectral lines associated to the chemical states of Sr(Ru_{1-x}Fe_x)O₃ were identified by XPS. Curves of ac magnetization vs. temperature shown for x ≥ 0.25 a behavior spin glass.

AS-TuP27 Surface Energy, Topography & Composition of SiOx on Polycarbonate by Proton-Induced X-ray Emission (PIXE), Atomic Force Microscopy & Sessile Drop Contact Angle Analysis using Young-Dupre Equation. Q.B. Xing, Arizona State University, C.F. Watson, SiO2 Associates, LLC, M.A. Hart, D.A. Sell, J.D. Bradley, R.J. Culbertson, A.S. Benitez-Brady, Arizona State University, B.J. Wilkens, LeRoy Eyring Center for Solid State Science at Arizona State University, N. Herbots, Arizona State University

The surface energy of silica is correlated with topography and composition in micron thick films on polycarbonate visors for football, hockey, ski and scuba diving.

Use of visors can be limited by condensation that occurs in during athletic performance. Control of the hydro-affinity of the surface requires an understanding of hydrophobic/hydrophilic behavior as well as of condensation kinetics and surface contamination for up to several continuous hours

Combining Proton-Induced X-ray Emission (PIXE), Tapping Mode Atomic Force Microscopy (TMAFM) & the Sessile Drop Method with Contact Angle Analysis (CAA) using Young-Dupre Equation, yields insights into nucleation and ripening of water droplets. Real-time observation via optical microscopy of both reflected and transmitted light, PIXE, TMAFM and CAA with previous Rutherford Backscattering Spectrometry (RBS) results ca establish a model to predict surface energy and hydro-affinity of silicates, phospho-silicates and other compounds used for high impact resistance vision wear coatings. Ultimately, the goal is to control condensation on such coated polymers for applications in sport eyewear used in hockey, skiing, football and other contact sports, swimming goggles, and diving masks.

Surface characterization techniques in this research combine the 4.265 ± 0.035 MeV 12C(alpha, alpha)12C and the 3.05 ± 0.005 MeV 16O(alpha, alpha)16O MeV Oxygen Nuclear Resonance to increase light atoms detection with 2.8 MeV Hydrogen Elastic Recoil Detection for compositional analysis with depth profiling, and Tapping Mode Atomic Force Microscopy for surface topography. The water affinity of the solid surface is measured via contact angle analysis using the Sessile Drop method calibrated with standards such as OH(1x1)Si(100), 100 nm thermal oxides on Si(100), Si(100) amorphized by high dose Si ion implantation at 35-175 keV, alpha-quartz crystals, and the Young-Dupre equation to compute surface energy. The surface energy is then correlated with statistical analysis of Tapping Mode Atomic Force Microscopy topographs and PIXE/RBS analysis to predict and determine the mechanism and kinetics of water condensation. Polymer adsorption on these surfaces is used to alter the surface hydroaffinity and maintain clarity when condensation occurs by making it hydrophilic [1].

[1] US Patent pending "Molecular films for controlling hydrophobic, hydrophilic, optical, condensation and geometric properties of Si-based surfaces. Inventor(s): N. Herbots, J. D. Bradley, M. A. Hart, D. A. Sell, S. D. Whaley, Q. Bradley (filed: November 9, 2009)

AS-TuP28 An Investigation of Primary Ion Choices in Depth Profiling Using Time-of-Flight Secondary Ion Mass Spectrometry. Z.H. Zhu, V. Shuththanandan, Pacific Northwest National Laboratory

Depth profiling is one of the important applications of time-of-flight secondary ion mass spectrometry (ToF-SIMS). Dual beam depth profiling strategy is commonly used because the current of the primary ion beam is normally very weak (~10⁻¹² A), and the second beam with high current (10⁻⁸-10⁻⁶ A) is introduced for sputtering. Recent years, a major development in ToF-SIMS field is application of cluster primary ions. It has been found that cluster primary ions can dramatically enhance signal intensity of molecular ions with a factor of 10-1000. So far, cluster primary ions have been introduced into commercial ToF-SIMS instruments for over five years. However, in presently available commercial ToF-SIMS instruments, the usable currents of cluster primary ion beams are considerably smaller than that of monatomic primary ion beams. More importantly, enhancements using cluster primary ions are not only material-dependent but also ion species-dependent. Therefore, large amounts of experimental data are needed to develop an understanding of how to choose an optimal primary ion for ToF-SIMS depth profiling.

In this work, we studied depth profiling of several representative systems: (1) Hydrogen depth profiling in silicon wafer, zinc oxide crystal and normal glass; (2) molecular depth profiling of a thin sucrose film on silicon substrate; (3) molecular depth profiling of Irganox "delta" layers prepared by NPL, United Kingdom. Six primary ion beams (25 keV Bi⁺, Bi₃⁺, Bi₅⁺, 50 keV Bi₃⁺⁺, 10 keV C₆₀⁺ and 20 keV C₆₀⁺⁺) were compared. Our data show that enhancement of cluster primary ions for elemental species is limited (~1.5-4.0 times) if compared to that for molecular species (>>10 times). Considering the highest usable currents of difference primary ion species on presently available commercial ToF-SIMS instruments, we suggest that monatomic primary ion beams may be the best choice for elemental depth profiling, and cluster primary ion beams are better choices for molecular depth profiling.

In this work, we studied depth profiling of several representative systems: (1) Hydrogen depth profiling in silicon wafer, zinc oxide crystal and normal glass; (2) molecular depth profiling of a thin sucrose film on silicon substrate; (3) molecular depth profiling of Irganox "delta" layers prepared by NPL, United Kingdom. Six primary ion beams (25 keV Bi⁺, Bi₃⁺, Bi₅⁺, 50 keV Bi₃⁺⁺, 10 keV C₆₀⁺ and 20 keV C₆₀⁺⁺) were compared. Our data show that enhancement of cluster primary ions for elemental species is limited (~1.5-4.0 times) if compared to that for molecular species (>>10 times). Considering the highest usable currents of difference primary ion species on presently available commercial ToF-SIMS instruments, we suggest that monatomic primary ion beams may be the best choice for elemental depth profiling, and cluster primary ion beams are better choices for molecular depth profiling.

Electronic Materials and Processing

Room: Southwest Exhibit Hall - Session EM-TuP

Electronic Materials and Processing Poster Session

EM-TuP1 Indium Nitride Epilayer Prepared by UHV- Plasma-Assisted Metalorganic Molecule Beam Epitaxy. W.-C. Chen, National Applied Research Laboratories, Taiwan, S.-Y. Kuo, Chang Gung University, Taiwan, F.-I. Lai, H.-Y. Wang, W.-T. Lin, Yuan-Ze University, Taiwan, C.N. Hsiao, National Applied Research Laboratories, Taiwan

Indium nitride films grown at various growth temperatures were prepared on GaN buffer layer using self-designed plasma-assisted metal-organic molecule beam epitaxy. The influence of substrate temperature on film crystal structure, surface morphology, optical and electrical properties is studied using x-ray diffraction (XRD), field emission scanning electron microscopy (FE-SEM), transmission electron microscopy (TEM), X-ray diffraction, Hall effect, and photoluminescence (PL) measurements. The results show that all InN films grown on the GaN template have good quality and the full width at half maximum is around 1000 arcsec. At 500°C, the optical measurements on the films revealed a luminescence feature in the vicinity of 0.7 eV. Also, TEM images of the films exhibit better structural properties indicated by a sharper InN/GaN interface. SEM images determine the growth rate of about 14 nm/min. These results indicate that the optoelectronic properties and crystalline quality can be improved significantly by increasing the growth temperature.

EM-TuP2 The Relationship between Surface Termination and Crystal Structure for HPCVD-grown InN Layers. A.R. Acharya, M. Buegler, S. Gamage, Georgia State University, J.S. Tweedie, R. Collazo, North Carolina State University, N. Dietz, B.D. Thoms, Georgia State University

The surface structure and termination of semiconductor thin films are important factors during epitaxial growth and may affect the interfacial properties of devices. The structure and surface bonding configuration of indium nitride layers grown by high pressure chemical vapor deposition (HPCVD) have been studied using high resolution electron energy loss spectroscopy (HREELS) and X-ray diffraction (XRD). HREELS analysis of InN layers suggests that the surface is primarily terminated with NH₂ species. This result is consistent with XRD, which shows the co-existence of different surface orientations. The observed termination by NH₂ is in contrast to previous HREELS work on HPCVD-grown InN layers, which showed only NH species on the nitrogen-terminated surface.

EM-TuP3 Rapid Thermal Ex-Situ Activation and Effect on Contacts to p-type GaN. J.H. Melby, L. Huang, R.F. Davis, L.M. Porter, Carnegie Mellon University

The difficulty of achieving ohmic contacts to p-type GaN is associated with the inherent difficulties involved in acceptor doping with Mg. Poor doping efficiency results in high contact resistance and high semiconductor sheet resistance. In GaN based devices, these issues lead to parasitic voltage drops and associated Joule heating. When grown via CVD methods a significant amount of Mg forms a complex with hydrogen. This complex

prevents Mg from participating in active doping. The challenge is to achieve large concentrations of free Mg in the films. In-situ post-growth annealing has been found to enhance p-type conductivity, but there is a large disparity in activated Mg acceptors versus incorporated Mg atoms. Furthermore, we know of no reports in the literature regarding optimization of the annealing conditions. In this study we have conducted I-V, C-V, Hall, and contact resistance measurements of Ni/Au contacts on Mg-doped GaN films grown on AlN/SiC (0001) substrates as a function of annealing temperature and time, and nitrogen or oxygen concentration for in-situ and ex-situ anneals. We found that in-situ cooling in nitrogen after growth is important for initial activation of Mg dopants; however, additional in-situ annealing in nitrogen after growth had little effect on the electrical properties. We also found that the electrical characteristics are particularly sensitive to the presence of oxygen and temperature during ex-situ annealing; > 200% improvements in hole concentration were observed for annealing in 1:1 N₂:O₂ at 800°C. The electrical data will be correlated with SIMS data of the hydrogen concentration as a function of annealing conditions.

EM-TuP4 Investigation of Crystal Structure and Optical Properties of Cd_{1-x}Mn_xS Epilayers, D.J. Kim, Y.D. Choi, Mokwon University, Republic of Korea, *J.W. Lee,* Hanbat University, Republic of Korea

EM-TuP5 Photovoltaic Characteristics of Sputtering-Deposited CdTe Thin Film Solar Cell by Hydrogen Doping Treatment, C.-H. Lim, S.-H. Ryu, J.-S. Park, Chosun University, Republic of Korea, *N.-H. Kim,* Chonnam National University, Republic of Korea, *G.-B. Cho, W.-S. Lee,* Chosun University, Republic of Korea

CdTe thin film has the near ideal band gap energy of 1.45 eV for the achievement of the theoretical maximum photovoltaic conversion efficiency of 31%. CdTe thin film also has a high optical absorption coefficient of over 99% of the incident sunlight with only about 2 μm of active thickness. However, the highest conversion efficiency of 16.5% was recorded in the CdTe/CdS heterostructured thin film solar cell. Therefore, the investigations would be strongly required to improve the conversion efficiency with the sufficiently absorbed light. In this study, hydrogen doping treatment was performed with the various hydrogen gas levels and doping temperature in the vacuum desiccator at the fixed doping time in order to improve the efficiency of CdTe/CdS heterostructured cell because the hydrogen affects the electrical properties of CdTe through the fast diffusion of the interstitial hydrogen. The effects of hydrogen doping treatment on the electrical and optical properties of CdTe thin film were investigated by UV-Visible spectrophotometer and Hall effect measurement. The role of hydrogen was examined by some analytical methods including photoluminescence (PL) spectra. The improved cell parameters of CdTe/CdS thin film solar cell were successfully obtained at the optimum condition including short-circuit current density (*J_{sc}*), open-circuit voltage (*V_{oc}*), fill factor (FF), and efficiency. Acknowledgement: This work was supported by National Research Foundation of Korea(NRF) grant funded by the Korean Government(MEST) (20 10-0016048).

EM-TuP6 Crystal Structure Analyses of Bis(triisopropylsilylethynyl)-Pentacene Nanofilms Deposited on OTS-SAM and Poly(3,4-ethylenedioxythiophene) Surfaces, S. Kim, S. Choi, Paichai University, Republic of Korea, *C. Yu,* Pohang Accelerator Laboratory, Republic of Korea, *T. Kim,* Paichai University, Republic of Korea, *J.-H. Boo,* Sungkyunkwan University, Republic of Korea

Highly pure 6,13-bis(triisopropylsilylethynyl)pentacene (TIPS-PEN) nanofilms were deposited on a very high quality OTS-SAM surface at two different substrate temperatures (70°C and 90°C) via the vacuum thermal evaporation (VTE) method. X-ray reflectivity (XRR) and grazing angle incidence x-ray diffraction (GID) measurements over a wide temperature range (30°C-284°C) revealed that out-of-plane crystallinity of the film (~10 nm) remains intact but in-plane crystallinity starts to become poor from ~100°C, and to become much worse from 260°C. Atomic force microscope images showed that TIPS-PEN films (~55 nm) prepared at the substrate temperature of 90°C or above commonly have a number of huge cracks between enormous crystal domains (up to 3mm) whereas the films didn't form such morphology below *T_s*=90°C. These results clearly suggest that an optimum substrate temperature of TIPS-PEN nanofilms on OTS-SAM surface must be somewhere between 70°C and 90°C, and the process temperature must be kept below 90°C in order to form and maintain a highly crystalline film for an organic thin film transistor device since in-plane crystallinity of a semiconductor channel deeply affects the performance of a transistor.

EM-TuP7 Atomic Imaging of Monolayer Nucleation of Atomic Layer Deposition Precursors, W. Melitz, J. Shen, J. Clemens, E. Chagarov, A.C. Kummel, University of California at San Diego

For highly scaled atomic layer deposition (ALD) of gate oxides (EOT < 1nm) on III-V semiconductors, the general requirements for an unpinned, high mobility oxide/III-V interface are as follows: (a) The metal precursor cannot disrupt the substrate during deposition; (b) The metal precursor must form a monolayer of nucleation sites in order for aggressive scaling of the equivalent oxide thickness (EOT); (c) The oxide has to be resistant to atom donation to/from the substrate; (d) The oxide needs to bond weakly to the interface or to form nearly covalent bonds to the interface to balance polarity. The nucleation/passivation layer has to enable all four requirements. Half cycle room temperature ALD of trimethylaluminum (TMA) and dimethylaluminum ethoxide (DEAE) have been performed on InAs and InGaAs surface to compare two precursors for the same oxide one of which is oxygen-free and one which contains oxygen. The electronic properties of the clean and deposited surfaces are probed via scanning tunneling spectroscopy and microscopy (STS and STM), and Kelvin probe force microscopy (KPFM). Previous STS and KPFM studies for both clean InAs and InGaAs (4x2) surfaces determined the Fermi level is pinned 0.3eV above the valance band; DFT studies show that the surface are pinned by homodimers in the trough. STM and STS show that TMA forms an ordered monolayer of adsorbates which unpin the Fermi level suggesting that an ordered monolayer layer might be a requirement for unpinning. However, STM of DEAE reacted InGaAs(001)-(4x2) shows a nearly amorphous monolayer layer while STS shows even this amorphous layer unpins the interface. The influence of larger ligands on the DEAE might account for more degeneracy in bonding configurations making order structures less probable. The results are consistent with a multitude of bonding configuration being able to unpin the Fermi level as long as the pinning sites are removed and the presence of oxygen in the precursor not being an impediment to passivation as long as there is still attractive interactions between the adsorbates which promote monolayer formation.

EM-TuP8 Synthesis and Magnetic Properties of Zn_{1-x}Mn_xO Hollow Nanospheres, D.R. Liu, T.C. Wu, Y.C. Yeh, W.H. Cho, National Applied Research Laboratories, Taiwan

ZnMnO is one of the most promising diluted magnetic semiconductors (DMS) materials due to its predicted above room temperature ferromagnetism. In this study, Al₂O₃ layer was conformally deposited on the surface of polystyrene (PS) nanosphere with different diameter (100nm~800nm) by atomic layer deposition (ALD). After removal of PS nanosphere by heating, Al₂O₃ hollow nanospheres were formed. Then the Zn_{1-x}Mn_xO (x=0.03, 0.05, 0.07) coatings were grown on Al₂O₃ hollow nanospheres by pulsed laser deposition (PLD). According to the results of high-resolution x-ray diffraction, the Zn_{1-x}Mn_xO hollow nanospheres are polycrystalline with a preferential growth direction of (002). The surface and cross-section morphologies of the hollow nanospheres were analyzed using a field-emission scanning electron microscope (FE-SEM). Photoluminescence spectra in applied magnetic field demonstrate ultraviolet emission peaks which have shift with the increase of Mn ion concentration. The magnetic properties of the nanospheres were measured by a superconducting quantum interference device (SQUID) magnetometer and x-ray magnetic circular dichroism (XMCD) spectroscopy. The results show the magnetic properties of Zn_{1-x}Mn_xO hollow nanospheres strongly depend on the Mn composition fraction and the size of nanospheres.

EM-TuP9 Fringing Field effects of Different Size Indium Gallium Zinc Oxide (IGZO) Active Layers Thin Film Transistors, J. Noh, S. Kwon, J.H. Noh, University of Tennessee, *P.D. Rack,* University of Tennessee at Knoxville; Oak Ridge National Laboratory

To realize the high performance-thin film transistors (TFTs) using amorphous indium gallium zinc oxide (a-IGZO) as the semiconducting active layer, we will present the how the a-IGZO with different active sizes affects the electrical characteristics of TFTs. The TFTs are fabricated with a bottom-gate staggered structure and the a-IGZO active size is photolithographically patterned to different lateral dimensions. A Cr gate is deposited on buffered silicon dioxide on a silicon substrate and SiN_x is the gate dielectric which is deposited via plasma enhanced chemical vapor deposition (PECVD). The a-IGZO semiconducting active layers are deposited using rf magnetron sputtering in a reactive Ar-O₂ atmosphere which controls the carrier concentration which can be metallic at low oxygen flow rates and insulating at high (>20% O₂) flow rates. The a-IGZO layer is patterned with different size by wet etch process with diluted HF. Finally, source and drain electrodes are formed and the device is annealed for activation. We will discuss the TFT characteristics based on fringing electric field effects in which the fringing electric field around the periphery of the patterned source and drain electrodes can induce electrical conduction as current paths in the semiconductor layer, changing electrical properties in the device, especially increasing the leakage current through the

backchannel on IGZO. Furthermore, we will correlate the different pattern size of IGZO to the electrical properties of the TFT devices. Finally, we will present a new application for our a-IGZO TFTs: an addressable microfluidic electrowetting channel device.

EM-TuP10 Optical Constant Measurements and Relation to Substrate Currents of Dielectric Layers under Vacuum Ultraviolet Irradiation, *D.B. Straight, H. Sinha, J. Lauer, University of Wisconsin-Madison, N.C. Fuller, S.U. Engelmann, Y. Zhang, IBM Research, G.A. Antonelli, Novellus Systems, Inc., Y. Nishi, Stanford University, J.L. Shohet, University of Wisconsin-Madison*

We report an inexpensive and rapid method to measure the reflectance of dielectrics in the vacuum ultraviolet (VUV) range of the spectrum using synchrotron radiation. Porous low- k organosilicate (SiCOH) dielectrics deposited on silicon were irradiated with VUV photons of various energies. Reflectance is calculated from ratio of the measured reflected photon flux to the measured incident photon flux. A 90% transmitting nickel mesh connected to a picoammeter was used to measure the incident and reflected photon flux. When the sample is absent from the path of the VUV photons, a photon dump is used to minimize any possible reflectance. Thus, the net photon flux incident on the nickel mesh is the synchrotron flux. Under these circumstances the reading from the picoammeter is proportional to the synchrotron flux. When the sample is present some of the photons are reflected from the sample. Since the sample is placed normal to the VUV photon flux, the reflected photons can travel back to the nickel mesh. Thus, under these conditions, the nickel mesh current is sum of the incident synchrotron photon flux and the reflected photon flux. The reflectance is calculated from the two current measurements. The reflectances of SiCOH of different porosities were compared. By using the Kramers-Kronig algorithm, [1] the index of refraction and the extinction coefficient as a function of energy can be obtained from the reflectance. We also find that during VUV irradiation, the reflectance of a dielectric and the substrate current are inversely correlated. Thus, the reflectance can be obtained from the substrate current and vice versa. We conclude that reflectance or substrate current measurements can determine which photon energies are more likely to be absorbed and can therefore cause dielectric damage during processing. [2] Reducing the flux of deleterious photon energies in processing systems can minimize dielectric damage.

This work has been supported by the Semiconductor Research Corporation under Contact 2008-KJ-1871 and by IBM Research. The UW-Madison Synchrotron is funded by NSF under Grant DMR-0084402.

[1] D. M. Roessler, *Brit. J. Appl. Phys.* **16**, 1119 (1965).

[2] G. S. Upadhyaya, J. B. Kruger, and J. L. Shohet, *J. Appl. Phys.* **105**, 053308 (2009)

EM-TuP11 Resistive Switching in Big Band Gap Material- beta - Ga₂O₃, *S.X. Zheng, T.C. Lovejoy, University of Washington, V. Garcia, S. Ueda, NIMS, Japan, A. Pakhomov, M.A. Olmstead, F.S. Ohuchi, University of Washington*

Gallium oxide has a unique combination of properties that hold significant promise for variety applications. Pure beta-Ga₂O₃ has band gap of 4.8 eV which has potentials as UV-transparent optics material. Recent findings suggest its n-type semiconducting behavior after treating it in reducing atmospheres, which place it in the group of new generation transparent conductive oxides. On the other hand, its conductivity change after gases like CO and NO₂ makes it a potential gas sensing material. Despite its unique optic/optoelectronic properties, incomplete mechanistic understanding of the origins of conductivity becomes a barrier to device development. According to recent findings, oxygen vacancy contribution to the conductivity is widely accepted due to inverse correlation of conductivity and oxygen partial pressure during material growth. However, other models were also proposed, e.g, experimental results show trace amount of impurities can enhance the conductivity of Ga₂O₃ without changing its crystal structure. On the other hand, formation energy calculation suggests possible vacancy alignment along conducting direction can also improve the electron hopping, thus enhance the conductivity. Unfortunately, most of the conclusions were either lack of experimental support, or based on samples prepared from different synthesizing techniques, whose properties can be substantially changed.

In this report, Single crystal beta-Ga₂O₃ prepared by float zone technique was used to investigate the electrical property change after heating under different atmospheres. It is discovered that by passing direct current through the material in the ultra high vacuum, resistivity of beta-Ga₂O₃ along [010] direction can have significant increase, which contradicts to the oxygen

vacancies model. A detailed investigation using X-ray Photoemission Spectroscopy (XPS), Scanning Tunneling Microscopy (STM), Physical Property Measurement System (PPMS) reveals the change in stoichiometry, work function, surface morphology and polaron hopping dimensions, which bring insight to the origins of conductivity in Ga₂O₃ along different crystal orientations. Based on the understanding on the single crystal conductivity, epitaxial Ga₂O₃ thin film with designated resistive switching properties using Pulse laser deposition can also be prepared.

EM-TuP12 Mass Fabrication of TiO₂-based Resistive Switching Arrays by Step and Flash Imprint Lithography, *K.D. Kim, D.K. Yun, Korea Institute of Machinery and Materials, Republic of Korea, H.Y. Jeong, ETRI, Republic of Korea, J.H. Lee, J.H. Jeong, Korea Institute of Machinery and Materials, Republic of Korea, S.Y. Choi, ETRI, Republic of Korea, H.H. Park, KANC, Republic of Korea, J.H. Choi, Korea Institute of Machinery and Materials, Republic of Korea*

EM-TuP13 Fabrication of Heavy Capacitive Organic Capacitor using All Ink Jet Process, *I.J. Bae, J.J. Han, I.S. Chung, Sungkyunkwan University, Republic of Korea*

We attempted to fabricate an organic capacitor on polyethersulphone (PES) substrate using ink jet printing. The capacitor cell was designed for the storage capacitor in E-paper backbone panel. Two different materials like Poly-4-vinylphenol (PVP) and Poly Methyl Methacrylate (PMMA) were examined by varying thickness and w%. The Area of the capacitor was 100 um x 100um. Silver was used as a metal electrode. All the processes were done using ink-jet printer. The dielectric properties were analyzed by measuring C-V, and the physical properties including the morphologies of the ink jet films were analyzed using optical microscope, SPM and SEM.

EM-TuP14 Copper-Electrochemical Mechanical Planarization (Cu-ECMP) Characteristics with a Change of Electrical Variables, *K.D. Myung, W.-S. Lee, Chosun University, Republic of Korea, N.-H. Kim, Chonnam National University, Republic of Korea*

Electrochemical mechanical planarization (ECMP) process for copper interconnects is an alternative process of the conventional chemical mechanical polishing (CMP) process due to its critical limitation in the recent industrial standards by the high pressure and abrasive. ECMP process dissolved the copper to copper ions for the generation of copper complex layer on the surface electrochemically by applying in an aqueous electrolyte with the electrical source, and then removed the copper complex layer by polishing with the lower pressure. In this study, ECMP was performed with changes of electrical variables including current, voltage, immersing time, size of electrodes, electrode materials, and distance between each electrode. ECMP characteristics such as removal rate, WIWNU%, RMS roughness, and peak-to-valley roughness were measured. The properties of electrolyte were examined as functions of the upper electrical variables in order to estimate the influences of the changed electrolyte on the ECMP characteristics in Cu-ECMP process. The surface of copper was also analyzed with various electrical variables by using XPS and nanoindentation to investigate the surface behaviors with chemical and mechanical properties. Acknowledgement: This work was supported by National Research Foundation of Korea(NRF) grant funded by the Korean Government(MEST) (2010-0016609).

EM-TuP15 Nanoparticle-enhanced Multilayered Thin Film Cooling Devices, *M. Hines, C. Cochran, Z. Xiao, Alabama A&M University*

Graphene Focus Topic

Room: Southwest Exhibit Hall - Session GR-TuP

Graphene Focus Topic Poster Session

GR-TuP1 Electronic and Magnetic Properties of Functionalized Graphene Nano-Ribbons, *Y. Fujii, J. Nakamura, The University of Electro-Communications (UEC-Tokyo), Japan*

Oxidation and reduction are the basic and most important processes for the carbon-based materials as initial processes for producing very thin graphitic materials composed of a single or several graphene layers [1]. Recently, Kosynkin *et al.* have reported that the graphene nano-ribbons (GNRs) can be produced using an oxidative process, and the edges of these GNRs are functionalized by carboxylic acids even after the reduction treatment [2]. On the other hand, it has been well-known that a certain type of GNR with zigzag edges exhibits the so-called flat-band magnetism, which stems from the localized states at the edges [3,4]. In this study, we reveal the electronic and magnetic properties of zigzag GNRs functionalized by carboxyl groups

using the first-principles total-energy calculations within the spin density functional theory.

The zigzag GNRs employed in this study have widths from $N=2$ to $N=8$. We have found that the ground state of the GNR with the zigzag edges functionalized by the carboxyl groups is ferromagnetic, if N is even. For the GNR with $N=4$, the ferromagnetic state is more stable by 17 meV per unit cell than the anti-ferromagnetic one. However, if N is odd, the ground state of the functionalized GNR becomes the anti-ferromagnetic: e.g., for $N=3$, the anti-ferromagnetic state is more stable by 12 meV per unit cell than the ferromagnetic one. We have also investigated the energy dispersions of the GNRs. In the anti-ferromagnetic states, the energy bands for both spins are degenerate, and their dispersions near the Fermi level are nearly-flat at the edge of the Brillouin zone, while for the ferromagnetic states, the up-spin and down-spin bands split from each other. The spin density for the ferromagnetic states is localized near the GNR edges. Thus, the onset of the finite magnetic moment of the functionalized GNR is due to the so-called flat-band magnetism.

- [1] S. Horiuchi *et al.*, Appl. Phys. Lett. **84**, 2403 (2004)
- [2] D. V. Kosynkin *et al.*, Nature Lett. **458**, 872 (2009)
- [3] M. Fujita *et al.*, J. Phys. Soc. Jpn. **65**, 1920 (1996)
- [4] J. Nakamura, T. Nitta, and A. Natori, Phys. Rev. B, **72**, 205429 (2005)

GR-TuP2 Aminocaproic Graphene Sheet Synthesized by Solution Plasma, N. Tsuda, Y. Aoki, J. Hieda, O. Takai, N. Saito, Nagoya University, Japan

Plasma in gas phase is widely used in many industrial fields such as electronic device manufacturing processes (plasma etching, sputtering, plasma-enhanced CVD, etc.), hard coating processes (ion plating, sputtering, etc.), surface treatment processes (low or atmospheric pressure plasma treatments, sputtering, plasma etching, etc.) and so on. Plasma in solid phase has been utilized finally for surface plasmon resonance (SPR) spectroscopy, nanoparticles, etc., and plasmonics is developing as a new research field. On the other hand, plasma in liquid phase is not generally well-known, although it has been partially utilized in water treatments and electrical discharge machining. The fundamentals of plasma in liquid phase have not been established, including its generation techniques, its state, and activated chemical species. However, it would be reasonable to expect a higher reaction rate under lower-temperature conditions, and the greater chemical reaction variability since the molecular density of liquid is much higher than that of gas phase. So we have named the plasma in liquid phase "solution plasma" because we make variety of plasma by choosing the combinations of solvents and solutes in solutions, and are developing solution plasma processing (SPP). In SPP, aqueous solutions, nonaqueous ones, liquid nitrogen, supercritical fluids, etc. can be utilized as solutions. Recently, we have investigated the features of SPP and the applications such as syntheses of nanoparticles and mesoporous silica, and surface modification of particles.

In this research, graphene sheet were modified by a glow discharge in solution. A pulsed power supply was used to generate discharges. The pulsed width was 2 micro seconds, the repetition frequency was 15 kHz. The electrode was tungsten wire in the diameter of 1 mm with electrode gap of 0.3 mm. ammonium aqueous solution was used as the medium around plasma. Graphene sheets were separated by oxidation. The graphene sheets were added to the ammonium solution and irradiated by glow discharge in the solution. The solution and the productants after the discharge were analyzed by optical emission spectroscopy, IR spectroscopy, Uv-Vis spectroscopy, AFM, XRD and TEM. After the discharge, the graphene sheets were modified by amino functional groups. Moreover, the aminocaproic acid was grafted into the amino functional groups on graphene sheets. Finally, graphene sheets were solidified because the space of sheets was measured.

GR-TuP3 Investigation of Diffusion Process between Many-Layers Graphene and Metallic Contacts, A.R. Vaz, CTI/CCS - UNICAMP, Brazil, F.P. Rouxinol, C.F. Fischer, S.A. Moshkalev, UNICAMP, Brazil, J.W. Swart, CTIRA, Brazil

Nanoscale graphitic carbon forms like nanotubes and few-layer graphene (graphite) or FLG layers have attracted much attention recently due to their unique physical-chemical properties and many potential applications in microelectronics, like sensors, MEMS (micro-electromechanical systems) and interconnections [1]. However, successful applications of these materials in microelectronic devices require development of reliable and compatible technologies for their controlled growth or deposition, manipulation, contacting, processing and measurements of electrical other properties. In particular, mechanisms responsible for formation of high-quality electrical contacts between graphitic layers and metals (this is imperative for applications like interconnections) is poorly understood and need thorough study and optimization. In this work, we studied

characteristics of the electrical contacts between FLG and metals like W, Ti, Ni, Cu, Pd and Au. For this, two different techniques were used. First, small flakes of FLG were prepared in solutions and deposited using ac dielectrophoresis [1] over metal electrodes pre-fabricated by photolithography and FIB milling processes that produced 5 μm deep gaps with varying widths (Fig. 1). The thickness of FLG flakes was evaluated using Raman spectra, AFM measurements and SEM images [2]. Then, electrical properties of deposited structures were measured before and after thermal annealing, using 2 terminals I-V method (Fig. 2). Electrical contacts between graphitic layers and metal electrodes were found to improve strongly with annealing. It was also found that metal-FLG contacts give usually the major contribution to the total measured 2-terminals resistance, and the contact resistivities were then evaluated for different metals. Better contacts were achieved using Ti and W electrodes. To study interaction between metals and graphitic layers during annealing (metal diffusion), a special study was undertaken. For this, metal layers of certain thickness were deposited in deep trenches prepared in thick HOPG layers using FIB based lithography followed by deep reactive ion etching of graphite in oxygen with high-density plasma source [3]. Then, after annealing in vacuum, FIB was used to make cross-sections and to study lateral (in-plane) and normal (between planes) diffusion of metal inside the graphite structure. For such study, several microscopy techniques with spatial resolution like EDX, EELS, HRSEM were employed.

- 1 R. Gelamo *et al.*, Chem. Phys. Lett. (2009)
- 2 F.P. Rouxinol *et al.*, to be published
- 3 H. Jansen *et al.*, J. of Micromech. Microeng. **16** (1995)

GR-TuP4 Optoelectronic Properties of Large Area Graphene Thin Films, C. Mattevi, H.K. Kim, G. Eda, M. Chhowalla, Imperial College London, UK

A scalable method to isolate graphene on insulating substrates is still a challenge. Recently it has been demonstrated that graphite can be exfoliated in certain solvents [1] and in water-surfactant solution [2] forming a stable colloidal suspension. Amongst several solvents investigated, exfoliation with 1-Methyl-2-pyrrolidone (NMP) has yielded the highest concentration of 1-5 graphene layers [1,3]. Here we present Langmuir-Blodgett (LB) films of pure graphene exfoliated in NMP and their optical and electronic characteristics [3]. For flakes with large lateral size, the films displayed sheet resistance of 5 K Ω /sq and transmittance of 75% at wavelength of 550 nm. Thin film transistor (TFTs) have been fabricated and tested at temperatures ranging from 77 K to 340 K. The field effect measurements displayed high degree of p-doping and this is possibly due to interaction between graphene and residual oxygen functional groups, as suggested by X-ray photoelectron spectroscopy (XPS). Below 150 K, the temperature dependence of the conductivity suggests transport by two-dimensional variable range hopping. Above 180 K, thermal activation of the charge carriers appears to be the dominant mechanism. A clear dependence of the optoelectronic properties with the lateral size of graphene flakes has been observed. A critical analysis on the prospects of improving the electrical properties of graphene obtained *via* non covalent exfoliation will be discussed.

- [1] Y. Hernandez *et al.* Nature Nanotech. Vol. 3, pp. 563-568, 2008.
- [2] M. Lotya *et al.* J. Am. Chem. Soc. Vol 131, pp.3611-3620, 2009.
- [3] H. Kim *et al.* submitted.

GR-TuP5 Tunneling Spectroscopy of Image Potential Derived States of Epitaxial Graphene on SiC(0001): Sample Annealing Effects, A. Sandin, A. Pronshinske, D.B. Dougherty, J.E. Rowe, North Carolina State University

Constant current tunneling spectroscopy has been used to study the high energy unoccupied electronic structure of single layer and bilayer epitaxial graphene on the Si-terminated face of SiC(0001) prepared with several different sample-annealing conditions that give different thicknesses of graphene film coverage. We identify a series of intense peaks in vertical sample-tip spacing versus voltage as derived from image-potential states of epitaxial graphene. These peaks shift in energy position between single-layer and bilayer graphene in a manner somewhat like the known work function difference (of ~ 4.4 eV and ~ 4.6 eV for single-layer and bilayer graphene respectively). We compare the series of image-potential-like-state energies measured experimentally with simple models of the tunneling potential due to a sharp tip protrusion and a flatter average tip radius that shows a variability of the energy series with spatial variation of the potential. In addition, we argue that variability in peak positions for nearly all of the observed image potential derived states arises from the variations

in the 3-D tip shape, which then determines the field dependent tunneling potential.

GR-TuP6 Characterization of Graphene Films Grown on Cu-Ni Foil by XPS and LEED, D.D. Moody, W. Priyantha, R. Droopad, C.A. Ventrice Jr., Texas State University - San Marcos, S. Chen, W. Cai, R.D. Piner, R.S. Ruoff, The University of Texas at Austin

Previous studies have shown that monolayer graphene films can be grown on Cu substrates by the catalytic decomposition of methane molecules.[1-5] The solubility of carbon in Cu is negligible at the growth temperatures typically used for graphene growth. This results in the formation of films that self-terminate at a monolayer coverage since there is very little (if any) carbon in the sub-surface region that can precipitate to the graphene overlayer during the cooling phase. Indeed, our prior work suggests that the growth is entirely surface mediated with no contribution from segregation of carbon from the bulk.[2] In an attempt to enhance the catalytic activity of the surface and to grow multilayer graphene rather than solely monolayer graphene, use of a commercial 70%-30% Cu-Ni alloy foil (which also has some Fe and Mn present) has been investigated. Growth was performed in a home-made, cold-wall, chemical vapor deposition (CVD) system [6] at a growth temperature of 1000 °C (as measured with a pyrometer through a quartz window) with pure CH₄ at a pressure of 8 Torr. To determine the surface alloy composition during the different phases of growth, X-ray photoelectron spectroscopy (XPS) measurements have been performed on the Cu-Ni foil before anneal, after anneal in H₂, and after growth of graphene in a CH₄ environment. XPS measurements were made at both normal emission, and at an exit angle of 50° to enhance the surface sensitivity. Before anneal, the measurements indicate that the surface is Ni-rich and heavily oxidized. After annealing in H₂, only a small amount of oxide remained, and the alloy fraction of the surface region was 21% Ni. This indicates that the outermost layer of atoms is probably Cu, but further study is indicated. Growth of the graphene overlayer resulted in an increase of the Ni composition of the surface region to 28%, with only trace amounts of oxygen present. Low energy electron diffraction (LEED) measurements of the foils showed only diffuse background for the Cu-Ni foils before anneal and after anneal in H₂. The LEED measurements of the foil after graphene growth showed diffraction spots and ring structures at 70 eV, which are attributed to the formation of multidomain graphene. *Support from the Office of Naval Research is appreciated.*

- [1] X. S. Li, et al., *Science* **324**, 1312 (2009).
- [2] X. S. Li, et al., *Nano Letters* **9**, 4268 (2009).
- [3] X. S. Li, et al., *Nano Letters* **9**, 4359 (2009).
- [4] X. S. Li, et al., *ECS Transactions* **19**, 41 (2009).
- [5] W. Cai, et al., *Nano Letters* (in-press).
- [6] W. Cai, et al., *Nano Research* **2**, 851 (2009).

GR-TuP7 Chemical Vapor Deposited Graphene-Based NEMS Resonators, I. Rivera, R. Joshi, J. Wang, University of South Florida

Graphene is a superb structural material for NEMS resonators because of its unique electrical and mechanical properties. Excellent material properties of graphene such as good conductivity, single atomic thickness layers, large surface area, low mass density, and high Young's modulus as compared to other materials allow optimization of the resonance response to approach the ultimate limit for two dimensional NEMs. Single device resonator has been studied extensively in the past with very high Q-factor and resonant frequency. However, for device technology, arrays of resonators provide a wider range of applications which appear to be possible in graphene based resonators. Figure 1 summarizes the fabrication process of the graphene resonators and Figure 2 presents a 3D schematic of graphene resonator array, indicating key parts and the materials. We have grown the monolayer quality graphene using thermal chemical vapor deposition method on Ni coated substrates at 1000°C using a mixture of argon, hydrogen and methane as precursor gases. It was observed that growth time and thickness of Ni films are key parameters for controlling the number of layers of graphene. Initial results suggest the formation of 1-5 layers of graphene which was estimated from AFM, TEM and 2D peak intensity of Raman spectra [Figure 3]. Hall Effect data show mobility ~ 1500 cm²/V and resistivity of 2X10⁻⁶ Ω-cm for 3 layer graphene. Graphene was released from Ni by wet chemical etching and the layers were transferred onto SiO₂/Si substrate. In order to employ graphene as a major building block, NEMS resonator structures were created by transferring a patterned graphene layer onto a silicon-on-insulator (SOI) substrate to act as mechanical interconnects. The Si device layer in SOI substrate is patterned by deep reactive ion etching (DRIE) using SiO₂ as hard mask to create the resonator body. An ultra-thin layer of high-k dielectric material is uniformly deposited by atomic layer deposition (ALD) followed by deposition and doping of a poly-Si layer. A lithography process is done to create the shape of the double side electrodes. Thereafter, the graphene is transferred and

attached to the resonator bodies to complete the array. Finally, the resonator array is released by removing the buried SiO₂ in the SOI substrate.

**Nanometer-scale Science and Technology
Room: Southwest Exhibit Hall - Session NS-TuP**

Nanometer-Scale Science and Technology Poster Session

NS-TuP1 Fabrication and Characterization of Piezoelectric Polymer Nanostructure, D. Kim, Y.-Y. Choi, H.W. Choi, M. Han, M. Park, G. Ahn, K. No, Korea Advanced Institute of Science and Technology (KAIST), Republic of Korea

We show the microstructures and ferroelectric domains of 200nm diameter poly(vinylidene fluoride-trifluoroethylene), P(VDF-TrFE) with composition of 75/25 mol%, nanorods fabricated by a porous template technique. In order to characterize the piezoelectric properties of P(VDF-TrFE) nanorods, both nanoscale manipulation and polarization switching were studied using piezoresponse force microscopy (PFM). Ferroelectric domains and their properties were confirmed using X-ray diffraction and PFM analysis. The ferroelectric domains in the nanorods were homogeneously switchable below 5V. This offers our rationale for a promise in energy harvesting and switchability would be good for plastic electronics.

NS-TuP2 Uniform Printing of PEG Hydrogel Arrays by Dip-Pen Nanolithography[®], J.-W. Jang, P.L. Stiles, S.R. Nettikadan, NanoInk Inc.

Dip Pen Nanolithography[®] (DPN[®]) is an established method of nanofabrication in which materials are deposited onto a surface via a sharp tip. DPN enables controlled deposition of a variety of materials with nanoscale registry onto various substrates. Recent advances in DPN technology has resulted in the ability to directly print larger, biologically relevant materials on to a variety of surfaces under ambient conditions.

A novel method for the construction of hydrogel patterns has been developed. Hydrogels are of great interest to tissue engineers and other biomedical researchers because of the versatility of PEG chemistry and excellent biocompatibility. Also the mechanical and swelling properties of PEG hydrogels can be easily tuned by controlling the degree of cross-linking and choosing the appropriate molecular weight. Patterning of hydrogels in submicron scale with defined mechanical properties is highly desirable as a scaffold for tissue engineering and *in vitro* cell culture studies.

We report a novel method for generation of hydrogel patterns at subcellular scales. Hydrogel precursors are directly deposited at defined location and then polymerized to form hydrogels. This method allows for rapid fabrication of high resolution patterns. We used a simple desktop nanolithography platform (NLP 2000[™], NanoInk, Inc.) for the deposition of the hydrogel precursors. The NLP 2000 consists of a stacked 3axis stage system with a travel range of 40 mm and a resolution of 25 nm. A high resolution optical microscope is available for monitoring the printing process. A custom fabricated array of cantilever based writing tools (M-Type, 12-pen, NanoInk, Inc.) were used to transport the hydrogel precursors on to the surface. Controlling the environmental conditions during the printing process allows for the transfer of defined volumes of hydrogel precursors. At 37°C, hydrogel domains of 6 μm were printed while at 25 °C 1.5 μm domains were printed. Patterning areas of 1 mm² with domains of less than 5 μm can be easily achieved in less than 30 min. AFM result confirmed the size and homogeneity of the printed hydrogel patterns.

NS-TuP3 Localized Surface Plasmons and Hot Spots from the Interstitial Sites in Linear Nano-Hole Array Structures of Gold Revealed by Near-Field Two-Photon Excitation, S.I. Kim, KAIST, Republic of Korea, K. Imura, Institute for Molecular Science, Japan, S. Sehun Kim, KAIST, Republic of Korea, H. Okamoto, Institute for Molecular Science, Japan

We analyzed spatial distribution of enhanced optical field at the gap between nano-holes in nano-hole array structures on gold thin film by near-field two-photon excitation imaging. We prepared linear chain-like array structures of circular nano-holes on gold thin film on a glass substrate, based on the method developed by Fischer [1]. A home-made scanning near field microscope [2] was used to observe two-photon excitation images for individual nano-hole array structures. We used a Ti:Sapphire laser (<100fs, 780 nm) to excite two-photon induced luminescence. Polarization dependences of the two-photon images were also measured. In the near-field two-photon excitation images of the nano-hole arrays, we found strong enhanced signal localized at interstitial sites between nano-holes, when the incident polarization is parallel to the chain axis of the array.

References

- [1] U. C. Fischer and H. P. Zingsheim., *J. Vac. Sci. Technol.* **19**, 881 (1981).
[2] K. Imura, T. Nagahara, and H. Okamoto, *J. Phys. Chem. B* **109**, 13214 (2005).

NS-TuP4 Band and Dielectric Discontinuities of the $\text{Si}_{1-x}\text{Ge}_x/\text{Si}_{1-y}\text{C}_y$ Superlattices, *T. Ohsumi, J. Nakamura*, The University of Electro-Communications (UEC-Tokyo), Japan

$\text{Si}_{1-x}\text{Ge}_x$ and $\text{Si}_{1-y}\text{C}_y$ alloys have attracted much attention from the perspective of the fabrication of novel devices, e.g., resonant tunneling diodes with strained alloys [1] and hetero bipolar transistors with double quantum wells [2]. It has been known that the lattice constants of these alloys are approximately proportional to their compositional ratios in accordance with Vegard's law [3]. Further, it has been reported that the band-gap of $\text{Si}_{1-x}\text{Ge}_x$, other than the lattice constant, changes with its composition [4]. In this study, we draw attention to the dependence of the dielectric constant on the composition of $\text{Si}_{1-x}\text{Ge}_x$ and $\text{Si}_{1-y}\text{C}_y$ as well as the dependence of other physical quantities such as lattice constants and band-gaps. We explore the band discontinuity and the spatial modulation of dielectric constants for the $\text{Si}_{1-x}\text{Ge}_x/\text{Si}_{1-y}\text{C}_y$ superlattices as novel device structures, using first-principles ground-state calculations in external electric fields [5, 6].

We have adopted the cubic supercells containing 8 atoms for the $\text{Si}_{1-x}\text{Ge}_x$ and $\text{Si}_{1-y}\text{C}_y$ bulk models. It has been shown that the lattice constants of $\text{Si}_{1-x}\text{Ge}_x$ and $\text{Si}_{1-y}\text{C}_y$ alloys increase and decrease linearly with their compositions, respectively, obeying the Vegard's law. In contrast, the nonlinearity with the composition is found for the band gap and the dielectric constants. In our presentation we discuss the origin of the onset of the nonlinearity and report the band and dielectric discontinuities of the $\text{Si}_{1-x}\text{Ge}_x/\text{Si}_{1-y}\text{C}_y$ superlattices from an atomic scale point of view.

- [1] P. Han *et al.*, *J. Crystal Growth*, **209**, 315 (2000)
[2] D. C. Houghton *et al.*, *Phys. Rev. Lett* **78** 2441 (1997)
[3] W. Windl *et al.*, *Phys. Rev. B* **57** 2431 (1998)
[4] J. Weber *et al.*, *Phys. Rev. B* **40** 5683 (1989)
[5] J. Nakamura *et al.*, *J. Appl. Phys.* **99**, 054309 (2006); *Appl. Phys. Lett.* **89**, 053118 (2006)
[6] S. Wakui *et al.*, *J. Vac. Sci. Technol. B* **26**, 1579 (2008)

NS-TuP5 Single Domain Homogeneous Monolayer at the Water/Oil Interface and its Application for Surface Enhanced Raman Scattering, *S.I. Kim, P.S. Fabien, H. Song, S. Kim*, KAIST, Republic of Korea

We made mm-range closely packed monolayer by using the water/oil interface with Au nanoparticles whose nominal sizes are about 32 nm. We transfer this monolayer to the hydrophilic Si substrates by pulling up the sample softly and we measure the surface enhanced Raman scattering of Rhodamine 6G dye molecules. For this structure, we simulate the electromagnetic field enhancement when the laser light shines the sample whose unit cell is hexagonal structures ideally. We suggest that the strong field enhancement comes from the every interstitial gap among nanoparticles.

NS-TuP6 Synthesis of Ge Nanostructures by Reactive RF Sputtering, *A. Hernández-Hernández, F.J. De Moure-Flores, J.G. Quiñones-Galvan, K.E. Nieto-Zepeda, J. Santoyo-Salazar*, CINVESTAV-IPN, Mexico, *V.T. Rangel-Kuoppa, T. Plach*, Johannes Kepler Universitat, Austria, *M.A. Melendez-Lira*, CINVESTAV-IPN, Mexico

In this work we report the results of the synthesis and structural and optical characterization of heterostructures $\text{SiO}_x/\text{Ge}/\text{SiO}_x$ by reactive RF sputtering. The characteristics of germanium along with its compatibility with silicon technology and the sensitivity of its band structure to confinement confer a high attractive to the synthesis of germanium nanostructures.

The samples were prepared on substrates of p-type Si monocrystalline (1 1 1) and commercial glass by reactive sputtering. The effect of the partial pressure of oxygen and Ge interlayer thickness on the electronic properties of the heterostructure is reported[1]. Structural characterization was carried out by grazing angle X-ray diffraction and atomic force microscopy. The electronic properties were studied by UV-Vis transmission, infrared and Raman spectroscopies. Surface roughness was quantified by atomic force microscopy. X-ray diffraction showed the amorphous characteristics of the heterostructures. UV-vis spectroscopy results do not presented relevant differences with respect to those from SiO_2 reference samples.

The Raman spectra shown modes associated to germanium indicating the formation of low dimensionality germanium particles embedded in an amorphous phase. Ellipsometry and electronic transmission micrographs

confirm the presence of Ge nanoparticles. Ohmic contacts were deposited in a van der Pauw geometry using AuSb. Temperature dependent Hall (T-Hall) measurements were done between 35K and 373K, using the van der Pauw method. The results indicate low resistivity values that could be explained due to the formation of a two dimensional electron gas o the presence of mini bands due to the quantum dots interaction.

*: partially funded by CONACyT-Mexico

- [1] E. Mota-Pineda, M. Meléndez-Lira, M. Zapata-Torres, A. Pérez-Centeno, M. A. Santana-Aranda and P. del Angel. *Semicond. Sci. Technol.* **24**, 105028 (2009).

NS-TuP7 Spinel $\text{M}_3\text{Co}_{3-x}\text{O}_4$ Nanoparticles: Facile Low Temperature Solution Synthesis and Characterization, *D. Davis, M. Bencomo, T.N. Lambert, P. Lu, S. Limmer, W.G. Yelton*, Sandia National Laboratories

The synthesis and characterization of spinel $\text{M}_3\text{Co}_{3-x}\text{O}_4$ (M = Mn, Fe, Ni, Cu) nanoparticles was undertaken. Cobalt oxide-based nanoparticles doped with transition metals have a wide variety of potential applications, ranging from new material coatings for concentrating solar power applications to performing as cathode catalysts in fuel cells and metal-air batteries. We have recently demonstrated that $\text{M}_3\text{Co}_{3-x}\text{O}_4$ nanoparticles can be prepared using simple, low temperature solution precipitation methods, and that the final size and morphology of the nanoparticle depends on the extent of doping. These materials have been characterized by powder X-ray diffraction (P XRD), high-resolution transmission electron microscopy (HR-TEM), N_2 adsorption-desorption, and thermal gravimetric analysis/differential thermal analysis (TGA/DTA). The synthesis, characterization, as well as some potential applications of these materials, will be presented.

This work is supported by the Department of Energy, Office of Basic Energy Science and the United States Department of Energy under contract number DE-AC04-94AL85000. Sandia is a multi-program laboratory operated by Sandia Corporation, a Lockheed-Martin Company, for the United States Department of Energy.

NS-TuP8 UV Induced Synthesis and XPS Characterization of Gold Nanoparticle-PMMA Composites, *E. Yilmaz, S. Suzer*, Bilkent University, Turkey

Polymer-nanoparticles are technologically important composite systems, gaining increasing interest from many different fields of science in the last decade. Many procedures were introduced for synthesis of gold and other metallic NPs in solution and their integration to polymer films afterwards. But a more efficient approach is to synthesize nanoparticles directly inside the polymer matrix. Irradiation of polymer-metal precursor mixtures with energetic light is a practical method for this purpose. In this study, we present in-situ synthesis of gold nanoparticles within poly(methylmethacrylate) (PMMA) films by UV irradiation.

An advantage of synthesizing gold NPs within polymer films is the opportunity of photo-patterning. Films having patterns made of regions with and without gold NPs can be produced, using masks designed to cut off the UV radiation at desired places. Such patterned films were investigated with secondary electron microscope (SEM) and dark regions between irradiated regions and masked regions were observed. These dark regions are speculated to be "ion free regions", where gold ions diffuse through irradiated regions during UV irradiation. These regions of about 10 μm width, suggests a very large distance for gold ions to diffuse through a rigid matrix like PMMA, which is very interesting. Supporting evidence for the existence and the properties of these regions was obtained from fluorescence studies with Rhodamine 6G molecule and x-ray electron spectroscopy (XPS). In XPS the gold content gradient shows, the border of the irradiated region contains more gold than the middle of the irradiated region which supports the diffusion of gold ions from masked regions through the irradiated regions.

Additionally, the electrical properties of PMMA with and without gold nanoparticles were investigated using XPS, while applying external bias to PMMA films with and without gold nanoparticles to probe the charging properties of the films. We observe an enhancement of conductivity of PMMA films containing gold nanoparticles.

NS-TuP9 Fabrication of Ordered Nanodot Arrays Utilizing Anodic Aluminum Oxide Template Formed on Si Substrate, *N.Y. Kwon, N.K. Kim, J.K. Yeon, G.Y. Yeom, I.S. Chung*, Sungkyunkwan University, Republic of Korea

We have fabricated anodic aluminum oxide (AAO) with two types of structures, namely, hexagonal and matrix arrays of pores. At first, Al thin films with the thickness of 2 μm grown on Si (100) substrates were

anodized in 0.3 M oxalic acid under conditions of 4 °C at 40 V. Then the hexagonal AAO templates with the thickness of 300 nm were obtained using two-step anodization. Alternatively, AAO template with a matrix pores was prepared utilizing focused ion beam milled indent. The size of pores was controlled between 30 nm and 60 nm by immersing in 5 % phosphoric acid at 20 °C. In order to obtain smaller size of pores, the barrier layer was removed by neutral ion beam etching. Finally, we successfully fabricated hexagonal and matrix AAO templates with the pore sizes between 10 nm and 60 nm. The Si surfaces at the AAO pore bottoms were cleaned with dilute hydrofluoric acid after annealing at 900 °C in Ar gas. We then fabricated ordered Au and Ni nanodots arrays with controllable size between 10 nm and 60 nm. Scanning probe microscopy (SPM) and field emission secondary electron microscopy (FE-SEM) were used for characterization on shape of AAO and nanodots arrays.

NS-TuP10 On the Photoluminescence of Zn₂GeO₄ Nanorods Synthesized by a Simple Solution Route, M.Y. Tsai, National Applied Research Laboratories, Taiwan, Republic of China, T.P. Perng, National Tsing Hua University, Taiwan, Republic of China

During the past decade, there has been increasing interest in ternary oxide nanomaterials due to their unique electronic, optical, and chemical properties. In the present study, Zn₂GeO₄ nanorods exhibiting intense white blue-green luminescence were synthesized using a reflux method. Stoichiometric GeO₂ (1 mmole) and zinc acetate (2 mmole) were pre-dissolved in deionized water separately, and the solution mixture was subsequently refluxed at 160°C with the aid of magnetic stirring. From scanning electron microscopic observation, the obtained product (denoted as sample A) was an aggregation of short nanorods. The diameter of nanorod ranges from 30 to 50 nm, and the length is approximately 300 nm. X-ray diffraction (XRD) analysis reveals that these nanorods exhibit a pure Zn₂GeO₄ phase of phenacite structure. If the concentration of reactants were increased by 5 times, the nanorods became longer and tended to aggregate to form bundles (denoted as sample B). Further, the full width at half maximum (FWHM) of XRD peaks measured from sample B was smaller than that of sample A, indicating a larger mean grain size. Since Zn₂GeO₄ is a self-activated phosphor, the photoluminescence (PL) of these two specimens was also measured. An intense white blue-green light emission was observed from sample A, and the broad PL band distributed from 400 nm to 600 nm, with the peak at 475 nm. The PL band profile of sample B was similar to that of sample A. However, the peak position red-shifted to 490 nm. The PL from Zn₂GeO₄ nanorods was quite different from that of sintered Zn₂GeO₄ powder which not only exhibited green PL peaked at 530 nm but also had a narrower FWHM. The luminescence of nanorods was rather likely associated with the native defects, and the red-shift phenomenon of PL peak may be correlated with the larger grain size.

NS-TuP11 Fabrication of Vertically Aligned Si Nanowires on Si (100) Substrates using AAO, N.K. Kim, N.Y. Kwon, J.H. Lee, D.M. Whang, I.S. Chung, Sungkyunkwan University, Republic of Korea

Vertically aligned Si nanowires were grown on using ordered AAO. At first anodic aluminum oxide (AAO) templates with both hexagonal pores and matrix pores were prepared. 2 μm Al thin film grown on Si (100) substrates were anodized in 0.3 M oxalic acid under conditions of 4 °C at 40 V. Then, the hexagonal AAO template with the thickness of 300 nm was obtained using a two-step anodization. On the other hand, AAO template with a matrix pores was obtained utilizing focused ion beam milled indent and anodization process. AAO template with pore sizes of 30 nm and that of 60 nm were obtained by immersing the AAO in 5 % phosphoric acid at 20 °C for 30 min and 60 min, respectively. The Si surfaces at the AAO pore bottoms were cleaned with dilute hydrofluoric acid after annealing at 900 °C. Then, Si was deposited using LPCVD on AAO templates grown on Si substrate. The mixture gas with SiH₄ and HCl was used for Si deposition. Finally, we can obtain vertically aligned Si nanowires by removing AAO template using 1.8 wt% H₂CrO₄ and 7.4 wt% H₃PO₄ at 65 °C for 120 min.

NS-TuP12 Controlled Hybrid Bioactive Nanostructures by Integrating Gold Nanoparticles and Peroxidase to the ssDNA Nanotemplate, M.-Y. Lin, F.H. Ho, Y.S. Yang, National Applied Research Laboratories, Taiwan, Republic of China

Controlled positioning of metallic nanoparticles to assembly nanostructure has drawn interests in the field of nano-architecture, because of their electronic and optical properties. To achieve this, scientists have adopted various materials and methods for “bottom-up” and “top-down” fabrication of nanostructures. DNA nowadays is more than just a carrier for genetic codes, but it has also been used as novel materials for building nano-architectures. In this study, we aim to assembly the long, periodic single-stranded DNA nanotemplate (ssDNA) on the silicon-based substrate covalently and couple the supramolecules into a functional bioactive system. The preparation of ssDNA nanotemplates is based on the aptameric recognition of tumor marker: platelet-derived growth factors and rolling

circle amplification (RCA) technology. Because of the periodic, repeated sequence with secondary structures on the ssDNA nanotemplate, the supramolecules, including gold nanoparticles and peroxidase enzyme will be incorporated on the specific sites of the ssDNA nanotemplate based on the Watson-Crick base-pairing strategy in a programmable way. The distance between the gold nanoparticles and peroxidase enzyme can be controlled by manipulated the sequence on each repeat. In addition, the distance can also be increased merely by thermal treatment (around 80 °C) to open up the secondary structure on the ssDNA nanotemplate. Gold nanoparticles and peroxidase were periodically allocated precisely on each repeating sequence. The property of the peroxidase was affected by the gold nanoparticles and demonstrated by the luminescence measurement. In this study, we attempt to incorporate the gold nanoparticles on the ssDNA nanotemplate through hierarchical self-organization. The gold nanoparticle chains integrated with ssDNA nanotemplate were confirmed and visualized by the atomic force microscopy. We anticipate this study will pave a way for assembling novel bioactive materials with metallic nanoparticles for the development of modern electronic devices.

NS-TuP13 Magnetic Properties of Fe-O Nanonetworks, C.V. Ramana, C.G. Franco, K.B. Karuppanan, University of Texas at El Paso

Nanostructures of Fe oxides and hydroxides with varying morphologies were prepared in aqueous media by precipitation of iron nitrate and ammonium hydroxide. The synthesis was carried out at room temperature (RT) involving two stages. The first stage is the precipitation of goethite and the second stage corresponds to the structural modification due to acetic acid. Initially, 250 ml of 3.52N NH₄OH was added to 250 ml of 1N Fe(NO₃)₃·9H₂O under magnetic stirring for 30 min at RT. The precipitates were washed with de-ionized water and maintained in water at 1.25N. AcOH was added to obtain three different concentrations: 2.4, 9.1, and 16.7 vol %. Powders were obtained heating the sols at 373 K until dry, and oxides were obtained by heat treatment at 773 K for 2 h. The samples with acetic acid addition show hematite (α-Fe₂O₃) with average size of 20 nm. Temperature variation of magnetization measurement was carried out for all the samples and the Curie temperature values for the 2.4, 9.1, and 16.7 vol % AcOH added samples were found to be 1004 K, 1024 K and 982 K respectively. Magnetization measurement was carried out at up to the magnetic field of 1000 Oe for 2.4 and 16.7 vol % AcOH added samples at room temperature as well as at higher temperatures. Magnetization value was found not to saturate at 1000 Oe for both the samples. For 16.7 vol % AcOH added sample, the saturation magnetization value at 300 K was calculated from Honda plot (1/H vs M plot) and it is found to be 38 emu/g. Coercive field value was found to be 255 Oe at 300 K. In the case of 2.4 vol% AcOH sample, magnetization measurements were carried out at different temperatures (from 300 K to 800 K) and the coercive field value was found to decrease with increasing temperature (130 Oe to 10 Oe).

NS-TuP14 Charge Transport across Phosphonate Molecular Wire-Indium Tin Oxide Junctions, D.M. Rampulla, J.G. Kushmerick, National Institute of Standards and Technology

Current-voltage analysis and transition voltage spectroscopy were used to measure the charge injection properties of monolayers of bi thiophene phosphonate, quarter thiophene phosphonate, and decyl phosphonate covalently bonded to an indium tin oxide surface. Hysteresis was observed for all three phosphonates, which is possibly explained by charge retention in the phosphonate. As compared to similar thiol/Au molecular junctions, there is no significant difference between the charge injection barriers of the three phosphonates, indicating that the phosphonate moiety dominates the observed charge injection properties.

NS-TuP16 Extreme Luminescent Signature of Coalesced Cd_{1-x}Zn_xSe Quantum-Rod Alloys, M. Plaisant, P.H. Holloway, University of Florida

Common ion semiconductor alloys in quantum structures such as dots and rods have the added benefit of control of the electron affinity of the material in addition to the fundamental spectral control provided by quantum confinement. Such alloys could be useful in mixed-material devices such as organic/inorganic photovoltaic cells, since inorganic valence and conduction energy levels can be appropriately matched to the HOMO/LUMO levels of the compatible organic phase. In this research we have synthesized common anion II-VI alloys consisting of a large band-gap core/small band-gap shell. We have been able to achieve a spectral signature ranging up to 200nm over the visible spectrum by a one-pot synthesis of Cd_xZn_{1-x}Se alloys. The morphology of the alloy (supported by TEM, XRD and PL characterization) was a prolate rod-like quantum structure resulting from coalesced quantum dots consisting of three regions, each of which provides for a specific spectral signature. The 440nm PL peak was from ZnSe, while intermediate wavelengths were due to alloyed Cd_xZn_{1-x}Se, and a peak at 640nm was due to a CdSe rich shell. With the judicious control of time and temperature of reaction, it was possible to create a multi-region quantum structure that mimicked the spectral

characteristics of a selected alloy composition, i.e. achieve emission over a much larger range of the electromagnetic spectrum.

NS-TuP17 Au-catalyzed Self Assembly of Ge-Sb-Te Nanowires by Metalorganic Chemical Vapour Deposition. *M.L. Longo, C. Wiemer, O. Salicio, R. Fallica, CNR-IMM, Italy, M. Fanciulli, CNR-IMM and University of Milano Bicocca, Italy, L. Lazzarini, L. Nasi, E. Rotunno, CNR-IMEM, Italy*

The Metalorganic Chemical Vapor Deposition (MOCVD), already promising for its potentialities in the scaling down of phase change memories (PCM, PRAM), was adopted for the Au-catalyzed self assembly of NanoWires (NWs) formed by Ge-Sb-Te alloys on SiO₂/Si substrates; the employed metalorganic precursors were tetrakisdimethylaminogermanium, trisdimethylaminoantimony and diisopropyltelluride; the process gas was N₂.

The NW properties were studied by X-ray Diffraction (XRD), Total Reflection X-ray Fluorescence (TXRF) and Scanning Electron Microscopy (SEM) observations. Local measurements were carried out on single nanostructures by High Resolution and Analytical Transmission Electron Microscopy (TEM).

Ge-Sb-Te (GST) NWs exhibited a mean diameter distribution centered on 35 nm and a length up to 1 μm. Two types of GST NWs were identified: i) "big" NWs, featured by mean cross size > 50 nm and aspect ratio (AR = length/mean width) distribution centered around 5 and ii) "small" NWs, featured by mean cross size < 50 nm and AR distribution centered around 12. Measurements indicated that GST NWs are compatible with both the Ge₁Sb₂Te₄ and Ge₁Sb₄Te₂ compositions and crystallographic phases.

The typical diameter of the GeTe NWs resulted to be around 50 nm and their length up to 4 μm. The structural measurements showed that both the cubic and rhombohedral crystalline phases of GeTe are present in the obtained NWs, whereas the compositional analyses yielded a Ge₃₆Te₆₄ composition. In particular, TEM observations revealed that the *fcc* wires are single crystals, 110 oriented.

NS-TuP19 Folate Functionalized Hollow Silica Nanoshells: Synthesis, Characterization and Application as an Intracellular Delivery Container. *A. Liberman, S. Sandoval, J. Yang, S. Aschemeyer, J.G. Alfaro, D. Martin, M. Makale, A.C. Kummel, W.C. Trogler, University of California, San Diego*

An important area of biomedical nanotechnology is based on the interaction of living systems with inorganic and organic materials at the nanoscale. Silica nanospheres (NS) are attractive biomaterials because of their advantages as readily functionalized transport and imaging devices: the porous amorphous structure of silica colloid allows small molecule storage; the surface of silica can be modified easily with trimethoxysilyl reagents; silica has low biotoxicity and good biocompatibility. Silica nanospheres potentially have multiple biomedical applications as imaging agents, targeted drug delivery agents or gene transferring motherships. A simple method to fabricate hollow silica nanospheres with 100 nm or 200 nm diameters has been developed and tested. Amino polystyrene beads were used as templates and a 5-10 nm thick silica gel coating was formed by the sol-gel reaction. After removing template by calcinations, porous dehydrated silica gel nanoshells of uniform size were obtained. The porous structure of silica shell wall was characterized by transmission electron microscopy measurements, while particle size and zetapotentials of the particles suspended in aqueous solution were characterized by dynamic light scattering. The surfaces of the NS have been functionalized with folic acid in order to specifically target cancer cells. Folic acid, also known as vitamin B₉ or Folate, is essential for the synthesis of nucleotide bases and binds with high affinity to Folate receptors, which are frequently over-expressed in tumor cells and epithelial lineaged tumors such as ovarian carcinomas. With the use of confocal and two-photon microscopy, it was found that as the amount of folate on the surface of the NS was increased, a higher amount of NS endocytose into HeLa cancer cells, a cervical cancer cell line. Cytotoxicity studies will quantify the effectiveness of using folate coated silica shells for enhancing endocytosis of chemotherapy drugs in cell lines and in animal studies.

NS-TuP20 New Insights to Coarsening Phenomena and Nanoparticle-Mediated Surface Patterning: Pt/TiO₂(110). *F. Behafarid, A. Naitabdi, B. Roldan, University of Central Florida*

Two technologically important aspects for the applications of metal nanoparticles in the fields of catalysis, molecular electronics, and plasmonics are discussed here: (i) the influence of the nanoparticle synthesis method and support morphology on thermally-driven coarsening phenomena, (ii) the high-temperature growth of oxide nanowires with tunable width, orientation, and spacing seeded by micellar metal nanoparticles (NPs). Along those lines, a comparison of the mobility of evaporated Pt NPs supported on pristine TiO₂(110) and on polymer-

modified TiO₂(110) and micelle-based Pt NPs is established. To gain additional insight into the NP coarsening mechanisms, simulations were conducted following the two most coarsening routes: (i) diffusion-coalescence, and (ii) Ostwald ripening. Some changes were introduced in these models to guarantee the correct temperature dependence and proper energetics in the diffusion model, and a new formulation of the critical radius in the Ostwald ripening model is introduced to satisfy the mass balance without the need to use very small time steps.

Furthermore, the growth of TiO₂ nanowires at high temperature starting from micellar Au and Pt nanoparticles supported on TiO₂(110) is discussed.

NS-TuP21 Some Effects of Iron Doping on Titanium Dioxide Nanoparticles. *D. González-Sánchez, J.L. González-Solis, G. Toriz, C.R. Michel-Urbe, G. Gómez-Rosas, A. Pérez-Centeno, M.A. Santana-Aranda, Universidad de Guadalajara, Mexico*

Iron doped titanium dioxide nanoparticles were synthesized using the sol-gel method. Solution was prepared in propanol, diluting Tween 80 surfactant (as pore directing agent), acetic acid and finally titanium tetrapropoxide (TTP); constantly stirred with a motor driven Teflon® palette. Doping iron was introduced by dissolving iron (III) chloride in propanol and adding to the solution; in the required amount to obtain 0.25; 0.5; 0.75; 1.0; 1.25 and 1.57 mol% iron with respect to titanium. Employed proportions of Tween80/PrOH/acetic acid/TTP were defined mostly following the values reported by Dionysiou's group on pure TiO₂ [1]. We obtained nanoparticles with sizes around 9 nm; being larger for lower iron content and smaller for higher iron content, as observed by electron microscopy and calculated from the full width at half maximum (FWHM) of X ray diffraction peaks, using Scherrer's formula. Raman spectroscopy and X ray diffraction measurements showed the presence of additional features, possibly related to a foreign phase into an almost pure anatase powder, increasing along with iron content.

[1] H. Choi, E. Stathatos, D.D. Dionysiou, Thin Solid Films 510 (2006) 107.

Aknowledgements: Authors want to thank the technical assistance of Gabriel Ramos Romo and Dr. Israel Ceja Andrade; as well as the financial support from UdeG (under program pro-SNI) and PROMEP (under project 103.5/07/2636).

NS-TuP22 Study on High-Current-Density CNT Field Emitter: Current Enhancement with Titanium Micro-powders. *V. Chouhan, The Graduate University for Advanced Studies, Japan, T. Noguchi, KEK-High Energy Accelerator Research Organization, Japan, H.R. Liu, Mie University, Japan, S. Kato, KEK-High Energy Accelerator Research Organization, Japan*

CNT film field emitters (FFE) with a high current density up to a couple of 100 A/cm² and a high total current up to 100 mA are applicable to electron sources such as accelerators and high intensity X-ray sources for medical and security examinations. Based on our previous work of FFE, it turned out that one of the most crucial factors for high current and long time operation is to select appropriate CNT junction and substrate materials so as to maintain high thermal and electric conduction with high tensile strength. Our FFE was prepared by dispersing MWCNTs over a titanium film deposited on a metallic substrate by magnetron sputtering technique followed with rooting of MWCNTs into the titanium film at high temperature. In this study, use of titanium micropowders was attempted to sprinkle on the dispersed MWCNTs. This powder would allow to enhance reaction for better carbide formation. This paper describes the detailed procedures and the experiments to achieve the high emission current density from the FFE.

NS-TuP23 Role of the pH Obtaining Microstructures and Size-Controlled SnO₂ Nanocrystals by the Precipitation Method. *C.E. Marín-Pineda, M.A. Santana-Aranda, C.R. Michel-Urbe, G. Gómez-Rosas, Universidad de Guadalajara, Mexico, O.E. Contreras-López, Universidad Nacional Autónoma de México, A. Pérez-Centeno, Universidad de Guadalajara, México*

In this work we present the results of the pH effect on the synthesis of SnO₂ by precipitation. This simple chemical route allowed us to obtain SnO₂ nanocrystals whose grain size depends linearly on the pH, ranging from 3 to 8nm, from basic to acid solutions, respectively. The most important, microstructures were also fabricated by this simple method, mainly whiskers and long fibers. The crystalline quality and the morphology were confirmed by X-ray diffraction and electron microscopy. The samples showed high-energy optical absorption as observed by UV-Vis measurements.

Aknowledgements:

The technical support of Israel Gradilla and Francisco Ruiz are greatly acknowledged. This work was partially supported by PROMEP (projects

103.5/07/2636 and 103.5/08/2919) and COECYTJAL (project PS-2009-873).

NS-TuP25 Nanoscale Roughness Analysis through System Evaluation by Atomic Force Microscopy, *C.Y. Su, Y.H. Lin, S.S. Pai, P.L. Chen, N.N. Chu, C.C. Yang, C.C. Chen, M.H. Shiao*, Instrument Technology Research Center, NRL, Taiwan, Republic of China

Atomic Force Microscopy (AFM) has become an essential tool in various applications of nanotechnology. Although roughness inspection is one of the most important and most common measurement since scanning probe microscopes (SPMs) have been invented, there is lack of international comparison on this application and it is in the early stage of prototype testing up to now. By combining a high precise three-axis closed-loop feedback scanner stage with the AFM, the mapping capability of surface roughness distribution from the sample topography with the sub-angstrom resolution is achievable. In this study, a procedure has been designed to optimize AFM parameters such as inspection area size, target amplitude, drive frequency, set-point, scan rate, integral gain, proportional gain, look-ahead gain and so forth for optimized surface roughness inspection. System evaluation of the measurement uncertainty is compliant to ISO, Guide to the Expression of Uncertainty in Measurement and ISO 5436-2:2001/Cor 2:2008, Geometrical Product Specifications (GPS) - Surface texture: Profile method; Measurement standards - Part 1: Material measures. Key factors such as repeatability, non-linearity, straightness, noise, probe deformation error, numerical error, system long-term stability and sample uniformity have been included for evaluation. By carefully control of probe deformation error, measurement uncertainty can be suppressed effectively.

NS-TuP26 Absorption based Model of Porous Silicon Photoluminescence, *C.G. Lowrie, S.B. Earles*, Florida Institute of Technology

Irradiating porous silicon with a 532 nm laser produces a photo luminescent (PL)

peak at 722 nm. This peak corresponds to the (3,1,1) absorption level of a cubic silicon

nanocrystal 3.79 nm in length.

NS-TuP27 Comparative Study on the Properties of ZnO Nanowires and Nanocrystalline Thin Films, *E. Broitman*, Carnegie Mellon University, *C. Bojorge*, CINSO-CITEFA-CONICET, Argentina, *F. Elhordoy, V. Kent*, Universidad de la Republica, Uruguay, *G. Zanini Gadioli*, Carnegie Mellon University, *R.E. Marotti*, Universidad de la Republica, Uruguay, *H. Canepa*, CINSO-CITEFA-CONICET, Argentina, *E.A. Dalchiale*, Universidad de la Republica, Uruguay

Nanostructures made of wurtzite ZnO, such as dots, nanobelts, nanowires, and nanocrystals, have recently attracted attention due to their proposed applications in electronic and optoelectronic devices. Here we present a comparative study on the properties of ZnO thin films containing nanocrystals and nanowires.

ZnO nanocrystalline (NC) films, obtained by the sol-gel process, were deposited from a precursor solution using zinc acetate dehydrate in ethyl alcohol. After a four-layer spin-coating on crystalline substrates, the films were transformed into nanocrystalline films by a thermal treatment at 370 °C during 3 hours. ZnO nanowires (NW) were electrochemically grown onto a ZnO seed layer sol-gel spin-coated using a conventional three electrode cell, with the substrate as the cathode, a Zn sheet as the counter electrode and a saturated calomel electrode (SCE) as the reference one. The electrolyte was an aqueous solution of the Zn²⁺ precursor (1 mM zinc acetate) and a supporting electrolyte (0.1 M sodium acetate), saturated with bubbling oxygen. The electrodeposition was carried out at 70 °C under potentiostatic conditions at two different potential values (-0.900 and -1.000 V vs. SCE) and during 70 min. The initial pH was adjusted to 6.76. Both, NC and NW samples, were deposited onto crystalline quartz substrates covered by a Au or Ag electrode, and ready to use in a quartz crystal microbalance (QCM).

Samples microstructure was characterized by X-ray Diffraction (XRD), Scanning Electron Microscopy (SEM), and Optical Diffuse Reflectance Spectroscopy (DRS). XRD measurements show in both cases a typical diffraction pattern of ZnO wurtzite structure. SEM micrographs of NC films have a smooth surface, while the NW sample reveal the presence of nanowires with hexagonal section and diameters ranging from 40 to 100 nm. No specific structure was observed by the DRS measurements on the seed layer, probably due to the fact that these films were not thick enough as required by the technique. For the NW onto seed layer samples, the optical characterization reveals the presence of ZnO with bandgap energy between 3.22 eV (for the ones grown onto Au metallic contacts) and 3.29 eV (for the Ag metallic contacts).

A QCM placed in a vacuum chamber was used to measure the water adsorption of the samples. Water vapour was introduced through a leak valve while a capacitance manometer was used to measure the partial pressure of water in the range 10¹-10⁵ Pa. The mass of water adsorbed on the surface of the quartz crystal was calculated using the Sauerbrey equation. The NW drastic increase of the surface area was revealed through a higher amount of water adsorption.

NS-TuP28 Effects of Surface-Sulfurization on Field Emission Characteristics of Al-doped ZnO Nanorods, *T. Hirate, T. Kaneshiro, T. Satoh*, Kanagawa University, Japan

ZnO is a promising material for ultraviolet (UV) and white light-emitting diode (LED) applications, because of its large exciton binding energy of 60 meV relative to the thermal energy of 25 meV, as well as its large band gap of 3.37 eV at room temperature. In the past several years, the fabrications and characterization of one-dimensional ZnO nanostructures have been extensively investigated for their applications, such as LEDs, gas sensors, field emission devices, nanolasers and photovoltaics. We have studied on application of vertically aligned ZnO nanorods grown by CVD to field emission devices. In this paper we report on surface-sulfurization of Al-doped ZnO nanorods and the effects on the field emission characteristics.

Al-doped ZnO nanorods are grown by low-pressure thermal CVD cooperated with 10Hz Nd-YAG pulsed laser ablation of Al₂O₃ target, which is developed by us. Precursors for CVD are Zn vapor and O₂. Substrates are n-Si(111) wafers. ZnO nanorods are grown in two stages. In first stage of growth no laser ablation is used to grow aligned ZnO nanorods and in second growth stage laser ablation is used to grow Al-doped ZnO layer on ZnO nanorods grown in 1st stage. Concentration of Al in ZnO nanorods is controlled by laser power. Finally surface-sulfurization is performed in H₂S atmosphere. It is revealed that the conditions of sulfurization have very complex effects on field emission characteristics. An example of the conditions are 39.6 Pa of H₂S partial pressure, 550 °C and 5 min. Field emission characteristics are measured in vacuum of 10⁻⁴ Pa using 12.7mm diameter metal ball as anode electrode with separation of 160 micron meter.

When laser power is high (2.0W), the low initial electric field of 4 V/micron meter for emission is obtained. In this case, however, ZnO nanorods with sharp tips are grown due to high laser power, thus the reason of improvement of field emission characteristics is not clear at present. We are studying on this point. We estimate that the surface-sulfurization of ZnO nanorods are effective to improve the field emission characteristics because the electronic affinity of ZnS is lower than ZnO.

Plasma Science and Technology

Room: Southwest Exhibit Hall - Session PS-TuP

Plasma Science and Technology Poster Session

PS-TuP1 Etching Characteristics of Ge₂Sb₂Te₅ in Chemical Effects for the Phase-Change Memory Applications, *J.T. Cheong, H.M. Lee, J.S. Yang, H.C. Jung, H.C. Lee, Y.S. Sohn, H.S. Kang*, Hynix Semiconductor

The present study aims at providing the fundamental data with respect to GST(Ge₂Sb₂Te₅) composition and GST damage depending on etch conditions. GST etching in this study was processed by changing etchants. By Cl₂ based GST etching, it was found that, there appeared degradation in the surface roughness due to GST damage, which is identified by XRD(x-ray diffraction) as an unknown phase different from FCC or HCP phases of GST, As for the sample etched by using CF₄ of high ratio and Ar gas, the GST were found damage area where Ge and Sb were deficient in stoichiometry. Meanwhile, GST etch by CF₄ of low ration and Ar gas exhibited the good results of this study, we have demonstrated the damage-free GST etching, which will be applicable for the Phase-Change Memory device.

PS-TuP2 Etch Characteristics of TiN for Metal/High-k Gate Stack using Inductively Coupled Plasma, *J.-S. Park, J.-C. Woo, C.-I. Kim*, Chung-Ang University, Republic of Korea

The ultra thinned body fully depleted silicon on insulator (UTB-FD SOI) is the solution to problems of short channel effect by shrinking the gate length. This device has many advantages of high drive current, high conductance and ideal sub threshold slope^{1,2}. This device uses the TiN/HfO₂ gate stack. The metal/high-k stack structure is being the core technology because reduction of device is faced with physical limitations.

So, we have to study about this metal/high-k stack³.

In this study is investigated the dry etching characteristics of the TiN in the TiN/HfO₂ gate stack using inductively coupled plasma system. TiN thin

film is etched by $\text{CF}_4/\text{Cl}_2/\text{He}$ plasma. We investigate the etching chemistry of the CF_4/Cl_2 gas mixture. Etching parameters are gas mixing ratio, the RF power, the process pressure in this study. The chemical reactions on surface of the etched TiN and etched HfO_2 are investigated by X-ray photoelectron spectroscopy. The profile of the etched TiN is investigated by Scanning electron microscope.

Reference

¹S. Mukhopadhyay, K. W. Kim, X. Wang, D. J. Frank, P. Oldiges, C. T. Chuang and K. Roy, *IEEE* 27(4), 284 (2006)

²S. Eminent, S. Cristoloveanu, R. Clerc, A. Ohata and G. Ghibauda, *Solid-state Electronics* 51(2), 239 (2007)

³D. P. Kim, X. Yang, J. C. Woo, D. S. Um and C. I. Kim *J. Vac. Sci. Technol. A* 27(6) 1320 (2009)

PS-TuP3 Etch Characteristics of HfAlO_3 Thin Films in High Density Plasma, T.-K. Ha, J.-C. Woo, C.-I. Kim, Chung-Ang University, Republic of Korea

With the permanent scaling down of complementary metal oxide semiconductor (CMOS) devices, the thickness of the gate oxide is expected to be reduced to less than 1 nm for the 45 nm and 32 nm technology nodes. Continuing to reduce the gate insulator thickness using SiO_2 is problematic as gate leakage current due to direct-tunneling increase.^{1,2} One solution to the problem is the replacement of SiO_2 by high- k material. HfAlO_3 have arisen as a promising material for gate oxide replacement due to their high dielectric constant, bandgap, and recrystallization temperature. Therefore, a further on the study of HfAlO_3 thin films is needed.³

In this work, HfAlO_3 thin films were etched in BCl_3/He plasma. The etching characteristics of HfAlO_3 thin films were investigated in terms of etch rates and selectivity as a function of gas mixing ratio, RF power, DC bias voltage, and chamber pressure. The total flow rate of BCl_3/He was fixed at 20 sccm. The other parameters were varied as follows; RF power = 400 ~ 600 W, DC-bias voltage = - 50 ~ - 200 V, process pressure = 1 Pa ~ 3 Pa. The plasma diagnosis was characterized by optical emission spectroscopy (OES) analysis. The chemical reaction on the surface of the etched HfAlO_3 thin films was investigated with X-ray photoelectron spectroscopy (XPS). Field emission scanning electron microscopy (FE-SEM) was used to investigate the etching profile.

Reference

¹G. D. Wilk, E. M. Wallace, J. M. Anthony. *J. Appl. Phys.* 89, 5243 (2001).

²A. I. Kingon, J. I. Maria, S. K. Streiffer, *Nature* 406, 1032 (2000).

³W. J. Zhu, T. Tamagawa, M. Gibson, T. Kurukawa, and T. P. Ma. *IEEE Electron Device Letters* 23, 649 (2002).

PS-TuP4 The Dry Etching of ITO Thin Films on Glass for Flat Panel Displays, J.H. Wi, J.-C. Woo, C.-I. Kim, Chung-Ang University, Republic of Korea

Amongst the most widely employed thin films in Flat Panel Displays (FPDs) belong to the described as Transparent Conducting Oxide (TCO) materials. When the thin films were applied for devices, etching characteristics is important process factor due to availability of patterning is directly linked with productivity. The TCO materials should have to proper etching characteristics for transparent electrode¹. By far the most common industrially employed TCO is Indium Tin Oxide (ITO), which is more correctly described as Sn-doped In_2O_3 . An n-type semiconductor, it offers an optimum performance in terms of conductivity and transparency. In order to utilize properties of thin films such as ITO it is usually necessary to pattern them to create functional structures. The conventional method for patterning is to use wet chemical etch process. Such techniques require multiple process stages, large expensive machinery, small-geometry patterning².

In this study, the relationship between patterning characteristics and other characteristics which depend on etch conditions, especially the RF power, the DC bias voltage, the process pressure, was investigated in ITO films etched by the inductively coupled plasma (ICP) system³. The analysis of x-ray photoelectron spectroscopy (XPS) was carried out to investigate the chemical reactions between the surfaces of ITO thin films and etch species.

References

¹Z. Wang, S. Naka, H. Okada, *Thin Solid Films*, 518 (2009) 497.

²C.J. Huang, Y.K. Su, S.L. Wu, *Materials Chemistry and Physics* 84 (2004) 146.

³J.C. Woo, D.S. Um, C.I. Kim, *Thin Solid Films* 518 (2010) 2905

PS-TuP5 Effect of N_2/Ar Flow Rates on Surface Roughness during High Speed Thinning of Si Wafer using F Radicals and NO Gas, W. Heo, N.-E. Lee, Sungkyunkwan University, Republic of Korea

In this work, we investigated on evolution of the surface roughness and morphology of thinned Si surface and die strength of thinned Si during high-speed chemical dry thinning of Si wafers ground by chemical mechanical polishing down to 100 nm. The direct injection of NO gas into the reactor during the supply of F radicals from NF_3 remote plasmas was very effective in increasing the Si thinning rate above 22.8 mm/min, due to the NO-induced enhancement of the surface reaction, but resulted in the significant roughening of the thinned Si surface. However, the addition of directly-injected N_2/Ar gas, together with NO gas, decreased the root mean square (RMS) surface roughness of the thinned Si wafer significantly. Therefore, rough surfaces of mechanically ground Si wafers could be effectively smoothed by adjusting the additive gas flow rates of N_2/Ar during chemical dry thinning of the Si thickness larger than 50 nm. We also measured mechanical strength of thinned Si wafer in order to understand the effect of chemical dry thinning on removal of mechanical damage generated during mechanical grinding. Fracture strength of the thinned Si wafers was measured using 3-point bending test and compared. The results indicated that chemical dry thinning with reduced surface roughness and mechanical damage effectively increased the fracture strength of the thinned Si wafer. It is expected that high-speed dry chemical thinning process has possibility of application to ultra-thin Si wafer thinning with controlled surface roughness and mechanical damage removal after mechanical grinding of silicon wafer.

PS-TuP6 Modelling of the Silica Glass Etching under ICP SF_6/Ar Plasma Discharge, L. Lallement, A. Rhallabi, M.C. Fernandez, C. Cardinaud, Institut des Matériaux Jean Rouxel, France

Quartz or pure fused silica is selected material for the fabrication of biochip devices and more specifically electrophoresis chips. Indeed, these materials benefit from transparency in the UV-visible range, and low dielectric breakdown. However material cost is higher in comparison to silica glass which offers similar properties with a low purity degree. Plasma deep etching techniques are well established for fused silica and quartz, but much more challenging for glass. In the present study, the etching simulator has been developed to study the etching of silica glass (Pyrex, D263, AF45, and Vycor) in SF_6/Ar plasma. The etching model is based on the development of the plasma kinetic model coupled to 2D Monte Carlo surface model to predict the etched surface morphology of glasses as a function of the operating conditions.

The gas phase kinetic model is based on the mass balance equations of reactive species. The kinetic constants of electron impact reactions are established as a function of electron temperature assuming Maxwellian distribution of electron energy. The additional equation of power balance in the ICP reactor allows to determine the electron temperature evolution with the plasma discharge parameters (RF power, reactor pressure and SF_6/Ar flow rates).

Langmuir probe is used to measure the electrical parameters of SF_6/Ar plasma mixture such as, electron temperature and density as a function of the plasma discharge parameters. A good agreement between the simulations and the experiments have been observed

One of the advantages of our model is the coupling between the plasma chemistry model and the surface etching model. The later is based on the Monte-Carlo approach which allows to describe, in a probabilistic manner, the surface mechanisms for silica glass etching.

The direct fluxes of the reactive species such as fluorine and ions are determined from the gas phase kinetic model and introduced as the input parameters in the glass etching model.

On the other hand, surface analyses such as the etch rate, surface roughness (profilometry), and surface topography (AFM) of silica glass as a function of operating conditions have been carried out.

The preferential redeposition mechanism of the etched products on the metallic sites seems to play an important role on the propagation of the etched surface roughness. A satisfactory agreement between experimental results and the model concerning the etching rate and the etched surface morphology have been obtained for different glasses.

PS-TuP7 Impact of Neutral Particles Ballistic Delivery Upon Sidewall Profile Formation During Dry Etching, S.I. Yanovich, V.A. Khrustalev, O.P. Gushchin, A.M. Islyaykin, E.V. Danilkin, S.I. Patyukov, A. Smirnov, Mikron JSC, Russia

Dry etching is a key process for topology formation and integrated circuit layers layout transfer on to a semiconductor substrate. Forced by Moore's law challenging demands dry etching technique was improved drastically for the decades. Development of fundamental plasma processing knowledge provides technical staff with the ideas for their engineering efforts in getting

the right hardware supported by right process recipe. Nevertheless there is still a room for further dry etching process development to fit the requirements of a variety of particular silicon, compound semiconductors, MEMS, fluidics and other application.

This paper presents an extension of a general model for plasma dry etching process in respect of impact of neutral particles delivery to the substrate surface and its influence on final window profile depending on window linear dimension. It is found that different size windows may have different side wall slope and bottom profile within the range of windows that might be present at actual IC layout of quarter micron mode and beyond. In many cases such a difference of etched profiles it is considered that neutral particles lateral delivery sheltering is responsible.

This effect is intrinsic for different dry etching processes including silicon dioxide etch, silicon etching, aluminum and its alloys etch. Sloping sidewall profile for larger lateral dimension of etched window may be considered both as advantage and disadvantage depending on each particular case. And therefore it is important to review precisely each case of window size extension or isolated element location and the elements located at array edge as well.

PS-TuP8 Using Pulsed Bias to Explore 2 μm AR 25:1 TSV, M. Kostermans, IMEC, Belgium, M. Brouri, Lam Research Corporation, Belgium

Since traditional 2-D planar architecture of ICs inevitably imposes restrictions on miniaturization, new interconnection and packaging technologies need to be developed to keep on track with the continuously scaling of electronic systems. 3-D integration is an interesting solution since it allows for reduction of the system size, both in area and volume. Furthermore, it improves performance since 3-D interconnects are shorter than traditional interconnects in a 2-D configuration, enabling a higher operation speed and smaller power consumption.

Plasma processing for dry etch purposes traditionally rely on a few basic parameters, allowing control of the discharge physics and chemistry: plasma power, substrate bias, flow of different gases, total gas flow, discharge pressure. In order to ensure a reliable pattern transfer, a basic requirement for the etch mechanism is to provide anisotropy. This means that patterned features usually need to be etched with vertical sidewalls, i.e. as little undercut/bowing/slope as possible. This can only be achieved, on one hand, by carefully tuning the plasma chemistry, in order to provide passivating species that will deposit on the feature sidewalls and protect them, and on the other hand by controlling the ion energy, which contributes to the removal of this passivating film on horizontal surfaces.

Another possibility to influence plasma characteristics is by pulsing the substrate bias power at different frequencies and duty cycles. Although deep Si via processes have been developed using this technology, little is known on the influence of the pulsing on etch rates, film selectivities, polymerisation curves, ... for state-of-the-art processes. For this study bias pulsing frequencies with different duty cycles are employed, in addition to the traditional deposition and etch Bosch cycles. The first step is C_4F_8 based and acts as a deposition step which passivates the via bottom and sidewall and enhances the resist selectivity. The second step, using SF_6 , is the actual etch step.

This study investigates the use of pulsed bias applied to the development of 2 μm diameter vias with an aspect ratio up to 25:1 taking into account profile, resist selectivity, roughness, bowing ... When varying the pulsing settings an impact on profile slope and resist selectivity is observed.

The resist based etch development was done on a ICP etch chamber optimised for deep Si etch (Lam Research 2300®Syndion®). The process used in the ICP etch chamber consists of two fast switching steps that are continuously repeated. To enable subsequent metallisation, these vias need to meet strict requirements.

PS-TuP9 Highly Selective and Low Damage Etching of TiN on HfO_2 Layer Gate Stack Structure using HBr/Cl_2 Neutral Beam, J.K. Yeon, W.S. Lim, Y.Y. Kim, B.J. Park, G.Y. Yeom, Sungkyunkwan University, Republic of Korea

As the critical dimension of metal-oxide-semiconductor field-effect transistor (MOSFET) shrinks to 45 nm and below, conventional poly silicon gates on ultrathin SiO_2 dielectric layers need be replaced by metal gates on high-k dielectric materials. However, the successful adoption of these new materials imposes new integration problems. Among many integration issues, selective etching of metal gate electrodes and the high-k gate dielectrics over the Si substrate is expected to be one of the critical steps in the process integration of the front end of the line. In the case of TiN etching on HfO_2 layer using conventional RIE etching, HfO_2 layer can be electrically damaged by charged particle leading to higher leakage current, the change of threshold voltage, etc. In order to solve these problems, in this study, we investigated etch characteristics of TiN on HfO_2 layer using low

angle forward reflected neutral beam and compared with those by conventional RIE etch process.

As a result, we observed nearly unlimited etch selectivity of TiN/ HfO_2 using HBr/Cl_2 gas mixing neutral beam by controlling energy (<100 eV). Also, using TEM and AFM, we observed an anisotropic etch profile and smooth surface roughness (0.109 nm). Neutral beam for metal gate etching process turns out to be very promising for gate/high-k dielectric complementary MOSFETs due to lower interface trap generation during etching process.

PS-TuP10 Atomic Scale Etch Depth Control and Low Damage Etching of III-V Compound Materials using Cl_2 Atomic-Layer Etching, Y.Y. Kim, W.S. Lim, J.K. Yeon, T.H. Kim, G.Y. Yeom, Sungkyunkwan University, Republic of Korea

III-V compound materials have been used for the devices such as high electron mobility transistors (HEMTs), light emitting diodes (LEDs), and quantum dot (QD) devices due to its excellent material properties including high carrier mobility, wide operating temperature range, direct energy band structure, etc. For the fabrication of these III-V compound materials devices, reactive ion etching techniques such as capacitively coupled plasma etching, inductively coupled plasma (ICP) etching, etc. are generally applied to obtain anisotropic etching properties. However, due to the energetic reactive ions involved in the reactive ion etch process, the surface of the etched III-V compound materials tends to be damaged physically and chemically by structural disruption, intermixing, stoichiometric modification, surface roughening, etc. In addition, it is difficult to control the etch depth precisely through the reactive ion etching due to the fluctuation of the etch process. To overcome these problems, various atomic layer etching techniques (ALETs) have been investigated especially as the application to the nano-device processing which requires atomic-scale precision in the etching in addition to the nearly no-damage to the surface during the etching.

The etch characteristics of III-V compound materials by ALET were investigated using a Cl_2 -based ALET. The effect of ALET on surface modification and etch-depth control was also examined. Self-limited etching of III-V compound materials could be obtained using Cl_2 ALET. In addition, the significant improvement in the electrical properties of the III-V device could be obtained by etching the damage sensitive layer using ALET.

PS-TuP11 Surface Model for Profile Simulation of SiO_2 Etching in Fluorocarbon Gas Chemistry, T.Y. Yagisawa, T.M. Makabe, Keio University, Japan

As the size of ULSI elements shrinks further, functional design for a top-down plasma processing will be strongly needed in order to solve many types of technological difficulties induced by plasma etching. Actually, under the present design rule for DRAM devices, a contact hole with high aspect ratio (> 20) is required.

The reactive ion etching (RIE) of high aspect contact hole (HARC) or inter layer dielectric has been traditionally performed by fluorocarbon gas chemistry in a two-frequency capacitively coupled plasma (2f-CCP) reactor. As is well known, SiO_2 etching in fluorocarbon chemistry proceeds under the competition of surface protection by the deposition of C_xF_y radicals and chemical sputtering by directional CF_x^+ ions. Under a practical condition for SiO_2 etching where the radical flux is larger than that of ions, a reactive mixing layer (SiO_xF_y), formed under excessive F radicals assisted by high-energy ion bombardment, is always covered with thick polymer layer (C_xF_y). Consequently, the etching is essentially carried out through the removal of polymer layer and the chemical reaction in a mixing layer. The side wall is simultaneously protected against the energetic ions by C_xF_y polymer deposition.

Under the circumstance, we have developed the two-layer surface model for the simulation of SiO_2 etching profile in fluorocarbon gas chemistry. This model clarified the effects of reactive species (ions and radicals) on the SiO_2 etching profile [1] and the dependence of etch rate on the pattern size (RIE-lag) [2].

In this paper, we will propose a new surface model for SiO_2 etching which accounts for the selectivity between SiO_2 and underlying Si substrate in HARC processing. Feature profile evolution and the selectivity during SiO_2 etching can be coincidentally discussed as functions of flux of reactive species and impact ion energy. In addition, the effect of resist mask erosion will also be discussed.

[1] T. Shimada et al, Jpn. J. Appl. Phys. **45**, p. 132, (2006).

[2] T. Makabe et al, Plasma Sources Sci. Technol. **18**(1), #014016, (2009).

PS-TuP12 General Approach to Feature Profile Evolution via Monte Carlo Simulations, P.E. Moroz, TEL US Holdings, P. Miller, HFS

This report will discuss numerical techniques used in the general feature profile evolution simulator FPS-3D. We call it general because it does not have any hardcoded dependencies, such for example, as etch or deposition rates, or dependencies on energy or angle of incident reactive particles (ions as well as neutral radicals and gases). The code thus can be applied to targets consisted of any set of solid materials and exposed to any fluxes of reactive particles with any distribution on energy and angle. Although the code is called FPS-3D, it actually has two options, 2D and 3D, which allow convenient comparison between 2D and 3D results for similar targets and fluxes. The 2D option has advantage of much higher speed of calculations, mainly because the number of cells is typically much smaller and the calculations are simpler than that for 3D, but the 3D option becomes indispensable when the target cannot be approximated by 2D geometry, or when the essentially 3D tasks are considered, such as roughness, for example. The FPS-3D code can comfortably treat up to one million cells, or maybe, a few times of that, depending on the speed of a computer. Correspondingly, the 2D option of FPS-3D allows consideration of a wide range of target sizes, from nanometers to micrometers, as well as treating them in great detail, such for example, as 1000x1000 cells. For the 3D option, a typical run is limited to about 100x100x100 cells, thus leading to each cell containing significantly more molecules than for 2D. One of the main advantages of FPS-3D relative to all other similar software is its GUI-graphics interface based on the TPSOFT package from HFS [1]. This interface is capable of producing high-speed and high-quality 2D and 3D graphics not only for initial parameters, distributions, geometry and fluxes, but also dynamically while the code is running and the feature profile and other parameters evolve, with a unique characteristic of not slowing down the calculations. The authors are thankful to S.-Y. Kang of TEL TDC for valuable discussions.

[1] www.highfactor.com [about:www.highfactor.com].

PS-TuP13 Warm Magnetized Vlasov Emission Equilibria, R.E. Terry, Naval Research Laboratory (retired)

A Vlasov equilibrium is developed for steady state emission into a magnetized gap in coaxial geometry. The cathode boundary conditions are those of a perfect conductor that emits a Maxwellian electron flux radially, azimuthally, and axially. The anode boundary conditions are those of a perfectly absorbing conductor. The cathode carries a fixed current and the radial gap is set to a fixed voltage. The angular momentum of emitted electrons around the cathode is found to materially change the orbit turning points. When energy conserving solutions are examined it is found that axial velocities must remain bounded above by a well defined function of radius, magnetic field, and voltage. A fully nonlinear and self consistent Vlasov-Poisson problem is formulated and solved for the space charge distribution implied by the Vlasov equilibrium. Moments of the Vlasov distribution then determine the shunt impedance of the gap and the criteria for "warm" magnetic insulation of the coaxial line. The theory limits to Ottinger's critical current magnetization picture for cold electrons, but shows a properly non-singular behavior in the electron density profile at the radial turning points and so properly reduces the enhancement of ion flux across the gap. Extensions of the model to include electron impact ionization of neutrals in the gap are also developed.

PS-TuP14 Inductive Plasmas in Cl₂/Ar : Comparison of Hybrid Model Results with Experimental Measurements, J.-P. Booth, E. Despiau-Pujo, R. Sarot, P. Chabert, CNRS-LPP, France, L. Gatilova, S. Bouchoule, CNRS-LPN, France

Inductively-coupled chlorine-based plasmas (often also containing HBr, O₂ and Ar) are widely used in the microelectronics industry for selective, anisotropic etching of silicon, and are currently being investigated for etching of III-V materials such as InP for the fabrication of photonic devices.

We have constructed a reactor, identical in geometry to an industrial 200mm etch tool, but adapted for advanced diagnostics and supplied with Cl₂/HBr/O₂ and Ar gases. It is excited by a flat spiral antenna through a dielectric window. In parallel we are developing a hybrid simulation code based on the HPEM (Hybrid Equipment Plasma Model) of Mark Kushner. Experimental measurements of internal plasma parameters (electron densities, temperatures, and also gas dissociation fraction and temperature) will be used to test and improve the simulation code. The aim is to reliably predict the plasma behaviour as a function of these parameters, and for arbitrary reactor geometries.

The electron density was measured using a microwave hairpin resonator, and with a Langmuir probe. Measurements were made as a function of pressure and power in pure Cl₂ and as a function of composition in Cl₂/Ar mixtures. The electron density decreased from 5x10¹⁰cm⁻³ to 2x10¹⁰cm⁻³ as the Cl₂ pressure was increased from 0.5 to 10 mTorr. The electron density

also decreases monotonically as the Cl₂ fraction is increased in Ar/Cl₂ mixtures. The Langmuir probe measurements of n_e showed the same trend as the hairpin probe, but gave lower values, particularly at the highest pressures and lowest powers and for high Cl₂ fractions.

PS-TuP15 Computer Simulation of a Controllable Electron Beam Exciter, D. Urrabazo, M.J. Goeckner, S. Thamban, University of Texas at Dallas, G. Padron-Wells, University of Texas at Dallas

We have developed a new chemical diagnostic based on a controlled electron beam. Specifically we make use of an inductively coupled plasma, electron extraction optics and traditional optical emission spectroscopy. In the work reported here, we make use of a computer simulation using the Comsol to investigate system characteristic and enhance the system performance. The axially-symmetric spatial distributions of the particle densities and electron temperature are calculated for varying pressure and power regimes. These simulation results will be compared to electrical probe measurements gathered from the experimental apparatus. This work is supported in part by NSF (Grant CBET- 0922962) and Verity Instruments.

PS-TuP16 Numerical Simulations of a Magnetron Plasma Sputtering System using VORPAL, C.M. Roark, C. Zhou, P.H. Stoltz, Tech-X Corporation

Three-dimensional numerical simulations are conducted for a magnetron sputtering plasma and target using the particle-in-cell code VORPAL. These simulations require accurate models of particle dynamics, Monte Carlo collisions and self-consistent electric and magnetic fields. The sputtering yield is calculated for materials commonly used in industrial applications. Sputter patterns are compared with experimental measurements, and in particular, we discuss non-uniformities in the sputter patterns and compare with the cross-corner effect. We also discuss the role of charge exchange and elastic scattering on the sputter patterns.

PS-TuP17 Multivariable PID Control of Oxygen and Fluorine Radicals in an Argon/Oxygen/Fluorocarbon Plasma, B. Keville, M. Turner, A. Holohan, Dublin City University, Ireland

Plasma enhanced processes such as etching are generally run open loop and hence are sensitive to disturbances such as substrate loading, wall effects and matching network drift. The deleterious effect of disturbances on process reproducibility could be mitigated by effective closed loop control of important reactive species in the plasma. The design of effective control algorithms is facilitated by control-oriented models of the causal relationships between plasma species to be controlled and actuators such as flow rate setpoints. For example, it may be demonstrated both experimentally and through simulation that the relationship between oxygen flow rate set point at the mass flow controller and atomic oxygen density in an oxygen plasma may be modelled adequately by a linear second order plus time delay (SOPTD) transfer function. Single input, single output (SISO) SOPTD processes may be controlled very effectively with a Proportional-Integral-Derivative (PID) controller. Suitable parameters for the controller may be determined using well established frequency domain methods such as Pole-placement, root-locus and frequency response, amongst others. Closed loop robustness to unmodelled dynamics, measurement noise and exogenous disturbances may be quantified by stability margins. Simultaneous control of two or more reactive species in a multigas plasma is a vastly more difficult problem due to the inherent multivariable nature of the problem. There are phenomena that arise in multi-input-multi-output (MIMO) systems that do not occur in SISO processes. In particular, due to interaction between variables, instability may arise in a multiloop PID control structure despite each loop being individually stable. Classical, frequency-based SISO design methods do not transfer directly to MIMO systems, and although a number of attempts have been made to adapt classical methods to MIMO systems, MIMO PID control remains relatively immature in comparison to the single variable case. MIMO PID represents a very fertile and active research area and this presentation considers application of current research to the simultaneous control of oxygen and fluorine radicals in an argon/oxygen/fluorocarbon plasma.

PS-TuP18 An Experimental Demonstration of Real-time Closed-loop Control of a Capacitively Coupled Argon Oxygen Plasma, Y. Zhang, B. Keville, A. Holohan, M. Turner, S. Daniels, Dublin City University, Ireland

Plasma processing of materials for advanced manufacturing is a key enabler for synthesis of nanoelectronic systems. In mainstream IC manufacturing, plasma processing is routinely used in etch and deposition steps. However, ensuring process repeatability and reproducibility is a major challenge for the IC manufacturing industry. Processing tools are, in general, run in open loop control mode and plasma parameters such as ion flux and radical densities at the substrate surface are sensitive to drift in tool subsystems,

changes in wall condition and wafer loading, for example. Disturbances to key plasma parameters may affect process metrics such as etch depth and anisotropy and result in a significant degradation in device yield and performance. Hence, process reproducibility may be improved significantly by effective closed loop control of the plasma process.

In this work we present an experimental demonstration of closed loop control of a capacitively coupled Ar/O₂ plasma using an optical emission spectrometer and a hairpin resonance probe as sensors. Design of the control algorithm is facilitated by a process model, which has been derived from a physics-based model and validated by taking step responses experimentally. The efficacy of the algorithm is demonstrated by setpoint tracking and disturbance rejection over a range of operating points.

PS-TuP19 Real Time Closed Loop Control of Plasma Processing. *B. Keiville, M. Turner, S. Daniels, Y. Zhang, A. Holohan*, Dublin City University, Ireland

In general, real time, closed loop control of plasma assisted processes has not been applied in IC manufacturing. In the case of etching, 'process control' is generally understood to mean ex situ statistical analysis of metrics such as etch depth, uniformity, anisotropy and selectivity and consequent adjustment of the process recipe, which is specified in terms of inputs such as gas flow rates, forward power and pressure. An alternative approach would be to specify a recipe in terms of plasma parameters such as ion fluxes and radical densities at the wafer surface and to regulate these in real time by adjusting the inputs with a suitable control algorithm. Such an approach would mitigate potential plasma process disturbances such as wall seasoning and substrate loading, leading to an improvement in process reproducibility. This presentation describes how suitable control algorithms for low pressure plasma processes may be derived from control-oriented process models. The stability and efficacy of the control algorithms are demonstrated using an plasma simulation. Some parameters of the control algorithm depend on unknown, possibly time-varying process parameters such as wall sticking coefficients. The presentation indicates how, given a process model and process measurements, the control algorithm may be adapted/gain-scheduled in order to maintain stability. Experimental implementation of control algorithms on a capacitively coupled plasma is presented and the results are compared to those of the simulation.

PS-TuP20 Adhesion Improvement of DLC Films on Polymer Substrates. *S.-M. Baek, T. Shirafuji, S.-P. Cho, N. Saito, O. Takai*, Nagoya University, Japan

Recently, diamond-like carbon (DLC) films have been performed on polymer substrates for improving scratch resistance and gas barrier properties. However, the DLC films deposited directly on polymers often encountered the problem of poor adhesion, which can reduce the performance of the DLC films. Low adhesion of the DLC films is recognized as a consequence of a residual stress due to high atomic density in comparison to polymers. Plasma pre-treatment is one of the most effective methods to modify the top surface of polymers involving surface cleaning, ablation and surface chemical functionalization. Since the bonding states of the interface are formed at the initial stage of the film growth, the adhesion strength of the films is controlled by the condition of plasma pre-treated surface. However, there have been few reports that directly dealt with the relation between the interface properties and adhesion of the DLC films.

In this study, the DLC films have been prepared on polyethylene terephthalate (PET), polycarbonate (PC) and (PMMA) substrates using a pulse biased ICP-CVD method. Plasma pre-treatments using Ar, O₂, CO₂, N₂ and CH₄ gases were performed on polymer substrates prior to DLC (non-doped, Si-doped, and oxygen-doped) coatings. The plasma pre-treated surfaces have been investigated by XPS and FT-IR ATR. The adhesion of the DLC films on polymer substrates has been characterized with a scratch test method. The scratched areas have been observed with optical microscope and SEM. Regarding the adhesion on the PET, at this moment, the doping oxygen in the films and the plasma pre-treatment have shown no effects on the adhesion of the DLC films. On the PC, on the other hand, the oxygen incorporation in the Si-doped DLC films has resulted in the enhanced adhesion of films. Furthermore, formation of the interfacial layer with N₂-plasma pre-treatment has markedly increased the adhesive strength of the DLC films on the PMMA.

Since the nitrogen atoms or NH bonds are considered to be a key factor to improve the interfacial adhesion properties, we have examined formation of the Self-Assembled Monolayer (SAM) which has NH groups at the top of the SAM. The SAM is composed of a bundle of relatively long molecular chains. Thus, we can expect the SAM layer to have mechanical flexibility. This will bring about further improvement of the adhesion properties of the DLC films, such as prevention of film-peeling due to thermal history, which is now under investigation.

PS-TuP22 2m Long-Linear Plasma Production by Microwave in a Narrowed Rectangular Waveguide with a Long Slot Antenna. *H. Shindo, Y. Kimura*, Tokai University, Japan

Long line-shaped plasmas are inevitable in material processing in manufacturing industries, such as solar cell film CVD, flat panel displays (FPDs), and various surface modification of large-area thin films. In this work, a newly proposed method of large-scaled line plasma production is studied. In this method, microwave power of frequency of 2.45 GHz in a narrowed and flattened rectangular waveguide is employed to produce a long uniform line plasma. Since the width of waveguide is very close to the cutoff condition, the wavelength of microwave inside the guide is very much lengthened, providing a condition of long line high density plasma with a great uniformity.

The narrowed rectangular wave-guide of 1.0 and 2.0 m in length and 5mm in height were prepared and the width of the waveguide is 62.0 to 61.5 mm which is very closed to the cut-off condition. The waveguide has a long slot on the top surface to launch the micro-wave into the discharge plasma chamber of 1.0 and 2.0 m in length. At the end of wave guide, a short plunger was equipped to adjust the phase of the standing microwave, hence the uniformity of the plasma thus produced. The plasmas of Ar at the pressures of 100 to 500 mTorr were produced by employing an extremely long microwave wavelength. The plasma thus produced was three-dimensionally measured by a Langmuir probe.

The axial profile of electron density in the plasma thus produced was quite flat and as the microwave power is increased, the uniformity becomes improved. In particular, the uniformity within 4 % was attained in the entire plasma of 2 m in length in the condition of microwave power above 1000 W. This kind of uniform linear plasma production showed a threshold in the microwave power, above which the electron density becomes high enough above the cut-off density of microwave of 2.45 GHz. It was also found that the profile of electron density was adjustable by the short plunger. To be specific, the electron density measured at a fixed Z position showed a standing wave-like profile, indicating the short plunger has functions of standing wave generation as well as the phase-shifter as expected. Thus we conclude that the present method of large-scaled linear plasma production is quite advantageous for large area processing.

PS-TuP23 A Study on the Characteristics of Multi-Hole Electrode RF Capacitive Discharge and its Application to Large Area Process. *H.S. Lee, Y.S. Lee, H.Y. Chang*, KAIST, Republic of Korea

Multiple-hole electrode RF capacitively coupled plasma source is experimentally characterized and the large area application of the plasma source is experimentally shown. The plasma density enhancement was measured at various pressure, hole diameter, RF current and gas species condition. The bulk plasma intrusion in the hole and the ionization avalanche in the sheath region facilitated high density plasma generation for fixed power when the diameter of the hole was slightly bigger than triple the sheath length. From the analysis of the multiple hole electrode RF capacitively coupled plasma, the condition to make uniform plasma density over large area plasma source is sought and analyzed. By use of the technique, high density and uniform large area capacitively coupled plasma discharge become possible.

Advanced Surface Engineering Room: Southwest Exhibit Hall - Session SE-TuP

Advanced Surface Engineering Poster Session

SE-TuP1 Effect of NiCr-based Bondcoat and Post Treatment Process on the Adhesion of Air Plasma Sprayed WC-Co Coatings. *F. Ghadami*, University of Tehran, Iran, *S. Ghadami*, University of Semnan, Iran

In this study WC-12wt%Co and NiCr-based powders were sprayed by the Air Plasma Spray (APS) method to form conventional WC-Co and double-layer NiCr-based/WC-Co coatings on steel substrates. The microstructure of as-sprayed samples with and without NiCr-based bondcoat were analyzed and found WC, W₂C carbides and an amorphous phases. The single layer WC-Co coating samples were also heat-treated at 650, 900 and 1150°C for 1 hr. Heat treatment at all temperatures examined resulted in phase changes within the coating layer by formation of W₃Co₃C, η-carbides. Adhesive strength as well as microhardness of the as-sprayed and heat-treated coatings were also investigated. Results indicated that, adhesive strength has improved by using NiCr-based bondcoat in WC-Co deposits. The results also showed that heat treatment at 900 and 1150°C improves adhesive strength and hardness in conventional WC-Co coating samples. In this case, heat treatment process at 900°C gave the highest adhesive strength among the WC-Co coatings, which was due to the

formation of η -carbides in interface of coating and substrate and formation of chemical bonding.

SE-TuP2 Nanostructured Surfaces for Electrodes Prepared by Glancing Angle Deposition, U.B. Jensen, E. Ferapontova, D.S. Sutherland, Aarhus University, Denmark

There are many potential applications for nanostructured surfaces. The aim of this work is making better electrodes for use in bio sensors and biofuel cells. One possible application is implantable medical devices, which could be a valuable tool for diagnosis and treatment of certain diseases, e.g. diabetes. If a biofuel cell could be made to deliver enough power, the signal from a bio sensor could be transmitted wirelessly to a computer capable of analysing and acting in response to the data. [1] Furthermore, if a bio sensor was functional and accurate for long times, an implantable medical device could work for months or longer.

The present approach to this challenge is to develop nanostructured surfaces on electrodes, onto which enzymes can be attached. Since the enzymes catalyze specific reactions, this can be used for sensing of a particular bio molecule. The proposition is that by changing the nanostructures one can improve and/or tailor electrodes for any bio sensing application.

The nanostructured surfaces were prepared by a combination of two techniques: colloidal lithography and glancing angle deposition [2]. This combination allows for control of critical parameters such as porosity, curvature and shape of the nanostructures. An example of nano-scale objects is shown in the figure – gold pillars protruding from a flat surface. This surface can be of almost any material, and the nano-scale objects uniformly covers large surface areas.

In terms of applications various enzymes will be immobilised on nanostructured surfaces. After changing various surface properties prior to enzyme immobilisation the efficiency of biofuel cells and bio sensors will be determined. This will make it possible to establish which properties are optimal, and it is therefore likely that better electrodes for bio sensing and fuel cells can be developed.

[1] C. Gomez, S. Shipovskov and E. E. Ferapontova, *J. Renewable Sustainable Energy* 2, 013103, (2010)

[2] K. Robbie and M. J. Brett, *J. Vac. Sci. Technol. A* 15(3), 1460–1465, (1997)

SE-TuP3 Spatially Controlled Heat Generation by Local Plasmon Resonator, K. Namura, M. Suzuki, R. Tabuchi, K. Nakajima, K. Kimura, Kyoto University, Japan

Heat generation from noble metal nanoparticles due to their local plasma resonance is attracting much attention because of the fast response and the flexibility to choose heating area. The conventional nanoparticle heaters are fabricated by simple lithography of Au thin films on glass or Si substrate so that they absorb only a few 10 % of the incident light even at the wavelength of the local plasma resonance. Therefore, they are ineffective from the viewpoints of not only the fabrication cost but also photothermal conversion. In addition, it is difficult to spatially control the generated heat because photothermal conversion efficiency is constant for all nanoparticles.

Recently, we demonstrated the self-assembling of Au nanoparticles/dielectric layer/ Ag mirror sandwiches, namely, the local plasmon resonator, by using a dynamic oblique deposition technique¹. Due to strong interference, their optical absorption can be controlled between 0.1% and 100% by changing the thickness of the dielectric layer. Although we focused our attention only on the local field enhancement in that work, now we notice that photothermal conversion efficiency can be spatially tuned by using the local plasmon resonators. This work is the feasibility study of application of the local plasmon resonator to the spatially controlled nanoheaters.

We prepared combinatorial local plasmon resonator chips which have different thicknesses of Au and the dielectric layers on a single substrate of 50×50 mm² by oblique deposition and measured the absorption spectrum on each element. In order to evaluate the heat generation from Au nanoparticles, we measured the temperature of the water, with which a small cell created on a local plasmon resonator was filled, irradiating the laser of the wavelength of 785 nm. The temperature of the water on the element with high absorption becomes higher than that on the element with low absorption. The change in temperature proportional to absorption of the element in the local plasmon resonator chips. This suggests that the photothermal conversion efficiency can be controlled by the interference. Consequently, local plasmon resonator can be applied to the nanoheaters, which can spatially control the heat generation.

This work was supported by KAKENHI 21656058 and by the Iketani Science Foundation.

1. M. Suzuki, *et al.*, *Journal of Nanophotonics*, 3, 031502 (2009).

SE-TuP4 Multifrequency Atomic Force Microscopy with Heated Cantilever Tips, J.L. Remmert, Universal Technology Corporation, J.G. Jones, A.A. Voevodin, Air Force Research Laboratory, W.P. King, University of Illinois at Urbana-Champaign

Multifrequency drive capabilities have recently been implemented on the atomic force microscope (AFM) to enhance imaging contrast and retrieve information about the material properties of the sample surface¹. Common to each technique is the use of a complex (amplitude-modulated) waveform to oscillate the cantilever tip in proximity to the substrate at two or more of its flexural resonances. Simultaneous measure of the amplitude and phase of the cantilever ac deflection is used to characterize the tip-sample coupling and may, for example, relay mechanical and chemical information through the separation of short- and long- range forces between distinct resonance modes^{2,3}. In this way, bimodal imaging has also advanced magnetic³ and electrostatic⁴ force mapping with the application of appropriate fields. Related techniques track spatial variations in the contact resonance by evaluating the cantilever response across either a frequency band (band excitation, BE) or at fixed limits bracketing the peak (dual ac resonance tracking, DART). Resonance tracking also reduces crosstalk between the surface topography and frequency-dependent material properties, and has been employed to measure energy dissipation⁵, as well as for piezoelectric domain characterization⁶ and local thermal analysis⁷ with drive signals modulating the local electrical bias and temperature gradient, respectively. This work focuses on the latter approach: the use of dual frequency excitation to resistively heat and actuate an AFM tip for thermomechanical imaging of sample surfaces. Evaluation of the ac deflection at two frequency limits provides the amplitude and phase data required to extract the quality factor (dissipation) by the simple harmonic oscillator model¹. The experimental procedure (thermal DART) has been demonstrated along with data post-processing to establish a temperature-dependent study of surface mechanical properties.

¹R. Proksch and C. Callahan, United States Patent Application Publication US 2009/0013770 A1 (2009).

²R. Proksch, *Applied Physics Letters* 89, 113121 (2006).

³J.W. Li, J.P. Cleveland, and R. Proksch, *Applied Physics Letters* 94, 163118 (2009).

⁴R. W. Stark, N. Naujoks, A. Stemmer, *Nanotechnology* 18, 065502 (2007).

⁵S. Jesse, S.V. Kalinin, R. Proksch, A.P. Baddorf, and B.J. Rodriguez, *Nanotechnology* 18, 435503 (2007).

⁶B. J. Rodriguez, C. Callahan, S. V. Kalinin, and R. Proksch, *Nanotechnology* 18, 475504 (2007).

⁷M.P. Nikiforov, S. Jesse, A.N. Morozovska, E.A. Eliseev, L.T. Germinario and S.V. Kalinin, *Nanotechnology* 20, 395709 (2009).

SE-TuP5 Time Domain Thermoreflectance and 3-Omega Comparison Studies of Polymer-Metallic-Ceramic Nanolaminate Coatings, A.R. Waite, Air Force Research Laboratory/Universal Technology Corp., J.J. Gengler, Air Force Research Laboratory/Spectral Energies, LLC, J.G. Jones, C. Muratore, A.A. Voevodin, Air Force Research Laboratory

Multilayered polymer-metal-ceramic nanolaminate coatings were grown by room temperature plasma enhanced chemical vapor deposition (PECVD) and magnetron sputtering processes in a dual chamber PVD-CVD system to examine optical coatings with tailored, through-thickness thermal conductivity. Highly cross-linked fluoropolymer films were grown by PECVD from an octafluorocyclobutane gas precursor. High refractive index ceramic layers were deposited by pulsed DC magnetron sputtering of a TiO₂ target. Thin (5–20 nm) silver interlayers with thicknesses on the order of phonon mean free paths were also integrated into the nanolaminate stack. The thickness and position of the layers with high and low refractive index layers could be adjusted to develop optical coatings with desired functionality for different wavelengths of incident light, while metal layers were integrated to distribute heat and eliminate decomposition of the polymer films during heating by incident light. The through-thickness thermal conductivity of the films with and without the integrated silver layers was compared by time domain thermoreflectance (TDTR) and 3-Omega techniques. The 3-Omega analysis provides the bulk thermal conductivity of the nanolaminate stack which was compared to the constructed thermal transport model from the TDTR analysis of each film material and their respective interfaces.

SE-TuP6 Water Adsorption on TiN and TiCN Hard Coatings. E. Broitman, Carnegie Mellon University, M. Rebelo de Figueiredo, University of Leoben, Austria, W. Michalak, Carnegie Mellon University, R. Franz, University of Leoben, Austria, G. Zanini Gadioli, Carnegie Mellon University, C. Mitterer, University of Leoben, Austria

It is known that ceramic coatings with substantial amounts of structurally incorporated carbon show low-friction behavior, in particular at intermediate temperatures. However, the mechanisms behind activation, formation and modification of the required free carbon in the friction contact are still not fully understood, especially in the case of Ti_xCN_y , a widely used commercial coating. In a previous study the importance of the presence of water vapor for the formation of a friction-reducing layer has been revealed by tribological tests at different water vapor pressures in the surrounding atmosphere. In the present work, water adsorption studies on titanium nitride (TiN) and titanium carbon nitride (TiCN) coatings are carried out in order to gain a new insight about the active chemical processes on the coating surface.

The TiN and TiCN coatings were prepared by dc magnetron sputtering of a TiN and Ti_2CN compound target, respectively, in a lab-scale deposition system. X-ray diffraction was used to study the crystal structure and the obtained patterns show a face-centered cubic structure with a [111] texture for TiCN and a [200] texture for TiN. Both X-ray Photoelectron Spectroscopy (XPS) and Temperature Program Desorption (TPD) experiments in the range 110-700 K were conducted in an Ultra High Vacuum chamber with a base pressure of $\sim 3 \times 10^{-10}$ Torr. Also, the water adsorption on the coatings as a function of % relative humidity was measured using a quartz crystal microbalance.

XPS measurements reveal the presence of a surface oxide, with the composition of the coatings being $Ti_{2.0}N$ and $Ti_{1.75}CN_{1.35}$. TPD experiments show that water adsorption has a zero-order desorption mechanism. After low coverage and temperature of exposure of 110 K, the spectra yield calculated desorption energies of 22.96 ± 4.17 kJ/mol and 18.42 ± 4.73 kJ/mol for the TiN and TiCN surfaces, respectively, based on a leading-edge analysis. Measurements from higher coverage indicate the strength of the water-water attractive interactions which cause clustering of H_2O into 2-D islands and then multilayers. The desorption energies from this regime are calculated to be 47.45 ± 2.31 kJ/mol and 41.73 ± 4.06 kJ/mol for the TiN and TiCN surfaces, respectively. These values are higher than the water's combined heats of vaporization and fusion: $\Delta H_v + \Delta H_f = 9.72$ kcal/mol + 1.44 kcal/mol. The water adsorption results can be correlated to the microstructure, composition and tribological properties.

SE-TuP7 Effects of Ag/Cu Ratios on the Annealing Temperature and Mechanical Properties of TaN-(Ag,Cu) Nanocomposite Thin Films. J.H. Hsieh, S.Y. Hung, Ming Chi University of Technology, Taiwan, Republic of China, S.Y. Chang, C.C. Tseng, National Chung Hsing University, Taiwan, Republic of China

TaN-(Ag,Cu) nanocomposite films were deposited by reactive co-sputtering on Si(110) substrates. The samples were then annealed using RTA (Rapid Thermal Annealing) at various temperature (200 °C ~ 400 °C) for 2, 4, 8 minutes respectively to induce the nucleation and growth of Ag/Cu particles in TaN matrix and on film surface. This study was attempted to find out if annealing temperature and mechanical properties were affected by Ag/Cu ratios. C-AFM (Conductive Atomic Force Microscopy) and FESEM (Field Emission Scanning Electron Microscopy) were used to confirm the emergence of Ag/Cu nano-particles on the surface of TaN-(Ag,Cu) thin films. Nano-indenter was used to examine the mechanical properties of the films. The results reveal that annealing temperature could be as low as 200 °C for the sample with Ag/Cu ratio at 4:6, while the hardness values could be at their highest. Accordingly, the films may be applied on polymeric substrate in the future for the purpose of anti-wear and anti-bacteria.

Surface Science

Room: Southwest Exhibit Hall - Session SS-TuP

Surface Science Poster Session

SS-TuP1 MORTON S. TRAUM AWARD FINALIST: Uptake of Copper Acetamidate ALD Precursor on Metal Surfaces and the Effect of Coadsorption of Hydrogen. Q. Ma*, F. Zaera, University of California, Riverside

Acetamidate precursors have shown great promise for atomic layer deposition (ALD) applications, but potentially deposit impurities that may

degrade the quality of the films and hinder their practical applications. To help solve this problem, the uptake and thermal activation of bis[(N,N'-di-sec-butylacetamidate)Cu] and N,N'-di-sec-butylacetamidate on metals were characterized under ultrahigh vacuum (UHV) conditions by using a combination of X-ray photoelectron spectroscopy (XPS), low-energy ion scattering (LEIS), and temperature programmed desorption (TPD).

In initial studies on a Ni(110) single crystal, a temperature window between approximately 350 and 450 K was identified for the ALD of the Cu acetamidate on Ni surface: lower temperatures are insufficient for activation of the dissociative adsorption, and higher temperatures lead to continuous decomposition beyond Cu monolayer saturation. Approximately three dosing cycles are required to reach full Cu monolayer saturation, the equivalent of a film growth rate of ~ 0.75 Å/cycle in ALD. Preadsorption of hydrogen on the surface does not modify any of this behavior because of its rapid desorption at temperatures below 350 K once the gas-phase H_2 is removed.

The surface chemistry of the Cu precursor is complex, leading to the desorption of not only hydrogen but also butene and N-sec-butylacetamidate ($H_2N-C(CH_3)=N-CH(CH_3)(CH_2CH_3)$), it seems that the amidine ligands decompose via beta-hydride elimination from one of their terminal sec-butyl moieties. Copper precursors leading to relatively stable organic surface intermediates are required in ALD because their clean removal can only happen in the second half-cycle of processes that rely on hydrogenation reactions. The ligand of the copper acetamidate precursors further decomposed on Ni (110) surfaces. The free hydrogenated amidine ligand is less reactive and no N-sec-butylacetamidate is produced by its thermal activation, but the remaining chemistry is seen with similar temperature transitions.

SS-TuP2 MORTON S. TRAUM AWARD FINALIST: Understanding and Controlling Rotation at the Single-Molecule Level: Turning Rotors into Motors. H.L. Tierney*, A.D. Jewell, A.E. Baber, E.V. Iski, E.C.H. Sykes, Tufts University

While molecular machines driven by chemical, light or thermal energies can be found throughout nature, little progress has been made toward creating synthetic counterparts. The gap between nature and nanotechnology remains due to the limited fundamental understanding of the transfer of energy to mechanical motion at the nanoscale. Understanding and actuating the rotation of individual molecules on surfaces is a crucial step towards the development of nanoscale devices such as fluid pumps, sensors, delay lines, and microwave signaling applications. Towards this end we have used a group of small molecules in order to understand the fundamental aspects of molecular rotation. Thioethers constitute a simple, robust system with which molecular rotation can be actuated thermally, mechanically and electrically, and can be studied using scanning tunneling microscopy (STM) as a function of molecular chemistry and proximity of neighboring molecules. Interestingly, the thermal onset to rotation was found to be nearly identical for studied thioether molecules with alkyl tails of two carbons or more. It is proposed that this plateau in thermal onset was due to an interplay between degrees of freedom in the alkyl tail vs. the S-metal bond length. While small amounts of thermal energy are capable of inducing rotation, thermodynamics dictates that thermal energy alone cannot be used to perform useful work in the absence of a temperature gradient. Therefore, for molecules to meet their full potential as components in molecular machines, methods for coupling them to external sources of energy that selectively excite the desired motions must be devised. To this end, we have studied using an electrical current to rotate individual dibutyl sulfide molecules on command. For these studies the source of energy is supplied via high energy electrons from the STM tip. By monitoring the rate of rotation as a function of tunneling electron energy (action spectroscopy) we have demonstrated that the rotors can be driven electrically via a mechanism that involves excitation of a C-H stretch. Finally, using theoretical methods the minimum energy adsorption site was determined and the mechanism of rotation was elucidated for the simplest thioether, dimethyl sulfide. These theoretical results indicate that the rotation of a small, simple molecule is actually rather complex; as the CH_3 groups of dimethyl sulfide rotate around the Au-S bond, the central S atom precesses around a surface Au atom.

SS-TuP3 MORTON S. TRAUM AWARD FINALIST: Growth of Ag on Ge(110) and Ge(111) Studied by LEEM. C. Mullet*, University of California, Davis, S. Chiang, University of California at Davis

We studied Ag island growth on reconstructed Ge(110) and Ge(111) surfaces with low energy electron microscopy (LEEM). At 480 °C, one-dimensional (1D) island growth was observed on Ge(110). Island nucleation proceeds from defects in the Ge substrate, with island thickness corresponding to the size of the substrate defect where the island nucleation occurred. As Ag is deposited, islands lengthen but do not thicken. At 9 ML, Ag coverage islands were up to 10 μm long, and thicknesses varied from 100 nm to 250 nm. One-dimensional islands were also produced by Ag

* Morton S. Traum Award Finalist

deposition at room temperature followed by sample heating. Round Ag islands resolvable in LEEM were observed and coalesced into many long 1D islands as temperature was increased. Islands formed by deposition at room temperature followed by heating to a particular temperature were shorter and thicker than islands grown by deposition on a substrate held at that same temperature. Ag growth on Ge(111) is Stranski-Krastanov. Multilayer Ag island formation begins after the Ag ($\sqrt{3}\times\sqrt{3}$)R30° phase completes at one monolayer. Ag islands exhibit hexagonal faceting. For both the Ge(111) and Ge(110) surfaces, Ag islands induce changes in the Ge substrate that leave a “footprint” observable in LEEM after all Ag has been desorbed from the surface.

*Funding from NSF CHE-0719504; NSF PHY-0649297 (REU)

SS-TuP4 Kinetics and Mechanism of NO Reduction with CO on Ir Surfaces, T. Fujitani, A. Takahashi, I. Nakamura, National Institute of Advanced Industrial Science and Technology (AIST), Japan

The reaction of NO and CO has been studied over various transition- and noble-metal catalysts because of its importance for three-way catalytic converters. Recently, Ir-based catalysts were found to be effective for the selective reduction of NO with CO in the presence of O₂. However, the reaction mechanism, kinetics, and adsorption behavior for the NO + CO reaction on Ir-based catalyst surfaces are not fully understood.

In this study, we investigated the adsorption and thermal reactivity of NO and CO over Ir single crystals to clarify the influence of the Ir surface structure. Furthermore, we examined the kinetics and mechanism of the NO + CO reaction over Ir single crystals at high-pressure and compared the results with results for a conventional Ir/SiO₂ powder catalyst.

The kinetics of the NO reduction with CO over the Ir single crystal and the powder Ir/SiO₂ catalyst were investigated under real reaction conditions. N₂ and CO₂ were formed by the reaction of NO + CO. The Ir(111) plane showed low activity for N₂ and CO₂ production compared with the Ir(100) and Ir(211) planes. The TOFs for N₂ and CO₂ formation for the Ir planes decreased in the order (100) > (211) >> (111). The apparent activation energies for N₂ and CO₂ formation were estimated to be 107–115 kJ/mol and 110–120 kJ/mol, respectively; and these values were almost the same, regardless of the changes of the Ir surface structure. Furthermore, the order of the pre-exponential factors for the various surface structures was in good agreement with the order of the planes with respect to NO dissociation activity, indicating that the catalytic activity for NO reduction over Ir surfaces was strongly dependent on the NO dissociation activity.

The activation energies for N₂ and CO₂ formation over an Ir/SiO₂ catalyst were estimated to be 117.2 kJ/mol and 123.1 kJ/mol, respectively, and these values were similar to those of the Ir single crystal. The TOFs for N₂ and CO₂ formation over Ir/SiO₂ were almost same for those for Ir(211), which indicates that the Ir surface structure of Ir/SiO₂ was close to that of Ir(211). That is, the Ir(211) surface can be regarded as an appropriate model catalyst for the NO + CO reaction over an Ir/SiO₂ catalyst because the apparent activation energies and the TOFs for N₂ and CO₂ formation over Ir(211) were in good agreement with those over the Ir/SiO₂ catalyst.

SS-TuP5 Development of Boundary Layer in the Flowing Water on the Solid Surface with Various Wettability, M. Sakai, Kanagawa Academy of Science and Technology, Japan, *M. Nishimura, T. Furuta, A. Nakajima,* Tokyo Institute of Technology, Japan, *A. Fujishima,* Tokyo University of Science, Japan

Recently, the importance of controlling wettability on the solid surface is recognized in various industries. Superhydrophobic surfaces with water contact angles exceeding 150° are currently the subject of great interest and intensive study. Superhydrophobic coatings that produce rough surfaces at the micro- and nanoscale level with low surface energies have been prepared by several methods. On the other hands, highly hydrophilic surface is obtainable, when the photocatalyst TiO₂ is irradiated by ultraviolet light. In the current paper, we evaluated friction drag of water on various surfaces including these surfaces. The amount of friction drag was evaluated by the static pressure during flowing in the tubes coated by various materials. Compared to Darcy-Weisbach's equation, a superhydrophobic coating and highly hydrophilic coating decreased the friction drag of the flowing under the condition of small Reynolds number. However, a highly hydrophilic coating contributed significantly to the reduction of friction drag, when Reynolds number is large. Moreover, the velocity gradient of the flowing water in the tube was measured by particle image velocimetry (PIV). The development of boundary layer depended on the wettability in the tubes, when the flowing was the same in the flow rate. The mechanism was discussed from the viewpoints of fluid mechanics and surface materials science.

SS-TuP6 Hydrogen Termination of Si(110) Surface in UHV Conditions, M. Yoshimura, A. Visikovskiy, Toyota Technological Institute, Japan

Hydrogen termination on silicon surfaces is very important in science and technology. Hydrogen (H) is used for surface passivation, and may play role of surfactant for epitaxial growth and also present in many technological processes including chemical vapor deposition. The behavior of H on Si(100) and Si(111) surfaces is extensively studied. However, the information on interaction of H with Si(110) is very limited. The (1x1) bulk-terminated structure was reported for chemically hydrogenated Si(110) in solution [1,2]. The surface structure and processes occur on Si(110) hydrogenated in ultra-high vacuum (UHV) may be very different from chemically treated samples. There are very few reports on *in situ* hydrogenation of Si(110) surface. Here, we report scanning tunneling microscopy (STM) study of atomic H adsorption on Si(110) in UHV.

The high efficiency hot capillary source was used to produce atomic H flux. The large concentration of highly reactive H atoms in the flux allows us to reach surface saturation for hydrogenation at ~2 L exposure. Chemically etched tungsten tips have been used for STM (Omiron VT-system).

The initial adsorption process of hydrogen reveals itself as suppression of individual protrusions of pentagon pairs on STM image. The number of these “missing” protrusions increases with H coverage, although the overall “16x2” structure of clean Si(110) preserves. More drastic changes were observed on unreconstructed areas exposed to small amount of H at elevated temperatures. Si pentagon pairs, usually randomly distributed on these areas, were arranged in patches with local “5x4” periodicity. Further exposure at room temperature (RT) led to losing of atomic resolution on STM images. At higher temperatures (400~500°C) the surface have reconstructed to the zigzag row structures. Depending on relative shift of neighboring zigzag rows the local periodicity was either (2x3) or (2,1)x(0,3). The up-and-down terrace structure of “16x2” reconstruction could still be observed, probably, due to insufficient temperature to initiate massive Si transport to smooth out the surface. At temperatures more than ~550°C the H atoms start to desorb from Si(110). These kinds of structure have not been observed before for H/Si(110) surface. No (1x1) reconstruction reported for chemically hydrogenated Si(110) was confirmed. Only small patches of (1x1) were observed in very narrow temperature window at ~350°C.

References

- [1] K. Arima, J. Ktoh, and K. Endo, Appl. Phys. Lett. 85 (2004) 6254.
- [2] S. Horie, K. Arima, K. Hirose, J. Katoh, T. Ono, and K. Endo, Phys. Rev. B 72 (2005) 113306.

SS-TuP7 Spectroscopic Investigation on Water Behavior in Mesoporous Silica, Y. Aoki, J. Hieda, O. Takai, N. Saito, Nagoya University, Japan

Mesoporous materials are widely used in industrial fields such as biotechnology and chemical engineering; catching and filtering a specific molecule, supplying novel reaction field for nanocatalysis. In particular, mesoporous silica is defined as a material with size-regulated mesopores (2–50 nm). Generally, highly-ordered arrangement of pores is attractive for chemists because the most of properties are controlled by the arrangement.

Recently some researchers reported that the internal water trapped by mesopores extraordinary behaved compared with bulk water. For examples, the water showed the lower melting point and increasing effect of non-freezing water. These phenomena were originated from the increasing ratio of interactions to water molecules from surface.

In this research, we aimed to reveal water behaviors in mesoporous silica from IR spectroscopy, Raman spectroscopy, and DSC. Mesoporous silica was synthesized conventional thermal calcinations with several organic templates because it control the pore diameters. The synthesized mesoporous silica was characterized by XRD, TEM and N₂ adsorption-desorption isotherm curve.

The complete removal of organic template and the OH-termination in inside wall resulted in the presence of water in the mesopores. As the water features, we observed the both types of non-freezing and freezing water. Finally, the types of water were separated in the properties by both spectroscopy and DSC.

SS-TuP8 Mechanism of Laser Assisted Field Evaporation from Oxides, M. Tsukada, H. Tamura, Tohoku University, Japan, *K. Mckenna,* University College London, UK

Recently, experimental methods for 3D-atom probe microscopy for a wide class of oxides and semiconductor materials have been developed by Hono et al using laser assisted field evaporation. Though this method is really epoch-making, the mechanism of laser assisted field evaporation has not been clarified so far and the best operation condition is still unexplored.

Therefore we studied theory on the mechanism of laser assisted field evaporation from MgO crystal, as a prototype of oxides. As a result, we found the mechanism is explained by electronic excitation model, which is remarkably different from the usual field induced evaporation from metal tips.

An important fact we clarified is that a certain amount of holes at the evaporation region exert a driving force of the evaporation by reducing the potential barrier of the ion desorption. The holes are generated by a strong positive electric field on the tip, as well as by the laser irradiation.

Using MRMP2 ab initio calculations, we obtained the potential energy surfaces of the ground states and photo-excited states of somewhat larger MgO clusters leading to the photo-induced desorption of corner ions. We found when two holes are captured in the MgO clusters, the activation barrier height of the excited diabatic potential energy surface is remarkably reduced, indicating such an excited potential energy surface provides an effective evaporation pathway. Using ab initio embedded cluster method with 6-311G*/B3LYP for much larger MgO cluster models including more than 1000 ions, we calculated the effect of positive charging on the sublimation energy of the corner ions and found only two holes captured by the cluster remarkably reduce the sublimation energy. We also obtained analytic expressions of the potential energy surfaces from phenomenological analyses, from which evaporation rates are estimated as the function of the applied voltage. The holes generated and accumulated near the evaporation region play an important role for triggering the ion desorption. We also discuss how such surface hole accumulation can be detected by the FIM images.

Based on theoretical analyses as above, we establish a systematic scenario leading to the laser assisted field evaporation from oxides and semiconductors. Moreover, theoretical clue will be provided towards finding a condition for the best resolution of the 3D-atom probe method using the laser assisted field evaporation.

SS-TuP9 Surface Roughness of Anodized Titanium Coatings, D.A. Chinn, M.T. Dugger, Sandia National Laboratories

Samples of grade five 6Al4V titanium alloy were coated with two commercial fluoropolymer anodizations (Tiodize and Canadize) and compared. Neither coating demonstrates significant outgassing. The coatings show very similar elemental analysis, except for the presence of lead in the Canadize coating, which may account for its lower surface friction in humid environments. Surface roughness has been compared by SEM, contact profilometry, optical profilometry, power spectral density and bidirectional scattering distribution function (BSDF). The Tiodize film is slightly smoother by all measurement methods, but the Canadize film shows slightly less scatter at all angles of incidence. Both films exhibited initial friction coefficients of 0.2 to 0.4, increasing to 0.4 to 0.8 after 1000 cycles of sliding due to wear of the coating and ball. The coatings are very similar and should behave identically in most applications.

SS-TuP10 Measurement of the Dielectric Properties of SiO₂ Wafers using Optical Spectroscopy, D. Popovic, A. Zekic, University of Belgrade, Serbia, V. Milosavljevic, Dublin City University, Ireland & University of Belgrade, Serbia

Low dielectric constant materials (low-k) are used as interlevel dielectrics in integrated circuits. As components have scaled and transistors have gotten closer and closer together, the insulating dielectrics have thinned to the point where charge builds up and crosstalk adversely affects the performance of the device. It is this reduction in scale which drives the need for insulating materials with lower dielectric constant. A 'low-k' material is one with a small value for dielectric constant relative to silicon dioxide (SiO₂) a former dielectric of choice. There are many materials with lower dielectric constants, but few of them can be suitably integrated into a semiconductor manufacturing process.

The SiO₂ is frequently used in a plasma chamber as a wafer for etching. The interaction of the plasma and the SiO₂ surface leads to incorporations/removing material for structure of SiO₂ and also to increasing of the dielectric constant. So the optimization problem in materials development for semiconductors is to lower the permittivity of the dielectric material as far as possible without compromising mechanical integrity.

The dielectric function spectra of low dielectric constant (low-k) materials have been determined using spectroscopic ellipsometry, near-normal incidence spectroscopic reflectometry, and Fourier transform infrared transmission spectrometry over a wide spectral range from 0.03 to 5.4 eV (230nm to 40.5μm wavelength region). The electronic and ionic contributions to the overall static dielectric constant were determined for representative materials used in the semiconductor industry for interlayer dielectrics. The main contributions to the static dielectric constant of the low-k materials studied were found to be the electronic and ionic absorptions.

To perform the study, square shape wafers (15x15mm) are placed in the discharge tube. The angle between wafers plane and a constructed channel is 45°. The DC discharge is produced in a Pyrex tube of 5mm inner diameter and an effective plasma length of 72mm. The discharge tube is evacuated using a vacuum pump that gives a base pressure of 2Pa. The working pressures from 50 to 266 Pa are achieved using a gate valve positioned above the rotary pump. Gas flow into the chamber is controlled via mass flow controllers that precisely determine gas content in the discharge tube. The working gas is a sulphur-hexafluoride (SF₆) with flow rate up to 40 sccm. The power supply used was a Keithley Model 248 high voltage supply with a maximum voltage of 5kV and discharge current of 5 mA. In this experimental campaign the maximum voltage is 2.2kV. The wafer processing time is 30 min.

SS-TuP11 Stereoselective Adsorption Configurations of S-Proline Molecules via N Dative Bonding on Ge(100), Y.-S. Youn, Korea Advanced Institute of Science and Technology (KAIST), Korea, K.-J. Kim, B. Kim, Pohang Accelerator Laboratory, Korea, D.H. Kim, Daegu University, Korea, H. Lee, Sookmyung Women's University, Korea, S. Kim, Korea Advanced Institute of Science and Technology (KAIST), Korea
The adsorption configurations of S-proline on Ge(100) were studied using scanning tunneling microscopy (STM), density functional theory (DFT) calculations, and high-resolution core-level photoemission spectroscopy (HRCLPES). We identified three adsorption structures of S-proline on Ge(100) through analysis of the STM images, DFT calculations, and HRCLPES results: (i) an 'intrarow O-H dissociated and N dative bonded structure', (ii) an 'O-H dissociation structure', and (iii) an 'N dative bonded structure'. Moreover, because adsorption through the N atom of S-proline produces a new chiral center due to symmetry reduction by N dative bonding, we found that the adsorption configurations have either (R,S) and (S,S) chirality with a preference for reaction at the Re face.

SS-TuP12 Islands and Holes as Measures of Mass Balance in Growth of the (√3x√3)R30° Phase of Ag on Si(111), A. Belianinov, Iowa State University & Ames Laboratory U.S. D.O.E.

It is well-known that conversion of Si(111)-(7x7) into the (√3x√3)R30° phase of adsorbed Ag requires a change in the Si density, and causes formation of islands and holes at the surface. By mass balance, the ratio of areas of islands and holes (R_{IH}) should be approximately 1. However, we find that the ratio is significantly higher, depending on preparation conditions. A possible explanation would be that there are different types of (√3x√3)R30° structures. However, neither scanning tunneling microscopy nor density functional theory (implemented as a genetic algorithm search) supports this explanation. The reason for the unexpectedly high values of R_{IH} is unknown.

P.A.C.S. Numbers 68.37.Ef, 68.55.-a, 81.15.Aa, 68.47

SS-TuP13 Secondary Electron Yield for As-Received, Electrodeposited, and Crystalline Silver Surfaces, T.P. Graves, P.D. Fuqua, P.M. Adams, R. Spektor, J.R. Lince, D.B. Witkin, The Aerospace Corporation

Silver electroplating is commonly used to provide low electrical loss characteristics for RF and microwave devices. These RF devices can also be susceptible to multipactor discharge, a resonant electron phenomenon that relies on electron density growth by secondary electron emission. The secondary electron yield (SEY) can determine whether a multipactor discharge can form; therefore, understanding SEY variations in silver surfaces is necessary for accurate multipactor breakdown prediction. In this work, SEY is measured for a variety of silver surfaces using a retarding potential method. Starting with as-received silver with no specific surface preparation, SEY values are shown to be considerably increased due to adsorbed gases on both bulk and electrodeposited silver substrates. Auger analysis was performed to determine the contaminant layers, as it is these technical silver surfaces that are realistic for space hardware where in-situ surface conditioning is not possible. Additional SEY measurements were performed on both polycrystalline and single crystal silver surfaces to determine the effect of the crystalline orientation on the SEY. Different crystallographic orientations at the surface of the electrodeposit may arise due to differences in plating variables such as bath chemistry, electrode geometry and localized current density. These measurements serve to better understand possible improvements in plating processes to minimize secondary electron emission and multipactor risk. Lastly, the effect of baking and multipactor conditioning on silver SEY is presented. Formation of thin carbon films are observed as a result of multipactor exposure, and x-ray photoelectron and Raman spectroscopy film analysis results are presented.

SS-TuP14 Characterization and Chemical Activity of Supported Ni-Au and Pt-Au Bimetallic Clusters: Reactions of Methanol. *S.A. Tenney, B.A. Cagg, W. He, D.A. Chen*, University of South Carolina

The activity of methanol on Ni-Au and Pt-Au clusters deposited at 300 K on TiO₂ (110) was investigated using temperature programmed desorption (TPD), scanning tunneling microscopy (STM), and low energy ion scattering (LEIS). Bimetallic clusters were grown by first depositing the metal with stronger metal-support interactions (Ni or Pt) onto the surface in order to seed the more mobile Au at existing Ni or Pt clusters. The preexisting Ni or Pt clusters also inhibited the sintering of Au at higher temperatures. The composition at the surface of the clusters was established by the major products observed in TPD experiments. Methyl (~717 K) was produced on the TiO₂ support, CO (~429 and ~775 K) and H₂ (~357 K) were produced at Ni sites, and formaldehyde (~580 K) production was attributed to the Au-titania interface. CO (~503 K) and H₂ (~503 K) were also characteristic of Pt at the surface. LEIS data for 0.25 ML of total coverage shows that for clusters with > 50% bulk Au composition, the surface of the cluster is almost entirely pure Au. TPD of methanol on clusters with > 50% bulk Au composition still show activity characteristic of Ni or Pt at the surface, suggesting that methanol is able to induce the migration of Ni and Pt to the surface of the clusters. Increasing the amount of Au on the surface for pure Au clusters beyond 1 ML resulted in a decrease of the formaldehyde signal, which is attributed to a subsequent decrease in the Au-TiO₂ interface as more Au is deposited onto the surface. Formaldehyde production on 0.25 ML of pure Au and 25% Ni / 75% Au clusters showed no decrease in activity even after 6 consecutive TPD cycles to 800 K.

SS-TuP15 Growth of Nanoparticles and Reactivity of a Copper Metal-Organic Precursor on Functionalized Silicon Surfaces. *K.A. Perrine, J. Lin, A.V. Teplyakov*, University of Delaware

As the sizes of the devices are quickly approaching the nanometer scale in the microelectronics industry, the need to control reactions at the molecular level and at the interface becomes very important for developing cleaner deposition techniques. For example, metal contacts grown using atomic layer deposition (ALD) have already made an impact on modern devices.

A common precursor used to grown copper metal contact, Cu^I (hexafluoroacetylacetonato) vinyltrimethylsilane or Cu(hfac)VTMS, has been previously studied at the molecular level on Si(100)-2x1 and other surfaces using surface sensitive techniques. Here we use this precursor as a reactant on several functionalized silicon surfaces to produce and control the size distribution of metallic nanoparticles.

We compare the reaction of Cu(hfac)VTMS with H-Si, NH₂-Si, NH-Si, and OH-Si surface reactive sites and follow it by *in situ* infrared spectroscopy (FTIR), temperature-programmed desorption (TPD), X-ray photoelectron spectroscopy (XPS), atomic force microscopy (AFM), and complement with Density Functional Theory calculations. The growth of the hfac vibrational signatures indicates reaction on these functionalized surfaces and losses in the Si-H stretch spectral region can be used to follow the deposition kinetics. The surface is used here as a reducing agent providing the hydrogen to remove the ligands of the copper deposition precursor and to produce metallic nanostructures.

SS-TuP16 Preparative Mass Spectrometry: A Novel Approach for the Creation of Catalyst Materials. *G. Johnson*, Pacific Northwest National Laboratory, *W.-P. Peng*, National Dong Hwa University, Taiwan, Republic of China, *R.G. Cooks*, Purdue University, *J. Laskin*, Pacific Northwest National Laboratory

Soft- and reactive landing of mass-selected ions onto surfaces is a unique approach for the highly controlled preparation of catalyst materials that are often inaccessible using conventional synthesis techniques. Mass selection allows polyatomic ions with known charge and chemical identity to be deposited onto surfaces under carefully controlled conditions, thereby avoiding purification steps which are typically necessary with traditional catalyst preparation methods. A new apparatus has been designed and assembled at PNNL that allows *in situ* reactivity and time of flight secondary ion mass spectrometry analysis of surfaces prepared or modified through soft- and reactive landing. The capabilities of this instrument for the preparation and analysis of catalyst materials are demonstrated for two different systems consisting of monolayer catalysts produced by the deposition of organometallic metal-salen and ruthenium bipyridine cations onto self assembled monolayer surfaces. It is shown that through soft landing of vanadium-salen cations and a proton donor it is possible to achieve proton mediated reactivity in an inert fluorinated monolayer that is normally only observed in highly acidic solutions. In addition, it is demonstrated that gas-phase ligand stripping may be used to generate highly reactive undercoordinated metal complexes which exhibit enhanced activity towards reactive landing in comparison to fully ligated species. The

immobilized complexes, which are covalently bound to the surface, are shown to exhibit catalytic activity when exposed to gaseous reagents.

SS-TuP17 Charge Transfer and Shake Satellites in XPS: A Unified View. *C.J. Nelin*, Maury's Trail, *P.S. Bagus*, University of North Texas, *H.-J. Freund*, Fritz-Haber-Institut der Max-Planck-Gesellschaft, Germany

The satellites in X-Ray photoemission spectroscopy, XPS, can provide information about the electronic structure, especially for ionic materials. [1,2] We present a new analysis of the XPS satellites that, when applied to CeO₂ which is an important substrate for model studies of catalysis, enables a new understanding of this material. While the origin of intra-atomic effects in terms of atomic near-degeneracies is well understood, [1] there are two different ways of describing the inter-atomic effects that lead to satellites. The first is to ascribe the satellites to charge transfer, CT, from ligands, or other neighboring atoms, into unoccupied or partly occupied shells of the ionized atom. This interpretation is commonly applied to oxides and other ionic crystals. [2] In the CT model, the satellites gain intensity through the mixing of XPS allowed configurations with XPS forbidden configurations. However, changes in the orbitals between the initial and final states are normally neglected in the CT model. On the other hand, the second way of understanding satellites as shake satellites, [3,4] ascribes the driving force for the loss of intensity from the main peak into the satellites to the orbital relaxation, which screens the core-hole. This orbital relaxation allows valence excited, or shake, states to obtain intensity. [3] However, both mechanisms must be taken into account to correctly describe the inter-atomic contributions to XPS satellites and, in the present work, we reconcile these two different points of view. We show that the covalent mixing of metal and ligand orbitals in the wavefunctions, for both initial and final states, is a powerful way to understand the intensities of satellites due to inter-atomic effects. For the XPS of NiO, where both intra and inter-atomic effects must be taken into account, our analysis of the CI wavefunctions shows the underlying covalent character of the main and satellite peaks. We also stress the importance of covalent mixing in the initial state in order for there to be substantial satellite intensity. We show that different degrees of covalent character in the initial states of CeO₂ and LaAlO₃ lead to very different satellite energies and intensities for the isoelectronic metal cations. Our analysis provides direct and unambiguous evidence that the inter-atomic satellite features are closely related to the covalent binding in the material.

- (1) PS Bagus, ES Ilton: Phys. Rev. B **73**, 155110 (2006).
- (2) FMF de Groot: J. Electron Spectrosc. Relat. Phenom. **67**, 529 (1994).
- (3) T Aberg: Phys. Rev. **156**, 35 (1967).
- (4) L Sangaletti, F Parmigiani, PS Bagus: Phys. Rev. B **66**, 115106 (2002).

SS-TuP18 XPS Investigation of Volcanic Ash and Other Basalt Materials. *P. Mack, T. Nunney, R.G. White, A. Wright*, ThermoFisher Scientific, UK

XPS has been used to analyse the ash released from a number of volcanoes, including that from Mount St Helens, USA and Eyjafjallajökull, Iceland. The results indicate that the differences in the composition of the basalt from different regions reflect the geological structure of the region. Some of the compositional differences depend upon whether the geological plates are moving together, causing more crust material to be mixed with the lava or whether the plates are moving apart and so the lava is predominantly from sub-surface sources. Further complications arise from the fact that the ash from some eruptions (e.g. Eyjafjallajökull) also contains material from an overlying glacier. It has been found that the material from Eyjafjallajökull is richer in calcium than that from Mt St Helens.

The use of XPS to fingerprint this type of material has been investigated. The effect of ion sputtering of the material has also been investigated as a means to generate more representative data.

SS-TuP19 Combined Surface Analysis and Electrochemistry Studies on SnO₂-Pt and Sn-Pt Electrocatalysts for Ethanol Oxidation Reaction. *S. Axnanda, W.-P. Zhou, M.G. White, J. Hrbek*, Brookhaven National Laboratory

Recently, the ethanol electro-oxidation reaction has attracted considerable attention because of the advantages of using ethanol as fuel in liquid fuel cells.¹ Ethanol can be produced from renewable biomass sources, and has high energy density and less toxic than methanol. However, the ethanol oxidation kinetics is slow, impeding its use in the direct ethanol fuel cells (DEFCs). Tremendous efforts have been made to develop new ethanol oxidation catalysts to improve its efficiency. Binary Pt-Sn alloy catalysts are some of the more extensively investigated anode materials for DEFCs. It was found that the increased activity of binary electrocatalysts with respect to Pt alone was attributed to the bifunctional effect and electronic interaction between Pt and alloyed metals.^{2,3,4} However, studies from supported nanocatalyst show disagreements in mechanism of what degree

of alloying between Pt and Sn and what amount of Sn alloyed with Pt will improve the activity of the electrocatalysts towards EOR.^{5, 6, 7, 8} It is still unclear whether the alloyed Sn, or the SnO₂ phase is the reason in the increase in Pt-Sn electrocatalysts activity towards EOR.^{1, 5-8}

In the work presented here, we are investigating surface alloy of Pt-Sn/Pt(111) and SnO₂/Pt(111) as model catalysts for ethanol electro-oxidation. Characterization is performed by a combination of surface science techniques (X-Ray photoelectron spectroscopy (XPS), low energy electron diffraction (LEED), temperature programmed desorption (TPD), and low energy ion scattering spectroscopy (LEISS)) and classical electrochemical measurements. This integrated approach can be used to identify the fundamental properties of SnO₂/Pt(111) and Sn-Pt/Pt(111) electrodes and to correlate them with the activity of each electrode towards EOR.

1. E. Antolini, J. Power Sources 170 (2007) 1-12
2. Rigsby, M. A., Zhou, W. -P, Lewera, A., Duong, H. T., Bagus, P. S., Jaegermann, W., Hunger, R., and Wieckowski, A., Experiment and Theory of Fuel Cell Catalysis: Methanol and Formic Acid Decomposition on Nanoparticle Pt/Ru. J. Phys. Chem. C, 2008 112 (39) 15595-15601
3. N. M. Markovic, H. A. Gasteiger, P. N. Ross, X. Jiang, I. Villegas, M. J. Weaver, Electrochim. Acta 40 (1995) 91
4. S. L. Goikovic, T. R. Vidakovic, D. R. Durovic, Electrochim. Acta 48 (2003) 3607
5. C. Lamy, S. Rousseau, E. M. belsirs, C. Countanceau, J.-M Leger, Electrochim. Acta 49 (2004) 3901
6. W. Zhou, Z. Zhou, S. Song, W. Li, G. Sun, P. Tsiakaras, Q. Xin, Appl. Catal. B 46 (2003) 273
7. L. Jiang, G. Sun, S. Sun, J. Liu, S. Tang, H. Li, B. Zhou, Q. Xin, Electrochim. Acta 50 (2005) 5384
8. F. Colmati, E. Antolini, E. R. Gonzalez, J. Electrochem. Soc. 154 (2007) B39

SS-TuP20 One-dimensional Coordination Chains of 4,4'-azopyridine on Cu(100) by Self-assembly, H.A. Lim, S.L. Tait, Indiana University

We have observed highly-ordered 1D chains of 4,4'-azopyridine (AZPY) formed by self-assembly on the pristine Cu(100) surface at room temperature. AZPY is of particular interest as a building block due to its π -conjugated system, photoactive azo site and coordinative bonding with transition metals in metal organic framework materials. Scanning tunneling microscopy shows that the APY molecules grow in one-dimensional chains, mostly starting from copper step edges, with an end-to-end pyridine-Cu-pyridine interaction. The APY chain structure, oriented along the [110] direction, is a significant departure from the side-to-side molecular arrangement in self-assembled azobenzene chains at surfaces. As the coverage increased mobile molecules are observed to be confined inside 2D APY corrals composed of a framework of intersecting chains. X-ray photoelectron spectroscopy is also used for characterization. Further studies are underway to investigate these assemblies on other surfaces as well as functionality of these systems for applications such as nano-electronics, molecular magnetism and single-site heterogeneous catalysis.

SS-TuP21 Surface Adhesion Properties of Block Copolymer Films, M. Palacio, S. Schrickler, B. Bhushan, The Ohio State University

Block copolymers are of interest as scaffold materials for cell growth and regeneration because novel, structurally diverse polymers can be synthesized from biocompatible blocks. The nanostructure and surface morphology of block copolymers can be modulated using synthetic techniques and the nanostructures can be used to affect surface mechanical behavior. We present atomic force microscopy (AFM) studies on the morphology and corresponding protein adhesion interactions of a novel class of methyl methacrylate and acrylic acid diblock and triblock copolymers. Distinct nanomorphologies were found on diblock and triblock copolymers even though their chemical compositions are identical. This has implications on the role of nanomorphology in cell-polymer interactions. Protein adhesion on a biomaterial surface is critical to understanding its biocompatibility. Bovine serum albumin (BSA) was attached to the AFM tip in order to model protein-block copolymer interactions.

SS-TuP22 XPS Organic Depth Profiling Analysis of Poly-glycidyl Methacrylate Brushes, S. Alnabulsi, J.F. Moulder, Physical Electronics, R. Barbey, H.A. Klok, Ecole Polytechnique Fédérale de Lausanne, Switzerland

The application of XPS C₆₀ sputter depth profiling to characterize synthesized poly-glycidyl methacrylate (PGMA) brush-like thin film structures will be presented. In contrast to low voltage (250 V) Ar sputtering, C₆₀ sputtering with XPS analysis was able to obtain quantitative chemical state information as a function of depth with minimal ion beam

induced chemical damage. To minimize sputtering artifacts and improve interface definition, Zalar (azimuthal) rotation and appropriate instrument geometry for C₆₀ sputter depth profiling was used for this work. The XPS depth profiles show the chemical changes associated with various solutions applied to these organic films.

SS-TuP23 Particles from the Ozonolysis of Unsaturated Silane Self-Assembled Monolayers, T.M. McIntire, O. Ryder, University of California, Irvine, P. Gassman, Z.H. Zhu, Pacific Northwest National Laboratory, S. Ghosal, Lawrence Livermore National Laboratory, B. Finlayson-Pitts, University of California, Irvine

Airborne particles have well-documented effects on human health, visibility, and the chemistry of the atmosphere. Particles play a major role in climate change and are a large source of uncertainty in model predictions of global warming. A significant part of this uncertainty is the lack of understanding of the nature of the organic component. This deficiency includes the chemical speciation and the distribution of the organics between the surface and the bulk of liquid particles, as well as changes due to oxidation during transport in the atmosphere.

Self-assembled monolayers (SAMs) represent a well-defined system for elucidating mechanisms of mixed gas-condensed phase reactions and serve as proxies for organic-coated airborne dust particles. Previous studies have shown that ozone reactions of terminal alkene-silane SAMs generates surface-bound acids, aldehydes, and secondary ozonide (SOZ), as well as gaseous products such as CO, CO₂, HCHO, and HCOOH. In addition, the surprising formation of large, hydrophobic organic particles was observed by AFM and Auger electron spectroscopy. A particularly noteworthy result of atmospheric interest is that the uptake of water was not increased upon oxidation of these films, despite the formation of polar carbonyl-containing groups, and SOZ. This has important implications for particles in the atmosphere, since it is generally assumed that oxidation converts hydrophobic surfaces to hydrophilic which take up water more readily, thereby affecting visibility and cloud formation.

The goal of this work was to determine the product functional groups and the 3-D structure of particles produced from the ozonolysis of SAMs formed by attachment of 7-octenyltrichlorosilane (C8= SAM) to silica substrates. A combination of analytical techniques such as single particle FTIR, NanoSIMS, and TOF-SIMS were utilized to study the surface composition and morphology after oxidation. Atmospheric implications for the 3-D structure of SOA, SAM reactions and stability in air, ozonolysis of alkenes on surfaces, and the oxidation of alkenes on airborne dust particles will be discussed.

SS-TuP24 Temperature Programmed Desorption Study of CO on Cr(110) and Cr₂O₃(0001)/Cr(110), J.L. Walters, G. Arellano, W.A. Harrison, C.A. Ventrice Jr., H. Geisler, Texas State University - San Marcos

The adsorption kinetics of CO on Cr(110) and on Cr₂O₃(0001)/Cr(110) was investigated using temperature programmed desorption (TPD). The adsorption of CO was performed with the substrate maintained at 120 K, and a feedback control system was used to generate linear heating rates. For the Cr₂O₃(0001)/Cr(110) surface a saturation coverage of CO was measured to occur at 0.5 L. The desorption kinetics is estimated to be 1st order with an attractive lateral interaction between CO molecules. The Redhead method was used to measure the activation energy for desorption of the CO. This analysis resulted in a value of 49.2 kJ/mol \pm 2.6 kJ/mol for the activation energy. For the adsorption of CO on Cr(110) no CO desorption is detected for coverage below 0.5 L. This indicates that at this coverage all of the CO is dissociating and reacting with the Cr(110) surface. Deposition of 1L CO on clean Cr(110) shows only one broad signal at 300 K. By deposition of 2 L of CO or larger, a shift of the signal to 280 K and the appearance of a second signal at 210 K can be observed. The broadening and shifting of the desorption signals can be attributed to the lateral interact between the CO molecules and their adsorption on different binding sites on the Cr(110) surface.

SS-TuP25 Creation of NO Dissociation Sites Over the Pd/Al₂O₃ Surface, I. Nakamura, T. Fujitani, National Institute of Advanced Industrial Science and Technology (AIST), Japan

The reduction of Rh in three-way catalysts is currently required. Pd catalysts, which have shown a high initial activity for NO reduction compared with that of Rh catalysts, have received much attention as possible substitutes for Rh. To develop high performance Pd catalysts, the nature of active sites must be clarified, as well as the effect of oxide supports on the supported Pd. In this study, we investigated the influence of an Al₂O₃ support on the electronic state and NO dissociation activity of supported Pd using a Pd-deposited Al₂O₃/NiAl(110) surface. NO was exposed at 300 K to the 2 ML Pd/Al₂O₃ surfaces annealed at different temperatures. Only molecularly adsorbed NO was observed on the Pd/Al₂O₃

surface after deposition of Pd at 300 K. In contrast, the formation of atomic nitrogen was seen on the Pd/Al₂O₃ surface annealed above 350 K, suggesting that NO dissociation sites were created after annealing. The adsorbed NO was completely dissociated over the Pd/Al₂O₃ surface annealed above 500 K. We compared the NO dissociation activity over the 500-K-annealed Pd/Al₂O₃ surface with that observed over a stepped Pd(311) single crystal surface, since the step sites on Pd surfaces are known to be active sites for NO dissociation. It was clearly shown that the NO dissociation reaction over the Pd/Al₂O₃ surface proceeded at a much lower temperature compared with that required for NO dissociation over the Pd(311) surface. We found that the active sites created on the annealed Pd/Al₂O₃ surface had a high NO dissociation ability. To clarify the nature of the Pd active sites for NO dissociation, we examined the electronic state of the Pd particles deposited on the Al₂O₃ surface. It was shown that the Pd was oxidized to Pdⁿ⁺ ($n < 2$) by lattice oxygen atoms in Al₂O₃ after annealing above 500 K. Therefore, we concluded that the positively charged Pdⁿ⁺ species created by annealing the Pd-deposited Al₂O₃ surface at temperatures higher than 500 K were effective for NO dissociation at low temperatures.

SS-TuP26 Analysis of the Characteristics of Nickel-Plating Baths. *A.O. Gezerman, B.D. Corbacioğlu*, Yıldız Technical University, Turkey

Nickel plating processes, popularly used in Europe in the 1950s, have been increasingly employed in Turkey in recent years; as a result, industrial usage has developed rapidly. Nickel plating is the preferred process for this study because of the uniformity of the plating thickness on the plated surface and the ease with which complex components can be plated. It is also resistant to corrosion and has good hardness levels.

In this experiment, the following parameters were investigated: the effect of varying the amount of nickel, the thickness of the plating, and sheen (whether shiny or dull).

In this study, brightener and carrier agents have been used to determine the best operational parameters for the Kale Kilit Factory. The compositions of the brightener and carrier agents used in the experiment is included in this text.

Thin Film

Room: Southwest Exhibit Hall - Session TF-TuP

Thin Film Poster Session I

TF-TuP2 Electrical and Optical Properties of Very Thin Ag Films with Surface and Interface Nanolayers. *M. Kawamura, K. Nishida, R. Kiyono, Y. Abe, K. Sasaki*, Kitami Institute of Technology, Japan

We have attempted improvements of thermal stability of Ag thin films which are candidates of electrodes in various electronic devices. Consequently, we have found that an introduction of very thin (about 3 nm thick) Al oxide surface and interface layers was very effective. For example, we confirmed a high thermal stability up to 600 °C even the Ag layer thickness was reduced to 50 nm in Al/Ag/Al films.

In the present work, we have further reduced the thickness of Ag layer in Al/Ag/Al films to obtain high transparency and investigated possibility to apply them as transparent electrodes. As a result, the Ag layer thickness could be reduced to 10 nm in Al/Ag/Al films, keeping a low electrical resistivity. On the other hand, Ag single layers thinner than 14 nm were discontinuous state having a high electrical resistance. Transmittance above 70% was obtained for the Al/Ag(10nm)/Al films. In addition, the property change of the films was found to be very little even after keeping them in air at 60 °C for 300 hrs, or in pure water at room temperature for 200 hrs. Consequently, it is found that the Al/Ag/Al thin films have good properties as transparent conductive electrodes.

TF-TuP3 Synthesis and Characterization of Cubic BC₂N Deposited by Reactive Laser Deposition. *H.A. Castillo*, Universidad Nacional de Colombia Sede Manizales, Colombia, *J.M. Vélez*, Universidad Nacional de Colombia Sede Medellín, Colombia, *W.H. de la Cruz*, Universidad Nacional Autónoma de México

Boron carbide nitride is considered a very important material, used for industrial applications due to their high hardness. Cubic BC₂N films were synthesized in a laser ablation system using a target of B₄C with 99.9% wt. Films were grown on (111) silicon wafers in an ultra high vacuum system with a base pressure in a low 1×10^{-9} Torr range. Target ablation was performed by means of a KrF excimer laser ($\lambda=248$ nm). During the grown process, the substrate temperature was varied in order to identify the influence of this parameter in the structure, composition and morphology of the coating. The composition, bonding configuration was obtained by X-ray

photoelectron (XPS) and the mechanical properties hardness and Young's modulus were determined using a Berkovich nanoindenter. Structural analyses with X-ray diffraction exhibited only 111, 200 and 220 lines of the cubic lattice.

TF-TuP4 Comprehensive Comparison of Electrical and Reliability Characteristics for Various Copper Barrier Films. *Y.J. Cheng, C.-T. Jung, J. Wu*, NCNU, Taiwan, Republic of China

The physical, electric and reliability characteristics of various Copper (Cu) barrier layers, including SiC, SiCN, SiCO, SiCNO, and SiN, were investigated. The reliability results associated with film characteristics were also reported in this work. The SiN film still shows the better Cu barrier performance, adhesion strength with Cu, and electromigration (EM) reliability, but its dielectric constant is too high. Nitrogen-doped or oxygen-doped silicon carbide barrier films (SiCN or SiCO) can reduce the dielectric constant, but show a traded-off reliability performance. A newly developed SiCNO film with doping nitrogen and oxygen can meet the better reliability (EM/SM) requirements at the same time, and has a comparable physical and electrical performance to the SiN film.

TF-TuP5 Growth of Silicon-Germanium-Carbon Alloys Using Modified Laser Ablation. *J.G. Quiñones Galván, F. de Moure Flores, A. Hernández Hernández, S. Cerón Gutiérrez, K. Nieto Zepeda, M.A. Meléndez Lira*, CINVESTAV-IPN, Mexico

Laser ablation technique allows depositing thin films with the same stoichiometry of the target material. The common use of solid targets is a limitation when there is a need to produce ternary alloys. In order to overcome that limitation we designed a modification of the laser ablation technique to employ powders as target.¹

The incorporation of carbon in a SiGe alloy is an alternative for achieving larger band gap and strain compensation. The main problem to control substitutional carbon concentration in SiGeC is the low solubility coefficient of carbon in silicon. Laser ablation technique allows exploring deposition parameters far from the equilibrium that could improve the content of substitutional carbon.

In this work we present the growth and characterization of thin films of Si_{1-x-y}Ge_xC_y alloys in the compositions range $0.27 \leq x \leq 0.29$ and $0.01 \leq y \leq 0.03$ deposited at different temperatures using the Modified Laser Ablation technique.

The samples were characterized by scanning electron microscopy, atomic force microscopy, X ray diffraction, energy dispersive X-ray spectroscopy, Raman, photoluminescence and photoreflectance spectroscopies. Results indicate the modification of the electronic properties of the alloys depending on the carbon content.

¹ M. González-Alcudia, A. Márquez-Herrera, M. Zapata-Torres, M. Meléndez-Lira and O. Calzadilla-Amaya, Adv. in Tech. of Mat. And Mat. Proc. J. 9, 81 (2007).

TF-TuP6 Interface and Properties of ALD Ta₂O₅ Films on Si (100) and GaAs (100) Surfaces. *T. Gougousi, J.W. Lacin*, UMBC

Tantalum pentoxide (Ta₂O₅) films have been deposited using an Atomic Layer Deposition (ALD) process based on the reaction of pentakis dimethyl amido tantalum (PDMAT) and H₂O at 250°C. Films were deposited on native oxide Si(100) surfaces and native oxide and etched GaAs(100) surfaces. Linear growth at ~0.6 Å/cycle has been confirmed using spectroscopic ellipsometry. Atomic Force Microscopy indicates that the films are smooth and x-ray diffraction data indicate that the as-deposited films are amorphous, and begin to crystallize after anneals at 800°C (3 min, Ar). These observations are mirrored in the infrared spectra. Film composition has been studied using x-ray photoelectron spectroscopy (XPS) and it has been found that the films are slightly over oxidized. The interface of films deposited on native oxide and etched GaAs surfaces has also been studied using XPS and high resolution transmission electron microscopy. Data from both techniques indicate that an interface cleaning mechanism similar to that observed for other amide based ALD processes may be present.

TF-TuP7 The Mechanical Properties and Thermal Stability of CrZrSiN/AlN Multilayer Coatings Synthesized by Closed Field Unbalanced Magnetron Sputtering. *S. Lee*, Korea Aerospace University, Republic of Korea

In this work, for the high temperature applications, CrZrSiN/AlN multilayer coatings with various bilayer thicknesses (Λ) were synthesized using a closed-field unbalanced magnetron sputtering (CFUBMS) and their chemical composition, crystalline structure, morphology, mechanical properties, and thermal stability were characterized by glow discharge optical emission spectroscopy (GDOES), X-ray photoelectron spectroscopy (XPS), X-ray diffraction (XRD), scanning electron microscopy (SEM),

atomic force microscopy (AFM), and nanoindentation. Also, the thermal stability of the CrZrSiN/AlN multilayer coatings was evaluated and compared with that of the CrZrSiN coatings by annealing the thin films at temperatures between 500 °C and 1200 °C for 30 min in air and under vacuum. The experimental results revealed that the hardness of the CrZrSiN/AlN coating was much superior to that of the CrZrSiN coating after annealing at various temperatures due to the presence of alternating AlN thin films. Furthermore, in the CrZrSiN/AlN coating with the bilayer thicknesses of 2.4 nm, the relatively high hardness of 28.3 GPa was maintained even after annealed at 1100 °C. The detailed experimental results will be presented.

TF-TuP8 First Reset Resistance Switching Characteristics with the Crystallinity of Ta₂O₅ Films, H.-C. Sohn, H.D. Na, K.-M. Lee, J.G. Kim, S.-H. Lee, Yonsei University, Republic of Korea

In this work, we investigated the effect of the crystallinity on the first reset resistance switching characteristics of Ta₂O₅ films. Ta₂O₅ films annealed by Rapid Temperature Process (RTP) at above 650 °C were changed from amorphous to poly-crystal structure. The post-annealing temperature of above 650 °C produced the resistance switching behavior of first reset process, indicating the disappearance of forming process due to high current level. For indentifying the formation of local conductive path, the ratio of High Resistance States (HRS) and Low Resistance States (LRS) in 200 x 200 μm² pattern of Ta₂O₅ was measured with the regular interval of 25 points at read voltage of 0.2 V. The crystallinity of Ta₂O₅ films with the annealing temperature was measured by X-Ray Diffraction (XRD) and Transmission Electron Microscopy (TEM). TEM and Fast Fourier Transform (FFT) images showed the nano-crystal structure in local region of Ta₂O₅ film annealed at 650 °C. We expected that the local crystal structure in Ta₂O₅ films formed by RTP is expected to be closely related to the local conductive path.

TF-TuP9 Preparation and Characterization of Ta-doped Indium Tin Oxide Films Deposited by DC Magnetron Sputtering, S.M. Chung, J.H. Shin, W.-S. Cheong, C.-S. Hwang, S.H. Park, K.I. Cho, ETRI, Republic of Korea

Transparent conductive oxide (TCO) films have been widely used as transparent electrodes for various applications such as smart windows, flat panel display (FPD), touch panel, light-emitting diodes, optical wave guides, and solar cells. It is well known that the TCO films require the properties of wide band gap (>3.0eV), high conductivity, and high transmittance (>80%) in the visible range. Current applications of the TCO films emphasize minimizing resistivity. Among the technologies available for producing ITO films, DC magnetron sputtering can produce high quality films and be adapted to large-area coatings. In general, the characteristics of indium tin oxide (ITO) depend on its oxidation state and the content of impurities. The carrier concentration may also be modified by the dopant activation state because a donor atom can substitute the lattice site producing more than one free electron to increase conductivity. Ta also can be a donor because the indium is replaced by Ta in the In₂O₃-matrix ITO film, which releases one free electron contributing the electrical conductivity.

In this work, ITO and ITO:Ta films were deposited on corning glass substrates by DC magnetron sputtering using ITO and Ta-doped ITO targets, respectively, at room temperature. Effects of Ts dopant on the structural and opto-electrical properties of the ITO films were investigated. The detailed results will be revealed in this presentation.

TF-TuP10 Deposition of Ga-doped ZnO Films by Atomic Layer Deposition Using Ozone as the Oxygen Source, H. Yuan, B. Luo, S.A. Campbell, W.L. Gladfelter, University of Minnesota

Gallium-doped ZnO (GZO) films were grown on Si and SiO₂/Si substrates at 250°C by atomic layer deposition using diethylzinc as zinc precursor and ozone as the oxygen source. Trimethylgallium were used as the dopant precursor, and two approaches to doping were studied. In one a nanolaminate was formed by interspersing a trimethylgallium/ozone cycle in between the diethylzinc/ozone cycles. The overall gallium concentration depended on the number of diethylzinc/ozone cycles. The second approach involved co-injection of both metal precursors in which their relative concentrations were controlled by adjusting the precursor vessel temperature. The influence of the deposition method on the composition, structural, electrical, and optical properties of the GZO thin films as a function of doping metal concentration will be reported. X-ray diffraction patterns showed all the samples were polycrystalline and exhibited (0001) preferential orientation. The carbon content of the films was below the detection limit of Auger electron spectrometry. The lowest resistivity (4.7×10⁻⁴ Ω·cm) of the as-deposited films was obtained through use of the co-injection process. The average optical transmission was over 85 % in the range of 400-800 nm and the optical band gap increased with increasing

doping in accordance with the Burstein-Moss effect. The effect of rapid thermal annealing will be presented.

TF-TuP11 Fabrication and Structural Analysis of W-Ti-O Thin Films, N.R. Kalidindi, S.K. Gullapalli, R.S. Vemuri, F.S. Manciu, K.B. Karuppanan, C.V. Ramana, University of Texas at El Paso

Semiconductor oxide based chemical sensors are widely used for detecting very small amounts of toxic gases. Tungsten (W) oxide thin films have been used for measuring small amounts of H₂S gas. The present work was performed on tungsten-titanium mixed oxide (W-Ti-O) thin films for application in H₂S sensors. W-Ti-O were deposited by r.f. magnetron sputtering from a W-Ti alloy target with 5 % (wt %) Ti. W-Ti-O films were grown at different substrate temperatures ranging from 30 to 500°C. All the films were grown with argon/oxygen ratio of 1:9. Structural characterization was performed using X-ray diffraction (XRD) and scanning electron microscopy (SEM) measurements. The results indicate that the W-Ti-O films grown up to the substrate temperature of 200°C were amorphous while films grown at 300-500 °C were crystalline. The peak broadening was found to increase with increase in substrate temperature from 300°C to 500°C due to the increase in disorder with the inclusion of Ti. XRD and SEM results confirm significant disordering at the Si-film interface at higher processing temperatures. Based on the results, which will be presented and discussed, the effect of substrate temperature on the microstructure of W-Ti-O films is established.

TF-TuP12 O K and Si (Ge) L_{2,3} (M_{2,3}) Spectra of Non-Crystalline Plasma-Deposited Thin Film nc-SiO₂ and nc-GeO₂, D.J. Zeller, K. Wu, G. Lucovsky, North Carolina State University

Four-fold coordinated Si-atoms in nc-SiO₂ are bonded to two-fold coordinated O-atoms in a bent 3-atom group with Si 3d-associated T_{2g} symmetries on the Si-atoms [1]. These constrain the dihedral angles bridging O-atoms, and contribute to medium range order (MRO) with correlation a length of ~0.4 to 0.45 nm, and a coherence length of ~1 nm, each obtained from analysis of the first sharp diffraction peak in X-ray/electron diffraction [2]. Similar considerations apply to nc-GeO₂. Analysis of O K edge spectra for nc-SiO₂ reveals conduction band states with 3s-state symmetries at the band edge, and stronger 3d-state symmetries at higher energy. The s-state features define the respective band gaps of ~9 eV for nc-SiO₂, and ~6 eV for nc-GeO₂. In nc-SiO₂, the energy difference between band edge non-degenerate A₁ features, and the triply degenerate T₂ and doubly degenerate E d-state features is ~3 eV, whereas in c-Si it is smaller, ~1 eV. The relative energies are these features are the same as band edge features obtained from transmission and reflectivity studies in the visible and VUV where this d-state character was not previously recognized [3]. This correspondence derives from O 1s core hole localization, and a coherent process whereby these core states are filled by electrons from valence band O 2p p states. Additionally, there is a one-to-one correspondence between Si A₁ features and the Si T_{2g} features in the O K edge and the Si L_{2,3} spectra of SiO₂. Studies of L_{2,3} transitions by electron energy loss spectroscopy (EELS) did not detect the Si 3s features in the 100 to 104 eV regime of nc-SiO₂, or in the 98 to 100 eV regime of c-Si. Analysis of O K and L_{2,3} spectra are based on the charge transfer multiplet (CTM) formalism [4]. The ground state is Si2p⁶3d⁰ $\bar{\underline{L}}$ + Si2p⁶3s⁰ $\underline{\underline{L}}$, where $\underline{\underline{L}}$ describes a coherent process in which Si 1s core level holes are neutralized by electrons from the O 2p states. Ground states have ¹A symmetries, excited states are Si2p⁵3d¹ $\underline{\underline{L}}$ + Si2p⁵3s¹ $\underline{\underline{L}}$ with ¹F and ¹P symmetries, respectively. Degeneracies are lifted by different J values associated with the orbital angular momentum. Similar spectral features are observed for nc-plasma-deposited GeO₂, and these films exhibit the same correspondence between Ge 4s- and 4p-derived features in the O K edge and the Ge M_{2,3} edge.

- [1] Whitten J, et al., J. Vac. Sci. Technol. B 20, 1710 (2002).
- [2] Lucovsky G, et al. physica status solidi (a) 207, 631 (2010).
- [3] Laughlin RB, Phys. Rev. B 22, 3021 (1980).
- [4] de Grott F, Kotani A. Core level spectroscopy of solids (Boca Raton, CRC Press, 2008).

TF-TuP13 High Temperature Oxidation Performance of Multilayered Al_xTi_{1-x}N/CrN Coatings, Y.Y. Chang, W.H. Wu, Mingdao University, Taiwan, Republic of China

The high temperature oxidation behavior of Al_xTi_{1-x}N and multilayered Al_xTi_{1-x}N/CrN coatings was studied. These coatings were synthesized by cathodic-arc evaporation with plasma enhanced duct equipment. Chromium and AlTi alloy alloy (70/30 at. % ratio) cathodes were used for the deposition of Al_xTi_{1-x}N/CrN coatings. During the coating process of multilayered Al_xTi_{1-x}N/CrN, CrN was deposited as an interlayer. The multilayered structure was obtained by regulation of cathode power at a constant rotation speed of sample holders. The nanolayer thickness and

alloy content of the deposited multilayered coating were correlated with the emission rate of alloy cathode materials. In this study, field emission scanning electron microscope (FESEM), and X-ray diffraction using glancing angle parallel beam geometries were used to characterize the microstructure of the deposited films. High resolution transmission electron microscope (HRTEM) was used for nanolayered structure analyses of the multilayered $Al_xTi_{1-x}N/CrN$ coatings. For the high temperature oxidation test, the coated samples were annealed in the temperature range 700–1000 °C in air for 2 hours. After oxidation, the deposited $Al_xTi_{1-x}N$ had completely transformed to TiO_2 and Al_2O_3 at 900 °C. Interestingly, the multilayered $Al_xTi_{1-x}N/CrN$ possessed superior oxidation resistance than the graded $Al_xTi_{1-x}N$. The different oxidation mechanisms of $Al_xTi_{1-x}N$ and multilayered $Al_xTi_{1-x}N/CrN$ at high temperature are developed in this study.

TF-TuP14 Formation of Ti-Doped DLC Films by Inert-gas Ion Beam Assistance in a $C_{10}H_8$ Atmosphere, S. Narita, I. Takano, Kogakuin University, Japan

Diamond-like carbon (DLC) has the amorphous structure that is chiefly composed by graphite (sp^2) and disordered graphite (sp^3) state. Therefore mechanical properties of DLC generally show high hardness and low friction. DLC film has been prepared by various method of chemical vapor deposition (CVD) or physical vapor deposition (PVD) including the sputtering method. Commercial applications of DLC have been already performed as engine parts of an automobile or surface coating of a hard disk.

In this study, Ti-doped DLC films were formed using He^+ or Ar^+ ion beam assistance in a naphthalene ($C_{10}H_8$) atmosphere. The formation conditions of DLC film were changed with ion-beam accelerating voltage and current density. Ti doping was performed by using the electron-beam deposition method with Ti evaporation rate from 0.0 to 0.2 nm/sec. The mechanical properties of hardness and friction coefficient were determined using the dynamic micro knoop hardness tester and the ball-on-disk tribotester respectively. Atomic concentration and structure of the films were investigated by X-ray photoelectron spectroscopy, X-ray diffraction and Raman spectroscopy.

The suitable mechanical property of DLC films was obtained by the condition with accelerating voltage of 5 kV at current density of 10 $\mu A/cm^2$. The maximum hardness was 5.37 GPa using Ar^+ ion beam, while the minimum friction coefficient was 0.117 using He^+ ion beam. It was clear that properties of DLC film was changed by ion species. In the case of Ar^+ ion beam, the higher hardness film contained much sp^3 state, while the film with lower friction coefficient contained much sp^2 state. From the other side the higher hardness film has a large crystal grain size as compared with the film with lower friction coefficient.

TF-TuP15 On the Optics of Thin Films Applied in Aerospace Telescope, C.N. Hsiao, H.P. Chen, P.K. Chiu, Y.W. Lin, W.H. Cho, F.Z. Chen, National Applied Research Laboratories, Taiwan, D.P. Tsai, National Taiwan University

Optical thin films designed for space grade multi-spectral assembly in CMOS sensor and reflective Ag mirror were deposited on radiation-resistant glass by ion-beam-assisted deposition for a Cassegrain-type aerospace telescope. The patterned multi-spectral assembly contained the blue, green, red, near infrared, and panchromatic multi layers high/low alternated dielectric band-pass filters arrays in a single chip which was fabricated by photolithography process. The corresponding properties of the films were investigated by in-situ optical monitoring, ellipsometry, spectrometry, and high-resolution transmission electron microscopy. It was found that the average transmittances are above 88% for the multi-spectral assembly, with a rejection transmittance below 1% in the spectral range of 350–1100 nm. The average reflectance of the Ag mirror (with a protective interference coating) is boosted above 99% in visible spectrum. The polarization sensitivity of the optical payload is below 5%. Furthermore, to estimate the optical stability of optical thin films for aerospace applications, a space environment that the satellite orbiting above the earth surface at an altitude near 900 kilometers were simulated by Co^{60} gamma (γ) radiation test (total dose effects) and thermal vacuum test (pressure below 10^{-7} Torr with thermal cycles). The optical stability of the films with the environmental test will be discussed.

TF-TuP16 Modification of Band Gap Structure of Cu-implanted TiO_2 Catalytic Thin Films by using Metal Plasma Ion Implantation Technique, D.Y. Wang, Mingdao University, Taiwan, C.C. Yen, L.S. Chang, National Chung Hsing University, Taiwan, M.H. Shih, Mingdao University, Taiwan, H.C. Shih, National Chung Hsing University, Taiwan

The anstae TiO_2 thin film has long been identified as the potential photocatalytic materials for various industrial applications. The Cu-implanted TiO_2 catalytic films were prepared by the sol-gel process in conjunction with the metal plasma ion implantation (MPII) technique at an

acceleration voltage of 20 keV with various ion dosages. The surface chemical states and compositions of Cu-implanted TiO_2 films were investigated by XPS. The optical band gap of the films was calculated by using Tauc formula. The photocatalytic activity was evaluated by the photodegradation of methylene blue (MB) under visible light irradiation. The correlation between the band gap structure and the photocatalytic behaviors of Cu-implanted TiO_2 were investigated. The electronic band structure and the location of Cu atom in anatase TiO_2 were studied by the first-principle calculations based on the density functional theory. The result demonstrated the dependence of the band gap structure on Cu dosage, which induced the formation of impurity energy levels in the band gap.

Keywords: TiO_2 , band structure, photocatalysis, MPII.

TF-TuP17 Nanofabrication of Insulated Scanning Probe Microscopy for Electromechanical Imaging in Liquid Solutions, J.H. Noh, University of Tennessee, M. Nikiforov, S.V. Kalinin, Oak Ridge National Laboratory, A.A. Vertegel, Clemson University, P.D. Rack, University of Tennessee at Knoxville; Oak Ridge National Laboratory

The fabrication and electrical and electromechanical characterization of insulated scanning probes have been demonstrated in liquid solutions. The silicon cantilevers were sequentially coated with chromium and silicon dioxide, and the silicon dioxide was selectively etched at tip apex using focused electron beam induced etching (FEBIE) with XeF_2 . The chromium layer acted not only as the conductive path from the tip, but also as an etch resistant layer. The relevant nanofabrication issues relative to the metallization and the insulator deposition process have been discussed. This insulated scanning probe fabrication process is compatible with any commercial AFM tip and can be used to easily tailor the scanning probe tip properties because FEBIE does not require lithography. The suitability of the fabricated probes is demonstrated and discussed by imaging of standard grid as well as piezoresponse force microscopy (PFM) and electrical measurements.

TF-TuP18 The Observation of Strain-Induced InN Nanorods Hetero-Epitaxially Grown by MOMBE, F.-I. Lai, W.-T. Lin, Yuan-Ze University, Taiwan, W.-C. Chen, C.N. Hsiao, National Applied Research Laboratories, Taiwan, S.-Y. Kuo, Chang Gung University, Taiwan, H.C. Hsu, National Cheng Kung University, Taiwan

In this study, we discussed the evolution of morphology and crystal structure of wurtzite indium nitride (InN) hetero-epitaxially grown on $GaN/sapphire(0001)$ by metal-organic molecular beam epitaxy (MOMBE) system with growth temperature. In order to investigate the influences of growth temperature, the stoichiometry of In/N was identical $\sim 1:1$ during the InN growth. The optical and structural properties of InN films samples were characterized by temperature-dependence photoluminescence (PL), field-emission scanning electron microscopy (FE-SEM) and x-ray diffraction (XRD). With increasing growth temperature, the surface morphology of InN varied from 1-dimensional (1D) nanorods to 2-dimensional-films. XRD results reveal that the strain of InN were released while increasing growth temperature. The PL emission peaks of InN nanorods and films were about 0.77 eV and 0.83 eV, respectively. In addition, it is noteworthy that the interface between GaN and InN nanorods exist massif-like structure as growth at lower temperature. These observation implied that the formation of 1D InN nanorods was ascribed to the strain-induced mechanism and will be discussed in detail.

TF-TuP19 Protecting Polymers from the Natural Space Environment with Films Grown Using Atomic Layer Deposition, M. Groner, ALD NanoSolutions, Inc., A.I. Abdulagatov, R. Fitzpatrick, S.M. George, University of Colorado, B. Wu, T. Minton, Montana State University

Polymers used on spacecraft are subjected to various threats including hyperthermal oxygen atoms, UV and VUV photons, and ions. These threats can degrade the polymer and lead to static charge accumulation. Nanometer thick inorganic films grown by atomic layer deposition (ALD) can protect polymers including Kapton, Teflon, and PMMA. We are developing multifunctional multilayer ALD films incorporating Al_2O_3 layers for preventing oxygen atom erosion, TiO_2 to minimize UV/VUV radiation damage, and ZnO to dissipate static charge. Such ALD-coated polymeric films are currently being tested in low Earth orbit on the International Space Station on MISSE-7b. In the laboratory, we are further exploring the mechanisms of polymer degradation by atomic oxygen and VUV radiation, as well as the cracking of inorganic films on polymers resulting from different thermal expansion coefficients. Field emission scanning electron microscopy images and profilometry measurements revealed that Kapton H samples coated with 25 ALD cycles (~ 3 nm) of Al_2O_3 completely resisted atomic oxygen erosion. Quartz crystal microbalance measurements of TiO_2 films deposited on PMMA substrates with an Al_2O_3 interfacial adhesion layer showed that 100 cycles (~ 6.2 nm) of TiO_2 resisted PMMA degradation upon VUV exposure. Mass losses of VUV-exposed PMMA

samples coated with similar overall bilayer thicknesses but different Al_2O_3 thicknesses were compared to decouple the role of the overall $\text{Al}_2\text{O}_3/\text{TiO}_2$ bilayer coating acting as a physical barrier from the role of TiO_2 acting as a VUV filter.

TF-TuP20 Effects of Pulse Frequency on the Structural, Electrical and Optical Properties of Al-doped ZnO Films by Pulsed dc Magnetron Sputtering. *C.T. Lee, B.H. Liou, W.H. Cho, C.N. Hsiao*, National Applied Research Laboratories, Taiwan, Republic of China, *K.S. Tang, C.C. Jaing*, Minghsin University of Science and Technology, Taiwan, Republic of China

The ZnO:Al (AZO) thin film was prepared on Si and glass substrates at 200 °C by pulsed dc magnetron sputtering deposition. Effects of pulse frequency on the structural, electrical and optical properties of AZO films were investigated by field emission scanning electron microscopy, X-ray diffraction, Hall measurement and spectrometer. The columnar structures are observed by field emission scanning electron microscopy. X-ray diffraction analysis reveals that AZO films were polycrystalline and have preferred orientation along (002). The grain size and resistivity of AZO films were investigated as a function of pulse frequency (5-100 kHz). The maximum grain size and minimum sheet resistivity of AZO film with 20 kHz were 37.5 nm and 650 ohm/sq, respectively. The average transmittance of AZO thin films was above 80% in the visible range. The presented results illustrate that the optimum properties of AZO films can be obtained at a pulsing frequency in the range of 5-100 kHz.

TF-TuP21 Fabrication of Cu-DLC Films by Cathodic arc Plasma Deposition. *J. Yun*, National Chung Hsing University, Taiwan, *S. Han*, National Taichung Institute of Technology, Taiwan

Copper-doped diamond-like carbon (Cu-DLC) films with varying Cu concentrations were deposited on 7050 aluminum alloy substrates using cathodic vacuum arc (CVA) system. Acetylene reactive gases were also activated at a pressure of 20 mTorr to 30 mTorr and a temperature fixed at 180 °C to provide the DLC. Structure, interface, and chemical bonding state of the investigated film were analyzed by transmission electron microscope (TEM), FTIR spectra, and X-ray photoelectron spectroscopy (XPS). The Cu-DLC film deposited exhibited an amorphous structure, while different fracture feature and surface morphologies was observed in these carbon films prepared under various acetylene reactive gases pressure. With increasing acetylene reactive gases pressure, the friction coefficient of the thin films is lower than 0.21 and the residual stress between the DLC thin films and aluminum alloy substrates can be substantially decreased after the effective doping of Cu into the films, which implies that the Cu-DLC films are suitable to be used as a protective coating on aluminum alloys.

Vacuum Technology

Room: Southwest Exhibit Hall - Session VT-TuP

Vacuum Technology Poster Session and Student Posters

VT-TuP1 Vacuum Pressure Simulation for the Hard X-Ray Insertion Device Beamline 17A at NSLS. *J.-P. Hu*, Brookhaven National Laboratory

Built in the 1980's, the insertion device beamline-17 at the X-ray storage ring of the Brookhaven Lab's National Synchrotron Light Source (NSLS) has been using superconducting-wiggler generated hard X-rays to facilitate cutting edge research. By sharing the wiggler's horizontal beam fan, three inline and one adjacent beamlines (17B1-B3 and 17C) have been designed to perform material stress-strain mapping, mineral phase transition under high-pressure, laser heating, and diffraction crystallography. To meet present-day high demand of hard X-rays for nano-structure probing via surface and interface scattering experiments and for large-volume high-pressure studies, a new beamline dubbed 17A, which also shares the wiggler's beam fan, has been constructed at immediately downstream to the common monochromator for all the branch beamlines at 17. For the purpose of improving beam quality, user safety and system vacuum, the degraded monochromator was replaced during the 17A construction by a custom-made monolithic unit to accommodate (1) a Si-crystal for the white beam bending (7.6-deg) into the 17A line, (2) a water-cooled white-beam filter followed by a collimated aperture for beam steering, (3) a Hevi-Met alloy of tungsten for bremsstrahlung shielding, (4) an ASME-certified burst disk for high pressure release, and (5) a sputter ion pump for outgas removal and high vacuum upkeep. Flanged to the beam exit port at the SS monochromator chamber is a round SS spool piece and a copper-brazed Be-window, installed to separate the beamline-17A vacuum from its upstream beamline-17 vacuum. At 1.4-meter downstream of the Si-crystal in monochromator is a 6-way cross, set to install a phosphor screen and a

CCTV for the beam image viewing and profile recording. Along the beam path of 2.6-meter from the 6-port optical enclosure, a 200 L/s sputter ion pump is hooked and sealed beneath the round beam pipe to remove desorbed gases from photon-stimulated scattering amid two Be-windows. For beam size confinement, residual gas analysis, synchrotron radiation blockage and shock wave monitoring, a tungsten slit, a tee-port, a tantalum-plated safety shutter and a Be-window are respectively installed at 0.7-, 1.5-, 1.8- and 2.5-meter off the ion pump. Prediction of pressure profile along the 17A was performed using the Monte-Carlo based Molflow code for gas conductance estimate and the finite-difference based Vaccum code for pressure distribution calculations. Details of beamline vacuum versus pre-cleaned and pre-baked assemblies encompassing the segmented beampipe will be presented. (Work performed under auspices of the US DOE, under contract DE-AC02-98CH10886)

VT-TuP2 Yttria/ Rhenium Alloy Emission Filaments for Analytical Instrumentation. *J. Manura, R. Shomo, C. Baker*, Scientific Instrument Services

Historically filaments used in most scientific instruments have been constructed from pure Rhenium. Rhenium has been the preferred material due to its resistance to oxidation and good emission qualities. However, Rhenium tends to be soft and has a tendency to warp and change shape during its operation. A new Yttria/Rhenium alloy has been developed for the purpose of improving the performance of filaments used in analytical instrumentation. The Yttria/Rhenium alloy filament exhibits the same electrical properties as pure Rhenium but has the advantage of not warping or changing shape, thereby improving the performance and lifetime of filaments used in analytical instrumentation.

Yttria alloys of rhenium were formed by sintering various concentration of yttria into rhenium. The sintered yttria/rhenium alloy bars were then drawn down to wires with diameters between 0.010" and 0.003".

Pure Rhenium filaments and Rhenium/Yttria alloy filaments of different configurations were tested to compare their properties. Testing was done using a custom filament station to measure the various filament electrical characteristics. Filaments were also tested in commercial instruments to monitor their performance. Electron microscopy studies were performed to study the grain characteristics.

Electrical studies in the filament testing station on pure rhenium filaments and various Yttria/Rhenium alloy filaments demonstrated that Yttria/Rhenium alloy filaments exhibited similar electrical properties as Rhenium. This enables these new alloy filaments to be used interchangeably with the standard rhenium filaments in analytical instrumentation.

Studies on the rhenium/yttria alloy filaments in commercial instruments demonstrated increased cycle lifetime as compared to standard rhenium filaments. The enhanced lifetime was attributed to the improved structural strength of the Yttria/Rhenium alloy filament. The Yttria/Rhenium filaments manufactured into different configurations all demonstrated less tendency to sag, warp or change shape as compared to pure Rhenium filaments.

Electron microscopy studies demonstrated that yttria oxide particles intermixed with the rhenium particles which minimized the grain growth in the alloy filament. In comparison, the pure rhenium filaments exhibited larger grain sizes. This smaller grain size in the alloy filament appears to strengthen the filament wire to provide a more stable filament that displays less sag or warping than pure rhenium filaments. The property of holding its shape has been demonstrated for multiple configurations. The Yttria/Rhenium material improves the performance of emission filaments used in analytical instrumentation.

VT-TuP3 Calibration of Ultra-High Vacuum Gauge from 10^9 Pa to 10^5 Pa by Two-Stage Flow-Dividing System. *H. Yoshida, K. Arai, M. Hirata, H. Akimichi*, National Institute of Advanced Industrial Science and Technology (AIST), Japan

A new two-stage flow dividing system has been developed for the calibration of ultrahigh vacuum gauges from 10^9 Pa to 10^5 Pa for N_2 , Ar, and H_2 . This system is designed based on the techniques of the calibration system in high vacuum region from 10^7 Pa to 10^2 Pa [1].

The system consists of four chambers: an initial chamber V_0 , a flow divider V_1 , a calibration chamber V_2 , and an evacuation chamber V_3 . Chambers between V_0 and V_1 and chambers between V_1 and V_2 are connected to each other with a capillary and a sintered filter, respectively. The chamber V_2 is evacuated by a turbo molecular pump (1100 L/s for N_2) through an orifice of 30 mm in diameter. The flow divider V_1 is evacuated by a subsidiary turbo molecular pump (220 L/s for N_2). The pressure P_0 in the initial chamber is changed in 12 steps using a pressure controller in the range from 10^2 Pa to 10^5 Pa. The time interval for each step is 600 seconds. Following the change in the P_0 , the pressure P_1 in the flow divider and the pressure P_2 in the calibration chamber similarly change from 10^4 Pa to 10 Pa and from

10^9 Pa to 10^5 Pa, respectively. The pressure P_2 is determined from the pressure P_1 using a pressure ratio of P_2 to P_1 . The ratio is pressure independent because the conductances of sintered filter C_1 and the effective pumping speed of the turbo molecular pump through the orifice C_{main} are pressure independent at molecular flow region.

The modifications of this system from the previous one are listed below. (1) TiN coated stainless steel vacuum chambers are used as V_2 and V_3 to decrease outgassing from the chambers [2]. (2) The conductance of the sintered filter is 1000 times smaller than that of previous system to control the pressure in the range from 10^9 Pa to 10^5 Pa. (3) The ratio P_2/P_1 is measured using a calibrated ionization gauge and a calibrated spinning rotor gauge. The ratio for N_2 , Ar, and H_2 is obtained to be 6.41×10^{-7} , 6.26×10^{-7} , and 8.36×10^{-7} , respectively.

The pressure P_2 is measured by an Extractor gauge (EXG) and an Axial-Symmetric Transmission gauge (ATG). The typical background pressure was $(2-4) \times 10^9$ Pa. These gauges were calibrated from 10^9 to 10^5 Pa for N_2 , Ar, and H_2 with an uncertainty of about 5% with the confidence level of 95% ($k=2$). The linearities of these gauges were within $\pm 2\%$. The fluctuations of pressure indications were within $\pm 2\%$ for 1 hour.

[1] H. Yoshida, K. Arai, H. Akimichi, M. Hirata, J. Vac. Sci. Technol. A 26 128 (2008)

[2] H. Akimichi, M. Hirata, Metrologia 42 S184 (2005)

VT-TuP4 Simultaneous Measurement of Pressure and Viscosity with a Resonant Sensor in a Viscous Flowing Gas, A. Kurokawa, AIST, Japan, H. Hojo, T. Kobayashi, VPI Co., Japan

With a quartz tuning-fork resonator vibrating at the resonant frequency in the viscous flowing gas, we found that the measurement of the resonator's Δf and ΔZ enabled to derive the pressure and the viscosity of the viscous flowing gas simultaneously. The parameter of Δf is the frequency change from its vibrating frequency in high vacuum. Another parameter of ΔZ is the impedance change from the resonator impedance in high vacuum. Also the ΔZ is related to the pressure and the viscosity of the gas. We focused on the pressure dependence of Δf and of ΔZ to derive the pressure and the viscosity.

In this experiment, to achieve the precise measurements of Δf and ΔZ , we paid careful attention to the temperature control because Δf was very sensitive to the temperature. We used the constant-temperature chamber in which the resonator, the driving circuit for the resonator, mass flow controllers, and the absolute pressure gauge were installed. The temperature variation was $\pm 0.1^\circ\text{C}$ during the experiment. In addition the driving circuit was stored in a thermostatic box which temperature was maintained at $30 \pm 0.02^\circ\text{C}$ to minimize the frequency drift. The driving circuit applied constant driving voltage (V_d) to the resonator and the driving current (I_d) passing through the resonator was monitored. The impedance of the resonator (Z) was given by the ratio of V_d to I_d . The resonator was a tuning-fork type quartz resonator and had a vibration frequency of 32 kHz. The measured gases were Ne, Ar, N_2 , O_2 , Kr. The gas was charged at 130 kPa initially, and was vacuumed at the rate of 20 Pa/sec. The pressure of the gas was measured with the capacitance manometer.

The results showed that $P-\Delta Z$ for every gas showed the same characteristics; the ΔZ has larger value for higher pressure. For the higher mass of the gas showed the larger ΔZ at atmospheric pressure except for Ne. The every $P-\Delta Z$ curve did not cross each other except for Ne.

The $P-\Delta f$ graph showed also the same tendency. The Δf has larger value for higher pressure, however, for the higher mass of the gas showed the larger Δf at atmospheric pressure including Ne. The every $P-\Delta Z$ curve did not intersect one another except for Ne. Then showed close but not the same characteristics.

The $\Delta Z-\Delta f$ plot revealed the difference between the $P-\Delta Z$ and $P-\Delta f$. The $\Delta Z-\Delta f$ curves did not intersect one another above 1 kPa and that the $\Delta Z-\Delta f$ curves were arranged in order of the viscosity of the gas. Then the pressure and the viscosity of the gas can be derived simultaneously from $\Delta Z-\Delta f$ curve.

VT-TuP5 Study on Calibration Methods of Discharge Coefficient of Sonic Nozzles using Constant Volume Flow Meter, W.S. Cheung, J.H. Shin, S.B. Kang, K.A. Park, J.Y. Lim, KRISS, Republic of Korea

This paper address technical issues in calibrating discharge coefficients of sonic nozzles used to measure the volume flow rate of low vacuum dry pumps. The first challenging issue comes from the technical limit that their calibration results available from the flow measurement standard laboratories do not fully cover the low vacuum measurement range of 10^{-3} ~ 10^0 mbar although the use of sonic nozzles for precision measurement of gas flow has been well established in national metrology institutes. The second one is to make an ultra low flow sonic nozzle sufficient to measure the throughput range of 10^{-2} mbar-l/s. Those small-sized sonic nozzles exploited in this study not only to achieve the noble stability and

repeatability of gas flow but also to minimize effects of the fluctuation of down stream pressures for the measurement of the volume flow rate of vacuum pumps. These distinctive properties of sonic nozzles are exploited to measure the pumping speed of low vacuum dry pumps widely used in the vacuum-related academic and industrial sectors.

Sonic nozzles have been standard devices for measurement of steady state gas flow, as recommended in ISO 9300. This paper introduces two small-sized sonic nozzles of diameter 0.03 mm and 0.2 mm precisely machined according to ISO 9300. The constant volume flow meter (CVFM) readily set up in the Vacuum center of KRISS was used to calibrate the discharge coefficients of the machined nozzles. The calibration results were shown to determine them within the 3 % measurement uncertainty. Calibrated sonic nozzles were found to be applicable for precision measurement of steady state gas flow in the vacuum process in the ranges of $0.6 \sim 2,050$ cc/min. Those flow conditions are equivalent to the very fine gas flow with Reynolds numbers of $26 \sim 8,500$. Those encouraging results may confirm that calibrated sonic nozzles enable precision measurement of extremely low gas flow encountered very often in the low vacuum processes. Both calibrated sonic nozzles are demonstrated to provide the precision measurement of the volume flow rate of the dry vacuum pump within one percent difference in reference to CVFM. Calibrated sonic nozzles are applied to a new 'in-situ and in-field' equipment designed to measure the volume flow rate of low vacuum dry pumps in the semiconductor and flat display processes.

VT-TuP6 High-k Gate Dielectric and Electrical and Surface Studies of Al_2O_3 , HfO_2 , La_2O_3 , $Al_xHf_yO_z$, and ZrO_2/HfO_2 on Silicon via Atomic Layer Deposition, G. Hernandez, R. Candler, S. Franz, Y.S. Lin*, UCLA

As the dimensions of the metal oxide semiconductor transistor shrink, quantum mechanical effects become more prominent. We are quickly reaching the limitations of SiO_2 thickness of 10 -12 Å in which the tunneling current degrades device performance. Therefore, high dielectric constant materials are needed to replace SiO_2 as the gate dielectric as we proceed to smaller devices. High-dielectric materials we study are Al_2O_3 , HfO_2 , La_2O_3 , $Al_xHf_yO_z$, and ZrO_2/HfO_2 deposited via Atomic Layer Deposit. We expect the aforementioned materials to have a lower leakage current and a band gap close to SiO_2 . We expect the nanolaminates to have a smoother interfaces as the expense of a band-gap in between each of its constituents. In order to characterize the electrical properties of each oxide, capacitors will be fabricated with oxide thicknesses of 50,100, and 150 Å. We will study the effects of different annealing /deposition temperature at the silicon-oxide interface by TEM. We also characterize the films with the material by XPS, AFM, and spectroscopic ellipsometry. The electrical properties will be determined by C-V and I-V measurements.

VT-TuP7 Overview of Anharmonic Resonant Ion Trap Mass Spectrometry Technology, P. Acomb, G. Brucker, K. Van Antwerp, M.N. Schott, Brooks Automation, Inc.

The poster will present the basics of an economical and commercially available mass spectrometer based upon Anharmonic Resonant Ion Trap Technology for mass selection. The mass separation method using electrostatic fields for ion trapping and the property of Autoresonance for mass selection will be shown. The key elements of gauge biasing, gas ionization, low-power RF-based mass separation and ion detection will be highlighted. Key performance characteristics of the anharmonic resonant ion trap will be summarized.

VT-TuP8 Elements of Vacuum Quality Measurement using an Anharmonic Resonant Ion Trap Mass Spectrometry Technology, L. Landman, Brooks Automation, Inc.

The poster will present the basics of a Vacuum Quality Measurement System using the inputs from commercially available mass spectrometer based upon Anharmonic Resonant Ion Trap Technology for mass selection, a total pressure gauge, external signals and a scripting tool to transform complex measurements into a single valued output.

VT-TuP9 A Computationally Simple, Wafer-to-Feature-Level Model of Etch Rate Variation in Deep Reactive Ion Etching, J.O. Diaz*, H.K. Taylor, Massachusetts Institute of Technology, R.J. Shul, R.L. Jarecki, T.M. Bauer, Sandia National Laboratories, D.S. Boning, Massachusetts Institute of Technology, D.L. Hetherington, Sandia National Laboratories

Modeling etch rate variation in Deep Reactive Ion Etching (DRIE) helps to identify possible defects in MEMS and IC devices arising from sub-optimal etching depths and times. Besides tool-specific properties, such as the chamber design, another cause for the observed non-uniformity effects is the particular wafer pattern employed. At the wafer scale, previous studies

* VT Student-Built Vacuum Systems Poster Competition

have shown that wafers with a large percentage of open (exposed Si) area, or pattern density, exhibit a radial center-low etch-rate distribution, while those with low pattern density achieve radial center-high etch rates. At the die scale, it is widely known that etch rate decreases as local pattern density increases. Furthermore, at the feature scale, the microloading effect describes how adjacent features tend to compete for radical species, thus decreasing overall etch rates within individual features.

We present a model to capture these pattern-dependencies by tracking the spatial and temporal distribution of the ion and radical species within the DRIE chamber. The model implementation uses a time-stepped algorithm with three levels – corresponding to the three different length scales – and a coarse-grain approach where multiple features in a given region are characterized by a particular shape, size and density. The local radical species concentration distribution above the wafer is determined at each time step using current feature geometries to compute their Knudsen transport coefficient which is linked to the radical transport mechanisms within other areas in the chamber. At the end of each time step, etch rate estimates based on this radical concentration distribution and current feature geometries are used to update feature depth information for the next time interval. At the wafer scale, our modeling results achieve a success comparable to that of previously-developed wafer-level models with an etch rate RMS error percentage between 2.1% and 8.2%. The results also show that feature-level etch evolution substantially impacts the wafer-level fluorine concentration and thereby modifies the wafer and die etch rate uniformity. We expect a similar model could be incorporated into CAD software tools to evaluate masks and correct potential design issues before they are made. Our results also shed light on possible tool and process modifications to allow users the capability of altering across-wafer etch rate variability. Sandia National Laboratories is a multi program laboratory operated by Sandia Corporation, a Lockheed Martin Company for the United States Department of Energy's National Nuclear Security Administration under contract DE-AC04-94AL85000.

VT-TuP10 Design, Simulation, and Implementation of Plasma Enhanced Atomic Layer Deposition in a Laminar Flow Reactor. *K. Kellogg**, *P. Falvo*, University of South Florida, *S. Lee*, University of South Florida, *T. Wright*, *J. Wang*, University of South Florida

A plasma enhanced atomic layer deposition reactor (PE-ALD) was built for the purpose of growing thin films on wafers up to 2.5" in diameter. Internationally, papers have been published describing characteristics of both homebuilt [1,2,3] and commercially available ALD reactors [4]. The construction of this reactor was strategically designed using these descriptions, within an allowable project time and budget. Design characteristics include an inert carrier gas, millisecond speed precursor valves, a remotely generated inductively coupled plasma, and a chamber with a high volume to surface ratio geometry. The reactor will act to complement and increase the current application repertoire versus our commercially available reactor located in the University's thin films laboratory. In this regard, the chamber must be optimized to accommodate unique recipe applications currently unattainable with the in-house system. The functionality of this reactor will include three separate modes of operation: a thermal reaction mode (thermal ALD) for use with general recipe applications, an isolated chamber mode necessary for high aspect ratio substrates, and a plasma enhanced mode (plasma enhanced ALD) for greater process recipe versatility such as metals and nitrides. ALD allows for a precision unattainable with other deposition processes. Unlike CVD, ALD is not dependent upon precursor flux upon the substrate surface, instead relying upon step-wise $A + B = P$ synthesis. Reactor characteristics such as laminar gas flow and plasma ion locality concentration and intensity will be modeled with COMSOL finite element simulations. ALD deposition cycle times are optimized according to ALD chemical reactions and by in-situ monitoring of sample growth rates by means of fiber optic spectroscopy. Important considerations included an optimized pumping rate and a minimization of unavoidable deposition upon all surfaces other than the process wafer. Process optimization was also pursued by means of vacuum gauge feedback and automation of precursor valve cycle sequence by means of a Lab View enabled PC. Other automated controllable growth parameters include substrate heater temperatures, reactor wall temperatures and the energies of plasma ion bombardment upon the substrate surface species. Safety concerns have also been addressed by ensuring suitable gas exhaust, pump maintenance, hard-wired safety valve shut-off programming and gas cylinder and hazardous materials safety training of individual users. The chamber design, multitude of process optimizations, and comparisons with existing designs and models allow for substantial research parameters to be explored and discussed.

References: [1] J. W. Elam, M. D. Groner, and S. M. George, "Viscous Flow Reactor with Quartz Crystal Microbalance for Thin Film Growth by

Atomic Layer Deposition," Review of Scientific Instruments, Vol. 73 No. 8, Aug. 2002, pp. 2981-2987 [2] H. C. M. Knoops, L. Baggetto, E. Langereis, M. C. M. van de Sanden, J. H. Klootwijk, F. Roozeboom, R. A. H. Niessen, P. H. L. Notten, and W. M. M. Kessels, "Deposition of TiN and TaN By Remote Plasma ALD for Cu and Li Diffusion Barrier Applications," Journal of the Electrochemical Society, Vol. 155, No. 12, Oct 2008, pp. G287-G294 [3] G. A. Ten Eyck, J. J. Senkevich, F. Tang, D. Liu, S. Pimanpang, T. Karaback, G. Wang, T. Lu, C. Jezewski, and W. A. Lanford, "Plasma-Assisted Atomic Layer Deposition of Palladium," Chemical Vapor Deposition, Vol 11, No. 1, 2005, pp. 60-66. [4] S. B. S. Heil, J. L. van Hemmen, C. J. Hodson, N. Singh, J. H. Klootwijk, F. Roozeboom, M. C. M. van de Sanden, and W. M. M. Kessels, "Deposition of TiN and HfO₂ in a Commercial 200mm Remote Plasma Atomic Layer Deposition Reactor," Journal of Vacuum Science and Technology A, Vol. 25, No. 5, Sept/Oct 2007, pp. 1357-1366.

VT-TuP11 A Cryogenic Vacuum Chamber for Low Temperature Thermophotovoltaic Testing. *D. DeMeo**, *T. Vandervelde*, Tufts University

Thermophotovoltaics (TPV) are devices capable of converting infrared electromagnetic radiation into electricity. Strained Layer Superlattices allow TPV devices to operate at longer wavelengths. In order to determine the performance of these devices, a unique test apparatus was designed and constructed. As the devices become sensitive to longer wavelengths (lower temperatures) in the infrared, the need to control the sample's ambient temperature becomes paramount. Here, we present a custom, cryogenic vacuum chamber specifically designed to test long wavelength TPV cells. The tester utilizes two copper heat shields cooled via conduction with two liquid nitrogen reservoirs to block outside thermal radiation. A blackbody source illuminates a temperature controlled sample at high vacuum, $\sim 10^{-6}$ Torr. The chamber is also connected to multiple thermocouples and a source-meter for measurement and testing purposes. This test apparatus will enable future research into low temperature TPV and other optoelectronic devices.

VT-TuP12 Experimental Approach to Equalizing the Orifice Method with the Throughput One for the Measurement of TMP Pumping Speed. *J.Y. Lim*, *S.B. Kang*, *J.H. Shin*, Korea Research Institute of Standards and Sciences, Republic of Korea, *D.J. Cha*, Kunsan National University, Republic of Korea, *D.Y. Koh*, Korea Institute of Machinery and Materials, Republic of Korea, *W.S. Cheung*, Korea Research Institute of Standards and Sciences, Republic of Korea

Methods of the characteristics evaluation of turbo-molecular pumps (TMP) are well-defined in the international measurement standards such as ISO, PNEUROP, DIN, JIS, and AVS. The Vacuum Center in the Korea Research Institute of Standards and Science (KRISS) has recently designed, constructed, and established the integrated characteristics evaluation system of TMPs based on the international documents by continuously pursuing and acquiring the reliable international credibility through measurement perfection.

The measurement of TMP pumping speed is normally performed with the throughput and orifice methods dependent on the mass flow regions. However, in the UHV range of the molecular flow region, the high uncertainties of the gauges, mass flow rates, and conductance are too critical to precisely accumulate reliable data. With UHV gauges of uncertainties less than 15% and a calculated conductance of the orifice, about 35% of pumping speed uncertainties are experimentally derived in the pressure range of less than 10^{-6} mbar. In order to solve the uncertainty problems of pumping speeds in the UHV range, we introduced an SRG with 1% accuracy and a constant volume flow meter (CVFM) to measure the finite mass flow rates down to 10^{-3} mbar-L/s with 3% uncertainty for the throughput method. In this way we have performed the measurement of pumping speed down to less than 10^{-6} mbar with an uncertainty of 6% for a 1000 L/s TMP. In this article we suggest that the CVFM has an ability to measure the conductance of the orifice experimentally with flowing the known mass through the orifice chambers, so that we may overcome the discontinuity problem encountering during introducing two measurement methods in one pumping speed evaluation sequence.

VT-TuP13 Implementation of a Lambertson Magnet in an Ultrahigh Vacuum Electron Storage Ring. *V. Anferov*, *J. Doskow*, *G. East*, *S.Y. Lee*, *T. Rinckel*, *C. Romel*, *T. Sloan*, *P. Sokol*, Indiana University

The Advanced Electron-Photon Facility (ALPHA), built at Indiana University, is a multipurpose electron accelerator to be used for DoD radiation effects testing as well as IU's interest in a compact high-brightness x-ray source. ALPHA consists of a 50 MeV linear accelerator source and 20 m storage ring which operates at 1×10^{-11} Torr. A Lambertson magnet, used to inject/extract the electron beam into and out of the ring, has been uniquely designed for optimal vacuum behavior and septum straightness

* VT Student-Built Vacuum Systems Poster Competition

while maintaining magnetic field quality. The design minimizes the ultrasonically-tested, 1018 steel pole tip exposure to UHV via a nickel plated surface and an exterior stainless steel vacuum body, welded to the pole tip. The magnet assembly yielded positive results in magnetic field and vacuum testing and is currently being commissioned in the ring.

Wednesday Morning, October 20, 2010

Applied Surface Science

Room: Cochiti - Session AS-WeM

New Ion Beam Technologies for Imaging, Sample Preparation and Analysis

Moderator: J.A. Gardella, Jr., SUNY at Buffalo

8:00am **AS-WeM1 Ion Photon Emission Microscopy: A Novel Method for Studying Radiation Effects**, *J.V. Branson, K. Hattar, G. Vizkelethy, C.J. Powell*, Sandia National Laboratories, *P. Rossi*, University of Padua and INFN, Italy, *B.L. Doyle*, Sandia National Laboratories

The development of a new radiation effects microscopy (REM) technique is crucial as emerging semiconductor technologies demonstrate smaller feature sizes and thicker back end of line (BEOL) layers. To penetrate these materials and still deposit sufficient energy into the device to induce single event effects, high energy heavy ions are required. Ion photon emission microscopy (IPEM) is a new technique that utilizes coincident photons, which are emitted from the location of each ion impact to map out regions of radiation sensitivity in integrated circuits and devices, circumventing the obstacle of focusing high-energy heavy ions. The (x,y) coordinates are instead determined with a single photon, position-sensitive detector. Thus, a high energy broad beam can be used to achieve high LETs, while still mapping out radiation-sensitive regions with sufficient resolution. Several versions of the IPEM have been developed and implemented at Sandia National Laboratories (SNL). The initial IPEM was a tabletop system, which utilized a Po-210 alpha source as the incident radiation. The second version has been utilized on the microbeam line of the 6 MV tandem accelerator at SNL, which allows for direct results comparisons between data obtained with a scanned, focused microbeam, and that from IPEM. Another IPEM was designed for ex-vacu use at the 88" cyclotron at Lawrence Berkeley National Laboratory (LBNL). That facility allows for the use of a heavy ion cocktail, with beam energies up to several GeV. Extensive engineering is involved in the development of these IPEM systems, including resolving issues with electronics, event timing, optics, phosphor selection, and mechanics. The various versions of the IPEM and the obstacles, as well as benefits associated with each will be presented. In addition, the current stage of IPEM development as a user instrument will be discussed in the context of recent results.

*Sandia National Laboratories is a multi-program laboratory operated by Sandia Corporation, a wholly-owned subsidiary of Lockheed Martin company, for the U.S. Department of Energy's National Nuclear Security Administration under contract DE-AC04-94AL85000.

8:20am **AS-WeM2 Synthesis and Characterization of Gold Nanocluster-Cavity Pairs in SrTiO₃**, *S.V. Shuthanandan, C.M. Wang, B. Arey, W. Jiang, Y. Zhang, T. Thevuthasan*, Pacific Northwest National Laboratory, *G. Duscher*, Oak Ridge National Laboratory

Dispersion of gold nanoclusters in single crystal TiO₂, MgO, and SrTiO₃ have been found to influence the optical properties of the materials. One way to make these clusters in these oxide media is through Au ion implantation followed by annealing at high temperatures for extended period of time. The Au clusters generated by this ion beam synthesis method often associated with vacancies as a cluster-vacancy pair in the matrix. These nanometer scale vacancy clusters are generally called quantum antidotes and they are believed to be spatially located at the interface between the Au clusters and the matrix. To verify this proposition, Au nanoclusters dispersed in SrTiO₃ single crystals were prepared using ion implantation at 975 K and subsequent annealing at 1275 K for 10 hours. We have used a suite of imaging capabilities including newly developed Helium ion microscopy (HIM) and scanning transmission electron microscopy (STEM) with high-angle-annular-dark-field (HAADF) imaging to understand the structural properties and spatial distribution of the Au and vacancy clusters. The results indicate that gold nanocluster-cavity pairs were formed uniformly throughout the implanted region. Size of the Nanocluster-cavity pairs ranges from 5 to 30 nanometers. In cluster free regions where the Au concentration is low, the HAADF results clearly indicate the substitution of Au for cations. The Au clusters and the cavity show spatial association, indicating a strong interaction during their respective clustering process.

9:00am **AS-WeM4 Material Contrast Mechanisms in FIB and SEM Images**, *L.A. Giannuzzi*, FEI Company, *M. Utlaut*, Portland State University

The relative contrast of both FIB and SEM images in metals yield a non-monotonic function with target atomic number. Material contrast from FIB

images is similar to the material contrast observed from SEM images, with differences that can be directly attributed to particle-solid interaction theory. The non-monotonic particle stopping power and the sputter yield (for those particles that cause sputtering) are directly responsible for material contrast. The term "Z-contrast" is shown to have a different meaning than universally understood.

9:20am **AS-WeM5 A High Brightness Plasma Source for Next Generation FIB, SIMS and Surface Engineering**, *N. Smith, P.P. Tesch, N.P. Martin, R.W. Boswell*, Oregon Physics

INVITED
Milling speeds with a gallium focused ion beam (FIB) are often much too slow for many sample preparation and surface engineering applications. For example, cross-sectioning stacked-die semiconductor devices, prototyping micro-mechanical structures and delayering IC's for circuit mapping are growing applications that require a milling rate that far exceeds that provided by the gallium FIB.

Furthermore, secondary ion mass spectrometry (SIMS) imaging has been limited to a lateral resolution of 200nm when using an oxygen focused ion beam for high sensitivity surface analysis. Many applications in material science could benefit from an ability to image trace level surface chemistry with <20nm resolution. Example applications include, sub-cellular imaging of trace metals in the brain for neurodegenerative disease studies, analysis of trace element segregation in metal alloys and studying isotope distributions in meteorites and interplanetary dust particles.

In the more general area of direct-write surface engineering, precision milling and deposition with nanometer precision is limited to volumes of <10⁴um³ when using gallium FIB systems. Also, engineered devices must generally be tolerant of high gallium concentrations being implanted in the near-surface region. These are major restrictions when fabricating devices that require nanometer precision across dimensions of several hundred micrometers. Additionally, inherent gallium implantation can render structures bio-incompatible and compromise the electrical properties of many materials.

Here, we review a plasma ion source technology (Hyperion™) that can provide a focused ion beam capable of milling silicon at a rate of >5000um³/s with <4um milling resolution and <20nm imaging resolution with 30keV xenon ions. The same ion source is also readily operated as a high brightness source of oxygen, hydrogen and any inert ions.

By transferring energy to plasma electrons via a RF induction field, it is possible to create a plasma state without a cathodic electrode. This approach can create high plasma densities (>1x10¹³ ion cm⁻³), with very low mean thermal ion energies (<0.05eV), providing the conditions for an energy normalized beam brightness that now exceeds 1x10⁴ Am²sr⁻¹V⁻¹. This high brightness can be attained with long lifetimes (>>2000 hours), stable beam current (<±0.5% drift per 30 minutes) and an axial energy spread for the extracted beam of 5-6eV and for an array of ion species.

This paper presents FIB and SIMS data from this new ion source. The operating principles of the ion source, the properties of the beam(s) being created and the projected future for this technology are also described.

10:40am **AS-WeM9 XPS Comparison of Ar, Coronene, C₆₀, and Ar Gas Cluster Ion Beam Depth Profiling of Polyimide Films**, *J.S. Hammond*, Physical Electronics, *T. Miyayama, N. Sanada*, ULVAC-PHI, Japan, *J.F. Moulder*, Physical Electronics, *M. Suzuki*, ULVAC-PHI, Japan, *A. Takuhara*, Kyushu University, Japan

Polyimide thin films have found wide-spread use in many industrial products such as microelectronics and thin film display panels due to their excellent insulating properties, high resistance to heat in manufacturing processes and its excellent flexibility and other mechanical properties. To increase the adhesion of metal films to polyimide substrates, ion beam and plasma surface modification steps are frequently incorporated in the manufacturing processes. It is therefore highly desirable to find a quantitative chemical depth profiling technique to characterize the surface modification layer and the polyimide thin film itself. A comparison of the use of XPS depth profiling of thin polyimide films with Ar, Coronene, C₆₀, and Ar Gas Cluster Ion Beam (GCIB) sputter sources will be presented. The GCIB sputter source produces an Ar_{2,500}⁺ ion beam with user definable incident beam energy. XPS elemental quantification and chemical state spectroscopy reveals that Ar, Coronene and C₆₀, ion sources produce rapid damage of the polyimide with a wide range of ion gun experimental conditions. Optimized conditions for the incident ion beam energy of the GCIB will be presented to provide minimal chemical state damage during the depth profiling of 100 nm thick films. Results will also be presented showing that the GCIB source can be used to remove Ar⁺ induced damage layers.

11:00am **AS-WeM10 XPS Sputter Depth Profiling of Organic Materials Using a Coronene Ion Source**, *S.J. Hutton, C.J. Blomfield, A.J. Roberts, G. Mishra, I.W. Drummond, S.C. Page*, Kratos Analytical Ltd., UK
The X-ray photoelectron spectroscopic (XPS) analysis of thin film or multilayer organic materials has recently been improved by the introduction of cluster ion sources for sputter depth profiling. One such commercially available cluster ion source uses the polyaromatic hydrocarbon (PAH) coronene. This source has successfully produced useful depth profiles of a number of model polymer films [1] [2] and mixed organic systems. [3] Results demonstrate a significant reduction in ion induced damage, as measured by XPS between ion etch sputter cycles, compared with conventional ion sources. High ion yields have been found for several polymers including poly(lactic-co-glycolic acid) (PLGA); Polyacrylic acid (PAA); and polylactic acid (PLA), however, other polymers, such as polystyrene (PSS), appear to be resistant to sputter profiling using cluster ion sources under previously investigated conditions. [4]

In this study we investigate a range of experimental parameters which influence ion yields and surface damage with the aim of optimising sputtering conditions for a number of different organic materials. Experimental factors include incident ion energy; ion beam angle of incidence; and sample temperature.

[1] D.E. Weibel, N. Lockyer, J.C. Vickerman, *App. Surf. Sci.*, **2004**, 231-232, 146-152.

[2] A.J. Roberts, S.J. Hutton, C.J. Blomfield, I. Drummond, S.C. Page, *J. Surf. Anal.*, **2009**, 3, 287.

[3] A. Rafati, M.C. Davies, A.G. Shard, S. Hutton, G. Mishra, M.R. Alexander, *J. Controlled Release*, **2009**, 138, 40-44

[4] R. Mollers, N. Tuccitto, V. Torrisi, E. Niehuis, A. Licciardello, *Applied Surface Science* **2006**, 252, 6509-6512.

11:20am **AS-WeM11 The Application of Digital Techniques to the Calibration of Depth Scales in XPS Sputter Profiling**, *P. Mack, T. Nunney, R.G. White, A. Wright*, ThermoFisher Scientific, UK

When sputter profiling a multi-layer material using XPS, it is often difficult to obtain an accurate calibration of the depth scale. In part, this is due to the fact that the sputter rate in each material is different and a post profile measurement of crater depth will only yield an average value for the sputter rate. The purpose of this paper is to provide a method for an internal, standardless calibration of the depth scale which can be applied to single profiles through multilayer materials.

As a layer is etched to a thickness of a few nanometres, the spectrum from the underlying layer can be seen. With knowledge of the electron attenuation lengths in the layers it is then possible to calculate the thickness of the remaining upper layer. If this calculation is carried out following each of a number of sputter cycles then the sputter rate within the layer can be calculated. This value can then be applied to sputtering within the whole of the upper layer. If this is repeated for each layer in a multilayer sample then an accurate depth scale can be constructed.

This method will be applied to a number of samples including standard multilayer materials and the value of the method assessed.

Biomaterial Interfaces

Room: Taos - Session B11-WeM

Biomolecules at Interfaces

Moderator: P. Kingshott, Aarhus University, Denmark

8:00am **B11-WeM1 Lipid Membrane Interface Mediated Protein Misfolding and Aggregation**, *E.Y. Chi*, University of New Mexico, *J. Majewski*, Los Alamos National Laboratory, *E. Mandelkow*, Max Planck Unit for Structural Molecular Biology, Germany, *K.Y. Lee*, University of Chicago

The misfolding and aggregation of the amyloid-beta (Ab) peptide and tau protein into fibrillar deposits are linked to the pathogenesis of Alzheimer's disease (AD). However, the molecular basis of the early events during the aggregation process and the nature of the structural fluctuations that triggers the misfolding and association of Ab and tau remain poorly understood. The lipid membrane interface has been implicated to mediate the fibrillogenesis of both proteins. Using model lipid membranes, we studied the nature and mode of lipid-protein interactions and characterized the effect of these interactions on the conformation and assembly of Ab and tau.

Both Ab and tau exhibit strong interactions with membranes composed of charged lipids, but interact weakly with zwitterionic lipids. To elucidate the molecular-scale structural details of Ab-membrane association, we used complementary X-ray and neutron scattering techniques (grazing-incidence X-ray diffraction, X-ray reflectivity, and neutron reflectivity) to investigate *in situ* the association of Ab with lipid monolayers at the air/water interface composed of either the negatively charged lipid DPPG, the zwitterionic lipid DPPC, or the cationic lipid DPTAP at the air/water interface. We found that the anionic lipid DPPG uniquely induced crystalline ordering of Ab at the membrane surface that closely mimicked the beta-sheet structures in fibrils, revealing an intriguing templated ordering effect of DPPG on Ab. Furthermore, incubating Ab with lipid vesicles containing the anionic lipid POPG induced the formation of amyloid fibrils, confirming that the templated ordering of Ab at the membrane surface seeded fibril formation. By measuring the interaction between different tau constructs (hTau40, K18 and K32) with membranes composed of different lipids, our data showed that tau's C-terminus, the microtubule binding domain, is responsible for its association with the lipid membrane. Moreover, hyperphosphorylation which is an early and critical event in the pathogenesis of AD, as mimicked by a tau mutant, did not prevent tau from binding to lipid membrane.

Our study provides a detailed molecular-scale characterization of the early structural fluctuation and assembly events that may trigger the misfolding and aggregation of Ab *in vivo*. Our study suggests that the "soft", intrinsically unfolded nature of both Ab and tau can give rise to rich dynamic behaviors at interfaces, such as the lipid membrane interface. Our data implicate that the adsorption of Ab and tau to anionic lipids in the cell membrane may serve as an *in vivo* mechanism of templated aggregation and drive the pathogenesis of AD.

8:20am **B11-WeM2 Effect of Metal Ions on Lipid Bilayer Formation on Semiconductor Surfaces**, *R. Jain, A.J. Muscat*, University of Arizona

Lipid bilayers have applications in drug delivery, bio-sensing for clinical diagnosis, and device fabrication. Just as in a living cell where a lipid bilayer separates aqueous compartments from their surroundings, a lipid membrane supported on a surface can function as a mask that allows selective mass transport via intermembrane proteins. Lipid bilayers have been used primarily to support proton channel proteins in sensors, but there are many other types of intermembrane proteins with different functions. With an aim to extend the use of biomolecules in device fabrication, the effect of heavy metal ions on bilayer formation was investigated using atomic force microscopy (AFM) and x-ray photoelectron spectroscopy (XPS). 1,2-dimyristoyl-*sn*-glycero-3-phosphocholine (DMPC) lipid molecules were used to form supported bilayers by the vesicle fusion method on hydroxylated Si, As₂O₃-terminated GaAs, and Al₂O₃ surfaces. Alumina was deposited on a p-Si(100) surface by atomic layer deposition (ALD) at 170°C using trimethylaluminum (TMA) and water as precursors. The bilayer was formed on an AFM stage for 6 hr and the stage was heated to 41.5±5°C, which is 17.5°C above the DMPC phase transition temperature. The height of lipid membranes measured with AFM after digging a hole was 4.9±0.5 nm on a hydroxylated Si surface and 4.0±0.6 nm on an alumina surface, which correspond to the thickness of a bilayer. The mechanical strength, uniformity, and integrity of membranes were measured after flowing copper sulfate solutions (100-3000 ppm) through a liquid flow cell over the formed bilayer on the Al₂O₃ surface. Al₂O₃ was chosen because Cu²⁺ ions are reduced to Cu⁰ on alumina, but not on SiO₂. It was found by XPS that the copper permeates through the lipid bilayer and deposits on the alumina surface as Cu⁰. Force distance measurements were made to understand copper permeation. The adhesion force of copper on Al₂O₃ was 2-3 times higher than that of lipid molecules, leading to breaking of the bilayer and deposition of copper. AFM confirmed the breakage and the bilayer thickness after copper exposure was 1.4±0.2 nm. This study shows that metal ions with a higher adhesion force than lipid molecules on an insulator surface disrupt bilayer formation, placing limitations on how bilayers can be used in device fabrication. These results also suggest an additional mechanism for the antibacterial properties of copper.

8:40am **B11-WeM3 Characterizing Carbohydrate-Modified Surfaces: Advancing the Glycomics Paradigm**, *D.M. Ratner*, University of Washington **INVITED**

Carbohydrates and glycoconjugates are involved in a myriad of biological processes, including fertility, cancer, the immune response, and host-pathogen interactions. The carbohydrate microarray (or glycoarray) has emerged as one of the most promising technologies capable of revealing the complex roles played by carbohydrates in biology and medicine. While the glycoarray has had a significant impact on the field of glycomics (the study of carbohydrates in biology), little is known about the function of surface chemistry on array performance. In addition, existing glycoarray technologies are non-standardized, utilize disparate chemistries, and are only partially optimized to interrogate low affinity interactions or discriminate between mono- and multivalent binding. To help realize the

glycoarray's full potential in glycomics research, new label-free and high-throughput diagnostic tools are needed to screen glycan-dependent interactions and expand our fundamental understanding of glycobiology. The reengineered glycoarray must also include a quantitative picture of glycan surface chemistry to advance our ability to match array results with the biological question or hypothesis being tested.

This study details the development a panel of carbohydrate-functionalized ultrasensitive label-free biosensors based on surface plasmon resonance imaging (SPRi), novel silicon photonic devices, and microelectrode microarrays. To define the role of biosensor surface chemistries, we describe the application of advanced surface analytical techniques to exhaustively characterize the biointerface of carbohydrate-modified surfaces for biosensor applications. X-Ray Photoelectron Spectroscopy (XPS), Time-of-Flight Secondary Ion Mass Spectrometry (ToF-SIMS), and Scanning Probe Microscopy (SPM) are used to examine the chemistries of glycoarray surfaces to establish the relationship between biosensor performance and glycan surface density and molecular conformation—highlighting the contributions of the surface analysis and biointerfaces communities in advancing the nascent field of glycomics.

9:20am **B11-WeM5 *In situ* Characterization of DNA Films, C. Howell, P. Koelsch, University of Heidelberg and Karlsruhe Institute of Technology, Germany**

Films of thymine, adenine and cytosine single-stranded DNA (homooligonucleotides) immobilized on gold were characterized in liquid under various conditions using broadband sum-frequency-generation (SFG) spectroscopy. Spectra of the three film types under these *in situ* conditions in the C-H stretching region were significantly different than those obtained in air and appeared to show unique contributions based on the nucleobase composition of the film. This could be the result of base-specific hydration differences for these films. Data in air showed no identifiable unique base contributions in this region; however, significant differences in peak intensities among the three film types were evident in the spectra. These differences appeared to correlate with the degree of order of the films, suggesting that SFG spectroscopy can be useful for detecting overall order in these types of systems. Hybridization behavior of these systems was also studied, with results showing detectable differences between hybridized and unhybridized films. These results contribute to the understanding of DNA films and help to establish a foundation for the investigation of more complex biomolecules *in situ* using SFG spectroscopy.

9:40am **B11-WeM6 Surface Characterization of Mixed DNA/Mercaptoundecanol Assembly on Gold, N. Vandencastele, L. Arnadottir, J.E. Baio, T.M. Weidner, L.J. Gamble, University of Washington**

The hybridization efficiency of DNA microarrays and biosensors is determined in part by variables such as the density and orientation of the single stranded DNA oligomers used to build the devices. In order to better understand the chemistry on the microarray surfaces, and therefore improve their response, we study model surfaces of DNA adsorbed on gold with x-ray photoelectron spectroscopy (XPS), near-edge x-ray absorption fine structure (NEXAFS) spectroscopy and time-of-flight secondary ion mass spectrometry (ToF-SIMS) to characterize the surface order and structure. We previously showed that varying the amount of diluent molecule, and thus the probe density, affects the hybridization efficiency of a 20mer thiolated single stranded DNA probe and the target.^{1,2} In this study we compare the density and orientation of a 40mer single-stranded thiolated DNA (HS-ss-DNA), when varying amounts of the diluent molecule 11-mercapto-1-undecanol (MCU) are adsorbed. DNA is detected on the surface using XPS (N1s and P2p peaks) and ToF-SIMS analysis. ToF-SIMS results for various backfill times and various backfilling media are compared using PCA analysis. In the first set of experiments the MCU backfill reaction takes place in water (ultra pure 18 M Ω), in the second set of experiment it takes place in sodium Tris EDTA buffer solution (STE). We showed that when the co-adsorption reaction is done with a solution of MCU in water, the amount of MCU that incorporates into the surface saturates at 18h and the amount of DNA on the surface remains relatively constant. When the same experiment is carried out using a MCU solution in STE buffer the MCU binding removes the surface bound DNA and all of the HS-ss-DNA is removed from the surface after 2h, suggesting a better hydration of the DNA in the STE medium. The improved hydration of the DNA increases it's mobility in the solution allowing an easier access of the MCU to the gold surface. Angle dependent NEXAFS spectra taken for DNA layers after different MCU backfill times in water showed the highest degree of orientational order after a 30 min MCU backfilling step. The data also indicate that the DNA nucleotide base rings are ordered parallel to the surface. Hybridization efficiencies of the 40 mer DNA layer with various densities will be compared with surface plasmon resonance (SPR).

(1) Gong, P.; Lee, C.-Y.; Gamble, L. J.; Castner, D. G.; Grainger, D. W. *Analytical Chemistry* 2006, 78, 3326-3334.

(2) Lee, C.-Y.; Gong, P.; Harbers, G. M.; Grainger, D. W.; Castner, D. G.; Gamble, L. J. *Analytical Chemistry* 2006, 78, 3316-3325.

Biomaterial Interfaces

Room: Taos A - Session B12-WeM

Proteins & Peptides on Surfaces

Moderator: P. Kingshott, Aarhus University, Denmark

10:40am **B12-WeM9 The Surface Mediated Assembly of Small Biomolecules Relevant to Prebiotic Chemistry, D.J. Frankel, L. Donlon, Newcastle University, UK**

On prebiotic Earth where the absence of large molecules such as enzymes would be a barrier to the formation of complex biological structures, self assembly mediated by surfaces could have offered an alternative mechanism for polymerisation. In this work we examine the interactions between various monomers of biological relevance including nucleic acid bases and amino acids. Unlike related studies the assembly was conducted in an aqueous environment which is the most prebiotically relevant solvent. STM shows that chiral amino acids form two dimensional crystals completely independently of the underlying graphite surface. Moreover the chiral amino acids can interact with nucleic acid bases to produce unique crystal structures. Unlike UHV single crystal studies the surface/adsorbate interaction is less relevant and the structures assembled in essence forgets the surface. We propose a mechanism by which subsequent solution based molecules can interact with these ordered surfaces to produce selective interactions.

11:00am **B12-WeM10 Stabilization of Proteins by Sol-Gel Encapsulation and Study of its Interactions with the Host Matrix, S. Sammeta, G. Doroudian, G.P. Lopez, E.Y. Chi, University of New Mexico**

Utilization of biological molecules such as proteins in biosensing and biofuel cell applications is one of the most innovative research fields. A major challenge that needs to be overcome in these applications is the adequate stabilization of proteins. Porous silica material made by the sol-gel process provides a promising host matrix for the encapsulation of proteins to increase their stability. The main objective of this study is to elucidate protein-host matrix interactions for the stabilization of proteins. In our study, lysozyme and cytochrome c were used as model proteins. We have developed two novel vapor exposure sol-gel techniques to encapsulate proteins using tetra methyl orthosilicate (TMOS) as a precursor: (I) *in-situ* protein exposure method, where a buffer containing a protein is directly exposed to TMSO vapor, and (II) buffer exposure method, where a buffer was first exposed to TMOS vapor and then a protein was added. Additionally, organically-modified glasses are used to study the effect of host-matrix hydrophobicity on protein structure and stability. Circular dichroism and high resolution derivative UV spectroscopy are used to evaluate the structure and thermal stability of encapsulated proteins. The effect of protein concentration and sucrose (a model osmolyte) on the structure and stability of encapsulated proteins are characterized. Cytochrome c retained native-like structures while lysozyme becomes partly unfolded when encapsulated in the silica matrix. Entrapment generally increases the thermal stability of proteins. Proteins encapsulated via the *in situ* technique are found to have higher thermal stability compared to those encapsulated using method II. In general, method II gave rise to proteins with more secondary structure. However, proteins in this matrix are less resistant to thermal denaturation. In addition, there are concentration-dependent decreases in protein secondary structure when encapsulated by method II. We believe that the trends are due to protein adsorption onto silica which causes denaturation. Osmolytes shift the protein native state ensemble towards more compact conformations, thereby increasing the conformational stability of proteins. We observed enhanced secondary structure of cytochrome c with the addition of 0.5 M sucrose and this enhanced structure and stability is preserved when the protein is encapsulated in silica gel in the presence of sucrose. The effect of increasing the host-matrix hydrophobicity by incorporating alkyl group substituted alkoxy silanes into the silica matrix on protein structure and stability will be presented.

11:20am **B12-WeM11 ToF-SIMS Imaging to Characterize DNA Microarray Surfaces, L.J. Gamble, N. Vandencastele, L. Arnadottir, D.G. Castner, University of Washington, D.W. Grainger, University of Utah**

Commercial DNA array slides are commonly made by microprinting techniques. These nanoliter droplets evaporate within seconds and this fast

drying may contribute to heterogeneous spots and inconsistent results. Successful development and optimization of DNA-functionalized surfaces for microarray and biosensor applications requires a better characterization of immobilized DNA. In this work, time-of-flight secondary ion mass spectrometry (ToF-SIMS) is applied to the study of spotted DNA surfaces on commercial microarray slides. ToF-SIMS results are directly compared to fluorescence images. Maximum Autocorrelation Factor (MAF) image analysis, a technique independent of the scaling of the raw data, is used to analyze the ToF-SIMS images. An IONTOF TOF.SIMS 5-100 instrument using a Bi source is used to analyze the samples. Immobilized DNA probes with 10, 20 and 40 μ M DNA concentrations as well as different Cy3 label concentrations are spotted on a commercially available microarray polymer slide. The effect of the spotting solution concentration as well as the amount of Cy3 label on spot uniformity is studied. MAF analysis of the ToF-SIMS image for a 20 μ M DNA spot shows that the areas seen as having high fluorescence intensities are related to higher concentrations of phosphate groups (from the DNA backbone) as well as sulfates and peaks with masses corresponding to the DNA bases. A comparison of MAF analysis of ToF-SIMS images for different DNA spotting concentrations indicates that the concentration of the spotting solution has an effect on the uniformity of the spot.

11:40am **B12-WeM12 Protein Nanopatterning for Studying Cell Adhesion**, *S. Kristensen, J. Malmström, J. Lovmand, M. Duch, D.S. Sutherland*, Aarhus University, Denmark

Synthetic materials are often used for biomedical applications. Interaction of cells with the interfaces and tissue components determine the biological outcome of the device. Knowledge about the interaction between the cells and biointerfaces is hence of importance in areas such as biomaterials, tissue engineering and cell culture. The interaction of the cells with its surroundings is mediated at the molecular and macromolecular level. Specific interaction with the extracellular matrix components or macromolecules in the outer membrane of adjacent cells provides signaling and communication pathways. Here patterns of extracellular matrix protein are used to study the development of cellular adhesion complexes.

Protein nanopatterns at the 100-3000 nm scale and with lateral ordering between independent ligands and controlled lateral mobility has been made by using a nanoscale chemical contrast of Au patches in a background of SiO₂ by colloidal lithography. The nanostructured surfaces are made by depositing a triple polyelectrolyte layer (PDDA/PSS/PAX) at Au substrates. Latex particles self assemble at the surface governed by electrostatic forces followed by SiO₂ evaporation and removal of the particles. The generated short range ordered arrays were further modified by octadecylmercaptane adsorption. The samples were subsequently treated with PLL-g-PEG for 30 min. followed by adsorption of fibronectin for 2 h. Myoblast cell(C2C12) or MDA-MB-435 cells were added to the samples and allowed to adhere to the surfaces for 6 h or 24 hours.

Fibronectin distribution at the nanopatterned surfaces was studied via liquid AFM showing that protein were adsorbed preferentially on the alkane thiol patches. SEM images showed that protein was patterned over large areas. Protein patterns of several other proteins such as Osteopontin, Vitronectin and Laminin were also demonstrated. Fluorescent microscopy showed that cells adhered to the patterns of size from 200nm and up. Small focal complexes were observed at the 200nm structures which were not linked to the actin cytoskeleton. For 500nm and 1000nm patches cell showed small focal adhesions connected to thin actin fibers and the adhesions were limited to individual patches.

We utilize colloidal lithography to fabricate protein patterns of size from nano to micro scale and from different proteins. The patterned areas are of a sufficiently large area to carry out large scale cellular characterisation in terms of adhesion morphology and differentiation. The protein patterning makes it possible to limit the length of developing focal adhesions to single patches and hence alter the cells ability to generate forces, spread and move.

Energy Frontiers Topical Conference

Room: Mesilla - Session EN+NS-WeM

Organic Photovoltaics

Moderator: R.J. Holmes, University of Minnesota

8:00am **EN+NS-WeM1 Interface Properties between Organic Blend Films and Metallic Substrates for Solar Cell Applications**, *L. Lozzi, S. Santucci*, University of L'Aquila, Italy

In the last years a strong effort has been devoted to develop new solar cells based on organic compounds. These organic compounds can be mixed with other molecules, as, for example fullerene or its derivatives, forming a blend

film to increase the charge separation efficiency. An important issue to evaluate the properties of these devices is to investigate the interface properties between these films and the metallic substrates generally used to realize the contacts.

In this work we have analysed, by using the photoemission spectroscopy (X-ray, Soft X-ray and Ultraviolet photons) the core levels and the valence band structures, in particular the HOMO states, of copper phthalocyanine (CuPc) and fullerene (C₆₀) blend films, composed by different CuPc:C₆₀ concentrations, deposited onto several metallic substrates (Au, oxidized Al and ITO), generally used as metallic contacts.

The molecular levels show, as a function of the blend film thickness and composition, a different behaviour depending on the substrate type. On Au the organic molecular level show, as the blend film thickness increases, a shift towards high binding energy. This shift depends on the organic composition. Depositing the blend film onto oxidized Al, a small shift in the opposite direction, i.e. towards lower binding energy, has been observed. Instead, when ITO substrate have been used, no shift have been observed.

The core levels generally show a different behaviour with respect to the molecular levels suggesting that no strong interaction with the substrates exist but a small redistribution of the molecular levels is present.

8:20am **EN+NS-WeM2 Energy Level Alignment at Conductive Polymer/Metal Interfaces**, *M.M. Beerbom, W. Wang, R. Schlaf*, University of South Florida

The energy level alignment between two prototypical conductive polymers, poly(3-hexylthiophene) (P3HT) and poly[2-methoxy-5-(2'-ethyl-hexyloxy)-1,4-phenylene vinylene] (MEH-PPV) and metals was investigated with ultraviolet and x-ray photoemission spectroscopy (XPS, UPS) dependent on the metal substrate work function. In these experiments thin films of the polymer material were grown in several steps on in-vacuum cleaned metal substrates. In between deposition steps the surface was characterized with UPS and XPS without breaking the vacuum. This was enabled by electrocoat polymer thin film deposition directly from solution, which allows the growth of clean macro-molecular films in vacuum. This enabled the measurement of the hole injection barriers and interface dipoles unaffected by environmental contamination artifacts. The presented results demonstrate a systematic dependence of the interface dipole on the substrate work function. This indicates that the charge neutrality level-based "induced density of interface states" (IDIS) model also holds for non-reactive conductive polymer/metal interfaces.

8:40am **EN+NS-WeM3 Electronic Structure of Key Interfaces in Organic Photovoltaic Cells**, *A. Kahn*, Princeton University **INVITED**

This talk reviews recent work on two types of interfaces that are important for organic photovoltaic cells. In the first part, we present the first direct determination via ultra-violet and inverse photoemission spectroscopy (UPS, IPES) of molecular level alignment between donor (D) and acceptor (A) in a bulk heterojunction.[1] We take the example of the interface between poly(3-hexyl thiophene) (P3HT) and [6,6]-phenyl C₆₁-butyric acid methyl ester (PCBM). The P3HT/PCBM blend is a standard, prototypical system for bulk heterojunction organic photovoltaic (OPV) cells. In question here is the relative position of the molecular levels of the donor (D) and acceptor (A) materials in the blend, given that LUMO(D) - LUMO(A) is linked to the charge separation process, and LUMO(A) - HOMO(D) is linked to the open circuit voltage (V_{oc}) of the OPV cell. A precise measurement of these molecular level offsets provides a firm basis for the accurate modeling of V_{oc} produced by these cells. The second part of the talk looks at the electronic structure of transition metal oxide films, such as MoO₃ or WO₃, and their role as hole-collecting electrode or central element of a charge recombination layer (CRL) in a tandem solar cell. Recent work has shown that these compounds exhibit exceptionally large electron affinity and work function.[2,3] N-doped by oxygen vacancies, they can act as efficient high work function hole-extractor (via electron injection through their conduction band) on the anode side of the solar cell. Similarly, combined with a low work function interlayer electrode, they form the central element of a CRL in a tandem cell.

[1] Z. Guan, J. Kim, Y.-L. Loo, and A. Kahn, *Org. Electr.* (submitted)

[2] M. Kröger, S. Hamwi, J. Meyer, T. Riedl, W. Kowalsky, and A. Kahn, *Appl. Phys. Lett.* **95**, 123301 (2009)

[3] J. Meyer, M. Kröger, S. Hamwi, T. Riedl, W. Kowalsky and A. Kahn, *Appl. Phys. Lett.* (in press, 2010)

9:20am **EN+NS-WeM5 Photocarrier Generation and Transport Characteristics in Organic Heterojunction Solar Cells**, *J.D. Myers, W.T. Hammond, J.P. Mudrick, J. Xue*, University of Florida

There have been many recent advances in improving the efficiency of organic photovoltaics (OPVs) by using new organic active materials and/or employing improved device architectures. However, our understanding of

fundamental OPV device operation principles is still incomplete. A new measurement technique for OPVs, synchronous photocurrent measurement, can give insight into the generation and transport characteristics of photogenerated charge carriers. In synchronous photocurrent measurements, a device is illuminated with chopped monochromatic light in addition to a constant white light bias with an intensity close to 1 sun. With the device biased at any given voltage, the current of the OPV is fed into a lock-in amplifier, which extracts the relevant photocurrent response to the monochromatic light with a varying wavelength.

With this technique, we have shown the bias dependence of the photocurrent for various small-molecule device structures. In planar (or bilayer) and planar-mixed organic heterojunctions (HJs), the photocurrent under forward bias is negative (flowing from the cathode to the anode, opposite to the direction of the dark current), up to high forward biases (~1 V), well in excess of the built-in potential. This reveals the surprisingly dominant nature of the diffusion photocurrent in these architectures. However, for mixed HJ cells, the photocurrent reverses direction at a certain forward bias with the reversal of directions for the electric field and the drift current inside the active layer. There exists a strong correlation between the zero-photocurrent voltage and charge generation profile in mixed HJ OPVs.

This technique can also determine the relative contributions of field-induced exciton dissociation and donor-acceptor interface exciton dissociation in planar HJ cells. Traditionally, exciton dissociation in planar HJ cells is assumed to occur almost exclusively at the donor-acceptor interface; field-induced dissociation is taken as a negligible contributor to the photocurrent in these devices. However, as the thickness of an active layer (either donor or acceptor) increases, field-induced dissociation becomes more important. The field-induced contribution increases as the average location of exciton generation moves greater than one exciton diffusion length away from the interface, as demonstrated by using optical field simulations.

We have further used photocurrent measurements as an instrument in analyzing the recombination behavior in planar organic HJs utilizing different materials. Synchronous photocurrent measurement is a useful technique in determining the photocarrier behavior in organic HJ solar cells.

9:40am EN+NS-WeM6 Interface Engineering for Improved Organic Photovoltaic Performance, C.K. Chan, D.S. Germack, P. Haney, L.J. Richter, D.M. DeLongchamp, D.J. Gundlach, National Institute of Standards and Technology

Organic photovoltaic (OPV) cells are attractive for flexible, low-cost, large-area, and lightweight solar conversion applications. Despite this demand, robust and efficient devices have been limited by the quality of organic semiconductor materials and by the poor understanding and control of their interfaces. Interface modification using self-assembled monolayers or conducting polymers can be leveraged to tune the composition and phase segregation in binary bulk heterojunction photovoltaic cells. In this work, the interface composition of a 1:1 mixture of poly(3-hexylthiophene):[6,6]-phenyl-C61-butiric-acid-methyl-ester (P3HT:PCBM) was characterized using near-edge x-ray absorption fine structure (NEXAFS) spectroscopy as a function of surface energy. The substrates consisted of a low surface energy Nafion-based copolymer, 4-phenylbutyltrichlorosilane or octyltrichlorosilane self-assembled monolayers on SiO₂, or high surface energy native SiO₂. It was observed that while the free surface of the film was always P3HT-rich (7:3 P3HT:PCBM), the bottom interfacial composition varied from P3HT-rich (4:1 P3HT:PCBM) to PCBM-rich (1:4 P3HT:PCBM) as the surface energy of the substrate increased from 20 mN/m² to 80 mN/m². These observations were further supported by electrical characterization of bulk heterojunction films deposited on thin-film transistor structures where the surface energy of the gate dielectric was modified with self-assembled monolayers. The transistor performance exhibited higher hole mobility at P3HT enriched organic-dielectric interfaces (low surface energy substrates), while ambipolar transport was observed in devices with a PCBM enriched interface (high surface energy substrates). These observations of surface energy dependant interfacial composition should have clear implications for optimizing photovoltaic cell design in regards to "conventional" and "inverted" device architectures. However, P3HT:PCBM bulk heterojunction solar cells constructed on low and high surface energy substrates in conventional and inverted device structures exhibit nominally identical performance. Early efforts at modelling the effect of compositional gradients on photovoltaic performance suggest that this is expected given that current densities increase in constricted percolation pathways to maintain constant overall current. Although this may have little impact on initial device performance, the effects of higher current densities in the constricted interfacial regions on device lifetime are currently being investigated.

10:40am EN+NS-WeM9 Experimental and Theoretical Investigation of Excitonic Energy Transfer in Organic Photovoltaic Cells, W.A. Luhman, R.J. Holmes, University of Minnesota

This work demonstrates a novel approach for measuring the Förster radius of energy transfer between electron donating and accepting materials commonly used in organic photovoltaic cells (OPVs). Typically an exciton must diffuse to an electron donor-acceptor interface in order to be dissociated and contribute to photocurrent. Alternatively, if an exciton in the donor layer is instead able to undergo long-range energy transfer to the acceptor layer, diffusion is no longer required, and dissociation occurs from the acceptor layer. While such processes are surprisingly common in OPVs, they are often incorrectly ignored in measurements of the exciton diffusion length and in models of device performance. In this work, the efficiency of energy transfer between an emissive donor and an absorptive acceptor is investigated using complementary experimental and theoretical techniques. This is accomplished by spatially separating the donor and acceptor materials using a wide energy gap spacer layer to suppress charge transfer, and tracking the donor photoluminescence as a function of spacer layer thickness. Fitting experimental data obtained for a variety of small molecule and polymer donor materials allows for the extraction of Förster radii that correlate very well with predicted values. The effect of energy transfer on device performance and on measurements of the exciton diffusion length is also investigated using the archetypical small molecule donor material boron subphthalocyanine chloride (SubPc). An exciton diffusion length of (7.5±0.4) nm is extracted from photoluminescence quenching experiments that carefully account for the role of energy transfer. These results will ultimately provide insight into the fundamental processes of exciton diffusion and dissociation in OPVs.

11:00am EN+NS-WeM10 Molecular Architecture and Charge Separation at Abrupt Donor-Acceptor Interfaces, G.J. Dutton, NIST, W. Jin, University of California at San Diego, D.B. Dougherty, North Carolina State University, W.G. Cullen, University of Maryland, S.W. Robey, NIST, J.E. Reutt-Robey, University of Maryland

Photocurrent production in organic photovoltaic structures differs fundamentally from current generation in inorganic semiconductor solar cells. Dissociation of excitons formed by optical absorption in organic materials requires heterointerfaces between electron donor and acceptor components. The extent to which molecular architecture, particularly along the donor-acceptor interface, impacts electronic level alignment and charge separation is of fundamental interest. In this work, we prepare well-defined molecular interfaces by the physical vapor deposition of select donor (MPc, Pn) and acceptor (C₆₀) components under UHV conditions. We determine the detailed structure of the donor-acceptor interface with Scanning Tunneling Microscopy and establish a correlation with electron band alignment (PES) and exciton dynamics (2PPES).

For technologically relevant interfaces between C₆₀ and donors such as pentacene (Pn) or phthalocyanines (Pc), distinct structures/molecular orientations can be selectively engineered by organic MBE through deposition sequence and flux. For the case of C₆₀ and Pn, "co-facial" C₆₀-Pn interfaces are formed by C₆₀ deposition on crystalline Pn bilayer films supported by Ag(111), whereas "edge-on" C₆₀-Pn interfaces result from Pn deposition on hexagonal close-packed C₆₀ monolayers supported by Ag(111). Such "edge-on" interfaces expand into large dendritic islands, as per reported "thin-film" phases, and support C₆₀ cluster formation under subsequent C₆₀ deposition. We show how electronic level alignments critical to V_{oc} and charge separation efficiency are impacted by these structural changes, and extend this information to other small-molecule cases, ZnPc:C₆₀ and perfluorinated ZnPc, as time permits.

Finally, for interfaces between CuPc and C₆₀, we will present the first studies of charge separation at well-characterized organic donor-acceptor interfaces using TR-2PPE. By pumping the CuPc Q-band at 1.65eV, a time-delayed UV pulse then probes the excited state population. We identify dominant relaxation processes on timescales from 100fs to >100ps. By varying the CuPc film thickness, we observe significantly enhanced charge transfer of the singlet exciton at the interface with C₆₀. Following the population dynamics as a function of energy also provides evidence for recombination from charge transfer states back to the low-lying CuPc triplet.

This work has been supported in part by the NSF under the UMD MRSEC (DMR0520471) and the Surface & Analytical Chemistry Program (CHE0750203).

11:20am EN+NS-WeM11 **Hybrid Organic/Inorganic Solar Cells Based on Silicon Nanowires**, *M. Pietsch*, Max Planck Institute for the Science of Light, Germany, *V.A. Sivakov, B. Hoffmann, G. Broenstrup, F. Talkenberg*, Institute of Photonic Technology, Germany, *T. Seyller*, Friedrich-Alexander Universität Erlangen-Nürnberg, Germany, *T. Fritz, B. Schroeter*, Friedrich-Schiller University Jena, Germany, *S.H. Christiansen*, Max Planck Institute for the Science of Light, Germany

Organic polymer solar cells have received a lot of attention as a promising approach to future photovoltaic energy sources due to their mechanical flexibility and their potential for low cost mass production, high open-circuit voltage values. From another side the hybrid organic/inorganic solar cells containing nanocrystals/nanowires of inorganic semiconductors (e.g. silicon) are promising for several reasons: (i) inorganic semiconductors have a much broader absorption spectrum than organic semiconductors; (ii) nanostructures can be doped to a specific *n*- or *p*-type doping level; (iii) nanostructures provide a large interface to the organic counter part due to their high surface to volume ratio.

The main topic of our research is focused on the formation of the hybrid organic/inorganic solar cells based on the silicon 1D nanostructures. The hybrid solar cells (presented here) are based on silicon nanowires (SiNWs) performed by two different approaches. A Vapor-Liquid-Solid (VLS) mechanism in a conventional chemical vapor deposition (CVD) chamber or electroless wet-chemical etching procedure was applied for the SiNWs realization. As-grown SiNWs are single crystalline and have a smooth (VLS SiNWs) or rough (etched SiNWs) surface covered with a thin oxide layer. Both types of SiNWs show enhanced absorption compared to bulk silicon in the visible spectrum and best results were achieved with etched arrays exhibiting absorption of 90 % over a broad spectral range (300-2000 nm). In a further step the huge nanowire surface was functionalized into a charge separation interface for solar cells by the depositing of semiconducting polymers upon them. To get a detailed picture of charge carrier separation at the organic/inorganic interface XPS/UPS measurements were performed to estimate band alignment between SiNWs and different polymers like PEDOT:PSS or P3HT. The Al:ZnO transparent conductive oxide (TCO) as a contact to the polymer coated SiNWs was realized by applying atomic layer deposition (ALD) technique which allowed us to cover SiNWs with precise ly uniformed Al:ZnO thin layer. For all device concepts based on SiNWs, the crystal structure, geometry (alignment of SiNW with respect to the substrate), interfacial properties between the SiNW and polymers are a key of importance for functioning of the PV devices. For this reason, the microstructure and optoelectronic properties (optical, microstructure) of the organic/inorganic solar cell will be presented and discussed in details during our presentation.

11:40am EN+NS-WeM12 **Influence of UV Radiation on Charge Injection Barriers in Dye-Sensitized Solar Cells**, *S. Gutmann, M.A. Wolak, M.M. Beerbom, R. Schlaf*, University of South Florida

The electronic structure of the interfaces in dye-sensitized solar cell structures was investigated using x-ray and ultraviolet photoemission spectroscopy (XPS, UPS). Electro spray thin film deposition in high vacuum was used to build the interfaces of interest directly in vacuum without exposure to the ambient. Electro spray enables the fabrication of clean, essentially uncontaminated thin films of organic molecules and nanoparticles directly in vacuum.

The experiments focused on the investigation of the indium tin oxide (ITO)/nanocrystalline TiO₂ interface, as well as the characterization of the TiO₂/RuL₂(NCS)₂ [cis-bis(4,4'-dicarboxy-2,2'-bipyridine)-bis(isothiocyanato)-ruthenium(II)] ("N3", a prototypical dye used in many currently pursued device structures)-dye interface. Both TiO₂ and N3 films were built up in several steps. After each step, characterization by XPS and UPS was performed. The resulting sequence of spectra allowed the determination of charge injection barriers and interface dipoles at the ITO/TiO₂ and TiO₂/N3 interfaces. Our experiments revealed a strong influence of the UV radiation during UPS measurements on the band line-up at these interfaces. This was revealed though low intensity x-ray photoemission spectroscopy (LIXPS) measurements, which allow the measurement of the work function prior to UV exposure. These results suggest that even low-level UV radiation, such as encountered in an encapsulated solar cell, may lead to cell degradation over time due to a re-alignment of the electronic structure with detrimental effect on charge transport.

Energy Frontiers Topical Conference
Room: Pecos - Session EN+TF-WeM

CIGS, CZTS and Chalcopyrite Films & Solar Cells
Moderator: E.S. Aydil, University of Minnesota

8:00am EN+TF-WeM1 **CIGS and CZTS Nanocrystal-Ink Solar Cells**, *H.W. Hillhouse, R. Agrawal, Q. Guo, G.M. Ford*, Purdue University
INVITED

The development of suitable colloidal nanocrystal inks are a key step in the development of low-cost solar cells since they enable the use of fast and inexpensive coating processes such as spray coating and roll coating to form a thin film photoabsorbing layer. Chalcopyrite structure copper indium gallium diselenide (CIGSe) and stannite or kesterite copper zinc tin sulfides (CZTS) are key photoabsorbing materials for thin film solar cells due to their near ideal band gap and their serendipitous defect chemistry (CIGSe) and Earth abundance (CZTS). Although several methods have been reported that describe the synthesis of CIGSe and related nanocrystals, precise control of the composition for these ternary and quaternary compounds has been problematic [1]. We have reported the solution-phase synthesis of stoichiometric chalcopyrite structured CuInSe₂ nanocrystals [2], Cu(In,Ga)S₂ [3], and the very first synthesis of CuZnSnS₄ nanocrystals [4]. The syntheses proceed rapidly from elemental and halide reagents via a simple batch reaction without "hot injection" in a single component coordinating solvent. We have demonstrated the use of these nanocrystals for low-cost solar cells by fabricating devices without using any oxygen-free techniques (after NC synthesis) and employing a scalable roll coating method. The nanocrystal inks are first coated on a back contact (Mo coated sodalime glass in this case). The nanocrystal layer is then easily consolidated into large crystalline domains by a brief thermal treatment in a selenium rich atmosphere to prevent selenium loss or to replace sulfur with selenium. The fabricated cells are robust and increase in efficiency with time, exhibiting similar serendipitous defect chemistry as layers formed by vacuum co-evaporation. We have fabricated solar cells by roll coating CIGS or CZTS nanocrystal-inks over large areas. CIGS devices fabricated by roll coating over large areas with a device architecture of Mo/CIGSSe/CdS/i-ZnO/ITO/Ni/Al are (at the time of the abstract submission) 12.0% efficient under standard AM1.5G illumination. The presentation will focus on the key aspects of the nanocrystal synthesis, ink coating, nanocrystal consolidation, and device fabrication and characterization for both CIGS and CZTS solar cells.

[1] Hillhouse H.W. & Beard M.C., Current Opinion in Colloid & Interface Science, 14, 245 (2009).

[2] Guo, Q.J., Kim, S.J., Kar, M., Shafarman, W.N., Birkmire, R.W., Stach, E.A., Agrawal, R., Hillhouse, H.W., Nano Letters 8, 9, 2982 (2008).

[3] Guo, Q.J., Ford, G.M., Hillhouse, H.W., Agrawal, R., Nano Lett. 9, 8 3060 (2009).

[4] Guo, Q.J., Hillhouse, H.W., Agrawal, R., J. Am. Chem. Soc. 131, 11672 (2009).

8:40am EN+TF-WeM3 **Compositional (non)Uniformity and its Effect on CIGS Solar Cell Performance**, *W. Li, S.R. Cohen, K. Gartsman, P. von Huth, R. Popovitch-Biro*, Weizmann Institute of Science, Israel, *Th. Rissom*, Helmholtz Zentrum Berlin, Germany, *D. Cahen*, Weizmann Institute of Science, Israel

CIGS is a promising material for solar cell applications. Uniformity of the polycrystalline composition and structure is an important factor in the solar cell performance. This work is an attempt to study CIGS (non)uniformity systematically as a function of depth, employing independent, complementary high resolution techniques which also reveal inter- and intra-grain compositional, structural, and electronic nonuniformities. In particular, thin cross-sections, prepared by field ion beam (FIB), were studied using TEM-based techniques to achieve higher spatial resolution of the composition than is normally possible. It was found that the Ga/In ratio in the devices drops initially with depth, then rises sharply again near the Mo contact. Furthermore, large variations of this ratio are observed from grain to grain. This variation is even observed within individual single crystal grains along their growth direction. Our measurements confirm the formation of a MoSe₂ phase at the Mo - CIGS interface. The lattice constant, measured by selected area diffraction (SAD), varies with the Ga composition, in agreement with Vegard's law. The extent of compositional variation was found to vary inversely with the temperature of sample preparation. Additionally, our measurements confirm the formation of a MoSe₂ phase at the Mo - CIGS interface.

A series of scanning probe (SPM)-based techniques, including scanning capacitance microscopy (SCM) and conducting probe atomic force microscopy (CP-AFM) were applied to correlate local device performance

and doping concentration with the compositional (non)uniformity revealed in these TEM results and will be presented here.

This compositional non-uniformity may well be of relevance for the properties and performance of solar cells made with such films, and this issue will be addressed in the talk.

9:00am **EN+TF-WeM4 Combinatorial Cd_{1-x}Zn_xS Thin Films Deposited with a Continuous Flow Microreactor**, *K.M. McPeak*, Drexel University, *H.P. Bui, T.P. Beebe*, University of Delaware, **J.B. Baxter**, Drexel University

Chemical bath deposited CdS thin films are commonly used as buffer layers in CdTe and CIGS photovoltaics because they form a high quality *p-n* junction with the absorber. However, light absorption by the CdS reduces solar cell efficiency. Cd_{1-x}Zn_xS has a wider band gap than CdS, offering the potential to reduce deleterious absorption of light in the 300-550 nm range and improve current densities by over 2 mA/cm². To maximize energy conversion efficiency, the Cd_{1-x}Zn_xS should be a single-phase ternary alloy and the stoichiometry should be optimized to ideally position the conduction band edge for increased transmissivity while retaining good junction properties.

We report on chemical bath deposition of combinatorial Cd_{1-x}Zn_xS thin films using a continuous flow microreactor. The microreactor uses a sub-millimeter reaction channel, with the substrate acting as one reactor wall. The microreactor behaves like a plug flow reactor whereby the bath composition changes as flowing material is deposited on the substrate. While the bath composition changes with respect to position down the reaction channel, the composition at any position is time-invariant. The graded bath composition results in deposition of graded thin films whose stoichiometry and optoelectronic properties change significantly over length scales of millimeters to centimeters. Spatially resolved characterization of the substrate enables rapid and direct correlation of material properties to growth conditions, which is not possible with a batch reactor where bath composition changes with time.

Graded Cd_{1-x}Zn_xS films grown with 1:200 Cd:Zn bath composition at the inlet had composition that varied from *x*=0.0 to *x*=0.17 over a distance of 12 mm on a single substrate. Film stoichiometry was determined by x-ray photoelectron spectroscopy (XPS) mapping. Stoichiometry changes because of differences in speciation and reaction kinetics of the cation species as they flow down the channel. XPS and XRD confirm that CdZnS is a single phase material. Deep level emission in photoluminescence and XPS indicate that O and OH is also incorporated into the film and is bound to Zn, with amount increasing further down the reaction channel. The graded stoichiometry causes the absorption edge to blue-shift by over 80 nm, as determined by UV-vis transmission and reflectance measurements. Blue-shifting band edge and changes in defect density are also seen by photoluminescence. The continuous flow microreactor offers new potential for deposition of graded thin films that act as combinatorial libraries for high throughput screening and accelerated materials discovery.

9:20am **EN+TF-WeM5 A Chemical Bath Process for Depositing Cu₂ZnSnS₄ Photovoltaic Absorbers**, *A. Wangperawong, J.S. King, S.M. Herron, B.P. Tran, K. Pangan-Okimoto, S.F. Bent*, Stanford University

Inorganic thin film photovoltaics are an attractive technology for achieving large-scale deployment of inexpensive, stable, and efficient solar cells. However, current leading thin-film materials, such as CdTe and CIGS, face production limitations at a global scale as they contain both non-abundant and toxic elements. A material that has gained significant attention is Cu₂ZnSnS₄ (CZTS), which is not constrained by the drawbacks of CdTe and CIGS and has an ideal bandgap for a single junction photovoltaic device of 1.4-1.5 eV. Several groups have studied the fabrication of CZTS solar cells using a variety of methods ranging from sol-gel processing to sputter deposition, with a record efficiency of 9.6% recently reported. In the present work, we report an alternative water-based method for large area deposition of CZTS thin films that does not require expensive or complex equipment. Specifically, thin films of CZTS were fabricated on silicon, glass and molybdenum-coated substrates through a combination of chemical bath deposition, ion exchange and sulfurization heat treatment. The film composition could be controlled through a combination of number and length of chemical bath steps and ion exchange time. The resulting samples were analyzed by scanning electron microscopy (SEM), Auger electron spectroscopy (AES), X-ray diffraction (XRD), Raman spectroscopy, inductively-coupled plasma optical emission spectroscopy (ICP-OES), and diffuse reflectance absorption spectroscopy. XRD, Raman, and UV-Vis optical spectra are consistent with the formation of CZTS. The results show that the process produces thin films of CZTS exhibiting uniform composition, well-defined crystal structure, and good optical properties with a bandgap of 1.45 eV. Complete solar cell devices made with chemical bath-deposited CZTS were fabricated. Measurements on

these devices exhibit photovoltaic and rectifying behavior, and the results will be discussed.

9:40am **EN+TF-WeM6 Synthesis Routes for CuIn_{1-x}Ga_xSe₂ Thin Film Absorbers**, *R. Krishnan, T.B. Song, V.U. Chaudhari*, University of Florida, *E.A. Payzant*, Oak Ridge National Laboratory, *R. Noufi*, National Renewable Energy Laboratory, *T.J. Anderson*, University of Florida

Chalcopyrite Cu(In,Ga)Se₂ is one of the most promising absorber materials for high efficiency thin film solar cells with reported conversion efficiency exceeding 20%. The National Solar Technology Roadmap for CIGS PV specifically calls for deposition rates of "30-40 μm/h and <1 μm CIGS absorber thickness" by 2015. This is compared to the current estimate in the Roadmap of "5 μm/h and 1.25-3 μm CIGS absorber thickness." The comparison translates into a reduction of the absorber synthesis time from ~15 to 36 min to ~1.5 to 2 min. The challenge is to get high throughput and yield with columnar grain growth while retaining the high efficiency. In this work *in-situ* high temperature X-ray diffraction with and without selenium overpressure is used to determine absorber synthesis mechanisms for various precursors structures. Qualitative analysis of the data gives information on the reaction pathway and quantitative analysis of the data yields rate constants.

This presentation summarizes studies on the selenization of elemental stacked layers of copper, indium, gallium and selenium in two different configurations. In the first configuration (sample A), copper was first deposited on glass/Mo substrates, followed by gallium, indium and selenium. In the other configuration (sample B), gallium was first deposited followed by indium, copper and selenium. ICP results showed that both the samples were copper poor. Reaction pathways were followed with and without selenium overpressure and isothermal soaking experiments were performed to obtain the kinetic parameters using the Avrami growth model to reduce the data. The reaction pathways were similar for both the configurations, showing formation In, Cu₉Ga₄, and Cu₂Se initially, followed by Se crystallization and formation of the intermediates In₄Se₃, CuSe₂, CuSe and CIS, and finally yielding product CuIn_{1-x}Ga_xSe₂. The value of *x* computed from Vegard's law yielded 0.35 for sample A and 0.37 for sample B. The activation energy computed from the Avrami model yielded 88.4(±12) and 125.1(±9) kJ/mole for samples A and B, respectively. The decrease in the local Avrami exponents (0.21-0.26) suggests the existence of an inhomogeneous distribution of nuclei during growth or interdiffusion of gallium and indium with simultaneous grain growth. Additional characterization such as SEM and TEM were performed to provide physical and compositional support of the pathway.

10:40am **EN+TF-WeM9 Atmospheric Processing Approaches to Low Cost Scalable Photovoltaics**, *M.F.A.M van Hest, A. Miedaner, C.J. Curtis, J. Leisch, P. Hersh*, National Renewable Energy Laboratory, *K. Steirer, R.M. Pasquarelli, J.A. Nekuda, R.P. O'Hayre*, Colorado School of Mines, **D.S. Ginley**, National Renewable Energy Laboratory

INVITED
Solar photovoltaics are becoming an increasing part of the energy supply mix, however to have a really significant impact they must become cost competitive with more conventional energy sources. Direct write ink based methods could help toward this significant cost reduction. We are investigating solution precursors and ink based atmospheric deposition approaches to a variety of solar cell materials and processes. The first application we are studying is inkjet printing of contacts for photovoltaics in particular for Si solar cells. We have developed metal organic decomposition inks for silver, nickel, copper and aluminum for example. Conductivities close to that of bulk metals were obtained. The second application is the formation of the absorber layer in CuInSe₂ (CIS) based photovoltaics. CIS/CIGS is the most efficient thin film photovoltaic technology, but typically employ capital-intensive PVD materials deposition and subsequent selenization steps. Our approach uses liquid based precursors that can be inkjet printed and processed under atmospheric conditions. Various precursors were identified leading to In₂Se₃, Cu₂Se and CuInSe₂ films without a selenization step on various substrates. Similar chemistries are applicable to copper zinc tin sulfide (CZTS) materials which are potentially more scalable. Details of film deposition and processing for these systems will be discussed. The third application is in the field of organic photovoltaics. Here inkjet printing is used to deposit the photoactive layer such as a polythiophene, for example P3HT, and the conducting contact layer such as PEDOT/PSS. Details will be shown on how solvents can influence the quality of the printed material. Direct write processing of these materials may be enabling for this technology leading to an all printed photovoltaics.

Exhibitors & Manufacturers Technology Spotlight Room: Southwest Exhibit Hall - Session EW-WeM

Exhibitors & Manufacturers Technology Spotlight Moderator: D.J. Surman, Kratos Analytical Inc., R. Langley, Consultant

10:00am EW-WeM7 TwisTorr: A New Molecular Drag Technology, W. Vissers, Agilent Technologies, Vacuum Products Division

Agilent Technologies presents the new TwisTorr molecular drag technology. Our new and innovative molecular drag stages, composed of a specific array of pumping channels with spiral design, greatly increase the pumping efficiency in a very compact space. This technology represents a next step in the evolution of hybrid turbo high vacuum pumps, providing significant improvements in pumping performance. The Turbo-V TwisTorr series represents a new category of Turbo Molecular Pumps offering unmatched performance in both pumping speed and compression ratio in the most compact space available. The innovative TwisTorr stages allow reaching the highest levels of compression ratio for light gases in commercially available Turbo Molecular Pumps. Using the patented TwisTorr molecular drag technology, Agilent has developed the Turbo-V 750 TwisTorr, the Turbo-V 850 TwisTorr and the Turbo-V 2300 TwisTorr.

10:20am EW-WeM8 Measure Ion flux to Substrate with Novel OCTIV™ RF Current-Voltage Probe, M.B. Hopkins, D. O'Sullivan, D. Gahan, P. Scullin, Impedans Ltd.

The Octiv Single Frequency VI Probe measures the Voltage, Current, Phase, Impedance, Harmonics, Real Power, Forward Power and Reflected Power delivered to a plasma chamber by an RF source. Octiv is a single frequency, inline RF VI Probe. The probe contains an RF VI sensor and high speed data acquisition system, utilising an ultra high-speed digital Fourier Transform for high accuracy measurement of fundamental RF voltage, current and phase.

The Octiv probe is housed in a single, compact enclosure, and is easily installed on all high power RF equipment encountered in the laboratory or industrial environment. A USB connection provides power and data access to the sensor. An adaptor kit can be supplied with the probe to enable connection with standard RF equipment. The Octiv also operates in Pulsed RF plasmas.

Impedans has recently added a unique feature to the Octiv product to allow the capture of the real and imaginary current to an RF biased electrode. In this presentation we will explain how this unique patent pending feature allows the user to measure the ion flux to an RF biased substrate in a processing plasma. The technique works well even when the Substrate is insulating. The ion flux is a key parameter in process control of many plasma processes.

Graphene Focus Topic Room: Brazos - Session GR+EM+MS+TF+MI-WeM

Graphene and Carbon-based Devices

Moderator: N.P. Guisinger, Argonne National Laboratory

8:00am GR+EM+MS+TF+MI-WeM1 Epitaxial Graphene: Effects of Dielectric Overlayers and Device Design on FET Performance, M.J. Hollander, R. Cavalero, D. Snyder, M. LaBella, K. Trumbull, Z. Hughes, J. Robinson, The Pennsylvania State University

The realization of a graphene-based electronic technology necessitates large-area graphene production, as well as the ability to integrate graphene with highly insulating films that act as the gate dielectric in field effect transistors (FETs). Graphene's two dimensional nature allows for phenomenal electronic properties and ultimate scalability, but also makes it susceptible to doping and scattering by charged impurities, dangling bonds, and other defects that may derive directly from choice in gate dielectric and deposition technique. The nature and extent of the effect of the dielectric over-layer on conduction within the graphene channel is of fundamental interest in designing and producing graphene based FETs. Atomic layer deposition (ALD) has proven to be an excellent technique toward the integration of dielectrics with graphene and provides a means to produce high quality films for gate dielectrics at temperatures below 300C, but requires the use of a thin nucleation layer to promote complete coverage and to protect the graphene.

We present results on graphene FETs utilizing various gate dielectrics and various nucleation layers. Graphene was grown epitaxially on 100 mm SiC

wafers and processed using standard photolithographic techniques. Al₂O₃ and HfO₂ gate dielectrics were investigated using SiO₂, TiO₂, and Al₂O₃ nucleation layers in various combinations. We show that choice of gate dielectric and nucleation layer can have a dramatic effect on transistor performance and charge carrier mobility. Saturation current, transconductance, and device hysteresis were examined in the fabricated FETs while charge carrier mobility and charge carrier density within the epitaxial graphene were evaluated using Van der Pauw structures. Graphene FETs utilizing Al₂O₃ and SiO₂ seeded dielectrics exhibit the best performance while TiO₂ seeded and unseeded devices exhibit large gate leakage currents resulting in non-functioning FETs. Additionally we provide evidence that the choice of dielectric and seed can significantly impact the Dirac point (minimum conduction), amount of hysteresis, and on/off ratio of the graphene FETs. Trends in saturation current, and transconductance appear to be independent of nucleation layer and gate dielectric choice, indicating that conduction through the channel may be limited by mechanisms independent of the nucleation layer and gate dielectric.

In addition to the aforementioned performance metrics, FET performance after continued application of high electric fields across the channel will be reported. Finally, we examine how choice of channel length and width, along with transistor design, effect performance.

8:20am GR+EM+MS+TF+MI-WeM2 Graphene Oxide on Patterned Self-Assembly Monolayer for Cancer Marker Detection, D.-J. Kim, C.Y. Jung, O.J. Yoon, N.-E. Lee, Sungkyunkwan University, Republic of Korea, J.-S. Park, Korea Electronics Technology Institute, Republic of Korea

Graphene, two-dimensional sheet of sp²-hybridized carbon atom, has received much attention in recent years for many applications such as energy storage and conversion, batteries, fuel cells, optoelectronic device, field-effect transistors, electromechanical resonators, chemical sensors, and biotechnologies. Oxidized form of graphene, graphene oxide, which has functional groups of epoxide, carbonyls, hydroxide, and phenol groups at both sides can also provide various functionalities for biomedical applications because the high densities of defective sites can provide many active sites for electron transfer to biological species, similarly to graphene. In this study, we demonstrate the graphene oxide based immunosensor for cancer marker detection. Graphene oxide pattern was formed selectively on self-assembly monolayer (SAM) pattern formed by using inkjet printing. The hydroxyl terminated ITO electrode was first selectively functionalized by the amine (-NH₂) group by inkjet printing of SAM, and the graphene oxide flakes were adsorbed selectively on the SAM pattern. After immobilization of monoclonal antibody to PSA (prostate specific antigen) which is the biomarker in prostate cancer, the electrochemical performance of immunosensor was evaluated by varying the concentration of PSA-ACT (prostate specific antigen/ α 1-antichymotrypsin) complex. And the PSA polyclonal antibody conjugated with gold nanoparticles was applied to amplification of electrochemical signal because the attachment of nanoparticles onto electrodes drastically enhances the conductivity and electron transfer from the redox analytes. The results showed that graphene oxide based immunosensor can be possibly applied to the delicate diagnosis of various disease markers as well as PSA at the extremely low level and with ultra-high sensitivity.

8:40am GR+EM+MS+TF+MI-WeM3 Spintronics in Graphene Based Nanostructures, J. Fernández-Rossier, Universidad de Alicante, Spain INVITED

Spintronics in graphene has received attention from two complementary points of view. On one side, the small spin orbit coupling and nuclear spin density suggest that graphene should have very long spin relaxation and decoherence times, which would make it suitable for long distance spin transport and, eventually, for spin-based quantum computing. Although small, spin orbit interaction turns graphene into a spin hall insulator, at very small temperatures, so that the edges of graphene should carry spontaneous spin currents. Independently of the above, the zigzag edges of graphene nanostructures, like graphene ribbons and islands, are predicted to present ferromagnetic spin order due to electron electron coupling. In this talk I will discuss the properties of graphene nanostructures when both the spin-orbit coupling and the Coulomb interactions are included. I will show how the combined action of spontaneous spin order and spin orbit coupling results in persistent charge currents flow in the edges of a variety of graphene nanostructures.

9:20am GR+EM+MS+TF+MI-WeM5 CVD Gate Dielectrics and Bandgap Engineering of Graphene Layers, W.J. Zhu, D. Neumayer, V. Perebeinos, P. Avouris, IBM T.J. Watson Research Center

Graphene is very promising for electronic devices, particularly for analogue high frequency devices due to its high intrinsic mobility. One challenge in graphene devices is the formation of gate dielectrics on graphene due to its

hydrophobic nature. We found a new CVD gate insulator that provides uniform coverage on graphene while preserving the channel mobility, thus making it a very promising gate dielectric for graphene devices. We also studied the channel resistance and the modification of the band structure as a function of the vertical electric field near the Dirac (neutrality) points in the fabricated top-gated graphene devices. We found that as the vertical field increases, in bi- and tri-layer graphenes, the band-gap increases, while in multi-layer graphene, the band-overlap increases. The values of band-gap/overlap in bi-, tri- and multi-layer graphenes were estimated using a simple model which takes into account the variations of the surface electrostatic potential at the Dirac/neutrality point.

9:40am **GR+EM+MS+TF+MI-WeM6 Characterization of Devices Fabricated from Electrostatically Transferred Graphene: Comparison with Epitaxial based Devices**, *S.W. Howell, L.B. Biedermann, T. Ohta, T.E. Beechem, W. Pan, A.J. Ross, D.C. Trotter*, Sandia National Laboratories

In this paper, we present our recent advancements in electrostatically transferring epitaxial graphene (EG) from SiC(0001) and SiC(000-1) to arbitrary glass substrates (including Pyrex). We will compare the electronic properties of electrostatically transferred EG and nominally-equivalent as-grown EG on SiC. These properties are measured using magnetoresistive, four-probe, and field effect transistor geometries. We feel this is a potential enabling technology for integration of graphene with structured and electronically-active substrates, such as MEMS and CMOS.

CVD-grown graphene on Cu has attracted wide interest since it can be readily transferred to arbitrary substrates. However, CVD-grown graphene has been shown to have lower mobilities and smaller domain sizes than EG. EG is difficult to transfer to arbitrary substrates. Currently two techniques exist to transfer EG – a gold/polymer film handle and thermal tape exfoliation [1,2]. While transfer is possible with these techniques, problems exist including contamination and damage, as measured by Raman spectroscopy.

To overcome the issues with the above mentioned transfer techniques, we have developed a technique capable of electrostatically transferring both patterned and chip-scale regions of EG to arbitrary glass substrates. We start with high-quality graphene (mobility 14,000 cm²/Vs and domains >100 um²) grown using an Ar-mediated approach [3,4]. In electrostatic graphene transfer, a large electric field is applied between the donor graphene sample (anode) and the acceptor insulating substrate (cathode). This strong electrostatic force deposits graphene on the insulating surface. Electrostatic transfer of EG is a clean technique which, unlike other EG transfer methods, does not contaminate the graphene with adhesive residue or gold contaminants. Both few-layer graphene from SiC(000-1) and monolayer graphene from SiC(0001) have been transferred using this technique.

Our initial attempts at EG transfer have been extensively characterized with Raman spectroscopy and atomic force microscopy. Raman spectroscopy shows that the inherent strain in EG has been partially relaxed. Furthermore, a defect peak (D peak) is frequently not seen in the transferred graphene indicating that the procedure does not significantly damage the graphene film.

Sandia is a multiprogram laboratory operated by Sandia Corporation, a Lockheed Martin Company, for the United States Department of Energy under contract DE-AC04-94AL85000.

- [1] D. Lee *et al.* *Nano Lett.* **8**, 4320 (2008)
- [2] S. Unarunotai *et al.* *APL* **95**, 202101 (2009)
- [3] W. Pan *et al.* submitted to *APL* (2010)
- [4] K. Emtsev *et al.* *Nature Mat.* **8**, 203 (2009)

10:40am **GR+EM+MS+TF+MI-WeM9 Electron Transport in Dual-Gated Mono- and Bilayer Graphene Devices with High-k Dielectrics**, *E. Tutuc, S. Kim, B. Fallah, K. Lee, J. Nah, S.K. Banerjee*, The University of Texas at Austin, *L. Colombo*, Texas Instruments, Inc.

INVITED

A key issue for graphene-based devices is the deposition of thin high-k dielectric layers combined with a minimum electron mobility degradation. Here we examine the carrier transport in mono and bilayer graphene field-effect transistors with top Al₂O₃ and HfO₂ dielectrics. The high-k dielectric films are grown by atomic layer deposition (ALD), and using a 1nm-thick Al interfacial layer in order to create intentional nucleation centers for the ALD. We show that this deposition technique allows the realization of high mobility graphene devices with aggressively scaled top dielectrics. We investigate the carrier mobility dependence on dielectric thickness and temperature in mono-layer graphene field-effect transistors with high-k dielectrics. The electron transport in dual-gated graphene bilayers with Al₂O₃ top dielectric reveals an interesting band-gap energy dependence on transverse electric field and perpendicular magnetic field in this system.

11:20am **GR+EM+MS+TF+MI-WeM11 In-situ X-ray Photoelectron Spectroscopy Studies of Ozone-based ALD Al₂O₃ Dielectrics on Graphite and Graphene**, *A. Pirkle, S. McDonnell*, University of Texas at Dallas, *L. Colombo*, Texas Instruments, Inc., *R.M. Wallace*, University of Texas at Dallas

We present a study of ozone-based atomic layer deposition (ALD) of Al₂O₃ films on graphene and bulk graphite. Uniform deposition of scalable device-quality high-k dielectrics on graphene is a substantial hurdle for the implementation of conventional FET devices as well as novel device structures exploiting the unique transport properties of graphene. Trimethylaluminum (TMA) / O₃ processes are found to result in uniform Al₂O₃ depositions on graphite and graphene surfaces (1), in contrast to common TMA / H₂O-based processes which result in nonuniform nucleation at defects and step edges.

In order to further examine the nature of interactions between TMA / O₃ and graphene, we utilize *in-situ* x-ray photoelectron spectroscopy (XPS) coupled via a UHV transfer line to an ALD reactor. Morphology of deposited films is also examined *ex-situ* using atomic force microscopy (AFM). We examine the impact of several parameters on Al₂O₃ deposition. Choice of deposition temperature is critical, as etching of graphene by O₃ is observed at elevated temperatures (2) but dielectric quality is degraded at low temperature (3). We also examine the impact of surface condition on Al₂O₃ composition particularly with regard to partially reacted TMA precursor molecules; various surface treatments are employed to approximate realistic device processing conditions. Finally, the effect of variations in purge time between ALD precursor pulses is studied; a reduction in deposition with increased purge time indicates that weakly bonded precursor molecules (TMA and O₃) are easily desorbed from the graphene surface.

This work is supported by the NRI SWAN and MIND centers.

- 1: B. Lee, *et. al.*, *Appl. Phys. Lett.* **92** (20), 203102 (2008)
- 2: G. Lee, *et. al.*, *J. Phys. Chem. C* **113** (32), 14225 (2009)
- 3: S. K. Kim, *et. al.*, *J. Electrochem. Soc.* **153** (5), F69 (2006)

In Situ Microscopy and Spectroscopy Topical Conference

Room: Acoma - Session IS+AS+NS+MI-WeM

In Situ Microscopy/Spectroscopy – In Situ Nanoscale Processes

Moderator: A. Mkhoyan, University of Minnesota

8:00am **IS+AS+NS+MI-WeM1 Low-dimensional Superconductivity of Pb Nanostructures**, *J. Kim, H. Nam, G.A. Fiete, C.K. Shih*, The University of Texas at Austin

The influence of low-dimensional geometries on superconductivity is an important issue to study because in low dimensions it is key to understanding coherence and robustness of the superconducting state in quantum-mechanically confined geometries. The lateral size dependence of superconductivity on 2 dimensional Pb islands is studied by using *in-situ* low temperature Scanning Tunneling Microscopy/Spectroscopy (STM/S). The superconducting transition temperature (T_c) of each island is obtained by fitting the STS data with a BCS-like density of states. It is found that superconductivity shows a clear dependence on the Pb island lateral size even when it is larger than the bulk coherence length (~80nm), and it is also found that T_c drops very quickly below a certain lateral size. In addition, an intriguing lateral proximity effect is observed at the interface of different local superconducting regions of Pb islands. Current imaging tunneling spectroscopy (CITS) is used to visualize this proximity effect in real space.

8:20am **IS+AS+NS+MI-WeM2 Enabling the Measurement of In-Situ, Site-Specific Mineral Transformation Rates in Supercritical CO₂ through Development of a High Pressure AFM**, *S. Lea*, Pacific Northwest National Laboratory, *S.R. Higgins*, Wright State University, *K.G. Knauss*, Lawrence Berkeley National Laboratory, *K.M. Rosso*, Pacific Northwest National Laboratory

Capture and storage of carbon dioxide in deep geologic formations represents one promising scenario for minimizing the impacts of greenhouse gases on global warming. At issue is the ability to demonstrate that CO₂ will remain stored in the geological formation over the long-term and so knowledge of mineral-fluid transformation rates is critical for this determination. The majority of previous research on mineral-fluid interactions has focused primarily on the reactivity of minerals in aqueous solutions containing CO₂. However, caprock integrity would be dictated primarily by mineral interaction with supercritical CO₂ (scCO₂) as the

buoyant phase slowly displaces or desiccates residual aqueous solution at these surfaces. Many of the mechanisms of mineral interfacial reactions with hydrated or water-saturated CO₂ are unknown and there are unique challenges to obtain kinetic and thermodynamic data for mineral transformation reactions in these fluids.

A high-pressure atomic force microscope (AFM) is currently under development that will enable *in-situ* site-specific measurements of metal carbonate nucleation and growth rates on mineral surfaces in contact with scCO₂ fluids. This apparatus is based on the hydrothermal AFM that was developed by Higgins et al.¹, but includes some enhancements and is designed to handle pressures up to 1500 psi. The noise in our optically-based cantilever deflection detection scheme is subject to perturbations in the density (and therefore index of refraction) of the compressible supercritical fluid. Consequently, variations in temperature and pressure within the fluid cell can have a significant impact in our ability to discern atomic steps on mineral surfaces. We demonstrate with our test fluid cell that the equivalent rms noise in the deflection signal is similar to (and in some cases less than) the equivalent noise for an AFM in its 'standard configuration' under controlled pressures of ~80 bar and temperatures of 60-80 °C and therefore *in-situ* atomic scale imaging of mineral surfaces in scCO₂ should be possible. This talk will also focus on recent progress in the development of this instrumentation, which will enable a unique platform for elucidating the role of water in mineral transformations, providing a means for determining effective kinetic constants.

1. Higgins, S. R.; Eggleston, C. M.; Knauss, K. G.; Boro, C. O., A hydrothermal atomic force microscope for imaging in aqueous solution up to 150°C. *Review of Scientific Instruments* **1998**, 69 (8), 2994-2998.

8:40am **IS+AS+NS+MI-WeM3 Au on VLS-grown Si Nanowires: Spreading of the Liquid Metal Seed**, E. Dailey, P. Madras, J. Drucker, Arizona State University **INVITED**

In situ TEM shows that liquid AuSi spreads from the seed along the NW sidewalls to form a thin liquid sheath for some growth conditions. The thin liquid film phase separates to form small solid Au clusters when the NW is cooled below the solidus temperature. Quantitative composition maps show that the Au composition is highest near the NW tip. The thickness and length that the liquid film spreads from the seed is growth condition and NW diameter dependent and represents a steady state during growth. These observations can be related to the spreading thermodynamics of liquid droplets along cylinders. Growth conditions for which the liquid AuSi spreads from the seed stabilize 'vertical' growth along <111> by lowering the surface energy of the high-energy {112} bounding facets. In contrast, the NWs kink toward <112> when grown using conditions that favor growth with Au-free sidewalls since these NWs are bound by facets that are found on the Si equilibrium crystal shape.

9:20am **IS+AS+NS+MI-WeM5 Advanced Study of Nanoscale Mechanisms: Plans for In-Situ TEM Microreactor, Gas Cell, and Multi-Beam Irradiation Experiments**, B.G. Clark, K. Hattar, Sandia National Laboratories, D. Nckashi, J. Damiano, S. Mick, Protochips, Inc., B.L. Doyle, Sandia National Laboratories

Over the years, in-situ TEM experiments have allowed for observation of material mechanisms at high resolution and in real time; a feat often not possible with any other experimental technique. With increasing demand for understanding nanoscale material mechanisms, both with growth in the applications of nanomaterials and in the development of predictive materials models based on experimental observation, the realm of in-situ TEM experiments has continued to expand. Highlighted in this presentation will be the development of three, exciting new capabilities for in-situ TEM experiments at Sandia National Labs.

The first part of the talk will focus on the development of two new in-situ TEM stages. Expanding on the success of static and single inlet-outlet liquid cells, we are designing a new in-situ TEM microreactor liquid cell with the capability to mix fluids in controlled temperature regimes, to view reactions as a function of time, and to capture and analyze reaction products. Research programs using this stage will pursue studies of self-assembly, directed assembly, and nanoparticle formation and growth. In addition, for observation of advanced degradation of materials in the presence of gases and/or vapor, a new in-situ TEM gas cell stage is being developed. This stage will have the capability to study a variety of gas-solid and vapor-solid interactions, such as corrosion, oxidation, and hydriding, with accurate control over temperature and pressure. Envisioned research will include understanding environmental degradation of materials during storage of spent nuclear fuels, an issue of critical importance for the future of nuclear energy.

The second part of the talk will highlight the development of a new, triple-ion-beam in-situ irradiation TEM. By combining expertise in in-situ TEM experiments with expertise in ion beam studies, planning is currently underway that would culminate in the construction of an instrument capable

of studying the effects of bombardment by up to three ion beams simultaneously within the TEM. This unique, triple-ion-beam capability would enable advanced experiments such as real-time studies of neutron induced damage and transmutation in a fission/fusion reactor by combining Fe, He, and H ions.

*This work is supported by the Division of Materials Science and Engineering, Office of Basic Energy Sciences, U.S. Department of Energy. Sandia National Laboratories is a multi-program laboratory operated by Sandia Corporation, a wholly owned subsidiary of Lockheed Martin company, for the U.S. Department of Energy's National Nuclear Security Administration under contract DE-AC04-94AL85000.

9:40am **IS+AS+NS+MI-WeM6 In Situ TEM Investigation into the Thermal Stability of Nanograin FCC Metals and Alloys**, K. Hattar, B.G. Clark, Sandia National Laboratories, J. Kacher, University of Illinois at Urbana-Champaign, J.A. Knapp, D.M. Follstaedt, L.N. Brewer, Sandia National Laboratories, I.M. Robertson, University of Illinois at Urbana-Champaign

Nanostructured materials often display very unique properties related to their far-from-equilibrium nature. Due to these unique structures, many of these materials transform into other, more stable microstructures with minimal thermal excitation. This work will highlight examples of the unexpected routes taken during the microstructural evolution of pulsed-laser deposited (PLD) free-standing face-centered cubic (FCC) thin films as a function of deposition condition and annealing temperatures. A direct comparison between the grain growth dynamics observed during *in situ* TEM annealing experiments in PLD films of high-purity aluminum, copper, gold and nickel films, as well as aluminum-alumina alloys shows a multitude of kinetics. For high-purity systems film thickness, void density, grain size distribution, and deposition temperature were found to be the primary factors observed controlling the rate, extent, and nature of the grain growth. The growth dynamics ranged from nearly classical normal grain growth to abnormal grain growth resulting in a bimodal grain size distribution. The grain growth rate was found to be highly dependent on the materials system despite all of the films being nanograin FCC metals produced by similar PLD parameters. The investigation of the aluminum-alumina alloys produced under various compositions and deposition parameters suggests that particle pinning can be used to maintain nanostructured films, even after annealing treatments at high homologous temperatures.

In addition to investigating the grain growth dynamics and the resulting grain size distribution, the variety of internal microstructures formed from thermal annealing were evaluated. These structures ranged from intergranular voids to stacking-fault tetrahedra. An unexpected, metastable hexagonal-closed packed phase was identified in the high-purity nickel films. These *in situ* TEM observations have provided key insight into the microstructural evolution of nanograin free-standing metal films and the defect structure present in the grains resulting from various growth dynamics, in addition to suggesting multiple methods to tailor the structure and the resulting properties of nanostructured free-standing films.

*This work is supported by the Division of Materials Science and Engineering, Office of Basic Energy Sciences, U.S. Department of Energy both at Sandia and under grant DE-FG02-07ER46443. Sandia National Laboratories is a multi-program laboratory operated by Sandia Corporation, a wholly owned subsidiary of Lockheed Martin company, for the U.S. Department of Energy's National Nuclear Security Administration under contract DE-AC04-94AL85000.

10:40am **IS+AS+NS+MI-WeM9 In Situ TEM Studies of Nanomagnetism and Thermal Transport**, J. Cumings, University of Maryland **INVITED**

The transmission electron microscope is a powerful tool for many areas of nanoscience. The combination of high spatial resolution and high time resolution, giving video-rate imaging, makes it uniquely capable of many types of studies of phenomena in-situ during imaging. Here I will present two areas where we have made recent advances. In nanomagnetic structures, it is possible to image in real-time the reversal process of coupled systems called artificial spin ice. These systems exhibit frustration, leaving disorder in their lowest energy magnetic configurations. I will present studies showing the magnetic reversal processes for these structures, revealing that microscopically correlated events lead to avalanche phenomena. A second topic that I will present is electron thermal microscopy of carbon nanotubes. Here, a new technique will be introduced that allows thermal imaging with nanoscale spatial resolution. This technique has been used to study the thermal transport through carbon nanotubes, and I will present results showing that thermal contact resistance can limit the thermal transport in nanotubes. I will show that this contact resistance can be tuned by two orders of magnitude by appropriately controlling the fabrication of the contacts. Together these results serve to

demonstrate the capabilities of studies utilizing in-situ transmission electron microscopy.

11:20am **IS+AS+NS+MI-WeM11 In-situ Infrared Transmission Analysis of Atomic Layer Deposition Reactions on Polymer Films and Fibers.** *G.N. Parsons, B. Gong, J.S. Jur, C. Oldham, K. Lee*, North Carolina State University

Many new product applications related to packaging, filtration, protection and others offer substantial opportunities and raise new demands for polymer/inorganic thin film integration and surface modification. In-situ transmission infrared spectroscopy can provide critical insight into reaction mechanisms that proceed during inorganic film deposition on organics. We are particularly interested in low-temperature atomic layer deposition (ALD) which ideally proceeds through a binary sequence of self-limiting surface reactions to form highly conformal and uniform films on high surface area structures. In-situ IR spectroscopy allows us to probe and identify specific polymer/precursor reaction mechanisms that occur during precursor and reactant exposure. Typical atomic layer deposition precursors and reactants include trimethylaluminum (TMA), diethyl zinc (DEZ) and water, and polymer materials studied to date include polypropylene, polyamide-6, polyesters (such as polybutylene terephthalate), cellulose, polyvinyl alcohol and others. We have investigated deposition reactions on planar polymer sheets as well as micro- and nano-scale polymer fibers.

In-situ IR transmission data demonstrates that typical non-reactive materials such as polypropylene will take up precursors with minimal precursor/polymer reaction, resulting in subsurface alumina nucleation. Polymers with more reactive backbone or side chain groups, such as cellulose, polyvinyl alcohol or polyamide-6 react readily with the precursor. For example, when polyamide-6 is exposed to TMA, N-H and C-O stretching modes decrease markedly, indicating that TMA attacks the electrophilic carbon atom in the carbonyl group leading to methyl insertion and formation of C-O-Al- and C-CH₃ bonds. Electron micrograph images of polyamide fibers after TMA exposure confirms significant extent of reaction. Deposition on cellulose cotton fibers, however, shows primarily surface adsorption, resulting in true ALD growth and highly conformal film coatings by TEM. We will show details of the in-situ transmission ALD reactor, and illustrate how the tool is especially amenable and adaptable to in-situ surface reaction analysis on polymer fiber networks.

Nanometer-scale Science and Technology

Room: La Cienega - Session NS+AS+MN-WeM

Characterization and Imaging at Nanoscale

Moderator: E.I. Altman, Yale University

8:20am **NS+AS+MN-WeM2 Surface Preparation of Supported Flat Gold Nanoparticles for use as Au(111) Single Crystal Substrates.** *D.H. Dahanayaka, L.A. Bumm*, The University of Oklahoma

Flat gold nanoparticles (FGNPs) grown in aqueous solution have large Au(111) facets that are excellent substrates for scanning probe microscopy. However adsorbed stabilizers (e.g. polyelectrolytes) must be removed or displaced before the FGNP surfaces can be used as single crystal surfaces. We have explored the effects of plasma cleaning, UV ozone, and thermal annealing on the surface roughness and the Au(111) terrace structure using STM.

This work has been supported by NSF CAREER grant No. CHE- 0239803, NSF MRSEC No. DMR-0080054, NSF No. DMR-0805233d NSF, and AFOSR No. FA9550- 06-1-0365.

8:40am **NS+AS+MN-WeM3 Determination of the Adsorption Site for Alkanethiol Monolayers on Au(111).** *Q. Guo*, University of Birmingham, UK

The bonding sites for Au-atom-octanethiolate within the ($\sqrt{3}\times\sqrt{3}$)R30° structure on Au(111) has been investigated with high-resolution scanning tunneling microscopy (STM) imaging. By establishing the relationship between the lateral positions of adsorbates on the top layer of gold and those inside an etch pit, we are able to determine the adsorption configuration with a high degree of accuracy for the illusive ($\sqrt{3}\times\sqrt{3}$)R30° molecular layer. Within any one particular domain, the Au-atom-octanethiolate species are found to occupy either the fcc hollow or the hcp hollow site.

9:00am **NS+AS+MN-WeM4 Atomic Co Wires: Room and Low Temperature STM/STS Measurements.** *N. Zaki*, Columbia University, *D. Acharya*, Brookhaven National Laboratory, *D.V. Potapenko*, Columbia University, *P. Johnson, P. Sutter*, Brookhaven National Laboratory, *R.M. Osgood*, Columbia University

We recently reported [1] on a new surface phase of the Co-*vicinal*-Cu(111) system which exhibits self-assembled uniform Co quantum wires that are stable at 300K. STM images show that the wires form along the leading edge of the step rise, differentiating it from previously theoretically predicted atomic-wire phases as well as experimentally observed step-island formation. Our observations allow us to comment on the formation kinetics of the atomic-wire phase and on the fit of our data to a recently developed lattice-gas model. Low-temperature STS measurements, taken on self-assembled Co chains, reveal a resonance at the Fermi energy. While it has been shown that single Co atoms and Co-Cu_n clusters [2] exhibit a Kondo effect, a Co chain at a Cu step may exhibit a different many-body effect that is the cause for our Fermi-energy resonance observation. Furthermore, we have observed different charge-density modulation that is dependent on tip bias. Since these charge-modulations are observed for tip-bias relatively far away from the Fermi level, we suspect that these modulations are not ground state charge-density-waves (CDW), but rather excited states of this 1-D system.

[1] N. Zaki et al, Phys. Rev. B 80, 155419 (2009)

[2] N. Néel et al, Phys. Rev. Lett. 101, 266803 (2008)

9:20am **NS+AS+MN-WeM5 Atomic-Resolution Spin Mapping by Exploiting Magnetic Exchange Forces.** *R. Wiesendanger**, University of Hamburg, Germany

INVITED
While Spin-Polarized Scanning Tunneling Microscopy (SP-STM) [1] is nowadays well established for revealing atomic spin configurations at surfaces, its application is limited to electrically conducting samples such as magnetic metals or semiconductors. In order to map atomic spin structures at surfaces of insulators and to open up the exciting possibility of studying spin ordering effects with atomic resolution while going through a metal-insulator transition, we have developed Magnetic Exchange Force Microscopy (MExFM) [2]. This technique is based on the detection of short-range spin-dependent exchange and correlation forces at very small tip-sample separations (a few Angstroms), in contrast to Magnetic Force Microscopy (MFM) where the magnetic dipole forces are probed with a ferromagnetic probe tip at a typical tip-to-surface distance of 10-20 nm [3]. MExFM has allowed a first direct real-space observation of spin structures at surfaces of antiferromagnetic bulk insulators [2] as well as ultrathin films [4]. Moreover, it provides a powerful new tool to investigate different types of spin-spin interactions based on direct-, super-, or RKKY-type exchange down to the atomic level. By combining MExFM with high-precision measurements of damping forces [5] localized or confined spin excitations in magnetic systems of reduced dimensions become experimentally accessible [1].

[1] R. Wiesendanger, Rev. Mod. Phys. **81**, 1495 (2009).

[2] U. Kaiser, A. Schwarz, and R. Wiesendanger, Nature **446**, 522 (2007)

[3] Y. Martin and K. Wickramasinghe, Appl. Phys. Lett. **50**, 1455 (1987); J. J. Saenz, N. Garcia, P. Grütter, E. Meyer, H. Heinzelmann, R. Wiesendanger, L. Rosenthaler, H. R. Hidber, and H.-J. Güntherodt, J. Appl. Phys. **62**, 4293 (1987)

[4] R. Schmidt, C. Lazo, H. Hölscher, U. H. Pi, V. Caciuc, A. Schwarz, R. Wiesendanger,

and S. Heinze, Nano Lett. **9**, 200 (2009).

[5] M. Ashino, D. Obergfell, M. Haluska, S. Yang, A. N. Khlobystov, S. Roth,

and R. Wiesendanger, Nature Nanotechnol. **3**, 337 (2008);

M. Ashino, R. Wiesendanger, A. N. Khlobystov, S. Berber, and D. Tomanek,

Phys. Rev. Lett. **102**, 195503 (2009)

10:40am **NS+AS+MN-WeM9 Chemical Imaging and Interaction Quantification on the Surface Oxide Layer of Cu(100) Using High-Resolution Atomic Force Microscopy.** *M.Z. Baykara, T.C. Schwendemann, H. Mönig*, Yale University, *M. Todorovic, R. Pérez*, Universidad Autónoma de Madrid, Spain, *E.I. Altman, U.D. Schwarz*, Yale University

Chemistry is governed by the interactions between atoms and molecules. On surfaces, chemical forces extending into the vacuum direct the behavior of many scientifically and technically important phenomena including surface catalysis. Therefore, it would be useful to map and quantify the

* NSTD Recognition Award

interactions between a catalytically active surface and a probe with atomic resolution in order to study the role and effectiveness of various surface defects such as vacancies, impurities, steps, kinks, and domain boundaries as active sites. An ability to discriminate between different chemical species on the sample surface would offer further insight. In this talk, we will show with the example of an oxygen-reconstructed copper (100) surface that much of this information can be derived from combining the new method of three-dimensional atomic force microscopy (3D-AFM) [1], a variant of noncontact atomic force microscopy, with scanning tunneling microscopy. The surface oxide layer of Cu(100) features domain boundaries and a distinct structure of the Cu and O sublattices that is ideally suited for such model investigations. While different tips show different chemical contrasts, 3D data sets enable site-specific quantification of force interactions and tunneling currents. In order to clarify the different contrast modes data, DFT total-energy calculations and Non-equilibrium Green's Function (NEGF) methods for electronic transport have been used to determine the interaction and the tunneling current [2-4] for a large set of tip models. These calculations provide insight into (1) the fundamentals of contrast formation in this experimental technique and (2) into the correlation between tip-sample forces and local chemical reactivity, factors that are essential for the further development and application of this novel approach to characterizing catalytic activity.

- [1] B. J. Albers et al., *Nature Nanotechnology* **4**, 307 (2009)
- [2] Y. Sugimoto et al., *Nature* **440**, 46 (2007)
- [3] P. Jelinek et al., *Phys. Rev. Lett.* **101**, 176101 (2008)
- [4] J. M. Blanco, F. Flores, and R. Perez, *Prog. Surf. Sci.* **81**, 403 (2006)

11:00am NS+AS+MN-WeM10 Comparison of Resonant-Frequency Techniques for AFM Nanomechanical Mapping. *D.C. Hurley, J.P. Killgore, A.B. Kos, NIST, A. Gannepalli, R. Proksch, Asylum Research*
 Contact-resonance force microscopy (CR-FM) is an emerging AFM technique for quantitative imaging of near-surface nanoscale mechanical properties. In CR-FM, the resonant frequency f of the cantilever is measured when the tip is in contact with the sample. Mechanical-property values are obtained from the frequency data with the use of models for the vibrating cantilever and the tip-sample contact. Contact-resonance measurements were originally made at a fixed sample position with off-the-shelf electronics. However, to achieve sufficient speed for CR-FM imaging, it has been necessary to develop new instrumentation approaches. Here we describe work to directly compare three methods for CR-FM imaging: the SPRITE (Scanned Probe Resonance Image Tracking Electronics) approach developed at NIST, the DART (Dual AC Resonance Tracking) approach developed by Asylum Research, and the BE (Band Excitation) method originally developed at Oak Ridge National Laboratory and implemented by Asylum Research. Each method enables contact-resonance frequency mapping but achieves it through different practical implementations. First, we will discuss the concepts on which each method is based. Next, results of comparison experiments will be presented in which images were acquired with each method in succession on the same AFM instrument. A variety of specimens were imaged to probe the strengths and limitations of each method. For example, we found that DART could operate at higher scan speeds, while SPRITE and BE were better able to track very asymmetric peaks that presumably originate from nonlinear tip-sample interactions. Both DART and BE provide values of the resonance quality factor Q in addition to the resonant frequency f , while currently SPRITE measures f only. Despite these differences, the methods yielded similar results in many cases. The availability of a broader array of frequency mapping tools will ultimately facilitate the widespread application of CR-FM to nanoscale materials science.

11:20am NS+AS+MN-WeM11 Single Molecule Structural Transitions of Water Polymer Chains in a Nanoscale Confined Space Studied by COIFM. *B.I. Kim, Boise State University*
 Interfacial water structures have been investigated in an ambient environment between two silica surfaces using a newly developed cantilever based optical interfacial force microscope (COIFM). As the gap distance decreases between the tip and the substrate, a remarkable oscillatory behavior is observed in normal and friction forces. Our further analysis suggests that water molecules confined between tip and substrate in an ambient environment form a bundle of water chains through hydrogen bonding. Each chain length is analyzed by a model called "freely jointed chain" (FJC) model in which the individual segments can rotate freely. The bundle of water chains experiences multiple layering transitions (without single layer transition) from $l = 36$ diameters to $l = 12$ diameters as the tip approaches the surface. The analysis shows that the number of links (l) decreases by 5,4,3,3,3,3,4,5 in water diameters. The result indicates that, as the gap between the tip and the substrate decreases, the interfacial water molecules favor multilayer transitions to stepwise, single layer transitions. The multilayer transitions consist of a sequential reduction of total chain

length by integer number of water diameters. The loss of one water diameter in overall chain length represents a highly cooperative transition, whereas the loss of two additional water diameter along the sigmoidal shape is reminiscent of a well-known two state transition. As a model to describe these transitions, a kink is introduced in the chain by rotating one water molecule 90 degrees while maintaining the number of hydrogen bonds in the chain. The other remaining molecules still follow the freely jointed chain model.

Plasma Science and Technology
Room: Galisteo - Session PS+MN-WeM

Plasma Processing for 3D Integration, TSV, and MEMS
Moderator: M. Darnon, CNRS-LTM, France

8:00am PS+MN-WeM1 High Etch Rate of TSV using by Ultra Self-Confined VHF-CCP. *Y. Morikawa, M. Yoshii, N. Mizutani, K. Suu, ULVAC, Inc., Japan*

Thru silicon via (TSV) etch process for deep and high-aspect ratio structure has been studied thoroughly for applications such as MEMS devices. Recently, TSV used in 3D-LSI devices, the via diameter and depth would be several tens of microns, and, the package for CMOS image sensors using TSV may have via diameters and depths up to 100 microns. A diameter of above 50um account for 50 % of TSVs. Therefore, development of high etch rate about 50um via is very important for realizing these applications. In this study, a large via size of 50 um etching in a low-pressure process was focused by using very high frequency capacitive coupled plasma (VHF-CCP) with an ultra self-confined system. This plasma system is simple parallel plate CCP. And the cathode has a structure designed to minimize the stray capacitance (C_s) and impedance (L) to get a low-pressure process of about 100Pa or more. Low-pressure process was carried out on the plasma confined, because mean free pass is very short. And, ion energy distribution (IED) is also controllable by low-pressure process with VHF bias. The bimodal IED changes under low-pressure. The peak of high-energy side is reduced, and a charge exchange peak appears. It is considered that the charge exchange is important to anisotropic Si etching with VHF bias. Finally, an etch rate of more than 60 $\mu\text{m}/\text{min}$ was realized. It was found that the Si etch rate depended on fluorine radical density and ion energy distribution, so, the high rate was obtained by creating a high fluorine radical density condition by using a high pressure condition of 100Pa using a VHF-CCP reactor with an ultra confined system and SF6 gas chemistry.

8:20am PS+MN-WeM2 Very Uniform and High Rate TSV Etching Process in Advanced NLD Plasma. *Y. Morikawa, T. Murayama, K. Suu, ULVAC, Inc., Japan*

The high-density of thru silicon via (TSV) is indispensable to the utilization and improvement in performance of 3D-LSI. Advanced high aspect ratio TSV etching technologies are required for high-density TSV formation. We have developed a new etching system for TSV application. This system is a planer type magnetic neutral loop discharge (NLD) plasma, which is named as advanced NLD. For high rate silicone etching, it is very important to understand not only the high density of the plasma generation but also the high density of fluorine atoms. In this study, a novel RF antenna 'Multi Stacked rf Antenna' has also been developed for the purpose of high rate etching. This antenna consists of multistage spiral turn rf antennas to reduce self-inductance (L), and is increased from turn of spiral to extend the inductive coupling discharge region. The L feature of this antenna is 0.95 uH and it is a low L antenna compared to the standard spiral antenna (1.7uH). As a result of performing the electron density measurement of the NLD plasma using this MS antenna, it succeeded in the high-density plasma production of $1 \times 10^{12} / \text{cm}^3$ by the process pressure of 7 Pa. Next, the Si etching process development was performed using the advanced NLD etcher. Si etching characteristics employing advanced NLD plasma were studied with respect to distance from an antenna. As a result, the etching rate improved 4 times more compared to the standard NLD. Finally, the diameter of 1.5 um was attained by the anisotropic etching of 8.5 um/min, and the aspect ratio is 5.3 using the advanced NLD etcher.

8:40am PS+MN-WeM3 Deep Reactive Ion Etch Process Optimization for Control of Sidewall Profile and Morphology as a Function of Aspect Ratio. *R.J. Shul, R.L. Jarecki, T.M. Bauer, Sandia National Laboratories, M. Wiwi, LMATA Government Services*

Deep reactive ion etching (DRIE) has become an enabling technology for the fabrication of many integrated microsystems, including accelerometers and gyroscopes, micro-fluidic devices, sensors, electrostatically actuated devices, and devices requiring back side optical access. The ability to etch

deep Si structures with anisotropic sidewalls hundreds of microns deep has established a new set of devices in the MEMS area. Significant improvements in equipment and understanding of the process conditions have improved device yield and performance, and process reliability. Even with these improvements, several process issues are not well understood and often limit applications for the process. For example, sidewall morphology is often dominated by scalloping created by the iterative deposition-depassivation-etch cycle. Scalloping may make it difficult for deposition of materials on the sidewalls post DRIE or create non-optimal flow conditions for micro-fluidic devices. In addition, profile control of deep structures as a function of aspect ratio has not been optimized. For example, we have observed that creating positively tapered trench sidewalls often results in a trench bottom that exhibits a characteristic micromasked, grassy appearance. Conversely, eliminating the grass often results in a profile that undercuts the etch mask. Depending on the application, these phenomenon prevent the use of DRIE for device fabrication or cause the process to be optimized for specific structures thus preventing yield of other structures. In this presentation, we report on our efforts to vary DRIE process conditions to optimize sidewall profile and sidewall morphology as a function of aspect ratio. Structures considered in this study range from 10 microns to 700 microns in width, with etch depths to several hundred microns. We observe that passivation time, as well as ion energy, and ion flux in both the depassivation and etch cycles, have significant effect on the sidewall profile as a function of aspect ratio. We have also included morphing experiments in this study, where morphing is changing DRIE process parameters as a function of total process time. To optimize sidewall profile and morphology, the magnitude of the process changes during the morphing process is not necessarily linear with time. Results of these experiments will also be reported.

Sandia National Laboratories is a multi program laboratory operated by Sandia Corporation, a Lockheed Martin Company for the United States Department of Energy's National Nuclear Security Administration under contract DE-AC04-94AL85000.

9:00am PS+MN-WeM4 XeF₂ Vapor Phase Silicon Etch used in the Fabrication of Movable SOI Structures, J. Stevens, R.J. Shul, Sandia National Laboratories, M. Wiwi, C.L. Ford, LMATA Government Services, T. Plut, T.M. Bauer, Sandia National Laboratories

Vapor phase XeF₂ has been used in the fabrication of various types of devices including MEMS, resonators, RF switches, and micro-fluidics, and for wafer level packaging. In this presentation we demonstrate the use of XeF₂ Si etch in conjunction with deep reactive ion etch (DRIE) to release single crystal Si structures on Silicon On Insulator (SOI) wafers. XeF₂ vapor phase etching is conducive to the release of movable SOI structures due to the isotropy of the etch, the high etch selectivity to silicon dioxide (SiO₂) and fluorocarbon (FC) polymer etch masks, and the ability to undercut large structures at high rates. Also, since XeF₂ etching is a vapor phase process, stiction problems often associated with wet chemical release processes are avoided. Monolithic single crystal Si features were fabricated by etching continuous trenches in the device layer of an SOI wafer using a DRIE process optimized to stop on the buried SiO₂. The buried SiO₂ was then etched to handle Si using an anisotropic plasma etch process. The sidewalls of the device Si features were then protected with a conformal passivation layer of either FC polymer or SiO₂. FC polymer was deposited from C₄F₈ gas precursor in an inductively coupled plasma reactor, and SiO₂ was deposited by plasma enhanced chemical vapor deposition (PECVD). A relatively high ion energy, directional reactive ion etch (RIE) plasma was used to remove the passivation film on surfaces normal to the direction of the ions while leaving the sidewall passivation intact. After the bottom of the trench was cleared to the underlying Si handle wafer, XeF₂ was used to isotropically etch the handle Si, thus undercutting and releasing the features patterned in the device Si layer. The released device Si structures were not etched by the XeF₂ due to protection from the top SiO₂ mask, sidewall passivation, and the buried SiO₂ layer. Optimization of the XeF₂ process and the sidewall passivation layers will be discussed. The advantages of releasing SOI devices with XeF₂ include avoiding stiction, maintaining the integrity of the buried SiO₂, and simplifying the fabrication flow for thermally actuated devices. Sandia National Laboratories is a multi program laboratory operated by Sandia Corporation, a Lockheed Martin Company for the United States Department of Energy's National Nuclear Security Administration under contract DE-AC04-94AL85000.

9:20am PS+MN-WeM5 SF₆/O₂/HBr Plasma Processes for the Etching of High Aspect Ratio through Silicon Via, S. Avertin, STMicroelectronics, France, E. Pargon, T. Chevolleau, Ltm - Umr 5129 Cnrs, France, F. Leverd, P. Gouraud, C. Verove, STMicroelectronics, France, O. Joubert, Ltm - Umr 5129 Cnrs, France

Today, the integration density and the chip dynamic power consumption are limiting and restricting phenomena. More than 50% of this consumption is due to long horizontal interconnects, and this rate is projected to increase.

One solution to resolve these problems is 3D-Integration which provides smaller wire-length distribution by minimizing the connection length thanks to the fabrication of vertical vias through the silicon substrate or/and the chip. The ITRS roadmap requirement is to etch vias with 2-5 μm in diameter and high aspect ratio (>5). For deep silicon etching, the Bosch etch process which consists in alternating isotropic etching and deposition steps leads to the formation of the so-called scalloping phenomenon on the sidewalls (>100nm). In this paper, we propose to characterize and develop conventional plasma etching processes as an alternative to the Bosch process. The etching development is carried out in ICP reactor accepting 300mm wafers (DPSII from AMATTM) using SF₆/O₂/HBr plasma chemistries. The scientific objectives are to study the etching mechanism and passivation layer formation in order to get high etch rate (>3μm.min⁻¹), straight profiles and a controlled undercut (<50nm). The etching profiles and etch rates have been analysed using Scanning Electron Microscopy while etch and passivation mechanisms have been studied by quasi-in-situ X-ray Photoelectron Spectroscopy (XPS) and plasma diagnostics (Mass Spectroscopy, ion flux probe..). Preliminary results indicate that the etch mechanisms are strongly driven by the ratio of neutral over ion fluxes and that the etch process is very sensitive to microscopic effects such as the local loading of fluorine and oxygen radicals which is directly correlated to the local pattern density. Through a better understanding of the etch mechanisms, high aspect ratio silicon via with anisotropic profiles and minimized undercut have been obtained.

9:40am PS+MN-WeM6 Study on the High Aspect Ratio Si Etch for D2x Devices, Y. Gwangyong, P. Jongchul, Samsung Electronics, Republic of Korea

As the design rule of the semiconductor devices decreases, the device fabrication technology is facing many difficulties. One of issues is the STI trench etching profile in case of the aspect ratio(A/R) over 20, and the traditional etching technology is not working properly any more. One among those problems is intra-cell loading which is due to the insufficient exhaustion of by-product from the narrow space (less than 30nm). The other is the bowing profile which results in the bad STI filling to generate the severe electrical short fails of a DRAM device. In this study, we researched and developed the innovative STI trench etching technologies to improve those problems. The one is the bias-pulsed plasma etching that repeats periodically plasma ON and OFF, which gave the dramatic decrease of the intra-cell loading. In addition that gave the side passivation effect to result in straight side-slope without bowing. These two effects are due to the byproduct exhaustion and the radical attaching during the plasma OFF time. And the high temperature etching process and the multi-step Oxygen flashing process also improved the intra-cell loading significantly. We got to know that these new Si etching technologies are successfully applied to the future high A/R(> 15:1) STI process for D2x DRAM devices.

10:40am PS+MN-WeM9 Key Challenges in Extremely High-Aspect-Ratio Dielectrics Etching at 3x nm DRAM and Beyond, S.K. Lee, J.-H. Sun, S.O. Lee, J.-S. Bang, S.-I. Lee, C.-M. Lim, S.-Y. Kim, D.-G. Lim, S.-K. Park, J.-G. Jung, HYNIX Semiconductor Inc., Republic of Korea

One of key issues in fabricating the dynamic random access memories (DRAM) is to control the vertical profile effectively during the etching of a SiO₂ high aspect ratio contact holes (HARC). In order to ensure acceptable Cs (>25fF/Cell) for DRAM at half pitch (HP) 3x nm and beyond generation, it is required of fabricating cell capacitors having very highly aspect ratio above 50:1. Thus, the HARC etching technology to get smaller bowing width as well as larger opening area becomes the most difficult challenges among numerous DRAM fabrication steps. This is because of trade-off between both bowing and opening requirement during HARC etching. Although the mechanism of bowing and not-opening has reported in several studies at above 70nm technology nodes, still has not yet been reported at hp 3x nm and beyond. In this presentation, especially, we will focused on the HARC etching issues at Nitride Fence supported Capacitor (NFC) scheme which is used to prevent leaning. Capping is arose by several factors, which reduce the etch rates and cause the contact opening failure, then eventually affects on the electrical characteristics. The types of capping studied in this work can be divided into three categories as the etching proceeded, such as polymer pinch-off, excess polymer capping originating from polymer rich chemistry at top region, and non-steady polymer deposition and removal at etch front. In this study, we investigated that capping issues become more serious when 2MHz range power is added to increase contact opening margin. To avoid these types of different failures aforementioned, it is necessary to understand the plasma etching behavior at hp 3x nm and beyond compared to previous technology nodes. In addition, beyond typical bowing position, an additional bowing position at NFC is also key concern issues within oxide layer between hard mask (HM) and Nitride from the wafer top surface. This is caused by the ions scattered from the mask side-wall slope on the contact-hole. It can be reduced effectively by adjusting HM material, thickness, and etching conditions. Especially,

HARC etching parameters also play an important role to suppress the bowing and capping. We will report here how contact hole's opening and bowing are enhanced, and how they can be controlled by adjusting etching conditions also. It is suggested that optimizing the etching condition with a suitable concept in this work would be the most effective solution during the HARC etching process. Consequently, Key approaches on HARC etch processes for fabricating of a contact hole in SiO₂ with aspect ratios of 50:1 and beyond were evaluated in this work in detail.

11:00am **PS+MN-WeM10 Microstructures Etching on Silicon with the STiGer Process**, *T. Tillocher*, GREMI, France, *J. Ladroue*, GREMI - STMicroelectronics, France, *F. Moro*, *G. Gommé*, *P. Lefauchaux*, GREMI, France, *M. Boufnichel*, STMicroelectronics, France, *P. Ranson*, *R. Dussart*, GREMI, France

The STiGer cryoetching process can be alternatively used to the Bosch process or the cryogenic process to etch high aspect ratio structures. It has been developed thanks to our knowledge of the passivation mechanisms in cryoetching. In the standard cryogenic process, patterned Si substrates cooled down to very low temperatures are exposed to continuous SF₆/O₂ plasmas. A SiO_xF_y-type passivation layer is formed on the sidewalls and prevents etching. This film has the property to desorb under ion bombardment or when the substrate is heated. We also showed that SiF₄/O₂ plasmas can be used to create or reinforce a passivation layer in cryogenic etching.

The STiGer process consists of cycling passivation steps (SiF₄/O₂ plasmas) and etching steps to get vertical structures. The etching steps can be either isotropic (SF₆ plasmas) or anisotropic (SF₆/O₂ plasmas). Like the cryogenic process, it is required to cool the Si substrate with liquid nitrogen.

The STiGer process combines advantages of both Bosch process and cryogenic process. Due to the cyclic passivation steps, the SiO_xF_y film is stronger than in "standard" cryoetching. In addition, the passivation layer desorbs when the substrate is heated back to room temperature. Thus, unlike the Bosch process, there is no need to clean the microstructures and the chamber walls after each process run. Moreover, the robustness is enhanced in comparison with "standard" cryoetching: the profiles are less sensitive to temperature variations.

But, like the standard cryogenic process, a cooling is required and like in Bosch etching, a scalloping is present on the sidewalls. However, it is possible to minimize this effect by tuning the etching and the deposition steps.

We will present our most recent performances with the STiGer process. Our objectives are to etch sub-micron trenches and holes that will be further used for the realization of integrated capacitors and Through Silicon Vias (TSV). But obviously, the STiGer process can be utilized for silicon micromachining in general.

Finally, we will see how such a process can amplify Columnar MicroStructures (CMS).

Plasma Science and Technology Room: Aztec - Session PS-WeM

Plasma Surface Interactions (Fundamentals & Applications) I

Moderator: M. Hori, Nagoya University, Japan

8:00am **PS-WeM1 On the Mechanism of Plasma Surface Interactions in Electron Beam-Generated Plasma in Nitrogen Environment**, *E.H. Lock*, *S.G. Walton*, *R.F. Fernsler*, Naval Research Laboratory

There are numerous features of electron beam-generated plasmas that distinguish them from discharges. In particular, most of the electron beam energy is spent on gas ionization ($\approx 50\%$), some on gas dissociation and very small amount on excitation. Thus, less radicals and photons are produced in electron beam-generated plasmas compared to discharges. Moreover, the electron temperature is low ($< 1\text{eV}$) so that the plasma potential is low and therefore the energy of the ions ($1\text{-}5\text{eV}$) that attack the surface is low. These low ion energies minimize the undesirable physical sputtering and ion-assisted chemical etching of polymer surfaces, thereby limiting changes to the polymer surface morphology and the depth of modification. Despite these differences, the chemical structure of the polymer surface exposed to electron beam plasma is changed. In this work, we focus on understanding the mechanism of plasma induced polystyrene modification in nitrogen through a careful analysis of the functional groups formed and their distribution with depth.

This work was supported by the Office of Naval Research.

8:20am **PS-WeM2 Breakthrough of Compatibility between Bowing-free Profile and Bottom CD in High Aspect Ratio Dielectric Etch Using DC Superimposed Capacitively-Coupled Plasma**, *A. Nakagawa*, *H. Mochiki*, *M. Dojun*, *K. Yatsuda*, *S. Okamoto*, Tokyo Electron AT Limited, Japan

Fabrication of latest DRAM capacitor structure requires precise etch profile control of silicon dioxide due to the continuous trend of narrowing pitch and high aspect ratio (HAR) features. While a number of issues are recognized such as twisting and bottom distortion, bowing became an outstanding subject for DRAM technology development for its complexity to cope with the bottom CD; even slight bowing leads to interference with the adjoining structures, and adjustment of process conditions frequently accompanies decreased bottom CD. In the present report we explore the effect of DC superimposition in capacitively-coupled plasma (CCP) as a countermeasure, taking advantage of its controllability on necking level at the mask facet.

Generally speaking, bowing is induced by the reflected ions at the mask facet attacking silicon dioxide sidewalls. Moreover, shrunk mask entrance interferes with incident radicals to transfer to the hole bottom, narrowing its size. One of the solutions utilizes high ion energy, but our results demonstrated a strong correlation between mask necking and bottom CD, thus the evaluation focused on optimization of mask necking.

Next, observation of deposition at the silicon dioxide sidewall varied by process parameters lead to systematic understandings of its physical amount and local enhancement, as well as the declining behavior at the removal process. By means of process parameters, the necking degree of the mask opening was controlled and the relationship among necking, bowing and bottom CD was examined.

As a result, it is necessary to improve necking at mask opening to minimize bowing and to keep bottom CD simultaneously. Optimization of process parameters enables etch profile enhancement by dispersing necking location, which normally decreases selectivity to mask. However, DC-superimposed CCP facilitated maintaining selectivity to mask with preferable etch profile, and less bowing with sufficient bottom CD.

8:40am **PS-WeM3 High Resolution Cryogenic Silicon Etch Process Development for Nanoscale Trenches**, *Y. Wu*, Oxford Instruments, Lawrence Berkeley National Laboratory, *D. Olynick*, Lawrence Berkeley National Laboratory, *A. Goodyear*, Oxford Instruments, *C. Peroz*, Abeam Technologies, *S. Dhuey*, *X. Liang*, *S. Cabrini*, Lawrence Berkeley National Laboratory

We present work on the development of a cryogenic silicon etch process suitable for etching shallow and high aspect ratio nanoscale features below 50 nm for use in nanophotonics applications. With shrinking feature sizes, profile and critical dimension control tolerance is reduced and appropriate processes must be developed. Cryogenic silicon etching using SF₆-O₂ offers several advantages over fluorocarbon or heavier halogen based processes. For example, low bias voltages can be used, reducing mask erosion and ion damage. In addition, the etching process is not purely ion dependent which reduces some of the problems at small feature sizes associated with the ion angular distribution and ion interaction with the sidewall which can cause less than ideal profiles. Furthermore, sidewall contamination is minimal eliminating critical dimension (CD) variations due to etch residue cleaning. Two challenges to creating a suitable cryogenic SF₆-O₂ process for 50-100 nm features and below, is optimizing the passivant to eliminate undercut and reducing the etch rate enough to control the process. Furthermore, an etch process which changes in time accordingly to the etch depth and aspect ratio may be necessary for features below 20 nm.

The cryogenic SF₆-O₂ based silicon etching process was investigated in an Oxford Instruments ICP 380 using a L18 Taguchi design of experiments (DOE) matrix. For the DOE, trench type features sized 300-500 nm are investigated. Parameters varied include pressure, temperature, RF power, ICP power, He backing pressure, and oxygen content. The effects on the etch rate, selectivity, profile angle, and surface roughness were examined. The process was then finely tuned for etching of densely packed silicon trenches ranging from 100 to 10 nm. These features are patterned both with electron beam lithography and nano-imprint lithography techniques. Resist selectivity is high in both cases: from 10:1 to 20:1. Vertical and smooth sidewalls were obtained. Etched patterns were used to create nanophotonic devices such as nanospectrometers and laser waveguides and imprint masks for high resolution applications.

9:00am **PS-WeM4 Quantitative Analysis and Modeling of Dry Etch Induced Physical Damage in Si Surface Layer**, *J.H. Yoon*, *W.S. Kim*, *J.W. Han*, *D.H. Kim*, *J.Y. Lee*, *K.S. Shin*, *C.J. Kang*, Samsung Electronics, Republic of Korea

As the size of memory cell is scaled down, due to the structural limitation of planar transistor, new structural device is needed, like a recessed channel or FinFET. When using the etch process for a new structure patterning,

however, exposure of Si surfaces to a reactive plasma can result physical damages. These effects lead to degradation of electrical properties of silicon substrates. Therefore, it is necessary to identify the measurable damage and then to design for reducing physical damage and/or removing the damaged layers without any further damage. In this study, using SRIM(Stopping and Range of Ions in Matter), we simulate ion distribution and damage region in the Silicon with etch species and Vdc, and using TEM, SE(Spectro Ellipsometry), RBS (Rutherford backscattering spectroscopy), we analyze the physical thickness of the damaged layer that depends on etch condition (Ion energy, selectivity to Si). In order to quantify the damage of exposed Silicon surface by etch process, the amount of defect was electrically calculated, respectively for Si/SiO₂ interface and Silicon bulk defect, using the charge pumping and gate controlled diode pattern at the MOSFET TEG. We found that defect density of high ion energy and high selectivity condition is bigger over a few order than low energy and low selectivity condition. In the latter case, the ion penetration depth is shallower and even damaged layer was also simultaneously etched during the process, but, in the former case, highly damaged layer was formed in the early stage of plasma exposure and defects were accumulated by increasing exposure time. To remove the damaged layers, normally we're using the light etch as post etch treatment. That is very effective to remove in case of highly damaged surface, but, in case of low damaged Silicon surface, light etch itself increase the amount of damage. So we have to choose well controlled treatment process with the degree of damage for improving the properties of Silicon substrate. The obtained results enable us to predict the etching induced physical damage to the devices in advance at the stage of plasma etch process design.

9:20am **PS-WeM5 On the Role of CF in Fluorocarbon Plasmas: Gas-Phase Reactions and Surface Interactions**, *M.F. Cuddy, E.R. Fisher*, Colorado State University

A complete understanding of the nature of fluorocarbon (FC) plasma systems necessarily includes a description of CF_x species behavior, including CF, CF₂, and CF₃. Our current research focuses primarily on understanding the gas-phase properties and reactions and gas-surface interactions of CF molecules produced from sparsely polymerizing CF₄ and C₂F₆ plasmas. An enriched understanding of these systems can elucidate the mechanisms contributing to film growth and may pave the way for enhanced plasma deposition and etching applications. To this end, we have employed laser induced fluorescence spectroscopy (LIF) and optical emission spectroscopy (OES) to probe the gas-phase behavior of CF, including calculations of rotational and vibrational temperatures. From these analyses, we determine that CF rotational states equilibrate with the plasma gas temperature at around 300 K. In addition, time-resolved actinometry has been employed to investigate gas-phase kinetics of the CF molecule as well as other CF_x species in a range of FC systems. We have also extended the LIF studies to our unique imaging of radicals interacting with surfaces (IRIS) technique which probes the gas-surface interface during plasma processing. CF species exhibit a surface gain in density, with surface scattering coefficients greater than unity for Si and ZrO₂ substrates, indicating production of the molecule at film-passivated surfaces. For comparison, IRIS results for CF₂ in the same plasmas will also be discussed. Surface analyses by high-resolution x-ray photoelectron spectroscopy (XPS) and variable angle spectroscopic ellipsometry along with the gas-phase data have culminated in a proposed mechanism for gas-surface interactions of these molecules during plasma processing of Si and ZrO₂ whereby the contributions of both CF and CF₂ molecules to film formation is summarily developed.

9:40am **PS-WeM6 "Designer" Ion Energy Distributions on Substrates Immersed in a Plasma**, *P. Diomede, D.J. Economou, V.M. Donnelly*, University of Houston

The energy of ions bombarding the substrate is critical in plasma etching (and deposition) of thin films. In conventional plasma processing, employing a sinusoidal substrate electrode voltage, the ion energy distribution (IED) is often very broad. However, as film dimensions approach the atomic level, control of the IED becomes critical. For example, selectivity considerations often dictate a narrow IED with a specified peak energy. In this work, semi-analytical models and particle-in-cell (PIC) simulations are employed to achieve "designer" IEDs, i.e., distributions with a desired shape and energy spread. This is accomplished by applying tailored voltage waveforms on the substrate electrode (spike, staircase, judiciously distorted square wave, etc.). Such waveforms can provide, for example, nearly mono-energetic IEDs or other desired shapes. Semi-analytic model results are compared with those of PIC simulation to identify the range of validity of the semi-analytic model. Predicted IEDs are also compared with experimental data under both collisional and collisionless sheath conditions. Strategies to control the energy flux of bombarding ions or to distribute the total energy flux to different energies will also be discussed.

Work supported by DoE Plasma Science Center and NSF.

10:40am **PS-WeM9 Modeling of Plasma-Induced Damage and Its Impacts on Parameter Variations in Advanced Electronic Devices**, *K. Eriguchi*, Kyoto University, Japan

INVITED

With scaling of advanced electronic devices, plasma-induced damage (PID) has been investigated extensively from various viewpoints. Although suppressing PID is one of the critical issues in plasma process optimization, there have been few reports which correlate the plasma parameters to device performance in terms of PID.

This study discusses one of the PID mechanisms, physical damage induced by ion bombardment on Si surface. We propose a new comprehensive framework linking an ion energy and the distribution function to device parameters, i.e., a unified PID design.¹⁾ The framework is based on a modified range theory²⁾ and an analytical device-degradation model.^{3,4)} To verify the validity, we performed both experiments to clarify the damaged-layer structures (the thickness, defect site density, and the electrical properties) by novel techniques⁵⁾ and simulations (molecular dynamics and device simulations) to understand the quantitative effects.

We demonstrate prediction of performance degradation in metal-oxide-semiconductor field-effect transistors (MOSFETs) damaged by an inductively coupled plasma reactor which can apply the bias with two different frequencies (400 kHz and 13.56 MHz). The model prediction indicates that, in typical etching processes, the damaged-layer thickness can be determined primarily by an average self-dc-bias voltage rather than applied bias frequencies. This implication is found to be in good agreement with experimental results. Moreover, one can estimate also variation in device parameters from basic plasma parameters. Thus, it is concluded that the proposed framework is a key concept for future process and device designs.

- 1)K. Eriguchi et al., IEDM Tech. Dig. (2008) 443.
- 2)K. Eriguchi et al., to be published in Jpn. J. Appl. Phys., 2010.
- 3)K. Eriguchi et al., Proc. Symp. Dry Process (2009) 267.
- 4)K. Eriguchi et al., IEEE Electron Device Lett. 30, 1275 (2009).
- 5)K. Eriguchi et al., Jpn. J. Appl. Phys. 47 (2008) 2446.

11:20am **PS-WeM11 Time Resolved Diagnostics of a Pulsed Dual-Source Inductively Coupled Plasma**, *H. Shin, W. Zhu, X. Lin, V.M. Donnelly, D.J. Economou*, University of Houston

A novel dual-source inductively coupled plasma (ICP) system was designed and built to control the electron energy distribution function (EEDF) in the plasma, and the ion energy distribution (IED) on the substrate. The main ICP source has a Faraday shield to minimize the RF component of the plasma potential. The substrate electrode, as well as a "boundary" electrode in contact with the plasma, can be independently biased by DC or RF voltages, of the desired waveform, to influence the IED. A secondary tandem ICP source can inject plasma, radicals or metastable atoms to the main ICP to influence the EEDF. The main ICP source was characterized using a Langmuir probe (LP), trace rare gas optical emission spectroscopy (TRG-OES), and an electrostatic ion energy analyzer. Emphasis was placed on pulsed plasma operation to achieve better control of the IED (as well as the ion angular distribution). With the Faraday shield installed, the plasma potential was several volts lower, and the peak-to-peak RF voltage of the plasma potential was suppressed to 1-2 V, as compared to the case without Faraday shield, allowing for smaller spread of the IED. The plasma potential, and thus the peak of the IED could be precisely controlled by the voltage applied to the boundary electrode. Accurate control of the ion energy and width of the IED is important for processes such as atomic layer etching, for which the threshold energies between etching and sputtering differ by only several volts. During the OFF period of a square wave modulation of the plasma power (50 μs ON, 50 μs OFF), the electron temperature decayed from 3.1 eV to less than 0.25 eV, with only a 20 % drop in plasma density for a 10 mtorr pressure, 200 W (average) power argon plasma. Time resolved EEDFs were also measured by the LP and compared to those extracted from TRG-OES experiments during the ON and first few ms of the OFF time. Tailored voltage waveforms were used to obtain "designer" ion energy distributions on the substrate. Finally, results for other gases (such as krypton and oxygen) will be discussed and compared to those obtained for argon plasmas.

Work supported by the DoE Plasma Science Center and NSF

11:40am **PS-WeM12 Investigations on Physical Processes for Low Temperature Plasma Activated Wafer Bonding**, *T. Plach, K.H. Hingerl*, University of Linz, Austria, *D.V. Dragoi, G.M. Mittendorfer, W.M. Wimplinger*, EV Group, Austria

Direct wafer bonding is a "simple" method of directly connecting wafers, with suitable (in terms of micro-roughness and flatness) surfaces,

permanently to each other, by bringing them into contact and subsequently annealing them. The conventional process for hydrophilic oxidized Silicon surfaces (native as well as thermal oxide) is well understood, and explained the following way:

Up to 100°C the substrate surfaces are held together via van der Waals interaction which is mediated by a few monolayers of water. In the range of 100-200°C the water diffuses away from the interface both along the interface and through the oxide into the crystalline bulk, where it reacts with the silicon and forms oxide. The increase of the bond strength from 50% to 100% of Si bulk strength is usually attributed to a closing of gaps at the interface [1], which starts at the softening temperature of the thermal oxide at around 850-900°C.

Low temperature plasma activated direct wafer bonding for a pair of native oxide – thermal oxide interfaces is a process that lowers the required annealing temperatures necessary for reaching high bond strength. Bulk strength can be realized by plasma activation with subsequent annealing at 300°C. At this temperature conventional wafer bonding reaches half of Si bulk strength, and is limited by gaps at the bonding interface. The mechanism behind this improvement compared to the non activated process is still under discussion.

To clarify the mechanism for this commercially available process, different bonding experiments were performed to evaluate the lifetime of the surface activation and the achievable bond strength when using substrates with various orientations. Interfaces of bonded wafer pairs were investigated by transmission electron microscopy (TEM). TEM images clearly show that there is no discernible interface between the native oxide on one side and the thermal oxide on the other side.

By covering half of the wafer during plasma activation, comparisons between the activated and non-activated region could be made by atomic force microscopy, by spectroscopic ellipsometry, by Auger analysis and by X-ray photoelectron spectroscopy.

It was found that the top surface stoichiometry is chemically changed, which favors bonding. Finally a model for the mechanism that explains the experimental results will be presented.

[1] Q.-Y. Tong, U. Gösele, *Semiconductor Wafer Bonding: Science and Technology*, Wiley, (1998)

Surface Science

Room: Picuris - Session SS1-WeM

Oxide Surface Structure

Moderator: C.H.F. Peden, Pacific Northwest National Laboratory

8:00am **SS1-WeM1 How Valuable Is Information from *Ab Initio* Phase Diagrams Beyond the Thermodynamically Allowed Region - the Puzzling (1 × 1)-H Structure on Polar ZnO(0001)-Zn**, *M. Valtiner, M. Todorova, J. Neugebauer*, Max-Planck-Institut fuer Eisenforschung, Germany

The (1 × 1) hydrogen reconstruction observed on Zn-terminated polar ZnO(0001) surfaces [1] is a prominent surface structure, which has so far defied any explanation attempts: none of the surface reconstructions observed in *ab initio* based equilibrium surface phase diagrams is consistent with the experimental observations [2]. Extending these equilibrium phase diagrams into the region of non-equilibrium conditions for the hydrogen chemical potential we show the occurrence of a new and so far not reported surface structure. The new structure consists of a (1 × 1) H covered triangular shaped reconstructions. It is stabilised and obeys electron counting, due to a simultaneous protonation of step-edge oxygen and surface terminating Zn atoms. It will be shown that the experimental conditions justify the consideration of hydrogen chemical potential outside the stability range of the H₂ molecule [3].

[1] T. Becker et al., *Surf. Sci.* 486, L502 (2001).

[2] M. Valtiner et al., *Phys. Rev. Lett.* 103, 065502 (2009).

[3] M. Valtiner et al., submitted (2010).

8:20am **SS1-WeM2 Hydroxylation of the MgO(001) Surface and its Effect on Metal Nucleation**, *M. Brown, E. Carrasco, M. Sterrer, H.-J. Freund*, Fritz-Haber-Institut der Max-Planck-Gesellschaft, Germany

The water-oxide interaction is of great importance in a number of technologically relevant fields, among them heterogeneous catalysis. Several studies report on the promoting effect of water in catalytic reactions, the participation of surface hydroxyls in reaction mechanisms, and the influence of hydroxylation on the binding of metals to oxide

surfaces. Achieving a fundamental atomic scale understanding of water-oxide interaction at environmentally and catalytically relevant conditions (e.g. ambient pressure) represents, therefore, a challenge for surface science studies related to heterogeneous catalysis. Here, we present a detailed study of water interaction with the surface of thin MgO films in a wide pressure range and the effect of surface hydroxylation on metal nucleation.

Adsorption of water on the surface of MgO(001) thin films of different thickness (2-20 ML) has been studied extensively from UHV to mbar pressure conditions using IRAS, XPS and TDS. Hydroxylation studies at room temperature were carried out in a high pressure cell up to water pressures of 1 mbar. The hydroxylation behavior of thick MgO films obtained from analysis of the O1s photoemission signal is comparable to MgO(001) single crystal studies showing a threshold pressure of 10⁻³ mbar H₂O for hydroxylation. With decreasing MgO film thickness the threshold pressure gradually shifts to lower H₂O pressures. In the limit of 2 ML MgO it is three orders of magnitude lower than for thick MgO films. Corresponding IR spectra confirm the enhanced reactivity of thin MgO films at high pressure conditions. The influence of surface hydroxylation on nucleation and sintering of gold nanoparticles was studied by comparison of Au deposition and thermal sintering on ideally terminated MgO(001) and hydroxylated MgO thin films, respectively. A combination of different spectroscopic techniques (TDS, XPS, IRAS) allows to establish a correlation between the degree of surface hydroxylation and the stability of gold atoms and clusters. Hydroxyl groups destabilize gold atoms on the MgO surface at 90 K; however, they enhance the stability of small gold clusters towards sintering at higher temperatures.

8:40am **SS1-WeM3 First, Find the Atoms: Mapping Epitaxial Nanostructures with Direct X-ray Methods**, *R. Clarke*, University of Michigan, Ann Arbor

INVITED

Epitaxial heterostructures constitute a large fraction of the materials systems used in current optoelectronics technology. As device dimensions continue to shrink to the nanoscale, atomic interfaces play an increasingly dominant role in their characteristics and performance. Moreover, new classes of devices are envisioned based on novel phenomena emerging from the complex ionic and electronic rearrangements occurring at interfaces. Energy harvesting, catalysis, quantum information processing and smart sensors are but a few of the possible applications. An essential requirement for harnessing these transformative developments is to provide accurate and detailed maps of the structure, chemical composition and strain at epitaxial interfaces prepared by various deposition methods, including molecular beam epitaxy, metallorganic chemical vapor deposition, focused ion beam and pulsed laser deposition. This presentation will describe some of the exciting science that can be done with current and envisioned capabilities in x-ray surface scattering. Examples include the use of direct methods for achieving sub-Ångstrom resolution maps of complex oxide interfaces, quantum-dot tailoring and focused ion beam directed assembly. Such experiments provide a basis for understanding how local structure can give rise to novel properties.

*Supported by DOE Basic Energy Sciences Contract DE-FG02-06ER46273 and the University of Michigan Energy Frontiers Research Center. </P>

9:20am **SS1-WeM5 W-oxide Clusters on Cu(110) Surfaces: Electronic Structure and Selforganisation**, *M. Wagner, A. Gumbsch, S. Surnev*, Karl-Franzens University Graz, Austria, *Z. Dohnalek*, Pacific Northwest National Laboratory, *A. Fortunelli*, CNR Pisa, Italy, *F.P. Netzer*, Karl-Franzens University Graz, Austria

Oxide clusters with well-defined size and stoichiometry supported on metal surfaces are interesting nanoscale objects with attractive features for both fundamental research and technological applications. It has been shown recently that (WO₃)₃ cluster molecules, formed by vacuum sublimation of WO₃ powder, can be deposited as monodisperse clusters on TiO₂ (110) surfaces [1]. In the present work, we investigate the interaction and electronic properties of (WO₃)₃ species at the single molecule level with Cu(110) and reconstructed Cu(110)-O surfaces using low-temperature (5K) scanning tunneling microscopy (STM) and spectroscopy (STS). In order to decouple the (WO₃)₃ cluster states from the metal substrate states, the clusters have been deposited also on a NaCl buffer layer (grown on Cu(110)). The comparison of the STM (STS) fingerprints of the (WO₃)₃ clusters on the NaCl and the Cu surfaces, together with respective DFT calculations, allows us to gauge the cluster-Cu interaction and to determine the hybridisation of the cluster orbitals with metal states. At low temperature (<20K) the (WO₃)₃ clusters are stable as individual units on the Cu(-O) surfaces, but at elevated temperature (room temperature and above) the clusters react with Cu substrate atoms. They selforganise via condensation and, depending on the coverage, form 1-D W-oxide line structures (nanowires) or arrange into ordered 2-D W-oxide nanolayer phases with well-defined atomic structures. These 2-D structures are investigated experimentally with STM and LEED and theoretically by DFT calculations.

Supported by the ERC Advanced Grant SEPON

[1] O. Bondarchuk, X. Huang, J. Kim, B.D. Kay, L.-S. Wang, J.M. White, Z. Dohnalek, *Angew. Chem. Int. Ed.* 45 (2006) 4786

9:40am **SS1-WeM6 Growth and Properties of Iron Oxides on YSZ(001)**, *I. Ermanoski, G.L. Kellogg*, Sandia National Laboratories

We have used low energy electron microscopy (LEEM) to study in real time the growth of iron oxides on the (001) surface of yttria-stabilized zirconia - YSZ(001). The FeO_x-YSZ system is currently used as a working material for solar thermochemical splitting of H₂O and CO₂ [1], but little fundamental information is available concerning the structure and composition of the mixed oxides and their surfaces. Upon Fe deposition in ~10⁻⁶ Torr of O₂ background pressure, iron oxides grow on the surface. Observation of low energy electron diffraction (LEED) patterns during growth shows the development of 3 distinct patterns with 12-fold symmetry, and one pattern with 4-fold symmetry. Dark field LEEM imaging shows a complicated domain structure where each of the 12-fold patterns corresponds to 2 or 4 rotationally equivalent domains. Some of the domains overlap laterally, pointing to a layered arrangement of different oxide structures. We use LEEM I-V and LEED to determine the oxide composition (hematite, magnetite, wüstite) and surface structure, both of which depend on the layer thickness, substrate temperature, and background oxygen pressure.

Sandia National Laboratories is a multi-program laboratory operated by Sandia Corporation, a wholly owned subsidiary of Lockheed Martin Company, for the U.S. Department of Energy's National Nuclear Security Administration under contract DE-AC0494AL85000. Funding for this work was provided through Sandia's LDRD Office.

[1] Diver, R.B., Miller, J.E., Allendorf, M.D., Siegel, N.P., Hogan, R.E., "Solar thermochemical water-splitting ferrite-cycle heat engines", *Journal of Solar Energy Engineering*, **130** (2008) 041001

10:40am **SS1-WeM9 Growth and Characterization of Ordered Tungsten Trioxide Films on Pt(111)**, *Z. Li, Z. Zhang, Y.K. Kim, S. Smith*, Pacific Northwest National Laboratory, *F.P. Netzer*, Karl-Franzens University Graz, Austria, *R.J. Rousseau, B.D. Kay, Z. Dohnalek*, Pacific Northwest National Laboratory

Catalysts based on WO₃ have been found to be active in a number of reactions including isomerization of alkanes and alkenes, partial oxidation of alcohols, selective reduction of nitric oxide, and metathesis of alkenes. In the present study we explore the growth of novel ordered WO₃ thin films on Pt(111) via direct sublimation of monodispersed (WO₃)₃ clusters. The prepared films are characterized using x-ray photoelectron spectroscopy (XPS), temperature-programmed desorption (TPD), low energy electron diffraction (LEED), reflection-adsorption infrared spectroscopy (RAIRS), and scanning tunneling microscopy (STM). The factors that affect the WO_x structure such as WO₃ exposure and substrate temperature were explored. At submonolayer coverages, the as-deposited (WO₃)₃ clusters are partially reduced leading to chainlike tungsten oxide structures with W in (6+) and (5+) oxidation states. Higher substrate temperatures (< 800 K) lead to further reduction of deposited (WO₃)₃. At higher coverages, an ordered (3 × 3) structure composed of (WO₃)₃ trimers is observed upon 700 K deposition. The experimental findings are complemented by DFT calculations that provide further insight into the observed WO₃ structures.

This research was performed in the Environmental Molecular Sciences Laboratory, a national scientific user facility sponsored by the Department of Energy's Office of Biological and Environmental Research and located at Pacific Northwest National Laboratory.

11:00am **SS1-WeM10 Towards a Reliable Characterisation of Oxide Layers on Pure Aluminium using High Energy Resolution FE-AES**, *I. Vandendael, T. Hauffman, Y. Van Ingelgem, A. Hubin, H. Terryn*, Vrije Universiteit Brussel, Belgium

Al₂O₃ on metallic aluminium is a widely used material of high technological importance. For the local chemical characterisation of these substrates FE-AES bears potential thanks to its high lateral resolution. In this study, the O KLL and Al KLL Auger electron spectral lines are recorded with a high energy resolution from pure aluminium, thin Al₂O₃ and thick Al₂O₃ layers on metallic aluminium. The behaviour of these aluminium oxide layers under electron beam irradiation is investigated.

It is demonstrated that, thanks to the high energy resolution used, it is possible to discriminate between the metallic and oxidised aluminium on the basis of the Al₀ KL_{2,3}L_{2,3} and Al³⁺ KL_{2,3}L_{2,3} Auger electron peaks recorded within one and the same spectrum. Oxygen electron-stimulated desorption is observed for both aluminium oxides. Effective cross-sections for this oxygen desorption are estimated for the thin and thick oxide layers. It is shown that when an Al₂O₃ layer is irradiated with an electron beam surface charging occurs. These phenomena remain limited thanks to the

presence of the underlying metallic aluminium substrate. The electron beam-induced effects are compensated by setting the angle of incidence of the primary electron beam to 15°. Finally, it is shown that inhomogeneities at the surface of the analysed oxides result in significant chemical shifts of the O KLL and Al KLL Auger electron transitions. It is investigated whether these inhomogeneities can be linked with lateral differences in hydroxyl fraction at the surface.

Surface Science

Room: Santa Ana - Session SS2-WeM

Electron, Photon and Ion Beam Induced Surface Modification

Moderator: J.A. Yarmoff, University of California, Riverside

8:00am **SS2-WeM1 Focused Electron Beam Induced Processing: Experiments, Simulations, and Applications**, *P.D. Rack*, University of Tennessee **INVITED**

The rapid and precise direct-write growth of nanoscale features by electron-beam-induced deposition (EBID) and etching (EBIE) requires the optimization of the growth parameters to maintain nanoscale feature dimensions. The tremendous and complex EBID/EBIE parameter space includes the precursor gas pressure, primary electron beam energy, electron beam current, surface diffusion rates of adsorbed precursor species, thermal effects on desorption, and the cascade of electron species produced by elastic and inelastic scattering processes. These variables affect the probability of precursor dissociation and hence determine the feature growth velocity and the size of the structure through a series of complex, coupled nonlinear interactions. In this presentation, a variety of experimental studies will be presented to demonstrate the various electron-gas, gas-solid, and electron-solid interactions that are germane to the electron beam induced processing technique. A dynamic computer simulation based on Monte-Carlo calculation sequences will then be described and compared to various experimental observations. Finally, several nanoscale device applications will be demonstrated.

8:40am **SS2-WeM3 Electron Beam Deposition for Nanofabrication: Insights from Surface Science**, *H. Fairbrother*, Johns Hopkins University, *J. Wnuk*, Princeton University, *J. Gorham*, National Institute of Standards and Technology, *S. Rosenberg*, Johns Hopkins University, *C.W. Hagen*, TU Delft, the Netherlands, *W. van Dorp*, University of Groningen, the Netherlands

Electron beam induced deposition (EBID) is attracting increased interest as a single-step, direct-write process capable of depositing free standing, nanometer-sized structures with high spatial resolution (~1 nm). However, the largest single limitation of EBID is that the deposited metallic nanostructures typically contain unacceptable levels of organic contamination which adversely affects the material's properties, thereby limiting potential applications. A more detailed understanding of the electron stimulated, decomposition of EBID precursors is needed to rationalize the relationships between organometallic ligand architecture and the composition of the deposits. Such mechanistic detail will allow greater control over the composition and function of nanostructures deposited by EBID while providing the necessary rational design criteria to fashion new organometallic precursors. Other scientific issues associated with EBID include a lack of quantitative information on the fundamental surface dynamics and deposition processes as well as overcoming the challenges of implementing successful purification strategies. The application of surface analytical techniques enables changes in the metal oxidation state, surface and gas phase composition as well as structure and chemical composition that accompany electron interactions with organometallic precursors to be studied in situ and in real time. In addition, I will describe how these various electron stimulated processes can be studied to extract data on reaction cross-sections and kinetics, information that would facilitate the development and testing of predictive models that can accurately describe EBID. Mechanistic insights into purification strategies that can be obtained through surface analytical techniques are also detailed. Throughout, I will discuss unresolved challenges and opportunities associated with EBID.

9:00am **SS2-WeM4 Multi-Electron Effects in Low Energy Sr⁺ Ion Scattering**, *X. He, J.A. Yarmoff*, University of California, Riverside

A system of many electrons can display emergent phenomena that cannot be extrapolated from the behavior of independent electrons. Non-adiabatic resonant charge transfer is used to reveal this multi-electron behavior by employing singly charged alkaline earth ions in a low energy ion scattering

experiment. The spin of the single valence electron of such an ion behaves as a magnetic impurity that interacts with the continuum of many-body excitations in the metal, resulting in Kondo and mixed valence resonances near the Fermi energy.^{1,2} The occupation of these resonances is acutely sensitive to changes of surface temperature, which leads to an anomalous temperature dependence of the ion neutralization probability. We report a maximum in the neutralization probability near 600 K for 2-4 keV Sr⁺ ions scattered from polycrystalline gold. Correlated electron effects, which have traditionally been manifest at low temperature, are observable well above room temperature because the projectile's ionization level shifts and crosses the target's Fermi energy as it approaches the surface where the interaction between the localized and extended electrons is very strong. This interaction becomes more pronounced as the work function of the surface is lowered by Sr implantation into the near-surface region. Further study will involve well-characterized single crystal surfaces that will enable detailed investigation of the relationships between the formation of correlated electron states and the atomic structure of the solid.

¹H. X. Shao, P. Nordlander, and D. C. Langreth, Phys. Rev. Lett. **77**, 948 (1996).

²J. Merino and J. B. Marston, Phys. Rev. B **58**, 6982 (1998).

9:20am **SS2-WeM5 Parallel Scanning Near-Field Photolithography: The Snomipede**, *E. ul Haq*, University of Sheffield, UK, *Z. Liu*, University of Nottingham, UK, *S. Alang Ahmad*, University of Sheffield, UK, *Y. Zhang*, University of Glasgow, Ireland, *L.S. Wong*, University of Manchester, UK, *J.K. Hobbs*, *G.J. Leggett*, University of Sheffield, UK, *J. Micklefield*, University of Manchester, UK, *C.J. Roberts*, University of Nottingham, UK, *J.M.R. Weaver*, University of Glasgow, UK

There has been enormous interest in the organisation of molecules at interfaces with nanometre spatial resolution, but important challenges still remain to be addressed. Of the established techniques, electron beam lithography is expensive, and requires exposure under vacuum, while scanning probe methods are slow and (with few exceptions) do not permit fabrication over large areas. Here, a new approach is described that yields arbitrary pattern fabrication over macroscopic areas. Scanning near-field photolithography enables the arbitrary fabrication of molecular structures as small as 9 nm ($\lambda/30$). We have developed a parallel near-field lithography device that fuses scanning near-field optical techniques with the 'Millipede' concept of massively parallel serial fabrication: a 'Snomipede'. Two Snomipede designs will be described, one based around the use of a liquid crystal spatial light modulator to direct diffraction-limited spots into an array of sixteen cantilevers with hollow, pyramidal tips, and the other based around the use of a Brewster angle zone plate, coupled to a digital mirror array, to direct the light spots. Their use for nanopatterning will be demonstrated by patterning siloxanes self-assembled monolayers formed from amino siloxanes molecules with a photocleavable protecting group. Structures with line widths of 100 nm have been formed in parallel over regions over 1 mm wide. Resulting structures have been derivatised with initiators for atom transfer radical polymerisation, from which biocompatible brushes have been grown. The potential of the Snomipede for reactive processing at the nanoscale will be demonstrated by fabricating 70 nm structures in photoresist using a probe array submerged under water.

9:40am **SS2-WeM6 Understanding the Effects of Radiation on the Cerium Oxide Thin Films by Experiment and Simulation**, *A. Kumar*, University of Central Florida, *V. Shuthanandan*, *R. Devanathan*, *S. Kuchibhatla*, *S. Thevuthasan*, Pacific Northwest National Laboratory, *S. Seal*, University of Central Florida

The damaging effect of radiation in applications such as immobilization of toxic radionuclides, fission and fusion reactors, and radiation therapy has attracted considerable scientific interest. The search for radiation tolerant materials has revealed that fluorite structural derivatives, such as zirconia and cerium oxide, have the ability to accommodate high energy radiation induced defects. Particularly for biomedical applications, cerium oxide is of more interest because not only it can prevent the damage from radiation but also it has the ability to quench free radicals and reactive oxygen species produced as the result of high energy radiation by regenerative switching between the +3 and +4 valence states of cerium. However the underlying mechanisms of radiation interaction and the resulting physicochemical and structural changes of cerium oxide are not well understood. In order to gain a fundamental understanding of radiation tolerance of cerium oxide nanostructures, we explored the behavior of single and polycrystalline ceria thin films were grown on YSZ and sapphire respectively by using oxygen plasma assisted molecular beam epitaxy and exposed to 2 MeV He⁺ radiation at fluences extending over three order of magnitude (10^{14} to 10^{17} ions/cm²) using the ion beam accelerator at EMSL, in Pacific Northwest National Laboratory. The chemical changes occurring in the thin films due to radiation exposure were characterized *in situ* by x-ray photoelectron spectroscopy (XPS). The experimentally observed changes in valence state

were correlated by simulating the nanoceria thin film by molecular dynamics and studying the displacement cascades produced by cerium and oxygen as primary knock on atom. The structural evolution of nanoceria thin films due to radiation exposure will be discussed in detail with implications for the use of cerium oxide as a radiation tolerant material.

10:40am **SS2-WeM9 Methyl Radical Velocity Distributions from Ketone Photooxidation on TiO₂(110)**, *D. Wilson*, *M. White*, Stony Brook University

The velocity distributions of methyl radical desorption from a photoinduced reaction of three ketones (acetaldehyde, acetone, and acetophenone (coadsorbed with O₂)) on TiO₂(110) was studied to determine the mechanism of reaction for these model systems. The data was collected using a pump-probe Time-of-Flight (TOF) method. The firing delay time between pump (initiates surface chemistry) and probe (ionizes desorbing neutrals) can be varied over a wide time range to map the velocities of the desorbing methyl species. Excitation occurs using 3.7 eV photons followed by ionization using 13.05 eV photons. Differences in the velocity distributions are observed and potential explanations of these differences is explained.

11:00am **SS2-WeM10 Laser Nitriding for Niobium Superconducting Radio-Frequency Accelerator Cavities**, *S. Singaravelu*, Old Dominion University, *J.M. Klopff*, *G. Krafft*, Jefferson Lab, *M.J. Kelley*, College of William & Mary

Particle accelerators are a key tool for scientific research ranging from fundamental studies of matter to analytical studies at light sources. Cost-performance is critical, both in terms of initial capital outlay and ongoing operating expense, especially for electricity. It depends on the niobium superconducting radiofrequency (SRF) accelerator cavities at the heart of most of these machines.

Presently Nb SRF cavities operate near 1.9 K, well (*and expensively*) below the 4.2 K atmospheric boiling point of liquid He. Transforming the 40 nm thick active interior surface layer from Nb to delta NbN (T_c = 17 K instead of 9.2 K) appears to be a promising approach. Traditional furnace nitriding appears to have not been successful for this. Further, exposing a complete SRF cavity to the time-temperature history required for nitriding risks mechanical distortion.

Gas laser nitriding instead has been applied successfully to other metals [P.Schaaf, Prog. Mat. Sci. 47 (2002) 1]. The beam dimensions and thermal diffusion length permit modeling in one dimension to predict the time course of the surface temperature for a range of per-pulse energy densities. As with the earlier work, we chose conditions just sufficient for boiling as a reference point.

We used a Spectra Physics HIPPO nanosecond laser ($\lambda = 1064$ nm, $E_{\max} = 0.392$ mJ, beam spot @ 34 microns, PRF = 15 – 30 kHz) to obtain an incident fluence of 1.73 - 2.15 J/cm² for each laser pulse at the target. The target was a 50 mm diameter SRF-grade Nb disk maintained in a nitrogen atmosphere at a pressure of 550 – 625 torr and rotated at a constant speed of 9 rpm.

The materials were examined by scanning electron microscopy (SEM), electron probe microanalysis (EPMA) and x-ray diffraction (XRD). The SEM images show a sharp transition with fluence from a smooth, undulating topography to significant roughening, interpreted here as the onset of ablation. EPMA measurements of N/Nb atom ratio as a function of depth found a constant value to depths greater than the SRF active layer thickness. Certain irradiation conditions resulted in values consistent with formation of delta NbN. Under certain irradiation conditions, XRD data were consistent only with delta NbN on top of Nb metal.

Funding: authored by Jefferson Science Associates LLC under US DOE Contract De-AC05-06OR23177. We are indebted to Prof. P. Schaaf (Goettingen) for the simulation code and helpful discussions.

11:20am **SS2-WeM11 A Model for the Hydroaffinity OH(1x1)-Si(100) and SiO₂ via Ion Beam Analysis (IBA), Tapping Mode Atomic Force Microscopy (TMAFM) and Surface Energy Analysis from Contact Angle Analysis**, *Q.B. Xing*, *N. Herbots*, *M.A. Hart*, *R.J. Culbertson*, *J.D. Bradley*, Arizona State University

The hydroaffinity of Si-based surfaces is investigated as a function of surface defect density, topography and electrical carrier concentration via either doping and/or point defect concentration. Surface energy and the resulting hydrophobic or hydrophilic behavior of two surfaces of application for wafer bonding, OH(1x1)-Si(100) and beta-crystalobite SiO₂. A series samples are implanted with increasing doses, annealed to obtain a uniform dopant depth profile in the first 10 nm. Their electrical activation is measured via substitutional fraction detected by ion channeling and sheet resistance measurements.

A combination of ion channeling, 4.265 ± 0.035 MeV $^{12}\text{C}(\alpha, \alpha)_n^{12}\text{C}$, 3.05 ± 0.005 MeV $^{16}\text{O}(\alpha, \alpha)_n^{16}\text{O}$ Nuclear Resonance and 2.8 MeV Hydrogen Recoil Detection are used for high resolution compositional depth profiling of the first 10 nm of the surface. Tapping Mode Atomic Force Microscopy (TMAFM) provides statistical analysis of the topography of these Si-based surfaces at a length scale ranging from a few nm to several μm . Extended atomic terraces with low edges and defects density on $\text{OH}(\text{1x1})\text{Si}(100)$ and crystalline silicates such as beta-cristobalite and alpha-quartz can render an insulating surface hydrophobic, while small scale roughness and surface defects makes it more hydrophilic. The water affinity and surface energy is measured using the Sessile Drop method and the Young-Dupré analysis as a function of topographical, compositional and micro-structural surface analysis using TMAFM, IBA combined with ion channeling and X-ray diffraction respectively. This correlation explains the behavior of water condensation at the liquid/air interface of intraocular implants during vitro-retinal surgery after cataract extraction and intraocular lens (IOL) implantation.

Polymer adsorption on surfaces alters their hydroaffinity, can control condensation on silicone IOL's [1] and enable for hermetic bonding in silica-based sensors in medical electronic implants [2]

[1] US Patent pending: "Molecular films for controlling hydrophobic, hydrophilic, optical, condensation and geometric properties of silicone implants surfaces, including intraocular lenses used in cataract surgeries." Inventor(s): N. Herbots, J. D. Bradley, M. Hart, D. A. Sell, S. Whaley, Q. Bradley (November 09, 2009)

[2] US Patent Pending: "Methods for Wafer Bonding, and for Nucleating Bonding Nanophases". Inventor(s): N. Herbots, J. D. Bradley, M. Hart, D. A. Sell, S. Whaley, R. J. Culbertson (April 30, 2010)

11:40am **SS2-WeM12 UV Induced Work Function Changes of Metal Oxide Surfaces**, M. Conrad, S. Gutmann, M.M. Beerbom, R. Schlaf, University of South Florida

The work function of a number of metal oxide thin films was measured using low intensity x-ray and ultraviolet photoemission spectroscopy (LIXPS, UPS).

Our experiments revealed that UPS based work function measurements of a variety of metal oxide surfaces previously exposed to the ambient or in contact with water vapor caused an immediate work function reduction of the order of 0.5 eV. This artifact was demonstrated using LIXPS work function measurements, which expose the sample surface to only a small fraction of the radiation flux encountered during UPS measurements. This enabled the measurement of the work function prior to the UPS characterization, revealing the UPS-related work function reduction. LIXPS measurement performed after the UPS measurements showed that sample charging effects can be ruled out as causes of the work function reduction, and that the work function change is permanent. These results suggest that a photochemical hydroxylation of the surface through photodissociation of water molecules occurs during the UPS measurement, which results in a surface dipole reducing the work function. Additional experiments investigated the influence of standard XPS measurements as well as LIXPS measurements on the work function. These experiments demonstrated that XPS measurements also cause a work function reduction similar to UPS measurements, albeit during a longer exposure time frame. In contrast, LIXPS measurements do not result in a significant work function reduction, i.e. can be used as a reliable work function characterization tool for oxide surfaces.

Thin Film

Room: Dona Ana - Session TF+EM-WeM

High K Dielectrics for Si Electronics

Moderator: S. Gupta, University of Alabama

8:00am **TF+EM-WeM1 Moore's Law - From Simple Scaling to Integrating New Materials and Introducing New Device Architectures**, R. Hendel, Periodic Structures Inc. **INVITED**

Moore's Law has been the driver for semiconductor integrated circuits over more than 40 years. Relentless scaling of dimensions switching provided increasing functionality and performance, resulting in leading edge single chips today that incorporate more than 1 Billion transistors.

All attempts on predicting the end of Moore's Law have been futile – innovations have always allowed continued scaling at reduced cost. However, while Moore's Law appears to be a continuous curve, we rarely reflect on the underlying changes that had to occur to enable this rate of progress. These changes comprised device architecture, the introduction of new materials and break-through processes.

Since Moore's Law describes a learning curve for which cost reduction is central, process simplicity frequently won out over performance advantages if the latter came at high cost. Self-aligned implanted poly-gate over the early metal gate structures is a prime example. Aggressive reduction in the cost per function also provided performance benefits: Smaller transistors switched faster and used less power to do so – truly a win-win situation.

Key innovations along this path were:

- The switch from thermal diffusion doping to implant
- The introduction of CMP, which was key in increasing the number of metal layers that could be integrated.
- The introduction of high-k dielectrics in conjunction with metal gates which addressed the critical gate leakage problem and will allow the introduction of new and better performing channel materials.

Compared to the past, the future will require even more innovation along three potential directions:

- Continuous improvements of current methodologies along existing technologies, consisting of solid engineering and hard work.

Innovations pursued in this category are: highly regular layouts, new channel materials in conjunction with modified hi-k/MG (yet planar) structures.

- Significant changes to traditional device structures and processes.

An example of innovations pursued in this category is the FinFET, which presents significant challenges in materials and processes that must be resolved before introduction into the manufacturing cycle.

- Radical new structures and approaches resulting in major deviation from today's mainstream technologies.

An example is new fundamental circuit components such as the Memristor or new approaches available if considering device operations at cryogenic temperatures (which may be feasible for server farms), allowing the exploration of concepts such as superinsulators.

This presentation will highlight the state-of-the-art in process technology and discuss challenges that require attention and timely solutions.

8:40am **TF+EM-WeM3 Non-destructive Depth Profiles of Hafnium Silicate Films by Angle-Resolved and Variable-Kinetic Energy XPS**, C. Weiland, N. Lorenz, R. Opila, University of Delaware

High dielectric constant, or high-k films are currently being employed in semiconductor devices. Hafnium silicate ($\text{Hf}_x\text{Si}_{(1-x)}\text{O}_2$) films are a promising material system for such applications, as they combine the high dielectric constant of HfO_2 with the high stability against crystallization of SiO_2 . The $\text{Hf}_x\text{Si}_{(1-x)}\text{O}_2/\text{Si}$ interface must be defect free as defects at this interface can create charge centers which decrease channel mobility. Atomic layer deposition (ALD) is frequently used to deposit high-k films, and provides excellent thickness control and conformality by reacting only one saturating layer of reactant at a time. This work focuses on studying the composition and interface quality of $\text{Hf}_x\text{Si}_{(1-x)}\text{O}_2$ films deposited by ALD using novel silicon precursors and water as the oxidizer. Films are analyzed using non-destructive depth profiles by angle-resolved and variable-kinetic energy X-ray photoelectron spectroscopy (ARXPS, VKE-XPS). In ARXPS, the effective probe depth is varied by changing the takeoff angle between surface and detector. As a complementary technique, VKE-XPS provides depth profiles by adjusting the incident X-ray energy, and thus the corresponding inelastic mean free path of the photoemitted electrons. VKE-XPS also allows the ability to probe deeper into films than conventional lab-based sources, providing the possibility of analyzing thicker films or entire gate stacks. Using these techniques, we have studied the composition and interface quality of $\text{Hf}_x\text{Si}_{(1-x)}\text{O}_2$ films deposited using various Si precursors. The presence of charge at the interface manifests itself as shifts in the energy of the photoelectron peaks. Using this data, we can determine charge at the high-k/silicon interface as well as measure band offsets.

9:20am **TF+EM-WeM5 Study of SiO_2 and SiN_x Passivation of HfInZnO Oxide Semiconductor Thin Film Transistor**, J.C. Lee, E.H. Lee, J.G. Chung, B. Anass, J.H. Lee, J.S. Park, M.K. Ryu, Samsung Advanced Institute of Technology, Korea

ZnO based oxide semiconductor is a promising material for thin film transistor which has transparent, high electric mobility, and the advantage of low temperature process. Several kinds of ZnO based oxide semiconductors (InZnO , GaInZnO , HfInZnO , etc.) have been adapted to the active material of thin film transistor. However most of ZnO based oxide semiconductors have very sensitive property to ambient environment. It is essential to prevent the penetration of moisture into ZnO based oxide thin film transistor (TFT). In the purpose of preventing moisture penetration and/or protecting damage from TFT processes, SiN_x or SiO_2 passivation layer is used frequently.

In this study, we investigated the interface reactions between amorphous HfInZnO (Hf:In:Zn= 10:35:55, 40nm thickness) oxide semiconductor active layer and the passivation layer of SiN_x or SiO₂ (20 nm thickness). TEM, XPS and SIMS were used to investigate the interface reactions such as atomic diffusion, reduction of HfInZnO, chemical state, microstructure.

According to experimental results, a SiO₂ phase and Indium metallic state were observed at the interface between SiN_x and HfInZnO active layer. On the other hand, there was not observed Indium metallic state at the interfaces between SiO₂ and HfInZnO layers. In the case of SiN_x passivation, it is considered that some Si took oxygen from Indium oxide in HfInZnO and oxidized to SiO₂. And some of Indium oxide reduced to metallic Indium at the interface. Indium diffusions from HfInZnO layers into passivation layers were observed at the both of SiN_x and SiO₂ samples. In the case of SiN_x passivation, it was a little bit higher diffusion than that of SiO₂ passivation. The low binding energy shift was observed at the Zn_{2p} XPS spectra at the both samples. However, there was no distinct difference at the Hf_{4d} spectra.

If there is metallic Indium between passivation and HfInZnO active layers, the metallic Indium may influence the conductance of active layer. The threshold voltage (V_{th}) shift of thin film transistor (TFT) could be affected by the change of conductance of active layer.

We observed that the V_{th} negative shift of the TFT used SiN_x passivation was higher than that of SiO₂ passivation. It may be due to the existence of metallic Indium at the interface.

In this report, it will be described the relationships between interface reactions and the property of HfInZnO oxide TFT in detail.

9:40am **TF+EM-WeM6 Capacitance-Voltage (C-V) and X-ray Photoelectron Spectroscopy (XPS) Study of the Effect of a La₂O₃ Layer in the TiN/HfO₂/SiO₂/p-Si Stack.** *E.J. Bersch, M. Di, University at Albany, S.A. Consiglio, R.D. Clark, G.J. Leusink, Tokyo Electron America Inc., A.C. Diebold, University at Albany*

There has been much attention paid recently to the lowering of the threshold voltage (V_t) that is accomplished by including an additional ultrathin (~5-10 Å) oxide layer in the high-k/metal gate metal oxide semiconductor field effect transistor (MOSFET) gate stack. We have investigated the TiN/HfO₂/La₂O₃/SiO₂/p-Si stack, where the La₂O₃ layer is the so-called V_t-shift layer. For several variations of this stack, where both the thickness and the position of the La₂O₃ layer were systematically varied, we measured two quantities directly related to the V_t, the flatband voltage (V_{fb}) and the Si band bending. The V_{fb} was measured using capacitance-voltage (C-V) measurements on stacks with 500 Å TiN layers, and the Si band bending was measured on sister wafers with 30 Å TiN layers. For a set of samples where the thickness of the La₂O₃ between the HfO₂ and SiO₂ layers was varied, we observed that the V_{fb} and Si band bending both become more negative as the thickness of the La₂O₃ was increased. For a set of samples where position of the La₂O₃ within the HfO₂ layer was varied, we observed that the V_{fb} and Si band bending became less negative as the amount of HfO₂ between the La₂O₃ and the SiO₂ was increased. These observations support the proposition that there is a dipole at the La₂O₃/SiO₂ interface which affects the Si band bending, as has been reported in the literature.^{1,2} We have also observed that there is a difference in the V_{fb} and Si band bending in TiN/HfO₂/La₂O₃/SiO₂/p-Si stacks with thermally grown and chemically grown SiO₂ layers. Results of this study as well as one where the thickness of thermally grown SiO₂ layers was varied will be presented, and its implications on the theory of the interface dipole will be discussed.

1. K. Kita, et al., *Appl. Phys. Lett.*, 94, 132902 (2009).

2. P.D. Kirsch, et al., *Appl. Phys. Lett.*, 92, 092901 (2008).

10:40am **TF+EM-WeM9 Modification of Defect-State Concentrations with Vacuum Ultraviolet and Ultraviolet Irradiation of Hafnium-Oxide Dielectric Layers.** *H. Ren, University of Wisconsin-Madison, S.-L. Cheng, Y. Nishi, Stanford University, J.L. Shohet, University of Wisconsin-Madison*

The effects of 7.2 eV vacuum ultraviolet (VUV) and 4.9 eV ultraviolet (UV) irradiation on a 20 nm HfO₂ layer atomic layer deposited (ALD) on (100) Si substrate are explored with electron-spin resonance (ESR). Silicon dangling-bond defect concentrations (*Pb* centers) and positively charged oxygen vacancies (*E'* centers) were measured with *g*-factor fitting. The concentrations of the defect states are presented. VUV irradiation increases the level of *Pb0* and *Pb1* states, while UV decreases the level of *Pb0* and *Pb1* states, but increases the level of *E'* states significantly. [i] [#_edn1] In addition, rapid thermal annealing (RTA) mitigates the effects of both VUV and UV irradiation. Surface-potential measurements with a Kelvin probe show that electron photoemission process dominate VUV irradiation. On the other hand, electrons are transferred from *E'* states to the silicon substrate during UV irradiation. At the same time, electrons are photo-injected into the dielectric layer from the substrate. Furthermore, VUV

spectroscopy measurements show that the Fermi level for *E'* defect states is around 4.7 eV, which is within the bandgap of the dielectric layer. Also, previous work [ii] [#_edn2] shows that the *E'* states, as oxygen-interstitial defects (OID), are located within the HfO₂ layer. We conclude that VUV irradiation modifies the concentrations of the silicon dangling-bond defect states and UV irradiation can be a potential source for positively charge oxygen vacancies during the processing.

Work Supported by the Semiconductor Research Corporation under contract 2008-KJ-1781

[i] [#_ednref] H. Ren, S.L. Cheng, Y. Nishi and J.L. Shohet, *Applied Physics Letters* (to be published)

[ii] [#_ednref][ii] J.L. Lauer, J.L. Shohet and Y.Nishi, *Applied Physics Letters* 94, 162907 (2009)

11:00am **TF+EM-WeM10 Plasma Enhanced Atomic Layer Deposition of Ruthenium Ultra-Thin Films for Advanced Metallization.** *J. Swerts, S. Armini, L. Carbonell, D.A. Annelies, F.A. Alexis, S. Mertens, T. Witters, M. Schaeckers, Z. Tökei, G. Beyer, IMEC, Belgium, V. Gravey, A. Cockburn, K. Shah, J. Aubuchon, Applied Materials Inc., S. Van Elshocht, IMEC, Belgium*

Electrochemical deposition of Cu for interconnect metallization traditionally uses Physical Vapor Deposition (PVD) of a Cu seed layer on top of a PVD Ta/TaN barrier to conduct the current. However, the limitations of PVD in respect of step coverage compromise its use in future technology nodes. Atomic Layer Deposition (ALD) for barrier deposition combined with seedless Cu electroplating is one of the metallization routes explored for sub-25 nm line widths. However, compatibility with seedless electroplating seriously limits the choice of materials. Among the different candidates, Ru-based layers have been identified as very promising.

We report the growth and scalability of Ru films by plasma-enhanced ALD (PE-ALD) from MethylCyclopentadienylPyrrolylRuthenium (MeCpPyRu) and N₂/NH₃ plasma. The layers were deposited using a 300 mm showerhead type reactor (AMAT) with direct plasma capability. The substrate temperature during deposition was 330C. The Ru growth per cycle was 0.04 nm. As substrates we used Si wafers with 100-300 nm SiO₂ on which a thin TaN or TiN layer was deposited by ALD or PVD.

The metal nitride is needed as a growth enabler since Rutherford backscattering spectrometry (RBS) showed that only 1E14 Ru atoms/cm², i.e. less than a monolayer, were deposited on SiO₂ after 120 PE-ALD cycles. The minimal thickness of the metal nitride to enable Ru growth has been determined to be as low as 0.7-0.8 nm which is promising for scaling. Growth studies on scaled and thick ALD TiN or TaN still showed a limited growth inhibition during the first 40 cycles followed by a linear growth behavior. Static time-of-flight secondary ion mass spectroscopy (TOFSIMS) suggests Ru layer closure for a film thickness around 2 nm.

Atomic force microscopy revealed that the root mean square roughness values were below 0.4 nm for film thicknesses up to 20 nm. X-ray diffraction showed that the Ru layers have a hexagonal structure. The density of the Ru layer was 11.75 g/cm³ as derived from X-ray reflectivity and RBS. Elastic recoil detection analysis and TOFSIMS indicate that the N, O, C-levels in the bulk Ru layers were << 1%. Surface analysis by static TOFSIMS showed the presence of organic contamination identified as MeCp ligands from the Ru precursor. In contrast, the Pyrrolyl ligand was not observed. A post deposition thermal treatment of the Ru film removes the ligand organic contamination. The impact of this surface contamination on the seedless Cu electroplating efficiency will be discussed. Finally, the step coverage of TiN/Ru and TaN/Ru stacks in narrow lines (65-15 nm width) was evaluated by transmission electron microscopy.

11:20am **TF+EM-WeM11 Effects of Hydrogen Plasma Pretreatment on Superconformal Gap-Filling of Cu-Al Alloy.** *H.K. Moon, N.-E. Lee, Sungkyunkwan University, Republic of Korea*

As the feature of microelectronic interconnects has continued to shrink, Cu resistivity is expected to increase at the nanoscale due to increased surface and grain boundary scattering of electrons. To prevent increase of the resistivity in nanoscale interconnects, alloying Cu with other metal elements such as Al, Mn, and Ag is being considered to increase the mean free path of the drifting electrons. The formation of Al alloy with a slight amount of Cu broadly studied in the past. The investigation of Cu alloy with a very small Al fraction, by contrast, recently started. The formation of Cu-Al alloy is limited in wet chemical bath and was mainly conducted for fundamental studies by sputtering or evaporation system. However, these deposition methods have a limitation in production environment due to poor step coverage in nanoscale Cu metallization. In this work, gap-filling of Cu-Al alloy was conducted by cyclic MOCVD (metal organic chemical vapor deposition), followed by thermal annealing for alloying, which prevented an

unwanted chemical reaction between Cu and Al precursors and hydrogen in the gas phase. To fill the Cu-Al alloy into sub-100nm trench without overhang and void formation, furthermore, hydrogen plasma pretreatment of the trench pattern with Ru barrier layer was introduced in order to suppress of Cu nucleation and growth near the entrance area of the nanoscale trench by minimizing adsorption of metal precursors. As a result, superconformal gap-fill of Cu-Al alloy could be achieved successfully in the 40-nm trench with an aspect ratio of 4. Examined morphology, microstructure, chemical composition, and electrical properties of superfilled Cu-Al alloy will be discussed in detail.

11:40am **TF+EM-WeM12 Depth Resolved Cathodoluminescence Spectroscopy of Amorphous High- k Dielectric LaLuO₃**, *S. Shen*, Ohio State University, *Y. Liu, R.G. Gordon*, Harvard University, *L.J. Brillson*, Ohio State University

We have used depth-resolved cathodoluminescence spectroscopy (DRCLS) to measure the native point defects and reaction-induced defects within ultrathin LaLuO₃ dielectric films. The rare earth oxide LaLuO₃ is gaining much attention because of its high dielectric constant (28 ~ 32) and its potential application to replace SiO₂ as a gate dielectric for Si microelectronics, requiring both sub-nanometer thick gate oxide layers and low leakage currents. LaLuO₃ deposited by atomic layer deposition (ALD) provides films with high crystallization temperature and relatively high conduction band offset, but they have non-negligible leakage currents that are attributed to electronic trap states in the band gap. Annealing can partially reduce these traps but can also induce diffusion/reaction at the LaLuO₃ interfaces. We used DRCLS to determine the changes in defect levels of WN/20 nm LaLuO₃/Si gate structures as a function of annealing and the introduction of an Al₂O₃ diffusion barrier at the Si interface. A 10 nm WN/20nm LaLuO₃/Si structure as-grown exhibits defect emissions at 2.4, 3.2, 3.8, 4.2 and 4.7 eV as well as a 5.48 eV band gap. With 300°C cyclic annealing, 10 nm WN/20nm LaLuO₃/Si, the band gap emission is absent and high energy emissions at 4.2 and 4.7 eV shift to 3.8 eV. A 10 nm WN/20nm LaLuO₃/0.4 nm Al₂O₃/Si interlayer structure exhibits negligible difference from the interlayer-free stack without anneal. However, with annealing, the WN/20nm LaLuO₃/0.4 nm Al₂O₃/Si defects at high energy and the band gap remain unchanged while the lower energy defects are suppressed. The 5.48 eV band gap emission agrees with an internal photoemission gap of 5.3 eV measured previously. The 4.2 and 4.7 eV emissions are consistent with weighted density function approximation calculations showing two oxygen-vacancy-related states at similar energies near the LaLuO₃ conduction band edge. The DRCLS-measured degradation of optical features with annealing of the interlayer-free structure is attributed to Si diffusion and reaction with LaLuO₃ as observed by cross sectional TEM. This degradation is suppressed with the Al₂O₃ barrier layer. Furthermore, the annealing of the interlayer structure reduces all the low energy defect emissions. Finally, the highest lying state at 4.7 eV above the valence band (0.78 eV below the conduction band) agrees reasonably well with the 0.6-0.7 eV electrical measurements of leakage current. These results highlight the importance of annealing with a diffusion barrier at the Si interface to suppress defects within LaLuO₃ without Si reaction at the LaLuO₃ interface.

Thin Film

Room: San Miguel - Session TF+SE-WeM

Glancing Angle Deposition (GLAD) I

Moderator: T. Karabacak, University of Arkansas at Little Rock

8:00am **TF+SE-WeM1 Soft Nanostructured Films for Biomedical Applications**, *M.C. Demirel*, Pennsylvania State University **INVITED**

Anisotropic textured surfaces represent key structural components utilized by various animals and plants to gain a competitive advantage for survival. For example, a closer look at complex structures in insect wings and lizard toes reveal organized structured features at the microscopic scale. These structures are composed of millions of aligned columns per square millimeter, which create novel anisotropic properties. We have demonstrated that these structures can be fabricated synthetically by an oblique angle polymerization (OAP) method. OAP allows us to tune the chemical properties of nanostructured surfaces and film morphology to control the physicochemical properties of the resulting films, such as hydrophobicity, porosity, electrochemistry, chemical reactivity, surface energy and crystallinity. In this talk, we will describe unique anisotropic physicochemical properties (i.e. morphing/folding, wetting, and friction) of well-ordered arrays of nano-rods/tubes, which mimic biological structures

at the microscopic scale. We will also present results concerning the use of these films for biomedical and biosensors applications.

8:40am **TF+SE-WeM3 Growth Temperature Controlled Morphology of Ge Nanocolumns**, *C. Khare, J. Bauer, J.W. Gerlach*, Leibniz Institute of Surface Modification (IOM), Germany, *B. Fuhrmann, Martin-Luther-University Halle, Germany, T. Höche, B. Rauschenbach*, Leibniz Institute of Surface Modification (IOM), Germany

Germanium films with manifold nanostructures are grown by ion beam sputter glancing angle deposition (GLAD). Morphological shape variations were introduced through variation of the substrate temperature (T_S) and differently patterned silicon substrates. Pre-patterned substrates served as seeds for growing structures assisting the formation of a periodic nanostructure array. Nanocolumns grown on a bare Si(100) substrate demonstrated an altered morphology that can be controlled by the substrate temperature. At elevated substrate temperature ($T_S / T_M > 0.3$), surface diffusion-driven mass transport as a result of increased adatom mobility augmented fibrous-columnar and intra-columnar growth. Further increment of the substrate temperature ($T_S / T_M > 0.45$) exhibited column merging and column broadening. Additionally, significant changes in the overall film thickness representing changes in the film porosity were observed. Similar merging and broadening characteristics were also exhibited on SiO₂ nanosphere templated substrates. For the films deposited at elevated substrate temperatures, XRD measurements showed the growth of polycrystalline films. TEM analysis confirmed the growth of large crystallites at elevated substrate temperatures. Thus, growth of Ge nanostructures with tailored morphology can be grown by substrate pre-patterning and by utilizing substrate temperature induced effects.

9:00am **TF+SE-WeM4 Glancing Angle Deposited Platinum Nanorod Arrays with Enhanced Electrocatalytic Activity for Oxygen Reduction Reaction in PEM Fuel Cells**, *W.J. Khudhayer, A.U. Shaikh, T. Karabacak*, University of Arkansas at Little Rock

In this work, we have investigated the electrochemical properties of vertically aligned, single-layer, low loading, carbon-free and single crystal Pt nanorod arrays as a potential cathode material in polymer electrolyte (PEM) fuel cells. These nanorods of different lengths in the range of 20-600 nm were produced by glancing angle deposition (GLAD) technique with Pt loading values of 0.016-0.5 mg/cm². Electrodes of conventional carbon supported Pt nanoparticles (Pt/C) were also prepared for comparison with Pt nanorods for their electrochemical properties. Scanning electron microscopy (SEM) and X-ray diffraction (XRD) were utilized to study the morphology and crystallography of Pt nanorods. SEM and XRD results reveal that Pt nanorods are well-isolated, vertically aligned, and single-crystal with atomically sharp tips. The single-crystal property allows enhanced electrochemical activity and reduced surface oxidation, while the isolated nature of the rods in lateral directions can provide a channeled porosity for effective transportation of gases in a PEM fuel cell. The electrochemical activity of Pt nanorods as well as Pt/C was evaluated using cyclic voltammetry (CV). CV results show that Pt nanorod electrocatalysts reduce oxygen to water at a more positive potential than Pt/C, indicating that our catalyst has a lower oxygen overpotential due to the enhanced electrode porosity, single-crystal property, and the dominance of the preferred crystal orientation for oxygen reduction reaction (ORR). In addition, a series of CV scans show that our catalyst is more stable than Pt/C in the acidic environment. Finally, in order to get a fair comparison for high surface area catalysts, detailed thin-film rotating disk electrode measurements at room temperature were performed on 200 nm long Pt nanorods as well as Pt/C for comparison to calculate the most important kinetics parameters (Tafel slopes, exchange current density, Pt mass-specific activity and area-specific activity), which are the accepted measures of true catalysts activity towards ORR. These results reveal the enhanced mechanism and kinetics of ORR on Pt nanorods compared to Pt/C.

9:20am **TF+SE-WeM5 Hydrogen Storage Properties of Magnesium Nanotrees by Glancing Angle**, *M.F. Cansizoglu, T. Karabacak*, University of Arkansas at Little Rock

Among many solid state materials for hydrogen storage, magnesium hydride (MgH₂) combines a hydrogen capacity of 7.6 wt % with the benefit of the low cost of production and abundance. The main difficulties for implementing MgH₂ are slow absorption/desorption kinetics and high reactivity towards air and oxygen, which are also common issues in most lightweight metal hydrides. Previously, improvements in hydrogen storage and release properties have been reported by using nanostructured magnesium that can be obtained through various fabrication methods including ball-milling, mechanical alloying, and vapor transport. In this study, we investigate the hydrogen absorption and desorption properties of magnesium "nanotrees" fabricated by glancing angle deposition (GLAD) technique, and also conventional Mg thin films deposited at normal incidence. Mg nanotrees are about 15 μ m long, 10 μ m wide, and

incorporate “nanoleaves” of about 20 nm in thickness and 1,2 μm in lateral width. A quartz crystal microbalance (QCM) gas absorption/desorption measurement system has been used for our hydrogen storage studies. Nanostructured and thin film Mg have been deposited directly on the surface of the gold coated unpolished quartz crystal samples. QCM hydrogen storage experiments have been performed at temperatures ranging between 100-300oC, and at H₂ pressures of 10 and 30 bars. QCM measurements revealed that Mg nanotrees have better storage characteristics compared to Mg thin films. They can reach hydrogen storage values of about 4.80 wt% at 100oC, and up to about 6.71 wt% (which is close to the theoretical maximum storage value of Mg) at temperatures lower than 150oC. The significant enhancement in hydrogen absorption properties of Mg nanotrees is believed to originate from novel physical properties of their nanoleaves. These structures are very thin (~20 nm) and both surfaces are exposed to hydrogen enhancing the diffusion of hydrogen together with a decreased diffusion length. In addition, nanostructured Mg have been observed to be quite resistant to surface oxidation, which is believed to be due to the single crystal property of the Mg nanoleaves.

9:40am **TF+SE-WeM6 Fabricating Crystalline ZnO Nanorods by Glancing Angle Deposition, J.M. LaForge, M.T. Taschuk, M.J. Brett, University of Alberta, Canada**

Zinc oxide possesses a combination of properties, including semiconductor electronic behaviour, optical transparency, and piezoelectricity, that make it an interesting candidate for energy scavenging, photovoltaics, and chemical sensing applications (1, 2). Several unique nanostructures may be formed with ZnO, with a variety of growth methods that exploit the difference in surface energy between the low-index crystal faces of the wurtzite ZnO crystal leading to preferential growth along the c-axis.

Glancing angle deposition (GLAD) is assumed to operate effectively under conditions of limited surface diffusion so that growth occurs from geometric shadowing of an incoming particle flux. While amorphous GLAD films are typical, there are numerous crystalline films reported in the literature, including ZnO (3). This suggests that in certain material systems growth kinetics play a role in GLAD growth. However, the conditions under which GLAD produces crystalline films has not been thoroughly investigated or explained.

We have selected ZnO to investigate these issues for two reasons: first, the technological applications outlined above, and second, to explore the material growth properties which can produce crystalline structures. This makes it an ideal candidate for studying nanostructure morphology and crystal properties as a function of process parameters, including deposition rate, pitch and throw distance. Optimal growth conditions for zinc oxide nanorod films occurred for pitch values in the vicinity of 1 nm to 10 nm. Study of the post aspect ratio and areal post density suggests that typical GLAD growth occurs for deposition rates <0.005 nm sec⁻¹ and that growth kinetics begin to contribute significantly at deposition rates >0.01 nm sec⁻¹. Films deposited at pitch values between 0.001 nm to 6.5 μm are crystalline and textured, and greater texturing is achieved for conditions of decreased surface diffusion.

(1) Wang, Z. L. *Journal of Physics: Condensed Matter*. **2004**, *16*, R829-R858.

(2) Ye, C.; Fang, X.; Hao, Y.; Teng, X.; Zhang, L. *The Journal of Physical Chemistry. B*. **2005**, *109*, 19758-65.

(3) Teki, R.; Parker, T.; Li, H.; Koratkar, N.; Lu, T.-M.; Lee, S. *Thin Solid Films*. **2008**, *516*, 4993-4996.

10:40am **TF+SE-WeM9 Optical, Magnetic, Magneto-Optical and Electrochemical Properties of Sculptured Thin Films, E.B. Schubert, D. Schmidt, T. Hofmann, A.C. Kjerstad, E. Montgomery, S. Schöche, M. Schubert, University of Nebraska - Lincoln**

Bottom-up and self-organized three-dimensional (3D) structure design on the nanoscale opens a new field in nanostructure based thin film engineering with a broad range of practical applications for sensors, optical coatings, photovoltaic devices or biomaterials, for example. Sculptured thin films (STF's) belong to this group of thin films and current research creates exciting new knowledge about the unique material properties that are related to shape, dimension, and distribution of the nanostructures within the thin film ensemble. The following paper presents new sculptured thin film properties obtained from material analysis using optical, magnetic, magneto-optical and electrochemical characterization techniques. [1-5] Material properties have been quantified from model analysis and results from our investigations lead to original device designs for applications such as highly-sensitive mass balances, subwavelength antireflection coatings, magneto-optical memory and chemical sensors.

[1] E. Schubert, *Contributions to Plasma Physics* **47**, 545 (2007).

[2] D. Schmidt, B. Booso, T. Hofmann, E. Schubert, A. Sarangen, and M. Schubert, *Appl. Phys. Lett.* **94**, 011914 (2009).

[3] D. Schmidt, B. Booso, T. Hofmann, E. Schubert, A. Sarangan, and M. Schubert, *Opt. Lett.* **34**, 992 (2009).

[4] D. Schmidt, A. C. Kjerstad, T. Hofmann, R. Skomski, E. Schubert, and M. Schubert, *J. Appl. Phys.* **105**, 113508 (2009).

[5] D. Schmidt, T. Hofmann, E. Schubert, and M. Schubert, *Appl. Phys. Lett.* **96**, 091906 (2010).

11:00am **TF+SE-WeM10 Stress Behavior of Obliquely Sputtered Ta Films on Glass Substrates, S.U. Jen, P.H. Chiang, Academia Sinica, Taiwan, Republic of China**

Ta films were obliquely deposited on glass substrates by magnetron sputtering method using the parameters: deposition angle $\alpha = 60^\circ$; deposition temperature $T_s = 298, 373, 473, \text{ and } 573 \text{ K}$; Ar working gas pressure $P_{AR} = 2, 7.5, \text{ and } 15 \text{ mTorr}$; film thickness $t_f = 100 \text{ nm}$. From X-ray diffraction, atomic force microscopy, cross-section transmission electron microscopy, and Auger depth profile analysis, we conclude that: [1] the axis of each columnar grain is inclined at an angle $\beta \approx 35^\circ$ with respect to the film normal; [2] in-plane grain aggregates show some vestiges of the chain-like structure, whose long axis is perpendicular to the plane of incidence (i.e. the transverse or width direction of the sample); [3] oxygen atoms are found inside the film; especially located in the columnar gaps (or microvoids) between neighboring grains. The stress of each film was measured via Stoney equation. The main results in regard to the stress behavior of this series of Ta films are summarized below: [a] the intrinsic stress S_i is always tensile and dominant over the thermal stress S_T ; [b] the total stress is anisotropic with the longitudinal stress being larger than the transverse stress; [c] as T_s increases, S_i becomes less tensile. Result [a] is reasonable because Ta is a high melting point material.¹ Especially, in the oblique-deposition case, the formation of gaps becomes more obvious. Hence, much larger tensile stress (than in the normal-deposition case) arises from the attractive interaction of oxygen atoms across the gaps. Result [b] is a consequence of the self shadowing effect, which is already manifested in the conclusion [2] above. Result [c] is due to the fact that as T_s is higher, there is a structure transition from zone 1 to zone T, and oxygen atoms are less likely to be incorporated into the film.

¹. G. Guisbiers, O. Van Overschelde, M. Wautelet, *Acta Materialia* **55**, 3541(2007).

11:20am **TF+SE-WeM11 Role of Columnar Nanostructures on Static and Dynamic Wetting Properties of Silver Film, D. Singh, J. Singh, IIT Delhi, India**

The study of wetting has always been a very active field of research. In recent years, the interest in this field is stimulated by nanoengineering the surface to meet the requirements of various biological, chemical and industrial applications by modifying their wetting properties. In the present study, we have investigated the effect of silver nanocolumns on the static as well as dynamic wettability of surface. The nanocolumns of about 400 nm length and 150 nm diameter ($\alpha = 85^\circ$) were grown by oblique angle deposition method over the Si(100) substrate. The effect of these nanocolumns on static wetting behavior was studied by performing sessile drop contact angle measurements using de-ionized water. A significant enhancement in the hydrophobicity of silver surface with contact angle value of 108° was observed (see supplement file, Fig. 1). To ensure that the observed changes in wetting behavior are due to the influence of nanocolumns, the measurements were carried out for different surface features ranging from plane to nanocolumnar film (grown for $\alpha = 0^\circ, 65^\circ, 75^\circ$ and 85° , see SEM images in supplement file, Fig.2). Contact angle was observed to increase gradually from 94° to 96° with increase in oblique angle (α) from 0° to 75° . A drastic increase in contact angle was observed for nanocolumnar surface grown at $\alpha = 85^\circ$. For these silver samples the rms (root mean square) surface roughness was found to follow almost the same pattern as that of contact angle with α , suggesting the dependence of wettability on surface roughness. The observed results were explained following the Cassie-Baxter model considering the silver nanocolumns to form a silver-air composite surface. To investigate the effect of nanocolumns on dynamic wetting property, the contact angle measurements for higher sample surface temperature ($T_s = 80^\circ\text{C}$) were performed and the rate of change of contact angle of water drop for an interval of 10 sec was measured. This transition rate of contact angle values was found to increase drastically for the nanocolumnar surface (see the supplement file, Fig.3). It shows that the nanocolumnar growth affects not only the static contact angle by making the surface hydrophobic but also greatly influences the surface temperature dependent dynamic wetting behavior of water drop. This study provides a basic understanding of the wetting behavior of nanocolumnar surface as well as shows the possibility to tune the surface wettability for meeting the requirements of various industrial applications.

Thin Film

Room: Ruidoso - Session TF-WeM

ALD: Nanostructure, Magnetics and Biological Applications

Moderator: E.W.M.M. Kessels, Eindhoven University of Technology, the Netherlands

8:00am **TF-WeM1 Magnetic Nano-Objects Based on Atomic Layer Deposition: Switching Modes in Nanotubes and Core-Shell Nanowires.** *J. Bachmann, K. Nielsch*, University of Hamburg, Germany **INVITED**

Atomic layer deposition (ALD) is uniquely suited to the conformal deposition of magnetic thin films in pore structures of high aspect ratio, while offering precise tuning of the layer thickness and high uniformity. Combining one or several layers of ALD with self-ordered porous anodic alumina membranes used as templates yields arrays of magnetic nanotubes with diameters tunable between 20 and 200 nm, wall thicknesses from 2 to 40 nm, and lengths set anywhere between 0.1 and 100 microns. The magnetic properties of such nanotubes strongly depend on their geometry, as evidenced on the ensemble and single-object levels by SQUID and MOKE magnetometries, respectively. The structural parameters can be chosen so as to favor a certain mechanism of magnetization reversal or another.

Further structural complexity can be created by introducing additional preparative steps. Interference lithography can be exploited for sculpting tubes with controlled modulations in diameter. Electrodeposition enables us to synthesize wires in which a core and a shell of two distinct magnetic materials are separated by a non-magnetic spacer layer. In those cases, the geometric parameters are still accurately controlled and tunable. The particular geometric characteristics of the system directly transpire into their magnetic properties: diameter modulations may hinder the propagation of magnetic domain boundaries, whereas core-shell structures may give rise to two distinct magnetic reversal events.

8:40am **TF-WeM3 Structural and Magnetic Properties of Anatase Mn-doped TiO₂ Film Synthesized by Atomic Layer Deposition.** *M.C.K. Sellers, E.G. Seebauer*, University of Illinois at Urbana-Champaign

Transition metal doped semiconductors exhibiting room temperature ferromagnetism are intensely investigated for spintronics applications. Devices leveraging the spin-dependent effects of these materials would allow for increased data processing speeds, decreased power consumption, and improved integration densities in comparison to standard charge-based electronics. In the past ten years, experimental and computational studies have demonstrated room temperature ferromagnetism (RTFM) for several TiO₂-based dilute magnetic semiconductors (DMSs) namely TiO₂ doped with Mn, Cr, Fe, and Co. Most DMS TiO₂ films are synthesized via sol-gel, pulsed laser deposition (PLD), and plasma-assisted molecular beam epitaxy (PAMBE). Atomic layer deposition (ALD) of DMS TiO₂ has never been demonstrated, although this method has been used to deposit Mn-doped ZnO with DMS properties. ALD circumvents complications with solvent and byproduct removal and with calcination-induced shrinkage that arise during sol-gel synthesis. PLD and PAMBE are ill-suited to the high throughput requirements of commercial manufacturing. In addition, PLD can result in high particulate composition and uneven coverage, while PAMBE films suffer from thickness-dependent morphologies. ALD avoids such problems. The present work involves the synthesis of Mn-doped anatase TiO₂ (0 to 5 at% Mn) thin films on Si(100) via ALD at 200°C and 400°C. Ti(OCH(CH₃)₂)₄ and H₂O are utilized as ALD precursors and Mn(DPM)₃ as a dopant source. The effect of substrate temperature, number of cycles, precursor and oxidant injection times, purge time, and distance between sample and delivery tube on film thickness and uniformity have been investigated. X-ray photoelectron spectroscopy measurements indicate that Mn is successfully doped in the TiO₂ matrix and reveal information about film composition and elemental chemical states. Microstructure, crystallinity, bulk density, and roughness were investigated with scanning electron microscopy, x-ray diffraction, and x-ray reflectivity. SQUID magnetometry was used as a probe of RTFM; the bulk density, microstructure, and magnetic moment of the TiO₂ vary with the concentration of Mn. The results provide insight into the properties of DMS TiO₂ synthesized via ALD and underscore the advantages of the technique - precise thickness, compositional control, and higher process throughput - in comparison to alternative techniques of DMS growth.

9:00am **TF-WeM4 Fabrication of Refractory Nanoporous Structures by ALD of Tungsten on High Surface Area Silica Aerogels.** *A.U. Mane, Argonne National Laboratory, U. Sampathkumaran, T. Owen, R. Winter, Innosense LLC, J. Nolen, J. Greene, J.W. Elam*, Argonne National Laboratory

Refractory nanoporous materials with high porosity could serve as efficient catchers for the fast release of unstable nuclei in rare isotope accelerators. The unique, self-limiting capability of atomic layer deposition (ALD) offers an attractive synthetic route for fabricating refractory nanoporous materials. Here we demonstrated a method using high surface area silica aerogel monoliths as templates for the growth of conformal thin films by ALD. Static mode ALD of W using Si₂H₆ and WF₆ at 200°C was employed to coat the inner surfaces of the low density, nanoporous silica aerogel monoliths. To facilitate nucleation and improve adhesion of the ALD W, the aerogels were coated with 2 Å Al₂O₃ using alternating exposures to Al(CH₃)₃ and H₂O prior to the W ALD. After coating, scanning electron microscopy revealed a porous microstructure in which the ALD W completely encapsulates the silica aerogel. The porosity of the aerogels was preserved during the first ~10 W ALD cycles allowing the density to be controlled by adjusting the number of W ALD cycles and values as high as 5 g/cc were obtained. BET surface area measurements revealed a gradual decrease in the surface area of the silica aerogel with increasing numbers of W ALD cycles consistent with a gradual filling of the aerogel voids. Next, we heated the W-coated aerogels to 1500°C in an inert atmosphere and observed that they maintained their integrity and porosity with almost no loss in density. These results are very encouraging for the deployment of these materials as isotope catchers.

9:20am **TF-WeM5 Nucleation and Ultra-Thin Film Formation during ALD on Multiwall Carbon Nanotubes.** *C. Devine, J.S. Jur, C. Oldham, J. Bonner, G.N. Parsons*, North Carolina State University

Atomic layer deposition is widely studied as a means to coat and encapsulate polymers to impede diffusion of water, oxygen or other species. ALD is also a viable means to coat and surface functionalize carbon nanotubes and other nanostructured materials. Previous work suggests that ALD nucleation proceeds differently on single and multiwalled carbon nanotubes, where the more defective nature of multiwalled tubes allows more rapid nucleation and film growth. In this work, we are interested in using ALD to encapsulate multiwall carbon nanotubes with as thin a layer as possible, to modify the chemical signature of the nanotubes while maintaining their advantageous mechanical and physical properties. Our motivation for this work is to explore means to alter potential toxic inhalation effects that carbon nanotubes may present, for example, in manufacturing facilities producing nanotube-based products. We have worked with multiwall nanotubes from Helix Materials Solutions as well as from Mitsui. The Mitsui tubes are 30-50 nm in diameter and contain many concentric nanotubes. TEM analysis shows that ALD using TMA/water at 90 °C proceeds slowly at first, producing isolated nuclei for the first 15 cycles. Films are smoother after 25 cycles, and continuous film coatings are observed after 80 cycles, corresponding to film thickness of 3.8 nm. After complete film coverage, the film growth rate increases to values close to that expected for TMA/water at this process temperature. We will present results regarding how these coatings affect physical properties of the nanotubes, including surface wetting, as well as possible new means to coat large numbers of nanotubes in a conventional viscous flow reactor system.

9:40am **TF-WeM6 Chemical Vapor Deposition of Sandwiched Antibacterial Layers.** *F. Schamberger, T.H. Huber, G. Franz*, Hochschule Muenchen, Germany

To deposit organic polymers on three-dimensional, even rugged surfaces, (pe)cvd is the method of choice. Thickness and film quality are mainly controlled by the number density of the precursors and their mixing ratio which determine the equilibrium of polymerization between reactions in the gas phase at high densities or at the surface for low densities. In most cases, MFCs can be used. Since MFCs can be heated only up to about 80 °C, precursors with low vapor pressure cannot be discharged into the reactor by this method, and the flow is mainly controlled by vapor pressure which limits the controlled deposition of thin layers.

We have recorded the vapor pressure curves for diparylene N and diparylene C applying a dynamic and a static method, resp. [1], and correlated flow and deposition rate with vapor pressure. To meet the demands for exact layer thickness even for values below 1 µm, an almost digital grow method is required. We introduce such a simple, low-cost method for the coating of antibacterial layers which have been deposited by subsequent wet chemical methods and galvanic plating. For very thin layers, the increase in pinhole density with shrinking film thickness has been investigated as functions of total pressure and process time by qualitative visual inspection (sem) and quantitative measurements by comparing the permeability of thin films against water vapor and oxygen. For swiss cheese layers, the antibacterial film below is but partly protected,

however, the antibacterial action can be prolonged over years. Eventually, the change in mechanism from polymerization at the surface to volume polymerization has been investigated by varying the doping levels of the ambient gas (argon or oxygen), and has been correlated in-situ by mass spectrometry and ex-post to some film properties; among them are surface roughness and surface energy and the refraction index as well as the IR spectrum which has been modeled for the dimeric and the polymeric species applying a Gaussian method.

[1] Council Regulation (EC) No 440/2008 of 30 May 2008 laying down test methods pursuant to Regulation (EC) No 1907/2006 of the European Parliament and of the Council on the Registration, Evaluation, Authorisation and Restriction of Chemicals (REACH) (Text with EEA relevance), Official Journal L 142 , 31/05/2008 P. 0001 - 0739

10:40am **TF-WeM9 ALD for Nano and Micro Electro-Mechanical Systems, V.M. Bright**, University of Colorado at Boulder **INVITED**

Atomic Layer Deposition (ALD) can be effectively used to deposit custom-designed, multi-material layers with atomic resolution on any micro- or nano-scale device surfaces. The nano-scale ALD coating can protect the devices from electrical short, charge accumulation, moisture-induced adhesion, wear, corrosion, creep, fatigue or anodic oxidation during prototyping or long-term product life. ALD films for N/MEMS achieve these goals similar to what CVD Si_3N_4 has been for CMOS. As MEMS scales further shrink toward nano-electro-mechanical systems (NEMS), ALD processes offer a new strategy for depositing conformal and precise films that may have important applications as a novel dielectric, a sacrificial layer for gap control in nanofabrication, or as a structural layer for NEMS realization.

ALD relies on sequential, self-limiting surface reactions to deposit ultra thin, conformal films. The following characteristics of ALD films and processes make them flexible and multifunctional, and represent their appeal for N/MEMS: ALD film thicknesses can be precisely deposited from a few Å to hundreds of nm; ALD films can be deposited at temperatures ranging from 33°C to over 200°C; ALD films are pinhole-free, dense, smooth and highly conformal; ALD films can be deposited on silicon, polysilicon, silicon nitride, metals, polymers, and ceramics; ALD films can be conformally deposited on any size or shape device or any substrate; ALD can coat high surface area to volume ratio structures with complex geometries; ALD can deposit dielectric or conductive layers; ALD can deposit hydrophobic or hydrophilic layers covalently bonded to the surface; ALD can deposit on lithographically defined selective areas; ALD films can be micromachined to create nano-scale gaps and free standing structures; ALD coating process' deposition rate can be high, e.g. 0.5 nm/min at 177°C for Al_2O_3 .

These ALD techniques for N/MEMS, pioneered at the University of Colorado – Boulder, represent breakthrough in nano-scale processes that can be used to fabricate custom-designed, multi-material layers with atomic resolution. The ALD processes developed are proven, mature, and are available to serve the N/MEMS community.

References

- S. George, et al, *J. Physical Chem.*, **100**, 13121 (1996).
- N. Hoivik, et al, *Sensors and Actuators A*, **103**, 100 (2003).
- C. Herrmann, et al, *J. Micromech. Microeng.*, **15**, 984 (2005).
- C. Stampfer, et al, *Nano Letters*, **6** (2), 233, (2006).
- T. Helbling, et al, *Nanotech.*, **20**, 434010 (10pp), (2009).
- D. Seghete, et al, *Sensors and Actuators A*, **155**, 8, (2009).
- B.D. Davidson, et al, *Sensors and Actuators A*, on line.

11:20am **TF-WeM11 Understanding Plasma Enhanced Chemical Vapor Deposition for the Production of Composite Nanomaterials with Biomedical Applications, J.C. Shearer, E.R. Fisher**, Colorado State University

Fe_2O_3 and other magnetic nanoparticles are becoming key components of both chemical and biological applications, including drug delivery schemes and magnetic resonance imaging contrast agents. Nanoparticles coated with organic and inorganic films have distinct properties and enhanced functionalities over those of uncoated nanoparticles. Plasma-enhanced chemical vapor deposition (PECVD) was employed to conformally coat Fe_2O_3 with SiO_2 or polyallyl alcohol films, thereby creating composite nanomaterials. Comparisons will be made between composite nanoparticles created with an in-house atmospheric pressure plasma system and similar composite materials created in a traditional low-pressure PECVD system. In other studies, surface sites were activated with O_2 and Ar plasmas to plasma graft SiO_2 and polyallyl alcohol monolayer films onto the nanoparticles. Compositional and morphological data demonstrate that conformal SiO_2 and polyallyl alcohol coatings were achieved and that the use of PECVD methods allowed specific tailoring of the film structure, composition, and

growth characteristics. The performance of the composite materials was explored through dispersion, UV-vis spectroscopy, and chemical functionalization studies. Further insight into the deposition process is provided by actinometric optical emission spectroscopy (AOES) and laser induced fluorescence spectroscopy (LIF), which allow characterization of the gas-phase species and their energetics (i.e. internal and kinetic energies) for each system. Preliminary data from our Imaging of Radicals Interacting with Surfaces (IRIS) technique provides additional information on the molecular-level chemistry that occurs at the interface between gaseous plasma species and nanoparticle substrates.

Tribology Focus Topic

Room: Tesuque - Session TR+MN+NS+SS-WeM

Influence of Atmosphere, Temperature, and Materials on Friction

Moderator: J.D. Schall, Oakland University

8:00am **TR+MN+NS+SS-WeM1 'Demystifying' Gas Phase Lubrication: Tribochemistry, Third Bodies and Competition, I.L. Singer**, Naval Research Laboratory **INVITED**

Gas phase lubrication, also called vapor phase lubrication, refers to processes in which the gas surrounding a sliding (or rolling) contact contributes to lubrication [1]. It has wide ranging applications from internal combustion engines to MEMS. Some gases simply condense on surfaces, others decompose and deposit lubricating films on the surface, e.g. hydrocarbon films decompose and deposit graphite. Some can be made to react on the surface, as do various monomers that tribochemically form and form lubricious third bodies at the contact. Alternatively, gases can react with the surface to form films; the most ubiquitous example is the oxide film formed on metals, which prevents (on earth, but not in outer space) surfaces from weld upon contact. Reaction films have been studied extensively by surface scientists; less well understood are tribofilms, films formed by rubbing action. Another important component to the lubrication process is film removal, which can occur during sliding or rolling; the competition between film formation and film removal always needs to be considered. In some cases, gas lubrication provides low friction and low wear; in other cases, it can increase friction and wear. In this talk, I will review gas phase lubrication processes and present several gas phase lubrication studies that still mystify me.

[1] For overview, see http://nsf.fresh.org/wiki/index.php?title=Gas_Phase_Lubrication

8:40am **TR+MN+NS+SS-WeM3 Understanding Vapor Phase Lubrication Mechanism of Alcohol for MEMS and Other Materials, S.H. Kim**, Pennsylvania State University

Microelectromechanical systems (MEMS) are usually fabricated from silicon-based materials which have poor tribological properties such as high friction, high adhesion, and low wear-resistance. We have recently demonstrated unprecedented success of MEML lubrication using alcohol vapor. The main difference of alcohol vapor phase lubrication (VPL) from other coating-based approaches is that it allows continuous replenishment of lubricant molecules from the vapor phase, rather than relying on one-time loaded coating layers. In our precious studies, we have observed tribochemically-formed polymeric species. Then, an interesting question is if the polymeric species is responsible for effective lubrication or not. This talk addresses the origin of tribochemical reaction products and the lubrication mechanism for alcohol VPL for silicon oxide surfaces. In summary, the tribochemical polymerization appears to be associated with the substrate wear process occurring due to insufficient adsorbate supply or high mechanical load. The tribochemical reactions do not seem to be the primary lubrication mechanism for vapor phase lubrication of SiO_2 surfaces with alcohol, although they may lubricate the substrate momentarily upon failure of the alcohol vapor delivery to the sliding contact.

9:00am **TR+MN+NS+SS-WeM4 Mechanistic Aspects of Vapor Phase Lubrication of Silicon, M.T. Dugger, J.A. Ohlhausen, S.M. Dirk**, Sandia National Laboratories

The lubrication of silicon surfaces with alcohol vapors has recently been demonstrated [D.B. Asay, et. al, *Langmuir* 24 (2007) p.155]. With a sufficient concentration of pentanol vapor present, sliding of a silica ball on an oxidized silicon wafer can proceed with no measurable wear. The initial results of time-of-flight secondary ion mass spectrometry (ToF-SIMS) analysis of wear surfaces revealed a reaction product having thickness on the order of a monolayer, and with an ion spectrum that included fragments having molecular weights of 200 or more that occurred only inside the wear

tracks. The parent alcohol molecule (pentanol) has molecular weight of 88 amu, suggesting that reactions of adsorbed alcohols on the wearing surfaces allowed polymerization of the alcohols to form higher molecular weight species. In addition to pin-on-disk studies, lubrication of silicon surfaces with pentanol vapors has also been demonstrated using MicroElectroMechanical Systems (MEMS) devices. Extraordinary increases in the operating life of MEMS devices have been observed with vapor phase lubrication. Devices with thermal actuators as well as electrostatic actuators have been successfully operated, demonstrating that the heated surfaces of the thermal actuators do not form prohibitively large amounts of reaction product from the alcohol vapor. The same reaction product between pentanol and the silicon surface observed in pin-on-disk tests has also been found on MEMS contacting surfaces using ToF-SIMS analysis.

Recent investigations of the reaction mechanisms of the alcohol molecules with the oxidized silicon surfaces have shown that wearless sliding requires a concentration of the alcohol vapor that is dependent upon the contact stress during sliding, with higher stress requiring a greater concentration of alcohol. Different vapor precursors including those with acid functionality, olefins, and methyl termination also produce polymeric reaction products, and can lubricate the silica surfaces. Doping the operating environment with oxygen was found to quench the formation of the polymeric reaction product, and demonstrates that polymer formation is not necessary for wearless sliding.

9:20am **TR+MN+NS+SS-WeM5 Tribological Study of Octadecylphosphonic Acid Self-Assembled Monolayers Across Velocity Regimes**, O. Matthews, S. Barkley, Luther College, C. Bouxsein, M. Deram, N. Eigenfeld, St. Olaf College, A. Poda, W.R. Ashurst, Auburn University, B. Borovsky, St. Olaf College, E. Flater, Luther College

Microelectromechanical systems (MEMS) are critically-limited by interfacial phenomena such as friction and adhesion. The most common method of reducing friction between MEMS surfaces is the use of molecularly-thin self-assembled monolayer (SAM) coatings. Typically silicon MEMS have been coated with silane-based SAMs, such as octadecyltrichlorosilane (OTS), and have resulted in some modest improvement in device performance and lifetime. Continued progress in the development of MEMS may require new materials systems to be implemented. Through a collaborative effort, we investigate the frictional properties of octadecylphosphonic acid monolayers deposited on aluminum oxide surfaces across speed regimes. Measurements using an atomic force microscope (AFM) and a nanoindenter-quartz crystal microbalance are performed each with a microsphere-terminated probe. This allows for a comparative study with similar contact sizes, pressures, surface roughness, and interfacial chemistry. Speeds between the different instruments range from microns per second to meters per second. Preliminary AFM friction vs. load and friction vs. velocity measurements are presented, with the goal of investigating phosphonate SAM/ metal oxide systems as alternative MEMS materials.

9:40am **TR+MN+NS+SS-WeM6 Triboelectrification and Triboplasma Generation and its Application for Surface Modification**, S.V. Singh, P.K. Michelsen, Y. Kusano, Technical University of Denmark

Triboplasma gas discharges are often induced by triboelectrification around a sliding contact. Only an empirical classification is available for triboelectrification, whereas a detailed physical mechanism behind it is still unknown. Laboratory triboplasmas are mostly characterized by using optical diagnostics, and the optical emissions are reported to be observed mostly in ultraviolet region, corresponding to nitrogen emission lines. These measurements do not directly address triboelectrification. Here we present the evidence of electrostatic charging at the sliding contact and gas break down between the contacts through electrical measurements. Furthermore, the applicability of triboplasma for surface modification on polymeric materials was studied. Two capacitive probes were used for the investigation of a triboelectrification and triboplasma generated in a pin-on-rotating disk apparatus. These probes were mounted above the disk and on the pin, respectively. Measurements show a clear evidence of tribocharging, charge decay and triboplasma generation. Several combination of sliding contact materials with tendency to gain opposite charging and different sliding speeds, as high as 1000 rotation per minute, were carefully chosen. In addition, influence of different gas environment and pressure were investigated. Triboplasma induced surface modifications were characterized by water contact angle and X-ray photoelectron spectroscopy measurements.

10:40am **TR+MN+NS+SS-WeM9 Friction at Cryogenic Temperatures**, S.S. Perry, University of Florida **INVITED**

There are a number of applications where operation over a wide temperature range is required for device success. These extreme conditions

are often the motivation for variable temperature studies in tribology; however, a paucity of relevant tribology data exists for temperatures below 273 K.

In the range from 300 K to 100 K the friction coefficient of various solid lubricants has recently been shown to increase with decreasing temperature. Molecular scale measurements employing an atomic force microscope over a temperature range from 140 K to 750 K at a vacuum level of 2×10^{-10} torr have identified a temperature activated behavior of the friction and friction coefficient for the solid lubricants graphite and molybdenum disulfide. These molecular scale experiments were performed under conditions for which interfacial sliding was confirmed, interfacial wear was absent, and the role of adsorbed contaminants could be dismissed.

The potential influence of interfacial wear as well as the mechanism underlying the measured temperature dependence will be discussed.

11:20am **TR+MN+NS+SS-WeM11 In-Situ Scanning Auger Analysis of a Tribological Wear Scar in UHV Conditions**, B.P. Miller, O.J. Furlong, W.T. Tysoe, University of Wisconsin-Milwaukee

Lubrication of sliding copper-copper interfaces for use in brushes in electrical motors provides a particular challenge. Not only is a reduction in friction and wear required, but also allowing for high conductivity through the contact. Therefore, a self-limiting tribofilm is essential. The following explores the surface chemistry and tribology of dimethyl disulfide (DMDS) on copper surfaces to establish whether it is sufficiently reactive to potentially form a tribofilm near room temperature as required for lubrication of the sliding copper-copper contact in an electric motor. The surface chemistry and decomposition pathways of DMDS on copper surfaces are analyzed using temperature-programmed desorption (TPD), reflection-absorption infrared spectroscopy (RAIRS) and X-ray photoelectron spectroscopy (XPS). It is shown that DMDS reacts to form methyl thiolate species on the copper surface at room temperature. After heating to about 430K, methane and C₂ hydrocarbons desorb leaving molecular sulfur adsorbed onto the surface. A UHV tribometer chamber was equipped with a scanning electron gun having a ~100 micron diameter spot size. DMDS was dosed in the gas phase while performing friction measurements so that *in-situ* elemental analysis of the wear scar could be made. An increase in the sulfur signal is witnessed inside compared to outside of the tribological wear scar. A depth profile Auger analysis of the sample showed selective diffusion of sulfur into the bulk only inside the wear scar attributed to tribologically induced effects. This novel method of analysis can give important insights into the fundamentals of tribological systems.

11:40am **TR+MN+NS+SS-WeM12 First Principles Calculations and Atomistic Simulations of Tribology at Sliding Molybdenum Disulfide Surfaces**, T. Liang, S.R. Phillpot, S.B. Sinnott, University of Florida

Molybdenum disulfide is the most commonly used solid lubricant coating in aerospace applications. In this work, we carry out first principles density functional theory (DFT) calculations of the potential energy surface between two MoS₂ surfaces and examine the influence of oxidation on the results. In addition, we present the results of a recently developed empirical many-body potential for Mo and S systems and examine nano-scale friction between sliding MoS₂ surfaces using classical molecular dynamics (MD) simulations. In particular, MD simulations of interfacial sliding at various loads, temperatures and sliding directions are carried out. The loads and friction forces are extracted to calculate the friction coefficient of the MoS₂ as a function of temperature, and the results are compared to experimental pin-on-disk measurements of MoS₂ coatings and atomic force microscopy measurements on single crystal MoS₂ surfaces. The results from both the DFT calculations and the MD simulations help us to better understand the origins of lubricity on MoS₂.

Vacuum Technology

Room: Laguna - Session VT-WeM

Accelerators, Large Vacuum Systems, and Vacuum Surfaces

Moderator: R.F. Berg, National Institute of Standards and Technology

8:00am **VT-WeM1 Architecture and Operation of the Z Pulsed Power Facility Vacuum System**, J.W. Weed, Sandia National Laboratories, D.W. Petmecky, Ktech Corporation, A.C. Riddle, Sandia National Laboratories **INVITED**

The Z Pulsed Power Facility at Sandia National Laboratories in Albuquerque, New Mexico, USA is one of the world's premier high energy

density physics facilities. The Z Facility derives its name from the z-pinch phenomena which is a type of plasma confinement system that uses the electrical current in the plasma to generate a magnetic field that compresses it. Z refers to the direction of current flow, the z axis in a three dimensional Cartesian coordinate system. The multiterawatt, multimegajoule electrical pulse the Facility produces is 100-400 nanoseconds in time. Research and development programs currently being conducted on the Z Facility include inertial confinement fusion, dynamic material properties, laboratory astrophysics and radiation effects. The Z Facility vacuum system consists of two subsystems, center section and load diagnostics. Dry roughing pumps and cryogenic high vacuum pumps are used to evacuate the 40,000 liter, 200 square meter center section of the facility where the experimental load is located. Pumping times on the order of two hours are required to reduce the pressure from atmospheric to 10^{-5} Torr. The center section is cycled from atmosphere to high vacuum for each experiment. The facility is capable of conducting one to two experiments per day. Numerous smaller vacuum pumping systems are used to evacuate load diagnostics. The megajoules of energy released during an experiment causes damage to the Facility that presents numerous challenges for reliable operation of the vacuum system.

Sandia is a multiprogram laboratory operated by Sandia Corporation, a Lockheed Martin Company, for the United States Department of Energy's National Nuclear Security Administration under contract DE-AC04-94AL85000.

8:40am VT-WeM3 Vacuum System for the Large-Scale Cryogenic Gravitational Wave Telescope (LCGT). *R. Takahashi*, National Astronomical Observatory of Japan, *Y. Saito, T. Suzuki*, KEK-High Energy Accelerator Research Organization, Japan

The large-scale cryogenic gravitational wave telescope (LCGT) project is proposed to open a new window for astronomy, which will be able to detect signals from the binary neutron star coalescence at 240Mpc away. LCGT requires an ultra-high vacuum tubes which the laser beams pass through. Two 3-km vacuum tubes are kept in $\sim 10^{-7}$ Pa of vacuum pressure so as to reduce scattering-effects due to residual gas molecules.

Mirrors of the main interferometer are cooled to 20K to reduce thermal noises. The super-insulator (SI) which consists of multi-layered organic films is generally used for a thermal insulation of cryostat. However, the SI should not be applied to the cryostat of LCGT to avoid contamination on the extremely sensitive mirrors. We plan to use multi-layered metal shields with low emissivity and low outgassing for a thermal insulation.

9:00am VT-WeM4 Working toward XHV: Characterization and Improvements of the Vacuum System for GaAs Photoemission Electron Sources. *M.L. Stutzman, P.A. Adderley, A. Comer, M. Poelker*, Jefferson Lab

The operational lifetime of a DC electron source using GaAs photocathode material is limited primarily by the system vacuum; the residual gasses ionized by the electron beam are accelerated into the photocathode where they cause damage and limit photocathode yield. Though we operate in the deep-UHV range, improvements to the vacuum should increase lifetime for today's electron sources, and is essential for proposed future accelerators needing considerably higher average current. This talk describes our efforts to improve vacuum in the Jefferson Lab polarized electron source, including efforts to characterize NEG and ion pumps in the deep-UHV range, carefully determine the x-ray limit of our Leybold extractor gauges, and quantify the reduction in outgassing from stainless steel chambers after a long 400°C heat treatment. The goal of these studies is to determine which factors primarily limit our ultimate pressure, to find ways to lower the ultimate pressure for future electron sources, and to quantify these improvements.

9:20am VT-WeM5 The Role of Vacuum Technology in the Production of Neutron Generators. *J.L. Provo*, Sandia National Laboratories

Neutron generators are neutron source devices which are composed of small linear accelerators that produce neutrons by fusing isotopes of hydrogen. Such devices were first used in the ignition of nuclear weapons but many commercial applications have been developed over the past 50 years. The critical component of a neutron generator is a small particle accelerator called a neutron tube. Neutron tubes are composed of several components which include an ion source, ion optic elements, and a target on to which ions are accelerated. All components are enclosed in a vacuum tube enclosure with a high voltage insulator between the ion source and the target. The ion source and accelerator high voltages are provided by external power supplies either of electronic design or of a ferroelectric explosive design. Electronic generators can be used after function testing while explosive generators are destroyed.

Neutron tubes thus are similar to vacuum tubes previously used in televisions, radios, etc., and processes used for production of these devices

can also be used for neutron tubes. Because of their application, the quality requirements for manufacturing such devices for weapons are very rigorous and are of the highest quality standards. These devices typically are designed and fabricated to operate over a temperature range of -65 °F to +168°F with 99.99+% reliability at over 95% confidence. These are quality levels rarely found in any industry. To support these requirements, the latest in applied science and technology in analysis of materials and chemical and vacuum processes were utilized.

Described will be analyses and processes used in the characterization of materials and components used in vacuum neutron tube manufacture. These include surface analysis techniques used to prove materials have specified constituents with no impurities. Cleaning processes used to prepare tube components prior to sub-assembly, which include plasma cleaning, and vacuum firing, vacuum brazing assembly processes as well as thin film deposition processes for tube ion sources and targets, occluder film hydrating processes, and final tube exhaust processes, all of which use vacuum technology will be briefly described.

Some weapon and commercial versions of neutron tubes will also be described with external photos, their history, and their applications. It is very evident that the application of vacuum technology was absolutely necessary to produce the controlled environments that meet the quality standards for neutron tube weapon application as well as for the many commercial applications that require advanced-materials processing and manufacture in use now and in the future.

10:40am VT-WeM9 Application of Electrochemical Buffing to Niobium Superconducting RF Cavity. *S. Kato, M. Nishiwaki, P.V. Tyagi, S. Azuma, F. Yamamoto*, KEK-High Energy Accelerator Research Organization, Japan

Niobium electropolishing for SRF cavities are generally considered to be the best technology today.

However, hydrofluoric and sulfuric acid mixture usually used in the EP process is harmful and requires us carefully controlled handling of it and the many additional facilities. In this article, we propose a new application of electrochemical buffing onto niobium SRF cavity. In the method of electrochemical buffing, a rotating disk with abrasive fine particles where electrolyte is supplied is pressed against the workpiece. The disk and the work function as a cathode and an anode, respectively and an aqueous solution of sodium nitrate is used for the electrolyte. This technique brings us a couple of advantages like high etching rate, ultra small surface roughness, cost-effective and environment-compatible polishing.

11:00am VT-WeM10 Development of UHV Field Emission Scanner for Surface Study of Niobium SRF Cavity. *S. Kato, M. Nishiwaki, V. Chouhan, P.V. Tyagi, T. Noguchi*, KEK-High Energy Accelerator Research Organization, Japan

It is mandatory to investigate field emission on Nb SRF cavity systematically since strong field emission often limits the cavity performance. The field emission strength and the number of emission sites strongly depend on Nb surface properties which are determined by its surface treatment and handling. Field emission scanner developed allows us to measure a distribution of the field emitting sites over a sample surface at a given field strength along with its FE-SEM (field emission scanning electron microscope) observation and energy dispersive x-ray analysis. The field emission scanner consists of a sample stage driven by piezo actuators and an anode needle driven by precise 3D stepping motors. In addition, this system was newly equipped with a sample load-lock system for existing UHV suitcases. The compact scanner was installed into the space between the object lens and the SEM sample holder. The UHV pumps were additionally installed in order to improve the base pressure down to UHV to reduce adsorbates during the measurement. This article describes development of the field emission scanner and its preliminary results of the application to niobium samples.

Wednesday Lunch, October 20, 2010

Exhibitors & Manufacturers Technology Spotlight

Room: Southwest Exhibit Hall - Session EW-WeL

Exhibitors & Manufacturers Technology Spotlight

Moderator: D.J. Surman, Kratos Analytical Inc., R.

Langley, Consultant

12:00pm **EW-WeL1 Novel Detectors and Electron Sources for Vacuum and Elevated Pressure Environments**, *P. Holmes, W. Netolicky, B.N. Laprade*, PHOTONIS USA, Inc.

This presentation will address several unique applications, including electron multiplier and MCP detector operation in high pressure applications, such as RGA's; "cold" electron source arrays for vacuum environments; and novel microchannel plate shapes and configurations for specialized instruments.

12:20pm **EW-WeL2 Simplicity Solutions™ from the Granville-Phillips® Portfolio will be Introduced as a New Line of Gas Analysis Instrumentation**, *K. Van Antwerp, G. Brucker*, Brooks Automation, Inc.

Simplicity Solutions™ from the Granville-Phillips® portfolio will be introduced as a new line of gas analysis instrumentation and two new vacuum quality monitoring products based on Anharmonic Resonant Ion Trap Technologies for use in low mass range mass spectrometry and vacuum quality measurement applications. A brief description of the technology will be provided, a comparison to other low mass range separation technologies will be described and examples of key mass spectrometer performance characteristics will be shown. We will further stress the importance of the vacuum quality index as a method to reduce complex measurements into easy to understand instrumentation outputs.

12:40pm **EW-WeL3 Synchronous Motion, Close Proximity Sputtering System**, *R. Belan*, Kurt J. Lesker Company

Conventional sputtering systems have a well defined relationship between the size of the substrate being coated, sputtering gun target size, and the throw distance that separates the substrate from the sputtering gun. Substrate size and the required thin film uniformity are the key factors from which the sputtering gun size and the throw distance are then derived. We report on a sputtering system developed at the Kurt Lesker Company that breaks these geometric dependencies while at the same time delivering thin film uniformity of +/-1% or better and sputtering rates that are 5 to 10 times greater than most standard sputtering systems which follow conventional codependent geometries. This rate improvement can be achieved with metal or insulating targets using RF, DC, or pulsed DC power. This sputtering system works by placing the sputtering gun very close to the substrate (<1") and then synchronizing the travel of the sputtering gun across the face of a rotating substrate, controlling the rotational speed of the substrate, and controlling the power that the sputtering gun is operating at as the sputtering gun deposits its target materials. The advantages of this sputtering system, the economy of scale, and the versatility will be explained.

1:00pm **EW-WeL4 Internet Access to your Thin Film Deposition Systems**, *C. Malocsay, T. Haight*, Semicore

For years, field service by factory personnel for a deposition system meant getting in a car, plane or other mode of transportation, sometimes spending as much time in travel as the actual service, and, of course, adding that cost. After many years of arm twisting, cajoling or direct threats from a manager, internet access to many high end deposition systems has come to reality. It has taken 20 years for computer control to become a mainstay in the operational architecture of thin film deposition systems. Now with that hurdle gone, resistance to on-line service and support is the next obstacle to overcome.

1:20pm **EW-WeL5 BIG SIMS, LITTLE SIMS**, *N. Long*, SAI, UK

ToF-SIMS has become the tool of choice in a wide variety of today's surface and interface analysis tasks. The level of performance required of these tasks varies enormously, resulting a wide range in the capability of available instruments. SAI's expertise in ToF-MS technology has enabled it to offer instruments both at the top end of the scale and at the entry level making sure customers are uniquely well served in their quest to match investment levels to their task set. Illustrative data will be presented in the talk to demonstrate the concept across the gamut of SIMS applications.

Wednesday Afternoon, October 20, 2010

Applied Surface Science

Room: Cochiti - Session AS-WeA

Surface Mass Spectrometry: SIMS and Beyond

Moderator: C. Szakal, National Institute of Standards and Technology

2:00pm **AS-WeA1 Exploring the Surface Sensitivity of ToF-SIMS: Measuring the Implantation Depths and Sampling Depths of Bi_n⁺ and C₆₀⁺⁺ Ion Sources in Organic Films**, S. Muramoto, J. Brison, D.G. Castner, University of Washington

When a pulsed Bi_n⁺ analysis beam and a direct current C₆₀ etching beam are used in ToF-SIMS dual-beam depth profiling, we observed that increasing the ion dose of the analysis beam decreased the molecular signal as a function of depth. This decay was seen to occur much earlier in the depth profile for less clustered ions, suggesting that damage is related to the implantation depth of the primary ion. Recent experimental and simulation results in this field indicate that implantation depth is inversely related to the clustering of the primary ion, and are observed to affect outcomes such as sputter yield and escape depth (sampling depth). There is a need to characterize these parameters on organic systems, since a better understanding of these parameters will help us choose experimental parameters for the optimal analysis of samples.

In this study, the above mentioned quantities for Bi_n^{q+} (n = 1, 3, 5, q = 1, 2) and C₆₀⁺⁺ ions were characterized on molecular and polymeric organic films; a spin-cast trehalose and a plasma polymerized tetraglyme, both about 100 nm thick. The implantation depths of Bi ions were determined using C₆₀ single-beam depth profiling of the same area bombarded by bismuth. The depth scale was calibrated using AFM. The sputter yield was obtained by AFM imaging of the sputter crater. The molecular escape depth was determined by capping a protein-adsorbed mica with tetraglyme overlayers of varying thicknesses and monitoring the protein fragment intensities as a function of thickness. Results show that an ion's penetration depth is directly proportional to the energy-per-constituent of the ion. For example, increasing the number of Bi atoms from 1 to 3 (Bi₁⁺ to Bi₃⁺) for 25 keV single charged ions decreased the average penetration depth from 18 to 10 nm. When the energy of Bi₃ was increased from 25 to 50 keV, the implantation depth increased from 10 to 14 nm. When implanting bismuth ions, we observed etching of the sample surface, with the crater depths proportional to the cluster size of the bismuth ion. These crater depths were also proportional to the escape depth of the protein fragments. Bi₁⁺ at 25 keV was found to be the most surface sensitive; its sampling depth was only 1.8 nm despite its implantation of 18 nm. The second most surface sensitive was C₆₀⁺⁺ at 20 keV with a molecular escape depth of 2.4 nm. It turned out that the single most important factor that determined the surface sensitivity of the ion source was its sputter depth; both Bi₁⁺ and C₆₀⁺⁺ eroded 0.3 and 1.0 nm, respectively, whereas Bi₅⁺⁺ with a sputter depth of 1.8 nm was the least surface sensitive with a molecular escape depth of 4.7 nm.

2:20pm **AS-WeA2 A New Cluster Ion Beam for Advanced Molecular Depth Profiling of Polymers by TOF-SIMS**, T. Miyayama, S. Iida, N. Sanada, M. Suzuki, ULVAC-PHI, Japan, G.L. Fisher, J.S. Hammond, S.R. Bryan, Physical Electronics

The introduction of C₆₀⁺ as a sputter beam for TOF-SIMS made it possible to acquire molecular depth profiles on a wide variety of polymers. Previous studies by many different groups have demonstrated that not all polymers can be successfully depth profiled and that certain classes of polymers undergo sputter-induced chemical reduction when bombarded by C₆₀⁺ ions. If the polymer sputter yield is not high enough, the subsurface sputter-induced damage will accumulate as a function of sputter ion dose and the secondary molecular ion signals will not be stable. A number of different analytical parameters have been previously explored in attempts to improve depth profiling of these difficult polymers including sample temperature, beam energy, and incidence angle. We reported last year that glancing C₆₀⁺ incidence angle (76° from surface normal) significantly improved the ability to depth profile polycarbonate and polystyrene, which were previously unsuccessful at a typical incidence angle of 48°. However, even under these optimized conditions, the depth profiles eventually fail after several hundred nanometers due to accumulated sputter damage to the polymer and a concurrent reduction of the secondary ion and sputter yields. In the present study, we report the efficacy of an argon gas cluster ion beam (GCIB) for steady-state molecular depth profiling the same polymer systems. Depth profiles using different GCIB experimental conditions will be reported and compared to C₆₀⁺ depth profiles acquired under optimized conditions.

2:40pm **AS-WeA3 Nanoparticle Surface Analysis by Time-of-Flight Secondary Ion Mass Spectrometry (ToF-SIMS) and Low Energy Ion Scattering (LEIS)**, T. Grehl, P. Bruener, E. Niehuis, ION-TOF GmbH, Germany, N. Havercroft, ION-TOF USA, Inc., R. ter Veen, M. Fartmann, D. Breitenstein, Tasccon GmbH, Germany

Due to their extraordinary properties nanoparticles enter more and more fields of industrial production and daily life. They facilitate the protecting effect of sun creams, make car coatings and spectacle lenses scratch resistant and reliably protect shoes from wetness. Nanoparticles with antibacterial properties are used in clothing and refrigerators.

Nanoparticles' properties are influenced by their high surface to volume ratio. In addition, specifically tailored nanoparticles are increasingly composed of core shell structures. In order to understand and further develop the properties of nanoparticles it is therefore important to develop tools to investigate the elemental and molecular composition of their surfaces and interfaces.

Two ion beam technologies show promising features in this respect: On the one hand Time-of-Flight Secondary Ion Mass Spectrometry (ToF-SIMS) is able to probe the outermost 3-5 atomic layers of a sample. It reveals the elemental as well as the molecular composition of the samples' surface in a semi-quantitative manner. On the other hand, Low Energy Ion Scattering (LEIS) is a quantitative technique to probe the elemental composition of the outermost atomic layer. Combining these two complementary techniques allows a comprehensive overview on the sample composition.

In our study we will present combined ToF-SIMS and LEIS data on model-nanoparticle systems and will give examples for their prospects to enable nanoparticle development, product control and failure analysis. Amongst others, the layer growth of a shell of Al₂O₃ on LiMn₂O₄ nanoparticles deposited by an ALD process was investigated. Both techniques are able to determine the increased coverage of the core. While ToF-SIMS yields additional information about organic residues, LEIS is able to quantify the surface composition and assess the integrity of the layer.

3:00pm **AS-WeA4 Dual Beam Depth Profiling of Organic Materials by Time-of-Flight Secondary Ion Mass Spectrometry under Optimized Ion Beam Conditions**, D. Rading, R. Moellers, F. Kollmer, T. Grehl, ION-TOF GmbH, Germany, N. Havercroft, ION-TOF USA, Inc., E. Niehuis, ION-TOF GmbH, Germany

In recent years the development of sputter depth profiling of organic materials using Time of Flight instruments has made rapid progress. In particular, the use of a high energy C₆₀ cluster ion beam for sputtering has drawn considerable interest [1-3]. However, it has also been demonstrated that a variety of organic compounds cannot be profiled in a satisfactory way as characteristic molecular secondary ion signals are lost under high dose cluster ion bombardment [4-6]. In a number of studies various approaches were applied in order to overcome this problem. These approaches included sputtering at low incident angles [7], sputtering with low energy Cs ions [8], cooling or heating of the sample [5,9,10] and using alternative cluster ion sources such as massive argon clusters [11]. As a suitable sample for more detailed studies on properties, such as depth resolution was not available, most of the work so far was of phenomenological kind, i.e. it was checked whether characteristic organic signals survived the sputter process.

In this contribution, we investigate the influence of sputtering and analysis beam conditions on the signal intensity of characteristic high-mass molecular ions under high primary ion flux. For this purpose a series of primary ion species (C₆₀, Bi_n, Cs) at various energies and angles has been applied. In a second step an Irganox multilayer sample introduced by NPL [10] was used to investigate the influence of energy and angle of a C₆₀ sputter beam as well as the influence of sample rotation on depth resolution, constancy of the sputter rate and quantification possibilities in organic depth profiling.

[1] N. Winograd, *Anal. Chem.* **2005**, April 1, 143A-149A

[2] J. Cheng, A. Wucher and N. Winograd, *J. Phys. Chem. B.* **2006**, *110*, 1829-8336

[3] J.S. Fletcher, X.A. Conlan, J.C. Vickerman, N.P. Lockyer, *Appl. Surf. Sci.* **2006**, *252*, 6513-6516

[4] M.S. Wagner, *Anal. Chem.* **2005**, *77*, 911-922

[5] R. Möllers, N. Tuccitto, V. Torrisi, E. Niehuis, A. Licciardello, *Appl. Surf. Sci.* **2006**, *252*, 6509-6512

[6] H.-G. Cramer, T. Grehl, F. Kollmer, R. Moellers, E. Niehuis, D. Rading, *Appl. Surf. Sci.* **2008**, *255*, 966

- [7] J. Kozole, D. Willingham, N. Winograd, *Applied Surface Science* **2008**, 255, 1068-1070.
- [8] N. Mine, B. Douhard, J. Brison and L. Houssiau, *Rapid Commun. Mass Spectrom.* **2007**, 21, 2680-2684
- [9] C. M. Mahoney, S.V. Roberson, G. Gillen, *Analytical Chemistry* **2004**, 76, 3199-3207
- [10] P.J. Sjövall, D. Rading, S. Ray, L. Yang and A.G. Shard, *J. Phys. Chem.* **B2010**, 114, 769-774
- [11] S. Ninomiya, K. Ichiki, H. Yamada, Y. Nakata, T. Seki, T. Aoki, J. Matsuo, *Rapid Communications in Mass Spectrometry* **2009**, 23, 1601-1606

4:00pm AS-WeA7 Fundamental Sputtering Yields of Nanoparticles using SIMS, J.L.S. Lee, I.S. Gilmore, D.C. Cox, M.P. Seah, S.J. Spencer, National Physical Laboratory, UK

Nanoparticles are front-runner nanotechnologies key to high innovation products, such as biodiagnostics, drug delivery, medical imaging (contrast agents), cosmetics, sunscreens and catalysts. The surface and bulk chemistries of nanoparticles are crucial for their unique properties. There is also increasing concern over the potential health, environmental and safety risks of nanomaterials. Robust and consistent methodologies for characterising nanoparticle surface and bulk chemistries are urgently needed to support standardisation, regulatory requirements and toxicology studies [1].

Secondary ion mass spectrometry (SIMS) has been applied in nanoparticle characterisation [2,3]. However, the fundamentals of the sputtering of nanoparticles are not yet well understood. The sputtering yield is expected to be significantly different for nanoparticles compared to bulk materials, due to the dimension of nanoparticles being similar to the size of the SIMS collision cascade, and the larger available surface area for secondary emission. In this study, SIMS depth profiles were obtained for model Au nanoparticles, with diameters ranging from 10 nm – 100 nm, dispersed and mounted onto a silanised silicon substrate. The sputtering yields and profile shapes are evaluated for both atomic and cluster primary ion beams (Ar^+ , Bi^+ , Bi_3^+ and C_{60}^{n+}), using a range of primary ion energies. The nanoparticles are characterised by SEM and AFM both before and after sputtering. There is a significant increase in the sputtering yield for nanoparticles compared with bulk materials, in agreement with predictions from a recent molecular dynamics study [4]. In addition, for the first time, we observed the sputtering of nanoparticles in real time using a focused ion beam system with simultaneous SEM imaging. This provides valuable information for interpreting the SIMS depth profiles of nanoparticles and an interesting phenomenon of nanoparticle coalescence was observed. These results contribute towards developing the essential underpinning metrology and providing a practical procedure to analysts for the chemical characterisation and compositional depth profiling of nanoparticles.

References

- [1] D R Boverhof and R M David, *Anal Bioanal Chem* **2010**, 396, 953.
- [2] D R Baer, D J Gaspar, P Nachimuthu, S D Techane and D G Castner, *Anal Bioanal Chem* **2010**, 396, 983.
- [3] W Szymczak, N Menzel, W G Kreyling, K Wittmaack, *Int. J. Mass Spectrom.* **2006**, 254, 70.
- [4] S Zimmermann and H M Urbassek, *Int. J. Mass Spectrom.* **2008**, 272, 91.

4:20pm AS-WeA8 SIMS: Cluster Primary Ion Sputtering - Practical Reference Data and Outlook for High-Resolution Organic Imaging, I.S. Gilmore, T.L. Salter, J.L.S. Lee, F.M. Green, M.P. Seah, National Physical Laboratory, UK

Cluster ions have become the ion beam of choice for the analysis of organics in ToF-SIMS, owing to the large enhancement of the molecular ion yield [1] and the ability to depth profile through certain organic materials [2,3]. However, there is currently a lack of practical reference data on the sputtering yield volumes and damage cross-sections for commonly encountered materials in industry. Aside from having fundamental importance, these data can aid analysis by informing optimal analysis parameters, such as the useful lateral resolution achievable [4]. In this work, a systematic study using Bi^+ , Bi_3^+ , Bi_5^+ and C_{60}^+ ions is conducted for industrially relevant organics (PMMA, PVP, hydroxypropyl cellulose, phenylalanine, cholesterol, rhodamine and Irganox 1010). We provide general recommendations to help analysts.

For some organic materials thicker than a monolayer, the traditional static SIMS limit may be exceeded since the secondary ion intensity is retained as the material is consumed. The useful lateral resolution may therefore be improved by integrating intensity. However, the ultimate lateral resolution is also limited by the ion source brightness. The reference data here and ion

source design constraints define the present frontier of SIMS in terms of spatial resolution and molecular information. We show how this frontier has moved forward dramatically over the last 10 years and what barriers need to be overcome to allow nanoscale molecular imaging in SIMS.

References

- [1] M P Seah, *Surf. Interface Anal.* 2007; 39: 890.
- [2] J Cheng, A Wucher, N Winograd, *J. Phys. Chem. B* 2006; 110: 8329.
- [3] A G Shard, F M Green, P J Brewer, M P Seah and I S Gilmore, *J. Phys. Chem. B* 2008; 112: 2596.
- [4] D Touboul, F Kollmer, E Niehuis, A Brunelle, O Laprevote, *J. Am. Soc. Mass Spectrom.* 2005; 16: 1608.

4:40pm AS-WeA9 Sample Preparation of Cellular Samples for ToF-SIMS Analysis, M.A. Robinson, D.G. Castner, University of Washington

Over the last decade time-of-flight secondary ion mass spectrometry (ToF-SIMS) has been increasingly used for examining (imaging) biological samples ranging from surface immobilized proteins to tissue sections to single cells. Due to the ultra high vacuum requirement of the ToF-SIMS technique careful and stringent sample preparation protocols are necessary to preserve the native state of these samples. There are a variety of preparation procedures that have been developed to address this need. However, there is still debate as to which procedure best preserves cell chemistry and morphology. The goal of this study is to further elucidate the differences in information that can be obtained when comparing cellular samples that have been plunge cooled and then freeze dried versus those that have been plunge cooled and analyzed in the frozen hydrated state.

Freeze drying biological samples after cryofixation is a much simpler method of sample preparation compared to frozen hydrated. We have shown that freeze drying cryofixed samples preserves the native morphology as well as the K^+/Na^+ gradient in single NIH 3T3 fibroblasts, as shown in Figures 1a and 1b. Given optimal preparation procedures, images of subcellular compartments can be realized, as seen in Figure 1c. A single cell is shown after C_{60}^{++} sputtering (C_{60}^{++} ion dose = 4.3×10^{14} ions/cm²). The nucleus can be seen in the circular area within the cell that lacks $\text{C}_3\text{H}_8\text{N}^+$ signal. A nucleolus is observed as the bright spot within the nucleus. Also noticeable is the $\text{C}_3\text{H}_8\text{N}^+$ signal is the Golgi apparatus in the perinuclear region.

The question that remains is what type of information can be obtained from samples that have been freeze dried? Some groups have reported that freeze drying will cause cellular damage [1], while others have reported detrimental effects from frozen hydrated analysis [2]. Freeze drying continues to be the most popular preparation method after cryofixation, most likely because it is less complex than frozen hydrated analysis, as well as the fact that few ToF-SIMS instruments are setup to easily perform this type of investigation. We are adapting a liquid nitrogen cooled sample stage to allow for the rapid entry of cellular samples at liquid nitrogen temperatures to avoid sample warming and ice crystal formation. Ice crystal formation must be avoided in frozen hydrated analysis of biological material, as ice crystal formation will rupture cell membranes causing a loss of morphological and chemical information.

The results from this study shows the differences in information obtained when analyzing similar cellular samples in the freeze dried state versus the frozen hydrated state.

5:00pm AS-WeA10 "Wet SIMS": A Novel Molecular Imaging Technique for Biological Material Analysis, J. Matsuo, Kyoto University, CREST, Japan, H. Yamada, Y. Wakamatsu, Kyoto University, Japan, T. Aoki, T. Seki, Kyoto University, CREST, Japan

Because of the complexity of the structure and chemical composition in living organisms, much progress has been made in realizing mass imaging for biological samples. Secondary ion mass spectrometry (SIMS) imaging technique has the significant advantage of high spatial resolution, free of matrix deposition and with good reproducibility. In conventional SIMS the primary probes are keV-energy ion beams, which deposit their energy to atomic nuclei. As a result, primary ions break molecular bonding, and molecular information is lost. On the other hand, MeV-energy ions enhance ionization of high mass molecules, because of their dense electronic excitation. Molecular images with lateral resolution of around 5 nm have been demonstrated for peptides or lipids using MeV-energy ion beams [1].

In addition, MeV-energy ions, which have a long projection range in matter, can be utilized for material analysis under low vacuum. The low-vacuum condition prevents evaporation of water from the biological sample and helps maintain the shape of the sample. A new instrument has been developed to realize SIMS measurements under low vacuum. Biological samples were analyzed with swift heavy ions, and secondary molecular ions

were introduced into a quadrupole ion guide combined with a differential pumping system. An orthogonal time-of-flight (o-ToF) retaining high vacuum was employed to measure secondary ion mass spectra. This system allows the use of continuous beam, because of collisional cooling and orthogonal extraction. The mass resolution of this system is better than 6000, and is independent on the primary beam. Molecular imaging of cells and tissues was observed with a sample-scanning system. Secondary emitted biomolecular ions, such as lipids or cholesterol, were clearly observed with sufficiently high intensity. This new technique opens new possibilities for SIMS analysis, and we called it "wet SIMS".

Recent progress in this novel technique will be presented and discussed in view of its possible application in the analysis of biological matter.

[1] Y. Nakata, et al. *J. Mass Spectrom.* (2009) 44, 128–136

5:20pm AS-WeA11 Improvement of Organic Ion Yields in Secondary Ion Mass Spectrometry via Water Vapor Injection, T. Mouhib, A. Delcorte, C. Poleunis, P. Bertrand, Université Catholique de Louvain, Belgium

Even though significant progress has been achieved in molecular characterization by secondary ion mass spectrometry (SIMS) of organic compounds, some challenges still exist. One important limitation concerns the sensitivity the technique, often insufficient for high resolution molecular imaging. Several approaches have been proposed to increase the useful molecular signal intensities. The first one involves specific sample preparation procedures, such as the use of special matrices or metal-assisted SIMS (MetA-SIMS), in which metal nanoparticles are condensed on the sample surface. The second type of improvement directly involves the choice of the projectile, i.e. atomic projectiles are replaced by clusters, such as Au_n⁺, B_n⁺, C₆₀⁺ and SF₅⁺.

In this contribution, we investigate a new protocol to improve the analytical performance in organic SIMS, using water vapor injection at relatively high pressure near the sample surface. A significant enhancement of the positive secondary ion intensities is observed for organic materials irradiated with 12 keV Ga⁺ ions in the presence of H₂O gas. In addition, our results show that the enhancement depends on the type of secondary ion and that the formation of protonated ions is specifically favored. For the low molecular weight additive Irgafos 168 (C₄₂H₆₃O₃P), the normalized [M+H]⁺ intensity increases by more than 50 times upon H₂O flooding. The enhancement factors are lower with high molecular weight polymers. Nevertheless, the intensity of the protonated monomer ions is also enhanced preferentially in comparison with those of the deprotonated and the bare monomer ions. In the next phase of this work, we consider the combination of H₂O vapor flooding with polyatomic projectile bombardment.

5:40pm AS-WeA12 IonCCDTM for Charged Particle Detection: From sub-keV Electrons and keV Atomic and Molecular Ions to Hyperthermal Biomolecular Ions, O. Hadjar, OI Analytical, W.C. Schmutz, Dionex Corporation, J. Laskin, Pacific Northwest National Laboratory

We will present the latest data using a pixel array for charged-particle detection based on a modified charge-coupled device technology (IonCCDTM). The array is 51 mm long, consists of 2126 pixels (1.5 mm long) with 0.024 mm pitch. The charged particle beam is collected individually by each pixel, and hence, the IonCCD signal response is proportional to the beam flux and the collection time (integration time). With an integration time of 82 μs and a readout time of 2.7 ms, the IonCCD produces 360 frames a second. We will present data showing the direct use of the IonCCD as a beam profiler (one dimensional) to characterize the positively and negatively charged ion beams exiting an RF-only collisional quadrupole. The latter is used to thermalize and collimate the ions produced by an atmospheric pressure electrospray source. When mounted on the focal plane of a miniature Mattauch-Herzog geometry sector-field analyzer, the IonCCD produces a mass-over-charge (m/z) spectrum of the produced ions. For high sensitivity measurements we coupled the IonCCD to a micro-channel plate (MCP). In this manner, the IonCCD is used as an anode to read the electrons produced by the MCP. We will present MCP-IonCCD mass spectra using an electron-impact (EI) source to produce singly and doubly charged Xe ions. We compare the performance of the MCP-IonCCD hybrid detector to that of the IonCCD itself. We will apply this technology to the simultaneous m/z separation and detection of negative ions produced by electrospray ionization that generates beams of deprotonated molecules that are typically 10 times weaker than ion beams produced in the positive mode.

Biomaterial Interfaces

Room: Taos - Session BI-WeA

Proteins & Peptides on Surfaces

Moderator: H.E. Canavan, University of New Mexico

2:00pm BI-WeA1 Interaction of Amphiphilic Antimicrobial Peptides with Phospholipid Membranes, Bacteria, and Cells, M. Malmsten, Uppsala University, Sweden
INVITED

Due to increasing resistance development, antimicrobial peptides (AMPs) are receiving increasing attention since these may provide rapid and broad-spectrum response to a host of pathogens. In addition, some of these peptides provide also strongly antiinflammatory responses, and are therefore promising in therapies of both acute and chronic inflammation. Critical for their antimicrobial action is the interaction between AMPs and bacteria membranes, where significant current efforts are directed to identifying peptides being potent antimicrobials, yet simultaneously displaying low toxicity. In inflammation, additional aspects are of importance, including interaction with lipopolysaccharide and other bacterial components. In our efforts to address these and other challenges in the development of such peptides to practical therapeutics, our research addresses various aspects of interaction of AMPs with lipid membranes, bacteria, and cells. Focusing on endogenous peptides generated during normal microbial infections, we combine basic biophysical investigations on various aspects of AMP-membrane interactions with modern biotechnological tools for peptide design, and with biological experiments including bacteria, cells, and various animal models. Some recent examples of the work done in these contexts will be provided, aiming at synthesizing biophysical and biological aspects of these peptides.

2:40pm BI-WeA3 Curcumin Offers Neuroprotection by Inhibiting amyloid-β Insertion into Membranes, A. Thapa, B. Gilver, E.Y. Chi, University of New Mexico

Alzheimer's disease (AD) is a major cause of dementia in elderly people, affecting 5 million people in USA alone. AD is caused by the abnormal accumulation of aggregated amyloid beta peptides (39 to 43 amino acid residues) in the brain. Amyloid beta peptides are proteolytic products of the amyloid precursor protein of unknown function. Unfortunately, there are no cures available for this disease. However, there are several mechanisms proposed to cause and cure AD. The lipid membrane has been shown to mediate the fibrillogenesis and toxicity of Alzheimer's disease amyloid beta (Aβ) peptide. Several reports have linked the insertion of Aβ peptide into membranes as a possible mechanism of neurotoxicity. We hypothesized that small molecules capable of preventing the insertion of Aβ into membranes may ameliorate Aβ toxicity. Therefore, we investigated the effect of curcumin, a naturally occurring anti-inflammatory and antioxidant compound that suppresses oxidative damage, inflammation, cognitive deficits, and amyloid accumulation, on Aβ40 induced toxicity and in Aβ40 insertion into 1,2-dimyristoyl-*sn*-glycero-3-phosphoglycerol (DMPG) monolayer using surface pressure insertion isotherms and fluorescence microscopic techniques. We found that curcumin attenuates Aβ40 induced neuronal toxicity by inhibiting the insertion of Aβ into membranes possibly by interacting with membranes. Our data also demonstrated that neuroprotective action of curcumin in Aβ induced toxicity does not exclusively come through oligomerization inhibition, indicating that curcumin-membrane interaction but not curcumin-Aβ is associated in curcumin mediated neuroprotection. Altogether, our study suggests that curcumin-like small molecules inhibitors of Aβ insertions into membranes could be potential target to cure AD.

3:00pm BI-WeA4 Nonspecific Protein Adsorption Requires Large Adhesive Domains on the Surface, L. Shen, X.-Y. Zhu, University of Texas, Austin

We study the dynamics of protein adsorption using nm – mm scale patterns involving hydrophobic domains in hydrophilic matrices. We report the discovery of a critical requirement on the sizes of adhesive pads for protein adsorption: the area of each adhesive pad must be more than two orders of magnitude larger than the footprint of a protein molecule before irreversible adsorption occurs. We attribute this to the minimal surface area sampled by a mobile protein molecule in a precursor state before irreversible adsorption occurs.

4:00pm BI-WeA7 Study of Adsorption and Orientation of FnIII₇₋₁₀ Fibronectin Fragment on Self-Assembled Monolayers using Time of Flight Secondary Ion Mass Spectrometry, L. Arnadóttir, J. Brison, L.J. Gamble, University of Washington

Protein adsorption and orientation plays a critical role in many biomedical applications. Fibronectin (FN) is an extracellular matrix protein that is

involved in many cell processes such as adhesion, migration and growth. The orientation and conformation of FN adsorbed onto surfaces can therefore play a critical role on cell-surface interactions. In this study, the adsorbed orientation and conformation of the 7-10 fragment of FNIII was studied on three different model surfaces (self-assembled monolayers (SAMs) of C₁₁ alkanethiols on Au with -CH₃, -NH₂, and -COOH functional groups). X-ray photoelectron spectroscopy (XPS) was used to quantify the amount of protein adsorbed on the different surfaces and time-of-flight secondary ion mass spectrometry (ToF-SIMS) was used to characterize their orientation and conformation. A trehalose coating was also used to inhibit the conformation changes due to the dehydration of the sample. With the help of principal component analysis (PCA), the peaks which are responsible for the variance observed between the spectra relative to the protein adsorbed on the different surfaces could be identified. Because the surface sensitivity of the ToF-SIMS technique is lower than average protein size, these changes in the spectra reflect differences in the conformation and the orientation of the FN fragment. Comparison of trehalose protected and unprotected samples show a significant difference in the ratio between hydrophilic and hydrophobic amino acids. The results suggest that the more hydrophilic amino acids stay on the outside of the trehalose protected protein while the more hydrophobic ones get exposed to the protein air interface upon drying. Comparison of the trehalose protected fragment on -CH₃ and -COOH terminated SAMs show more intense signals of Arg and Asp on the -COOH surface and more intense Val, Pro and Leu signals on the -CH₃ SAMs. The detection of these different amino acids for the protein on the different SAMs suggests that the fragment might partly denature upon adsorption to the hydrophobic surface.

4:20pm BI-WeA8 Temperature Controlled Dehydration of Protein Films: Time-of-flight Secondary Ion Mass Spectrometry Study of Conformational Mobility of Proteins in Vacuum, H.P. Bui, T.P. Beebe, Jr., University of Delaware

Once a biomaterial is implanted, a film of protein will adsorb onto the surface and it is this protein film that will dictate how the biomaterial will interact with the surrounding cells and tissue. Two strategies to increase the success rate of biomaterials are to passivate the surface so that it is resistant to protein adsorption, or to activate the surface to obtain a desired cell response. One method of activation is the grafting of one or more proteins onto the surface that direct specific cellular interactions. However a thorough understanding of the protein film's composition, conformation and orientation is needed in the development of these advanced biomaterials. Time-of-flight secondary ion mass spectrometry's (TOF-SIMS) high surface specificity, analytical sensitivity and ability to provide long-range molecular information can be used to probe protein composition, conformation and orientation. In this study, we demonstrate that the use of temperature-programmed dehydration and principal component analysis can be used as a method of determining the conformation and orientation of protein films. We have found that TOF-SIMS is sensitive to the dehydration of the protein film and the accompanying conformational changes

4:40pm BI-WeA9 Structure and Function of von Willebrand Factor on Glass, Polystyrene, and Tissue Culture Polystyrene, E. Hillenmeyer, R.A. Penkala, W. Thomas, D.G. Castner, University of Washington

von Willebrand Factor (vWF) is a blood-soluble clotting protein responsible for binding platelets through the glycoprotein 1b (GP1b) receptor on the platelet surface. vWF can become activated and bind platelets when bound to exposed collagen in blood vessels or when vWF experiences increased shear.

vWF can also bind platelets when adsorbed to synthetic surfaces and participate in clot formation, which is not desirable for blood-contacting biomaterials. There is evidence that surface properties can influence vWF adsorption. Previous studies showed differences in protein topography (1) and conformation (2) when vWF was adsorbed on mica (1), octadecyltrichlorosilane modified glass (1,2), and collagen VI (2). However, studies were not performed to relate adsorption differences to vWF function.

To more fully characterize the adsorption properties of vWF, we adsorbed the platelet binding domain of vWF (A1 domain) to three surfaces: polystyrene, tissue culture polystyrene, and glass. Protein structure was investigated using x-ray photoelectron spectroscopy (XPS) and time of flight secondary ion mass spectrometry (ToF-SIMS). Protein function was tested by measuring platelet binding in a physiologically relevant flow assay.

Using nitrogen as a marker of protein, XPS showed similar amounts of vWF A1 adsorbed to the three surfaces. However, the flow assay showed significantly different platelet binding to vWF A1 on each surface, as measured by platelet rolling velocity. Rolling velocity was highest on glass, indicating lowest platelet binding. The slowest rolling velocity was observed on polystyrene, indicating the highest level of platelet binding.

ToF-SIMS data was analyzed using principle component analysis (PCA). PCA showed separation of the three surfaces with adsorbed vWF A1, indicating conformational differences between the proteins on each surface.

These studies show that surface properties influence structure and function of adsorbed vWF domains. Although there was a similar amount of protein on each surface, protein function was different. Polystyrene, the most hydrophobic of the surfaces, appeared to have the strongest activating effect on vWF. ToF-SIMS studies showed conformational differences, suggesting that conformational differences contribute to the observed functional differences.

Understanding the structure and function of adsorbed vWF gives insight into how vWF behaves on biomaterial surfaces and how this might affect platelet binding. Characterizing vWF adsorption also allows *in vitro* behavior to be more accurately related to *in vivo* thrombosis events.

Raghavachari. *Colloids Surf B* (2000) 19:315.

Kang. *Thromb Res* (2007) 119: 731.

5:00pm BI-WeA10 Secondary Structures of Soft- and Reactively Landed Multiply Charged Protein Ions, Q. Hu, P. Wang, J. Laskin, Pacific Northwest National Laboratory

Soft- and reactive landing of mass-selected ions enables highly selective preparation of uniform thin films of a variety of complex molecules on surfaces. We previously demonstrated that conformationally-selected peptide arrays can be prepared using SL of peptide ions onto self-assembled monolayer (SAM) surfaces. In this work we studied the secondary structures of protein ions soft- and reactively landed onto SAM surfaces using infrared reflection absorption spectroscopy (IRRAS). Different charge states of ubiquitin were generated by electrospray ionization (ESI). The structure of the low charge state corresponds to the pseudo-native state of the protein and the high charge state corresponds to an unfolded state. Inert CH₃-terminated SAM (HSAM) and hydrophilic COOH-terminated SAM (COOH-SAM) were used as soft- landing targets. Detailed analysis of IRRAS spectra, especially the amide I band, provides valuable information on the secondary structures of the immobilized protein species. This technique allows us to study the effect of the initial conformation and the properties of the surface on the secondary structure of immobilized proteins. Secondary structure of ubiquitin ions reactively landed onto SAM of N-hydroxysuccinimidyl ester terminated alkylthiol on gold (NHS-SAM) was also studied by IRRAS, and the reaction rate was determined from the depletion of the strong asymmetric carbonyl stretching band of the NHS group.

5:20pm BI-WeA11 Analysis of Unspecific Protein Adsorption onto Polymer Materials using Radioactive Labeling, Atomic Force Microscopy and ELISA, M. Holmberg, X.L. Hou, Technical University of Denmark

In this study radioactive labeling is used in combination with ELISA measurements and Atomic Force Microscopy (AFM) analysis to investigate aspects of unspecific protein adsorption onto polymer materials. The radioactive labeling is a setup in which different proteins are labeled with isotopes that emit gamma radiation with different energies. This makes it possible to detect several proteins simultaneously onto the same sample and thus to investigate competitive protein adsorption and how the presence of some proteins influence the adsorption of others. Results from protein adsorption onto polymer materials using the radioactive labeling setup have shown adsorption levels higher than expected for monolayer adsorption and suggest the existence of protein multilayers on some surfaces. Results from fibrinogen adsorption onto surfaces that are pre-adsorbed with albumin show that fibrinogen can adsorb on top of albumin and that exchange of already adsorbed albumin is not a dominant process during the competitive adsorption with fibrinogen. Preliminary results on QCM-D (quartz crystal microbalance with dissipation monitoring) also strengthen the idea of the existence of an interface between polymer surface and protein solution in which proteins interact with both each other and the surface in a matrix structure that have multilayer character. To further illustrate the impact on (or lack of) unspecific protein adsorption using blocking buffers and pre-adsorption of proteins, we show results from ELISA measurements of unspecific protein adsorption onto TCPS (tissue culture polystyrene) and PS (polystyrene). We can detect large difference in adsorption level between proteins with and without a HIS tag (six histidines) onto TCPS, but not onto PS, with the HIS tagged proteins showing much higher adsorption onto TCPS compared to the same protein without a HIS tag. Furthermore, low or none impact on the level of adsorption of these HIS tagged proteins is observed when the TCPS surfaces are blocked with BSA (bovine serum albumin). We are combining quantitative results from radioactive labeling (and QCM-D) with AFM analysis performed in liquid to obtain data regarding homogeneity and topography of adsorbed protein layers. Furthermore, ELISA is used as a supplementary technique to acquire more knowledge regarding unspecific adsorption of proteins onto polymer

materials. The obtained information is of importance when evaluating interactions between proteins and biomaterials.

5:40pm **BI-WeA12 Surface Interactions of GG-X-GG and X_n Oligopeptides with Inorganic Substrates**, K.P. Fears, J.L. Kulp, T.D. Clark, D.Y. Petrovykh, Naval Research Laboratory

The adsorption behavior of model GG-X-GG and X_n oligopeptides on Au and native Si oxide substrates was investigated to elucidate the contributions of different amino acids (AAs) to peptide-surface interactions. The manner in which peptides and proteins interact with surfaces is of critical importance in many biological and technological systems. The mechanisms underlying surface adsorption of proteins, however, are poorly understood, largely due to the inherent complexity of natural proteins. Accordingly, in this work simple model peptides were chosen to systematically examine the interactions between natural AAs and inorganic surfaces. Surface interactions of a series of AAs were probed by incubating inorganic substrates in aqueous solutions of model GG-X-GG pentapeptides, in which an AA of interest was flanked with Gly. The effects of cooperative adsorption were also examined using model X_n oligopeptides ($n = 5, 10$). The amount of peptides that irreversibly adsorbed on each substrate was quantified by X-ray photoelectron spectroscopy (XPS), the resulting systematic data revealed several trends in surface adsorption of oligopeptides as a function of their composition and length. On the negatively-charged, hydrophilic native SiO_x layer of a Si wafer, only peptides containing positively-charged residues (Lys and Arg) and polar residues (Ser and Thr) adsorbed at significant levels. Peptides adsorbed more readily on Au-coated Si wafers, on which the maximum surface coverage was ca. 3 times greater than that on the native SiO_x . For a particular AA (X), adsorption tended to increase, sometimes dramatically, with increasing units of X (GG-X-GG < X_5 < X_{10}). In pairs of AAs having side chains that only vary by alkyl chain length (L and V, Q and N, R and K, E and D), the AA with the longer alkyl chain adsorbed more readily, although this trend diminished with the increasing number of X residues.

Electronic Materials and Processing

Room: Dona Ana - Session EM+SS-WeA

High-k Dielectrics for III-V Electronics

Moderator: A.C. Kummel, University of California at San Diego

2:00pm **EM+SS-WeA1 High-k III-V MOSFETs Enabled by Atomic Layer Deposition**, P. Ye, Purdue University **INVITED**

The principal obstacle to III-V compound semiconductors rivaling or exceeding the properties of Si electronics has been the lack of high-quality, thermodynamically stable insulators on III-V materials. For more than four decades, the research community has searched for suitable III-V compound semiconductor gate dielectrics or passivation layers. The literature testifies to the extent of this effort. The research on ALD approach is of particular interest, since the Si industry is getting familiar with ALD Hf-based dielectrics and this approach has the potential to become a manufacturable technology.

Using In-rich InGaAs as surface channel, high-performance inversion-mode high-k/III-V NMOSFETs have been demonstrated. By further improving on-state performance, such as maximum drain current I_{dss} and peak transconductance G_m , the off-state performance or subthreshold characteristics need to be seriously evaluated for digital applications. In this talk, we review some new progresses on deep-submicron inversion-mode $\text{In}_{0.7}\text{Ga}_{0.3}\text{As}$ NMOSFETs using 2.5 nm-5.0 nm ALD Al_2O_3 as high-k gate dielectrics. The G_m exceeds 1.1-1.3 mS/ μm and starts to approach the values from InGaAs HEMTs. The scaling metrics, such as threshold voltage (V_T), $I_{\text{on}}/I_{\text{off}}$ ratio, sub-threshold swing (S.S.), the drain induced barrier lowering (DIBL), as a function of the gate length from 150 nm to 250 nm are systematically studied. Retro-grade structure and halo-implantation are also applied to III-V MOSFET field to improve the off-state performance of InGaAs MOSFETs. In order to achieve better gate control capability, new structure design like FinFET demonstrated successfully in Si devices, is strongly needed for short-channel III-V MOSFETs. However, unlike Si, the dry etching of III-V semiconductor surface has been believed to be difficult and uncontrollable, especially related with surface damage and integration with high-k dielectrics. We also review some results on the first experimental demonstration of inversion-mode $\text{In}_{0.53}\text{Ga}_{0.37}\text{As}$ tri-gate FinFET using damage-free etching and ALD Al_2O_3 as gate dielectric. The SCE is greatly suppressed.

The work is in close collaborations with Y.Q. Wu, Y. Xuan, J.J. Gu and M. Xu. We also would like to thank valuable discussions with D. Antoniadis, M.S. Lundstrom, R.M. Wallace, K.K. Ng, M. Hong, and J. Woodall.

2:40pm **EM+SS-WeA3 Passivation of $\text{Al}_2\text{O}_3/\text{InGaAs}(100)$ Interfaces by Atomic Layer Deposition and Annealing**, F.L. Lie, B. Imangholi, University of Arizona, W. Rachmady, Intel Corp., A.J. Muscat, University of Arizona

Identification of the source of interfacial defects between high-k films and III-V substrates is crucial for developing passivation methods. Efforts have been made to isolate defects based on a specific chemical moiety at an interface. A study reported that doubly-O coordinated Ga and displaced As formed when GaAs is exposed to oxygen, induces mid-gap states¹. Another study suggested that high activity interface defects originate from structural disorder instead of specific chemical moieties². This project aims to understand the nature of $\text{Al}_2\text{O}_3/\text{InGaAs}$ interface defects by relating composition to electrical performance. The modification of InGaAs(100) surfaces due to surface cleaning, Al_2O_3 deposition, and post deposition annealing (PDA) was investigated using capacitance-voltage (CV) curves, large AC signal conductance (LSC), and x-ray photoelectron spectroscopy (XPS). Al_2O_3 films were deposited by atomic layer deposition (ALD) using trimethylaluminum (TMA) and water precursors on native oxide covered and aqueous HF etched InGaAs(100) surfaces. XPS analysis on a native oxide sample revealed ~8Å oxide (52% As, 29% Ga, and 21% In) and a monolayer excess of As on an As-terminated substrate. TMA reacted on this surface during ALD, thinning the oxide to ~4.2 Å (45% As, 29% Ga, and 27% In). Aqueous HF treatment removed the native oxide and produced an As-rich surface, which re-oxidized in air. Surfaces consisted of ~4.2 Å oxide (91% As) and 1.5 monolayer excess As on an As-terminated surface. ALD Al_2O_3 on the liquid-cleaned surface produced a chemically sharp $\text{Al}_2\text{O}_3/\text{InGaAs}$ interface with less than a monolayer of As oxide. CV and LSC measurements were performed on Au/Ni/10 nm $\text{Al}_2\text{O}_3/\text{InGaAs}$ stacks. The deep-level surface recombination velocity (SRV) values extracted represent the net effect of interface defects, which includes the defect density and capture cross section. The similar SRV values obtained for native oxide (34±6 cm/s) and aqueous HF (29±13 cm/s) prepared surfaces suggest that the presence or absence of oxides was not the only determining factor. PDA in forming gas and NH_3 ambients significantly improved the electrical quality, as reflected in SRV values of 1 to 5 cm/s for both surfaces. XPS analysis showed increased excess As and Ga_2O_3 at the interface of both surfaces, likely due to thermally or H-induced reactions between interfacial As oxide and Ga atoms in the substrate. These results suggest that high activity defects in III-V's could be associated with interfacial dangling bonds and are amenable to standard passivation methods used in Si technology.

¹Hale M. J. et al, J. Chem. Phys. 119(13), 2003

²Caymax M. et al, Microelectron. Eng. 86, 2009

3:00pm **EM+SS-WeA4 An In Situ Examination of Atomic Layer Deposited $\text{Al}_2\text{O}_3/\text{InAs}(100)$ Interfaces**, A.P. Kirk, M. Milojevic, D.M. Zhernokletov, J. Kim, R.M. Wallace, University of Texas, Dallas

An in situ half-cycle atomic layer deposition/X-ray photoelectron spectroscopy (ALD/XPS) procedure was conducted in order to learn more about the evolution of the Al_2O_3 dielectric interface with undoped InAs(100). Without breaking vacuum, monochromatic XPS was used to examine the InAs(100) surface following ammonium sulfide passivation or ammonium hydroxide etching and then after each individual ALD pulse of trimethyl aluminum (TMA) and deionized water (DIW) precursors (e.g. single TMA pulse/XPS scan; single DIW/XPS scan; etc.). Ammonium sulfide was more effective at minimizing native oxides than ammonium hydroxide. Regardless of chemical cleaning technique, after depositing up to 1 nm of Al_2O_3 , elemental arsenic (As⁰ or As-As bonds) remained at the interface which may have adverse implications for devices such as metal oxide semiconductor field effect transistors (MOSFET). After heating to 300 °C (typical ALD reactor temperature), As-S bonding was reduced below the XPS detection limit. The In^{1+} chemical state (e.g. In_2O) was preserved while trivalent In and As oxidation states were minimized following exposure to TMA. The chemical reaction pathways appear to be similar to that observed for GaAs and InGaAs. We will also present electrical characterization studies and examine the correlation to the in situ interface analysis.

4:00pm **EM+SS-WeA7 Fermi-level Unpinning of $\text{HfO}_2/\text{In}_{0.53}\text{Ga}_{0.47}\text{As}$ Gate Stacks using Hydrogen Anneals**, *R. Engel-Herbert, Y. Hwang, N.G. Rudawski, S. Stemmer*, University of California, Santa Barbara

4:20pm **EM+SS-WeA8 Valence Band Alignment in low-k Dielectric/Cu Interconnects as Determined by X-ray Photoelectron Spectroscopy**, *S. King, M. French, M. Jaehnig, M. Kuhn*, Intel Corp.

Electrical leakage in low-k/Cu interconnect structures is becoming a growing vital concern as the nano-electronics industry moves to increasingly tighter metal spacing's for sub 22 nm technology nodes and continues to replace dense SiO_2 dielectrics with low density / porous SiOC:H "low-k" dielectric materials. In order to understand the various possible leakage mechanisms in low-k/Cu interconnects, a knowledge of the basic band alignment between Cu and low-k dielectric materials is needed but has gone largely unreported. In this regard, we have utilized X-ray Photoelectron Spectroscopy (XPS) to measure the Valence Band Alignment and Schottky Barrier at interfaces of importance to Cu/low-k interconnects. XPS has been used extensively for determining the band alignment of numerous semiconductors to other semiconductors, metals, and dielectrics. In this paper, we demonstrate that XPS can also be utilized to determine the band alignment at interfaces between amorphous dielectrics and metals of interest to the low-k/Cu interconnects industry. Specifically, we have utilized XPS to determine the Schottky Barrier between Cu and low-k dielectric SiC and SiCN capping layers deposited on Cu via Plasma Enhanced Chemical Vapor Deposition (PECVD). We have also utilized XPS to determine the valence band alignment at SiCN:H/SiOC:H interfaces. Lastly, the impact of various plasma surface treatments on the band alignment at these interfaces was also investigated.

4:40pm **EM+SS-WeA9 III-V CMOS: A sub-10 nm Electronics Technology?**, *J.A. del Alamo*, Massachusetts Institute of Technology
INVITED

CMOS scaling is at the heart of the microelectronics revolution. The ability of Si CMOS to continue to scale down transistor size while delivering enhanced performance is becoming increasingly difficult with every generation of technology. For Moore's law to reach beyond the limits of Si, a new channel material with a high carrier velocity is required. A promising family of materials for this is III-V compound semiconductors.

III-Vs are well known for their unique suitability for high frequency electronics. III-V-based integrated circuits are currently in use in a variety of communications and defense applications. The prospect of III-Vs entering the logic roadmap is tantalizing. This work reviews some of the critical issues.

The barrier for insertion of a new channel material into the CMOS roadmap is huge. Any new technology has to beat Si designs in performance at device footprints that allow the integration of billions of transistors on the same chip. In addition, cost-effective manufacturing must be realized.

To make this work, a III-V CMOS technology has to solve a number of challenging technical problems. The development of a gate stack that includes a high-K dielectric and yields a high-quality semiconductor interface with a III-V compound semiconductor is up there as one of the greatest and most fascinating problems in modern semiconductor technology. Recent research suggests that this is an eminently attainable goal. Transistor size scalability is also a major worry. Will it be possible to scale future III-V transistors to the required dimensions while preventing excessive short-channel effects and attaining the demanding parasitic resistance objective? This is a topic that will call for extensive experimental and simulation research. Fortunately, calibrated simulators today reproduce quite well the characteristics of 30 nm gate length III-V FETs and should be valuable in projecting to devices in the 10 nm range. If planar device designs are unsuitable, 3D designs might offer a viable path. Recent 3D device demonstrations with impressive characteristics give hope that this is a promising strategy. A future III-V CMOS technology will also have to "look and feel" as much as Si as possible. This calls for the formation of thin high-quality III-V layers on top of large Si wafers. In fact, depending on what emerges as the best option for the p-channel device, a major challenge in itself, two dissimilar materials might need to be integrated side by side in very close proximity on top of a Si wafer. These are all great problems that will require the coordinated attention of scientists and technologists with expertise in many different domains.

5:20pm **EM+SS-WeA11 Potential Profiles of III-V MOSCAPs with Kelvin Probe Force Microscopy *In Situ***, *W. Melitz, J. Shen, S. Lee, J.S. Lee, A.C. Kummel*, University of California at San Diego, *S. Bentley, D. Macintyre, M. Holland, I. Thayne*, University of Glasgow, UK

Energy Frontiers Topical Conference Room: Mesilla - Session EN+NS-WeA

Nanostructures for Energy Conversion & Storage I Moderator: S. Agarwal, Colorado School of Mines

2:00pm **EN+NS-WeA1 Electrochemical Performance of Nanostructured Sn Thin Films as Anodes of Thin film Li-ion Battery**, *C.S. Nimisha, G. Venkatesh, T. Dhivya, G. Mohan Rao, N. Munichandraiah*, Indian Institute of Science, India

Nanostructured Sn thin films have been prepared by rf sputtering and thermal evaporation on to silicon substrates for evaluating the electrochemical performance to use as anode layer of thin film Li-ion battery. The scanning electron microscopy (SEM) shows different film morphologies for evaporated and sputtered films which directly control the electrochemical performance. Crystallinity of the deposited films were ensured by X-ray diffraction (XRD). Bio-Logic SA potentiostat / Galvanostat (model:VPM3) is used for testing electrochemical performances. Sn thin films prepared by thermal evaporation from Sn granules of 99.99% purity resulted in films with nanograins of ~200nm size homogeneously distributed over the surface. Whereas films made by rf sputtering from Sn target (99.99% purity) with Ar as sputtering gas at a pressure of 5×10^{-3} mbar, resulted in highly porous film surface with 'nanobead' (~50nm size) formation inside the edges.

For electrochemical studies half cells were assembled using lithium as counter and reference electrodes in 1M LiAsF_6 dissolved in ethylene carbonate and dimethyl carbonate electrolyte. Charging was done with a constant current density of $10 \mu\text{A} / \text{cm}^2$ up to 1.2 V, followed by discharging at $10 \mu\text{A} / \text{cm}^2$ down to 0.2 V. The capacity obtained from both evaporated and sputtered films clearly shows the three plateau regions of lithiation and delithiation for both evaporated and sputtered films. From the evaporated film, a discharge capacity of $83.6 \mu\text{Ah}/\text{cm}^2$ is obtained, whereas from sputtered film a much higher capacity of $886 \mu\text{Ah}/\text{cm}^2$ is obtained.

We speculate that the increased surface area of the rf sputtered Sn film due to the porous nature and the presence of nano beads, resulted in higher capacities than the evaporated Sn films, which have relatively bigger sized grains. Also the presence of more nano sized features in the sputtered film surface reduces the pulverization of Sn films during cycling since the absolute volume change would be minimized. The reduction in diffusion length for Li-ion and increased effective surface area ensures higher discharge capacity from rf sputtered Sn films compared to evaporated films. The higher discharge capacity obtained from rf sputtered Sn thin films makes it ideal candidate for integrating as anode layer of thin film Li-ion battery.

2:20pm **EN+NS-WeA2 Lithographically Defined Porous Carbon Electrodes**, *R. Polsky, B. Burckel, X. Xiao, C.M. Washburn, M. Roberts, B. Bunker*, Sandia National Laboratories, *A. Raub, S. Brueck*, University of New Mexico, *S. Brozik, D.R. Wheeler*, Sandia National Laboratories

Pyrolyzed Photoresist Films (PPF) have electrochemical properties similar to glassy carbon electrodes with the unique feature that they can be lithographically defined to create microstructures and microfeatures. Previously we reported that the near atomically flat surface of PPF results in the deposition of gold nanoparticles (1-3 nm) with narrow size distributions. [1] Herein we describe the fabrication of porous carbon structures using interference lithography (IL) to generate 3-D structures in PPF that contain five patterned layers with microporous hexagonal lattices (~ 800 nm in diameter). [2] Because IL is a maskless approach porous carbon structures are able to be patterned over large volumetric areas (2.5 X 2.5 cm). We demonstrate the porous carbon structures can be used as a highly adaptable electrode material suitable for the deposition of metal nanoparticles (Au, Ag, and Pt) and conducting polymers with possible applications in such areas as fuel cells, ultracapacitors, and biosensors.

References

- [1] R. Polsky, C.M. Washburn, G. Montano, H.Q. Liu, T.L. Edwards, D.M. Lopez, J.C. Harper, S.M. Brozik, D.R. Wheeler, *Small*, **2009**, 5, 2510-2513.
- [2] D.B. Burckel, C.M. Washburn, A.K. Raub, S.J. Brueck, D.R. Wheeler, S.M. Brozik, R. Polsky, *Small*, **2009**, 5, 2792-2796.

2:40pm **EN+NS-WeA3 Designing Inorganic Nanostructures for Solar Cells and Energy Storage Devices**, *Y. Cui*, Stanford University **INVITED**
The capability of synthesizing materials with nanometer size and shape control has enabled exciting opportunities to engineer materials for controlling and understanding electronic, photonic, mechanical and ionic processes, which are important for applications such as energy conversion and storage devices. In this talk I will show two examples on how we design nanoscale materials towards high performance photovoltaics and energy storage devices. In the first example, nanocone- and nanodome-shaped substrates are designed for efficient photon management and charge carrier separation, which result in significant improvement of solar cell power efficiency compared to the flat film devices. Second, nanowires are exploited to maximize efficiency of simultaneous electron and ionic insertion with facile strain relaxation, which enable novel ultrahigh charge storage capacity materials towards next generation of high energy density batteries.

4:00pm **EN+NS-WeA7 Synthesis of Rare Earth Ion Co-Doped Core-Shell Nanostructures for Improved Energy Generation Efficiency**, *J.A. Dorman, J. Hoang, J.H. Choi, J.P. Chang*, University of California, Los Angeles

The development of rare-earth ion (RE) doped phosphors allows for the conversion of photons at various wavelengths to those at energies similar to that of the photovoltaic band gap. Work has been shown that through the incorporation Er^{3+} and Yb^{3+} into complex metal oxides, specifically yttrium based compounds, both energy upconversion and downconversion can be utilized to convert absorbed photons to a more desirable energy for Si based solar cells. However, both photoluminescence and energy transfer mechanisms are highly susceptible to the local crystal environment, including the overall crystal field and surrounding molecules. The addition of a shell layer increases luminescence by decreasing the effect of surface quenching sites while promoting energy transfer between layers.

This work focuses on the synthesis of core-shell nanostructures while controlling the luminescence spectrum through the spatial distribution within the particle architecture using a combination of wet chemical synthesis and atomic layer deposition (ALD). $\text{Y}_2\text{O}_3: \text{Er}^{3+}, \text{Yb}^{3+}$ core nanoparticles (NPs) were synthesized using the molten-salt synthesis. Enhanced luminescence was observed after deposition of a high quality shell of $\text{Y}_2\text{O}_3: \text{Yb}^{3+}$, roughly 5-10 nm thick, by radical enhanced ALD. However, the deposited shell layer has a slightly lower density, as shown in TEM imaging. The downconversion and upconversion luminescence spectra was collected for $\text{Y}_2\text{O}_3: \text{Er}^{3+}, \text{Yb}^{3+}$ NPs, 1 mol % Er^{3+} and the Yb^{3+} mol % ranging from 0 to 8 %, with a 980 nm diode excitation. The various NPs cores emitted strongly in the green (532 nm) and red (650 nm) upconversion luminescence and IR (1540 nm) downconversion luminescence, the ${}^2\text{H}_{11/2}, {}^3\text{S}_{3/2} \rightarrow {}^4\text{I}_{15/2}$, ${}^4\text{F}_{9/2} \rightarrow {}^4\text{I}_{15/2}$ and ${}^4\text{I}_{13/2} \rightarrow {}^4\text{I}_{15/2}$ transitions, respectively. A systematic luminescent red shift, ~2 nm, was observed when comparing the core to core-shell structures for all samples. Visible luminescence occurs via an energy transfer process, requiring two absorbed photons (red) and three absorbed photons (green), between the $\text{Yb}^{3+} {}^2\text{F}_{5/2}$ and $\text{Er}^{3+} {}^4\text{I}_{11/2}$ and ${}^4\text{I}_{13/2}$ energy levels. The proposed energy transfer mechanism incorporates the interaction between RE ions at the core-shell interface based on the local binding environment modeled using enhanced x-ray absorption fine structure (EXAFS) spectroscopy. Additionally, the energy transfer coefficients are extracted using the excitation lifetimes and the red-to-green ratio is correlated to key spectroscopic parameters, such as the Judd-Ofelt parameters and branching ratio. These values can be compared to the bulk Y_2O_3 luminescence and the actual measured lifetimes, 200 ms (green) and 600 ms (red), as the figure of merit.

4:20pm **EN+NS-WeA8 High Figure of Merit Nanostructured Bulk Thermoelectrics from Doped Pnictogen Chalcogenide Nanoplate Crystals**, *R.J. Mehta, C. Karthik, B. Singh, Y. Zhang, E. Castillo, T. Borca-Tasciuc, G. Ramanath*, Rensselaer Polytechnic Institute

Nanostructured pnictogen chalcogenides are attractive for realizing high thermoelectric figure of merit (ZT) materials for solid-state refrigeration and electrical power harvesting from heat. Here, we report a scalable surfactant-assisted microwave synthesis approach to realize bulk assemblies of sulfur-doped nanostructures with 25% to 250% higher room temperature ZT than the non-nanostructured bulk counterparts of both n- and p-type nanostructured bulk materials with room temperature ZT ~ 1. We synthesized ~5- to 20-nm-thick single-crystal hexagonal sulfur-doped nanoplates of the pnictogen chalcogenides in a microwave oven, followed by compaction and sintering to obtain bulk nanostructured pellets. The n-type material was obtained from single-component nanostructure assemblies of bismuth chalcogenides, while the p-type material was obtained by mixing bismuth telluride and antimony telluride nanostructures. Electron spectroscopy shows that <1% sulfur doping from thioglycolic acid, used as a nanoplate-sculpting and surface-passivating agent, increases the power factor $\alpha^2\sigma$ to ~5% greater than that of the state of the art alloys.

Electron microscopy analyses reveal that measured k values as low as 0.5 – 1.4 W/mK, which are ~50% lower than bulk alloys, are due to 50-100 nm grains with intragrain structural modulations with characteristic wavelengths between 3-10 nm. Our findings open up completely new possibilities for realizing novel high ZT thermoelectric materials through the assembly of doped single-crystal nanostructures.

4:40pm **EN+NS-WeA9 Core-Shell Nanodielectrics through Hybrid Wet Chemistry/Laser Process for Embedded Energy Storage Capacitors**, *B. Rajesh*, University of Houston, *N. Badi*, University of Houston and Integrated Micro Sensors, Inc., *A. Bensaoula, R. Supparesk, T.R. Lee*, University of Houston

Extensive interest is being invested into the research of nanodielectrics because of their promising applications in energy storage solutions as both discrete and embedded capacitors. They are useful in integral passive technology for miniaturization, improvement of power distribution and as decoupling capacitors. Their applications include, but are not limited to, high speed computing boards (servers, routers, super computers) and module boards (cell phones, PDA, note book computers). We fabricated high capacitance density dielectrics for flexible electronics by embedding core-shell type gold-silica nanoparticles in a polymer matrix using a coupled sol-gel procedure with laser engineering technique.

We report on fabrication of nanodielectric capacitors based on core-shell nanoparticles embedded in polyvinyl pyrrolidone (PVP) dielectric matrix. We developed a process chain to optimize the use of PVP as dielectric and measured its dielectric constant (K) as 7 at 10 KHz and breakdown field as 130V/ μm . Monodispersed core-shell nanoparticles (NPs) are prepared with two different structures: 1) 35nm gold core – 95nm silica shell and 2) coating 35nm gold NPs with polymer compatible self assembled monolayer (SAM). Pre-processing is performed to uniformly disperse the NPs in a polymer matrix and to selectively form the polymer shell around each of the nanoparticles. Post-processing is carried out to spin coat on substrates and to cure under UV light to make capacitor slabs.

The results from SEM and AFM analysis, thermal and frequency response, breakdown dielectric strength and dielectric loss of the films for different loadings of NPs will be reported in the talk. K value of 20 and breakdown field of 50V/ μm were measured for a dielectric with 10% loading of Au/SiO₂ NPs. Resulting capacitance value of 11.5nF/In² is in par with commercially available capacitor devices. It is worth mentioning that currently manufacturers use ceramic based dielectric material which makes it hard to manufacture (reproducibility, stability and cost) and shows limited flexibility (a requirement in modern printed circuit board technologies) due to high ceramic loading. Our fabricated nanodielectrics have the advantage of ease of fabrication and high flexibility due to the low metal loading.

It is forecasted that the effective permittivity of the dielectric and thereby the K value increases with loading of NPs till a percolation threshold is reached and then rapidly decreases with further loading. Future research is aimed at using other inexpensive metal NPs like silver and testing different polymers for best desirable characteristics of the capacitors.

5:00pm **EN+NS-WeA10 Characterization of Vertical InN Nanorods and InN-GaN Core-Shell Structures Grown by Merged Metal Organic Hydride Vapor Phase Epitaxy**, *V.U. Chaudhari, D. Wood, R. Krishnan, T.B. Song, T.J. Anderson*, University of Florida

The pseudobinary solid solution $\text{Ga}_x\text{In}_{1-x}\text{N}$ alloys exhibits a direct band gap in the range 3.4 to 0.7 eV and thus suitable for optoelectronic device applications. Recent simulations from our group have also suggested this alloy could produce high efficiency thin film photovoltaic devices on the order of 18% efficiency, similar to CIGS devices. The use of nanorod structures for light emitting and absorbing applications promises relatively high junction area, crystalline quality, and collection efficiencies. In addition, the nanorod assemblies are less rigid, and thus open to flexible substrates. The synthesis of nanorods with specific orientation, however, remains a challenge.

The synthesis of self-assembled, vertical InN nanorods and InN-GaN core shell nanostructures on Si without the need for a catalyst or template is reported. This self-catalyzed approach has made it possible to grow nanorods with uniform yet tunable diameter without any patterning of the substrate. The synthesis is performed in a Merged Metal Organic Hydride Vapor Phase Epitaxial growth system. This system allows growth of $\text{Ga}_x\text{In}_{1-x}\text{N}$ by either metal organic CVD, using trimethylgallium, trimethylindium and NH_3 , or hydride VPE in which the metal organic precursor is reacted with HCl. This presentation summarizes properties of the nanorods grown in the temperature range 560 to 600 °C at atmospheric pressure in N_2 . As revealed by transmission electron spectroscopy, the grown nanorods are defect-free, single crystal showing the wurtzite structure. Scanning electron microscopy and X-ray diffraction results reveal growth in vertical direction with (002) preferred orientation. The InN-GaN core shell structures exhibited a polycrystalline GaN shell with (002) and (101) preferred

orientations. This particular behavior of GaN is attributed to the high growth rates used. Annealing studies of these microstructures under ammonia atmosphere showed the absence of alloy formation with virtually no inter-diffusion of In and Ga.

5:20pm EN+NS-WeA11 Fabrication of InAs/GaAs Nanocomposites Using Ion Implantation, M.V. Warren, C. Uher, R.S. Goldman, University of Michigan, Ann Arbor

The controlled formation of semiconductor nanocomposites offers a unique opportunity to tailor functional materials with a variety of novel properties. In particular, nanocomposites consisting of InAs nanostructures embedded in GaAs have been proposed for high efficiency photovoltaics and high figure-of-merit thermoelectrics. A promising approach to nanocomposite synthesis is matrix-seeded growth, which involves ion-beam-amorphization of a semiconductor film, followed by nanoscale re-crystallization via annealing [1]. In earlier studies of In⁺ implantation into GaAs, the formation of InGaAs alloys upon annealing was reported [2-4]. Due to the large size difference between In and Ga, it is likely that phase separation occurs, especially for high indium fraction InGaAs alloys. Therefore, we are examining the possibility of selective formation of InAs-rich nanocrystals in a GaAs matrix using high dose In implantation into GaAs. However, Profile Code simulations suggest that the retained In dose in GaAs, $4.5 \times 10^{20} \text{ cm}^{-3}$, is limited by sputtering. To increase the concentration of implanted In, we have developed a sputter-mask method, for which a sacrificial layer with sputter yield lower than that of GaAs is used to prevent sputtering of GaAs:In. Using 100kV ions with fluences ranging from 3.8×10^{15} to $3.8 \times 10^{17} \text{ cm}^{-2}$, we have implanted In⁺ ions into GaAs with 50 nm sputter-masks consisting of AlAs. Following implantation, the films were annealed at 500 to 600°C for 30 to 60 s. We will discuss the influence of In⁺ dose and annealing conditions on the nucleation and growth of InAs, as well as the influence of nanostructuring on the temperature dependence of the resistivity and Seebeck coefficient of the implanted structures.

This work is supported in part by the GAANN Fellowship and the US Department of Energy, Office of Basic Energy Sciences as part of an Energy Frontier Research Center

[1] X. Weng, W. Ye, S. Clarke, A. Daniel, V. Rotberg, R. Clarke, and R.S. Goldman, *J. Appl. Phys.* **97**, 064301 (2005).

[2] M.V. Ardyshev and V.F. Pichugin, *Russian Physics Journal* **47**, 175 (2004).

[3] M. Kulik, F.F. Komarov, and D.D. Maczka, *Vacuum* **63**, 755 (2001).

[4] M. Kulik, A.P. Kobzev, D. Jaworska, J. Zuk, and J. Filiks, *Vacuum* **81**, 1124 (2007).

Graphene Focus Topic

Room: Brazos - Session GR+MS-WeA

Low Dimensional Carbon Device Manufacturing

Moderator: A.C. Diebold, The University at Albany-SUNY

2:00pm GR+MS-WeA1 Material Properties of Epitaxial Graphene in RF Devices, D.K. Gaskill, U.S. Naval Research Laboratory, J.S. Moon, HRL Laboratories, LLC, G.G. Jernigan, J.C. Culbertson, J.L. Tedesco, U.S. Naval Research Laboratory, J. Robinson, The Pennsylvania State University, P.M. Campbell, N. Garces, V.D. Wheeler, J.K. Hite, R.L. Myers-Ward, C.R. Eddy, Jr., A.L. Friedman, U.S. Naval Research Laboratory, M. Fanton, The Pennsylvania State University **INVITED**

The advent of the world's first epitaxial graphene (EG) RF field effect transistors (FETs), grown on semi-insulating SiC wafers, has generated tremendous interest in the electronics community since devices can be fabricated using conventional photolithographic approaches [1]. Recently, RF FETs have shown an f_{max} of 14 GHz at 5 V_{ds} for a 2 μm gate width and better results are expected as gate widths are scaled down. To push the performance metrics for wafer-scale EG FETs significantly higher, key materials issues must be addressed. Some of these issues are morphology and thickness control, enhanced mobility, uniformity of sheet carrier density and resistivity, and substrate defects. Here we describe NRL-HRL-Penn State approach in the DARPA CERA program for forming EG via Si sublimation from SiC wafers and the impact of material issues on RF device performance will be discussed.

Epitaxial graphene was synthesized using an Aixtron VP508 reactor on the Si- and C-faces of 4H- and 6H-SiC semi-insulating 0° oriented substrates from 1225 to 1700°C and for 10 to 300 min. Samples were 50.8 and 76.2 mm wafers and 16 x 16 mm² witnesses. Both *in-vacuo* (10⁻⁶ to 10⁻⁴ mbar) and Ar ambient (50-200 mbar) sublimation conditions were investigated. Growth conditions resulted in continuous EG on Si-face witnesses < 1 nm

thick as measured by atomic force microscopy, x-ray photoelectron spectroscopy and Raman spectroscopy, whereas growth on C-face witnesses could be varied, depending upon growth conditions, from island formation to continuous sheets > 10 nm thick. Using the witness samples, 300 K mobilities over 2,100 and 27,000 cm²V⁻¹s⁻¹ were found for 10x10 μm² sized Hall patterns for EG on the Si- and C-face of SiC, respectively.

The growth of EG on 50.8 mm Si-face wafers resulted in excellent relative resistivity uniformity of 2.8% and 300 K Hall mobilities up to 2,700 cm²V⁻¹s⁻¹ were found. Raman spectroscopy mapping of the 2D peak on the wafers determined: (1) the majority of the film was monolayer, (2) two layers of EG could be found at step edges and (3) EG was continuous across the wafer. RF FETs exhibited state-of-the-art ambipolar behavior such as electron field-effect mobility of 6,000 cm²V⁻¹s⁻¹ with I_{on}/I_{off} ratio of 19 and peak transconductance of 600 mS mm⁻¹ per 1 fF μm² gate oxide capacitance. The f_T•L_g performance metric of 10 GHz•μm was established. Additionally, we will discuss our recent work on EG growth on 76.2 mm wafers as well as the impact of morphological features and Ar ambient controlled graphenization on future RF devices.

Supported by DARPA CERA (N66001-08-C-2048) and ONR.

[1] J.S.Moon *et al.*, *IEEE Electron Dev Lett* **31**, 260 (2010)

2:40pm GR+MS-WeA3 In situ Growth, Microscopy, and Spectroscopy of Graphene Films, J. Hannon, IBM T.J. Watson Research Center **INVITED**

I will describe *in situ* low-energy electron microscopy (LEEM) studies of graphene synthesis on SiC and polycrystalline Ni substrates. Using spatially-resolved electron diffraction (LEED-IV), we have determined the atomic structure, layer thickness, and stacking sequence of individual graphene domains with sub-micron precision. Using spatially-resolved electron energy loss spectroscopy (EELS), we have correlated the local electronic and atomic structure. I will discuss how these measurements aid in interpreting transport measurements from these same samples. This work was performed in collaboration with Ruud Tromp.

4:00pm GR+MS-WeA7 High-frequency Transistors from Wafer-scale Epitaxial Graphene, Y.-M. Lin, IBM T.J. Watson Research Center **INVITED**

Graphene has generated enormous research interest because of its unique physical and electronic properties. In particular, a large part of the research interests and activities arise from the high intrinsic carrier mobility and saturation velocity in graphene that may lead to higher-frequency electronic devices/circuits than can be achieved by conventional semiconductor materials. Here we present the top-gated graphene transistors fabricated on two-inch graphene wafer.

Graphene was epitaxially grown on the Si face of a high-purity semi-insulating SiC 4H(0001) wafer by thermal decomposition, yielding a film of 1-2 layers of graphene over the entire wafer. The as-grown graphene film possesses an electron (*n*-type) carrier density of ~ 3x10¹² cm⁻² and a Hall-effect mobility between 1000–1500 cm²/V.s. In order to preserve the intrinsic mobility of graphene in the top-gated device structure, an interfacial polymer layer was spin-coated on the graphene prior to the oxide deposition. The carrier mobility of top-gated Hall bar devices varied between 900-1520 cm²/V.s across the two-inch wafer, indicating that little degradation in graphene mobility.

The cutoff frequency *f*_T is obtained from the high-frequency S-parameters measurements, which signifies the highest frequency at which a transistor can propagate an electrical signal. For a gate length of 550 nm, the measured *f*_T ranges between 20 to 53 GHz. For a shorter gate length of 240 nm, *f*_T as high as 100 GHz was measured. This 100 GHz cutoff frequency is the highest speed achieved to date for any type of graphene devices, including exfoliated and CVD -grown graphene. Further enhancement in the device performance is expected to be achieved by continued improvements in the electrical characteristics of epitaxial graphene and the gate length scaling.

*In collaboration with K. Jenkins, D. Farmer, C. Dimitrakopoulos, H.-Y. Chiu, A. Valdes-Garcia, A. Grill, and P. Avouris.

4:40pm **GR+MS-WeA9 Graphene-on-SiC and Graphene-on-Si MOSFETs on 75 mm Wafers**, J.S. Moon, D. Curtis, M. Hu, S. Bui, D. Wheeler, T. Marshall, HRL Laboratories, LLC, D.K. Gaskill, P.M. Campbell, Naval Research Laboratory, P. Asbeck, University of California at San Diego, G.G. Jernigan, J.L. Tedesco, R.L. Myers-Ward, C. Eddy Jr., Naval Research Laboratory, X. Weng, J. Robinson, M. Fanton, Penn State University **INVITED**

In this talk, we present recent progress in epitaxial graphene n-MOSFETs and p-MOSFETs on both SiC and Si substrates for graphene-on-SiC and graphene-on-Si technologies. Both graphene MOSFETs were fabricated in a self-aligned manner on 75 mm wafers and exhibited gate-controlled ambipolar characteristics. For the graphene MOSFETs on SiC substrates, the graphene was grown by Si-sublimation of Si-face 6H-SiC substrates in a commercial Aixtron VP508 epitaxial reactor. For the graphene MOSFETs on Si substrates, the graphene was synthesized by graphitizing a thin 3C-SiC layer grown on float-zone Si (111) substrates using a halogen process. Figure 1 shows sheet resistance maps of 3-inch graphene-on-SiC and graphene-on-Si wafers. Typical Hall mobility ranges from 500 to 2000 cm^2/Vs depending on electron carrier density. Both graphene MOSFETs were fabricated with a gate oxide layer and metal gate stack. The gate length was 3 μm . The graphene-on-SiC MOSFETs showed excellent I-V saturation behavior as shown in Figure 2(a). Figure 2(b) shows measured ambipolar behaviors with n-type MOSFET at $V_{\text{gs}} = 0 \text{ V}$, while p-type behaviors are observed at $V_{\text{gs}} < -1.5 \text{ V}$. An $I_{\text{on}}/I_{\text{off}}$ ratio of 33 was measured. Figure 2(c) shows measured peak transconductance of 600 mS/mm at $V_{\text{ds}} = 3 \text{ V}$. Figure 3 shows the extrinsic field-effect mobility of 6000 cm^2/Vs for electron and of 3200 cm^2/Vs for hole obtained at an effective electric field of $\sim 0.27 \text{ MV}/\text{cm}$, approaching Dirac point. The measured graphene field-effect mobility is eight to 10 times higher than that of ITRS Si n-MOSFETs and ~ 80 times higher than that of ultra-thin-body SOI n-MOSFETs.

The graphene-on-Si MOSFETs are fabricated in a similar manner. Figure 4 shows measured transfer curves of graphene-on-Si MOSFETs, showing ambipolar behaviors with the Dirac point close to zero gate bias, unlike the graphene-on-SiC MOSFETs. The on-state current is measured at 50 to 125 mA/mm with $I_{\text{on}}/I_{\text{off}}$ ratio of 3 to 2, respectively. This is the highest performance observed among graphene-on-Si technologies so far. RF performance of graphene FETs will be discussed. This work was supported by DARPA, monitored by Dr. M. Fritze, under SPAWAR contract number N66001-08-C-2048.

The views, opinions, and/or findings contained in this article/presentation are those of the author/presenter and should not be interpreted as representing the official views or policies, either expressed or implied, of the Defense Advanced Research Projects Agency or the Department of Defense.

[1] C. Berger et al., Science, vol. 312, p. 1191, 2006; J.S. Moon et al., IEEE EDL, vol 30, p650, 2009

[2] H. Kang et al., ISDRS, 2009

In Situ Microscopy and Spectroscopy Topical Conference

Room: Acoma - Session IS+BI+AS-WeA

In Situ Microscopy/Spectroscopy – Biological Interfaces

Moderator: M. Grunze, University of Heidelberg, Germany

2:00pm **IS+BI+AS-WeA1 Adsorption and Phase Transition of Liposomes via Attenuated Total Reflectance Fourier Transform Infrared Spectroscopy**, M.R. Hernandez, T.C. Ng, E.N. Towns, B.C. Walsh, D.P. Land, University of California at Davis

Liposomes are becoming increasingly prevalent as an important part of drug delivery systems in modern medicine, however a better understanding of the physical characteristics is needed. In this study we present our results on the stability and adsorption of liposomes formulated from dipalmitoylphosphatidylcholine (DPPC) via attenuated total reflectance Fourier transform infrared (ATR-FTIR) spectroscopy. The phase transition temperature of liposome formulations of pure DPPC, DPPC and cholesterol, and DPPC, cholesterol, and 1,2-Distearoyl-phosphatidylethanolamine-methyl-polyethyleneglycol-2000 (DSPE-mPEG2000) is determined using a temperature dependant study (25°C to 50°C) and been found to occur abruptly around 41°C for pure DPPC liposomes and exhibit gradual temperature changes from 35°C to 43°C for the other two liposome formulations. We have studied the adsorption characteristics of different formulations of liposomes with both hydrophobic and hydrophilic surfaces created by different self-assembled monolayers, and will present a new method for studying an in vitro way of studying the adsorption of different formulations of liposomes onto a surface of immobilized proteins. Knowing

the stability of liposomes and liposome-protein adsorption characteristics allows for a better understanding of their use and design of future formulations in drug delivery systems.

2:20pm **IS+BI+AS-WeA2 Synchrotron Based Infrared Imaging at the Diffraction Limit**, J. Nasse, University of Wisconsin-Milwaukee, C. Gohr, A. Rosenthal, Medical College of Wisconsin, C. Hirschmugl, University of Wisconsin-Milwaukee

A new mid-infrared beamline (IRENI) extracting a large horizontal swath of radiation ($320 \text{ hor.} \times 25 \text{ vert. mrad}^2$) to homogeneously illuminate a commercial IR microscope equipped with an infrared Focal Plane Array (FPA) detector has recently been commissioned at the Synchrotron Radiation Center in Stoughton, WI. This new facility provides the opportunity to obtain chemical images with diffraction-limited resolution, for all wavelengths in the mid-IR concurrently, in minutes. The design of this facility and an initial application will be presented.

IRENI combines a bright IR synchrotron source to an FTIR microscope with a multi-element detector for wide-field imaging as opposed to the common dual-aperture geometry with raster scanning that is available at most synchrotron IR beamlines. The swath of radiation from the SRC is extracted as 12 beams and recombined into a 3×4 bundle of beams that is refocused onto a sample plane of an infrared microscope illuminating $40 \times 60 \text{ micron}^2$ sample area. The sampled spatial resolution is defined by both the magnification after the sample and the FPA pixel size. Here, a 74x Schwarzschild objective achieves effective geometric pixel sizes of $0.54 \times 0.54 \text{ micron}^2$, which is approximately $\lambda/4$ for even the shortest wavelength of $2 \mu\text{m}$. This spatial oversampling provides adequate information to obtain concurrent, diffraction-limited images across the entire spectral range. In addition, the spectral quality is excellent, since the high density, stable, broadband flux from the synchrotron achieves high quality spectra for $0.54 \times 0.54 \text{ micron}^2/\text{pixel}$ using similar measuring times as table-top instruments that image $5.5 \times 5.5 \text{ micron}^2/\text{pixel}$.

The presence of calcium-containing crystals, including calcium pyrophosphate dihydrate (CPPD) and hydroxyapatite-like basic calcium phosphate (BCP), in synovial fluids plays a major role in cartilage degeneration in osteoarthritis. Models of calcium crystal formation tend to produce small, sparse crystals embedded in debris enriched in proteins, lipids, and carbohydrates, which interfere with many identification techniques. Synchrotron FTIR imaging circumvents difficulties in identifying these crystals and also allows for characterization of the surrounding matrix. We present results from well-characterized models of calcium crystal formation that demonstrate our ability to both identify crystals *in vitro* and characterize the matrix surrounding these crystals.

This work has been done with support from an NSF Major Research Instrumentation grant (DMR-0619759) and the Synchrotron Radiation Center, which is also supported by NSF (DMR-0537588).

2:40pm **IS+BI+AS-WeA3 Proteins and Lipids at Liquid/Solid Interfaces: In situ Studies by Neutron Reflectometry and Infrared Spectroscopy**, M. Strobl, M. Kreuzer, University of Heidelberg, Germany, M. Reinhardt, R. Steitz, Helmholtz Zentrum Berlin, Germany, M. Grunze, R. Dahint, University of Heidelberg, Germany **INVITED**

Proteins and lipids at liquid/solid interfaces are of crucial importance in the design of biofunctional interfaces. For example, adsorbed protein layers determine the biocompatibility of implants and may control bacterial adhesion. Upon surface contact, proteins commonly undergo structural changes, which will alter their activity and biological function. In combination with lipids, proteins are valuable model systems to mimic cell membrane function. Thus, in order to improve our understanding of biofunctional interfaces, a strong need exists to develop surface analytical tools, which facilitate *in situ* characterization on a molecular level.

Due to its *in situ* capability, non-destructive character and the short wavelength of neutron beams, neutron reflectometry offers a very attractive approach to the analysis of layer structures on the nanometer scale. It provides detailed information on the amount of adsorbed species as well as on the thickness, density and hydration of the adsorbate. In combination with surface sensitive infrared spectroscopy (ATR-FTIR), additional information is obtained on specific molecular groups of the adsorbate as well as on molecule conformation.

We will report on the set-up of a new time-of-flight neutron reflectometer at the Helmholtz Center Berlin, which is especially adapted to biological samples and, for the first time, facilitates simultaneous *in situ* ATR-FTIR characterization. Dedicated sample environments have been developed to study biological films as a function of applied pressure, shearing forces and temperature. As a potential application, we discuss the phase behavior and stability of immobilized oligolamellar lipid bilayer films under load and shear, which are important in bio-lubrication and the search for advanced implant materials, such as artificial joints. A second example will focus on

the impact of surface chemistry and structure on the activity of immobilized proteins.

4:00pm **IS+BI+AS-WeA7 Biological Imaging with Coherent X-rays: The Lens-less Approach to High Resolution**, *A. Beerlink*, Universität Göttingen, Germany **INVITED**

Understanding molecular functions in complex environments such as biological cells or novel composite materials are a prerequisite for the advancement of nano and biomedical sciences. They require a combination of high spatial resolution, quantitative contrast and

full compatibility with environmental conditions, such as aqueous media. To this end, the potential of x-ray imaging is not yet fully developed, but currently undergoes rapid progress. While classical x-ray microscopy based on Fresnel zone plates has matured and provides useful structural information in a growing range of applications, this technique is severely limited by the nanostructuring process of the lenses. In

recent years, novel lens-less approaches for imaging have emerged, where the object functions are reconstructed from the measured intensities

either in the far-field regime, or under near-field conditions (propagation imaging). We present experiments using x-ray quasi point sources to illuminate the sample in combination with digital recording of the resulting diffraction patterns. One focus is the applicability towards biological samples, for which the imaging properties of the different coherent microscopy approaches will be compared. In this context, recent results obtained with ultrabright femtosecond pulses provided by the free electron laser FLASH will be presented and accessible information complementary to synchrotron imaging will be discussed.

4:40pm **IS+BI+AS-WeA9 Dielectric Constant and Polarization of Biomolecules Determined by Torsional Resonance Nanoimpedance Microscopy**, *K. Kathan-Galipeau, S.U. Nanayakkara, P.A. O'Brien, B.M. Discher, D.A. Bonnell*, University of Pennsylvania

We have developed a new technique, torsional resonance nanoimpedance microscopy (TR-NIM), that allows for the measurement of frequency-dependent local transport properties on soft materials. AFM measurements at torsional resonances provide a key advantage: the ability to achieve low-force scanning while maintaining the tip in the near-field. As a result, it is possible to measure impedance between the tip and sample without damaging the sample.

This technique has been used to determine the resistance, capacitance, and dielectric properties of a novel class of biomolecules. These redox active molecules, known as maquettes, consist of dimers and tetramers of alpha helix polypeptides and provide a convenient functional alternative to natural proteins. Maquettes are capable of binding a range of cofactors; this study examines the properties of iron and zinc porphyrins. Maquettes serve as a benchmark for integrating electronics with biologically inspired materials that possess unique characteristics, such as electron-transfer capability, the possibility of gating redox activity, optoelectronic functionality, and nanometer size.

In order to determine the behavior of these functional biomolecules on electrodes, PDMS stamping was used to create stripes that alternate between maquettes and bare graphite. Stamping also allowed us to control the assembly of the redox-active maquettes from multilayers to horizontally oriented monolayers (maquettes laying down) and vertically oriented monolayers (maquettes standing up) by varying the stamping time and the concentration of the maquettes in organic solvents.

Interestingly, we observe that the resistance decreases with increased height of maquettes, which is explained in terms of the configurations of the molecules on the electrode. The dependence of local impedance on exposure to optical radiation revealed an increase in capacitance and decrease in resistance when the maquettes are exposed to 425 nm light. This is true for both zinc and iron porphyrin cofactors. We attribute the decrease in resistance to photoactivated current. The increase in capacitance is due to an increase in the polarizability of the maquettes.

5:00pm **IS+BI+AS-WeA10 Dynamic Observation of Phospholipid Model Cell Membranes and Particles by STM and Vibrational Spectroscopy**, *T. Yamada*, RIKEN, Japan, *S. Matsunaga*, The University of Tokyo, Japan, *T. Kobayashi*, RIKEN, Japan, *M. Kawai*, The University of Tokyo, Japan

Scanning tunneling microscopy (STM) and other surface-scientific techniques can be utilized to explore the microscopic dynamics of biological molecules in the context that the techniques are applicable for solid surfaces immersed in aqueous solutions. We devised STM and vibrational spectroscopies to make usable for molecular monolayers at solid-liquid interface. We attempted to observe phospholipid layers formed on octanethiol-terminated gold (111) single-crystalline substrates placed in aqueous buffer solutions (in situ STM). By in situ STM we could observe

dihexanoyl-*sn*-glycero-3-phosphocholine (DHPC), a relatively short kind of lipid, forming a fluidic monolayer. A crystalline phase of this monolayer was observed by applying an electrode potential compatible with the membrane potentials of real cells. Furthermore, mixed lipid layers have been examined by STM [1]. We found some nanometer-scale raft structures (phase-separated domains), which are functionally characteristic for real cell membranes. We also studied phospholipid particles suspended in buffer solutions. Suspensions were prepared from a phosphocholine (PC) and an ethanolamine (PE), consisting of nanometer-scale phospholipid particles with narrow size distribution. In situ STM revealed particles with a diameter ~ 10 nm (named "minimal lipid particles (MLP)"), forming a monolayer along the Au(111). It is known that some categories of antibiotics selectively attack lipids contained in germ cell membranes and disintegrate the whole cells. We chose "duramycin", a 19-residued peptide antibiotic, which specifically binds PE. When the total concentration of phospholipid was controlled between 100 μ M and 500 μ M, a layer of MLP was discerned. During STM scanning, 7 μ M of duramycin solution was added into the suspension, and the PC+PE MLP became fragile and seemed to be scratched by the tip, ending up with a widespread multilayer. This sort of highly leveraged effect of duramycin is characteristic in the action of antibiotics [2]. These works demonstrated the advantage of STM in monitoring the live nanometer-scale reactions of biological entities, which have not been recognized experimentally so far. We expect more application of STM in physiological investigation in cell biology.

[1] S. Matsunaga et al., *Electrochem. Commun.* **9** (2007) 645.

[2] S. Matsunaga et al., *Langmuir* **25** (2009) 8200.

5:20pm **IS+BI+AS-WeA11 Rapid In-Situ Assessment for Microbes on Simultaneously Prepared Plate with Substrate and Zirconium Based Thin Film Metallic Glasses (TFMGs)**, *P.T. Chiang*, I-Shou Univ./Fooyin Univ. Hospital, Taiwan, Republic of China, *G.J. Chen, H.H. Liu, Y.H. Shih*, I-Shou Univ., Taiwan, Republic of China, *J.P. Chu*, National Taiwan Univ. of Science and Technology, Taiwan, Republic of China, *J.S.C. Jang*, National Central Univ., Taiwan, Republic of China

ZrAlNiCuSi TFMGs could modify the stainless steel's surface with high hardness, scratch-adhesion capabilities. Zr-based TFMGs' smooth surface could decrease and prolong the lag phase of microbes' growth for at least 24 hours.

The actual numbers of pathogenic bacteria might be underestimated by conventional methods due to sublethal injury, malnutrient's and other physiological factors which reduce bacterial viability. Moreover, these methods would limit the real-time quantitative detection and easily cause contaminations with bias.

Rapid comparisons in the same culture condition are obtained on a simultaneously prepared plate with substrate and Zr based TFMGs. By utilization of GFP plasmid (pGLO) into HB101 with 10mM arabinose induction, we could measure the intensity of green fluorescence by LAS-3000 fluorescent detector to setup the real-time monitor system for observation of bacterial growth on TFMGs' surface.

This integrated method was time-saving, cost-effective and simple. The serially rapid in situ monitor of the microbial growth will emerge as a novel tool to realize the TFMGs or other materials' antimicrobial properties.

Late Breaking Session

Room: Cimmaron - Session LB-WeA

Late Breaking Session Featuring Talks on Energy, Graphene and Atom-Probe Tomography

Moderator: E.S. Aydil, University of Minnesota

2:00pm **LB-WeA1 Studying Low-Resistance Silicide Contacts using Atom-Probe Tomography**, *P. Adusumilli*, Northwestern University and PNNL, *C.E. Murray*, IBM Thomas J. Watson Research Center, *L.J. Lauhon*, *D.N. Seidman*, Northwestern University

Improvements in energy efficiency of electronic devices are receiving increased attention. The increasing power consumption of complementary-metal-oxide-semiconductor (CMOS) transistors leads to large power dissipation and high chip-temperatures and has implications for device performance and battery life. Scaling of contact area, source/drain junction depth, and contact silicide thickness leads to an increase in the parasitic resistance in the circuit. The fundamental contact-scaling problem arises from the lateral scaling of the contact area in two dimensions. Therefore, the contact resistivity associated with the interface between the source/drain contact and doped contact silicon ultimately becomes the dominant component of the overall source/drain parasitic resistance. There is a need

for low barrier height contacts, which can lead to low parasitic resistance and consequently to lower power consumption, heat dissipation and longer battery life times.

Nickel monosilicide has been the material of choice for source/drain contacts to CMOS transistors in recent technology generations. Alloying with nominal amounts of transition metals, such as Pt or Pd, has been employed to overcome the integration challenges faced during processing. These include agglomeration of this low resistivity NiSi phase; and phase transformation to the higher resistivity NiSi₂ phase during fabrication. Local-electrode atom-probe (LEAP) tomography is used in this study to map three-dimensional (3D) distributions of Pt or Pd in Ni monosilicide thin films to obtain insights into the role played by these transition metal elements in phase stabilization. Solid-solutions of Ni_{0.95}M_{0.05} (M = Pd or Pt) thin films on Si (100) substrates are subjected to rapid thermal annealing to form the monosilicide phase. Focused-ion-beam milling is employed to implement the lift-out technique to prepare LEAP tomography samples.

Pt and Pd segregate at the silicide/silicon heterophase interface for Ni_{0.95}Pt_{0.05} and Ni_{0.95}Pd_{0.05} thin films. A measured decrease of the interfacial Gibbs free energy due to segregation at the silicide/silicon interface is most likely responsible for the stabilization of the monosilicide phase at elevated temperatures. Quantitative evidence for short-circuit diffusion of Pt via grain boundaries in the NiSi phase is observed in 3D direct space, providing valuable insights into the kinetics of the reactive diffusion process. The high spatial resolution and the unique 3D nature of the measurements yields accurate and precise measurements of both the lattice and grain boundary diffusivities of Pt. This discovery underscores the importance of interfacial phenomena in the stabilization of this low-resistivity phase and may help explain modification of NiSi texture, grain size, and morphology caused by Pt. The silicide surface work function shifts to the Si valence band edge with Pt incorporation. Additionally, the silicide/Si heterophase interface was reconstructed in three-dimensions on an atomic scale and its chemical roughness evaluated.

This research is supported by the Semiconductor Research Corporation/Global Research Collaboration. The specimens employed were obtained from IBM T. J. Watson Research Center. Acknowledgements are due to IBM Research for an IBM PhD Fellowship for the academic year 2009-2010.

2:20pm LB-WeA2 Epitaxial Graphene Growth on Step Free Mesas: Towards Layer Thickness Homogeneity, L.O. Nyakiti, V.D. Wheeler, N. Garcés, R.L. Myers-Ward, J.C. Culbertson, J.K. Hite, C.R. Eddy, Jr., F.J. Bezares, J.D. Caldwell, G.G. Jernigan, E.A. Imhoff, D.K. Gaskill, U.S. Naval Research Laboratory

Epitaxial graphene (EG) has exciting material properties that promise advancements in electronics, specifically in the fabrication of RF field-effect transistors. When EG is grown on the 4H- or 6H-SiC (0001), step-bunching occurs [1] with vertical morphology of 5 – 10 nm which poses a challenge to device development. Additionally, surface steps in graphene show a conductance difference between paths parallel and perpendicular to the step direction [2]. Hence to fabricate device structures, it is highly desirable to place devices on the relatively narrow (~2-4µm) terraces. In this work, we use large area, step-free 4H-SiC mesas (SFMs) to form EG and the results are found to mitigate the terrace (step bunching) related challenges present in traditional on-axis 4H-SiC (0001) wafer growth

Hexagonal and square SFMs with side dimensions ranging from 40 to 200 µm were formed by homoepitaxial growth of (0001) 4H-SiC layers [3] using a kinetically-controlled lateral step flow growth process at 1580°C, resulting in atomically flat mesas devoid of surface defects. This was followed by EG growth in a 100 mbar Ar ambient at 1620°C for 1.5 or 2.5 hours. Nomarski microscopy was used in the identification of mesas having specular surfaces, or single stepped and defective surfaces. Micro-Raman spectroscopy and surface mapping using a laser excitation of 514.5 nm was employed to confirm the presence, thickness and strain variation of EG across the mesas. Veeco D3100 AFM (tapping mode) and LEO Supra 55 Scanning Electron Microscope was used to extract surface morphology variations across mesas.

Preliminary results show that 1.5 and 2.5 hours of EG growth were more than sufficient for complete uniform monolayer and bilayer graphene coverage on the mesas, respectively. The surface of the EG on SFMs had atomic steps ≤ 0.6 nm, a reduction in step-height by a factor of 30 from typically grown step-bunched graphene on 4H-SiC (0001) substrates. Raman 2D peak position maps for monolayer and bilayer regions show relatively low strain (~2700cm⁻¹) coverage with the former approaching values close to exfoliated graphene (~2696cm⁻¹). Thus, the use of large area SFMs for EG has resulted in novel characteristics that holds great promise towards controlling layer thickness homogeneity without step bunching and having minimal strain.

References

[1] Tedesco, J. L.; et al *ECS Trans.* 2009, 19, 137-150.

[2] Yakes, M. Y.; et al *Nano lett.* 2010, 10, 1559-1562.

[3] Neudeck, P. G.; et al *MRS symp. Proc.* 911, 2006

2:40pm LB-WeA3 Functionalizing Graphene for ALD using a Simple Wet Chemical Treatment, V.D. Wheeler, N. Garcés, J.L. Tedesco, L.O. Nyakiti, R.L. Myers-Ward, G.G. Jernigan, J.K. Hite, D.K. Gaskill, C. Eddy Jr., U.S. Naval Research Laboratory

Realizing graphene-based technologies requires both large-area graphene production and integration with scalable high-k gate dielectrics. Thermal atomic layer deposition (ALD) provides a means to achieve high-quality ultrathin dielectric films below 300 °C, but the hydrophobic and chemically inert nature of the graphene surface inhibits direct application of ALD oxides. Several methods have been utilized to functionalize the surface of graphene for ALD including: deposition of a metal seed layer^[1], an ozone pretreatment^[2], and using a low-κ polymer seed layer^[3]. Although some success has been achieved, these techniques are complex and often result in degradation of the graphene mobility. In this work, we present a simple wet chemical surface treatment which functionalizes the surface of graphene and results in conformal, uniform Al₂O₃ films.

Epitaxial graphene was synthesized on semi-insulating, on-axis 4H- and 6H-SiC substrates (16x16mm²) using an Aixtron/Epigress VP508 SiC growth reactor at temperatures from 1600 to 1650 °C for a duration of 60 to 180 min. Samples were grown in an Ar ambient at a constant pressure of 100 mbar. All samples underwent an optimized wet chemical surface treatment before oxide deposition to render the graphene susceptible to ALD process. This *ex-situ* treatment consisted of an HF dip (25 wt. %) for 2 min. at room temperature followed by soaking in SC1 (1 H₂O₂:1 NH₄OH:5 H₂O) at 80 °C for 10 min. Samples were then rinsed in DI and blown dry in N₂. ALD of Al₂O₃ was carried out in a Cambridge NanoTech 200 at 225 °C with trimethylaluminum and deionized (DI) water precursors, under conditions which yielded a growth rate of ~1.1 Å/pulse cycle. Initial pulse sequences and final oxide thickness (10-30 nm) were varied to determine the effect on oxide coverage. Al₂O₃ coverage and uniformity was characterized with atomic force microscopy, scanning electron microscopy, and X-ray photoelectron spectroscopy, while mobility changes were ascertained with van der Pauw Hall measurements.

Results show that a 30 nm conformal, uniform Al₂O₃ film can be obtained using a simple wet chemical surface treatment prior to ALD. Mobility was maintained indicating little impact of the pretreatment or deposited oxide on the underlying graphene properties. While the initial pulse sequence had minimal effect on the coverage and uniformity of thick films, it is a significant factor in obtaining conformal thin films (< 30 nm). Better coverage with thinner films was achieved using 10 initial water pulses. Key to the success of this approach is the ability to nucleate on both terraces and step edges. Variations in coverage as a function of oxide thickness and deposition temperature will also be discussed.

Since graphene growth on Si-face SiC substrates results in a surface morphology with step heights on the order of 5-10 nm, only the 30 nm oxide was completely uniform. We hypothesize that the steps inhibit deposition of ultrathin conformal films (≤ 10 nm) needed for scaling of devices. Therefore, we have deposited thin Al₂O₃ films on step-free graphene mesas^[4] to elucidate the affect of steps on oxide uniformity and obtain the ultimate limit of this wet chemical approach.

[1] J.A. Robinson, et.al. *ACS Nano* **4**(5) 2667-2672 (2010).

[2] B.Lee, et.al. *ECS Transactions* **19**(5) 225-230 (2009).

[3] D.B. Farmer, et. al. *Nano Letters* **9**(12) 4474-4478 (2009).

[4] L.O.Nyakiti, et.al. presented at STEG conference, Amelia Island, FL 2010.

3:00pm LB-WeA4 Photoelectrochemical Water Splitting by Hematite Nanorod Arrays Prepared by Aqueous Solution Growth, R. Moorish, Colorado School of Mines, M. Rahman, D. MacElroy, University College Dublin, Ireland, C.A. Wolden, Colorado School of Mines

Hematite (α-Fe₂O₃) is a promising material for sustainable generation of H₂ due to its low cost, widespread availability, chemical stability, and ability to absorb a significant fraction of visible light. However numerous challenges remain in order for this material to approach its theoretical potential of 15% solar to hydrogen efficiency. The two most important metrics for photocurrent are its onset potential and the current plateau. The latter is a measure of the fraction of photo-generated carriers that are extracted to perform water splitting. In this work we address this challenge through the production of oriented nanorod arrays on fluorine-doped tin oxide (FTO) coated glass using the approach developed by Vayssieres and coworkers.[1] This simple aqueous solution method is scalable and employs low cost precursors. In previous studies well-developed arrays of vertical nanorods were formed, by unfortunately such structures yielded poor

photoelectrochemical performance ($<5 \mu\text{A}/\text{cm}^2$). [2] In this paper it is shown that the temperature used for post-deposition calcination has a profound impact on material properties and performance. The critical temperature is found to be $\sim 725^\circ\text{C}$. Films calcined below this temperature displayed negligible photocurrent, while samples treated at above had dramatic improvement in photocurrent density. The enhanced performance is correlated with increased optical absorption and improved crystallinity, which are thought to enhance carrier generation and transport, respectively. Electron microscopy and energy dispersive spectroscopy suggests that significant diffusion of tin from the FTO into the Fe_2O_3 matrix occurs during high temperature annealing process. The benefits of this process may include enhanced conductivity as well as improvement of the FTO/ Fe_2O_3 interface. Initial testing of these films under simulated sunlight produced photocurrent densities $>300 \mu\text{A}/\text{cm}^2$ at 1.23 V versus the reversible hydrogen electrode, a 100-fold increase over previous reports. In this presentation we will discuss the sensitivity to process conditions, and update further improvements achieved to the system.

References

[1] L. Vayssieres, N. Beermann, S. E. Lindquist, and A. Hagfeldt, "Controlled aqueous chemical growth of oriented three-dimensional crystalline nanorod arrays: Application to iron(III) oxides," , 233-235, (2001).

[2] N. Beermann, L. Vayssieres, S.-E. Lindquist, and A. Hagfeldt, "Photoelectrochemical Studies of Oriented Nanorod Thin Films of Hematite," , 2456-2461, (2000).

4:00pm **LB-WeA7 Polymer Molded Templates for Nanostructured Vertical Amorphous Silicon Photovoltaics**, L. Pei, A. Balls, C. Tippets, M.R. Linford, R. Vanfleeter, R.C. Davis, Brigham Young University

Although amorphous silicon photovoltaics is a mature commercial technology, these potentially low cost thin film photovoltaic devices still suffer from either incomplete absorption of the light that excites electrons to higher energy states where they can generate electrical power or the loss of these energetic electrons in the material before they can be collected. This results in a tradeoff between producing a cell thick enough to absorb the incident light but thin enough that excited electrons can be extracted from the silicon before they are lost to recombination through electron traps (that are present at high density in these low cost thin films). To overcome these problems, complicated triple junction cells are fabricated that reduce these problems but increase the costs to rival that of crystalline cells.

We propose to address this trade off by changing the amorphous silicon layers from planar to a vertical 3-D nanostructured geometry that will result in long optical absorption paths and high light absorption even for very thin silicon layers. Choosing the dimensions of the nanostructured vertical geometry carefully will also result in low top surface reflection. The combination of low surface reflection, long optical absorption path length, and reduced electron trapping will yield significantly higher thin film device quantum efficiencies. The much thinner required layers will also result in higher throughput for expensive Si deposition equipment.

Modeling the increased path length in amorphous Si:H indicates the increase in absorption due to the vertical geometry could be in the range of 30 %. The vertical geometry will introduce several other effects that should increase efficiency over current practice, these effects include improved series resistance, electrical contact geometries, reduced reflection, and stability gains. There are also negative secondary factors that must be considered; these include a larger junction interfacial area resulting in both a larger dark current and a larger doped semiconductor absorption loss. Factoring in these positive and negative effects, we fully expect to demonstrate vertical cells with efficiency gains of at least 15% relative to planar control cells. This would be a very significant gain as amorphous silicon is currently considered a relatively stable, well developed technology.

It is essential that these vertical structures be fabricated at low cost. To fabricate these structures, we formed three dimensional nanoscale vertical patterns in a polymer layer on a glass substrate. This pattern acts as a template during Si device layer deposition to generate the desired vertical device geometry. The nanostructured template has high aspect ratio features down to 300 nm and would add far too much cost if standard nanofabrication patterning and etching processes were used, consequently we have developed templates using a low cost high aspect ratio polymer molding process that allows us to rapidly create these structures. Amorphous silicon PIN layers have been deposited on these templates and we have performed optical transmission and reflection studies on the patterned and unpatterned regions of the samples to determine the effects of templated fabrication on light capture.

4:20pm **LB-WeA8 Nanocrystalline Silicon Film Growth Morphology Control through RF Waveform Tailoring**, J.-P. Booth, LPP-CNRS, Ecole Polytechnique, France, E.V. Johnson, LPICM-CNRS, Ecole Polytechnique, France, T. Verbeke, LPP-CNRS, Ecole Polytechnique, France, J.-C. Vanel, LPICM-CNRS, Ecole Polytechnique, France

Deposition of device-quality microcrystalline silicon thin films at an adequate rate is a key challenge in the fabrication of thin film silicon tandem photovoltaic modules for viable large-scale power generation. Conventionally films are deposited using sinusoidal RF excitation of parallel plate reactors containing lean $\text{H}_2\text{-SiH}_4$ mixtures. Higher voltages increase the deposition rate, but also increase the ion bombardment energy which degrades the film, thus limiting the deposition rate of high quality films to $>1 \text{ nm/s}$ for RF excitation at 13.56 MHz. We have investigated plasma excitation using non-sinusoidal waveforms to decouple the injected RF power from the ion bombardment. Films were deposited in $\text{Ar/SiF}_4/\text{H}_2$ plasmas and were characterised using in-situ spectroscopic ellipsometry.

We demonstrate the application of RF waveform tailoring to generate an electrical asymmetry in a capacitively coupled plasma-enhanced chemical vapor deposition system, and its use to control the growth mode of hydrogenated amorphous and nanocrystalline silicon thin films deposited at low temperature (150°C). A dramatic shift in the DC bias potential at the powered electrode is observed when simply inverting the voltage waveform from "peaks" to "troughs", indicating an asymmetric distribution of the sheath voltage. By enhancing or suppressing the ion-bombardment energy at the substrate (situated on the grounded electrode), the growth of thin silicon films can be switched between amorphous and nanocrystalline modes, as observed using in-situ spectroscopic ellipsometry. The effect is observed at pressures sufficiently low that the collisional reduction in average ion bombardment energy is not sufficient to allow nanocrystalline growth ($<100\text{mTorr}$).

4:40pm **LB-WeA9 Numerical Ellipsometry: N-K Plane Analysis of Transparent Conducting Films for Solar Applications**, D. Barton, F. Urban, Florida International University

This work presents a new kind of ellipsometric data analysis applied to an Indium Tin Oxide thin film, characterized by an energy window of electromagnetic transparency capable of passing solar energy and at the same time having usable electron conductivity elsewhere. The work presents very recent advances in the n-k plane data analysis method that allow greatly improved accuracy in modeling these films for multiple layers. Solution accuracy is orders of magnitude better than least squares, the method in common use. It is well known that such materials are optically opaque (have high extinction coefficients, k) both at energies higher than the high energy window edge and at energies below the lower window edge. Such materials present a particular challenge to ellipsometry data analysis due to these different optical behaviors across the measurement wavelength range. Data reported here were taken on an Indium Tin Oxide (ITO) film grown on a silicon substrate to a nominal thickness of 400 nm. Measurements were taken at 293 wavelengths, every 5 nm from 280 to 1700 nm, and at each of three incidence angles of 55° , 65° , and 75° . Thus at each wavelength (experiment) there are three measurements providing 6 real numbers, three each of Ψ and Δ . Each Ψ - Δ pair results in set of solution curves on different root and logarithm planes, for which the one containing the film solution is readily identifiable. If measurements had no experimental uncertainty, the three curves per experiment would intersect at the value of film n, k, and d. In actual fact they come close to intersecting and have a point of closest approach. In cases for which the intersection is well defined, and there are six real number unknowns which may, in principle, be determined. We have chosen the six variables to represent the thickness and optical properties of two layers on the substrate, one computation per wavelength. In the transparent region from approximately 300 to 980 nm the ITO matches a 2 layer film divided into two near-equal thicknesses with somewhat differing index real part and with an extinction coefficient near zero. At longer wavelengths the film corresponds to an absorbing layer which appears vertically inhomogeneous but which cannot be well characterized due to the light interaction depths at the three incidence angles. Results will be presented across the entire measurement wavelength range.

Magnetic Interfaces and Nanostructures

Room: Zuni - Session MI-WeA

Spintronic Devices and Proximity Effects

Moderator: R.A. Lukaszew, College of William and Mary

2:00pm **MI-WeA1 A New Twist on Spin Devices, S. Wolf**, University of Virginia **INVITED**

The use of a spin polarized current to rotate the magnetization direction of a ferromagnetic has a number of important implications for novel magnetic devices. Spin torque can switch the resistivity of a magnetic tunnel junction, create spin waves over a very wide range of frequencies, and move magnetic domain walls. I will describe some of the recent advances in Spin Torque Magnetic Random Access Memory (STT-RAM), spintronic nano-oscillators and flux shuttle memory. In addition I will describe a very novel logic array based on electrical control of magnetism called a Reconfigurable Array of magnetic Automata which uses the ferroelastic strain on a magnetic nanopillar to rotate the direction of magnetization. I will show how this can be used to perform logic at very low power approaching zeptojoules per switch..

2:40pm **MI-WeA3 Thermal Stability and Switching Distributions in Nanoscale Spin Torque Transfer Random Access Memory Devices, S.E. Russek, R. Heindl, W.H. Rippard, M.R. Pufall, T. Cecil**, NIST-Boulder

Thermal stability and switching distributions of MgO magnetic tunnel junction (MTJ) devices, that are being developed for spin-torque-transfer random access memory (STT-RAM), have been modeled using single domain simulations. The simulations incorporate realistic current-voltage characteristics, a field-like torque term and thermal heating. These elements are required to allow the single domain model to fit data from standard STT-RAM devices. Simulations were performed with a stochastic thermal field with 10,000 repetitions for each value of applied current and pulse duration. For a typical STT-RAM device with dimensions of 50 nm x 150 nm, at room temperature, with a 10 ns pulse width, the write error rate (WER = 1- switching probability) falls off at a rate of 40 mV/decade. To achieve a write error rate below 10⁻⁹, which is a typical value for current memory, the switching voltage must be 360 mV above the intrinsic switching voltage. The direction of the spin polarizer was systematically varied and it was found that switching probability decreases as the polarizer is moved off the device easy axis. The fall off in WER with pulse amplitude remained roughly constant.

The simulations are compared to data from devices consisting of a Co₄₀Fe₄₀B₂₀ free layers, 1.1 nm MgO tunnel barrier, and a synthetic antiferromagnetic fixed layer. The average resistance area product (RA) and tunneling magnetoresistance (TMR) are RA=5 Ohm micrometer² and TMR=150%, respectively. The devices were patterned using e-beam lithography and ion beam etching into ellipsoids of sizes ranging between 50 nm x 150 nm to 100 nm x 300 nm (all with aspect ratios 1:3). The devices were embedded in a high frequency coplanar wave guide structure to allow high-speed switching and high-frequency thermal ferromagnetic resonance (FMR) measurements. The high speed switching measurements confirmed that simple thermally activated switching models cannot accurately fit the measured data. The single domain simulations, with a field like torque term and thermal heating, can replicate several key features of the measured switching distribution. The thermal FMR data, however, often show a complex mode structure indicating that the real devices deviate considerably from simple single domain behavior.

These results indicate that slow fall off of the WER may be a key problem for STT-RAM technology. Within the single domain model, the slow fall off of the WER is intrinsic. To obtain a more rapid fall off in the WER, micromagnetic design concepts must be employed to prevent the device from accessing low torque configurations during the switching process.

3:00pm **MI-WeA4 Growth and Magnetism of Mn-nanostructures Embedded in a Group IV Semiconductor Matrix, K.R. Simov**, University of Virginia, C.A. Jenkins, M. Liberati, Lawrence Berkeley National Laboratory, P. Reinke, University of Virginia

The magnetic doping of the group IV semiconductors Si and Ge with Mn is coveted as valuable component in novel spintronics devices. Their magnetic doping is hampered by the low solubility of Mn in both elements, and the formation of silicide and germanide phases which modify or suppress the magnetic response of the material. We therefore investigate Mn-nanostructures which are synthesized on the Si(100)(2x1) surface and then capped with a layer of Si or Ge to protect the integrity of the nanomaterial.

The Mn-nanostructure is therefore embedded as a delta-doped layer within a group IV semiconductor matrix.

The first section of our presentation focuses on nanostructure synthesis, in particular the growth of monoatomic Mn-wires on the Si(100)(2x1) surface, where the dimer row structure guides the wire formation. A scanning tunneling microscopic (STM) study establishes the relation between the nanostructure type and the quality of the substrate, which is expressed in the concentration of defects prior to Mn deposition. An increasing defect concentration (1.0 % to 18.2%) leads to a suppression of wire formation and the growth of ultrasmall Mn-clusters is favored, which allows for an excellent control of nanostructure type. Surface structuring through the presence of dimer vacancy lines, or narrow terraces offer an additional route to control Mn-wire formation. A Monte-Carlo based model is introduced to describe the surface processes which lead to wire-formation.

The second section of our presentation assesses the stability of the nanostructures during the growth of the Si or Ge caps. The capping of nanostructures is indispensable for preservation of the nanostructures' unique capabilities in devices, and is critical for magnetic measurements such as VSM (vibrating sample magnetometry) and XMCD (X-ray magnetic circular dichroism, Advanced Light Source, Lawrence Berkeley National Laboratory). An STM observation of the growth process of the Si and Ge caps shows that the Mn-nanostructures are indeed preserved, and we are therefore able to assess the magnetic properties of Mn-wires and ultrasmall clusters.

The third section of our presentation is devoted to the discussion of the magnetic properties of the Mn-wire and Mn-cluster structures. The role of magnetic anisotropy, the ionic and metallic contributions from the Mn-nanostructure, and the nature of the magnetic coupling within the respective nanostructure, and with the cap-material will be discussed.

The support from NSF-Chemistry and DOE are gratefully acknowledged.

4:00pm **MI-WeA7 Exchange Bias Using Ideal Antiferromagnets, D. Lederman**, West Virginia University **INVITED**

Exchange bias is the interaction at the interface between an antiferromagnetic material and a ferromagnetic thin film or nanoparticle which causes the center of the ferromagnetic hysteresis loop to shift away from zero field, effectively resulting in a unidirectional anisotropy. Despite the fact that this effect was discovered approximately fifty years ago, and that it is used in magnetic sensors found in hard drives, the fundamental mechanism responsible for this interaction was poorly understood until recently. Important advances using ideal antiferromagnets (antiferromagnets with well understood and relatively simple properties) have been made during the past few years to assess or validate theories that explain exchange bias. My group has used transition metal difluoride epitaxial thin films, such as Fe_xZn_{1-x}F₂ and Fe_xNi_{1-x}F₂, which allow us to vary the magnetic disorder and anisotropy of the antiferromagnet in a controlled manner. Traditional magnetometry techniques, as well as more sophisticated experiments sensitive to the depth profile of the magnetization, such as x-ray magnetic circular dichroism (XMCD) and polarized neutron reflectivity (PNR), have allowed us to understand the interface processes responsible for the effect. I will discuss the important results from these experiments, including 1) the effects of short range order at the surface of the antiferromagnet above its Néel temperature; 2) the observation of pinned and unpinned magnetic moments at the ferromagnet/antiferromagnet interface; and 3) the effects of the magnetic anisotropy of the antiferromagnet on the temperature dependence of the exchange bias and the possibility of reversing the effect at low temperatures.

This work was supported by the National Science Foundation.

4:40pm **MI-WeA9 Spintronic Effects in Molecular Materials: The Past, Present, and Future, G.J. Szulczewski**, The University of Alabama **INVITED**

In this talk I will introduce the general concepts of spintronics and highlight some of the key experimental results that have catalyzed the emerging research area known as "organic spintronics". The confluence of spin-electronics, which combines transition metal ferromagnets and inorganic semiconductors, and molecular-electronics, which combines organic semiconductors and non-magnetic metals, has led to the evolution of organic spintronics. Furthermore, the development of organic light emitting diodes and organic photovoltaic cells has proven that molecular thin films can reliably function as the active layer in commercial products. Consequently it often envisioned that spin dependent conduction in organic-based semiconductors, rather than traditional charge transport, can be manipulated and detected to fabricate low-power, non-volatile, multifunctional devices because electron spin coupling to orbital angular momentum and nuclear spin is weak. Recent experimental evidence is beginning to demonstrate this view is too simplistic and hyperfine coupling

is very important in the hopping transport mechanism characteristic of disordered organic semiconductors.

The focus of this talk will be on the phenomena of magnetoresistance; specifically in vertical device structures with conducting electrodes used to separate an organic semiconductor layer(s). In many laboratories around the world such devices are observed to change resistance when placed in an external magnetic field. If both electrodes are magnetic and the change in the resistance corresponds to the coercive fields of the electrodes, then the magnetoresistance can be interpreted as spin-polarized injection, transport, and ejection of carriers from one ferromagnetic layer, through the non-magnetic spacer layer, and into the second ferromagnetic layer, respectively. However, when neither of the electrodes is magnetic the magnetoresistance must arise some other phenomena and there are several competing theories to describe the effects. The bulk of this talk will be devoted to reviewing case studies from the former class of devices, since there are well-accepted criteria to support the interpretation of device magnetoresistance when using magnetic electrodes. In addition I will cite examples where the interfaces of the devices have been examined by surface sensitive spectroscopy/microscopy techniques and correlated to device performance. Finally I will conclude by recommending some new experiments that could reveal more knowledge of the fundamental spintronics effects in molecular materials and suggest some possible applications.

5:20pm MI-WeA11 Probing Induced Magnetism in Vanadium Nano-islands on Cr by Spin-polarized STM, C. Clavero, College of William & Mary, M. Bode, Argonne National Laboratory, G. Bihlmayer, S. Bligel, Institut für Festkörperforschung, Germany, R.A. Lukaszew, College of William & Mary

The growth mode and magnetism at V(001)/Cr(001) interfaces are still controversial and in recent years have attracted considerable theoretical and experimental interest since they strongly affect the properties of multilayered structures prepared with these materials. Both V and Cr are *bcc 3d* transition metals with approximately half-band filling. Cr exhibits antiferromagnetism along the $\langle 001 \rangle$ direction which converts the (001) surfaces to ferromagnetic (001) planes that couple antiferromagnetically from layer to layer. Interestingly, it has been theoretically predicted that a single V layer on Cr couples antiferromagnetically to Cr with an induced V moment of $2.1 \mu_B/\text{atom}$, but drastically reducing the Cr magnetic moment[1]. Previous reports using Mössbauer spectroscopy[2] applied to Cr/V multilayers have given direct experimental evidence for a reduction of the Cr magnetic moment near the interface region. In addition, recent neutron scattering experiments have shown that proximity effects in Cr/V multilayers lead to the appearance of a 50 Å magnetically dead Cr layer near the interfaces[3].

Despite the interest in V/Cr(001) interfaces, possible magnetic polarization of V by proximity to the antiferromagnetic Cr(001) substrate has not been yet fully investigated. We report on our spin-polarized scanning tunneling microscopy (SP-STM) studies on subatomic layer coverings of V on Cr(001) substrates and experimentally demonstrate antiferromagnetic coupling between V islands and the Cr(001) underlying surface. V was evaporated on Cr(001) substrates under ultra-high vacuum conditions (base pressure in the low 10-11 mbar) and at 250 °C, temperature reported as optimum to achieve high quality multilayers with abrupt interfaces. V coverages ranging from 0.1 to 1.5 atomic layers (AL) were explored. Antiparallel coupling between the V islands and the Cr(001) substrate is found, with the magnetic contrast disappearing when the V islands start to coalesce for increasing coverages starting at 0.9 AL. In addition, using Scanning Tunneling Spectroscopy and density functional theory calculations, it was found that during the early stages of growth the islands exhibit radial symmetry in their chemical composition, with Cr-rich composition in the center and V-rich regions at the rims. Interestingly, for higher coverages such islands coalesce evidencing an island assisted interface alloying mechanism.

References

- [1.] G. Bihlmayer, T. Asada and S. Bligel, Phys. Rev. B **62** (18), 11937 (2000).
- [2.] K. Mibu *et al.*, J. Magn. Magn. Mat. **226-230** (Part 2), 1785-1787 (2001).
- [3.] E. Kravtsov *et al.*, Phys. Rev. B **76** (2), 024421 (2007).

Nanometer-scale Science and Technology Room: La Cienega - Session NS+EM+EN-WeA

Photonic and Plasmonic Materials and Devices Moderator: P. Cheng, Cornell University

2:00pm NS+EM+EN-WeA1 Spatially-Resolved Study of Luminescence and Composition in III-Nitride Nanowires, G.T. Wang, Q. Li, Sandia National Laboratories

Given the strong interest in III-nitride-based nanowires for optoelectronic and energy applications, a better understanding of their optical properties and structure-composition is required, particularly at nanoscale spatial resolutions, which could shed light into issues such as the nature and distribution of radiative defects and alloy compositional variations. Here, we present a spatially-resolved, correlated study of luminescence and composition in GaN, Al(Ga)N/GaN, and InGaN/GaN core-shell nanowires grown by metal-organic chemical vapor deposition. For GaN nanowires, a surface layer exhibiting strong yellow luminescence (YL) near 566 nm in the nanowires was directly revealed by high resolution, cross-sectional cathodoluminescence (CL) imaging, compared to weak YL in the bulk. In contrast, other defect related luminescence near 428 nm (blue luminescence) and 734 nm (red luminescence), in addition to band-edge luminescence (BEL) at 366 nm, were observed in the bulk of the GaN nanowires but were largely absent at the surface. As the nanowire width approaches a critical dimension, the surface YL layer completely quenches the BEL. The surface YL is attributed to the diffusion and piling up of mobile point defects, likely isolated gallium vacancies, at the surface during growth. AlGaN/GaN and AlN/GaN core-shell nanowires were observed to exhibit stronger BEL and weaker YL as compared with bare GaN nanowires, which may relate to the passivation of nanowire surface states. InGaN/GaN core-shell nanowires were also investigated by correlated CL and cross-sectional scanning TEM (STEM). Dislocation-free InGaN layers with up to ~40% indium incorporation were achieved on GaN nanowires. The indium composition distribution in the InGaN layers were qualitatively correlated to the strain energy density distribution as calculated by finite element analysis models. The observed high indium incorporation and high crystalline quality in the heteroepitaxial InGaN layers is attributed to strain-relaxed growth on the nanowires. Sandia National Laboratories is a multi-program laboratory operated by Sandia Corporation, a wholly owned subsidiary of Lockheed Martin company, for the U.S. Department of Energy's National Nuclear Security Administration under contract DE-AC04-94AL85000.

2:20pm NS+EM+EN-WeA2 Photonic Crystal Cavities and Vertical Confinement to Increase the Conversion Efficiency of a Thermophotovoltaic Cell, C. Shemelya, T. Vandervelde, Tufts University

For many years researchers have attempted to efficiently harvest waste heat and transform it into a usable energy via thermophotovoltaics (TPVs). The low quantum efficiency (QE; i.e. the probability that a photon will be absorbed) in most TPV cells is probably the biggest limiting factor in achieving an economically viable device and directly affects the conversion efficiency (CE; i.e. the probability that a photon will be converted into a carrier that is collected). In many cases, top of the line TPV cells might only have a CE of 20%. Recent advances in micro-/nano-fabrication techniques have enabled the creation of novel structures to enhance the absorption and, therefore, the conversion of the incident thermal photons. In particular, photonic crystals (PhC) interface enhancements have been shown to increase the efficiency of photon to current conversions for infrared photodetectors. The addition of a back reflecting layer, or vertical confinement layer can further increase conversion efficiencies. Here, we report on the enhancement of photon conversion by integration of PhC structures and vertical confinement layers into the TPV cells. To this end, photonic crystals consisting of rods of either air or dielectric surface-passivation material are placed into the base semiconductor TPV cells to increase duration of thermal photon absorption, resulting in significantly enhanced QE and CE. The use of photonic crystals and vertical confinement in augmenting the conversion efficiency of TPV cells is applicable for most IR wavelengths, making this a widely useful technology. The ability to harvest waste heat for energy will help make many processes and/or systems more energy efficient, which will be a critical component in ushering in an era of energy independence.

2:40pm NS+EM+EN-WeA3 Unconventional and Broadband Plasmonics, T.W. Odom, Northwestern University INVITED

Breakthroughs in photonics and optoelectronics demand actively controlled materials that are inexpensive, robust, and scalable. The interaction of light with surface plasmons—collective oscillations of free electrons—in metal nanostructures has resulted in exceptional displays of enhanced optical

transmission, collimation of light through a subwavelength aperture, and negative permeability and refraction at visible wavelengths. The structures that display these phenomena typically consist of ordered arrays of particles or holes with sizes of the order 100 nm. Surface plasmons can interact with each other over much longer distances, however, and thus the ability to organize nanoscale materials over multiple length scales could lead to new plasmonic metamaterials with novel optical properties.

This talk will describe how superlattices and low symmetry plasmonic lattices provide an important first step to meet these goals. We will introduce new soft nanolithography tools for creating new plasmonic structures, including PEEL (a procedure combining Phase-shifting photolithography, Etching, Electron-beam deposition, and Lift-off) and solvent assisted nanoscale embossing (SANE). These methods can achieve arrays of 50-nm features simultaneously over 6-in² areas without needing electron, ion, or photon-based lithographies. We will then discuss how the optical properties of the plasmonic crystals and the nanoparticle arrays can be engineered and then manipulated by external factors to produce large optical responses.

4:00pm NS+EM+EN-WeA7 Controlling Plasmon Enhanced Photoconduction in Porphyrin-Gold Nanoparticle Assemblies, D.J. Conklin, S.U. Nanayakkara, T.-H. Park, University of Pennsylvania, J.T. Stecher, M.J. Therien, Duke University, D.A. Bonnell, University of Pennsylvania

Recently we demonstrate plasmon-induced electronic transport in hybrid metal nanoparticle-molecular devices that realized enhancements of up to a factor of 200. This was realized in a hybrid structure that consists of an array of gold nanoparticles linked by (porphinato)zinc(II) oligomers. Here we examine the role of metal particle size, spacing, molecular length and radiation power on the photoconductive properties. Controlling these parameters allows the relative roles of nano antennae focus increasing effective photon flux and hot electron distribution to the current enhancement to be compared.

This phenomenon offers a pathway to selectively enhance specific optical energies or to design a hybrid structure that can simultaneously enhance a range of optical wavelengths. Applications in optical devices and a range of photovoltaics could exploit this new phenomenon [ACS Nano, 2010, 4 (2), pp 1019-1025].

4:20pm NS+EM+EN-WeA8 From Red-Coloured Coatings to Light Trapping in Solar Cells: on the Tunability and Control of the Surface Plasmon Resonance Behaviour, M. Creatore, H. Takeke Beyene, M. Ponomarev, M.C.M. van de Sanden, Eindhoven University of Technology, Netherlands

The combination of (noble) metal nanoparticles (NPs) with dielectrics is an on-going research subject, due to the generated surface plasmon resonance (SPR) effect, relevant in several technological applications such as color filters, optical switching devices and sensors, to name a few.

In this contribution, we report on the tunability and control of the surface plasmon resonance behaviour through the engineering of metal NP/dielectric interfaces for two applications, i.e. thickness- and viewing angle- independent red- coloured decorative coatings and light trapping enhancement in silicon- based tandem thin film solar cells. Both studies have been carried out by making use of a vacuum chamber where plasma-enhanced chemical vapour deposition for the dielectric layer and magnetron sputtering for the metal NP deposition are combined.

Multilayer structures composed of gold NPs sandwiched between SiO₂ layers represent a valid solution for the independent control of NP size and density: while a constant NP size guarantees a narrow surface plasmon frequency, an increased NP density leads to an enhancement in the absorption [1]. A multi-diagnostic approach consisting of spectroscopic ellipsometry, transmission electron microscopy and Rutherford backscattering analysis has allowed the characterization of the deposited coatings: gold NPs (diameter 10-15 nm) with a surface area coverage of 26% and sandwiched between 40 nm- thick SiO₂ layers, exhibit a red colour, whereas the color intensity (i.e. from cool to warm deep red) increases with the layer number, i.e. NP density.

While in this first application the main mechanism contributing to extinction is *absorption*, for an efficient sun light management/ trapping within a solar cell, *scattering* plays a dominant role. In particular, for amorphous (a-Si:H)/microcrystalline (μ c-Si:H) silicon tandem solar cells a promising approach consists in the incorporation of an intermediate layer (e.g. ZnO) sandwiched between the top a-Si:H and the bottom μ c-Si:H cell, able to efficiently scatter photons of a specific frequency range back to the top cell or forward to the bottom cell. In this respect, copper NPs (30-150 nm diameter) when coupled to ZnO layers, are responsible for the generation of a plasmon peak at 700 nm, which shifts towards higher

wavelengths with an increase in NP size, therefore showing its potential towards low energy photon forward scattering into the bottom μ c-Si:H cell.

[1] H. T. Beyene, F.D. Tichelaar, P. Peeters, I. Kolev, M.C.M. van de Sanden, M. Creatore, accepted for publication in Plasma Processes and Polymers (2010).

4:40pm NS+EM+EN-WeA9 Index-Matching at the Nanometer Scale, G. Broenstrup, C. Leiterer, N. Jahr, B. Hoffmann, F. Talkenberg, Institute of Photonic Technology, Germany, S.H. Christiansen, Max Planck Institute for the Science of Light, Germany

Silicon nanowires (SiNW) show high potential as future building blocks for photonic devices. They show strong resonant enhancement effects resulting in high absorption efficiencies and even higher scattering efficiencies. Since both effects are based on the same underlying physical principles the resonant enhancement of the absorption as well the resonant enhancement of the scattering of light occurs at the same wavelength. These large scattering efficiencies could result in an increased reflectivity of structures based on these SiNWs.

To overcome the increased scattering efficiencies we show an index matching core-shell approach.

The SiNWs are wrapped with a thin oxide layer with a refractive index smaller than the refractive index of silicon. The thickness of the wrapping layer is formed using atomic layer deposition (ALD), which allows to control the thickness of the layer at the Angstrom scale. The microstructure is analyzed using transmission electron microscopy (TEM).

The scattering behavior of these individual SiNWs with an oxide layer are measured using an optical microscope with a coupled spectrometer. The experimental data is analyzed using an extended Mie theory.

It will be shown, that this method can be used to tune the absorption efficiencies and the scattering separately to different wavelengths.

5:00pm NS+EM+EN-WeA10 20 μ s Photocurrent Response from Lithographically Patterned Nanocrystalline Cadmium Selenide Nanowires, S.-C. Kung, W.E. van der Veer, F. Yang, K.C. Donovan, R.M. Penner, University of California, Irvine

Lithographically patterned nanowire electrodeposition (LPNE) provides a method for patterning nanowires composed of nanocrystalline cadmium selenide (*nc*-CdSe) over wafer-scale areas. We assess the properties of (*nc*-CdSe) nanowires for detecting light as photoconductors. Structural characterization of these nanowires by X-ray diffraction and transmission electron microscopy reveals they are composed of stoichiometric, single phase, cubic CdSe with a mean grain diameter of 10 nm. For *nc*-CdSe nanowires with lengths of many millimeters, the width and height dimensions could be varied over the range from 60 to 350 nm (*w*) and 20 to 80 nm (*h*). Optical absorption and photoluminescence spectra for *nc*-CdSe nanowires were both dominated by band-edge transitions. The photoconductivity properties of *nc*-CdSe nanowire arrays containing ~350 nanowires were evaluated by electrically isolating 5 μ m nanowire lengths using evaporated gold electrodes. Photocurrents, i_{photo} , of 10-100 \times (i_{dark}) were observed with a spectral response characterized by an onset at 1.75 eV. i_{photo} response and recovery times were virtually identical and in the range from 20 to 40 μ s for 60 \times 200 nm nanowires.

5:20pm NS+EM+EN-WeA11 Efficient, Single Layer Organic Light-Emitting Devices Based on a Graded Composition Emissive Layer, N.C. Erickson, R.J. Holmes, University of Minnesota

We demonstrate efficient electrophosphorescence from devices comprised of a single organic active layer. High efficiency is realized by combining both hole- and electron-transporting host materials (HTM and ETM, respectively) into a single, graded composition emissive layer with the green emitter, *fac*-tris(2-phenylpyridine) iridium (III). The composition of the host-material is continuously graded to realize 100% HTM at the anode, and 100% ETM at the cathode. A peak external quantum efficiency of $\eta_{\text{EQE}}=(19.3 \pm 0.4) \%$ is realized in the forward-viewing direction at a luminance level of 600 cd/m², corresponding to a power efficiency of $\eta_{\text{p}}=(66.5 \pm 1.3) \text{ lm/W}$. This performance is similar to that realized in more conventional and complex, multi-layered structures. The graded composition of the structure balances electron and hole injection and transport leading to efficient exciton formation, permitting high efficiency using a single active layer. The graded composition architecture may be further utilized to realize simple, efficient organic light-emitting devices for use in display and lighting applications.

Plasma Surface Interactions (Fundamentals & Applications) II

Moderator: J. Guha, Lam Research Corporation

2:00pm **PS1-WeA1 VUV-Induced Bond Scission and Site-Specific Nitridation in Organosilicate Glass: Bulk and Surface Effects, S. Behera***, University of North Texas, *J. Lee*, University of California-Berkeley, *S. Gaddam, S. Pokharel*, University of North Texas, *D.B. Graves*, University of California-Berkeley, *J.A. Kelber*, University of North Texas

In-situ XPS and ex-situ FTIR have been used to characterize the effects of ionizing vacuum ultraviolet (VUV— 147 nm) photons on the surface composition of organosilicate glass (OSG; $k = 3.0$). VUV irradiation is an important component of the plasma environment, and both the types and kinetics of VUV-induced effects must be understood in order to accurately control and model plasma effects. Irradiation was carried out in vacuum (10^{-6} Torr), and in the presence of 10^{-4} Torr NH_3 so that NH_3 reactions with VUV-induced reactive sites would cause chemical shifts in XPS core level spectra, permitting a more detailed characterization of photo-induced chemistry. The effects of photo-excited gas phase species are negligible under these conditions, as confirmed by experiments with the light path parallel to the surface. FTIR and XPS data after photoirradiation in vacuum indicate photon-induced Si-C and Si-O bond scission. Lifetimes of bulk Si reactive sites are ~ 6 days, as determined by Si-OH, but \sim minutes at surface sites due to reaction with chamber ambient. Core level XPS spectra recorded after irradiation in the presence of NH_3 show similar effects, but with nitridation at Si sites, and not at carbon sites. Si-C/Si-O bond breaking and C-C bond formation obey first order kinetics. At longer exposure times, the nitridation process saturates while the Si-C/Si-O bond scission and C-C bond formation processes do not, consistent with photo-induced surface densification inhibiting NH_3 diffusion into the solid. However, similar increases in surface carbon intensity were observed for photoirradiation of SiO_2 with ~ 1 monolayer of surface carbon, indicating that reaction of background gases with surface reactive sites may also be a factor. Preferential Si-N bond formation and absence of C-N bond formation were also reported¹ for OSG bombardment by Ar^+ in the presence of NH_3 and suggest fundamentally different dissociation pathways/kinetics at Si vs. C sites created by either ion bombardment or ionizing photoirradiation. C-C and C-H bond dissociation enthalpies are larger than those of Si-H or Si-C bonds, but smaller than that of Si-O, so this site specificity is not readily explainable on the basis of bond strengths alone.

¹J. A. Wilks and J. A. Kelber, *Applied Surface Science* **255** (2009) 9543

Acknowledgements: This research was supported by the Semiconductor Research Corporation under Task IDs 1862.001 and 1862.002.

2:20pm **PS1-WeA2 Real-time Measurements of Material Modifications by VUV Radiation during Plasma Etching of 193nm PR, F. Weilnboeck, R. Bruce, G.S. Oehrlein**, University of Maryland, *T.-Y. Chung, D.B. Graves*, University of California, Berkeley, *M. Li, D. Wang*, Dow Electronic Materials, *E.A. Hudson*, Lam Research Corporation

Plasma radiation in the ultraviolet (UV) and vacuum ultraviolet (VUV) spectral range is a fundamental component of plasma processes used for pattern transfer of nanometer structures. Photons in this wavelength range can lead to severe modification of photoresist (PR) materials in depths exceeding 100nm. We studied the material modifications of fully formulated 193nm PR by plasma photon radiation in Ar plasma discharges. A novel filter approach was applied allowing to probe PR surface modifications in real time by *in-situ* ellipsometry during plasma processing while protecting the PR against ion bombardment. Different filter materials enable to test dependencies on wavelength ranges of the plasma radiation from visible to VUV light. Material modifications were also characterized by Fourier transform infrared spectroscopy and scanning electron microscopy. By combining these data with optical multilayer ellipsometric simulations, material thickness reduction and changes in optical properties could be understood on a molecular level.

Radiation in the UV/VUV spectral range was found to modify the PR at a depth of $\sim 100\text{nm}$ leading to thickness reduction of up to 12nm , whereas radiation in the VIS spectral range modifies the entire film ($\sim 400\text{nm}$) leading to marginal changes in the film thickness. The thickness reduction is caused by material loss, mainly by detachment and loss of lactone, and to a larger extent by densification of up to 9% following the detachment of the PR pendant groups.

Radiation exposure also leads to a change in film optical properties which is discussed in terms of a bond polarizability model. This enables correlation of the measured data with changes of the PR structure on a molecular level. For exposure of the PR to UV/VUV radiation it was found that besides loss of lactone and detachment of the PR pendant groups a significant amount of C-C bonds were lost which can be directly correlated to changes in the polymer structure by chain scissioning reactions.

Real time measurements allow for extracting the temporal evolution of material removal, densification and changes in film optical properties as a function of photon flux and degree of modification. It was found that material modification can be separated into two fundamentally different regimes. In the initial exposure period to plasma radiation in the UV/VUV spectral range changes in film properties are rapid and mainly limited by the photon flux. For extended exposure times modification is flux dependent but limited by the unmodified material remaining in the film after the initial exposure period.

2:40pm **PS1-WeA3 Deciding Factors for Line-Edge-Roughness (LER) Formation and Plasma-Resistance of ArF Photoresist during Plasma Etching Processes, T. Uesugi, K. Koyama, B. Jinnai**, Tohoku University, Japan, *S. Maeda, K. Kato, A. Yasuda, H. Momose*, Mitsubishi Rayon Co., Ltd, Japan, *S. Samukawa*, Tohoku University, Japan

ArF excimer laser (193nm) lithography is used in the fabrication of sub-100-nm devices. However, during plasma etching processes, activated species radiated from plasma, such as ions, radicals, and photons, degrade ArF photoresist, resulting in low etching resistance and the formation of line-edge roughness (LER). To solve these issues, it is important to understand the interaction of plasma and ArF photoresist and to clarify deciding factors for the plasma resistance and the formation of LER in ArF photoresist. For this purpose, using our developed neutral beam process, effects of the activated species from plasma are divided into physical bombardment (by ions), chemical reactions (by radicals), and UV radiation. UV radiation drastically increased the etching rates of ArF photoresist films, and, in contrast, chemical reactions enhanced the formation of surface roughness in ArF photoresist. FTIR analysis shows that UV radiation preferentially dissociates C-H bonds in ArF photoresist, rather than C=O bonds, because of these bond dissociation energies; $E(\text{C-H}, 4.25\text{eV}) < E(\text{C=O}, 7.71\text{eV})$. This indicates that the etching rates of ArF photoresist are determined by UV radiation, because UV radiation can break C-H bonds, which are a majority of structures in ArF photoresist. On the other hand, according to the FTIR analysis, chemical species, such as radicals and ions, are likely to react with C=O bonds, especially C=O bonds in lactone groups of ArF photoresist due to the structural and electronic effects of lactone groups. As a result, the etching rates of ArF photoresist can microscopically vary in different bond structures, leading in the enhancement of surface roughness in ArF photoresist. To reduce the chemical reactivity and the surface roughness, radical trap additives were injected into ArF photoresist. Radical trap additives, which can reduce surface roughness by 30%, are very effective to suppress the roughness formation in ArF photoresist.

3:00pm **PS1-WeA4 Smoothing of 193 Immersion Resist by 172 nm VUV Exposure, E. Kunnen, A. Vaglio Pret**, IMEC, Belgium, *O. Luere*, CNRS-LTM, France, *L. Azarnouche*, STMicroelectronics, France, *E. Pargon*, CNRS-LTM, France, *P. Foubert, R. Gronheid, D. Shamiryani, M.R. Baklanov, W. Boullart*, IMEC, Belgium

At today's date 193 immersion lithography is used in semiconductor industry to print lines of less than 40nm half pitch, continuing the scaling. One of the challenges is to reduce line edge variations, or Line Width Roughness (LWR). It has already been pointed out earlier that LWR can be significantly reduced during the subsequent dry etch step. One of the important components acting on LWR during the dry etch is the VUV light emitted from the plasma, however, the exact mechanism is not yet revealed.

The photoresist pattern profile and its chemical modifications are studied as a function of VUV dose. A 172 nm Xe_2^* excimer 30mW/cm² light source is used to expose patterned and blanket (resist & organic BARC) wafers, exposing them from 2 to 256 seconds under nitrogen ambient and controlling the temperature within 2°C. SEM-CD top-down image analysis gives us spatial and information in both spatial and frequency domain through Critical dimension (CD), CD-Uniformity, LWR and Power Spectral Density (PSD). Three dimensional information is recorded by CD AFM measurements. The thickness, refractive index and extinction coefficient are deduced from spectral ellipsometric (SE) measurements. Mass measurements provide density. Fourier Transformed Infrared Spectroscopy (FTIR) analyses provide information on the molecular bonds. Finally, chemical analysis will be performed by elastic recoil detection (ERD) and Time of flight secondary ion mass spectrometry (TOFSIMS).

Significant changes in CD and LWR are observed up to 12s (360 mJ/cm²) of VUV exposure time corresponding to a dose of about 1 photon per atom. For higher exposures the integrity of the lines deteriorates compromising

* Coburn & Winters Student Award Finalist

the accuracy in the SEM-CD analyses. Initially, CD and LWR decreases while the correlation length increases. PSD analysis shows that the reduction is attributed to a decrease in the high frequency roughness region. For longer exposure, a CD increase is observed and finally low frequency roughness increases, the total LWR. The CD evaluation indicates a resist reflow that is driven by surface tension towards a more rounded shape. Mass and thickness measurements over the whole exposure range show a decrease that goes linearly with the logarithm of the exposure time, while density remains about constant. FTIR indicate a correlation of the observed changes with the removal of the lactone bonds at 1800 cm⁻¹.

In conclusion the dose range at which VUV impacts LWR is measured to be around 1 photon/atom. Initially a CD and LWR decrease is observed while for larger doses the trend is the opposite. Change of mass and thickness follows a first order kinetic equation, which is quite typical for simple desorption processes.

4:00pm PS1-WeA7 Ion and Vacuum Ultraviolet Photon Beam Effects in 193 nm Photoresist Surface Roughening: the Dependence on Polymer Structure. *T.-Y. Chung, D.B. Graves, University of California, Berkeley, F. Weilnboeck, G.S. Oehrlein, University of Maryland, E.A. Hudson, Lam Research Corporation, M. Li, The Dow Chemical Company*

Previous vacuum beam studies showed that methacrylate-based 193 nm photoresist (PR) will roughen due to the synergistic effects of ion bombardment, vacuum ultraviolet (VUV) photon and substrate heating [1]. The surface roughness and surface morphology is similar to that after inductively coupled argon plasma exposure under similar ion and VUV fluences and energies [2]. However, 193 nm PR is a heteropolymer, with three separate side-groups that could be photolyzed due to the plasma-generated VUV, and this could complicate analysis of roughening mechanisms. We therefore examined several associated homopolymers to better understand the role of the side groups in roughening under plasma exposure. We chose two homopolymers: 2-methyl-2-adamantyl methacrylate (MAMA, leaving group) and R-functionalized adamantyl methacrylate (RAMA, polar group). At a substrate temperature of 65°C, MAMA undergoes considerable loss of material under VUV-only exposure. In addition to the loss of CH₂/CH₃, C=O and C-O-C bonds in the polymer bulk observed by transmission Fourier transform infrared (FTIR) spectroscopy, mass spectroscopy analysis shows that the adamantane leaving group is lost from the film. In contrast, RAMA is relative insensitive to VUV irradiation. After simultaneous ion/VUV exposure at a substrate temperature of 65°C, MAMA shows very high surface roughness while RAMA shows little surface roughening. The surface of MAMA is also significantly rougher than that of 193 nm PR processed under the same condition. It therefore appears that the leaving group in 193 nm PR, designed to cleave in the presence of photoacid during lithographic exposure and post-exposure bake, is the primary cause of 193 nm PR roughening, when combined with energetic ion bombardment, VUV irradiation and elevated heating.

[1] D. Nest, T.-Y. Chung, D. B. Graves, S. Engelmann, R. L. Bruce, F. Weilnboeck, G. S. Oehrlein, D. Y. Wang, C. Andes, and E. A. Hudson, *Plasma Process. Polym.* 6 (2009) 649.

[2] M. J. Titus, D. G. Nest, T.-Y. Chung, and D. B. Graves, *J. Phys. D, Appl. Phys.* 42 (2009) 245205.

4:20pm PS1-WeA8 Polymer Surface Modification: Vibrational Sum Frequency Generation Study for Plasma Etching. *K. Ishikawa, K. Takeda, H. Kondo, M. Sekine, M. Hori, Nagoya University, Japan*

A comprehensive understanding of interaction between plasmas and nano-materials is essential for advanced plasma processing technology. By means of plasma-beams apparatus, complicated processes are expectedly convolved individual contributions such as ion, radical, and photons. The vibrational sum-frequency-generation (SFG) is a beneficial tool for addressing best sensitivity at surface and interface, breaking their centrosymmetry[1]. In this study, we have investigated polymer surfaces exposed to the plasma-beams by using SFG.

Samples used were spin-on methyl-siloxane polymer, which is able to used as low-dielectric-constants (Low-k) film for interconnects. Hydrophobic property exhibits since methyl end group, -CH₃, is terminated at end on siloxane.

Plasma beams, which directly extracted from a argon plasma by acceleration between 100 and 400 eV, were irradiated.

The SFG spectroscopy setup consists of a 1064 nm Nd:YAG laser, and optical systems, which create both visible (532 nm) and tunable infrared (1000-4000 cm⁻¹) radiations (Ekspla). The SFG spectra taken were decomposed into individually spectral features by fitting spectra calculated to that measured. Intensity of SFG signal emitted from the surface is phenomenologically expressed as the summation of non-resonant

susceptibility and damped Lorentian oscillators, which are characterized by phases, strength, resonant, and damping wavenumber.[2]

Before plasma exposure, peaks at ~2930 and ~2970 cm⁻¹ are arisen from C-H stretch of Si-CH₃. This strength coincides with that for a peak at around 1275 cm⁻¹ in infrared spectra. After plasma exposure, surface methyl group is disappeared. At the present, it was interpreted that at early stage under ion irradiation, hydrogen is released from the end-on methyl group to create surface radicals, namely rupture of chemical bonds to methyl group is essential for elimination from end-groups on the surface.[3] Further detailed considerations should be conducted.

The surface modifications of plasmas have been studied by using the plasma-beam apparatus and the SFG spectroscopy. The end-groups of the polymer surface were changed only physical ion bombardments. To understanding surface chemical reactions and physical properties, nano- and atom- scaled views of not only bulk materials but also surface end-groups are informative.

Acknowledgments

This study was partly supported by the Tokai region knowledge cluster, Aichi Science and Technology Foundation.

References

[1] M. Buck, *et al.*, *J. Vac. Sci. Technol. A* 19, 2717 (2001).

[2] A. G. Lambert *et al.*, *Appl. Spectrosc. Rev.* 40, 103 (2005).

[3] K. Ishikawa, *et al.*, *J. Appl. Phys.* 99, 083305 (2006).

4:40pm PS1-WeA9 Plasma-induced Mechanical Degradation of Silicon Microcantilever. *C.H. Huang, M. Tomura, Y. Yoshida, T. Ono, Tohoku University, Japan, S. Yamasaki, National Institute of Advanced Industrial Science and Technology (AIST), Japan, S. Samukawa, Tohoku University, Japan*

Miniaturization of microcantilever realized increasing resonant frequency and achieving high resolution in image sensing devices such as scanning probe microscopy. Thin film deposition and etching are widely used in micro fabrication process. Therefore, it is indispensable to use plasma process. However, the plasma process usually generates defects in the micro structure due to the high-energy ion bombardment, charge build-up and UV photon radiation from the plasma, which might degrade the mechanical characteristics of the micro elements, such as microcantilever, and result in MEMS malfunction.

In this study, a Si microcantilever was adopted to investigate the influence of plasma irradiation to mechanical characteristic. The Si microcantilever was fabricated with silicon on insulator wafer. After the fabrication, the microcantilevers were irradiated by inductively coupled plasma and neutral beam (NB) with argon gas at room temperature. The influences of the plasma and NB irradiations on Si microcantilevers were evaluated with Q factor and resonant frequency (f) using laser Doppler vibrometer before and after irradiation. After plasma irradiation, Q factor ratio [Q factor after irradiation/ Q factor before irradiation] and f ratio [f factor after irradiation/ f factor before irradiation] drastically decreased. The Q factor ratio didn't depend on the irradiation time and the f ratio decreased as the plasma irradiation time increased. On the other hand, the Q factor ratio and f ratio only slightly decreased after Ar NB irradiation, which indicates that NB process have great potential for MEMS application. To understand the degradation mechanism of Si microcantilever, defect (E' center) density on microcantilever surface was measured by electron spin resonance. The defect density increased when plasma irradiation time increased. The Young's modulus (E) of microcantilever calculated from f suddenly decreased and became plateau when E' center was over a threshold defect density. The Q ratio decreased when the microcantilever thickness decreased. It is because the ratio of defect depth to microcantilever thickness being higher. Given these results, plasma irradiation degrades the E resulting in the variation of the f . Degradation of Q factor is determined by the ratio of defect depth to microcantilever thickness.

5:00pm PS1-WeA10 Gas-phase Diagnostics for Understanding Plasma Processing to Tailor the Surfaces of Inorganic Thin Films and Nanoparticles. *K.J. Trevino, S.M. Thagard, J.C. Shearer, J.M. Stillahn, E.R. Fisher, Colorado State University*

Plasma-enhanced chemical vapor deposition (PECVD), plasma etching, and plasma modification of surfaces are emerging as important tools in the development of biomaterials, hard coatings and other diverse applications. Recently, we have explored the use of both low-pressure rf plasmas as well as atmospheric plasmas to specifically tailor the surface properties of a variety of inorganic materials with a range of morphologies from flat substrates to membranes and nanoparticle systems. Despite the broad range of applicability of plasma processing for producing materials with specific surface properties (e.g. hydrophilicity, chemical functionality, etc.), many mechanistic details remain unknown. Understanding the contributions of

gas-phase species is critical to understanding the chemistry that leads to specific surface modifications. In addition, the surface interactions of gas-phase plasma species provide critical molecular level information about plasma processing, especially at interfaces. In addition, power dissipation and energetics are also important for elucidation of mechanistic details in plasmas. The imaging of radicals interacting with surfaces (IRIS) technique uses laser-induced fluorescence (LIF) to provide spatially-resolved images of plasma species. Furthermore, IRIS provides direct information on the energetics of plasma-generated radicals as well as for species scattering off of surfaces. Combined with quantitative optical emission spectroscopy (OES) data, we have measured the internal and translational temperatures for a range of species in a variety of plasma environments. This work concentrates on OH radicals in H₂O plasmas used to create hydrophilic metal oxide surfaces, CH radicals in plasma polymerization systems for nanocomposite materials, and, SO₂ and CF_x species in dielectric etching systems. For many of these molecules, vibrational temperatures are significantly higher than rotational temperatures and the partitioning of energy is correlated to surface reactivity. Comparison between atmospheric and low temperature plasmas as well as flat vs. nanostructured substrates will be made. Preliminary results from computational models of our plasma systems will also be presented. The gas-phase data are complemented by a range of surface and materials analysis data that reveal a more detailed picture of the overall plasma process in each system.

5:20pm **PS1-WeA11**, *D.L. Gilbert*, Mattson Technology Singapore PTE LTD

High Dose Implantation (HDI) for source/drain (S/D) is one of the critical steps for transistor formation. It becomes more complicated due to S/D junctions are designed to be shallower at proportional scaling down of the entire transistor. The photo resist (PR) mask is exposed to increasing number of implant species, higher dosages and energy levels. The top layer of the PR transforms to hard and cross-linked crust. Meanwhile, the sidewall of the PR mask collects a lot of spattered substrate (inorganic) materials. As a consequence, HDI photo resist strip (HDIS) is increasingly difficult to get residue free with controlled material loss and growth as required at lower node. One of widely used HDIS process solutions is remote O₂/CF₄ plasma followed by a wet chemical clean, such as dilute HF and/or SC1 solutions. However, these strip / clean processes also attack the underlying SiO₂ films. It is critical to control such SiO₂ loss for future IC production, as device sizes shrink. Therefore, a delicate balance is to be discovered between effectively cleaning the wafer surface and etching into the SiO₂ substrate. This paper discusses the significant synergy between the O₂/CF₄ processes and subsequent wet clean. It has been observed that the overall oxide removal through combined O₂/CF₄ dry clean and wet chemical clean is significantly higher than the sum of the independent oxide loss through dry clean and wet clean. The effect on CF₄ concentration in the plasma, O₂/CF₄ processing time, and temperature on the wet etch rate enhancement are explored. In an effort to reduce the etch rate enhancement, several post O₂/CF₄ processes such as a O₂ only plasma, a forming gas plasma, and a simple water rinse are employed. Results show that the oxide loss enhancement is due to the presence of a highly fluorinated surface post O₂/CF₄ dry clean. This fluorinated oxide surface readily dissolves in wet etch chemistries. Furthermore, once desorbed from the wafer surface, the fluorine may increase the local concentration of species responsible for etching oxide films.

Plasma Science and Technology

Room: Galisteo - Session PS2-WeA

Neutral Beam Processing

Moderator: J. Joo, Kunsan National University, Republic of Korea

2:00pm **PS2-WeA1 Possible Applications of Neutral Beam Generated by Low Angle Reflection of a Reactive Ion Beam to Nanoscale Semiconductor Processing**, *G.Y. Yeom*, Sungkyunkwan University, Republic of Korea **INVITED**

Reactive ion etching (RIE) is one of the key technologies in the fabrication of deep submicrometre silicon-based integrated circuits. However, conventional RIE techniques can have serious disadvantages for future device fabrication due to charged particles and UV photons causing increased gate oxide breakdown, charging, etc. It is believed that these problems will become more serious as the critical dimensions of the device shrink to a few nanometres size. Therefore, there is a need to develop novel semiconductor processing equipment and processing techniques that can cope with the issues caused by the integration of future semiconductor devices and the decrease in the design rule to the sub-nano scale. One of the

methods being investigated by many researchers is etching using a reactive neutral beam.

This presentation introduces a neutral beam generated by surface neutralization of an ion beam using a low angle forward reflection technique and explains its possible application to various areas such as surface treatment and etching. When a metal-oxide-semiconductor device was etched using a reactive neutral beam instead of conventional reactive ion etching, it was confirmed that charge-related problems such as aspect-ratio-dependent etching and gate oxide charging could be removed. Neutral beams can be beneficial to the fabrication of other devices such as the III-V devices, SOI devices, etc

2:40pm **PS2-WeA3 Numerical Simulation of Neutral Beam Generation by Quantum Electrons Dynamics**, *N. Watanabe, S. Ohtsuka, T. Iwasaki, K. Ono, Mizuho Information & Research Institute, Inc., Japan, Y. Iriye, O. Nukaga, S. Ueki, T. Kubota, M. Sugiyama*, BEANS Project 3D BEANS Center and University of Tokyo, Japan, *S. Samukawa*, BEANS Project 3D BEANS Center and Tohoku University, Japan

We have developed numerical simulation method which analyses neutral beam generated by collisions with aperture sidewalls.

The neutral-beam etching system developed by Samukawa, et al [1] has a carbon plate which has numerous apertures, where positive or negative ions pass through. In this system, we had found experimentally that most of those ions passing through the apertures are efficiently converted into neutral atoms with maintaining the motion energy. We consider ions are neutralized by the collision with aperture sidewall, namely, a negative ion transfers some of their valence electrons to the aperture sidewall by the collision, on the other hand, a positive ion receives some valence electrons from the aperture sidewall.

To realize more efficient neutral-beam etching system, we have to understand the dynamical process of electron transfer by the collision. The process of electron transfers can be described by the Quantum Mechanics as a time-evolution of wavefunction during the collision. For this purpose, we have developed computational simulation software named QuickQD[2,3] which can calculate the time-evolution of wavefunction of electrons around both an ion and the carbon plate during the whole process of collision. QuickQD is based on the density functional theory, and it can calculate the time-evolution of wavefunctions stably and efficiently.

Our numerical model consists of an ion and several carbon atoms forming a graphite sheet. We have taken the following ions and neutral atoms as the colliding ion respectively; Cl⁻, Cl, Cl⁺, Cl₂⁻, Cl₂, and Cl₂⁺.

We have performed the numerical simulation of the collision of each ion and the carbon sheet. QuickQD has calculated the time-evolution of several ten wavefunctions of both the ion and carbon atoms. During the time-evolution, the ion has been moved to collide with the graphite sheet and then bounce back to its original position. At the end of time-evolution, we have counted the electron distribution left around the ion, and have estimated the valence number of the ion after the collision. In this way, we have determined the probability of neutralization of each ion. We have obtained results which show a Cl⁻ is converted into Cl with a high probability, meanwhile a Cl₂⁺ is converted into a Cl₂ with a low probability. These numerical results agree well with the experimental results. We have established a numerical method that analyzes the neutralization process based on the Quantum Electrons Dynamics.

[1] S. Samukawa et al., Jpn. J. Appl. Phys., 40, L779 (2001).

[2] N. Watanabe and M. Tsukada, Phys. Rev. E. 65 036705 (2002).

[3] <http://www.mizuho-ir.co.jp/science/meso/index.html>

3:00pm **PS2-WeA4 Development of a Defect-Free GaAs/AlGaAs Heterostructure Etching Process Utilizing Chlorine and Argon Mixed Neutral Beam**, *X.Y. Wang, C.H. Huang, Y. Ohno, M. Igarashi*, Tohoku University, Japan, *A. Murayama*, Hokkaido University, Japan, *S. Samukawa*, Tohoku University, Japan

Dry etching is a key technique in top-down process for the fabrication of GaAs/AlGaAs nanometer-scale heterostructures such as quantum wire and quantum dot. For nanostructures, surface condition would affect the quantum-effect substantially. Therefore, it is important to suppress the effect of dry etching process by defect-free, atomically smooth etching profile, and control of etching selectivity. Plasma dry etching such as reactive ion etching process induces the etched defect since it has high energy ultraviolet (UV) photon irradiation and charged particles. The etched defect would reduce the optical and electrical properties of semiconductor materials. Alternatively, neutral beam has great potential for developing a defect-free dry etching process by its characteristics of completely suppressing UV photon irradiation and only generating the low energy neutral beam (below 100eV). In this work, we study on a GaAs/Al_{0.3}Ga_{0.7}As heterostructure etching process by neutral beam etching with chlorine and argon mixed etching gas. The effect of different mixed ratio of chlorine and

argon has been investigated. The results shows when 100% chlorine neutral beam used, the etching grass formation was observed on etched surface. To increase the argon mixed ratio in etched gas, the grass was eliminated and the etched surface roughness was smoother. As the best we know until now, when the 22% chlorine and 78% argon of mixed etched gas used, both the root-mean-square (rms) etched surface roughnesses of GaAs and $\text{Al}_{0.3}\text{Ga}_{0.7}\text{As}$ are about 0.6 nm (the rms surface roughness of as-received sample is about 0.4nm). Meanwhile, the etching rate of GaAs and $\text{Al}_{0.3}\text{Ga}_{0.7}\text{As}$ are 16 nm/min and 17 nm/min, respectively. It means the etching selectivity of GaAs/ $\text{Al}_{0.3}\text{Ga}_{0.7}\text{As}$ is about 0.94. Additionally, to verify the defect-free property of neutral beam etching, the cross-section of etched GaAs etched profile was analyzed by transmission electron microscopy. The result shows that no crystalline defect can be observed at the top region of etched surface. In summary, we developed a promising dry etching process for nanometer-scale GaAs/ $\text{Al}_{0.3}\text{Ga}_{0.7}\text{As}$ heterostructure with defect-free, etching selectivity of GaAs/ $\text{Al}_{0.3}\text{Ga}_{0.7}\text{As}$ closes to 1, and atomically smooth etching surface roughness.

4:00pm **PS2-WeA7 Development of Sputter and CVD using the Hyperthermal Neutral Beam**, *B.J. Lee, S.W. Choi, D.C. Kim, J.S. Kim, K.S. Oh, S.J. Yoo*, National Fusion Research Institute, Republic of Korea, *J.N. Jang, Y.J. Lee, M.P. Hong*, Korea University, Republic of Korea, *Y.C. Park*, Handong Global University, Republic of Korea

New deposition processes using Hyperthermal Neutral Beam, which has energy between 1 ~ 100 eV, have been developed for the damage-free deposition below 80 °C. Many studies concerning the plasma and heat damage problems during the deposition of transconductive oxide such as Indium Tin Oxide (ITO) on various organic materials which are vulnerable to those damages. This presentation discusses characteristics of ITO thin films deposited by brand-new plasma-damage - free sputtering process on cross-linked Poly 4-vinylphenol (PVP) layer at the room temperature using HNB. Nano-crystal (nc) Si TFT manufactured at low temperature (< 100 °C), namely CVD using HNB to satisfy the stability, V_{th} Shift, mobility and on/off ratio for OLED operation is also discussed. Very thin (< 5 nm) incubation layer for the transition from amorphous to crystal occurred while growing the nc-Si thin film on the glass was grown.

4:20pm **PS2-WeA8 Silicon Etching using Large Diameter Neutral Beam Source**, *T. Kubota*, BEANS Project 3D BEANS Center and University of Tokyo, Japan, *S. Ueki*, BEANS Project 3D BEANS Center, Japan, *O. Nukaga, M. Sugiyama*, BEANS Project 3D BEANS Center and University of Tokyo, Japan, *H. Ohtake*, Tohoku University, Japan, *S. Samukawa*, BEANS Project 3D BEANS Center and Tohoku University, Japan

Plasma etching is widely used for fabricating semiconductor electronic devices, microelectromechanical systems (MEMS), but plasma etching is known to cause damages due to the charge-up and UV irradiation. To overcome plasma-induced damages, neutral beam is widely studied by several groups in the world. Samukawa proposed a neutral beam source using negative ions in plasma and carbon aperture plate for neutralization [S. Samukawa, K. Sakamoto, and K. Ichiki, Jpn. J. Appl. Phys., 40, L779 (2001)]. The neutral beam source achieved high neutralization efficiency by using negative ions from pulse-time modulation plasma, and UV irradiation was drastically reduced. To apply this neutral beam source to mass production, we developed a large-diameter neutral beam source by using an 8-inch-diameter inductively coupled plasma etcher (Panasonic Factory Solutions Co., Ltd. E620) as an ion source. We measured flux and energy of neutral particles, ions, and photons and it was revealed that an argon neutral beam flux of more than 1 mA/cm² in the equivalent current density and a neutralization efficiency of more than 99%. Spatial uniformity of the neutral beam flux was within ±6%. Si etching with vertical profile using an F₂-based neutral beam was achieved with a high etch rate of about 100 nm/min. The spatial uniformity of the etch rate was better than ±5%. The etch rate was increased by applying bias power to the neutralization aperture plate, demonstrating that an accelerated neutral beam was successful in operation. This neutral beam source will enable the usage of damage-free neutral beam processes for practical use in the near future. A part of this work was supported by the New Energy and Industrial Technology Development Organization (NEDO). This work is partly supported by Formation of Innovation Center for Fusion of Advanced Technologies, Special Coordination Funds for Promoting Science and Technology, Ministry of Education, Culture, Sports, Science and Technology.

4:40pm **PS2-WeA9 Microwave Plasma Source for the High Flux Hyperthermal Neutral Beam**, *B.J. Lee, H.J. You, S.W. Jang, Y.H. Jung, D.W. Kim, M. Koo*, National Fusion Research Institute, Republic of Korea, *Y.C. Park, J.T. Kim*, Handong Global University, Republic of Korea

In order to incident the high flux of Hyperthermal Neutral Beam (HNB) on the substrate the high plasma density and the shortest distance between the

reflector, which converts ions to neutrals, namely neutralizer, and the substrate are required. ECR plasma source can both requirements. This presentation shows the features of ECR plasmas due to the Lisitano antenna, the vertical slotted antenna (VSLAN), the incline slotted antenna (ISLAN), and the rectangular slotted antenna (RESLAN) for the scanning type CVD. The characteristics of HNB Cu sputter for the Cu seed layer for Cu interconnect line of semiconductor as an application of plasma source from Lisitano antenna and HNB Al sputter for the thin film deposition of Al₂O₃ as one from RESLAN are also presented.

5:00pm **PS2-WeA10 Low Temperature, Lattice-plane-free, Anisotropic and Damage-free Oxidation by Neutral Beam Technology**, *A. Wada*, Tohoku University, Japan, *K. Endo, M. Masahara, S. Yamasaki*, National Institute of Advanced Industrial Science and Technology (AIST), Japan, *S. Samukawa*, Tohoku University, Japan

To fabricate a metal-oxide-semiconductor field-effect transistor (MOSFET) with a three-dimensional (3D) structure several problems arise in the conventional thermal oxidation process, such as high temperature, the dependence of the oxidation rate on the lattice plane of silicon (Si) and non-oriented oxidation process. After high temperature processing, compression stress remains in the SiO₂ film due to the difference in thermal expansion coefficient between the Si substrate and SiO₂ film. The compression results in defects in the SiO₂ film, which leads to increased leakage current. Furthermore, in the case of gate oxidation in the fabrication of 3D MOSFETs, the oxide film on a 3D structure and substrate is not consistent due to the different oxidation rates resulting from different lattice planes between them, which cause a concentration of the electric field and dielectric breakdown. Moreover, conventional thermal oxidation (TO) process is non-oriented oxidation process which forms oxide film on whole Si surface, and hence, it is difficult to independently control the thickness of the dual-gate dielectric film such as a four-terminal FinFET. To overcome these problems, we propose low-temperature (< 300°C) damage-free neutral beam oxidation (NBO) as an alternative oxidation process. We found that oxide film grown by NBO (NBO film) even at a low substrate temperature (300 °C) exhibits performance characteristics of a gate dielectric film that are as high as that of thermal oxide film in terms of the relationship between equivalent oxide thickness (EOT) and leakage current. This is because beam-induced oxidation plays a dominant role in the formation of NBO films by bombardment with an oxygen neutral beam. Also, the oxidation rate of NBO is independent of the lattice plane of silicon, and the oxidation is anisotropic. Therefore, oxide film grown by NBO is advantageous in that it can be applied to a gate dielectric film for a 3D fin structure of MOSFET.

5:20pm **PS2-WeA11 Structure-designable Method to form Super low-*k* SiOC Film by Neutral-Beam-Enhanced Chemical Vapour Deposition**, *T. Sasaki, S. Yasuhara*, Tohoku University, Japan, *T. Shimayama, K. Tajima, H. Yano, S. Kadomura, M. Yoshimaru, N. Matsunaga*, Semiconductor Technology Academic Research Center (STARC), Japan, *S. Samukawa*, Tohoku University, Japan

To precisely control the dielectric constant and the structure of a low-*k* SiOC film, we have developed a neutral-beam-enhanced chemical vapour deposition (NBECVD) method. Using Ar NBECVD with precursors of methyl trimethoxy silane (MTMOS), dimethyl-dimethoxy-silane (DMDMOS), and dimethoxy-tetramethyl-disiloxine (DMOTMDS), we can precisely control the dielectric constant and the film modulus of low-*k* SiOC deposited on Si substrates because this method avoids precursor dissociation that results from electron collisions and UV photons in plasma. Optimizing the ratio between Si-O and Si-(CH₃)_x as well as the proportions of linear (two-dimensional SiOC), network and cage (three-dimensional SiOC) structures by changing the precursor and neutral beam energy, we obtained a *k* value of less than 1.9 and a reasonable modulus of more than 4GPa with an extremely water resistant and very thermally stable

Additionally, we investigated the resistance of the NBECVD low-*k* SiOCH to plasma-irradiation damage in comparison with conventional plasma CVD (PECVD) techniques. We found that the durability of a low-*k* SiOCH film structure to plasma irradiation strongly depended on the kind of Si-O structure the film had. In particular, a linear Si-O structure was less affected by plasma exposure than were network/cage Si-O structures. In addition, this linear Si-O structure helped to reduce the number of methyl groups removed from the film by plasma irradiation, which preserved the dielectric constant. Since the NBECVD technique can generate a low-*k* SiOCH film with more linear Si-O structures than conventional plasma CVD, the NBECVD film has very strong plasma durability.

Glancing Angle Deposition (GLAD) II

Moderator: K. Robbie, Queen's University, Canada

2:40pm SE+TF-WeA3 Nanorods by Extreme Shadowing: New Pictures and New Physics, D. Gall, Rensselaer Polytechnic Institute INVITED

Glancing angle deposition (GLAD) uses an oblique deposition angle to exacerbate atomic shadowing during physical vapor deposition to create underdense layers consisting of nanorods with engineered shapes and three-dimensional composition variations. This growth process is intrinsically chaotic. However, initial substrate patterning combined with temporal changes in the deposition fluxes yield surprisingly regular nanostructure arrays. The questions about the theoretical minimum feature size as well as rod branching, merging, and broadening is discussed by presenting statistical morphology data from various metals deposited over a large temperature range. The rod width follows a power law scaling where the growth exponent depends linearly on the island nucleation length scale, but exhibits a discontinuity at 20% of the melting point, associated with a transition from a 2D to a 3D island growth mode. Different metals show excellent quantitative agreement when scaled to the melting point, yielding a single homologous activation energy of 2.46 for surface diffusion on curved nanorod growth fronts, applicable to all metallic systems at all temperatures. The onset of bulk diffusion near 50% of the melting point during such growth under exacerbated shadowing conditions leads to a direct transition from an underdense (zone I) structure to a dense (zone III) structure. Applications include nanostructured fuel cell electrodes, active components of nano pressure sensors, and lubricant transport channels for high-temperature self-lubrication.

4:00pm SE+TF-WeA7 Quasi-periodic Pattern Formation on Columnar Thin Films by Ion Beam Erosion at Oblique Incidence, M. Suzuki, H. Moriwaka, K. Nakajima, K. Kimura, Kyoto University, Japan

It is well known that obliquely deposited thin films show various shape related properties due to not only their complex columnar shapes but also their unique surface morphology. For example we have succeeded to prepare in-line aligned noble metal nanorod arrays on a template layer with anisotropic surface roughness originating from the bundled columns created by serial-bideposition technique (SBD)¹. Our nanorod arrays show the excellent surface enhanced Raman scattering properties. However, it is difficult to avoid the irregularities in size and shapes of the columns in the obliquely deposited thin films. On the other hand, recently, much attention has been paid on the pattern formation by ion beam erosion (IBE) at oblique incidence. When the flat surface is irradiated with the ion beam, quasi-periodic ripple patterns are self-organized. These ripple patterns seem to be more regular than the morphology found in the obliquely deposited thin films. However, the ripples in IBE surface are too gentle to use their functionalities or to use them as a template for the shadowing growth. In this work, we tried to reduce the irregularities of columnar shapes of obliquely deposited thin films by IBE.

Layers of Ge with an anisotropic surface morphology were prepared by SBD technique on a Si substrate. During the SBD, the deposition angle for Ge measured from the surface normal was fixed at an angle of 82°, while the azimuthal angle was changed rapidly by 180° with each deposition of an approximately 10 nm thick layer. After 15 cycles of SBD, Ge layers with a thickness of 300 nm were obtained. The surface of the Ge layer was irradiated with Xe⁺ ions of 5 keV up to the fluence of 0.5, 1.5, 3.0×10¹⁶ ions/cm² at an angle of incidence of 45° or 70°. The planes of incidence of Ge vapor and Xe⁺ ions are perpendicular to each other.

The average aspect ratio of the surface corrugation is 1.4 for the non-irradiated Ge films and significantly increases with increase of fluence. At the fluence of 3.0×10¹⁶ ions/cm², the aspect ratio reaches 7 mainly due to the elongation of the surface corrugation along the incident direction of the ion beam. The width of the surface corrugation is wider for 45° incidence than 70° incidence. Remarkably, distinct periodicity is found in the autocorrelation images of the SEM of the surface. These results are understood in terms of the directive sputtering toward the forward direction of the ion beam and the redeposition of the sputtered atoms, and are characteristic for the ion beam erosion of the porous materials.

1. M. Suzuki, et al., Appl. Phys. Lett., **88**, 203121 (2006).

4:20pm SE+TF-WeA8 Shadowing Effect of Patterned Seeds in Glancing Angle Deposition, D. Soma, D.-X. Ye, Virginia Commonwealth University

Glancing angle deposition (GLAD) technique has been developed by several groups including us in the past few years to produce three-dimensional nanostructures of a large variety of material. This technique combines oblique angle deposition with substrate manipulations in a physical vapor deposition system. The shadowing effect is the dominant growth mechanism resulting in the formation of various nanostructure arrays by programming the substrate rotation in polar and/or azimuthal direction. On patterned seeds, the shadowing effect strongly depends on the geometric parameters of the seed arrays, i.e. the aspect ratio of individual seeds, and the separation and arrangement of the seeds. In this talk, we will study those geometric parameters using a (2+1)-dimensional Monte Carlo simulation. In our simulation, we couple the shadowing effect and ballistic aggregation with rotating oblique incident particles. The uniformity of the nanostructures grown on the seeds will be investigated. The results of this study will provide a guideline for the design of seeds to achieve uniform size nanostructures by using GLAD.

4:40pm SE+TF-WeA9 Control of Phase Formation in Metal Oxide GLAD Films, R.T. Tucker, University of Alberta, Canada, A.E. Schoeller, M.D. Fleischauer, NRC - National Institute for Nanotechnology, Canada, M.J. Brett, University of Alberta, Canada

Glancing angle deposition (GLAD) has found application in a wide range of fields requiring porous, high surface area thin films, including sensors, optics, and energy devices. [1] This diversity is due in large part to the wide range of compatible materials, including metals, semiconductors, and organic compounds. Metal oxides are of particular interest for energy storage and conversion applications since they can be tuned for a combination of transparency, electrical conductivity, and chemical and thermal stability. Achieving the desired stoichiometric phase is essential for controlling desirable metal oxide properties. Here we discuss the challenges associated with achieving phase control in porous GLAD films.

Metal oxide GLAD films typically deposit in an amorphous state, so post-deposition processing is one route used to access a particular crystallinity and stoichiometry. Thermal annealing conditions depend on the desired phase: anatase TiO₂ readily forms at a few hundred degrees Celsius in air; Ti₄O₇ generally requires longer anneals at high temperatures (1000 °C) in a reducing atmosphere (eg. H₂ in carrier gas). [2] Annealing temperature, duration, and environment (e.g. oxidizing vs. reducing atmosphere) can all have an impact on film morphology, since coalescence or softening of structures is greatly enhanced at temperatures near the melting point of the metal oxide. Both the porosity of the film and the strength of the reducing atmosphere affect the extent of oxygen removal and morphology changes at relatively high temperatures, while still allowing access to a wide range of compositions (e.g. Ti_nO_{2n-1}, n = 2 - 9), phases (e.g. monoclinic, tetragonal, or orthogonal Nb₂O₅) and the associated optical, electronic, and thermal properties.

We will present methods to retain the porosity and structure of GLAD thin films while achieving desired stoichiometry and phase via post-deposition annealing, with a specific focus on phase and crystallinity characterization using x-ray diffraction. We will attempt to correlate results from the Ti-O and Nb-O systems with results from other systems of interest (e.g. W-WO₃) [3] as part of a better understanding of phase formation in porous thin films.

[1] M.M. Hawkeye and M.J. Brett, J. Vac. Sci. & Tech. A, **25**, 1317 (2007).

[2] J.R. Smith *et al.*, J. Appl. Electrochem., **28**, 1021 (1998).

[3] D. Deniz *et al.*, Thin Solid Films, **518**, 4095 (2010).

We thank NSERC, iCORE, Micralyne, and the National Research Council - Technology Development Program for financial support.

5:00pm SE+TF-WeA10 A Fan-Shadowing Model in Oblique Angle Deposition, B. Tanto, Rensselaer Polytechnic Institute, G.A. Ten Eyck, Sandia National Laboratories, T.-M. Lu, Rensselaer Polytechnic Institute

Recently oblique angle deposition has been used in a wide range of important, unique applications. The column angle of the obliquely deposited columnar structures is an important parameter that determines their mechanical, optical, and chemical properties. Unfortunately this angle can be greatly affected by materials and processing conditions which are too complex to model and predict. Existing models such as the tangent rule and cosine rule are independent of materials and processing conditions and therefore in general have a limited ability to predict the column angle. We present a semi empirical model that includes the effects of materials and processing conditions. We show that our model is able to accurately predict column angle analytically for a wide range of obliquely deposited amorphous Ge for two different sets of processing conditions. We also show how this model can be used to predict other useful quantities, such as porosity and column width.

The model uses the fact that the deposition on a line (or wire) results in a fan structure due to a self-shadowing effect with a fan angle that depends on materials and processing conditions. We first show how columnar structures can be generated by analytically applying global shadowing between the fan structures growing on adjacent lines. The columnar structures obtained possess geometrical properties (such as column width and column merging) that are consistent with columnar structures observed in experiment and simulation. We show how the exact shape and time evolution of the columnar structure can be calculated based on the knowledge of the fan shape. Once the exact shape of the columnar structure is known, various useful quantities can also be obtained: column angle, porosity, and column width. We experimentally verified our model by depositing amorphous Ge on line seeded substrate and on a flat substrate. The model agrees with experiments done on both substrates.

Finally, we describe relatively simple experimental setups that can be used for fast and convenient measurement of the fan geometry at various processing conditions, such as flux rates and temperatures. These fan geometry data obtained on normal incident flux can then be used to predict the columnar structure geometries for the whole range of incident flux angles and for all the various processing conditions.

5:20pm SE+TF-WeA11 Investigation of the Nanorod-Structuring Threshold in Glancing Angle Deposition (GLAD), D. Deniz, R.J. Lad, University of Maine

Thin films of tin (Sn), aluminum (Al), gold (Au), ruthenium (Ru), tungsten (W), ruthenium dioxide (RuO₂), tin dioxide (SnO₂) and tungsten trioxide (WO₃) were grown by glancing angle deposition (GLAD) to determine whether a nanostructuring threshold condition can be quantified as a function of both substrate temperature and melting point of the material. Films were grown using both DC and pulsed DC magnetron sputtering with continuous substrate rotation over the temperature range from 18 – 800°C. Film morphologies, structures, and compositions were characterized by high resolution scanning electron microscopy (SEM), X-ray diffraction (XRD) and X-ray photoelectron spectroscopy (XPS). Films were also grown in non-GLAD configurations for comparison. For the elemental metals, it is found that nanorod-structuring occurs for materials with melting points higher than that of Al (660°C) when films are grown at room temperature with a relatively small rotation rate of ~5 rpm. For the oxide materials, our results indicate that a critical substrate temperature (TS) to melting point (TM) ratio exists, above which GLAD nanorod-structuring becomes ineffective because the adatom mobilities become large enough for non-kinetically limited film nucleation and growth processes to occur, similar to those operative in a non-GLAD growth configuration.

Surface Science

Room: Santa Ana - Session SS-WeA

Chemisorption and Surface Reactions

Moderator: A. Utz, Tufts University

2:00pm SS-WeA1 Characterization of the Chemical Signal Created by CO Oxidation on Pt/GaN Nanodiodes, J.R. Creighton, M.E. Coltrin, R.P. Pawlowski, K.C. Baucom, Sandia National Laboratories

Previous results from Gabor Somorjai's group demonstrated the production of chemi-current during catalytic reactions on Pt and Pd surfaces using a Schottky diode structure described as a "catalytic nanodiode" [1-2]. During the exothermic oxidation of CO, some fraction of the chemical energy may be dissipated by formation of hot electrons in the catalytic metal via electronic excitation. If the catalytic metal film is thin enough (nanometer scale) some of these hot electrons may be collected on the semiconductor side of the Schottky barrier in the form of a "chemi-current". We have fabricated several versions of catalytic nanodiodes, and during CO oxidation we also detect a current that is unambiguously a result of the chemical reaction. We typically measure current densities up to 100 nA/mm² and reaction conversion efficiencies in the range of 10⁻⁵-10⁻³ electrons per CO₂ produced; results which are quantitatively similar to reports in more recent publications [3-4].

However, details of the electronic nature this chemical signal indicates that it is derived from a **voltage source**; not from a current source. In fact, the chemical signal is primarily, if not entirely, due to the thermoelectric voltage generated by changes in the **lateral** temperature gradient between the two electrical contacts in the nanodiode. We have used a 3D heat transfer model to simulate the time dependent temperature profile in the nanodiode during CO oxidation on Pt/GaN devices. This information, along with independent experimental measurements of the Seebeck coefficient allows us to quantitatively simulate the thermoelectric voltage signal generated during a typical experiment involving time-dependent CO

oxidation. Our results indicate that the nanodiode is simply operating as a **thermal detector** via a thermoelectric voltage. Unfortunately we have not yet found evidence supporting true "chemi-current" formation during CO oxidation on Pt/GaN nanodiodes.

References:

- [1] Z.J. Xiao and G.A. Somorjai, J. Phys. Chem. B 109 (2005) 22530.
- [2] J. Xiaozhong, A. Zupero, J.M. Gidwani, and G.A. Somorjai, J. Amer. Chem. Soc. 127 (2005) 5792.
- [3] J.Y. Park, J. R. Renzas, B.B. Hsu, and G.A. Somorjai, J. Phys. Chem. C, 111 (2007) 15331
- [4] J.Y. Park, J. R. Renzas, A.M. Contreras, and G.A. Somorjai, Topics in Catalysis, 46 (2007) 217

2:20pm SS-WeA2 Structural Investigation of Methylthiolate/Au (111) Interface: A Photoemission Core Level Shift Study, A. Chaudhuri, University of California, Irvine

Self assembled monolayers have been the subject of considerable interest for the last two decades. The high order, dense and stable structures, and bio compatible nature of these systems make them interesting for a wide range of technological application in industry. The thiolate /Au(111) interface is regarded as one of the classical examples of self assembled monolayer systems and is ideal for study in laboratories, due to the robust nature of the surface.

Despite of a number of studies, the adsorption sites of the thiolate and, hence, the structure of this interface is a long standing controversial issue. The conflict between theoretical calculations and the experimental observations for thiol-Au system has been fuelled by contradictory models to determine the adsorption site based on different experimental techniques. These models are different from each other and fail to depict a mechanism for a complete structure formation. In this present work, we have investigated the local structure of methylthiolate in the ordered Au(111) - (√3x√3)R30° phase using core-level- shifts measurements of the surface and bulk components of Au 4f_{7/2} photoelectron binding energy.

2:40pm SS-WeA3 Mechanistic Study of Photochemical Grafting of Alkenes to Group IV Semiconductors, X. Wang, R.J. Hamers, R. Ruther, University of Wisconsin-Madison

The grafting of organic molecules on semiconductor surfaces initiated by UV light has become an efficient means to tailor the chemical and physical properties of surfaces of materials, enabling their integration with various applications of the devices. The mechanism of photochemical grafting of alkenes to group IV semiconductors (diamond, silicon, germanium, etc) has remained poorly understood. We have demonstrated that a previously unrecognized process—photoelectron emission from semiconductors to reactant liquid—is a nearly universal mechanism for initiating grafting of alkenes to surfaces and is broadly applicable to a wide range of semiconductors.

The charge transfer processes that occur during the photochemical grafting to diamond surfaces were investigated by spectrally resolved photoelectron yield experiments. X-ray and ultraviolet photoelectron spectroscopy measurements (XPS, UPS) establish a clear correlation between the photoelectron yield, the grafting efficiency at different wavelengths, and the valence electronic structure of the substrate and of the reactant molecule.

While our initial work focused on detailed studies on diamond, more recently we have shown that this mechanism is also responsible for initiating UV-induced grafting onto other semiconductors, most notably both silicon and germanium. By intentionally reducing the bulk carrier lifetime in Si (by doping with Au) and comparing the grafting efficiency, we showed that the rate of UV-induced grafting is independent of the bulk carrier lifetime. This observation is important as it allows us to immediately rule out the bulk exciton mechanism as the primary pathway. Our results also showed that the rate of grafting was directly connected to the electron affinity of the reactant molecules. These results are important because they show that photoemission can also dominate as an initiation process with smaller bandgap semiconductors, such as silicon and germanium, where photoemission and exciton processes can both take place. We have hypothesized that the reason why the photoemission can be dominant even on silicon is that photoemission is an irreversible process, while in an exciton process the concentration of holes is reduced by recombination processes. Our studies provide new insights into the nature of photochemical functionalization on the surfaces of semiconductors and a fundamental understanding of the mechanism will facilitate the design and synthesis of well defined functional interfaces.

3:00pm **SS-WeA4 Reaction of Diisocyanates at the Ge(100)-2 × 1 Surface.** *K.T. Wong, S.N. Chopra, S.F. Bent*, Stanford University

Interest in organic functionalization of semiconductors has increased in recent years, as it offers the ability to mate existing knowledge of microelectronics fabrication with the tailorability of organic molecules to precisely control interfacial properties. Such control is necessary for today's microelectronics with continually decreasing feature sizes. In particular, this study focuses on organic functionalization of the germanium surface; germanium is a group IV semiconductor, like silicon, which may be used in devices for its favorable electronic properties. Here, we study the adsorption of two diisocyanate molecules on the Ge surface: 1,3-phenylene diisocyanate, in which the isocyanate functional groups are connected by a relatively stiff phenylene ring, and 1,4-diisocyanatobutane, in which they are connected by a more flexible alkyl chain. Using multiple internal reflection Fourier transform infrared spectroscopy in ultra high vacuum, we show that both molecules bind to the Ge(100)-2×1 surface primarily by a [2+2] cycloaddition reaction across the C=N bond of one isocyanate functional group. This result is similar to previous results for other isocyanate-containing molecules reacted with the Ge(100)-2×1 surface. X-ray photoelectron spectroscopy results agree with the [2+2] cycloaddition assignment and provide evidence that some isocyanate functional groups interact with the surface via a dative bond through an oxygen lone pair. We propose that this is likely the result of some adsorbates forming an additional interaction with the surface through the second isocyanate functional group. Density functional theory calculations demonstrate the feasibility of such products. The relatively weak binding of a second functional group by dative bonding may make these molecules ideal candidates for studying displacement by subsequent exposure to a second precursor. It may be possible to displace the dative-bonded isocyanate functional group, thereby creating additional free isocyanate groups on the surface.

4:00pm **SS-WeA7 Multiple Time and Length Scales in Nanocatalysts Probed in a Single Synchrotron Experiment: The Combined use of XAFS, XRD, DAFS and IR.** *A.I. Frenkel*, Yeshiva University INVITED

X-ray absorption fine structure (XAFS) and x-ray diffraction (XRD) techniques give complementary information about the structure of catalytic materials. XRD is effective in crystalline materials that possess medium to long range order (bulk catalysts, substrates and templates) while XAFS provides short range structural details in disordered, amorphous and/or low-dimensional materials. In addition, XAFS gives information about the electronic properties of the catalysts. These two methods have been developed and advanced *independently* from each other at synchrotron sources in the US and abroad. To analyze catalysts *in situ*, in particularly *in operando* (under their operating conditions), a new approach is needed, namely, the simultaneous collection of the XRD and XAFS data in real time as the reaction progresses, together with the online product analysis. Diffraction Anomalous Fine Structure (DAFS) is a structure-sensitive technique that allows to deconvolute multiple phases of the same element (e.g., metal nanoparticles and metal oxide) that can coexist in the sample. Application of quick scanning monochromator mode to XAFS measurement (called QEXAFS) allows to study kinetics of structural transformations within the reactants, catalysts and the reaction products. Such combinations allow to measure the time-dependent changes in the *actual* structure (in the short, medium and long range order), electronic properties and chemical activity of catalysts synchronously.

The first in US dedicated instrument for such combined measurements was built at the beamlines X18A and X18B of the National Synchrotron Light Source at Brookhaven National Laboratory. The current setup includes transmission and fluorescence XAFS detectors, QEXAFS monochromator enabling 10ms time EXAFS scan time, 2D area detector for XRD, residual gas analyzer and the automated gas mixing system. The upgrades currently under way include the addition of Diffuse Reflectance Infrared Fourier Transform Spectroscopy (DRIFTS) instruments developed jointly by members of Synchrotron Catalysis Consortium at BNL and HARRICK Scientific.

I will present several applications of the combined use of these instruments for catalysis research, including the studies of kinetics of reduction and oxidation of Cu-ceria catalysts, the investigation of the mechanism of reduction of CuFe₂O₄ with CO, and others.

4:40pm **SS-WeA9 The Interaction of Oxygen with Single Crystal Stepped Copper Surfaces: a XPS and STM Study.** *E. Broitman*, Carnegie Mellon University, *V.V. Pushkarev*, Lawrence Berkeley National Laboratory, *B.S. Holsclaw*, Carnegie Mellon University, *T.J. Lawton*, *A.E. Baber*, *E.C.H. Sykes*, Tufts University, *A.J. Gellman*, Carnegie Mellon University

Fundamental knowledge of metal oxidation processes is an important problem for the understanding of corrosion. In particular, the oxygen

reaction with copper surfaces is considered to be a model system and has consequently been extensively studied. However, to our knowledge, most of the studies have been carried out in individual samples of single orientations. In this work, the influence of steps on the oxidation of copper surfaces is studied by the use of a spherically-shaped sample with a (111) plane in its center. This sample allows the possibility to study the orientation dependence continuously up to a deviation of 10° from the (111) plane.

The copper crystal was cleaned in a UHV preparation chamber with a base pressure < 1X 10⁻¹⁰ Torr using several cycles of sputter cleaning with Ar⁺ ions of 1 KeV energy and annealing up to 600°C. The sample, kept at room temperature, was subsequently exposed to oxygen using a leak valve with dosing values in the range 100 to 1000 Langmuir. Two-dimensional surface imaging chemical analysis was carried out at room temperature using a Theta Probe monochromated Al K_α x-ray photoelectron spectroscopy (XPS) system (Thermo Scientific) in snapshot mode with a 100 μm spot size. Data processing was performed using the software Advantage provided with the instrument. Scanning Tunneling Microscopy (STM) was also done at room temperature using a commercially available STM Variable Temperature system (Omicron).

XPS images have shown that the oxygen content in the surface increases in the areas with higher step density. STM images revealed a complex oxidation mechanism. Adsorption of oxygen leads to the formation of a surface oxide by preferential incorporation of Cu atoms from step edges. It was observed at higher dosing that the descending step edge to a large terrace results to be more faceted and jagged than a descending step edge of a smaller terrace. It can be assumed that oxygen landing on the terrace diffuses to the descending step edge and oxidizes it. In this way, larger terraces above a step edge would have more oxygen diffusing to the descending step edge, producing more faceting than in the descending steps of the smaller terraces.

5:00pm **SS-WeA10 Cu(100) Oxidation: Potential Copper-Releasing Pathways for c(2x2) to Missing-Row Reconstruction Transition.** *M. Lee, A.J.H. McGaughey*, Carnegie Mellon University, *J.C. Yang*, University of Pittsburgh

Previous experimental and theoretical results show that the (2√2x√2)R45° missing-row reconstruction is a stable intermediate state during the early stages of Cu(100) oxidation. When the oxygen coverage on a Cu(100) surface reaches 0.5 monolayers [the c(2x2) phase], the surface structure transforms into the missing-row reconstruction by the release of every fourth row of copper atoms from the top copper layer. The released copper atoms are assumed to then diffuse away. The specific mechanisms and energetics of this transition are not yet fully understood. To investigate this transition, we use density functional theory calculations to predict potential copper-releasing pathways and their energy barriers using the climbing image nudged elastic band method. In the p(2√2x√2) unit-cell, there are two potential copper releasing pathways. For each pathway, two energy barriers are predicted because there is an intermediate state between the c(2x2) phase and the missing-row reconstruction. The energy barriers are 1.61 eV and 1.04 eV for the first pathway and 2.19 eV and 0.38 eV for the second pathway. To assess system size effects and alternative pathways, we also investigate the p(2√2x2√2) and p(4x4) unit-cells. In applying the copper releasing pathways analyzed for the p(2√2x√2) unit-cell to the larger unit-cells, there will be multiple ways to arrive at the final state. For example, in the p(2√2x2√2) unit-cell, two copper atoms should be released to form a complete missing-row. There are two ways for the missing-row formation: moving the copper atoms one by one or moving two copper atoms together. We expect that the copper releasing pathways and energy barriers will vary with the nature of the releasing copper movements.

5:20pm **SS-WeA11 Formation, Characterization and Reactivity of Adsorbed Oxygen on BaO/Pt(111).** *K. Mudiyansele*, Pacific Northwest National Laboratory, *C.-W. Yi*, Sungshin Women's University, Republic of Korea, *J. Szanyi*, Pacific Northwest National Laboratory

The formation of O_{ad} species and their reactivities in CO oxidation on BaO/Pt(111) were studied with temperature programmed desorption (TPD), infrared reflection absorption (IRA) and X-ray photoelectron (XP) spectroscopies. Two BaO/Pt(111) model systems with different BaO coverages were prepared and studied. The Pt(111) surface in both of these systems was not completely covered with BaO. On the system with lower BaO coverage (~50 % of the Pt(111) surface was free of BaO), two different O_{ad} species form following the adsorption of O₂ at 300 K; O adsorbed on clean Pt(111) sites and at the Pt-BaO interface. On the system with higher BaO coverage (~70 % of the Pt(111) surface is covered by BaO) two types of O_{ad} are seen at the Pt/BaO interface. The desorption of oxygen from the BaO-free portion of the Pt(111) surface gives an O₂ desorption peak with a maximum desorption rate at ~ 690 K. Recombinative desorption of interfacial O_{ad} gives two explosive-desorption features at ~ 760 and ~ 790 K in the TPD spectrum. The reactivities of these

adsorbed O species with CO to form CO₂ follow their order of desorption; i.e., the O_{ad} associated with the clean Pt(111) surface and desorbs at 690 K reacts first with CO, followed by the O_{ad} species at the BaO/Pt(111) interface (first the one that desorbs at ~ 760 K and finally the one that is bound the most strongly to the interface, and desorbs at ~ 790 K).

5:40pm **SS-WeA12 Molecular Vibrations at Surfaces by First-Principles Molecular Dynamics: Hydrogen-Bonded Networks of Amino Acids on Copper**, *A. Ievins, S.J. Jenkins*, University of Cambridge, UK

We present first-principles molecular dynamics simulations, obtained at the density functional level of theory, for molecular vibrations of amino acids on copper surfaces. Specifically, we have studied the hydrogen-bonded networks formed by glycine and alanine on the Cu{110} and Cu{311} surfaces. Fourier transformation of the autocorrelation function in each case leads to frequency spectra that may be compared with data from infra-red absorption experiments, where available. Moreover, by separately Fourier transforming key structural parameters such as individual bond lengths or bond angles, it is possible to make confident band assignments that aid in the interpretation of experiment. By tracking the motion of atoms over time, it is also possible to extract mean atomic positions, and realistic thermal ellipsoids, which may in turn be of use in understanding results from diffraction experiments and/or scanning tunneling microscopy.

Thin Film

Room: Pecos - Session TF-WeA

Thin Films: Growth and Characterization

Moderator: N.P. Guisinger, Argonne National Laboratory

2:00pm **TF-WeA1 Growth and Characterization of Thin Films for Organic Electronics Applications**, *D.J. Gaspar, L. Wang, Z.H. Zhu, M.H. Engelhard, B.J. Tarasevich, J.S. Swensen, R.E. Williford, M.E. Gross, W.D. Bennett, D.W. Matson*, Pacific Northwest National Laboratory **INVITED**

There are two basic ways of generating organic thin films for electronics applications – vacuum-based processes and solution processes (each with many variations). Each has advantages and disadvantages in film purity, morphology, deposition rate, process control, molecular design and materials choices. This presentation will describe the deposition, characterization and performance of organic thin films deposited using variants of both methods for organic light emitting diodes (OLEDs), organic thin film transistors (OTFTs), and other applications utilizing electroactive organic thin films. Specific advantages in film purity and access to different classes of materials are discussed. Surface characterization using time of flight secondary ion mass spectrometry (TOF-SIMS), X-ray photoelectron spectroscopy (XPS), atomic force microscopy (AFM) and conductive AFM), ellipsometry and Fourier transform infrared spectroscopy (FTIR) are used to characterize thin films, highlighting the challenges in characterizing these often sensitive and usually amorphous films, as well as need to develop a solid experimental understanding of the composition and structure of thin films deposited for organic electronics applications to understand performance.

2:40pm **TF-WeA3 Bio Modification of Titanium Surfaces with Grafted Sodium Styrene Sulfonate Thin Films**, *G. Zorn, D.G. Castner*, University of Washington

Ti and its alloys are commonly used as biomaterials due to their unique mechanical properties and good corrosion resistance. Still, Ti implants can induce the formation of a fibrous layer that can compromise bonding at the interface with the living tissue. The lack of proper integration of Ti with tissue can lead to implant failure. Since the biological response to implanted biomaterials is initiated at their surfaces, the performance of Ti and Ti alloys can be improved by modifying their surfaces. A promising approach for surface bio-modification is grafting a bioactive polymer onto Ti implant surfaces. For optimal grafting, it is important to fully understand the nature of the bio-modified surfaces since it has a pivotal role in the biomaterial performance. The main thrust of this work is to graft bioactive sodium styrene sulfonate (NaSS) onto Ti surfaces to control and improve their response in biological environment.

Smooth Ti films evaporated onto silicon wafers were used as substrates. XPS showed that the surfaces of these films are covered with a layer of TiO₂. The roughness of these surfaces, as measured by AFM, was 0.7nm. Methacryloxypropyltrimethoxysilane (MPS) was used as a cross linker between the Ti and the NaSS; the substrates were soaked in a solution of MPS in chloroform (5%v/v) for 1 hr at room temperature and then removed

from the solution and heated at 140°C for 4 hrs. After attaching the MPS molecules, XPS surface composition and high resolution XPS data suggested that the Ti substrates were covered with a uniform thin film. Additional evidence for the MPS attachment to the Ti surfaces was the appearance of the C_xH_yO_z fragments from the methacrylate group along with the decrease of the Ti and TiO_x fragments in the ToF-SIMS data. The NaSS grafting was then done at 90°C in an oxygen free environment for 15hrs using a 0.7M solution of NaSS monomer in dimethyl sulfoxide (DMSO). After NaSS grafting the XPS composition showed an increase of the C/Ti ratio and an appearance of sulfur and sodium. ToF-SIMS successfully detected the sulfonate group, C₈H₇SO₃, and a decrease of the Ti containing fragments. Fourier transform infrared spectroscopy (FTIR) and near edge absorption fine structure (NEXAFS) indicated an ordered array of the grafted NaSS layer on the Ti surfaces and AFM showed a uniform coverage with a roughness of 1.11nm.

Currently the mechanism of competitive protein adsorption on titanium surfaces before and after NaSS grafting is being studied. The XPS nitrogen signal indicates a higher amount of bovine serum albumin (BSA) or fibrinogen is adsorbed onto the titanium surfaces after modifying them with the NaSS layer.

3:00pm **TF-WeA4 Probing Stability of the Molecule-Substrate Interface in Self-Assembled Monolayers by Ion-Beam-Induced Desorption**, *P. Cyganik*, Jagiellonian University, Poland, *S. Wyczawska, F. Vervaecke, E. Vandeweert, P. Lievens*, Catholic University Leuven, Belgium

Due to the ease of preparation and their relatively high stability, self-assembled monolayers (SAMs) are very promising candidates to be used in the development of micro- and nano-structured materials. With numerous detailed studies available nowadays for SAMs, the identification of SAMs adsorption geometry and stability of molecule-substrate interface still remains controversial and rather difficult to access experimentally. In this presentation we report experiments on ion-induced desorption and resonance enhanced ionization mass spectrometry of SAMs on Au(111) substrate.¹ Although ion-induced desorption is commonly considered as a very invasive process when used for probing monomolecular films, our experiments demonstrate that this method can be successfully applied to monitor fine changes in the molecule-substrate interface stability of model SAMs systems based on thiols (CH₃-C₆H₄-C₆H₄-(CH₂)_n-S-Au(111), n = 2-6) and selenols (BPnSe, CH₃-C₆H₄-C₆H₄-(CH₂)_n-Se-Au(111), n = 2-6). Current desorption experiments will be discussed together with recent microscopic² and spectroscopic³ analysis of the molecular structure and stability of these SAMs. We demonstrate that lower or higher ion-induced bond scission efficiency can be correlated with, respectively, higher or lower chemical stability of particular chemical bonds. Thus, a new method for probing the stability of the substrate-SAM interface can be proposed.

References

- (1) S. Wyczawska, F. Vervaecke, et al. *in preparation*.
- (2) P. Cyganik, K. Szelagowska-Kunzman, et al. *J. Phys. Chem. C* **2008**, *112*, 15466.
- (3) K. Szelagowska-Kunzman, P. Cyganik, et al. *Phys. Chem. Chem. Phys.* **2010**, *12*, 4400.

4:00pm **TF-WeA7 Benzene Adsorption on Self-Assembled Monolayers**, *S.J. Sibener, H. Yuan, D.R. Killelea, K.D. Gibson*, The University of Chicago

Non-dissociative deposition of gas-phase species onto surfaces of alkanethiol self-assembled monolayers (SAMs) allows creation of new types of multi-component nanoscale materials. Systems such as these have garnered much attention due to their central role as model systems for studies of orientation-controlled adsorption and non-dissociative attachment of functional molecules on organic surfaces of technological importance, including molecular electronics.

Benzene (C₆H₆), perdeuterobenzene (C₆D₆) or a 50:50 mixture of these two isotopologues were deposited on SAM surfaces using a supersonic molecular beam. Supersonic molecular beam techniques permitted precise control over the dynamics of the deposition process by changes in the incident reagent's translational energy (E_{trans}) and incident angle. The results presented here highlight the role these dynamical variables play in the adsorption, desorption and conformation of the resultant multilayer molecular film. A combination of *in-situ* infrared reflection absorption spectroscopy (FT-IRAS) and mass spectrometry was used to determine the surface coverage, molecular orientation and the sticking coefficient as a function of the surface coverage of the benzene molecules deposited on SAM surfaces. The interaction between adsorbates and the SAM substrate was also investigated by varying the SAM chain length and whether the SAM contains an odd or even number of carbon atoms. These results were compared to analogous results from adsorption on clean Au surfaces.

The results of these experiments uncovered the details of the adsorption process. The effects of E_{trans} and substrate temperature on sticking show the central role dynamics plays in the physisorption of molecules on surfaces. Most significantly, the sticking of gas-phase benzene was found to have a novel dependence on surface coverage, and non-Langmuirian uptake was observed.

4:20pm TF-WeA8 Ex and In Situ Analysis of the Growth of Ultrathin Organic Films from Ethanol Solutions, T. Hauffman, E. Tourwé, A. Hubin, H. Terryn, Vrije Universiteit Brussel, Belgium

In order to form stable self-assembling organic monolayers on numerous substrates, dipping deposition from organic solvents is a widespread technique. However, it is rarely investigated what is the influence of the solvent on the substrate and the molecules which are supposed to be deposited. In this study we present the self assembly of phosphonic acids from an ethanolic solution on aqueous based pretreated aluminium oxides. Following the deposition behavior with XPS and AFM throughout deposition time, it was concluded that the nature of the deposition is random and fluctuating. In order to understand better what is going on, the deposition was followed in situ with odd random phase multisine impedance spectroscopy. This technique gives the opportunity to follow the behavior of the organic molecules as well as the behavior of the buried substrate. It was observed that ethanol adheres on the surfaces, changing the water based chemistry which was obtained through the pretreatment. Furthermore, a competition between the adsorption of the phosphonic acids and ethanol was seen, explaining the non-stable behavior previously analysed with XPS and AFM.

This statement was proven by characterizing ethanol-stabilised aluminium oxide samples during different immersion times. Although here no monolayer was formed, the trend observed corresponded with continuous organic layer growth.

4:40pm TF-WeA9 Effect of Deposition Pressure on the Structural, Optical and Electrical Characteristics of Y_2O_3 Thin Films by Reactive Magnetron Sputtering, V.H. Mudavakkat, K.B. Karuppanan, C.V. Ramana, University of Texas at El Paso

Significant research efforts have been directed in recent years on the growth of Y_2O_3 films because of their interesting physical, electronic, and optical properties. The diverse range of potential applications of Y_2O_3 films includes storage capacitors, random access memory (RAM) and metal-insulator-semiconductor (MIS) devices, protective and antireflective coatings for IR detectors, and optical filters. In the present work, Y_2O_3 films have been produced by the magnetron sputter-deposition. The effect of pressure on the structure, optical and electrical properties of Y_2O_3 films has been investigated. The rate of deposition found to be significantly influenced by the overall pressure during deposition. Optical characterization carried out using transmittance analysis indicate that the samples at lower deposition rates showed weaker absorption in comparison to the samples with higher deposition rates. X-ray diffraction (XRD) showed that the as-is deposited films at room-temperature exhibit [111] oriented cubic structure. Electrical characterization indicate that films are insulating with a very high resistivity. The capacitance-voltage characteristics are also obtained for Y_2O_3 films. The results will be presented and discussed.

5:00pm TF-WeA10 Effect of Partial Pressure on Structural and Optical Properties of WO_3 Thin Films, R.S. Vemuri, S.K. Gullapalli, R.V. Chintalapalle, University of Texas at El Paso

Tungsten oxide (WO_3) is a wide band gap semiconductor (~ 3.2 eV), which exhibits excellent properties suitable for the development of integrated chemical sensors and electrochromics. N-type conductivity coupled with selectivity and sensitivity to certain type of chemicals make WO_3 thin films interesting for NO_x and H_2S sensors. The present work was performed to understand the effect of oxygen partial pressure on the microstructure, optical and electrical properties of WO_3 thin films and optimize the conditions to produce materials suitable for sensor applications. WO_3 thin films were produced by the reactive RF magnetron sputtering. The films were grown at various reactive gas pressures (2.3 – 5.6 mTorr) by changing the oxygen flow rate while keeping the deposition temperature fixed at 400°C. Optical spectroscopy analysis of the grown films indicates that optical properties are sensitive to the oxygen partial pressure. The spectral transmission of the films increased with the increase in oxygen concentration. The band gap of these films was found to be increasing from 2.6 eV to 3.25 eV with increasing oxygen pressure. Electrical conductivity $\{\sim 10^{-2} (\Omega\text{-cm})^{-1}\}$ measurements indicate that there is a correlation between the growth conditions, optical and electrical properties.

5:20pm TF-WeA11 Effects of Deposition Temperature on Al doped ZnO Thin Film for Solar Cells by dc Magnetron Sputtering, W. Yang, J. Joo, Kunsan National University, Republic of Korea, S.M. Rossnagel, IBM Research

5:40pm TF-WeA12 Influence of Growth Rate on the Epitaxial Orientation and Crystalline Quality of CeO_2 Thin Films Grown on $Al_2O_3(0001)$ by Oxygen Plasma-Assisted Molecular Beam Epitaxy, M. Nandasiri, S. Kuchihbatla, P. Nachimuthu, T. Varga, V. Shutthanandan, W. Jiang, S. Thevuthasan, Pacific Northwest National Laboratory, S. Seal, University of Central Florida, A. Kayani, Western Michigan University

Cerium oxide thin films were grown on $Al_2O_3(0001)$ substrates with different growth rates (1-10 Å/min) by oxygen plasma-assisted molecular beam epitaxy (OPA-MBE). The growth rate induced epitaxial orientations and crystalline quality of CeO_2 thin films were studied by in-situ reflection high-energy electron diffraction (RHEED), ex-situ atomic force microscopy (AFM), and high-resolution x-ray diffraction (HRXRD) techniques. CeO_2 grows as three-dimensional (3-D) islands and two-dimensional (2-D) layers at growth-rates of 1-7 Å/min and ≥ 9 Å/min, respectively. The average surface roughness of 5-10 Å shows high-quality surfaces of CeO_2 thin films. The formation of epitaxial $CeO_2(100)$ and $CeO_2(111)$ thin films occurs at growth rates of 1 Å/min and ≥ 9 Å/min, respectively. Glancing incidence XRD measurements have indicated that the films grown at intermediate growth rates (2-7 Å/min) consist of some polycrystalline CeO_2 along with $CeO_2(100)$. The thin film grown at 1 Å/min showed six in-plane domains, characteristic of well-aligned $CeO_2(100)$ crystallites. All six of the repeating rectangle units of O atoms from the oxygen sub-lattice in $Al_2O_3(0001)$ that bind to Ce atoms are nonequivalent which produces six in-plane domains. This also minimizes the lattice mismatch between the thin film and the substrate leading to well-aligned $CeO_2(100)$ crystallites. When increasing the growth rate from 1 Å/min to 2-7 Å/min, the lack of sufficient time to stabilize the Ce atoms on all the rectangle units of O atoms from oxygen sub-lattice in $Al_2O_3(0001)$ results in poorly-aligned $CeO_2(100)$ crystallites that start to coexist along with well-aligned crystallites. Furthermore, the content of the poorly-aligned $CeO_2(100)$ crystallites increases with increasing growth rate up to 7 Å/min, and three out of six in-plane domains gradually decrease and eventually disappear. At growth rates ≥ 9 Å/min, $CeO_2(111)$ film with single in-plane domain was identified. In order to accommodate the $CeO_2(111)$ unit on top of the $Al_2O_3(0001)$, the cerium sub-lattice undergoes compression in all three axes by $\sim 24\%$ resulting in poorly-aligned $CeO_2(111)$ crystallites. The formation of $CeO_2(100)$ 3D-islands at growth rates of 1-7 Å/min is a kinetically-driven process unlike at growth rates ≥ 9 Å/min which result in an energetically and thermodynamically more stable $CeO_2(111)$ surface.

Tribology Focus Topic

Room: Tesuque - Session TR+NS+SS-WeA

Mechanical & Chemical Effects on Friction and Wear

Moderator: S.S. Perry, University of Florida

2:00pm TR+NS+SS-WeA1 Quantitative Assessment of Sample Stiffness and Sliding Friction from Force Curves in Atomic Force Microscopy, J.R. Pratt, G.A. Shaw, NIST, L. Kumanchik, University of Florida, N.A. Burnham, Worcester Polytechnic Institute

It has long been recognized that the angular deflection of an atomic force microscope (AFM) cantilever under "normal" loading conditions can be profoundly influenced by the friction between the tip and the surface. It is shown here that a remarkably quantifiable hysteresis occurs in the slope of loading curves whenever the normal flexural stiffness of the AFM cantilever is *greater* than that of the sample. This situation arises naturally in cantilever-on-cantilever calibration, but also when trying to measure the stiffness of nanomechanical devices or test structures, or when probing any type of surface or structure that is much more compliant along the surface normal than in transverse directions. Expressions and techniques for evaluating the coefficient of sliding friction between the cantilever tip and sample from normal force curves, as well as relations for determining the stiffness of a mechanically compliant specimen are presented. The model is experimentally supported by the results of cantilever-on-cantilever spring constant calibrations. The cantilever spring constants determined here agree with the values determined using the NIST electrostatic force balance within the limits of the largest uncertainty component, which had a relative value of less than 2.5%. This points the way for quantitative testing of micromechanical and nanomechanical components, more accurate calibration of AFM force, and provides nanotribologists access to information about contact friction from normal force curves [1].

1. J. Appl. Physics **107**, 044305 (2010), doi:10.1063/1.3284957

2:20pm **TR+NS+SS-WeA2 Nanotribological Properties of Polyzwitterionic Brushes**, Z. Zhang, A.J. Morse, S.P. Armes, University of Sheffield, UK, A.L. Lewis, Biocompatibles UK Ltd., UK, G.J. Leggett, University of Sheffield, UK

The frictional properties of surface grown zwitterionic polymer brushes: poly(2-(methacryloyloxy)ethyl phosphorylcholine) (PMPC) have been characterized using friction force microscopy (FFM) in different liquid media.

1. Effect of molecular weight and solvent on the frictional properties

For brushes thicker than 192 nm, the coefficient of friction decreased with increasing brush thickness, while for brush layers with smaller thicknesses, the coefficient of friction varied little with molecular weight. It is suggested that water molecules bound to PMPC chains act as an interfacial lubricant; as brush thickness increases, the amount of bound water increases and the coefficient of friction decreases. This hypothesis is supported by comparative studies of the approaching parts of force-displacement plots acquired for PMPC brush samples with different molecular weights under water. In particular, it was found that thicker brushes exerted a greater repulsive force to the AFM probe. Gold-coated probes were used throughout this part to avoid any complication might be caused by tip surface chemistry. FFM has also been used to investigate the consolvency behaviour of PMPC. Friction force was measured for PMPC brushes with a dry thickness of 307 nm while immersed in alcohol/water binary mixtures with different compositions. A distinct increase was observed in the coefficient of friction at an ethanol-water ratio of 90:10, and a 2-propanol-water ratio of 70:30, but not for methanol/water mixtures. This result is attributed to the conformational change of the polymer brush, which induced the loss of hydration layer.

2. Influence of solvent and tip chemistry on the contact mechanics

To study the contact mechanics of tip-sample interactions in FFM, AFM probes were chemically functionalized by deposition of three different types of self-assembled monolayer of dodecanethiol ($C_{11}CH_3$) or mercaptoundecanoic acid ($C_{10}COOH$), or cysteamine (C_2NH_2). In alcohol solvents, friction force acquired using acid- or CH_3 - functionalized tip has a linear relationship with the applied load, but nonlinear for amine-terminated tip. It is also noted that the coefficient of friction is highest in 2-propanol for all three types of probe, which again suggests that conformation of PMPC brush is one of the key factors. In aqueous medium, the friction-load relationships were nonlinear and characterized by the Derjaguin-Muller-Toporov model of contact mechanics. Coefficient of friction measured by amine-functionalized probes were greater than that of acid-functionalized probes, and than CH_3 -ones, which was attributed to the interaction between polymeric chains and probes.

2:40pm **TR+NS+SS-WeA3 Atomic-scale Processes in Friction and Wear: From Diamond to Graphene**, R.W. Carpick, University of Pennsylvania **INVITED**

Nanoscale friction and wear are primary limitations for small-scale devices such as atomic force microscopy (AFM) probes and micro- or nano-electronic mechanical systems with contacting surfaces, and is also relevant to understanding friction and wear in larger-scale contacts. We first present studies that quantify the nanoscale volume loss in sliding wear using AFM and periodic *ex-situ* transmission electron microscopy (TEM) imaging. Novel carbon-based AFM tip materials, including ultrananocrystalline diamond and diamondlike carbon, exhibit superior wear resistance compared to conventional materials (silicon and silicon nitride)¹⁻³. We then present results from wear tests performed inside of the TEM using modified *in-situ* indentation techniques. This permits real-time visualization of the contact geometry and shape evolution of a single asperity with sliding over a countersurface. This allows us to measure wear with a higher degree of precision than previously possible. Insights comparing the wear resistance of carbon-based and Si-based materials, particularly in the context of atom-by-atom wear processes, will be discussed⁴. Finally, we will discuss how nanoscale friction in graphene and other atomically-thin sheets is governed by the high flexibility intrinsic to the atomic scale⁵.

1. *Prevention of nanoscale wear in atomic force microscopy through the use of monolithic ultrananocrystalline diamond probes*. J. Liu, D.S. Grierson, J. Notbohm, S. Li, S.D. O'Connor, K.T. Turner, R.W. Carpick, P. Jaroenapibal, A.V. Sumant, J.A. Carlisle, N. Neelakantan & N. Moldovan, **Small**, in press (2010).

2. *Ultra-low nanoscale wear through atom-by-atom attrition in silicon-containing diamond-like-carbon*. H. Bhaskaran, B. Gotsmann, A. Sebastian, U. Drechsler, M. Lantz, M. Despont, P. Jaroenapibal, R.W. Carpick, Y. Chen & K. Sridharan, **Nature Nanotechnology** 5, 181-185 (2010).

3. *Wear resistant diamond nanoprobe tips with integrated silicon heater for tip-based nanomanufacturing*. P.C. Fletcher, J.R. Felts, Z. Dai, T.D. Jacobs,

H. Zeng, W. Lee, P.E. Sheehan, J.A. Carlisle, R.W. Carpick & W.P. King, **ACS Nano**, accepted (2010).

4. *On the application of transition state theory to atomic-scale wear*. T.D. Jacobs, B. Gotsmann, M.A. Lantz & R.W. Carpick, **Tribol. Lett.**, accepted (2010).

5. *Frictional characteristics of atomically-thin sheets*. C. Lee, Q. Li, W. Kalb, X.-Z. Liu, H. Berger, R.W. Carpick & J. Hone, **Science** 328, 76-80 (2010).

4:00pm **TR+NS+SS-WeA7 Lubricin Reduces Microscale Cartilage Wear**, J.M. Coles, D.P. Chang, Duke University, L. Zhang, G.D. Jay, Brown University / Rhode Island Hospital, F. Guilak, S. Zauscher, Duke University

Articular cartilage is the load bearing surface of mammalian joints. Relatively little wear occurs in cartilage and the tissue is able to sustain millions of loading cycles despite limited regenerative capacity. Though many studies of cartilage friction and lubrication have been performed, often with a stated goal of understanding cartilage wear prevention, very few have measured wear directly and none have directly assessed the effects of synovial fluid constituents in mediating wear. Here we show that the synovial fluid glycoprotein lubricin reduces microscale cartilage wear *in vitro*. We used colloidal probe microscopy to induce wear and use the change in the average height of the surface as a measure of worn volume. The height change in locations worn in the presence of lubricin was significantly less than in those worn in the control solution. These data indicate that lubricin is important for cartilage preservation physiologically and may have implications for treating or preventing joint disease.

4:20pm **TR+NS+SS-WeA8 Friction of Metallic Nanoparticles: The Influence of Particle Morphology, Orientation and Air Exposure**, D. Dietzel, T. Moeninghoff, C. Herding, M. Feldmann, H. Fuchs, Westfälische Wilhelms-Universität Muenster, Germany, C. Ritter, U.D. Schwarz, Yale University, A. Schirmeisen, Westfälische Wilhelms-Universität Muenster, Germany

The contact area dependence of the interfacial friction experienced during the translation of the antimony is studied under different conditions using the tip of an atomic force microscope as a manipulation tool [1]. In vacuum a dual behavior in the friction-area curves is found had been found earlier, characterized by the observation that some particles exhibit friction below the detection limit while other similarly sized particles showed constant shear stress values [2]. New investigations with improved sensitivity confirm the reproducibility of this effect and that neither the particle's morphology nor their relative orientation towards the substrate lattice change this behavior. In contrast, we find that a temporary exposure to ambient air can lead to a drastic increase in the particle's friction.

[1] A. Schirmeisen and U. D. Schwarz, *ChemPhysChem* 10 (2009) 2358

[2] D. Dietzel et al., *Physical Review Letters* 101 (2008) 125505

4:40pm **TR+NS+SS-WeA9 Modeling Materials in Contact using Molecular Simulation**, J.D. Schall, R.V. Petrach, Oakland University **INVITED**

Molecular dynamics (MD) simulation has become an extremely powerful tool for materials science research due to the wealth of atomic level information it provides. In this talk an overview of the MD simulation method will be given. Then a number of applications where MD simulations have been applied to study materials in contact will be discussed. Topics will include the tribology of amorphous carbon films in the presence of hydrogen, and recent work involving the indentation of free-standing graphene sheets. In simulation of the tribology of amorphous carbon, chemical reactions between opposing films were monitored and used to elucidate the mechanisms for enhanced friction and wear properties and to discover the mechanisms of transfer layer formation. These simulations illustrate the need for surface passivation of amorphous carbon films in applications where low friction is desired. We have also investigated the role of silicon on the properties of these films using a parametrization of Brenner's second generation reactive empirical bond order potential for Si-C-H interactions. Recent results of the simulation of indentation of free-standing graphene films will be shared.

5:20pm **TR+NS+SS-WeA11 Modeling Tribochemistry of DLC vs DLC in the Presence of Water**, J.A. Harrison, P.T. Mikulski, M.T. Knippenberg, United States Naval Academy

Because the structure and properties of diamond-like carbon (DLC) can vary depending upon deposition conditions, the tribological response of DLC (and diamond) is very sensitive to environmental conditions. For instance, the presence of water vapor has been shown to negatively impact the friction performance of hydrogenated DLCs but to improve the performance of nanocrystalline and ultrananocrystalline DLCs.

Tribochemical reactions of the water with the DLC are thought to be at the heart of this long-standing puzzle.

With that in mind, we have been working to develop a potential energy function that is capable of modeling DLC in the presence of water. To be realistic, such a potential energy function should be able to model tribochemical reactions that may occur as a result of the sliding. In addition, because H, C, and O have very different electronegativities, the potential energy function must be capable of modeling charges and fluctuating charges that arise from electronegativity differences in a realistic way. This talk will outline our efforts at potential development and present some preliminary results of DLC friction in the presence of water.

**Supported by The Air Force Office of Scientific Research.

5:40pm **TR+NS+SS-WeA12 Effects of Impact and Sliding Forces on Failure Behavior of a DLC Coating.** *J.F. Su, L. Wang, X. Nie*, University of Windsor, Canada

The wear and tribological properties of diamond-like carbon (DLC) coatings have been investigated and well documented under various laboratorial and industrial conditions. However, investigations into failure behavior of the coatings when subjected to cyclic impact-sliding loads are scarce. In this study, an inclined ball-on-plate impact-sliding tests were used to evaluate the fatigue cracking and peeling failure behavior of a DLC (a-C:H) coating and a TiN coating as comparison. By adjusting the impact velocity of a steel impacting ball that is connected to and driven by air cylinder, various dynamic impact loads can be obtained. The impact load vs. time curves were recorded and showed three stages, i.e., impact loading stage, vibration stage and quasi-static sliding stage for each impact-sliding cycle. Four loading combinations of impact/static forces (50N/100N, 100N/100N, 50N/200N and 100N/200N) were used in the tests. The test results showed that the DLC coating performed better than the TiN coating under the impact forces but worse under the sliding stages where the quasi-static force was applied by the air cylinder.

Thursday Morning, October 21, 2010

Applied Surface Science

Room: Cochiti - Session AS1-ThM

Advanced Automation and Data Processing

Moderator: V. Smentkowski, GE Global Research Center

8:20am **AS1-ThM2 Chemical State Thin Film Characterisation by Angle Resolved XPS Using the Maximum Entropy Method**, *A.J. Roberts, G. Mishra, K. Macak*, Kratos Analytical Ltd., UK, *C. Moffitt*, Kratos Analytical Inc., UK

The application of thin films with nanometre thickness is being driven by their use in many industries. Angle resolved x-ray photoelectron spectroscopy (ARXPS) is a uniquely placed technique providing non-destructive quantitative chemical state depth distribution of elements in the first few nanometres of a surface.

Acquisition of ARXPS using modern instrumentation is now straight forward but determining the depth distribution of elements and their chemistry is more challenging. One numerical method for the reconstruction of depth profile data from ARXPS is the maximum entropy method (MEM). The precision of the reconstructed depth profile depends both on the noise in the experimental data and on the accuracy of the physical model. Furthermore effects of elastic scattering of the photoelectrons and analyser acceptance angle of the analyser must also be adequately accounted for. The influence of the fitting algorithm on reconstructed depth profiles from ARXPS has recently been reviewed [1] for high-k multilayer materials with emphasis on the importance of prior knowledge and/or constraints to achieve high quality profiles. Work presented here expands on the previous conclusions and explores the effect of data collection conditions such as instrument operating mode, analyser collection angle and signal to noise on the reliability of reconstructed profiles for multilayer thin films and modified surfaces.

[1] T. Conard, K. Macak, G. Mishra, W. Vandervorst IUVSTA-59 Workshop

8:40am **AS1-ThM3 Strategies for Multivariate Analysis of Very Large Spectral Images**, *M.R. Keenan*, Consultant **INVITED**

The sizes of spectral image data sets, always large, are becoming truly huge with modern spectral imaging techniques. Taking ToF-SIMS as one example, image depth profiling can yield data sets comprising several million individual mass spectra arrayed in three spatial dimensions. Spectral complexity is also increasing, particularly in biological applications where more mass channels and higher spectral resolution are required to separate and identify the species of interest. The tools of multivariate statistical analysis (MVA) have proven valuable aids to interpreting complex, high-dimensional data. Given the realities of huge data sets, however, straightforward application of these techniques strains the computing resources available in the typical analytical laboratory. In this paper, we propose a two-stage strategy for multivariate analysis of very large spectral images. In the extraction phase, we seek to efficiently distill the chemical information contained in the data into a minimum number of components that describe the spatial and spectral characteristics the species making up the sample. Principal Component Analysis (PCA) of data suitably preprocessed to account for non-uniform noise is the maximally parsimonious method for extracting information. Techniques for exploiting characteristics of the raw data, such as sparsity, and approaches to estimating the noise covariance on-the-fly can make order-of-magnitude computational improvements in PCA. Owing to the physically irrelevant constraints imposed on the principal components, however, they are notoriously abstract in appearance and difficult to interpret. In the second, or interpretive, stage of MVA, we will perform rotations or transformations of the principal components that are inspired by physically meaningful sample or spectral features such as component non-negativity, sparsity, independence and simplicity. Abstract factor rotations, such as the Varimax method, are time-honored tools in Factor Analysis, but appear to be underutilized in chemometrics. In this talk, we will discuss a general and rapid method for performing factor rotations based on arbitrary optimization criteria. Besides making a connection between factor rotation and seemingly disparate techniques such as Independent Component Analysis (ICA) and Maximum Autocorrelation Factors (MAF), we will present several novel rotations that have potential use in spectral image analysis. An important point, here, is that the rotations entail relatively low computational cost allowing us to examine our results from multiple points of view with an eye toward find representations that best help us solve the chemical problem at hand.

9:20am **AS1-ThM5 Report on the 59th IUVSTA Workshop: Surface Chemical Analysis – Improving Data Interpretation by Multivariate & Informatics Techniques**, *J. Tyler*, University of the West Indies, Trinidad and Tobago

The 59th IUVSTA Workshop: Surface Chemical Analysis - Improving Data Interpretation by Multivariate & Informatics Techniques was held at the Salybia Nature Resort in the Republic of Trinidad and Tobago from April 11 -16, 2010. The purpose of the workshop was to provide a forum for presentations and discussions in order to advance the field of Surface Chemical Data Analysis and Interpretation. Thirty-two scientists attended the meeting, including representatives from industry, academia and National Laboratories. The participants ranged from senior scientists to graduate students. Experts in surface science and chemometrics participated alongside those who were relative neophytes in one area or the other. The workshop was organized into 14 sessions, each with two to three formal presentations and an extended discussion period, and a final summary session. Many discussions lasted for more than an hour. During the discussions it was evident that there is no single data analysis method that is ideally suited to all problems and that guidelines are needed to assist analysts in selecting the most appropriate techniques for their objectives. The necessity for appropriate preprocessing of data, including peak selection, dead time correction, normalization and scaling was an oft repeated theme. A variety of approaches to enhance correct chemical interpretation of results were discussed. One full day of the workshop focused on biological applications, highlighting the value of multivariate methods when dealing with chemically and spatially complex samples and the difficulties of handling very large data sets. Although SIMS was a focus of much of the discussion, emerging issues in analysis of imaging XPS, NEXAFS, MALDI and multi-technique data sets were addressed. Key issues that arose during the discussions included the need to create guidelines and best practices, the value of mentoring, and the critical demand for a rapid, easy to use interface between vendor software and advanced data analysis packages. A series of action items were developed to address these critical issues, including creation of a website for exchange of data, software programs and bibliographical information; creation of a blog for continued community discussion; completion of an ISO technical report that would provide guidelines and establish best practices and a request to instrument vendors to improve the transparency and to simplify the interface between their software and data reduction programs. A full report on the conference and progress to date on these action items will be presented.

9:40am **AS1-ThM6 Multivariate Analysis of NEXAFS Spectrum Images**, *J.A. Ohlhausen, M.T. Brumbach*, Sandia National Laboratories, *C. Jaye, D.A. Fischer*, NIST, *E. Principe, P. Sobol*, Synchrotron Research, Inc. Multivariate analysis methods have been applied to Near Edge X-ray Absorption Fine Structure (NEXAFS) spectrum images acquired at the National Synchrotron Light Source (NSLS) at Brookhaven National Laboratories (BNL). NEXAFS has typically been a large spot technique, but with the new imaging system on U7a at NSLS, spectrum images can now be acquired. These spectrum images can be processed univariately, but many issues confound the analysis. Issues include overlapping peaks, broad spectral features, poor contrast, non-zero backgrounds and unique synchrotron-related data artifacts. We will discuss these issues and their implications to successful multivariate analysis. Strategies for removing non-uniform illumination and time-dependent illumination decay will be shown. Additionally, the energy of secondary electrons can be filtered so that the depth of analysis is varied, leading to depth and spatially-resolved (3D) chemical information. We will demonstrate the multivariate analysis of data acquired by this technique as well.

Sandia National Laboratories is a multi-program laboratory operated by Sandia Corporation, a wholly owned subsidiary of Lockheed Martin Company, for the U.S. Department of Energy's National Nuclear Security Administration under contract DE-AC04-94AL85000.

Applied Surface Science

Room: Cochiti A - Session AS2-ThM

Forensics, Failure Analysis, and Practical Surface Analysis

Moderator: I.S. Gilmore, National Physical Laboratory, UK

10:40am **AS2-ThM9 Characterization of Composition C4 Explosives using Time-of-Flight Secondary Ion Mass Spectrometry (ToF-SIMS) and X-Ray Photoelectron Spectroscopy (XPS).** *C. Mahoney, K.L. Steffens, A.J. Fahey, B.A. Benner*, National Institute of Standards and Technology, *R.T. Lareau*, Transportation Security Laboratory **INVITED**
Over the past decade, we at the National Institute of Standards and Technology have been working closely with the Department of Homeland Security to stop the threat of terrorist-based attacks in the form of explosives or explosive-based devices. Our program encompasses many different aspects of this threat, from development of measurement standards for trace explosives detection at airports, to the development and application of new metrology for the characterization these explosives. Here we present, to our knowledge, the first investigation into the application of surface analytical techniques, such as Secondary Ion Mass Spectrometry (SIMS) and X-Ray Photoelectron Spectroscopy (XPS) for the characterization and differentiation of plastic explosives. This particular work is focused on the characterization of composition C-4 explosives from several different regions.

Unlike traditional analytical techniques such as GCMS and/or LCMS, these powerful surface analytical tools allow for the simultaneous and direct characterization of all the components in C-4 (explosive components, additives, binders, contaminants etc.), as opposed to a partial analysis of extracted portions. Furthermore, the characterization of the explosive samples with ToF-SIMS and XPS will enable rapid identification of both organic and inorganic constituents as well as their characteristic isotopic abundances with excellent sensitivity. Most importantly, these techniques are well-suited for direct analysis of small explosive particulates collected directly in the field, and are already employed for homeland security applications that effect national policy.

11:20am **AS2-ThM11 Chemical Speciation of Engineered Nanoparticle Surface Chemistry with Secondary Ion Mass Spectrometry.** *C. Szakal, R.D. Holbrook*, National Institute of Standards and Technology

As the sizes of nanostructures decrease, the surface-to-volume ratios increase immensely such that the smallest nanoparticles are theoretically seen by their surroundings as only the chemistry exposed on the surface and not the bulk of the nanoparticle interiors. We believe that the ability to track the surface chemistry of nanoparticles vs. size and vs. environmental exposures will show dramatically altered surface chemistry, and thus altered chemical reactivity of the nanoparticles. This concept has widely been suspected and/or believed to be true within the nanoparticle field, but experimentalists have yet to devise a standard approach at measuring what the surface chemistry is and to what extent that surface chemistry can be altered in real-world conditions. Since we are interested *only* in the surfaces of the nanoparticles and not necessarily the bulk, we have worked to develop a new paradigm for monitoring the surface chemistry of engineered nanoparticles with secondary ion mass spectrometry (SIMS). When kept in a static mode analysis, SIMS can be highly surface-sensitive to just a few nm, where other commonly employed techniques for measuring nanoparticle chemistries either cannot separate bulk vs. surface information, or only arrive at surface information indirectly. We will present progress made towards reaching our aims, including nanoparticle preparation considerations, sensitivity of SIMS to monitoring changes in the nanoparticle surfaces, and projections into the future of this methodology for such a purpose.

11:40am **AS2-ThM12 Complementary XPS and SEM/EDS Characterization of Gunshot Residue (GSR).** *A.J. Schwoeble, B.R. Strohmeier, J.D. Piasecki*, RJ Lee Group, Inc.

Discharged firearm cartridges produce unique microscopic particles referred to as gunshot residue (GSR). GSR is the product of combustion of the primer material. Depending on the type and brand of ammunition, GSR particles typically contain varying amounts of lead, barium, and antimony, along with one or more other elements, such as aluminum, silicon, phosphorus, sulfur (trace), chlorine, potassium, iron (trace), nickel, copper, zinc, zirconium, and tin. If particles containing lead, antimony, and barium are detected on a crime suspect's hands or clothing, it is taken as sufficient evidence that the person has either recently handled a discharged firearm, was present in the general vicinity of a weapon while it was discharged, or came in contact with a surface contaminated with GSR. Scanning electron

microscopy (SEM) combined with energy dispersive X-ray spectroscopy (EDS) is the most commonly used technique for detecting the presence of GSR particles. GSR samples are collected from a suspect's hands and clothing using adhesives mounted on standard SEM sample stubs. SEM imaging is used to verify the characteristic size, shape, and morphology of GSR particles and EDS can identify the elemental composition of individual particles.

Determining the presence of lead, barium, and antimony fused together in a single particle having the correct morphology is all that is normally required for the positive identification of GSR. However, because of the high temperatures (~1,500-3,600 °C) and pressures (~14,000-65,000 psi) that result within 1 millisecond of discharging a firearm cartridge, highly complicated chemical interactions are likely to occur that will affect the chemical composition of the GSR particles. Because of its nanometer-scale sampling depth and the ability to provide detailed chemical state information, X-ray photoelectron spectroscopy (XPS) can provide important information regarding the surface chemistry of GSR; therefore, XPS offers potential as a complementary technique to SEM/EDS analysis. The aim of this investigation was to use XPS to gain further knowledge regarding the surface chemistry of GSR.

Biomaterial Interfaces

Room: Taos - Session B11+NS-ThM

Replicating Biological Environments and Processes

Moderator: E.O. Reimhult, University of Natural Resources and Applied Life Sciences, Switzerland

8:00am **B11+NS-ThM1 Biofunctionalized Micro- and Nano-cup Arrays by Plasma Polymer Templating.** *R. Ogaki, M.A. Cole, D.S. Sutherland, P. Kingshott*, Aarhus University, Denmark

We present a novel fabrication method for creating an array of 'cups' on the micro- and nano scale by using a combination of plasma polymerization (pp), self assembled monolayers (SAMs) and colloidal lithography (CL). The method uses polystyrene (PS) particles that are first self-assembled into a hexagonal close-packed (HCP) structure onto a desired substrate over a large area via the lift-off method. The assembled particles are reduced in size by plasma etching and a plasma polymer is deposited into the interstitial spaces between the particles. The particles are subsequently removed by ultrasonication, forming an array of plasma polymerized cups with controllable sizes (through particle choice) and chemistries (through plasma monomer choice). The plasma polymer does not coat the contact region between the particles and the substrate. Thus a chemical pattern is generated, in our case, when SAMs are assembled onto the exposed substrate region. This provides a platform for site specific immobilization of biomolecules and cells with a diversity of chemistries possible. The method can be extended to other types of coatings such as those from physical vapor deposition (PVD), prior to the removal of the particles. As a result, up to three different chemistries can be presented on the array, with the first chemistry on the uppermost surface, the second chemistry on the internal wall and the final chemistry on the particle-substrate contact region inside the cup. The structural and chemical success of the cups and the patterns are determined by scanning electron microscopy (SEM), atomic force microscopy (AFM), X-ray photoelectron spectroscopy (XPS), time of flight secondary ion mass spectrometry (ToF-SIMS). The method is adaptable to create micro- and nano-sized cups by the appropriate choice of particle sizes. The versatility of the method to tune the cup sizes and the potential to incorporate up to three chemistries is apparent, thus the presented fabrication method could be potentially utilized for immobilizing a range of multiple biological cells and molecules of different sizes inside the cups for applications such as multi-functional biosensors or for carrying out specific reactions inside the cups for biological studies.

8:20am **B11+NS-ThM2 Fabrication of Functional Hydrogel Nanostructures for Biomolecule Immobilization.** *R.T.S. Lam, J.-W. Jang, P.L. Stiles, S.R. Nettikadan*, NanoInk Inc.

Hydrogels have been used extensively for tissue engineering scaffolds and other biomedical applications because of their unique three-dimensional cross-linked polymer network that provide structural support while endowing an environment similar to natural tissue. Fabrication of hydrogels in submicron scale is greatly desirable; however structures with well-defined organization and high uniformity are not easily achievable by using traditional methods. Herein, we have demonstrated the printing of thiolated PEG hydrogels on a glass chip with precise control over the architecture

and feature size using dip-pen nanolithography (DPN) techniques. This direct and reliable method for generating hydrogel patterns may serve as useful tools to explore cell-substrate interactions. In addition, conjugating different proteins through the free thiol functional groups in hydrogels is a promising approach of functionalizing the substrate with different biomolecules. This can be used as a platform for high throughput screening of protein-cell interaction studies. We have shown specific immobilization of thiol-reactive rhodamine red maleimide molecules on to the hydrogel patterns. Yellow-fluorescent was observed exclusively at the patterned area. By adjusting the ratio between the two PEG hydrogel precursors, we should be able to fine-tune the number of free thiol functional groups in the hydrogels, and hence the density of conjugated biomolecules. These hydrogels with different composition can be also printed simultaneously by DPN techniques to create gradient pattern in a single array. In a nutshell, our studies has combined the top-down approach of generating 3D nanostructures surfaces with controlled surface chemistry which creates an ideal interface for solving various fundamental questions in the field of cell biology.

8:40am **B11+NS-ThM3 Engineering Cell Behavior in Microfabricated Substrates: Adding Dimensionality to the Sensory Toolbox**, *M.H. Textor, M. Ochsner, V. Vogel*, ETH Zurich, Switzerland, *M.L. Smith*, Boston University **INVITED**

The physical properties of the local cell microenvironment regulate cell behavior in concert with soluble or matrix bound signaling molecules. *In vivo*, these properties are defined by a fibrillar ECM and adjacent cells and have implications for human health and disease. Our understanding of their role in regulating cell physiology resulted from technological advances which led to reductionist cell culture systems with tunable substrate stiffness, ligand density, or cell adhesive area and shape in two dimensions (2-D). Most of these studies were performed on flat, 2-D culture surfaces where studies have shown that these properties regulate a seemingly endless variety of observable cell responses. Regulating these processes with engineered cell culture platforms might prove useful in tissue engineering or regenerative medicine applications where a specific cell phenotype needs to be stimulated or maintained.

The extent to which observations made in 2-D Petri dishes can be transferred to predict cell behavior in a 3-D environment is a focus of current research. However, only a limited number of studies investigated the different microenvironmental parameters as a function of dimensionality, often with no or limited control of cell shape and substrate stiffness, and thus cannot be directly compared to observations made on (patterned) 2-D culture systems.

The focus of this talk is to demonstrate how the surface area of adhesive contact and substrate rigidity differentially regulate actin cytoskeleton assembly in 2-D versus 3-D environments, and how this impacts cell phenotype and function. PDMS polymeric substrates (compatible with inverted stage microscopy) for the organization of single cells in engineered quasi-3-D microenvironments were fabricated presenting arrays of microwells of different shape/aspect ratios, and stiffness (typically 1 MPa to 10 kPa Young's Modulus). The walls and bottom of wells were backfilled with extracellular matrix proteins such as fibronectin or mobile lipid bilayers.

On rigid substrates cytoskeleton assembly within single fibroblast cells was found to occur in 3-D microwells at shapes that inhibited stress fiber assembly in 2-D. In contrast, cells did not assemble a detectable actin cytoskeleton in soft 3-D microwells (20 kPa), but did so on flat, 2-D substrates that were otherwise equivalent. These data indicate that neither cell shape nor rigidity are orthogonal parameters directing cell fate. The sensory toolbox of cells seems to integrate mechanical (rigidity) and topographical (shape and dimensionality) information differently when cell adhesions are confined to 2-D or occur in a 3-D space.

9:20am **B11+NS-ThM5 Uniform Spheroid Formation Using a "Smart" Polymer**, *J.A. Reed, J.P. Freyer, H.E. Canavan*, University of New Mexico Spheroids are small (~50-1000 μm diameter) sphere-shaped aggregates of cells that have been developed as 3D models for tumors. In addition to providing a model that more closely approximates the microenvironments of tissues and tumors than 2D cultures, spheroids can be more easily controlled than tests performed on animal models. Current approaches for spheroid formation result in spheroids with a wide size distribution (>25% standard deviation), requiring the use of secondary sorting to obtain a uniformly-sized population. To increase the efficacy of these models for drug discovery in cancer therapeutics, it is necessary to develop an efficient way to fabricate a large number of uniform spheroids. Using a thermoresponsive polymer, poly(*N*-isopropyl acrylamide) (pNIPAM), cell aggregates of reproducible size and cell density can also be obtained. In this work, we pattern pNIPAM on an anti-fouling substrate to direct cell attachment, and ultimately cell sheet detachment for uniform spheroid

formation. Using plasma polymerization, pNIPAM is patterned on Pluornic® F-127, which is nonfouling, to form 300 μm diameter reversibly cell adhesive "islands" in non-fouling Pluornic® F-127 "seas." EMT6 cells are grown to confluence on the islands in 2 days, at which time their growth media is exchanged to stimulate cell detachment to form 70 spheroids of ~100 μm from each 35mm diameter substrate. To verify pattern fidelity, X-ray photoelectron spectroscopy (XPS), time-of-flight secondary ion mass spectrometry (ToF-SIMS), atomic force microscopy (AFM), and contact angle goniometry are used. In addition to developing a novel technique for the formation of tumor analogs, we also find that use of the larger surface area: volume ratio accelerates the speed of cell release.

9:40am **B11+NS-ThM6 Parylene Peel-Off Technology: A Tool for Nano- and Microengineering Biological Environments**, *C.P. Tan, B.R. Cipriany, B.R. Seo, D.J. Brooks, E.M. Chandler, C. Fischbach, D.M. Lin, H.G. Craighead*, Cornell University

Spatial manipulation of biomolecules and cells on a surface with nano- and micrometer scale precision is important in engineering biological microenvironments for tissue engineering, micro total analysis systems (biosensors, microfluidics and microarrays), and fundamental biophysical studies. We present Parylene Peel-Off, a simple and adaptable tool that can be used to improve current patterning/engineering of biological environments. In this work, we describe the fabrication process for creating a polymer (parylene-C) template to serve as a stencil for printing nano- and microscale regions of nucleic acids, proteins, lipids and cells. Afterwards, the parylene template can be easily peeled away to yield arrays of highly uniform biomolecular features in a large area format. We demonstrate the use of our Parylene Peel-Off technology to micropattern tumor cell arrays, for investigations into the role of cell-cell interactions in angiogenesis and cancer progression. By combining Parylene Peel-Off with current inkjet printing technologies, we have also generated multi-component, combinatorial protein arrays with array feature sizes down to 90nm. We anticipate that Parylene Peel-Off will be useful for enabling high-resolution studies of subcellular biological processes, integrating biochemical functionalities with miniaturized sensors, and engineering cellular and tissue microenvironments. Beyond basic science, our Parylene Peel-Off technology can be a useful tool to pattern chemically sensitive materials that are difficult to manipulate on the nano-scale, improve drug screening, and enable current inkjet printing technologies to extend their resolution to the sub-micrometer scale.

Biomaterial Interfaces

Room: Taos A - Session B12+NS-ThM

Quantitative Sensing at Biointerfaces

Moderator: E.O. Reimhult, University of Natural Resources and Applied Life Sciences, Switzerland

10:40am **B12+NS-ThM9 Membranes on Solid Surfaces**, *A.P. Shreve*, Los Alamos National Laboratory **INVITED**

Lipid assemblies on solid substrates provide a means of integrating biological and non-biological systems. They serve as a basis for a number of technological applications, particularly biological sensing and imaging platforms. They also provide important materials for the study of fundamental biophysical processes, and additionally are a platform for the study of the structure and dynamics of low-dimensional complex fluids. Working with a number of collaborators [1-4], we have been investigating how lipids interact with variously textured and functionalized solid surfaces, with an emphasis on the use of optical microscopy and spectroscopy as means of interrogating structure, dynamics and function within membrane assemblies on surfaces. Selected examples from recent and ongoing work will be discussed, including the use of diffusion measurements to infer the nature of membrane interactions with nanotextured surfaces, preparation and characterization of controlled multilayer architectures, study of how electrostatic interactions with surfaces affect the structure and asymmetry of membranes, the interaction of functionalized nanoparticles and nanomaterials with membranes, and the development and characterization of multicomponent membranes on patterned nanoporous and nanostructured substrates. All of these topics are related to long-term interests in the application of solid-substrate supported lipid assemblies in sensing and characterization of biological systems.

[1] T.H. Yang, C.K. Yee, M.L. Amweg, S. Singh, E.L. Kendall, A.M. Dattelbaum, A.P. Shreve, C.J. Brinker, A.N. Parikh, "Optical detection of ion-channel-induced proton transport in supported phospholipid bilayers," *Nano Letters* 7 (2007) 2446. [2] A.E. Oliver, E.L. Kendall, M.C. Howland, B. Sanii, A.P. Shreve, A.N. Parikh, "Protecting, patterning, and scaffolding supported lipid membranes using carbohydrate glasses," *Lab on a Chip* 8

(2008) 892. [3] A.P. Shreve, M.C. Howland, A.R. Sapuri-Butti, T.W. Allen, A.N. Parikh, "Evidence for leaflet-dependent redistribution of charged molecules in fluid supported phospholipid bilayers," *Langmuir* **24** (2008) 13250. [4] J.H. Werner, G.A. Montaña, A.L. Garcia, N.A. Zurek, E.A. Akhadov, G.P. Lopez, A.P. Shreve, "Formation and dynamics of supported phospholipid membranes on a periodic nanotextured substrate," *Langmuir* **25** (2009) 2986.

11:20am **BI2+NS-ThM11 2010 AVS Albert Nerken Award Lecture - AlGaIn/GaN High Electron Mobility Transistor Based Sensors for Bio-Applications**, *F. Ren**, *S.J. Pearton*, *B.H. Chu*, *C.Y. Chang*, University of Florida, *W.J. Johnson*, Nitronex, *A. Dabiran*, *P.P. Chow*, SVT Associates
INVITED

It is highly desirable to have a programmable, single chip sensor with an array of sensors for different purposes that is handheld and capable of wireless communication. This kind of sensor can be very useful for environmental, safety, and biomedical applications. For example, the sensor can be programmed in the doctor office for specific uses to give it to patients to use at home, transmitting the sensing results to their doctor directly to monitor the effectiveness of prescribed medicines. Thus, patients can get better, prompt and adequate health care. It can also reduce the number of unnecessary visits to the emergency room and the cost of the national health system. AlGaIn/GaN high electron mobility transistor based sensors are good candidates for low cost, handheld, and wireless chemical and biomedical sensor due to their excellent thermal as well as chemical stability and sensitivity to the changes of ambient. We have demonstrated AlGaIn/GaN HEMT based individual sensors for protein, DNA, kidney injury molecules, prostate cancer, pH values of the solutions, pH in the exhaled breath condensate, and mercury ions with specific surface functionalizations. Recently, we integrated ZnO nanorods with AlGaIn/GaN HEMT to detect glucose. This approach offers a possibility of integrating AlGaIn/GaN HEMT based sensors with ZnO nanorod sensors on a single "smart sensor chip" for bio-sensing applications.

Electronic Materials and Processing

Room: Dona Ana - Session EM+SS-ThM

Nitride Surfaces and Interfaces

Moderator: Engel-Herbert, Penn State University

8:00am **EM+SS-ThM1 Recent Advances in the MOCVD Growth of III-N Light Emitting Diodes**, *R.D. Dupuis*, *J.-H. Ryou*, *H.-J. Kim*, *J. Liu*, *Z.M. Lochner*, *J. Kim*, *S. Choi*, *S.-S. Kim*, Georgia Institute of Technology
INVITED

Group III-nitride-based green light-emitting diodes (LEDs) are increasingly used in applications for full-color displays, back-lighting, and color-mixing-based general illumination lighting systems. Recently, the potential for III-N LEDs to replace all forms of conventional lighting sources has been discussed and advanced white-light LEDs have entered the market place for general consumer use. However, significant fundamental and technical challenges remain for III-N LEDs to achieve their full potential, such as the improvement of the peak internal quantum efficiency (IQE) and the minimization of the efficiency droop with increasing injection current density. For full-color lighting based upon III-N RGB LEDs, other impediments remain. The peak IQE of green LEDs are significantly lower than shorter-wavelength InAlGaIn-based blue and longer-wavelength InAlGaP-based red LEDs, a feature referred to as a "green gap". In addition, the efficiency of green LEDs at high drive currents decreases with increasing injection current more significantly than in blue LEDs. In this paper, we will review some of the recent work and advances in the area of improving the high-current-density performance of III-N LEDs.

8:40am **EM+SS-ThM3 Microstructural Comparison of InGaIn/GaN Multi Quantum Wells Grown on SiC and GaN Substrates**, *F. Liu*, *L. Huang*, Carnegie Mellon University, *E.A. Preble*, *T. Paskova*, *K. Evans*, Kyma Technologies, Inc., *R.F. Davis*, *L.M. Porter*, Carnegie Mellon University

Light emitting diodes (LED) with InGaIn/GaN multi-quantum wells (MQW) as the active region are now being widely investigated for blue and green light sources. However, InGaIn/GaN MQWs grown on sapphire or SiC substrates commonly contain V-shaped defects with densities as high as 10^9cm^{-2} . These V-defects, which are believed to degrade the internal quantum efficiency of the LED, are remarkably reduced via growth on GaN substrates. In this study, we present a detailed microstructural comparison

between $\text{In}_{0.2}\text{Ga}_{0.8}\text{N}$ (3nm)/GaN (8nm) MQWs grown on AlGaIn/ SiC (0001) and GaN (0001) substrates via metalorganic chemical vapor deposition at 790°C . The composition was determined by analyses of x-ray diffraction (XRD) and photoluminescence measurements. The microstructure was characterized using a variety of techniques, including transmission electron microscopy (TEM), scanning electron microscopy (SEM), electron channeling contrast imaging (ECCI), and photoelectrochemical (PEC) etching. SEM images revealed that the V-defect density decreased from $1 \times 10^{10}\text{cm}^{-2}$ to $7 \times 10^6\text{cm}^{-2}$ in MQWs grown on SiC and GaN substrates, respectively. Cross-sectional TEM images on MQWs grown on SiC substrates indicated that V-defects invariably originated from threading dislocations. To test this hypothesis, we investigated the threading dislocation densities prior to the growth of the MQWs (i.e., in (300-500 nm) GaN films grown on SiC and GaN substrates) via PEC etching and ECCI. The dislocation densities observed in these samples ($\sim 6 \times 10^9\text{cm}^{-2}$ on SiC; $\sim 4 \times 10^6\text{cm}^{-2}$ on GaN) are close to the respective densities of V-defects observed in samples after growth of the MQWs. These results from multiple techniques provide convincing evidence that the dislocation densities in the GaN layer above the substrate determine the densities of V-defects in the MQW. The introduction of dislocations directly from GaN substrates into the homoepitaxial layers is also under investigation using the techniques described herein.

9:00am **EM+SS-ThM4 Switching GaN Polarity on Homoepitaxial Substrates**, *J.K. Hite*, *M.E. Twigg*, *M.A. Mastro*, *F.J. Kub*, *C.R. Eddy, Jr.*, Naval Research Laboratory

Gallium nitride (GaN), a highly advantageous material for both optical and electronic devices, can be grown in the (+/-) c-direction of its lattice with two different polar faces, nitrogen- (N-) or gallium- (Ga-) polar. The face or polar orientation of the material establishes many quite varied properties of the material, from chemical reactivity to dopant incorporation to spontaneous and piezoelectric-induced electric field directions in the crystal. Control of the polarization fields and, thus, polarization induced doping is the basis of Ga-polar and N-polar GaN-based high electron mobility transistor operation. On heterogeneous substrates, such as silicon carbide (SiC) and sapphire (Al_2O_3), the growth conditions, doping levels, and buffer or nucleation layer properties are used to control the polarity of resulting GaN epilayers. Further, in the case of heavily doped p-type layers, spontaneous polarity inversion has been demonstrated even on GaN epilayers, switching from Ga-polar to N-polar in the doped layer.¹ However, this approach leads to uncontrolled inversion domain boundaries and often results in dopant clustering² in the film, impacting film quality and resultant device performance.

In contrast, this new approach enables the controlled formation of Ga-polar GaN from a N-polar crystal. Instead of using concentrated doping, the polarity switch in this case hinges on both surface treatment and the addition of an optimized polarity inversion layer. Initial material characterization verified that the film was without N-polar inclusions or inversion domain boundaries. Chemical etching of the material in 4M KOH under slightly elevated temperatures (40°C) for 10-40 minutes as well as convergent beam electron diffraction³ are employed to verify the polarity of the films. The structural quality of the films is ascertained with transmission electron microscopy and x-ray diffraction. In addition, the dislocation density and grain size are determined through the use of electron channeling contrast imaging.⁴ While lateral polarity heterostructures have been of interest due to their unique electrical and structural properties,⁵ this method offers the promise of engineering both lateral and vertical polarity heterostructures and the potential of novel variable polarity-based devices.

¹V. Ramachandran et al., Appl. Phys. Lett. **75**, 808, 1999.

²M. Hansen et al., Appl. Phys. Lett. **80**, 2469, 2002.

³F.A. Ponce et al., Appl. Phys. Lett. **69**, 337, 1996.

⁴Y.N. Picard et al., Appl. Phys. Lett. **91**, 094106, 2007.

⁵M. Stutzmann et al., Phys. Status Solidi b **288**, 505, 2001.

9:20am **EM+SS-ThM5 Studies of InGaIn Growth Morphology and Its Relationship to Multiple Quantum Well Luminescence**, *D. Koleske*, *S.R. Lee*, *M.H. Crawford*, *M.E. Coltrin*, *J.M. Kempisty*, *K.C. Cross*, Sandia National Laboratories

It has been suggested that InGaIn quantum well (QW) thickness fluctuations, acting in conjunction with piezoelectric fields, are sufficient to cause exciton localization and reduce non-radiative recombination at dislocations [1]. Consequently, the study of InGaIn step morphology and the control of InGaIn/GaN interfaces may be crucial for understanding and improving blue and green LED quantum efficiency. To this end, a variety of InGaIn QW and thin film structures have been grown to determine how the surface roughens when GaN is alloyed with InN. Statistical analysis of the step-height distributions from AFM images shows that the nominally single-layer step heights transition to multiple-layer step heights as InGaIn

* Albert Nerken Award Winner

is grown on GaN. Further analysis of the surface-roughness power spectral density suggests that the main smoothing mechanism changes from an evaporation/recondensation mechanism to a surface diffusion mechanism as the growth temperature is lowered to incorporate indium into GaN. Exploiting these two smoothing mechanisms allows the construction of otherwise identical MQW structures with smoother or rougher InGaN QW interfaces. Initial studies of the correlations between QW interface roughness and luminescence intensity suggest that some degree of InGaN QW roughness leads to higher luminescence efficiency, lending credibility to theories that propose a structural-based enhancement of exciton localization. [1] D. M. Graham, *et al.*, *J. Appl. Phys.* 97 103508 (2005).

This research was supported by the U.S. Department of Energy, Office of Basic Energy Sciences. Sandia National Laboratories is a multi-program laboratory operated by Sandia Corporation, a wholly owned subsidiary of Lockheed Martin Company, for the U.S. Department of Energy's National Nuclear Security Administration under contract DE-AC04-94AL85000.

9:40am EM+SS-ThM6 High-Quality, Large-Area, and Free-Standing GaN Epilayer Growth and Liftoff using Self-Assembled Interlayer of Silica Microspheres, Q. Li, G.T. Wang, Sandia National Laboratories

We demonstrate that self-assembled monolayers of silica microspheres can be used as inexpensive, selective growth masks for both significant threading dislocation density reduction and laser-free lift-off of GaN epilayers and devices. Silica microspheres self-assemble into close-packed monolayers on the surface of an initial GaN epilayer on sapphire using a Langmuir-Blodgett method. In a subsequent GaN regrowth, the silica microspheres effectively terminate the propagation of threading dislocations. As a result, the threading dislocation density, measured by large area AFM and CL scans, is reduced from $3.3 \times 10^9 \text{ cm}^{-2}$ to $4.0 \times 10^7 \text{ cm}^{-2}$. This nearly two orders of magnitude reduction is attributed to a dislocation blocking and bending by the unique interface between GaN and silica microspheres. The sequential wet etching of the samples in HF solution removes the silica microspheres sandwiched between the GaN epilayers and the growth template. Further wet etching of the samples in KOH solution successfully detaches the GaN epilayers from the growth templates. Sandia is a multiprogram laboratory operated by Sandia Corporation, a Lockheed Martin Company, for the United States Department of Energy under contract DE-AC04-94AL85000.

10:40am EM+SS-ThM9 GaN(0001) Surface at Various Conditions: Fundamental Properties and Basic Dynamic Processes - Ab Initio Study, S.K. Krukowski, Polish Academy of Sciences, Poland INVITED

Due to its polar nature, gallium nitride, GaN properties strongly depend on its orientation. Therefore various GaN surfaces have different physical properties, which is related to their different atomic structure and also to the different electric fields in the subsurface layers. A new developed procedure allows to simulate these fields exactly, in a controlled fashion, within the slab model, by modification of the termination of the opposite side of the slab. These techniques will be discussed using bare Ga-terminated GaN(0001) surface as a working example. It will be shown that the field causes shift of the energy of the surface and band states, which is known as Surface States Stark Effect (SSSE). This approach will be employed also in the discussion of the hydrogen covered GaN(0001) surface. Both equilibrium properties and dynamic processes will be investigated with the account of the role of electric field, or equivalently doping in the bulk semiconductor, in shaping of the surface electronic and energetic properties. Equilibrium properties such as hydrogen adsorption sites and energy, and also the thermodynamic and energetic stability will be discussed for various coverage. It will be shown that adsorption of molecular hydrogen on bare GaN(0001) surface leads to its dissociation and location of H atoms in the sites, above the Ga surface atoms. The interaction with adsorbed species leads to strong relaxation of the surface with Ga atoms moving upwards towards H adatoms. Generally, the hydrogen adatoms are strongly confined at the GaN(0001) surface, having their energy 1 eV below that in the GaN bulk. Thus the hydrogen coverage of GaN (0001) surface is stable, and its removal is extremely difficult. The energy of H - induced surface states strongly depend on the doping in the bulk: in p-type GaN the state is close to valence band maximum, but for n-type it is located 2 eV lower. The determined dynamic properties include the adsorption paths showing that the adsorption of molecular hydrogen depends on the coverage: for small coverage, molecular hydrogen is chemically adsorbed at the surface while for 1ML H-coverage it encounters significant energy barriers, drastically lowering the probability of this process. Adsorption of atomic hydrogen does not depend on the coverage, leading at some instances to creation of H₂ admolecules which subsequently could be desorbed from the surface.

The research was partially supported by the European Union within European Regional Development Fund, through grant Innovative Economy (POIG.01.01.02-00-008/08).

11:20am EM+SS-ThM11 Surface Photovoltage Behavior for p-type vs. n-type GaN, A.A. Baski, M. Foussekis, M.A. Reshchikov, Virginia Commonwealth

Devices based on wide-bandgap GaN are successfully being used today, but a better understanding of surface effects such as band bending could further improve their performance. Many results have been reported on the upward surface band bending for n-type GaN, but fewer exist on the downward band bending for p-type GaN. Surface photovoltage (SPV) measurements using a Kelvin probe can directly measure the change in surface potential during UV illumination, and thereby indirectly measure the resulting decrease in band bending. We have studied steady-state and transient SPV for band-to-band (365 nm) illumination on a variety of p-type (Mg-doped) and n-type (Si-doped) GaN samples grown by hydride vapor phase epitaxy and metal organic chemical vapor deposition.

For n-type and p-type GaN samples, short (5 s) UV exposures generate an SPV magnitude of about 0.5 eV in both air and vacuum environments. The sign of the SPV signal is positive for n-type GaN and negative for p-type GaN, corresponding to a positive or negative change in surface potential, respectively. This fast component of the SPV corresponds to the accumulation of photo-generated holes (n-type) or electrons (p-type) at the semiconductor/oxide interface and leads to a corresponding decrease in band bending. As expected, this "internal" mechanism does not appear to depend on the sample environment. After ceasing illumination, decay of the SPV in dark and under all environments is slow with a logarithmic time dependence.

It is during longer UV exposures that the SPV behavior becomes noticeably different for n- vs. p-type samples. For n-type GaN, a long UV exposure (1 h) typically causes the SPV to decrease to 0.35 eV in air, but to increase to 0.6 eV in vacuum. This SPV behavior is consistent with the photo-induced adsorption of negatively charged oxygen species in air and their desorption in vacuum. In contrast, long UV exposure for some p-type samples has caused the SPV to reach a surprisingly large value of -1.1 eV in air, but to not change significantly in vacuum. The more negative SPV in air again indicates the adsorption of negative surface species, but the rather large change over extended illumination is not expected, particularly given that a comparable opposite change does not occur in vacuum (as for n-type). Therefore, the charging of the surface layer on p-type GaN and how it affects band bending is still under investigation. We have developed a phenomenological model that is able to distinguish contributions from internal (fast) and external (slow) mechanisms in SPV transients, and have demonstrated that the native oxide layer can play a significant role.

11:40am EM+SS-ThM12 Investigation of the Structure of GaN(0001) Pseudo-1x1 Structure at Low Temperature, A.R. Smith, T. Chen, K. Wang, Y. Liu, Ohio University Nanoscale and Quantum Phenomena Institute

The wurtzite GaN(0001) surface has previously been determined to be in a pseudo-1x1 structure which includes approximately 2 monolayers (ML's) of Ga sitting atop the last GaN bilayer [1]. This metallic structure, commonly observed, was initially determined using a combination of reflection high energy electron diffraction (RHEED), Auger electron spectroscopy, and scanning tunneling microscopy (STM). In addition, there has been theoretical work performed for this surface. [2,3] In RHEED, the main observation is the appearance of satellite streaks located at 1/6th (or 1/12th) of the primary streak spacing outside of the primary streaks. It was initially modeled as a bi-axially contracted Ga bi-layer, contracted by approximately 16% relative to the GaN bulk. Theoretical calculations found only the top Ga ML to be contracted bi-axially. More recent theory work by Rinehimer et al. suggest that instead it is uniaxially contracted but having a similar structure. [3]

We investigate the pseudo-1x1 structure experimentally using a new growth and analysis system consisting of a molecular beam epitaxy (MBE) chamber for preparation of the surface and a RHEED system to monitor it. The sample growth stage also has the feature of allowing cooling to cryogenic temperatures as well as heating. The pseudo-1x1 structure is prepared by MBE growth on MOCVD-grown GaN substrates. Following this, the sample is cooled down, and the diffraction pattern is monitored. At low temperature, we observe the onset of new diffraction streaks located at approximately 5/12 and 7/12 of the primary streak positions, as well as disappearance of the pseudo-1x1 satellite streaks.

Models for the low-temperature GaN(0001) structure are currently being formulated which may give new insights into the structure of the pseudo-1x1, based on this new low-temperature RHEED data. As one model currently under consideration, a uniaxial, aperiodic superstructure is proposed in which the top Ga layer freezes into a coherent layer but with the resultant extra Ga atoms being displaced vertically. To further probe this model, low-temperature STM experiments are currently being planned, to be conducted in an adjacent in-situ STM system. This work is supported by

the National Science Foundation (Grant No. 0730257) and by a grant from Ohio University.

[1] A. R. Smith, R. M. Feenstra, D. W. Greve, M.-S. Shih, M. Skowronski, J. Neugebauer, and J. E. Northrup, *J. Vac. Sci. Technol. B* **16** (4), 2242 (1998).

[2] J. E. Northrup, J. Neugebauer, R. M. Feenstra, A. R. Smith, *Phys. Rev. B* **61**, 9932 (2000).

[3] J.A. Rinehimer, M. Widom, J.E. Northrup, and R.M. Feenstra, *Phys. Stat. Sol. (b)* **245**(5), 920 (2008).

Energy Frontiers Topical Conference

Room: Pecos - Session EN+AS-ThM

Surface and Interface Analysis of Materials for Energy

Moderator: S.M. Han, University of New Mexico

8:00am EN+AS-ThM1 **Functionalization of Carbon Materials for the Controlled Deposition of Pt Electrocatalysts for Fuel Cell Applications.** *S. Pylypenko*, Colorado School of Mines, National Renewable Energy Lab, *A. Dameron, T. Olson, K.C. Neyerlin, J. Bult, C. Engtrakul*, National Renewable Energy Lab, *A. Queen*, Colorado School of Mines, *K. O'Neill, T. Gennett, H.N. Dinh, B. Pivovar*, National Renewable Energy Lab, *R.P. O'Hayre*, Colorado School of Mines

Catalyst-support interactions are essential in the design of materials for a variety of applications related to renewable energy technologies. In the fuel cell field, improved understanding of these interactions enables controlled improvement in the catalytic activity and durability of carbon-supported fuel cell electrocatalysts. Carbon surface chemistry and structure can be altered to achieve a desired coverage, morphology and composition of the metal nanoparticle. For example, doping a model HOPG surface with argon or nitrogen results in structural and chemical modification of its surface that leads to improved dispersion, decreased nanoparticle phase and, at certain conditions, enhanced stability. In this work, the role of surface defects, oxygen and nitrogen groups introduced during doping and their effect on electrocatalyst deposition and performance is evaluated through a combination of spectroscopic (XPS, Raman, EELS) and microscopic (SEM, TEM) methods. The same methods are used to evaluate the effect of various surface modifications (via Ar plasma, O₂ plasma and their mixture, HNO₃, TMA functionalization, etc.) on high surface area carbon materials (CNTs, for instance) and their effect on nucleation and growth of Pt in a controlled nanoparticle or continuous coating phase.

8:20am EN+AS-ThM2 **Structural and Morphological Properties of Carbon Supports studied by XPS and SEM: Effect on Catalyst Degradation.** *A. Patel, K. Artyushkova, P. Atanassov*, University of New Mexico, *A. Young, M. Dutta, Z. Ahmad, V. Colbow, S. Wessel*, Ballard Power Systems, Canada

Understanding the chemical structure and morphology of Pt electrocatalysts and their supports, and linking these parameters to electrocatalytic activity, corrosion stability and overall performance of the fuel cell is essential for elucidation of failure mechanisms and optimization of support properties. The strategy presented in this work can be viewed as universal methodology that allows correlation between multiple variables relevant to fuel cell technology.

In this work we have investigated the performance and corrosion stability of Pt electrocatalysts supported on different carbon supports in order to understand the effect of the carbon support on catalyst degradation. Low surface area (LSA), mid-range surface area (MSA), high surface area (HSA) and heat treated (to induce graphitization) high surface area carbons were extensively studied and characterized.

X-ray Photoelectron Spectroscopy (XPS) has been chosen to obtain information on graphiticity and amount of surface oxides on carbon supports. The ability to discriminate between different carbon chemical environments, not just elemental compositions, is one of the primary advantages of XPS in the characterization of carbon corrosion.

Morphological properties such as size of particles, size of particles agglomerates, surface area, roughness and porosity are equally contributive to corrosion process. Digital Image Processing (DIP) can be applied to SEM and TEM images to extract statistical parameters, such as roughness, particle size distributions, shape parameters, texture parameters, which all are related to morphology of carbon blacks.

Performance and durability of Pt electrocatalysts supported on various carbon blacks were evaluated extensively electrochemically to provide activity from rotating disk electrode measurements, capacitance and photon

resistance from Electrode Impedance Spectroscopy, voltage degradation rates, effective platinum surface area and kinetic losses.

This multi-analytical approach provides a large set of variables (structural, physical and microscopic properties) which must be related to corrosion and performance behaviour of carbon blacks. Multivariate statistical methods of data analysis (MVA) become, thus, of critical importance in structure-to-property relationship modeling. Principal Component Analysis (PCA) is used as a visualization tool to find samples which are globally correlated or anti-correlated, and to facilitate visualization of the variables responsible for the correlations. Through this methodology, we have determined which set of structural and morphological parameters are responsible for durable and active electrocatalyst.

8:40am EN+AS-ThM3 **Anchoring of N3, N719 and Z907 Dye Molecules on TiO₂(110) Surface.** *P. Nachimuthu, A. Pandey, Z.Q. Yu, Z.H. Zhu, K.M. Beck, S. Thevuthasan, M.A. Henderson, D.R. Baer*, Pacific Northwest National Laboratory

In dye-sensitized solar cells, the alignment of the energy levels for the dye and TiO₂ resulting from the electronic coupling between these states determines the photoinduced electron transfer across the dye-TiO₂ interface. The electronic coupling which in turn is strongly modified by the mode of binding of the dye molecules onto TiO₂ surface, its relative orientations and geometrical structures. In order to understand the mode of binding of the dye molecules on TiO₂(110) surface, the N3, N719 and Z907 dye molecules in the powder form and adsorbed on TiO₂(110) surface using 0.25-1.0 mg/ml in ethanol were investigated using high-resolution x-ray photoelectron spectroscopy. The S 2p XPS data from N3 dye molecules adsorbed onto TiO₂ surface show two S components in addition to SO_x, suggesting that the S atoms in the -NCS functional groups exist in two different chemical environments with a binding energy difference of ~1 eV and the intensity ratio of ~1 indicating that in each intact N3 molecule on TiO₂, one -NCS group is bound to TiO₂(110) surface and the other is projected away from TiO₂ surface. The O 1s XPS data show components at 531.2 eV and 533.1 eV which are arising from C=O / COO⁻ and C-OH bonds from carboxylic acid groups in N3 molecule, respectively, in addition to a peak at 529.7eV from TiO₂. The relative intensity ratio of the O 1s XPS components at 533.1 eV to 531.2 eV signifies the presence of protonated carboxylic acid groups in N3 molecule and is found to be 0.388 suggesting that only one carboxylic acid group in each N3 molecule is deprotonated and it is most likely bound to TiO₂ surface. In contrast, both the -NCS groups in the N719 and Z907 dye molecules were projected away from the TiO₂ surface and are not involved in binding with TiO₂ surface. One of the carboxylic acid groups in Z907 is deprotonated and it is most likely bound to TiO₂ surface. Furthermore, with decreasing the dye concentration in ethanol results in a gradual dissociation of -NCS groups from Ru in these dye molecules.

9:00am EN+AS-ThM4 **Characterization of Minority Carrier Lifetime in Ge Films Epitaxially Grown on Si by Nanoscale Interfacial Engineering.** *J.J. Sheng, D. Leonhardt*, University of New Mexico, *J.G. Cederberg, M.S. Carroll*, Sandia National Laboratories, *M.J. Romero, S. Johnston*, National Renewable Energy Laboratory, *S.M. Han*, University of New Mexico

High-quality Ge-on-Si (GoS) heterostructures are pursued for many applications, including near infrared (NIR) photodetectors and integration with III-V films for multijunction photovoltaics. However, such integration poses many engineering challenges, ranging from lattice mismatch, to thermal expansion coefficient mismatch, to non-planar morphological evolution. We have previously demonstrated a scale-up of growing low-dislocation-density Ge on Si by manipulating the Ge-Si interface at the nanoscale, using a thin chemical SiO₂ layer and a surface reaction involving Ge and SiO₂. We have also developed a slurry-free, chemical-mechanical polish step to planarize the GoS surface resulting in a Ge surface with a root mean square (RMS) roughness of less than 1 nm. Herein, we focus on the characterization of carrier lifetime in the Ge epilayers grown on Si by the said nanoscale Ge-Si interfacial engineering. Using photoconductivity decay techniques, minority carrier lifetime is measured in the GoS substrates to extract surface recombination velocity as well as carrier lifetime in bulk Ge. The effective surface recombination velocity, representing both Ge-Si interface decorated with chemical SiO₂ and Ge surface, is approximately 1.26x10⁶ cm/sec, largely dominated by recombinations at the oxide. We observe that the extracted lifetimes, which vary with the Ge film thickness, correlate well with the dislocation density that varies as a function of distance from the Ge-Si interface. In this presentation, we will further discuss capacitance-voltage characterization of metal-oxide-semiconductor structures fabricated on our GoS substrates.

9:40am **EN+AS-ThM6 A Multi-technique Approach to the Characterization of New Materials for Energy Production**, *T. Nunney, R.G. White, N. Bulloss, P. Camus, J. Konopka*, ThermoFisher Scientific, UK, *H.M. Meyer III*, Oak Ridge National Laboratory

In order to meet the challenges of more economical and environmentally benign energy production, a new generation of complex materials and devices is being developed, these include thin film solar cells, fuel cells, and batteries. In all stages of development there is a requirement for materials characterization and analysis; from the initial development stages, through to testing of the finished article. Most materials need to be analyzed for compositional homogeneity across the sample surface and also for layer chemistry, interface chemistry and thickness through the sample. It is rare that a single technique can achieve all of these testing requirements, and therefore a complementary approach involving several techniques is demanded.

In this presentation we will discuss how a multi-technique approach can address a variety of technical problems, illustrated by examples from real applications case studies. We will mainly concentrate on the information supplied from two techniques, XPS and EDS, but we will also consider the additional data that can be obtained from other sources such as Raman spectroscopy.

X-ray photoelectron spectroscopy (XPS) is ideally suited to the quantitative determination of the surface chemistry and the way in which that chemistry changes in the surface, near-surface and interface region of the materials.

Energy Dispersive Spectroscopy (EDS) collects characteristic X-rays generated by rastering an electron beam over a solid sample to generate a full elemental X-ray spectrum at each pixel of the electron image. The latest generation silicon drift detectors for EDS are capable of collecting and storing hundreds of thousands of X-ray counts per second. This large volume of X-ray data, collected across the sample, allows for rapid identification and characterization of surface defects and lateral compositional variations. Software advances now allow rapid, multivariate statistical analysis processing of very limited amounts of X-ray data to determine not only the elemental distribution across the sample but also the chemical phase distribution.

10:40am **EN+AS-ThM9 Novel Visible-Light Photo-Sensitive Zirconium Oxynitride (ZrO_xN_y) Thin Films**, *C.V. Ramana, N.E. Esparaza, I. Fernandez*, University of Texas at el Paso, *A.L. Campbell*, Wright Patterson Air Force Base

Zirconium oxide (ZrO_2) exhibits excellent optical properties such as high refractive index, large band gap, low optical loss, high transparency in the visible and near-infrared regions, and high dielectric constant. However, ZrO_2 is UV-light sensitive. In addition, interfacial reactions during thin-film growth suppress the effective dielectric constant and degrade the optical performances. The present work was performed on ZrO_xN_y thin films to effectively alter the electronic structure by the method of nitridation, which well-known to suppress the interfacial reactions. ZrO_xN_y thin films were produced by magnetron-sputter deposition under the reactive pressure of nitrogen and oxygen. The effect of nitrogen/oxygen flow rate on the structure and optical properties of ZrO_xN_y thin films was investigated and compared with that of ZrO_2 . The optical measurements of ZrO_2 films show a very high optical transmission with a band gap of 5 eV. The optical absorption measurements on ZrO_xN_y thin films grown at various reactive nitrogen pressures indicate a progressive shift from insulating to semiconductor behavior. The corresponding changes in the profiles of index of refraction were also remarkably distinct. The results indicate that tailoring the electronic structure and optical constants of ZrO_xN_y thin films to meet the requirements of visible-light functionality can be achieved by carefully controlling the reactive pressure. The results will be presented and discussed in detail.

11:00am **EN+AS-ThM10 Quantification of Hydrogen and Deuterium in Niobium and Niobium Oxide**, *P. Maheshwari, F.A. Stevie*, North Carolina State University, *G.R. Myneni, G. Ciovati*, Jefferson Lab, *M. Rigsbee, D.P. Griffis*, North Carolina State University

Superconducting Radio Frequency (SRF) cavities provide enhanced efficiency and reduced energy utilization in present day particle accelerators. Niobium (Nb) is the material of choice for these cavities due to its high critical temperature and critical magnetic field. In order to understand why certain treatments, especially a low temperature bake, improve performance, it is important to study Nb surface characteristics and identify elemental contamination that can affect the performance of the cavity. H, C, O, and N are of interest because they are interstitial impurities in Nb. In earlier work,[1] SIMS analysis using a CAMECA IMS-6F with Cs⁺ primary beam showed that C and N were probably not significant factors impacting performance and that there was a very high level of H in the Nb. TEM analysis also showed that the surface niobium oxide was a uniform layer with typical thickness about 6nm. Ion implants of C, N, O,

and D into Nb provided quantification of C, N, O and indicated that D is very mobile in the Nb.[2]

Analysis of samples before and after heat treatment showed that the H level could be dramatically reduced after certain heat treatments. Removal of the oxide with HF caused the H to return to its former level and the native oxide was again established. SIMS measurement of H in the niobium oxide showed a low H level and, as noted above, the oxide appears to be a very effective H barrier. One possible cause for the removal of H by low temperature heat treatment is the possible formation of openings in the oxide barrier which allows the hydrogen to exit the Nb surface, followed by the renewal of the oxide after heat treatment which does not allow H to re-enter. Another theory is that the heat treatments drive the H deeply into the Nb.

In order to better understand the role of the niobium oxide, implants have now been made into a specially prepared 120nm thick niobium oxide layer on Nb substrate. H is shown to have an implant shape in the oxide and verify that H is not mobile in the oxide. An implant of D with peak at the oxide/Nb interface showed an implant shape up to the interface and a sharp drop once the Nb was reached. If the H relative sensitivity factor from the oxide is used to quantify the H in a Nb sample without heat treatment, the H concentration is measured as $2E22$ atoms/cm³.

[1] A. D. Batchelor, D. N. Leonard, P. E. Russell, F. A. Stevie, D. P. Griffis, G. R. Myneni, Proceedings of Single Crystal Niobium Technology Workshop, Brazil, AIP Conference Proceedings, Melville, NY (2007) 72-83.

[2] P. Maheshwari, H. Tian, C. Reece, G. Myneni, F. Stevie, M. Rigsbee, A. Batchelor, D. Griffis, Surf. Int. Anal. (in press 2010)

11:20am **EN+AS-ThM11 Study of Thin Film Solar Cell Materials using Variable-Wavelength Electric Force Microscopy**, *J. Luria, J.J. Chot, T. Hanrath, J.A. Marohn*, Cornell University

Organic electronics offer a clear path to large scale, low cost photovoltaics. But efficiency issues such as charge transport, extraction, and device degradation keep these materials from being market-viable. Electric Force Microscopy (EFM) allows us to probe electronic properties of various materials and meso-scale morphologies. By observing the photo-induced response and degradation, we are able to inform synthetic and fabrication processes.

We have developed a general approach to illuminate samples in our custom-built vacuum electric force microscope. We will describe experiments using variable-wavelength light to characterize lead sulfide, PFB/F8BT polymer blend, and other thin film photovoltaic devices.

Energy Frontiers Topical Conference Room: Mesilla - Session EN+NS-ThM

Nanostructures for Energy Conversion & Storage II Moderator: K.S. Leschgies, Applied Materials

8:00am **EN+NS-ThM1 Rare Earth Oxide Nanocavity Upconversion**, *V.D. Jankovic, J. Hoang, J.P. Chang*, UCLA

Rare-earth (RE) oxides represent an important class of photonic materials owing to their nonlinear optical and upconversion (UC) properties which find applications in high power lasers, remote sensing, optical communications and photovoltaics. In the context of solar cells, these materials could increase cell efficiencies by upconverting photons with energies below and near the silicon bandgap (1.1eV) which are poorly absorbed by the indirect band-gap semiconductor to higher energy photons that can be absorbed more efficiently. Unfortunately, up-conversion efficiencies in rare-earth ions are usually low due to non-radiative processes such as concentration quenching. One strategy to address this problem is to couple RE ions with metal nanoparticles. Noble metal nanoparticles exhibit localized surface plasmon resonances which can readily be tuned to a particular spectral range of interest by means of size, shape and local dielectric environment. By coupling metal nanoparticles' plasmon resonances to rare earth ion energy transitions, the absorption cross sections of rare earth ions can be significantly improved.

In this work, we designed and synthesized Au|Yb:Er:Y₂O₃ core|shell nanorods as a potential route to improve solar cell efficiencies in the near infrared regime. A modified Mie scattering algorithm determined the optimum theoretical Au nanorod aspect ratio to be 9, for a resonance close to the Yb 980-nm energy transition. The Au nanorods were synthesized using a surfactant mediated growth technique, in which

cetyltrimethylammoniumbromide micelles were used to direct the growth of Au nanoparticles in the [111] direction while suppressing the growth in [100] and [110] directions. Au nanorods with aspect ratios from 6 to 12 have been synthesized by varying the concentration of the reducing agent, ascorbic acid. Spatially and compositionally controlled Yb:Er Y₂O₃ shells were deposited using sequential radical enhanced atomic layer deposition process. The plasmon-ER color center and plasmon-Yb sensitizer distance was systematically varied by controlling the thickness of the Y₂O₃ spacer layer from 1nm to 10nm. The length, aspect ratio, nanorod monodispersity and shell thickness were verified using transmission electron microscopy, while the shell composition was verified by energy dispersive X-Ray spectroscopy. Photoluminescence and radiative lifetime measurements with 980 nm excitation were used to investigate the distance dependence effects of the noble metal-emitter coupling on the optical properties of the core/shell nanorods. Quantitative measurements of the absorption cross section are underway and will also be presented

8:20am **EN+NS-ThM2 Thermal Transport Property of SiGe Nanowire**, *E.K. Lee*, Samsung Advanced Institute of Technology, Republic of Korea, *J.W. Lee*, Sungkyunkwan University, Republic of Korea, *L. Yin*, Texas A&M University, *B.L. Choi*, *S.J. Lee*, Samsung Advanced Institute of Technology, Republic of Korea, *D.M. Whang*, Sungkyunkwan University, Republic of Korea, *C.H. Yu*, Texas A&M University, *J.M. Kim*, Samsung Advanced Institute of Technology, Republic of Korea

Thermoelectric power conversion of waste heat is one of the promising energy harvesting method in the future.

The developments of bulk thermoelectric material are studied by many researchers, but the results are limitedly progressed. However, when the size of material becomes small enough comparable to the mean free path of phonons, the thermal conductivity is remarkably reduced. The thermal conductivities of some nanowires show a few orders of magnitude lower than those of bulk materials due to enhanced boundary scattering. In this point, SiGe nanowire is one of attractive candidates for thermoelectric energy conversion. Here we report the thermal property of SiGe nanowire grown by vapor-liquid-vapor mechanism and the correlation between thermal conductivity and morphology of nanowires. The thermal conductivity of SiGe nanowires was measured using micro-fabricated devices over temperature range of 60K to 450K.

8:40am **EN+NS-ThM3 Hydrogen Storage in Metal Organic Frameworks (MOFs)**, *N. Nijem*, *J.-F. Veyan*, University of Texas at Dallas, *L. Kong*, *K. Li*, *J. Li*, *D.C. Langreth*, Rutgers University, *Y.J. Chabal*, University of Texas at Dallas

Hydrogen storage is one of the most challenging problems in hydrogen-based energy technologies. One of the goals of hydrogen storage is the ability to store a high volumetric density of hydrogen at room temperature. As a result, studies exploring molecular hydrogen interaction in storage materials are important to facilitate further development of materials. Metal-organic Frameworks are promising candidates for hydrogen storage because their high surface area and porosity facilitate high hydrogen physisorption on specific sites of the structures and because many options are possible to enhance the interaction of molecular hydrogen with the host.

This work explores the incorporation of hydrogen into various MOFs using infrared (IR) absorption spectroscopy to characterize its interaction. IR spectroscopy can distinguish possible H₂ binding sites based on the perturbation of the internal H₂ stretch mode. IR measurements are performed on saturated metal center MOFs varying the ligand and/or the metal center and on unsaturated metal center MOF-74-M (M=Zn, Mg and Ni). We combine room temperature, high pressure with low temperature (20-100K) measurements and theoretical van der Waals density functional (vdW-DF) calculations to derive quantitative information from IR shifts and dipole moment strengths.

Our results show that, in contrast to the current understanding, IR shifts are independent of binding energies and depend instead on the chemical environment of the molecule, including effects such as H₂-H₂ interactions. For example, we see little difference in IR shifts between saturated MOFs with low binding energy (~4kJ/mol), and unsaturated MOFs with higher binding energy (~10kJ/mol) sites at room temperature. Furthermore, we show that dipole moments of adsorbed H₂ depends greatly on parameters such as geometry of adsorption site and H₂-H₂ interactions. Measurements performed at low temperatures on MOF-74 show that IR shifts of H₂ is greatly red shifted (an additional ~30 cm⁻¹) due to H₂-H₂ interactions on close proximity adsorption sites, and that dipole moments of adsorbed H₂ can appreciably vary with loading.

Our analysis indicate that the intensity of H₂ IR band cannot always be a measure of the amount of H₂ adsorbed, therefore methods such as variable temperature IR (VTIR) used to deduce binding energies cannot always be implemented.

9:00am **EN+NS-ThM4 The Influence of Acid Treatment of TiO₂ Film Prepared by FFCVD on the Performance of Dye-Sensitized Solar Cell**, *B.R. Chen*, *Y.J. Chen*, National Dong Hwa University, Taiwan, Republic of China

In this study, we use the acid treatment to enhance the dye-sensitized solar cell (DSSC) efficiency from 4.58% to 5.87%. Comparing with the untreated films, the photocurrent and efficiency both largely increase ~28%. We also found that the use of acetic acid, as well as hydrochloric acid, can easily enhance the performance of DSSCs. The untreated film was prepared using a one-step method by the flat-flame chemical vapor deposition (FFCVD) system which deposits the nanoporous TiO₂ film directly as working electrode used in the DSSC. The TiO₂ film was grown on ITO substrate at the temperature of 400°C and the pressure of 20 torr. The efficiency of DSSC using as-synthesized TiO₂ electrode approaches 4.58% with the film thickness about 11~13 nm with proper tuning of carrier gas flow rate in the TiO₂ deposition process. We know that the DSSCs with best efficiency about 11% were prepared exclusively by hydrothermal method. The efficiency we have is among the highest for DSSCs prepared through non-hydrothermal process. The influence of acid treatment increase conversion efficiency was largely attributed to the short circuit current increase. In previous studies, some group improved the acid treatment to make the dye absorption increase effectively. However, most of them performed the treatment during hydrothermal process for the powder synthesis, which cannot be incorporated with the direct film preparation process. Therefore, we take the dipping method to treat our nanoporous TiO₂ film, and try to determine if the treatment can enhance the dye absorption as well. The crystalline quality and morphologies of surface modified TiO₂ electrodes were characterized by using XRD and FESEM. FT-IR and XPS were used to perform the surface characterization. The dye absorption of the DSSCs was also characterizes by UV-vis spectrophotometer. The efficiency of DSSCs using these working electrodes were measured under AM 1.5G 100 mW/cm² by Keithley 2400 sourcemeter. The optimized cell efficiency is 5.87% with the short-circuit photocurrent density of 14.50 mA/cm² and open-circuit voltage of 0.60 V at 0.1M hydrochloric acid solution and half-an-hour soaking.

9:20am **EN+NS-ThM5 Development of Novel Nanomaterials as the Building Blocks for Next-Generation Solar Cells**, *J.M. Pietryga*, *D.C. Lee*, *I. Robel*, *V.I. Klimov*, Los Alamos National Laboratory **INVITED**

The use of colloiddally synthesized nanomaterials in devices is attractive not only because of the low-cost and scalability of solution-based fabrication methods, but because of the facile control over electronic and optical properties of these materials made possible by structural fine-tuning. As the range of applications-of-interest has become more sophisticated, such tuning has progressed beyond simple control over effective band gap using quantum size effects to include much more fundamental modification of electronic structure and dynamics. Design and synthesis of novel nanomaterials that exploit such effects to create unique materials for use in next-generation solar cells are an important part of the ongoing effort within the Center for Advanced Solar Photophysics, a DOE Energy Frontier Research Center. I will examine a number of specific examples from this work, including germanium nanocrystals with partial direct-gap behavior and unique infrared-active heterostructures with extremely long-lived charge-separated excited states, and how such materials may be incorporated into devices.

10:40am **EN+NS-ThM9 CdSe-Coated ZnO Nanowires for Extremely Thin Absorber Solar Cells**, *H. Majidi*, *J.B. Baxter*, Drexel University

Solar cells can provide an abundant, clean, and sustainable source of electricity, but high costs have limited their implementation. Extremely thin absorber (ETA) cells are robust solid state cells that utilize low cost processing while promising potential efficiencies above 15%. However, the highest reported efficiency of ETA cells is only 2.5%. Improving this efficiency will require fundamental understanding and control of the charge transfer in materials and interfaces within the cell.

We report on materials synthesis and photovoltaic response of ETA cells consisting of a vertical array of *n*-type ZnO nanowires coated with CdSe absorber and with the pores between nanowires filled with *p*-type CuSCN. CdSe absorbs visible light and injects photoexcited electrons into the ZnO nanowires. The architecture of the ETA cell enables use of absorbers with smaller carrier lifetimes than those used in thicker planar films, and elimination of liquid electrolytes renders them more robust than conventional dye sensitized solar cells. However, CdSe deposition must be carefully controlled to obtain highly crystalline, uniform, and conformal coatings with an optimal thickness to achieve maximum light harvesting and charge injection efficiency.

We have deposited CdSe coatings at room temperature using electrodeposition with precise control over morphology and material properties. Detailed information about nucleation, crystal growth, and

morphology of the coating on both planar ZnO films and ZnO nanowire arrays was obtained by electrochemical probes and electron microscopy at the early stages of deposition. Under potentiostatic deposition, applied potential of ~ -1.25 V resulted in instantaneous nucleation and high areal density of nuclei and, hence, conformal coatings. Smaller applied potentials ~ -1.05 V resulted in sparse and progressive nucleation and non-uniform coatings. However, deposition at potentials larger than -1.6 V resulted in precipitation in electrolyte solution. After annealing, x-ray diffraction and transmission electron microscopy show nanocrystalline CdSe in both hexagonal and cubic phases. Using the optimal potential range determined from the potentiostatic studies, we investigated galvanostatic deposition of CdSe coatings on ZnO nanowire arrays. The thickness of CdSe coating is precisely controlled by electrodeposition charge density, and the deposition is conformal and uniform, which is ideal for ETA cells. UV-Vis transmission spectroscopy and photoelectrochemical solar cell measurements demonstrate that CdSe coatings effectively sensitize ZnO nanowires to visible light.

11:00am **EN+NS-ThM10 Titanium Dioxide Nanowires for Dye-Sensitized Solar Cells, Lithium Ion Batteries and Photocatalysis, E.S. Aydil, B. Liu, A. Khare, University of Minnesota**

One-dimensional titanium dioxide nanowires find applications ranging from photocatalysis to lithium ion batteries and dye sensitized solar cells. A simple and environmentally benign method was developed for growing oriented single-crystalline TiO₂-B and/or anatase TiO₂ nanowire arrays on titanium foil over large areas. These nanowire arrays are suitable for use as the anode in lithium-ion-batteries; they exhibit specific capacities ranging from 200-250 mAh/g and retention of these capacities at high charge-discharge rates and over as many as 200 charging-discharging cycles. These promising properties are attributed to both the nanometer size of the nanowires and their oriented alignment. The comparable electrochemical performance to existing technology, improved safety, and the ability to roll titanium foils into compact three-dimensional structures without additional substrates, binders or additives suggest that these TiO₂ nanowires on titanium foil are promising anode materials for large scale energy storage. Another application of these nanowires is in photocatalysis. Ideally, after photogeneration, electrons and holes must be segregated to different parts of the photocatalyst to take part in separate oxidation and reduction reactions. One way to achieve spatial control of electron-hole separation is by building junctions into the catalyst with built-in electric fields that tend to separate the electron and the hole into two different regions of the catalyst. We sought to accomplish this by controllably forming junctions between different phases of TiO₂. A solution method followed by a subsequent heating process has been developed to prepare core-shell TiO₂ nanowires made of TiO₂-B core and anatase shell. We control the anatase phase surface coverage on the TiO₂-B phase and show that the maximum photocatalytic activity is obtained when the solution containing the reactants can contact both the anatase and TiO₂-B phases. The photocatalytic activity drops both with bare TiO₂-B nanowires and with completely anatase covered TiO₂-B nanowires. In contrast, nanowires partially covered with anatase phase gives the highest photocatalytic activity. The improved photocatalytic activity is attributed to the effective electron-hole separation at the junction between the anatase and TiO₂-B phases, which reduces charge recombination and increases the electron and hole lifetimes. Finally, we have developed a method to grow rutile TiO₂ nanowires on transparent conducting oxide substrates for use in dye-sensitized solar cells (DSSC). A light-to-electricity conversion efficiency of 3% could be achieved by using 4 mm-long TiO₂ nanorod films as the photoanode in a DSSC.

11:20am **EN+NS-ThM11 Device Characteristics of Dye Sensitized Solar Cells Based on Evaporated TiO₂ Nanowire Photoanodes, S.M. Pursel, S.H.A. Lee, T.E. Mallouk, M.W. Horn, The Pennsylvania State University**

Dye sensitized solar cells (DSSCs) continue to be the subject of intensive research because of their potential low cost with efficiencies near 11%. In this talk, we report on engineered one-dimensional TiO₂ nanowire photoanodes as an alternative to the standard colloidal based photoanodes currently used in most DSSC's. By using one dimensional nanowire photoanodes, there is potential to speed up electron collection thereby permitting the use of faster acting redox couples in future electrolytes. The nanowire photoanodes are made by evaporation of TiO₂ at an oblique deposition angle. Dense arrays of nanowires, of any thickness, can be deposited with an orientation normal to the front contact. Deposition methods that enable growth of nanowires with a consistent diameter (~ 30 nm) and interwire spacing ($\sim 5-10$ nm) have been developed for use with DSSCs, unlike most sputtered wires. Optically uniform films have been deposited over 7 cm diameter substrates. These arrays are improvements over past lithographically or hydrothermally deposited nanowires in terms of dye loading, which in our case match or improve upon the dye loading of

standard colloidal based photoanodes. Dye loading data, obtained through spectroscopic measurements of desorbed dye, is presented along with SEM images of the various architectures of nanowire arrays. Devices are constructed using ruthenium based N719 dye, I⁻/I₃⁻ based electrolyte, and Pt coated FTO counter electrodes and temporary sealing. Performance data is obtained under AM 1.5G or D simulated solar illumination. Electron transport data is obtained through electrochemical impedance spectroscopy (EIS) and open circuit voltage decay (OCVD). Data is analyzed using published theoretical models to quantify transport properties.

11:40am **EN+NS-ThM12 Dye Sensitized Solar Cells with Aerogel-Templated Nanostructured Photoanodes Fabricated using Atomic Layer Deposition, A. Yanguas-Gil, J.W. Elam, Argonne National Laboratory, V.O. Williams, Northwestern University, M. Mushfiq, D.M. Hess, R. Winter, U. Sampathkumar, Innosense LLC, M.J. Pellin, Argonne National Laboratory, J.T. Hupp, Northwestern University**

The combination of sol/gel processing techniques with Atomic Layer Deposition is a versatile and scalable route to fabricate nanostructured electrodes with different functional materials. By controlling the sol/gel process it is possible to create scaffolds with very different microstructures and pore-size distributions, while ALD allows a layer-by-layer control of the electrode composition. One of the main advantages of this approach is the possibility of creating nanostructured electrodes with multiple functional coatings that lead to a faster transport of the injected electrons to the transparent conducting oxide, [1, 2] thus paving the way for the use of alternative redox shuttles that would allow higher photovoltages and higher efficiencies.

In this work we present results on the influence that the sol/gel process and the ALD steps have on the microstructure and transport properties of the photoanodes, and the optical properties and efficiency of the cells. In particular, we have studied the influence of the aging and drying steps in the aerogel/xerogel growth, and we have compared the performance of TiCl₄ and Ti(OiPr)₄ as precursors during the ALD step. Our results show that aerogel-templated nanostructured electrodes are a promising alternative to nanoparticle-based photoanodes for dye sensitized solar cells. Our work is funded by the US Department of Energy, Office of Energy Efficiency and Renewable Energy, Industrial Technologies Program.

[1] A. B. F. Martinson, J. W. Elam, M. J. Pellin and J. T. Hupp, *Nano Lett.* **7**, 2183 (2007).

[2] T. W. Hamann, A. B. F. Martinson, J. W. Elam, M. J. Pellin and J. T. Hupp, *J Phys. Chem. C* **112**, 10303 (2008).

Graphene Focus Topic

Room: Brazos - Session GR+AS+TF-ThM

Graphene Synthesis on Metals

Moderator: A.W. Ghosh, University of Virginia

8:00am **GR+AS+TF-ThM1 Contrast Behavior of Carbon Adatom Diffusion and Nucleation in the Initial Stage of Graphene Epitaxial Growth on Stepped Metal Surfaces, H. Chen, W. Zhu, University of Tennessee at Knoxville; Oak Ridge National Laboratory, Z. Zhang, Oak Ridge National Laboratory; University of Tennessee at Knoxville**

Using first-principles calculations within density functional theory, we study the energetics and kinetics of carbon adatom diffusion and nucleation on three stepped metal surfaces: Ir(111), Ru(0001) and Cu(111). We find that on the flat surfaces, two carbon atoms repel each other on Ir(111) and Ru(0001), while they prefer to form a dimer on Cu(111). Moreover, the step edges on Ir and Ru surfaces cannot effectively trap single carbon adatoms either, whereas it is strongly favorable to form carbon dimers at the step edges. The different behaviors are attributed to the competition between C-C bonding and different types of C-metal bonding, and the picture is generalized to other C-on-metal systems with predicted results. These findings provide an insight into the understanding of experimentally observed carbon nucleation in the initial stage of graphene epitaxial growth on metal surfaces.

8:20am **GR+AS+TF-ThM2 Density and Height Distribution of Ru and Bimetallic Pt/Ru Nanoclusters Self-Assembled on Ru(0001) Supported Monolayer Graphene, A.K. Engstfeld, S. Beckord, H.E. Hoster, R.J. Behm, Ulm University, Germany**

The Moiré-type nm-scale patterns of graphene monolayers on metal single crystals were recently shown to allow facile fabrication of ordered arrays of virtually monodisperse metal nanoclusters by simple metal vapour deposition in UHV [1-3]. In view of a potential utilization as model systems in electrocatalysis, we have tested the possibility of preparing Ru and

bimetallic PtRu clusters by an analogous procedure. This included an extended study on the growth behaviour of the pure Ru clusters. Statistically evaluated STM images indicate that density and height distribution of Ru clusters are largely independent from the evaporation rate at room temperature. Lower/higher cluster densities along with larger/smaller cluster sizes were only achieved by higher/lower substrate temperatures during evaporation. For a given temperature, the lateral density of Ru clusters is higher than that of Pt clusters. Hence, the fabrication of bimetallic clusters can be performed more reliably when Ru is deposited first. We discuss in how far the found growth behaviour can be understood using classic nucleation theory.

8:40am GR+AS+TF-ThM3 From Perfect Graphene to Cluster Superlattices, T. Michely, University of Cologne, Germany INVITED

Through pyrolysis of hydrocarbons on noble metal surfaces monolayer graphite – graphene – is readily formed. Using scanning tunneling microscopy (STM) and low energy electron microscopy (LEEM) we investigate the temperature dependent growth and the nature of point and line defects in the graphene layer on Ir(111). We identify heptagon-pentagon pairs of carbon atom rings to accommodate for slight misalignments of graphene domains, and wrinkles in the graphene layer for the mismatch in thermal expansion of graphene and Ir. After a systematic optimization of the growth procedure we obtain a single sheet of well oriented graphene on Ir(111) with a minimum of point and line defects.

Angle resolved photo emission finds graphene on Ir(111) to be only marginally doped and to display the characteristic Dirac cone at the K-point of the graphene Brillouin zone. The absence of hybridization of Ir and graphene states is consistent with the weak graphene - Ir interaction, as inferred from the large graphene - substrate separation as measured by the X-ray standing wave method and calculated by density functional theory including van der Waals interactions. The moiré resulting from the incommensurate epitaxy of graphene on Ir(111) gives rise to a large graphene supercell. In the graphene electronic structure it is reflected by the opening of minigaps at the boundaries of the induced mini-Brillouin zone.

The graphene moiré with Ir(111) is an active template allowing one to grow superlattices of metal clusters (Ir, Pt, Au, W, Fe, Re, Co, etc), spatially and thermally stable below 450 K. The graphene moiré enables also patterned adsorption of molecules and the template effect is not limited to the Ir(111) substrate. Based on STM and XPS measurements as well as density functional theory calculations it is proposed that at geometrically defined locations within the supercell and if sandwiched between substrate and cluster metal the graphene rehybridizes from sp^2 graphitelike to sp^3 diamondlike bonding, resulting in strong covalent bonds between metal and graphene. The relevance of the graphene template effect for nanocatalysis, nanomagnetism and electrochemistry will be outlined.

9:20am GR+AS+TF-ThM5 Graphene on Pd(111): In situ Low-Energy Electron Microscopy Studies of Growth Kinetics and Structure – Work Function Relationship, S. Kodambaka, Y. Murata, University of California Los Angeles, E. Starodub, N.C. Bartelt, K.F. McCarty, Sandia National Laboratories

Using *in situ* low-energy electron microscopy, we investigate the dynamics of graphene layer formation and the relationship between domain structure and its work function on Pd(111). We observe, in real time, the nucleation and growth of graphene islands during cooling via surface segregation of C atoms from the Pd bulk. Interestingly, we observe rapid motion of Pd substrate surface steps during graphene growth. Using low-energy electron diffraction, we identify at least five different orientations (domains) of monolayer graphene islands on the surface. We determine their relative orientations with respect to the substrate as approximately 2°, 6°, 11°, 19°, and 26°. We measured electron reflectivity (image intensity) values for each of the domains as a function of incident electron energy. From this data, we extracted the work functions of graphene domains which are found to vary with the domain orientation. Our results suggest that the substrate-graphene interactions influence the growth kinetics as well as the electronic structure of graphene.

9:40am GR+AS+TF-ThM6 Second-Layer Graphene on Ir(111) – Relating Growth Mechanism to Physical and Electronic Structure, S. Nie, Sandia National Labs, A.L. Walter, Lawrence Berkeley National Lab and Fritz-Haber-Institut der Max-Planck-Gesellschaft, Germany, E. Starodub, K.F. McCarty, K. Thürmer, Sandia National Labs, K. Horn, Fritz-Haber-Institut der Max-Planck-Gesellschaft, Germany, A. Bostwick, Lawrence Berkeley National Lab, N.C. Bartelt, Sandia National Labs, E. Rotenberg, Lawrence Berkeley National Lab

An interesting question is how the second layer of graphene grows on transition-metal substrates. First-layer graphene on Ir(111) [1] exists with four discrete in-plane orientations relative to substrate directions [2]. Thus, this system offers potential to better understand the relationship between

second-layer growth and first-layer structure. We use low-energy electron microscope (LEEM) to characterize where the second-layer graphene forms on Ir(111) covered by domains of differently oriented first-layer graphene. We find that the second layer does not grow easily where the lattice of the first-layer graphene is aligned with the lattice of the substrate. Instead the second-layer graphene forms most easily where the first-layer graphene is rotated, by 30°, for example. Angle-resolved photoemission spectroscopy (ARPES) confirms this strong preference. So how does the orientation of the first layer control the growth of the second layer? ARPES and Raman spectroscopy provide insight, revealing that the rotated variants of first-layer graphene are even less strongly bound to the substrate than the more abundant, non-rotated variant [3]. This information suggests the following growth mechanism. Carbon atoms segregating from the substrate build up in concentration under the first layer. The second layer nucleates and grows where it is easier to debond the first layer from the substrate, that is, under the rotated first-layer domains. Electron diffraction also reveals that the second graphene layers are usually but not always aligned with the first-formed layer. Finally, we will discuss the doping of the different types of second-layer graphene, as revealed by ARPES.

This work was supported by the Office of Basic Energy Sciences of the US DOE under Contracts No. DE-AC04-94AL85000 (SNL) and No. DE-AC02-05CH11231 (LBL).

[1] A. T. N'Diaye, J. Coraux, T. N. Plasa, C. Busse, and T. Michely, *New J. Phys.* 10, 16 (2008).

[2] E. Loginova, S. Nie, K. Thürmer, K., N. C. Bartelt, and K. F. McCarty, *Phys. Rev. B* 80, 085430 (2009).

[3] I. Pletikosic, M. Kralj, P. Pervan, R. Brako, J. Coraux, A. T. N'Diaye, C. Busse, and T. Michely, *Phys. Rev. Lett.* 102, 056808 (2009).

10:40am GR+AS+TF-ThM9 Graphene on Transition Metals – Growth and Interfacial Processing, P. Sutter, E. Sutter, Brookhaven National Laboratory INVITED

Graphene has been used to explore the fascinating properties of two-dimensional sp^2 bonded carbon, and shows great promise for applications. A key bottleneck lies in synthesizing the required starting material: structurally perfect, macroscopically large graphene sheets with uniform thickness, into which active device structures can be patterned.

Epitaxial growth on transition metals has recently become one of the most promising methods for large-scale graphene synthesis. Here we discuss the fundamental mechanisms of graphene growth on ruthenium [1] and platinum [2], both single crystals and polycrystalline thin films, studied by a combination of *in-situ* surface microscopy methods. Real-time observations by low-energy electron microscopy (LEEM) show that epitaxy on Ru(0001) produces arrays of macroscopic monolayer graphene domains, whose coalescence is followed by the formation of large bilayer areas in a controlled layer-by-layer fashion. LEEM imaging together with diffraction, selected-area angle resolved photoemission spectroscopy (micro-ARPES), and scanning tunneling microscopy provide unique insight into the interaction between graphene and transition metal substrates, key to the synthesis of high-quality graphene [2, 3].

Beyond large-scale synthesis, potential applications of graphene will require novel approaches to processing and functionalization. We will highlight experiments by real-time surface microscopy to understand chemical reactions at graphene-metal interfaces, which may become part of novel processing strategies for graphene devices.

Work performed under the auspices of the U.S. Department of Energy under contract No. DE-AC02 98CH1-886.

[1] P. Sutter, J.I. Flege, and E. Sutter, *Nat. Mater.* 7, 406 (2008).

[2] P. Sutter, J.T. Sadowski, and E. Sutter, *Phys. Rev. B* 80, 245411 (2009).

[3] P. Sutter, M.S. Hybertsen, J.T. Sadowski, and E. Sutter, *Nano Lett.* 9, 2654 (2009).

11:20am GR+AS+TF-ThM11 Real-time Analysis of Graphene Growth on Polycrystalline Copper Foils, J.M. Wofford, University of California at Berkeley and Lawrence Berkeley National Lab, S. Nie, N.C. Bartelt, K.F. McCarty, Sandia National Laboratories, O. Dubon, University of California at Berkeley and Lawrence Berkeley National Lab

Despite the potentially significant technological impact of graphene synthesis on Cu, little is understood about both the growth kinetics of this system and the morphology of the resulting heterostructure. We use low-energy electron microscopy (LEEM) to observe directly the UHV growth of graphene on polycrystalline Cu foils by the electron-beam evaporation of carbon. The temperatures required to synthesize highly ordered graphene simultaneously induce significant Cu sublimation and step flow, leading to a dynamic growth surface. As a result a complex interdependence develops between the graphene growth behavior and Cu surface morphology, with the graphene islands limiting Cu step mobility, and Cu step bunching

distorting the propagation of the graphene growth front. This interplay becomes increasingly dramatic over time as the inhomogeneous sublimation of Cu leads to considerable surface roughening. In addition, the graphene islands are not compact in shape. Instead, the islands are ramified, consisting of several distinct lobes extending from a common nucleation site. Diffraction analysis reveals that each constituent lobe has a different in-plane orientation relative to the copper grain below and that the growth velocity of a given lobe depends strongly on its orientation relative to the underlying Cu at the growth front. We will describe the relationship between the orientation-dependent growth velocity and the local atomic geometry at the edge of the graphene sheet. Finally, the implications of this unexpected nucleation and growth mechanism on the formation of high-quality graphene films on Cu foils are evaluated.

Work at Sandia was supported by the Office of Basic Energy Sciences, Division of Materials Sciences, U. S. Department of Energy under Contract No. DE-AC04-94AL85000. Work at LBNL was supported by the Director, Office of Science, Office of Basic Energy Sciences, Division of Materials Sciences and Engineering, of the U.S. Department of Energy under Contract No. DE-AC02-05CH11231. JMW acknowledges the support from an NSF fellowship.

11:40am **GR+AS+TF-ThM12 Moiré Superstructures of Graphene on Faceted Nickel Islands**, *Y. Murata*, University of California Los Angeles, *V. Petrova*, University of Illinois at Urbana-Champaign, *B.B. Kappes*, *A. Ebnoumasir*, Colorado School of Mines, *I. Petrov*, University of Illinois at Urbana-Champaign, *Y.-H. Xie*, University of California Los Angeles, *C.V. Ciobanu*, Colorado School of Mines, *S. Kodambaka*, University of California Los Angeles

Using scanning tunneling microscopy and spectroscopy, in combination with density functional theory (DFT), we investigated the morphology and electronic structure of monolayer graphene grown on the (111) and (110) facets of three-dimensional nickel islands on highly oriented pyrolytic graphite substrate. We observed hexagonal and stripe moiré patterns with periodicities of 22 Å and 12 Å, respectively, on (111) and (110) facets of the Ni islands. Graphene domains are also observed to grow, as single crystals, across adjacent facets and over facet boundaries. We suggest that the unexpected observation of moiré patterns of graphene on lattice-matched Ni(111) and the formation of single-crystalline domains across different surface orientations are a consequence of the kinetic limitations of growth, rather than of the strength of the C-Ni interactions. Scanning tunneling spectroscopy data indicate that the graphene layers are metallic on both Ni(111) and Ni(110), in agreement with the DFT calculations. We attribute this behavior to strong hybridization between the *d*-bands on Ni and the *p* bands of carbon. Our findings point to the possibility of preparing large-area epitaxial graphene layers even on polycrystalline Ni substrates.

Magnetic Interfaces and Nanostructures

Room: Zuni - Session MI+TF-ThM

Magnetic Nanostructures, Thin Films and Heterostructures

Moderator: C. Clavero, College of William & Mary

8:00am **MI+TF-ThM1 AC Susceptibility of Ni Bars with Magnetic Single Domain**, *X.G. Zhang*, *I.I. Kravchenko*, *S.T. Retterer*, *J.F. Wendelken*, *Z. Gai*, Oak Ridge National Laboratory

For thin films, the generalized Curie-Weiss law extends the power law scaling well above T_c by replacing the linear reduced temperature t_l by a nonlinear reduced temperature $t_{NL}=1-T_c/T$. The film thickness *d* and temperature *T* are usually not independent variables in the scaling. Using the nonlinear reduced temperature, the power law scaling was shown to be accurate over the entire paramagnetic regime [1-3]. However, at low temperature, thermally activated domain wall motion is expected to contribute significantly to the temperature dependence of magnetic properties, therefore the scaling law is generally believed not to extend far below T_c . Such belief was contradicted by a very recent experiment [4] that showed a surprising power law scaling for the in-plane susceptibility of sputtered Ni films deposited on silicon for the entire temperature range between zero and T_c . In addition, thickness and temperature dependence are completely decoupled. This scaling result implies that even in the ferromagnetic regime, there is no domain wall motion contribution to the low field susceptibility [4]. To clarify the role of domain wall motion, arrays of single domain Ni microstructures are studied experimentally and theoretically. We will show the results of the AC susceptibility measurements of Ni microstructures with magnetic single domain, in which the contributions of domain wall motion and spin fluctuation to the susceptibility are separated.

This research at Oak Ridge National Laboratory's Center for Nanophase Materials Sciences was sponsored by the Scientific User Facilities Division, Office of Basic Energy Sciences, U.S. Department of Energy.

[1] H. Lutz, P. Scobisria, J. E. Crow, and T. Mihalism, Phys.Rev. B 18, 3600 (1978).

[2] M. Fahnle and J. Souletie, J. Phys.c 17, L469 (1984).

[3] A. S. Arrott, Phys. Rev. B 31, 2851 (1985).

[4] X. H. Song, X.-G. Zhang, J. Fan, Y. R. Jin, S. K. Su, and D. L. Zhang, Phys. Rev. B 77, 092408 (2008).

8:20am **MI+TF-ThM2 Deuterium Absorption in Co/Pd Multilayers**, *K. Munbodh*, *F.A. Perez*, *D. Lederman*, West Virginia University, *M. Zhernenkov*, *M. Fitzsimmons*, Los Alamos National Laboratory

The absorbed concentration of deuterium was calculated in Co/Pd multilayers at standard temperature and pressure using in-situ neutron reflectometry. The out-of-plane film expansion and deuterium concentration-depth profiles were determined from the fitting of the neutron reflectivity data. The measurements demonstrated that deuterium is absorbed in all the Pd layers. However, the concentration of the hydrogen varies with Pd layer thickness. Polarized neutron reflectometry with applied field of 6.5 kOe in the plane of the sample was performed and the detailed magnetic depth profile was established. These results showed an overall increase in magnetization upon deuterium absorption.

8:40am **MI+TF-ThM3 Correlated Structural and Magnetic Studies of Capping and Seed Layer Dependent Epitaxial FePd Thin Films**, *L. Wang*, *J.R. Skuza*, College of William & Mary, *T. Mewes*, University of Alabama, *C. Clavero*, *R.A. Lukaszew*, College of William & Mary

FePd binary alloys can form a chemically ordered phase ($L1_0$) that exhibits interesting properties such as high perpendicular magnetic anisotropy (PMA). This property has drawn great attention for many technological applications such as ultrahigh density magnetic recording media and spin transfer torque random access memory (STT-RAM). We investigate the influence of different capping layers (Au, Pd and V and compare with an insulating capping layer such as MgO) on the magnetic properties, particularly the magnetic anisotropy and damping, of highly anisotropic $L1_0$ FePd films which were grown onto MgO (001) substrates using magnetron sputtering in an ultra-high vacuum deposition system. We use x-ray diffraction techniques to study the chemical ordering of the films, and vibrating sample magnetometry (VSM), magnetic force microscopy (MFM) and ferromagnetic resonance (FMR) to investigate the magnetic properties. Our aim is to investigate and tailor the structural and magnetic properties of highly ordered FePd thin films with strong PMA via adequate choice of capping and seed layer materials.

We thank W. Chen and S. A. Wolf for their collaboration. Funding for this project was obtained from NSF grants DMR 0804243 and DMR 0605661 and a Cottrell Scholar Award from the Research Corporation.

9:00am **MI+TF-ThM4 Microstructural, Magnetic Anisotropy, and Magnetic Domain Structure Correlations in $L1_0$ Ordered Thin Films**, *J.R. Skuza*, *L. Wang*, College of William & Mary, *W. Chen*, *J. Lu*, University of Virginia, *T. Mewes*, University of Alabama, *C. Clavero*, *R.A. Lukaszew*, College of William & Mary

Understanding microstructural, magnetic anisotropy, and magnetic domain structure correlations in materials with strong perpendicular magnetic anisotropy (PMA) is of fundamental interest and it is also important in many technological applications such as next generation magneto-recording, magneto-optical, and patterned media. The $L1_0$ ordered phase of some binary alloys (FePt, FePd, MnAl, etc.) has strong PMA due to chemical ordering that can be controlled with adequate thin film deposition parameters and/or subsequent thermal annealing treatments. A detailed structural (XRD and AFM) and magnetic (MFM, SQUID, and FMR) study on two of these $L1_0$ ordered alloys will be presented. Epitaxial FePd thin films with various capping layers were grown by dc magnetron sputter deposition onto MgO(001) substrates. A quantitative analysis and correlation of the strong PMA to magnetic domain structure in these FePd films was accomplished with good agreement using an analytical energy model [1]. MnAl thin films were grown by reactive biased target ion beam deposition onto MgO(001) substrates. Effects of the growth conditions and subsequent thermal annealing treatments on the microstructure and magnetic properties will be discussed.

This work was supported by the Virginia Space Grant Consortium, National Science Foundation (DMR Grants #0355171, #0605661, and #0804243), the American Chemical Society (PRF Grant #41319-AC), and the Research Corporation Cottrell Scholar Award. K. Yang, B. Wincheski, and S. A. Wolf are acknowledged for their collaboration.

[1] J. R. Skuza, C. Clavero, K. Yang, B. Wincheski, and R. A. Lukaszew, IEEE Trans. Magn. **46**, 1886 (2010).

9:20am **MI+TF-ThM5 Correlating Microstructure with Magnetic Properties Variation in Patterned Magnetic Nanostructures with Transmission Electron Microscopy, J.W. Lau**, National Institute of Standards and Technology **INVITED**

Patterned magnetic nanostructures are keystone components in technologies such as hard drive media, sensors, and the magnetoresistive device variants (read-head, random access memory, logic). During manufacturing, different processes produce defects that are the source of variations in magnetic properties in magnetic nanostructures. One example is the Co/Pd nanodot array, interesting for its potential in realizing the bit-patterned media data storage platform. We showed that grains of a particular orientation formed during the film deposition can act as trigger sites for magnetization reversal. Therefore, the ease of switching a particular nanodot among millions of nominally identical nanodots depends on the random presence of trigger grains within it. When considered as an ensemble, the nanodot array will exhibit a switching field distribution; this is the superposition of the individual switching fields unique to each nanodot. In general, switching field distribution and other magnetic property variations in patterned magnetic nanostructures can present major problems for devices development where uniform magnetic performances are required.

The fact that magnetic phenomena in patterned magnetic nanostructures, whether it be magnetization reversal or magnetoresistance, are always observed as distributions means that it is important to identify the root causes to these distributions. An essential aspect to furthering the progress in developing magnetic nanostructure devices is therefore, to correlate nanostructure, defects and interfaces, and chemical composition to magnetic behaviors on the nanoscale. To this end, one of our main focuses is in developing ways to measure variations in magnetic properties using transmission electron microscopy (TEM). TEM is one of the few tools that can provide structural, chemical and magnetic information all at the same time.

In this presentation, I will highlight specific examples of measurements developed for patterned magnetic nanostructures using a TEM. The first example is the microstructure correlation to the switching field distribution in Co/Pd nanodots, described earlier. The second example is a set of *in situ* tunneling measurements where we succeeded in measuring unique energy barrier height and tunneling magnetoresistance (TMR) on fully functional nano-magnetic tunnel junctions (MTJ) built as a TEM sample. Finally, I will show how single nanostructure magnetometry can be achieved within a TEM.

10:40am **MI+TF-ThM9 Partial Perpendicular Anisotropy of CoFeB with Vanadium Capping, A. Natarajathinam, Z.R. Tadisina, S. Gupta**, University of Alabama

Magnetic tunnel junctions with vanadium-based capping layers on top of the CoFeB free layer have been studied. The interest in the effect of capping on the free layer originated from reports⁽¹⁾ that cap layers influence the crystallization of the CoFeB free layer through diffusion of the B into the cap, as well as induce a partial perpendicular magnetic anisotropy (PPMA or PPA) in the free layer^(2,3). Different cap layers differently accelerate the diffusion of the B from the free layer. In this study, we have sputter-deposited V/Ru and V/Ta capping layers on CoFeB and subsequently characterized these films by magnetometry and ferromagnetic resonance (FMR). We have found that V/Ru and V/Ta capping of CoFeB induces partial perpendicular anisotropy (PPA) in CoFeB, as well as reduces the Gilbert damping parameter, confirming results reported by other researchers⁽⁴⁾. The origin of this PPA is believed to be caused by the interface anisotropy between the free layer and the capping layer. The effect of post-deposition annealing, CoFeB thickness, and doping of CoFeB with vanadium on the anisotropy and damping of these V/Ru and V/Ta capped samples has been studied for the free layers. Doping CoFeB with vanadium greatly reduces the $4\pi M_s$ and $4\pi M_{eff}$ values, resulting in an effective increase in the PPA, as well as the damping parameter. X-ray magnetic circular dichroism (XMCD) has also been performed on a series of V-doped films over a range of V concentrations. Magnetic tunnel junctions were fabricated to study device properties of the V-capped and V-doped films. The mechanisms for increasing TMR in these types of pMTJ's will be discussed.

This work is supported by the U.S. Department of Defense DARPA-MTO STT-RAM Universal Memory contract, and Grandis Inc., Milpitas, CA.

1. T. Miyajima, T. Ibusuki, S. Umehara, M. Sato, S. Eguchi, M. Tsukada, and Y. Kataoka, Appl. Phys. Lett. **94**, 122501 (2009).

2. E. Chen, D. Apalkov, Z. Diao, A. Driskill-Smith, D. Druist, D. Lottis, V. Nikitin, X. Tang, S. Wang, S. A. Wolf, A. W. Ghosh, J. W. Lu, S. J. Poon, M. Stan, W. H. Butler, S. Gupta, C. K. A. Mewes, T. Mewes, and P. B. Visscher, (invited paper), IEEE Trans. Magn. **46**, 1 (2010).

3. S. M. Watts, X. Tang, Z. Diao, D. Apalkov, D. Druist, E. Chen, V. Nikitin "Low switching current in conventional in-plane STT-RAM structure with partial perpendicular anisotropy", Digest FV-11, 11th Joint MMM-Intermag Conference, Washington, DC (2010).

4. D. Worledge, D. Abraham, S. Brown, M. Gaidis, G. Hu, C. Long, J. Nowak, E. O'Sullivan, R. Robertazzi, J. Sun, P. Trouilloud, 11th Joint MMM-Intermag Conference, Washington, D. C. (2010).

11:00am **MI+TF-ThM10 Magnetic Properties of Fe_xNi_{1-x}Fe/Co Bilayers, F.A. Perez, D. Lederman**, West Virginia University

Fe_xNi_{1-x}Fe/Co bilayers were deposited on single-crystal MgF₂ (110) substrates via molecular-beam epitaxy. The RHEED patterns were used to characterize the surface crystallinity during growth. The high angle x-ray diffraction (XRD) allowed establishing epitaxial growth directions and in- and out-of-plane crystallinity coherences. The x-ray reflectivity (XRR) patterns were used to establish the layer thicknesses and the interface roughness parameters. The Fe-concentration was estimated from XRD lattice parameters and the XRR fittings and it was according with that from XPS analysis. The magnetic anisotropies of the Co layer were measured via standard magnetometry measurements.

11:20am **MI+TF-ThM11 Electrical Properties of Ni_{1-x}Fe_xO₃ Thin Films, K.B. Karuppanan**, University of Texas at El Paso, *M. Garimalla*, IIT Madras, India, *C.V. Ramana*, University of Texas at El Paso

Nickel ferrite is one of the most versatile and technologically important ferrite materials because of its high Curie temperature, high saturation magnetization, low conductivity and thus lower eddy current losses, high electrochemical stability, catalytic behavior. The focus of the present work was to grow Ni_{1-x}Fe_xO₃ and NiO.Fe_{1.925}Sm_{0.075}O₃ thin films by RF magnetron sputtering and study their structural and electrical properties. Ni_{1-x}Fe_xO₃ and NiO.Fe_{1.925}Sm_{0.075}O₃ films were grown by sputtering the bulk NiO.Fe_{1.925}Sm_{0.075}O₃ and NiO.Fe_{1.925}Sm_{0.075}O₃ targets prepared by solid state chemical reaction. The results indicate that the as-grown films were amorphous. Samples annealed at 1073 K were crystalline. DC electrical conductivity measurements performed in the temperature range 60-300 K indicate the insulating behavior of the materials. The room-temperature conductivity of the NiO.Fe_{1.925}Sm_{0.075}O₃ film is less than that of pure Ni ferrite film. Analysis of the conductivity indicates that the small polaron and variable-range-hopping (VRH) mechanisms are operative in 180-300 K and 60-180 K temperature regions, respectively. Frequency variation of the electrical resistivity measurements in the range 1 kHz - 13 MHz indicate that the resistivity decreases with increasing frequency. The mean relaxation time and spreading factor values were found to be larger for the NiO.Fe_{1.925}Sm_{0.075}O₃ film which could be due to the fact that larger Sm³⁺ ion leads to increased bond distance.

11:40am **MI+TF-ThM12 Structural, Transport and Magnetic Properties of SrSn_{0.95}Fe_{0.05}O₃ Thin Films, G. Prathiba**, IIT Madras, India, *S. Venkatesh*, Tata Institute of Fundamental Research (TIFR), India, *N. Harish Kumar*, IIT Madras, India

Transparent magnetic semiconductors are potential materials for multifunctional magneto-opto-electronic devices. Wide band gap oxides are the best candidates for transparent semiconductors. Following the prediction of Dietl et al.,¹ on possible ferromagnetic ordering in wide band gap semiconductors doped with magnetic elements, the focus was on oxide dilute magnetic semiconductors. SrSnO₃ is a wide band gap material with a direct band gap of 4.27 eV. At room temperature it crystallizes in perovskite orthorhombic structure. The electrical resistivity of SrSnO₃ on forming solid solution with SrFeO₃ decreases. SrSn_{0.95}Fe_{0.05}O₃ thin films were prepared by RF magnetron sputtering on oxidized silicon (100) substrates at room temperature. The films were annealed at 1073 K for two hours. The as deposited films were found to be amorphous whereas the annealed films were polycrystalline in nature. The surface morphology of the films studied using Atomic Force Microscopy (AFM) showed low roughness value (Root mean square value of surface roughness - 2.02 nm). The resistivity of the film was measured using two probe method in the temperature range 200 to 300 K. The variation of resistivity with temperature exhibits semiconducting behaviour. Using Arrhenius plot [$\rho = \rho_0 \exp(E/kT)$] the activation energy was found to be 0.39 eV. The magnetic measurements done using Superconducting Quantum Interference Device (SQUID) magnetometer showed ferromagnetic ordering below 20 K.

Reference:

¹T. Dietl, H. Ohno, F. Matsukura, J. Cibert and D. Ferrand, *Science*, 287 (2000) 1018

MEMS and NEMS

Room: Santo Domingo - Session MN-ThM

Multi-scale Interactions of Materials at the Micro- and Nano-scale

Moderator: R.B. Ilic, Cornell University

8:00am MN-ThM1 Mechanical Devices Incorporating Ultra-Thin Membranes, H.G. Craighead, Cornell University INVITED

We have fabricated resonant mechanical structures from different membrane materials, including single-atom-thick graphene, and explored their function as sensors and devices. Silicon nitride can be lithographically fabricated to form electromechanical devices, and these structures have been widely studied, often in the form of cantilevers, as resonators and sensors. We have explored different geometries of silicon nitride as resonant mass sensors and also studied a new stress-based resonant device for sensing atmospheric gasses. With advances in processing methods we can now create similar devices from lithographically patterned graphene atomic sheets and monitor their mechanical response by methods similar to those used for surface patterned silicon nitride. The ability to integrate membranes into nanomechanical devices and systems creates the possibility for new sensing modalities and systems.

8:40am MN-ThM3 Functionalized CMOS Nanomechanical Resonators for Trace Explosives Detection, J.W. Baldwin, Naval Research Laboratory, J.S. Burgess, National Research Council, M. Zalaludinov, F.A. Bulat, Global Strategies Group, B.H. Houston, Naval Research Laboratory

We used functionalized CMOS integrated Nanoelectromechanical (NEM) resonators to selectively detect specific families of analyte. Unfunctionalized resonators have femtogram sensitivity in air, but have little selectivity. To address this problem, our resonators have been functionalized with adsorbate groups (e.g. perfluoroalkane and hexafluoroisocarbonol). These groups were bound to the surface using a spatially selective process using UV hydrosilation reactions. This process allows for the functionalization of the resonator without functionalizing the whole surface, leading to increased sensitivity. These functionalized resonators showed enhanced selectivity towards target molecules. For example, the hexafluoroisocarbonol group showed selectivity towards nitrobenzene but not towards cyclohexane or water. The operation of these devices in air, functionalization methods, and limits of detection will be discussed. This work was supported by the Office of Naval Research.

9:00am MN-ThM4 Performance of Nanomechanical Mass Sensors Containing Nanofluidic Channels, R.A. Barton, R.B. Ilic, S.S. Verbridge, B.R. Cipriany, J.M. Parpia, H.G. Craighead, Cornell University

Nanomechanical resonators operating in vacuum are capable of detecting and weighing single biomolecules, but their poor performance in liquid, a consequence of strong viscous damping, hinders many biological applications. One approach that has been demonstrated to improve the performance of resonant MEMS operating in contact with liquid, encapsulating the liquid within the resonator, had until this work not been extended to devices with effective mass smaller than ~100 ng. Here, we show that the practice of confining liquid within a resonator improves the performance of NEMS with mass as small as 100 pg. We optically actuate and detect the motion of doubly clamped beams containing fluidic channels with height 100 nm, which show quality factors as high as 800 when filled with fluid. We use these devices to measure fluid density, demonstrating a mass responsivity of 100 Hz/fg and a noise equivalent mass of 2 fg. We also demonstrate that the quality factor of the fluid-filled resonators is limited by the fluid, and discuss the physical mechanisms causing the enhanced dissipation. Our analysis suggests methods of improving the mass resolution of fluid-filled resonators and demonstrates their promise for novel biological applications.

9:20am MN-ThM5 Fabrication of Integrated Nanomagnets Overhanging Batch-Fabricated Attonewton-Sensitivity Cantilevers, J.G. Longenecker, S.A. Hickman, E.W. Moore, S.G. Lee, S.J. Wright, Cornell University, L.E. Harrell, United States Military Academy, J.A. Marohn, Cornell University

Mechanical detection of magnetic resonance opens up exciting possibilities for characterizing soft materials and biomolecules with elemental specificity at nanometer-scale, and potentially atomic-scale, resolution. Achieving atomic-scale resolution requires using cantilevers with a low minimum detectable force at small tip-sample separations and fabricating magnetic tips with only a few nanometers of damage at the leading edge. We address these challenges by 1) fabricating cantilevers with overhanging magnetic

tips, 2) protecting the nanomagnet leading edge by atomic layer deposited (ALD) alumina, and 3) characterizing the extent and chemical mechanism of damage by nanometer-resolution electron energy loss spectroscopy (EELS).

After determining by EELS analysis that the nickel magnet leading edge incurred substantial damage during processing, we introduced tantalum and ALD alumina interdiffusion barriers into our forty-two step fabrication process. We demonstrate that these modifications have significantly reduced the damage layer thicknesses. The nanomagnet grain structure, point-by-point relative atomic concentrations at the leading edge, and magnetization are determined by high-resolution transmission electron microscopy (TEM), EELS, and frequency-shift cantilever magnetometry, respectively. We will also detail ongoing work to reduce the number of processing steps after magnet deposition, which could greatly improve magnet yield and quality. Our findings suggest that fabricating a cantilever suitable for single proton detection, while a materials processing challenge, should be possible.

9:40am MN-ThM6 Fabrication and Characterization Ultra-Sensitive, Nickel-Tipped Silicon Cantilevers for Magnetic Resonance Force Microscopy, S.A. Hickman, E.W. Moore, S.G. Lee, S.J. Wright, Cornell University, L.E. Harrell, United States Military Academy, J.A. Marohn, Cornell University

Magnetic Resonance Force Microscopy is a technique which combines the elemental discrimination and three-dimensional imaging of magnetic resonance with the spatial resolution of scanned probe microscopy. Key to this technique is attonewton-sensitivity mechanical oscillators with magnetic particles at the tip.

The aim of this work was to create silicon cantilevers with nickel magnets which extended past the tip of the cantilever body - a design conceived to minimize surface-induced force noise.

The fabrication challenges of this design, including alignment across multiple lithographic modes and silicide prevention, will be covered. As well, characterization data of successfully produced devices will be presented.

10:40am MN-ThM9 Parametric Excitation of Large Amplitude Out-of-Plane Vibrations of Micro Beams By Fringing Electrostatic Fields, S.L. Krylov, Tel Aviv University, Israel, N. Molinazzi, Medica Group, Italy, T. Shmilovich, U. Pomerantz, S. Lulinsky, Tel Aviv University, Israel

We report on an approach for efficient parametric excitation of large amplitude flexural out-of-plane vibrations of cantilever and double-clamped micro beams and present results of theoretical and experimental study of the suggested principle. An actuating electrode is located symmetrically at the two sides of the beam and is fabricated from the same layer of the wafer. The beam is free to deflect in the out-of-plane direction, whereas its stiffness in the lateral in-plane direction is significantly higher. The distributed electrostatic force, which is zero in the initial configuration, is engendered by the asymmetry of the fringing fields in the deformed state and acts in the direction opposite to the deflection.

The force can be effectively viewed as a reaction of an elastic foundation, which increases the stiffness of the system. The time-varying voltage applied to the electrode results in the modulation of this electrostatic stiffness and consequently in the parametric excitation of the structure. The device is distinguished by a simple single-layer architecture and may exhibit large vibrational amplitudes, which are not limited by the pull-in instability common in close-gap actuators. In contrast to previously reported devices excited by the fringing fields, the force considered here is of distributed character. The reduced order model was built using the Galerkin decomposition with undamped linear modes as base functions and the resulting system of nonlinear differential equations was solved numerically. The electrostatic forces were approximated by means of fitting the results of three-dimensional numerical solution for the electric fields. The devices fabricated from a silicon on insulator (SOI) substrate using deep reactive ion etching (DRIE) based process combined with the critically timed etching were operated in ambient air conditions and the responses were registered by means of Laser Doppler Vibrometry. The experimental resonant curves were consistent with those predicted by the model. Theoretical and preliminary experimental results illustrated the feasibility of the suggested approach.

11:00am MN-ThM10 The Effect of Temperature on Etch Rate and Surface Roughness for Si Etched with Vapor Phase XeF₂, Z.C. Leseman, J. Butner, University of New Mexico

In this work we present results from a pulsed etching system with XeF₂ over an expanded temperature range while at the same time determining the roughness of the substrate left behind. The experimental apparatus used for the work presented in this paper is capable of temperature ranges from

approximately 100 K to 800 K. Data was taken at a constant etching pressure (1 Torr) so the effect of temperature on etch rate and roughness could be studied. Etch rates were determined by varying the duration of the pulse and surface roughness was characterized using an AFM.

11:20am MN-ThM11 Fabrication of High Density Single Crystal Silicon Nanowires for Ensemble Measurements, D.A. Czaplewski, L.E. Ocola, M.V. Holt, Argonne National Laboratory

Silicon nanowires have shown promise in applications such as photovoltaic cells, lithium storage for batteries, transducers, sensors, and many more. Single crystal silicon nanowires (SCSN) have been used to study materials and electrical properties of Si as the nanowires have been scaled down towards several nanometers. These experiments have been designed to test the classical predictions of materials behavior as the assumption of continuum mechanics starts to break down. Due to the small sizes of SCSNs, measurements of materials properties have been inconsistent due to the variation in dimensions and fabrication methods from wire to wire. Typically, SCSNs are fabricated at very low densities, which make measurements of ensembles very difficult. Here we present two top-down processes to create SCSNs at relative densities approaching 50% of a continuous film with dimensions as small as 30 nm. Both fabrication processes start with e-beam lithography. In the first fabrication process, a positive e-beam resist is patterned and developed. The resist is exposed to a second dose of electrons to increase the etch selectivity during reactive ion etching. The silicon structures are reactive ion etched in a CHF₃-O₂ plasma chemistry to define the structures. In the second approach, a negative e-beam resist, hydrogen silsesquioxane (HSQ), is patterned and developed on a thin thermally-cured HSQ layer. After development, the pattern is transferred into the silicon via a reactive ion etch using a Chlorine chemistry followed by a HBr-O₂ chemistry. After the wires are defined, they are subsequently released in a dilute HF-DI water mixture and then dried using a super critical CO₂ drying technique. The released structures are being used for studies of coupled mechanical oscillators and to study materials and electrical properties in ensembles of 1-D wires.

11:40am MN-ThM12 Analysis of a Dip-Solder Process for Self Assembly, M.R. Rao, J. Luth, S.L. Burkett, University of Alabama

Dip-soldering is a crucial step in forming certain self-assembled metal structures. However, this particular use of dip-soldering is not well described in the literature. The goal of this work is to characterize the thickness and roughness of solder layers deposited by dipping metallic films into solder melt over a range of temperatures. Control of the solder thickness and roughness will improve the yield of structures whose self-assembly is driven by surface area minimization during solder reflow. Film thickness and overall film roughness for four solder alloys, each with different melting points, were measured on unpatterned and patterned copper films. Additionally, two variations in flux treatment were investigated: flux maintained at room temperature and flux preheated to 98 °C. Findings include the determination of critical temperatures, particular to each alloy, above which the roughness and thickness of the deposited solder dramatically decreases. Preheating the flux improves the nature of the deposition below these critical points. Above the critical points, thickness and roughness of the solder vary little and preheating the flux does not provide significant improvements. This study provides insight into designing a process flow that optimizes the folding characteristics of self-assembled metal polyhedra by controlling the volume and quality of the solder layer.

Nanometer-scale Science and Technology

Room: La Cienega - Session NS-ThM

Nanowires and Nanoparticles

Moderator: L. Bartels, University of California at Riverside

8:00am NS-ThM1 Enantioselective Separation on Chiral Au Nanoparticles, N. Shukla, M. Bartel, N. Ondeck, A.J. Gellman, Carnegie Mellon University

The surfaces of chemically synthesized Au nanoparticles have been modified with D- or L- cysteine to render them chiral and enantioselective for adsorption of chiral molecules. Their enantioselective interaction with chiral compounds has been probed by optical rotation measurements when exposed to racemic propylene oxide. The ability of optical rotation to detect enantiospecific adsorption arises from the fact that the specific rotation of polarized light by R- and S-propylene oxide is enhanced by interaction Au nanoparticles. The enhancement of the specific optical rotation of polarized light by R- and S-propylene oxide is sensitive to excitation wavelength. Longer the excitation wavelength, smaller is the specific rotation of

polarized light. This effect is related to previous observations of enhanced circular dichroism by Au nanoparticles modified by chiral adsorbates. More importantly, chiral Au nanoparticles modified with either D- or L- cysteine enantioselectively adsorb one enantiomer of propylene oxide from a solution of racemic propylene oxide, thus leaving an enantiomeric excess in the solution phase. Au nanoparticles modified with L- cysteine (D- cysteine) selectively adsorb the R-propylene oxide (S-propylene oxide). A simple model has been developed that allows extraction of the enantiospecific equilibrium constants for R- and S-propylene oxide adsorption on the chiral Au nanoparticles.

8:20am NS-ThM2 Unique Optical Properties in Wet - Chemically Etched Silicon Nanowires, V.A. Sivakov, B. Hoffmann, F. Voigt, G. Broenstrup, F. Talkenberg, Institute of Photonic Technology, Germany, G. Bauer, University of Oldenburg, Germany, S.H. Christiansen, Max Planck Institute for the Science of Light, Germany

Silicon nanowire (SiNW) ensembles with vertical and zig-zag architectures have been realized using wet chemical etching of bulk silicon wafers (p-Si(111) and p-Si(100)) with an etching hard mask of silver nanoparticles that are deposited by wet electroless deposition on polystyrene patterned silicon surfaces.

Strong visible (red-orange) room temperature photoluminescence has been observed in wet chemically etched heavily (1020 cm⁻³) and lowly (1015 cm⁻³) doped SiNWs. Our observations strongly suggest that visible light emission at room temperature of SiNWs is a result of the rough sidewall structure that can be such that nanoscale features form that make quantum confinement most probable. Significant light absorption (over 90% in a range between 300-2000 nm) was observed in the SiNWs covered by the TCO (Al doped ZnO) thin layers performed via Atomic Layer Deposition. The strong absorption, less reflection of visible and infra-red light and room temperature photoluminescence of the SiNW ensembles strongly suggest that such a material has a real potential to be applied in the fields of optoelectronics, photonics, sensoric and photovoltaics. The morphology, crystallographic and surface structure, and optical properties of SiNWs will be presented and discussed in details.

8:40am NS-ThM3 Size, Composition and Support Effects in Nanocatalysis: I. Bridging the Sub-Nanometer and Nanometer Size Range & II. Coupling the Studies of Model and "Real" Catalysts, S. Vajda, Argonne National Laboratory

The elucidation of the size/composition/shape/structure and function correlation is instrumental for the design of new catalysts. Uniform particles are prerequisites for such studies, making size-selected clusters of few atoms to several nm in size as ideal model systems. The experiments are based on 1) size-selected cluster deposition, 2) electron microscopy and 3) *in situ* synchrotron X-ray characterization under working conditions (scattering and absorption), combined with 4) mass spectroscopy of products. DFT calculations performed by our collaborators are instrumental at the understanding of the catalytic properties of these materials. In this presentation, examples will be given on bridging the size gap between the sub-nanometer and nanometer cluster size regime and on coupling studies of model size-selected [1-3] and "real"- with wet chemical methods prepared [4-6] catalysts. Processes discussed will include dehydrogenation, Fischer-Tropsch synthesis and partial oxidation of alkenes. For example, our studies led to the identification of a new class of silver-based direct propylene epoxidation catalyst which works at considerably lower temperatures than existing ones [1]. The role of the size in catalyst's activity and the evolving morphology of silver nanoclusters under epoxidation conditions will be addressed [1-3], followed by the discussion of strong size, composition and support effects in dehydrogenation [4,5], hydrogenation [6] and Fischer-Tropsch reactions.

[1] Y. Lei, F. Mehmood, S. Lee, J. P. Greeley, B. Lee, S. Seifert, R. E. Winans, J. W. Elam, R. J. Meyer, P. C. Redfern, D. Teschner, R. Schlögl, M. J. Pellin, L. C. Curtiss, and S. Vajda, *Science* **328**, 224 (2010)

[2] S. Vajda, S. Lee, K. Sell, I. Barke, A. Kleibert, V. von Oeynhausen, K.-H. Meiwes-Broer, A. Fraile-Rodriguez, J. W. Elam, M. J. Pellin, B. Lee, S. Seifert, R. E. Winans, *J. Chem. Phys.*, **131**, 121104 (2009),

[3] L. M. Molina, S. Lee, K. Sell, G. Barcaro, A. Fortunelli, B. Lee, S. Seifert, R. E. Winans, J. W. Elam, M. J. Pellin, I. Barke, A. Kleibert, V. von Oeynhausen, Y. Lei, R. J. Meyer, J. A. Alonso, A. Fraile-Rodriguez, S.

Giorgio, C. R. Henry, K.-H. Meiwes-Broer, and S. Vajda, *Catal. Today*, invited, under review

[4] M. Di Vece, S. Lee, X. Wang, B. Lee, S. Seifert, R.E. Winans, M. Neurock, G. Haller, L. D. Pfefferle, and S. Vajda, in preparation

[5] M. Di Vece, S. Lee, R. Si, B. Ricks, S. Seifert, R.E. Winans, M. Flytzani-Stephanopoulos, and S. Vajda, in preparation

[6] S. A. Wyrzgol, S. Schäfer, S. Lee, B. Lee, M. Di Vece, X. Li, S. Seifert, R. E. Winans, M. Stutzmann, J. A. Lercher, and S. Vajda, 2010, *Phys. Chem. Chem. Phys.* feature article, on-line April 27, 2010

9:00am **NS-ThM4 Electrochemistry of Surface-Passivated Nanocrystals**, *P. Szymanski, A.Y. Kopsosov, V.I. Klimov, M. Sykora*, Los Alamos National Laboratory

We have combined electrochemical and optical measurements to investigate the effects of charging on the optical properties of semiconductor nanocrystals (NCs). We show that cyclic voltammetry with simultaneous monitoring of absorption and photoluminescence is necessary to accurately determine the energy offset of the NC conduction-band minimum. The combination of electrochemical and optical studies also reveals the different location of charges - surface vs. NC core. The studies of photoluminescence dynamics show that carrier relaxation dynamics is significantly enhanced in charged NCs. In addition, we have studied the effect of inorganic passivating layers on the NC charging. The addition of a shell with a wide band gap, such as ZnS, creates an energetic and kinetic barrier for charging the nanocrystal core under an applied potential. We find that a significant shift in the charging potential can occur with shell thicknesses as thin as 2 monolayers. Our results demonstrate the broad applicability of spectroelectrochemical methods for characterizing materials of potential interest in photovoltaic and light-emitting devices.

9:20am **NS-ThM5 Single-nanoparticle Catalysis at Single-turnover Resolution**, *P. Chen*, Cornell University **INVITED**

Metal nanoparticles can catalyze many chemical transformations for energy conversion, petroleum processing, and pollutant removal. Characterizing their catalytic activity is important, but challenging in ensemble measurements due to their morphology dispersions and variable surface active sites. Using single-molecule microscopy of fluorogenic reactions, we monitor the redox catalytic reactions on the surface of individual Au-nanoparticles in an aqueous environment in real time at single-turnover resolution. We find that for catalytic product generation, all Au-nanoparticles follow a Langmuir-Hinshelwood mechanism, but individual nanoparticles show drastically different reactivity. And for product dissociation, three nanoparticle subpopulations are present that show differential selectivity between parallel dissociation pathways. Individual nanoparticles show large temporal activity fluctuations, attributable to both catalysis-induced and spontaneous dynamic surface restructuring that occurs at different timescales at the surface catalytic and product docking sites. Individual Au-nanoparticles also show reactant-concentration dependent dynamic surface switching between a low reactivity state and high reactivity state. Strong size dependences are also observed in the catalytic activity, selectivity, and dynamics of these Au-nanoparticles. Smaller particles are more reactive but bind the reactant weaker. Larger particles are less selective in the parallel reaction pathways. The smaller particles are more prone to dynamic surface restructuring, whose activation energies and timescales are quantified. The results exemplify the power of the single-molecule approach in revealing the interplay of catalysis, heterogeneous reactivity, and surface structural dynamics in nanocatalysis.

10:40am **NS-ThM9 Size Effects in the Synthesis of Ge and Ge/Si Nanowire Heterostructures**, *S.A. Dayeh, S.T. Picraux*, Los Alamos National Laboratory

Progress in the synthesis of semiconductor nanowires has prompted intensive discussions of the science of their growth and the technological applications they promise. Fundamental aspects of their growth have been postulated for nearly five decades for larger diameter nanowires and debated more recently in detailed growth studies for different materials systems. Here, we exploit an extreme level of control over diameter, morphology, and placement in VLS synthesized germanium nanowires to establish systematic size effects on their growth at small diameters, down to sub-10 nm, where quantum effects become relevant. We observe reproducible reduction in Ge nanowire growth rates with decreased diameter coupled to a measured increase in the Ge equilibrium solubility¹ for the same wires, validating the role of the Gibbs-Thomson effect in nanowire growth at small diameters. We show how this sets a practical thermodynamic limit on the lowest achievable nanowire diameters (~ 3 nm) and present comprehensive studies of the effects of temperature, pressure, and the introduction of dopant precursors on the size dependences and cutoff diameters for nanowire growth. We also discuss methods to control and eliminate Au diffusion during the growth of Ge/Si core/shell

heterostructures. Single crystal core/multi-shell Ge/p+Ge/Si nanowires were grown using such a process and their transport properties benchmarked. Using field-effect transistors as a test-bed for their transport properties, we observe up to 2X mobility enhancement in such heterostructured nanowires without Au diffusion and obtain record geometry-normalized on-currents for p-type FET devices of up to 430 $\mu\text{A/V}$. These studies provide an in-depth understanding for the control of the growth of Ge/Si nanowires and for exploiting their bandgap engineering possibilities for unique nanoscale device performance.

¹ E. Sutter et al., 2010 (to be published).

11:00am **NS-ThM10 Formation and Characterization of Metallic Glass Nanowire**, *K.S. Nakayama, Y. Yokoyama, T. Ono, M.W. Chen, K. Akiyama, T. Sakurai, A. Inoue*, Tohoku University, Japan

Metallic glasses have exciting potential for structural, chemical, and magnetic applications with the sizes ranging from micrometer to centimeter, but the fabrication and characterization down to nanoscale remains an important challenge. Progress has been hindered by the lack of bottom-up methodologies to produce amorphous nanostructures. Recently, we show the self-organized amorphous nanowires that are formed on the fracture surfaces of bulk metallic glasses [Nakayama et al., *Nano Lett.* 8, 516-519 (2008)]. However, it is difficult to control their morphologies because they were created by instantaneous fracture processes. Here we report the controlled formation and mechanical characterization of individual amorphous nanowires. We find that they have a high strength with the excellent flexibility where the elastic modulus is much smaller than that of the bulk owing to the hyper-excess free volume in nanowire. The nanowire composed of amorphous materials leading to outstanding mechanical properties would offer a new paradigm for development in nanotechnology and materials science.

11:20am **NS-ThM11 Diameter Dependence of the Minority Carrier Diffusion Length in Semiconductor Nanowires**, *A. Soudi, Y. Gu*, Washington State University

Carrier transport in semiconductors is of both fundamental and technological significance, as it not only reflects fundamental aspects such as electron-phonon interactions, but also controls electronic and optoelectronic device characteristics. Minority carrier transport is particularly important, as it determines the performance of p-n junction based devices. A fundamental understanding of carrier transport properties, especially those of minority carriers, provides a critical basis for material engineering and device design efforts.

In advancing semiconductor nanowire-based device technologies, a quantitative knowledge of carrier transport parameters, such as the carrier diffusion length, is required for a rational design of devices with controlled performance. From a fundamental perspective, in semiconductor nanowires, the one-dimensional confinement of carriers and phonons, together with the high surface-to-volume ratio, can render carrier transport characteristics significantly different from those in the bulk. Here, using the near-field scanning photocurrent microscopy technique, we have directly measured the minority carrier diffusion length in single ZnO nanowires. In particular, a near-field scanning optical microscope was used to locally generate minority carriers in single nanowire Schottky diodes; the spatial variations of the resulting photocurrent images near the Schottky contact were used to obtain the minority carrier diffusion length, L_D . The diameter dependence of L_D suggests a *diameter-dependent* surface electronic structure, particularly an increase in the density of mid-bandgap surface states with the decreasing diameter. This diameter dependence of the surface electronic structure might be a universal phenomenon in wurtzite-type nanostructures, and is critical in interpreting and understanding the effects of surfaces on various material properties.

11:40am **NS-ThM12 Photocatalytic Deposition of Pt or Ag Nanoparticles on Ordered Linear Arrays of TiO₂ Nanoparticles**, *J. Taing, J.C. Hemminger*, University of California, Irvine

TiO₂ nanoparticles are generated on step edges of highly oriented pyrolytic graphite (HOPG) via physical vapor deposition of Ti followed by air oxidation. Deposition of Ti on HOPG while the substrate is held at 900 K results in nanoparticle growth exclusively at the graphite step edges. Since the steps on high quality HOPG are long (>1 micron) and very parallel, the result is highly ordered arrays of nanoparticles. Photodeposition of Pt on the TiO₂ nanoparticles results in the decoration of the TiO₂ with Pt nanoparticles (≤ 5 nm). Photodeposition of Pt is accomplished by submersion in an aqueous solution of 0.25 mM K₂PtCl₄ and 0.5 mM trisodium citrate followed by photolysis with TiO₂ bandgap radiation (365 nm radiation from a 200 W Mercury lamp). Similarly, Ag nanoparticles can be deposited by photolysis of the sample in an aqueous solution of 0.25 mM Ag(NO₃)₃ and 0.5 mM trisodium citrate. Scanning electron microscopy (SEM), atomic force microscopy (AFM), transmission electron microscopy

(TEM), x-ray dispersive spectroscopy (EDS), and x-ray photoelectron spectroscopy (XPS) characterize the morphology, crystal structure, and chemical identity of the nanoparticles. Images of decorated TiO₂ nanoparticles are included in the supplement.

Plasma Science and Technology

Room: Galisteo - Session PS+TF-ThM

Plasma Deposition and Plasma Enhanced ALD

Moderator: M. Shiratani, Kyushu University, Japan

8:00am **PS+TF-ThM1 High Rate Synthesis of Crystalline Si Film by Control of High Density Radicals with Dual Frequency PECVD, J.G. Han, Y.S. Choi, Y.J. Kim, I.S. Choi**, Sungkyunkwan University, Republic of Korea **INVITED**

One of prime hurdle for high efficiency and cost effective Si film solar cell is enhancement of deposition rate of crystalline Si film with low defects at least higher than 1.0 nm/sec for cost effective solar cell device manufacturing. Crystalline Si thin films are synthesized at low temperature less than 350 °C on glass by various dual frequency plasma CVD utilizing dual power inputs in a frequency range of RF to UHF. The deposition rate of crystalline Si film is significantly enhanced in a range of 0.8 nm/s to 2.0 nm/s by RF plasma CVD using SiH₄ and H₂ gas mixture with additional power input of very high frequency (VHF) and ultra high frequency (UHF). The volume ratio of crystalline and amorphous Si film structure is also controlled in a range of 45 % to 70 % with change of dual frequency power inputs and partial pressure ratio of SiH₄ and H₂. The significant improvement of deposition rate with additional power input of VHF and UHF is closely associated with enhanced generation of SiH_x radicals from SiH₄ molecules due to the secondary high density plasma generated by additional high excitation frequency. Hydrogen radical which contribute the formation of crystalline Si film with surface diffusion and chemical annealing is also generated intensively. This paper illustrates the results of change of deposition rate as well as microstructure with variation of dual power inputs and process parameters. The corresponding mechanism is discussed with plasma diagnostic data of silane and hydrogen radicals using optical emission spectroscopy (OES), Langmuir probe and radical monitors.

8:40am **PS+TF-ThM3 Room Temperature PECVD Synthesis of Hybrid Organic-Inorganic Nanolaminates, R. Patel, C.A. Wolden**, Colorado School of Mines

Nanolaminates enable a new class of optoelectronic structures that are ultra lightweight, dimensionally stable, and have low cost with increased durability and flexibility. They are integral components in various applications serving as advanced dielectrics, flexible barrier coatings, and as optical components. In this work plasma enhanced chemical vapor deposition (PECVD) is employed to deposit functional polymer thin films on flexible substrates in order to make hybrid organic-inorganic nanolaminates for the applications described above.

Silicone-like coatings were deposited using hexamethyldisiloxane (HMDSO) and oxygen as precursors at room temperature. Film composition was assessed by spectroscopic ellipsometry and FTIR. A wide range of coatings, from inorganic SiO₂-like films to flexible polymeric films could be deposited by appropriate control of parameters including the O₂/HMDSO ratio, rf power, and working pressure. In this work we report on how these variables impact deposition rate, film composition, and nanolaminate performance. Growth rates as high as 100 nm/min were obtained, and crack free silica and polymeric films have been deposited on polyethylene.

For the production of organic-inorganic nanolaminates, two approaches were used for the formation of the inorganic layer. In one case HMDSO was used for deposition of both the silicone- and silica-like layers. In this case, the flowrate of HMDSO was held constant while other variables (power/O₂ flowrate) were adjusted. In the second case, the inorganic layer was aluminum oxide that was formed using tri-methyl aluminum (TMA) and oxygen at room temperature. Self-limiting growth of alumina (~Å/pulse) was achieved by both plasma-enhanced ALD and pulsed PECVD. No impurities were detected in Al₂O₃ by FTIR by either technique under optimum conditions. Nanolaminates were constructed as a function of dyad composition and total number of dyads. In this paper we compare the performance of these various nanolaminates with respect to metrics such as adhesion and barrier properties.

9:00am **PS+TF-ThM4 Role of PEALD System Plasma Source Operation on Substrate Ion Bombardment and the Impact on HfO₂ and TiN Film Properties, M.J. Sowa, G.M. Sundaram, E.W. Deguns, R. Bhatia, M.J. Dalberth, A. Bertuch, G. Liu, J.S. Becker**, Cambridge NanoTech, Inc.

Plasma enhanced atomic layer deposition (PEALD) has seen increased interest in recent years. Replacing one of the half cycles of the ALD process with a plasma generated radical dose has been successfully demonstrated to improve film electrical properties, improve deposition rates, enable lower temperature processing, and enable the use of precursors unsuitable for thermal processes. It is typically advantageous to operate the plasma source of PEALD systems in a "remote" mode, such that the substrate being processed does not have any exposure to energetic charged species. Rather, the longer-lived radicals generated in the remote plasma source react with the chemisorbed precursor from the previous half-cycle to form the desired film. Exposure of the substrate to energetic ion bombardment during the plasma half cycle has been demonstrated to lead to decomposition of the chemisorbed precursor which gives thick, non-uniform films with poor electrical properties. We have observed that, depending on the processing conditions utilized for generating the plasma, the plasma may be confined to the remote plasma source or may extend into the ALD processing reactor to varying degrees. The remote plasma source on our system is an inductively coupled plasma design consisting of a cylindrical quartz tube surrounded by a water-cooled copper inductor. We have investigated the quality of HfO₂ and TiN films grown in our PEALD system with various, controlled levels of substrate ion bombardment. Up to 300W of 13.56MHz rf is coupled to the copper inductor through an L-type matching network. Plasma gas mixtures of Ar with commonly used PEALD gases, O₂ or N₂, over a wide range of flow rates and pressures were investigated. We have quantified the encroachment of the plasma into the ALD reactor through the placement of Langmuir probes on the surface of a 200mm substrate which is placed onto the heated substrate holder of our PEALD system. We then deposited films of HfO₂ with tetrakis(dimethylamino)hafnium and Ar/O₂ plasmas and TiN with tetrakis(dimethylamino)titanium and Ar/N₂ plasmas at various levels of substrate surface bombardment. Resulting films were evaluated for stoichiometry, impurities, crystallinity, and relevant electrical properties including dielectric constant and leakage current for the HfO₂ and resistivity for the TiN.

9:20am **PS+TF-ThM5 HfTiSiON Film Growth by N₂ Plasma Exposure to Hf-Ti Liquid Nano Particles on SiO₂/Si, T. Kitajima, T. Nakano**, National Defense Academy, Japan, T.M. Makabe, Keio University, Japan

1. Introduction

HfSiON is the most applicable chemistry for the high-k gate dielectrics with proper energy band alignment, large area uniformity, and thermal stability. The direct formation of HfSiO film from the Hf overlayer and underlying SiO₂ utilizing the thermal interfacial reaction was previously proposed [1]. The process enables remarkably low leak current of the film due to the lack of carbon impurity. We applied N₂ plasma for the interfacial reaction and nitridation and realized plasma-based nanoparticle involved non-thermal chemistry for HfSiON.

2. Experiment

The system consists of a UHV-SPM chamber with an e-beam metal evaporation source, a separate VHF (50MHz) low pressure ICP plasma source [2], and ex-situ XPS. Commercial Si(100) wafer with native oxide is introduced to the chamber and Hf and Ti metal beam is exposed to the surface at room temperature. The morphological development of the surface is analyzed with the in-situ non-contact AFM. The N₂ ICP is exposed to the sample without any temperature control. The grown film surface is again evaluated on its surface flatness with nc-AFM. The change of the chemistry of the sample surface is analyzed with the XPS.

3. Results and discussion

The AFM image of self-assembled Hf nanoparticles on SiO₂ surface after the deposition reveals dome shaped particles with 3-6 nm width are close-packed on the surface with high density of 8.5×10¹² cm⁻². The N₂ ICP exposure induces the interfacial reaction of the Hf nanoparticle/SiO₂/Si structure and forms Hf(Ti)SiON(film)/SiON/Si. The angle-resolved Si2p XPS spectrum at 101.5 eV in 30deg. shows the Si included in the film is nitrided. Hf silicate formation is found in the component around 100 eV. The total amount of nitrogen atoms in the film well corresponds to the total supply from the N₂ ICP due to the absorption spectroscopy of N(¹S) and N(²D) [2].

The AFM image shows the film has superior flatness of RMS roughness of 0.3 nm except the dips of 0.8 nm depth which disappear with Ti addition to the film.

5. Conclusions

The novel film growth process with plasma induced reaction of metal nanoparticles and the substrate is demonstrated for Hf(Ti)SiON. The

process scheme is widely applicable to the nano-scale feature modification and chemistry with non-thermal reactions of non-equilibrium plasma.

References

- [1] H. Watanabe, M. Saitoh, N. Ikarashi, and T. Tatsumi, Appl. Phys. Lett. 85, 449 (2004).
[2] T. Kitajima, T. Nakano, S. Samukawa, and T. Makabe, Plasma Sources Sci. Technol., 17(2), 024018 (2008).

9:40am **PS+TF-ThM6 Platinum and Platinum Oxide Films Prepared by Using Low Temperature Plasma Enhanced ALD**, *B.H. Liu, C.C. Kei, C.C. Yu, D.R. Liu, C.N. Hsiao*, National Applied Research Laboratories, Taiwan, Republic of China

In this study, smooth and pinhole-free platinum films were deposited on Si substrates by plasma enhanced atomic layer deposition (PEALD). Ar/O₂ inductively coupled plasma was applied to decompose the ligands of Pt precursor, MeCpPtMe₃. Partial pressures of Ar and O₂ were held at 0.3 and 0.1 Torr during the PEALD process, respectively. The substrate temperatures were varied between 100 and 200 °C to obtain Pt films. Crystal structure of deposited films was studied using an X-ray diffraction (XRD). Film morphology was obtained by using a field-emission scanning electron microscope (SEM). Electric properties of deposited films were measured by using a Hall effect measurement system. XRD pattern shows that the film prepared at 200 °C has the fcc structure of platinum. Only a broad (102) peak of hexagonal alpha-PtO₂ was appeared for the films deposited at 100 and 150 °C, implying that oxidized Pt can not be reduced at a temperature less than 200 °C. The growth rate of Pt films is about 0.04 nm/cycle based on the SEM observation. The sheet resistances of Pt and PtO₂ film prepared by using 200 cycles are 30.57 and 85.19 Ω/sq, respectively.

Keywords: inductively coupled plasma, PEALD, sheet resistance

10:40am **PS+TF-ThM9 Dielectric Performance of Al₂O₃ Films Prepared by Direct Plasma PEALD**, *C.C. Yu*, Instrument Technology Research Center, Taiwan, Republic of China, *Z.Y. Han*, National Chiao Tung University, Taiwan, Republic of China, *C.C. Kei, M.Y. Tsai, W.H. Cho, C.N. Hsiao*, Instrument Technology Research Center, Taiwan, Republic of China, *C.H. Chien*, National Chiao Tung University, Taiwan, Republic of China, *C.Y. Su, N.N. Chu*, Instrument Technology Research Center, Taiwan, Republic of China

In this study, plasma enhanced atomic layer deposition system (PEALD) was used to deposit Al₂O₃ films at room temperature. Trimethylaluminum (TMA) and O₂ plasma were used as metal precursor and oxidant, respectively. A DC power supplier was applied to generate O₂ plasma with a parallel-plate electrode configuration. Nitrogen purge was applied between the exposures of TMA and O₂ plasma to prevent vapor phase reaction. Cycle numbers of PEALD were varied from 100 to 500 nm. The thicknesses of Al₂O₃ films were obtained from x-ray reflectivity measurement. Surface morphology and roughness was given by using scanning electron microscopy (SEM) and atomic force microscopy (AFM), respectively. C-V measurement was performed by using a HP4194 impedance analyzer to obtain the capacitance and dielectric constants. I-V curves were characterized by measuring with a Keithley 4832 multimeter. The growth rate of Al₂O₃ film increases with the increasing plasma power and reaches a saturation value of 1.7 Å/cycle when the plasma power exceeds 50 W. SEM images imply PEALD prepared Al₂O₃ films have a pinhole free structure, and AFM result shows that Al₂O₃ film deposited for 100 PEALD cycles has a smooth surface roughness as 0.211 nm. The dielectric constant for Al₂O₃ films prepared by using 100 PEALD cycles is 4.53. A leakage current density of 3 × 10⁻⁹ A/cm² can be achieved for the 100 PEALD cycles prepared Al₂O₃ film. The interface charge trap density given by the C-V measurement increases with an increasing plasma power. This implies that high energy oxygen ion bombardment would lead to damage at interface and formation of the charge traps.

Key : PEALD, Parallel-plate electrode, Direct plasma, High-k material, C-V, I-V, D_{it}

11:00am **PS+TF-ThM10 Improving the Quality of PVD Cu Seed Layer for Interconnect Metallization**, *A. Dulkan, E. Ko, L. Wu, I. Karim, K. Leaser, K.J. Park*, Novellus Systems, Inc., *L. Meng, D.N. Ruzic*, University of Illinois at Urbana-Champaign

Physical Vapor Deposition (PVD) of Ta(N) barrier and Cu seed layers has been traditionally used in interconnect metallization process flow in VLSI manufacturing. Reliability of the manufactured devices greatly depends on the quality of different interfaces, particularly the barrier/seed one. Failure to ensure continuous seed coverage with good adhesion to the barrier may result in voided electrofill, post-CMP defects, and stress/electro-migration failures. Quality of the barrier/seed interface was greatly improved by enhancing Cu nucleation on the Ta surface through filtering of non-

energetic species from the deposition flux, increasing the fraction of Cu ions, improving flux uniformity, and minimizing gas ion bombardment. The self-sputtering ability of Cu was combined with magnetically confined high density plasma in the Novellus HCM™ PVD source. Spatial profiles of plasma density and temperature, as well as ion flux, ion metal fraction, and ion energy, were measured by planar Langmuir probes, quartz crystal microbalance, and gridded energy analyzer, all located at the wafer level. Multiple criteria, such as seed step coverage and roughness, its resistance to agglomeration, and its stability in the plating bath, have been used to evaluate interface quality. As a result new and improved Cu PVD process which demonstrated superior stability during subsequent process steps and ensured successful electrofill performance with more than 50% reduction in minimal sidewall thickness requirement has been developed.

11:20am **PS+TF-ThM11 Pulsed Plasma Polymerization of 2-Chloro-p-xylene**, *I.C. Estrada-Raygoza, P.L.S. Thamban, G. Padron-Wells, L.J. Overzet, M.J. Goeckner*, University of Texas at Dallas

Parylene C is a high-quality protective layer used in a wide array of areas that includes dielectric applications, biomedicine and micro-electromechanical systems (MEMS). Using traditional deposition, poor adhesion to a broad range of substrates remains a main concern. Adhesion is greatly improved to almost any type of substrate if the deposition is via plasma polymerization. In the work reported here we use a wide set of data to predict the film growth mechanisms during pulsed plasma polymerization of parylene C. Specifically, we examine plasma gas phase chemistry in a 2-Chloro-p-xylene pulsed discharge using of a novel e-beam probe as well as more traditional Fourier-Transform Infrared Spectroscopy and WISE[®] probe measurements. We contrast the gas phase chemistry with the bulk properties of the films deposited. Work supported in part by CONACYT Scholarship number 170201 and NSF (Grant CBET- 0922962).

11:40am **PS+TF-ThM12 Morphological Variation of Plasma Polymerized TiO_xC_y Films as a Function of Oxygen Concentration during PECVD**, *L. Sun, H. Jiang*, General Dynamics Information Technology, *J. Grant*, University of Dayton Research Institute, *P. Lloyd*, UES, Inc., *T. Bunning, R. Jakubiak*, Air Force Research Laboratory

Amorphous titanium oxide derivative films have relatively high index of refraction compared to purely organic thin films, retain much of the functionality of their crystalline counterparts and can be deposited at low temperature. Using PECVD operated at room temperature and in a remote configuration, plasma-polymerized (PP-) TiO_xC_yN_z films were derived from titanium (IV) isopropoxide using a mixture of argon and nitrogen as carrier gases. Upon exposure to ambient, the PP-TiO_xC_yN_z films undergo a continual decrease in film thickness and increased index of refraction that does not stabilize for several days after deposition. After one hour in air, the thickness of the films rapidly decreased by 14% and after three weeks the thickness decreased 30% (128 - 90 nm). This was accompanied by an increase of the refractive index from n₅₈₉ = 1.72 to 1.84. Broadly, the densification results from oxidation of low valence titanium moieties prevalent in films formed in an oxygen-poor environment. From AFM and SEM studies we know that the thin films possess a featureless, smooth (RMS - 0.5 nm) one phase 3-D crosslinking amorphous structure. When oxygen was substituted for nitrogen as a carrier gas, most of the titanium atoms retained the Ti⁴⁺ state of the monomer and little, if any densification was noted; however, the film morphology was strongly dependent on the argon to oxygen ratio in the carrier gas mixture. In oxygen rich conditions, the films contained granular columns (approximately 10 to 50 nm in diameter) composed of amorphous TiO₂, with void and crack defects between 10-20 nm in width. Films deposited in oxygen poor conditions exhibited a uniform, amorphous structure as seen in the nitrogen/argon case.

Plasma Science and Technology

Room: Aztec - Session PS-ThM

Plasma Surface Interactions (Fundamentals & Applications) III

Moderator: S. Sriraman, Lam Research Corporation

8:20am **PS-ThM2 Etching of MTJ by using Non-Corrosive Gas Mixtures**, *S.K. Kang, M.H. Jeon, J.Y. Park, G.Y. Yeom*, Sungkyunkwan University, Republic of Korea

Magnetic random access memory (MRAM) has made a prominent progress in memory performance and has brought a bright prospect for the next generation nonvolatile memory technologies due to its excellent advantages. Dry etching process of magnetic thin film is one of the important issues for the magnetic devices such as magnetic tunneling junctions (MTJs) based MRAM. MTJs which are the basic elements of MRAM can be used as bits

for information storage. CoFeB is a well-known soft ferromagnetic material, of particular interest for magnetic tunnel junctions (MTJs) and other devices based on tunneling magneto-resistance (TMR), such as spin-transfer-torque MRAM. One particular example is the CoFeB–MgO–CoFeB system, which has already been integrated in MRAM. In all of these applications, understanding and control over the etching properties of CoFeB is crucial. Recently, transferring the pattern by using an Ar⁺ ion milling is a commonly used, although the redeposition of sputter etch products on the sidewalls and the low etch rate are main disadvantages of this method. Other method, which reported the etch rates higher than 50 Å/s for magnetic multilayer structures using Cl₂/Ar plasmas, is also proposed. However, the chlorinated etch residues on the sidewalls of the etched features tend to severely corrode the magnetic material. To prevent corrosion of MTJ layer, the etching of MTJ layer using organic-based gases such as CO/NH₃, CH₃OH, etc. are actively investigated currently.

In this work, MTJ materials such as CoFeB, MgO, etc. were etched using various gas mixtures which can be expected to form volatile metallo-organic compounds and the results were compared with those etched using Cl₂-based gas mixture. As one of the gas mixtures, gas mixtures of carbon monoxide (CO) and ammonia (NH₃) were used as etching gases to form carbonyl volatiles, and the etched features of CoFeB thin films under by Ta cap-material were observed with transmission electron microscopy. The etch results showed the enhanced etch rates higher than 3 times by using a gas mixture of CO/NH₃ compared to that etched by pure CO or NH₃ possibly indicating the formation of products composed of carbonyl volatiles. The composition of etched sidewall was less damaged compared with that etched with Cl₂-based gas. The characteristics of etched MTJs were also compared to the MTJs etched by the other method such as neutral beam etching, etc.

8:40am PS-ThM3 Effect of SiH₄ Addition on the Sidewall Passivation Mechanism during the Anisotropic Etching of III-V Materials in Cl₂-based ICP Discharges, L. Gatilova, S. Bouchoule, G. Patriarche, S. Guilet, Cnrs - Lpn, France

III-V semiconductors remain unequalled materials to fabricate high efficient emitters. Anisotropic etching of III-V heterostructures is a key building-block for the processing of such photonic devices (e.g. low-optical loss waveguides or optical cavities with high quality factors, ...) and the ICP etching technique is now widely used for this purpose. Several Cl₂-containing chemistries have been proposed to date for the smooth and high-aspect-ratio etching of InP-based or GaAs-based heterostructures required to reach the NIR region. We have evidenced that in many cases anisotropic etching is due to a passivation mechanism involving SiOx deposition on the III-V sidewalls [JVSTB 26, 666 (2008)]. SiOx passivation simply occurs when a Si wafer is used as the sample tray; this configuration corresponds actually to most commercial ICP etch systems having an electrode diameter of 4-in or more, used to etch III-V samples of not more than 2-in size. However this will not be the case in future large surface processing of III-Vs, when the III-V wafer becomes of the same size of the electrode, or when III-V dies bonded onto a 200/300mm wafer have to be etched, with the wafer surface covered by protecting layer that is not silicon as it may be the case in III-V/Si photonic technologies. Other passivation mechanisms have therefore to be found. For example a Si-containing gas could be added in order to maintain SiOx passivation. In this work we have investigated the Cl₂-SiH₄ chemistry for this purpose. It is found that highly anisotropic etching (aspect ratio > 30 for micropillars) of III-V patterns with a high etch rate (> 0.6 μm/min) can be obtained by optimizing the SiH₄/Cl₂ ratio, independently from the nature of the sample tray. A high selectivity > 1:30 is also obtained with the process using a metallic/ dielectric mask. Ex-situ EDX-TEM analysis of the thin (10-50 nm thick for a 3-μm etch depth) passivation layer deposited on the sidewalls of etched sub-micrometer pillars shows that in optimized conditions this layer consists of micro-crystalline silicon. We also confirm that the deposition of the passivation layer is enhanced by H addition, as previously proposed in Cl₂-H₂ chemistry [JVSTA 27, 262, 2009]. We will further discuss the possibility to use HBr/SiH₄ plasma for the anisotropic etching of InP-based or GaAs-based heterostructures, and the effect of oxygen or nitrogen addition in the gas phase on the composition of the passivation layer. We also will compare the respective effects of SiCl₄ and SiH₄ addition on the etched surface passivation process.

9:00am PS-ThM4 Deep Inductively Coupled Plasma Etching of GaN, J. Ladroue*, GREMI - STMicroelectronics, France, M. Boufnichel, STMicroelectronics, France, T. Tillocher, P. Lefauchaux, P. Ranson, R. Dussart, GREMI, France

III-Nitride semiconductors such as gallium nitride are widely used in light emitter device manufacturing¹. GaN physical properties also open new

prospects in microelectronics developments². Combining a wide bandgap (3.4eV), strong chemical bonds and high electron mobility, GaN based devices should operate under higher temperature, higher power and higher frequency than typical silicon devices. Due to inert chemical nature of GaN, wet etching is limited³. As a consequence, it is necessary to use dry etching method⁴ to obtain a reliable MESA structure. Chlorine based plasmas are commonly used because GaCl₃ is the most volatile etching product. Etch rate is also found to strongly depend on physical sputtering. GaN etching requirements for power device applications are different from those concerning photonic devices. Due to the power density supplied to the next generation of power devices, deep structures as high as 10μm should be build. As a comparison, the etched depth needed for light emitter are of the order of a few hundreds of nanometers. Deep GaN etching implies etch rate issues as well as surface roughness defects. We showed that these etching defects are linked with dislocations and nanopipes inherent to the substrates and revealed during etching⁵. Experiments were mainly performed in two Inductively Coupled Plasma (ICP) reactors: an industrial Alcatel 601E, composed of an ICP source and a diffusion chamber and an ICP-RIE Corial 200IL without diffusion chamber. For a better understanding of the etching mechanisms, different diagnostics are used to characterize the plasma. Optical emission spectroscopy, Langmuir probe and mass spectrometry are performed as a function of process parameters. We observe that etching behaviour depends on cover plate material. An optimum etch rate as a function of source power is measured by using a silicon cover plate. OES and Langmuir probe measurements suggest that silicon cover plate, which is etched by chlorine radicals, can be a limitation in the etching performance of the process. Different chemistries are studied as source of active species, sputtering ions or molecule scavenging impurities. We have shown that oxygen impurities are responsible for the columnar defects. We also show that adding a small amount of nitrogen in the chemistry could increase the selectivity with SiO₂ mask.

¹S. Nakamura & al., Appl. Phys. Lett., 67, 1868 (1995)

²G.T. Dang & al., IEEE Trans. On Elec. Dev., 47, 692-696 (2000)

³D. Zhuang and J.H. Edgar, Mat. Sci. and Eng., 48, 1-46 (2005)

⁴S.J. Pearton & al., J. Appl. Phys., 86 (1999)

⁵J. Ladroue, A. Meritan, M. Boufnichel, P. Lefauchaux, P. Ranson and R. Dussart, JVST A submitted (2010)

9:20am PS-ThM5 Mass-selected Ion Beam Study on Reactive Ion Etching Mechanisms for Pt, Co and PtCo Thin Films, K. Karahashi, T. Ito, S. Hamaguchi, Osaka University, Japan

Recently limited choices of microfabrication techniques for magnetic thin film processing have been recognized as one of the major impediments for the development of microelectronics devices such as magnetic random access memory (MRAM) and read/write heads for magnetic data storage. For magnetic films, Ar ion milling is essentially the only etching technique that is currently available in actual manufacturing processes. Whereas Ar ion milling is a well established technology, it does not provide etching selectivity that the industry currently desires. For magnetic thin films, reactive ion etching processes based on Cl₂ or CO chemistry have been considered so far as good candidates. In this study, therefore, we have examined etching processes of PtCo alloy thin films by energetic Cl⁺ ions. More specifically we have measured desorbed products and etching yields of Pt, Co, and PtCo, using a mass-selected ion beam system. With the use of the ion beam system, we inject mono-energetic single-species ions (i.e., Cl⁺ or Ar⁺ ions) to the sample surface in ultra-high vacuum conditions. The reaction chamber, where the sample is placed, is equipped with a quadrupole mass spectrometer (QMS), a temperature programmed desorption (TPD) system, and an X-ray photoelectron spectroscopy (XPS). It has been found that the etching yields of Pt films by Cl⁺ ion injections are larger than those of Co films by Ar⁺ ion injections, and the etching yields of PtCo depend on its composition ratio. It has been also found that platinum chloride (PtClx) desorption are detected with QMS under Cl⁺ ion injections. These results indicate that the yield of Pt is increased by the formation of PtClx on the surface. We have also studies temperature dependence of the etching yield. With a higher temperature, the yield of Pt by Cl⁺ ion injections is lower because chlorine coverage on the surface is also lower at a higher surface temperature. Therefore temperature control in Pt or PtCo etching processes is of significant importance for better process control. Etching characteristics of PtCo by CO⁺ ion beams will be also discussed.

9:40am PS-ThM6 Oxygen and Chlorine Atom Recombination on TiO₂, SiO₂, and SiO₂Cl₂-Coated Plasma Chamber Wall Surfaces, R. Khare, V.M. Donnelly, University of Houston

Recombination and other possible reactions of Cl and O on chamber walls in chlorine and oxygen plasmas were studied by the "spinning wall" technique. With this method, a small cylinder (1"dia. x 1"high) in the chamber wall was rapidly rotated, periodically exposing its surface to the

* Coburn & Winters Student Award Finalist

plasma and then to the differentially pumped diagnostic chamber housing an Auger electron spectrometer for *in-situ* surface analysis. The plasma chamber also contained a silicon electrode that can be rf-biased and sputtered in an inert (Ar) plasma, or etched in a chlorine plasma. Using this technique, we previously measured Cl and O atom recombination on plasma-conditioned anodized Al and stainless steel surfaces by monitoring desorption of Cl₂ and O₂ with a mass spectrometer or through a pressure rise. We also previously found a substantial increase in O atom recombination probabilities due to trace amounts of Cu deposited *in-situ* by thermal evaporation. In the current study, a smooth Ni-coated Al substrate was used. This substrate was exposed to Si sputtered from the rf-biased electrode and was then oxidized and conditioned by long exposure to oxygen plasma. Traces of Ti were deposited on this surface with the evaporator, followed by the oxygen plasma conditioning (Ti:Si:O::5:47:48 atomic percents, averaged over the ~10 nm depth probed by Auger). The O atom recombination probability on this Ti-contaminated substrate was found to be ~30% lower than on the Ti-free substrate, i.e. the opposite to that observed for Cu contamination. Ti was then etched away in the chlorine plasma, leaving an oxy-silicon-chloride surface (Si:O:Cl:: 47:39:14). The Si electrode was then etched in the chlorine plasma while rotating the substrate, coated the rotating substrate with etching products changing the substrate surface composition to Si:O:Cl :: 54:19:27. Immediately after extinguishing the rf bias to the Si electrode, the Cl atom recombination probability was found to be lower than on the more oxygen-rich Si surface. During rf bias, however, the total product yield is higher, indicating that other products (i.e. SiCl_x) could also be desorbing from the substrate as a result of the etching of the Si electrode.

10:40am **PS-ThM9 Characteristics of Silicon Nitride Etching by Reactive Plasmas Containing CHxHy Ions**, *T. Ito, K. Karahashi*, Osaka University, Japan, *M. Fukasawa, T. Tatsumi*, Sony, Japan, *S. Hamaguchi*, Osaka University, Japan

Selective etching of silicon oxide (SiO₂) over silicon nitride (SiN) has been widely used in microelectronics fabrication processes such as contact hole etching in self-aligned processes, formation of a stress liner, and dual/triple hard mask (DHM/THM) etching processes of dual-damascene structures. The etching gases used in these plasma processes typically include fluorocarbon gases and etching chemistry by CxHyFz+ ions emitted from the plasma is considered to play an important role for the determination of etching selectivity. In this work, etching characteristics of SiO₂ and SiN by CHxHy+ ion beams are discussed with a special emphasis on effects of hydrogen provided by CHxHy+ ions on etching selectivity. The ion beams are generated by a mass-selected ion beam system and injected with a monochromatic energy into a sample substrate (SiO₂ or SiN) placed in an ultra-high vacuum chamber. The multi-beam injection system that we employed for this study also allows simultaneous irradiation of the sample by charge-neutral radical species during ion beam injection. In this way, the system enables us to simulate experimentally plasma-surface interactions that take place during the corresponding plasma etching processes. The change in chemical nature of the substrate surface during the process can be observed *in situ* by X-ray photoelectron spectroscopy (XPS) that is installed in the reaction chamber. Time of Flight (ToF) measurement of sputtered species from the sample surface is also possible with a mass and energy analyzer placed near the sample. In the experiments, sputtering yields of SiO₂ and SiN by CF+, CHF+, CF₂+, CF₂+, and CH₂F₂+ ion beams generated from CH₂F₂ or CHF₃ gases were examined. A typical ion dose for each ion irradiation was 1.6·10¹⁵ /cm²/sec. It has been found that the sputtering yield of SiN depends on the amount of hydrogen provided by the CHxHy+ ion beam whereas the sputtering yield of SiO₂ is less sensitive to such hydrogen. Energy dependence of the sputtering yields and effects of fluorocarbon film deposition by a low-energy ion beam on hydrogen accumulation on the surface will be also discussed.

11:00am **PS-ThM10 H₂/Ar and D₂/Ar Plasma Interactions with a-C:H Surfaces: A Detailed Study of Modified Layer Formation and Erosion**, *N. Fox-Lyon, F. Weirnboeck, G.S. Oehrlein*, University of Maryland, N. Ning, D.B. Graves, University of California at Berkeley

The interaction of H₂ gas discharges with carbon-based materials has been of sustained interest in many technological fields. In this work we have used a well characterized, inductively coupled plasma system (ICP) to study the interaction of H₂/Ar and D₂/Ar discharges with hard a-C:H films. The erosion of a-C:H is monitored in real time by ellipsometry, optical emission spectroscopy and plasma properties are characterized by a Langmuir probe. Our experimental setup allows for varying the reactor geometry over a wide range by changing the plasma generation substrate distance. H₂/Ar and D₂/Ar plasma interaction with a-C:H were performed using low pressure (30 mTorr) 600 W 13.56 MHz RF inductive power plasma with different substrate bias voltages. Employing real-time ellipsometry, we were able to monitor the detailed kinetics of the formation of a 1-5 nm thick hydrogenated layer of lower density than the a-C:H substrate, followed by

steady-state erosion. The influence of various plasma parameters on modified surface properties and erosion will be reported. We also will present real-time data which gives insight into the dynamic flux of carbon atoms into the plasma produced by erosion a-C:H for different conditions. The measurements of the modified surface layers are compared with "Stopping and Range of Ions in Matter (SRIM)" simulations for different conditions. The atomistic details of surface processes will also be compared with molecular dynamics simulations of the UCB group.

We gratefully acknowledge support of this work by DOE's *Plasma Science Center for Predictive Control of Plasma Kinetics: Multi-phase and Bounded Systems (University of Michigan)*.

11:20am **PS-ThM11 Plasma Surface Interactions for Low-k Material Etching**, *M. Hori*, Nagoya University, Japan **INVITED**

Porous low-dielectric-constant (low-k) materials such as porous SiOCH film are essential for interlayer dielectric film in high performance ULSI devices. To establish extremely precise etching processes of the low-k film for the next generation devices, it is required to understand the surface reaction and damage formation mechanism during plasma processing, while developing a sophisticated methodology to control the etching and ashing processes. We developed an integrated monitoring system equipped with *in-situ* spectroscopic ellipsometry, Fourier transform infrared reflection absorption spectroscopy (FT-IR RAS), a substrate temperature monitor using an optical fiber-type low-coherence interferometer [1] and an absolute density monitor for H and N radicals [2,3]. The integrated monitoring system was installed in a dual frequency capacitively coupled plasma etch reactor and we investigated H₂/N₂ plasma interactions on the low-k film. The *in-situ* monitoring during the plasma etching or ashing is crucial for the clarification of damage mechanism because the damaged films are easily modified during air exposure. Furthermore, the effect of each particle, i.e. ions, photons and radicals, was investigated individually by 'PAPE' method [4] that uses small plates, such as Si, SiO₂ and MgF₂, on or above the film substrate during the plasma exposures. So far, we considered that damages on the p-SiOCH are determined by chemical reactions of H radicals that reduce the Si-CH₃ bonds and N radicals that have an effect of inhibition of the damages. It was also confirmed that a portion of Si-O-Si linear structure in the SiOCH film changed to network and cage structures with decrease in Si-CH₃ bond during the plasma exposure. The effects of the temperature during etching on the etch profile were also examined for a variety of H₂/N₂ gas mixture ratio. The higher the H radical density and the temperature, the larger the undercut in the low-k pattern profile. Especially, the temperature increase after plasma ignition was found to be a cause of the profile deformation. Based on the above results, we proposed an autonomously-controlled etch system that realized a real-time feedback control for the fine pattern etching while monitoring the wafer temperature, radical densities and so on. It was demonstrated that real-time radical-density control upon the temperature was effective for obtaining precise pattern profiles.

[1] K. Takeda, et al., *J. Appl. Phys.*, **43**, 7737 (2004).

[2] S. Takashima, et al., *Appl. Phys. Lett.*, **75**, (25), 3929 (1999).

[3] S. Takashima, et al., *J. Vac. Sci. Technol.*, **A 19**, 599 (2001).

[4] S. Uchida, et al., *J. Appl. Phys.* **103**, 073303 (2008).

Surface Science

Room: Picuris - Session SS-ThM

Adsorption and Reactivity on Oxide Surfaces

Moderator: G. Williams, Jefferson Laboratory

8:00am **SS-ThM1 Adsorption and Reaction on Poorly Crystalline γ -Al₂O₃ Surfaces**, *J.H. Kwak, D. Mei, R.J. Rousseau, J. Szanyi, Y. Wang, C.H.F. Peden*, Pacific Northwest National Laboratory **INVITED**

γ -alumina (γ -Al₂O₃), one of the metastable 'transition' alumina structural polymorphs, is an important catalytic material both as an active phase and as a support for other catalytically active phases, with widespread applications ranging from petroleum refining to automotive emission control. As such, the bulk and surface structure of γ -Al₂O₃, and its formation and thermal stability have been and continue to be the subject of a considerable research. However, due to the low crystallinity and very fine particle size of γ -Al₂O₃, it is very difficult to apply well-established analytical techniques for determining its surface structures. Of particular importance for understanding the catalytic properties of γ -alumina, relating its surface structure to the origin of Lewis and Brønsted acidity has been of considerable interest and has been studied by solid state NMR and FTIR spectroscopies, and most recently by theoretical calculations. In this presentation, we describe recent studies using ultra-high resolution NMR spectroscopy as an especially useful probe of the γ -Al₂O₃ surface structure,

and its relevance to catalytic behavior. In particular, we correlate the NMR spectra with measurements of the adsorption and reaction of light alcohols. In this way, we demonstrate a strong dependence of this chemistry on the presence of specific 5-coordinate Al^{3+} ions. These sites, in turn are a function of the dehydration temperature of the alumina material before use. From these correlations, we are able to explain a considerable number of prior observed phenomena.

8:40am SS-ThM3 Evolution and Growth of Polar ZnO Nanostructures and their Correlation with Native Point Defects, D.R. Doutt, T.A. Merz, Y.F. Dong, L.J. Brillson, Ohio State University

We have used a complement of depth-resolved cathodoluminescence spectroscopy (DRCLS), Kelvin probe force microscopy (KPFM), atomic force microscopy (AFM), and surface photovoltage spectroscopy (SPS) to measure how polarity, morphology, and nanoscale growth on ZnO surfaces correlate with electrically-active native point defects. Previous DRCLS showed that ZnO nanostructures can grow spontaneously on bare, air-exposed ZnO surfaces and produce electronically-active defects. SPS measures the filling and emptying of these states and thereby their energy level position in the band gap. CLS associates these optical transitions with V_{Zn} and V_O -related (V_{O-R}) defects, respectively. Positron annihilation spectroscopy shows that 2.1eV DRCLS emission correlates with V_{Zn} vs. depth, anticorrelating with 2.5 eV V_{O-R} emission. SPS correlates these emissions with optical unfilling and filling transitions, respectively, within the same near-surface region on a nanometer scale. The SPS V_{Zn} trap state features vary laterally, increasing in nanostructured regions common to ZnO surfaces versus atomically-flat regions. Near both hexagonal pits on (0001) and individual ZnO nano-mounds on both polar faces, 2.1 eV trap densities increase with radial proximity. KPFM maps before and after 2.25 eV illumination show increased potential that reveals large concentrations of V_{Zn} distributed non-uniformly around and extending away from the hexagonal surface pits. These observations all suggest that ZnO nanostructures grow by oxidation of Zn at the free ZnO surface due to mobile Zn atoms extracted from the underlying lattice.

We measured the morphology, potential, and defect distributions of these structures vs. annealing temperature in flowing oxygen over a 400°C range. AFM/KPFM maps of room temperature and annealed (0001) surfaces reveal deep (~150 nm) hexagonal pits with spoke-like *trenches* extending from both the corners and faces of the hexagonal formation and >50 meV positive potentials that increase with temperature. Conversely, (000-1) surfaces initially show few pits with random geometry and *raised* spoke-like ridges extending from pits. After 1 hr at 200 °C, pitting increases with strong (~150 mV) negative potentials and newly formed spoke-like *trenches*. At 300°C, nanoscale mounds grow 5 – 50 nm high and potentials vary further. From AFM increases in nanorod mass vs. temperature, Arrhenius plots yield 130±10 meV (0001) and 150±10 meV(000-1) activation energies, consistent with the low (0.57 eV) activation energy for Zn interstitial diffusion. Overall, this complement of techniques reveals the interplay between ZnO surface nanostructure, polarity, and electronic defects.

9:00am SS-ThM4 Atomic Structure and Site Specific Reactivity at Ferroelectric Oxide Surfaces, L. Kraya, D.A. Bonnell, The University of Pennsylvania

The functionality of ferroelectric compounds are inspiring new approaches for catalysis, water splitting, information storage, and nanofabrication. The atomic details of interactions at ferroelectric surfaces are as important as those on other oxides but have been less amenable to examination. Recently we have determined the thermodynamic stability of a wide range of reconstructions on BaTiO₃ (100) and also demonstrated that surface reactions depend on the orientation of the ferroelectric polarization. Here we examine the 3x1 and R5xR5 reconstruction in atomic detail. Reaction of the R5xR5 structure with CO₂ is imaged by scanning tunneling microscopy as a function of exposure and the site occupation quantified. In addition, the effect of locally reorienting the ferroelectric polarization with an STM tip is determined by scanning tunneling spectroscopy. Offsets in local I/V curves are related to energy level shifts due to the local field induced by the polarization.

These results will be contrasted with those on non ferroelectric oxides.

9:20am SS-ThM5 Selective Oxidation of Ammonia on RuO₂(110): a Combined DFT and KMC Study, T.S. Rahman, S. Hong, University of Central Florida, A. Karim, Brookhaven National Laboratory

We have used a combination of density functional theory (DFT) and kinetic Monte Carlo (KMC) simulations to calculate the reaction rates for the selective oxidation of ammonia on the RuO₂(110) surface. We find that the overall energy barrier for $NH_3 + O \rightarrow NH + H_2O$ is 0.56 eV, while that for $N + N \rightarrow N_2$, and $N + O \rightarrow NO$ to be 0.27 and 0.14 eV, respectively. In accompanying KMC simulations, in which we include in addition to the

above key processes, several intermediates and their reactions (18 processes), we find selectivity towards NO and N₂ formation, as a function of O₂ pressure range, in excellent qualitative and quantitative agreement with experiment [1]. As for the high reactivity of RuO₂(110) we concur that hydrogen bonding between ammonia, and its intermediates, with adsorbed and substrate oxygen play a critical role by making H abstraction facile such that NH decomposition is a spontaneous, non-activated process. As for the high selectivity of RuO₂(110) for ammonia oxidation, the significantly-restricted N diffusion caused by reaction intermediates present on the RuO₂(110) surface severely affects the recombination rate for $N+N \rightarrow N_2$ while $N+O \rightarrow NO$ is much less affected by such reduced N diffusion due to dissociatively-adsorbing O₂ species on RuO₂(110). As a result, NO production is remarkably favored than N₂ production even at low O₂ pressure. These results highlight the important role of the chains of undercoordinated Ru atoms on this surface.

[1] Y. Wang, K. Jacobi, W.-D. Schoene, and G. Ertl, J. Phys. Chem. B 109, 7883 (2005).

Work supported in part by DOE Grant DE-FG02-07ER15842

9:40am SS-ThM6 Electron Paramagnetic Resonance Evidence for the Formation of O₂⁻ on the Surface of Ultra Thin MgO/Mo Films, A. Gonchar, T. Risse, H.-J. Freund, Fritz-Haber-Institut der Max-Planck-Gesellschaft, Germany

Theoretical calculations [1, 2] have predicted novel catalytic properties of ultra thin MgO films for CO oxidation. In particular, molecular oxygen is thought to be activated on ultra thin MgO films due to a charge transfer from the metal substrate resulting in the formation of paramagnetic O₂⁻.

We have investigated the adsorption of O₂ on ultra thin MgO(001) films grown on Mo(001) single crystals using in situ Electron Paramagnetic Resonance (EPR) spectroscopy. Adsorption of oxygen on 4 ML thick MgO(001) films creates an EPR signal associated with the formation of O₂⁻ radicals. The orientation of these radicals on the MgO surface is deduced from angular dependent EPR measurements. The properties of O₂⁻ radicals with respect to thermal stability and external parameters such as the film thickness will be discussed.

References

[1] A. Hellman, S. Klacar, and H. Grönbeck, JACS 2009, 131, 16636–16637

[2] P. Frondelius, H. Häkkinen, and K. Honkala, PCCP 2010, 12, 1483–1492

10:40am SS-ThM9 Franck-Condon Broadening of the XPS of Ionic Materials, P.S. Bagus, University of North Texas, C.J. Nelin, Maury's Trail, E.S. Ilton, Pacific Northwest National Laboratory

We present an analysis of the width of X-Ray photoelectron spectroscopy, XPS, features that relates the broadening of these features to the chemical activity and reactivity of oxide surfaces. The use of synchrotron radiation allows high resolution measurements of core-level XPS with instrumental resolutions of ~250 meV, or even higher. However, the XPS spectra of many materials, especially oxides and other ionic systems, have features that are much broader than would be expected from instrumental and lifetime broadenings. For example, there are four levels that contribute to the main Mn 2p_{3/2} XPS peak of MnO that are not fully resolved with high resolution synchrotron measurements [1] even though the levels are separated from each other by ~1.5 eV. [2] In another example for the XPS of CeO₂, [3] broadenings of the theoretical results of ~2.5 eV FWHM are required to have the theory match experiment. While surface effects or other inhomogeneities might, in principle, account for large broadenings, we investigate here the contribution to XPS broadening due to vibrational excitations in the final ionic states. Large Franck-Condon broadenings are known for photoemission from molecules [4] but have not been studied in connection with the broad features in the XPS of ionic crystals. We investigate changes in the metal-oxygen bond length for ionic states of MnO and CeO₂, where a metal core-level has been ionized, using wavefunctions and energies for embedded cluster models of these materials. Initial and final state potential energy surfaces are determined for breathing motions of the nearest oxygen neighbors of the ionized metal cation. These surfaces allow us to determine the Franck-Condon envelope for transition from the $v=0$ initial, unionized state to vibrationally excited levels of the final, ionized state and show the broadenings that arise from these excitations. Furthermore, we make correlations between the changes in the metal-oxygen bond distances in the ionic states with changes, increases, in the final state covalent metal-oxygen bonding over the initial state covalent character. This correlation may provide a new and novel way to use high resolution photoemission to obtain information about the nature and strength of the bonding in ionic materials.

(1) V Bayer, R Podloucky, C Franchini, F Allegretti, X Bo, G Parteder, MG Ramsey, S Surnev, FP Netzer: Phys. Rev. B 76, 165428 (2007).

- (2) PS Bagus, ES Ilton: Phys. Rev. B **73**, 155110 (2006).
- (3) PS Bagus, CJ Nelin, ES Ilton, M Baron, H Abbott, E Primorac, H Kühlenbeck, S Shaikhutdinov, HJ Freund: Chem. Phys. Lett. **487**, 237 (2010).
- (4) PS Bagus, EK Viinikka: Phys. Rev. A **15**, 1486 (1977).

11:00am **SS-ThM10 Ethylene Glycol Adsorption and Decomposition over CeO₂ (111) Surfaces**, *T.-L. Chen, F.C. Calaza, S.H. Overbury, D.R. Mullins*, Oak Ridge National Laboratory

Hydrogen production from the reforming of oxygenated hydrocarbons is highly dependent on the heterogeneous reactions provided by its catalysts. Cerium oxide supported metal catalysts can offer a means of reducing precious metal loading and achieving higher selectivity. Thus studying the direct contribution from the metal oxide surface to the decomposition of the molecules can give insight into the catalytic reforming process.

In light of our previous characterization on C₁-C₃ oxygenate reactions on well-defined cerium oxide thin films, we further examine ethylene glycol as a model system for bio-mass derived hydrocarbons. As the simplest diol, ethylene glycol has two symmetric hydroxyl groups which are available to interact with the surface. The adsorbates can bond to the surface through either one or both of these oxygens, which may lead to a different decomposition pathways.

On the surface of the fully oxidized ceria ethylene glycol appears to initially bond to the surface through only one of the C-O groups. As the temperature is increased both ends interact with the surface and one C-O group is converted into a carboxylate group (COO). The primary reaction products are acetaldehyde, ethylene, acetylene, water and H₂. CO desorption was also observed indicating some of the oxygenates experienced C-C bond breaking. On a reduced surface one end of the molecules undergoes C-O cleavage resulting in a C-Ce bond rather than an additional C-O bond. The surface intermediate is a carbanion, similar to what was observed for acetaldehyde. More acetylene is observed from a reduced surface.

The dependence of the reaction pathways on the coverage of ethylene glycol was also examined on the oxidized and reduced surfaces. At larger coverage, the formation of carboxylates or carbanions is hindered which suggests that the formation of these species may be sterically limited.

Research sponsored by the Division of Chemical Sciences, Geosciences, and Biosciences, Office of Basic Energy Sciences, US Department of Energy, under contract DE-AC05-00OR22725 with Oak Ridge National Laboratory, managed and operated by UT-Battelle, LLC. Use of the National Synchrotron Light Source, Brookhaven National Laboratory, was supported by the US Department of Energy, Office of Science, Office of Basic Energy Sciences, under Contract No. DE-AC02-98CH10886.

11:20am **SS-ThM11 Synthesis and Characterization of Cerium Oxide Nanoparticles with Well-defined Crystallographic Terminations**, *S.H. Overbury, M. Li, Z. Wu, D.R. Mullins, J. Howe*, Oak Ridge National Laboratory

Through hydrothermal synthesis techniques it is possible to create oxide nanoparticles with highly uniform dimensions and shapes and therefore with crystallographically well-defined terminations. These mono-faceted nanocrystals provide an opportunity to examine structure dependence in surface chemistry with the advantage of using methods appropriate to high surface area materials. We have synthesized cubic, octahedral and rod-shaped nanoparticles of CeO₂ that are terminated exclusively in (100), (111) or a mixture of (100) + (110) crystallographic terminations, respectively. These have been used to compare reducibility, stability and adsorption of water, oxygen and alcohol with the goal of characterizing and understanding the effect of surface structure upon the reaction of these molecules with the surface or with other adsorbates. Multi-wavelength Raman and FTIR in the DRIFTS mode are performed in controlled ambient pressure gas streams, and are combined with pulsed / switched chemisorption and temperature programmed techniques. UV Raman reveals that the CeO₂ nanocrystals contain stable bulk-like Frenkel defects, identified by a characteristic Raman feature, and these are more prevalent in the rod-like particles with (110) + (100) termination. Reduction of the nanoparticles in hydrogen at 673 K leads to oxygen vacancies that are identified by a Raman feature near 560 cm⁻¹ and the rods are more easily reduced while the octahedral are the least. Oxygen vacancies are immediately removed by O₂ at room temperature on all ceria polymorphs. Upon adsorption of isotopically labeled O₂ at 80 K on reduced surfaces, peroxide and superoxide species are observed and these dissociate or desorb as the temperature is increased. Clustered and isolated peroxides are distinguished by their Raman frequency and their relative ratio depends upon degree of reduction and surface structure. Adsorption of D₂O and H₂O on each of the surfaces was probed by DRIFTS at room temperature following dehydroxylation at 673 K. Following a pulse of water, OD (OH) features are observed with characteristic IR frequencies. These results are

compared to “single crystal” RAIRS studies on CeO₂(111) oriented films and with previously published IR studies of highly dispersed, polycrystalline CeO₂ crystals of undefined structure terminations. The features observed agree with previous work but their prevalence differ between the faceted nanocrystals and the differences allow structural assignments of the IR features. The results lead to a re-assignment of the IR features.

11:40am **SS-ThM12 Surface Analysis of Selected Metal-Doped Adsorbent Materials for Logistics Fuels Desulfurization**, *R.A. Quinlan*, NSW, Carderock Division, *J.M. Heinzl*, NSW, *A.N. Mansour*, NSW, Carderock Division

Transportation fuels, i.e., gasoline, diesel and jet fuels have been identified as a potential hydrogen source for fuel cell applications due to their high energy densities, ease of storage and availability. However, these liquids, especially the diesel and jet fuels, can contain extremely high concentrations of sulfur. If hydrogen or reformat syngas is to be produced from these high sulfur content fuels, catalyst degradation of the reformer system can occur. Additionally, sulfur compounds such as H₂S and COS are capable of poisoning follow-on processing operations and the electrode catalyst of the fuel cell. Therefore, desulfurization is paramount for the development of logistics fuels as a hydrogen production source. Recently titania and silica supported silver have shown high performance as regenerable desulfurization sorbents. A variety of techniques have been employed to specifically investigate the active form of the material, and the nature of the adsorptive sites and their interactions with the support, as well as the adsorbed species. Specifically, x-ray photoelectron spectroscopy (XPS) to study the surface chemistry and x-ray absorption spectroscopy (XAS) to study the bulk structure of composite materials were utilized. This provides insight into how the Ag/support system enables such high adsorptive capacities.

Thin Film

Room: Ruidoso - Session TF-ThM

Modeling and Analysis of Thin Films

Moderator: S.B. Sinnott, University of Florida

8:00am **TF-ThM1 Thermodynamics of Clustering and Magnetism in Ti_{1-x}Al_xN and Ti_{1-x}Cr_xN Thin Film Materials from First-Principles**, *B. Alling, I.A. Abrikosov, L. Hultman*, Linköping University, Sweden

Multinary nitride materials are widely used as coatings for wear protection of cutting tools, e.g. TiAlN, as well as in thin film electronic applications. One important aspect of the success of TiAlN is a composition dependent thermodynamically driven age-hardening process through spinodal decomposition into TiN and cubic AlN at cutting tool operational temperatures. To understand this phenomena and to be able to tailor optimal compositions for different applications, we perform a thorough theoretical thermodynamics investigation based on first principles calculations.

By mapping the complete quantum mechanical complexity of the system onto a generalized Ising Hamiltonian for the configuration of Ti and Al atoms, we are able both to predict thermodynamics using accurate Monte Carlo simulations and achieve a deeper understanding of the interactions governing the system.

One physical property that is difficult to find in nitrides and which disfavors the usage of the materials class in spintronics, is room temperature ferromagnetism. TiCrN is one of the rare nitride systems where strong ferromagnetism is seen. We use our methodological framework to analyze and explain why the magnetic interactions that favor anti-ferromagnetism in pure CrN is changed in the TiCrN solid solution, as well as the intricate dependence of the Curie temperature on the CrN content.

8:20am **TF-ThM2 Electronic Mechanism for Toughness Enhancement in V_xM_{1-x}N Thin Films**, *D.G. Sangiovanni, V. Chirita, L. Hultman*, Linköping University, Sweden

We use Density Functional Theory (DFT) calculations in the generalized gradient approximation (GGA) to predict the properties of a number of novel V-M-N thin films in the B1 (NaCl) structure. The new compounds are obtained by alloying VN with Nb, Mo and W, in concentrations of 50 %. We evaluate the elastic moduli and constants of these ternaries and perform a detailed analysis of their electronic structure. These results are compared with the corresponding properties of typical binaries such as TiN and VN. Our calculations show that the new ternaries have hardness comparable with TiN and VN, and significantly, a resolute ductile behavior. This unique combination of hardness/ductility, which is in contrast to the hardness/brittleness relationship typically found in hard coatings, equates to

significantly increased toughness, as confirmed by the stress-strain relationship we obtain for all these compounds. The electronic structure results presented herein reveal a layered charge density, consisting in alternating high and low electron density regions, similar to that recently reported for Ti-Mo/W-N thin films [1]. To fully understand the mechanism responsible for this interleaved arrangement of electrons, we carry out crystal orbital overlap population (COOP) and electron localization function (ELF) calculations, and succeed to energetically resolve the bonding/antibonding contributions, of the first and second neighbors, to the chemical bonds in these compounds. Based on the results of this analysis, we find that the electronic mechanism responsible for the observed toughness enhancement in these compounds is rooted in the increased metal-metal (second neighbors) interaction of $d-t_{2g}$ orbitals.

[1] D.G. Sangiovanni, V. Chirita and L. Hultman, Phys. Rev. B **81**, 104107 (2010)

8:40am **TF-ThM3 2010 Gaede-Langmuir Award Lecture- X-ray Absorption Spectroscopy and Many Electron Theory Applied to O-vacancy State Differences between (i) Non-crystalline SiO₂ and (ii) Nano-crystalline HfO₂ Thin Films, G. Lucovsky***, North Carolina State University **INVITED**

Correlated atomic positions of Si-atoms bonded to 2-fold coordinated O-atoms are determined by Si $3d$ -derived T_{2g} states on these atoms [1]. These states constrain dihedral angles contributing to medium range order with correlation lengths of ~ 0.4 and 0.45 nm, and, a coherence length of ~ 1 nm, each obtained from the first sharp diffraction peak in X-ray diffraction [2]. O K edge soft X-ray SiO₂ spectra reveal conduction band edge states with singly degenerate A_1 symmetry, and stronger doubly and triply degenerate E and T_2 d -state beginning at energies ~ 3 eV higher. This difference is smaller in c-Si, ~ 1 eV. Analysis of O K and $L_{2,3}$ spectra are based on a charge transfer multiplet many electron theory [3]. Energy differences are the same for band edge features obtained from transmission/reflectivity studies in the visible/VUV where the d -state character was not previously recognized [4]. The correspondence derives from O $1s$ core hole localization, and a coherent process in which $1s$ core holes are filled by electrons from valence band O $2p$ p states, accounting for the one-to-one correspondence between sequenced features in the O K edge, and in the Si $L_{2,3}$ spectrum of SiO₂. $L_{2,3}$ spectra, studied by electron energy loss spectroscopy (EELS), have not detected the weaker Si A_1 features in the 100 to 104 eV regime of SiO₂, or 98 to 100 eV regime of c-Si. The O K edge X-ray spectra of transition metal elemental and complex oxides are qualitatively different with either doubly or triply degenerate d -state derived spectral features at the band edge. This results in significant quantitative differences in (i) the high-spin excited d -states of O-atom vacancy occupied d^2 states, and (ii) the negative ion electronically active d -state traps populated by charge injection. O-vacancy states in SiO₂ are close to mid-gap, and do not contribute to gate stack tunneling processes. This explains the order of magnitude higher interfacial trap densities, d_{it} , and trap-assisted tunneling in HfO₂ gate stacks. It also accounts for significant differences in radiation hardness. XAS spectra are presented for the first time for remote plasma deposited GeO₂. These deposited films display significantly different O K edge spectra than those obtained by oxidation of Ge; more importantly A_1 , and E and T_{2g} features stronger and narrower than those of SiO₂. Electrical data for deposited GeO₂ dielectrics on Si and Ge substrates are compared for the first time with SiO₂ test devices on the same substrates.

[1] Whitten J, et al., J. Vac. Sci. Technol. B **20**, 1710 (2002).

[2] Lucovsky G, et al. physica status solidi (a) **207**, 631 (2010).

[3] de Grott F, Kotani A. Core level spectroscopy of solids (Boca Raton, CRC, 2008).

[4] Laughlin RB, Phys. Rev. B **22**, 3021 (1980).

9:20am **TF-ThM5 New Parameterization of the Modified Embedded Atom Potential for Large Scale Simulations of TiN Thin Films Growth, D.G. Sangiovanni, V. Chirita, L. Hultman**, Linköping University, Sweden
Classical Molecular Dynamics (MD) has become an indispensable tool in thin films modeling, as it allows the study of systems and phenomena reaching far beyond the inherent limitations of ab-initio and/or Density Functional Theory (DFT) methods. Generally, the range of systems to which the method can be applied has typically been limited to materials characterized by single-type bonding, such as ionic, covalent or metallic. This situation has been considerably improved in the last decade within the formalism of the Modified Embedded Atom Method (MEAM), which allows the treatment of mixed-type bonding materials, and in recent years, a number of studies have been devoted to MD simulations of important model systems such as TiN. Nevertheless, the very few MEAM parameterizations

for TiN reported thus far are able to reasonably reproduce bulk, as well as some surface properties of this material. However, if meaningful MD simulations of TiN thin films growth are to be performed, a number of critical nucleation and diffusion phenomena have to be accounted for besides basic bulk/surface properties. Herein, we propose a new parameterization of the MEAM interaction potential for TiN, which in addition to correctly predicting bulk and surface properties, reproduces the experimentally observed trends in the diffusion of single species (Ti, N) and Ti-N dimers, on the most representative steps/surfaces for TiN growth, the (100) and (111) respectively. Our estimations of activation energies for diffusion and Ehrlich-Schwoebel (ES) step-edge barriers are in good agreement with previous ab-initio calculations and experimental observations. Consequently, this new MEAM parameterization has the potential to adequately account for most essential processes during the initial stages of TiN nucleation, which, as it is well known, dramatically affect the growth mode and properties of thin films in laboratory and computer experiments.

9:40am **TF-ThM6 DSMC Modeling of Metal Vapor Flow in Vacuum in Application to Thin-Film Depositions, V. Ayyaswamy, A. Alexeenko**, Purdue University

Electron beam assisted physical vapor deposition (EBPVD) is widely used in a number of vacuum material processing applications for deposition of thin films of metals. The properties of these thin films including thickness uniformity, growth rates and other material properties are dependent, to a great extent, on the geometric configuration of the deposition source and electron gun power. A complete understanding of the deposition process requires the ability to accurately simulate the vapor flow that varies from highly collisional in regions near the source to being free-molecular near the substrate location. The direct simulation Monte Carlo technique, which is by far the most powerful technique to simulate such flows rapidly expanding into vacuum, requires an accurate molecular model for the interaction between the metal vapor atoms. A molecular model has been formulated [1] for the interaction of Cu atoms and validated with experimental data for electron-beam deposition of copper. The main goal of this work is to formulate molecular models for common metal vapors including Gold, Titanium, Nickel, and Aluminium and validate them with experimental data[2,3] for thin-film growth rates at various evaporation rates. The ability to accurately model deposition processes of thin films of metals would greatly assist in the design and control of such vacuum deposition systems and processes.

References

[1] A. Venkatraman and A.A. Alexeenko, "DSMC Modeling of E-beam Metal Deposition", J. Vac. Sci. & Tech. A, July 2010 (*accepted*).

[2] D. Chaleix, P. Choquet, A. Bessaudou, L. Frugier, and J. Machet, "A spatial distribution study of a beam vapour emitted by electron-beam-heated evaporation sources", J. Phys. D: Appl. Phys. **29**(1996) 218-224.

[3] K.B. Thakur and G.K.Sahu, "Spatial distribution of copper vapour flux during strip electron beam vaporation", J. Phys. D: Appl. Phys. **35**(2002) 1812-1820.

* Gaede Langmuir Award Winner

Thursday Afternoon, October 21, 2010

Spectroscopic Ellipsometry Focus Topic

Room: Cochiti - Session EL+AS+EM+MS+TF-ThA

Spectroscopic Ellipsometry

Moderator: A.M. Creatore, Eindhoven University of Technology, the Netherlands

2:00pm **EL+AS+EM+MS+TF-ThA1 Developments in Spectroscopic Ellipsometry for Characterization of Organic and Inorganic Surfaces, Interfaces and Complex Layered Materials, M. Schubert**, University of Nebraska - Lincoln **INVITED**

In this paper we will review new developments in Spectroscopic Ellipsometry for characterization of organic and inorganic surfaces, interfaces and complex layered materials. Ellipsometry has matured over the past two decades with instrumentation and methodology capable of addressing today's and tomorrow's challenges in materials characterization and metrology. Ellipsometry measures the general state of polarization of light reflected or transmitted from samples. Owing to its nondestructive and generally applicable concept of investigating light emerging from specimens under investigations, and owing to its extreme accuracy and precision, ellipsometry has paved the way for almost all our modern technologies, continues to enable next-generation devices in electronics and optoelectronics, and emerges into fields of chemical, biochemical and biological platform technologies. Originating from the identification that the information carried upon the polarization within a light beam emerging from surfaces is extremely sensitive to mono and submonolayer characteristics, ellipsometry started decades ago pioneering development of microprocessors and electronic devices, which still today are based on planar thin film technology. Without ellipsometry, today's computation and information technology would be still in its infancy. In this paper, emerging developments and applications for metrology of optical and electrical properties of semiconductors and nanostructures by Terahertz Magneto-optic generalized ellipsometry, also referred to as the Optical Hall effect, will be highlighted. Examples will include state-of-the-art nitride semiconductor device structures and epitaxial graphene, candidates for tomorrow's next-generation devices. Likewise, new approaches for characterizing precise structural, magnetic and optical properties of three-dimensional nanostructure hybrid materials will be discussed. Examples will describe how ellipsometry characterization enables understanding and tailoring of electromagnetic properties of materials created by human intelligence, rather than by nature. New horizons are being explored currently by combining ellipsometry with independent surface sensitive techniques, such as acoustic Quartz-Crystal microbalance techniques. Combinations allow for identification of new information not accessible otherwise. Examples include observation of in-situ formation of self-assembled monolayers, protein adsorption onto sensitized surfaces, and formation of micelle-assisted bilayer configurations. Prospects, challenges and future developments will be reviewed from today's perspective.

2:40pm **EL+AS+EM+MS+TF-ThA3 Characterizing the Adsorption – Desorption Behavior of Organic Molecules Within Thin Mesoporous Carbon Composite Films using Spectroscopic Ellipsometry, B.D. Vogt, L.Y. Song, M.Z. Dai**, Arizona State University

Porous carbon materials are commonly utilized as adsorbants (i.e. activated carbon) and as catalyst supports. Direct templated synthetic routes to form ordered mesoporous carbons have recently been developed. By utilizing these concepts, mesoporous carbon composite films containing metal oxides can be synthesized. As a wide range of metal oxides can be utilized, these materials could be utilized in chemical sensing applications or as catalysts in fuel cell membranes. For both of these applications, the porous material will be exposed to organic vapors (such as ethanol in fuel cells). The condensation and evaporation of organic vapors from these materials is therefore an important consideration for their ultimate utilization in these applications. In-situ spectroscopic ellipsometry measurements of the mesoporous films exposed to controlled vapor pressures of organic vapors such as toluene, hexane and ethanol are utilized to understand the adsorption-desorption behavior of these films. Activated desorption of all three compounds is observed for pure carbon films, but addition of a small fraction of metal oxide enables the organics to be desorbed for the porous framework. These adsorption-desorption isotherms can also be utilized to estimate the pore size distribution and porosity of these films.

3:00pm **EL+AS+EM+MS+TF-ThA4 Mueller-Matrix Ellipsometry Studies of Chirality in Chitin-Based Structures and Thin Films of Al_{1-x}In_xN, K. Järrendahl, H. Arwin, R. Magnusson, P. Sandström, C.-L. Hsiao, J. Landin, S. Vallyukh, J. Birch**, Linköping University, Sweden

A limited number of natural structures are known to reflect light that has circular or near circular polarization. This is for instance, the case for some scarab beetles where it is suggested that the polarization is caused by chiral structures in the form of helicoids in the cuticles. In this study, Mueller-matrix spectroscopic ellipsometry is applied in the spectral range of 250 to 1000 nm to investigate optical response and structures of the cuticle of various scarab beetles of the Cetoniinae subfamily. We will present our measurements showing how the polarization changes with wavelength as well as incidence angle and specify the conditions for when the reflected light is circularly left- or right-polarized. In most cases the reflected light is left-polarized as described by negative values of the M41 Mueller matrix element. For *Cetonia aurata*, a green beetle with metallic appearance, this is clearly seen in a rather narrow spectral range (470-550 nm). For other beetles (*Potosia cuprea* and *Licola lugubris*) similar polarization behavior is observed but the polarization features occur in a broader spectral region. We will show that there are even beetles (e.g. *Plusiotis argentiola*) reflecting both left- (M41 < 0) and right-polarized light (M41 > 0) in different parts of the spectral region. The Mueller data, including observations of the degree of polarization, are used to obtain structural and optical parameters from model calculations.

Our attempts to fabricate artificial structures with similar polarization properties will also be presented. Al_{1-x}In_xN thin films were grown on sapphire substrates by magnetron sputtering of indium and aluminum in a nitride atmosphere. Utilization of different seed layers and a substrate rotation gave chiral structures constituted by layers with a compositional gradient. Mueller-matrix results from these structures will be compared with the results from the natural structures. The Mueller data is also in this case very rich on information. In the initial steps to model these samples a similar approach as for the natural structures has been employed. Similarities and differences of the natural and artificial polarization response will be discussed in detail.

3:40pm **EL+AS+EM+MS+TF-ThA6 Mueller Polarimetry as a Tool for the Evaluation of the Diffraction Grating Profile Asymmetry, T. Novikova, P. Bulkin, LPICM, CNRS, Ecole Polytechnique, France, V. Popov, Moscow State University, Russia, A. De Martino, LPICM, CNRS, Ecole Polytechnique, France**

Mueller polarimetry in conical diffraction has proved to be a powerful optical technique for the metrological characterization of diffraction gratings. It was already shown that the shape of grating profile can be successfully reconstructed via appropriate optical modeling using full Mueller matrix measurements [1]. We also demonstrated that this approach can be of particular interest in microelectronics technology for the detection of overlay errors, which frequently result from the alignment deficiencies in lithography [2]. In some cases the asymmetrical distortion of grating profile can be induced by the etch process, or even be intentional, like in blazed gratings fabrication. For these applications a technique that allows for fast non-contact evaluation of the profile asymmetry may be of great value.

We studied the Mueller matrix spectra of symmetrical [3] and asymmetrical photoresist diffraction gratings on chromium using MM16 spectroscopic polarimeter, commercially produced by Horiba Jobin-Yvon, in the most general geometry of conical diffraction. At this configuration the 0th order cross-polarization complex reflection coefficients are antisymmetrical ($r_{sp}^0 = -r_{ps}^0$), provided that the grating is composed of only reciprocal materials and is invariant under the rotation by 180° about the normal incidence [4]. It leads to the following relations between the elements of 2x2 off-diagonal blocks of Mueller matrix: $M_{ij} = \pm M_{ji}$.

The lack of rotational symmetry violates the electromagnetic reciprocity theorem for the 0th-order diffraction on the asymmetrical gratings and, consequently, breaks the symmetry of the off-diagonal blocks of Mueller matrix ($|M_{ij}|$ is not equal to $|M_{ji}|$). This property of Mueller matrix of asymmetrical gratings was experimentally observed and numerically modeled at any illumination condition with exception of planar and pure conical mounting. We showed that the non-reciprocity in diffraction gratings can be used for the unambiguous detection of the grating profile asymmetry. The optimal choice of measurement configuration, i.e. azimuthal and polar angles considerably increases the sensitivity of the above mentioned technique.

References:

[1] T. Novikova, A. De Martino, S. Ben Hatit, and B. Drévilion, Appl. Opt. **45**, 3688 (2006).

- [2] T. Novikova, A. De Martino, R. Ossikovski and B. Drévilion, *Europ. Phys. J. Appl. Phys.* **31**, 63 (2005).
- [3] T. Novikova, A. De Martino, P. Bulkin, Q. Nguyen, B. Drévilion, V. Popov, and A. Chumakov, *Opt. Express* **15**, 2033 (2007).
- [4] L. Li, *Opt. Soc. Am. A* **17**, 881 (2000).

4:00pm EL+AS+EM+MS+TF-ThA7 Monitoring Ultra-Thin Organic Film Growth, In-Situ, with Combined Quartz Crystal Microbalance and Spectroscopic Ellipsometry, K.B. Rodenhausen, B.A. Duensing, A.K. Pannier, M. Schubert, University of Nebraska-Lincoln, M. Solinsky, The Procter & Gamble Company, T.E. Tiwald, J. A. Woollam Co., Inc.

We report a combinatorial approach to study ultra-thin organic films. This novel technique consists of *in-situ* spectroscopic ellipsometry and quartz crystal microbalance methods. In contrast to the quartz crystal microbalance, which is sensitive to the total mass attached to the surface, including the trapped solvent, spectroscopic ellipsometry only measures the amount of adsorbent on the surface. We also introduce a new "virtual separation approach" ($2\pi nd/\lambda \ll 1$) of analysis for the ellipsometry measurements. By using these two techniques in tandem, we are able to determine the thickness and solvent fraction of viscoelastic thin films.

We investigate cetyltrimethylammonium bromide (CTAB) thin films deposited onto a gold-coated quartz crystal as a model system. CTAB grown from a 2.5 mM solution demonstrates several phases in porosity evolution, including a temporary hold in water fraction as the film is rinsed off the substrate with water; these effects may be related to the structure of a CTAB bilayer.

In addition, a variety of self-assembled monolayers (SAMs) of alkanethiols on gold-coated quartz crystals are used as model biomaterials to determine the water fraction of an adsorbed prion layer. The porosity information distinguishes the proteins' conformation, dictated by the defined surface chemistries of the SAMs.

4:20pm EL+AS+EM+MS+TF-ThA8 Ellipsometric Studies of Electronically Coupled PbSe and PbS Quantum Dot Thin Films, S.G. Choi, National Renewable Energy Laboratory, O.E. Semonin, University of Colorado, J.M. Luther, M.C. Beard, A.G. Norman, National Renewable Energy Laboratory, Z. Lin, Colorado School of Mines, A. Franceschetti, National Renewable Energy Laboratory, M.T. Lusk, Colorado School of Mines, A.J. Nozik, National Renewable Energy Laboratory

Discovery of multiple exciton generation from colloidal suspensions of semiconductor quantum dots (QDs) has generated growing interests in realization of high-efficiency QD-based solar cells. Among a number of semiconductor QDs explored up to date, lead chalcogenides such as PbSe and PbS have been of great interest as a result of their wide tuning range of bandgap energy, abundance of materials, and large exciton Bohr radius.

In this presentation, I discuss optical properties of electronically coupled PbSe and PbS QD thin films. A series of QD multilayer thin films were prepared by a layer-by-layer dip-coating method onto glass substrates. Diameter of the QDs varies from 3.2 to 7.2 nm and from 3.5 to 8.3 nm for PbSe and PbS, respectively. Room-temperature pseudo-optical functions of the samples were measured by a rotating compensator-type, variable-angle spectroscopic ellipsometer. Transmittance data were also acquired in a normal-incidence configuration.

First, I determined refractive index $N = n + ik$ of the QD films using the B-spline basis functions within the multilayer model (ambient/surface roughness/QD film/substrate). We use the N obtained as the input parameters for modeling the internal quantum efficiency of the QD-based solar cell devices. Then, I extracted dielectric function $\epsilon = \epsilon_1 + i\epsilon_2$ for the ensemble of electronically coupled QDs using the Maxwell-Garnett effective medium approximations. The ϵ spectra show the first exciton peaks, and the E_1 and E_2 critical-point (CP) structures whose energies are higher than the corresponding bulk values probably due to the quantum confinement effects. This abstract is subject to government rights.

4:40pm EL+AS+EM+MS+TF-ThA9 In-situ Temperature Measurements by Spectroscopic Ellipsometry: Application to a-Si based Thin Films, D. Daineka, LPICM, CNRS, Ecole Polytechnique, France, V. Suendo, Institut Teknologi Bandung, Indonesia, P. Roca i Cabarrocas, LPICM, CNRS, Ecole Polytechnique, France

Accurate measurement of the substrate temperature is of crucial importance in many semiconductor technologies such as plasma enhanced chemical vapor deposition (PECVD). Traditional tools, both thermocouples and pyrometers, are not always reliable for in situ measurements in vacuum when the substrate can be out of thermal equilibrium. On the other hand, non-contacting optical methods allow to determine the surface temperature with great accuracy, provided the temperature dependence of optical constants for the studied material is known. Since recently, spectroscopic ellipsometers are widely available and often installed on the research

deposition systems, which provides an opportunity to use them for temperature monitoring. We have studied the optical functions of amorphous silicon based thin films with spectroscopic ellipsometry in the temperature range from 290 to 520 K. The experimental data were modeled using Tauc-Lorentz dispersion law for amorphous materials. We have found that the temperature coefficients of Tauc-Lorentz parameters, such as the optical gap, are rather close for a few different materials. That similarity suggests that these values can be used to determine the surface temperature for a broad range of amorphous silicon based materials with a good accuracy. Practical examples of using spectroscopic ellipsometry for temperature measurements in the low pressure PECVD environment are given.

5:00pm EL+AS+EM+MS+TF-ThA10 Real Time Spectroscopic Ellipsometry Studies of Amorphous and Nanocrystalline Si_{1-x}Ge_x:H Thin Films for Microbolometer Applications, D.B. Saint John, H.-B. Shin, M.-Y. Lee, E.C. Dickey, T.N. Jackson, N.J. Podraza, Penn State University

Hydrogenated amorphous and nanocrystalline silicon (a/nc-Si:H), germanium (a/nc-Ge:H), and their alloys have been used and continue to be assessed for use in uncooled infrared microbolometer applications. These materials may be deposited as uniform layers using equipment common to the manufacturing of displays and photovoltaics and are thus more amenable to manufacturing considerations than the ion beam deposited vanadium oxide films used in most commercial microbolometers. Real optimization of material in the a/nc-Si_{1-x}Ge_x:H system for use in these devices requires a better understanding of the relationship between the key electrical properties of interest including resistivity (ρ), temperature coefficient of resistance (TCR), and the 1/f noise character as a function of the degree of order and composition of the films. Si_{1-x}Ge_x:H thin films were deposited using plasma enhanced chemical vapor deposition using SiH₄, GeH₄, and H₂ at variable H₂- dilution. These films have been monitored using in situ real time spectroscopic ellipsometry (RTSE) over a spectral range from 0.75 to 5.15 eV during deposition to detect changes in the film thickness and optical properties in the form of the complex dielectric function spectra ($\epsilon = \epsilon_1 + i\epsilon_2$) as a function of deposition time. From the RTSE measurements and analysis it is possible to determine the structure of the material as amorphous, nanocrystalline, or mixed-phase and track the evolution of nanocrystallinity as a depth profile into the film. Ex situ Fourier transform infrared spectroscopic ellipsometry measurements over a spectral range from 0.05 to 0.75 eV were also performed to augment the complex dielectric function spectra and study absorption features relating to bonding. For electrical measurements, contacts were deposited in an isolated transfer length pattern for measurement of resistivity and TCR, while resistors with different volumes were made for volume normalization of the 1/f noise measurements. The TCR was measured from 20°C to 55°C. This study explores correlations between the electrical and optical properties of a-Si_{1-x}Ge_x:H and nc-Si_{1-x}Ge_x:H as functions of film processing conditions, resultant composition, and order. a-Si_{1-x}Ge_x:H films were prepared as a function of germanium content and hydrogen dilution to identify the impact that germanium and improved order at higher hydrogen dilution conditions have on the electrical properties (ρ , TCR, 1/f noise). The impact on the electrical properties due to the incorporation of small fractions of nanocrystallites are explored using mixed-phase (a+nc)-Ge:H films with nanocrystallite profiles guided by depth profile studies.

5:20pm EL+AS+EM+MS+TF-ThA11 Roll-to-Roll Fabrication of Thin Film Si:H Solar Cells: Real Time Monitoring and Post Deposition Mapping by Spectroscopic Ellipsometry, L.R. Dahal, Z. Huang, D. Attygalle, M.N. Sestak, C. Salupo, S.X. Marsillac, R.W. Collins, University of Toledo

Real time spectroscopic ellipsometry (RTSE) has been used to monitor the roll-to-roll deposition of thin film Si:H n-i-p solar cells on flexible plastic substrates coated with a Ag/ZnO back-reflector. In this process, the RTSE monitoring position is located directly above the ZnO sputtering target (i.e., at the closest target-substrate separation). RTSE data collection is initiated before the plasma is ignited so that ZnO nucleation can be observed. The film thickness increases with time until a steady state is reached, after which the bulk layer thickness at the monitoring point is constant with time. This occurs when the elapsed deposition time equals the time required for the moving substrate to travel from the leading edge of the deposition zone to the monitoring point. Although a constant substrate speed is selected such that the final film thickness is achieved in the time required to move through the entire deposition zone, this speed does not allow study of film growth that occurs after the substrate passes the monitoring point. To solve this problem, the substrate speed is reduced only in the early stage of growth such that the final film thickness of interest is reached at the monitoring point. In this way, RTSE can be used to analyze the entire layer on an initial length of the roll before the full length of the roll is processed. The thickness evolution of ZnO in the case of both normal and reduced

speeds shows good agreement with a simple inverse square variation of the deposition flux from the target to the flexible substrate.

After cell deposition, spectroscopic ellipsometry (SE) has also been applied for large area mapping of the completed 15 cm wide roll, at up to 1.5 m long sections at a time. Key information such as critical point, oscillator amplitudes, band gap energies, and widths have been extracted from which material density, composition, grain structure, disorder, and defect density can be determined. In this paper, optical mapping was applied for the intrinsic absorber layer in a full device a-Si:H solar cell structure. The results clearly show the degree to which thickness uniformity of the absorber layer depends on the gas flow and the electrode configuration. Also, by parameterizing the optical functions of the intrinsic absorber layer using single Lorentz oscillator modified by a low energy absorption cut-off, a map of its band gap and oscillator width can be deduced. Such an SE application is ideal for evaluation of uniformity in bulk thickness d_b , surface roughness thickness d_s , index of refraction, and extinction coefficient (n , k); the critical parameters for fabricating uniform and high efficiency solar modules.

Energy Frontiers Topical Conference Room: Mesilla - Session EN+SS+TF-ThA

Transparent Conductors

Moderator: S. Gupta, University of Alabama

2:00pm EN+SS+TF-ThA1 **Synthesis of ZnO:F by DC Reactive Magnetron Sputtering**, X. Noirfalise, University of Mons, Belgium, T. Godfroid, Matera Nova, Belgium, G. Guisbiers, IEMN Lille, France, R. Snyders, University of Mons, Belgium

Nowadays, numerous applications in the electronics and/or optoelectronics field need transparent thin films presenting a good electrical conductivity. The transparent conductive oxides (TCO) which reveal a large band gap and a good electrical conductivity fulfil these requirements. Recently, due to the significant increase of the demand, the prize of the most employed TCO, namely indium tin oxide (ITO) has strongly increased. Therefore, an alternative to this material becomes necessary. Among all the candidates, ZnO:F and Cd₂SnO₄ present the best performance in term of transparency and electrical conductivity. For obvious environmental reasons the latter cannot be considered. Therefore, ZnO:F is identified as the best candidate to replace ITO in TCO applications.

The most employed techniques for the synthesis of ZnO:F are Chemical Vapor Deposition and Spray Pyrolysis which both require organometallic precursor and high temperature processing. Another drawback of these technologies is the low chemical purity of the synthesized films because of the presence of the precursor decomposition products. At the contrary, reactive magnetron sputtering is an environmentally friendly technology allowing the synthesis of thin films with very fine control of the chemistry. Therefore, the aim of this works is to study the reactive magnetron sputtering of ZnO:F.

Thin films were prepared by DC reactive sputtering using a zinc target in an Ar/O₂/F₂ mixture. In a first attempts, ZnO films have been synthesized in order to optimize the matrix properties in terms of crystallinity and transparency. The studied parameters were the DC power (P_{DC}), the total pressure (P_{Tot}) and the O₂ flow (f_{O_2}). Our data reveal that the ZnO films presenting the best features are prepared for $P_{DC} = 70$ W, $P_{Tot} = 30$ mTorr and $f_{O_2} = 3$ sccm.

The second step was to introduce fluorine in this matrix. Therefore, we have studied the crystallographic, chemical, electrical and optical properties of the deposited films as a function of the fluorine content. In our deposition window, all films present a high transmission in the visible (> 80%). Our XRD data reveal decrease of the crystallite size with the increase of the fluorine content. Above a fluorine concentration of 2-3%, the ZnO:F crystallinity decreases. Our XPS and XRD data suggest that F atoms substitute O atoms in the ZnO structure. Finally, the electrical properties have been investigated by Hall effect measurements. For the optimal synthesis conditions (~ 2% of fluorine in the film), a charge carrier density of $\sim 10^{20}$ cm⁻³, an electrical resistivity of 10^{-2} Ω.cm and charge mobility of about 4 cm²/V.sec have been measured.

2:20pm EN+SS+TF-ThA2 **Relationship Between Resistivity Stability and Structure of Transparent Conducting Impurity-doped ZnO Thin Films**, J.-I. Nomoto, T. Hirano, T. Miyata, O. Ueda, T. Minami, Kanazawa Institute of Technology, Japan

Recently reported results show that the resistivity stability for moisture-resistance and heat-resistance tests in transparent conducting impurity-doped ZnO thin films prepared on low temperature glass substrates is

considerably affected by the film thickness as well as the kind and content of doped impurity. In this paper, we discuss the relationship between the obtainable resistivity stability and the structure in Al-, Ga- and B-doped ZnO (AZO, GZO and BZO) thin films prepared with a thickness in the range from 30 to 3000 nm by various deposition methods. Transparent conducting AZO, GZO and BZO thin films were prepared on glass substrates at 200°C by dc or rf magnetron sputtering, vacuum arc plasma evaporation and pulsed laser depositions. The resulting film structures were evaluated using a scanning electron microscope (SEM), an atomic force microscope (AFM) and a transmission electron microscope (TEM). The surface morphology of the impurity-doped ZnO films was found to change significantly after exposure to a highly moist environment (air at 85% relative humidity and 85°C) for 1000 h, as evidenced from AFM and SEM images; although the resistivity stability in these tests tended to improve with increasing impurity-doped ZnO thin film thickness, the effect was considerably dependent on the kind of doped impurity. In contrast, the surface morphology changed only slightly even after exposure to an oxidizing atmosphere (air at a temperature of 200°C) for 1000 h. The resistivity stability in the heat-resistance tests was found to depend significantly on whether the testing temperature was lower or higher than approximately 300°C. The amount of resistivity increase in the moisture-resistance and heat-resistance tests was found to correlate with the structure of the impurity-doped ZnO thin films, as evidenced from TEM images. The variation exhibited in the resistivity stability in these resistance tests is mainly attributed to micro-structural differences associated with the crystallinity of the deposited impurity-doped ZnO thin films.

2:40pm EN+SS+TF-ThA3 **Bulk and Surface Physics of Indium Oxide Thin Films Grown on Cubic Zirconia by O-plasma Assisted Molecular Beam Epitaxy**, R.G. Egdell, University of Oxford, UK INVITED

Tin doped indium oxide (In₂O₃) aka ITO is one of the most important transparent conducting oxides, yet it is only recently that many fundamental aspects the bulk and surface physics of indium oxide itself and of ITO have been addressed [1-3]. We have an ongoing programme concerned with growth of In₂O₃ on Y-stabilised ZrO₂ by oxygen plasma assisted molecular beam epitaxy and will review our most recent work in this area. Issues that will be addressed include the following:

The influence of surface energies and strain on the growth of In₂O₃ on low index zirconia surfaces. Mechanisms for relief of strain, including crystallographic tilting and development of nanostructures during high temperature MBE growth.

The influence of strain on the optical properties of ultrathin In₂O₃ films.

Surface structure and surface physics of In₂O₃ and ITO surfaces, including development of electron accumulation layers for material with low bulk doping levels.

References

- 1 P D C King *et al.*, Physical Review Letters 2008 **101** 116808
- 2 A Walsh *et al.*, Physical Review Letters 2008 **100** 167402/1-4
- 3 K H L Zhang *et al.*, Chemistry of Materials 2009 **21** 4353-4355

3:40pm EN+SS+TF-ThA6 **Recent Developments in Transparent Conducting Oxides for Thin-Film Solar Cells**, J. Burst, M. Scott, T. Gessert, National Renewable Energy Laboratory, S. Weiss, B. Rogers, Vanderbilt University, T. Coutts, Timothy J. Coutts Consulting, Inc

Transparent conducting oxides (TCOs) are utilized in all thin-film solar cells. Their function is to reduce electrical losses associated with collection of photogenerated current. However, they exhibit optical and electrical losses of their own and many researchers have tried to reduce these losses either by adjusting deposition conditions, post-deposition annealing, or by using completely novel materials. In our own work, we have shown that it is important to develop TCOs with high free-carrier mobility rather than high concentrations, which causes increased optical losses. Our latest results suggest significant gains in the performance of thin-film solar cells may be made via relatively minimal changes to the TCOs.

We have shown that the properties of transparent conducting oxides (TCOs) can be improved by doping them with approximately 1 atomic % cations whose oxides exhibit high dielectric permittivity. Our experiments have shown that TCOs doped with "high permittivity" cations have increased permittivity compared to the undoped TCO. Also, for similar carrier concentrations and mobilities, the doped TCOs have free-carrier absorption bands shifted to longer wavelengths (1500 nm doped v. 1300 nm undoped), thereby reducing optical losses compared to the undoped TCO. These observations are consistent with predictions based on the Drude free-electron model. In addition, there is evidence that the increased permittivity helps screen scattering centers, thereby leading to enhanced mobility. We will demonstrate that increasing film permittivity reduces optical losses in several standard TCO materials (ZnO, SnO₂, and In₂O₃). Film resistivity as low as 6×10^{-2} Ω.cm (corresponding to a sheet resistance of about 1 Ω/ sq

for a film 500 nm thick) has been achieved without compromising the high optical transmittance. The study has also indicated that TCO films with additions that alter permittivity appear to be less sensitive to variation in deposition ambient and temperature. Although this insight will clearly assist development of future TCO materials, we believe the results are even more relevant to present TCOs that may embody industrial advantages but remain limited by low mobility. *This abstract is subject to government rights.*

4:00pm EN+SS+TF-ThA7 The Study of AZO/Au/AZO as a Transparent Electrode for Organic Light Emitting Diodes, J.H. Park, Hanyang University, Republic of Korea

Transparent conducting oxide (TCO) thin films and coatings are an important and integral part of a number of electro optical devices because TCOs play an important role as transparent electrodes for flexible optoelectronic devices such as liquid crystal displays, solar cell panels, and organic light emitting devices (OLEDs). Typical TCOs are impurity-doped indium oxides, tin oxides and zinc oxides that offer commercially acceptable performance in terms of conductivity transmittance, environmental stability, reproducibility and surface morphology. The Al-doped ZnO (AZO) films show low resistance and high transmittance in the visible range of the spectrum. However, their resistivity is rather high in some case to adapt as a transparent electrode for advanced applications. Recently, in order to improve properties of TCO, thin metal or metal alloy film was embedded between TCO layers. In this study, we will discuss the effect of Au middle layer thickness on the electrical and optical properties of the multilayer TCOs and OLED applications. The AZO films were deposited on Corning eagle 2000 glass substrates by atomic layer deposition (ALD). The Optimization conditions of AZO films were 1/19 ratio of TMA/DEZ and 180°C. And Au middle layer were deposited by e-beam evaporator. The AZO/Au/AZO films exhibit better electrical properties compared to the AZO films. The carrier concentration was increased from 1.9×10^{20} to 5.8×10^{20} cm^{-3} . The mobility was decreased from 12.6 to 12.4 cm^2/Vs . The resistivity was decreased from 2.6×10^{-3} to 8.5×10^{-4} $\Omega \cdot \text{cm}$. However transmittance was decreased from 91 to 76 %, on average. The AZO/Au/AZO films were used as anode electrodes for red emission OLED application. The device showed that a maximum luminance of 2.4×10^3 cd/m^2 at 11 voltage. More detailed electrical and physical results will be discussed and presented.

4:20pm EN+SS+TF-ThA8 Origin of the Distribution of Electrical Properties of ITO Sputtered Films on Substrate, Y. Hoshi, Y. Yasuda, Tokyo Polytechnic University, Japan, H. Shimizu, Niigata University, Japan

The ITO films deposited by magnetron sputtering and facing target sputtering at low substrate temperature have quite different distributions of film properties. However, their origin was still not clear. In this paper, we clarify the origin of the different distributions between the sputtering methods, and will propose a sputtering method to deposit the ITO films with good uniformity.

In the deposition of ITO films by a conventional planar magnetron sputtering, the films deposited at the center of the substrate have higher oxygen content than the films deposited at the end of the substrate. It should be noted that the film deposited by a facing target sputtering has much lower oxygen content than the films deposited by conventional planar magnetron sputtering. As a result, the ITO films with poor transparency were always obtained by the sputtering in pure Ar gas, when a Facing Target Sputtering system was used.

These phenomena can be explained by the following model; When sputter-deposition of ITO films was performed at a low temperature, only oxygen atoms produced by the sputter-emission from the target surface promote the oxidization of indium atoms on the film surface. In other words, oxygen molecules cannot oxidize the indium atoms at a low temperature.

In addition, oxygen atoms sputter-emitted from the target have different angular distributions than indium atoms have. That is, the emission ratio of oxygen atoms to indium atoms sputter-emitted from the target surface changes depending on the emission angle and gradually decreases with an increase of the emission angle. This phenomenon mainly causes the distribution of the properties of ITO films on the substrate, although bombardment of high energy negative oxygen ions also affects the distribution of film properties in planar magnetron sputtering.

In order to deposit uniform film on the substrate, compensation of the angular distribution in the emission ratio of oxygen atoms to indium atoms is necessary. Use of two sputtering sources arranged like a facing target sputtering system is one of the solutions to compensate the distribution and obtain the films with more excellent uniformity.

4:40pm EN+SS+TF-ThA9 Deposition of Al-doped ZnO by Atomic Layer Deposition Using Ozone as the Oxygen Source, W.L. Gladfelter, H. Yuan, B. Luo, S.A. Campbell, University of Minnesota

Transparent conducting oxide (TCO) films are used in many photovoltaic and optoelectronic devices. The need to deposit conformal films at relatively low temperature has raised interest in atomic layer deposition (ALD). Literature reports establish that n-doped zinc oxide has been deposited by ALD using water as the source of oxygen and aluminum or gallium as the dopant. The interest in replacing water with ozone has led to many new ALD routes to metal oxide films, including ZnO. In this presentation we will describe an effective ALD route to Al-doped ZnO. Aluminum-doped ZnO (AZO) films were grown on Si and SiO₂/Si substrates in the temperature range from 150 - 300°C using diethylzinc as the zinc precursor and ozone as the oxygen source. Trimethylaluminum was used as the aluminum precursor. Two approaches to doping were studied. In one a nanolaminate was formed by interspersing a trimethylaluminum/ozone cycle in between the diethylzinc/ozone cycles. The overall aluminum concentration depended on the number of diethylzinc/ozone cycles. The second approach involved co-injection of both metal precursors in which their relative concentrations were controlled by adjusting the precursor vessel temperature. The influence of the deposition method on the composition, structural, electrical, and optical properties of the AZO films as a function of doping metal concentration will be reported. X-ray diffraction patterns showed all the samples were polycrystalline and exhibited preferential (0001) orientation. The (0002) reflection for AZO films shifted in opposite directions depending on the deposition method. The carbon content of the films was below the detection limit of Auger electron spectrometry. The lowest resistivity (6×10^{-4} $\Omega \cdot \text{cm}$) of the AZO films was obtained using the co-injection process. The average optical transmission was over 85 % in the range of 400-800 nm and the optical band gap increased with increasing doping in accordance with Burstein-Moss effect. The resistivity of AZO films grown by the co-injection method decreased to 3×10^{-4} $\Omega \cdot \text{cm}$ after rapid thermal annealing (RTA) in an Ar atmosphere.

5:00pm EN+SS+TF-ThA10 Atomic Layer Deposited (ALD) Al-doped ZnO Films for Transparent Conductor Applications, P. Banerjee, University of Maryland, W.-J. Lee, G.-Y. Bae, Dong-Eui University, Republic of Korea, S.-B. Lee, G.W. Rubloff, University of Maryland

Among various materials for thin film transparent conductor applications, Al-doped ZnO (AZO) is a particularly attractive material because of its excellent properties, such as higher thermal stability, good resistance against damage by hydrogen plasma and potentially, low cost compared to indium tin oxide (ITO). Of the various available deposition techniques, Atomic layer deposition (ALD) provides superb control at the nanoscale for thickness, uniformity, conformality and Al doping of AZO films. This is particularly attractive for use in nanostructures, as well as in more conventional applications such as liquid crystal displays.

We report here results for structural, optical and electrical properties of ultrathin ALD AZO films as a function of at% Al. AZO films of ~ 100nm thickness were deposited on quartz substrates at 150C using a commercial BENEQ TFS 500 reactor using diethyl zinc (DEZ) and H₂O as precursors for ZnO, and trimethyl aluminum (TMA) and H₂O as precursors for Al₂O₃. Al-doping was incorporated in a film by introducing a single cycle of TMA-H₂O after fixed cycles of DEZ-H₂O pulses. This 'super' cycle was repeated until the desired thickness was achieved. Al-doping was varied from 0.0at% to 24.5at%, on various samples, as determined by EDX. In addition, XRD, AFM, UV-Vis spectroscopy and temperature-dependent (80K-340K) Hall measurements were carried out to understand the structural, optical and electrical properties in these films.

Strong texture effects were observed in the AZO films on the quartz substrates as the films preferentially crystallized along the [100] direction. This texturing effect is different from the [002] normally reported for AZO films deposited using established methods other than ALD. Crystallinity and electrical conductivity peaked at 3at% Al, consistent with previous published work. AFM results show a dramatic drop in surface roughness with Al doping. Optical transmittances of over 80% were obtained for all films in the visible region.

Calculation of lattice parameter constants from XRD data and analysis within the framework of the Burstein-Moss effect, reveal that AZO films act as substitutionally doped films for Al doping less than ~7.3at%. Beyond this value of doping, phase segregation and possible formation of a low conductivity phase cause a reduction in the concentration and mobility of free carriers and hence a degradation of the electrical properties.

5:20pm **EN+SS+TF-ThA11 Silicon-Titanium Oxides as Transparent Conductors for Photovoltaic Applications**, *J. Chivers, T. Vandervelde*, Tufts University

We report on the use of Earth-abundant silicon-dioxide and titanium-dioxide as a transparent conducting oxide (TCO) and antireflective (AR) coating. TCOs are a critical component in modern photovoltaic devices, used as a front-side contact that won't block incident light. At present, many TCOs require rare-Earth materials (e.g. Indium), which is problematic for large-scale manufacturing. The abundant, well characterized materials used here can be integrated into an existing product line quickly and cheaply. The varied band gap and index of refraction conditions inherent in the SiTiO₂ system allow controlled variation of material properties during monolithic growth. Some TCOs may also act as an AR coating, further increasing light absorption. The ideal AR coating would gradually change from the index of refraction of air to that of the underlying semiconductor. Most AR coatings used today make this transition in a small number of steps, which limits their efficacy. In this work, we investigate deposition processes that slowly grade the index of refraction while maintaining conductivity and transparency.

Graphene Focus Topic

Room: Brazos - Session GR+AS+TF+MI-ThA

Graphene: Surface Characterization

Moderator: P. Sutter, Brookhaven National Laboratory

2:00pm **GR+AS+TF+MI-ThA1 Scanning Tunneling Microscopy and Spectroscopy of Impurities on a Gated Graphene Device**, *R.T. Decker, V.W. Brar, M.H. Solowan, Y.C. Wang, A. Zettl, M.F. Crommie*, University of California Berkeley **INVITED**

2:40pm **GR+AS+TF+MI-ThA3 Graphene Defect States in a Magnetic Field Studied by Scanning Tunneling Spectroscopy**, *K.D. Kubista, D.L. Miller, M. Ruan, W.A. de Heer, P.N. First*, Georgia Institute of Technology, *G.M. Rutter, J.A. Stroscio*, National Institute of Standards and Technology
We present tunneling differential conductance (dI/dV) spectra and 2D conductance maps acquired over both positive and negative defects in magnetic fields up to 8 T. The measurements were performed on multilayer epitaxial graphene using scanning tunneling microscopy and spectroscopy at 4 K under ultrahigh vacuum conditions. Landau level drift states are found to follow the local potential (determined independently at near-zero magnetic field), but near a negatively-charged defect a bound (or quasibound) state originates from the $n = -1$ Landau Level. The defect state Stark shifts and finally ionizes under the influence of the STM tip electric field.

3:00pm **GR+AS+TF+MI-ThA4 Atomic-Scale Maps of Quantum Hall States in Epitaxial Graphene**, *D.L. Miller, K.D. Kubista*, Georgia Institute of Technology, *G.M. Rutter*, National Institute of Standards and Technology, *M. Ruan, W.A. de Heer, P.N. First*, Georgia Institute of Technology, *J.A. Stroscio*, National Institute of Standards and Technology
When a perpendicular magnetic field is applied to a graphene sheet, the resulting eigenenergies (Landau Levels or LLs) have a nonlinear energy distribution that includes a four-fold degenerate zero-energy state (LL₀). Maps of the energy-resolved local density of states (LDOS) acquired via cryogenic scanning tunneling spectroscopy (STS) provide atomic-scale imaging of the LL spatial distribution. Focusing on LL₀, we use STS maps to image the *localized* and *extended* quantum Hall states. Unexpectedly, we find atomic-scale variations of the LDOS above a critical magnetic field. We attribute this to an energy gap in LL₀ and show how it depends on the local A-B lattice symmetry. The gap is observed only within patches of at least a few magnetic lengths in size, which forces the splitting to "turn off" below the critical field. This behavior implies a breaking of the local sublattice symmetry imposed by moiré layer stacking.

3:40pm **GR+AS+TF+MI-ThA6 Imperfect Graphene: Point Defects, Edges, Dislocations and Grain Boundaries**, *O.V. Yazyev*, University of California, Berkeley **INVITED**

In two dimensions, properties of materials can be heavily affected by defects. In this talk, I will review our recent efforts directed towards understanding various types of structural irregularities in graphene.

Firstly, I will present the results of theoretical studies of the magnetism induced by point defects and edges in graphene and graphite. We show that in graphene single-atom defects such as vacancies and hydrogen chemisorption induce the spin-polarized defect states [1, 2]. The coupling between the magnetic moments is either ferromagnetic or

antiferromagnetic, depending on whether the defects correspond to the same or to different sublattices of the graphene lattice, respectively. These results are able to clarify some experimental observations of high-temperature ferromagnetism in proton-irradiated graphite. Similarly, zigzag edges of graphene are predicted to induce spin-polarized edge states which can serve as a basis for novel spintronic devices. We address the question of the spin correlation length at finite temperatures in this one-dimensional magnetic system and establish the limitations of the proposed spintronic devices [3].

Then, I will talk about our latest results on dislocations and grain boundaries in graphene [4], topological defects which are still not well understood despite the growing number of experimental observations. We introduce a general approach for constructing dislocations in graphene characterized by arbitrary Burgers vectors as well as grain boundaries, covering the whole range of possible misorientation angles. By using ab initio calculations we investigate thermodynamic, electronic and transport properties of grain boundaries, finding energetically favorable large-angle symmetric configurations, strong tendency towards out-of-plane deformation in the small-angle regimes, pronounced effects on the electronic structure, and two distinct behaviors in the electronic transport [5] - either perfect reflection or high transparency for low-energy charge carriers depending on the grain boundary structure. Our results show that dislocations and grain boundaries are important intrinsic defects in graphene which may be used for engineering graphene-based functional devices.

[1] O. V. Yazyev and L. Helm, Phys. Rev. B 75, 125408 (2007).

[2] O. V. Yazyev, Phys. Rev. Lett. 101, 037203 (2008).

[3] O. V. Yazyev and M. I. Katsnelson, Phys. Rev. Lett. 100, 047209 (2008).

[4] O. V. Yazyev and S. G. Louie, arXiv:1004.2031 (2010).

[5] O. V. Yazyev and S. G. Louie, submitted.

4:20pm **GR+AS+TF+MI-ThA8 Spectroscopic Ellipsometry for Thickness Measurement and Optical Dispersion Modeling of CVD-Grown Graphene**, *F.J. Nelson, V.K. Kamineni, A.C. Diebold*, The University at Albany-SUNY

Graphene has attracted much research over the past several years due to its electrical and mechanical properties. It is a prime candidate for electronic and optoelectronic devices, yet much of the research has utilized the exfoliation, or "scotch-tape" technique of sample preparation. More scalable growth methods have been investigated, such as the thermal decomposition of SiC, and the resulting graphene films have properties dependent on their fabrication parameters. One potentially scalable technique is that of hydrocarbon gas-based CVD onto metallic substrates. Here, we report on the ellipsometric measurement of Few-Layer-Graphene (FLG) grown on copper foils and subsequently transferred to a different substrate (i.e. glass). One of the challenges with development of a dispersion model for FLG is that the CVD graphene has many "grains" inside the measured area while previous reports of exfoliated graphene were done on single crystal samples. The work explores finding an average thickness, as well as the optical dispersion modeling, of the graphene layers on different substrates, such as SiO₂/Si and glass slides.

MEMS and NEMS

Room: Santo Domingo - Session MN-ThA

Integration, Packaging and Reliability of MEMS and NEMS

Moderator: M. Metzler, Cornell University

2:00pm **MN-ThA1 Electrothermal Tuning of Bistability in a Large Displacement Micro Actuator**, *Y. Gerson*, Tel Aviv University, Israel, *R.B. Ilic*, Cornell University, *S.L. Krylov*, Tel Aviv University, Israel

We report on an approach allowing efficient tuning of the bistability properties in large displacement micro actuators. The devices fabricated from highly doped silicon on insulator (SOI) wafers using Deep Reactive Ion Etching (DRIE) based process incorporate elastic suspension realized as a pair of initially curved beams and are operated electrostatically by a comb-drive transducer. The tuning principle is based on the control of the initial elevation and consequently of stability characteristics of the suspension by passing a current through the beams and electrothermal heating of the beams's material. Experimental results, which are in good agreement with the Finite Elements model predictions, demonstrate the feasibility of the suggested approach and show that the application of a tuning current significantly increases the device deflection and allows efficient control of the critical snap-through and snap-back voltages.

2:20pm **MN-ThA2 Measured and Predicted Temperature Profiles along MEMS Bridges at Pressures from 0.05 to 625 Torr**, *L.M. Phinney, J.R. Serrano, E.S. Piekos, J.R. Torczynski, M.A. Gallis, A.D. Gorby*, Sandia National Laboratories

We will present experimental and computational investigations of the thermal performance of microelectromechanical systems (MEMS) as a function of the surrounding gas pressure. Lowering the pressure in MEMS packages reduces gas damping, providing increased sensitivity for certain MEMS sensors; however, such packaging also dramatically affects their thermal performance since energy transfer to the environment is substantially reduced. High-spatial-resolution Raman thermometry was used to measure the temperature profiles on electrically heated, polycrystalline silicon bridges that are nominally 10 microns wide, 2.25 microns thick, 12 microns above the substrate, and either 200 or 400 microns long in nitrogen atmospheres with pressures ranging from 0.05 to 625 Torr. Finite element modeling of the thermal behavior of the MEMS bridges is performed and compared to the experimental results. Noncontinuum gas effects are incorporated into the continuum finite element model by imposing temperature discontinuities at gas-solid interfaces that are determined from noncontinuum simulations. The experimental and simulation results indicate that at pressures below 0.5 Torr the gas-phase heat transfer is negligible compared to heat conduction through the thermal actuator legs. As the pressure increases above 0.5 Torr, the gas-phase heat transfer becomes more significant. At ambient pressures, gas-phase heat transfer drastically impacts the thermal performance. The measured and simulated temperature profiles are in qualitative agreement in the present study. Quantitative agreement between experimental and simulated temperature profiles requires accurate knowledge of temperature-dependent thermophysical properties, the device geometry, and the thermal accommodation coefficient.

Sandia National Laboratories is a multi-program laboratory operated by Sandia Corporation, a wholly owned subsidiary of Lockheed Martin Corporation, for the U.S. Department of Energy's National Nuclear Security Administration under contract DE-AC04-94AL85000.

2:40pm **MN-ThA3 Micro- and Nanoswitches: Materials, Design, Packaging and Reliability**, *M.P. De Boer*, Sandia National Laboratories, *D.A. Czaplewski*, Argonne National Laboratory, *M.S. Baker*, Sandia National Laboratories

INVITED

Ohmic micro- and nanoswitches are of interest in numerous potential applications including phased-array radars, cell-phone circuitry, circuit breakers and power savings in advanced CMOS circuits. However, many challenges remain with respect to materials, design, packaging and reliability. An important issue is maintaining a low contact resistance as switch cycling approaches high counts. In this talk, a prototype ohmic microswitch will be presented, and its electrical performance when coated by Pt and Ru films will be compared. A whole-wafer singulation, post-processing and metallization process will be demonstrated. Then, a nanoswitch design will be introduced and initial results including processing and test will be discussed. Continued progress in micro- and nanoswitch technology will lead to insertion in multiple applications.

Sandia is a multiprogram laboratory operated by Sandia Corporation, a Lockheed-Martin Company, for the United States Department of Energy under contract DE-AC04-94AL85000.

3:40pm **MN-ThA6 Bulk Focused Ion Beam Fabrication of Nanoelectromechanical Systems**, *W.K. Hiebert, D. Vick, V. Sauer*, National Institute for Nanotechnology (NRC Canada), *A.E. Fraser, M.R. Freeman*, University of Alberta, Canada

Although the focused ion beam (FIB) has previously been used for fabrication of nanostructures and devices, including MEMS and NEMS, FIB nanomilling out of bulk material has rarely been discussed. In this talk, we will present our methods and results for using FIB to fabricate NEMS devices out of bulk materials. Ion impingement from multiple directions allows sculpting with considerable 3-dimensional control of device shape, including tapering and notching. The tailoring of large gaps between device layer and bulk allows large amplitude NEMS motion, access to a nonlinear readout regime, and a novel calibration method for optical interferometric displacement detection. Finite element modeling of device frequencies agrees with interferometric measurements, including for the effect of a localized notch. The measurements are sensitive enough to determine the thermomechanical noise floor of a bulk FIBed NEMS device with displacement sensitivity of $166 \text{ fm} / \text{Hz}^{1/2}$, limited only by a combination of optical shot noise and detector dark current. We envision that bulk FIB fabrication will be useful for NEMS prototyping, milling of tough-to-machine materials, and generalized nanostructure fabrication with 3-dimensional shape control.

4:00pm **MN-ThA7 NanoFIBrication of UHAR Vias Using a Material Shaping Technique for Phononic Crystals**, *D.F. Goettler, Z.C. Leseman*, University of New Mexico

In this paper we present both experimental and theoretical results showing the effective use of material shaping to fabricate ultra-high-aspect-ratio (UHAR) vias with a focused ion beam (FIB). With this technique, one can create vias with aspect ratios of 50:1 and higher. This is achieved by placing a 'lower sputter rate' material on top of a 'higher sputter rate' material. We model the FIB as a Gaussian beam with an angular dependent sputter rate. With our model we predict a high sputter rate ratio (high/low) can achieve vias with aspect ratios near 50:1. Experimental results support this prediction. By placing a thin layer of pyrolyzed carbon on top of silicon, we fabricated UHAR vias. For completeness, we also reversed the sputter rate ratio by placing a 'higher sputter rate' material on top of a 'lower sputter rate' material. Once again, experimental results support the model's predictions. Vias with radii 15 nm have been NanoFIBricated. Using these techniques we have created phononic crystals operating in the GHz regime.

4:20pm **MN-ThA8 Highly Robust Hydrogen Selective MEMS Nanogap Sensor Utilizing the Schottky Barrier at Electrode/Sensing Material**, *A. Kumar, P. Zhang, H.J. Cho, S. Seal*, University of Central Florida

The growing need to explore hydrogen as a near future fuel demands a robust hydrogen sensor which offers high sensitivity, selectivity and response time in order to avoid the danger associated with storage, transportation and use of this highly combustible gas. The sensor platform with Au interdigitated electrodes (IDE) having 8 fingers in each electrode and a gap of 100 nm was fabricated using E-beam lithography on a silica substrate. The Au IDE was dip coated with sol-gel preparation of nanocrystalline 6.5 mol % Indium oxide (In_2O_3)-doped tin oxide (SnO_2) to yield an excellent thin film room temperature hydrogen sensor. The variation in the I/V response of the sensor with atmosphere suggested that the Schottky barrier height could be modulated to sense hydrogen and utilizing this a large sensitivity (~ 2000) and fast response time (~ 27 seconds) was observed at a low applied voltage of 0.4 V in 0.09 vol% hydrogen gas atmosphere. The sensing characteristics were severely affected in presence of moisture ($>40\%$). Various polymeric coatings on the sensor were compared in an effort to make the hydrogen sensor robust even in high moisture environment. It was observed that the fluoropolymer coatings improved the sensor behavior in varying moisture environment without deteriorating other characteristics such as sensitivity, response time and recovery of a sensor.

4:40pm **MN-ThA9 Development of Lab-on-a-chip on Mn Induced Nano-arrayed Structures in Sol-gel Derived TiO₂ Platforms for Biosensing Applications**, *R.R. Pandey*, Centre for Cellular and Molecular Biology, India, *K.K. Saini*, National Physical Laboratory, India, *M. Dhayal*, Centre for Cellular and Molecular Biology, India

Development of low cost point-of-care diagnostic system for effective health care is important for rapid screening of routine biochemical tests. To address this, we have used sol-gel derived process in which Mn induced nano-arrayed structures were developed in TiO₂ as a platform for lab-on-a-chip. Mn doped nanopore TiO₂ platforms were prepared by using wet chemistry deposition with the help of metal alkoxide precursor and assembled with micro-fluidics networks to screen multiple interactions. To demonstrate usefulness of this, enzymatic biocatalyst has been used to determine the specificity of multiple interactions on these platforms. These platforms have been characterized by XRD, XPS, FTIR, SEM, cyclic voltammetry to determine structure, surface chemistry and electron transfer characteristics for biosensor applications. Mono-enzyme ChOX, urease and GOX were prepared by immobilizing the separate enzymes onto nanopore TiO₂ surfaces modified with Mn doping. The electrochemical detection sensitivity for detection of low concentrations of cholesterol, urea and glucose has been enhanced.

**Nanometer-scale Science and Technology
Room: La Cienega - Session NS+BI-ThA**

**Biomolecular Templates & Bioinspired Nanomaterials
Moderator: B. Borovsky, St. Olaf College**

2:00pm **NS+BI-ThA1 Bio-functionalization of Nanopatterned Surfaces and their Integration with DNA Nanostructures**, *M. Palma, J.J. Abramson, E. Penzo, A. Gorodetsky, R. Wang, M.P. Sheetz, C. Nuckolls, J. Hone, S.J. Wind*, Columbia University

The ability to control biomolecules on surfaces with nanometer resolution is of great interest in the field on nanoscience and nanotechnology. DNA

nanarrays, in particular, are of interest in the study of DNA-protein interactions, for biodiagnostic investigations and as a tool to drive self-organization of nanomaterials on surfaces. In this context, achieving a highly specific nanoscale assembly of oligonucleotides at surfaces is critical.

Here we describe different strategies to control the immobilization of single- and double-stranded DNA, as well as DNA nanostructures (DNA "origami"), on nanopatterned surfaces, with features down to the sub-10nm regime.

Using electron-beam and nanoimprint lithography we fabricated sub-10nm metal dots arranged in multiple configurations on Si or glass substrates. We have developed strategies for the selective bio-functionalization of these patterns, at the single nanodot level: each step of the biochemical functionalization has been monitored by Fluorescence Microscopy. The bio-functionalization approach used allowed for the formation of non-sterically hindered DNA nanodomains where the dsDNA attached to the dots maintains its native conformation, as confirmed by restriction enzymes studies. This allowed us, moreover, to follow the activity (at surfaces) of a restriction enzyme in real time and at the nanoscale: the monitoring of protein-DNA interactions with such biological nanoarrays will be discussed.

We will highlight the broader utility and application of such nanopatterned surfaces for the self-organization of DNA nanostructures. In-situ hybridization between the complementary strands on DNA nanostructures and on functionalized nanodots has been achieved, resulting in the ordered placement of the origami on the dot patterns, as demonstrated by Atomic Force Microscopy (AFM) imaging, both in liquid and in air.

Finally, we will discuss the application of DNA origami as functional scaffolds for the assembly of different nanomaterials (e.g Au nanoparticles and carbon nanotubes): highly complex arrangements can be created with high resolution and high throughput, opening the possibility for the realization of electronic devices at the molecular scale.

2:20pm NS+BI-ThA2 De Novo Nanostructure Design: from Protein Folding to Self-Assembly-Templated Nanomaterials, *M. Ryadnov*, National Physical Laboratory, UK

Rational design of self-assembled nano-to-micro scale structures offers an efficient tool for molecular nanotechnology improving our ability to engineer nanostructured materials at whim. Such attention is driven by the need for approaches leading to specialist nanostructures whose properties can relate to particular biological functions. Critical in this respect becomes the hierarchical nature of self-assembly rendering the process a "bottom-up" strategy in challenging different levels of nanostructural complexity [1].

Generic protein folding motifs are proving to be instrumental for prescriptive nanoscale engineering. Of particular demand are nanostructures which can be made functionally and architecturally amenable in cellular environments. In this report, bioinspired nanoscale designs based on peptide self-assembling systems possessing antimicrobial [2], cell-supporting [3], encapsulating[4] and tuneable morphological[5] properties will be discussed.

1. Ryadnov, M. G. (2009) *Bionanodesign: Following the Nature's touch*. RSC Publishing, 250 pp.
2. Ryadnov, M. G., Mukamolova, G. V., Hawrani, A. S., Spencer, J. & Platt, R. (2009) RE-coil: An antimicrobial peptide regulator. *Angew. Chem. Int. Ed.* 48, 9676-9679.
3. Ryadnov, M. G., Bella, A., Timson, S. & Woolfson, D. N. (2009) Modular design of peptide fibrillar nano- to microstructures. *J. Am. Chem. Soc.*, 131, 13240-13241.
4. Ryadnov, M.G. (2007) A self-assembling peptide polyanoreactor. *Angew Chem Int Ed Engl.* 46, 969-972.
5. Ryadnov, M. G. & Woolfson, D. N. (2003) Engineering the morphology of a self-assembling protein fibre. *Nature Mater.*, 2, 329-332.

2:40pm NS+BI-ThA3 Rare Earth Nanoparticles to be used as Both Fluorescent Probes and MRI Contrast Agents, *L. Axelsson, M. Åhrén, L. Selegård, F. Söderlind*, Linköping University, Sweden, *P. Nordblad*, Uppsala University, Sweden, *M. Lindgren*, Norwegian University of Science and Technology, Norway, *K. Uvdal*, Linköping University, Sweden Nanotechnology continuously explores new fields, and nanomedicine presents an entirely new research area with unlimited possibilities. For the last 20 years, gadolinium complexes have been used clinically as contrast enhancing agents for Magnetic Resonance Imaging (MRI). Simultaneously, Quantum Dots (QDs), with its excellent photostability and high quantum yield, are developed to replace organic fluorophores for medical diagnosis. The aim of this study is to develop nanoprobe that possess both the

magnetic properties suitable for a contrast agent, and luminescent properties.

We have designed a novel nanomaterial of gadolinium oxide nanoparticles doped with europium (Eu:Gd₂O₃) or terbium (Tb:Gd₂O₃). Using nanoparticles, the local signal intensity in MRI can be increased compared to Gd complexes with only one Gd ion per complex. When introducing luminescent europium or terbium ions into the gadolinium oxide nanocrystal, fluorescent properties are added, creating a bifunctional nanocrystal. In addition to the favorable size for biomedical applications, nanoparticle contrast agents can bring advantages such as longer rotational correlation time to obtain increased relaxivity, and surface-coating possibilities for attaching targeting molecules. This will enable tailored design of a new generation of contrast agents. We present highly crystalline, 5 nm large nanoparticles, showing typical Eu³⁺ or Tb³⁺ fluorescence with a long luminescent lifetime. The strength of both europium and terbium ions is the suitable properties for excitation in an ordinary confocal microscope, which makes them promising as components when designing nanoprobe for cell studies. Relaxation measurements show relaxivity ratios in the same range as the pure Gd₂O₃ nanoparticles. The nanoparticles present a promising bifunctional core material, acting as a platform when developing advanced nanoprobe for future applications in biomedical imaging.

3:00pm NS+BI-ThA4 Plasma Polymerized Amino Acids used for Bio-Assisted Fabrication of Nanostructures, *R. Jakubiak*, Air Force Research Laboratory, *K. Anderson*, Georgia Institute of Technology, *J. Slocik*, UES, Inc., *M. McConney*, Georgia Institute of Technology, *J. Enlow*, UES, Inc., *T. Bunning*, *R. Naik*, Air Force Research Laboratory, *V. Tsukruk*, Georgia Institute of Technology

Plasma-enhanced chemical vapor deposition (PECVD) allows deposition of conformal, ultrathin, and uniform polymer coatings from gaseous, liquid or solid precursors onto a variety of materials. Our process uses a modified afterglow plasma reactor operated at room temperature where plasma polymerization occurs downstream from plasma generation. This allows controllable retention of the precursor's functionality needed for surface-induced biomineralization on soft or delicate substrates that cannot withstand high temperature or multiple wet-chemistry treatments. Amine-functionalized substrates, derived from the plasma polymerization of L-tyrosine, enabled biomineralization of gold nanoparticles from a solution of gold chloride. Templated gold nanoparticle coatings were formed by the placement of a shadow mask on the substrate during plasma deposition creating a micropatterned plasma polymerized tyrosine film. Subsequent gold chloride exposure created a gold nanoparticle network replica of the initial micropattern. Similar processing conditions were used to biomineralize titania on highly ordered three-dimensional structures.

3:40pm NS+BI-ThA6 Molecular Shuttles for 'Smart Dust' Biosensors, Active Self-Assembly, and Protein-Resistant Coatings, *H. Hess*, Columbia University

Biomolecular motors, such as the motor protein kinesin, can serve as biological components in engineered nanosystems. Initially, a nanoscale transport system termed molecular shuttle has been explored by others and us as a model system. The development of this system has revealed a number of challenges in engineering at the nanoscale, particularly in the guiding, activation, and loading of these shuttles. Overcoming these challenges requires the integration of a diverse set of technologies, and continues to illustrate the complexity of biophysical mechanisms.

A proof-of-principle application of the developed technologies is a "smart dust" biosensor for the remote detection of biological and chemical agents, which is enabled by the integration of recognition, transport and detection into a submillimeter-sized microfabricated device.

The application of nanoscale forces introduces an interesting element into self-assembly processes by accelerating transport, reducing unwanted connections, and enabling the formation of non-equilibrium structures. The formation of nanowires and nanospools from microtubules transported by kinesin motors strikingly illustrates these aspects of motor-driven self-assembly.

Finally, a critical aspect of the design of these hybrid systems is the controlled adsorption of proteins. In pursuit of this goal of controlled adsorption, we have utilized kinesin motors as probes of residual protein adsorption to non-fouling coatings and achieved the detection of a few adsorbed molecules per square micrometer (adsorbed mass on the order of pg/cm²). Furthermore, we have developed a Random Sequential Adsorption model which successfully explains residual protein adsorption as the result of randomly occurring "bald" spots on a surface covered with PEG-chains.

4:20pm **NS+BI-ThA8 Probing Biom mineralization Protein Interactions with Hydroxyapatite Using SFG and NEXAFS Spectroscopy**, T.M. Weidner, M. Dubey, N.F. Breen, J. Ash, J.E. Baio, University of Washington, C. Jaye, D.A. Fischer, National Institute of Standards and Technology, G.P. Drobny, D.G. Castner, University of Washington

The structural integrity of hydroxyapatite (HAP) in tooth enamel is maintained through the saliva environment that is supersaturated with calcium and phosphate salts. The biom mineralization protein statherin adsorbs onto HAP surfaces with high binding affinity. It regulates HAP growth and prevents the buildup of excess HAP on the tooth surface by inhibiting spontaneous calcium phosphate growth. Owing to the importance of the underlying physiological processes and a general interest in biom mineralization mechanisms, the binding of statherin to HAP has attracted significant interest in the biomaterials community. Sum frequency generation (SFG) spectroscopy can probe protein orientation and secondary structure at the solid-liquid interface and we have recently shown it can address specific protein regions with atomic resolution when combined with isotopic labeling.¹ Near edge X-ray absorption fine structure (NEXAFS) spectroscopy can give valuable information about the structure and binding chemistry of proteins on surface. We have combined both techniques to characterize the structure of the binding domain of statherin, SN15, a short peptide with 15 residues (Ac-DSSEENKFLRRIGRFG-OH) adsorbed onto a model HAP surface. Protein adsorption was verified using X-ray photoelectron spectroscopy and time-of-flight secondary ion mass spectrometry. SFG confirmed a loosely helical secondary structure of SN15 on HAP. Deuteration was used to specifically probe the orientations of the hydrophobic leucine and isoleucine side chains with SFG in situ. Side-chain orientations were determined using ratios of the symmetric and asymmetric CD₃ stretching modes. The leucine chain was tilted 120° from the surface normal (pointing towards the surface) and the isoleucine was tilted 5° from the surface normal. For the first time, element labels were employed to probe individual side chain orientations with NEXAFS spectroscopy. Para- and perfluorination of the phenylalanine rings F7 and F14 allowed us to precisely measure their orientations using angle dependent NEXAFS data. The tilt angles from the surface normal were determined to be 26° for F7 and 35° for F14.

[1] T. Weidner, N. F. Breen, K. Li, G. P. Drobny, D G. Castner, submitted.

4:40pm **NS+BI-ThA9 Assembly of Nanoparticles for Patterning and Functional Materials in Nature's Way at Liquid-Liquid Interfaces**, L. Isa, E. Amstad, M.H. Textor, E.O. Reimhult, ETH Zurich, Switzerland

An interesting aspect of the self-organization in Nature resulting in precise patterning of hierarchically structured materials is that the "synthesis" and patterning of the materials occur at liquid amphiphilic interfaces such as membranes. That particles can be organized and change the properties of liquid interfaces has long been known and explored as e.g. Pickering emulsions in foams, food processing and other large-scale, bulk materials applications. However, self-assembly of nanometer-sized colloids with defined surface properties at liquid-liquid interfaces is also a process with huge potential for the fabrication of controlled two-dimensional nanoscale structures and patterns as well as "nanomaterials". This is due to three key factors: a) the particles are trapped at the interface, but b) retain lateral mobility and c) exhibit specific interactions, which when properly understood and controlled lead to assembly of controlled structures. We have recently explored both how the oil-water interface can be used for unprecedented control of the assembly of nanoparticle patterns and transferred to substrates for low-cost nanolithography, and how tailored core-shell nanoparticles with functional cores can be assembled at such interfaces.

I will describe how self-assembly at the liquid-liquid interface (SALI) can be used for the deposition of non-close-packed crystalline arrays of NPs for lithographic masks and the physical control parameters for the successful application of this method. Our approach allows us to control the spacing of particles in a wide range; we have demonstrated reproducible and homogeneous patterns with spacing between 3 to 20 particle diameters using colloids from 40 to 500 nm over chip-sized areas. The use of bimodal size distributions at controlled ratios also allows for induced phase separation and thus hierarchically ordered patterns to emerge.

By optimization of a simple Schäfer-type deposition setup and the choice of the proper oil phase, the particle patterns can be transferred to a substrate with few limitations. We will demonstrate use of the deposited particle patterns to fabricate a range of nanostructures for electrochemical and nanoplasmonic biosensing which previously could not be fabricated by particle lithography, and this at a fraction of cost to other available patterning techniques.

5:00pm **NS+BI-ThA10 Characterization of Folate Receptor Targeting Drug Loaded PLGA-Lipid Hybrid Nanoparticles**, S. Sandoval, A. Liberman, J. Yang, S. Aschemeyer, L. Zhang, W.C. Trogler, A.C. Kummel, University of California, San Diego

The response rate of breast cancer to first line chemotherapies is encouraging, but 20-30% of patients develop chemoresistance to these drugs, and consequently, have a cancer recurrence 7-10 months after their last treatment. Chemoresistance is believed to be due to drug efflux proteins responsible for the removal of many commonly used anti-neoplastic agents. One possible way to overcome these drug efflux pumps is to give higher doses of chemotherapy, but high doses of such agents commonly lead to chemocytotoxicity. Targeted PLGA-Lipid hybrid nanoparticle (NP) drug delivery systems have been developed that can deliver high doses of chemotherapy agents specifically to breast cancer cells. A practical cancer targeting drug delivery system will reduce the overall amount of chemotherapy agents given to patients for a given amount of targeted NPs endocytosed by cancer cells. Biodegradable NPs were synthesized using a novel nano-precipitation lipid-polymer hybrid platform which also allows for the encapsulation of hydrophobic chemotherapy drugs within the NPs. Using this method, drug free NPs have been shown to have an average diameter size of 81.78 nm (PDI: 0.25), while single loaded NPs, with Paclitaxel or Doxorubicin, show an average size between 72.33 to 89.64 nm (PDI: 0.242 to 0.339), signifying that the synthesis technique creates consistent sub 100nm particles. The majority of all NPs show a zeta-potential value of > -30 mV consistent with the NPs having sufficient repulsive interaction to be mono-dispersed in solution under physiological conditions. Folate receptors are often over expressed on the surfaces of cancer cells; therefore, folic acid was incorporated to the surface of these NPs as a cancer targeting ligand. Previous studies have shown that HeLa cells, a cervical cancer cell line, over expresses folate receptors. Immunofluorescence studies show that folic acid coated PLGA-Lipid hybrid NPs are readily endocytosed by HeLa cells compared to non-targeted NPs. Cytotoxicity studies will determine the increased effectiveness of drug delivery with targeted PLGA-Lipid hybrid NPs vs. untargeted PLGA-Lipid hybrid NP in cell lines and in animal models.

5:20pm **NS+BI-ThA11 Controlled Surface Modification of Ultra-stable Superparamagnetic Iron Oxide Nanoparticles**, E. Amstad, M.H. Textor, E.O. Reimhult, ETH Zurich, Switzerland

Biocompatibility, magnetic properties and ease of synthesis renders iron oxide nanoparticles (NPs) attractive for many especially biomedical applications such as magnetic resonance (MR) contrast agents, triggered drug release and cell separation. Good NP stability under physiologic conditions and controlled surface chemistry are key to successful application not only in the biomedical field but also for assembly into various materials.

NPs with close control over the interfacial chemistry and good stability at high salt concentrations and elevated temperatures can only be achieved if dispersants are irreversibly bound to the NP surface. The dispersant binding affinity is determined by its anchor group. Low molecular weight dispersants which consist of one high affinity anchor covalently linked to poly(ethylene glycol) (PEG) spacers have been proven well suited to sterically stabilize Fe₃O₄ NPs. However, we found that electronegatively substituted catechols such as nitrocatechols vastly outperform the well-known and often used catechol anchors such as DOPA and dopamine. Because of the optimized binding affinity of nitrocatechols, PEG-nitrocatechol coated Fe₃O₄ NPs remained stable under physiologic conditions up to 90 °C whereas e.g. PEG-dopamine stabilized Fe₃O₄ NPs started to agglomerate below body temperature.^[1] Further investigations showed that the optimal binding affinity of nitrocatechols to Fe₃O₄ is closely related to a redox reaction between Fe²⁺ located at the Fe₃O₄ NP surface and nitrocatechols, which leads to electron delocalization in the adsorbed catechol ring, and a close to covalent bond of nitrocatechols to Fe₃O₄ surfaces. Irreversible binding of PEG-nitrocatechols to Fe₃O₄ NPs allowed us to closely control and investigate the influence of dispersant layer thickness by varying the nitrocatechol-PEG molecular weight. Furthermore, NPs could easily be functionalized by co-adsorbing differently end-functionalized dispersants on the Fe₃O₄ NP surface.^[2]

In summary, nitrocatechols have a close to optimal binding affinity to Fe₃O₄ surfaces. This optimized binding affinity not only leads to ultra-stable PEG-nitrocatechol coated superparamagnetic Fe₃O₄ NPs but also allows for close control over the hydrodynamic diameter and interfacial chemistry, factors which crucially determine NP performance especially in biomedical applications.

[1] E. Amstad, T. Gillich, I. Bilecka, M. Textor, E. Reimhult, *Nano Letters* **2009**, *9*, 4042.

[2] E. Amstad, S. Zurcher, A. Mashaghi, J. Y. Wong, M. Textor, E. Reimhult, *Small* **2009**, *5*, 1334.

Plasma Modeling

Moderator: Z. Chen, Applied Materials Inc.

2:00pm **PSI-ThA1 Molecular Dynamics Simulation of Fluorocarbon/hydrogen Ion Beam Interaction with a PMMA (Polymethyl Methacrylate) Surface**, *Y. Morita, M. Isobe, S. Hamaguchi*, Osaka University, Japan

Beam-surface interaction between fluorocarbon ions (mainly CF₃⁺) or hydrogen ions (H⁺) with a polymethyl methacrylate (PMMA) surface has been examined at the atomic level with the use of molecular dynamics (MD) numerical simulations. The work is motivated by the desire to control line edge roughness (LER) or line width roughness (LWR) observed after plasma etching processes, which is incurred by deterioration of photoresist polymers exposed to reactive plasmas. Molecular structures of commercially available photoresist polymers are complex in general and typically not disclosed in the public domain, so we use PMMA in this work as a model polymer in a hope that, combining this study with other previous studies on plasma-polymer interaction based on other simple organic polymers, an insight into the mechanism of photoresist deterioration due to plasma exposure will be gained. For example, PMMA contains ester bonds (R-COO-R') and their interactions with plasmas are a subject of this study. In this presentation, we shall focus on two specific issues. One is to evaluate sputtering yields of PMMA by Ar⁺ or CF₃⁺ ion injections with various injection energies. With Ar⁺ injection simulations, we shall clarify the nature of physical sputtering of PMMA whereas, with CF₃⁺ injection simulations, we hope to understand the modification mechanism of a polymer mask during oxide etching processes. Our MD simulation results have so far indicated that there is a strong dependence of sputtering yields on the direction of polymer chains against the incoming beam angle at the atomic level. The other issue is solidification of polymer by hydrogen plasma exposure, which may be used to cure polymers after the mask formation process by photolithography. In the simulations, hydrogen beams are injected into PMMA and we have observed increase of the relative carbon density in the polymer due to hydrogen abstraction reactions.

2:20pm **PSI-ThA2 Molecular Cross-Section Calculations Enabling Etch-Profile Simulations of a Microwave Source Silicon Etch using Ar/HBr/O₂**, *J. Munro, J. Tennyson*, University College London, UK, *S.-Y. Kang*, Tokyo Electron Limited, Japan, *D. Brown*, Quantemol Ltd., UK

The introduction of new microwave plasma sources for Silicon and Silicon-Nitride etch processes has renewed interest in a more detailed understanding of the etch process in a microwave regime. The use of Ar/HBr/O₂ for Silicon etching in this regime is common. In particular the inclusion of HBr has been found to reduce "microtrenching" [1]. The etching yields of high density HBr plasmas have been studied previously [2]. Here we study the additional effects of the etching products SiBr and SiBr₂ near the wafer.

A set of quantum electron scattering calculations are performed on SiBr and SiBr₂ using the electron-molecule code Quantemol-N [3]. The resulting cross-sections are used to complete a set of gas-phase reactions contributing to the etch process. Etch-profile simulations are then performed using the Monte Carlo Feature Profile Model code (MCFPM) [4]. Here we use incident species fluxes derived from simulations of Ar/HBr/O₂ plasmas. Results are presented which include an analysis of the contribution of the etch products SiBr and SiBr₂.

[1] J. M. Lane, F. P. Klemens, K. H. A. Bogart, M. V. Malyshev, and J. T. C. Lee, *J. Vac. Sci. Technol. A* 18, 188 (1999)

[2] S. A. Vitale, H. Chae, H. H. Sawin, *J. Vac. Sci. Technol. A*, 19, 2197 (2001)

[3] J. Tennyson, D. B. Brown, J. J. Munro, I. Rozum, H. N. Varambhia and N. Vinci, *J. Phys.: Conf. Ser.*, 86, 012001 (2007)

[4] R. J. Hoekstra, M. J. Grapperhaus, and M. J. Kushner, *J. Vac. Sci. Technol. A* 15, 1913 (1997)

2:40pm **PSI-ThA3 Gas/Ion Temperatures in Multi-Frequency Capacitively Coupled Plasma Sources**, *A. Agarwal, S. Rauf, K. Collins*, Applied Materials Inc.

Plasma etching of high aspect ratio (HAR) features is extremely challenging as it places great emphasis on uniformity of just about every characteristic of the plasma: density, fluxes, fields, energy and angular distributions to mention a few. At large aspect ratios, even minor variations in the bulk plasma can translate into huge deviations on the feature scale. One important plasma characteristic that influences etch properties is the ion

temperature. Small variations in ion temperature can lead to non-uniform or tapered etch profiles since even marginally cold ions when accelerated through the sheath (having large voltage drops for HAR process) can deviate significantly from the normal leading to offset of the bottom of the feature compared to the top.

In this work, a 2/3 dimensional plasma equipment model (CRTRS) [1] has been used to assess the consequences of ion and neutral temperature on etching processes. CRTRS previously only included continuity and momentum equations for charged species. The model has been improved to include solution of the energy equations for all heavy neutral and charged species to obtain the ion and neutral temperatures. The model results have been validated using experimental data from laser induced fluorescence measurements.[2] In this talk, results of this validation exercise will be discussed. We found that while ion temperatures peak in the sheath region near the electrodes under the influence of high electric fields, neutral radicals' temperature peak predominantly in the bulk via collisions with ions (for example, charge exchange reactions). Consequently, inclusion of Franck-Condon heating sources is important for low fragmenting gas mixtures such as pure Ar compared to, for example, N₂ to accurately predict neutral temperatures.

The validated model is then applied to a typical high-power HAR etch process. Modeling results are used to understand the impact of gas and ion temperatures on electron heating and power deposition mechanisms, ion energy and angular distributions, plasma uniformity and neutral radical composition. Plasma characteristics are investigated for etch-relevant feed gas mixtures over a wide range of pressures (20 – 100 mT).

¹ A. Agarwal, P.J. Stout, S. Rauf and K. Collins, 56th AVS Symposium 2009.

² G.A. Hebner and A.M. Paterson, *Plasma Sources Sci. Technol.* 19, 015020 (2010).

3:00pm **PSI-ThA4 Control of Electron Energy Distributions in Pulsed Capacitively Coupled Plasmas Sustained in Noble and Electronegative Gas Mixtures**, *S.-H. Song, M.J. Kushner*, University of Michigan, Ann Arbor

In capacitively coupled radio frequency (rf) discharges, as used in plasma processing of semiconductor materials, controlling the electron energy distribution function $f(\epsilon)$ is important for controlling the flux of radicals and ions to the substrate. The strategies for controlling $f(\epsilon)$ include varying the gas mixture, frequency, pressure and pulse power format. Customizing the $f(\epsilon)$ is related to balancing the electron heating and cooling mechanisms. Multi-frequency capacitively coupled plasmas (CCPs) provide an opportunity to customize $f(\epsilon)$ through using pulsed plasmas. For example, a low frequency (LF) is typically applied to the lower electrode to control ion energy distributions and a high frequency (HF) is applied to the upper electrode to heat electrons. By pulsing the HF one can modulate $f(\epsilon)$ to produce shapes that are not otherwise attainable using continuous wave excitation. For example, an $f(\epsilon)$ may be produced that has both a high energy tail and a large thermal component. These $f(\epsilon)$ will produce different dissociation patterns in the feedstock gases. The choice of pressure, duty cycle and pulse repetition frequency (PRF) are important to the time average $f(\epsilon)$ as these determine the relative role of thermalization. Pressure also has a role in determining the dominant electron heating mechanism between ohmic heating and stochastic heating.

The customization of $f(\epsilon)$ in 2-frequency CCPs will be discussed using results from a 2-dimensional plasma equipment model. The electron $f(\epsilon)$ are obtained using a Monte Carlo simulation including electron-electron collisions. The consequences of PRF, duty cycle and HF power on $f(\epsilon)$ will be discussed for pressures of tens of mTorr in argon and fluorocarbon gas mixtures. The correlation between these parameters and $f(\epsilon)$ on the identity of radical and ion fluxes onto the substrate will be made.

* Work supported by the Department of Energy Office of Fusion Energy Sciences and the Semiconductor Research Corp.

3:40pm **PSI-ThA6 Impact of Frequency Mixing on Plasma Characteristics in Low Pressure Capacitively Coupled Discharges**, *J.A. Kenney, S. Rauf, K. Collins*, Applied Materials Inc.

As high aspect ratio (HAR) etch requirements have grown more stringent, the strategies used to deliver an appropriate combination of species to the wafer have evolved considerably. One common approach is to use a capacitively coupled plasma (CCP) reactor with a combination of generator frequencies and complex feed gas mixtures. The use of multiple frequencies allows for generation of a large plasma density using a high frequency source while biasing the wafer substrate at low frequency to control the flux and energy of impinging ions. Complex feed gases provide etch precursors from which to make volatile products as well as passivating species to protect certain features (e.g. sidewalls). Such a large parameter space of frequencies, powers, pressures, and feed gases to employ, however, has

made modeling an increasingly attractive option to gain insight and understanding, both during engineering design and process development. Here, we use a plasma model to investigate the impact of frequency mixture in low pressure capacitively coupled discharges.

In our 2/3-dimensional fluid plasma model, charged species densities are computed by solving continuity equations for all species coupled with the full momentum equation (ions) or the drift-diffusion approximation (electrons). These equations, combined with the Poisson equation, which governs the electrostatic fields, are solved implicitly in time. The electron temperature is determined by solving the electron energy equation. The model also includes the full set of Maxwell equations in their potential formulation, Kirchhoff equations for the external circuit, and continuity equations for neutral species, along with non-uniform mesh generation to better resolve regions of interest. Ion energy and angular distributions are computed using a Monte Carlo-based particle simulation, which uses the spatially and temporally-resolved species densities, species fluxes, and electric fields from the plasma model as inputs.

In this work, we look at the impact of multiple frequencies on plasma density, uniformity, fluxes of neutrals and ions, and ion energy distributions. We consider frequencies in the range of 1 to 150 MHz in single-, dual-, and three-frequency configurations in CCP systems using a simple etch-relevant feed gas mixture (Ar/CF₄) at 20 mT. Radio-frequency (RF) bias powers in the 1.0 – 7.0 kW range are employed.

4:00pm **PS1-ThA7 Predicting the Surface Response Upon Simultaneous Plasma Etching and Deposition**, *N.P. Marchack, C. Pham, J. Hoang, J.P. Chang*, University of California Los Angeles

As the downscaling of integrated circuit devices continues, minute variations in the feature profiles from processing techniques such as plasma etching significantly affect device performance. Thus, there is a need to predict the surface response during etching of a variety of materials, such as complex oxides. To accurately represent the kinetics involved, experiments are conducted in this work in an inductively coupled plasma (ICP) reactor equipped with a quadrupole mass spectrometer (QMS) for analyzing etch products and a quartz crystal microbalance (QCM) for measuring the etch rate *in situ*. This reactor is connected to a UHV transfer tube which allows the surface composition to be studied via x-ray photoelectron spectroscopy (XPS) without exposure to ambient conditions. The materials system studied include Hf-based high-k materials and YMnO₃, a multiferroic oxide, etched in Cl₂/BCl₃ plasmas. A surface site-based phenomenological model¹ that was previously developed for binary and ternary oxides is shown to be applicable to the prediction of how these complex oxides were etched. To use this model in a cell based Monte Carlo simulator to predict feature profile evolution, a translated mixed layer (TML) kinetics model² is utilized to describe the surface reactions such as ion impingement, neutral adsorption, physical sputtering and chemically enhanced ion etching. Reaction parameters that cannot be measured directly are extracted by comparing the model to etch yield data and validated against the phenomenological model. Ion incident angle dependence and an elliptical energy deposition model were used to capture the effects of surface morphology on the profile evolution under the bombardment of energetic and directional ions. Simulated profiles are compared to cross-sectional SEM images of the patterned material systems and display reasonable agreement.

¹ Martin et al. Journal of Vacuum Science and Technology A 27(2) 2009

² Kwon et al. Journal of Vacuum Science and Technology A. 24(5) 2006

4:20pm **PS1-ThA8 Computational Modeling of DC and Pulsed Microplasmas-Based Space Propulsion Devices**, *L. Raja*, The University of Texas at Austin **INVITED**

Very small microplasma-based propulsion is gaining importance as a viable propulsion concept for small satellites that weigh less than 100 kg. These devices involve complex multiple physical phenomena associated with high-density plasma discharge in small volumes and coupling of plasma phenomena with high-speed viscous dominated flows. Specific requirements of minimal wall erosion and wall heat transfer are also driving oscillatory dielectric-barrier microdischarge designs, which introduced additional physics complexity associated pulsed microplasmas. We present computational modeling studies of microplasma propulsion devices. The model describes the plasma dynamics, gas-phase chemical kinetics, neutral dynamics, and coupling of plasma phenomena with high-speed flow for both DC and pulsed mode microdischarges. Unique computational challenges associated with this problem are described and solutions to these challenges as addressed in our model are presented. Results show the dominant mechanism for thruster performance improvement is the gas heating in the microplasma. The gas heating is primarily a result of near-wall ion Joule heating in the case of DC discharges and is also accompanied by significant wall heat loss. The use of dielectric-barrier microdischarge

configuration accompanied by oscillatory excitation is shown to mitigate wall heat loss while sustaining off-wall gas heating.

5:00pm **PS1-ThA10 Feature Profile Simulator FPS-3D**, *P.E. Moroz*, TEL US Holdings

Reliable and predictive feature profile evolution simulation is an extremely important topic for nanotechnology and semiconductor industry. If successfully solved, it will allow significant saving of time and resources presently spent on numerous design experiments directed on finding proper chemistries and conditions in a multi-parameter space of search for advanced etching or deposition. FPS-3D is a Monte Carlo code, where launched particles corresponding to the specified fluxes, each particle typically consisting of many gas molecules, or ions, or electrons, interacts with solid materials of the target. A cellular model is used for presenting solid materials. Each cell is a complex object consisting of the body of the cell and its surface layer, and is typically includes many molecules. All material properties and all reaction mechanisms are specified in the chemistry file. The output of gas and ion reactions is characterized in terms of probabilities and yields. The incoming fluxes could be specified via two different options. One option is to use the flux file, where all the data for fluxes of each gaseous species is provided for each energy-angular bin. This file is typically generated by a plasma simulation code (for example, such as HPEM [1], which we are currently using). A second option is to generate fluxes of species according to a few parameters specified in the input file. The second option is especially convenient for considering interactions of particle beams with solid materials. Upon collision of a flux particle with the target, the code determines a particular cell where the reaction occurs. The result of such an interaction could be a removal of some of molecules from the cell, or deposition of similar or different molecules to the cell, or both. The code considers low-energy gaseous species very differently from the high-energy species. The low-energy species are interacting only with the surface layer of the cell by mainly depositing or altering molecules in the surface layer, although spontaneous etching from the surface layer is taken into account as well. The energetic species, on the other hand, could do much more. They could also lead to removal of molecules from the surface layer and from the body of the cell with the yield corresponding to their energy and angle of incidence. Such yields could be larger than one for higher energies. This report will present technical details of FPS-3D and give a few examples of its operation in 2D and 3D. The author is thankful to Drs. S.-Y. Kang of TEL TDC and P. Miller of HFS for valuable discussions.

[1] M.J. Grapperhaus, M.J. Kushner, J. Appl. Phys. 81, 669 (1997).

5:20pm **PS1-ThA11 3D Numerical Modelling of VHF MHC type SiH₄ PECVD for Solar Cells**, *J. Joo*, Kunsan National University, Republic of Korea

Full 3D numerical modelling is done for a VHF (very high frequency > 30 MHz) MHC (multi hollow cathode) based PECVD (plasma enhanced chemical vapor deposition) of Si thin film in tandem or triple junction solar cells. The purpose of VHF-MHC is confining high density plasma into small holes while maintaining large area deposition uniformity. ICP gives high plasma density (> 10E11 #/cm³) but poor uniformity and thin film quality (electron mobility and photo sensitivity) in addition to particle generation issues. For optimization of hole geometry and hole array configurations, numerical models for Ar, H₂, and SiH₄ are developed based on fluid model. CFD-ACE+ is used for calculation of each parameter set. For Ar, 1 Torr and 40 MHz was good enough for confining into a few mm diameter holes, but H₂ needs higher plasma density. SiH₄ needs more complicated plasma chemistry sets including negative ions and higher order silanes. The concentration ratio of SiH₃/SiH₂ was accurately modeled using electron energy distribution function calculation.

Plasma Science and Technology

Room: Galisteo - Session PS2+BI-ThA

Plasmas for Medical and Biological Applications

Moderator: S. Hamaguchi, Osaka University, Japan

2:00pm **PS2+BI-ThA1 Activation of Cell under the Atmospheric Pressure Plasma Irradiation**, *T. Hirata, C. Tsutsui, A. Mori, T. Yamamoto, A. Taguchi*, Tokyo City University, Japan **INVITED**

The researches in the case of “novel plasma” have been widely conducted in the fields of chemistry, solid physics, and nanomaterial science. Such plasma uses a boundary reaction field in a liquid or gaseous-liquid phase based on application of liquid plasma, micro plasma, and atmospheric pressure plasma. In particular, atmospheric pressure plasma is indispensable not only for sterilization, disinfection, decomposition of hazardous

materials, and surface modification but also for the cultivation and development of complex new areas which require a diverse perspective, involving biomedical science. From the above-mentioned background, we are conducting basic experiments on direct irradiation of cells using a micro-spot atmospheric pressure plasma source.

The device is a coaxial structure having a tungsten wire (1 mm I.D.) installed inside a glass capillary (plasma generation area: 8 mm I.D.; tip area: 1 mm I.D.), and a grounded tubular electrode wrapped on the outside. The high voltage for the plasma generation is provided by the high voltage power supply. The conditions of plasma generation are as follows: applied voltage: 5-9 kV, frequency: 1-3 kHz, helium (He) gas flow rate: 1 L/min, and plasma irradiation time: 1-300 sec. The experiment was conducted by preparing a culture medium containing mouse fibroblasts (NIH3T3) on a culture dish (made of polypropylene). A culture dish irradiated with plasma was introduced into a CO₂-incubator.

According to the dependency of cell numbers against the plasma irradiation time, when only He gas was flowed, the growth of cells was inhibited as the floatation of cells caused by gas agitation inside the culture was promoted. On the other hand, there was no floatation of cells and healthy growth was observed when plasma was generated. Therefore, it appears that the interaction due to ion/radical collisions on the culture surface causes a substantial effect on the proliferation of growth factors such as epidermal growth factor (EGF), nerve growth factor (NGF), and transforming growth factor (TGF) that are present in the cells.

2:40pm **PS2+BI-ThA3 Stability of Highly Functionalised Plasma Polymerised Acrylic Acid Thin Films in Aqueous Environments, C.D. Easton, A. Pegalajar Jurado, A. Badri, S.L. McArthur**, Swinburne University of Technology, Australia

Plasma polymerisation provides a convenient one step method for creating a functionalised organic surface on virtually any substrate. This technique has attracted considerable attention in recent years for application within the biomedical field as a substrate for cell culture and as a surface functionalisation for polymer grafting and protein immobilisation [1-4]. Detailed stability studies of these coatings in aqueous solutions have focused on water rather than more biological relevant solutions including phosphate buffered saline (PBS). Critically, the interplay between coating stability and protein and polymer adsorption on the coating behaviours have rarely been examined.

Within this study, highly functionalised acrylic acid thin films have been fabricated via RF plasma polymerisation and the stability of these coatings in aqueous environments examined. The chemical and physical stability of these coatings in water and PBS were investigated using X-ray Photoelectron Spectroscopy (XPS), Atomic Force Microscopy (AFM) and Quartz Crystal Microbalance with Dissipation (QCM-D). The results have shown that the physical behaviour of the coatings changes significantly when they are exposed to water and buffers with differing pH and ionic strength. The significance of these stability observations in an application setting has been explored where the plasma polymerised acrylic acid coating has been used in the assembly of polyelectrolyte layers and biomolecule immobilisation.

References:

- [1] K. S. Siow, L. Britcher, S. Kumar, H. J. Griesser, *Plasma Process. Polym.* **2006**, *3*, 392.
- [2] R. Forch, A. N. Chifen, A. Bousquet, H. L. Khor, M. Jungblut, L. Q. Chu, Z. Zhang, I. Osey-Mensah, E. K. Sinner, W. Knoll, *Chem. Vapor Depos.* **2007**, *13*, 280.
- [3] H. E. Colley, G. Mishra, A. M. Scutt, S. L. McArthur, *Plasma Process. Polym.* **2009**, *6*, 831.
- [4] G. J. S. Fowler, G. Mishra, C. D. Easton, S. L. McArthur, *Polymer* **2009**, *50*, 5076.

3:00pm **PS2+BI-ThA4 Scalable Atmospheric DBD Device for Biomedical Processing, S. Kitazaki, T. Iwao, G. Uchida, K. Koga, M. Shiratani**, Kyushu University, Japan, *N. Hayashi*, Saga University, Japan

Nonthermal atmospheric discharge plasmas have been employed for biomedical processing applications, because they offer low temperature processing [1-3]. We have developed a scalable atmospheric dielectric barrier discharge (DBD) device for biomedical processing in a large area. The device consists of 12 electrodes of a stainless rod of 1 mm in outer diameter and 60 mm in length covered with a ceramic tube of 2 mm in outer diameter. In principle, the device size can be extended to a large area by increasing the electrode length as well as the number of electrodes. The electrodes are arranged parallel with each other at a distance of 0.5 mm. The frequency of applied voltage was 10 kHz, and its peak-to-peak voltage was 10 kV. The peak discharge current was about 0.15 A and the duration of each current pulse was about 10 ns. To obtain information about radicals generated in the discharges, UV-Visible emission spectra were measured

with a multi-channel spectrometer. Spectral lines of N₂ 2nd positive band (280-400 nm) were observed in air DBD discharges. We apply the device to process seeds of radish sprouts. We compare germination and growth of seeds with one minute plasma irradiation to those of seeds without irradiation. While the germination periods of these two kinds of seeds are 2 days, being nearly the same with each other, the growth rate of irradiated seeds is 20-50% faster than that without irradiation. These results suggest that the DBD device is useful for such biomedical processing applications.

- [1] J. Raiser and M. Zenker, *J. Phys. D*, **39**, 3520 (2006).
- [2] M. G. Kong, et al., *New J. Phys.*, **11**, 115012 (2009).
- [3] A. Helmke, et al., *New J. Phys.*, **11**, 115025 (2009).

3:40pm **PS2+BI-ThA6 2010 AVS Medard Welch Award Lecture - Controlling Plasma Sources: Nano to Bio, N.Yu. Babaeva, S.-H. Song**, University of Michigan, Ann Arbor, *J. Shoeb, M. Wang*, Iowa State University, *Y. Yang*, Applied Materials, Inc., *M.J. Kushner**, University of Michigan, Ann Arbor

INVITED

The development of technologies for plasma modification of surfaces is in large part based on controlling plasma sources to deliver desired fluxes of radicals and ions to surfaces. Doing so ultimately rests on the ability to control the energy and velocity distributions of charged and neutral particles. Controlling electron energy distributions, $f(e)$, ultimately specifies the production rates of radicals and ions. Controlling the velocity distributions, $f(v)$, of ions and neutrals ultimately specifies the activation energy delivered to surfaces. There has been an evolution of techniques to control $f(e)$ and $f(v)$ utilizing type of excitation (e.g., ICP vs CCP), frequency, pulse power and, most recently, multiphase plasmas. These techniques are being challenged to provide the specificity required for nano-scale processing, particularly given the synergistic and presently uncontrolled relationship between fluxes into and returning from surfaces. Control of $f(e)$ and $f(v)$ becomes even more challenging in biological applications of plasmas and plasma medicine, typically performed at atmospheric pressure, where timescales for plasma formation are shorter than conventional control techniques can address. In this talk, techniques to control $f(e)$ and $f(v)$ in plasma sources in the context of plasma modification of biological and nano-scale surfaces will be discussed. Examples of control techniques will be taken from using pulsed, multi-frequency and multiphase plasmas. Applications will be discussed from nano-scale cleaning and sealing of porous dielectrics; and dielectric barrier discharge treatment of wounded skin. Challenges facing researchers in developing plasma sources having the ability to control $f(e)$ and $f(v)$ will be discussed.

* Work supported by the Department of Energy Office of Fusion Energy Sciences, Semiconductor Research Corp., Applied Materials, Tokyo Electron., Agilent, Inc.

4:20pm **PS2+BI-ThA8 Spectral Signatures of Amine Species at Aminated Surfaces Prepared by using Plasma Techniques, Self Assembling of Thiols and Silanization, W.E.S. Unger, N. Graf, P.M. Dietrich, H. Min, P.-L. Girard-Lauriault, A. Lippitz, T. Gross**, BAM Federal Institute for Materials Research and Testing, Germany

The determination of amines on surfaces capable of binding biomolecules is important for the understanding and optimization of technologically relevant coupling processes. Different relevant types of amino-functionalized model surfaces have been investigated by complementary tools of surface analysis: XPS, NEXAFS spectroscopy and ToF-SIMS with Principal Component Analysis. Amino-terminated surfaces have been prepared from aliphatic and aromatic aminosilanes and aminothiols by self assembly, plasma polymerization of allyl amine and plasma activated polyethylene foils reacted with 1,2-diaminoethane. The determination of those amino groups which are available to serve as attachment sites for biomolecules in technical applications by wet chemical derivatization (CD) XPS using 3,5-bis(trifluoromethyl)phenyl isothiocyanate was a special issue of interest. In another experiment the in-depth homogeneity of a pulse plasma polymerized allyl amine film after derivatization with 4-trifluoromethyl benzaldehyde (TFBA) was investigated by using variable excitation energy XPS. Finally, effects of aging in air and damage by X ray radiation on aminated surfaces are addressed.

Problems of the CD XPS approach for a determination of amines will be discussed with a focus of comparability of results obtained in different labs.

4:40pm **PS2+BI-ThA9 Correlation of Properties of Polymeric Organic Layers with Plasma Parameters, S. Umrath, F. Schamberger, G. Franz**, Hochschule Muenchen, Germany

For exact deposition of thin films out of the vaporous phase (cvd), an entire knowledge of the process parameters such as flows, pressure and gaseous

* Medard W. Welch Award Winner

temperature is required. In the case of pecvd, this means the extension on influencing plasma variables like plasma density and electron temperature, in particular in large reactors for production purposes to meet the demands for flat layer qualities (growth and composition) over the whole reactor volume.

In an almost cubical reactor 80 l in volume, the microwave power is coupled into the volume via a quartz window which exhibits approximately 1/10 of the sidewall area. The spatial compilation of these plasma quantities along with plasma potential has been accomplished with a bendable Langmuir probe. To isolate the tungsten wire against its grounded housing tube, it was coated with polyarylene. After having compared this construction with our Langmuir probe which has been now in use for more than a decade, we have taken data of the whole reactor with argon and with mixtures of monomers of parylene and argon or oxygen in a pressure range between 10 mTorr and 150 mTorr (1 1/2 Pa to 20 Pa) applying a new evaluation procedure [1]. Over the covered range, the plasma density remains in the dielectric regime (plasma degree less than 100 ppm).

Compared to discharges through pure argon, the plasma parameters exhibit opposing behavior: at same discharge pressure and power input, the plasma density is lower, whereas the electron temperature goes up. The layers are highly transparent with a slightly yellow color. Ftir measurements reveal that the ring structure still remains intact. Adding oxygen to the ambient to the monomeric vapor leads to hydrophilic surfaces which is caused by the formation of CO bonds and OH bonds. The creation of these features is confined by power input. If it is raised beyond 4 W/l, the reaction mechanism drastically changes from surface polymerization to volume polymerization leading to thick, low-density films which can be easily be scratched away. This change has been traced by plasma diagnostics and mass spectrometry. At a threshold density of about $1 \times 10^{10} \text{ cm}^{-3}$ (plasma degree about 1000 ppm), all peaks beyond 44 (CO_2) vanish. In the resulting mass spectrum, no CH vibrations beyond 3000 cm^{-1} can be detected indicating the complete destruction of the aromatic system.

[1] Peter Scheubert: Modelling and Diagnostics of Low Pressure Plasma Discharges, PhD thesis, Bochum, 2002

Surface Science

Room: Picuris - Session SS-ThA

Environmental Interfaces

Moderator: H. Fairbrother, Johns Hopkins University

2:00pm **SS-ThA1 Environmental Interfaces: Where the Vacuum, Cleanliness, and Size Gaps Must Be Minimized.** *G. Brown, Jr.*, Stanford University, *S. Yamamoto*, University of Tokyo, Japan, *T. Kendelewicz*, Stanford University, *J. Newberg*, *H. Bluhm*, *M. Salmeron*, Lawrence Berkeley National Laboratory, *A. Nilsson*, Stanford Synchrotron Radiation Lightsource, *Y. Wang*, *M. Michel*, Stanford University, *Y. Choi*, *P. Eng*, University of Chicago, *J. Ha*, University of California at Berkeley, *A. Spormann*, Stanford University

INVITED

Environmental interfaces come in many varieties, including solid-water, solid-gas, solid-microbial biofilm-water, solid-organic film-water, etc., and they exist under a variety of conditions, none of which involve UHV. In addition, the solids involved in environmental interfaces are often in the nanoparticle size range, which may result in properties, such as surface structures and reactivities, that differ from their bulk counterparts. Another common complication is that the surfaces of environmental solids are often coated by natural organic matter and/or microbial biofilms, which could have dramatic effects on their surface charge properties, extent of aggregation, and reactivity. In contrast, most surface science studies involve clean single crystal surfaces on which metals, molecules, or organic molecules are attached under carefully controlled conditions, typically involving UHV. In order to increase our understanding of the chemical and biological processes at environmental interfaces, the pressure, cleanliness, and size gaps must be overcome to the extent possible in surface science studies. We will discuss recent near-ambient pressure XPS studies of the interfaces between alpha-Fe₂O₃ (0001) and water and Fe₃O₄ and water, which have revealed the extent of dissociation of water and hydroxylation of these surfaces. We will also present the results of new x-ray standing wave fluorescence yield spectroscopy studies of the interaction of aqueous metal ions with alpha-Fe₂O₃ nanoparticles coated by polyacrylic acid and natural organic matter thin films as well as with microbial biofilm-coated single crystal metal oxides. The results of these studies have revealed that the intrinsic order of reactivities of different metal oxide surfaces coated by organic matter or microbial biofilms is not affected by the coatings. However, time-dependent studies have shown that the rates of partitioning of metal ions between aqueous solutions and metal oxide surfaces are diffusion controlled. Finally, we will discuss differences in surface

structures of nanoparticulate (avg. diameter = 10 nm) vs. microparticulate (avg. diameter = 550 nm) of alpha-Fe₂O₃ derived from XAFS spectroscopy studies of Zn(II) ions sorbed on the particle surfaces.

2:40pm **SS-ThA3 Ion Segregation and Deliquescence of Alkali Halide Nanocrystals on SiO₂ Revealed by Scanning Polarization Force Microscopy.** *K. Arima*, Osaka University, Japan, *P. Jiang*, Lawrence Berkeley National Laboratory, *D.-S. Lin*, National Tsing Hua University, Taiwan, Republic of China, *A. Verdaguer*, CSIC-ICN, Spain, *H. Bluhm*, *M. Salmeron*, Lawrence Berkeley National Laboratory

The adsorption of water on alkali halide (KBr, KCl, KF, NaCl) nanocrystals on SiO₂ and their deliquescence was investigated as a function of relative humidity (RH) from 8% to near saturation by scanning polarization force microscopy (SPFM). SPFM is a noncontact AFM operation mode based on electrostatic forces, which gives two images (topographic image modulated by a local dielectric constant and surface potential image) simultaneously. At low humidity water adsorption solvates ions at the surface of the crystals and increases their mobility. This results in a large increase in the dielectric constant, which is manifested in an increase in the electrostatic force and in an increase in the apparent height of the nanocrystals. Above a critical RH (58% RH in the case of KBr nanocrystals) the diffusion of ions leads to Ostwald ripening, where larger nanocrystals grow at the expense of the smaller ones. At the deliquescence point droplets were formed. For KBr, KCl and NaCl, the droplets exhibit a negative surface potential relative to the surrounding region, indicative of the preferential segregation of anions to the air-solution interface. We will also show spectra obtained by ambient pressure X-ray photoelectron spectroscopy to complement the SPFM results.

3:00pm **SS-ThA4 Investigation of H/D Exchange in Water Layers on Hydrophilic/Hydrophobic Organic Surfaces.** *N.M. Barrentine*, *R.L. Grimm*, *J.C. Hemminger*, University of California, Irvine

Water interactions with organic surfaces are of great importance to chemistry in the environment as well as a variety of device manufacturing and performance issues. We have carried out studies of the interaction of D₂O with organic surfaces as a function of the hydrophilic/hydrophobic nature of the surface. Temperature programmed desorption (TPD) experiments are used to follow the strength of the interaction of adsorbed D₂O with the surface and to follow the extent of H/D exchange that occurs on the surface. Self-assembled monolayers (SAM) of alkanethiols on Au(111) surfaces are used as a highly characterized organic surface. Hydrophilic SAMs are generated using 6-mercapto-1-hexanoic acid (HSC₆H₁₀COOH) on Au(111). Similarly, hydrophobic SAMs are generated using 1-octanethiol (HSC₇H₁₄CH₃). TPD experiments were carried out following adsorption of D₂O on the SAM surface at a temperature of 120 K. H/D exchange was observed by simultaneously monitoring m/z = 20 (D₂O⁺), 19 (HDO⁺), and 18 (OD⁺ and H₂O⁺) in the TPD experiments. Our experiments showed an increase in the m/z 19/20 ratio for experiments with the hydrophilic SAM in comparison to the hydrophobic SAM, indicative of H/D exchange with the acidic proton of the 6-mercapto-1-hexanoic acid SAM. Results will also be presented for mixed hydrophilic/hydrophobic monolayers as a function of the hydrophilic/hydrophobic ratio.

3:40pm **SS-ThA6 Photochemistry of O₂ on Reduced Rutile TiO₂(110).** *G.A. Kimmel*, *N. Petrik*, Pacific Northwest National Laboratory

We investigate the adsorption and photon-stimulated reactions of O₂ on reduced, rutile TiO₂(110). After adsorption at 28 K and annealing to 100 K, at least 85% of the O₂ has not dissociated. Typically, less than 50% of this molecularly adsorbed O₂ desorbs via hole-mediated reactions during irradiation with ultraviolet (UV) photons. However, UV irradiation dissociates ~20 – 45 % of the chemisorbed O₂, which we propose to occur through electron attachment reactions. In addition, weakly bound (physisorbed) O₂ readily reacts with chemisorbed O₂ during UV irradiation. A simple model based on the oxygen coverage and the charge of the chemisorbed oxygen, which accounts for the observations, is presented. These results show that the photochemistry of oxygen on TiO₂(110) is both diverse and more complicated than previously appreciated.

4:00pm **SS-ThA7 Pentagons and Heptagons in the First Water Layer on Pt(111).** *S. Nie*, *P.J. Feibelman*, *N.C. Bartelt*, *K. Thürmer*, Sandia National Laboratories

We present STM observations of the first layer of water on Pt(111). Because scanning parameters typically used for high-resolution imaging can easily disturb the fragile water layer, acquiring images is particularly challenging. Nonetheless, employing an extremely small tunneling current, we were able to extract enough structural detail to decipher how individual water molecules arrange themselves.

At a growth temperature of 140K, we found large regions consisting of the $\sqrt{37}$ and $\sqrt{39}$ phases previously observed in diffraction experiments [1]. The

main characteristic of both are triangularly-shaped regions, which appear as depressions in STM. The triangles are embedded in a hexagonal lattice of water molecules, which, remarkably, is rotated by approximately 30° relative to the $\sqrt{3}\times\sqrt{3}$ -R30° structure that is the usual starting point for discussions of ice films. We propose that the triangular regions consist of a central hexagon of water molecules surrounded by alternating pentagons and heptagons. Twelve water molecules in the center of this (“575757” di-interstitial) defect lie approximately flat, with O atoms directly atop Pt atoms. Elsewhere, the water molecules lie “H-down,” i.e., with an H atom beneath the O. Image simulations based on DFT calculations are consistent with this non-conventional model.

The dramatic structural differences between the $\sqrt{39}$ phase and 3-D ice consisting of stacked unrotated classic bilayers suggests that 3-D islands do not grow on top of the wetting layer, rather the wetting-layer molecules substantially rearrange when 3-D ice nucleates.

This work was supported by the DOE Office of Basic Energy Sciences, Division of Materials Sciences and Engineering under contract DE-AC04-94AL85000.

[1] For example, A. Glebov, A. P. Graham, A. Menzel and J. P. Toennies, *J. Chem. Phys.* **106**, 9382 (1997).

4:20pm **SS-ThA8 Wetting Monolayer Structure on Metals, P.J. Feibelman, N.C. Bartelt**, Sandia National Laboratories

The $\sqrt{37}$ and $\sqrt{39}$ rotated H₂O-molecule adlayers that form at low T on Pt(111) have been a mystery since 1997. [1] Their structures must optimize among : 1) forming as many H-bonds as possible, 2) allowing the maximum number of H₂O's to lie flat, with O-atoms in atop sites, and 3) minimizing strain in bond lengths and angles. But, 1) rules out vacancy structures, 2) begs why rotation, leaving few O atoms in atop sites, would be preferred, and 3) is troublesome in the models proposed in Ref. 1, given their areal compression relative to ordinary ice.

Haq, et al. spun off a clue in an effort to interpret a spectroscopically observed metastable water monolayer on Ru(0001). Flat-lying molecules that have each other as neighbors can lie closer to the metal than in the conventionally imagined “ice-like” adlayer, where adjacent molecules’ dangling H-bonds force the flat molecules up. [2] Thus, they proposed a water layer on Ru(0001) comprising chains of flat H₂O molecules separated by molecules whose dangling H-bonds point toward the metal. Elaborating, we find that a *checkerboard* of compact flat-lying and H-down phases is even somewhat better bound, and this, together with new, telling STM images, has led us to plausible, low-energy structures for water on Pt(111).

STM images of these structures show $\sqrt{37}$ and $\sqrt{39}$ arrays of dark triangles separated by ribbons of H₂O-molecule hexagons. [3] We assign the triangles to di-interstitial molecular “defects,” wherein six flat-lying H₂O's, with O atoms $\sim 2.2\text{\AA}$ directly atop Pt's, anchor the water layer to the metal. In DFT calculations, these “defect” structures, containing three 5-member and three 7-member rings of H₂O molecules, have lower energy than any purely hexagonal mesh. A competing explanation of the dark triangles as vacancy islands [4] is significantly less bound, because of its many dangling bonds. Remarkably, analogous 555777 structures on Ru(0001), never observed, are better bound than any purely hexagonal structure tried to date.

[1] A. Glebov, et al., *J. Chem. Phys.* **106**, 9382(1997).

[2] S. Haq, et al., *Phys. Rev. B* **73**, 115414 (2006).

[3] S. Nie, et al, unpublished.

[4] S. Standop, et al., unpublished.

*Work supported by the DOE Office of Basic Energy Sciences, Div. of Mat. Sci. and Eng., under contract DE-AC04-94AL85000.

4:40pm **SS-ThA9 Experimental Evidence for Mixed Dissociative and Molecular Adsorption of Water on a Rutile TiO₂(110) Surface without Oxygen Vacancies, L.E. Walle, A. Borg**, Norwegian University of Science and Technology, P. Uvdal, Lund University, Sweden, A. Sandell, Uppsala University, Sweden

Rutile TiO₂(110) has for many years been regarded as the benchmark surface for fundamental studies of metal oxide surface chemistry. Since water is an integral part of the environment, the H₂O/TiO₂(110) system has received more attention than any other comparable system [1,2]. While the dissociation of water on the oxygen deficient TiO₂(110) surface has been characterized in detail, there is as of yet no consensus reached between experimentalists and theorists regarding a very fundamental question: Does water dissociate upon adsorption on the defect-free TiO₂(110) surface?

We have studied the interaction of water with the rutile TiO₂(110) surface using synchrotron radiation photoemission at beamline D1011 at the MAX-

lab synchrotron radiation source, and in this contribution we demonstrate that O 1s spectra recorded at grazing emission angle at optimized photon energy in conjunction with valence spectra allow for the observation of OH on the surface even when substrate oxygen is present. The surface was prepared free from oxygen vacancies following the recipe in ref. [3].

Here we find evidence for mixed molecular and dissociative water adsorption at monolayer coverage on the rutile TiO₂(110) surface free from oxygen vacancies. At monolayer coverage the OH:H₂O ratio is close to 0.5 and reducing the coverage by heating yields an increased OH:H₂O ratio. At room temperature neither species originating from the monolayer on the defect free surface can be detected. The OH species of the monolayer hence recombines and leaves the surface at much lower temperatures than OH formed by water dissociation on oxygen vacancies.

References

U. Diebold, *Surf. Sci. Rep.* **48**, 53 (2003).

C. L. Pang, R. Lindsay, and G. Thornton, *Chem. Soc. Rev.* **37**, 2328 (2008).

S. Wendt, P. T. Sprunger, E. Lira, G. K. H. Madsen, Z. Li, J. Ø. Hansen, J. Matthiesen, A. Blekinge-Rasmussen, E. Laegsgaard, B. Hammer, and F. Besenbacher, *Science* **320**, 1755 (2008).

5:00pm **SS-ThA10 Atomic Scale Study of Surface Corrosion and Wet Oxidation of Cu(110) Surface by Water, B.-Y. Choi**, Lawrence Berkeley National Laboratory, Y. Shi, University of California, Berkeley, M. Salmeron, Lawrence Berkeley National Laboratory

Dissociated water molecules are at the origin of corrosion and wet oxidation of metals. An atomic scale research is necessary to understand the processes involved in many material industries and the environment science. We investigate the steps leading to corrosion and wet oxidation of Cu(110) surface due to adsorption and dissociation of water molecules using scanning tunneling microscopy. Water is dissociated at 150K and seems to form H₂O-OH mixed chain structures along the [110] direction. Growth of a single atomic Cu wire is observed nucleating at the step edges, along with the mixed water chain at high temperature around 180K. The strong bond between hydroxyl molecules and Cu produces the nonvolatile molecule-metal combined structure which is the alternating stripe of them. Further annealing the substrate over 300K dissociates water molecules to leave oxygen atoms on a surface, which form single atomic rows of Cu-O along the [001] direction. This allows us to analyze the initial steps of wet oxidation of Cu at the atomic scale. The results provide fundamental views of the water related surface chemistry of Cu, with applications to surface engineering of copper-based electrode and catalyst.

Thin Film

Room: Ruidoso - Session TF-ThA

Multifunctional Thin Films and Characterization

Moderator: J.M. Fitz-Gerald, University of Virginia

2:00pm **TF-ThA1 Structural and Dielectric Properties of Epitaxial BiFeO₃:BiMnO₃ Nanocomposite Films on Flexible Hastelloy, J. Xiong, J. Zhai, V. Matias, G. Zou, M. Zhuo, Y. Zhang, D.T. Trugman**, Los Alamos National Laboratory, B. Tao, Y. Li, University of Electronic Science and Technology of China, J. Driscoll, University of Cambridge, UK, Q. Jia, Los Alamos National Laboratory

Growth of multifunctional thin films on flexible substrates is of great technological significance since such a platform is needed for the fabrication of flexible electronics. In this study, we report the growth of nanocomposite (BiFeO₃)_{0.5}:(BiMnO₃)_{0.5} [BFO:BMO] films on polycrystalline hastelloy. To grow epitaxial BFO:BMO films on polycrystal substrates, we have used a template consisting of biaxially aligned TiN seed layer deposited by ion-beam-assisted deposited (IBAD) and a La_{0.7}Sr_{0.3}MnO₃ (LSMO) buffer layer deposited by pulsed laser deposition. It should be noted that LSMO is used not only as a buffer layer but also as the bottom electrode of the nanocomposite dielectric films. Microstructural characterization by X-ray diffraction and transmission electron microscopy showed that the nanocomposite thin films were epitaxy with orientation relations of (001)_{BFO:BMO}||[(001)_{LSMO}](001)_{TiN} and [100]_{BFO:BMO}||[100]_{LSMO}||[100]_{TiN}. Electrical measurements indicated good dielectric and ferroelectric properties which are comparable to that reported for ferroelectric films on single crystal substrates.

2:20pm **TF-ThA2 Comparison of Ion Beam and Magnetron Sputtered Vanadium Oxide Thin Films**, *O.M. Cabarcos, B.D. Gauntt, J. Li*, The Pennsylvania State University, *S. Antrazi*, 4Wave Inc., *E.C. Dickey, D.L. Allara, M.W. Horn*, The Pennsylvania State University

Uncooled Infrared (IR) focal plane arrays are an enabling technology for both military and commercial high sensitivity night vision cameras. The IR imaging is accomplished using MEMS microbolometers fabricated on read-out integrated circuits (ROIC's) and depends critically on the material used to absorb the incoming IR radiation. A typical detector works by monitoring changes in the electrical resistance of the detector material as it absorbs the radiation. Thus, suitable detector materials must exhibit a large temperature coefficient of resistance (TCR) and low noise characteristics to efficiently detect IR photons while also maintaining compatibility with standard IC processing. The most commonly used material in uncooled infrared imaging detectors is vanadium oxide deposited by reactive ion beam sputtering. Here we present a comparison of vanadium oxide thin films grown via reactive ion beam sputtering to films grown using reactive pulsed DC magnetron sputtering. Films deposited using both methods were optically and structurally characterized using Raman spectroscopy, transmission electron microscopy, atomic force microscopy, grazing incidence X-ray diffraction and Rutherford backscattering spectroscopy. Electrical properties of the films were also measured and were found to be very sensitive to the deposition conditions used. The ion beam sputtered films were determined to contain twinned FCC VOx nanocrystals with sub-nanometer scale twin spacing, in the form of large 10-20 nm wide columnar/conical grains. In contrast, the magnetron sputtered films consisted of equiax grains of FCC VOx (5-10 nm) encapsulated in an amorphous matrix. Subtle differences in composition and structure could also be determined from the Raman spectra of the films. These differences in microstructure and composition were then correlated to the measured resistivities and TCRs of the films.

2:40pm **TF-ThA3 Mapping Li-ion Diffusion on the Nanoscale in Thin Film Battery Materials**, *S.V. Kalinin*, Oak Ridge National Laboratory
INVITED

The electrochemical energy storage systems based on Li-based insertion and reconstitution chemistries are a vital aspect of energy technologies. Despite the wealth of device-level and atomistic studies, little is known on the mesoscopic mechanisms of ion diffusion and electronic transport on the level of grain clusters, individual grains, and extended defects.

The development of the capability for probing ion transport on the nanometer scale is a key to deciphering complex interplay between structure, functionality, and performance in these systems. Here we demonstrate how Scanning Probe Microscopy can be utilized to measure Li-ion mobility based on the strong strain-bias coupling in the system when local Li concentrations are changed by electrical fields. The imaging capability, as well as time- and voltage spectroscopies analogous to traditional current based electrochemical characterization methods are developed. The reversible intercalation of Li and mapping electrochemical activity in LiCoO₂ is demonstrated, illustrating higher Li diffusivity at non-basal planes and grain boundaries. In Si-anode device structure, the direct mapping of Li diffusion at extended defects and evolution of Li-activity with charge state is explored. The electrical field-dependence of Li mobility is studied to determine the critical bias required for the onset of electrochemical transformation, potentially allowing reaction and diffusion processes in the battery system to be separated at each location. The Scanning Probe Microscopy measurements are compared with classical characterization methods such as cyclic voltammetry and electrochemical impedance spectroscopy. The prospects of Scanning Probe Microscopy for battery characterization are discussed.

This material is based upon work supported as part of the Fluid Interface Reactions, Structures and Transport (FIRST) Center, an Energy Frontier Research Center funded by the U.S. Department of Energy, Office of Science, Office of Basic Energy Sciences under Award Number ERKCC61. Part of work is performed as a user proposal in the Center for Nanophase Materials Sciences at ORNL.

3:40pm **TF-ThA6 Composition and Intermixing at the LaAlO₃/SrTiO₃ Interface by Rutherford Backscattering Spectrometry**, *S.V. Shutthanandan, A. Cohen, L. Qiao, S.A. Chambers*, Pacific Northwest National Laboratory

There is a strong and growing interest in complex oxide interfaces because of the wide range of functional properties exhibited. It is well known that the LaAlO₃/SrTiO₃ (LAO)/(STO) interface exhibits novel electronic conductivity when grown in certain ways. LAO and STO are both band insulators in the bulk, but their interface exhibits n-type electrical conductivity when LAO is grown on TiO₂-terminated STO. Rutherford backscattering spectrometry (RBS) was used to determine interface composition in several pulsed laser deposition (PLD) grown LAO/STO samples prepared at leading laboratories. RBS data collected on these

samples clearly show that La diffuses deep into the STO substrate. The clear presence of a shoulder between the low energy side of the La peak and the high energy side of the Sr peak suggests La indiffusion, although this shoulder could also be caused by pulse pile up in the detector, straggling, and/or multiple/dual scattering effects. Therefore, RBS data were taken as a function of beam current, incident beam energy, and film thickness to determine if this shoulder is due to these artifacts, or La indiffusion. It was determined that none of the aforementioned artifacts occur, thereby implicating La indiffusion. The presence of substitutional La at Sr sites in the substrate provides a plausible explanation for the observed n-type conductivity, as La is a shallow donor in STO.

4:00pm **TF-ThA7 Low Work Function CsI Coatings for Enhanced Field Emission Properties**, *P.T. Murray*, University of Dayton, *T.C. Back, S.B. Fairchild*, Air Force Research Laboratory

The use of CsI coatings on graphite fiber cathodes has been shown to reduce the field strength required for field emission from approximately 10⁴ V/cm to 250 V/cm. Interestingly, the mechanism for enhanced field emission is poorly understood. We have explored the enhancement mechanism by using simulated cathode structures consisting of CsI films deposited (by thermal evaporation and by pulsed laser deposition) onto graphite and Si surfaces; the films were characterized by x-ray photoelectron, Auger electron, ultraviolet photoelectron, and electron energy loss spectroscopy. Two aspects of the enhancement mechanism have been explored. The first, cathode conditioning, was addressed by characterizing the surfaces of CsI-coated cathodes and (stainless steel) anodes before and after conditioning. The results allow us to assess the change in cathode surface chemistry as well as the extent to which material is transferred between electrodes during conditioning. The second aspect concerns the reported observation that CsI coated cathodes, after use, exhibit the disappearance of I and the appearance of a coating that appears to have wetted the cathode surface. We hypothesize that I depletion leaves behind a film of Cs which, with its low melting point, will flow during cathode operation. To test this hypothesis, we have characterized I depletion from CsI by carrying out electron and photon stimulated desorption from CsI surfaces. The talk will conclude with a discussion of our findings and their relevance to the enhancement mechanism.

4:20pm **TF-ThA8 Characterization of SiO₂ Thin Films Prepared by Pulsed Electron Deposition**, *V.C. Rincon, S. Kotru, H.V. Nampoori, M. Chen, R.M. Frazier*, The University of Alabama

Pulsed Electron Deposition (PED) is an ablation-based physical vapor deposition technique similar to Laser Deposition (PLD), where electrons are used as the ablation source. Silicon dioxide is a material which is extensively used by the microelectronic industry and also finds various applications as insulators, protective layers, antireflection coatings etc. There are many different techniques as thermal oxidation of silicon, low pressure chemical vapor deposition (LPCVD), plasma enhanced chemical vapor deposition (PECVD), to grow SiO₂. This work presents growth of thin films of SiO₂ deposited on Si (100) using PED. Films were deposited at oxygen pressure of 4.1mTorr and a pulse frequency of 3 Hz. Substrate temperature was varied from RT- 850 °C, along with varying the source's voltage in the range of 18-12 KV. Characterization tools such as ellipsometry, FTIR and AFM were employed to study the dependence of optical constants and roughness on the quality of SiO₂ films.

4:40pm **TF-ThA9 Growth and Characterization Studies of CdS_{1-x}Se_x (0.0 ≤ x ≤ 1.0) Alloy Thin Films by Spray Pyrolysis**, *E. Masumdar, Rajarshi Shahu Mahavidyalaya, India*

The n-CdS_{1-x}Se_x thin films of variable composition have been deposited on amorphous glass and FTO coated glass substrates by simple and cost effective spray pyrolysis technique. The various deposition parameters have been optimized by using photoelectrochemical technique. The structural, surface morphological, compositional, optical and electrical properties have been studied. The X-ray diffraction studies indicated that all the films are polycrystalline in nature with hexagonal structure irrespective of the composition. The lattice parameter 'a' and 'c' varies from 4.1034 to 4.2615Å and 6.6664 to 6.9243 Å respectively with change in composition parameter from x = 0.0 to x = 1.0. Polycrystalline texture with nearly smooth surface and clearly defined grains has been observed for all samples from scanning electron microscopy (SEM). EDAX studies confirmed that CdS_{1-x}Se_x films have approximately same stoichiometry both initially and finally. The absorption coefficient 'α' is of the order of 10⁴ cm⁻¹. The optical absorption studies reveal that direct allowed transition with band gap energy between 2.44 and 1.74 eV. It is found that resistivity of the films decreased with increase in 'x' up to 0.8 and further it increases for x = 1.0. Semi-conducting behavior has been observed from resistivity measurements.

Key words: X-ray diffraction; Cadmium compounds; Semiconducting II-VI materials; Optical Properties; Electrical properties.

Corresponding author. Tel.: +919421363009; E-mail address: emasumdar@yahoo.com

5:00pm **TF-ThA10 *In situ* Stoichiometry Control using Reflection-High-Energy-Electron-Diffraction Generated X-rays**, *C. Keenan*, *S. Chandril*, West Virginia University, *T.H. Myers*, Texas State University - San Marcos, *D. Lederman*, West Virginia University

One major challenge in the stoichiometric growth of complex oxides, such as YMnO_3 , is the control of the relative compositions of the constituent materials. Desirable properties of oxide materials, such as ferroelectricity, are highly dependent upon material stoichiometry, making stoichiometry control an important issue. While RHEED (Reflection High Energy Electron Diffraction) analysis is typically used as a qualitative tool, RHEED generated x-rays can be used to give quantitative compositional information. The relative compositions of Y and Mn in MBE grown YMnO_3 samples were studied using the grazing exit x-rays generated by RHEED electrons. Comparing the results with RBS characterization suggested that the technique has the potential for real-time compositional analysis.

This work was funded by the Office of Naval Research (Grant N00014-02-1-0974), the Air Force Office of Scientific Research (MURI grant F49620-03-1-0330), and the National Science Foundation (CIAM-DMR grant 0502825).

Thursday Afternoon Poster Sessions

Biomaterial Interfaces

Room: Southwest Exhibit Hall - Session BI-ThP

Biomaterial Interfaces Poster Session

BI-ThP1 Temperature Gradient Device for Investigation of Cell Detachment from Thermoresponsive Surfaces, M.A. Cooperstein, H.E. Canavan, University of New Mexico

Poly(*N*-isopropyl acrylamide) (pNIPAM) undergoes a phase change in a physiologically relevant temperature range that leads to cell release. Above its lower critical solution temperature (LCST, ~32°C), pNIPAM is relatively hydrophobic, and when grafted to a surface, it takes on a packed conformation. There have been numerous studies on the conformation change of pNIPAM across its LCST. Although it is known how pNIPAM chains tethered to a substrate behave when the temperature is changed, no study has probed the influence of a temperature gradient on the behavior of cells attached to the polymer. In this work, we present the investigation of cell detachment from pNIPAM-grafted surfaces resting on a temperature-gradient device. The polymer was deposited on the surface using plasma polymerization. This deposition technique creates a conformal, sterile film that is compatible with any surface chemistry, including the transparent well plates required for these experiments. Prior to their use for cell culture, it is imperative to characterize the pNIPAM films for film thickness, surface chemistry, and thermoresponse, as the surface characteristics determine cell attachment and detachment. The characterization was performed via interferometry, X-ray photoelectron spectroscopy (XPS), and contact angle measurements. Using a device fabricated in our laboratory, we studied whether there is a gradual progression of cellular detachment from the polymer along the temperature gradient, or if there is an abrupt step-change in the detachment. This work will have valuable insights regarding the optimal temperature for cell detachment from pNIPAM.

BI-ThP2 Protein Resistant Oligo(ethylene glycol) Terminated Self-Assembled Monolayers of Thiols on Gold by Vapor Deposition in Vacuum, L. Kankate, University of Bielefeld, Germany, H. Großmann, Johann Wolfgang Goethe-University, Germany, U. Werner, University of Bielefeld, Germany, R. Tampé, Johann Wolfgang Goethe-University, Germany, A. Turchanin, A. Götzhäuser, University of Bielefeld, Germany

Protein resistant oligo(ethylene glycol) terminated (OEG) self-assembled monolayers (SAMs) of thiols on gold are commonly used for suppression of nonspecific protein adsorption in biology and biotechnology. The standard preparation for these SAMs is the solution method (SM) that involves immersion of the gold surface in an OEG solution. Here we present the preparation of 11-(mercaptoundecyl)-triethylene glycol (HS(CH₂)₁₁(OCH₂CH₂)₃OH) SAMs on gold surface by vapor deposition (VD) in vacuum. We compare the properties of SAMs prepared by VD and SM using X-ray photoelectron spectroscopy (XPS), polarisation modulation infrared reflection absorption spectroscopy (PM-IRRAS) and surface plasmon resonance (SPR) measurements. VD and SM SAMs exhibit similar packing density and show a similar resistance to the nonspecific adsorption of various proteins (bovine serum albumin, trypsin, and myoglobin) under physiological conditions. A very high sensitivity of the OEG SAMs to X-ray radiation is found, which allows tuning their protein resistance. These results show a new path to *in situ* engineering, analysis and patterning of protein resistant OEG SAMs by high vacuum and ultra high vacuum techniques.

[1] L. Kankate, H. Großmann, U. Werner, R. Tampé, A. Turchanin, A. Götzhäuser, *Biointerphases* 5, 30 (2010)

BI-ThP3 Spontaneous Micro-Fluidic Flow Driven by Marangoni Effect, Y.C. Hu, Y.H. Lin, Y.C. Ou, National Applied Research Laboratories, Taiwan, Republic of China

This article presents an innovative new type of micro-fluidic chips; the marangoni effect is used as the driving force of the fluidics, while the fluidics is confined in "Surface tension-confined micro-fluidics" chips for regularly transportation. "Surface tension-confined micro-fluidics" is an open structure micro-fluidic chip, there is no micro-channels, only hydrophobic and hydrophilic coating patterns on the chips to confined fluidic flow. Normally the fluidics is driven by surface tension force, since there is no micro-channels structure, there is no way to use conventional pumps. In this study we propose a initiative driving force source that can be applied in "Surface tension-confined micro-fluidics" chips; low surface energy surfactants (such as alcohol) after atomization is sprayed on local area of the fluidics so that the fluidics surface can render surface energy gradient, according to the marangoni effect liquids with higher surface

energy will attract liquids from lower surface energy area and generate fluidic flow, while the fluidic flow is confined along the hydrophilic pattern channel, with carefully designed patterns one can control the fluidic flow to a designed location. The surfactants spraying nozzle can be moved to any position so that one can easily control the fluidic flow just by simply move the spraying nozzle along the pattern channel. If one want to separate the fluidic flow in to two parts, just move the spraying nozzle to the middle area of the fluidic flow, it will be cut into two parts. By reciprocating oscillate the spraying nozzle one can disturb the fluidics and enhance the mixing efficiency.

This innovative micro-fluidic chip has the following advantages: the process is simple, low cost, easy to integrate and it is easy to use.

BI-ThP4 Printable Biological Ink on Gelatin for Self Crosslinking Wound Dressings, M. Yanez, T. Boland, University of Texas at el Paso

The printable biological ink on gelatin is a biopolymer that could be use in a handheld, portable device, such as a ink jet of printer and become a substrate for advanced wound care. Skin is very affected by when burned, and also by diabetic venous ulcers. Currently, some skin substitutes exist that for treatment of diabetic foot ulcers, but these products are really expensive. Based on this we want to create a low cost wound care material that helps not only people with diabetic foot ulcers and venous leg ulcers, but also with burned skin. We selected sodium alginate because it is a FDA approved carbohydrate that has many applications for tissue regeneration and cell therapy, and it is very compatible with human body. Oxidation of sodium alginate has been investigated to obtained alginate dialdehyde (ADA). Alginate dialdehyde is a fast acting self-crosslinking degradable polymer, when applied over collagen or gelatin. We investigated, the degree of oxidation, the degree of cross-linking and mechanical properties of the materials. The degree of crosslinking was determined by trinitrobenzene sulphonic acid assay maintaining constant ADA concentration in borax or PBS buffer and varying concentration of gelatin in borax or PBS. An increase of the degree of oxidation of sodium alginate, an increase in the cross-linking and a decrease of the gelling time was observed with increasing ADA concentration. We investigated the effect of ADA concentration on viscosity and found that at concentrations of about 10% ADA, the solutions are viscous. We will present data on the use of ADA solution as an ink in a printing device and the effect of printed ADA to cross-link gelatin. In general, control over the concentrations of ADA as well as the spatial dispensing via printing should allow us to generate wound dressings of tunable properties. The use of a portable device makes this solution attractive to low resource settings. Future work will include testing the wound dressing in a small animal model and investigating the effect of adding keratinocytes as well as endothelial cells to the material on healing and wound contraction.

BI-ThP5 Carbohydrate-functionalized Surfaces: Analysis by a Multi-Method Approach, P.M. Dietrich, BAM Federal Institute for Materials Research and Testing, Germany, T. Horlacher, Max Planck Institute of Colloids and Interfaces, Germany, T. Gross, T. Wirth, BAM Federal Institute for Materials Research and Testing, Germany, R. Castelli, Max Planck Institute of Colloids and Interfaces, Germany, A. Lippitz, BAM Federal Institute for Materials Research and Testing, Germany, P.H. Seeberger, Max Planck Institute of Colloids and Interfaces, Germany, W.E.S. Unger, BAM Federal Institute for Materials Research and Testing, Germany

Carbohydrate microarrays formed by hundreds of different sugars, covalently or non-covalently bound, have enabled an emerging field of applications in the last decade, i.e. in diagnostics or high-throughput analysis.[1-5] Saccharide microarrays are valuable tools to investigate interactions with other molecules since many glycans are involved in fundamental biological processes.

Carbohydrate-based microarrays are commonly prepared by covalent attachment of chemically modified saccharides that bind selectively to a functionalized solid support such as gold, glass or polymers. Arrayed structures of spotted sugars can be printed with standard robotic microarray printers.

For future applications a reliable surface chemistry combined with an advanced surface analysis is required for improved microarray qualities and performances.

Herein, we report on the combined XPS, NEXAFS and ToF-SIMS surface analysis of carbohydrate functionalized gold and glass surfaces containing synthetic glycans. Advanced characterization of spot shape, size and chemical composition across a spot surface are provided by surface sensitive methods as ToF-SIMS and XPS, used in their imaging modes.

References

- [1] T. Feizi, F. Fazio, W. Chai, C.-H. Wong, *Curr. Opin. Struct. Biol.* **2003**, 13, 637.
- [2] D. M. Ratner, E. W. Adams, M. D. Disney, P. H. Seeberger, *ChemBioChem* **2004**, 5, 1375.
- [3] S. Injae, P. Sungjin, L. Myung-ryul, *Chem.--Eur. J.* **2005**, 11, 2894.
- [4] J. L. De Paz, P. H. Seeberger, *QSAR Comb. Sci.* **2006**, 25, 1027.
- [5] T. Horlacher, P. H. Seeberger, *Chem. Soc. Rev.* **2008**, 37, 1414.

BI-ThP6 Enzymeless Flow Injection Analysis of 2,4,6-Trichlorophenol Based on Preoxidation by Ammonium Cerium (IV) Nitrate, J.S. Wang, National Applied Research Laboratories, Taiwan, Republic of China

Enzymeless flow injection analysis of 2,4,6-trichlorophenol (2,4,6-TCP) based on preoxidation by ammonium cerium (IV) nitrate is present in this work. A preoxidation scheme is applied for 2,4,6-TCP determination without any enzyme treatment. This preoxidation scheme can provide a determination method with low cost and non-conductive polymerization reaction of 2,4,6-TCP. In proposed scheme, the 2,4,6-TCP is oxidized to 2,6-dichloro-1,4-benzoquinone by ammonium cerium (IV) nitrate and the 2,6-dichloro-1,4-benzoquinone can be detected at low reduction potential. The linear range of 2,4,6-TCP determination was 0.4 to 750 mM with correlation coefficient (R^2) 0.9999 and the estimated detection limit (S/N=3) was 40 nM which were demonstrated by flow injection analysis. Twenty consecutive successive detection of 100 mM 2,4,6-TCP showed the relative standard deviation was 1.56%. Several 2,4,6-TCP structure-like compounds were studied as interferences including 2,4-dichlorophenol, 2-chlorophenol, phenol and 4-aminophenol. No obvious influences were observed. Two water samples which were collected from local farm and pool were adopted as analytical application. The recoveries of two water samples are 105.2% and 107.5%, respectively. An easy operation and enzymeless treatment detection scheme of 2,4,6-TCP is illustrated at this work.

BI-ThP7 Evaluation of Electrochemical Impedance Spectroscopy with an ITO Culture Chip, S.-Y. Hsiao, Instrument Technology Research Center, NARL, Taiwan, Y.-S. Lin, Hungkuang University, Taiwan, Y.-P. Lu, Instrument Technology Research Center, NARL, Taiwan, C.-Y. Lin, Taipei Medical University, Taiwan, H.-S. Huang, Instrument Technology Research Center, NARL, Taiwan, H.-M. Huang, Taipei Medical University, Taiwan, D.-C. Chen, National Yang-Ming University, Taiwan, T.-S. Liao, J.-S. Kao, Instrument Technology Research Center, NARL, Taiwan

An electrochemical impedance spectroscopic (EIS) instrument with indium-tin oxide (ITO) culture chip module and lock-in impedance readout module was developed. The lock-in impedance readout module achieves impedance measurements with a small, bio-harmless AC signal. Moreover, transparent ITO culture-chip module is experience friendly; other optical inspections can be applied on the chip. The impedance readout module is designed to perform in a range from 1 to 10 kHz; the phase measuring errors are within 5.1% in that range. Typical examples of PBS solutions, BSA proteins and cell culturing tests are discussed in experiments. Higher concentration levels of PBS produced lower impedance. Higher concentration level of BSA solution also produced lower impedance. Furthermore, experiments of 0.25% BSA dissolved in sDDW and 1X PBS show that the mediums influence system impedance. Moreover, the log phase (period of cell proliferation) of B16F10 cell culture tests ended at 9, 16, 23, and 65 h for seeded cell densities of 5×10^4 , 1×10^5 , 2×10^5 , and 4×10^5 /mL, respectively. Finally, cultures are incubated and doped to demonstrate the monitoring of cell proliferation.

An EIS using microelectrode arrays has gained much attention as a promising, label free, fast, and real-time method for cellular analysis. The electric cell substrate impedance sensing (ECIS; Applied BioPhysics) and real time cell electronic sensing (RT-CES; Roche Applied Sciences) systems are widely applied in measuring cell proliferation, attachment and spreading, motility, toxicology, barrier function, wounding, and migration. The sensing chips are opaque and the influence of solutions is generally disregarded. However, transparent chips for optically related detection are required in many applications. And, in fact, chemical additives for biochemical treatments induce impedance variations.

This study develops an EIS instrument with an ITO culture chip module and lock-in impedance readout module. The instrument can apply and extract bio-harmless small signals by lock-in technology. Experimental results prove impedance readout module performance. The ITO culture chip module electrodes are connected via the electrolyte medium and the route of cell/tissue. Typical examples of the effects of solutions and cell culturing tests are discussed. A higher level of PBS causes lower impedance. Further study of solution ingredients will improve the measurement accuracy and results analysis. The ESI instrument with an ITO culture chip module and lock-in impedance readout module can be applied in other conductive liquid sample investigations.

BI-ThP8 Molecular Interactions between Lubricin and Type II Collagen Surfaces: Adsorption, Adhesion, Steric Repulsion, and Boundary Lubrication, D.P. Chang, F. Guilak, Duke University, G.D. Jay, Brown University / Rhode Island Hospital, S. Zauscher, Duke University

Although many studies have tried to elucidate the lubrication mechanisms that occur in articular cartilage, the molecular details of how constituents of the synovial fluid interact with cartilage surfaces and mediate cartilage to cartilage interaction still remain poorly understood. One of the major constituents of the synovial fluid that is thought to be responsible for boundary lubrication is the glycoprotein lubricin; however, details of the molecular mechanisms by which lubricin carries out its vital functions still remain largely unknown. Here, we examine i) the molecular details in which lubricin interacts with type II collagen, the main component of cartilage that provides structural integrity and tensile strength, ii) whether collagen structure can affect lubricin binding and change the adhesive interactions and boundary lubrication between collagen surfaces. We found that lubricin adsorbed strongly onto denatured, amorphous and fibrillar collagen surfaces. Furthermore, we found large repulsive interactions, between the collagen surfaces in presence of lubricin, increase with increasing lubricin concentration. Lubricin attenuated the large friction and also the long-ranged adhesion between the fibrillar collagen surfaces. Interestingly, lubricin mediated the frictional response between the denatured and native amorphous collagen surfaces equally, and showed no preference on the supramolecular architecture of collagen. We speculate that in mediating interactions at the cartilage surface, an important role of lubricin is to attach to the cartilage surface and provide a protective coating that maintains the contacting surfaces in a sterically repulsive state.

BI-ThP9 A Study of the Effect of Solvent-based Sterilization on the Reversible Adhesion of Biological Cells to a Thermoresponsive Surface, L.J. Pawlikowski, V.J. Eriacho, H.E. Canavan, University of New Mexico

Poly(*N*-isopropyl acrylamide) (pNIPAM) is a thermoresponsive polymer that is widely used in bioengineering applications, including tissue culture engineering, single cell adhesion/detachment, and biofouling prevention. Although there are many ways to treat surfaces with pNIPAM, plasma polymerization is one of the more adaptable ways for coating surfaces for the use in tissue culture experiments. While plasma polymerization creates a sterile environment useful for tissue culture, occasionally, additional sterilization techniques must be used. Some sterilization methods include using UV light to sterilize the surfaces, and the use of different solvents, such as ethanol. To date, there have been no studies on the effect of these sterilization techniques on the reversible adhesion of biological cells on pNIPAM treated surfaces. In this work, we investigate the effect of different sterilization techniques (e.g., ethanol and UV light) on the thermoresponsive nature of pNIPAM. Substrates were coated using plasma polymerization (ppNIPAM), after which they were sterilized using solvents, and characterized to determine if the solvents changed the thermoresponsive nature of the polymer. X-ray photoelectron spectroscopy (XPS) and interferometry were used to determine the surface chemistry and thickness of our ppNIPAM surfaces. Goniometry was used to confirm the thermoresponsive nature of our surfaces. Finally, we tested the adhesion and detachment of cells on the surfaces using bovine aortic endothelial cells (BAECs). We found that the use of solvents as sterilizing agents does have an effect on the thermoresponsive nature of pNIPAM (as demonstrated by the decreased detachment of cells from the surfaces), even when the pNIPAM film's chemistry appears unaffected.

BI-ThP10 Probing the Molecular Interactions at Bio-Inorganic and Bio-Organic Interfaces using X-ray Photoelectron Spectroscopy, R.A. Rincón, K. Artyushkova, D. Ivniiski, University of New Mexico, M. Eby, Universal Technology Corporation, H.R. Luckarjft, G.R. Johnson, Air Force Research Laboratory, P. Atanassov, University of New Mexico

Our recent work has made extensive use of X-ray photoelectron spectroscopy (XPS) in order to identify molecular interactions at a series of bio-inorganic and bio-organic interfaces.

In the first project, biologically-synthesized silica-enzyme and silica-peptide nanocomposite materials were analyzed by means of high resolution XPS. Biosilicification, i.e., rapid precipitation of silica mediated by a biological catalyst at ambient conditions, provides an efficient method for controlled synthesis of complex nanoscale structures. The process mimics reactions that organisms use to form rigid structures such as diatom exoskeletons and sponge spicules. The molecular interactions that allow these peptides to induce silica mineralization have not been elucidated. The focus of our study used the antimicrobial decapeptide KSL (KKVVFKVKFK), which induces rapid biosilica formation from pre-hydrolyzed tetramethyl orthosilicate in phosphate buffer. XPS was used to probe elemental composition and coordination chemistry of hybrid peptide-silica nanoparticle surfaces and ultimately identify the molecular interactions at the bio-inorganic interface.

In separate work, XPS was used to define interactions between biomolecules and various materials molecules used for bioelectrochemical architectures. One complex used the in vitro biosilicification process to help associate glucose oxidase (GOx) and carbon nanotubes (CNT) to yield a conductive composite matrix. Silica encapsulation of GOx provided an immobilization efficiency of ~25% in the presence of CNT. XPS analysis confirmed that the formation of a heterogeneous silica matrix had incorporated lysozyme, GOx and CNT. Another materials approach used layer-by-layer assembly (LBL) to immobilize a redox enzyme. The LBL approach fixed bilirubin oxidase (BOD) on an electrode surface by using a glutaraldehyde as a "cross-linker" in combination with electrostatic interactions between the negatively charged enzyme and the positively charged polymer. The composite matrix was characterized using angle resolved XPS and multivariate analysis. The methods defined: the physical architecture of BOD layers immobilized on the electrode, the relative thickness of each assembled layer, along with their elemental and chemical composition.

In the third project we have studied poly-azines, which have been popular electrocatalysts of choice for NADH oxidation for sensors and biofuel cell applications using NAD-dependent enzymes. Little is known about their structure and mechanism of polymerization. Through detailed XPS analysis of monomers and polymers we were able to propose mechanism of electropolymerization and elucidate polyazine structure.

BI-ThP11 Polysomes Interaction with Self-Assembled Monolayers, L. Marocchi, L. Lunelli, Center for Materials and Microsystems - FBK, Italy, G. Viero, CiBio - University of Trento, Italy, F. Piras, Center for Materials and Microsystems - FBK, Italy, N. Arseni, A. Provenzani, CiBio - University of Trento, Italy, C. Pederzoli, Center for Materials and Microsystems - FBK, Italy, A. Quattrone, CiBio - University of Trento, Italy, M. Anderle, Ict - Pat, Italy

The cellular machinery dedicated to the synthesis of the polypeptide chain translated from the mRNA template is the ribosome. Clusters of translating ribosomes held together by mRNA form the so-called polysome. The study of such supramolecular assemblies has interests both in structural and functional aspects as addressed in this study. As consequence the analyses of polysomal mRNA are emerging as good estimators in directly representing cell phenotypes. Since traditional methods of polysome purification are still a time consuming and laborious procedures, high throughput polysomal purifications are attracting growing interest. Recently, more modern approaches have been developed, based on the specific affinity between genetically modified ribosomes and functional surfaces. However, native ribosomes are required for several analytical applications. This work is a first step in developing a convenient and fast strategy to purify native polysomes thanks to their adhesion ability to appropriate substrates. We studied the interaction between functionalized gold surfaces and polysome fractions purified from human cultured cells or ribosomes derived from rabbit reticulocyte lysate. Surfaces endowed with different chemical properties were obtained using functional thiols able to form self assembled monolayers on gold substrates. Substrate surface properties were studied with XPS, ToF-SIMS and AFM. The interaction of rabbit ribosomes with the surfaces was assessed with AFM and confocal microscopy.

Despite different imaging approaches have been used to visualize bacterial and eukaryotic polysomes, human native polysomes have never been observed in physiological conditions. Moreover nothing is known about the formation of the mRNA-ribosomes macroassembly. Here we present the very first AFM images of native polysomes from mammalian cell lines adherent to surfaces. For the first time to our knowledge, we could observe ribosome aggregates associated to RNA, providing the imaging of polysome assemblies. Our imaging approach suggests the existence of a complex pattern of conformations and reveals novel levels of polysomal organization.

BI-ThP12 Adsorption of a Therapeutic Monoclonal Antibody on Surfaces Characterized by X-Ray Photoelectron Spectroscopy and Atomic Force Microscopy, K.L. Steffens, J.R. Wayment, National Institute of Standards and Technology

As the number of FDA-approved monoclonal antibody therapeutics increases, the need to understand and control aggregation and surface adsorption of these therapeutics becomes more critical. Aggregation of protein therapeutics is a concern, because aggregates may lead to serious immunological responses in patients. Currently, the cause of protein aggregation is not clearly understood. Recent evidence from several studies has suggested that the interaction of proteins with surfaces may influence solution phase aggregation processes. Therefore, investigation of these effects is critical in order to reduce or eliminate aggregation in biopharmaceutical products. In this study, we investigate the interaction of Rituxan™, a therapeutic monoclonal antibody, with various surfaces including alkanethiol self-assembled monolayers on gold, polyethylene

glycol on gold, gelatin on gold, and bare glass. Both as-prepared and heat-stressed (aggregated) protein solutions were investigated with size exclusion chromatography (SEC) before and after contact with the surfaces to measure the presence of small antibody aggregates (monomers to trimers). The presence of larger antibody aggregates formed in solution was assessed by performing AFM of protein solutions deposited and dried on mica. Protein adsorption on the various surfaces was measured using x-ray photoelectron spectroscopy (XPS) to probe the surfaces before and after exposure to the protein solutions. In addition, the standard overlayer model was used to estimate the thickness of adsorbed protein layers. Results show that adsorption of the protein is highly dependent on the surface character as well as on the presence of solution phase aggregates.

BI-ThP13 Univariable Synthetic Material for the Study of Cell Response to Substrate Rigidity, A.T. Leonard, J.R. Funston, University of New Mexico, K.N. Cicotte, Sandia National Laboratories, M.N. Rush, E.L. Hedberg-Dirk, University of New Mexico

There is a strong indication that the mechanics of a substrate plays an important role in many cellular functions. Native human soft tissue has elastic modulus in the range of 0.01 to 1000 kPa. The synthetic materials commonly used to fabricate cell culture platforms with varied moduli, including polyacrylamide and polydimethylsiloxane, are limited in applicability due to a restricted range of achievable moduli and/or surface chemistry instabilities. The copolymer network of n-octyl methacrylate (nOM) and diethylene glycol dimethacrylate (DEGDMA) offers attractive material properties that overcome these limitations. In our laboratory, copolymer networks were fabricated with 3 to 33 wt% DEGDMA. The compressive modulus was 25±2 kPa for the 3% DEGDMA network and increased with increasing DEGDMA fraction to 4700±300 kPa at 33 wt%. The networks demonstrated consistent surface wettability over the range of gel formulations examined as determined by goniometry. Surface interrogation with x-ray photoelectric spectroscopy (XPS) at the two extremes of formulations, 3 and 33 wt% DEGDMA, showed similar elemental and chemical bond compositions. The formulation 3% DEGDMA had elemental composition of 82.1±2.0 % Carbon 1s and 16.8±0.7 % Oxygen 1s. The higher DEGDMA composition of 33 wt% DEGDMA showed 83.2±0.8 % Carbon 1s, 15.4±0.2 % Oxygen 1s. High resolution carbon XPS indicated similar ratios of ether, ester and alkyl groups at the two extremes of DEGDMA compositions. The murine osteoblastic cell line MC-3T3 was used as a model for cell attachment and viability at six and 72 hours, respectively. Scanning electron spectroscopy was used to visualize the long range nano and micro surface topology. Atomic force microscopy was used to map as well as quantify the surface roughness for each of the formulations. Our results indicate nOM/DEGDMA substrates can vary in modulus over three orders of magnitude while maintaining comparable chemical and topographical surface features. These networks are the first that allow for the study of the effects of material mechanics without the interference of other material properties.

BI-ThP14 In Vitro Cytotoxicity Studies of Antimicrobial Conjugated Polyelectrolytes, K.N. Wilde, L. Ding, Y. Wang, E. Ji, T.S. Corbitt, L.K. Ista, D.G. Whitten, H.E. Canavan, University of New Mexico

An estimated 19,000 deaths and \$3-4 billion in health care costs per year in the U.S. are attributed to methicillin-resistant *Staphylococcus aureus* (MRSA) infections. Infected individuals inevitably touch a wide variety of surfaces. Therefore, making these surfaces antimicrobial would reduce or prevent the spread of potentially untreatable strains of bacteria. Current sterilization and disinfection techniques tend to be temporary and surface-specific, and require constant vigilance on the part of medical and support staff. Certain conjugated polyelectrolytes (CPEs) with arylene ethynylene repeat unit structure have been demonstrated to exhibit dark and light-activated antimicrobial activity. Both in solution and anchored to a support, these polymers have been effective at killing Gram-negative bacteria, specifically *Pseudomonas aeruginosa* strain PAO1 and *Cobetia marina*. This light-activated antimicrobial activity enables their use in a wide range of potential applications. However, until recently, it was unknown if the CPEs would exhibit similar biocidal activity toward mammalian cells. In this study, bovine aortic endothelial cells were exposed to two different CPEs for increasing periods of time, from 10 minutes to 24 hours, in both light and dark conditions. The relative cytotoxicity was then assessed using a live/dead fluorescence assay, and imaged via epi-fluorescence microscopy. While CPEs demonstrate biocidal activity toward *P. aeruginosa* strain PAO1 and *C. marina*, these polymers do not appear to be toxic toward mammalian cells when the cells are exposed to the polymers in both light and dark conditions. Further work is underway to evaluate cytotoxicity at concentrations above the micromolar concentrations tested to date, to correlate mammalian test conditions to bacterial test conditions, and to include an epithelial cell line. Because membrane disruption is a common mechanism of action for antimicrobial agents, molecular dynamic simulations will also be performed to model polymer insertion into a

hydrated zwitterionic phospholipid bilayer. These combined data are important to determine how to best incorporate CPEs into antibacterial household and health care products.

BI-ThP15 Aptamer-based Protein Recognition using CMOS Single-Photon Detector Arrays for Time-Resolved Analysis. *L. Pasquardini*, Center for Materials and Microsystems - FBK, Italy, *M. Benetti*, University of Trento, Italy, *L. Lunelli*, Center for Materials and Microsystems - FBK, Italy, *D. Iori*, University of Trento, Italy, *L. Pancheri*, *F. Borghetti*, *L. Gonzo*, Center for Materials and Microsystems - FBK, Italy, *G.F. Dalla Betta*, University of Trento, Italy, *D. Stoppa*, *C. Pederczoli*, Center for Materials and Microsystems - FBK, Italy

There is a high demand for convenient methodologies for detecting and measuring the levels of specific proteins in biological samples because their detection, identification and quantification can be very complex, expensive and time consuming. Biosensors are interesting tools offering certain operational advantages over standard photometric methods, especially with respect to sensibility, duration, ease-of-use, cost, simplicity and portability. Regarding this research field we are developing a monolithic silicon biochip suitable for detecting traces of proteins in biological fluids that are not detected by conventional immunoassays. Particularly in this contribute we discuss the performances of SPAD (Single-Photon Avalanche Diode) detector arrays fabricated in CMOS technology utilized within a lab-on-chip system consisting of a micro-reactor (MR) array for bioaffinity assays based on fluorescence markers. In a typical fluorescence lifetime experiment a pulsed laser is used to excite the fluorescent dyes and the emitted light is revealed by means of high sensitivity detectors. The utilized SPAD detector module, having a total area of 600 x 900 μm^2 per MR, can be arranged to build a small pixel array to be directly coupled to the MRs. No emission filters are needed, since the ultra-short laser pulse is cut off in the time domain. Every module consists of a 10x10-SPAD sub-array, where each SPAD cell is equipped with dedicated active quenching and recharging circuit. A memory has also been implemented in order to enable only low dark count rate (DCR) SPADs, so that a total DCR of about 100kHz can be achieved for the whole photosensitive area. Two time-windows have been implemented in this architecture, with a time width that can be set within the range 500ps-10ns with a resolution of 500ps.

The bifunctional layer is based on a dual-site binding strategy with aptamers, that are short single-stranded DNA folded into well-defined three-dimensional structures to form binding pockets and cleft for the specific recognition and tight binding of the molecular target. The biological model chosen for the present work is the protein thrombin (factor IIa). Two aptamer sequences able to bind to different sites of this protein are used. The first aptamer, anchored to substrate, specifically immobilizes the target protein to the sensor surface, while the second sequence, carrying a fluorescent molecule, allows target detection.

BI-ThP16 Adsorption of Beta-Helical Peptides. *J.L. Kulp*, *K.P. Fears*, *T.D. Clark*, Naval Research Laboratory

This poster will describe surface adsorption of beta-helical scaffolds derived from peptides composed of alternating D- and L-amino acids. The monomeric and stable conformation of beta-helical peptides in solution provides a well-defined starting point for discriminating the changes in secondary structure of peptides induced by surface adsorption. NMR, CD, VCD, and XPS results will be presented.

BI-ThP17 Surface Characterization of Baked-on Siliconized Vials for Biopharmaceuticals. *G. Torraca*, *A. Vance*, *P. Masatani*, *L. Wong*, *B. Eu*, *M. Pallitto*, *M. Ricci*, *Z.-Q. Wen*, Amgen, Inc.

Protein formulations have been found to interact with the glass container surface, resulting in protein adsorption, glass delamination, or glass dissolution. To mitigate surface interactions, alternative primary containers with chemically modified surfaces are actively investigated. One container coating technology that was studied utilized a method of coating the vial interior with a dilute emulsion of polydimethylsiloxane (PDMS) and then baking the vials to form a durable layer. The baked-on layer is meant as an isolation layer that insulates the drug product from the glass surface to prevent glass degradation as well as product interactions. Baked-on siliconized vials from two primary container vendors were examined for changes in surface properties over a 6-mo stability timecourse. To better understand and compare representative samples, three analytical techniques were employed to study the interior surface of the vials. These were Polarized Light Microscopy, X-ray Photoelectron Spectroscopy (XPS) which is also referred to as Electron Spectroscopy for Chemical Analysis (ESCA) and Contact Angle Measurement. The baked-on PDMS layer of the vial container was determined to be incompatible with the formulations that were studied. The coating characteristics and the robustness of these coatings from each vendor are discussed.

BI-ThP18 Accurate Delivery and Detection of Single Biomolecules Using Sub-Attoliter Pipettes on a Confocal/AFM Microscope. *Y. Hu*, *S. Tadayyon*, *R. Taylor*, *J. Dechene*, *P.R. Norton*, University of Western Ontario, Canada

The development of novel techniques to accurately deliver, manipulate, and detect single molecules is one of the most interesting but challenging subjects in modern biotechnology and molecular biology. Most of the recent studies are focused on electrochemical methods using glass micro/nano pipettes that are mechanically pulled and an electrical field used to move molecules through microchannels. However, "single-molecule delivery" has not yet been achieved.

We report on our recent studies of single molecule delivery using a sub-attoliter reservoir formed at the end of what is essentially an NSOM optical fiber, mounted on a combined AFM/confocal fluorescence microscope. The reservoir is formed by chemical etching and focused ion beam (FIB) milling and is then coated with Al to confine the light for fluorescence detection in an NSOM geometry, and for the expulsion of the solution containing the molecule of interest. The volume of the reservoir can be in the range of attoliters by control of the etching and/or milling conditions. Initial experimental results using fluorescein dye indicates that when the solution concentration is low enough, single molecule delivery is achievable. Further study on cell labeling is discussed.

References

1. C. W. Park, J. P. Knemeyer, N. Marmé, M. Möller, J. Spatz, J. Wolfrum and M. Sauer, *Chem. Phys.* 2004, 301 (1) 105-110.
2. A. Bruckbauer, P. James, D. Zhou, J. Yoon, D. Excell, Y. Korchev, R. Jones, and D. Klenerman, *Biophys. J.* 2007 vol. 93, no. 1, 3120-3131.
3. S. Uehara, M. Karhanek, R. W. Davis, and N. Pourmand, *Proc. Natl. Acad. Sci. USA*, 2009, 106 (12), 4611-4616.
4. R. Taylor and C. Hantovsky, *J. Appl. Phys.* 2004, 95 (12), 8444-8449.

BI-ThP19 Exploring Critical Parameters in Biointerface Design using Plasma-Modified Polymers. *S.H. North*, NUARI-Institute for Advanced Sciences Convergence, *E.H. Lock*, *J. Wojciechowski*, *C.R. Taitt*, *S.G. Walton*, U.S. Naval Research Laboratory

The development of new transducing substrate materials, such as polymers, has spurred a growing interest in assessing the influences of surface topography and chemistry of the abiotic layer on the bio-functionality of the biotic layer. However, it is a challenge to differentiate the contributions of surface roughness and surface chemistry to biointerface functionality, as most surface modification methods tend to alter *both* at the same time. In this work, we discuss a dry and wet chemistry approach to biointerface development on polymeric substrates aimed at minimizing changes in the surface morphology. Specifically, an NRL developed electron beam-generated plasma processing system was used to functionalize the surface of polystyrene microtitre plates, which were then silanized to covalently immobilize biomolecules. Electron beam plasmas are unique in that they deliver high flux of low energy (< 5 eV) ions to substrate surfaces enabling selective, chemical alteration of the top few nanometers of any material *without* significant morphological modification. Thus, reactive hydroxyl groups, that make the characteristically inert material amenable to silane chemistry, can be introduced while maintaining substrate morphology. Silanization is an easy, controllable, and conformal covalent immobilization method that supports a wide variety of bio-immobilization schemes. Biomolecules covalently immobilized using this combined dry-wet chemistry approach retained functionality and demonstrated attachment efficiency comparable (and in some cases superior) to specialized commercial microtitre plates. We have used a combination of complementary surface analytical techniques to evaluate the relationships between the physical and chemical properties of the treated polymer surfaces, with particular emphasis on attachment of a functional silane layer, which is a critical parameter for efficient covalent bio-immobilization. Based on our results, we conclude that the development of novel interface materials with superior transducing capabilities is contingent on the deeper understanding of the complex physicochemical interactions between substrate polymer and the chemical/biological components attached to it.

Spectroscopic Ellipsometry Focus Topic

Room: Southwest Exhibit Hall - Session

EL+AS+EM+MS+TF-ThP

Spectroscopic Ellipsometry Focus Topic Poster Session

EL+AS+EM+MS+TF-ThP1 Temperature Dependence of the Dielectric Function of AlSb Measured by Spectroscopic Ellipsometry, J.J. Yoon, Y.W. Jung, J.S. Byun, S.Y. Hwang, Y.D. Kim, Kyung Hee University, Republic of Korea, **S.H. Shin, S.Y. Kim, J.D. Song,** Korea Institute of Science and Technology, Republic of Korea

AlSb is a promising material for applications in heterostructure devices such as long-wavelength detectors, quantum-well lasers, and laser diodes. However, to understand and properly design these devices, information about its electronic properties and its dielectric function $\epsilon = \epsilon_1 + i\epsilon_2$ is needed. While room-temperature ϵ data for AlSb exist, very little information is available about its behavior at elevated temperatures. Here, we report pseudodielectric function data $\langle\epsilon\rangle$ from 300 to 800 K and from 0.7 to 5.0 eV, determined by spectroscopic ellipsometry. The samples were 1.5 μm thick layers grown on GaAs (001) substrates by molecular beam epitaxy (MBE). This thickness significantly exceeds the critical value for AlSb, so the layers are fully relaxed. The MBE station features an integrated spectroscopic ellipsometer and strain-free windows, thereby allowing ϵ data to be obtained without exposing the samples to air. For AlSb this is critical, because the removal of its oxides is not feasible owing to its reactivity. As a result of these precautions and the method by which these $\langle\epsilon\rangle$ data were obtained, we consider them to be the most accurate representation of ϵ to date. We also analyzed these data for critical-point (CP) parameters by fitting numerically calculated second energy derivatives of standard analytic CP lineshape expressions. A parametric model was used, which describes dielectric functions by a combination of energy-bounded polynomials and poles, and encodes information in terms of amplitudes, critical-point energies, and broadening parameters. The reconstructed spectra are in excellent agreement with the data. We use these parameters to obtain information about the individual oscillators, including phonon effects, and interpolate them to obtain an analytic representation of the dielectric response of AlSb as a function of temperature. We expect these results to be an important database supporting engineering design, device technologies, and in-situ monitoring and control of device fabrication.

EL+AS+EM+MS+TF-ThP2 Optical Properties and Humidity Effects on Thin Films of Micro Fibrillated Cellulose Studied by Spectroscopic Ellipsometry, H. Arwin, E. Antunez de Mayolo, Linköping University, Sweden, **M. Eita,** Royal Institute of Technology (KTH), Sweden, **H. Granberg,** Innventia Ab, Sweden, **L. Wågberg,** Royal Institute of Technology (KTH), Sweden

High quality micro fibrillated cellulose (MFC) prepared from wood fibers can be used to prepare thin films on solid substrates by a layer-by-layer deposition technique. In applications MFC layers can be used alone or as a constituent in functional coatings, where the MFC can make a significant contribution to mechanical properties of the coating. Examples of potential applications are sensor layers, decorative coatings or mirrors. Here the optical properties in terms of the refractive index of MFC are studied with *in situ* spectroscopic ellipsometry (SE) and the effects on thickness and index due to humidity are investigated.

Films of MFC and polyethyleneimine (PEI) in the thickness range 30 - 300 nm are deposited on silicon substrates. Such MFC/PEI samples are exposed to water vapor in nitrogen (0-90% RH) and the ellipsometric response are measured *in situ* in the spectral range 245 - 1700 nm at an angle of incidence of 70 degrees using a dual-rotating compensator ellipsometer. From the SE-data the MFC/PEI film thickness and layer index are modeled.

Due to water exposure, the thickness of an MFC/PEI film is found to increase up to 15% or more, whereas the refractive index decreases. The effects are fully reversible and the dynamics of these changes are monitored with SE and are discussed.

EL+AS+EM+MS+TF-ThP3 Spectroscopic Ellipsometry and X-ray Photoelectron Spectroscopy of La₂O₃ Thin Films Deposited by Reactive Magnetron Sputtering, V. Atuchin, Institute of Semiconductor Physics, Russia, **A.V. Kalinkin,** Boreskov Institute of Catalysis, Russia, **V.A. Kochubey, V.N. Kruchinin,** Institute of Semiconductor Physics, Russia, **R.S. Vemuri, C.V. Ramana,** University of Texas at El Paso

Lanthanum trioxide (La₂O₃) is one among the most promising high-k dielectric materials to replace SiO₂ and Si₃N₄ in advanced metal-oxide-semiconductor devices in gate stack. La₂O₃ can be prepared by various techniques but the film properties are strongly dependent on the fabrication

conditions. Reactive magnetron sputtering deposition is widely used for the preparation of high quality transition multivalent metal oxide films with reproducible parameters and controlled thickness. The technique is preferred since it usually offers a high deposition rate for oxide films and a possibility to control the chemical composition of the film by reactive atmosphere in vacuum chamber. The aim of the present study is to understand the surface structure and evaluate the optical parameters of La₂O₃ films deposited on Si substrates by magnetron sputtering. La₂O₃ thin films were deposited onto Si(100) substrates in an argon/oxygen atmosphere using a high purity La target (99.9%). Structural parameters of the films were estimated by reflective high energy electron diffraction (RHEED) method at electron energy of 50 keV. All the films show no diffraction pattern indicating their amorphous nature in the near surface layers. Chemical state examined by the X-ray photoelectron spectroscopy (XPS), SPECS device, monochromatic Al K α radiation (1486.6 eV) before and after Ar⁺ (2.5 keV, 2 min) sputtering indicates the stoichiometric film formation. Chemical nature of the species was identified with using binding energy (BE) difference parameter $DL_a = BE(\text{La } 3d_{5/2}) - BE(\text{O } 1s)$ [1]. Optical parameters of the films were measured with spectroscopic ellipsometry (SE) using a Spectroscan ellipsometer in the spectral range of 250 nm < λ < 1100 nm at the incidence angle of 70°. The La₂O₃ films with thickness 500-850 nm were transparent over the spectral range and dispersion relations of refractive index n were well derived using a model of (air)/(single homogeneous layer)/(Si substrate). The curves $n(\lambda)$ were approximated by Cauchy polynomials. Good relation between experimental points and theoretical curves confirms applicability of this simple model for the films. The optical parameters of La₂O₃ defined with SE are related to film bulk and are insensitive to top surface effects induced by hydration or carbonate formation. These parameters will be used as a basis for SE evaluation of nanometric lanthanum oxide films with thickness below 10 nm.

I.V.V. Atuchin, T.A. Gavrilova, J.-C. Grivel, V.G. Kesler, Electronic structure of layered ferroelectric high-k titanate La₂Ti₂O₇, J. Phys. D: Appl. Phys. 42 (2009) 035305.

EL+AS+EM+MS+TF-ThP4 Analysis of Anomalous Film Growth when Yttrium Oxide Thin Films are Exposed to 7.2eV Light, D. Mortensen, D.D. Allred, Brigham Young University

We have recently found that exposure of reactively sputtered yttrium oxide thin films to 7.2 eV photons in air produces a dramatic (factor of 4) increase in the films' thickness. This result was completely unexpected, Y₂O₃ is exceptional stable, and demanded further investigation. This is particularly important since yttria and neighboring metal oxides such as ZrO₂ have been considered, and HfO₂ is being used, as components in gate oxides for silicon devices. The excimer lamp used for the study was of the type used in cleaning the surfaces of silicon wafers in the semiconductor industry. It is vital to understand how metal oxides might swell during cleaning.

We have experimentally observed the following:

1. The film-thickness increase is linear with exposure time up to a point.
2. Over a factor of four increase in film thicknesses, as measured by spectroscopic ellipsometry, has been observed. E.g., film which was about 20 nm thick as deposited reached a thickness of about 100nm.
3. When the yttrium oxide sample is placed in a furnace the changes rendered to the yttrium oxide sample are reversed.
4. A film placed in a plasma cleaner does not show this increase.
5. These effects are noticeably absent under the same conditions for a silicon wafer.
6. The refractive index of the film decreased with exposure time, suggesting the film could becoming more porous, though effective media optical models were unsuccessful in modeling the optical properties.

In addition to ellipsometry the films were studied by XPS and STEM.

EL+AS+EM+MS+TF-ThP5 In-Situ Spectroscopic Ellipsometry of Lithium Ion Intercalation in GLAD Three-Dimensional Nanostructured Thin Films, E. Montgomery, M. Schubert, E.B. Schubert, T. Hofmann, D. Schmidt, University of Nebraska - Lincoln, **R.A. May,** University of Texas at Austin

Lithium intercalation in thin nanostructured and bulk films from metals and semiconductors has been studied using in-situ spectroscopic ellipsometry. Nanostructured thin films have a large surface area, and the stress caused by the intercalation of lithium is reduced in comparison to continuous films. The films are deposited using electron beam evaporation at a glancing angle or Glancing Angle Deposition (GLAD).

The charge capacity of the films can be observed as a change of index of refraction using ellipsometry. We will study intercalation as a function of structure geometry in chiral and achiral 3D GLAD thin films deposited from different metals onto silicon and other dielectric substrates. We report the anisotropic dielectric functions of the 3D nanostructures and their changes as a function of intercalation time and period.

EL+AS+EM+MS+TF-ThP6 Multi Phase Model Generation of Reflection Anisotropy Spectra of Copper Phthalocyanine Films on Vicinal Silicon Substrates, F. Seidel, L. Ding, O.D. Gordan, D.R.T. Zahn, Chemnitz University of Technology, Germany

In this work the in-plane anisotropy of copper phthalocyanine (CuPc) thin films grown on vicinal silicon substrates is explained by simulating Reflection Anisotropy Spectroscopy (RAS). In RAS the complex difference in reflection along two perpendicular directions is measured at an incidence angle close to 0° . While RAS has strong similarities with another polarisation related measurement technique, Spectroscopic Ellipsometry (SE), simulations of RA spectra using a similar mathematical formalism like in SE is not common.

One difference is that in SE the measurements are usually performed at an incidence angle close to the Brewster angle, where the difference between s and p reflected polarisation is maximal. However due to the similarities between the two techniques the evaluation of RA spectra can be performed in a similar way like for SE after some simple mathematical transformations. This is particularly useful when thickness induced interference can lead to incorrect interpretations of RA spectra. Therefore in this work we show that the RA spectra evaluation of CuPc layer with increasing thickness is mainly given by the optical interference effect and not by a change in the optical anisotropy of the film.

Energy Frontiers Topical Conference

Room: Southwest Exhibit Hall - Session EN-ThP

Energy Frontiers Topical Conference Poster Session

EN-ThP1 N-doped TiO₂ Photocatalytic Thin Films : Synthesis with Controlled Nitrogen Partial Pressure and Study on Their Catalytic Activity, J.-H. Boo, S.-J. Cho, C.-K. Jung, Y.-H. Song, Sungkyunkwan University, Republic of Korea, S.-S. Kim, Paichai University, Republic of Korea

We have deposited N-doped TiO_xNy thin films on Si(100) substrates at 500°C using PEMOCVD method. Titanium iso-propoxide was used as precursor with different nitrogen flow rate to control oxygen and nitrogen contents in the films. Changes of chemical states of constituent elements in the deposited films were examined by XPS analysis. The data showed that with increasing nitrogen flow rate, the total amounts of nitrogen and titanium were increased while that of oxygen was decreased, resulting in a binding energy shift toward high energy side. The characteristics of film growth orientation and structure as well as morphology change behavior were also analyzed by XRD, TED, TEM, AFM, and SEM. Deposition at higher nitrogen flow rate results in finer clusters with a nano-scale grain size and a slower growth rate.

In order to elevate photocatalytic activity of the as-grown N-doped TiO_xNy films, argon and oxygen plasmas ignited by atmospheric discharge at 300 W were also used within 5 min. at room temperature. Photocatalytic activity was evaluated by the measurements of the contact angle, UV-Visible spectroscopy. In this work, the effect of the plasma on the improvement of hydrophilic property of N-doped TiO_xNy photocatalysts has mainly been investigated. Superhydrophilic property and smooth surface morphology appeared in the UV light irradiation with O₂ plasma treatment.

Keywords : N-doped TiO_xNy Thin Film, Photocatalyst, PEMOCVD, Atmospheric Plasma, Surface Modification

EN-ThP2 Optical and Electrical Properties of Transparent Conducting B-doped ZnO Thin Films Prepared by Various Deposition Methods, J.-I. Nomoto, S. Hotta, T. Miyata, T. Minami, Kanazawa Institute of Technology, Japan

Recently, transparent conducting impurity-doped ZnO films with a high transmittance in the near-infrared region have attracted much attention for transparent electrode applications in thin-film solar cells. It is necessary to achieve a reduction of the plasma resonance frequency resulting from a decrease of carrier concentration. However, in order to maintain a low resistivity in impurity-doped ZnO films, any decrease in carrier concentration should be compensated by an appropriate increase of mobility. In this paper, we describe the preparation of transparent conducting B-doped ZnO (BZO) thin films with a lower carrier

concentration as well as a higher Hall mobility by various deposition methods. BZO thin films were prepared on low temperature glass substrates by dc or rf magnetron sputtering deposition, pulsed laser deposition (PLD) and vacuum arc plasma evaporation methods. The optical and electrical properties were evaluated in BZO thin films prepared with various thicknesses up to about 3 μm and doped B contents (B/(B+Zn) atomic ratio) up to 5 at.%. In addition, long-term resistivity stability was evaluated with exposure to a highly moist environment (air at 85% relative humidity and 85°C) as well as an oxidizing atmosphere at a high temperature (air at a temperature up to 250°C). In the moisture-resistance tests, the BZO thin films exhibited an increase in resistivity during long-term testing; increasing the thin film thickness tended to lessen this increase in resistance, irrespective of the deposition method. In the heat-resistance tests, the resistivity of thin films thicker than approximately 200 nm was found to be stable for 1000 h at a testing temperature up to 200°C. A Hall mobility of 42 cm^2/Vs and a carrier concentration of $3.4 \times 10^{20} \text{ cm}^{-3}$ were obtained in a BZO thin film prepared by PLD. Resistivities of $4\text{--}6 \times 10^{-4} \Omega\text{cm}$ were obtained in 500 nm-thick-BZO thin films prepared with a B content of 1 at.%, irrespective of deposition methods. The low-resistivity BZO thin films exhibited an average transmittance in the visible range above 80 %; transmittances were above 80% at a wavelength of 1100 nm and 75% at 1300 nm.

EN-ThP3 Enhanced Performance of Dye-Sensitized Solar Cell by Inorganic/Organic Core-Shell Formation using Dip-Coating Method, M.J. Shin, J.M. Kim, H.J. Kim, B. Hong, Sungkyunkwan University, Republic of Korea

Dye-sensitized solar cell (DSSC) is considered as alternative to traditional solar cells due to its environment-friendly energy conversion capability and low fabrication cost. However, DSSC still suffers from efficiency loss due to a high recombination rate between the injected electrons and the oxidized dye or ions in electrolyte.

In this work, we present a very efficient but simple method is presented to improve the efficiency of DSSC using inorganic/organic core-shell electrode. This core-shell electrode consists of an inner nanoporous TiO₂ matrix covered with an aminopropyltriethoxysilane (APS) monolayer. It is relatively easy to control the shell density by controlling the concentration of APS using the dip-coating method. We confirmed that the efficiency of DSSC with TiO₂/APS core-shell instead of conventional TiO₂ was significantly dependent on the shell density. Relative change in surface chemistry with APS concentration was investigated by various analysis methods. The power conversion efficiency under AM 1.5 G spectral illumination of 100 mWcm^{-2} was improved by 20 % (from 4.37 % to 5.28 %) when APS concentration was optimized. This TiO₂ nanoparticles covered with APS are supposed to increase dye adsorption on TiO₂ surface and to prevent interfacial recombination of charge carriers. For the various analysis, it was used UV-absorbance spectroscopy, FT-IR (Fourier transfer IR), EIS (Electrochemical Impedance spectroscopy), TOF-SIMS (Time-of-Flight Secondary Ion Mass Spectrometry) and HR-TEM (High Resolution-Transmission Electron Microscope).

EN-ThP4 Characteristics of Undoped ZnO as Window Layer for CIGS Thin Film Solar Cell using Nano-Inks, E.C. Choi, J. Chang, D.Y. Jung, B. Hong, Sungkyunkwan University, Republic of Korea

ZnO is a very useful material as II-VI compound semiconductor with a wide band gap of 3.3 eV and a property of native n-type semiconductors. It has been studied actively due to its excellent optical, electrical and structural properties suitable for many applications such as transparent conductive oxide (TCO), solar cell window layer and surface acoustic wave (SAW) devices. In particular, n-type and undoped ZnO films are used as the window layer of CIGS solar cell (n-ZnO/i-ZnO/CdS/CIGS/Mo/glass).

The surface morphology of CIGS film deposited on Mo/glass substrate by liquefied deposition method using nano-inks is severely uneven and the film has many crevices. Also, the CBD-CdS layer with the thicknesses of about 50 nm does not perfectly cover the surface of the CIGS layer. Consequently, these crevices, which remain before the TCO deposition, lead to the formation of shunt path between TCO and CIGS layers.

Therefore, in this study, we investigate the role of undoped ZnO film with high resistivity to prevent the shunt path between TCO and CIGS layers, and ZnO films are deposited varying the thickness and the plasma power to investigate characteristics of undoped ZnO film for CIGS solar cell. It is confirmed that the efficiency of CIGS solar cell depends on the properties of the undoped ZnO films. The films are deposited using magnetron sputtering system in argon ambient and are analyzed using Hall measurement, UV-visible spectrometer and XRD.

EN-ThP5 Effect of Hydrogen and Deuterium Gas on the Thermionic Electron Emission from Nitrogen Doped Diamond Films, M. Zumer, V. Nemanic, B. Zajec, Jozef Stefan Institute, Slovenia, R.J. Nemanich, F.A.M. Koeck, Arizona State University

Nitrogen doped, hydrogen terminated diamond films have shown a work function of less than 1.5 eV and thermionic electron emission has been detected at temperatures as low as 300 °C. This report explores the influence of hydrogen and deuterium gas on the electron emission using a triode setup with an applied electric field that ranges from low values to 4 MV/m. The extracting grid and phosphor screen were set to the same potential. The hydrogen terminated, nitrogen doped diamond films were deposited on 25 mm diameter molybdenum substrates by microwave plasma assisted chemical vapour deposition. The process involves a nucleation layer, nitrogen doped layer and surface termination which were all optimized to enhance the emission. The thermionic electron emission from 300 to 500 °C was quite intense. A typical average emission current density at 500 °C was of the order of 2E-6A/cm² at a base pressure of the order of 10⁻⁷ mbar. The emission was relatively stable exhibiting only a weak tendency to decrease with time. The emission was relatively uniform across the surface as opposed to the intense emission sites often observed in field emission. When hydrogen was leaked into the chamber, the emission current density increased by greater than an order of magnitude as the pressure was increased from UHV to 10⁻⁵ mbar. Results indicated that atomic hydrogen generated by a nearby Bayard-Alpert ionization gauge induced the effect. An identical leak rate of deuterium causes a similar but less intense increase of the emission current. At both cases, the initial value of the thermionic emission was restored by establishing again the UHV. The question of whether the hydrogen (deuterium) improves the surface through bonding and forming a NEA or whether it assists in the charge transfer process is assessed. These results should guide the development of an efficient thermionic cell for direct conversion of heat to electricity.

EN-ThP6 Hot Electron Transfer from Semiconductor Nanocrystals, W. Tisdale, University of Minnesota, K. Williams, University of Texas at Austin, B. Timp, D. Norris, E.S. Aydil, University of Minnesota, X.-Y. Zhu, University of Texas at Austin

In typical semiconductor solar cells, photons with energies above the semiconductor bandgap generate hot charge carriers that quickly cool before all of their energy can be captured, a process that limits device efficiency. Although fabricating the semiconductor in nanocrystalline morphology can slow this cooling, the transfer of hot carriers to electron/hole acceptors has not yet been thoroughly demonstrated. We use time-resolved optical second harmonic generation to observe hot electron transfer from colloidal lead selenide nanocrystals (PbSe NCs) to a titanium dioxide electron acceptor (TiO₂). With appropriate chemical treatment of the nanocrystal surface, this transfer occurs much faster than expected. Moreover, the electric field resulting from sub-50 femtosecond charge separation across the PbSe-TiO₂ interface impulsively excites coherent vibrations of the TiO₂ surface atoms, whose motions can be followed in real time.

EN-ThP7 Synthesis and Characterization of Free-Standing Si Nanocrystals using PECVD, R. Chaukulkar, B.N. Jariwala, S. Weeks, Colorado School of Mines, N.J. Kramer, Eindhoven University of Technology, Netherlands, S. Agarwal, Colorado School of Mines

Si nanocrystals (NCs) (size <5nm) are generating an increased interest as a material to be used in third generation photovoltaics (PVs) owing to their size-dependent band gap, visible photoluminescence and multiple exciton generation (MEG). Synthesis of both liquid and gas phase NCs have been reported in the literature. We synthesize the Si NCs using a capacitively-coupled SiH₄/Ar plasma generated using radio-frequency power. The Si NCs are characterized using *in situ* attenuated total reflection Fourier-transform infrared spectroscopy (ATR-FTIR) and *ex situ* techniques such as transmission electron microscopy (TEM), energy-dispersive X-ray spectroscopy, infrared spectroscopy, photoluminescence spectroscopy, Raman spectroscopy and X-ray diffraction. The size of the NCs can be controlled by varying the residence time in the plasma volume. The residence time is adjusted to attain a particle size of 5nm collected on a grid. The crystallinity of the NCs depends on the amount of rf power put in the plasma. By varying the input rf power we were successful in demonstrating the transition from amorphous to crystalline nanoparticles using X-ray diffraction and TEM.

EN-ThP8 Physical Properties of Zinc Oxide Thin Films for Hybrid Solar Cell Application, S.-H. Nam, M.-H. Kim, Sungkyunkwan University, Republic of Korea, S. Kim, Paichai University, Republic of Korea, B. Hong, J.-H. Boo, Sungkyunkwan University, Republic of Korea
Zinc oxide (ZnO) films have been investigated in recent years as transparent conducting oxide layers, because of their good electrical and optical properties in combination with large band gap, abundance in nature, and

absence of toxicity. Zinc oxide thin films were prepared at deposition thickness in the range of 50 nm to 150 nm by RF magnetron sputtering on glass substrates with pure zinc oxide target. The crystallinity nanostructure and surface morphology of zinc oxide thin films were investigated by X-ray diffraction (XRD), scanning electron microscopy (SEM). As the thickness of the films increased, the grain size and surface roughness increased. Also, we studied the optical-electrical properties of the zinc oxide thin films such as carrier concentration, mobility, and resistivity by hall measurement. As changed by thickness of zinc oxide thin films, concentration become increasing. But mobility and resistivity become decreasing.

EN-ThP9 Al and N co-doped ZnO:(Al,N) Thin Films for Solar Driven Hydrogen Production, S. Shet, National Renewable Energy Laboratory

ZnO thin films with significantly reduced bandgaps were synthesized by doping N and co-doping Al and N at 100°C. All the films were synthesized by radio-frequency magnetron sputtering on F-doped tin-oxide-coated glass. We found that co-doped ZnO:(Al,N) thin films exhibited significantly enhanced crystallinity as compared to ZnO doped solely with N, ZnO:N, at the same growth conditions. Furthermore, annealed ZnO:(Al,N) thin films exhibited enhanced N incorporation over ZnO:N films. As a result, ZnO:(Al,N) films exhibited improved photocurrents than ZnO:N films grown with pure N doping, suggesting that charge-compensated donor-acceptor co-doping could be a potential method for bandgap reduction of wide-bandgap oxide materials to improve their photoelectrochemical performance.

EN-ThP10 Optical and Thermal Studies on CdSe Quantum Dots and Rods, H. Awad, S. Abdallah, Ain Shams University, Egypt, K. Easawib, S. Negm, Benha University, Egypt, H. Talaat, Ain Shams University, Egypt

CdSe nanoparticles have attracted a great deal of scientific interest recently, because of the sensitivity of their optical and non-radiative properties to their size and shape, and their applicability in high efficiency photovoltaic solar cells [1]. As the size of a material falls to the nanometer length scale, the material properties become sensitive not only to the particles size, but also to their shapes. The optical (band gap width) and thermal properties of different sized CdSe quantum dots (QDs) and nano rods (NRs) of different aspect ratios have been characterized and compared using photoacoustic (PA) techniques. CdSe colloidal nanocrystals were prepared by the method of Talapine et al. [2], on the other hand, CdSe nanorods were prepared according to Manna et al [3]. A conventional PA setup with (PAR model 6003) PA cell was used to measure the optical absorption spectrum, and the thermal parameters. The PA absorption spectra for CdSe QDs and NRs in Figures (1.a) and (2.a), respectively, show a significant red shift in all cases as the nanoparticles increase in size. We used the second-derivative technique, to determine the peaks positions for QDs and NRs (Figure (1.b) and (2.b), respectively). The lowest energy transition is between 1S(e) and 1S_{3/2}(h) states in case of QDs and between 1S(e) and 1S_{1/2} states in case of NRs. The UV-Vis absorption spectra were also obtained for the samples and give a comparable values for the first excitonic transition peaks. The band gap of the nanoparticles $E_g(\text{NC})$ is determined by the energy of the lowest 1S(e)-1S_{3/2}(h) transition corrected for the coulomb e-h interaction, NOTE: WE ARE UNABLE TO INCLUDE FORMULAS where m_{hh} is the heavy hole mass, e is the electron charge, and ϵ is the dielectric constant for bulk CdSe. The QDs radii were found to be within 2.52 nm and 2.86 nm in agreement with the dimensions obtained by XRD. In the case of NRs, the radial dimensions determined in the same way, were found to be between 2.28 nm and 2.89 nm in good agreement with STM measurements, which gave the rod lengths as 19-50 nm. The second peak in the PA spectra could be described by the transition coupling the 1P_e electron state with the 1P_{1/2} hole state. Furthermore, the thermal parameters of the CdSe nanoparticles (diffusivity α , effusivity e and conductivity k) as determined by PA technique for both the QD's and NR's show an increase by almost an order of magnitude from the bulk values, however, there is no observable variations between the QD's and the NR's thermal parameters.

NOTE: WE ARE UNABLE TO INCLUDE FIGURES

1. E. Hendry, M. Koeberg, F. Wang, H. Zhang, C. deMello Donega', D. Vanmackelbergh, and M. Bonn, Phys. Rev. Lett. 96, 057408, 2006.
2. D. V. Talapin, A. L. Rogach, A. Kornowski, et al, Nanoletters, 1, 207, 2001.
3. L. Manna, E. C. Scher, A. P. Alivisatos, J. Am. Chem. Soc. 122,12700, 2000.

EN-ThP11 Study of Optical and Thermal Properties Of CdTe Quantum Dots Using Photoacoustic Spectroscopy. *A. Badawi, N. Al-Hosiny*, Taif University, Saudi Arabia, *S. Abdallah*, Taif University, Saudi Arabia and Ain Shams University, Egypt, *S. Negm, H. Talaat*, Ain Shams University, Egypt

Semiconductor nanoparticles are currently of great interest for their industrial applications in a variety of optoelectronic devices specially solar cells. Recently, CdTe semiconductor quantum dots (QDs) have become one of the promising materials for high efficiency photovoltaic solar cell. Therefore, massive attention has been devoted to investigate their optical and thermal properties in order to improve the performance of the solar cell. In this work, CdTe QDs were fabricated by the chemical solution deposition (CD) technique [1]. Four samples of increasing time of growth leading to different sizes labeled (a–d) were obtained. The sizes of these samples were estimated using transmission electron microscope (TEM); as an example (d) is shown in Fig. (1)

NOTE: WE ARE UNABLE TO INCLUDE FIGURES

Photoacoustic spectroscopy (PA) was employed to study both the optical and thermal properties of the samples at room temperature and modulation frequency $f = 15\text{Hz}$. Fig (2) show the PA spectra for the four different particle sizes samples (a–d) in the wavelength range 400–700 nm. The absorption edges shift towards lower energy region with increasing size, from (a) at 540 nm to (d) at 595 nm. The PA spectra give typical results with those obtained by regular UV-Vis absorption, though the samples were in colloidal form for UV-Vis and in powder form for the PA. The sizes of the CdTe nanocrystals were calculated using the effective mass approximation (EMA) model [2].

NOTE: WE ARE UNABLE TO INCLUDE FORMULAS

where m^* is the reduced electron-hole mass, E_g is the bulk crystal band gap, R is the average radius of the nanocrystal, $E_{g(\text{nano})}$ is the lowest energy for electronic transition and h is the Planck's constant. The calculated average diameters of CdTe nanocrystal show an increase from 2.13 nm for (a) to 2.43 nm for (d), in agreement with the values determined by TEM.

NOTE: WE ARE UNABLE TO INCLUDE FIGURES

The PA technique was also employed to investigate the thermal properties of the CdTe QDs which are of great importance to solar energy conversion. The powder of each sample size was compressed into a disk. The PA signal amplitude was recorded at various chopping frequencies for each sample (depth profile analysis) using the Argon laser at wavelength 514 nm. The plot of \ln PA amplitude versus the $\ln f$. (Fig. 3) shows a distinct change in slope, at the characteristic frequency (f_c) where the sample changes from being thermally thick to thermally thin. The thermal diffusivity (D), was then calculated using the relation [4].

NOTE: WE ARE UNABLE TO INCLUDE FORMULAS

where L is the thickness of the sample. The calculated diffusivity varies from $0.65\text{ cm}^2/\text{s}$ for (a) to $0.38\text{ cm}^2/\text{s}$ for (d). These values of the thermal diffusivity are at least one order of magnitude larger than the bulk value ($0.05\text{ cm}^2/\text{s}$) [4]. Our results are in agreement with the results of other authors [4,5], where the decrease in thermal diffusivity with increasing the particle size is attributed to the decrease in the population of phonons.

[1] Guo-Yu Lan, Zusing Yang, Yang-Wei Lin, Zong-Hong Lin, Hao-Ying Liao and

Huan-Tsung Chang, *J. Mater. Chem.*, 2009, 19, 2349–2355

[2] Y.-S. Yuang, Y.-F. Chen, Y.-Y. Lee, L.-C. Liu, *J. Appl. Phys.* 76, 3041 (1994)

[3.] Al.L. Efros, A.L. Efros, *Sov. Phys. Semicond.* 16, 772 (1982)

[4] P. Raji, C. Sanjeevrajaa, K. Ramachandran, *Cryst. Res. Technol.* 39, 617 (2004) [5] T. El- Brolossy, S. Abdallah,, S. Negm and H. Talaa *Eur. Phys. J.* 153, 361–

364 (2008)

EN-ThP12 CdTe Quantum Dots Sensitized TiO₂ Electrodes for Photovoltaic Cells. *A. Badawi, N. Al-Hosiny, S. Abdallah*, Taif University, Saudi Arabia, *S. Negm, H. Talaat*, Ain Shams University, Egypt

Semiconductors quantum dots (QDs) has been paid much attention in QDs sensitized solar cell because of their high potential in light harvesting under visible region along with particle size tuning properties. CdTe semiconductor quantum dots (QDs) have become one of the promising materials for high efficiency photovoltaic solar cell [1]. It has a high extinction coefficient ($4.4 \times 10^4\text{ M}^{-1}\text{ cm}^{-1}$) at 370 nm and valence band, conduction band, and band gap energies of -3.9, -5.5, and +1.6 eV, respectively, would behave as sensitizers capable of effectively injecting electrons into TiO₂ NPs (band gap: 3.4 eV) [2]. CdTe QDs were fabricated by the chemical solution deposition (CD) technique [3]. In this article we describe the preparation and photovoltaic characterization of CdTe quantum dot-sensitized solar cells (QDSSCs). We coated Fluorine doped Tin Oxide

(FTO) substrates with 20 nm-diameter TiO₂ nanoparticles (NPs) by the doctor blade method. Then, the as prepared CdTe quantum dots of different sizes were deposited on the TiO₂-coated substrates by the chemical bath deposition (CBD) technique for various periods of dipping times under ambient conditions. Other FTO substrates were coated with platinum to form the counter electrode, while the electrolyte containing I⁻/I₃⁻ redox species was sandwiched between the two electrodes. The I-V characteristic curve of the QDSSCs was measured under AM1.5-simulated sunlight at 100 mW/cm². As a result, the open-circuit photovoltage V_{oc} and the short circuit photocurrent density J_{sc} were about 0.48 volts and 300 $\mu\text{A}/\text{cm}^2$ respectively. The fill factor FF and efficiency for energy conversion η of the photovoltaic cell were calculated to be about 0.48 and 0.113 %, respectively. Our results are comparable with that obtained by Guo-Yu Lan et al [2].

References

[1] Y. Shen, J. Bao, N. Dai, J. Wu, F. Cu, J. C. Tao, J. C. Zhang. *Appl. Surf. Sci.* 255 (2009).

[2] Guo-Yu Lan, Zusing Yang, Yang-Wei Lin, Zong-Hong Lin, Hao-Ying Liao and

Huan-Tsung Chang. *J. Mater. Chemistry* (19), 2349 (2009).

[3] Dmitri V. Talapin, Stephan Haubold, Andrey L. Rogach, Andreas Kornowski, Markus Haase, and Horst Weller, *J. Phys. Chem. B* 2001, 105, 2260-2263

In Situ Microscopy and Spectroscopy Topical Conference

Room: Southwest Exhibit Hall - Session IS-ThP

In Situ Microscopy and Spectroscopy Topical Conference Poster Session

IS-ThP2 Surface Studies of Ionic Liquids and Their Interaction with Water and CO₂. *A.M. Margarella, T.M. McIntire, M.H. Cheng*, University of California, Irvine, *H. Bluhm, Z. Lui*, Lawrence Berkeley National Laboratory, *J.C. Hemminger*, University of California, Irvine

Ionic liquids are substances composed entirely of ions which have a low melting point, typically below 100° C, and other unique properties such as very low vapor pressure. These properties, in addition to ionic conductivity, make them useful as solvents for a number of applications, such as gas separation and solar cells. Using Ambient Pressure X-ray Photoelectron Spectroscopy (AP-XPS), the surface composition of different room temperature ionic liquids has been investigated. AP-XPS offers the advantage of doing photoelectron spectroscopy under higher pressures, up to a few torr, so the sample can be exposed to a variety of chemical environments. The AP-XPS used in these experiments is at the Advanced Light Source synchrotron facility. Utilizing synchrotron radiation, depth profiles of the elements in the compounds can be obtained by varying the photoelectron kinetic energy. We first investigated the surface composition of imidazolium halides under humid conditions; our results indicate that with added water vapor in the chamber, up to 15% relative humidity, the surface composition does change slightly. Higher relative humidity environments are currently being explored. The effect of water vapor on the surface of ionic liquids is important because many ionic liquids are hygroscopic, and when using them in applications, it is difficult to keep them dry. Using AP-XPS, we are also exploring the effect of CO₂ on the depth profiles of the ionic liquids. Ionic liquids have the potential to be used for CO₂ capture because the solubility for CO₂ is generally high and, when compared to other absorbents, the ease of recovery is straight-forward. For this application, the surface plays an important role in this process because the surface of the ionic liquid is the first part that interacts with the gas stream containing CO₂. Depending on the nature of the ionic liquid, it can either dissolve the CO₂ or react with it to form a carbamate. Additionally, we will investigate the role of water on the interaction with CO₂. Near Edge X-ray Absorption Fine Spectroscopy (NEXAFS) will also be used to study these interactions. By combining the surface science techniques XPS and NEXAFS, we can understand the role of different ionic liquids in capturing CO₂.

Magnetic Interfaces and Nanostructures

Room: Southwest Exhibit Hall - Session MI-ThP

Magnetic Interfaces Poster Session

MI-ThP1 Investigations of Magnetic Overlayers at the Advanced Photon Source, G.D. Waddill, Missouri University of Science and Technology, *S.W. Yu, M.T. Butterfield,* Lawrence Livermore National Laboratory, *T. Komesu,* Missouri University of Science and Technology, *J.G. Tobin,* Lawrence Livermore National Laboratory

Magnetic overlayers of Fe and Co have been investigated with X-ray Magnetic Circular Dichroism in X-ray Absorption Spectroscopy (XMCD-XAS) and Photoelectron Spectroscopy (PES), including Spin-Resolved Photoelectron Spectroscopy (SRPES), at Beamline 4 at the Advanced Photon Source (APS). Particular emphasis was placed upon the interrogation of the 2p levels of the Fe.

MI-ThP2 Magnetic Properties of Size-Selected Fe (FeAu) Nanoparticles, K. Paredis, University of Central Florida

We report the magnetic properties of size-selected Fe and FeAu nanoparticles (NPs) supported on SiO₂/Si(001). These microscopic properties are dominated by two key parameters: finite size effects and surface effects.

In order to systematically study size effects, we use the method of inverse micelle encapsulation (PS-P2VP diblock - copolymers) for the growth of the nanoparticles. This approach results in Fe (and FeAu) NPs with a high homogeneity in size, shape and inter-particle distance. Following this method, the NP size can be tuned by changing the length of the polymer head (P2VP) while the interparticle distance can be modified by changing the length of the polymer tail (PS). Investigating these NPs in-situ (ultrahigh vacuum) after the removal of the encapsulating ligands by means of a variable temperature magneto-optical Kerr effect set-up enables the determination of: (i) the temperature dependence of the coercivity and remanence of the NPs, (ii) the blocking temperature for the ferromagnetic-superparamagnetic transition, and (iii) the direction of magnetization in anisotropic nanostructures. This new insight constitutes a step forward towards unravelling the influence of the NP geometrical structure (size and shape) on its magnetic properties. Additionally, by varying the interparticle distance we can probe the role played by particle-particle interactions in the collective magnetic behavior.

MI-ThP3 Fabrication of a Non Local Spin Logic Device with Exfoliated Graphene Channel, J.R. Abel, A. Matsubayashi, J.J. Garramone, V.P. LaBella, University at Albany

The use of the electron spin has gained considerable attention lately as a possible substitute for charge-based electronics [1,2]. This poster will focus on the fabrication of a spin logic device that utilizes graphene as the spin transport channel since graphene has been shown to have a long spin lifetime at room temperature [3]. The device is prepared utilizing exfoliated graphene on SiO₂. The injection and readout contacts were fabricated with and without aluminum oxide as a tunnel barrier which was deposited using thermal evaporation of Al in ultra high vacuum (UHV) and then subsequent oxidation in O₂. Then Co/Au was deposited under high vacuum and 100-200-nm-wide contacts were patterned using e-beam lithography followed by a standard liftoff technique. Scanning electron microscopy and optical images will be presented of the fabrication process and the device. Non-local spin valve and Hanle measurements are being pursued to characterize the spin injection polarization and the spin relaxation in the graphene channel.

[1] Behin-Aein, B., Datta, D., Salahuddin, S., Datta, S. *Nat Nano* 5:266-270 (2010)

[2] Dery, H. Dalal, P., Cywinski, L. & Sham, L.J. *Nature* 447, 573-576 (2007)

[3] Tombros, N., Jozsa, C., Popinciuc, M., Jonkman, H.T., Van Wees, B.J. *Nature*, 448 (7153), pp. 571-574 (2007)

MI-ThP4 Magnetic Properties of Zn_{1-x}Mn_xO Thin Film Grown by Pulsed Laser Deposition, T.C. Wu, Y.C. Yeh, D.R. Liu, National Applied Research Laboratories, Taiwan, *H.J. Lin, M.J. Huang,* National Synchrotron Radiation Research Center, Taiwan

In this paper, Zn_{1-x}Mn_xO (x=0-0.1) thin films were grown on corning glass, sapphire (0001) and silicon (100) substrates by pulsed laser deposition (PLD). Atomic force microscopy (AFM) and magnetic force microscopy (MFM) were used to characterize the surface properties of Zn_{1-x}Mn_xO thin film, and the high-resolution x-ray diffraction (XRD) was used to measure the crystallographic structure of this film. Moreover, superconducting quantum interference device (SQUID) magnetometer was employed to

investigate the magnetic moments. X-ray magnetic circular dichroism (XMCD) spectra of Zn_{1-x}Mn_xO films were also measured to clarify their spin and orbital magnetic moment properties. Integrating above measurements, these results reveal that substrate plays an important role and oxygen is the key factor for magnetic properties of Zn_{1-x}Mn_xO thin films.

MEMS and NEMS

Room: Southwest Exhibit Hall - Session MN-ThP

MEMS and NEMS Poster Session

MN-ThP1 A Novel Micro-droplet Proteomic Identification Chip for Protein Digestion and MALDI-TOF MS, T.T. Huang, Instrument Technology Research Center, Taiwan, Republic of China

Proteomic identification at the point of care would be valuable for a wide variety of applications and importance, including clinical diagnostics, food safety, and environmental monitoring. Traditional proteomic identification makes use of protein digestion of interesting sample and could be detected using matrix assisted laser desorption/ionization time-of-flight mass spectrometry (MALDI-TOF MS). Protein digesting reaction in vitro often wastes much time (usually overnight) and reagent volume, and then the reaction products should be transferred to the MS sample plate and air-dried. The analysis process is not effective for convenience and wastes time and analysis sample.

For more effective protein identification, we construct a novel micro-droplet chip system with auto-positioning and enriching the sample for rapid analysis. Presently, MALDI-TOF MS has been widely used in proteomic research, and it is the important issue to identify the micro sample. Utilizing the novel micro-droplet chip, protein sample would be co-crystallized with MS matrix and concentrated on the detection area. Through drying the sample and matrix mixture, protein digestion would be reacting at the same time. The sample would be digested to smaller dried peptides on chips and then detected with matrix assisted laser desorption/ionization time-of-flight mass spectrometry (MALDI-TOF MS). Comparing to the traditional methods, the proteomic identification chip offers four advantages: 1. shortening reaction and analysis time (total ~2.5 hours); 2. auto-positioning and enriching the sample concentration; 3. lower reaction volumes (1~5 µL); 4. entire process sequentially on the chip.

MN-ThP2 Test Instrument for the Mechanical Strength of Micro-Nano Materials, A. Kasahara, H. Suzuki, M. Goto, H. Araki, M. Tosa, National Institute for Materials Science, Japan

There is considerable research at present on the performance and properties of nanosheets, nanofibers and other functional nanomaterials such as fullerenes and nanotubes. This is particularly true of carbon nanotube, made from carbon atoms, where many research projects throughout the world are looking at measurement techniques for evaluating electrical and electronic characteristics with a view to developing electronic device applications such as high-intensity field-emitted electron sources and ultra-fast transistors. We have prepared long crystal silicon wires with a diameter of several tens of nano meters at a temperature lower than 523K by using the low-pressure low-temperature CVD method. To use these as materials for application to micro-nano electromechanical system, we need to fully understand their electric, chemical and mechanical properties. However, we have not yet to see a genuine, flexible methodology for evaluating the key characteristic of mechanical strength essential to micro-nano structural materials development the nanoscale equivalent of mechanical strength testers for ordinary materials. This is due to the inherent difficulties associated with the manipulation and transportation of materials at the micro-nano scale level. The most difficult part of the handling of small materials is to fix material samples.

We have improved it to the device with an easy fixation of the sample from the last time. Here, we will discuss our recent results on mechanical strength measurement of micro-nano wires in diameter several nm through several thousand nm and in length several mm by means of prepared micro-nano tensile strength tester device.

MN-ThP3 A Micro-droplet PCR Device with Low Volume Reaction and Rapid Amplification, T.T. Huang, Y.C. Ou, Instrument Technology Research Center, Taiwan, Republic of China

Nucleic-acid amplification and analyses techniques have become the most significant tools for many important applications. Besides the frequent molecular diagnosis of diseases and assessments of therapies in clinics and hospitals, they are also broadly applied in environment surveillances, food processing industry and agricultural researches. The amplification of the amount of nucleic-acid analyte in the test sample is essential for sufficient detection. Polymerase chain reaction (PCR) is the major process to amplify

interesting nucleic-acid. However, it always spends too much analyte volume and 3~4 hours for carrying out the reaction. In the study, we construct a novel micro-droplet PCR device and PCR chips utilizing MEMS techniques.

The temperature variation of the micro-droplet PCR device achieves 1 °C per second. Moreover, we develop the micro-droplet PCR chips fabricated by silicon wafer with two concentric circles structure. Then, the chip is coated with a layer of PPFC (plasma polymerization fluorocarbon) film on its surface. Utilizing the MEMS process, the solution of nucleic-acid reactants is concentrated in the inner circle and 5 μ L the mineral oil in the outer circle is covered on the reaction solution. Comparing to the traditional PCR method, the micro-droplet PCR device and chips have the advantages of extremely low-volume reaction solution (only 1~2 μ L) and rapid amplification time (~30 minutes). The novel micro-droplet PCR device is quite promising to efficiently DNA amplify.

MN-ThP4 Boundary Slip and Nanobubble Study in Micro/Nanofluidics with Atomic Force Microscope, B. Bhushan, The Ohio State University

The boundary condition at the liquid-solid interface in micro/nano scale is an important issue in micro/nanofluidics systems. Recent studies have shown that the fluid velocity near solid surfaces is not equal to the velocity of the solid surface on hydrophobic surfaces, which is called boundary slip. The degree of boundary slip is evaluated by a slip length. Theoretical and experimental studies suggest that at the solid-liquid interface, the presence of nanobubbles is responsible for the breakdown of the no-slip condition. Nanobubbles are long lasting on hydrophobic surfaces, and movement and coalescence of nanobubbles are observed with higher scan loads during imaging with tapping mode AFM.

In this study, both contact and dynamic AFM methods have been applied to study the boundary slip on hydrophilic, hydrophobic, and superhydrophobic surfaces. An AFM based technique is developed to study boundary slip. Nanobubble movement and coalescence, as well as tip-bubble interaction, are studied in detail. The physical interaction between nanobubbles and the surfaces supporting them is investigated.

MN-ThP5 Rapid Point-Of-Care (POC) Diagnostics by Droplet-Based Detection Instrument, C.S. Yu, Y.C. Hu, H.-S. Huang, J.-S. Kao, ITRC, Taiwan, Republic of China

This paper proposes a novel point-of-care (POC) instrumentation, provides fast, simple, low cost detection and easy used. This instrument including three main parts, micro fluid chip module, electronic module and optics detection module. We use the standard the LIGA-Like process to complete the micro fluid chip. Metal master which using the electroplating technology, the massive manufactures uses the Hot-Embossing process. We characterize a gradient of surface tension force to manipulation droplet and a droplet-based reagent can be transported, precisely positioning, and mixed on the detection zone without any power source. A variety of applications are also possible such as food testing, drinking water testing, alcohol testing, anti-oxidation measurement and cosmetic analysis.

MN-ThP6 Absorption and Emission of Plasmonic Antenna Arrays, K.E. O'Brien, M.R. Davidson, P.H. Holloway, University of Florida

New and more portable means of generating narrow band radiation is of interest, especially in the terahertz (THz) range. One potential method for generating radiation involves photo-mixing over nano/micro scale plasmonic structures. The plasmonic structures can serve as antennas for absorbing incoming photons and conversely emit radiation of a lower frequency. Designs include 2-dimensional and 3-dimensional arrays of these resonant structures fabricated on Ag thin films using electron-beam lithography and lift-off. Patterns vary from arrays of structures of identical lengths and widths, to those with alternating and increasing lengths and widths. We have shown emission of visible radiation from similar structures when excited by space charge from electrons. The absorption and emission of light by the arrays has been measured. The effect of different antenna structures on the in absorption and emission will be discussed.

MN-ThP7 Biomimetic Application of Localized Hydrophobicity for Increased Drag Reduction Performance on Shark Skin-Inspired Riblet Surfaces, B. Dean, B. Bhushan, The Ohio State University

The skin of fast swimming sharks exhibits riblet structures aligned in the direction of flow which are known to reduce skin friction drag in the turbulent flow regime. Fish secrete mucus through their skin which greatly reduces drag during swimming. Small amounts of mucus have been seen on the scales and riblets of fast swimming sharks, which affect the near-skin flow properties in some way. The drag reduction effect of this trace amount of mucus on the surface of the shark skin is approximated by the slip length present in water flowing over a hydrophobic surface. A biomimetic study is done in which the drag reduction benefit of localized and non-localized

hydrophobic surface applications onto drag reducing riblet structures are studied. The combined effect of turbulent drag reduction by localized or non-localized hydrophobicity and by riblet mechanisms is presented.

MN-ThP8 Development of High-Density Cylindrical Ion Trap Array for Mass Spectrometer, T. Wu, A. Chaudhary, F. Amerom, T. Short, J. Wang, University of South Florida

This paper presents the development of high-density cylindrical ion trap array for mass spectrometer (CIT-MS). The previous research has mainly focused on the adjusting the ring electrode radius r_0 , cylinder length z_0 , and endplate hole electrode r_H (Figure 1) and developing a fabrication process involving a back-to-back bonding of two half CIT structures. However, recently it has been noticed that a key factor that limits the performance of the CIT is the high capacitance between endplate electrodes and ring electrode due to the small gap; besides, the back-to-back bonding of two half structures could bring a maximum 5 micron misalignment. Based on these concerns, a new geometry of CIT array for mass spectrometer has been designed; also a new fabrication process has been developed accordingly.

In the newly developed generation of CIT-MS, the geometry design of CIT has been focusing on increasing the gap between the ring electrode and endplate electrode. Several simulations have been done on this subject. Other important improvements include better ring-to-endplate aperture alignment using dedicated alignment marks during flip-chip bonding, hexagonal orientation of traps leading to smaller pitch between each trap to increase density (thereby more trapping volume per unit area of wafer), larger vacuum gaps for operation at higher voltages for increased mass range and selective metallization using lithography techniques to reduce the overlap area of ring and endplate electrodes for lower capacitance.

A new fabrication process has been designed to achieve the improvements mentioned above. A suspended endplate electrode structure, using KOH/DRIE etching techniques, was used to increase the gap and reduce the overlapping area at the same time. To avoid surface charging of the dielectric surface that is exposed to ions, Atomic Layer Deposition (ALD) was investigated to deposit highly resistive (ZnO) layer on the dielectric surface to dissipate charge, while adding minimum to the capacitance. Flip-chip bonding was used to bond the ring-electrode and endplate electrodes and minimize the misalignment between the two substrates. With these considerations, both the resolution specificity and sensitivity are expected to improve. The design of optical mask for this process is underway and we report preliminary progress based on the latest findings.

MN-ThP9 Development of Optimum Ti/TiN Dark Reference Structure to Improve Dark Leakage Characteristics in CMOS Image Sensor, S.-Y. Kim, Korea Polytechnic College IV, Republic of Korea, N.-H. Kim, Chonnam National University, Republic of Korea, K.-G. Oh, Chosun University, Republic of Korea

MN-ThP10 Improvement of Optical Properties in 3D CMOS Image Sensor (CIS) by Using Insertion Structure of Metal Slot, S.-Y. Kim, Korea Polytechnic College IV, Republic of Korea, G.-M. Han, N.-H. Kim, Chonnam National University, Republic of Korea

High integrated CMOS image sensor (CIS) has continuously decreased the area of photodiode in CIS structure. This is the originated reason to decline the optical characteristics of CIS including optical generation collection efficiency (CE), and crosstalk. Although the conventional structure used the PD structure with shallow trench isolation (STI) for pixel-to-pixel isolation, this structure brought out the high leakage characteristics. To improve this leakage problem, the conventional process employed the counter-doping method of impurities; however, this method could not solve the crosstalk problem by the obliquely incoming light. In this study, both the counter-doping of impurities and insertion of metal slot into the center of counter-doping were proposed to form the pixel-to-pixel isolation. This structure carried out the role of wave-guide with the excellent light reflection characteristics of metal as well as the conventional ground of contact. The crosstalk issue was successfully improved with the enhancement of the optical generation characteristics of 3D CIS by using this novel structure instead of the conventional STI pixel-to-pixel isolation method.

MN-ThP11 Modeling of Diffusion, Nucleation and Growth in the Chemical Vapor Infiltration of Vertically-Aligned Carbon Nanotube Forests for MEMS, A.M. Konneker, D.D. Allred, R.C. Davis, Brigham Young University

We present preliminary results using computer simulation of chemical vapor deposition into vertically aligned carbon nanotube (VACNT) forests. The model is based upon deposition processes used in the carbon nanotube templated microfabrication (CNT-M) process. It utilizes VACNT arrays as a framework into which matter is infiltrated via a chemical vapor deposition (CVD)-type process to create solid microstructures and

microelectromechanical systems (MEMS). These can have large aspect ratios (200:1) and startling heights (to date up to a mm). Long nozzles with narrow ID and other structures have been made that would be difficult by subtractive techniques. One of the biggest advantages of CNT-M is the promise of being able to prepare MEMS from any desired solid material that can be deposited by CVD, though to date this has only been amorphous and polycrystalline Si, SiO₂, SiC, silicon nitride and amorphous carbon.

This work was inspired by the desire to understand how the gas diffusion, reaction and nucleation and growth models used to describe, mostly 2-D, thin-film CVD can be applied to understanding growth on the individual carbon nanotubes and nanotube bundles that make up a VACNT structure. This scaffolding is 3-dimensional, but "rarified"- that is > 99% empty and geometrically complex, and is vital for use of the CNT-M process. How it changes from mostly emptiness to a filled structure was a puzzle. Without optimized growth parameters, deposition is limited to the exterior of the VACNT forests and the structural integrity of the MEMS is poor. In addition, the adhesion of the MEMS devices to the substrate is often inadequate, which leads to low yields and frequent device failure.

Our model explores how the deposition rate, VACNT geometry, and VACNT forest density affects the filling of the forest. We base the parameters in our model on data from the TEM analysis of MEMS devices fabricated using the CNT-M process with CVD-deposited polysilicon, amorphous carbon, and silicon nitride.

Plasma Science and Technology

Room: Southwest Exhibit Hall - Session PS-ThP

Plasma Science and Technology Poster Session

PS-ThP1 Transition in Intensities of the Forbidden Atomic Oxygen Spectral Lines and its Application to Plasma Monitoring. *V. Milosavljevic*, Dublin City University, Ireland & University of Belgrade, Serbia, *A. Jasenko*, Faculty of Pharmacy, Serbia, *Z. Simic, L.C. Popovic*, Astronomical Observatory, Serbia

To decouple the optical contributions of surfaces in a process chamber to the plasma chemistry from those of other constituents present in the plasma is one of the most demanding tasks today. In this work oxygen spectral emission is used for purposes to increase understanding of plasmas such as those used in industry and particularly those used in semiconductor device manufacture, when plasma-surface interactions are of critical importance.

We analyze the intensity of forbidden oxygen lines at 630.0, 636.3, 297.23 and 557.73 nm as well as the (NLTE afflicted) oxygen triplet lines around 777.4 nm. The emission of forbidden spectral lines is used to establish a threshold for actinometry. Actinometry suffers from signal masking by molecular species due to molecular dissociation and trace gas emission. To establish the threshold for actinometry we monitor the emission of forbidden spectral lines and search for "phase transition" in the intensities of forbidden spectral lines (in most cases the upper energy levels of atomic forbidden lines are below the threshold for dissociation of any constituent molecule so that any sudden increase in the emission intensity of forbidden lines indicates molecular dissociation has occurred). Concurrently the forbidden spectral line is used for determination of the main plasma parameters too.

Radiative emission of the forbidden spectral lines follows a three level atomic model that characterizes the radiative transfer processes, and can help to understand the contribution of molecular dissociation processes to the emission spectrum of atomic oxygen. This represents a major contribution to the current state of the art and eliminates the requirement for trace gas based actinometry which will overcome not only the molecular masking problem but the intrinsic problem of having a trace gas in the plasma discharge. Thus, this work develops the method based on OES as a non-invasive technique for quantifying complex chemistry which has direct application in plasma processing in semiconductor and other industries. This approach enables greater understanding of complex processes allowing, optimization, fault detection, increased productivity and yields. The challenge in this case lies in the complex plasma chemistry that is commonly used in surface treatment and the constraint of applying intrusive sensors to industrial plasma reactors. These constraints make OES ideal for industrial use, however interpreting the spectra and extracting useful information is the challenge. This work is done with ICP 13.56 MHz RF plasma discharge at pure oxygen, as well as oxygen-argon-hydrogen mixture.

PS-ThP2 Optical Emission and Mass Spectrometric Characterization of a Dual Plasma PE-CVD System. *Z. Chen, V.M. Donnelly, D.J. Economou*, University of Houston

Initial diagnostic studies will be presented of a novel PE-CVD reactor suitable for self-limiting growth of thin films through a repetitive, step A / step B, process. In a single vacuum system, two independent plasma sources are operated to separate step A from step B. An Ar gas curtain minimizes mixing of the gases of the two plasma sources. As an example, this reactor could be used to deposit a very thin hydrogenated amorphous silicon (a-Si:H) film in step A, followed by exposure of this film to a hydrogen plasma in step B, to induce formation of silicon nano-crystallites. In the present reactor configuration, one plasma source is a capacitively-coupled plasma (CCP) reactor and the other is an inductively-coupled plasma (ICP) reactor. The substrate is moved back and forth between the two sources. Optical emission spectroscopy (OES) and mass spectrometry (MS) are used to detect radicals (OES) and stable feed gas and products (MS) in the two plasma sources. Results will be presented for a SiH₄/He CCP and H₂, N₂ or O₂ ICPs operating simultaneously. The degree of separation of the two plasma sources will be presented as a function of the Ar flow rate to the gas curtain, as well as the feed gas flow rates and pressures of the plasma sources.

PS-ThP3 Diagnosis of Gold Nanoparticle Synthesis in Solution Plasma by Coherent Anti-Stokes Raman Spectroscopy. *D. Fujimoto, J. Hieda, M.A. Bratescu, O. Takai, N. Saito*, Nagoya University, Japan

The performance of the electrical discharges in the aqueous solution presents modern and ecologically very attractive way of the synthesis of nanoparticles. Such kind of techniques are known for the production of very active species like hydrogen radicals, hydroxyl radicals, ozone, aqueous electrons, UV light, etc., which are characterized by its very high reactivity. Although both oxidation and reduction agents were generated in the plasma, gold, platinum, and copper ions were reduced by the plasma. In order to control the reactions in solution plasma, the understandings of activated species and their behaviour are needed.

In this paper we present process diagnosis of gold nanoparticles synthesis in solution plasma based on coherent anti-stokes Raman spectroscopy (CARS). This discharge is generated between two wire type electrodes faced one to each other and driven by bipolar dc pulse power supply. Utilization of this power supply gave us a possibility of an intensive and stable working condition even at lower liquid conductivities. Operation conditions of this power supply lie in the frequency range 0-50 kHz, with minimum pulse length, 2 ms, and maximum voltage, 1.5 kV. In order to obtain desired conductivity of liquid, a small amount of KCl was added into the water. Initial [AuCl₄⁻] concentration and pH were varied. The reactor was placed on the stage of the optical microscope with CARS system. The morphology of the nanoparticles obtained was observed by transmission electron microscopy (TEM). The solution after discharge was also analyzed by UV-Vis spectroscopy and ICP-MS.

PS-ThP4 Characterization of a Faraday-shielded Inductively Coupled Plasma using Langmuir Probe and Optical Emission Spectroscopy. *W. Zhu, H. Shin, L. Xu, V.M. Donnelly, D.J. Economou*, University of Houston

A novel plasma reactor was designed and built to control the electron energy distribution function (EEDF) in the plasma, as well as the ion energy distribution (IED) and ion angular distribution (IAD) on the substrate electrode. The main inductively coupled plasma (ICP) source has a Faraday shield to minimize the RF component of the plasma potential. The substrate electrode and another electrode in contact with the plasma (boundary electrode) can be biased independently with DC or RF voltages to influence the IED and IAD. A second tandem ICP plasma source may be used to inject a secondary plasma or metastable atoms to the main source, to influence the EEDF. A continuous wave argon plasma in the main ICP was characterized with a Langmuir probe (LP), with and without the Faraday shield installed. With the Faraday shield, the DC value of the plasma potential decreased from 25 to 17 V, and the corresponding peak-to-peak amplitude of the RF oscillation dropped from ~15-20 V to ~0.8-1.5 V, compared to the case without the Faraday shield. A low plasma potential is critical for certain processes such as atomic layer etching with monolayer precision. The electron "temperature" as well as the ion and electron densities were measured for a range of powers and pressures. The plasma density was $1.5 \times 10^{12} \text{ cm}^{-3}$ at 40 mtorr and 300 W. The EEPF was also measured with the LP; comparisons with EEPFs extracted using trace rare gas-optical emission spectroscopy (TRG-OES) will be presented. In addition to argon, oxygen and krypton plasmas were studied and their similarities and differences with the argon plasma will be shown. Control of the plasma potential and hence energy of ions impacting surfaces was achieved by applying a positive DC voltage to a boundary electrode immersed in the plasma. Finally, preliminary results of plasma injection from the secondary to the main plasma source and its effect on the EEDF will be presented.

Work supported by the Department of Energy Plasma Science Center and NSF

PS-ThP5 Diagnostic of Laser Ablation Air Plasma using Wide Field Spectroscopy. *N. Abundiz*, UNAM-CICESE, Mexico, *C. Velez*, UABC, Mexico, *E. Luna*, *S. Zazueta*, Universidad Nacional Autónoma de México, *R. Machorro*, Universidad Nacional Autónoma de México

Plasmas generated by pulsed laser have a brief existence and their properties are far from uniform. Optical spectroscopy provides information about the spatial and temporal evolution of transient species produced by the laser-matter interaction, such as excited atoms, ions or molecules. This knowledge is essential to understand the ablation phenomenon, and develop better models.

In this work, we use a Nd-YAG laser with 3J energy, 1064nm wavelength, and 7 ns duration pulsed beam, focused with a 20cm focal length biconvex lens into ambient air. Fluence of the order of 3×10^6 J/m² creates an electric field of 3×10^9 V/m, enough to ionize the air atoms, creating a plasma.

A camera lens forms the plume image into the image plane, where an optical fiber array with 12*12 fibers is placed. The array is re-arranged to form a one-dimensional column with 144 fibers, which becomes the entrance slit of the spectrograph. A gated image intensified CCD captures the output plane of the spectrograph. An electronic device produces a precise time delay between laser pulse and image capture. From this data is possible to get density and temperature maps of the species, and its discrete time evolution. Moving the camera lens and fiber array along the optical axis, we make a confocal scanning of the plasma.

In the high density regime, the plasma is dominated by collisions, and intensity ratios of lines from the same ion will depend exclusively on the temperature in the manner prescribed by the Boltzmann distribution. We present reconstruction of spectral images of the plasma, as a function of time and axial displacement.

Partial support from the CONACyT project 60351 and DGAPA-UNAM project IN100910 is acknowledged, student NA thanks Conacyt for her scholarship.

PS-ThP6 In-situ Monitoring of Organic Pollutants Degradation in Pulsed Plasma by Coherent Anti-Stokes Raman Spectroscopy. *M.A. Bratescu*, *N. Saito*, *O. Takai*, Nagoya University, Japan

Water pollution and storage is becoming an important problem to the people worldwide. Conventional water treatment processes, such as chlorination and ozone oxidation suffer a lot of limitations. The application of pulsed electrical discharges in water solutions for degradation of organic pollutants offers the advantage of simultaneous using of different physical effects (UV light) and chemical effects by the active species like OH, H, O, HO₂, H₂O₂, O₃ able to decompose the harmful organic compounds. In this study we analyzed the degradation of the benzoquinone molecule by using *in-situ* Coherent anti-Stokes Raman Spectroscopy (CARS) in order to monitor the active species during the decomposition process.

In the present experiment a pulsed plasma in an aqueous benzoquinone solution was used. The plasma was generated in a reaction glass cell, between two rods electrodes. The plasma electrical characteristics were: the peak to peak voltage of 2 – 4 kV, the pulse frequency of 10 – 15 kHz and the pulse width of 2 μs. The reaction cell was set on the optical microscope stage of the CARS system. Benzoquinone was dissolved in a potassium sulfate solution (4 g/L) and the pH was adjusted with dilute sodium hydroxylate or dilute sulfuric acid.

The CARS benzoquinone signal was observed at 1230 cm⁻¹, 1050 cm⁻¹ and 1667 cm⁻¹ corresponding to COH bending CH₂ bending and CC stretching vibrations, respectively. Degradation of the benzoquinone molecule was monitored by the peak at 1667 cm⁻¹, characteristics to benzene ring vibration. The shift and the amplitude of the absorption peak at 427 nm were observed by *ex-situ* measurements by the UV-visible spectroscopy.

The degradation of benzoquinone molecule depends on solution pH and plasma electrical characteristics.

PS-ThP7 Study of Plasma-based Ion Implantation Sterilization using High Resolution Rutherford Back Scattering. *T. Tanaka*, *T. Hironaka*, Hiroshima Institute of Technology, Japan, *S. Hayashi*, Japan Medical Creative, Japan, *I. Koyama*, Saitama Medical University, Japan

Plasma base ion implantation (PBI) with negative voltage pulses to the test specimen has been applied to the sterilization process as a technique suitable for three-dimensional work pieces. Pulsed high negative voltage (5μs pulse width, 300 pulses/s, -800 V to -13 kV) was applied to the electrode in this process at a gas pressure of 2.4 Pa of N₂. We found that the PBI process reduced the numbers of active *Bacillus pumilus* cell using N₂ gas self-ignited plasma generated by only pulsed voltages. The number of bacteria survivors was reduced by 10⁻⁵ x with 5 min exposure. As the ion

energy is the most important processing parameter, a simple method to estimate the nitrogen ion energy calculated using distribution for nitrogen in Si implanted by PBI was estimated. The ion implanted surface using PBI sterilization is discussed from measurements data using the High Resolution Rutherford Back Scattering (HR-RBS).

PS-ThP8 A Novel Current-Voltage Probe for Diagnostics in Deposition Plasma. *M.B. Hopkins*, *D.M. O'Sullivan*, Impedans Ltd., Ireland

Current- voltage probes monitor power parameters, such as the voltage, current and phase angle of an RF power used to generate the plasma (source) or to bias a substrate. A number of commercial systems are available and a key feature is that the sensors work in non-50Ω environment. This allows the sensor be placed either pre-match or post-match and still make accurate measurements.

The most important plasma parameters in a capacitively coupled plasma source or bias configurations are the flux and energy of ions arriving at the substrate. The ion flux is difficult to establish in deposition tools as the plasma often deposits insulating layers, such as in the manufacture of solar panels.

We report on a novel IV sensor, which is placed post-match in series with a capacitively coupled RF biased plasma electrode. The sensor integrates the current into voltage bins. We show that the resulting characteristic represents the real current-voltage (IV) characteristic of the electrode. The measured IV trace is similar to a DC Langmuir probe IV trace and we determine the ion flux to the biased electrode. We compare ion flux measured by the IV probe with the ion flux determined by a retarding field analyzer placed on the electrode.

Other parameters such as electron temperature and plasma potential are also obtained and compared to direct measurements taken in the source.

PS-ThP9 Hardness and Roughness of SiCN Thin Films Deposited at 500 °C by RF-PECVD. *T. Wydeven*, *T. Kawabe*, SAMCO International, Inc.

The experimental difficulties encountered in attempting to synthesize super hard high purity polycrystalline or single crystal beta carbon nitride (β-C₃N₄) films has prompted research on the synthesis of hard silicon carbon nitride (SiCN) films(1). Current research interest in SiCN is motivated by several reported desirable properties of this material(2). Among those properties are short bond length, high bond strength and therefore high hardness, adjustable friction coefficient, high resistance to wear and corrosion and wide band gap.

The work reported on here is a continuation of our earlier research (3) on the deposition and characterization of near stoichiometric SiCN films deposited at ambient temperature from a gas mixture (SiH₄, CH₄, N₂) and using RF-PECVD. In this work, we report on the hardness and characterization of surface topography by roughness measurements and SEM photographs of SiCN films deposited at 500 °C on silicon wafer substrates using RF-PECVD. These measurements are important in applications involving friction, lubrication and wear(4).

References

1. J. C. Sung, *New Diamond and Carbon Technology* **12** (2002) 47.
2. Fei Zhou, Bin Yue, Xiaolei Wang and Lanjian Zhuge, *Journal of Alloys and Compounds* **492** (2010) 269-276.
3. T. Wydeven and T. Kawabe, *Deposition and characterization of silicon carbon nitride films prepared by RF-PECVD with capacitive coupling*, Proceedings of the 19th International Symposium on Plasma Chemistry, Bochum, Germany, July 26th-31st, 2009.
4. T.R. Thomas, *Rough Surfaces*, 2nd ed., Imperial College Press, London (1999).

PS-ThP10 The Role of Negative Oxygen Ions in the Pulsed-Plasma Deposition of Titania Films. *J.W. Bradley*, *R. Dodd*, *S.D. You*, University of Liverpool, UK

Reactive pulsed magnetron sputtering is the process of choice to deposit commercially important oxide-based thin films and coatings. The technique relies on the plasma ions (e.g. Ar⁺, O⁺) assisting the deposition process through energetic impact at the substrate leading to good, dense coating structures.

However, in these systems copious amounts of negative ions (O⁻, O₂⁻, O₃⁻, MO_x⁻) can be created at the cathode target. These ions are accelerated through the cathode sheath to bombard the substrate with upper energies equivalent to the target potential, (i.e. hundreds of eV). These ions easily overcome the negative substrate bias potentials, used to attract positive ions and can be wholly destructive to growth of engineering quality films.

In this study we use an eclipse laser photo-detachment technique combined with a Langmuir probe to measure the density of negative ions in the pulsed

sputtering of titanium in oxygen-argon mixtures. This has been done at different positions in the plasma during different phases of the driving pulsed-voltage waveform. The results show that the total negative ion density can exceed that of the electrons and at positions close to the substrate on the discharge centre line, the fraction of very fast negative ions can be over 10% of the total observed. The power fluxes of these species at the substrate have been calculated and the effect on the growing TiO₂ film is discussed.

PS-ThP11 Investigation of the Plasma Parameters and Plasma Process-Induced Damage in Physical Vapor Deposition, X. Tang, T.-J. Gung, S. Gandikota, P. Gopalraja, R. Wang, G. Liu, Applied Materials Inc.

The introduce of the high K and metal gate enables significant gate leakage reduction (>100x) with excellent transistor performance. Physical vapor deposition process plays an important role in its manufacturing process because of its film composition tunability, excellent step coverage and thin film uniformity. However there are growing concerns about the potential process damage induced by the physical vapor deposition process since in some cases these films are directly deposited on thin (~20Å) high k films. It is well known that PID can be classified into three categories: charging damage by plasma non-uniformity, bombardment damage by high energy ions, neutrals, and electrons, and radiation damage from plasma emission. In this paper, we mainly focus on high energy components in plasma itself and the process induced damage caused by the plasma non-uniformity. Both the discharge plasma properties (such as n_e, T_e, target voltage, ion energy etc) and their correlations to the potential plasma process induced damage were discussed. Two types of PVD chamber designs were evaluated in this study. One is a short throw rf PVD chamber which has both RF and DC power capability on the sputtering target. Another one is a long throw dc sputtering chamber with a special high ionization magnetron. Ti target material is used in this study. Discharge plasma parameters such as (plasma density n_e, electron temperature T_e, and plasma potentials V_{pl}) were monitored by a Langmuir probe inserted into the discharge cavity. The corresponding neutral and ion energy were further derived based on the measured target voltage and wafer self-induced dc bias. The plasma uniformity is characterized by an ion current probe biased at the ion saturation region. Two test vehicles: the 'Spiders' wafer with different ANT ratios and MOS cap were used to quantify the plasma process induced damage.

Langmuir probe studies show that the rf plasma density increases linearly with the rf power while

the electron temperature remains constant in RF PVD chamber. Very high metal ionization was achieved as a result of the high plasma density by high rf power and high pressure (>50mT) operation. Interestingly, no plasma process induced damage were observed by RF PVD Chamber under a broad range of process conditions even with different ion energy. On the other hand, with the dc high ionization (magnetron with a UB>3.5) operation, significant plasma damage was observed under most conditions. The damage was later correlated to the plasma non-uniformity. These results clearly demonstrates that plasma non-uniformity needs to be optimized for any PVD hardware for the damage sensitive applications.

PS-ThP12 Realization of Silicon Antireflection Subwavelength Structure using Simple One Step Plasma Fabrication Process, B.S. Kim, J.H. Sung, M.W. Lee, C.H. Choi, H.D. Yim, S.G. Park, S.G. Lee, E.H. Lee, B.H. O, INHA University, Republic of Korea

Polished flat silicon surfaces have high reflectivity in visible lays. The minimization of reflection losses is very important for solar cells. Lowering surface reflectivity of silicon by texturization is one of the most important processes for improving the conversion photovoltaic efficiency of silicon solar cells.

Many texturing techniques for fabricating antireflective silicon surfaces have been proposed, including mechanical diamond saw cutting, optical interference lithography, wet etching using catalysis of metal, and reactive ion etching, to produce so-called "black silicon".

In this paper, we attempted to one step etching for formation of black silicon using combined Cl₂, C₄F₈, and O₂ gases. It uses inductively coupled plasma (ICP) and Cl₂ gas for etching, C₄F₈ and O₂ gas for masking.

The substrate temperature was -10 °C ~ 10 °C, the fluorocarbon film deposited in a C₄F₈ plasma was thicker and more strongly bonded than the lower substrate temperature. Then combined O₂ gas, fluorocarbon film was locally etching which is self-masking effect. The diameter of fluorocarbon mask was dozens nanometer size.

With Cl₂ etching, many processes were developed for producing vertical sidewalls, smooth surface morphology, fine critical dimension control, and high aspect ratio microstructures for MEMS. The main advantage of Cl₂ etching is that etching is anisotropic since it is an ion assisted process rather than a spontaneous etching process. The subwavelength silicon pillar

structure was grown up because physical etching characteristic of Cl₂ plasma.

The etched silicon surface shows almost zero reflectance in the visible region. The silicon surface is covered by columnar microstructures. The diameter and height of subwavelength silicon columnar structures were depends on substrate temperature, etching, and gas contain ratio.

PS-ThP13 Synthesis of Zinc Oxide Nanoparticles Using an Atmospheric Pressure Plasma Jet, S.M. Chang, C.C. Hsu, National Taiwan University, Taiwan, Republic of China

Nanocrystalline zinc oxide particles have been synthesized using a gas-phase process by atmospheric pressure plasma jets (APPJ). The APPJ used is sustained by a repetitive pulse source with nitrogen or oxygen as the plasma gas. Zinc-containing salt solutions, namely Zn(NO₃)₂ and ZnCl₂, are nebulized into μm-sized droplets and fed into the downstream of the APPJ. Liquid droplets undergo vaporization and reaction and form solid particles in the downstream of the jet. The particles are collected using de-ionized water or buffer solutions. The particle size and its distribution are measured using the dynamic light scattering method and scanning electron microscopy. It is found that the reactivity and the temperature of the jet downstream are able to efficiently convert the droplets into crystalline ZnO particles, as confirmed by the X-ray diffractometer. When O₂ is used as the plasma gas, the fabricated ZnO particles readily dissolve in the particle-collecting solution due to the decrease in the pH of this solution. The pH drops to as low as 1 within 2 min. It suggests the need of using the buffer solution as the particle collector. When using N₂ as the plasma gas, a relative small change in pH is found and results in decent collection yield. When using Zn(NO₃)₂ solution as the precursor under 275 V applied voltage and 30 ~ 60 slm N₂ gas flow, the fabricated ZnO particles show a double-peak distribution: small and large particles with the averaged sizes of 120 nm and 1000 nm, respectively. Preliminary studies found that the particle size distribution can be altered by changing the precursor solution concentration, the carrier gas flow rate, and the plasma conditions. Finally, the potential using this apparatus to fabricate more complex metal oxides will be discussed.

PS-ThP14 Studies of Interactions between the Plasma in Salt Solutions and Organic Compounds, S.H. Wang, H.W. Chang, C.C. Hsu, National Taiwan University, Taiwan, Republic of China

Plasmas in salt solution have shown to be reactive due to the produce of reactive species such as OH, H, O, and H₂O₂. In this study, interactions between the plasma in salt solutions and organic compounds are studied. The plasma is ignited in sodium-, zinc-, or calcium-containing salt solutions using DC or AC power sources. The electrode at which the plasma is ignited is a platinum wire 0.5 mm in diameter covered by a glass tube while the grounding electrode is a bare platinum wire of the same diameter. Cellulose, glucose and lactose are used as the organic compounds studied. Diagnostics include a voltage probe and a current probe to monitor the electrical characteristics; the conductivity and pH of the solution before and after the plasma treatment are monitored; an optical emission spectrometer is used to monitor the time-averaged emission spectra. It is observed that with the existence of the cellulose particles in the solution, the plasma appears to be much less stable. In addition, a much stronger light emission and larger current fluctuations are seen. This is possibly due to the fact that stable bubble is not able to form due to the existence of the cellulose particles. When glucose or lactose are added in NaCl solution, a much brighter plasma is seen and the optical emission shows a hump-like continuous emission band between 400~800 nm while this emission band does not exist without the addition of glucose and lactose. The total organic carbon (TOC) and high performance liquid chromatography (HPLC) measurements strongly suggest the possibilities that the cellulose, glucose, and lactose are decomposed due to the interaction with the plasma ignited in salt solution, especially when the plasma electrode is negatively biased. The identification of the decomposed products is currently underway. In this presentation, how the existence of the organic compounds influences the plasma behavior and how the organic compounds are decomposed in the plasma will be discussed.

PS-ThP15 The Optical Diagnostics of Microplasmas in Different Types of Electrolyte Solutions, A.H. Hsieh, C.C. Hsu, National Taiwan University, Taiwan, Republic of China

The optical diagnostics of microplasmas in various electrolyte solutions are performed. This microplasma is sustained by using a DC power source with the voltage up to 600 V. The powered electrode, the electrode where the plasma is ignited, consists of a thin platinum wire 0.5 mm in diameter covered by a glass tube. The grounding electrode is a bare platinum wire of the same diameter. Both electrodes are immersed in the solution. The electrolyte solutions studied include NaCl, NaNO₃, Na₂SO₄, ZnCl₂, Zn(NO₃)₂ and ZnSO₄ with the concentration of 0.01 M ~ 2 M. Time-

averaged optical emission and time-resolved intensities of the light emanating from the plasma are studied. With an applied voltage greater than 500V and the concentration below 0.02 M, there exists a bubble that stays steadily at the electrode tip for many seconds, and microplasma is ignited inside the bubble. Under this condition, the emission of H, OH, O and atomic metal emissions are observed regardless of the electrolyte type. In the high concentration conditions and low applied voltages, atomic metal emissions dominate and nearly no H, OH, and O emissions are seen. It is observed that for all electrolyte solutions studied except NaCl, there exist a hump-like continuous emission band in the optical emission spectra between 400~900 nm. The source of this continuous band is not identified yet but can potentially be a result of the thermal emission or free-bound transition. In this presentation, the implication of the optical emission to the plasma reactivity will be discussed.

PS-ThP16 Polyimide Surface Treatment by Using Atmospheric Pressure Plasma to Improve Metal Adhesion, J.B. Park, J.S. Oh, E.L. Gil, G.Y. Yeom, Sungkyunkwan University, Republic of Korea

Polyimide [(N, N'-oxydiphenylene) pyromellitimide], (PI) is one of the representative high-performance polymer films that has been widely used for the substrate in the microelectronic and flexible electronics industries because PI has desirable properties of high temperature resistance, good mechanical strength, and good dimensional stability. However, in spite of the extensive usage as well as the detailed characterization of the PIs, the poor adhesion of metals to PI, which is a consequence of its low specific surface energy, has to be overcome to render the fabricated devices reliable because the general polyimide-metal composites have limited adhesion strength. Therefore, many researchers have studied on the surface modification of PIs for adhesion improvement to metals.

In this study, the surface of PDMA-ODA PI films before and after atmospheric pressure plasma surface treatment by using remote type modified DBD module was investigated to improve the adhesion between the PI substrate and metal thin film using various gas compositions such as N₂/He/SF₆, N₂/He/O₂, N₂/He/SF₆/O₂, N₂/He/SF₆/O₂. Among the plasma treatments of the PI substrate surface using various gas mixtures, the plasma treatment with N₂/He/SF₆/O₂ showed the lowest contact angle value due to the high C=O bondings formed on the PI surface while that with N₂/He/SF₆ showed the highest contact angle value due to the high C-F_x chemical bondings on the PI surface. Especially, when O₂ gas was varied from 0 to 2.0 slm in N₂(40 slm)/He(1 slm)/SF₆(1.2 slm)/O₂ (x slm) gas composition, the lowest contact angle value of about 9.3° could be obtained at 0.9 slm of O₂ gas due to the highest oxygen radicals in the plasma, which forms the highest C=O bondings on the PI surface. When the interfacial adhesion strength between the Ag film and the PI substrate was measured after the treatment with N₂(40 slm)/ He(1 slm)/SF₆(1.2 slm)/O₂(0.9 slm) followed by the deposition of Ag, the peel strength of 111 gf/mm which is close to the adhesion strength between metal and the PI treated by a low pressure plasma could be observed.

PS-ThP17 Atmospheric Pressure Plasma Ashing of Photoresist using Remote-type Pin-To-Plate Dielectric Barrier Discharge, J.S. Oh, J.B. Park, E.L. Gil, G.Y. Yeom, Sungkyunkwan University, Republic of Korea

In these days, many researchers are developing glow discharges generated at atmospheric pressure for various thin films and surface processing such as dielectric barrier discharge (DBD), microwave discharge, pulsed corona plasma, etc. Various atmospheric pressure plasma sources have been reported with the claim of low running cost, low gas temperature, and wide applicability to surface treatment, cleaning, etching, and thin film deposition. Among the various atmospheric pressure plasmas, DBDs are studied mostly due to the easy generation of stable plasma.

In this study, ashing of photoresist (PR), AZ 1512, has been investigated using a pin-to-plate remote type DBD. The pin-to-plate type DBD showed higher power consumption and higher discharge current compared to the conventional DBDs at a given applied voltage. But glow discharge, which is generated by DBD, is easily transferred to filamentary/arc discharge, and the substrate is more likely to be damaged under arc discharge condition. Also, thermal damage can occur due to direct contact of the plasma to the substrate. But, remote plasma does not contact the substrate directly, therefore, the substrate can avoid damaging. In this study, using the remote type pin-to-plate DBD, the effect of various gas combinations such as N₂/O₂, N₂/O₂+SF₆ on the changes of PR etch rate and the electrical characteristics was investigated.

The addition of SF₆ gas to N₂/O₂ showed higher consumed power, higher discharge current at a given voltage, and lower turn-on voltage. For example, the plasma turn-on voltage for N₂ (50 slm)/O₂ (200 sccm) was 3.16 kV while that for N₂ (50 slm)/O₂ (200 sccm)/SF₆ (2.5 slm) was 2.7 kV, therefore, a lower turn-on voltage was obtained by adding 2.5 slm of SF₆. The consumed power for N₂ (50 slm)/O₂ (200 sccm)/SF₆ (2.5 slm) was 2330 W while that for N₂ (50 slm)/O₂ (200 sccm) was 1119 W. Therefore, the

addition of 2.5 slm of SF₆ increased the power consumption in the plasma by ionizing and dissociation the gas mixture further possibly through the penning ionization and dissociation. At N₂ (70 slm)/ O₂ (200 sccm) + SF₆ (3 slm), the maximum PR etch rate of about 1850 nm/min could be achieved.

PS-ThP18 SiO₂ Thin Films Deposition by using a Modified Pin-To-Plate Dielectric Barrier Discharge Source in Atmospheric Pressure, E.L. Gil, J.B. Park, J.S. Oh, G.Y. Yeom, Sungkyunkwan University, Republic of Korea

SiO₂ films are used in various areas due to the excellent physical and chemical properties such as optical transparency, chemical inertness, scratch resistance, and sufficient hardness. In this study, as an application to a thin film passivation layer for flexible substrates, the deposition of SiO₂ thin film has been investigated. Especially, for the in-line and the roll-to-roll processing of flexible substrate, SiO₂-like thin film was deposited by an atmospheric pressure plasma-enhanced chemical vapor deposition (AP-PECVD) technique at atmospheric pressure and at room temperature. A modified dielectric barrier discharge (DBD) called a "pin-to-plate-type DBD" having the combined characteristics of the remote-type DBD was used with a gas mixture of hexamethyldisilazane (HMDS)/O₂/He/Ar in order to generate high-density plasmas and to limit the damage to the substrate. The characteristics of SiO₂-like thin film were varied with gas mixture. As HMDS flow rate was increased, higher -(CH₃)₂ bonds and lower -OH bonds were obtained due to the decreased recombination of carbon or hydrogen with oxygen, and consequently more particles and rough surface were observed. Although the increase of oxygen in the plasma was beneficial in removing all impurities relating to carbon, further increase of O₂ more than 14 slm obstructed forming the pure SiO₂-like films resulting in a rough surface. By using a gas mixture of HMDS (150 sccm)/O₂ (14 slm)/He (5 slm)/Ar (3 slm), SiO₂-like thin films with a low impurity could be obtained at a deposition rate of approximately 42.7 nm/min.

PS-ThP19 Studies of the Metal Electrode Erosion by Microplasmas in Saline Solution, C.Y. Sie, C.L. Chen, C.C. Hsu, National Taiwan University, Taiwan, Republic of China

The studies of the erosion of metal electrode by microplasmas in saline solutions are preformed. The plasma is ignited in saline solution of concentrations ranging from 0.01 to 2 M. This plasma is sustained by a DC power source with the voltage up to 600 V or a AC power source with the same voltage range and the frequency between 50 ~ 1000 Hz. The electrode on which the plasma is ignited is a metal electrode covered 0.5 mm in diameter by an alumina tube to precisely define the length exposes to the solution. The erosion of tungsten, titanium, and platinum electrodes is studied. During the plasma processing, the electrode erosion appears to be inevitable. It is found that when tungsten is used as the electrode, the most severe erosion occurs when the electrode is positive biased with the applied voltages at which no plasma is ignited, suggesting the electrolytic reaction plays an important role in the electrode erosion. With the plasma ignited at a higher applied voltage, increase in the applied voltage leads to a decrease in the erosion rate. When the AC power source is used, the erosion rate increases with the power frequency. In this presentation, the major erosion mechanism will be proposed and the strategy how the erosion rate can be minimized will be presented.

PS-ThP20 Formation of Size Regulated Platinum Nanoparticles Synthesized by Solution Plasma Process, T. Ishizaki, AIST, Japan, N. Saito, O. Takai, Nagoya University, Japan

Platinum nanoparticles have been applied to high activation of photo catalysis, catalysis for fuel cells, and cosmetics. Platinum nanoparticles have been synthesized by various techniques including chemical reduction, photo reduction and electrochemical technique. However, in these techniques, it takes few hours to synthesize the nanoparticles or chemically toxic substances leave in a product. Thus, it is required to develop an environmentally friendly technique to synthesize nanoparticles. We have developed 'Solution Plasma', which is defined as plasma in aqueous solution. Solution plasma has attracted much attention as a novel chemical reaction field. As solution plasma generates UV light, electrons, and radicals, it would reduce metal ions to nanoparticles without reduction agents. In this study, we aimed to synthesize platinum nanoparticles by solution plasma. In addition, we investigated influence of solution pH on the sizes of the platinum nanoparticles. Optical absorption of nanocolloidal platinum was measured by UV-vis spectrometer. The nanoparticles were observed by transmission electron microscopy (TEM).

H₂PtCl₆·6H₂O (1.44mM) and PVP (Polyvinylpyrrolidone, 12.1mM) were used as raw materials. The pH of solution was varied from 2.5 to 4.5. The electrical conductivity was adjusted to 1.5μS/cm by the addition of KCl. A pulsed power supply was utilized to generate plasma. Pulsed voltage of

1.6kV was applied between the tungsten electrodes in the solution. Pulse width and frequency were varied from 2.0 to 3.0 μ s, respectively.

Solution color changed from orange to dark brown at discharge times of more than 40 min. An absorption peak at 262 nm originated from PtCl₆²⁻ became weaker with the increases of the discharge time, while baselines in the spectra became higher in all the range. These results indicate the formation of platinum particles. TEM image shows that the mean diameter of the nanoparticles was 10nm. Debye rings by (111), (200), (220), (311) were also observed by diffraction patterns. The effects of pulse width, frequency and pH on the particle size distribution were also discussed.

PS-ThP21 Effects of Dirty Walls on the Plasma Potential of a Multi-Dipole Chamber, J.P. Sheehan, N. Hershkowitz, University of Wisconsin-Madison

In a multi-dipole chamber with dirty walls, the plasma potential is observed to be negative with respect to grounded wall in the tens of volts. The plasma is generated by hot filaments releasing monoenergetic primary electrons ranging from 35 to 60eV. The primaries can exist in significant concentrations relative to the plasma electrons (up to 0.5% primaries as measured by a planar Langmuir probe) and contribute to charge neutrality, but not significantly to current balance. It is observed that the plasma potential becomes more negative with increasing relative concentrations of primary electrons. The potential profile next to the wall was measured using an emissive probe in the limit of zero emission[1]. The negative potential in the bulk plasma drops an additional few Te radially to the wall. The radial and axial potential profiles resemble those found in a chamber with clean walls and a positive plasma potential except the entire profile is shifted 10–20V lower. Possible mechanisms for these observations are suggested.

References

[1] J. R. Smith, N. Hershkowitz, and P. Coakley, Rev. Sci. Instrum. **50**, 210 1979.

PS-ThP22 New Solutions for Magnetron Sputtering Technology, M. Cichowlas, Huettinger Electronic, Poland

Traditionally, DC-pulsed units are advised to number of applications like: AZO, reactive sputtering with SN target, etc. This recommendation is based on the assumption that a DC-pulsed unit is enough to match process requirements.

Typical recommendations for usage of DC-pulsed units are as follows:

- high ARC rate,
- reactive process (reactive gas in the chamber),

The aim of this article is to introduce DC-non pulsed and High-Power (HIPIMS) units as more interesting alternative for expensive DC-pulsed units.

1. DC non-pulsed units

Advanced, powerful functions implemented into DC-non pulsed units, gives beneficial solution for processes affected by highly arcing materials like AZO. Ability to stable operation with extremely highly arcing frequency is one of most interesting features of DC power supplies developed by Huettinger Electronic. Mentioned units are able capably to work with 8000 ARCs/sec with 60kW output power.

Fig. 1. Behavior of AZO - extremely high arcing rates-70.000 arcs/s.

2. HIPIMS units

The other potentially interesting technique is HIPIMS coating. Looking for DC pulsed or DC non-pulsed processes, HIPIMS is going to serve fully dense, defect free films. Additionally, HIPIMS process leaves substrate temperature at lower level, compared to DC units. This gives a possibility for usage of completely new materials to be coated, like polymeric, foil or rubber. Moreover, power supplies for HIPIMS applications are equipped with CompensateLine (cable length compensation circuit), this allows to reduce arc energy to 0,3mJ.

Fig. 2. Behaviour of HIPIMS unit with arc during a HIPIMS pulse.

DC non-pulsed units can be used for advanced reactive processes, efficiently competing with DC pulsed units. The HIPIMS gives new possibilities for fully dense films on material required substrate temperatures.

Thin Film

Room: Southwest Exhibit Hall - Session TF-ThP

Thin Film Poster Session II

TF-ThP1 Effects of Substrate Temperature on the Microstructure and Mechanical Properties of Multi-Element (TiVCrZrTa)N Coatings, M.H. Shiao, National Applied Research Laboratories, Taiwan, Republic of China, C.C. Jaing, K.S. Tang, Minghsin University of Science and Technology, Taiwan, Republic of China, C.T. Lee, C.Y. Su, Instrument Technology Research Center, Taiwan, Republic of China, Z.C. Chang, National Chin-Yi University of Technology, Taiwan, Republic of China, C.N. Hsiao, National Applied Research Laboratories, Taiwan, Republic of China

Multi-element nitride thin films of TiVCrZrTa high-entropy alloy were prepared by reactive RF magnetron sputtering technique with different substrate temperatures ranging from 25 °C to 400 °C. The microstructure and mechanical properties of the deposited nitride thin films were investigated by scanning electron microscope (SEM), atomic force microscope (AFM), transmission electron microscope (TEM), X-ray diffraction (XRD), nanoindenter, and phase shifting interferometry techniques. SEM and TEM results show that (TiVCrZrTa)N thin films exhibit a columnar structure. XRD and TEM diffraction results show a face-centered-cubic structure, and the intensity of (111) and (200) peaks increases with substrate temperatures in X-ray diffraction result. AFM measurements show the surface roughness of TiVCrZrTa nitride thin films increases slightly from 2.9 to 3.5 nm. Furthermore, the residual stress of (TiVCrZrTa)N thin films presents compressive stress and increases from 1.5 to 1.9 GPa with increasing substrate temperatures. The hardness and elastic modulus of TiVCrZrTa nitride thin films are approximate 26.5 and 240 GPa respectively, independent of the substrate temperatures.

TF-ThP2 Pulsed DC Magnetron Sputtered Nickel Thin Films: A Study of Stress, Density and Electronic Properties, E.D. Jones Jr., D.P. Adams, M.A. Rodriguez, Sandia National Laboratories

With the advent of pulsed magnetron direct current (DC) sputter deposition technology, there have been gains made in the deposition of various inorganic thin films.¹ Most notably used for reactive sputtering of oxides and nitrides, pulsed DC sputtering has led to the deposition of dense coatings with improved properties such as adhesion and wear. The property changes have been attributed to the differences in flux and energy of the species involved with growth.

In this work, we explore the effects of using pulsed DC methods for sputtering monolithic ~ 200 nm-thick nickel films. The power supply used for this study is the Advanced Energy Pinnacle Plus 10kW series, which allows for continuous or pulsed DC sputtering modes. We demonstrate the effects of argon sputter pressure (1-25mT) on residual stress, film density and film resistivity for various pulsed DC processes and contrast these with the properties formed during continuous DC sputtering. For the pulsed DC experiments we show how these three film properties (stress, density and resistivity) depend on argon pressure for each of four different pulse frequencies (50, 150, 250 and 350 kHz - reversal time is held at 1.0 μ s). Residual stress is determined through wafer curvature methodologies – working within the assumptions of Stoney's equation². Film density determined using x-ray reflectivity. Room temperature resistivity is determined using four-point probe instruments.

In general, the stress can be tailored during pulsed DC and constant DC sputtering by adjusting argon sputter pressure. For most conditions, the films are in a state of in-plane tensile stress after deposition and cooldown although near-zero stress can be obtained at lower pressures. Pulse frequency is shown to have a minor effect on residual stress for most processes. However, frequency has a greater effect on stress at the lower sputter pressures (1-5mT). We further evaluate the stress of all films in terms of intrinsic and extrinsic contributions to isolate the role of pulsed DC sputtering process parameters on intrinsic stress. Extrinsic stress effects (due to mismatch in thermal expansion coefficients) are factored out from the final, residual stress using known temperatures achieved during deposition and the mechanical properties of the film and substrate.

Sandia is a multiprogram laboratory operated by Sandia Corporation, a Lockheed Martin Co., for the United States Department of Energy's National Nuclear Security Administration under Contract No. DEAC04-94AL85000.

References:

- 1) J. Lin, J.J. Moore, W.D. Sproul, B. Mishra and Z. Wu, Thin Solid Films **518** (2009) 1566.
- 2) G.G Stoney, Proc. Roy. Soc. Ser A, **82** (1909) 172

TF-ThP3 Photoluminescence Characterization using Hanle Effect in $\text{Al}_x\text{Ga}_{1-x}\text{As}/\text{GaAs}$ Quantum Wells Grown on Processed Surfaces, J. Hernández-Rosas, C. Mejía-García, IPN, Mexico, A. Winter, Universität Bayreuth, Germany, M. López-López, IPN, Mexico, A. Gilinsky, Institute of Semiconductor Physics SB RAS, Russia, H. Pascher, Universität Bayreuth, Germany

In this work, we report the photoluminescence spectroscopy using Hanle effect of a series of quantum well (QW) structures of $\text{Al}_{0.3}\text{Ga}_{0.7}\text{As}/\text{GaAs}$ grown by molecular beam epitaxy, which were prepared using different processing of the GaAs buffer layer surface. Each sample consists of three QW's with thicknesses of 7, 5, and 3 nm, respectively. The characterization by photoluminescence spectroscopy was done using several fixed wavelength lasers with circularly polarized excitation at 1.6 K. By means of Hanle effect the interband lifetime τ and the spin lifetime τ_s of the electrons were determined. A polarization change was observed if the photon energy of the exciting light exceeds the difference between the spin orbit band and the conduction band. The intensity of the inverse circular polarization seems to be increased in the samples with better quality. Interband transitions associated to the QW's were calculated using the effective mass approximation method in order to verify the experimental results.

TF-ThP4 Electrical Characterization of GLAD Thin Films, A. Lalany, R.T. Tucker, University of Alberta, Canada, M.D. Fleischauer, National Institute for Nanotechnology (NRC Canada), M.J. Brett, University of Alberta, Canada

Glancing Angle Deposition (GLAD)¹ thin films are increasingly used in optical and sensor devices that benefit from the unique refractive properties or ultra-high surface area. Extending the use of GLAD films to energy devices, epitomised by the fields of photovoltaics² and fuel cell catalysis³, increases the complexity in desired film requirements. High electrical conductivity along the length of GLAD structures - normal to the substrate plane - is necessary in order to exploit the high surface area of GLAD films in electronic devices. To date, GLAD has been applied to a variety of metals and conductive oxides^{4,6}, and preliminary trends outline a relationship between the angle of incident flux, film density and in-plane resistivity. More specifically, it has been found that as the oblique deposition angle increases, the in-plane resistivity also increases. This relationship has been attributed to a decrease in film density resulting in diminished conductive pathways. Electrical anisotropy has also been observed, with differing in-plane resistivity for parallel and perpendicular directions with respect to the nanocolumns formed.^{4,6} A thorough study of both in-plane and through-post conductivity as a function of film composition, morphology, porosity, and crystallinity / phase is required to understand the complex interplay between film morphology and corresponding electrical properties. Quantifying differences between vertical and lateral-plane characteristics of GLAD films requires expanding on established techniques for in-plane measurements (which largely neglect morphological effects) and tailoring techniques to apply directly to GLAD films. It has been found that external boundaries begin to dominate standard bulk scattering mechanisms as film thickness decreases, resulting in an inverse relationship between film thickness and resistivity.⁷ Subsequently, the extensive boundaries present in GLAD films between and within individual features can result in complex electrical behaviour. We will quantify the variations in both in-plane and through-post conductivity through the use of direct and indirect experimental approaches, and relate the results to deposition parameters suitable for forming GLAD films of desirable conductivity.

[1] M.M. Haweye *et al.*, J. Vac. Sci. Technol. A, **25**, 1317, (2007).

[2] N. Li *et al.*, Appl. Phys. Lett., **95**, 123309, (2009).

[3] A. Bonakdarpour *et al.*, Appl. Catal. A., **349**, 110 (2008).

[4] J. Lintymer *et al.*, Surf. & Coat. Tech. **174-175**, 316, (2003).

[5] K.D. Harris *et al.*, Adv. Funct. Mater., **18**, 2147, (2008).

[6] D. Vick *et al.*, J. Vac. Sci. Technol. A, **24**, 156, (2006).

[7] A.F. Mayada, M. Shatzkes, Phys. Rev. B, **1**, 1382 (1970).

TF-ThP5 Atomic Layer Deposition of Titanium Nitride Using Titanium Tetrachloride and Hydrazine, D. Seghete, A.I. Abdulagatov, V.R. Anderson, A.S. Cavanagh, W. Wang, S.M. George, University of Colorado at Boulder

The atomic layer deposition (ALD) of high quality metal nitrides at low process temperatures has remained a challenge. The use of organometallic precursors to reduce the deposition temperature can lead to carbon incorporation and poor electrical performance. One possibility is to use halide precursors together with hydrazine instead of ammonia for the ALD of metal nitrides. Thermochemical calculations indicate that heats of reaction are more favorable and reaction temperatures should be lower with hydrazine. In this work, TiN ALD was performed using titanium tetrachloride (TiCl_4) and hydrazine (N_2H_4). *In situ* quartz crystal

microbalance (QCM) measurements revealed a TiN ALD growth rate of 16 ng/cm^2 at 225°C. The TiCl_4 and N_2H_4 reactions were both observed to be self-limiting. At higher temperatures, TiN ALD is difficult to examine using the QCM because of thermal stability issues. X-ray diffraction (XRD) and X-ray reflectivity (XRR) studies revealed that TiN ALD deposited at 275°C resulted in the purest cubic polycrystalline TiN film. TiN ALD at 275°C also displayed the highest growth rate of 0.36 Å/cycle and a film density of 4.7 g/cm^3 . Fourier transform infrared (FTIR) studies of the TiCl_4 and N_2H_4 reactions at 275°C observed that primary ($-\text{NH}_2$) and secondary ($-\text{NH}$) amines are formed after hydrazine exposures. The FTIR spectra contained no evidence of any chlorine-containing salt on the surface. Elemental analysis of the TiN ALD grown at 275°C revealed no chlorine impurities within the X-ray photoelectron (XPS) instrument detection limit of 1 at%. However, oxygen was present at 14 at% that is attributed to oxidation after exposure to air. The use of hydrazine should facilitate the deposition of TiN ALD films at process temperatures <300°C.

TF-ThP6 Understanding Some Pitfalls and Loopholes in Routine Characterization and Metrology of Thin Films for Solar Cells, M. Scott, J. Burst, T. Gessert, National Renewable Energy Laboratory

We show that even the more ordinary metrology tools routinely used to evaluate thin films demonstrate some subtle, and some not so subtle, pitfalls which may lead to unexpected, and perhaps unnoticed, error in the measurement. In the extreme case, of course, one may altogether get the "wrong" answer. We focus on some of the primary tools used in the evaluation of thin films for photovoltaic applications. Empirical results from commercially available spectrophotometer, Hall, profilometer and other characterization tools are presented. We show, for example, that the commonly presented, but often unnoticed and not discussed, mismatch in reflectance data at the detector changeover (~800 nm) is readily explained and satisfactorily eliminated.

TF-ThP7 Deposition of Relatively Thin Highly C-axis Oriented AlN Films for High Frequency Electro-Acoustic Devices, V. Felmetger, P. Laptev, OEM Group Inc.

Thin film bulk acoustic resonators (FBAR) and bulk acoustic wave (BAW) filters based on piezoelectric aluminum nitride (AlN) thin films are widely employed for different wireless applications. As the resonance frequency of the resonator is determined by the thickness of the AlN layer, there is essential interest of using ultra-thin 100-200 nm films to extend the current technology from 1-2 to 5-10 GHz range. Reactive magnetron sputtering is a method of choice enabling formation of the films with a high degree of c-axis texture; however it is challenging to deposit such thin films with acceptable piezoelectric coefficients due to their drastically downward crystallinity compared to 500-2000 nm thick films required for lower frequency devices.

In this study, we use reactive sputtering technology with a dual cathode ac powered S-Gun magnetron [1]. The quality of the c-axis crystal orientation is characterized by the full width at half maximum (FWHM) of the AlN (0002) X-ray diffraction peak. AlN films deposited by the S-Gun on low-doped Si wafers exhibit a strong crystal orientation, which is improved with increasing film thickness. It is more sophisticated to achieve the same crystal orientation when the film is deposited on a metal bottom electrode, as it is required for the FBAR and BAW devices. Therefore, formation of well-textured underlying electrodes is essential, especially if the AlN films are relatively thin.

The crystal orientation of common electrode metals and alloys deposited on Si, SiO_2 , SiC, and diamond-like substrates is greatly enhanced by depositing a thin AlN seed layer underneath the metal. In the paper, we will discuss the critical conditions and process steps required for producing ultra-thin highly textured AlN films. For this purpose, we have developed a two-step sputter deposition process enabling better conditions for AlN nucleation. After preliminary rf plasma treatment of the substrate surface, the first 20-50 nm thick AlN layer is deposited at elevated temperature with higher nitrogen concentration in Ar- N_2 gas mixture, stimulating growth of higher quality columnar grains with the increase of AlN film thickness.

The results obtained for 100 and 200 nm thick AlN films deposited onto different metal electrodes (Mo, Cr, Ir) are presented in the paper.

The sputter technology has demonstrated high efficiency in producing very thin (100 nm) AlN films exhibiting superior crystallinity with FWHM < 2.5° on Mo electrode, which is equal to or even better than the value for the deposition on Si substrates.

[1] V. V. Felmetger, P. N. Laptev, and S. M. Tanner, Surf. & Coat. Technol., **204** (2009) 840-844.

TF-ThP8 Properties of Transparent Conducting Sn-doped In₂O₃ Films Deposited by Pulsed Electron Deposition. *M. Chen, V.C. Rincon, H.V. Nampoori, R.M. Frazier, S. Kotru, The University of Alabama*

Sn-doped In₂O₃ (ITO) thin films find wide applications as an electrode material for photovoltaic devices. Optical transparency, electrical properties and surface roughness are the major parameters which need to be optimized for obtained device quality films for such applications. In the present work 100 nm thick ITO films were deposited on quartz substrates at room temperature using a vapor deposition technique, where a pulsed electron beam was used to ablate the target material. A series of films were deposited by varying the oxygen pressure in chamber during growth from 3.1mTorr to 20mTorr. Various characterization techniques were applied: x-ray diffraction, atomic force microscopy, four-point probe, Hall analysis, and Spectrophotometry were used to investigate the structure, surface morphology, electrical, and optical properties of these films. The best samples had a film resistivity of 6.8E⁻⁴ohm*cm, and an average transmittance of 80% in the visible spectrum. The influence of post annealing on the film properties was also be presented.

TF-ThP9 Synthesis and Characterization of Molybdenum Oxynitride Thin Films. *J.Y. Park, Y.C. Kang, Pukyong National University, Republic of Korea*

Molybdenum oxynitride films were deposited on the p-type Si(100) substrate using radio frequency (r.f.) magnetron sputtering technique at different nitrogen gas ratio from 0 to 100%. Molybdenum oxynitride films were investigated by atomic force microscopy (AFM), X-ray diffraction (XRD), scanning electron microscopy (SEM), spectroscopic ellipsometry (SE), and X-ray photoelectron spectroscopy (XPS).

The roughness of molybdenum oxynitride films were slightly increased up to 13% of nitrogen gas ratio then decreased significantly. XRD results show that the crystal structure was metallic Mo(110) at the 0% of nitrogen gas ratio. The thickness of molybdenum oxynitride films was decreased to 70 from 800 nm with increasing nitrogen gas ratio. The thickness deduced from SE experiment was well consistent with the result of SEM and band gap was calculated using extinction coefficient values obtained by SE. The high resolution XP spectra of Mo 3d, O 1s, and N 1s were deconvoluted to get more chemical information and valence band maximum was determined with valence band region XP spectra of molybdenum oxynitride thin films.

TF-ThP10 Effects of Non-Uniformity for GaN Deposition by the Structure of Gas Inlet in MOCVD. *W. Yang, K. Hong, J. Joo, Kunsan National University, Republic of Korea, S. Lee, T. Lee, JUSUNG Engineering, Republic of Korea*

GaN deposition equipment and processes for white LED (Light Emitting Diode) at MOCVD (Metalorganic Chemical Vapor Deposition) were numerically modeled to analyze the effects of reactive gas introduction strategy. The source gases, TMGa and NH₃, were injected from shower head on the top of chamber, and the carrier gases, H₂ or N₂, were introduced from two types of structure: vertical injection and horizontal injection. Wafers are setting on the holder at a radial distance of between 100 mm and 150 mm. The non-uniformity of deposition rate for vertical injection and horizontal injection was 1.9 % and 2.8 %, respectively. And In case of using the N₂ carrier gas instead of H₂, the uniform deposition zone was increased by 20%.

TF-ThP11 In Search of New Multiferroics: Thin Film Synthesis and Characterization of Titanates of the MTiO₃ (M=Ni, Fe, Mn, Co) Family. *R. Sanghavi, T. Varga, T. Droubay, P. Nachimuthu, V. Shutthanandan, S. Thevuthasan, Pacific Northwest National Laboratory*

Today's challenge in multiferroics is to identify materials in which polarization and magnetization – normally considered contraindicated properties are strongly coupled. Recent theory calculations predicted that the family of compounds MTiO₃ (M = Mn, Fe, Ni), in a certain polymorphic structure (acentric R3c), are promising candidates where a polar lattice distortion can induce weak ferromagnetism (WFM). Guided by these insights, a phase of FeTiO₃ has been prepared more recently, which exhibits both ferroelectricity (FE) and WFM. However, the possible coupling between its polarization and WFM remains to be demonstrated. This demonstration may require the use of aligned single crystals to show that the magnetic and polar domains can be switched in concert. Results of the synthesis of the thin films of structurally analogous MTiO₃ compounds, and their characterization with a focus on the possible coupling between FE and WFM are reported. This fundamental study can be used to develop functional magnetic devices such as bio-sensors in which the magnetization can be controlled by electric field

TF-ThP12 Properties of ALD Al₂O₃ Protective Coatings. *P.J. Evans, Australian Nuclear Science and Technology Organisation, Y. Murai, Nagaoka University of Technology, Japan, M. Lindsay, J. Davis, G. Triani, Australian Nuclear Science and Technology Organisation*

In recent years, atomic layer deposition (ALD) has emerged as a technology platform for nanofabrication [1]. This interest has evolved from its intrinsic advantages; inherent thickness control, the ability to prepare highly conformal pin-hole free films, low temperature film growth and its large area uniformity. These redeeming characteristics have broadened the application of ALD films in such diverse areas as encapsulation of nanoparticles [2], templating of complex structures [3] and the modification of membranes [4].

The deposition of atomic layer protective coatings on flexible polymers and metals is another target application to improve the lifetime performance of functional materials that may be susceptible to degradation [5]. In particular, the ingress of moisture and atmospheric gases as well as the effects of abrasion and thermal cycling can significantly diminish a material's suitability in cases where its bulk properties meet all other requirements. Inorganic barrier coatings on flexible substrates are subject to additional constraints where the mechanical strength and adhesion of the protective coating are particularly important.

In this study, ALD alumina coatings were deposited on flexible substrates including polycarbonate, polyethylene naphthalate (PEN), copper and titanium, to investigate their toughness and adhesion under tensile load. In addition, the effect of deposition conditions on the performance of these protective coatings will be presented.

References

- H. Kim, H.B.R. Lee, and W.J. Maeng, *Thin Solid Films*, **517** (2009) 2563-2580.
J.R. Scheffe, A. Frances, D.M. King, X. Liang, B.A. Branch, A.S. Cavanagh, S.M. George, and A.W. Weimer, *Thin Solid Films*, **517** (2009) 1874-1879.
G. Triani, P.J. Evans, D.J. Attard, K.E. Prince, J. Bartlett, S. Tan, and R.P. Burford, *J. Mater. Chem.*, **16** (2006) 1355-1359.
L.Velleman, G. Triani, P.J. Evans, J. G. Shapter, and D. Losic, *Micropor. Mesopor. Mater.* **126** (2009) 87-94.
T. Hirikikorpi, M. Vaha-Nissi, T. Mustonen, E.Iiskola and M. Karpinen, *Thin Solid Films*, **518** (2010) 2654-2658

TF-ThP13 Temperature Uniformity Issues of Inductive Heating in MOCVD Systems to Fabricate MQW White LEDs. *K. Hong, W. Yang, J. Joo, Kunsan National University, Republic of Korea*

Deposition temperature uniformity of GaN based MQW(multiple quantum well) layers is an important key which affects the wavelength uniformity of white LEDs. Two types of heater were tested: a resistive and inductive heater. Varying the gap between the heater and the susceptor, temperature uniformity was assessed by infra-red images for both cases of a static and a rotating susceptor. The best non-uniformity of resistive heater was obtained at 3 mm gap, 6.2%. Rotating the susceptor at 2.5 rpm over the induction heater gave 4.3% of temperature non-uniformity. Temperature distribution of the graphite susceptor over the induction heater was numerically modelled and agreed with experimental results.

TF-ThP14 Investigation on the Electrical and Optical Properties of ZnO:Al Thin Films by RF Magnetron Sputtering and Annealing. *C.T. Lee, B.H. Liou, D.R. Liou, C.N. Hsiao, Instrument Technology Research Center, Taiwan, Republic of China*

ZnO:Al (AZO) thin film was prepared on glass substrate with various substrate temperatures by RF magnetron sputtering deposition. Various substrate temperatures and 500 °C annealing on the electrical and optical properties of as-deposited AZO film were investigated by Hall measurement and spectrometer. The minimum resistivity of the as-deposited AZO film was 1.0 X 10⁻³ ohm cm at the substrate temperature of 300 °C. After annealing, the resistivity of all films was improved. The optimum resistivity of AZO thin film is 5.6 X 10⁻⁴ ohm cm. The average transmittance of AZO thin films in the visible range was decreased with increased substrate temperature. It was found that the minimum resistivity and maximum average transmittance of 82% in the visible range were at substrate temperature of 300 °C and after 500 °C annealing.

TF-ThP15 Photo-functional Properties for Fe-Added Titanium Dioxide Thin Films Prepared by Reactive Magnetron Sputtering. *S. Arahara, I. Takano, M. Sato, Kogakuin University, Japan*

Since the photoinduced decomposition of water on TiO₂ electrodes were discovered, semiconductor based on photocatalyst has attracted extensive interest. TiO₂ is anticipated as one of materials which are alternative for existing solar cell technology type based on a silicon type. TiO₂ shows

relatively high reactivity and chemical stability under UV light whose energy exceeds the band gap of 3.2 eV in the anatase crystalline phase. The sun can provide an abundant source of photons. However, UV light accounts for the only small fraction (~5 %) of the sun's energy compared to the visible region (45 %). Many techniques have been examined to achieve this purpose, including the doping of TiO₂ with transition metals (such as Cr, Fe, Ni, V).

In this study, TiO₂ film has been prepared by reactive magnetron sputtering using a Ti target in an Ar/O₂ gas mixture. Fe addition was performed by Fe sputtering onto those TiO₂ films. Composition and microstructure of these films were investigated by X-ray photoelectron spectroscopy and X-ray diffraction, respectively. Chromatic change of a methylene blue solution was applied to a photocatalytic property. Light irradiation to the TiO₂ film in a methylene blue solution was carried out using a commercial sterilizing lamp as ultraviolet light and artificial sun light as visible light. Transmittance of a methylene blue solution was measured by a spectrophotometer. Furthermore, photocurrent between the TiO₂ film and a platinum electrode was measured by a volt-ampere characteristic using an unresisted ammeter in a KCl solution of 0.5 mol/l.

The crystal structure of TiO₂ turned from a rutile type into an anatase type with increase of O₂ gas flow rate. Photocatalytic characteristic of an anatase type showed the higher value under ultraviolet light, while the difference in the crystallographic structure was not observed under visible light. The effect of adding Fe was obtained at the Fe-added sample basing TiO₂ prepared with O₂ gas flow rate of 1.5 and 2.0 sccm. It was considered that the charge separation between an electron and a hole was enhanced by adding Fe to the TiO₂ surface. The optimum thickness of the Fe film was about 0.1 nm.

TF-ThP16 Control of Reflectivity at Substrate/Resist Interface of Nanometer-scaled Devices by Inorganic Bottom Anti-Reflection Coating (BARC). *S.-Y. Kim*, Korea Polytechnic College IV, Republic of Korea, *N.-H. Kim*, Chonnam National University, Republic of Korea

As the device has become highly integrated, the more accurate critical dimension (CD) was demanded. High contrast resist was also required for the exposure threshold effect. However in this case, the reflectivity between substrate and resist became higher; therefore, the CD swing curve was intensified which was directly influenced by the change of resist thickness. Lastly, the resist notching phenomenon was appeared, which was caused by the reflectivity owing to the shape of sub-layer. It is very important to control the reflectivity between substrate and resist for the precise CD control. The bottom anti-reflective coating (BARC) is one of the most widely used methods. The conventional inorganic BARC has been employed in the metal pattern process of μm -scaled devices with oxynitride. Because the more accurate CD control is necessary for the nm-scaled devices, the resist thickness, the conditions of reflectivity and absorption coefficient, and metal stack as a sub-layer were changed. The standing wave was also observed in the resist profile after metal pattern process of nm-scaled devices. Therefore, the optimization of inorganic BARC was investigated for the application to the nm-scaled devices with the changes of resist thickness and sub-layer. The reflectivity in the interface between BARC (oxynitride) and resist was under the control of thickness, refractive index, and absorption coefficient. The refractive index and absorption coefficient were investigated by a function of the SiH₄/N₂O gas flow rate, which is the main control factor of the refractive index and absorption coefficient, in oxynitride deposition. Computational simulation was performed in order to obtain the reflectivity in the interface of BARC and resist with changes of the optical factors. The optimum thickness, refractive index, and absorption coefficient were obtained for the minimum reflectivity of oxynitride. The simulated results were successfully applied to the experiments, which was confirmed by the cross-sectional SEM. There is no standing wave in this optimum condition.

TF-ThP17 Ar/O₂ Plasma Treatment Effects on Structural, Optical and Electrical Properties of Sputtering-deposited CdS Thin Films. *S.-H. Ryu*, *K.D. Myung*, *J.-S. Park*, Chosun University, Republic of Korea, *N.-H. Kim*, Chonnam National University, Republic of Korea, *W.-S. Lee*, Chosun University, Republic of Korea

CdS thin film has been widely used in the heterostructured solar cell applications as a window layer, which is a well-known n-typed semiconductor material. The sputtering method was employed for a large-area preparation of CdS thin film by the author in the previous study. It was good quality and had the high transmittance through it. In this study, the sputtering-deposited CdS thin films were treated by the plasmas under the various conditions with some process parameters including RF power, gas flow rate and treatment time with Ar or O₂ gases. Surface morphology and structure of them were analyzed by AFM and XRD. The effects of each plasma treatment on the electrical and optical properties of CdS thin film were investigated by UV-Visible spectrophotometer and Hall effect measurement. The roles of morphology and structure of plasma-treated CdS

thin films were compared by the optical and electrical characteristics. The improved cell parameters of CdTe / the plasma-treated CdS thin film solar cells, including short-circuit current density (J_{sc}), open-circuit voltage (V_{oc}), fill factor (FF), and efficiency, were also obtained at the condition for the good properties of the plasma-treated CdS thin film. Acknowledgement: This work was supported by National Research Foundation of Korea(NRF) grant funded by the Korean Government(MEST) (20 10-0016048).

TF-ThP18 Photodissolution and Photodiffusion Effects of Silver on Electrical Characteristics of CdTe Thin Film for CdTe/CdS Solar Cells. *J.-S. Park*, *C.-H. Lim*, *S.-H. Ryu*, Chosun University, Republic of Korea, *N.-H. Kim*, Chonnam National University, Republic of Korea, *W.-S. Lee*, Chosun University, Republic of Korea

The maximum efficiency of CdTe/CdS solar cell was just 16.8% although the CdTe thin films shows the excellent absorbance above 99% with only about 2 μm of active thickness. The enhanced electrical characteristics of CdTe thin film are required for the improvement of the efficiency. Doping of polycrystalline CdTe thin film is thought to be one of the effective methods to control the conductivity of CdTe thin film. The group I elements including copper are generally known as substitutional acceptors in CdTe thin films, which increase the p-doping of CdTe thin films. However, there have been many reports on the degradation of solar cell by the high diffusivity of copper. In this study, silver was employed to dope the sputtering-deposited CdTe thin film. Silver was deposited on the 1 μm -thickness of CdTe thin film by the sputtering method with 10 nm-thickness. He-Ne laser (632.8 nm) was exposed with a small energy by a change of exposure time. The remained silver layer was removed with HNO₃+3HCl and H₂SO₄+H₂O₂ solutions. The photodissolution and photodiffusion effects of silver on the CdTe thin films were investigated by analyzing the electrical and optical properties of CdTe thin films including absorption coefficient, carrier mobility, resistivity and carrier density. AES depth profile was employed to examine the Ag-doped CdTe thin film with a change of He-Ne laser exposure time. Acknowledgement: This work was supported by National Research Foundation of Korea(NRF) grant funded by the Korean Government(MEST) (2010-0016048).

TF-ThP19 Surface and Interface Characterization of ALD and PVD Thin Films for Microelectronic Applications. *L. Zhang*, *K.G. Lloyd*, *G. Blackman*, DuPont Corporate Center for Analytical Sciences, *J. Thompson*, DuPont CR&D, *L. Bao*, *J. Ryley*, DuPont Engineering, *D. Reardon*, DuPont CR&D, *M.A. Plummer*, *J.R. Marsh*, DuPont Corporate Center for Analytical Sciences

Surface and interface properties of thin films are critical for the growth and commercialization of microelectronics and Photovoltaics (PV) products. During the development of these thin film materials, chemical and structural characterization of surfaces at each film layer and interfaces between different layers are essential to aid product development and manufacture process for optimum products.

This presentation will focus on the applications of applying integrated methods/techniques to support thin film construction using Atomic Layer Deposition (ALD) and Physical Vapor Deposition (PVD) methods, including the study of surface composition and morphology, surface treatment, inter-layer diffusion, and film stoichiometry.

TF-ThP20 Enhancing of Optical Properties of TiO₂ Thin Films by N⁺ Ion Beam Irradiation. *H.A. Shukur*, *I. Takano*, Kogakuin University, Japan

Titanium dioxide (TiO₂) has considerable properties such as photocatalytic effect, dye-sensitized photovoltaic effect, photoinduced hydrophilicity and transparent electrode. Among all these properties photocatalytic property has been interested by many researchers because of its promised application such as antifouling effect and ability to decompose environmental pollution materials. However, TiO₂ has a high band gap (3.0 ~ 3.2 eV) so that the most photocatalytic effect occurs under UV irradiation. In order to improve TiO₂ behavior under visible light, there is many researchers have used various methods such as gas or metal doping.

In this study N⁺ ion implantation was used to improve the optical properties of TiO₂ films, which were prepared by reactive magnetron sputtering on glass substrate (corning #1737). The substrate was sputtered by Ar ions in order to clean the surface before the TiO₂ thin film formation. Titanium (Ti) was sputtered from Ti target in an Ar / O₂ gas and the substrate was heated at 200 °C. The total film thickness was around 145nm with a deposition rate of 0.025nm/sec. N⁺ ion was irradiated to TiO₂ thin film at 15keV in acceleration voltage and 40 $\mu\text{A}/\text{cm}^2$ in ion current density with a various irradiation doses from 2.5 $\times 10^{15}$ to 250 $\times 10^{15}$ ions/cm². Film thickness of the samples was measured by Avantes optical spectrometers system (AvaSpe-2048). The structure was determined by X-ray diffraction (XRD: MAC Science High quality XG M18XCE) with CuK α (0.154nm) radiation at an incident angle of 0.3°, and the composition was characterized by X-ray

photoelectron spectroscopy. The photocatalytic property was measured by a methylene blue immersion test. The spectrophotometer (SHIMADZU UV-2550) was used to measure the difference in light absorption at a wave length of 665nm and also was used to measure the optical band gap for ion irradiated films.

N⁺ ion implanted TiO₂ films showed a narrower optical band gap than unirradiation films, i.e. N⁺ was substituted for O and created a new energy level. Optical band gap was changed from 3.58 to 3.5 eV at sample of 12.510¹⁵ ions/cm² ion irradiation dose, this sample was showed a maximum photocatalytic activity for visible light.

TF-ThP21 Influence of the Fluorine Doping on the Properties of SnO₂ Thin Films, F.J. De Moure-Flores, K.E. Nieto-Zepeda, J.G. Quiñones-Galvan, A. Hernandez-Hernandez, M. Olvera, M.A. Melendez-Lira, CINVESTAV-IPN, Mexico

We propose the addition of fluorine in SnO₂ to increase n-type doping be used as transparent electrode in photovoltaic heterostructure. The thin films were deposited on glass substrates (at different temperatures) by RF magnetron sputtering using a SnO₂:F target employing an argon atmosphere. The thin films were thermal annealed using a nitrogen flux. We present results of the structural and chemical characterization obtained through X-ray diffraction, atomic force microscopy (AFM), scanning electron microscopy (SEM) and energy dispersive X-ray microanalysis (EDX). The electrical, optical and structural properties were determined before and after heat treatment; the results are discuss in terms of growth details.

Tribology Focus Topic

Room: Southwest Exhibit Hall - Session TR-ThP

Tribology Focus Session Poster Session

TR-ThP1 A Study of Sliding Friction Across Velocity Regimes for Alternative MEMS-type Interfaces using Proximal Probes and Quartz Microbalance, S. Barkley, Luther College, C. Boussein, M. Deram, N. Eigenfeld, St. Olaf College, L. Matthews, Luther College, A. Poda, W.R. Ashurst, Auburn University, E. Flater, Luther College, B. Borovsky, St. Olaf College

As mechanical devices have shrunk to microscopic sizes, the need for a more fundamental understanding of friction and other surface phenomena has become urgent. While the emerging technology of microelectromechanical systems (MEMS) shows promise as the mechanical counterpart to integrated circuits, progress remains slow as structural materials and lubricant strategies continue to be developed. We report on the results of a collaborative effort to study the frictional properties of organic monolayers on metal oxide surfaces. Both a nanoindenter-quartz crystal microbalance (NI-QCM) and an atomic force microscope (AFM) in lateral force mode have been used to perform tribological experiments at sliding velocities spanning the range from microns per second to meters per second. Our initial studies have employed octadecylphosphonic acid self-assembled monolayers chemisorbed onto aluminum oxide components with realistic contact roughness, sizes, and pressures. These interfacial systems have the potential to offer an alternative to silicon-based device fabrication. We present the development of custom microsphere probes for the NI-QCM and AFM systems, as well as the fabrication and characterization of the phosphonate monolayers. We discuss preliminary data from frictional studies across velocity regimes.

TR-ThP2 Deposition and Characterization of TiAlN/WN Multilayer Thin Films Deposited by dc Magnetron Sputtering, O. Jimenez-Aleman, J. Garcia, Universidad de Guadalajara, Mexico, L. Huerta, Universidad Nacional Autonoma de Mexico, M. Flores, Universidad de Guadalajara, Mexico

TiAlN/WN multilayer thin films with a range of different compositions and number of layers were deposited by PVD magnetron sputtering onto a variety of metallic substrates in a mixture of Ar/N₂ atmospheres. The utilisation of different nitride-formers elements and nitrogen (as a reactive gas) allows the deposition of alternative coatings with improved properties (e.g. wear and corrosion resistance) to those observed in individual commercial nitrides. The structure and morphology of the coatings were studied by means of X-ray Diffraction and Scanning Electron Microscopy. The elemental compositions and the surface chemistry (to gain precise information on the bonding environment) of these coatings were obtained by XPS. Microhardness and scratch tests were used to evaluate the mechanical properties and the adhesion of TiAlN/WN thin films respectively. The corrosion resistance was studied by potentiodynamic polarisation experiments in saline solutions of 0.5 M. The tribological

properties were studied through reciprocating sliding against ceramic counterparts and different loads. In this paper we report the results relating to the influence of deposition conditions such as deposition temperature, period size and nitrogen content on coating properties. The improvement of corrosion and wear resistance by the utilisation of a multilayered TiAlN/WN arrangement is also presented and discussed.

TR-ThP3 Tribocorrosion Behavior of TiAlN and TiAlN/TiAl Multilayers, M. Flores, E. Rodríguez, O. Jiménez, J. García, Universidad de Guadalajara, Mexico, L. Huerta, Universidad Nacional Autonoma de Mexico

In the present work we investigate the tribocorrosion behavior of TiAlN, TiAlN/TiAl and TiAlN/TiAl/Pt coatings deposited on 316L stainless steel by magnetron sputtering. The period size of the multilayers was from 250nm to 1350 nm. The friction and wear tests were performed on a ball-on-flat tribometer and conducted in dry (unlubricated) conditions at room temperature. The loads used were 1 to 10 N, the oscillating frequencies were 1-5 Hz. The corrosion was studied using open circuit potential (OCP) measurements and potentiodynamic polarization in ringer solutions. Tribocorrosion tests were performed using a ball-on-flat tribometer where the sliding contact is fully immersed in a Ringer's solution. The potentiodynamic polarizations and OCP measurements were performed during, and after sliding test. The structure and composition of multilayers were studied by means of XRD and XPS techniques respectively. The surface topography and worn surface were studied by means of optical microscopy and profilometry. The results indicate that coefficient of friction (COF) of TiAlN coatings decreased when metal layers are introduced and the corrosion resistance of TiAlN/TiAl coatings is improved when Pt layers are introduced. The synergy effect of the tribocorrosion tests is reported.

TR-ThP4 A Reactive, Fluctuating-Charge Potential for Carbon, Hydrogen, and Oxygen, M.T. Knippenberg, P.T. Mikulski, J.A. Harrison, United States Naval Academy

A classical bond-order potential energy function that incorporates fluctuating charges and reactions for carbon-, hydrogen-, and oxygen-containing molecules is presented. The model treats atomic charges as separate degrees of freedom that can be integrated over the course of the simulation, with charge fluctuations arising from the difference in electronegativity in bonds between atoms. Using the bond order that is already calculated, fluctuating charges are equilibrated during the course of the simulation. To test the validity of the potential, the dipole moments of oxygen-containing molecules are examined. Additional tests compare surface energies and structure of oxygen-containing diamond films.

TR-ThP5 Radial Compression Studies of Tungsten Disulfide Nanotubes, E. Kalfon-Cohen, O. Goldbart, R. Schreiber, Weizmann Institute of Science, Israel, D. Barlam, Ben Gurion University, Israel, T. Lorenz, G. Seifert, Technical University Dresden, Germany, S.R. Cohen, Weizmann Institute of Science, Israel

Understanding the mechanical properties of nanotubes is of significant practical and fundamental interest. Multiwalled nanotubes and nanoparticles of metal dichalcogenides such as WS₂ express unique mechanical and tribological characteristics.[1] The structure of WS₂ nanotubes consists of layers of covalently bound trigonal bipyramidal WS₂. The interaction between the layers is a van der Waals interaction between adjacent sulfur sheets. One of the intriguing aspects of these structures is the response of these layers under mechanical stress. Whereas some of the elastic constants of these unique structures have been addressed by experimental and theoretical work, the radial compression mode has not yet been studied. Relatively few studies of radial modulus of multiwalled carbon nanotubes have been made, and these also do not explicitly include the multilayered aspect of the structures. Here, we report an experimental and modeling study of this mode in the WS₂ nanotubes.

Three independent atomic force microscope (AFM) experiments were employed to measure the nanomechanical response, using both large (R=200 nm) and small (R=3-15 nm) probe tips. Two different analytical models were applied to analyze the results.[2] For a large AFM tip, a Hertzian model presuming an elliptical contact was applied. A shell continuum model is applied in the case of the sharper AFM tips. This model treats the nanotube wall as a thin, curved membrane. The results indicate that the derived modulus varies with nanotube diameter and compression depth

The modulus values derived from the analytical models were used as initial input for finite element analysis (FEA). The FEA model described the nanotubes as alternating high stiffness (representing the covalent shells) and low stiffness (representing the vdW gap) layers for the outer two shells, with a homogeneous inner core. This model was fit with the experimental results over the initial linear elastic region of the first few nm of deformation. Values obtained varied for different nanotube diameters, and

compression depths, showing the importance of the inter-layer contact. In addition, first-principles calculations using density functional theory tight binding give qualitative agreement with a reversible collapse of the nanotubes, seen at larger deformations.

[1] L. Rapoport, et al, *Nature* **387**, 791-93 (1997); I. Kaplan-Ashiri et al, *Proc. Natl. Acad. Sci. USA*. **103**, 523 (2006); I. Kaplan-Ashiri et al, *J. Phys. Chem C*. **111** 8432-8436 (2007)

[2] W. Shen, et al, *Phys. Rev. Lett.* **84**, 3634 (2000); M. Minary-Jolandan et al., *J. Appl. Phys.* **103**, 073516 (2008).

TR-ThP6 Tribocorrosion Behavior of nc-TiN/a-Si₃N₄ Nanocomposite Deposited on Metallic Substrates for Biomedical Applications, J. García, M. Flores, E. Rodríguez, O. Jiménez, Universidad de Guadalajara, Mexico

The tribocorrosion property of a nc-TiN/a-Si₃N₄ nanocomposite deposited using DC and RF codeposition reactive magnetron sputtering technique on SS316L nitrated and Titanium Ti6Al4V alloy against ceramic and metallic balls was studied in comparison with substrate materials using a reciprocating tribotester in distilled water, 1% NaCl water solution and artificial saliva solution. The effects of load and reciprocating sliding speed on the tribocorrosion properties of the nanocomposite were investigated. The structure and composition of coatings were studied by means of XRD and XPS techniques respectively. Under the experimental conditions of the present study, the nc-TiN/a-Si₃N₄ nanocomposite showed excellent resistance against corrosion and lower wear rate compared with SS316L nitrated and Titanium substrates. Profilometer analysis shows that on both materials most of overall tribocorrosion damage is due to mechanical wear. The tests suggest that nc-TiN/a-Si₃N₄ nanocomposite is a promising biomaterial for applications where reciprocating conditions occur.

TR-ThP8 A Tribological Study on Plasma Electrolytic Oxidation Process of Al319, H. Eiliat, X. Nie, University of Windsor, Canada

In this study, a plasma electrolytic oxidation process is used in order to produce a layer of oxide on aluminum silicon alloy 316. A pulsed dc power mode with frequencies up to 2000 Hz is selected with current density variations from 0.06 to 1.4 A/cm². Surface morphology (roughness), microstructure (grain size) and other properties of the plasma induced layer such as hardness and toughness are studied. Various coating conditions are compared based on treatment time, wear scar and coefficient of friction. These are critical coating properties for automotive engine block applications. The study is concluded by selecting the best coating condition with the optimized thickness.

Friday Morning, October 22, 2010

Biomaterial Interfaces

Room: Taos - Session BI+MN-FrM

Sensors & Fluidics for Biomedical Applications

Moderator: S.L. McArthur, Swinburne University of Technology, Australia

8:20am **BI+MN-FrM1 Release of Biomolecules from a Photovoltaic Device for Targeted Drug Delivery**, *S.L. Ambure*, University of Texas at el Paso, *D. Terreros*, Texas Tech University Health Sciences Center, *T. Xu*, University of Texas at el Paso

Introduction

An important goal of targeted drug delivery is to minimize the exposure of normal tissues to the drugs while maintaining their therapeutic concentration in diseased parts of the body. However, current methodologies are not yet ideal for such goal; therefore, new strategies for targeted drug delivery are needed. A photovoltaic device (PD) is a system that converts lights into electricity as well as induces charge transfer by photovoltaic effect. Motivated by such unique property, we have hypothesized that a PD can serve as a new drug delivery system to carry chemotherapeutic drugs and release them upon external photo stimulation, such as near Near-Infrared (NIR) light or Laser source. Taking advantage of repulsion between a photovoltaic device and a substance is proposed to serve as a new drug delivery method. In this study, we have investigated if the charged molecules can be effectively released from the PV device upon photon stimulation.

Methodology

As proof of principle, we have first experimented coating of commercially available photovoltaic devices with positively charged poly-L-lysine and negatively charged bovine serum albumin (BSA) tested the release of the molecules upon photo stimulation. These molecules were physically absorbed onto the surface of the PDs before exposed to an IR LED illuminator, which was used as an external light source. Moreover, the pure glass slide was used as a control of the device with non-photovoltaic effect for drug delivery.

Results and Discussion

During the series of experiments, we have found that, the PD has a capability to release the charged drugs by photovoltaic effect. Compared to no light stimulation, the positively charged poly-L-lysine and the negatively charged BSA when exposed to IR illuminator for 3 hours were released about 2.0 folds and 2.1 folds respectively. Moreover, in the control group (pure glass slide with no photovoltaic effect), there was no significant release of both poly-L-lysine and BSA when exposed to the IR illuminator.

Conclusion

These data showed that the new PD can effectively carry either positively or negative charged molecules on its surface and release them upon external photo stimulation, which suggests the PD has potential to be used as a new drug delivery system to carry cancer chemotherapeutic drugs. Further experiments are planned on the micro-fabricated photovoltaic devices (Size 300µm to 500 µm). With this project a new approach for targeted drug delivery with micro- photovoltaic devices will be developed.

(*Proprietary: an IP application based on this study is pending)

8:40am **BI+MN-FrM2 Enzymatic Activity Enhancement on Nanostructured TiO₂ Platforms by Ru doping for Biosensor Applications**, *R.R. Pandey*, Centre for Cellular and Molecular Biology, India, *K.K. Saini*, National Physical Laboratory, India, *M. Dhayal*, Centre for Cellular and Molecular Biology, India

Devices based on nanomaterials platforms are emerging as a powerful tool for ultrasensitive sensors for the direct detection of biological and chemical species. In this work, we will report the preparation and the full characterization of Ru doped TiO₂ nanostructured platforms those have been used for electrochemical detection of enzymatic activity for biosensor applications. Ru doped TiO₂ platforms were prepared by sol-gel deposition onto conducting substrates and as test model cholesterol oxidase, urease and glucose oxidase were loaded onto the nanostructured platforms. Cholesterol /Urease/Glucose oxidase immobilized onto Ru doped TiO₂-based nanostructured surfaces exhibited a pair of well-defined and quasireversible voltammetric peaks in CV measurements. The electron exchange between the enzyme and the electrodes was greatly enhanced in the Ru doped TiO₂ nanostructured environment. The electrocatalytic activity of cholesterol, urease and glucose oxidase embedded on Ru doped TiO₂ electrodes had

enhanced significantly toward detection of low concentrations of cholesterol, urea and glucose.

9:00am **BI+MN-FrM3 A Microfluidic Single Cell Isolation Device for Ensemble Measurements of Viral Hemorrhagic Fever Pathogenesis in Macrophages**, *M.W. Moorman*, *J.B. Ricken*, *R.F. Renzi*, *R.P. Manginell*, *C.S. Branda*, *O.A. Negrete*, *C.D. James*, *B.D. Carson*, Sandia National Laboratories **INVITED**

Arenaviruses are a particular class of viruses that cause lethal hemorrhagic fever in humans, and a fundamental problem in understanding their pathogenicity is that many effects of viral infection are not mediated directly by the virus itself (primary immune response) but by the response of the immune system (secondary immune response). Thus, population level experiments on cells make it difficult to elucidate the timing of signaling events during pathogenesis in order to lay the groundwork for improved antiviral therapeutics, vaccines, and biological countermeasures. Our objective here is to deconvolute the pathogenic response by isolating and infecting individual macrophage host cells followed by real-time measurements of response-critical cytokines. We have developed a microfluidic cell isolation platform that can trap up to 150 individual host cells in fluidically isolated microchambers. The chip design eliminates chamber-to-chamber fluidic communication, thus signaling molecules that are secreted from infected cells are prevented from interacting with uninfected cells. This configuration allows us to differentiate between primary and secondary immune response when compared to bulk cell population level studies. The chip is made with a three level reactive-ion etch process in silicon that produces trapping features that place cells adjacent to an anodically-bonded coverslip to permit high-resolution confocal imaging. The microfluidic device is operated with a custom pressure controller system that permits computer-controlled delivery and routing of up to 10 different reagents. Currently, we are using experimental and computational techniques to identify the mechanisms by which arenaviruses provoke lethal cytokine production in host cells. This is accomplished with a fluorescent reporter fusion construct that we developed to measure the cytoplasm-to-nucleus translocation dynamics of a transcription factor. This construct allows us to assess the early (< 1 hour) response of host cells to viral infection and when combined with a second reporter construct for real-time monitoring of cytokine induction, we are also able to monitor a late (>1 hour) immune response event. Initial studies using a viral mimic challenge showed oscillation of the transcription factor in and out of the nucleus over the first several hours of pathogen exposure, and a rapid 2X increase in cytokine induction over the first five hours post-infection. Future work will use a live Pichinde virus to examine transcription factor (NFκB) translocation and cytokine (TNFα, IFNβ) induction dynamics.

9:40am **BI+MN-FrM5 Elastomeric Microparticles that Exhibit Negative Acoustic Contrast in Bioassays**, *K.W. Cushing*, *M.E. Piyasena*, *B.A. Lopez*, *N. Carroll*, *T. Woods*, *D.N. Petsev*, *S. Graves*, University of New Mexico, *G.P. Lopez*, Duke University

The development of more sensitive and rapid medical assays is imperative to decreasing time-to-diagnosis in diseased state individuals, and thus to improving patient outcomes. Enhanced detection limits afford the ability to detect the presence of low concentrations of biomarkers that may be present during the early-onset stages of a disease. Reduction in sample preparation requirements can further decrease assay time and the expertise level of the user. Our research aims to develop a sensitive and rapid bioassay platform using elastomeric capture microparticles (ECµPs) coupled to an acoustic sample preparation chamber and a flow cytometer. ECµPs possess unique physical and mechanical properties enabling the separation of ligand-bound ECµPs from biological particles (e.g., red blood cells) within a collected fluid sample (e.g., whole blood) by placing them under acoustic pressure. ECµPs have acoustic properties (negative contrast) that allow their positioning separately from many biological particles, which typically exhibit positive contrast, (e.g., cells) within an acoustic pressure field. Hence, an in-line acoustic sample preparation instrument can be used to separate unwanted biological particles (along with interfering soluble molecules) from ligand-bound ECµPs within biological fluids. The acoustic field will also concentrate the ECµPs, and so combined with removal of unwanted biological particles, much higher analysis rates of ECµPs may be possible. Since the acoustic sample preparation system operates continuously and can be mounted to feed separated ECµPs directly into a flow cytometer, this approach may decrease sample preparation time. Our studies show that simple emulsion polymerization methods using commercially available silicone precursors can be used to easily form elastomeric microparticles that exhibit negative contrast.

10:00am **BI+MN-FrM6 Optimization of Biosensors using Selective Chemistry**, *O. Seitz, P.G. Fernandes*, University of Texas at Dallas, *H.C. Wen*, Texas Instruments, Inc., *H.J. Stiegler, R.A. Chapman, E.M. Vogel, Y.J. Chabal*, University of Texas at Dallas

There is currently a strong need to develop sensitive and reliable biosensors, based on electronic detection, such as field-effect transistors (FET). Most of the focus has been on improving sensitivity by decreasing the FET channel size, using nanowires instead of similar devices on planar silicon. Issues of silicon functionalization, important for device reliability have been mostly ignored.

In this work, we present a robust approach to functionalize the channel region of a SOI wafer, thus achieving better reliability and sensitivity to very low analyte concentrations. The process leads to attachment of active SAM on oxide-free (H-terminated) silicon through formation of a Si-C bond on the channel. Combining IR absorption (IRAS) and X-ray photoelectron (XPS) spectroscopies, photoluminescence, atomic force microscopy (AFM) and electrical measurements, we find that this configuration results in a stable device where the active SAM is more strongly attached to the Si than silane molecules do on oxides. This functionalization is achieved by immersion in carboxylic acid (COOH)-terminated alkene molecules to functionalize the H-terminated channel. After processing, XPS and IRAS confirm that the channel remains oxide-free, that the packing of the SAM on the channel is dense. Photoluminescence measurements confirm the high quality of the interface on the channel where non-radiative recombination (interface states) is not detected. The AFM pictures confirm that active molecules attach to the channel (imaged by attachment of nanoparticles). Electrical measurements, on these improved devices, indicate excellent response for both pH and protein sensing with sensitivity at least as good as the one of similar structure with a uniform SAM functionalization (i.e. using oxidized Si channels).

10:20am **BI+MN-FrM7 Nanopatterned Pores on a Gel-supported Membrane For On-chip Sample Preparation in Surface Plasmon Resonance Sensing**, *G.R. Marchesini*, Joint Research Centre, Italy, *S. Rebe Raz*, Wageningen University, the Netherlands, *M.G.E.G. Bremer*, RIKILT – Institute of Food Safety, *P. Colpo, G. Giudetti*, Joint Research Centre, Italy, *W. Norde*, Wageningen University, the Netherlands, *F. Rossi*, Joint Research Centre, Italy

We present a novel approach to tackle the most common drawback of using Surface Plasmon Resonance for analyte screening in complex biological matrices - the nonspecific binding to the sensor chip surface.

By using a perforated membrane supported by a polymeric gel structure that exceeds the evanescent wave penetration depth, we created a filter above the sensing region that prevents the diffusion of large particles or aggregates that bind non specifically to the polymeric gel and interfere with SPR sensing, thus increasing assay's sensitivity, reducing sample preparation steps and shortening the analysis time in total. A 10 nm thick non-fouling membrane with nanopatterned macropores was fabricated by means of colloidal lithography and plasma enhanced chemical vapor deposition of polyethylene oxide-like films. Such a membrane was supported by carboxymethyl-dextran, a polymeric gel matrix commonly used in surface plasmon resonance analysis. The surface was characterized using surface plasmon resonance imaging, contact angle, atomic force microscopy and scanning electron microscopy.

The performance of this surface in full fat milk and porcine serum was studied using an antibiotic detection immunoassay as a model system. Structurally, the 91.7 ± 14.7 nm diameter pores presented an hexagonal crystal lattice and a clearance of about 5 % of the total surface. Functionally, the nanopatterned macropores showed significant improvements in the quality of the obtained measurements in comparison to bare carboxymethyl-dextran, displaying 100 fold increase in the limit of detection of the enrofloxacin bioassay when performed in porcine serum.

10:40am **BI+MN-FrM8 Stability and Selectivity of Biorecognition Proteins Immobilized on Diamond Surfaces**, *R.J. Hamers, C.J. Stavis*, University of Wisconsin-Madison, *A. Radadia, R. Brashir*, University of Illinois at Urbana-Champaign, *J.A. Carlisle*, Advanced Diamond Technologies, *W.P. King*, University of Illinois at Urbana-Champaign, *H. Zeng*, Advanced Diamond Technologies

The use proteins, such as antibodies, for the detection of target biological species in water supplies or with *in situ* medical diagnostics will require immobilization of these proteins on surfaces that resist non-specific adsorption and maintain the protein's activity over time. Ultrananocrystalline diamond (UNCD) thin films are a promising material that may address several major challenges for the next generation of biosensors including detection of cellular mass loading, stability throughout multiple uses and regenerations of the sensor surface, and use at elevated temperatures.

We are currently investigating the chemical functionalization of diamond thin films with antibodies for selective recognition and detection of biological cells, using E. coli as a model system. Infrared spectroscopy and X-ray photoelectron spectroscopy measurements have been performed to characterize the covalent attachment of antibodies to the surface and to quantitatively characterize the antibody surface attachment via the N(1s) and S(2p) levels. To determine the factors controlling selectivity and stability, we have performed time-dependent cell capture studies and have correlated the time-dependent changes in cell capture efficiency with corresponding measurements of the surface composition. These measurements are used to establish whether long-term stability and selectivity for biomolecular recognition is limited by loss of the ligands directly linked to the diamond substrate, by removal of the biological layer, or by alteration of the antibody structure. Infrared measurements of the Amide I band is particularly useful in characterizing changes in the antibody secondary structures. These studies provide important fundamental insights into the chemical factors that control biological interactions at surfaces and provide guidance on efforts to make ultra-stable biological sensing platforms.

11:00am **BI+MN-FrM9 Saturated Ionic Conductance at Low Electrolyte Concentration Through Solid-State Nanopores**, *P. Waggoner, H. Peng, S. Harrer, B. Luan, S.M. Rossnagel*, IBM T.J. Watson Research Center

It has been observed that ion currents pass through biased nanopores in electrolyte solutions with bulk conduction properties until the concentration of ions decreases beyond a certain level. At this critical point, the conductance of the pores saturates at a constant value despite further decreasing the concentration of ions, an effect that has been attributed to charge shielding effects of surface charges within the pore. Below the critical concentration, the Debye length associated with screening the surface charges becomes larger and larger compared to the size of the pore and effectively cuts off bulk conduction. However, the conductance of the pore is not affected by the continuing growth of the space-charge region with the Debye length. In the following we present a model describing the nanopore-electrolyte system with an analytical solution that explains the experimentally observed behavior for five different salt solutions at low concentrations, including KCl, KCl in 50% glycerol, Tris-EDTA buffer, phosphate buffered saline, and CaCl₂. Conduction through the nanopore at low ion concentrations is analogous to hole extraction in reverse biased diodes and is related only to the diffusion of the minority carrier into the space charge region where it is then accelerated through the nanopore. These results also have important implications for solid-state nanopores being applied for DNA detection and sequencing technologies.

11:20am **BI+MN-FrM10 Fabrication of *in situ* Oligonucleotide Arrays by Inkjet Printing and their use in Gene Assembly**, *I. Saaem, J. Tian*, Duke University

In our studies, we utilized an inkjet based *in situ* oligonucleotide synthesis platform that uses salvaged printheads from commercial printers. The platform utilizes standard four-step phosphoramidite chemistry with some modifications in order to synthesize oligonucleotides on functionalized substrates. A sensitive pressurization system is used to ensure print quality and an on-board vision system enables substrate registration and synthesis monitoring. Using this platform we synthesized oligonucleotide on prepatterned functionalized plastic slides. Such patterned substrates help in proper droplet formation and fluid mixing on the surface while mitigating satellite and irregular drops, which can lead to cumulative synthesis errors. Functional integrity of synthesized oligonucleotides was confirmed by hybridization with complementary strands. Being able to hot emboss microfluidic structures directly onto plastic slides in combination with the ability to generate arbitrary sequences provides diagnostic capabilities as well as the means to harvest pools of cheap oligonucleotides on demand. Importantly, our combination of technologies has allowed formation of genes and large DNA constructs by amplifying oligonucleotides off of the synthesized arrays and assembling them in the on-chip chambers.

Spectroscopic Ellipsometry Focus Topic

Room: Cochiti - Session EL+AS+EM+MS+TF-FrM

Spectroscopic Ellipsometry - Inorganic Thin Films

Moderator: L.A. Giannuzzi, L.A. Giannuzzi & Associates LLC

8:20am **EL+AS+EM+MS+TF-FrM1 Spectroscopic Ellipsometry Study on Transparent Conductive Ga-doped ZnO Thin Films Deposited by Ion-Plating with DC Arc Discharge**, *T. Yamada, H. Makino, N. Yamamoto, T. Yamamoto*, Kochi University of Technology, Japan

Transparent conductive Ga-doped ZnO (GZO) thin films was one of promising candidates as transparent electrodes in flat panel displays and thin film solar cells. In this study, we investigated contributions of intra-grain scattering and grain boundary scattering on Hall mobility of polycrystalline GZO thin films based on the analysis of spectroscopic ellipsometry measurements. The GZO films were deposited by ion-plating method with DC arc discharge. Samples with a wide range of thicknesses from 70 to 500 nm were deposited at 200 degree C on glass substrates by controlling the deposition time. Sintered ZnO ceramic tablets doped with 1 wt% and 4 wt% Ga₂O₃ were used as evaporation sources. A systematic study has been done on the structural, electrical and optical properties of GZO films. In the case of GZO films using 4wt% Ga₂O₃ doped tablet, the minimum resistivity of $1.8 \times 10^{-4} \Omega\text{cm}$ was obtained at the film thickness of around 350 nm. The carrier concentration and Hall mobility was $1.2 \times 10^{21} \text{cm}^{-3}$ and $29 \text{cm}^2/\text{Vs}$, respectively. The GZO films showed c-axis preferential orientation nearly normal to the substrate surface with columnar grain structures. In XRD measurements, full width half maximum of (0002) omega rocking curve decreased with increasing the film thickness. It means that the fluctuation in the c-axis orientations among the grains improved with increasing the film thickness. Average grain size of columnar structure was estimated by Williamson-Hall plot on spectral width of in-plane XRD patterns. The average grain size increased with increasing film thickness. Optical mobility of the GZO films was estimated from analysis using the conventional Drude model on data obtained by spectroscopic ellipsometry. Differences between the optical mobility obtained by the spectroscopic ellipsometry and the Hall mobility obtained by Hall effect measurements suggest contribution from grain boundary scattering on the Hall mobility. It demonstrates that grain boundary scattering contributes to the Hall mobility in rather thinner film thickness. However, the very small contribution of grain boundary scattering to the Hall mobility was observed in the thick films. On the other hand, resistivity of $4.5 \times 10^{-4} \Omega\text{cm}$ with the carrier concentration of $3.6 \times 10^{20} \text{cm}^{-3}$ and Hall mobility of $39 \text{cm}^2/\text{Vs}$ was obtained for a 500 nm thick GZO film using the ZnO ceramic target doped with 1 wt% Ga₂O₃. The spectroscopic ellipsometry analysis on the GZO film suggests that the Hall mobility was dominated by intra-grain scattering.

8:40am **EL+AS+EM+MS+TF-FrM2 Spectroscopic Ellipsometry of Pulsed Laser Deposited ZnO on Atomic Layer Deposited Al₂O₃ and HfO₂**, *D.L. Agresta, K.D. Leedy*, U.S. Air Force Research Laboratory

Zinc oxide thin films and coatings are an integral part of a number of devices because of their wide range of properties. Depending on the conductivity and transparency, these materials are of interest for electronic (diodes, FETs), optoelectronic (detectors, modulators, flat-panel displays, solar cells, etc.) and piezoelectric (BAW,SAW) devices. In this study, we examine FET ZnO active device layers in conjunction with atomic layer deposited (ALD) Al₂O₃ and HfO₂ for isolation and gate dielectrics. Stacks of pulsed laser deposited (PLD) ZnO on thermal and plasma ALD Al₂O₃ and HfO₂ are prepared on a variety of large area substrates.

The surface morphologies of PLD grown ZnO-based films and ALD dielectrics are critical to optimize the interface quality in multilayer structures. Therefore, the control and optimization of surface properties over large areas is essential for the successful application of PLD ZnO thin films in device configurations. We have previously reported high quality ZnO films being obtained over large areas using off-axis PLD [1, 2]. Film thickness and compositional uniformity control is a critical issue associated with the scale-up of PLD systems. Thus, spectroscopic ellipsometry (SE) has a significant role in the characterization of these films.

A commercial Phase-Modulated Ellipsometer (PME) is employed to study the interplay between structural, electrical and optical properties of single-layers and PLD ZnO/ALD dielectric stacks. Known for its precision and non-destructiveness, SE is an indirect measurement technique in the sense that the film properties of interest are obtained by a nonlinear regression analysis of measured data to an optical model. We examine the effect on the goodness of fit parameter from the use of various optical models. Furthermore, since we are employing a PME, the time to scan a wide spectral region is limited by the slew rate of the monochromator. This can be a significant burden when making uniformity determination over large-

area substrates. Thus, we examine the effect on the goodness of fit parameter from minimizing data acquisition time. The optical properties of the individual thin films extracted by SE are compared to optical studies using normal incidence transmission. Film surface roughness is obtained from SE by employing the Bruggeman effective-medium approximation and subsequently compared to structural characterizations using atomic force microscopy and x-ray diffraction.

Reference:

K. D. Leedy, C. V. Varanasi, D. H. Tomich and B. Bayraktaroglu, 5th International Workshop on ZnO and Related Material (2008).

2. D. Agresta, K. Leedy, R. Scott, T. Dang and B. Bayraktaroglu., AVS-56 (2009).

9:00am **EL+AS+EM+MS+TF-FrM3 Processing and Stability Studies of Vanadium Oxide Thin Films for Microbolometer Applications**, *M.A. Motyka, B.D. Gauntt, E.C. Dickey, M.W. Horn, N.J. Podraza*, Penn State University

Vanadium oxide (VO_x) thin films are commonly used as an imaging material in uncooled infrared sensing devices. Material properties that make VO_x useful for this application are a high temperature coefficient of resistance (TCR), controllable resistivity (ρ), and low electrical noise. A difficulty in growing VO_x thin films arises from the many valence states of vanadium, which may result in formation of a film consisting of an undesirable phase or with the presence of multiple phases. Each phase has varying electrical properties and thus, the reliability and consistency in industrial fabrication is lowered. Furthermore, atmospheric exposure of the VO_x films has been shown to alter the electrical and optical properties. In order to prevent changes in the desired material, VO_x films are commonly capped with a thin layer of SiO₂ before atmospheric exposure. In this study, vanadium oxide thin films were studied using in situ real time spectroscopic ellipsometry (RTSE) over a spectral range of 0.75 to 5.15 eV during deposition via pulsed DC-magnetron sputtering in an argon and oxygen atmosphere, with the set of variables being the total pressure, the oxygen-to-argon ratio, target power and the target material (metallic V, VO₂, V₂O₅). These variables control the material growth and resulting optical and electrical properties. The growth evolution, complex dielectric function spectra ($\epsilon = \epsilon_1 + i\epsilon_2$), and structure obtained from RTSE have been shown to correlate with the electrical properties of the film. Ex situ Fourier transform infrared spectroscopic ellipsometry (FTIR-SE) measurements were also made to help characterize the materials in the spectral range of 0.05 to 0.75 eV, so that the optical properties in the range of microbolometer operation are obtained. Electrical measurements include temperature dependent I-V curve measurements to determine the VO_x film resistivity and TCR as a function of processing conditions. Changes in the optical and electrical properties as a function of processing conditions including film thickness are explored for materials exhibiting amorphous or nanocrystalline (V, V₂O, and VO phase) structures. RTSE is also used to monitor the changes in optical properties of the VO_x layer and interfacial formation arising from the deposition of the SiO₂ capping layer. The environmental stability of VO_x with and without capping layers is also monitored via RTSE as the samples are initially exposed to the atmosphere after deposition. In this manner both intentional variations in film microstructure and electrical properties as a function of processing conditions and unintentional variations arising from material instability are studied.

9:20am **EL+AS+EM+MS+TF-FrM4 Instrumentation of Far-infrared Mueller Matrix Ellipsometer and Its Application for Multiferroic Materials**, *T.D. Kang, P.D. Rogers, E. Standard, G.M. Nita, T. Zhou, New Jersey Institute of Technology, G.L. Carr, Brookhaven National Laboratory, S. Zollner, IBM Systems and Technology Group, M. Kotlyanskii, Rudolph Technologies, Inc., A. Sirenko, New Jersey Institute of Technology*

We develop a far-IR spectroscopic ellipsometer at the National Synchrotron Light Source (NSLS) in Brookhaven National Laboratory (BNL). This Ellipsometer is designed to measure a full-Mueller matrix of the sample by using compensators and wire-grid linear polarizers [1]. With the exceptional brightness of synchrotron radiation and the Fourier-transform infrared (FT-IR) spectrometer, we measure ellipsometric data with a high accuracy at multi-wavelengths between 10 and 4,000 cm⁻¹. Study in terms of temperature variation of the sample is available using the cryostat for temperature between 4.2 K and 450 K. The wide range of θ - 2θ rotation, c angle adjustment, and X-Y-Z translation of sample stage enables high accuracies in the alignment, calibration, and ellipsometric measurement. With the Labview program interface, the automated experiments with the pre-programmed measurement schedules are performed by controlling the motors, temperature, and FT-IR spectrometer. The ellipsometric data analysis is based on the Berreman's 4x4 propagation matrix formalism [2] to extract dielectric permittivity and magnetic permeability tensors for bulk and thin film samples from the Mueller matrix measured at variable

incidence angles and sample orientations across the broad far-IR spectral range. Applications of this far-IR ellipsometry for multiferroic materials with $\mu \neq 1$ will be discussed. This development effort is supported by NSF-MRI-0821224.

[1] P. S. Hauge, *J. Opt. Soc. Am.* **68**, 1519 (1978).

[2] D.W. Berreman, *J. Opt. Soc. Am.* **62**, 502 (1972).

9:40am **EL+AS+EM+MS+TF-FrM5 Roughness beyond Bruggeman's Effective Medium Approximation**, *H. Wormeester*, University of Twente, Netherlands **INVITED**

Surface roughness is regularly characterized with ellipsometry, which is especially sensitive for the short length scale roughness. Because of this, the roughness can be treated as a heterogeneous material modelled with an Effective Medium Approximation (EMA). The EMA layer thickness determined is often successfully related to the root mean square roughness from microscopy. A breakdown of this correspondence was recently shown [1]. This was attributed to the non-negligible influence of the characteristic length scale of the roughness. This typical characteristic length scale can approach the wavelength of the light used for many cases of surface roughness. In thus violates an important prerequisite of EMA, i.e. a variation limited to a length scale much smaller than the wavelength of light. This not only results in off-specular scattering, but also to a change in the polarization of the specular reflected light beam as probed with ellipsometry.

The applicability of an EMA to describe small surface roughness can be evaluated with the Rayleigh-Rice (RR) perturbation. In this perturbation method, the surface roughness is incorporated via its power spectral density function. Ohlidahl and co-workers [2] extensively compared Gaussian roughness distributions with EMA results. They reported that Bruggeman's equation describes the roughness well in many situations. However, the correspondence between EMA and RR breaks down for surface heterogeneity if noble metals are involved. For example for deposited colloids, the resonance energy of the induced surface plasmon is not correct [3]. Also the optical spectra calculated with EMA for a rough silver surface can only be reproduced by RR if a very specific power spectral density is used, showing a quite large characteristic length scale.

Roughness with various length scales created by oblique incidence ion sputtering on Ag(001) were experimentally studied with normal incidence ellipsometry, also known as Reflection Anisotropy Spectroscopy [4]. The observed plasmon resonances are the result of anisotropy in the local length scale. This system allows to probe quantitatively the adequacy of the RR. One of the limits discussed is the inability to discriminate between roughness and roughness length scale for small scale roughness. The ability to monitor in-situ the evolution of the anisotropy of the roughness distribution will be addressed.

[1] B. Sperling and J. Abelson, *J. Appl. Phys.* **101** 024915 (2007).

[2] D. Franta and I. Ohlidahl, *Opt. Commun.* **248** 459 (2005).

[3] H. Wormeester, E.S. Kooij and B. Poelsema, *Phys. Stat. Sol. A* **205** 756 (2008).

[3] F. Everts, H. Wormeester and B. Poelsema, *Phys. Rev. B* **78** 155419 (2008).

10:20am **EL+AS+EM+MS+TF-FrM7 Spectroscopic Ellipsometry on Graphene**, *J.W. Weber*, Eindhoven University of Technology, Netherlands, *V.E. Calado*, Delft University of Technology, Netherlands, *M.C.M. van de Sanden*, Eindhoven University of Technology, Netherlands

We show how we used spectroscopic ellipsometry to determine both the optical constants and thickness of graphene. We scanned a mechanically exfoliated graphene flake (150 x 380 μm) on an oxidized silicon wafer (98 nm SiO₂) with a spectroscopic ellipsometer with a focused spot (100 x 55 μm) at an angle of 55°, in the range 210-1000 nm. The spectroscopic ellipsometric data were analyzed with an optical model in which the optical constants of graphene were parameterized by B-splines. This parameterization was key in the uncorrelated, accurate and simultaneous determination of the optical constants and thickness of graphene. The thickness is in perfect agreement with the thickness as expected from the interlayer spacing in graphite: 3.4 Å. This work opens up the possibility for in situ monitoring of graphene growth.

References

[1] K. S. Novoselov, A. K. Geim, S. V. Morozov, D. Jiang, Y. Zhang, S. V. Dubonos, I. V. Grigorieva, and A. A. Firsov, *Science* **306**, 666 (2004).

[2] B. Johs and J. S. Hale, *Phys. Status Solidi A* **205**, 715 (2008).

[3] J. W. Weber, T. A. R. Hansen, M. C. M. van de Sanden, and R. Engeln, *J. Appl. Phys.* **106**, 123503 (2009).

10:40am **EL+AS+EM+MS+TF-FrM8 Free-charge Carrier Properties of Epitaxial Graphene by Terahertz and Infrared Ellipsometry**, *T. Hofmann*, *A. Boosalis*, *P. Kühne*, University of Nebraska-Lincoln, *J.L. Tedesco*, *R.L. Myers-Ward*, *P.M. Campbell*, *C.R. Eddy, Jr.*, *D.K. Gaskill*, U.S. Naval Research Laboratory, *V. Shields*, *S. Shivaraman*, *M.G. Spencer*, *W.J. Schaff*, Cornell University, *M. Schubert*, University of Nebraska-Lincoln

Graphene systems exhibit extremely high charge carrier mobilities highly suitable for the design of high speed terahertz (THz), Angstrom scale transistors [1]. The use of graphene for future electronic devices requires the growth of epitaxial graphene layers on suitable substrates.

We have grown highest-quality epitaxial graphene on Si- and C-faces of silicon carbide substrates under various conditions. We report on Terahertz (THz), Far-infrared (FIR) and Infrared (IR) ellipsometry and THz-IR Optical Hall-effect (generalized ellipsometry in magnetic fields) investigations of the free-charge carrier properties in epitaxial graphene samples. Furthermore, new developments on the tunable-wavelength frequency-domain THz ellipsometry instrumentation with and without external magnetic will be described [2,3].

Our ellipsometric data allows the identification of multiple, parallel sheet carrier densities within the single-to-few monolayer thick graphene layers, and which crucially depend on substrate orientation and growth condition. Analysis of the multiple two-dimensional carrier sheet densities reveals their extreme yet strongly varying mobility, effective mass, and density parameters as well as the vertical carrier sheet profile. Our findings reveal striking influences of the substrate. We discuss the physical mechanisms of the substrate that influence the free-charge carrier properties in epitaxial graphene such as surface polarity, dopant incorporation, surface roughness, and defects. We present a free-charge carrier model for epitaxial graphene, its implications due to the substrate, and discuss in light of previous implementations [4].

References:

[1] Y. Taur, *IBM J. of Res. & Dev.* **46**, 2 (2002).

[2] T. Hofmann, *et al.*, *Rev. Sci. Instrum.* **81**, 023101 (2010).

[3] T. Hofmann, *et al.*, *Appl. Phys. Lett.* **95**, 032102 (2009).

[4] Z. Q. Li, *et al.*, *Nature Physics* **4**, 532 (2008).

11:00am **EL+AS+EM+MS+TF-FrM9 Mueller-Matrix Studies of Scarab Beetles using Spectroscopic Ellipsometry and Imaging Polarimetry**, *H. Arwin*, Linköping University, Sweden, *S. Manhas*, LPICM, CNRS, Ecole Polytechnique, France, *J. Landin*, *K. Järrendahl*, Linköping University, Sweden, *A. De Martino*, LPICM, CNRS, Ecole Polytechnique, France

Many scarab beetles exhibit astonishing structural colors and polarization phenomena including circular polarization in the reflected light. Electron microscopy studies reveal that the cuticles of these beetles contain complex layered and/or chiral structures. From an applications point of view it is of large interest to explore these nanostructures as inspiration for biomimetic design based on structural colors and/or polarization.

In this work, spectroscopic ellipsometry as well as imaging polarimetry are used to determine normalized Mueller matrices of cuticles of several scarab beetle species. Mueller-matrix data in the visible spectral range are measured with a dual-rotating compensator ellipsometer. In addition real-space as well as Fourier-space Mueller-matrix images are recorded at 532 nm and 632 nm with an imaging polarimeter utilizing a microscope objective with a high numeric aperture.

The M41 Mueller-matrix element measured on the partly blue and partly green *Coptomia laevis* is very small and represents a beetle with a nanostructure without chirality. *Anoplognathus frenchi* is goldish and has a broad-band reflection with large values on M41. Very pronounced left-handed polarization effects are observed. *Cetonia aurata* has a narrow-band reflection and the color varies from green to red among species. In the color range of reflection, strong left-handed polarization is observed. Some beetles are also found to reflect right-handed polarization at certain wavelengths and angles of incidences.

The real-space Mueller-matrix images carry information about lateral variation of Mueller-matrix elements. In many cases beetle surfaces are laterally inhomogeneous. On the other hand, Fourier space images provide the azimuthal and angle of incidence variations of the Mueller-matrix elements, averaged over the spatial inhomogeneities. The Mueller-matrix images are found to be consistent with the spectroscopic Mueller-matrix results and provide complementary information. The spectral Mueller-matrix data are also used for modelling the nanostructure of beetle cuticles involving dielectric surface layers and heliocoidal structures. Parameterization in terms of layer thicknesses, refractive indices and pitch of the helix in cuticle structures are presented.

11:20am **EL+AS+EM+MS+TF-FrM10 Agent-Free Bio-Chemical Sensing with Sculptured Thin Films**, *D. Schmidt, K.B. Rodenhausen, S. Schöche, T. Hofmann, E.B. Schubert, M. Schubert*, University of Nebraska-Lincoln

A new concept of agent-free highly sensitive bio-chemical sensing is presented based on the change of birefringence of sculptured thin films (STFs). A mere intermixture of liquid or gaseous molecules with solid state STFs dramatically changes the overall optical properties of the porous film, which can be easily detected by means of ellipsometry or even the bare eye, i.e. light intensity changes upon interaction.

Previously, we have shown that STF exhibit highly anisotropic optical properties, which differ significantly from their bulk properties. Strong form birefringence and large dichroism can be tailored by appropriate deposition geometries to produce desired optical responses. In order to vary structure spacing (void fraction), and enable growth on defined sites self-assembled large-scale substrate patterning by diblock copolymer nanolithography can be exploited. We have demonstrated that generalized spectroscopic ellipsometry is ideally suited for determining geometrical structure and the anisotropic optical properties of STFs [1-3]. Recently, we have demonstrated that the combination of spectroscopic ellipsometry (SE) with quartz crystal microbalance (QCM) methods provides access to organic thin film thickness and porosity information and can further reveal structural properties of thin organic films [4].

Here we report on the application of STFs for bio-chemical sensing by simultaneous in-situ generalized ellipsometry (GE) and QCM measurements. STFs from different materials were deposited by glancing angle electron beam evaporation on gold-coated quartz crystals. Changes in the resonance frequency of the quartz crystals before and after STF deposition were used to determine the void fraction of the STF and agree well with scanning electron micrograph estimates.

In our in-situ experiments, we observe that the optical response of STFs is very sensitive to the ambient medium. We find that the filling of the STFs void fraction with solvents of different refractive index causes changes in birefringence as well as dichroism of the STFs.

Furthermore, the deposition of cetyltrimethylammonium bromide (CTAB), a well-known detergent molecule, is used here in order to demonstrate the detection of organic molecules. We find that the intriguing optical response of the STFs is changing drastically with the deposition of minute amounts of CTAB.

[1] D. Schmidt et al., *Opt. Lett.* **34**, 992 (2009).

[2] D. Schmidt et al., *Appl. Phys. Lett.* **94**, 011914 (2009).

[3] D. Schmidt et al., *J. Appl. Phys.* **105**, 113508 (2009).

[4] K. B. Rodenhausen et al. (*in submission*, 2010).

Energy Frontiers Topical Conference Room: Mesilla - Session EN+SS-FrM

Photocatalysis and Solar Fuels

Moderator: S.-H. Lee, University of Colorado

8:20am **EN+SS-FrM1 Hybrid Metal-Semiconductor Nanomaterials for Electrochemical Hydrogen Generation**, *M.R. Dirmyer, E.P. Luther, A.K. Burrell, B.C. Tappan, A.H. Mueller*, Los Alamos National Laboratory

For the full utilization of intermittent alternative energy sources such as wind and solar energy, issues regarding energy storage must be addressed. An attractive solution is the production of a chemical fuel, allowing for both storage and transportation from so called "stranded" production sites. The electrochemical splitting of water to generate hydrogen allows for the production of such fuel, be it in a denser chemical form or H₂. Electrode materials for such an electrocatalytic process must have a high surface area, and be catalytically efficient and robust in order to be viable for such a process.

The research presented addresses the aforementioned challenges using two elegant, Los Alamos National Lab exclusive nanotechnologies: 1) combustion synthesis of conducting noble metal nanofoam scaffolding to serve as the cathode and 2) Polymer Assisted Deposition (PAD) of catalytically active films onto a conductive metal scaffold to functionalize the anode. The resulting foams have ultralow densities, controlled nanopore diameters, and rank with the highest surface area metals ever produced, making them ideal candidates for various catalytic applications. The deposition mechanism of PAD, as well as the high conductivity of the metal foam, enables the utilization of the entire interior surface of the foam for electrochemical reactions, exploiting the advantages of the thin film form of the coating while retaining the electrical advantages of a bulk metal electrode. Metallic copper foams have been coated with CIS-based thin-film

absorber layers. These materials show photocurrent under illumination with 1.5 AM solar simulated light. Electrochemical water-splitting data will also be presented.

8:40am **EN+SS-FrM2 Surface Electronic Properties of Tantalum Oxynitride Perovskites**, *S. Balaz, S. Porter, P.M. Woodward, L.J. Brillson*, The Ohio State University

We used a complement of X-ray photoemission spectroscopy (XPS), depth-resolved cathodoluminescence spectroscopy (DRCLS), Kelvin Probe Force Microscopy (KPFM), and Atomic Force Microscopy (AFM) to measure the surface electronic properties of the tantalum oxynitride series ATaO₂N (A = Ca, Sr, Ba) and RTaON₂ (R = La, Pr), promising candidates for photocatalytic splitting of water under illumination by visible light. Besides creating perovskites with band gaps that straddle the redox potentials of water closely, a major challenge to conversion efficiency is the recombination of free carriers by trap states formed by lattice defects. We used DRCLS to measure the energies and densities of these recombination centers with respect to the bulk oxynitride energy bands and Fermi levels. Previously reported UV-VIS diffuse reflectance measurements indicate band gap absorption onsets at 2.4, 2.1, 1.8 [1], 2.0, and 2.0 eV [2] for CaTaO₂N, SrTaO₂N, BaTaO₂N, LaTaON₂ and PrTaON₂, respectively. DRCL spectra reveal both broad band-to-band transitions in the 2-5 eV range as well as intense and narrow sub-band gap peak features at 1.95, 1.70, 1.70, 1.70 and 1.79 ± 0.01 eV for the same oxynitride sequence. The relatively constant DRCLS gap state energies indicate similar defects derived from the oxygen and nitrogen 2p orbitals comprising the valence band for all five compounds. By varying the incident beam energy, we probed the surface to the bulk with DRCLS, showing these peak energies nearly unchanged as a function of depth. However 0.1-0.2 eV shifts within the outer 10 nm suggest surface interactions that modify these localized states. The higher energy CL features reflect the slowly rising conduction band densities of states plus more pronounced O 2p-Ta 5d transitions calculated by density functional theory [1]. XPS valence band spectra show Fermi levels 0.5-2 eV above the valence bands, while KPFM work functions vary in the range 4.7 – 4.9 eV, indicating valence band maxima comparable to the 5.67 eV oxidation potential of water. Charging and potentials that vary laterally with nanoscale thickness can affect the XPS and KPFM values significantly but not DRCLS. The appearance of strong defect emissions at energies well within the band gap is indicative of strong recombination that can limit optical conversion efficiencies. Hence, these studies reveal the importance of O- and N-derived native point defects in limiting the efficiency of oxynitride photocatalysts.

[1] Y.-I. Kim, P. M. Woodward, K.Z. Baba-Kishi, and C.W. Tai *Chem. Mater.* 2004, **16**, 1267.

[2] S. Porter, Y.-I. Kim, P. Woodward, Am. Phys. Soc. March Meeting, March 15-19, 2010, abstract X27.00003.

9:00am **EN+SS-FrM3 Zinc-Gallium Oxynitrides as Visible-Light Photocatalysts: Band Gaps and Formation Energies**, *H. Schmidt, D.J. Doren, V.B.R. Boppana, R.F. Lobo*, University of Delaware

Solid solutions of GaN and ZnO have been shown to be a promising class of photocatalysts, capable of splitting water under visible-light irradiation. The structural and electronic properties of Ga_{1-x}Zn_xN_{1-x}O_x have been studied using density-functional theory with the Linear Augmented Plane Wave (LAPW) method at varying values of x. A GGA+U approach is used to better describe the semicore 3d states of Ga and Zn. These calculations show that there exists a p-d coupling between the N 2p and Zn 3d states, leading to a decreased band gap. The band gaps in the mixed metal oxynitrides are lower than either ZnO or GaN, thus allowing excitation by visible light. The trend in band gaps over the range of Zn concentrations (x) is consistent with experimental results. The expected band gap minimum is at a composition that is difficult to synthesize. Formation energies have been calculated to understand the limitations on synthesis of these materials. Several starting materials and synthesis environments have been studied in the formation energy calculations to determine how the thermodynamically preferred products depend on experimental conditions and whether high concentrations of zinc can be obtained in these materials.

9:20am **EN+SS-FrM4 Electronic Structure Analysis and Photocatalytic Properties of Novel Spinel Zinc Gallium Oxy-Nitride Semiconductors**, *B. Boppana, H. Schmidt, D.J. Doren, R.F. Lobo*, University of Delaware

A sol-gel precursor was used to synthesize zinc gallium oxy-nitrides with visible light band gaps. At low temperatures, novel spinel oxynitrides were produced with band gaps of 2.5 to 2.7eV, surface areas of 16 to 36 m²/g, and nitrogen content less than 1.5%. As the temperature was raised, these spinels get consumed to form wurzitic oxy-nitrides also with band gaps less than 3 eV but with surface areas of 4 to 6 m²/g. The reduction in the band gap for the spinel oxy-nitrides is associated with the incorporation of N₂p

orbitals in the valence band with corresponding changes in the anion position parameter. We established that the presence of a small fraction of gallium tetrahedral centers and anion vacancies might affect its unique electronic properties. The changes associated with the gallium coordination environment as the spinel zinc gallate precursor transforms to a spinel oxynitride at 550°C and further changes into a wurzite oxynitride at 850°C are studied through x-ray diffraction, ultraviolet-visible diffuse reflectance spectroscopy, neutron powder diffraction, x-ray absorption spectroscopy and other techniques. Electronic structure and formation energies of the spinel and wurzite oxy-nitrides were studied using density-functional theory (DFT) with the Linear Augmented Plane Wave (LAPW) method at varying dopant concentrations. Furthermore, these novel spinel photocatalysts were found to be active in degrading methylene blue in visible light and oxygen production from silver nitrate. The protocol developed opens a different avenue for the synthesis of semiconductors possessing the spinel crystal structure and with band gaps engineered to the visible region with potential applications for both opto-electronics and photocatalytic applications.

9:40am **EN+SS-FrM5 Synthesis and Surface Characterization of Nano-Scaled Structures for Energy Conversion Devices**, *W. Patterson, M. Robson, K. Artyushkova, P. Atanassov*, University of New Mexico

Using a microemulsion-based synthesis approach to create silica particles with internal porosity characterized by a nano-scale, bi-modal pore size distribution, we have developed functional templates for non-Platinum catalysts for fuel cell technologies. This material is derived from novel silica particles synthesized through oil/water/surfactant microemulsion templating under controlled conditions to have two distinct pore size regimes (~5 nm and ~40 nm). The larger pores, determined by the volume of microemulsion droplets, allow for more facile infiltration of precursors as compared to fumed silica previously used as the templating material. The smaller pores are determined by micellar dimensions and allow sites for creation of active site centers.

After formation of the silica, a subsequent carbon/active-site precursor co-impregnation process is followed by pyrolysis and etching. This leads to formation of open-frame structures of synthetic carbon supports decorated with the nano-phase metallic catalyst of choice. The resulting high surface area material is a bi-porous, carbonaceous matrix decorated with a low loading of non-precious metal. Last year, this effort resulted in demonstrating Pt/C catalysts for oxygen reduction. We have since focused efforts towards non-Pt precursors for pyrolytic formation of a nitrogen-containing carbon backbone structure in combination with transition metals, Co and Fe.

Synthesis conditions, such as the amount of precursor, pyrolysis temperature, and etching conditions play an important role in formation of the porous structure of the resulting electrocatalyst. Well designed nanoporous structures can effectively minimize transport limitations, thus increasing the accessibility of the active sites by gas and electrolyte phases in the fuel cell active layer.

Thorough characterization including SEM, TEM, XRD, and XPS was performed. Detailed physisorption was performed to characterize the pore structure and surface area of the materials. A thorough analysis of the surface composition and structure as a function of pyrolysis temperature for the pyrolyzed Co-N precursor with sucrose was performed and high-resolution XPS spectra were acquired.

Using methodology previously developed for correlation of material structure to properties, we provide an enhanced characterization of composition and structure, identification of active sites, and some insight into the mechanism of reduction/oxidation reactions.

10:00am **EN+SS-FrM6 Enhancement of Visible-Light Photocatalytic Efficiency of TiO₂ Nanopowder by Anatase/Rutile Interface Formation**, *Y.J. Chen, C.S. Lin*, National Dong Hwa University, Taiwan, Republic of China

In this article we report that the presence of anatase/rutile interface is essential on realization of visible-light photocatalytic ability of TiO₂ produced by the novel flat-flame chemical vapor condensation (FFCVC) method. Previous study shows that when nitrogen is replaced by argon as precursor carrier gas as well as quench gas in the FFCVC process, the synthesized TiO₂ nanopowder changes from anatase/rutile dual phases to anatase single phase. The UV-vis absorption spectra suggest that the

synthesized TiO₂ with single anatase phase may still possess visible light absorption capability when the process parameters are carefully chosen. However, the photocatalytic efficiency drops to minimal value for the single-phase TiO₂ compared with that for dual-phase TiO₂. To confirm that the photocatalytic efficiency difference is caused by the formation of anatase/rutile interface, we synthesize the TiO₂ nanopowder using argon as carrier gas while using either nitrogen or argon as quench gas for comparison. Results show that when using nitrogen as quench gas, the TiO₂ powder is mostly anatase phase with minor rutile content, while when using argon as quench gas, the TiO₂ powder is almost anatase phase with hardly any rutile content. From the x-ray diffraction analysis, the grain size of anatase from both processes is similar, indicating that the choice of quench gas does not influence significantly on the nucleation process of the TiO₂ nanopowder. On the other hand, the use of nitrogen as quench gas does promote the formation of rutile phase, even though the rutile content is still minimal. This observation indicates that the nitrogen as quench gas does have some effect, although weak, on TiO₂ nanopowder during its final coalescence and growth stage. The visible-light photocatalytic experiment shows that even two powder samples are similar, the photocatalytic efficiency of TiO₂ with minor rutile content is significant while that of TiO₂ with single anatase phase is insignificant. Since the anatase from both processes is considered the same, the photocatalytic efficiency difference must be due to that minor rutile formation. Since the photocatalytic reaction occurs mostly on the anatase surface, the enhancement of photocatalytic efficiency by the formation of rutile phase leads to the conclusion that the anatase/rutile interface is the major cause for the efficiency enhancement. We will show the XPS, EPR, and XRD characterization of powders and discuss the materials science behind the phenomenon.

MEMS and NEMS

Room: Santo Domingo - Session MN-FrM

Characterization for MEMS and NEMS

Moderator: A.V. Sumant, Argonne National Laboratory

8:20am **MN-FrM1 Wafer-scale Processing of Diamond Thin Films for MEMS and NEMS**, *J.A. Carlisle*, Advanced Diamond Technologies **INVITED**

The key to enabling wafer-scale processing of thin film diamond are the specifications that the technology can meet on commercially relevant wafer sizes. Due to advances in reaction design and deposition chemistry, a variety of diamond materials can now be deposited onto wafers up to 300 mm in size, with excellent thickness and property uniformity, enabling high-yield production of microdevices. In this presentation advances made over the past several years to enable thin, smooth diamond films for MEMS will be reviewed with emphasis on materials and microfabrication strategies needed to integrate diamond with other materials for MEMS devices. UNCD® (ultranano-crystalline diamond) spans a family of thin smooth diamond materials. UNCD wafers serve to demonstrate the availability of the technology and to allow designers to integrate diamond into new process flows. NaDiaProbes®, which are all-diamond AFM probes used for metrology and nano-manufacturing, are the first example of a commercially available diamond MEMS device that leverages wafer-scale processing of UNCD wafers using established microfabrication techniques. How ADT looks at wafer-scale production of UNCD-based MEMS devices going forward as well as our technology roadmap for UNCD-enabled products under development will be presented. Particular emphasis will be placed on the development of UNCD coatings and MEMS devices for RF devices, nanomanufacturing, and chem/bio-sensing related applications.

9:00am **MN-FrM3 CMOS Integrated Ultrananocrystalline Diamond Capacitive RF-MEMS Switches**, *S. Balachandran, A.V. Sumant, O.H. Auciello*, Argonne National Laboratory, *S. O'Brien, C.L. Goldsmith*, Memtronics Corporation, *J.A. Carlisle*, Advanced Diamond Technologies, *C. Gudeman, S. Sampath*, Innovative Micro Technology

RF-MEMS DC contact and capacitive switches are being developed, involving a broad range of designs in series and shunt configurations. The work done until now has facilitated significant maturing of the technology to overcome technical challenges such as reliability, packaging, and high power operation. In particular, the reliability of RF-MEMS capacitive switches has been limited mainly by the electrical charging of the oxide or nitride dielectric layers used until now, which exhibit discharging times in the hundred of seconds range, resulting in failure of the switches. Therefore, it is critical to develop dielectric layers with fast charging/discharging performance. In this respect, the novel ultrananocrystalline diamond (UNCD) films developed and patented at Argonne National Laboratory exhibit a unique fast charging (50-100 μsec)/discharging (≤ 100 μsec)

behavior, which provides the reliability required by RF-MEMS switches. The charges are transported through a large network of grain boundaries, which occupy a large percentage of the total area of the films, characterized by a nanostructure formed by 2-5 nm grains with ~ 0.5 nm wide grain boundaries.

This paper focuses on a description of materials, materials integration strategies, device architecture and performance of prototype monolithically integrated RF-MEMS mm-wave shunt capacitive switches/CMOS devices in coplanar waveguides, using UNCD as the dielectric layer. The RF-UNCD MEMS switches are based on a MEMtronics, Inc. switch design, fabricated on sapphire wafers with high-voltage CMOS devices, provided by Peregrine Semiconductor, using standard lithography and surface micromachining techniques. Small signal measurements were performed in the frequency range of 1-20 GHz. Measurements of the UNCD dielectric layer charging and discharging were performed using both MEMS and metal-insulator-metal (MIM) capacitor device configurations, using standard I-V and C-V techniques. The charging and discharging time constants for RF-MEMS switches with UNCD dielectric were 5-6 orders of magnitude faster (≤ 100 μ sec) than the discharging times (100s of seconds) exhibited by conventional oxide or nitride dielectric materials. Although static power consumption is an issue with UNCD-based capacitors, they can be used in applications, which demand little to no degradation in performance and allow microwatts of power consumption.

This work was mainly supported by DARPA, under contract MIPR 06-W238. Use of the Center for Nanoscale Materials was supported by the U. S. Department of Energy, Office of Science, Office of Basic Energy Sciences, under Contract No. DE-AC02-06CH11357.

9:20am **MN-FrM4 Mechanical Stiffness and Dissipation in Ultrananocrystalline Diamond Resonators**, *V.P. Adiga*, University of Pennsylvania, *S. Suresh*, *A. Datta*, Innovative Micro Technology, *J.A. Carlisle*, Advanced Diamond Technologies, *A.V. Sumant*, Argonne National Laboratory, *R.W. Carpick*, University of Pennsylvania

Nanocrystalline materials exhibit unique mechanical properties depending on the nature of the bond, co-ordination number of atoms at grain boundaries. Tetragonal sp^3 -bonded diamond has the highest known atomic density. The nature of the bond and its high density enable diamond to have superior physical properties such as the highest Young's modulus, melting temperature and acoustic velocity of all materials. Recently, conformal thin diamond films have been grown at CMOS-compatible temperatures in the form known as ultrananocrystalline diamond (UNCD). We have measured the Young's modulus (E), Poisson's ratio and the quality factors (Q) for microfabricated overhanging ledges and fixed-free beams composed of UNCD films grown at lower temperatures. The overhanging ledges exhibited periodic undulations due to residual stress. This was used to determine a biaxial modulus of 838 ± 2 GPa. Resonant excitation and ring down measurements of the cantilevers were conducted under ultra high vacuum (UHV) conditions on a customized atomic force microscope to determine E and Q. At room temperature we found $E = 790 \pm 30$ GPa, which is ~20 % lower than the theoretically predicted value of polycrystalline diamond, an effect attributable to the high density of grain boundaries in UNCD. From these measurements, Poisson's ratio for UNCD is estimated for the first time to be 0.057 ± 0.038 . We also measured the temperature dependence of E and Q in these cantilever beams from 60 K to 450 K. Above ~ 150 K, temperature dependence of modulus is slightly higher than that of single crystal diamond averaged over all directions despite the presence of large fraction of disordered carbon at grain boundaries and below 150 K changes in modulus are extremely small. This is the first such measurement for UNCD and strongly suggests that the nanostructure plays a significant role in modifying the thermo-mechanical response of the material. We have measured a very low temperature coefficient of frequency at room temperature which has important technological applications including resonant mass sensors and filters. The room temperature Q varied from 5000 to 16000 and showed a moderate increase as the cantilevers were cooled below room temperature and it saturates resembling the plateaus observed in many disordered systems. The results suggest that defects in the grain boundaries significantly contribute to the observed dissipation.

"Mechanical stiffness and dissipation in ultrananocrystalline diamond resonators" *Adiga et al*, V 79, pp 245403.1-8, *Physical Review B*, 2009

9:40am **MN-FrM5 Theoretical and Experimental Investigation of Optically Driven Nanoelectromechanical Oscillators**, *R.B. Ilıc*, Cornell University, *S.L. Krylov*, Tel Aviv University, Israel, *H.G. Craighead*, Cornell University

Actuation of biologically functional micro and nanomechanical structures using optical excitation is an emerging arena of research that couples the fields of optics, fluidics, electronics and mechanics with potential for generating novel chemical and biological sensors. In our work, we

fabricated nanomechanical structures from 200nm and 250nm thick silicon nitride and single crystal silicon layers with varying lengths and widths ranging from 4 μ m to 12 μ m and 200nm to 1 μ m, respectively. Using a modulated laser beam, focused onto the device layer in close proximity to the clamped end of a cantilever beam, we concentrate and guide the impinging thermal energy along the device layer. Cantilever beams coupled to chains of thermally isolated links were used to experimentally investigate energy transport mechanisms in nanostructures. The nature of the excitation was studied through steady-periodic axisymmetric thermal analysis by considering a multilayered structure heated using a modulated laser source. Results were verified by finite element analysis, which was additionally implemented for the solution of steady-periodic and transient thermal, as well as steady thermoelastic problems. These theoretical investigations, coupled with our experimental results, reveal that the complex dynamics underpinning optical excitation mechanisms consist of two disparate spatial regimes. When the excitation source is focused in close proximity to the structure the response is primarily thermal. We show that as the source is placed farther from the clamped end of the structure, the thermal response progressively fades out indicating the possibility of mechanical wave propagation. Understanding the excitation mechanisms may be useful for applications including compact integration of nanophotonic elements with functionalized nanomechanical sensors for ultra-sensitive biochemical analysis.

10:00am **MN-FrM6 Nanotribological Studies of Adaptive Optics Sliding Components in Microprojectors**, *B. Bhushan*, *H. Lee*, The Ohio State University, *S. Chaparala*, *V. Bhatia*, Corning Incorporated

As portable devices are increasingly developed and used, the size of their displays are getting smaller, therefore becoming harder to view. Integrated micro-projectors are an alternative way to see a big image on any surface chosen by users. Microprojectors require red, blue, and green lasers to perform. However, unfortunately the green laser is not commercially available. In order to generate the green laser, frequency doubling technique is used, doubling a semiconductor laser of a wavelength 1060nm to 530nm green laser. The best alignment of the lenses in frequency doubling technique effects on energy efficiency and performance of the devices. To align the lenses, there are reciprocating and stick-slip motions between the components in the devices. Therefore, nanotribological studies of adaptive optics sliding components in microprojectors are needed. In this study, a methodology to measure lubricant thickness and distribution is developed. Lubricant bonding techniques are identified to bond the lubricant to the surfaces with thermal, UV or plasma treatments. Friction, adhesion and wear mechanisms of lubricant on the sliding components are studied in various environments, such as different humidity and temperature.

10:20am **MN-FrM7 Nonlinear Fracture Mechanics Model for Mode I & Mode II Stiction Failure**, *A. Mousavi*, *Z.C. Leseman*, University of New Mexico

The highly nonlinear nature of the crack propagation is studied using a completely nonlinear beam theory model. A model is described that is highly accurate for various deflections of microcantilevers and agrees with the experimental data with nanometer accuracy. The micro cantilever beams used are fabricated by SUMMIT V technology and the dimensions of the beams are 500 x 20 x 2 microns. A nonlinear method is also proposed to calculate the strain energy release rate of stiction failed micro cantilever beams. It is shown that at higher deflections the previous methods fail to accurately determine the stored strain energy and the strain energy release rate. The proposed method is used to accurately determine the beam's profile and strain energy release rate at higher deflections, and it is in good agreement with the other methods at small deflections.

The method developed here is completely applicable to both Mode I and mixed mode I & II crack development problems. It is shown that when it comes to micro cantilevers the so called Mode I crack propagation turns out to be a mixture of Mode I and Mode II. Longitudinal stresses developed inside the cantilevers increases rapidly as the beam gets nonlinear and starts to play a more important role in the crack length and strain energy release rate. The strain energy release rate can be formulated both using the elastic energy stored in the beam and also using the definition of stress intensity. In this paper, the two common methods for calculation strain energy release rate are discussed and stress intensity factors determined. The obtained stress intensity factors once again verify the fact that there is some Mode II component present during the crack propagation. These results also show that the strain energy release rate is not a constant value and increases as the crack develops. A highly linear relationship is observed between stress intensity components which are in good agreement with the analytical models of the phase angle. It is observed that the phase angle is almost a constant value for all crack heights.

10:40am **MN-FrM8 Novel NEMS Gas Detectors for Micro Gas Chromatograph**, C.-H. Chen, C.-J. Hsieh, H.-K. Lin, T.-S. Lee, P.-H. Chen, C.-H. Chou, National Taiwan University, Republic of China, C.-J. Lu, National Taiwan Normal University, Republic of China, W.-C. Tian, National Taiwan University, Republic of China

This research reports the developments and characterizations of two types of NEMS gas detectors, based on nano-scaled titanium oxide (TiO₂) and monolayer protected gold nanoclusters (MPCs) as a sensing film of chemiresistors. For sensing films based on chemically synthesized MPCs, the diversified selectivity (>10 compound detection based on various MPC shell structures), the fast response (<10 seconds) and the low power consumption (25 μ W) are its main advantages. However, the irreversible adsorption due to the strong affinity between MPCs and vapor molecules could be problematic. On the other hand, nano-structured TiO₂ film, which is operated at elevated temperature, is inherently immune from irreversible condensation. The TiO₂ sensing film is fabricated through E-beam lithography in the present study. Various shapes of nano-structures are precisely aligned and placed in between microelectrodes to mimic nanocrystalline structures for the enhancement of the detector sensitivity and robustness. In addition, these NEMS gas detectors are conditioned with integrated heaters at a controlled temperature to minimize any interfering gas adsorption in between analysis. Various performance evaluations including the characterizations of two types of detectors at different temperatures, test chemicals, detection limits, and the compatibility with a gas chromatography system, are investigated and to be presented.

11:00am **MN-FrM9 On the Impact of Relative Humidity and Environment Gases on Dielectric Charging Process in Capacitive RF MEMS Switches Based on Kelvin Probe Force Microscopy**, U. Zaghloul, B. Bhushan, The Ohio State University, P. Pons, LAAS-CNRS, France, G.J. Papaioannou, Universite de Toulouse, France, F. Cocetti, R. Plana, LAAS-CNRS, France

Dielectric charging is among the major reliability issues that have prevented the commercialization of RF-MEMS Capacitive switches in spite of the extensive study performed on the topic. Moreover, a little work has been performed to study the effect of the relative humidity (RH) and environment gases on the dielectric charging process.

In this work we present the effect of RH and the environment gases on the charging/discharging processes in PECVD silicon nitride films based on Kelvin Probe Force Microscopy (KPFM) methodology. The measurements have been performed in ambient air and under N₂ flow, both under different RH levels (from 6% to 40% RH). In addition, the influence of the dielectric film thickness, SiN deposition conditions and the substrate nature on the charging process have been investigated under different environment conditions. This has been done through depositing SiN films with different thicknesses ranges from 100nm to 400nm over bare silicon substrates and over evaporated Au layers and using both Low Frequency(LF) and High Frequency(HF) PECVD deposition modes.

For both measurements performed in ambient air and under N₂ flow, the surface potential decay with time follows the stretched exponential law. The decay time constant decreases strongly as the RH increases (1.230E+03 sec and 650 sec for 6%RH and 40%RH respectively, for the HF 200nm thick SiN film deposited over evaporated Au). The measured decay time constant is found to be shorter in case of N₂ than in ambient air measurements. The surface potential distribution is represented by the Full Width at Half Maximum (FWHM) for charges which have been injected in a single point with the AFM tip. The FWHM becomes smaller as RH decreases. Charge injection duration is controlled to range from 10 ms to 100 sec. The FWHM is found to be always larger in air comparing to FWHM measured in N₂ flow for different charge injection durations. Moreover, FWHM increases almost linearly with increasing the charge injection time for different RH measurements. Charge lateral diffusion has been observed at larger RH only and is attributed to the more hydrophobic SiN material at smaller RH levels which prevents water condensation at the surface and thereby inhibits lateral charge migration due to the electrical conductivity of a possible water film. The FWHM is found to be smaller in thinner SiN films than in thicker ones and the relaxation time is found to be larger in the thinner SiN films, independently of the substrate nature. Finally, the decay time constant is found to be smaller in case of dielectric films deposited over Au layers comparing to films deposited over bare silicon substrates.

11:20am **MN-FrM10 Feature Size Etch Rate Dependence in Bosch Process Deep Silicon Etching Due to Local Thermal Loading**, R. Kurkul, R. Gulotty, B. VanderElzen, University of Michigan, Ann Arbor

Aspect ratio dependent etching (ARDE) is a common issue in reactive ion etching. This phenomenon results in narrow, deeply etched features exhibiting slower etch rate and a more reentrant profile than larger, more open features. The common mechanism indicated for this effect is ion flux. The narrow features restrict the ability of ions that are not perfectly

perpendicular to make it to the bottom of the feature and drive the etch. Recent data obtained at the University of Michigan Lurie Nanofabrication Facility suggests that, in some circumstances, there is a feature size effect that is independent of aspect ratio. The mechanism proposed and studied herein is local thermal loading due to exothermic etch reactions.

The evolution of faster etch rates in silicon is a key enabling factor in MEMS production. However, this fast etching results in thermal management concerns. In an effort to understand these temperature effects better, as well as to determine the evolution of aspect ratio dependence, we performed a variety of rate tests at various stages of etching on different size features. A surprising result was that, after an initial substrate warm up time where etch rates increased slightly, etching rates were flat until aspect ratios approached 10:1 after which they began to drop off slightly. Even more notable is a very significant rate variance with feature size even at very early stages of the etch. This appeared in a regime where ion flux and ARDE should not be significant. This strongly suggests a mechanism of feature size dependence separate from aspect ratio.

The mechanism proposed for this etch rate variance is local thermal loading. This agrees with data collected. Temperature is a significant factor in determining etch rate. The fluorine silicon reaction is exothermic. This has been shown to elevate the temperature of the substrate over the first few minutes of the process. The thermal load will also result in heating and a higher temperature at the etch interface within the features. Larger features will have a higher local thermal load and thus get hotter. This heating accelerates the etch and likely inhibits the ensuing etch resistant fluorocarbon deposition step that is characteristic of the Bosch Process.

We will demonstrate the evolution of this thermal loading and its effects on etch rate within an etch step and through the first few etch cycles of a Bosch Process. We will then evaluate the effectiveness of possible methods of mitigating this effect.

Plasma Science and Technology **Room: Aztec - Session PS-FrM**

Liquids and Multiphase Discharges

Moderator: C. Labelle, GLOBALFOUNDRIES

8:20am **PS-FrM1 Dynamic of Plasma Ignition and Propagation in Water**, W.G. Graham, Queen's University Belfast, Northern Ireland, A. Rousseau, P.H. Ceccato, O. Guaitella, Ecole Polytechnique, France
INVITED

We present an experimental study of a filamentary microplasma discharge inside liquid water. Such plasmas are used for liquid electrical insulations tests and for pollution control of water [1-2]. It was recently shown that the propagation velocity was found to be surprisingly constant whatever the experimental parameters and especially as a function of the water conductivity [3]. The purpose of the present work is to understand the physical mechanisms responsible for initiation and propagation of the discharge. A point to plane electrode configuration submerged in water has been constructed and was submitted to a high voltage pulse. Filaments inception and propagation and several discharges modes have been characterized with electrical measurements and time resolved nanosecond imaging. A Shadow diagnostic using 2 fast cameras was implemented to study the gas content and the shock wave emission from the discharge. The influence of the applied voltage polarity and the water conductivity was investigated. At positive high voltage the growth of the discharge begins by the nucleation of a microbubble at the needle electrode within a few microseconds at an applied voltage of 40kV, a hemispheric branching filamentary structure grows at 3km/s during 100ns and is followed by the propagation of second filamentary structure ten time faster. This continuous propagation on a nanosecond time scale is followed by a stepwise propagation in case of distilled water. When the filaments reach the opposite electrode electrical breakdown occurs. At negative polarity the discharge is much slower 600m/s. The morphology of the gas cavity is driven by interface instability.

[1] P. Bruggeman et al. 2009, J. Phys. D: Appl. Phys. 42

[2] B. R. Locke et al. Ind. Eng. Chem. Res. 45 882-905

[3] P. Ceccato et al. J. Phys. D: Appl. Phys. 43 (2010) 175202

9:00am **PS-FrM3 Copper Nanoparticles Synthesized by Glow Discharge in Solution**, N. Saito, Y. Aoki, J. Hieda, O. Takai, Nagoya University, Japan

Plasma in gas phase is widely used in many industrial fields such as electronic device manufacturing processes (plasma etching, sputtering, plasma-enhanced CVD, etc.), hard coating processes (ion plating,

sputtering, etc.), surface treatment processes (low or atmospheric pressure plasma treatments, sputtering, plasma etching, etc.) and so on. Plasma in solid phase has been utilized finally for surface plasmon resonance (SPR) spectroscopy, nanoparticles, etc., and plasmonics is developing as a new research field. On the other hand, plasma in liquid phase is not generally well-known, although it has been partially utilized in water treatments and electrical discharge machining. The fundamentals of plasma in liquid phase have not been established, including its generation techniques, its state, and activated chemical species. However, it would be reasonable to expect a higher reaction rate under lower-temperature conditions, and the greater chemical reaction variability since the molecular density of liquid is much higher than that of gas phase. So we have named the plasma in liquid phase "solution plasma" because we make variety of plasma by choosing the combinations of solvents and solutes in solutions, and are developing solution plasma processing (SPP). In SPP, aqueous solutions, nonaqueous ones, liquid nitrogen, supercritical fluids, etc. can be utilized as solutions. Recently, we have investigated the features of SPP and the applications such as syntheses of nanoparticles and mesoporous silica, and surface modification of particles.

In this research, copper nanoparticles were synthesized by a glow discharge in solution. A pulsed power supply was used to generate discharges. The pulsed width was 2 micro seconds, the repetition frequencies were 10 – 15 kHz. The electrode was tungsten wire in the diameter of 1 mm with electrode gap of 0.3 mm. Ethanol was used as a solution. Monohydroxy copper acetate (II) was utilized as a raw material of copper. The molar concentration of raw material was adjusted to 5mM. Moreover sodium iodide was added to the solution up to 5 mM. The solution and the productants after the discharge were analyzed by ¹H NMR, Uv-Vis spectroscopy, XRD, TEM. Finally, TEM showed the synthesis of copper nanoparticles. Moreover ¹H NMR show the presence of acetaldehyde in the solution after discharge, which might work as a reducing agent.

9:20am **PS-FrM4 The Consequences of Bubbles in the Electrical Breakdown of Liquids**, *N.Yu. Babaeva, M.J. Kushner*, University of Michigan, Ann Arbor

Streamer discharges in liquids do not likely directly develop through the liquid phase. It is thought that breakdown occurs inside bubbles where streamers preferentially propagate along the surface of the bubbles and near gas-liquid interfaces [1]. In many applications, plasmas are intentionally generated inside bubbles in liquids to produce reactive species which then diffuse through the gas-liquid interface. For short (nanoseconds) time scales, one of the proposed mechanisms for electrical breakdown in liquids is the sequential linking of plasmas in bubbles (PBs). For example, the large E/N produced in the bubble compared to the adjoining liquid enables more rapid breakdown and charging of inner surfaces. If the bubbles are in favorable alignment, the inter-bubble electric field enhancement may provide a mechanism for propagating the streamer through the liquid. On longer timescales (microseconds) when heating of the gas-liquid interface becomes important, thermally induced breakdown likely occurs. The mechanism includes heating and evaporation of adjacent liquid layers, expansion of the gas phase accompanied by the deformation of the gas-liquid interface by electrical forces. In this case the favorable alignment of bubbles does not play an important role.

In this paper, properties of PBs and of streamers intersecting with liquids will be discussed based on results of computer simulations.[2] The model used in this investigation is *nonPDPSIM*, a 2-dimensional plasma hydrodynamics model in which the densities and momentum of charged and neutral particles are solved coincident with Poisson's equation and radiation transport. On short time scales liquids are computationally treated in the same manner as plasma with an appropriate density dependent polarization to provide the liquid density permittivity. On longer time scales, heating and evaporation of the adjacent portions of the liquid is addressed.

We will also address streamers intersecting with liquids in the context of plasma treatment of biological tissue or wounds. In this case the intersection of streamers with the liquid on time scales shorter than the dielectric relaxation time additionally produce electric fields within the underlying tissue. The values of these electric fields, as large as 100s kV/cm, are above the threshold for breakdown for atmospheric pressure gas bubbles or gas filled vacuoles. As such, it may be possible to produce plasmas below the surface of the liquid or within tissues.

[1] P. Bruggeman and C. Leys, *J. Phys. D* **42**, 053001 (2009).

[2] N. Yu. Babaeva and M. J. Kushner, *J. Phys. D* **42**, 132003 (2009).

* Work supported by the Department of Energy Office of Fusion Energy Sciences

9:40am **PS-FrM5 Diagnostic Studies of AC-driven Plasmas in Saline Solutions: the Effect of the Frequency on the Plasma Behavior**, *H.W. Chang, C.C. Hsu*, National Taiwan University, Taiwan, Republic of China
Plasmas in saline solutions receive considerable attention in recent years. How the electrical power frequency influences the plasma behavior remains unclear. In this presentation, diagnostic studies of plasmas ignited in saline solution driven by an AC power source are presented. An AC power source with tunable frequencies between 50~1000 Hz and a voltage up to 600 V is used. The electrode at which the plasma is ignited uses a Pt wire 0.5 mm in diameter covered by a glass tube to precisely define the area exposes to the solution. Saline solutions with concentrations 0.01 M ~ 2 M are used. Diagnostic tools used include a voltage and a current probe to monitor the electrical characteristics. A high speed camera with a frame rate up to 1200 frames/sec is used to capture the bubble and plasma dynamics. An optical emission spectrometer and a photomultiplier tube are used to monitor the optical emission emanating from the plasma. It is shown that the plasma behavior is strongly coupled with the bubble dynamic adjacent to the electrode tip. Two distinct modes, namely the static mode and the jetting mode, are identified. In the static mode, a bubble with a diameter 1~3 mm is attached at the electrode tip for many seconds. The oscillation of the bubble is found to be relevant to the plasma behavior and is partially responsible to the stability of the discharge. This mode occurs mostly at the frequency below 100 Hz. The jetting mode occurs at a frequency higher than 300 Hz. In this mode, the plasma is ignited intermittently and is less stable comparing with the bubble mode. Under low applied voltages, bubbles of hundreds of μm in diameter are continuously jetted from the electrode tip. As the applied voltage increases, the micro-bubbles tend to coalescence into large bubbles and attach back to the electrode thus the switching of the above two modes is observed. Further increase in the applied voltage leads to bright plasmas with high current and severe electrode damage occurs. It is also observed that under the applied voltage above 200 V, the plasma ignited in the negative half cycle of the power period shows a much stronger emission intensity than that in the positive half cycle. By the integration of the high speed image, the optical emission spectroscopy, and the electrical characteristics, the mechanism of the plasma formation under various frequencies and how it is affected by the bubble dynamics will be proposed.

10:00am **PS-FrM6 Solution Plasma Processing of Carbon Nano-Fillers in Ammonia Aqueous Solution for Preparation of Polymer Nano-Composite Materials**, *T. Shirafuji, Y. Noguchi, J. Hieda, N. Saito, O. Takai*, Nagoya University, Japan

Solution Plasma Processing (SPP) has been performed in ammonia aqueous solution for amino functionalization of multi-walled carbon nanotubes (MWCNTs). The MWCNTs, which do not disperse in aqueous solution, have uniformly dispersed after the SPP. The treatment time for obtaining 10 g of the well-dispersed MWCNTs was only 2 hours. Infrared absorption spectroscopy of the SPP-treated MWCNTs revealed that NH₂ bonds were formed on the MWCNTs. The destruction of the MWCNT structure was not observed as shown by the characteristic Raman spectrum. The composite materials were prepared with the SPP-treated MWCNTs and polyamide 6 (PA6), and showed better tensile, bending and impact strength than those of non-treated MWCNTs and polyamide 6. Grafting of the ϵ -aminocaproic acids has been performed on the NH₂ sites of the MWCNTs. Appearance of the amide-I and amide-II bands in the infrared absorption spectrum of the grafted sample indicated that the grafting was successfully achieved. By grafting the ϵ -aminocaproic acids, which has the molecular structure of one segment of the PA6, we can expect hydrogen bonding between the N-H and O=C sites in the PA6 and grafted epsilon-aminocaproic acids, and can expect further improvement in mechanical strength of the PA6/MWCNT composites.

Surface Science

Room: Santa Ana - Session SS-FrM

Reactivity of Oxides, Mainly TiO₂

Moderator: G.A. Kimmel, Pacific Northwest National Laboratory

8:20am **SS-FrM1 Electronic, Chemical, and Morphological Structure of Ag Nanoclusters Grown on FeO_x/Cu(100)**, *F.N. Womack, R. Singh, Y. Losovyi, O. Kizilkaya, R.L. Kurtz, P.T. Sprunger*, Louisiana State University
Iron oxides are used as catalysts in a number of processes crucial to our standard of living, most notably the water-gas shift reaction and the Haber process for producing ammonia. Recent work[1-3] on ultra-thin iron oxide films suggests that their catalytic efficiency can be improved by the addition of metal nanoparticles. We have performed ARPES and LEED experiments

on ultra-thin film FeOx grown on Cu(100). In agreement with our STM results, FeO structure (electronic) is observed at monolayer coverage, but Fe3O4 is observed above 2.5 ML. Moreover, Ag growth, at submonolayer coverages on both oxide phases, there is an increase in binding energy of the Ag 4d band indicating charge transfer from the iron oxide. This partial reduction of Ag may provide sites on the film surface for both oxidation and reduction of adsorbed species. In addition to electronic structure, STM atomic/morphological structure will be presented, as well as induced chemisorption changes, probed by both HREELS and TPD.

- [1] L. Giordano et al., Physical Review Letters 101, 1 (2008).
[2] C. Lemire et al., Surface Science 552, 27 (2004).
[3] Y. N. Sun et al., Surface Science 603, 3099 (2009).

8:40am SS-FrM2 Effect of Ti Dopant in Ceria on the Structure of Metal Nanoparticles. *Y. Zhou, J. Zhou*, University of Wyoming

Ceria plays a major role in the chemistry of supported metal nanoparticles. The nanostructure, redox properties and oxygen storage capacity of ceria can affect the morphology, structure, as well as catalytic reactivity of supported metal nanoparticles. The addition of other metal elements such as Ti can result in structural and electronic modifications of ceria, which not only can enhance the thermal stability of ceria, but also improve its redox properties and oxygen storage capacity. In this paper, we discuss the effect of Ti dopant in the ceria support on the structure of metal particles at the fundamental level. Ti-doped CeOx(111) thin films were prepared on Ru(0001) as model supports under ultrahigh vacuum conditions. Their structures were examined in detail by LEED, XPS and STM. The nucleation and growth of metal particles including Au and Ni on the doped-ceria surfaces were investigated upon deposition at 300 K as well as after heating to higher temperatures, which is compared to that on the pure ceria supports. The research is sponsored by University of Wyoming start-up fund and Wyoming NASA Space grant.

9:00am SS-FrM3 Nucleation Behavior of Supported Nanoparticles Fabricated from an Organometallic Precursor under Ultra High Vacuum: A DFT and STM Study. *H. Khosravian, Z. Liang, A. Uhl, R. Meyer, M. Trenary*, University of Illinois at Chicago

In this combined STM and DFT study, we examine the adsorption of Rh(CO)₂(acac) (acac is acetylacetonate) on a TiO₂(110) single crystal surface, which is aimed at developing an understanding of the relationship between the preferred adsorption sites of the supported organometallic species, and the nucleation behavior of this precursor compound on different surface terminations. The STM images of clean TiO₂(110) show large terraces with the characteristic row pattern that arises from alternating lines of bridging oxygen and uncapped titanium ions. After exposing Rh(CO)₂(acac) to the surface at room temperature the formation of small particles is observed, with diameters of 1 nm or less, and a height of 2.5 Å (i.e., monolayer height). After annealing the sample to 630°C the density and number of the particles is significantly reduced. The particles appear to be monodispersed, with their sizes increased to several nm in lateral directions, and about 5 Å in height (i.e., bilayer height). The findings can be rationalized in terms of deligation of the parent species and agglomeration of the denuded rhodium. The details of the adsorption and deligation Process have been characterized with DFT calculations.

9:20am SS-FrM4 Oxygen Adatom Formation and Charge Transfer upon O₂ Dissociation on Reduced TiO₂(110). *I. Lyubinetsky, Y. Du*, Pacific Northwest National Laboratory, *N.A. Deskins*, Worcester Polytechnic Institute, *Z. Zhang*, Baylor University, *Z. Dohnalek, M. Dupuis*, Pacific Northwest National Laboratory

Combination of the statistical analysis by scanning tunneling microscopy and density functional theory calculations has been used to investigate the initial stages of molecular oxygen dissociation on the reduced TiO₂(110) surface at 300 K. Major O₂ dissociation channel results in the bridging O vacancy (V_O) healing and deposition of a single O adatom (O_a), while minor channel results in formation of O_a pair on regular Ti sites. For latter channel, an intermediate, metastable nearest-neighbor O_a-O_a configuration is observed after O₂ dissociation. This initial configuration is destabilized by Coulomb repulsion of charged O_a's that separate further along the Ti row into energetically more favorable second-nearest neighbor configuration. The potential energy profile calculated for O₂ dissociation on Ti rows and following O_a's separation strongly supports the experimental observations. Our results also suggest that the itinerant electrons associated with the V_O's are being utilized in the O₂ dissociation process at the Ti rows, whereas at least two oxygen vacancies per O₂ molecule are required in order for this process to become viable. Overall, the electrons originating from V_O's provide a larger fraction of charge required for O₂ dissociation, while a smaller fraction can be attributed to Ti interstitials.

[1] Du, Y.; Dohnalek, Z.; Lyubinetsky, I. *J. Phys. Chem. C* 2008, 112, 2649.

[2] Du, Y.; Deskins, N. A.; Zhang, Z.; Dohnalek, Z.; Dupuis, M.; Lyubinetsky, I. *Phys. Chem. Chem. Phys.*

2010, DOI: 10.1039/C000250J.

9:40am SS-FrM5 Chemistry and Physics of Oxide Surfaces: New Insights from Spectroscopic Studies on ZnO and TiO₂ Single Crystals. *C. Wöll*, Karlsruhe Institute of Technology, Germany **INVITED**

A thorough understanding of microscopic mechanism governing chemical reactions at oxide surfaces requires precise knowledge about the nature of the molecular adsorbates and possible transition states. With regards to the economically very important applications in heterogeneous catalysis, where powder catalysts are being used, an ideal approach would be to first determine vibrational bands of molecular adsorbates on the surface of the powder particles, then to assign them by using a data-basis for the corresponding vibrations measured for single-crystal model substrates and finally relate the remaining bands to e.g. defect-related species using quantum chemistry calculations. Of course, these calculations should be validated by a comparison to the experimental results contained in the model substrates data base. Unlike the case of metal substrates, unfortunately, the corresponding experimental data base for metal oxide single crystal surfaces is very small, mostly a result of the rather severe technical difficulties in applying vibrational spectroscopies to these insulating, often defective surfaces.

In this talk the results of a systematic study carried out for ZnO and TiO₂ single crystals is presented. In particular for ZnO substrates a rather thorough understanding has been reached, both experimentally and theoretically, about atomic and molecular adsorbates (H, CO, H₂O, CO₂, methanol, ...) on ZnO single crystals as well as on powder particles [1]. This progress is largely based on being able to obtain high-quality experimental data using HREELS (high resolution electron energy spectroscopy) and IR-spectroscopy for single crystal surfaces and IR-spectroscopy for powder particles. The last part of the will focus on hydrogen atoms adsorbed on ZnO and TiO₂, some of which are rather surprising [2] and a short glimpse on photochemistry with oxides [3].

[1] Ch. Wöll, The Chemistry and Physics of Zinc Oxide Surfaces, Prog.Surf.Sci. 82, 55, 2007

[2] X. Yin, M. Calatayud, H. Qiu, Y. Wang, A. Birkner, C. Minot, C. Wöll, ChemPhysChem 9, 253, 2008

[3] Ch. Rohmann, Y. Wang, M. Muhler, J. B. Metson, H. Idriss, and Ch. Wöll, Chem. Phys. Lett. 460, 10, 2008

10:20am SS-FrM7 Imaging Hindered Rotations of Alkoxy Species on TiO₂(110). *Z. Zhang, R.J. Rousseau*, Pacific Northwest National Laboratory, *J. Gong*, University of Texas at Austin, *B.D. Kay, Z. Dohnalek*, Pacific Northwest National Laboratory

The first scanning tunneling microscopy (STM) study of the rotational dynamics of organic species on oxides is presented. Variable-temperature STM and dispersion-corrected density functional theory (DFT-D) are used to study the alkyl chain conformational disorder and dynamics of 1-, 2-, 3- and 4-octoxy species on rutile TiO₂(110). Initially, the geminate pairs of the octoxy and bridging hydroxyl species are created via octanol dissociation on bridging-oxygen (O_b) vacancy defects. The STM images provide time averaged snapshots of octoxy species rotating among multiple energetically nearly-degenerate configurations accessible at a given temperature. The calculations show that the underlying corrugated potential energy surface is a result of the interplay between attractive van der Waals dispersion forces leading to weak attractive C··Ti and repulsive C··O_b interactions which lead to large barriers of 50-70kJmol⁻¹ for the rotation of the octoxy alkyl chains across the O_b rows. The relative populations of various conformations as well as the rotational barriers are found to be perturbed as a result of additional C··hydroxyl repulsions when the geminate hydroxyl groups are present.

This research was performed in the Environmental Molecular Sciences Laboratory, a national scientific user facility sponsored by the Department of Energy's Office of Biological and Environmental Research and located at Pacific Northwest National Laboratory.

10:40am SS-FrM8 Hydrogen Bonding Controls the Dynamics of Catechol Adsorbed on a TiO₂(110) Surface. *S.-C. Li*, Tulane University, *L.-N. Chu, X.-Q. Gong*, East China University of Science and Technology, China, *U. Diebold*, Tulane University and Vienna University of Technology, Austria

Direct studies of how organic molecules diffuse on metal oxide surfaces can provide insights into catalysis and molecular assembly processes. We

studied individual catechol molecules, $C_6H_4(OH)_2$, on a rutile $TiO_2(110)$ surface with scanning tunneling microscopy (STM). Surface hydroxyls enhanced the diffusivity of adsorbed catechol molecules. The capture and release of a proton caused individual molecules to switch between 'mobile' and 'immobile' states within a measurement period of minutes. Density functional theory (DFT) calculations show that the transfer of H from surface hydroxyls to the molecule and its interaction with surface hydroxyls substantially lowered the activation barrier for rotational motion across the surface. Hydrogen bonding can play an essential role in the initial stages of the dynamics of molecular assembly.

11:00am **SS-FrM9 Design of Highly Stable Molecular Interfaces to TiO_2 Surfaces**, *R.A. Franking*, University of Wisconsin-Madison, *S.A. Chambers*, Pacific Northwest National Laboratory, *R.J. Hamers*, University of Wisconsin-Madison

The integration of molecular systems with TiO_2 is of interest in a wide range of emerging applications. Previously we developed a photochemical reaction which highly stably and covalently binds terminal alkenes to nanocrystalline and single crystal TiO_2 . Here we further develop the reaction to allow the controlled binding of short chain molecules with highly flexible, modular functionalities. Using XPS, FTIR and AFM, we demonstrate that by adding methyl substitutions around the alkene double bond, uniform grafting of the molecules can be controlled from the monolayer to the multilayer regime. Through secondary reactions, click chemistries can be used to attach photo sensitizers and biologically active molecules with the stable linker to the surface. These highly functional molecules grafted to TiO_2 facilitate the study of charge transfer and photo catalysis for wide range of applications involving organic semiconductor oxide interfaces.

11:20am **SS-FrM10 CO Photooxidation on Reduced $TiO_2(110)$ Surface**, *N. Petrik*, *G.A. Kimmel*, Pacific Northwest National Laboratory

Photo-induced reactions between O_2 and CO on reduced rutile $TiO_2(110)$ surface are studied at low temperature ($\sim 30K$). Photon stimulated desorption (PSD) of O_2 , CO_2 and CO (not reported earlier) are observed with comparable yields. Results indicate that CO_2 is produced from the chemisorbed O_2 molecule residing in the oxygen vacancy and CO molecule physisorbed on the Ti site next to it. The PSD angular distribution for CO_2 is non-cosine, narrow and off-normal: it peaks at ~ 40 degrees to the surface normal in the (001) plane (across the Ti and O rows on the surface). The results are consistent with CO_2 produced from the (Ti)-O-C-O-(V_O) transition state complex predicted theoretically. CO PSD from the $TiO_2(110)$ surface is enhanced dramatically by the presence of chemisorbed O_2 molecules, where photo-desorbing CO may be a by-product of the CO photooxidation process.

Authors Index

Bold page numbers indicate the presenter

— A —

Abbas, A.: EN+PS-MoM6, 4
Abdallah, S.: EN-ThP10, 218; EN-ThP11, 219; EN-ThP12, **219**
Abdulagatov, A.I.: TF-MoA2, **37**; TF-ThP5, 227; TF-TuA7, 89; TF-TuP19, 117
Abe, Y.: TF-TuP2, 115
Abel, J.R.: EM-TuM2, 46; MI-ThP3, **220**
Abraham, B.: SE+PS-MoA8, 34
Abraham, D.W.: TF2-TuM1, **63**; TF2-TuM6, 63
Abrahams, R.D.: SS2-TuM10, 60
Abramson, J.J.: NS+BI-ThA1, 202
Abrikosov, I.A.: TF-ThM1, 195
Abrikossova, N.: BI-TuM11, 45
Abundiz, N.: PS-ThP5, 223
Acharya, A.R.: EM-TuP2, **96**
Acharya, D.: NS+AS+MN-WeM4, 132
Acik, M.: GR+NS-MoA1, **26**
Acomb, P.: VT-TuP7, **119**
Adams, D.P.: TF-ThP2, 226
Adams, Jr., J.H.: AS-TuP19, 94
Adams, M.L.C.: TF+EN-MoM6, 20
Adams, P.M.: SS-TuP13, 112
Adderley, P.A.: VT-WeM4, 147
Adiga, V.P.: MN-FrM4, **238**
Adusumilli, P.: LB-WeA1, **158**
Agarwal, A.: PS1-ThA3, **205**; PS1-TuM5, 54
Agarwal, S.: EN+PS-MoM9, 4; EN-ThP7, 218; TF-TuA2, 89
Agrawal, R.: EN+TF-WeM1, 127
Agresta, D.L.: EL+AS+EM+MS+TF-FrM2, **234**
Ahmad, Z.: EN+AS-ThM2, 180
Ahn, G.: NS-TuP1, 100
Ahren, M.: BI-TuM11, 45
Ahrén, M.: NS+BI-ThA3, 203
Aijaz, A.: SE+PS-MoA6, 33
Akimichi, H.: VT-TuP3, 118
Akiyama, K.: NS-ThM10, 189
Aksoy, F.: IS+SS-TuM5, 50; SS1-MoM11, 15
Alang Ahmad, S.: SS2-WeM5, 139
Al-Bataineh, S.: B11-TuA3, 70; SE+PS-MoM8, **13**
Alcántara Ortigoza, M.: SS-TuA12, **88**
Aldred, N.: MB+BI-MoM3, 8
Alexander, J.: NS-TuM3, 52; SS2-MoA1, 36
Alexander, M.R.: B11-TuA1, **70**
Alexeenko, A.: TF-ThM6, 196
Alexis, F.A.: TF+EM-WeM10, 141
Alfaro, J.G.: NS-TuP19, 103
Al-Hosiny, N.: EN-ThP11, **219**; EN-ThP12, 219
Al-Jassim, M.: AS-TuA11, 69
Allara, D.L.: EM-TuM5, 46; TF-ThA2, 210
Allen, M.W.: EM-TuM3, **46**
Alling, B.: TF-ThM1, **195**
Allred, D.D.: AC+TF-MoA1, 23; EL+AS+EM+MS+TF-ThP4, 216; MN-ThP11, 221
Alnabulsi, S.: SS-TuP22, **114**
Altman, E.I.: NS+AS+MN-WeM9, 132; SS1-TuM12, **58**
Alves, O.: GR+NS-MoA8, 27
Ambrosch-Draxl, C.E.: SS2-TuM5, 59
Ambure, S.L.: BI+MN-FrM1, **232**
Amerom, F.: MN-ThP8, 221
Aminpur, M.: PS1-TuA10, 84
Amonette, J.E.: NS-MoA9, 29
Ams, D.: AC-TuA4, 67
Amstad, E.: NS+BI-ThA11, **204**; NS+BI-ThA9, 204
An, J.: EM+MI-MoA8, 25
Anass, B.: TF+EM-WeM5, 140
Anderle, M.: BI-ThP11, **214**
Andersen, J.N.: IS+SS-TuM1, **50**; IS+SS-TuM5, 50
Anderson, D.G.: B11-TuA1, 70
Anderson, K.: NS+BI-ThA4, 203

Anderson, T.J.: EN+NS-WeA10, 155; EN+TF-WeM6, 128; TF-TuA10, 90
Anderson, V.R.: TF-MoA2, 37; TF-ThP5, 227; TF-TuA7, **89**
Andersson, O.: MB+BI-MoM3, 8
Andreas, B.: VT+MN-MoM4, 21
Anferov, V.: VT-TuP13, 120
Anglin, E.: SE+PS-MoM8, 13
Annelies, D.A.: TF+EM-WeM10, 141
Anthis, J.: TF-TuA12, 90
Anthony, J.E.: SS2-TuM1, **59**
Antonelli, G.A.: EM-TuA10, 73; EM-TuP10, 98
Antony Premkumar, P.: PS2-MoA2, 31; SE+PS-MoM4, **12**
Antony, A.: SS1-MoM2, 14
Antrazi, S.: TF-ThA2, 210
Antunez de Mayolo, E.: EL+AS+EM+MS+TF-ThP2, **216**
Aoki, T.: AS-WeA10, 150
Aoki, Y.: GR-TuP2, 99; PS-FrM3, 239; SS-TuP7, **111**
Arahara, S.: TF-ThP15, **228**
Arai, K.: VT-TuP3, 118
Araki, H.: MN-ThP2, 220
Ardalan, P.: EN-MoA10, **26**; SS2+EM-MoM10, 16
Arellano, G.: SS-TuP24, 114
Arena, D.A.: EM+MI-MoA7, 24
Arey, B.: AS-TuA3, 68; AS-WeM2, 122
Arima, K.: SS-ThA3, **208**
Armes, S.P.: TR+NS+SS-WeA2, 173
Armini, S.: TF+EM-WeM10, 141
Arnadottir, L.: B12-WeM11, 124
Árnadóttir, L.: B11-WeM6, 124; BI-WeA7, **151**
Arnold, J.C.: PS-MoM5, 11
Arnold, P.C.: VT+MS-MoA8, **39**
Arseni, N.: BI-ThP11, 214
Arteaga, A.: IJ+BI+MN-MoM9, 7
Artyushka, K.: SS1-TuM11, 58
Artyushkova, K.: AS-TuA10, **69**; BI-ThP10, 213; EN+AS-ThM2, 180; EN+SS-FrM5, 237
Arwin, H.: EL+AS+EM+MS+TF-FrM9, **235**; EL+AS+EM+MS+TF-ThA4, 197; EL+AS+EM+MS+TF-ThP2, 216
Asbeck, P.: GR+MS-WeA9, 157
Asbury, J.B.: EN-MoA1, **25**
Aschemeyer, S.: NS+BI-ThA10, 204; NS-TuP19, 103
Ash, J.: NS+BI-ThA8, 204
Ashurst, W.R.: TR+MN+NS+SS-WeM5, 146; TR-ThP1, 230
Asscher, M.: SS2+EM-MoM2, 15
Asthagiri, A.: SS1-MoM2, 14
Atanassov, P.: BI-ThP10, 213; EN+AS-ThM2, 180; EN+SS-FrM5, 237; SS1-TuM11, 58
Atkinson, S.: B11-TuA1, 70
Attygalle, D.: EL+AS+EM+MS+TF-ThA11, 198
Atuchin, V.: EL+AS+EM+MS+TF-ThP3, **216**
Aubry, O.: PS2-MoA6, 32; PS2-MoA8, 32
Aubuchon, J.: TF+EM-WeM10, 141
Auciello, O.H.: MN-FrM3, 237; NS-MoM8, 10; VT+MN-MoM5, 21
Auger, R.: AS-TuM11, 43
Aurbach, D.A.: IS+SS-TuA7, **79**
Avertin, S.: PS+MN-WeM5, **134**
Avouris, P.: GR+EM+MS+TF+MI-WeM5, 129
Awad, H.: EN-ThP10, 218
Axelsson, L.: NS+BI-ThA3, **203**
Axnanda, S.: SS-TuP19, **113**
Aydil, E.S.: EN+NS-ThM10, **183**; EN-ThP6, 218; IS+SS-TuA11, 79
Ayyaswamy, V.: TF-ThM6, **196**
Azarnouche, L.: PS1-MoA11, **31**; PS1-WeA4, 164
Azuma, S.: VT-WeM9, 147

— B —

Babaeva, N.Yu.: PS2+BI-ThA6, 207; PS-FrM4, **240**
Baber, A.E.: NS-TuM9, 52; SS-TuP2, 110; SS-WeA9, 170
Babu, S.: AS-TuP9, 93
Bachmann, J.: TF-WeM1, **144**
Back, T.C.: TF-ThA7, 210
Badawi, A.: EN-ThP11, 219; EN-ThP12, 219
Baddorf, A.P.: NS-MoM9, 10
Badi, N.: EN+NS-WeA9, 155
Badri, A.: PS2+BI-ThA3, 207
Bae, G.-Y.: EN+SS+TF-ThA10, 200
Bae, L.J.: EM-TuP13, **98**
Baek, S.-M.: PS-TuP20, **108**
Baer, D.R.: AS-TuM6, 43; EN+AS-ThM3, 180; NS-MoA10, 29; NS-MoA9, **29**
Bagge-Hansen, M.: AC+SS-MoM9, **3**
Bagus, P.S.: SS-ThM9, **194**; SS-TuP17, 113
Bailly, A.: SS1-MoA1, 34
Bailly, F.: PS-MoM1, 10
Baio, J.E.: B11-WeM6, 124; B12+AS-TuA8, **70**; NS+BI-ThA8, 204
Baker, S.S.: SS1-TuM3, 58
Baker, C.: VT-TuP2, 118
Baker, L.: TF-TuA9, **90**
Baker, M.S.: MN-ThA3, 202
Bakke, J.R.: EN-MoA10, 26
Baklanov, M.R.: PS1-TuA3, 83; PS1-WeA4, 164
Balachandran, S.: MN-FrM3, **237**
Balakrishna, A.: PS1-TuM5, **54**
Balaz, S.: EN+SS-FrM2, **236**
Baldwin, J.W.: GR+NS-MoA7, 27; MN-ThM3, **187**
Ballard, J.B.: NS-TuM3, 52; SS2-MoA1, **36**
Ballav, N.: MI+EM-TuA9, **80**; SS2-TuM11, 60
Balls, A.: LB-WeA7, 160
Balmes, O.: IS+SS-TuM1, 50
Ban, C.: EN+EM-TuA1, 73
Banerjee, P.: EN+SS+TF-ThA10, **200**; TF1-TuM10, 62
Banerjee, S.: GR+TF-TuM12, 50
Banerjee, S.K.: GR+EM+MS+TF+MI-WeM9, 130
Bang, J.-S.: PS+MN-WeM9, 134
Bangsarutip, S.: PS1-MoA8, 30
Banna, S.: PS1-MoA1, 30; PS1-TuM4, 53
Bao, L.: TF-ThP19, 229
Baraket, M.: GR+TF-TuA8, **77**; PS2-TuM10, 55
Barankova, H.: SE+PS-MoM3, 12
Barbey, R.: SS-TuP22, 114
Bardos, L.: SE+PS-MoM3, **12**
Barghouty, N.: AS-TuP19, 94
Bar-Ilan, O.: NS-MoA8, 29
Barkley, S.: TR+MN+NS+SS-WeM5, 146; TR-ThP1, 230
Barlam, D.: TR-ThP5, 230
Barlow, D.E.: MB+BI+AS-MoA10, **28**; MB+BI+AS-MoA8, 28
Barrentine, N.M.: SS-ThA4, **208**
Bartel, M.: NS-ThM1, 188
Bartels, L.: SS2-TuM4, 59; SS-TuA11, 88; SS-TuA2, **87**
Bartelt, N.C.: GR+AS+TF-ThM11, 184; GR+AS+TF-ThM5, 184; GR+AS+TF-ThM6, 184; GR+NS-MoA10, 27; GR+SS+TF+EM-MoM2, 5; SS-ThA7, 207; SS-ThA8, 209
Bartnik, A.C.: EN-MoA8, 25
Barton, D.: LB-WeA9, 160
Barton, R.A.: MN-ThM4, **187**
Baski, A.A.: EM+SS-ThM11, **179**
Basse, F.H.-U.: SE-TuA10, 87; SE-TuA11, 87
Batan, A.: SE+PS-MoM2, 12
Batteas, J.D.: EM-TuM6, 46
Baucom, K.C.: SS-WeA1, 169
Bauer, E.: AC+SS-MoM5, 2

- Bauer, E.D.: AC+SS-MoM5, 2; AC+SS-MoM8, 2
 Bauer, G.: NS-ThM2, 188
 Bauer, J.: TF+SE-WeM3, 142
 Bauer, T.M.: PS+MN-WeM3, 133; PS+MN-WeM4, 134; VT-TuP9, 119
 Baugh, L.: AS-TuM6, 43; BI2+AS-TuA8, 70
 Baxter, J.B.: EN+NS-ThM9, 182; EN+TF-WeM4, 128; IJ+BI+MN-MoM5, 7; IS+SS-TuA2, 78
 Baykara, M.Z.: NS+AS+MN-WeM9, 132
 Beard, M.C.: EL+AS+EM+MS+TF-ThA8, 198; EN-MoA3, 25
 Beck, K.M.: EN+AS-ThM3, 180
 Becker, J.S.: PS+TF-ThM4, 190; SS2+EM-MoM4, 16
 Becker, M.: IS+SS-TuA2, 78
 Beckord, S.: GR+AS+TF-ThM2, 183
 Beebe, Jr., T.P.: BI-WeA8, 152
 Beebe, T.P.: BI-TuM1, 43; EN+TF-WeM4, 128
 Beechem, T.E.: GR+EM+MS+TF+MI-WeM6, 130
 Beerbom, M.M.: EN+NS-WeM12, 127; EN+NS-WeM2, 125; EN+TF-TuA10, 75; SS2-WeM12, 140
 Beerlink, A.: IS+BI+AS-WeA7, 158
 Behafarid, F.: NS-TuP20, 103
 Behera, S.: PS1-WeA1, 164
 Behm, R.J.: GR+AS+TF-ThM2, 183; GR+NS-MoA8, 27; GR+TF-TuA7, 77
 Behr, M.J.: IS+SS-TuA11, 79
 Belan, R.: EW-WeL3, 148
 Belashchenko, K.D.: EM+MI-MoA8, 25
 Belianinov, A.: SS-TuP12, 112
 Bell, N.S.: NS-TuA7, 81
 Bencomo, M.: NS-TuP7, 101
 Benetti, M.: BI-ThP15, 215
 Bengtsson, T.: BI-TuM11, 45
 Benitez-Brady, A.S.: AS-TuP27, 96
 Benner, B.A.: AS2-ThM9, 176
 Benner, M.S.: VT+MS-MoA3, 38
 Bennett, W.D.: TF-WeA1, 171
 Bensaoula, A.: EN+NS-WeA9, 155
 Bent, S.F.: EN+TF-WeM5, 128; EN-MoA10, 26; SS2+EM-MoM10, 16; SS-WeA4, 170
 Bentley, S.: EM+SS-WeA11, 154
 Bera, K.: PS2-TuA11, 85; PS2-TuM1, 54
 Berg, R.F.: VT+MS-TuM2, 64
 Bersch, E.J.: TF+EM-WeM6, 141
 Bertrand, P.: AS-WeA11, 151
 Bertuch, A.: PS+TF-ThM4, 190
 Besbes, R.: AC-TuA8, 67
 Bettac, A.: EM-TuM12, 47
 Beyer, A.: GR+TF-TuM3, 48
 Beyer, G.: TF+EM-WeM10, 141
 Bezars, F.J.: LB-WeA2, 159
 Bhatia, R.: PS+TF-ThM4, 190
 Bhatia, V.: MN-FrM6, 238
 Bhushan, B.: AS-TuP9, 93; MN-FrM6, 238; MN-FrM9, 239; MN-ThP4, 221; MN-ThP7, 221; SS-TuP21, 114
 Biedermann, L.B.: GR+EM+MS+TF+MI-WeM6, 130
 Biegalski, M.D.: AC+TF-MoA7, 24
 Bihlmayer, G.: MI-WeA11, 162
 Billington, S.: VT+MS-MoA10, 39
 Biolsi, P.: PS1-TuA10, 84
 Birch, J.: EL+AS+EM+MS+TF-ThA4, 197
 Bishop, S.: SS2+EM-MoM9, 16
 Bjelkevig, C.: GR+TF-TuA3, 76
 Blackman, G.: TF-ThP19, 229
 Blanc, R.: TF2-TuM5, 63
 Blessing, J.: VT+MS-MoA10, 39
 Blomberg, S.: IS+SS-TuM1, 50
 Blomfield, C.J.: AS-WeM10, 123; EW-TuL4, 66
 Blügel, S.: MI-WeA11, 162
 Bluhm, H.: IS+SS-TuM1, 50; IS+SS-TuM3, 50; IS+SS-TuM5, 50; IS+SS-TuM6, 51; IS-ThP2, 219; SS-ThA1, 208; SS-ThA3, 208
 Blum, M.: EM-TuA11, 73
 Bodart, P.: PS1-MoA1, 30; PS1-TuM4, 53
 Bode, M.: MI-WeA11, 162
 Boeckl, J.J.: NS-TuA3, 81
 Boggs, M.E.: BI-TuM1, 43
 Bohnen, K.P.: SS-TuA12, 88
 Boitnott, C.: EN+PS-MoM3, 3
 Borge, C.: NS-TuP27, 104
 Boland, T.: BI-ThP4, 212
 Boning, D.S.: VT-TuP9, 119
 Bonnell, D.A.: IS+BI+AS-WeA9, 158; NS+EM+EN-WeA7, 163; SS-ThM4, 194
 Bonner, J.: TF-WeM5, 144
 Bonucci, A.: VT+MN-MoM8, 21; VT+MN-MoM9, 21
 Bonvalot, M.: TF+EM-MoM4, 17
 Boo, J.-H.: EM-TuP6, 97; EN-ThP1, 217; EN-ThP8, 218
 Boosalis, A.: EL+AS+EM+MS+TF-FrM8, 235
 Booth, J.-P.: LB-WeA8, 160; PS-TuP14, 107
 Boppana, B.: EN+SS-FrM4, 236
 Boppana, V.B.R.: EN+SS-FrM3, 236
 Borca-Tasciuc, T.: EN+NS-WeA8, 155
 Borg, A.: SS-ThA9, 209
 Borghetti, F.: BI-ThP15, 215
 Boris, D.R.: PS2-TuM10, 55; SE+PS-MoM9, 13
 Borkowski, M.: AC-TuA4, 67
 Borovsky, B.: TR+MN+NS+SS-WeM5, 146; TR-ThP1, 230
 Borysiuk, J.: GR+SS+TF+EM-MoM5, 5
 Bose, R.K.: TF-MoA9, 38
 Bostwick, A.: GR+AS+TF-ThM6, 184
 Boswell, R.W.: AS-WeM5, 122
 Bottene, A.C.: AS-TuP15, 94
 Bouchoule, S.: PS-ThM3, 192; PS-TuP14, 107
 Boufnichel, M.: PS+MN-WeM10, 135; PS-ThM4, 192
 Boullard, F.: PS1-MoA1, 30
 Boullart, W.: PS1-WeA4, 164
 Bouxsein, C.: TR+MN+NS+SS-WeM5, 146; TR-ThP1, 230
 Bouyssou, R.: PS-MoM1, 10
 Bowers, J.K.: EN+PS-MoM6, 4
 Bowfield, A.: PS2-MoA11, 33
 Bradely, C.M.: SE-TuM6, 56
 Bradley, J.D.: AS-TuP27, 96; SS2-WeM11, 139
 Bradley, J.W.: PS2-MoA11, 33; PS-ThP10, 223
 Branda, C.S.: BI+MN-FrM3, 232
 Branson, J.V.: AS-WeM1, 122
 Brar, V.W.: GR+AS+TF+MI-ThA1, 201
 Brashir, R.: BI+MN-FrM8, 233
 Bratescu, M.A.: PS-ThP3, 222; PS-ThP6, 223
 Bravenec, R.: PS2-TuA2, 84
 Breen, N.F.: NS+BI-ThA8, 204
 Brehmer, D.: NS-TuA4, 81
 Breitenstein, D.: AS-WeA3, 149
 Breitwisch, M.: PS1-TuA11, 84
 Bremer, M.G.E.G.: BI+MN-FrM7, 233
 Brennan, A.B.: BP-SuA5, 1
 Brennan, T.P.: EN-MoA10, 26
 Brett, M.J.: SE+TF-WeA9, 168; TF+SE-WeM6, 143; TF-ThP4, 227
 Brewer, L.N.: IS+AS+NS+MI-WeM6, 131
 Brewster, B.: VT+MN-MoM11, 22
 Bright, V.M.: TF-WeM9, 145
 Brillson, L.J.: EM+MI-MoA4, 24; EN+SS-FrM2, 236; SS-ThM3, 194; TF+EM-WeM12, 142
 Brison, J.: EL+AS-WeA1, 149; BI-WeA7, 151
 Brison, J.P.: BI2+AS-TuA12, 71
 Broach, A.L.: AC+SS-MoM3, 2; AC+SS-MoM4, 2
 Broenstrup, G.: EN+NS-WeM11, 127; NS+EM+EN-WeA9, 163; NS-ThM2, 188; TF+EN-MoM5, 20
 Broitman, E.: NS-TuP27, 104; SE-TuP6, 110; SS-WeA9, 170
 Bronneberg, A.C.: EN+TF-TuA1, 74
 Brooks, D.J.: BI1+NS-ThM6, 177
 Brouri, M.: PS-TuP8, 106
 Brown, D.: PS1-ThA2, 205
 Brown, J.: VT+MS-TuM5, 64
 Brown, Jr., G.: SS-ThA1, 208
 Brown, M.: SS1-WeM2, 137
 Brown, R.D.: SS2+EM-MoM4, 16
 Brozik, S.: EN+NS-WeA2, 154
 Bruce, R.: PS1-WeA2, 164
 Bruce, R.L.: PS1-TuA7, 83
 Brucker, G.: EW-WeL2, 148; VT+MS-MoA6, 39; VT+MS-MoA8, 39; VT-TuP7, 119
 Brueck, S.: EN+NS-WeA2, 154
 Bruener, P.: AS-WeA3, 149
 Bruin, A.: MB+BI+AS-MoA3, 28
 Bruley, J.: TF1-TuM6, 61
 Brumbach, M.T.: AC+SS-MoM11, 3; AS1-ThM6, 175; AS-TuP24, 95; NS-TuA7, 81
 Brüner, P.: AS-TuP2, 92
 Bruns, M.: AS-TuP2, 92
 Bryan, S.R.: AS-TuA8, 69; AS-WeA2, 149
 Buegler, M.: EM-TuP2, 96
 Büenfeld, M.: GR+TF-TuA4, 77
 Bui, H.P.: BI-WeA8, 152; EN+TF-WeM4, 128
 Bui, S.: GR+MS-WeA9, 157
 Bulat, F.A.: MN-ThM3, 187
 Bulkin, P.: EL+AS+EM+MS+TF-ThA6, 197
 Bulloss, N.: EN+AS-ThM6, 181
 Bult, J.: EN+AS-ThM1, 180
 Bumm, L.A.: NS+AS+MN-WeM2, 132; SS2-TuM10, 60
 Bunker, B.: EN+NS-WeA2, 154
 Bunker, B.A.: IS+SS-TuA2, 78
 Bunker, K.L.: EW-TuA6, 76; IS+SS-TuA10, 79
 Bunning, T.: NS+BI-ThA4, 203; PS+TF-ThM12, 191
 Burckel, B.: EN+NS-WeA2, 154
 Burgess, J.S.: GR+NS-MoA7, 27; MN-ThM3, 187
 Burkett, J.R.: MB+BI-MoM5, 8
 Burkett, S.L.: MN-ThM12, 188
 Burnham, N.A.: TR+NS+SS-WeA1, 172
 Burns, S.: PS-MoM5, 11
 Burrell, A.K.: AC+SS-MoM5, 2; EN+SS-FrM1, 236
 Burst, J.: EN+SS+TF-ThA6, 199; TF-ThP6, 227
 Busscher, H.: BP-SuA3, 1
 Butail, G.: EN-MoA11, 26
 Butner, J.: MN-ThM10, 187; VT+MS-TuM9, 64
 Butterfield, M.T.: MI-ThP1, 220
 Buyanova, I.A.: EM-TuA3, 72
 Buzanska, L.M.: BI-TuM2, 44; BI-TuM4, 44
 Byrne, M.S.: SE-TuM3, 56
 Byun, J.S.: EL+AS+EM+MS+TF-ThP1, 216
- C —
- Cabailh, G.: SS1-MoA1, 34
 Caballero-Briones, F.: EN+TF-TuA12, 76
 Cabarcos, O.M.: TF+EM-MoM9, 18; TF-ThA2, 210
 Cabrini, S.: PS-WeM3, 135
 Cagg, B.A.: SS-TuP14, 113
 Cahen, D.: EN+TF-WeM3, 127
 Cahill, D.G.: SE-TuA9, 87
 Cai, W.: GR-TuP6, 100
 Calado, V.E.: EL+AS+EM+MS+TF-FrM7, 235
 Calaza, F.C.: AC+TF-MoA7, 24; SS1-MoM1, 14; SS-ThM10, 195
 Caldwell, J.D.: LB-WeA2, 159
 Callow, J.A.: BP-SuA5, 1; MB+BI+AS-MoA3, 28
 Callow, M.E.: BP-SuA5, 1; MB+BI+AS-MoA3, 28
 Camara, N.: GR+SS+TF+EM-MoM10, 6
 Camassel, J.: GR+SS+TF+EM-MoM10, 6
 Camillone III, N.: SS1-MoA10, 35
 Campbell, A.L.: EN+AS-ThM9, 181
 Campbell, C.T.: SS1-MoM8, 15; SS2-MoA8, 36
 Campbell, P.M.: EL+AS+EM+MS+TF-FrM8, 235; GR+MS-WeA1, 156; GR+MS-WeA9, 157; GR+NS-MoA7, 27; GR+SS+TF+EM-MoM1, 5; GR+SS+TF+EM-MoM8, 5
 Campbell, S.A.: EN+SS+TF-ThA9, 200; TF-TuP10, 116
 Campbell, V.: SS-TuA10, 88; SS-TuA9, 88
 Camus, P.: EN+AS-ThM6, 181
 Canavan, H.E.: BI1+NS-ThM5, 177; BI-ThP1, 212; BI-ThP14, 214; BI-ThP9, 213; BI-TuM9, 45

- Cancellieri, C.: NS-MoM5, 9
Candler, R.: VT-TuP6, 119
Canepa, H.: NS-TuP27, 104
Cano, M.F.: AS-TuP7, 93; AS-TuP8, 93
Cansizoglu, M.F.: TF+SE-WeM5, 142
Cao, Y.: TF1-TuM11, 62
Carbonell, L.: TF+EM-WeM10, 141
Cardinaud, C.: PS-TuP6, 105
Carlisle, J.A.: BI+MN-FrM8, 233; MN-FrM1, 237; MN-FrM3, 237; MN-FrM4, 238
Carmona, A.: BI-TuM12, 45
Carp, R.: SS-TuA2, 87
Carpick, R.W.: MN-FrM4, 238; TR+NS+SS-WeA3, 173
Carr, G.L.: EL+AS+EM+MS+TF-FrM4, 234
Carrasco, E.: SS1-WeM2, 137
Carroll, M.S.: EN+AS-ThM4, 180; EN+TF-TuA8, 75
Carroll, N.: BI+MN-FrM5, 232
Carryon, G.: IJ+BI+MN-MoM5, 7
Carson, B.D.: BI+MN-FrM3, 232
Carter, D.: EN+PS-MoM11, 4
Cartier, E.: TF1-TuM6, 61
Caruso, A.N.: MI+EM-TuA10, 80
Caruso, L.: VT+MN-MoM8, 21; VT+MN-MoM9, 21
Castañeda, J.N.: SE-TuA3, 86
Castelli, R.: BI-ThP5, 212
Castillo, E.: EN+NS-WeA8, 155
Castillo, H.A.: TF-TuP3, 115
Castner, D.G.: AS-TuM6, 43; AS-WeA1, 149; AS-WeA9, 150; BI2+AS-TuA11, 71; BI2+AS-TuA12, 71; BI2+AS-TuA8, 70; BI2-WeM11, 124; BI-WeA9, 152; NS+BI-ThA8, 204; TF-WeA3, 171
Cavalero, R.: GR+EM+MS+TF+MI-WeM1, 129
Cavanagh, A.S.: EN+EM-TuA1, 73; TF-MoA2, 37; TF-ThP5, 227; TF-TuA7, 89
Cavanaugh, A.S.: TF-TuA9, 90
Caviglia, A.D.: NS-MoM5, 9
Ceccato, P.H.: PS-FrM1, 239
Ceccone, G.: BI-TuM12, 45
Cecil, T.: MI-WeA3, 161
Cederberg, J.G.: EN+AS-ThM4, 180; EN+TF-TuA8, 75
Cerón Gutiérrez, S.: TF-TuP5, 115
Cha, D.J.: VT-TuP12, 120
Chabal, Y.J.: BI+MN-FrM6, 233; EN+NS-ThM3, 182; GR+NS-MoA1, 26; NS-TuM3, 52; SS2-MoA1, 36; SS2-MoA7, 36; TF-TuA12, 90
Chabert, P.: PS-TuP14, 107
Chagarov, E.: EM-TuP7, 97
Chambers, S.A.: SS-FrM9, 242; TF-ThA6, 210
Chan, C.K.: EN+NS-WeM6, 126
Chandarsekhar, N.: EM-TuM12, 47
Chandler, E.M.: BI1+NS-ThM6, 177
Chandril, S.: TF-ThA10, 211
Chang, C.Y.: BI2+NS-ThM11, 178
Chang, C.-Y.: BI1-TuA1, 70
Chang, D.P.: BI-ThP8, 213; TR+NS+SS-WeA7, 173
Chang, H.W.: PS-FrM5, 240; PS-ThP14, 224
Chang, H.Y.: PS-TuP23, 108
Chang, J.: EN-ThP4, 217
Chang, J.P.: AC+TF-MoA2, 23; EN+EM-TuA3, 73; EN+NS-ThM1, 181; EN+NS-WeA7, 155; PS1-ThA7, 206; TF1-TuM5, 61
Chang, L.S.: TF-TuP16, 117
Chang, S.M.: PS-ThP13, 224
Chang, S.Y.: SE-TuP7, 110
Chang, W.S.: EN+PS-MoM10, 4
Chang, Y.Y.: TF-TuP13, 116
Chang, Z.C.: TF-ThP1, 226
Chaparala, S.: MN-FrM6, 238
Chapman, R.A.: BI+MN-FrM6, 233
Chaudhari, V.U.: EN+NS-WeA10, 155; EN+TF-WeM6, 128
Chaudhary, A.: MN-ThP8, 221
Chaudhuri, A.: IS+SS-TuM2, 50; SS-WeA2, 169
Chaukulkar, R.: EN-ThP7, 218
Chavez, C.A.: NS-TuA7, 81
Chawla, J.S.: EM-TuM1, 45
Check, M.: SE-TuA7, 86
Chen, B.R.: EN+NS-ThM4, 182
Chen, C.C.: NS-TuP25, 104
Chen, C.-H.: MN-FrM8, 239
Chen, C.L.: PS-ThP19, 225
Chen, D.A.: SS-TuP14, 113
Chen, D.-C.: BI-ThP7, 213
Chen, F.: SS2-MoA6, 36
Chen, F.F.: PS2-TuA3, 85
Chen, F.Z.: TF-TuP15, 117
Chen, F.-Z.: VT+MS-TuM10, 64
Chen, G.J.: IS+BI+AS-WeA11, 158
Chen, H.: GR+AS+TF-ThM1, 183
Chen, H.P.: TF-TuP15, 117
Chen, L.: PS2-TuA2, 84; SE-TuM5, 56
Chen, M.: EM-TuA3, 72; TF-ThA8, 210; TF-ThP8, 228
Chen, M.W.: NS-ThM10, 189
Chen, N.: SS-TuA10, 88; SS-TuA9, 88
Chen, P.: NS-ThM5, 189
Chen, P.-H.: MN-FrM8, 239
Chen, P.L.: NS-TuP25, 104
Chen, R.: EM-TuA7, 72
Chen, S.: GR-TuP6, 100
Chen, T.: EM+SS-ThM12, 179
Chen, T.-L.: AC+TF-MoA7, 24; SS1-MoM1, 14; SS-ThM10, 195
Chen, W.: MI+TF-ThM4, 185
Chen, W.-C.: EM-TuP1, 96; TF-TuP18, 117
Chen, Y.: GR+TF-TuM5, 49
Chen, Y.J.: EN+NS-ThM4, 182; EN+SS-FrM6, 237
Chen, Z.: EN+PS-MoM3, 3; PS2-TuA7, 85; PS2-TuA8, 85; PS-ThP2, 222
Chen, Z.W.: SS1-MoA11, 35
Cheng, C.-M.: SS2-TuM3, 59
Cheng, H.: EM-TuA1, 72
Cheng, M.H.: IS-ThP2, 219
Cheng, S.-L.: TF+EM-WeM9, 141
Cheng, Y.J.: TF-TuP4, 115
Cheng, Z.H.: SS2-TuM4, 59; SS-TuA11, 88; SS-TuA2, 87
Cheong, J.T.: PS-TuP1, 104
Cheong, W.-S.: TF-TuP9, 116
Chesneau, F.: SS2-TuM11, 60
Cheung, W.S.: VT-TuP12, 120; VT-TuP5, 119
Chevolleau, T.: PS+MN-WeM5, 134; PS-MoM1, 10; TF2-TuM4, 63
Chew, A.: VT+MN-MoM11, 22
Chhasatia, V.: IJ+BI+MN-MoM4, 6
Chhowalla, M.: GR+NS-MoA1, 26; GR+NS-MoA3, 27; GR+TF-TuM4, 49; GR-TuP4, 99
Chi, E.Y.: BI1-WeM1, 123; BI2-WeM10, 124; BI-WeA3, 151
Chiam, S.Y.: EN+TF-TuA7, 75
Chiang, P.H.: TF+SE-WeM10, 143
Chiang, P.T.: IS+BI+AS-WeA11, 158
Chiang, S.: GR+SS+TF+EM-MoM10, 6; SS2-MoA10, 37; SS-TuP3, 110
Chiba, Y.: PS1-TuA10, 84; PS-MoM4, 11
Chien, C.H.: PS+TF-ThM9, 191
Chim, W.K.: EN+TF-TuA7, 75
Chinchore, A.V.: MI+EM-TuA3, 80; MI+EM-TuA4, 80
Chinn, D.A.: SS-TuP9, 112
Chinnathambi, K.: AS-TuP23, 95
Chintalapalle, R.V.: TF-WeA10, 172
Chirita, V.: TF-ThM2, 195; TF-ThM5, 196
Chistyakov, R.: SE+PS-MoA8, 34
Chiu, P.K.: TF-TuP15, 117
Chivers, J.: EN+SS+TF-ThA11, 201
Cho, C.H.: TF1-TuM1, 61
Cho, G.-B.: EM-TuP5, 97
Cho, H.J.: MN-ThA8, 202
Cho, H.Y.: AS-TuP4, 92
Cho, J.: EN+EM-TuA3, 73; SS2-MoA7, 36
Cho, J.-H.: NS-TuM2, 51
Cho, K.I.: TF-TuP9, 116
Cho, K.J.: GR+NS-MoA1, 26; SS2-MoA1, 36
Cho, S.H.: PS1-TuA12, 84
Cho, S.-J.: EN-ThP1, 217
Cho, S.-P.: PS-TuP20, 108
Cho, W.H.: EM-TuP8, 97; PS+TF-ThM9, 191; TF-TuP15, 117; TF-TuP20, 118
Choi, B.L.: EN+NS-ThM2, 182
Choi, B.-Y.: SS-ThA10, 209
Choi, C.H.: PS-ThP12, 224
Choi, E.C.: EN-ThP4, 217
Choi, H.-S.: SS2-MoA1, 36
Choi, H.W.: NS-TuP1, 100
Choi, I.S.: PS+TF-ThM1, 190
Choi, J.: AC-TuA1, 67; AC-TuA9, 67
Choi, J.H.: EM-TuP12, 98; EN+NS-WeA7, 155; PS1-TuM2, 53
Choi, J.J.: EN+AS-ThM11, 181; EN-MoA8, 25
Choi, S.: EM+SS-ThM1, 178; EM-TuP6, 97
Choi, S.G.: EL+AS+EM+MS+TF-ThA8, 198
Choi, S.W.: PS2-WeA7, 167
Choi, S.Y.: EM-TuP12, 98
Choi, W.J.: PS1-TuA12, 84
Choi, Y.: SS-ThA1, 208
Choi, Y.D.: IS+EM-TuP4, 97
Choi, Y.M.: IS+SS-TuA1, 78
Choi, Y.S.: PS+TF-ThM1, 190
Choi, Y.-Y.: NS-TuP1, 100
Chopra, S.N.: SS-WeA4, 170
Chorkendorff, I.: SS1-MoA3, 34
Chou, C.-H.: MN-FrM8, 239
Choudhuri, A.R.: SE-TuM6, 56
Chouhan, V.: NS-TuP22, 103; VT-WeM10, 147
Chow, P.P.: BI2+NS-ThM11, 178
Christen, H.M.: AC+TF-MoA7, 24
Christiansen, S.H.: EN+NS-WeM11, 127; NS+EM+EN-WeA9, 163; NS-ThM2, 188; TF+EN-MoM5, 20
Christou, Y.: TF+EM-MoM10, 18
Chu, B.H.: BI2+NS-ThM11, 178
Chu, D.: VT+MN-MoM1, 20
Chu, E.: SS-TuA2, 87
Chu, J.P.: IS+BI+AS-WeA11, 158
Chu, L.-N.: SS-FrM8, 241
Chu, N.N.: NS-TuP25, 104; PS+TF-ThM9, 191
Chu, Y.-H.: NS-MoM9, 10
Chu-Kung, B.: PS1-TuM10, 54
Chun, W.-J.: SS1-MoA11, 35
Chung, B.W.: AC+MI-TuM12, 42; AC+TF-MoA6, 23
Chung, H.J.: GR+TF-TuM11, 50
Chung, I.S.: EM-TuP13, 98; NS-TuP11, 102; NS-TuP9, 101
Chung, J.G.: AS-TuP4, 92; TF+EM-WeM5, 140
Chung, S.M.: TF-TuP9, 116
Chung, T.-Y.: PS1-WeA2, 164; PS1-WeA7, 165
Chung, Y.W.: SE-TuM11, 57
Chylarecka, D.: MI+EM-TuA9, 80
Cichowlas, M.: PS-ThP22, 226
Cicotte, K.N.: BI-ThP13, 214
Ciftlikli, E.Z.: SS2-MoA3, 36
Ciobanu, C.V.: EN+PS-MoM9, 4; GR+AS+TF-ThM12, 185; GR+TF-TuA11, 78
Ciovati, G.: EN+AS-ThM10, 181
Cipriany, B.R.: BI1+NS-ThM6, 177; MN-ThM4, 187
Clare, A.S.: MB+BI+AS-MoA3, 28; MB+BI-MoM3, 8
Clark, B.G.: IS+AS+NS+MI-WeM5, 131; IS+AS+NS+MI-WeM6, 131
Clark, R.D.: TF+EM-WeM6, 141
Clark, T.D.: BI-ThP16, 215; BI-WeA12, 153
Clarke, R.: SS1-WeM3, 137
Clavero, C.: MI+TF-ThM3, 185; MI+TF-ThM4, 185; MI-WeA11, 162
Clemens, J.: EM-TuP7, 97
Clendenning, S.: PS1-TuM10, 54
Clifton, P.: AS-TuA3, 68

- Cochran, C.: EM-TuP15, 98
Cockburn, A.: TF+EM-WeM10, 141
Coetsee, E.: TF+EN-MoM8, 20
Cohen, A.: TF-ThA6, 210
Cohen, S.: PS1-TuA7, 83
Cohen, S.R.: EN+TF-WeM3, 127; TR-ThP5, 230
Colbow, V.: EN+AS-ThM2, 180
Colburn, M.: PS-MoM5, 11
Cole, M.A.: B11+NS-ThM1, 176
Coleman, E.: AC-TuA3, 67
Coles, J.M.: TR+NS+SS-WeA7, 173
Collazo, R.: EM-TuP2, 96
Collins, K.: PS1-ThA3, 205; PS1-ThA6, 205; PS1-TuM5, 54; PS2-TuA11, 85; PS2-TuA7, 85; PS2-TuA8, 85; PS2-TuM1, 54
Collins, R.W.: EL+AS+EM+MS+TF-ThA11, 198
Colombo, L.: GR+EM+MS+TF+MI-WeM11, 130; GR+EM+MS+TF+MI-WeM9, 130
Colón, J.A.: EM+MI-MoA8, 25
Colpo, P.: BI+MN-FrM7, 233; BI-TuM2, 44; BI-TuM4, 44
Coltrin, M.E.: EM+SS-ThM5, 178; SS-WeA1, 169
Colvin, V.: NS-MoA6, 29
Comer, A.: VT-WeM4, 147
Conklin, D.J.: NS+EM+EN-WeA7, 163
Conlan, S.L.: MB+BI+AS-MoA3, 28
Conrad, M.: SS2-WeM12, 140
Consiglio, S.A.: TF+EM-WeM6, 141
Conte, A.: VT+MN-MoM8, 21; VT+MN-MoM9, 21
Contreras-López, O.E.: NS-TuP23, 103
Coocetti, F.: MN-FrM9, 239
Cooks, R.G.: SS-TuP16, 113; VT+MS-MoA1, 38
Cooperstein, M.A.: BI-ThP1, 212
Corbacioglu, B.D.: SS-TuP26, 115
Corbitt, T.S.: BI-ThP14, 214
Cornella, B.: VT+MS-TuM11, 64
Cornish, A.: IS+SS-TuM5, 50
Correa, F.: AS-TuP8, 93
Coss, B.E.: TF1-TuM11, 62
Cottle, H.: PS1-TuA10, 84
Coutts, T.: EN+SS+TF-ThA6, 199
Cox, D.C.: AS-WeA7, 150
Craighead, H.G.: B11+NS-ThM6, 177; MN-FrM5, 238; MN-ThM1, 187; MN-ThM4, 187
Crawford, M.H.: EM+SS-ThM5, 178
Creatore, A.M.: EN+TF-TuA1, 74
Creatore, M.: NS+EM+EN-WeA8, 163; PS2-MoA2, 31; SE+PS-MoM4, 12
Creighton, J.R.: SS-WeA1, 169
Crommie, M.F.: GR+AS+TF+MI-ThA1, 201
Cross, K.C.: EM+SS-ThM5, 178
Crowe, M.: SS1-MoM8, 15
Croy, J.R.: SS1-MoA2, 34
Cruguel, H.: SS1-MoA1, 34
Cuddy, M.F.: PS-WeM5, 136
Cui, Y.: EN+NS-WeA3, 155
Cui, Z.: PS-MoM10, 11
Culbertson, J.C.: GR+MS-WeA1, 156; GR+SS+TF+EM-MoM8, 5; LB-WeA2, 159
Culbertson, R.J.: AS-TuP27, 96; SS2-WeM11, 139
Cullen, W.G.: EN+NS-WeM10, 126
Cumings, J.: IS+AS+NS+MI-WeM9, 131
Cumpson, P.J.: AS-TuP17, 94; AS-TuP25, 95
Cunge, G.: PS1-MoA1, 30; PS1-TuM4, 53
Curtis, C.J.: EN+TF-WeM9, 128
Curtis, D.: GR+MS-WeA9, 157
Cushing, G.: SS1-MoM6, 14
Cushing, K.W.: BI+MN-FrM5, 232
Cyganik, P.: SS2-TuM11, 60; TF-WeA4, 171
Czaplewski, D.A.: MN-ThA3, 202; MN-ThM11, 188
Czarnetzki, U.: PS2-TuA9, 85
- D —
da Silva, R.: AS-TuP15, 94
Dabeux, F.: SE+PS-MoM2, 12
Dabiran, A.: BI2+NS-ThM11, 178
Dadson, A.: NS-TuA11, 82
Dahal, L.R.: EL+AS+EM+MS+TF-ThA11, 198
- Dahanayaka, D.H.: NS+AS+MN-WeM2, 132; SS2-TuM10, 60
Dahint, R.: IS+BI+AS-WeA3, 157
Dai, M.Z.: EL+AS+EM+MS+TF-ThA3, 197
Dai, Z.: NS-TuM6, 52
Dailey, E.: IS+AS+NS+MI-WeM3, 131
Daineka, D.: EL+AS+EM+MS+TF-ThA9, 198
Dalberth, M.J.: PS+TF-ThM4, 190
Dalchiale, E.A.: NS-TuP27, 104
Dalla Betta, G.F.: BI-ThP15, 215
Dameron, A.: EN+AS-ThM1, 180
Damiano, J.: IS+AS+NS+MI-WeM5, 131
Daniels, S.: PS-TuP18, 107; PS-TuP19, 108
Danilkin, E.V.: PS-TuP7, 105
Darling, S.B.: NS-TuM10, 52
Darnon, M.: PS1-MoA1, 30; PS1-TuA7, 83; PS1-TuM4, 53; PS-MoM1, 10
Dasaka, R.: PS1-TuA11, 84
Datta, A.: MN-FrM4, 238
Datye, A.: SS1-TuM11, 58
David, T.: PS-MoM1, 10
Davidson, M.R.: AC-TuA1, 67; AC-TuA9, 67; MN-ThP6, 221
Davies, M.C.: B11-TuA1, 70
Davies, T.E.: GR+TF-TuA11, 78
Davis, B.J.: VT+MN-MoM10, 22
Davis, D.: NS-TuP7, 101
Davis, J.: TF-ThP12, 228
Davis, M.: PS1-MoA6, 30
Davis, R.C.: LB-WeA7, 160; MN-ThP11, 221
Davis, R.F.: EM+SS-ThM3, 178; EM-TuP3, 96
Dayeh, S.A.: NS-ThM9, 189; NS-TuM5, 52
De Boer, M.P.: MN-ThA3, 202
De Gendt, S.: PS1-TuA3, 83
de Heer, W.A.: GR+AS+TF+MI-ThA3, 201; GR+AS+TF+MI-ThA4, 201; GR+SS+TF+EM-MoM9, 6
de la Cruz, W.H.: TF-TuP3, 115
De Martino, A.: EL+AS+EM+MS+TF-FrM9, 235; EL+AS+EM+MS+TF-ThA6, 197
de Moure Flores, F.: TF-TuP5, 115
De Moure-Flores, F.J.: NS-TuP6, 101; TF-ThP21, 230
de Vries, H.: PS2-MoA2, 31; SE+PS-MoM4, 12
Dean, B.: MN-ThP7, 221
Debrabandere, D.: SE+PS-MoM1, 12
Debray, P.: MI+EM-TuA1, 80
Dechene, J.: BI-ThP18, 215; BI-TuM5, 44
Decker, R.T.: GR+AS+TF+MI-ThA1, 201
Deguns, E.W.: PS+TF-ThM4, 190
Dekker, M.F.: VT+MS-MoA4, 39
del Alamo, J.A.: EM+SS-WeA9, 154
Delcorte, A.: AS-WeA11, 151
DeLongchamp, D.M.: EN+NS-WeM6, 126
DeMeo, D.: VT-TuP11, 120
Demirel, M.C.: TF+SE-WeM1, 142
Denecke, R.: AS-TuP10, 93; AS-TuP11, 93; SS1-TuM2, 57
Deng, X.: SS1-MoM11, 15
Deniz, D.: SE+TF-WeA11, 169
Deppert, K.: IS+SS-TuM1, 50
Deram, M.: TR+MN+NS+SS-WeM5, 146; TR-ThP1, 230
Derby, B.: IJ+BI+MN-MoM3, 6
Desai, T.V.: SS2-TuM9, 60
Deskins, N.A.: SS-FrM4, 241
Despiau-Pujo, E.: PS-TuP14, 107
Devanathan, R.: SS2-WeM6, 139
Deves, G.: BI-TuM12, 45
Devine, C.: TF-TuA3, 89; TF-WeM5, 144
Dewdney, J.: TF+EM-MoM11, 19
Dhayal, M.: BI+MN-FrM2, 232; MN-ThA9, 202
Dhivya, T.: EN+NS-WeA1, 154
Dhlamini, M.S.: TF+EN-MoM8, 20
Dhuey, S.: PS-WeM3, 135
Di Ventra, M.: EM-TuM10, 46
Di, M.: TF+EM-WeM6, 141
Diaz, J.O.: VT-TuP9, 119
- Dickey, E.C.: EL+AS+EM+MS+TF-FrM3, 234; EL+AS+EM+MS+TF-ThA10, 198; TF+EM-MoM9, 18; TF-ThA2, 210
Dickinson, G.H.: MB+BI+AS-MoA8, 28
Dickson, B.: AS-TuM12, 43
Diebold, A.C.: GR+AS+TF+MI-ThA8, 201; TF+EM-WeM6, 141
Diebold, U.: SS-FrM8, 241
Dieterle, W.E.: IJ+BI+MN-MoM6, 7
Dietrich, P.M.: BI-ThP5, 212; PS2+BI-ThA8, 207
Dietz, N.: EM-TuP2, 96
Dietzel, D.: TR+NS+SS-WeA8, 173
Dillon, A.C.: EN+EM-TuA1, 73; NS-MoM3, 9
Ding, L.: BI-ThP14, 214; EL+AS+EM+MS+TF-ThP6, 217
Dingemans, G.: TF+EN-MoM6, 20
Dinh, H.N.: EN+AS-ThM1, 180
Diomedea, P.: PS-WeM6, 136
Dirk, S.M.: TR+MN+NS+SS-WeM4, 145
Dirmyer, M.R.: EN+SS-FrM1, 236
Discher, B.M.: IS+BI+AS-WeA9, 158
Dockstader, T.: EN-TuM4, 47
Dodd, R.: PS-ThP10, 223
Doğan, İ.: EN+PS-MoM5, 4
Doherty, K.G.: PS2-MoA11, 33
Dohnalek, Z.: SS1-WeM5, 137; SS-FrM4, 241; SS-FrM7, 241
Dohnálek, Z.: SS1-WeM9, 138
Dohnalkova, A.: NS-MoA9, 29
Dojun, M.: PS-WeM2, 135
Dolle, P.: SS1-MoA1, 34
Dolo, J.J.: TF+EN-MoM8, 20
Donald, S.: SS1-MoM6, 14
Donavan, K.C.: NS+EM+EN-WeA10, 163
Dong, H.: SS2-MoA7, 36
Dong, Y.F.: SS-ThM3, 194
Doniat, F.: PS1-TuA4, 83
Donlon, L.: BI2-WeM9, 124
Donnelly, G.T.: MB+BI+AS-MoA3, 28
Donnelly, V.M.: PS-ThM6, 192; PS-ThP2, 222; PS-ThP4, 222; PS-WeM11, 136; PS-WeM6, 136
Doren, D.J.: EN+SS-FrM3, 236; EN+SS-FrM4, 236
Dorf, L.: PS2-TuM1, 54
Dorman, J.A.: EN+NS-WeA7, 155
Doroudian, G.: BI2-WeM10, 124
Doskow, J.: VT-TuP13, 120
Dougherty, D.B.: EN+NS-WeM10, 126; GR-TuP5, 99; SS2-TuM6, 60
Doutt, D.R.: SS-ThM3, 194
Dowben, P.A.: AC+MI-TuM3, 41; AS-TuM5, 43; EM+MI-MoA8, 25; GR+TF-TuA3, 76
Downs, C.: EN+EM-TuA9, 74
Doyle, B.L.: AS-WeM1, 122; IS+AS+NS+MI-WeM5, 131
Dozias, S.: PS2-MoA6, 32; PS2-MoA8, 32
Dragoi, D.V.: PS-WeM12, 136
Drain, C.M.: EM-TuM6, 46
Driscoll, J.: TF-ThA1, 209
Drobny, G.P.: NS+BI-ThA8, 204
Droopad, R.: GR-TuP6, 100
Droubay, T.: TF-ThP11, 228
Drube, W.: IS+SS-TuM9, 51
Drucker, J.: IS+AS+NS+MI-WeM3, 131
Drummond, I.W.: AS-WeM10, 123
D'Souza, F.: MB+BI+AS-MoA3, 28
Du, C.-X.: MB+BI+AS-MoA3, 28
Du, Y.: SE-TuM5, 56; SS-FrM4, 241
Dubey, M.: BI2+AS-TuA11, 71; NS+BI-ThA8, 204
Dubois, G.: PS1-TuA7, 83
Dubon, O.: GR+AS+TF-ThM11, 184
Dubourdieu, C.: TF1-TuM6, 61
Duch, M.: BI2-WeM12, 125
Ducote, J.: PS-MoM1, 10
Duda, L.: AC+TF-MoA6, 23
Dudis, D.S.: SE-TuA7, 86
Duensing, B.A.: EL+AS+EM+MS+TF-ThA7, 198

- Dufour, T.: PS2-MoA6, 32; PS2-MoA8, 32
Dugger, M.T.: SS-TuP9, 112; TR+MN+NS+SS-WeM4, **145**
Duguet, T.: SS2-MoA11, 37
Dulkin, A.: PS+TF-ThM10, 191
Dumais, H.: AC+TF-MoA1, **23**
Duncan, R.L.: BI-TuM1, 43
Dunham, S.: EM-TuA7, 72
Dunn, B.: EN+EM-TuA3, 73
Dupuis, M.: SS-FrM4, 241
Dupuis, R.D.: EM+SS-ThM1, **178**
Durakiewicz, T.: AC+SS-MoM5, 2; AC+SS-MoM8, **2**
Durbin, S.M.: EM-TuM3, 46
Duscher, G.: AS-WeM2, 122
Dussarrat, C.: PS1-TuA4, 83; PS-MoM9, 11; TF+EN-MoM3, 19
Dussart, R.: PS+MN-WeM10, 135; PS2-MoA6, 32; PS2-MoA8, **32**; PS-ThM4, 192
Dutta, M.: EN+AS-ThM2, 180
Dutton, G.J.: EN+NS-WeM10, 126
- **E** —
Earles, S.B.: NS-TuP26, 104
Easawib, K.: EN-ThP10, 218
East, G.: VT-TuP13, 120
Easton, C.D.: PS2+BI-ThA3, **207**
Ebnonnasir, A.: GR+AS+TF-ThM12, 185
Eby, M.: BI-ThP10, 213
Economou, D.J.: PS-ThP2, 222; PS-ThP4, 222; PS-WeM11, 136; PS-WeM6, 136
Eda, G.: GR+TF-TuM4, 49; GR-TuP4, 99
Eddy Jr., C.: GR+MS-WeA9, 157; LB-WeA3, 159
Eddy, Jr., C.R.: EL+AS+EM+MS+TF-FrM8, 235; EM+SS-ThM4, 178; GR+MS-WeA1, 156; GR+SS+TF+EM-MoM8, **5**; LB-WeA2, 159
Ederth, T.: MB+BI+AS-MoA3, **28**
Egdehl, R.G.: EN+SS+TF-ThA3, **199**
Ehiasarian, A.P.: SE+PS-MoA1, **33**
Eichler, M.: SE+PS-MoM5, 13
Eigenfeld, N.: TR+MN+NS+SS-WeM5, 146; TR-ThP1, 230
Eiliat, H.: TR-ThP8, **231**
Einstein, T.L.: SS-TuA11, 88
Eisenbraun, E.: PS1-TuA4, 83
Eita, M.: EL+AS+EM+MS+TF-ThP2, 216
Ekblad, T.: MB+BI+AS-MoA3, 28; MB+BI-MoM3, 8
El Gabaly, F.: IS+SS-TuM6, 51
El Saghir, A.E.: PS2-TuM11, **55**
Elam, J.W.: EN+NS-ThM12, 183; NS-TuM10, 52; TF+EN-MoM1, 19; TF-TuA4, **89**; TF-TuA8, 90; TF-WeM4, 144
Elhordoy, F.: NS-TuP27, 104
Ellefson, R.E.: VT+MS-MoA9, 39
Elsayed-Ali, H.: TF+EM-MoM6, 18
Enderes, R.: VT+MN-MoM4, 21
Endo, K.: PS2-WeA10, 167
Eng, P.: SS-ThA1, 208
Engelhard, M.H.: AS-TuP21, **95**; NS-MoA9, 29; TF-WeA1, 171
Engel-Herbert, R.: EM+SS-WeA7, **154**
Engelmann, S.U.: EM-TuP10, 98; PS1-MoA8, **30**; PS1-MoA9, 31; PS1-TuA7, 83
Engin, S.: AS-TuP2, 92
Engstfeld, A.K.: GR+AS+TF-ThM2, **183**
Engstrom, J.R.: SS2-TuM9, **60**; TF1-TuM3, 61
Engrakul, C.: EN+AS-ThM1, 180
Enlow, J.: NS+BI-ThA4, 203
Enriquez, H.: GR+SS+TF+EM-MoM10, 6
Epaminonda, P.: TF+EM-MoM10, 18
Er, A.O.: TF+EM-MoM6, **18**
Eralp, T.: IS+SS-TuM5, 50
Eriacho, V.J.: BI-ThP9, 213
Erickson, N.C.: NS+EM+EN-WeA11, **163**
Eriguchi, K.: PS1-MoA3, 30; PS-WeM9, **136**
Ermanoski, L.: SS1-WeM6, **138**
Escamilla, R.: AS-TuP26, 96
Esparaza, N.E.: EN+AS-ThM9, 181
Estrada-Raygoza, I.C.: PS+TF-ThM11, **191**
- Eu, B.: BI-ThP17, 215
Evans, J.: SS2-MoA11, 37
Evans, K.: EM+SS-ThM3, 178
Evans, P.J.: TF-ThP12, 228
Everett, R.K.: MB+BI+AS-MoA8, 28
Ewsuk, K.: VT+MN-MoM1, **20**
- **F** —
Fabien, P.S.: NS-TuP5, **101**
Faggin, M.F.: SS2+EM-MoM1, **15**
Fahey, A.J.: AS2-ThM9, 176
Fairbrother, H.: SS2-WeM3, **138**
Fairchild, S.B.: EN+EM-TuA4, 73; NS-TuA3, **81**; TF-ThA7, 210
Fallah, B.: GR+EM+MS+TF+MI-WeM9, 130
Fallica, R.: NS-TuP17, 103
Falta, J.: IS+SS-TuA1, 78
Falvo, P.: VT-TuP10, 120
Fanciulli, M.: NS-TuP17, 103
Fang, F.: EN+TF-TuA9, **75**
Fang, L.: VT+MN-MoM1, 20
Fanton, M.: GR+MS-WeA1, 156; GR+MS-WeA9, 157
Farach-Carson, M.C.: BI-TuM1, 43
Farr, J.D.: AC-TuA2, 67
Farruggia, G.: IJ+BI+MN-MoM11, 8
Fartmann, M.: AS-WeA3, 149
Faubel, M.: IS+SS-TuM2, 50
Favaloro, T.: AC-TuA3, 67
Fears, K.P.: BI-ThP16, 215; BI-WeA12, **153**
Feibelman, P.J.: SS-ThA7, 208; SS-ThA8, **209**
Feldmann, M.: TR+NS+SS-WeA8, 173
Felmetsger, V.: TF-ThP7, **227**
Feltz, A.: EM-TuM12, 47
Feng, H.: TF+EN-MoM1, 19
Fenton, J.L.: AS-TuM11, **43**
Ferapontova, E.: SE-TuP2, 109
Ferekides, C.S.: EN+TF-TuA10, 75
Ferguson, J.: SE-TuA7, 86
Feringa, B.L.: NS-TuM11, **53**
Fernandes, P.G.: BI+MN-FrM6, 233
Fernandez, I.: EN+AS-ThM9, 181
Fernandez, M.C.: PS-TuP6, 105
Fernández-Rossier, J.: GR+EM+MS+TF+MI-WeM3, **129**
Fernsler, R.F.: PS2-TuM10, 55; PS-WeM1, 135
Fête, A.: NS-MoM5, 9
Feulner, P.: EM-TuM5, 46
Feuprier, Y.: PS-MoM4, **11**
Fiete, G.A.: IS+AS+NS+MI-WeM1, 130
Finlay, J.A.: BP-SuA5, 1
Finlayson-Pitts, B.: SS-TuP23, 114
First, P.N.: GR+AS+TF+MI-ThA3, 201; GR+AS+TF+MI-ThA4, 201; GR+SS+TF+EM-MoM6, 5; GR+SS+TF+EM-MoM9, 6
Fischbach, C.: BI1+NS-ThM6, 177
Fischer, C.F.: GR-TuP3, 99
Fischer, D.A.: AS1-ThM6, 175; GR+TF-TuM12, 50; NS+BI-ThA8, 204
Fischer, K.: SS1-TuM2, 57
Fisher, E.R.: PS1-WeA10, **165**; PS-WeM5, 136; TF-WeM11, 145
Fisher, G.L.: AS-TuA8, **69**; AS-WeA2, 149
Fishman, R.S.: AC+MI-TuM11, 41
Fitz-Gerald, J.M.: TF+EM-MoM8, 18
Fitzpatrick, R.: TF-TuA1, **89**; TF-TuP19, 117
Fitzsimmons, M.: MI+TF-ThM2, 185
Flack, F.S.: SS2-MoA6, 36
Flake, J.: SS1-MoA9, 35
Flater, E.: TR+MN+NS+SS-WeM5, **146**; TR-ThP1, 230
Flege, J.L.: IS+SS-TuA1, 78
Fleischauer, M.D.: SE+TF-WeA9, 168; TF-ThP4, 227
Fletcher, R.: VT+MS-MoA10, 39
Flores, M.: AS-TuP26, 96; TR-ThP2, 230; TR-ThP3, **230**; TR-ThP6, 231
Fokin, A.A.: NS-TuA4, 81
Fokina, N.A.: NS-TuA4, 81
Follstaedt, D.M.: IS+AS+NS+MI-WeM6, 131
- Ford, C.L.: PS+MN-WeM4, 134
Ford, G.M.: EN+TF-WeM1, 127
Fortunelli, A.: SS1-WeM5, 137
Foubert, P.: PS1-WeA4, 164
Fouchier, M.: PS1-MoA11, 31
Foussekis, M.: EM+SS-ThM11, 179
Fowlkes, J.D.: TF+EM-MoM3, 17
Fox-Lyon, N.: PS-ThM10, **193**
Franceschetti, A.: EL+AS+EM+MS+TF-ThA8, 198
Franco, C.G.: NS-TuP13, **102**
Frank, M.M.: TF1-TuM6, 61
Frank, P.F.: SS2-TuM5, 59
Frankel, D.J.: BI2-WeM9, **124**
Franking, R.A.: SS-FrM9, **242**
Franz, G.: PS2+BI-ThA9, **207**; TF-WeM6, 144
Franz, R.: SE-TuM12, 57; SE-TuP6, 110
Franz, S.: VT-TuP6, 119
Fraser, A.E.: MN-ThA6, 202
Frazier, R.M.: TF-ThA8, 210; TF-ThP8, 228
Freeman, M.R.: MN-ThA6, 202
French, M.: EM+SS-WeA8, 154
Frenkel, A.I.: SS-WeA7, **170**
Freund, H.-J.: SS1-MoA7, 35; SS1-MoA8, 35; SS1-WeM2, 137; SS-ThM6, 194; SS-TuP17, 113
Freyer, J.P.: BI1+NS-ThM5, 177
Friedman, A.L.: GR+MS-WeA1, 156; GR+SS+TF+EM-MoM8, 5
Friend, C.: SS1-TuM3, **58**
Fritz, T.: EN+NS-WeM11, 127
Frot, T.J.: PS1-TuA7, 83
Fuchs, H.: TR+NS+SS-WeA8, 173
Fuhrmann, B.: TF+SE-WeM3, 142
Fujii, Y.: GR-TuP1, **98**
Fujimoto, D.: PS-ThP3, **222**
Fujishima, A.: SS-TuP5, 111
Fujitani, T.: SS-TuP25, 114; SS-TuP4, **111**
Fujiwara, Y.: AS-TuP1, **92**
Fukasawa, M.: PS1-MoA3, **30**; PS-ThM9, 193
Fukui, K.: SS1-MoA11, 35
Fukutani, K.: AS-TuM5, **43**
Fuller, N.C.: EM-TuP10, 98; PS1-MoA8, 30; PS1-MoA9, 31
Funk, M.: PS2-TuA2, 84
Funston, J.R.: BI-ThP13, 214
Fuqua, P.D.: SS-TuP13, 112
Furlani, E.P.: IJ+BI+MN-MoM11, 8
Furlong, O.J.: TR+MN+NS+SS-WeM11, 146
Furuta, T.: SS-TuP5, 111
Fyrner, T.: MB+BI+AS-MoA3, 28
- **G** —
Gabay, M.: NS-MoM5, 9
Gaddam, S.: GR+TF-TuA3, 76; PS1-WeA1, 164
Gahan, D.: EW-WeM8, 129
Gai, Z.: MI+TF-ThM1, **185**
Gaidarova, V.N.: AS-TuP22, **95**
Galiy, P.: AS-TuM5, 43
Gall, D.: EM-TuM1, 45; SE+TF-WeA3, **168**
Gallis, M.A.: MN-ThA2, 202; SE-TuA3, 86
Gamage, S.: EM-TuP2, 96
Gamble, L.J.: AS-TuM6, 43; BI1-WeM6, 124; BI2+AS-TuA8, 70; BI2-WeM11, **124**; BI-WeA7, 151
Gandikota, S.: PS-ThP11, 224
Gannepalli, A.: EW-TuM8, **48**; NS+AS+MN-WeM10, 133
Gao, Z.J.: IJ+BI+MN-MoM11, 8
Garaudée, S.: SS1-MoA1, 34
Garces, N.: GR+MS-WeA1, 156; LB-WeA2, 159; LB-WeA3, 159
Garcia Flores, H.G.: AC+SS-MoM3, 2; AC+SS-MoM4, 2
Garcia, J.: TR-ThP2, 230
Garcia, J.: TR-ThP3, 230; TR-ThP6, **231**
Garcia, V.: EM-TuP11, 98
Gardella Jr., J.A.: AS-TuA7, 69
Gardella, Jr., J.A.: AS-TuA9, 69
Garg, S.: AS-TuP23, **95**

- Gariglio, S.: NS-MoM5, 9
Garimalla, M.: MI+TF-ThM11, 186
Garramone, J.J.: EM-TuM2, 46; MI-ThP3, 220
Gartsman, K.: EN+TF-WeM3, 127
Gaskill, D.K.: EL+AS+EM+MS+TF-FrM8, 235;
GR+MS-WeA1, 156; GR+MS-WeA9, 157;
GR+SS+TF+EM-MoM1, 5; GR+SS+TF+EM-
MoM8, 5; LB-WeA2, 159; LB-WeA3, 159
Gaspar, D.J.: TF-WeA1, 171
Gassman, P.: SS-TuP23, 114
Gatilova, L.: PS-ThM3, 192; PS-TuP14, 107
Gatineau, J.: TF+EN-MoM3, 19
Gaunt, B.D.: EL+AS+EM+MS+TF-FrM3, 234;
TF+EM-MoM9, 18; TF-ThA2, 210
Geisler, H.: SS-TuP24, 114
Geiss, E.: PS1-TuA10, 84
Gellman, A.J.: NS-ThM1, 188; SS1-MoM5, 14;
SS-WeA9, 170
Gengler, J.J.: SE+PS-MoA3, 33; SE-TuA10, 87;
SE-TuA11, 87; SE-TuP5, 109
Gennett, T.: EN+AS-ThM1, 180
George, S.M.: EN+EM-TuA1, 73; TF-MoA10, 38;
TF-MoA2, 37; TF-ThP5, 227; TF-TuA1, 89;
TF-TuA7, 89; TF-TuA9, 90; TF-TuP19, 117
Gerlach, J.W.: TF+SE-WeM3, 142
Germack, D.S.: EN+NS-WeM6, 126
Gerson, Y.: MN-ThA1, 201
Gessert, T.: EN+SS+TF-ThA6, 199; TF-ThP6, 227
Getty, S.: VT+MN-MoM5, 21
Gezerman, A.O.: SS-TuP26, 115
Ghadami, F.: SE-TuP1, 108
Ghadami, S.: SE-TuP1, 108
Ghosal, S.: SS-TuP23, 114
Ghosh, A.W.: GR+TF-TuA1, 76
Giannuzzi, L.A.: AS-WeM4, 122
Gianoncelli, A.: BI-TuM12, 45
Gibbs, Z.M.: TF-MoA2, 37; TF-TuA1, 89; TF-
TuA7, 89
Gibson, K.D.: TF-WeA7, 171
Gil, E.L.: PS-ThP16, 225; PS-ThP17, 225; PS-
ThP18, 225
Gila, O.: PS2-MoA7, 32
Gilbert, D.L.: PS1-WeA11, 166
Gildea, A.G.: PS1-TuA4, 83
Gilinsky, A.: TF-ThP3, 227
Gilmore, I.S.: AS-WeA7, 150; AS-WeA8, 150
Gilver, B.: BI-WeA3, 151
Gimelshein, N.: VT+MS-TuM11, 64
Gimelshein, S.: VT+MS-TuM11, 64
Gin, A.: NS-TuM5, 52
Ginley, D.S.: EN+TF-WeM9, 128
Girard-Laurialt, P.-L.: AS-TuP12, 93; PS2+BI-
ThA8, 207
Giudetti, G.: BI+MN-FrM7, 233
Gladfelter, W.L.: EN+SS+TF-ThA9, 200; TF-
TuP10, 116
Glavin, D.: VT+MN-MoM5, 21
Glukhoy, Y.: SE+PS-MoM10, 13
Godfrey, T.: TF-MoA8, 38
Godfroid, T.: EN+SS+TF-ThA1, 199
Godignon, Ph.: GR+SS+TF+EM-MoM10, 6
Goeckner, M.J.: PS+TF-ThM11, 191; PS2-MoA6,
32; PS2-MoA8, 32; PS2-TuM6, 55; PS-TuP15,
107
Goettler, D.F.: MN-ThA7, 202
Gohr, C.: IS+BI+AS-WeA2, 157
Goldbart, O.: TR-ThP5, 230
Goldman, R.S.: EM-TuA1, 72; EN+NS-WeA11,
156
Goldsmith, C.L.: MN-FrM3, 237
Gözlhäuser, A.: BI-ThP2, 212; GR+TF-TuA4, 77;
GR+TF-TuM3, 48; SS2-TuM12, 60
Gómez-Rosas, G.: NS-TuP21, 103; NS-TuP23, 103
Gommé, G.: PS+MN-WeM10, 135
Gonchar, A.: SS-ThM6, 194
Gong, B.: IS+AS+NS+MI-WeM11, 132; TF-
MoA1, 37; TF-MoA8, 38; TF-TuA3, 89
Gong, C.: GR+NS-MoA1, 26
Gong, J.: SS-FrM7, 241
Gong, X.-Q.: SS-FrM8, 241
Gonon, P.: TF2-TuM4, 63
Gonzalez, J.M.: AS-TuP7, 93; AS-TuP8, 93
González-Sánchez, D.: NS-TuP21, 103
González-Solís, J.L.: NS-TuP21, 103
Gonzo, L.: BI-ThP15, 215
Goodyear, A.: PS-WeM3, 135
Gopal, P.: EN-MoA11, 26
Gopalraja, P.: PS-ThP11, 224
Gorai, P.: EM-TuA9, 72; SS2+EM-MoM11, 17
Gorby, A.D.: MN-ThA2, 202
Gordan, O.D.: EL+AS+EM+MS+TF-ThP6, 217;
EN+TF-TuA2, 74
Gordon, R.G.: TF+EM-WeM12, 142
Gorham, J.: SS2-WeM3, 138
Gorman, B.P.: AS-TuA11, 69
Gorman, J.: NS-TuM3, 52
Gorodetsky, A.: NS+BI-ThA1, 202
Gossard, A.: AC-TuA3, 67
Gothard, N.W.: EN+EM-TuA4, 73
Goto, M.: MN-ThP2, 220
Gouder, Th.: AC+TF-MoA3, 23
Gougousi, T.: TF-TuP6, 115
Gouraud, P.: PS+MN-WeM5, 134; PS1-MoA11,
31
Gourvest, E.: TF2-TuM5, 63
Grace, J.M.: IJ+BI+MN-MoM11, 8
Gracias, D.: NS-TuM2, 51
Graf, N.: PS2+BI-ThA8, 207
Graham, K.S.: AC+SS-MoM5, 2
Graham, W.G.: PS-FrM1, 239
Graham, W.S.: PS1-MoA8, 30; PS1-MoA9, 31
Grainger, D.W.: BI2+AS-TuA11, 71; BI2-WeM11,
124
Grampeix, H.: TF2-TuM4, 63
Granados, B.: TF-TuA11, 90
Granberg, H.: EL+AS+EM+MS+TF-ThP2, 216
Grant, J.: PS+TF-ThM12, 191
Grass, M.: IS+SS-TuM6, 51
Graves, D.B.: PS1-WeA1, 164; PS1-WeA2, 164;
PS1-WeA7, 165; PS-MoM8, 11; PS-ThM10,
193
Graves, S.: BI+MN-FrM5, 232
Graves, T.P.: SS-TuP13, 112
Gravey, V.: TF+EM-WeM10, 141
Green, E.: GR+SS+TF+EM-MoM6, 5
Green, F.M.: AS-WeA8, 150
Greene, J.: TF+EM-MoM5, 18; TF-WeM4, 144
Gregorczyk, K.: TF+EN-MoM3, 19
Gregorkiewicz, T.: EN+PS-MoM5, 4
Grehl, T.: AS-TuP2, 92; AS-WeA3, 149; AS-
WeA4, 149
Griesser, H.J.: BI1-TuA3, 70; SE+PS-MoM8, 13
Griesser, S.S.: BI1-TuA3, 70
Griffis, D.P.: EN+AS-ThM10, 181
Grimm, R.L.: SS-ThA4, 208
Griveau, J.-C.: AC+SS-MoM8, 2
Groner, M.: TF-TuP19, 117
Gronheid, R.: PS1-WeA4, 164
Gross, L.: SS-TuA3, 87
Gross, M.E.: TF-WeA1, 171
Gross, T.: AS-TuP12, 93; AS-TuP6, 93; BI-ThP5,
212; PS2+BI-ThA8, 207
Großmann, H.: BI-ThP2, 212
Gruner, Ph.: SE+PS-MoM8, 13
Grunze, M.: IS+BI+AS-WeA3, 157
Gu, Y.: NS-MoM10, 10; NS-ThM11, 189
Guaitea, O.: PS-FrM1, 239
Gudeman, C.: MN-FrM3, 237
Guenther, B.: EM-TuM12, 47
Guha, J.: PS1-MoA2, 30
Guilak, F.: BI-ThP8, 213; TR+NS+SS-WeA7, 173
Guilet, S.: PS-ThM3, 192
Gullorn, M.A.: PS1-MoA8, 30; PS1-MoA9, 31
Guisbiers, G.: EN+SS+TF-ThA1, 199
Gullapalli, S.K.: TF-TuP11, 116; TF-WeA10, 172
Gulotty, R.: MN-FrM10, 239
Gumbsch, A.: SS1-WeM5, 137
Gundlach, D.J.: EN+NS-WeM6, 126
Gung, T.-J.: PS-ThP11, 224
Guo, D.: GR+NS-MoA2, 26
Guo, Q.: EN+TF-WeM1, 127
Gupta, A.: SS2+EM-MoM1, 15; TF1-TuM9, 62
Gupta, R.: PS-MoM9, 11
Gupta, S.: MI+TF-ThM9, 186
Gushchin, O.P.: PS-TuP7, 105
Gustafson, J.: IS+SS-TuM1, 50
Guthrey, H.L.: AS-TuA11, 69
Gutmann, S.: EN+NS-WeM12, 127; EN+TF-
TuA10, 75; SS2-WeM12, 140
GUuo, Q.: NS+AS+MN-WeM3, 132
Guziewicz, E.: AC+SS-MoM8, 2
Gwangyong, Y.: PS+MN-WeM6, 134
— H —
Ha, J.: SS-ThA1, 208
Ha, T.-K.: PS-TuP3, 105
Haass, M.: PS1-MoA1, 30; PS1-TuM4, 53
Hadjar, O.: AS-WeA12, 151
Hagen, C.W.: SS2-WeM3, 138
Haight, T.: EW-WeL4, 148
Hakanoglu, C.: SS1-MoM2, 14
Halevi, B.: SS1-TuM11, 58
Hall, R.A.: TF-MoA10, 38
Halterman, R.L.: SS2-TuM10, 60
Ham, H.C.: SS1-TuM10, 58; SS1-TuM6, 58
Hamaguchi, S.: PS1-ThA1, 205; PS-ThM5, 192;
PS-ThM9, 193
Hamers, R.J.: BI+MN-FrM8, 233; NS-MoA8, 29;
SS-FrM9, 242; SS-WeA3, 169
Hammond, E.: EN+PS-MoM3, 3
Hammond, J.S.: AS-TuP14, 94; AS-WeA2, 149;
AS-WeM9, 122; EW-TuL3, 66
Hammond, W.T.: EN+NS-WeM5, 125
Han, G.-M.: MN-ThP10, 221
Han, J.G.: PS+TF-ThM1, 190
Han, J.J.: EM-TuP13, 98
Han, J.W.: PS-WeM4, 135
Han, M.: NS-TuP1, 100
Han, S.: TF-TuP21, 118
Han, S.M.: EN+AS-ThM4, 180; EN+TF-TuA8, 75
Han, Y.: SS2-MoA11, 37
Han, Z.Y.: PS+TF-ThM9, 191
Hanawa, H.: PS2-TuM2, 54
Haney, P.: EN+NS-WeM6, 126
Hannon, J.: GR+MS-WeA3, 156
Hanrath, T.: EN+AS-ThM11, 181; EN-MoA8, 25
Harish Kumar, N.: MI+TF-ThM12, 186
Harrell, L.E.: MN-ThM5, 187; MN-ThM6, 187
Harrer, S.: BI+MN-FrM9, 233
Harris, P.R.: AS-TuP19, 94
Harrison, I.: SS1-MoM6, 14
Harrison, J.A.: TR+NS+SS-WeA11, 173; TR-
ThP4, 230
Harrison, W.A.: SS-TuP24, 114
Hart, M.A.: AS-TuP27, 96; SS2-WeM11, 139
Haspert, L.C.: TF1-TuM10, 62
Hatakeyama, R.: EN+PS-MoM2, 3
Hattar, K.: AS-WeM1, 122; IS+AS+NS+MI-
WeM5, 131; IS+AS+NS+MI-WeM6, 131
Haubrich: SS1-TuM3, 58
Hauffman, T.: SS1-WeM10, 138; TF-WeA8, 172
Hauser, A.J.: EM+MI-MoA4, 24
Havercroft, N.: AS-WeA3, 149; AS-WeA4, 149
Hawkins, J.M.: SS1-MoM2, 14
Hayashi, H.: PS1-TuA2, 82
Hayashi, N.: PS2+BI-ThA4, 207
Hayashi, S.: PS-ThP7, 223
He, J.: PS1-TuM2, 53
He, W.: SS-TuP14, 113
He, X.: SS2-WeM4, 138
Hedberg-Dirk, E.L.: BI-ThP13, 214
Hederos, M.: MB+BI+AS-MoA3, 28
Heid, R.: SS-TuA12, 88
Heideman, W.: NS-MoA8, 29
Heindl, R.: MI-WeA3, 161
Heinrich, H.: SS1-MoA2, 34
Heinzel, J.M.: SS-ThM12, 195
Held, G.: IS+SS-TuM5, 50

- Hellberg, C.S.: GR+SS+TF+EM-MoM1, 5
Helmersson, U.: SE+PS-MoA6, 33
Hemminger, J.C.: IS+SS-TuM2, 50; IS-ThP2, 219; NS-ThM12, 189; SS-ThA4, 208
Hendel, R.: TF+EM-WeM1, 140
Henderson, M.A.: EN+AS-ThM3, 180
Hendricks, J.H.: VT+MN-MoM3, 20
Henn-Lecordier, L.: TF+EN-MoM3, 19; TF1-TuM10, 62
Henrich, V.E.: EM+MI-MoA7, 24
Heo, J.: GR+TF-TuM11, 50
Heo, S.: AS-TuP4, 92
Heo, W.: PS-TuP5, 105
Herbots, N.: AS-TuP27, 96; SS2-WeM11, 139
Herding, C.: TR+NS+SS-WeA8, 173
Hernández Hernández, A.: TF-TuP5, 115
Hernandez, G.: VT-TuP6, 119
Hernandez, M.R.: IS+BI+AS-WeA1, 157
Hernandez-Hernandez, A.: TF-ThP21, 230
Hernández-Hernández, A.: NS-TuP6, 101
Hernández-Rosas, J.: TF-ThP3, 227
Herrera-Gomez, A.: AS-TuM3, 42; AS-TuP3, 92
Herron, S.M.: EN+TF-WeM5, 128
Hersam, M.C.: GR+TF-TuA9, 77
Hersh, P.: EN+TF-WeM9, 128
Hershkowitz, N.: PS2-TuM12, 56; PS-ThP21, 226
Hess, D.M.: EN+NS-ThM12, 183
Hess, H.: NS+BI-ThA6, 203
Hesse, R.: AS-TuP10, 93; AS-TuP11, 93
Hetherington, D.L.: VT-TuP9, 119
Hickman, S.A.: MN-ThM5, 187; MN-ThM6, 187
Hiebert, W.K.: MN-ThA6, 202
Hieda, J.: GR-TuP2, 99; PS-FrM3, 239; PS-FrM6, 240; PS-ThP3, 222; SS-TuP7, 111
Higgins, S.R.: IS+AS+NS+MI-WeM2, 130
Hill, M.A.: AC+SS-MoM10, 3
Hill, R.W.: VT+MN-MoM10, 22
Hillmeyer, E.: BI-WeA9, 152
Hillhouse, H.W.: EN+TF-WeM1, 127
Hinch, B.J.: SS2-MoA3, 36
Hines, M.: EM-TuP15, 98
Hines, M.A.: SS2+EM-MoM1, 15
Hingerl, K.H.: PS-WeM12, 136
Hinojosa, Jr., J.A.: SS1-MoM2, 14
Hirano, T.: EN+SS+TF-ThA2, 199
Hirata, M.: VT-TuP3, 118
Hirata, T.: PS2+BI-ThA1, 206
Hirate, T.: NS-TuP28, 104
Hironaka, T.: PS-ThP7, 223
Hirschmugl, C.: IS+BI+AS-WeA2, 157
Hirvonen, J.K.: SE+PS-MoM9, 13
Hite, J.K.: EM+SS-ThM4, 178; GR+MS-WeA1, 156; GR+SS+TF+EM-MoM8, 5; LB-WeA2, 159; LB-WeA3, 159
Hlawacek, A.: SS2-TuM5, 59
Ho, F.H.: NS-TuP12, 102
Hoang, J.: AC+TF-MoA2, 23; EN+NS-ThM1, 181; EN+NS-WeA7, 155; PS1-ThA7, 206
Hobbs, J.K.: SS2-WeM5, 139
Höche, T.: TF+SE-WeM3, 142
Hochrein, J.: VT+MS-TuM5, 64
Hoepker, N.: EM-TuM11, 47
Hoffbauer, M.A.: EN+TF-TuA11, 75
Hoffmann, B.: EN+NS-WeM11, 127; NS+EM+EN-WeA9, 163; NS-ThM2, 188; TF+EN-MoM5, 20
Hofmann, T.: EL+AS+EM+MS+TF-FrM10, 236; EL+AS+EM+MS+TF-FrM8, 235; EL+AS+EM+MS+TF-ThP5, 216; TF+SE-WeM9, 143
Hoyo, H.: VT-TuP4, 119
Holbrook, R.D.: AS2-ThM11, 176
Holcombe, A.: EM+MI-MoA4, 24
Holec, D.: SE-TuM5, 56
Holland, M.: EM+SS-WeA11, 154
Hollander, M.J.: GR+EM+MS+TF+MI-WeM1, 129
Hollister, A.: EM-TuA9, 72
Holloway, P.H.: AC-TuA1, 67; AC-TuA9, 67; EN+TF-TuA3, 74; MN-ThP6, 221; NS-TuP16, 102
Holm, W.: IJ+BI+MN-MoM10, 7
Holmberg, M.: BI-WeA11, 152
Holmes, P.: EW-WeL1, 148
Holmes, R.J.: EN+NS-WeM9, 126; EN-TuM11, 48; NS+EM+EN-WeA11, 163
Holmes, S.: PS-MoM5, 11
Holohan, A.: PS-TuP17, 107; PS-TuP18, 107; PS-TuP19, 108
Holsclaw, B.S.: SS-WeA9, 170
Holt, M.V.: MN-ThM11, 188
Honda, M.: PS-MoM3, 10
Hone, J.: NS+BI-ThA1, 202
Hong, B.: EN-ThP3, 217; EN-ThP4, 217; EN-ThP8, 218
Hong, K.: TF-ThP10, 228; TF-ThP13, 228
Hong, M.P.: PS2-WeA7, 167
Hong, S.: NS-MoM8, 10; SS2-MoA3, 36; SS2-TuM4, 59; SS-ThM5, 194
Honma, Y.: GR+NS-MoA2, 26
Hook, A.L.: BI1-TuA1, 70
Hopkins, M.B.: EW-WeM8, 129; PS-ThP8, 223
Horak, D.: PS-MoM5, 11
Hori, M.: PS1-TuA2, 82; PS1-TuA8, 83; PS1-WeA8, 165; PS-MoM11, 12; PS-ThM11, 193
Horlacher, T.: BI-ThP5, 212
Horn, K.: GR+AS+TF-ThM6, 184
Horn, M.W.: EL+AS+EM+MS+TF-FrM3, 234; EN+NS-ThM11, 183; TF+EM-MoM9, 18; TF-ThA2, 210
Hosch, J.: PS2-TuM6, 55
Hoshi, Y.: EN+SS+TF-ThA8, 200
Hoster, H.E.: GR+AS+TF-ThM2, 183; GR+NS-MoA8, 27; GR+TF-TuA7, 77
Hotta, S.: EN-ThP2, 217
Hou, X.L.: BI-WeA11, 152
Houssiau, L.: BI2+AS-TuA12, 71
Houston, B.H.: GR+NS-MoA7, 27; MN-ThM3, 187
Howe, B.: TF+EM-MoM5, 18
Howe, J.: SS-ThM11, 195
Howell, C.: BI1-WeM5, 124
Howell, S.W.: GR+EM+MS+TF+MI-WeM6, 130
Hrbek, J.: IS+SS-TuA1, 78; SS1-MoM10, 15; SS-TuP19, 113
Hsiao, C.-L.: EL+AS+EM+MS+TF-ThA4, 197
Hsiao, C.N.: EM-TuP1, 96; PS+TF-ThM6, 191; PS+TF-ThM9, 191; TF-ThP1, 226; TF-ThP14, 228; TF-TuP15, 117; TF-TuP18, 117; TF-TuP20, 118
Hsiao, S.-Y.: BI-ThP7, 213
Hsieh, A.H.: PS-ThP15, 224
Hsieh, C.-J.: MN-FrM8, 239
Hsieh, F.-C.: VT+MS-TuM10, 64
Hsieh, J.H.: SE-TuP7, 110
Hsu, C.C.: PS2-MoA10, 33; PS-FrM5, 240; PS-ThP13, 224; PS-ThP14, 224; PS-ThP15, 224; PS-ThP19, 225
Hsu, H.C.: TF-TuP18, 117
Hsu, Y.W.: PS2-MoA10, 33
Hsue, C.-S.: SS2-TuM3, 59
Hu, J.-P.: VT-TuP1, 118
Hu, M.: GR+MS-WeA9, 157
Hu, Q.: BI-WeA10, 152
Hu, Y.: BI-ThP18, 215; GR+SS+TF+EM-MoM9, 6
Hu, Y.C.: BI-ThP3, 212; MN-ThP5, 221
Hua, X.: PS1-TuM2, 53
Huang, C.H.: PS1-WeA9, 165; PS2-WeA4, 166
Huang, H.-M.: BI-ThP7, 213
Huang, H.-S.: BI-ThP7, 213; MN-ThP5, 221
Huang, J.: IS+SS-TuA9, 79; NS-MoM4, 9; NS-TuM5, 52
Huang, L.: EM+SS-ThM3, 178; EM-TuP3, 96
Huang, M.: SS2-MoA1, 36; SS2-MoA6, 36; SS2-MoA7, 36
Huang, M.J.: MI-ThP4, 220
Huang, T.T.: MN-ThP1, 220; MN-ThP3, 220
Huang, Y.: SS1-MoM5, 14; SS-TuA9, 88
Huang, Z.: EL+AS+EM+MS+TF-ThA11, 198
Huber, T.H.: TF-WeM6, 144
Hubert, J.: SE+PS-MoM2, 12
Hubin, A.: SS1-WeM10, 138; TF-WeA8, 172
Hudak, N.: IS+SS-TuA9, 79
Hudson, E.A.: PS1-WeA2, 164; PS1-WeA7, 165
Huerta, L.: AS-TuP26, 96; TR-ThP2, 230; TR-ThP3, 230
Hughes, K.J.: TF1-TuM3, 61
Hughes, Z.: GR+EM+MS+TF+MI-WeM1, 129
Hultman, L.: SE-TuM4, 56; TF+EM-MoM5, 18; TF-ThM1, 195; TF-ThM2, 195; TF-ThM5, 196
Hung, S.-Y.: SE-TuP7, 110
Hupp, J.T.: EN+NS-ThM12, 183
Hurley, D.C.: NS+AS+MN-WeM10, 133
Hutter, H.: SE-TuM12, 57
Hutton, S.J.: AS-WeM10, 123; EW-TuL4, 66
Hwang, C.-S.: TF-TuP9, 116
Hwang, D.: EN+PS-MoM10, 4
Hwang, G.S.: GR+TF-TuA12, 78; SS1-TuM10, 58; SS1-TuM6, 58
Hwang, H.J.: TF1-TuM1, 61
Hwang, H.Y.: EM+MI-MoA1, 24
Hwang, S.-Y.: EL+AS+EM+MS+TF-ThP1, 216
Hwang, Y.: EM+SS-WeA7, 154
Hyun, B.-R.: EN-MoA8, 25
— I —
Iacovita, C.: MI+EM-TuA9, 80
Ilanakiev, K.D.: AC-TuA2, 67
Ichimura, S.: AS-TuP1, 92
Ilevins, A.: SS-WeA12, 171
Igarashi, M.: PS2-WeA4, 166
Iida, S.: AS-WeA2, 149
Ilic, R.B.: MN-FrM5, 238; MN-ThA1, 201; MN-ThM4, 187
Ilton, E.S.: SS-ThM9, 194
Imamura, T.: PS1-TuA2, 82
Imangholi, B.: EM+SS-WeA3, 153
Imhoff, E.A.: LB-WeA2, 159
Imura, K.: NS-TuP3, 100
Inoue, A.: NS-ThM10, 189
Inoue, M.: PS1-MoA10, 31
Iori, D.: BI-ThP15, 215
Iriye, Y.: PS2-WeA3, 166
Isa, L.: NS+BI-ThA9, 204
Ishikawa, K.: PS1-TuA2, 82; PS1-TuA8, 83; PS1-WeA8, 165; PS-MoM11, 12
Ishikawa, M.: PS-MoM4, 11
Ishizaki, T.: PS-ThP20, 225
Iski, E.V.: NS-TuM9, 52; SS-TuP2, 110
Islayaykin, A.M.: PS-TuP7, 105
Isobe, M.: PS1-ThA1, 205
Issacson, S.: TF1-TuM3, 61
Issaksson, U.: SE+PS-MoA6, 33
Ista, L.K.: BI-ThP14, 214; BP-SuA5, 1; MB+BI-MoM2, 8
Itagaki, N.: EN+PS-MoM1, 3
Ito, A.: PS1-TuA8, 83
Ito, T.: PS-ThM5, 192; PS-ThM9, 193
Ivnicki, D.: BI-ThP10, 213
Iwao, T.: PS2+BI-ThA4, 207
Iwasaki, T.: PS2-WeA3, 166
— J —
Jackson, L.P.: SS2-TuM10, 60
Jackson, S.: NS-MoM8, 10
Jackson, T.N.: EL+AS+EM+MS+TF-ThA10, 198
Jaehrig, M.: EM+SS-WeA8, 154
Jahr, N.: NS+EM+EN-WeA9, 163
Jain, A.: AS-TuP23, 95
Jain, R.: BI1-WeM2, 123
Jaing, C.C.: TF-ThP1, 226; TF-TuP20, 118
Jakubiak, R.: NS+BI-ThA4, 203; PS+TF-ThM12, 191
James, C.D.: BI+MN-FrM3, 232
James, T.: NS-TuM2, 51
Jang, J.N.: PS2-WeA7, 167

- Jang, J.S.C.: IS+BI+AS-WeA11, 158
 Jang, J.-W.: BI1+NS-ThM2, 176; NS-TuP2, **100**
 Jang, S.W.: PS2-WeA9, 167
 Janjua, S.J.: MI+EM-TuA10, 80
 Jankovic, V.D.: EN+NS-ThM1, **181**
 Jarecki, R.L.: PS+MN-WeM3, 133; VT-TuP9, 119
 Jariwala, B.N.: EN+PS-MoM9, 4; EN-ThP7, 218
 Järendahl, K.: EL+AS+EM+MS+TF-FrM9, 235; EL+AS+EM+MS+TF-ThA4, **197**
 Jasenko, A.: PS-ThP1, 222
 Jay, G.D.: BI-ThP8, 213; TR+NS+SS-WeA7, 173
 Jaye, C.: AS1-ThM6, 175; GR+TF-TuM12, **50**; NS+BI-ThA8, 204
 Jegal, W.: BI2+AS-TuA9, 71
 Jen, S.U.: TF+SE-WeM10, **143**
 Jena, D.: TF1-TuM11, 62
 Jeng, H.T.: SS2-TuM3, 59
 Jenkins, C.A.: MI-WeA4, 161
 Jenkins, S.J.: SS-WeA12, **171**
 Jenks, C.J.: SS1-TuM1, 57
 Jensen, D.S.: NS-TuA11, 82
 Jensen, U.B.: SE-TuP2, **109**
 Jeon, H.T.: TF1-TuM4, 61
 Jeon, M.H.: PS1-TuA9, **84**; PS-ThM2, 191
 Jeong, H.Y.: EM-TuP12, 98
 Jeong, J.H.: EM-TuP12, 98
 Jernigan, G.G.: GR+MS-WeA1, 156; GR+MS-WeA9, 157; GR+SS+TF+EM-MoM1, **5**; LB-WeA2, 159; LB-WeA3, 159
 Jesse, S.: EW-TuM8, 48; NS-MoM9, 10
 Jewell, A.D.: NS-TuM9, 52; SS-TuA1, **87**; SS-TuP2, 110
 Ji, E.: BI-ThP14, 214
 Ji, X.: PS1-TuM2, 53
 Jia, Q.: AC+SS-MoM5, 2; TF-ThA1, 209
 Jiang, H.: PS+TF-ThM12, 191
 Jiang, K.: SE-TuM9, 56
 Jiang, P.: SS-ThA3, 208
 Jiang, W.: AS-WeM2, 122; TF-WeA12, 172
 Jie, D.: EM-TuM12, 47
 Jiménez, O.: TR-ThP3, 230; TR-ThP6, 231
 Jimenez-Aleman, O.: TR-ThP2, **230**
 Jin, W.: EN+NS-WeM10, 126; SS2-TuM6, 60
 Jin, Y.: EM-TuA1, **72**
 Jinnai, B.: PS1-WeA3, 164
 Joachim, C.: EM-TuM12, 47
 Jock, R.M.: EM-TuA1, 72
 Johansson, E.: SS2+EM-MoM4, 16
 Johnson, D.P.: AC+SS-MoM10, 3
 Johnson, E.V.: LB-WeA8, 160
 Johnson, G.: SS-TuP16, **113**
 Johnson, G.R.: BI-ThP10, 213
 Johnson, J.C.: EN-MoA3, 25
 Johnson, L.J.S.: SE-TuM4, **56**
 Johnson, P.: NS+AS+MN-WeM4, 132
 Johnson, W.J.: BI2+NS-ThM11, 178
 Johnston, S.: EN+AS-ThM4, 180
 Jones Jr., E.D.: TF-ThP2, **226**
 Jones, J.G.: SE+PS-MoA3, 33; SE-TuA12, 87; SE-TuP4, 109; SE-TuP5, 109
 Jongchul, P.: PS+MN-WeM6, 134
 Joo, J.: PS1-ThA11, **206**; TF-ThP10, 228; TF-ThP13, 228; TF-WeA11, 172
 Joseph, E.A.: PS1-MoA9, 31; PS1-TuA11, **84**; TF2-TuM6, 63
 Joshi, A.: IJ+BI+MN-MoM4, 6
 Joshi, R.: GR-TuP7, 100
 Joubert, O.: PS+MN-WeM5, 134; PS1-MoA11, 31; PS1-TuM4, 53; PS1-TuM9, 54; PS-MoM1, 10
 Jourde, D.: TF2-TuM5, 63
 Jousseau, V.: TF2-TuM4, 63
 Joyce, J.: AC+SS-MoM5, 2; AC+SS-MoM8, 2
 Jun, S.: GR+TF-TuA11, 78
 Jung, C.-K.: EN-ThP1, 217
 Jung, C.-T.: TF-TuP4, **115**
 Jung, C.Y.: GR+EM+MS+TF+MI-WeM2, 129
 Jung, D.Y.: EN-ThP4, 217
 Jung, H.C.: PS-TuP1, 104
 Jung, J.-G.: PS+MN-WeM9, 134
 Jung, S.: GR+TF-TuM10, 49; GR+TF-TuM9, **49**; PS2-MoA9, 32; PS2-TuA1, 84
 Jung, T.A.: MI+EM-TuA9, 80
 Jung, U.J.: TF1-TuM1, 61
 Jung, Y.H.: PS2-WeA9, 167
 Jung, Y.S.: EN+EM-TuA1, 73
 Jung, Y.W.: EL+AS+EM+MS+TF-ThP1, 216
 Jupille, J.: SS1-MoA1, **34**
 Jur, J.S.: IS+AS+NS+MI-WeM11, 132; TF-MoA1, **37**; TF-MoA8, 38; TF-WeM5, 144
 Jurow, M.: EM-TuM6, 46
 Jyun, B.G.: PS1-TuA12, 84
 — **K** —
 Kacher, J.: IS+AS+NS+MI-WeM6, 131
 Kadomura, S.: PS2-WeA11, 167
 Kahn, A.: EN+NS-WeM3, **125**
 Kalfon-Cohen, E.: TR-ThP5, **230**
 Kalidindi, N.R.: TF-TuP11, **116**
 Kalinin, S.V.: NS-MoM9, 10; TF-ThA3, **210**; TF-TuP17, 117
 Kalinkin, A.V.: EL+AS+EM+MS+TF-ThP3, 216
 Kalugin, N.G.: GR+TF-TuM1, **48**
 Kamineni, V.K.: GR+AS+TF+MI-ThA8, 201
 Kaneko, T.: EN+PS-MoM2, **3**
 Kanesiro, T.: NS-TuP28, 104
 Kang, C.G.: TF1-TuM1, 61
 Kang, C.J.: PS-WeM4, 135
 Kang, H.J.: AS-TuP4, 92
 Kang, H.S.: PS-TuP1, 104
 Kang, S.B.: VT-TuP12, 120; VT-TuP5, 119
 Kang, S.K.: PS1-TuA9, 84; PS-ThM2, **191**
 Kang, S.-Y.: PS1-ThA2, 205
 Kang, T.D.: EL+AS+EM+MS+TF-FrM4, **234**
 Kang, Y.C.: TF-ThP9, 228
 Kanjolia, R.: TF-TuA12, 90
 Kankate, L.: BI-ThP2, 212; SS2-TuM12, 60
 Kao, J.-S.: BI-ThP7, 213; MN-ThP5, 221
 Kao, P.: EM-TuM5, 46
 Kappes, B.B.: GR+AS+TF-ThM12, 185; GR+TF-TuA11, **78**
 Karabacak, T.: TF+SE-WeM4, 142; TF+SE-WeM5, 142
 Karahashi, K.: PS-ThM5, **192**; PS-ThM9, 193
 Karakoti, A.: NS-MoA10, **29**
 Karim, A.: AS-TuP21, 95; SS-ThM5, 194
 Karim, I.: PS+TF-ThM10, 191
 Karp, E.: SS1-MoM8, **15**
 Karthik, C.: EN+NS-WeA8, 155
 Karuppanan, K.B.: MI+TF-ThM11, **186**; NS-TuP13, 102; TF-TuP11, 116; TF-WeA9, 172
 Kasahara, A.: MN-ThP2, **220**
 Kasemo, B.H.: SS1-MoA6, 35
 Kathan-Galipeau, K.: IS+BI+AS-WeA9, **158**
 Katiyar, R.: NS-MoM8, 10
 Kato, K.: PS1-WeA3, 164
 Kato, S.: NS-TuP22, 103; VT-WeM10, 147; VT-WeM9, **147**
 Kaufman-Osborn, T.: SS2+EM-MoM9, 16
 Kaulich, B.: BI-TuM12, 45
 Kavanagh, K.L.: EM-TuA11, **73**
 Kawabe, T.: PS-ThP9, **223**
 Kawai, M.: IS+BI+AS-WeA10, 158
 Kawamura, M.: TF-TuP2, **115**
 Kawashima, Y.: EN+PS-MoM1, 3
 Kay, B.D.: SS1-WeM9, 138; SS-FrM7, 241
 Kayani, A.: TF-WeA12, 172
 Kayser, S.: AS-TuP2, 92
 Keenan, C.: TF-ThA10, **211**
 Keenan, M.R.: AS1-ThM3, **175**; AS-TuP13, 93
 Kei, C.C.: PS+TF-ThM6, 191; PS+TF-ThM9, 191
 Kelber, J.A.: GR+TF-TuA3, **76**; PS1-WeA1, 164
 Kelley, M.J.: SS2-WeM10, 139
 Kellock, A.: TF1-TuM6, 61
 Kellogg, G.L.: GR+SS+TF+EM-MoM2, 5; SS1-WeM6, 138
 Kellogg, K.: VT-TuP10, **120**
 Kempisty, J.M.: EM+SS-ThM5, 178
 Kendelewicz, T.: SS-ThA1, 208
 Kenney, J.A.: EN+PS-MoM3, 3; PS1-ThA6, **205**; PS2-TuM1, 54
 Kennison, J.A.: AC+SS-MoM5, 2
 Kent, V.: NS-TuP27, 104
 Kersten, H.: PS2-TuM3, **54**
 Kessels, E.W.M.M.: TF+EN-MoM6, **20**; TF-TuA9, 90
 Ketsdever, A.: VT+MS-TuM11, 64
 Keville, B.: PS-TuP17, 107; PS-TuP18, 107; PS-TuP19, **108**
 Khaing, H.: AC-TuA4, 67
 Khan, A.: PS1-TuM2, 53
 Khare, A.: EN+NS-ThM10, 183
 Khare, C.: TF+SE-WeM3, **142**
 Khare, R.: PS-ThM6, **192**
 Khosravian, H.: SS-FrM3, **241**
 Khrustalev, V.A.: PS-TuP7, 105
 Khudhayer, W.J.: TF+SE-WeM4, **142**
 Kida, H.: PS-MoM4, 11
 Kiefer, B.: SS1-TuM11, 58
 Killelea, D.R.: SS-TuA10, 88; TF-WeA7, 171
 Killgore, J.P.: NS+AS+MN-WeM10, 133
 Kim, B.: SS-TuP11, 112
 Kim, B.I.: NS+AS+MN-WeM11, **133**
 Kim, B.S.: PS-ThP12, **224**
 Kim, C.-I.: PS-TuP2, 104; PS-TuP3, 105; PS-TuP4, 105
 Kim, D.: EN+PS-MoM10, 4; NS-TuP1, **100**
 Kim, D.C.: PS2-WeA7, 167
 Kim, D.H.: PS-WeM4, 135; SS2-TuM4, 59; SS-TuA11, 88; SS-TuA2, 87; SS-TuP11, 112
 Kim, D.J.: EM-TuP4, **97**
 Kim, D.-J.: GR+EM+MS+TF+MI-WeM2, **129**
 Kim, D.W.: PS2-WeA9, 167
 Kim, H.: TF1-TuM4, **61**
 Kim, H.J.: EN-ThP3, 217
 Kim, H.-J.: EM+SS-ThM1, 178
 Kim, H.K.: GR+TF-TuM4, 49; GR-TuP4, **99**
 Kim, H.-S.: TF+EN-MoM1, 19
 Kim, I.K.: EN+PS-MoM8, **4**
 Kim, J.: EM+SS-ThM1, 178; EM+SS-WeA4, 153; IS+AS+NS+MI-WeM1, **130**; TF1-TuM11, 62
 Kim, J.G.: TF2-TuM3, **63**; TF-TuP8, 116
 Kim, J.M.: EN+NS-ThM2, 182; EN-ThP3, 217
 Kim, J.S.: PS2-WeA7, 167
 Kim, J.T.: PS2-WeA9, 167
 Kim, K.: SS-TuA11, 88
 Kim, K.D.: EM-TuP12, **98**
 Kim, K.H.: SS1-MoA7, 35
 Kim, K.-J.: SS-TuP11, 112
 Kim, K.N.: EN+PS-MoM8, 4
 Kim, M.-H.: EN-ThP8, 218
 Kim, N.-H.: EM-TuP14, 98; EM-TuP5, 97; MN-ThP10, 221; MN-ThP9, **221**; TF-ThP16, 229; TF-ThP17, 229; TF-ThP18, 229
 Kim, N.K.: NS-TuP11, **102**; NS-TuP9, 101
 Kim, R.: PS-MoM5, 11
 Kim, S.: EM-TuP6, **97**; EN-ThP8, 218; GR+EM+MS+TF+MI-WeM9, 130; NS-TuP5, 101; SS-TuP11, 112
 Kim, S.H.: TR+MN+NS+SS-WeM3, **145**
 Kim, S.I.: NS-TuP3, **100**; NS-TuP5, 101
 Kim, S.-S.: EM+SS-ThM1, 178; EN-ThP1, 217
 Kim, S.W.: BI2+AS-TuA9, 71
 Kim, S.Y.: EL+AS+EM+MS+TF-ThP1, 216
 Kim, S.-Y.: PS+MN-WeM9, 134
 Kim, S.-Y.: MN-ThP9, 221
 Kim, S.-Y.: MN-ThP10, 221
 Kim, S.-Y.: TF-ThP16, **229**
 Kim, T.: EM-TuP6, 97
 Kim, T.H.: PS-TuP10, 106
 Kim, W.S.: PS-WeM4, 135
 Kim, Y.D.: EL+AS+EM+MS+TF-ThP1, 216
 Kim, Y.J.: PS+TF-ThM1, 190
 Kim, Y.K.: SS1-WeM9, 138
 Kim, Y.Y.: PS1-TuM6, 54; PS-TuP10, **106**; PS-TuP9, 106
 Kimmel, G.A.: SS-FrM10, 242; SS-ThA6, **208**
 Kimura, K.: SE+TF-WeA7, 168; SE-TuP3, 109

- Kimura, Y.: PS-TuP22, 108
King, D.: AS-TuP21, 95
King, J.S.: EN+TF-WeM5, 128
King, S.: EM+SS-WeA8, **154**
King, W.P.: BI+MN-FrM8, 233; GR+NS-MoA9, 27; NS-TuM6, 52; SE-TuA1, **86**; SE-TuP4, 109
Kingshott, P.: B11+NS-ThM1, 176
Kirk, A.P.: EM+SS-WeA4, **153**
Kirk, W.P.: SS2-MoA7, 36
Kisielowski, C.: GR+TF-TuA4, 77
Kiskinova, M.: BI-TuM12, 45
Kislov, N.: TF+EN-MoM4, 19
Kitajima, T.: PS+TF-ThM5, **190**
Kitazaki, S.: PS2+BI-ThA4, **207**
Kiyono, R.: TF-TuP2, 115
Kizilkaya, O.: SS-FrM1, 240
Kjerstad, A.C.: TF+SE-WeM9, 143
Klages, C.-P.: SE+PS-MoM5, **13**
Kleibert, A.: MI+EM-TuA9, 80
Klein, T.M.: TF1-TuM9, 62
Klimov, N.N.: GR+TF-TuM10, **49**; GR+TF-TuM9, 49
Klimov, V.I.: EN+EM-TuA7, 73; EN+NS-ThM5, 182; NS-ThM4, 189
Kline-Schoder, R.J.: VT+MN-MoM10, 22
Klok, H.A.: SS-TuP22, 114
Klopf, J.M.: SS2-WeM10, 139
Knapp, J.A.: IS+AS+NS+MI-WeM6, 131
Knauss, K.G.: IS+AS+NS+MI-WeM2, 130
Knippenberg, M.T.: TR+NS+SS-WeA11, 173; TR-ThP4, **230**
Ko, D.-H.: TF2-TuM11, 63
Ko, E.: PS+TF-ThM10, 191
Koay, C.: PS-MoM5, 11
Kobayashi, K.: EM-TuA7, 72
Kobayashi, N.P.: AC-TuA3, 67
Kobayashi, S.: PS2-TuM2, **54**
Kobayashi, T.: IS+BI+AS-WeA10, 158; VT-TuP4, 119
Koc, B.: AS-TuA9, 69
Kochubey, V.A.: EL+AS+EM+MS+TF-ThP3, 216
Kodama, S.: EN+PS-MoM2, 3
Kodambaka, S.: GR+AS+TF-ThM12, 185; GR+AS+TF-ThM5, **184**
Koeble, J.: EM-TuM12, 47
Koeck, F.A.M.: EN-ThP5, 218
Koel, B.: SS1-TuM9, **58**
Koelsch, P.: B11-WeM5, 124
Koga, K.: EN+PS-MoM1, 3; PS2+BI-ThA4, 207
Koh, D.Y.: VT-TuP12, 120
Koleske, D.: EM+SS-ThM5, **178**
Kollmer, F.: AS-WeA4, 149
Kolodziej, J.J.: SS2+EM-MoM8, **16**
Komesu, T.: MI-ThP1, 220
Kondo, H.: PS1-TuA2, 82; PS1-TuA8, 83; PS1-WeA8, 165; PS-MoM11, 12
Kondo, T.: EN-TuM3, 47; GR+NS-MoA2, 26
Kondo, Y.: PS1-TuA8, 83
Kondratenko, Y.: SS2+EM-MoM11, 17
Kong, L.: EN+NS-ThM3, 182
Konneker, A.M.: MN-ThP11, **221**
Konopka, J.: EN+AS-ThM6, 181
Konradsson, P.: MB+BI+AS-MoA3, 28
Konrath, M.: NS-MoA8, 29
Konstantinidis, S.: SE-TuM9, 56
Koo, M.: PS2-WeA9, 167
Koposov, A.Y.: NS-ThM4, 189
Kos, A.B.: NS+AS+MN-WeM10, 133
Köser, J.: BI-TuM6, 44
Koshimizu, C.: PS-MoM11, 12
Kostermans, M.: PS-TuP8, **106**
Kotelyanskii, M.: EL+AS+EM+MS+TF-FrM4, 234
Kotru, S.: EN+EM-TuA10, 74; TF-ThA8, 210; TF-ThP8, 228
Koyama, I.: PS-ThP7, 223
Koyama, K.: PS1-WeA3, 164; PS2-TuA2, 84
Kraemer, S.: AC-TuA3, 67
Krafft, G.: SS2-WeM10, 139
Kramer, N.J.: EN+PS-MoM5, 4; EN+PS-MoM9, 4; EN-ThP7, 218
Kravchenko, I.I.: MI+TF-ThM1, 185
Kraya, L.: SS-ThM4, **194**
Kreuzer, M.: IS+BI+AS-WeA3, 157
Krishna, L.R.: SE-TuM11, 57
Krishnan, K.M.: TF+EM-MoM1, **17**
Krishnan, R.: EN+NS-WeA10, 155; EN+TF-WeM6, **128**
Kristensen, S.: BI2-WeM12, **125**
Kruchinin, V.N.: EL+AS+EM+MS+TF-ThP3, 216
Krukowski, S.K.: EM+SS-ThM9, **179**; GR+SS+TF+EM-MoM5, **5**
Krupp, L.: PS1-TuA7, 83
Krylov, S.L.: MN-FrM5, 238; MN-ThA1, 201; MN-ThM9, **187**
Kub, F.J.: EM+SS-ThM4, 178
Kubista, K.D.: GR+AS+TF+MI-ThA3, **201**; GR+AS+TF+MI-ThA4, 201
Kubota, T.: PS2-WeA3, 166; PS2-WeA8, **167**
Kuchibhatla, S.: NS-MoA10, 29; SS2-WeM6, 139
Kuchibhatla, S.: AS-TuA3, 68; TF-WeA12, 172
Kudela, J.: EN+PS-MoM3, 3
Kühn, G.: AS-TuP6, 93
Kuhn, M.: EM+SS-WeA8, 154
Kühne, P.: EL+AS+EM+MS+TF-FrM8, 235
Kulp, J.L.: BI-ThP16, **215**; BI-WeA12, 153; MB+BI+AS-MoA10, 28
Kulsreshath, M.K.: PS2-MoA6, **32**; PS2-MoA8, 32
Kumar, A.: MN-ThA8, **202**; SS2-WeM6, 139
Kummel, A.C.: EM+SS-WeA11, 154; EM-TuP7, 97; NS+BI-ThA10, 204; NS-TuP19, 103; SS2+EM-MoM9, 16
Kung, S.-C.: NS+EM+EN-WeA10, **163**
Kunnen, E.: PS1-WeA4, **164**
Kuo, S.-Y.: EM-TuP1, 96; TF-TuP18, **117**
Kupfer, H.: EN+TF-TuA2, 74
Kurdak, C.: EM-TuA1, 72
Kurkul, R.: MN-FrM10, 239
Kurokawa, A.: VT-TuP4, **119**
Kurtz, R.L.: SS1-MoA9, 35; SS-FrM1, 240
Kusano, Y.: TR+MN+NS+SS-WeM6, 146
Kushmerick, J.G.: EM-TuM6, 46; NS-TuP14, 102
Kushner, M.J.: PS1-ThA4, 205; PS1-TuA1, 82; PS2+BI-ThA6, **207**; PS2-MoA7, 32; PS2-TuA12, 86; PS-FrM4, 240
Kwak, J.H.: SS-ThM1, 193
Kwan, M.: AS-TuM12, 43
Kweon, K.E.: GR+TF-TuA12, **78**
Kwon, J.: TF-TuA12, **90**
Kwon, K.-Y.: SS-TuA2, 87
Kwon, N.Y.: NS-TuP11, 102; NS-TuP9, **101**
Kwon, S.: EM-TuP9, 97
— **L** —
LaBella, M.: GR+EM+MS+TF+MI-WeM1, 129
LaBella, V.P.: EM-TuM2, 46; MI-ThP3, 220
Lacis, J.W.: TF-TuP6, 115
Lad, R.J.: SE+TF-WeA11, 169; SE-TuM3, **56**
Ladroue, J.: PS+MN-WeM10, 135; PS-ThM4, **192**
LaForge, J.M.: TF+SE-WeM6, **143**
Lagally, M.G.: SS2-MoA6, 36
Lai, F.-I.: EM-TuP1, 96; TF-TuP18, 117
Lalany, A.: TF-ThP4, **227**
Lallement, L.: PS-TuP6, 105
Lam, C.H.: PS1-TuA11, 84
Lam, R.T.S.: B11+NS-ThM2, **176**
Lambert, T.N.: NS-TuA7, 81; NS-TuP7, 101
Land, D.P.: IS+BI+AS-WeA1, 157
Landie, G.: PS-MoM5, 11
Landin, J.: EL+AS+EM+MS+TF-FrM9, 235; EL+AS+EM+MS+TF-ThA4, 197
Landman, L.: VT-TuP8, **119**
Landt, L.: NS-TuA4, 81
Lane, M.: AS-TuP23, 95
Lange, M.A.: SE+PS-MoA3, 33
Langer, R.: B11-TuA1, 70
Langhammer, C.: SS1-MoA6, 35
Langreth, D.C.: EN+NS-ThM3, 182
Lao, K.A.: VT+MS-TuM1, 64
Laoufi, I.: SS1-MoA1, 34
Laprade, B.N.: EW-WeL1, 148
Laptev, P.: TF-ThP7, 227
Laracuenta, A.R.: GR+NS-MoA9, 27; NS-TuM6, 52
Lareau, R.T.: AS2-ThM9, 176
Larson, T.C.: AS-TuM12, 43
Larsson, M.K.: SS1-MoA6, 35
Laskin, J.: AS-WeA12, 151; BI-WeA10, 152; SS-TuP16, 113
Latrous, H.: AC-TuA8, **67**
Lau, J.W.: MI+TF-ThM5, **186**
Lau, K.K.S.: TF-MoA9, 38
Lauer, J.: EM-TuA10, 73; EM-TuP10, 98
Lauhon, L.J.: LB-WeA1, 158
Law, M.: EN-TuM9, **48**
Lawton, T.J.: SS-WeA9, 170
Lazzari, R.: SS1-MoA1, 34
Lazzarini, L.: NS-TuP17, 103
Lea, S.: IS+AS+NS+MI-WeM2, **130**
Leclair, A.: BI-TuM5, 44
LeClair, P.R.: AC+MI-TuM11, 41
Lederman, D.: MI+TF-ThM10, 186; MI+TF-ThM2, 185; MI-WeA7, **161**; TF-ThA10, 211
Lee, B.G.: EN+PS-MoM9, 4
Lee, B.H.: TF1-TuM1, **61**
Lee, B.J.: PS2-WeA7, **167**; PS2-WeA9, 167
Lee, C.: PS1-MoA2, 30; PS1-MoA6, **30**
Lee, C.T.: TF-ThP1, 226; TF-ThP14, 228; TF-TuP20, **118**
Lee, D.C.: EN+NS-ThM5, 182
Lee, D.S.: TF2-TuM11, **63**
Lee, E.H.: AS-TuP4, 92; PS-ThP12, 224; TF+EM-WeM5, 140
Lee, E.K.: EN+NS-ThM2, **182**
Lee, G.: GR+NS-MoA1, 26
Lee, H.: AS-TuM12, 43; MN-FrM6, **238**; SS-TuP11, 112; TF1-TuM4, 61
Lee, H.C.: PS-TuP1, 104
Lee, H.-H.: MB+BI+AS-MoA3, 28
Lee, H.I.: AS-TuP4, 92; AS-TuP5, **92**
Lee, H.-J.: EN+PS-MoM10, **4**
Lee, H.M.: PS-TuP1, 104
Lee, H.S.: PS-TuP23, **108**
Lee, J.: PS1-WeA1, 164; PS-MoM8, **11**; SS1-MoM11, 15; TF1-TuM4, 61; TF-TuA10, **90**
Lee, J.-B.: PS2-MoA6, 32; PS2-MoA8, 32
Lee, J.C.: AS-TuP4, 92; TF+EM-WeM5, **140**
Lee, J.H.: EM-TuP12, 98; NS-TuP11, 102; TF+EM-WeM5, 140
Lee, J.L.S.: AS-WeA7, **150**; AS-WeA8, 150
Lee, J.R.I.: NS-TuA4, 81
Lee, J.S.: EM+SS-WeA11, 154; SS2+EM-MoM9, **16**
Lee, J.W.: EM-TuP4, 97; EN+NS-ThM2, 182
Lee, J.Y.: BI2+AS-TuA9, 71; PS-WeM4, 135
Lee, K.: GR+EM+MS+TF+MI-WeM9, 130; IS+AS+NS+MI-WeM11, 132; TF-TuA3, 89
Lee, K.-M.: TF2-TuM3, 63; TF-TuP8, 116
Lee, K.Y.: B11-WeM1, 123
Lee, M.: SS-WeA10, **170**
Lee, M.S.: PS1-TuA12, 84
Lee, M.W.: PS-ThP12, 224
Lee, M.-Y.: EL+AS+EM+MS+TF-ThA10, 198
Lee, N.-E.: GR+EM+MS+TF+MI-WeM2, 129; PS-TuP5, 105; TF+EM-WeM11, 141
Lee, S.: EM+SS-WeA11, 154; TF-ThP10, 228; TF-TuP7, **115**; VT-TuP10, 120
Lee, S.-B.: EN+SS+TF-ThA10, 200
Lee, S.G.: MN-ThM5, 187; MN-ThM6, 187; PS-ThP12, 224
Lee, S.-H.: EN+EM-TuA1, 73; GR+TF-TuM11, 50; TF2-TuM3, 63; TF-TuP8, 116
Lee, S.H.A.: EN+NS-ThM11, 183
Lee, S.-I.: PS+MN-WeM9, 134
Lee, S.J.: EN+NS-ThM2, 182
Lee, S.K.: PS+MN-WeM9, **134**
Lee, S.O.: PS+MN-WeM9, 134

- Lee, S.R.: EM+SS-ThM5, 178
Lee, S.Y.: TF1-TuM1, 61; VT-TuP13, 120
Lee, T.: TF-ThP10, **228**
Lee, T.G.: BI2+AS-TuA9, 71
Lee, T.R.: EN+NS-WeA9, 155
Lee, T.-S.: MN-FrM8, 239
Lee, V.: GR+TF-TuM12, 50
Lee, W.-J.: EN+SS+TF-ThA10, 200
Lee, W.-K.: GR+NS-MoA9, 27; NS-TuM6, **52**
Lee, W.-S.: EM-TuP14, 98; EM-TuP5, 97; TF-ThP17, 229; TF-ThP18, 229
Lee, Y.: TF-MoA10, 38
Lee, Y.-G.: TF1-TuM1, 61
Lee, Y.J.: PS2-WeA7, 167
Lee, Y.S.: PS-TuP23, 108
Leedy, K.D.: EL+AS+EM+MS+TF-FrM2, 234
Leeser, K.: PS+TF-ThM10, 191
Lefaucheux, P.: PS+MN-WeM10, 135; PS2-MoA6, 32; PS2-MoA8, 32; PS-ThM4, 192
Leggett, G.J.: SS2-WeM5, **139**; TR+NS+SS-WeA2, 173
Leisch, J.: EN+TF-WeM9, 128
Leiterer, C.: NS+EM+EN-WeA9, 163
Leonard, A.T.: BI-ThP13, **214**
Leonhardt, D.: EN+AS-ThM4, 180; EN+TF-TuA8, **75**
Leoni, N.: PS2-MoA7, 32
Lersch, T.L.: EW-TuA6, 76; IS+SS-TuA10, 79
Leschkies, K.S.: EN-MoA6, **25**
Leseman, Z.C.: MN-FrM7, 238; MN-ThA7, 202; MN-ThM10, 187; VT+MS-TuM9, **64**
Leusink, G.J.: TF+EM-WeM6, 141
Leverd, F.: PS+MN-WeM5, 134
Lewis, A.L.: TR+NS+SS-WeA2, 173
Lewis, N.S.: SS2+EM-MoM4, 16
Lewis, T.: IS+SS-TuM2, **50**
Lhostis, S.: TF2-TuM5, 63
Li, C.H.: SE-TuA4, **86**
Li, C.-P.: NS-MoM3, **9**
Li, J.: EN+NS-ThM3, 182; TF-ThA2, 210
Li, K.: EN+NS-ThM3, 182
Li, M.: PS1-WeA2, 164; PS1-WeA7, 165; SS1-TuM12, 58; SS-ThM11, 195
Li, N.: TF1-TuM9, **62**
Li, Q.: EM+SS-ThM6, **179**; NS+EM+EN-WeA1, 162
Li, S.-C.: SS-FrM8, **241**
Li, W.: EN+TF-WeM3, **127**; NS-MoM8, 10
Li, Y.: EN+PS-MoM2, 3; TF-ThA1, 209
Li, Y.-T.: AS-TuA4, **68**
Li, Z.: SS1-WeM9, **138**
Liang, H.D.: AS-TuA7, 69
Liang, T.: TR+MN+NS+SS-WeM12, 146
Liang, X.: PS-WeM3, 135
Liang, Z.: SS-FrM3, 241
Liao, T.-S.: BI-ThP7, 213
Libera, J.E.: TF+EN-MoM1, 19
Libera, M.: BI1-TuA2, 70
Liberati, M.: MI-WeA4, 161
Liberman, A.: NS+BI-ThA10, 204; NS-TuP19, **103**
Licitra, C.: TF2-TuM4, 63
Lie, F.L.: EM+SS-WeA3, **153**
Liedberg, B.: MB+BI-MoM3, 8
Liedberg, B.G.: MB+BI+AS-MoA3, 28
Lievens, P.: TF-WeA4, 171
Liljeröth, P.: SS-TuA3, 87
Lill, T.: PS1-MoA1, 30; PS1-TuM4, 53
Lim, C.-H.: EM-TuP5, **97**; TF-ThP18, 229
Lim, C.-M.: PS+MN-WeM9, 134
Lim, D.-G.: PS+MN-WeM9, 134
Lim, H.A.: SS-TuP20, **114**
Lim, J.H.: EN+PS-MoM8, 4
Lim, J.Y.: VT-TuP12, **120**; VT-TuP5, 119
Lim, S.K.: TF1-TuM1, 61
Lim, W.S.: PS1-TuM6, **54**; PS-TuP10, 106; PS-TuP9, 106
Lim, Y.-F.: EN-MoA8, 25
Limmer, S.: NS-TuP7, 101
Lin, C.-H.: SS2-TuM3, 59
Lin, C.S.: EN+SS-FrM6, 237
Lin, C.-Y.: BI-ThP7, 213
Lin, D.M.: BI1+NS-ThM6, 177
Lin, D.-S.: SS-ThA3, 208
Lin, H.J.: MI-ThP4, 220
Lin, H.-K.: MN-FrM8, 239
Lin, J.: SS-TuP15, 113
Lin, M.-Y.: NS-TuP12, **102**
Lin, W.-T.: EM-TuP1, 96; TF-TuP18, 117
Lin, X.: PS-WeM11, 136
Lin, Y.: PS2-MoA10, 33
Lin, Y.H.: BI-ThP3, 212; NS-TuP25, 104
Lin, Y.-M.: GR+MS-WeA7, **156**
Lin, Y.S.: VT-TuP6, **119**
Lin, Y.-S.: BI-ThP7, 213
Lin, Y.W.: TF-TuP15, 117
Lin, Z.: EL+AS+EM+MS+TF-ThA8, 198
Lince, J.R.: SS-TuP13, 112
Lindgren, M.: NS+BI-ThA3, 203
Lindsay, M.: TF-ThP12, 228
Linford, M.R.: LB-WeA7, 160; NS-TuA11, **82**
Liou, B.H.: TF-ThP14, 228; TF-TuP20, 118
Liou, D.R.: TF-ThP14, **228**
Lippitz, A.: BI-ThP5, 212; PS2+BI-ThA8, 207
Liu: SS1-TuM3, 58
Liu, B.: EN+NS-ThM10, 183
Liu, B.H.: PS+TF-ThM6, **191**
Liu, D.-J.: SS1-TuM1, 57
Liu, D.R.: EM-TuP8, **97**; MI-ThP4, 220; PS+TF-ThM6, 191; VT+MS-TuM10, 64
Liu, F.: BI2+AS-TuA11, 71; EM+SS-ThM3, **178**; SS2-MoA6, 36
Liu, G.: PS+TF-ThM4, 190; PS-ThP11, 224
Liu, H.H.: IS+BI+AS-WeA11, 158
Liu, H.R.: NS-TuP22, 103
Liu, J.: EM+SS-ThM1, 178; NS-MoA9, 29
Liu, P.: EM+MI-MoA8, 25
Liu, Q.: SS2-TuM6, 60
Liu, Y.: EM+SS-ThM12, 179; TF+EM-WeM12, 142
Liu, Z.: IS+SS-TuA10, 79; IS+SS-TuM5, 50; IS+SS-TuM6, 51; SS1-MoM11, 15; SS2-WeM5, 139
Liu, Z.Y.: TF-TuA9, 90
Lloyd, K.G.: AS-TuP20, **94**; TF-ThP19, 229
Lloyd, P.: PS+TF-ThM12, 191
Lobo, R.F.: EN+SS-FrM3, 236; EN+SS-FrM4, 236
Lochner, Z.M.: EM+SS-ThM1, 178
Lock, E.H.: BI-ThP19, 215; GR+TF-TuA8, 77; PS2-TuM10, 55; PS-WeM1, **135**
Lockwood, N.P.: AS-TuA3, 81
Lofaro, M.: PS1-TuA7, 83
Long, N.: EW-WeL5, **148**
Longenecker, J.G.: MN-ThM5, **187**
Longo, M.L.: NS-TuP17, **103**
Lopez, B.A.: BI+MN-FrM5, 232
Lopez, G.P.: BI+MN-FrM5, 232; BI2-WeM10, 124; BP-SuA5, 1; MB+BI-MoM2, 8; MB+BI-MoM8, **8**
López-López, M.: TF-ThP3, 227
Lorbek, S.B.: SS2-TuM5, 59
Lorenz, C.: GR+NS-MoA8, 27
Lorenz, N.: TF+EM-WeM3, 140
Lorenz, T.: TR-ThP5, 230
Losovyí, Y.: SS1-MoA9, 35; SS-FrM1, 240
Losovyj, Y.B.: AC+TF-MoA8, 24; AS-TuM5, 43; EM+MI-MoA8, 25
Lou, J.: IS+SS-TuA9, 79
Louis, K.: NS-MoA8, **29**
Lovejoy, T.C.: EM-TuA7, **72**; EM-TuP11, 98
Lovmand, J.: BI2-WeM12, 125
Lowrie, C.G.: NS-TuP26, **104**
Lozova, N.: AS-TuM5, 43
Lozzi, L.: EN+NS-WeM1, **125**
Lu, C.-J.: MN-FrM8, 239
Lu, H.: AC-TuA3, 67
Lu, J.: MI+TF-ThM4, 185; TF+EN-MoM1, 19
Lu, P.: AS-TuA8, 69; NS-MoM4, 9; NS-TuP7, 101
Lu, T.-M.: SE+TF-WeA10, 168
Lu, W.H.: SS2-TuM4, 59; SS-TuA11, 88
Lu, Y.-P.: BI-ThP7, 213
Luan, B.: BI+MN-FrM9, 233
Lucchini, J.-F.: AC-TuA4, 67
Luckarift, H.R.: BI-ThP10, 213
Lucovsky, G.: TF-ThM3, **196**; TF-TuP12, 116
Ludwig, W.: SS1-MoA8, 35
Luef, D.: SE-TuM5, 56
Luere, O.: PS1-WeA4, 164
Luhman, W.A.: EN+NS-WeM9, **126**
Lui, Z.: IS-ThP2, 219
Lukaszew, R.A.: MI+TF-ThM3, 185; MI+TF-ThM4, 185; MI-WeA11, 162
Lulinsky, S.: MN-ThM9, 187
Luna, E.: PS-ThP5, 223
Lundgren, E.: IS+SS-TuM1, 50
Lunelli, L.: BI-ThP11, 214; BI-ThP15, 215
Luo, B.: EN+SS+TF-ThA9, 200; TF-TuP10, 116
Luo, M.: PS1-TuA10, 84; SS2-TuM4, 59; SS-TuA11, 88; SS-TuA2, 87
Luria, J.: EN+AS-ThM11, **181**; EN-MoA8, 25
Lusk, M.T.: EL+AS+EM+MS+TF-ThA8, 198
Lusth, J.: MN-ThM12, 188
Luther, E.P.: EN+SS-FrM1, 236
Luther, J.M.: EL+AS+EM+MS+TF-ThA8, 198; EN-MoA3, 25
Lyding, J.W.: NS-TuM3, 52; SS2-MoA1, 36
Lysaght, P.: GR+TF-TuM12, 50
Lyubintsev, I.: SS-FrM4, **241**
— **M** —
Ma, Q.: SS-TuP1, **110**
Macak, K.: AS1-ThM2, 175
MacElroy, D.: LB-WeA4, 159
Machida, T.: GR+NS-MoA2, 26
Machorro, R.: PS-ThP5, **223**
Macintyre, D.: EM+SS-WeA11, 154
Mack, P.: AS-TuP2, 92; AS-WeM11, 123; EW-TuL2, **66**; SS-TuP18, 113
Mackus, A.J.M.: TF-TuA9, 90
Madix, R.J.: SS1-MoA8, 35; SS1-TuM3, 58
Madras, P.: IS+AS+NS+MI-WeM3, 131
Maeda, S.: NS-TuA8, **81**; PS1-WeA3, 164
Magbitang, T.P.: PS1-TuA7, 83
Magin, C.M.: BP-SuA5, 1
Magnusson, R.: EL+AS+EM+MS+TF-ThA4, 197
Mahaffy, P.: VT+MN-MoM5, 21
Maheshwari, P.: EN+AS-ThM10, 181
Mahoney, C.: AS2-ThM9, **176**
Maier, M.: EM-TuM12, 47
Maitrejean, S.: TF2-TuM5, 63
Majewski, J.: BI1-WeM1, 123
Majidi, H.: EN+NS-ThM9, **182**
Makabe, T.M.: PS+TF-ThM5, **190**; PS-TuP11, 106
Makale, M.: NS-TuP19, 103
Makino, H.: EL+AS+EM+MS+TF-FrM1, **234**; EN-TuM3, 47
Maksymovych, P.: NS-MoM9, **10**
Mallouk, T.E.: EN+NS-ThM11, 183
Malmsten, M.: BI-WeA1, **151**
Malmström, J.: BI2-WeM12, 125
Malocsay, C.: EW-WeL4, **148**
Manciu, F.S.: TF-TuP11, 116
Mandelkow, E.: BI1-WeM1, 123
Mandoc, M.M.: TF+EN-MoM6, 20
Mane, A.U.: TF-TuA8, 90; TF-WeM4, **144**
manef, A.: AC-TuA8, 67
Manginell, R.P.: BI+MN-FrM3, 232
Mangone, A.: MB+BI+AS-MoA3, 28
Manhas, S.: EL+AS+EM+MS+TF-FrM9, 235
Mani-Gonzalez, P.G.: AS-TuP3, **92**
Manini, P.: VT+MN-MoM8, 21; VT+MN-MoM9, **21**
Mankey, G.J.: AC+MI-TuM11, **41**
Mannequin, C.: TF2-TuM4, 63
Manos, D.M.: AC+SS-MoM9, 3
Mansour, A.N.: SS-ThM12, 195
Manura, J.: VT-TuP2, **118**
Marchack, N.P.: PS1-ThA7, **206**

- Marchany, M.D.: AS-TuA9, **69**
 Marchesini, G.R.: BI+MN-FrM7, **233**; BI-TuM4, 44
 Margarella, A.M.: IS-ThP2, **219**
 Marin-Pineda, C.E.: NS-TuP23, 103
 Marmorato, P.: BI-TuM12, 45
 Marocchi, L.: BI-ThP11, 214
 Marohn, J.A.: EN+AS-ThM11, 181; EN-MoA8, 25; MN-ThM5, 187; MN-ThM6, 187
 Marotti, R.E.: NS-TuP27, 104
 Marsella, M.: SS-TuA2, 87
 Marsh, J.R.: AS-TuP20, 94; TF-ThP19, 229
 Marshall, T.: GR+MS-WeA9, 157
 Marsillac, S.X.: EL+AS+EM+MS+TF-ThA11, 198
 Mårtensson, G.E.: IJ+BI+MN-MoM10, 7
 Martin, D.: NS-TuP19, 103
 Martin, E.M.: PS2-TuM11, 55
 Martin, N.: IS+SS-TuA1, 50
 Martin, N.P.: AS-WeM5, 122
 Martin, R.M.: PS1-MoA9, 31; TF2-TuM6, **63**
 Martinotti, D.: GR+SS+TF+EM-MoM10, 6
 Maruyama, B.: NS-TuA3, 81
 Masahara, M.: PS2-WeA10, 167
 Masatani, P.: BI-ThP17, 215
 Mastovich, J.: IS+SS-TuA10, **79**
 Mastro, M.A.: EM+SS-ThM4, 178
 Masumdar, E.: TF-ThA9, **210**
 Matias, V.: TF-ThA1, 209
 Matos-Perez, C.R.: MB+BI-MoM5, 8
 Matranga, C.: SS1-MoM11, 15
 Matson, D.W.: TF-WeA1, 171
 Matsubayashi, A.: MI-ThP3, 220
 Matsubayashi, N.: AS-TuP12, 93
 Matsuda, A.: PS1-MoA3, 30
 Matsumoto, K.: NS-TuA2, **81**
 Matsunaga, N.: PS2-WeA11, 167
 Matsunaga, S.: IS+BI+AS-WeA10, 158
 Matsunaga, T.: EN+PS-MoM1, 3
 Matsuo, J.: AS-WeA10, **150**
 Mattes, W.: AS-TuP15, 94
 Mattevi, C.: GR+NS-MoA1, 26; GR+TF-TuM4, **49**; GR-TuP4, 99
 Matthews, L.: TR-ThP1, 230
 Matthews, O.: TR+MN+NS+SS-WeM5, 146
 Matubayashi, Y.: EN-TuM3, 47
 May, R.A.: EL+AS+EM+MS+TF-ThP5, 216
 Mayer, J.: GR+TF-TuA4, 77
 Mayrhofer, P.H.: SE-TuM5, **56**
 Mazariego, J.L.: AS-TuP26, 96
 McArthur, S.L.: BI2+AS-TuA7, 70; PS2+BI-ThA3, 207
 McCandless, B.: EN+TF-TuA9, 75
 McCarthy, T.W.: MB+BI-MoM5, 8
 McCarty, K.F.: GR+AS+TF-ThM11, 184; GR+AS+TF-ThM5, 184; GR+AS+TF-ThM6, **184**; GR+NS-MoA10, 27; IS+SS-TuM6, 51
 McCleskey, T.M.: AC+SS-MoM5, 2
 McClory, J.W.: AC+TF-MoA8, 24
 McConney, M.: NS+BI-ThA4, 203
 McDaniel, A.H.: IS+SS-TuM6, **51**
 McDonnell, S.: GR+EM+MS+TF+MI-WeM11, 130; TF1-TuM11, 62
 McGaughey, A.J.H.: SS-WeA10, 170
 McHale, S.R.: AC+TF-MoA8, **24**
 McIntire, T.M.: IS-ThP2, 219; SS-TuP23, **114**
 Mckenna, K.: SS-TuP8, 111
 Mckenzie, B.B.: NS-TuA7, 81
 McNary, C.P.: IJ+BI+MN-MoM6, 7
 McPeak, K.M.: EN+TF-WeM4, 128; IS+SS-TuA2, **78**
 Mehn, D.: BI-TuM4, **44**
 Mehrhoff, T.K.: VT+MS-MoA3, 38
 Mehta, R.J.: EN+NS-WeA8, **155**
 Mei, D.: SS-ThM1, 193
 Mejía-García, C.: TF-ThP3, 227
 Melby, J.H.: EM-TuP3, **96**
 Meléndez Lira, M.A.: TF-TuP5, 115
 Melendez-Lira, M.A.: NS-TuP6, 101; TF-ThP21, 230
 Melitz, W.: EM+SS-WeA11, **154**; EM-TuP7, 97
 Mellhaoui, X.: PS1-TuM9, 54
 Membreno, D.: EN+EM-TuA3, 73
 Meng, L.: EN-TuM4, 47; PS+TF-ThM10, **191**; PS2-TuA1, 84
 Menguelti, K.: PS1-MoA11, 31
 Menkens, B.: IS+SS-TuA1, 78
 Menzel, D.: SS1-MoA7, **35**
 Merche, D.: SE+PS-MoM2, 12
 Mertens, S.: TF+EM-WeM10, 141
 Merz, T.A.: SS-ThM3, 194
 Messing, M.E.: IS+SS-TuM1, 50
 Methaapanon, R.M.: SS2+EM-MoM10, **16**
 Metz, A.: PS1-TuA10, **84**
 Mewes, T.: MI+TF-ThM3, 185; MI+TF-ThM4, 185
 Meyer III, H.M.: AS-TuP18, **94**; AS-TuP19, 94; EN+AS-ThM6, 181
 Meyer, F.W.: AS-TuP19, **94**
 Meyer, G.: SS-TuA3, **87**
 Meyer, R.: SS1-MoM9, 15; SS-FrM3, 241
 Meyer, T.: EM+MI-MoA4, 24
 Mi, Z.: GR+TF-TuA3, 76
 Michalak, W.: SE-TuP6, **110**
 Michallon, P.: TF2-TuM5, 63
 Michel, B.: SE+PS-MoM5, 13
 Michel, M.: SS-ThA1, 208
 Michelsen, P.K.: TR+MN+NS+SS-WeM6, 146
 Michel-Uribe, C.R.: NS-TuP21, 103; NS-TuP23, 103
 Michely, T.: GR+AS+TF-ThM3, **184**
 Mick, S.: IS+AS+NS+MI-WeM5, 131
 Micklefield, J.: SS2-WeM5, 139
 Midgett, A.G.: EN-MoA3, 25
 Miedaner, A.: EN+TF-WeM9, 128
 Migliori, A.: AC-TuA7, **67**
 Mignot, Y.: PS-MoM4, 11; PS-MoM5, 11
 Mikulski, P.T.: TR+NS+SS-WeA11, 173; TR-ThP4, 230
 Miller, B.P.: TR+MN+NS+SS-WeM11, **146**
 Miller, D.L.: GR+AS+TF+MI-ThA3, 201; GR+AS+TF+MI-ThA4, **201**; GR+SS+TF+EM-MoM6, 5
 Miller, P.: PS-TuP12, **107**
 Miller, S.: TF1-TuM12, **62**
 Milojevic, M.: EM+SS-WeA4, 153
 Milosavljevic, V.: PS-ThP1, **222**; SS-TuP10, 112
 Min, H.: PS2+BI-ThA8, **207**
 Minami, M.: PS1-MoA3, 30
 Minami, T.: EN+SS+TF-ThA2, 199; EN-ThP2, 217
 Minton, T.: TF-TuP19, 117
 Mirecki Millunchick, J.: SS2+EM-MoM5, 16
 Misewich, J.A.: NS-TuA1, 80
 Mishra, G.: AS1-ThM2, 175; AS-WeM10, 123; BI2+AS-TuA7, **70**; EW-TuL4, 66
 Misra, N.: PS2-TuM11, 54
 Mitchell, G.: AS-TuM11, 43
 Mitchell, J.N.: AC+SS-MoM5, 2
 Mittendorfer, G.M.: PS-WeM12, 136
 Mitterer, C.: SE-TuM12, **57**; SE-TuP6, 110
 Miyata, T.: EN+SS+TF-ThA2, 199; EN-ThP2, **217**
 Miyawaki, Y.: PS1-TuA8, **83**
 Miyayama, T.: AS-WeA2, 149; AS-WeM9, 122
 Mizutani, N.: PS+MN-WeM1, 133
 Mkhoyan, A.: IS+SS-TuA11, **79**
 Mochiki, H.: PS-WeM2, 135
 Modine, N.A.: SS2+EM-MoM5, 16
 Moellers, R.: AS-WeA4, 149
 Moennighoff, T.: TR+NS+SS-WeA8, 173
 Moffitt, C.: AS1-ThM2, 175; EW-TuL4, 66
 Moh, S.: EN+PS-MoM6, 4
 Mohan Rao, G.: EN+NS-WeA1, 154
 Mohn, F.: SS-TuA3, **87**
 Molinazzi, N.: MN-ThM9, 187
 Moll, N.: SS-TuA3, 87
 Momose, H.: PS1-WeA3, 164
 Mönig, H.: NS+AS+MN-WeM9, 132
 Montgomery, E.: EL+AS+EM+MS+TF-ThP5, **216**; TF+SE-WeM9, 143
 Moody, D.D.: GR-TuP6, **100**
 Moon, D.W.: BI2+AS-TuA9, **71**
 Moon, H.K.: TF+EM-WeM11, **141**
 Moon, J.S.: GR+MS-WeA1, 156; GR+MS-WeA9, **157**
 Moon, J.Y.: PS1-TuA12, **84**
 Moore, D.P.: AC+SS-MoM3, **2**; AC+SS-MoM4, 2; AC+SS-MoM5, 2; AC-TuA2, 67
 Moore, E.W.: MN-ThM5, 187; MN-ThM6, 187
 Moorish, R.: LB-WeA4, 159
 Moorman, M.W.: BI+MN-FrM3, 232
 Morales, C.: TF+EM-MoM11, **19**
 Mori, A.: PS2+BI-ThA1, 206
 Morikawa, Y.: PS+MN-WeM1, **133**; PS+MN-WeM2, 133
 Morita, Y.: PS1-ThA1, **205**
 Moriwaka, H.: SE+TF-WeA7, 168
 Moro, F.: PS+MN-WeM10, 135
 Moroz, P.E.: PS1-ThA10, **206**; PS-TuP12, 107
 Morris, P.A.: EM+MI-MoA4, 24
 Morse, A.J.: TR+NS+SS-WeA2, 173
 Mortensen, D.: EL+AS+EM+MS+TF-ThP4, **216**
 Moshkalev, S.A.: GR-TuP3, 99
 Motyka, M.A.: EL+AS+EM+MS+TF-FrM3, **234**
 Mouhib, T.: AS-WeA11, **151**
 Moulder, J.F.: AS-WeM9, 122; SS-TuP22, 114
 Mount, A.S.: MB+BI-MoM10, **9**
 Mousavi, A.: MN-FrM7, **238**
 Moyer, J.A.: EM+MI-MoA7, **24**
 Mudavakkat, V.H.: TF-WeA9, **172**
 Mudiyansele, K.: SS-WeA11, 170
 Mudrick, J.P.: EN+NS-WeM5, 125
 Mueller, A.H.: EN+SS-FrM1, 236
 Mueller, K.: MI+EM-TuA9, 80
 Müller, B.: BI-TuM6, **44**
 Mullet, C.: SS2-MoA10, **37**; SS-TuP3, **110**
 Mullins, D.R.: AC+TF-MoA7, **24**; SS1-MoM1, 14; SS-ThM10, 195; SS-ThM11, 195
 Mulugeta, D.: SS1-MoA7, 35
 Munbodh, K.: MI+TF-ThM2, **185**
 Munichandraiah, N.: EN+NS-WeA1, 154
 Munro, J.: PS1-ThA2, **205**
 Murai, Y.: TF-ThP12, 228
 Muramoto, S.: AS-WeA1, **149**
 Murata, Y.: GR+AS+TF-ThM12, 185; GR+AS+TF-ThM5, 184
 Muratore, C.: SE+PS-MoA3, 33; SE-TuP5, 109
 Murayama, A.: PS2-WeA4, 166
 Murayama, T.: PS+MN-WeM2, **133**
 Murray, C.E.: LB-WeA1, 158
 Murray, P.T.: EN+EM-TuA4, 73; TF-ThA7, **210**
 Muscat, A.J.: BI1-WeM2, 123; EM+SS-WeA3, 153; TF1-TuM12, 62; TF-TuA11, 90
 Musgrave, C.: TF-MoA3, **37**
 Mushfiq, M.: EN+NS-ThM12, 183
 Music, D.: SE-TuA10, **87**; SE-TuA11, 87; SE-TuM9, 56
 Muzik, H.: SS2-TuM12, **60**
 Myers, J.D.: EN+NS-WeM5, **125**
 Myers, T.H.: TF-ThA10, 211
 Myers-Ward, R.L.: EL+AS+EM+MS+TF-FrM8, 235; GR+MS-WeA1, 156; GR+MS-WeA9, 157; GR+SS+TF+EM-MoM8, 5; LB-WeA2, 159; LB-WeA3, 159
 Myneni, G.R.: EN+AS-ThM10, 181
 Myung, K.D.: EM-TuP14, **98**; TF-ThP17, 229
 — **N** —
 Na, H.D.: TF2-TuM3, 63; TF-TuP8, **116**
 Nabok, D.: SS2-TuM5, 59
 Nachimuthu, P.: EN+AS-ThM3, **180**; NS-MoA9, 29; TF-ThP11, 228; TF-WeA12, 172
 Nackashi, D.: IS+AS+NS+MI-WeM5, 131
 Nadesalingam, M.P.: SS2-MoA7, 36
 Nagamoto, K.: EN-TuM3, **47**
 Nagatomi, T.: AS-TuP4, 92
 Nagpal, P.: EN+EM-TuA7, **73**
 Nagpure, S.: AS-TuP9, **93**

- Nah, J.: GR+EM+MS+TF+MI-WeM9, 130
 Nahif, F.: SE-TuM9, **56**
 Naik, M.: PS-MoM10, 11
 Naik, R.: NS+BI-ThA4, 203
 Naitabdi, A.: NS-TuP20, 103
 Nakagawa, A.: PS-WeM2, **135**
 Nakajima, A.: SS-TuP5, 111
 Nakajima, K.: SE+TF-WeA7, 168; SE-TuP3, 109
 Nakakubo, Y.: PS1-MoA3, 30
 Nakamura, I.: SS-TuP25, **114**; SS-TuP4, 111
 Nakamura, J.: GR+NS-MoA2, **26**; GR-TuP1, 98; NS-TuP4, 101
 Nakamura, M.: PS1-TuA8, 83
 Nakamura, W.: EN+PS-MoM1, 3
 Nakanaga, T.: AS-TuP1, 92
 Nakano, T.: PS+TF-ThM5, 190
 Nakayama, K.S.: NS-ThM10, **189**
 Nakazaki, Y.: PS2-TuM9, **55**
 Nam, H.: IS+AS+NS+MI-WeM1, 130
 Nam, S.-H.: EN-ThP8, **218**
 Namkoong, W.: AS-TuM12, 43
 Nampoori, H.V.: EN+EM-TuA10, **74**; TF-ThA8, 210; TF-ThP8, 228
 Namura, K.: SE-TuP3, **109**
 Nanayakkara, S.U.: IS+BI+AS-WeA9, 158; NS+EM+EN-WeA7, 163
 Nandasiri, M.: TF-WeA12, **172**
 Narayanan, V.: TF1-TuM6, 61
 Narita, S.: TF-TuP14, **117**
 Nasi, L.: NS-TuP17, 103
 Nasse, J.: IS+BI+AS-WeA2, 157
 Natarajarathinam, A.: MI+TF-ThM9, **186**
 Nath Premnath, R.: NS-MoM8, 10
 Navin, J.: SS1-MoM6, 14
 Ndi, C.P.: B11-TuA3, 70
 Negm, S.: EN-ThP10, 218; EN-ThP11, 219; EN-ThP12, 219
 Negrete, O.A.: BI+MN-FrM3, 232
 Nekuda, J.A.: EN+TF-WeM9, 128
 Nelin, C.J.: SS-ThM9, 194; SS-TuP17, **113**
 Nelson, F.J.: GR+AS+TF+MI-ThA8, 201
 Nemani, S.: PS-MoM10, 11
 Nemanic, V.: EN-ThP5, 218
 Nemanich, R.J.: EN-ThP5, 218
 Neppi, S.: EM-TuM5, 46
 Netolicky, W.: EW-WeL1, **148**
 Nettikadan, S.R.: B11+NS-ThM2, 176; NS-TuP2, 100
 Netzer, F.P.: SS1-WeM5, **137**; SS1-WeM9, 138
 Neugebauer, J.: SS1-WeM1, 137
 Neumann, M.J.: EN-TuM4, 47; PS2-MoA9, 32; PS2-TuA1, 84
 Neumayer, D.: GR+EM+MS+TF+MI-WeM5, 129
 Newberg, J.: SS-ThA1, 208
 Newell, D.B.: GR+TF-TuM10, 49; GR+TF-TuM9, 49
 Neyerlin, K.C.: EN+AS-ThM1, 180
 Ng, K.C.: IJ+BI+MN-MoM11, 8
 Ng, T.C.: IS+BI+AS-WeA1, 157
 Nichols, M.: EM-TuA10, **73**
 Nie, S.: GR+AS+TF-ThM11, 184; GR+AS+TF-ThM6, 184; GR+SS+TF+EM-MoM2, 5; SS-ThA7, **208**
 Nie, X.: TR+NS+SS-WeA12, 174; TR-ThP8, 231
 Niehuis, E.: AS-WeA3, 149; AS-WeA4, 149
 Nielsch, K.: TF-WeM1, 144
 Nieto Zepeda, K.: TF-TuP5, 115
 Nieto-Zepeda, K.E.: NS-TuP6, 101; TF-ThP21, 230
 Nijem, N.: EN+NS-ThM3, **182**
 Nikiforov, M.: TF-TuP17, 117
 Nilsson, A.: SS-ThA1, 208
 Nimisha, C.S.: EN+NS-WeA1, **154**
 Ning, N.: PS-ThM10, 193
 Nishi, Y.: EM-TuA10, 73; EM-TuP10, 98; TF+EM-WeM9, 141
 Nishida, K.: TF-TuP2, 115
 Nishimura, M.: SS-TuP5, 111
 Nishino, M.: PS-MoM3, **10**
- Nishiwaki, M.: VT-WeM10, **147**; VT-WeM9, 147
 Nisol, B.: SE+PS-MoM2, 12
 Nita, G.M.: EL+AS+EM+MS+TF-FrM4, 234
 No, K.: NS-TuP1, 100
 Nobis, F.: EN+TF-TuA2, 74
 Noguchi, T.: NS-TuP22, 103; VT-WeM10, 147
 Noguchi, Y.: PS-FrM6, 240
 Noh, J.: EM-TuP9, **97**
 Noh, J.H.: EM-TuP9, 97; TF-TuP17, **117**
 Noirfalise, X.: EN+SS+TF-ThA1, 199
 Nolen, J.: TF-WeM4, 144
 Noll, R.J.: VT+MS-MoA1, 38
 Nolting, F.: MI+EM-TuA9, 80
 Nomoto, J.-I.: EN+SS+TF-ThA2, **199**; EN-ThP2, 217
 Nonaka, H.: AS-TuP1, 92
 Noor-A-Alam, M.: SE-TuM6, **56**
 Nordblad, P.: NS+BI-ThA3, 203
 Norde, W.: BI+MN-FrM7, 233; BP-SuA1, **1**
 Nordgren, J.: AC+TF-MoA6, 23
 Norman, A.G.: AS-TuA11, 69; EL+AS+EM+MS+TF-ThA8, 198
 Norris, D.: EN-ThP6, 218
 North, S.H.: BI-ThP19, **215**
 Norton, P.R.: BI-ThP18, 215; BI-TuM5, 44
 Nottbohm, C.T.: GR+TF-TuM3, 48
 Noufi, R.: EN+TF-WeM6, 128
 Novikova, T.: EL+AS+EM+MS+TF-ThA6, **197**
 Nowak, J.: BI-TuM4, 44
 Nozawa, T.: PS2-TuA2, 84
 Nozik, A.J.: EL+AS+EM+MS+TF-ThA8, 198; EN-MoA3, **25**
 Nsimama, P.D.: TF+EN-MoM8, 20
 Ntwaeeborwa, O.M.: TF+EN-MoM8, **20**
 Nuckolls, C.: NS+BI-ThA1, 202
 Nukaga, O.: PS2-WeA3, 166; PS2-WeA8, 167
 Nunney, T.: AS-WeM11, 123; EN+AS-ThM6, **181**; SS-TuP18, 113
 Nurmi, J.T.: NS-MoA9, 29
 Nyakiti, L.O.: GR+SS+TF+EM-MoM1, 5; LB-WeA2, **159**; LB-WeA3, 159
- **O** —
 O, B.H.: PS-ThP12, 224
 O'Brien, K.E.: MN-ThP6, **221**
 O'Brien, P.A.: IS+BI+AS-WeA9, 158
 O'Brien, S.: MN-FrM3, 237
 Ochsner, M.: B11+NS-ThM3, 177
 Ocola, L.E.: MN-ThM11, 188; NS-MoM8, **10**
 Odén, M.: SE-TuM4, 56
 Odum, T.W.: NS+EM+EN-WeA3, **162**
 Odysseos, A.: TF+EM-MoM10, 18
 Oehrlein, G.S.: PS1-WeA2, 164; PS1-WeA7, 165; PS-ThM10, 193
 Ogaki, R.: B11+NS-ThM1, **176**
 Oh, D.-W.: SE-TuA9, **87**
 Oh, J.: GR+NS-MoA2, 26
 Oh, J.S.: AS-TuP4, 92; PS-ThP16, 225; PS-ThP17, **225**; PS-ThP18, 225
 Oh, J.-S.: PS2-MoA11, **33**
 Oh, K.-G.: MN-ThP9, 221
 Oh, K.S.: PS2-WeA7, 167
 Oh, S.K.: AS-TuP4, 92
 O'Hayre, R.P.: AS-TuA11, 69; EN+AS-ThM1, 180; EN+TF-WeM9, 128
 Ohiwa, T.: PS1-TuA2, 82
 Ohlhausen, J.A.: AC+SS-MoM11, 3; AS1-ThM6, **175**; AS-TuP24, 95; TR+MN+NS+SS-WeM4, 145
 Ohno, Y.: PS2-WeA4, 166
 Ohsawa, Y.: PS1-MoA10, 31
 Ohsugi, T.: NS-TuP4, **101**
 Ohta, T.: GR+EM+MS+TF+MI-WeM6, 130; GR+SS+TF+EM-MoM2, **5**
 Ohtake, H.: PS2-WeA8, 167
 Ohtsuka, S.: PS2-WeA3, 166
 Ohuchi, F.S.: EM-TuA7, 72; EM-TuP11, 98
 Okamoto, H.: NS-TuP3, 100
 Okamoto, S.: PS-WeM2, 135
- Oldham, C.: IS+AS+NS+MI-WeM11, 132; TF-MoA8, **38**; TF-WeM5, 144
 Olmstead, M.A.: EM-TuA7, 72; EM-TuP11, 98
 Olsen, I.: VT+MN-MoM11, 22
 Olson, C.S.: MI+EM-TuA10, 80
 Olson, D.A.: VT+MN-MoM3, 20
 Olson, T.: EN+AS-ThM1, 180
 Olvera, M.: TF-ThP21, 230
 Olynick, D.: PS-WeM3, 135
 Omarjee, V.: PS1-TuA4, **83**; PS-MoM9, 11
 Ondeck, N.: NS-ThM1, 188
 O'Neill, K.: EN+AS-ThM1, 180
 Onishi, T.: AC-TuA3, **67**
 Ono, K.: PS1-MoA3, 30; PS2-WeA3, 166
 Ono, L.K.: SS1-MoA2, **34**
 Ono, T.: NS-ThM10, 189; PS1-WeA9, 165
 Ooya, Y.: PS-MoM3, 10
 Opila, R.: EN+TF-TuA9, 75; TF+EM-WeM3, 140
 Oppeneer, P.M.: AC+SS-MoM8, 2
 Orihuela, B.: MB+BI+AS-MoA8, 28
 Ormrod, S.: VT+MN-MoM11, 22
 Orr, G.: NS-MoA10, 29
 Ortega, R.: BI-TuM12, 45
 Osgood, R.M.: NS+AS+MN-WeM4, 132; SS-TuA7, 88
 O'Sullivan, D.: EW-WeM8, 129
 O'Sullivan, D.M.: PS-ThP8, 223
 Otte, A.F.: GR+SS+TF+EM-MoM9, 6
 Ou, Y.C.: BI-ThP3, 212; MN-ThP3, **220**
 Ouerfelli, N.: AC-TuA8, 67
 Oughaddou, H.: GR+SS+TF+EM-MoM10, 6
 Outlaw, R.A.: AC+SS-MoM9, 3
 Ouyang, Z.: PS2-MoA9, **32**; VT+MS-MoA1, 38
 Overbury, S.H.: AC+TF-MoA7, 24; SS1-MoM1, 14; SS-ThM10, 195; SS-ThM11, **195**
 Overzet, L.J.: PS+TF-ThM11, 191; PS2-MoA6, 32; PS2-MoA8, 32
 Owen, T.: TF-WeM4, 144
 Ozbolat, I.T.: AS-TuA9, 69
- **P** —
 Padron-Wells, G.: PS+TF-ThM11, 191; PS2-TuM6, **55**; PS-TuP15, 107
 Paffett, M.T.: AC-TuA2, **67**
 Page, S.C.: AS-WeM10, 123
 Pai, S.S.: NS-TuP25, 104
 Pai, W.W.: SS2-TuM3, **59**
 Pakhomov, A.: EM-TuP11, 98
 Pal, S.: TF+EM-MoM11, 19
 Palacio, M.: SS-TuP21, **114**
 Palacios-Padrós, A.: EN+TF-TuA12, 76
 Pallitto, M.: BI-ThP17, 215
 Palma, M.: NS+BI-ThA1, **202**
 Palmer, R.E.: SS-TuA8, 88
 Pan, J.S.: EN+TF-TuA7, 75
 Pan, W.: GR+EM+MS+TF+MI-WeM6, 130
 Panagopoulos, T.: PS1-TuM3, 53
 Pancheri, L.: BI-ThP15, 215
 Pandey, A.: EN+AS-ThM3, 180
 Pandey, R.R.: BI+MN-FrM2, **232**; MN-ThA9, 202
 Pangan-Okimoto, K.: EN+TF-WeM5, 128
 Pannier, A.K.: EL+AS+EM+MS+TF-ThA7, 198
 Papaioannou, G.J.: MN-FrM9, 239
 Pappas, D.D.: SE+PS-MoM9, 13
 Paredis, K.: MI-ThP2, **220**
 Pargon, E.: PS+MN-WeM5, 134; PS1-MoA1, 30; PS1-MoA11, 31; PS1-TuM4, 53; PS1-TuM9, 54; PS1-WeA4, 164
 Park, B.J.: PS-TuP9, 106
 Park, G.S.: AS-TuP4, 92
 Park, H.H.: EM-TuP12, 98
 Park, J.B.: PS-ThP16, **225**; PS-ThP17, 225; PS-ThP18, 225
 Park, J.H.: EN+SS+TF-ThA7, **200**
 Park, J.S.: TF+EM-WeM5, 140
 Park, J.-S.: EM-TuP5, 97; GR+EM+MS+TF+MI-WeM2, 129; PS-TuP2, **104**
 Park, J.-S.: TF-ThP17, 229
 Park, J.-S.: TF-ThP18, **229**
 Park, J.W.: PS1-TuA12, 84

- Park, J.Y.: PS1-TuA9, 84; PS-ThM2, 191; TF-ThP9, **228**
- Park, K.A.: VT-TuP5, 119
- Park, K.J.: PS+TF-ThM10, 191
- Park, M.: NS-TuP1, 100
- Park, S.G.: PS-ThP12, 224
- Park, S.H.: TF-TuP9, 116
- Park, S.-K.: PS+MN-WeM9, 134; PS1-TuA12, 84
- Park, T.-H.: NS+EM+EN-WeA7, 163
- Park, T.J.: TF1-TuM11, 62
- Park, Y.C.: PS2-WeA7, 167; PS2-WeA9, 167
- Parlinska-Wojtan, M.: SE-TuM10, 57
- Parpia, J.M.: MN-ThM4, 187
- Parsons, G.N.: IS+AS+NS+MI-WeM11, **132**; TF-MoA1, 37; TF-MoA8, 38; TF-TuA3, 89; TF-WeM5, 144
- Pascher, H.: TF-ThP3, 227
- Pascolo, L.: BI-TuM12, 45
- Paskiewicz, D.M.: SS2-MoA6, 36
- Paskova, T.: EM+SS-ThM3, 178
- Pasquali, M.: NS-TuA3, 81
- Pasquardini, L.: BI-ThP15, 215
- Pasquarelli, R.M.: EN+TF-WeM9, 128
- Patel, A.: EN+AS-ThM2, **180**
- Patel, R.: PS+TF-ThM3, **190**
- Paterson, A.: PS1-TuM3, 53
- Patriarche, G.: PS-ThM3, 192
- Patscheider, J.: SE-TuM10, **57**
- Patterson, M.: SS1-MoA9, 35
- Patterson, W.: EN+SS-FrM5, **237**
- Patyukov, S.I.: PS-TuP7, 105
- Paul, D.F.: AS-TuP14, **94**
- Pawel, S.J.: AS-TuP18, 94
- Pawin, G.: SS-TuA2, 87
- Pawlikowski, L.J.: BI-ThP9, **213**
- Pawlowski, R.P.: SS-WeA1, 169
- Payzant, E.A.: EN+TF-WeM6, 128
- Pearton, S.J.: BI2+NS-ThM11, 178
- Pecher, P.: SE-TuM10, 57
- Peden, C.H.F.: SS-ThM1, **193**
- Pedersen, J.: NS-MoA8, 29
- Pederzoli, C.: BI-ThP11, 214; BI-ThP15, **215**
- Peebles, H.C.: VT+MS-MoA3, **38**
- Pegalajar Jurado, A.: PS2+BI-ThA3, 207
- Pei, L.: LB-WeA7, **160**
- Péllisson, A.: SE-TuM10, 57
- Pellin, M.J.: EN+NS-ThM12, 183; TF+EN-MoM1, 19
- Pender, J.: PS-MoM10, 11
- Peng, H.: BI+MN-FrM9, 233
- Peng, Q.: NS-TuM10, 52; TF-MoA1, 37; TF-TuA3, 89; TF-TuA8, **90**
- Peng, W.-P.: SS-TuP16, 113
- Peng, X.: NS-TuA1, **80**
- Penkala, R.A.: BI-WeA9, 152
- Penn, R.L.: NS-MoA9, 29
- Penner, R.M.: NS+EM+EN-WeA10, 163
- Pensack, R.D.: EN-MoA1, 25
- Penzo, E.: NS+BI-ThA1, 202
- Perebeinos, V.: GR+EM+MS+TF+MI-WeM5, 129
- Pereira, J.: PS1-TuM9, **54**
- Perez, F.A.: MI+TF-ThM10, **186**; MI+TF-ThM2, 185
- Perez, L.M.: EM-TuM6, 46
- Pérez, R.: NS+AS+MN-WeM9, 132
- Pérez-Centeno, A.: NS-TuP21, 103; NS-TuP23, **103**
- Perkins, F.K.: GR+TF-TuA8, 77
- Perkins, K.: GR+NS-MoA7, 27
- Perng, T.P.: NS-TuP10, 102
- Perng, Y.-C.: EN+EM-TuA3, **73**; TF1-TuM5, 61
- Peroz, C.: PS-WeM3, 135
- Perrine, K.A.: SS-TuP15, **113**
- Perry, S.S.: TR+MN+NS+SS-WeM9, **146**
- Peterson, G.P.B.: SE-TuA4, 86
- Peterson, R.: NS-MoA8, 29
- Petit, L.: AC+MI-TuM5, **41**
- Petit-Etienne, C.: PS1-MoA1, 30; PS1-TuM4, 53
- Petkovic, L.M.: EM+MI-MoA9, **25**
- Petmecky, D.W.: VT-WeM1, 146
- Petrach, R.V.: GR+TF-TuM2, **48**; TR+NS+SS-WeA9, 173
- Petrik, N.: SS-FrM10, **242**; SS-ThA6, 208
- Petrosky, J.C.: AC+TF-MoA8, 24
- Petrov, I.: GR+AS+TF-ThM12, 185; TF+EM-MoM5, 18
- Petrova, V.: GR+AS+TF-ThM12, 185
- Petrovykh, D.Y.: BI-WeA12, 153
- Petsev, D.N.: BI+MN-FrM5, 232
- Pettitt, M.E.: MB+BI+AS-MoA3, 28
- Pham, C.: AC+TF-MoA2, 23; PS1-ThA7, 206
- Phang, I.Y.: MB+BI-MoM3, 8
- Phillips, M.: GR+SS+TF+EM-MoM6, 5
- Phillpot, S.R.: TR+MN+NS+SS-WeM12, 146
- Phinney, L.M.: MN-ThA2, **202**
- Piasecki, J.D.: AS2-ThM12, 176; EW-TuA6, 76
- Picraux, S.T.: NS-ThM9, **189**; NS-TuM5, 52
- Piekos, E.S.: MN-ThA2, 202
- Pietryga, J.M.: EN+NS-ThM5, **182**
- Pietsch, M.: EN+NS-WeM11, **127**
- Piner, R.D.: GR-TuP6, 100
- Pinna, N.: TF-MoA6, **37**
- Piras, F.: BI-ThP11, 214
- Pirkle, A.: GR+EM+MS+TF+MI-WeM11, **130**
- Pivovar, B.: EN+AS-ThM1, 180
- Piyasena, M.E.: BI+MN-FrM5, 232
- Plach, T.: NS-TuP6, 101; PS-WeM12, **136**
- Plaisant, M.: NS-TuP16, **102**
- Plana, R.: MN-FrM9, 239
- Plummer, M.A.: AS-TuP20, 94; TF-ThP19, 229
- Plut, T.: PS+MN-WeM4, 134
- Poda, A.: TR+MN+NS+SS-WeM5, 146; TR-ThP1, 230
- Podraza, N.J.: EL+AS+EM+MS+TF-FrM3, 234; EL+AS+EM+MS+TF-ThA10, 198
- Poelker, M.: VT-WeM4, 147
- Poggi, M.A.: MB+BI+AS-MoA11, **29**
- Pois, H.: AS-TuM12, 43
- Pokharel, S.: GR+TF-TuA3, 76; PS1-WeA1, 164
- Pokhodnya, K.I.: MI+EM-TuA10, 80
- Polcik, P.: SE-TuM10, 57
- Poleunis, C.: AS-WeA11, 151
- Polsky, R.: EN+NS-WeA2, **154**
- Pomerantz, U.: MN-ThM9, 187
- Ponomarev, M.: NS+EM+EN-WeA8, 163
- Pons, P.: MN-FrM9, 239
- Ponti, J.: BI-TuM12, 45
- Popov, V.: EL+AS+EM+MS+TF-ThA6, 197
- Popovic, D.: SS-TuP10, **112**
- Popovic, L.C.: PS-ThP1, 222
- Popovitch-Biro, R.: EN+TF-WeM3, 127
- Porter, L.M.: EM+SS-ThM3, 178; EM-TuP3, 96
- Porter, S.: EN+SS-FrM2, 236
- Portoles, J.F.: AS-TuP25, **95**
- Posseme, N.: PS-MoM1, **10**
- Potapenko, D.V.: NS+AS+MN-WeM4, 132; SS-TuA7, **88**
- Potocar, T.G.: SS2-TuM5, 59
- Powell, C.J.: AS-TuM1, **42**; AS-WeM1, 122
- Prathiba, G.: MI+TF-ThM12, **186**
- Pratt, J.R.: TR+NS+SS-WeA1, 172
- Preble, E.A.: EM+SS-ThM3, 178
- Priest, C.: SE+PS-MoM8, 13
- Principe, E.: AS1-ThM6, 175
- Priyantha, W.: GR-TuP6, 100
- Profijt, H.B.: TF+EN-MoM6, 20
- Proksch, R.: EW-TuM8, 48; NS+AS+MN-WeM10, 133
- Pronshinske, A.: GR-TuP5, 99
- Prosa, T.: AS-TuA3, 68
- Provenzani, A.: BI-ThP11, 214
- Provo, J.L.: VT-WeM5, **147**
- Puffall, M.R.: MI-WeA3, 161
- Pugmire, D.L.: AC+SS-MoM3, 2; AC+SS-MoM4, **2**
- Pursel, S.M.: EN+NS-ThM11, **183**
- Purushothaman, S.: PS1-TuA7, 83
- Puschign, P.C.: SS2-TuM5, 59
- Pushkarev, V.V.: SS1-MoM5, 14; SS-WeA9, 170
- Putnam, S.A.: SE-TuA12, **87**
- Pylypenko, S.: EN+AS-ThM1, **180**
- Q —**
- Qian, L.: EN+TF-TuA3, 74
- Qiao, L.: TF-ThA6, 210
- Quattrone, A.: BI-ThP11, 214
- Queen, A.: EN+AS-ThM1, 180
- Quickel, T.E.: TF1-TuM5, 61
- Quinlan, R.A.: SS-ThM12, **195**
- Quiñones Galván, J.G.: TF-TuP5, **115**
- Quiñones-Galvan, J.G.: NS-TuP6, 101; TF-ThP21, 230
- Quintana, M.: AS-TuP26, 96
- R —**
- Rachbauer, R.: SE-TuM5, 56
- Rachmady, W.: EM+SS-WeA3, 153
- Rack, P.D.: EM-TuP9, 97; SS2-WeM1, **138**; TF+EM-MoM3, 17; TF-TuP17, 117
- Radadia, A.: BI+MN-FrM8, 233
- Raddiar, M.: EN-MoA11, 26
- Rader, D.J.: SE-TuA3, 86
- Rading, D.: AS-WeA4, 149
- Radosavljevic, M.: PS1-TuM10, 54
- Rahman, M.: LB-WeA4, 159
- Rahman, T.S.: SS2-MoA3, 36; SS2-MoA4, 36; SS2-TuM4, 59; SS-ThM5, **194**; SS-TuA12, 88
- Rai, V.R.: TF-TuA2, **89**
- Raja, L.: PS1-ThA8, **206**
- Rajesh, B.: EN+NS-WeA9, **155**
- Ramana, C.V.: EL+AS+EM+MS+TF-ThP3, 216; EN+AS-ThM9, **181**; MI+TF-ThM11, 186; NS-TuP13, 102; SE-TuM6, 56; TF-TuP11, 116; TF-WeA9, 172
- Ramanath, G.: AS-TuP23, 95; EN+NS-WeA8, 155; EN-MoA11, 26
- Ramaswamy, K.: PS2-TuM2, 54
- Ramesh, R.: NS-MoM9, 10
- Ramirez, E.: AS-TuP26, 96
- Ramm, J.: SE-TuM1, 56
- Rampulla, D.M.: NS-TuP14, **102**
- Ranade, A.N.: SE-TuM11, **57**
- Randall, J.N.: NS-TuM3, **52**; SS2-MoA1, 36; SS2-MoA7, 36
- Rangel-Kuoppa, V.T.: NS-TuP6, 101
- Ranson, P.: PS+MN-WeM10, 135; PS2-MoA6, 32; PS2-MoA8, 32; PS-ThM4, 192
- Rao, M.R.: MN-ThM12, **188**
- Rao, Y.Q.: AS-TuM11, 43
- Rashkeev, S.N.: EM+MI-MoA9, 25
- Rathbone, J.: VT+MS-MoA6, 39; VT+MS-MoA8, 39
- Ratner, D.M.: BI1-WeM3, **123**
- Raub, A.: EN+NS-WeA2, 154
- Rauf, S.: EN+PS-MoM3, 3; PS1-ThA3, 205; PS1-ThA6, 205; PS1-TuM5, 54; PS2-TuA11, 85; PS2-TuA7, **85**; PS2-TuA8, 85; PS2-TuM1, 54; PS2-TuM2, 54
- Rauschenbach, B.: TF+SE-WeM3, 142
- Rauscher, H.: BI-TuM4, 44
- Ravishankar, N.: EN-MoA11, 26
- Reardon, D.: TF-ThP19, 229
- Rebe Raz, S.: BI+MN-FrM7, 233
- Rebello de Figueiredo, M.: SE-TuP6, 110
- Rebholz, C.: TF+EM-MoM10, 18
- Reed, A.N.: SE+PS-MoA3, **33**
- Reed, D.T.: AC-TuA4, 67
- Reed, J.A.: BI1+NS-ThM5, **177**
- Reichert, L.A.: EN+TF-TuA11, 75
- Reid, J.: PS1-TuM9, 54
- Reimhult, E.O.: NS+BI-ThA11, 204; NS+BI-ThA9, **204**
- Reinhardt, M.: IS+BI+AS-WeA3, 157
- Reinke, P.: MI-WeA4, 161
- Remmert, J.L.: SE-TuP4, **109**
- Ren, F.: BI2+NS-ThM11, **178**
- Ren, H.: TF+EM-WeM9, **141**
- Ren, M.: SS1-MoA9, 35

- Reniers, F.: SE+PS-MoM1, 12; SE+PS-MoM2, 12
 Renzi, R.F.: BI+MN-FrM3, 232
 Repp, J.: SS-TuA3, 87
 Reshchikov, M.A.: EM+SS-ThM11, 179
 Restrepo, J.S.: AS-TuP7, 93; AS-TuP8, 93
 Retterer, S.T.: MI+TF-ThM1, 185
 Retzko, I.: AS-TuP12, 93
 Reutt-Robey, J.E.: EN+NS-WeM10, 126; SS2-TuM6, 60
 Reyren, N.: NS-MoM5, 9
 Rhallabi, A.: PS-TuP6, 105
 Ricci, M.: BI-ThP17, 215
 Ricciardo, R.: EM+MI-MoA4, 24
 Richmann, M.K.: AC-TuA4, 67
 Richter, F.: EN+TF-TuA2, 74
 Richter, L.J.: EN+NS-WeM6, 126
 Ricken, J.B.: BI+MN-FrM3, 232
 Riddle, A.C.: VT-WeM1, 146
 Riedo, E.: GR+NS-MoA9, 27
 Rigsbee, M.: EN+AS-ThM10, 181
 Riley, L.A.: EN+EM-TuA1, 73
 Rinckel, T.: VT-TuP13, 120
 Rincón, R.A.: BI-ThP10, 213
 Rincon, V.C.: TF-ThA8, 210; TF-ThP8, 228
 Rippard, W.H.: MI-WeA3, 161
 Riseborough, P.S.: AC+SS-MoM8, 2
 Risse, T.: SS-ThM6, 194
 Rissom, Th.: EN+TF-WeM3, 127
 Ritter, C.: TR+NS+SS-WeA8, 173
 Rittschof, D.: MB+BI+AS-MoA8, 28
 Ritz, E.: EN-TuM4, 47
 Rivera, I.: GR-TuP7, 100
 Rizzoni, G.: AS-TuP9, 93
 Roark, C.M.: PS-TuP16, 107
 Robach, O.: SS1-MoA1, 34
 Robel, I.: EN+NS-ThM5, 182
 Roberts, A.J.: AS1-ThM2, 175; AS-WeM10, 123; BI2+AS-TuA7, 70; EW-TuL4, 66
 Roberts, C.J.: SS2-WeM5, 139
 Roberts, M.: EN+NS-WeA2, 154
 Robertson, I.M.: IS+AS+NS+MI-WeM6, 131
 Robertson, J.L.: AC+MI-TuM11, 41
 Robey, S.W.: EN+NS-WeM10, 126; SS2-TuM6, 60
 Robinson, J.: GR+EM+MS+TF+MI-WeM1, 129; GR+MS-WeA1, 156; GR+MS-WeA9, 157
 Robinson, J.A.: GR+NS-MoA7, 27; GR+NS-MoA9, 27; GR+TF-TuA8, 77; NS-TuM6, 52
 Robinson, M.A.: AS-WeA9, 150
 Robson, M.: EN+SS-FrM5, 237
 Roca i Cabarrocas, P.: EL+AS+EM+MS+TF-ThA9, 198
 Rochat, N.: TF2-TuM4, 63
 Rodenhausen, K.B.: EL+AS+EM+MS+TF-FrM10, 236; EL+AS+EM+MS+TF-ThA7, 198
 Rodríguez, E.: TR-ThP3, 230; TR-ThP6, 231
 Rodriguez, J.: IJ+BI+MN-MoM8, 7
 Rodriguez, J.A.: IS+SS-TuA1, 78; SS1-MoM10, 15
 Rodriguez, M.A.: TF-ThP2, 226
 Rodriguez-Santiago, V.: SE+PS-MoM9, 13
 Rogers, B.: EN+SS+TF-ThA6, 199
 Rogers, J.A.: EN-TuM5, 48
 Rogers, P.D.: EL+AS+EM+MS+TF-FrM4, 234
 Roh, J.S.: PS1-TuA12, 84
 Roldan Cuenya, B.: SS1-MoA2, 34
 Roldan, B.: NS-TuP20, 103
 Romel, C.: VT-TuP13, 120
 Romero, M.J.: EN+AS-ThM4, 180; EN+TF-TuA8, 75
 Roos, M.: GR+TF-TuA7, 77
 Rosaz, G.M.: TF+EM-MoM4, 17
 Rosenberg, S.: SS2-WeM3, 138
 Rosenhahn, A.: MB+BI+AS-MoA6, 28
 Rosenthal, A.: IS+BI+AS-WeA2, 157
 Ross, A.J.: GR+EM+MS+TF+MI-WeM6, 130
 Rossi, F.: BI+MN-FrM7, 233; BI-TuM12, 45; BI-TuM2, 44; BI-TuM4, 44
 Rossi, P.: AS-WeM1, 122
 Rossnagel, S.M.: BI+MN-FrM9, 233; TF1-TuM6, 61; TF-WeA11, 172
 Rosso, K.M.: IS+AS+NS+MI-WeM2, 130
 Rotenberg, E.: GR+AS+TF-ThM6, 184
 Rotunno, E.: NS-TuP17, 103
 Rousseau, A.: PS-FrM1, 239
 Rousseau, R.J.: SS1-WeM9, 138; SS-FrM7, 241; SS-ThM1, 193
 Roussel, P.: AC+SS-MoM3, 2; AC+SS-MoM4, 2
 Rouxinol, F.P.: GR-TuP3, 99
 Rowe, J.E.: GR-TuP5, 99
 Rowley, P.N.: EN+PS-MoM6, 4
 Roy, C.K.: SE-TuM6, 56
 Roy, D.: AS-TuA4, 68
 Ruan, M.: GR+AS+TF+MI-ThA3, 201; GR+AS+TF+MI-ThA4, 201
 Rubloff, G.W.: EN+SS+TF-ThA10, 200; TF+EN-MoM3, 19; TF1-TuM10, 62
 Ruda, H.: EM-TuA11, 73
 Rudawski, N.G.: EM+SS-WeA7, 154
 Ruden, A.: AS-TuP7, 93; AS-TuP8, 93
 Rudigier, H.: SE-TuM1, 56
 Ruiz, A.: BI-TuM2, 44; BI-TuM4, 44
 Ruoff, R.S.: GR-TuP6, 100
 Rush, M.N.: BI-ThP13, 214
 Russek, S.E.: MI-WeA3, 161
 Russell, N.M.: EM-TuA10, 73
 Russell, S.M.: SS1-TuM1, 57
 Ruther, R.: SS-WeA3, 169
 Rutkowski, M.M.: EM+MI-MoA4, 24
 Rutter, G.M.: GR+AS+TF+MI-ThA3, 201; GR+AS+TF+MI-ThA4, 201; GR+TF-TuM10, 49; GR+TF-TuM9, 49
 Ruzic, D.N.: EN-TuM4, 47; PS+TF-ThM10, 191; PS2-MoA9, 32; PS2-TuA1, 84
 Ryadnov, M.: NS+BI-ThA2, 203
 Ryder, O.: SS-TuP23, 114
 Ryley, J.: TF-ThP19, 229
 Ryou, J.-H.: EM+SS-ThM1, 178
 Ryu, M.K.: TF+EM-WeM5, 140
 Ryu, S.-H.: EM-TuP5, 97; TF-ThP17, 229; TF-ThP18, 229
- S —
- Saaem, I.: BI+MN-FrM10, 233
 Sadowski, J.T.: IS+SS-TuA1, 78
 Saini, K.K.: BI+MN-FrM2, 232; MN-ThA9, 202
 Saini, R.: NS-TuM3, 52; SS2-MoA1, 36
 Saint John, D.B.: EL+AS+EM+MS+TF-ThA10, 198
 Saint-Lager, M.-C.: SS1-MoA1, 34
 Saito, N.: AS-TuP1, 92; GR-TuP2, 99; PS-FrM3, 239; PS-FrM6, 240; PS-ThP20, 225; PS-ThP3, 222; PS-ThP6, 223; PS-TuP20, 108; SS-TuP7, 111
 Saito, T.: NS-TuA8, 81
 Saito, Y.: VT-WeM3, 147
 Sakai, I.: PS1-TuA2, 82
 Sakai, M.: SS-TuP5, 111
 Sakulsermsuk, S.: SS-TuA8, 88
 Sakurai, T.: NS-ThM10, 189
 Salfi, J.: EM-TuA11, 73
 Salicio, O.: NS-TuP17, 103
 Salmeron, M.: SS-ThA1, 208; SS-ThA10, 209; SS-ThA3, 208
 Salomé, M.: BI-TuM12, 45
 Salter, T.L.: AS-WeA8, 150
 Salupo, C.: EL+AS+EM+MS+TF-ThA11, 198
 Sammann, E.: TF+EM-MoM5, 18
 Sammeta, S.: BI2-WeM10, 124
 Sampath, S.: MN-FrM3, 237
 Sampathkumaran, U.: EN+NS-ThM12, 183; TF-WeM4, 144
 Samuelsson, M.: SE+PS-MoA6, 33
 Samukawa, S.: PS1-WeA3, 164; PS1-WeA9, 165; PS2-TuA2, 84; PS2-WeA10, 167; PS2-WeA11, 167; PS2-WeA3, 166; PS2-WeA4, 166; PS2-WeA8, 167
 Sanada, N.: AS-WeA2, 149; AS-WeM9, 122
 Sandell, A.: SS-ThA9, 209
 Sandin, A.: GR-TuP5, 99
 Sandoval, S.: NS+BI-ThA10, 204; NS-TuP19, 103
 Sandström, P.: EL+AS+EM+MS+TF-ThA4, 197
 Sanghavi, R.: TF-ThP11, 228
 Sanguiovanni, D.G.: TF-ThM2, 195; TF-ThM5, 196
 Sankaran, R.M.: PS2-MoA3, 31
 Santana-Aranda, M.A.: NS-TuP21, 103; NS-TuP23, 103
 Santoyo-Salazar, J.: NS-TuP6, 101
 Santucci, S.: EN+NS-WeM1, 125
 Sanz, F.: EN+TF-TuA12, 76
 Sarakinos, K.: SE+PS-MoA6, 33; SE-TuM9, 56
 Sardela, M.: TF+EM-MoM5, 18
 Sarkar, N.: NS-TuA3, 52
 Sarot, R.: PS-TuP14, 107
 Sasaki, K.: TF-TuP2, 115
 Sasaki, M.: PS1-MoA10, 31
 Sasaki, T.: PS2-WeA11, 167
 Sato, H.: AC+MI-TuM11, 41
 Sato, M.: TF-ThP15, 228
 Sato, Y.: EN-TuM3, 47
 Satoh, T.: NS-TuP28, 104
 Sauer, V.: MN-ThA6, 202
 Savage, D.E.: SS2-MoA6, 36
 Savara, A.: SS1-MoA8, 35
 Saveliev, I.: EM-TuA11, 73
 Schaeckers, M.: TF+EM-WeM10, 141
 Schäfer, P.: EN+TF-TuA2, 74
 Schaff, W.J.: EL+AS+EM+MS+TF-FrM8, 235
 Schall, J.D.: GR+TF-TuM2, 48; TR+NS+SS-WeA9, 173
 Schamberger, F.: PS2+BI-ThA9, 207; TF-WeM6, 144
 Schauerermann, S.: SS1-MoA8, 35
 Schiesser, H.: SE+PS-MoM10, 13
 Schirmeisen, A.: TR+NS+SS-WeA8, 173
 Schlaf, R.: EN+NS-WeM12, 127; EN+NS-WeM2, 125; EN+TF-TuA10, 75; SS2-WeM12, 140
 Schmidt, D.: EL+AS+EM+MS+TF-FrM10, 236; EL+AS+EM+MS+TF-ThP5, 216; TF+SE-WeM9, 143
 Schmidt, H.: EN+SS-FrM3, 236; EN+SS-FrM4, 236
 Schneider, J.M.: SE-TuA10, 87; SE-TuA11, 87; SE-TuM9, 56
 Schnoeller, J.: SE-TuM12, 57
 Schnute, W.C.: AS-WeA12, 151
 Schöche, S.: EL+AS+EM+MS+TF-FrM10, 236; TF+SE-WeM9, 143
 Schoeller, A.E.: SE+TF-WeA9, 168
 Schott, M.N.: VT+MS-MoA6, 39; VT+MS-MoA7, 39; VT-TuP7, 119
 Schreiber, R.: TR-ThP5, 230
 Schreiner, P.R.: NS-TuA4, 81
 Schrickler, S.: SS-TuP21, 114
 Schroeter, B.: EN+NS-WeM11, 127
 Schrott, A.G.: PS1-TuA11, 84
 Schubert, E.B.: EL+AS+EM+MS+TF-FrM10, 236; EL+AS+EM+MS+TF-ThP5, 216; TF+SE-WeM9, 143
 Schubert, M.: EL+AS+EM+MS+TF-FrM10, 236; EL+AS+EM+MS+TF-FrM8, 235; EL+AS+EM+MS+TF-ThA1, 197; EL+AS+EM+MS+TF-ThA7, 198; EL+AS+EM+MS+TF-ThP5, 216; TF+SE-WeM9, 143
 Schuckman, A.E.: EM-TuM6, 46
 Schulte, K.: IS+SS-TuM5, 50
 Schulze, R.K.: AC+SS-MoM10, 3; AC-TuA2, 67
 Schüpbach, B.: SS2-TuM11, 60
 Schwarz, U.D.: NS+AS+MN-WeM9, 132; TR+NS+SS-WeA8, 173
 Schwendemann, T.C.: NS+AS+MN-WeM9, 132
 Schwoeble, A.J.: AS2-ThM12, 176
 Scott, M.: EN+SS+TF-ThA6, 199; TF-ThP6, 227
 Scullin, P.: EW-WeM8, 129
 Seah, M.P.: AS-WeA7, 150; AS-WeA8, 150
 Seal, S.: MN-ThA8, 202; NS-MoA10, 29; SS2-WeM6, 139; TF-WeA12, 172

- Seebauer, E.G.: EM-TuA9, **72**; SS2+EM-MoM11, 17; TF-WeM3, 144
- Seeberger, P.H.: BI-ThP5, 212
- Seghete, D.: TF-ThP5, **227**; TF-TuA9, 90
- Sehgal, A.: EM-TuA10, 73
- Sehun Kim, S.: NS-TuP3, 100
- Seibert, A.: AC+TF-MoA3, 23
- Seidel, F.: EL+AS+EM+MS+TF-ThP6, **217**
- Seidel, J.: NS-MoM9, 10
- Seidman, D.N.: LB-WeA1, 158
- Seifert, G.: TR-ThP5, 230
- Seitz, O.: BI+MN-FrM6, **233**
- Seki, T.: AS-WeA10, 150
- Sekine, M.: PS1-TuA2, 82; PS1-TuA8, 83; PS1-WeA8, 165; PS-MoM11, 12
- Selegård, L.: BI-TuM11, 45; NS+BI-ThA3, 203
- Sell, D.A.: AS-TuP27, 96
- Sellers, M.C.K.: TF-WeM3, **144**
- Semonin, O.E.: EL+AS+EM+MS+TF-ThA8, 198; EN-MoA3, 25
- Semple, S.: BI1-TuA3, 70
- Senanayake, S.D.: IS+SS-TuA1, 78; SS1-MoM10, 15
- Senecal, K.: TF-MoA8, 38
- Seo, B.R.: BI1+NS-ThM6, 177
- Seo, S.: GR+TF-TuM11, 50
- Sequeda, F.: AS-TuP7, 93; AS-TuP8, **93**
- Serrano, J.R.: MN-ThA2, 202
- Sestak, M.N.: EL+AS+EM+MS+TF-ThA11, 198
- Severn, G.: PS2-TuM12, 56
- Seyller, T.: EN+NS-WeM11, 127; GR+SS+TF+EM-MoM3, **5**
- Sfeir, M.Y.: NS-TuA1, 80
- Shah, K.: TF+EM-WeM10, 141
- Shah, U.: PS1-TuM10, **54**
- Shaikh, A.U.: TF+SE-WeM4, 142
- Shakouri, A.: AC-TuA3, 67
- Shamiryan, D.: PS1-TuA3, 83; PS1-WeA4, 164
- Shannon, S.S.: PS2-TuM11, 55
- Shavorskiy, A.: IS+SS-TuM5, **50**
- Shaw, G.A.: TR+NS+SS-WeA1, 172
- Shaw, M.: PS1-TuM10, 54
- Shaw, M.J.: IS+SS-TuA9, 79
- Shaw, P.: VT+MS-MoA10, 39
- Shearer, J.C.: PS1-WeA10, 165; TF-WeM11, **145**
- Sheehan, J.P.: PS-ThP21, **226**
- Sheehan, P.E.: GR+NS-MoA9, **27**; NS-TuM6, 52
- Sheetz, M.P.: NS+BI-ThA1, 202
- Shemelya, C.: NS+EM+EN-WeA2, **162**
- Shen, J.: EM+SS-WeA11, 154; EM-TuP7, **97**
- Shen, L.: BI-WeA4, **151**
- Shen, M.: SS1-TuM1, 57
- Shen, S.: TF+EM-WeM12, **142**
- Sheng, J.J.: EN+AS-ThM4, **180**; EN+TF-TuA8, 75
- Shenoy, V.B.: GR+NS-MoA6, **27**
- Sherer, M.: VT+MS-TuM3, **64**
- Sheridan, C.M.: PS2-MoA11, 33
- Shet, S.: EN-ThP9, **218**
- Shi, M.: MI+EM-TuA4, 80
- Shi, X.Q.: SS2-TuM3, 59
- Shi, Y.: SS-ThA10, 209
- Shi, Z.: EM-TuM9, 46
- Shiao, M.H.: NS-TuP25, 104; TF-ThP1, **226**
- Shields, V.: EL+AS+EM+MS+TF-FrM8, 235
- Shiffler, D.A.: NS-TuA3, 81
- Shih, C.K.: IS+AS+NS+MI-WeM1, 130
- Shih, H.C.: TF-TuP16, 117
- Shih, M.: MI+EM-TuA3, 80
- Shih, M.H.: TF-TuP16, 117
- Shih, Y.H.: IS+BI+AS-WeA11, 158
- Shima, M.: AS-TuA2, **68**; AS-TuM10, 43
- Shimamura, K.: EM-TuA7, 72
- Shimayama, T.: PS2-WeA11, 167
- Shimizu, H.: EN+SS+TF-ThA8, 200
- Shimizu, R.: PS-MoM3, 10
- Shin, H.: PS-ThP4, 222; PS-WeM11, **136**
- Shin, H.-B.: EL+AS+EM+MS+TF-ThA10, 198
- Shin, J.: PS1-TuM9, 54
- Shin, J.H.: TF-TuP9, 116; VT-TuP12, 120; VT-TuP5, 119
- Shin, K.S.: PS-WeM4, 135
- Shin, M.J.: EN-ThP3, **217**
- Shin, S.H.: EL+AS+EM+MS+TF-ThP1, 216
- Shindo, H.: PS2-TuM9, 55; PS-TuP22, **108**
- Shirafuji, T.: PS-FrM6, **240**; PS-TuP20, 108
- Shiratani, M.: EN+PS-MoM1, 3; PS2+BI-ThA4, 207
- Shivaraman, S.: EL+AS+EM+MS+TF-FrM8, 235
- Shmilovich, T.: MN-ThM9, 187
- Shoeb, J.: PS1-TuA1, **82**; PS2+BI-ThA6, 207
- Shoheit, J.L.: EM-TuA10, 73; EM-TuP10, **98**; TF+EM-WeM9, 141
- Shomo, R.: VT-TuP2, 118
- Short, R.D.: SE+PS-MoM8, 13
- Short, T.: MN-ThP8, 221
- Shreve, A.P.: BI2+NS-ThM9, **177**
- Shukla, N.: NS-ThM1, **188**
- Shukur, H.A.: TF-ThP20, **229**
- Shul, R.J.: PS+MN-WeM3, **133**; PS+MN-WeM4, 134; VT-TuP9, 119
- Shutthanandan, S.V.: AS-WeM2, 122; TF-ThA6, **210**
- Shutthanandan, V.: AS-TuA3, 68; AS-TuP28, 96; SS2-WeM6, 139; TF-ThP11, 228; TF-WeA12, 172
- Sibener, S.J.: SS2+EM-MoM4, 16; TF-WeA7, 171
- Sie, C.Y.: PS-ThP19, **225**
- Sikorski, E.M.: PS1-MoA8, 30; PS1-MoA9, 31
- Silver, R.M.: NS-TuM3, 52
- Simic, Z.: PS-ThP1, 222
- Simov, K.R.: MI-WeA4, **161**
- Singaravelu, S.: SS2-WeM10, **139**
- Singer, I.L.: TR+MN+NS+SS-WeM1, **145**
- Singh, A.: SS2-TuM10, 60
- Singh, B.: AS-TuP23, 95; EN+NS-WeA8, 155
- Singh, D.: TF+SE-WeM11, **143**
- Singh, H.: PS1-TuM3, 53
- Singh, J.: TF+SE-WeM11, 143
- Singh, R.: SS-FrM1, 240
- Singh, S.V.: TR+MN+NS+SS-WeM6, **146**
- Sinha, H.: EM-TuA10, 73; EM-TuP10, 98
- Sinnott, S.B.: TR+MN+NS+SS-WeM12, **146**
- Sirenko, A.: EL+AS+EM+MS+TF-FrM4, 234
- Sitnitsky, I.L.: EM-TuM2, 46
- Sivakov, V.A.: EN+NS-WeM11, 127; NS-ThM2, **188**; TF+EN-MoM5, 20
- Sivasubramani, P.: TF1-TuM11, **62**
- Skidmore, S.: TF+EM-MoM11, 19
- Skoglund, C.: BI-TuM11, **45**
- Skuza, J.R.: MI+TF-ThM3, 185; MI+TF-ThM4, **185**
- Sloan, P.A.: SS-TuA8, 88
- Sloan, T.: VT-TuP13, 120
- Slocik, J.: NS+BI-ThA4, 203
- Smentkowski, V.: AS-TuP13, **93**; AS-TuP23, 95
- Smets, A.H.M.: EN+PS-MoM5, 4
- Smirnov, A.: PS-TuP7, 105
- Smith, A.R.: EM+SS-ThM12, **179**; MI+EM-TuA3, 80; MI+EM-TuA4, 80
- Smith, M.L.: BI1+NS-ThM3, 177
- Smith, N.: AS-TuA8, 69; AS-WeM5, **122**
- Smith, S.: SS1-WeM9, 138
- Snow, C.S.: AC+SS-MoM11, 3
- Snow, E.: GR+NS-MoA7, 27
- Snyder, D.: GR+EM+MS+TF+MI-WeM1, 129
- Snyders, R.: EN+SS+TF-ThA1, **199**
- Sobol, P.: AS1-ThM6, 175
- Sobolewski, M.A.: PS2-TuM5, **55**
- Söderlind, F.: NS+BI-ThA3, 203
- Soderlind, P.: AC+MI-TuM2, **41**
- Sohn, H.-C.: TF2-TuM3, 63; TF-TuP8, 116
- Sohn, Y.S.: PS-TuP1, 104
- Sokol, P.: VT-TuP13, 120
- Solinsky, M.: EL+AS+EM+MS+TF-ThA7, 198
- Solowan, M.H.: GR+AS+TF+MI-ThA1, 201
- Soma, D.: SE+TF-WeA8, 168
- Son, L.S.: AS-TuP4, 92
- Song, H.: NS-TuP5, 101
- Song, J.D.: EL+AS+EM+MS+TF-ThP1, 216
- Song, L.Y.: EL+AS+EM+MS+TF-ThA3, 197
- Song, S.-H.: PS1-ThA4, **205**; PS2+BI-ThA6, 207
- Song, T.B.: EN+NS-WeA10, 155; EN+TF-WeM6, 128
- Song, Y.-H.: EN-ThP1, 217
- Song, Y.J.: GR+SS+TF+EM-MoM9, **6**
- Sorensen, P.H.: VT+MN-MoM10, 22
- Soudi, A.: NS-MoM10, 10; NS-ThM11, **189**
- Soukiasian, P.: GR+SS+TF+EM-MoM10, 6
- Sowa, M.J.: PS+TF-ThM4, **190**
- Spagnola, J.C.: TF-MoA1, 37; TF-MoA8, 38
- Spektor, R.: SS-TuP13, 112
- Spencer, M.G.: EL+AS+EM+MS+TF-FrM8, 235
- Spencer, S.J.: AS-WeA7, 150
- Spila, T.: TF+EM-MoM5, 18
- Spillmann, C.M.: MB+BI+AS-MoA8, 28
- Spormann, A.: SS-ThA1, 208
- Spowart, J.E.: EN+EM-TuA4, 73
- Springell, R.S.: AC+MI-TuM9, **41**
- Sprunger, P.T.: SS1-MoA9, 35; SS-FrM1, 240
- Srikanth, H.: TF+EM-MoM11, 19
- Sriraman, S.: PS1-TuM3, **53**
- Srivastava, Y.: AS-TuM11, 43
- Stacchiola, D.J.: SS1-MoM10, **15**
- Stafford, N.: PS1-TuA4, 83; PS-MoM9, 11
- Stair, P.C.: TF+EN-MoM1, **19**
- Standard, E.: EL+AS+EM+MS+TF-FrM4, 234
- Starodub, E.: GR+AS+TF-ThM5, 184; GR+AS+TF-ThM6, 184; GR+NS-MoA10, 27
- Starostin, S.A.: PS2-MoA2, **31**; SE+PS-MoM4, 12
- Stavis, C.J.: BI+MN-FrM8, **233**
- Stayton, P.S.: AS-TuM6, 43; BI2+AS-TuA8, 70
- Stecher, J.T.: NS+EM+EN-WeA7, 163
- Steele, D.: SE+PS-MoM8, 13
- Steffens, K.L.: AS2-ThM9, 176; BI-ThP12, **214**
- Stein, B.E.: SE+PS-MoM9, 13
- Stein, O.: SS2+EM-MoM2, **15**
- Steiner, M.A.: TF+EM-MoM8, **18**
- Steirer, K.: EN+TF-WeM9, 128
- Steitz, R.: IS+BI+AS-WeA3, 157
- Stemmer, S.: EM+SS-WeA7, 154
- Stephens, J.A.: SS1-TuA10, 58; SS1-TuM6, **58**
- Sterrer, M.: SS1-WeM2, 137
- Stevens, J.: PS+MN-WeM4, **134**
- Stevie, F.A.: EN+AS-ThM10, **181**
- Stiegler, H.J.: BI+MN-FrM6, 233
- Stiles, P.L.: BI1+NS-ThM2, 176; NS-TuP2, 100
- Stillahn, J.M.: PS1-WeA10, 165
- Stiller, K.: SE-TuM4, 56
- Stojak, K.: TF+EM-MoM11, 19
- Stoltz, P.H.: PS-TuP16, 107
- Stoppa, D.: BI-ThP15, 215
- Stout, P.: PS1-TuM5, 54
- Stradins, P.: EN+PS-MoM9, 4
- Straight, D.B.: EM-TuP10, 98
- Strano, M.: NS-TuA9, **82**
- Streber, R.: SS1-TuM2, 57
- Streubel, P.: AS-TuP11, **93**
- Stringer, J.: IJ+BI+MN-MoM3, 6
- Strobl, M.: IS+BI+AS-WeA3, 157
- Strohmeier, B.R.: AS2-ThM12, **176**; EW-TuA6, **76**; IS+SS-TuA10, 79
- Stroschio, J.A.: GR+AS+TF+MI-ThA3, 201; GR+AS+TF+MI-ThA4, 201; GR+SS+TF+EM-MoM9, 6; GR+TF-TuM10, 49; GR+TF-TuM9, 49
- Sturgeon, J.L.: EW-TuA6, 76; IS+SS-TuA10, 79
- Stutzman, M.L.: VT-WeM4, **147**
- Su, C.Y.: NS-TuP25, **104**; PS+TF-ThM9, 191; TF-ThP1, 226
- Su, J.F.: TR+NS+SS-WeA12, **174**
- Su, Y.: AS-TuP21, 95
- Subrahmanyam, A.: NS-MoM2, **9**
- Subramanian, A.: IS+SS-TuA9, **79**
- Suendo, V.: EL+AS+EM+MS+TF-ThA9, 198
- Sugiyama, M.: PS2-WeA3, 166; PS2-WeA8, 167
- Sullivan, J.P.: IS+SS-TuA9, 79

- Sullivan, S.L.: NS-TuM1, **51**
Sumant, A.V.: MN-FrM3, 237; MN-FrM4, 238; VT+MN-MoM5, 21
Sun, D.Z.: SS2-TuM4, **59**; SS-TuA11, 88; SS-TuA2, 87
Sun, J.-H.: PS+MN-WeM9, 134
Sun, L.: EN-MoA8, 25; PS+TF-ThM12, **191**
Sun, Y.: IJ+BI+MN-MoM4, **6**; IJ+BI+MN-MoM5, 7
Sundaram, G.M.: PS+TF-ThM4, 190
Sundararajan, R.: PS2-TuA2, 84
Sung, J.H.: PS-ThP12, 224
Sung, S.H.: PS1-TuA10, 84
Sung, Y.H.: TF2-TuM11, 63
Supparesk, R.: EN+NS-WeA9, 155
Suresh, S.: MN-FrM4, 238
Surla, V.: PS2-MoA9, 32
Surman, D.J.: BI2+AS-TuA7, 70; EW-TuL4, **66**
Surnev, S.: SS1-WeM5, 137
Susac, D.: EM-TuA11, 73
Sutherland, D.S.: BI1+NS-ThM1, 176; BI2-WeM12, 125; SE-TuP2, 109
Sutherland, J.C.: MI+EM-TuA10, 80
Sutter, E.: GR+AS+TF-ThM9, 184
Sutter, P.: GR+AS+TF-ThM9, **184**; NS+AS+MN-WeM4, 132
Suu, K.: PS+MN-WeM1, 133; PS+MN-WeM2, 133
Suzer, S.: AS-TuM4, **42**; NS-TuP8, 101
Suzuki, H.: MN-ThP2, 220
Suzuki, M.: AS-WeA2, 149; AS-WeM9, 122; SE+TF-WeA7, **168**; SE-TuP3, 109
Suzuki, T.: VT-WeM3, 147
Svane, A.: AC+MI-TuM5, 41
Swanson, J.S.: AC-TuA4, 67
Swaraj, S.: AS-TuP12, 93
Swart, H.C.: TF+EN-MoM8, 20
Swart, J.W.: GR-TuP3, 99
Sweet, W.J.: TF-MoA1, 37
Swensen, J.S.: TF-WeA1, 171
Swerts, J.: TF+EM-WeM10, **141**
Sykes, E.C.H.: NS-TuM9, 52; SS1-TuM5, **58**; SS-TuA1, 87; SS-TuP2, 110; SS-WeA9, 170
Sykora, M.: NS-ThM4, **189**
Szakal, C.: AS2-ThM11, **176**; AS-TuA8, 69
Szanyi, J.: SS-ThM1, 193; SS-WeA11, **170**
Szelągowska-Kunstan, K.: SS2-TuM11, 60
Szili, E.: SE+PS-MoM8, 13
Szotek, Z.: AC+MI-TuM5, 41
Szulczewski, G.J.: MI-WeA9, **161**
Szymanski, P.: NS-ThM4, **189**
- **T** —
Tabuchi, R.: SE-TuP3, 109
Tadayyon, S.: BI-ThP18, 215
Tadisina, Z.R.: MI+TF-ThM9, 186
Taguchi, A.: PS2+BI-ThA1, 206
Tahi, D.: AS-TuP4, 92
Taing, J.: NS-ThM12, **189**
Tait, S.L.: SS-TuP20, 114
Taitt, C.R.: BI-ThP19, 215
Tajima, K.: PS2-WeA11, 167
Takahashi, A.: SS-TuP4, 111
Takahashi, H.: BI2+AS-TuA11, 71
Takahashi, R.: VT-WeM3, **147**
Takai, O.: GR-TuP2, 99; PS-FrM3, 239; PS-FrM6, 240; PS-ThP20, 225; PS-ThP3, 222; PS-ThP6, 223; PS-TuP20, 108; SS-TuP7, 111
Takai, Y.: AS-TuP4, 92
Takano, I.: TF-ThP15, 228; TF-ThP20, 229; TF-TuP14, 117
Takao, Y.: PS1-MoA3, 30
Takeda, K.: PS1-TuA2, 82; PS1-TuA8, 83; PS1-WeA8, 165; PS-MoM11, 12
Takeke Beyene, H.: NS+EM+EN-WeA8, 163
Takahara, A.: AS-WeM9, 122
Talaat, H.: EN-ThP10, **218**; EN-ThP11, 219; EN-ThP12, 219
Talkenberg, F.: EN+NS-WeM11, 127; NS+EM+EN-WeA9, 163; NS-ThM2, 188; TF+EN-MoM5, 20
Tampé, R.: BI-ThP2, 212
Tamura, H.: SS-TuP8, 111
Tan, C.P.: BI1+NS-ThM6, **177**
Tanaka, A.: AS-TuA2, 68
Tanaka, T.: EN+PS-MoM3, **3**; PS-ThP7, **223**
Tang, A.: EN+TF-TuA3, 74
Tang, J.: EM+MI-MoA8, 25
Tang, K.S.: TF-ThP1, 226; TF-TuP20, 118
Tang, X.: PS-ThP11, **224**
Tanto, B.: SE+TF-WeA10, **168**
Tao, B.: TF-ThA1, 209
Tappan, B.C.: EN+SS-FrM1, 236
Tarasevich, B.J.: TF-WeA1, 171
Taschuk, M.T.: TF+SE-WeM6, 143
Tatsumi, T.: PS1-MoA3, 30; PS-ThM9, 193
Taylor, H.K.: VT-TuP9, 119
Taylor, R.: BI-ThP18, 215
Tazawa, T.: AS-TuA2, 68; AS-TuM10, 43
Techane, S.: AS-TuM6, **43**
Tedesco, J.L.: EL+AS+EM+MS+TF-FrM8, 235; GR+MS-WeA1, 156; GR+MS-WeA9, 157; GR+SS+TF+EM-MoM1, 5; GR+SS+TF+EM-MoM8, 5; LB-WeA3, 159
Teichert, C.K.: SS2-TuM5, **59**
Teki, R.: AS-TuP23, 95; EN-MoA11, 26
Temmerman, W.M.: AC+MI-TuM5, 41
Ten Eyck, G.A.: SE+TF-WeA10, 168
Tenent, R.: NS-MoM3, 9
Tenney, S.A.: SS-TuP14, **113**
Tennyson, J.: PS1-ThA2, 205
Teplyakov, A.V.: SS2+EM-MoM3, **16**; SS-TuP15, 113
ter Veen, R.: AS-WeA3, 149
Terblans, J.J.: TF+EN-MoM8, 20
Terfort, A.: SS2-TuM11, 60
Terlinden, N.M.: TF+EN-MoM6, 20
Terrerros, D.: BI+MN-FrM1, 232
Terry, R.E.: PS-TuP13, **107**
Terry, H.: SS1-WeM10, 138; TF-WeA8, 172
Tesch, P.P.: AS-WeM5, 122
Tew, G.: MB+BI+AS-MoA1, **28**
Textor, M.H.: BI1+NS-ThM3, **177**; NS+BI-ThA11, 204; NS+BI-ThA9, 204
Thagard, S.M.: PS1-WeA10, 165
Thamban, P.L.S.: PS+TF-ThM11, 191; PS2-TuM6, 55
Thamban, S.: PS-TuP15, 107
Thapa, A.: BI-WeA3, **151**
Thayne, I.: EM+SS-WeA11, 154
Therien, M.J.: NS+EM+EN-WeA7, 163
Thevuthasan, S.: AS-TuA3, **68**; EN+AS-ThM3, 180; NS-MoA10, 29; SS2-WeM6, 139; TF-ThP11, 228; TF-WeA12, 172
Thevuthasan, T.: AS-WeM2, **122**
Thiel, P.A.: SS1-TuM1, 57; SS2-MoA11, 37
Thissen, A.: IS+SS-TuM11, **51**
Thomas, J.C.: SS2+EM-MoM5, **16**
Thomas, W.: BI-WeA9, 152
Thompson, J.: TF-ThP19, 229
Thompson, P.E.: GR+SS+TF+EM-MoM1, 5
Thompson, W.: BI-TuM1, 43
Thoms, B.D.: EM-TuP2, 96
Thornberg, S.: VT+MS-TuM5, 64
Thürmer, K.: GR+AS+TF-ThM6, 184; GR+SS+TF+EM-MoM2, 5; SS-ThA7, 208
Thuvander, M.: SE-TuM4, 56
Tian, J.: BI+MN-FrM10, 233
Tian, W.-C.: MN-FrM8, **239**
Tierney, H.L.: NS-TuM9, **52**; SS-TuP2, **110**
Tillocher, T.: PS+MN-WeM10, **135**; PS2-MoA8, 32; PS-ThM4, 192
Timp, B.: EN-ThP6, 218
Tinkey, H.: GR+SS+TF+EM-MoM6, 5
Tippets, C.: LB-WeA7, 160
Tiron, R.: PS1-MoA11, 31
Tisdale, W.: EN-ThP6, 218
Tiwald, T.E.: EL+AS+EM+MS+TF-ThA7, 198
Tkachenko, B.A.: NS-TuA4, 81
To, B.N.: PS1-MoA9, 31
Tobin, J.G.: AC+MI-TuM12, 42; AC+MI-TuM2, 41; AC+TF-MoA6, **23**; MI-ThP1, 220
Todorova, M.: SS1-WeM1, 137
Todorovic, M.: NS+AS+MN-WeM9, 132
Tökei, Z.: TF+EM-WeM10, 141
Tolbert, S.: TF1-TuM5, 61
Tomizawa, H.: PS-MoM5, 11
Tomoyasu, M.: EM-TuA10, 73
Tomba, G.S.: AC-TuA3, 67
Tomura, M.: PS1-WeA9, 165
Torczynski, J.R.: MN-ThA2, 202; SE-TuA3, 86
Toriz, G.: NS-TuP21, 103
Torraca, G.: BI-ThP17, **215**
Torrance, D.B.: GR+SS+TF+EM-MoM6, **5**; GR+SS+TF+EM-MoM9, 6
Tosa, M.: MN-ThP2, 220
Toth-Fejöl, T.: NS-TuM3, 52
Tourwé, E.: TF-WeA8, 172
Towns, E.N.: IS+BI+AS-WeA1, 157
Tran, B.P.: EN+TF-WeM5, 128
Tran, T.H.: MB+BI+AS-MoA4, **28**
Tratnyek, P.G.: NS-MoA9, 29
Trenary, M.: SS1-MoM9, 15; SS-FrM3, 241
Trevino, K.J.: PS1-WeA10, 165
Triani, G.: TF-ThP12, **228**
Triscone, J.-M.: NS-MoM5, 9
Trogler, W.C.: NS+BI-ThA10, 204; NS-TuP19, 103
Trompoukis, Ch.: PS1-TuA3, 83
Trott, W.M.: SE-TuA3, **86**
Trotter, D.C.: GR+EM+MS+TF+MI-WeM6, 130
Trouillet, V.: AS-TuP2, 92
Trugman, D.T.: TF-ThA1, 209
Trumbull, K.: GR+EM+MS+TF+MI-WeM1, 129
Trunk, J.: MI+EM-TuA10, 80
Tsai, D.P.: TF-TuP15, 117
Tsai, M.Y.: NS-TuP10, **102**; PS+TF-ThM9, 191
Tseng, C.C.: SE-TuP7, 110
Tseng, T.-K.: AC-TuA1, **67**; AC-TuA9, 67
Tseng, Y.-C.: NS-TuM10, 52
Tskipuri, L.: SS2-TuM6, **60**
Tsotsos, C.: TF+EM-MoM10, **18**
Tsuda, N.: GR-TuP2, **99**
Tsuei, K.-D.: SS2-TuM3, 59
Tsukada, M.: SS-TuP8, **111**
Tsukruk, V.: NS+BI-ThA4, 203
Tsutsui, C.: PS2+BI-ThA1, 206
Tsumumi, K.: AS-TuA2, 68; AS-TuM10, **43**
Tucker, R.T.: SE+TF-WeA9, **168**; TF-ThP4, 227
Turchanin, A.: BI-ThP2, 212; GR+TF-TuA4, **77**; GR+TF-TuM3, 48; SS2-TuM12, 60
Turkot, B.: PS1-TuM10, 54
Turley, R.S.: AC+TF-MoA1, 23
Turner, M.: PS-TuP17, **107**; PS-TuP18, 107; PS-TuP19, 108
Tutuc, E.: GR+EM+MS+TF+MI-WeM9, **130**
Tweedie, J.S.: EM-TuP2, 96
Twigg, M.E.: EM+SS-ThM4, 178; GR+SS+TF+EM-MoM8, 5
Tyagi, P.V.: VT-WeM10, 147; VT-WeM9, 147
Tyer, R.: AC+MI-TuM5, 41
Tyler, J.: AS1-ThM5, **175**
Tysoe, W.T.: TR+MN+NS+SS-WeM11, 146
- **U** —
Uchida, G.: EN+PS-MoM1, 3; PS2+BI-ThA4, 207
Ueda, O.: EN+SS+TF-ThA2, 199
Ueda, S.: EM-TuA7, 72; EM-TuP11, 98
Ueki, S.: PS2-WeA3, 166; PS2-WeA8, 167
Uesawa, F.: PS1-MoA3, 30
Uesugi, T.: PS1-WeA3, **164**
Uher, C.: EN+NS-WeA11, 156
Uhl, A.: SS-FrM3, 241
ul Haq, E.: SS2-WeM5, 139
Ulfig, R.: AS-TuA3, 68
Umrath, S.: PS2+BI-ThA9, 207

- Unger, W.E.S.: AS-TuP12, 93; AS-TuP6, 93; BI-ThP5, 212; PS2+BI-ThA8, **207**
- Unsworth, P.: PS2-MoA11, 33
- Upadhyaya, H.M.: EN+PS-MoM6, 4
- Urban, F.: LB-WeA9, **160**
- Urbanowicz, A.M.: PS1-TuA3, **83**
- Urquhart, S.G.: IS+SS-TuA3, **78**
- Urrabazo, D.: PS-TuP15, **107**
- Utgikar, V.: EM+MI-MoA9, 25
- Utlaut, M.: AS-WeM4, 122
- Utz, A.: SS-TuA10, **88**; SS-TuA9, 88
- Uvdal, K.: BI-TuM11, 45; NS+BI-ThA3, 203
- Uvdal, P.: SS-ThA9, 209
- **V** —
- Vaglio Pret, A.: PS1-WeA4, 164
- Vahedi, V.: PS1-MoA2, 30; PS1-MoA6, 30; PS1-TuM3, 53
- Vail, M.A.: NS-TuA11, 82
- Vajda, S.: NS-ThM3, **188**
- Vallée, C.: TF2-TuM4, **63**; TF2-TuM5, 63
- Vallier, L.: PS1-MoA1, 30; PS1-TuM4, 53
- Valtiner, M.: SS1-WeM1, **137**
- Valyukh, S.: EL+AS+EM+MS+TF-ThA4, 197
- Van Antwerp, K.: EW-WeL2, **148**; VT+MS-MoA6, 39; VT-TuP7, 119
- Van Besien, E.: PS1-TuA3, 83
- van Buuren, T.: NS-TuA4, 81
- van de Sanden, M.C.M.: EL+AS+EM+MS+TF-FrM7, 235; EN+PS-MoM5, 4; EN+PS-MoM9, 4; EN+TF-TuA1, 74; NS+EM+EN-WeA8, 163; PS2-MoA2, 31; SE+PS-MoM4, 12; TF+EN-MoM6, 20
- van der Loop, T.H.: EN+PS-MoM5, 4
- van der Veer, W.E.: NS+EM+EN-WeA10, 163
- Van der Ven, A.: SS2+EM-MoM5, 16
- van Dorp, W.: SS2-WeM3, 138
- van Duin, A.C.T.: GR+TF-TuA11, 78
- Van Elshocht, S.: TF+EM-WeM10, 141
- van Hest, M.F.A.M.: EN+TF-WeM9, 128
- Van Hove, M.A.: SS2-TuM3, 59
- Van Ingelgem, Y.: SS1-WeM10, 138
- van Rijn, R.: IS+SS-TuM1, 50
- Vance, A.: BI-ThP17, 215
- Vancso, G.J.: MB+BI-MoM3, 8
- Vandalon, V.: TF-TuA2, 89
- Vanden Eynde, X.: SE+PS-MoM1, 12
- Vandencastele, N.: BI1-WeM6, **124**; BI2-WeM11, 124; SE+PS-MoM2, 12
- Vandendaal, I.: SS1-WeM10, 138
- VanderElzen, B.: MN-FrM10, **239**
- Vandervelde, T.: EN+EM-TuA9, 74; EN+SS+TF-ThA11, 201; NS+EM+EN-WeA2, 162; VT-TuP11, 120
- Vandeweert, E.: TF-WeA4, 171
- Vanel, J.-C.: LB-WeA8, 160
- Vanfleet, R.: LB-WeA7, 160
- Vanstreels, K.: PS1-TuA3, 83
- Varga, T.: TF-ThP11, 228; TF-WeA12, 172
- Vasilev, K.: BI1-TuA3, 70
- Vaz, A.R.: GR-TuP3, **99**
- Vaz, C.A.F.: EM+MI-MoA7, 24
- Vazquez-Lepe, M.O.: AS-TuP3, 92
- Velez, C.: PS-ThP5, 223
- Vélez, J.M.: TF-TuP3, 115
- Vemuri, R.S.: EL+AS+EM+MS+TF-ThP3, 216; TF-TuP11, 116; TF-WeA10, **172**
- Venkatesh, G.: EN+NS-WeA1, 154
- Venkatesh, S.: MI+TF-ThM12, 186
- Ventrice Jr., C.A.: GR-TuP6, 100; SS-TuP24, 114
- Verbeke, T.: LB-WeA8, 160
- Verbride, S.S.: MN-ThM4, 187
- Verdaguier, A.: SS-ThA3, 208
- Verdonck, P.: PS1-TuA3, 83
- Verheijen, M.A.: EN+PS-MoM5, 4
- Verve, C.: PS+MN-WeM5, 134; PS1-MoA11, 31; PS-MoM1, 10
- Versluis, R.: VT+MS-MoA4, **39**
- Vertegel, A.A.: TF-TuP17, 117
- Vervaecke, F.: TF-WeA4, 171
- Vescovo, E.: MI+EM-TuA10, 80
- Veyan, J.-F.: EN+NS-ThM3, 182; SS2-MoA1, 36; SS2-MoA7, **36**
- Viale, L.: VT+MN-MoM8, 21; VT+MN-MoM9, 21
- Vick, D.: MN-ThA6, 202
- Viero, G.: BI-ThP11, 214
- Villora, E.G.: EM-TuA7, 72
- Visikovskiy, A.: SS-TuP6, 111
- Vissers, W.: EW-WeM7, **129**
- Vitiello, J.: TF2-TuM5, 63
- Vizkelethy, G.: AS-WeM1, 122
- Vizzini, S.: GR+SS+TF+EM-MoM10, 6
- Voelcker, N.: SE+PS-MoM8, 13
- Voevodin, A.A.: SE+PS-MoA3, 33; SE-TuA10, 87; SE-TuA11, 87; SE-TuP4, 109; SE-TuP5, 109
- Vogel, E.M.: BI+MN-FrM6, 233
- Vogel, V.: BI1+NS-ThM3, 177
- Vogt, B.D.: EL+AS+EM+MS+TF-ThA3, **197**
- Voigt, F.: NS-ThM2, 188
- Volksen, W.: PS1-TuA7, 83
- Vollero, M.F.: VT+MS-MoA9, **39**
- Von Ehr, J.R.: NS-TuM3, 52; SS2-MoA1, 36
- von Huth, P.: EN+TF-WeM3, 127
- **W** —
- Wada, A.: PS2-WeA10, **167**
- Waddill, D.G.: AC+MI-TuM12, 42
- Waddill, G.D.: AC+TF-MoA6, 23; MI-ThP1, **220**
- Waeckerlin, C.: MI+EM-TuA9, 80
- Wägberg, L.: EL+AS+EM+MS+TF-ThP2, 216
- Waggoner, P.: BI+MN-FrM9, **233**
- Wagner, F.T.: TF-TuA9, 90
- Wagner, M.: SS1-WeM5, 137
- Wahl, K.J.: MB+BI+AS-MoA10, 28; MB+BI+AS-MoA8, **28**
- Waite, A.R.: SE-TuP5, **109**
- Wakamatsu, Y.: AS-WeA10, 150
- Walde, H.: EN+PS-MoM11, 4
- Walker, A.V.: EM-TuM9, **46**
- Wallace, R.M.: EM+SS-WeA4, 153; GR+EM+MS+TF+MI-WeM11, 130; NS-TuM3, 52; SS2-MoA7, 36; TF1-TuM11, 62
- Wallace, W.: AS-TuP24, **95**
- Walle, L.E.: SS-ThA9, **209**
- Walls, J.M.: EN+PS-MoM6, 4
- Walsh, B.C.: IS+BI+AS-WeA1, 157
- Walter, A.L.: GR+AS+TF-ThM6, 184
- Walters, J.L.: SS-TuP24, 114
- Walton, S.G.: BI-ThP19, 215; GR+NS-MoA9, 27; GR+TF-TuA8, 77; PS2-TuM10, 55; PS-WeM1, 135; SE+PS-MoM9, 13
- Walukiewicz, W.: EN+TF-TuA11, 75
- Wang, A.: TF1-TuM9, 62
- Wang, C.: SS1-MoM11, 15
- Wang, C.M.: AS-TuA3, 68; AS-WeM2, 122; NS-MoA9, 29
- Wang, D.: GR+NS-MoA9, 27; PS1-WeA2, 164
- Wang, D.Y.: TF-TuP16, 117
- Wang, G.T.: EM+SS-ThM6, 179; NS+EM+EN-WeA1, **162**
- Wang, H.: NS-MoA10, 29
- Wang, H.-Y.: EM-TuP1, 96
- Wang, J.: GR-TuP7, 100; MN-ThP8, 221; TF+EM-MoM11, 19; TF+EN-MoM4, 19; VT-TuP10, 120
- Wang, J.-C.: PS2-MoA7, **32**
- Wang, J.S.: BI-ThP6, **213**
- Wang, K.: EM+SS-ThM12, 179; MI+EM-TuA3, 80; MI+EM-TuA4, **80**
- Wang, L.: MI+TF-ThM3, **185**; MI+TF-ThM4, 185; TF-WeA1, 171; TR+NS+SS-WeA12, 174
- Wang, L.L.: VT+MS-TuM1, **64**
- Wang, M.: PS2+BI-ThA6, 207
- Wang, P.: BI-WeA10, 152
- Wang, Q.: BI1-TuA2, 70
- Wang, R.: NS+BI-ThA1, 202; PS-ThP11, 224
- Wang, S.H.: PS-ThP14, **224**
- Wang, S.J.: EN+TF-TuA7, 75
- Wang, W.: EN+NS-WeM2, 125; TF-ThP5, 227
- Wang, X.: SS-WeA3, **169**; VT+MN-MoM5, **21**
- Wang, X.J.: EM+MI-MoA8, 25
- Wang, X.Y.: PS2-WeA4, **166**
- Wang, Y.: AS-TuP21, 95; BI-ThP14, 214; SS-ThA1, 208; SS-ThM1, 193
- Wang, Y.C.: GR+AS+TF+MI-ThA1, 201
- Wangperawong, A.: EN+TF-WeM5, 128
- Warren, M.V.: EN+NS-WeA11, **156**
- Washburn, C.M.: EN+NS-WeA2, 154; NS-TuA7, 81
- Watanabe, K.: SS1-MoA7, 35
- Watanabe, N.: PS2-WeA3, **166**
- Watson, C.F.: AS-TuP27, 96
- Watson, D.: IS+SS-TuM5, 50
- Watson, D.G.: AS-TuP14, 94
- Wayment, J.R.: BI-ThP12, 214
- Weaver, B.: AS-TuM11, 43
- Weaver, J.F.: SS1-MoM2, **14**
- Weaver, J.M.R.: SS2-WeM5, 139
- Webb, K.M.: EM-TuM6, 46
- Weber, D.H.: GR+TF-TuA4, 77
- Weber, J.W.: EL+AS+EM+MS+TF-FrM7, **235**
- Wedlich, D.: AS-TuP2, 92
- Weed, J.W.: VT-WeM1, **146**
- Weeks, J.: SS2-TuM6, 60
- Weeks, S.: EN-ThP7, 218
- Wehbe, N.: BI2+AS-TuA12, 71
- Wei, Z.: GR+NS-MoA9, 27
- Weidner, T.M.: BI1-WeM6, 124; BI2+AS-TuA8, 70; NS+BI-ThA8, **204**
- Weightman, P.: PS2-MoA11, 33
- Weiland, C.: TF+EM-WeM3, **140**
- Weilnboeck, F.: PS1-WeA2, **164**; PS1-WeA7, 165; PS-ThM10, 193
- Weimann, T.: GR+TF-TuA4, 77
- Weinberg, R.Y.: VT+MS-TuM1, 64
- Weiss, S.: EN+SS+TF-ThA6, 199
- Welland, M.E.: AS-TuA4, 68
- Weller, T.: TF+EM-MoM11, 19
- Wen, H.C.: BI+MN-FrM6, 233
- Wen, J.-G.: TF+EM-MoM5, 18
- Wen, Z.-Q.: BI-ThP17, 215
- Wendelken, J.F.: MI+TF-ThM1, 185
- Weng, X.: GR+MS-WeA9, 157
- Werner, U.: BI-ThP2, 212
- Wessel, S.: EN+AS-ThM2, 180
- Westerstrom, R.: IS+SS-TuM1, 50
- Whang, D.M.: EN+NS-ThM2, 182; NS-TuP11, 102
- Wheeler, D.: GR+MS-WeA9, 157
- Wheeler, D.R.: EN+NS-WeA2, 154; NS-TuA7, 81
- Wheeler, V.D.: GR+MS-WeA1, 156; GR+SS+TF+EM-MoM1, 5; LB-WeA2, 159; LB-WeA3, **159**
- White, J.D.: MB+BI-MoM5, 8
- White, M.: SS2-WeM9, 139
- White, M.G.: SS1-MoA10, 35; SS-TuP19, 113
- White, R.G.: AS-TuP2, 92; AS-WeM11, 123; EN+AS-ThM6, 181; EW-TuL2, 66; SS-TuP18, **113**
- Whitten, D.G.: BI-ThP14, 214
- Wi, J.H.: PS-TuP4, **105**
- Wi, S.-S.: EN+PS-MoM10, 4
- Wickert, S.: SS1-TuM2, 57
- Wiemer, C.: NS-TuP17, 103; TF2-TuM9, **63**
- Wiesendanger, R.: NS+AS+MN-WeM5, **132**
- Wiest, L.A.: NS-TuA11, 82
- Wilde, K.N.: BI-ThP14, **214**
- Wilkens, B.J.: AS-TuP27, 96
- Wilker, J.W.: MB+BI-MoM5, **8**
- Wilks, G.B.: EN+EM-TuA4, **73**
- Willemsen, P.R.: MB+BI+AS-MoA3, 28
- Willey, T.M.: NS-TuA4, **81**
- Williams, K.: EN-ThP6, **218**
- Williams, P.: BI1-TuA1, 70
- Williams, R.L.: PS2-MoA11, 33
- Williams, V.O.: EN+NS-ThM12, 183
- Williamson, T.L.: EN+TF-TuA11, **75**

Williford, R.E.: TF-WeA1, 171
 Wilson, D.: SS2-WeM9, **139**
 Wimplinger, W.M.: PS-WeM12, 136
 Wind, S.J.: NS+BI-ThA1, 202
 Winkler, A.H.: SS2-TuM5, 59
 Winter, A.: TF-ThP3, 227
 Winter, B.: IS+SS-TuM2, 50
 Winter, R.: EN+NS-ThM12, 183; TF-WeM4, 144
 Wirth, T.: BI-ThP5, 212
 Wise, F.W.: EN-MoA8, 25
 Wise, R.: PS1-TuA10, 84
 Witkin, D.B.: SS-TuP13, 112
 Witters, T.: TF+EM-WeM10, 141
 Wiwi, M.: PS+MN-WeM3, 133; PS+MN-WeM4, 134
 Wnuk, J.: SS2-WeM3, 138
 Wöckel, C.: SS1-TuM2, 57
 Wofford, J.M.: GR+AS+TF-ThM11, **184**
 Wojciechowski, J.: BI-ThP19, 215
 Wolak, M.A.: EN+NS-WeM12, 127; EN+TF-TuA10, **75**
 Wolden, C.A.: LB-WeA4, **159**; NS-MoM3, 9; PS+TF-ThM3, 190
 Wolf, S.: MI-WeA1, **161**
 Woll, A.R.: SS2-TuM9, 60
 Wöll, C.: SS-FrM5, **241**
 Womack, F.N.: SS-FrM1, **240**
 Wong, K.L.: SS-TuA2, 87
 Wong, K.T.: SS-WeA4, **170**
 Wong, L.: BI-ThP17, 215
 Wong, L.M.: EN+TF-TuA7, 75
 Wong, L.S.: SS2-WeM5, 139
 Wong, S.S.: NS-TuA1, 80
 Woo, J.-C.: PS-TuP2, 104; PS-TuP3, 105; PS-TuP4, 105
 Woo, S.: TF1-TuM4, 61
 Wood, D.: EN+NS-WeA10, 155
 Woods, T.: BI+MN-FrM5, 232
 Woodward, P.M.: EM+MI-MoA4, 24; EN+SS-FrM2, 236
 Wormeester, H.: EL+AS+EM+MS+TF-FrM5, **235**
 Wright, A.: AS-WeM11, **123**; EW-TuL2, 66; SS-TuP18, 113
 Wright, S.J.: MN-ThM5, 187; MN-ThM6, 187
 Wright, T.: VT-TuP10, 120
 Wu, B.: TF-TuP19, 117
 Wu, I.-T.: TF+EN-MoM4, **19**
 Wu, J.: TF-TuP4, 115
 Wu, K.: TF-TuP12, 116
 Wu, L.: PS+TF-ThM10, 191
 Wu, N.: AS-TuM5, 43
 Wu, T.: MN-ThP8, **221**
 Wu, T.C.: EM-TuP8, 97; MI-ThP4, **220**
 Wu, W.H.: TF-TuP13, 116
 Wu, Y.: BI1-TuA2, **70**; PS-WeM3, **135**; TF+EM-MoM3, **17**
 Wu, Z.: EN+EM-TuA1, 73; SS-ThM11, 195
 Wuest, M.: VT+MN-MoM4, **21**
 Wyczawska, S.: TF-WeA4, 171
 Wydeven, T.: PS-ThP9, 223
 Wyre, J.P.: AS-TuP20, 94
 Wyrick, J.: SS-TuA11, **88**

— X —

Xiao, J.: GR+TF-TuA3, 76
 Xiao, X.: EN+NS-WeA2, 154
 Xiao, X.D.: SS2-TuM3, 59
 Xiao, Z.: EM-TuP15, 98; NS-TuA12, **82**
 Xie, Y.-H.: GR+AS+TF-ThM12, 185
 Xing, H.: TF1-TuM11, 62
 Xing, Q.B.: AS-TuP27, 96; SS2-WeM11, **139**
 Xiong, J.: TF-ThA1, **209**
 Xiong, Z.: PS2-TuA12, **86**
 Xu: SS1-TuM3, 58
 Xu, F.: SS1-MoM5, 14
 Xu, G.: SS2-TuM3, 59
 Xu, L.: PS-ThP4, 222
 Xu, T.: BI+MN-FrM1, 232; IJ+BI+MN-MoM8, 7; IJ+BI+MN-MoM9, 7
 Xue, J.: EN+NS-WeM5, 125; EN+TF-TuA3, 74

— Y —

Yabutani, H.: NS-TuA8, 81
 Yagisawa, T.Y.: PS-TuP11, **106**
 Yakes, M.K.: GR+NS-MoA9, 27
 Yamada, H.: AS-WeA10, 150
 Yamada, T.: EL+AS+EM+MS+TF-FrM1, 234; IS+BI+AS-WeA10, **158**; NS-TuA8, 81
 Yamaguchi, T.: PS-MoM11, **12**
 Yamamoto, F.: VT-WeM9, 147
 Yamamoto, H.: PS1-TuA2, **82**
 Yamamoto, N.: EL+AS+EM+MS+TF-FrM1, 234; EN-TuM3, 47
 Yamamoto, S.: SS-ThA1, 208
 Yamamoto, T.: EL+AS+EM+MS+TF-FrM1, 234; EN-TuM3, 47; PS2+BI-ThA1, 206
 Yamasaki, S.: PS1-WeA9, 165; PS2-WeA10, 167
 Yamashita, Y.: EM-TuA7, 72
 Yan, Y.: AS-TuA11, 69; EN+EM-TuA1, 73
 Yanez, M.: BI-ThP4, **212**
 Yang, C.: NS-TuA8, 81
 Yang, C.C.: NS-TuP25, 104
 Yang, F.: IS+SS-TuA1, 78; NS+EM+EN-WeA10, 163
 Yang, F.Y.: EM+MI-MoA4, 24
 Yang, H.: GR+TF-TuM11, 50
 Yang, J.: BI1-TuA1, 70; EN+TF-TuA3, 74; NS+BI-ThA10, 204; NS-TuP19, 103
 Yang, J.C.: IS+SS-TuA10, 79; SS-WeA10, 170
 Yang, J.S.: PS-TuP1, **104**
 Yang, Q.: PS1-MoA9, 31
 Yang, S.: NS-MoA8, 29
 Yang, W.: TF-ThP10, 228; TF-ThP13, 228; TF-WeA11, **172**
 Yang, X.: SS1-TuM9, 58
 Yang, Y.: PS2+BI-ThA6, 207
 Yang, Y.J.: PS2-MoA10, **33**
 Yang, Y.S.: NS-TuP12, 102
 Yanguas-Gil, A.: EN+NS-ThM12, **183**; TF-TuA4, 89
 Yano, H.: PS2-WeA11, 167
 Yanovich, S.I.: PS-TuP7, **105**
 Yarin, A.L.: IJ+BI+MN-MoM1, **6**
 Yarmoff, J.A.: SS2-WeM4, 138
 Yasuda, A.: PS1-WeA3, 164
 Yasuda, Y.: EN+SS+TF-ThA8, 200
 Yasuhara, S.: PS2-WeA11, 167
 Yatsuda, K.: PS-WeM2, 135
 Yatzor, B.P.: AS-TuA7, **69**
 Zayzev, O.V.: GR+AS+TF+MI-ThA6, **201**
 Ye, D.-X.: SE+TF-WeA8, **168**
 Ye, P.: EM+SS-WeA1, **153**
 Yeh, Y.C.: EM-TuP8, 97; MI-ThP4, 220
 Yelton, W.G.: NS-TuP7, 101
 Yen, C.C.: TF-TuP16, **117**
 Yeom, G.Y.: EN+PS-MoM8, 4; NS-TuP9, 101; PS1-TuA9, 84; PS1-TuM6, 54; PS2-WeA1, **166**; PS-ThM2, 191; PS-ThP16, 225; PS-ThP17, 225; PS-ThP18, 225; PS-TuP10, 106; PS-TuP9, 106
 Yeon, J.K.: NS-TuP9, 101; PS-TuP10, 106; PS-TuP9, **106**
 Yi, C.-W.: SS-WeA11, 170
 Yildirim, H.: SS2-MoA4, **36**
 Yilmaz, E.: NS-TuP8, **101**
 Yim, H.D.: PS-ThP12, 224
 Yin, J.: SS1-MoM9, **15**
 Yin, L.: EN+NS-ThM2, 182
 Yin, Y.: PS-MoM4, 11; PS-MoM5, **11**
 Yip, C.-S.: PS2-TuM12, 56
 Yokoyama, Y.: NS-ThM10, 189
 Yoo, S.J.: PS2-WeA7, 167
 Yoon, B.: TF-MoA10, 38; TF-MoA2, 37
 Yoon, J.H.: PS-WeM4, **135**
 Yoon, J.J.: EL+AS+EM+MS+TF-ThP1, **216**
 Yoon, O.J.: GR+EM+MS+TF+MI-WeM2, 129
 Yordanov, Y.T.: AS-TuP22, 95
 Yoshida, H.: VT-TuP3, **118**
 Yoshida, Y.: PS1-WeA9, 165
 Yoshii, M.: PS+MN-WeM1, 133

Yoshikawa, H.: EM-TuA7, 72
 Yoshimaru, M.: PS2-WeA11, 167
 Yoshimura, M.: SS-TuP6, **111**
 You, H.J.: PS2-WeA9, **167**
 You, S.D.: PS-ThP10, 223
 Youn, Y.-S.: SS-TuP11, **112**
 Young, A.: EN+AS-ThM2, 180
 Ys, H.: BI1-TuA3, 70
 Yu, C.: EM-TuP6, 97
 Yu, C.C.: PS+TF-ThM6, 191; PS+TF-ThM9, **191**
 Yu, C.H.: EN+NS-ThM2, 182
 Yu, C.S.: MN-ThP5, **221**
 Yu, J.: AC+MI-TuM11, 41
 Yu, K.M.: EN+TF-TuA11, 75
 Yu, L.H.: EM-TuM6, 46
 Yu, P.: NS-MoM9, 10
 Yu, S.W.: AC+MI-TuM12, **42**; AC+MI-TuM2, 41; AC+TF-MoA6, 23; MI-ThP1, 220
 Yu, Z.Q.: EN+AS-ThM3, 180
 Yuan, H.: EN+SS+TF-ThA9, 200; TF-TuP10, **116**; TF-WeA7, **171**
 Yuen, C.: SS2-MoA11, **37**
 Yun, D.K.: EM-TuP12, 98
 Yun, J.: TF-TuP21, **118**

— Z —

Zaera, F.: SS1-MoM3, **14**; SS-TuP1, 110
 Zaghoul, U.: MN-FrM9, **239**
 Zahn, D.R.T.: EL+AS+EM+MS+TF-ThP6, 217; EN+TF-TuA2, 74
 Zajec, B.: EN-ThP5, 218
 Zaki, N.: NS+AS+MN-WeM4, **132**
 Zalalutdinov, M.: GR+NS-MoA7, 27; MN-ThM3, 187
 Zanini Gadioli, G.: NS-TuP27, 104; SE-TuP6, 110
 Zauscher, S.: BI-ThP8, 213; TR+NS+SS-WeA7, 173
 Zavadil, K.R.: AC+SS-MoM11, 3; NS-MoM4, **9**
 Zazueta, S.: PS-ThP5, 223
 Zekic, A.: SS-TuP10, 112
 Zeller, D.J.: TF-TuP12, **116**
 Zeng, H.: BI+MN-FrM8, 233
 Zettl, A.: GR+AS+TF+MI-ThA1, 201
 Zhai, J.: TF-ThA1, 209
 Zhan, Y.: IS+SS-TuA9, 79
 Zhang, F.: TF1-TuM5, **61**
 Zhang, L.: AS-TuP20, 94; NS+BI-ThA10, 204; TF-ThP19, **229**; TR+NS+SS-WeA7, 173
 Zhang, P.: MN-ThA8, 202
 Zhang, X.: GR+TF-TuM3, **48**
 Zhang, X.G.: MI+TF-ThM1, 185
 Zhang, X.Q.: SS2-TuM3, 59
 Zhang, Y.: AS-WeM2, 122; EM-TuP10, 98; EN+NS-WeA8, 155; PS1-MoA8, 30; PS1-MoA9, **31**; PS-TuP18, **107**; PS-TuP19, 108; SS2-MoA6, 36; SS2-WeM5, 139; TF2-TuM6, 63; TF-ThA1, 209
 Zhang, Z.: GR+AS+TF-ThM1, 183; SS1-MoA9, **35**; SS1-WeM9, 138; SS-FrM4, 241; SS-FrM7, 241; TR+NS+SS-WeA2, **173**
 Zhao, A.D.: SS2-TuM3, 59
 Zhao, J.P.: PS2-TuA2, **84**
 Zharnikov, M.: EM-TuM5, **46**; SS2-TuM11, 60
 Zheng, S.X.: EM-TuA7, 72; EM-TuP11, **98**
 Zheng, Y.: EN+TF-TuA3, 74
 Zherenkov, M.: MI+TF-ThM2, 185
 Zhernokletov, D.M.: EM+SS-WeA4, 153
 Zhitenev, N.B.: GR+TF-TuM10, 49; GR+TF-TuM9, 49
 Zhou, C.: PS-TuP16, 107
 Zhou, J.: SS1-MoA10, **35**; SS-FrM2, **241**
 Zhou, R.: EN+TF-TuA3, 74
 Zhou, T.: EL+AS+EM+MS+TF-FrM4, 234
 Zhou, W.-P.: SS-TuP19, 113
 Zhou, Y.: PS-MoM10, **11**; SS-FrM2, 241
 Zhu, W.: GR+AS+TF-ThM1, 183; PS-ThP4, **222**; PS-WeM11, 136
 Zhu, W.J.: GR+EM+MS+TF+MI-WeM5, **129**
 Zhu, X.-Y.: BI-WeA4, 151; EN-ThP6, 218

Zhu, Y.M.: SS2-TuM4, 59; SS-TuA11, 88; SS-TuA2, 87
Zhu, Z.H.: AS-TuP28, **96**; EN+AS-ThM3, 180;
SS-TuP23, 114; TF-WeA1, 171
Zhuo, M.: TF-ThA1, 209

Zin, K.: PS-MoM4, 11
Zollner, S.: EL+AS+EM+MS+TF-FrM4, 234
Zorić, I.L.: SS1-MoA6, **35**
Zorn, G.: TF-WeA3, **171**
Zou, G.: TF-ThA1, 209

Zuber, S.M.: AS-TuM5, 43
Zumer, M.: EN-ThP5, **218**
Zwolak, M.: EM-TuM10, **46**
Zychowicz, M.: BI-TuM2, 44